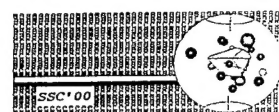


PROCEEDINGS OF SPIE



SPIE—The International Society for Optical Engineering



International Conference on Solid State Crystals 2000

Growth, Characterization, and Applications of Single Crystals

**Antoni Rogalski
Krzysztof Adamiec
Paweł Madejczyk**
Editors

**9–13 October 2000
Zakopane, Poland**

Organized by
Institute of Applied Physics, Military University of Technology (Poland)

In Co-operation with
Polish Society for Crystal Growth
SPIE—The International Society for Optical Engineering
in association with SPIE Poland Chapter

Sponsored by
State Committee for Scientific Research (Poland)
European Office of Aerospace Research and Development
Institute of Physics, Technical University of Łódź (Poland)
Institute of Physics, Wrocław University of Technology (Poland)



Volume 4412

DISTRIBUTION STATEMENT A
Approved for Public Release
Distribution Unlimited

20020110 059

REPORT DOCUMENTATION PAGE			Form Approved OMB No. 0704-0188	
Public reporting burden for this collection of information is estimated to average 1 hour per response, including the time for reviewing instructions, searching existing data sources, gathering and maintaining the data needed, and completing and reviewing the collection of information. Send comments regarding this burden estimate or any other aspect of this collection of information, including suggestions for reducing this burden to Washington Headquarters Services, Directorate for Information Operations and Reports, 1215 Jefferson Davis Highway, Suite 1204, Arlington, VA 22202-4302, and to the Office of Management and Budget, Paperwork Reduction Project (0704-0188), Washington, DC 20503.				
1. AGENCY USE ONLY (Leave blank)		2. REPORT DATE 24 October 2001		3. REPORT TYPE AND DATES COVERED Conference Proceedings
4. TITLE AND SUBTITLE International Conference on Solid State Crystals 2000 – Growth, Characterization, and Applications of Single Crystals			5. FUNDING NUMBERS F61775-00-WF	
6. AUTHOR(S) Conference Committee				
7. PERFORMING ORGANIZATION NAME(S) AND ADDRESS(ES) Military University of Technology (MUT) Kaliskiego 2 00-908 Poland			8. Performing Organization Report Number	
9. SPONSORING/MONITORING AGENCY NAME(S) AND ADDRESS(ES) EOARD PSC 802 Box 14 FPO 09499-0200			10. SPONSORING/MONITORING AGENCY REPORT NUMBER CSP 00-5035	
11. SUPPLEMENTARY NOTES Final report is published as Proceedings of SPIE, Vol. 4412, 414 pages, ISSN 0277-786X, ISBN 0-8194-4115-5				
12a. DISTRIBUTION/AVAILABILITY STATEMENT Approved for public release; distribution is unlimited.			12b. DISTRIBUTION CODE A	
ABSTRACT (Maximum 200 words) The Final Proceedings for the International Conference on Solid State Crystals - Growth, Characterization, and Applications of Single Crystals, 9-13 October 2000 This is an interdisciplinary conference. Topics include crystal growth, characterization and applications of solid materials, nanostructured materials and films, optoelectronic devices, and organic materials for electronics. Final report is published as Proceedings of SPIE, Vol. 4412				
14. SUBJECT TERMS EOARD,			15. NUMBER OF PAGES	
			16. PRICE CODE	
17. SECURITY CLASSIFICATION OF REPORT UNCLASSIFIED	18. SECURITY CLASSIFICATION OF THIS PAGE UNCLASSIFIED	19. SECURITY CLASSIFICATION OF ABSTRACT UNCLASSIFIED	20. LIMITATION OF ABSTRACT UL	



PROCEEDINGS OF SPIE

SPIE—The International Society for Optical Engineering

International Conference on Solid State Crystals 2000

Growth, Characterization, and Applications of Single Crystals

**Antoni Rogalski
Krzysztof Adamiec
Paweł Madejczyk**
Editors

**9–13 October 2000
Zakopane, Poland**

Organized by
Institute of Applied Physics, Military University of Technology (Poland)

In Co-operation with
Polish Society for Crystal Growth
SPIE—The International Society for Optical Engineering
in association with SPIE Poland Chapter

Sponsored by
State Committee for Scientific Research (Poland)
European Office of Aerospace Research and Development
Institute of Physics, Technical University of Łódź (Poland)
Institute of Physics, Wrocław University of Technology (Poland)

Published by
SPIE—The International Society for Optical Engineering



Volume 4412

SPIE is an international technical society dedicated to advancing engineering and scientific applications of optical, photonic, imaging, electronic, and optoelectronic technologies.

AQ F02-04-0480



The papers appearing in this book compose the proceedings of the technical conference cited on the cover and title page of this volume. They reflect the authors' opinions and are published as presented, in the interests of timely dissemination. Their inclusion in this publication does not necessarily constitute endorsement by the editors or by SPIE. Papers were selected by the conference program committee to be presented in oral or poster format, and were subject to review by volume editors or program committees.

This material is based upon work supported by the European Office of Aerospace Research and Development, Air Force Office of Scientific Research, Air Force Research Laboratory, under Contract No. F61775-00WF035. Any opinions, findings, and conclusions or recommendations expressed in this material are those of the author(s) and do not necessarily reflect the views of the European Office of Aerospace Research and Development, Air Force Office of Scientific Research, Air Force Research Laboratory.

Please use the following format to cite material from this book:

Author(s), "Title of paper," in *International Conference on Solid State Crystals 2000: Growth, Characterization, and Applications of Single Crystals*, Antoni Rogalski, Krzysztof Adamiec, Pawel Madejczyk, Editors, Proceedings of SPIE Vol. 4412, page numbers (2001).

ISSN 0277-786X
ISBN 0-8194-4115-5

Published by
SPIE—The International Society for Optical Engineering
P.O. Box 10, Bellingham, Washington 98227-0010 USA
Telephone 1 360/676-3290 (Pacific Time) • Fax 1 360/647-1445
<http://www.spie.org/>

Copyright© 2001, The Society of Photo-Optical Instrumentation Engineers.

Copying of material in this book for internal or personal use, or for the internal or personal use of specific clients, beyond the fair use provisions granted by the U.S. Copyright Law is authorized by SPIE subject to payment of copying fees. The Transactional Reporting Service base fee for this volume is \$15.00 per article (or portion thereof), which should be paid directly to the Copyright Clearance Center (CCC), 222 Rosewood Drive, Danvers, MA 01923 USA. Payment may also be made electronically through CCC Online at <http://www.directory.net/copyright/>. Other copying for republication, resale, advertising or promotion, or any form of systematic or multiple reproduction of any material in this book is prohibited except with permission in writing from the publisher. The CCC fee code is 0277-786X/01/\$15.00.

Printed in the United States of America.

Contents

xi	<i>Conference Committees</i>
xiii	<i>Preface</i>

BULK CRYSTAL GROWTH

1	Scope of ZnO growth (Invited Paper) [4412-01] R. Triboulet, CNRS (France)
9	Influence of mechanical stress on the growth of crystals (Invited Paper) [4412-02] J. N. Sherwood, Univ. of Strathclyde (UK)
18	Crystal growth of new functional materials for electro-optical applications (Invited Paper) [4412-03] T. Fukuda, K. Shimamura, A. Yoshikawa, E. G. Villora, Tohoku Univ. (Japan)
26	Possibilities and limitations of multioxide crystals growth (Invited Paper) [4412-04] M. Berkowski, J. Fink-Finowicki, R. Aleksiyo, Institute of Physics (Poland)
33	Single-domain HTC superconducting materials synthesis: BaZrO₃ substrates as a tool for optimized systems [4412-05] B. Robertz, F. Boschini, A. Rulmont, M. Ausloos, R. Cloots, Univ. of Liège (Belgium)
38	Very high quality crystals of wide-gap II-VI semiconductors: What for? (Invited Paper) [4412-06] A. Mycielski, A. Szadkowski, W. Kaliszek, B. Witkowska, Institute of Physics (Poland)
46	Annealing of GaSb single crystals in ionized hydrogen atmosphere [4412-07] B. Štěpánek, V. Šestáková, J. Šesták, Institute of Physics (Czech Republic)
50	Growth and structure of strontium-doped LaGaO₃ [4412-08] R. Aleksiyo, M. Berkowski, J. Fink-Finowicki, Institute of Physics (Poland); P. Byszewski, Institute of Physics (Poland) and Institute of Vacuum Technology (Poland); R. Didusko, E. Kowalska, Institute of Vacuum Technology (Poland)
55	Al-Cu-Co single quasi-crystals obtained by the method of inclined front crystallization [4412-09] W. Bogdanowicz, Z. Bojarski, Univ. of Silesia (Poland)
59	Correlation of Cu and V_{Zn} concentration within the diffusion region of ZnSe monocrystals [4412-10] T. Łukaszewicz, Technical Univ. of Białystok (Poland)
63	Chromium recharging processes in the Y₃Al₅O₁₂:Mg,Cr single crystal under the reducing and oxidizing annealing influence [4412-11] S. B. Ubizskii, S. S. Melnyk, National Univ. Lviv Polytechnic (Ukraine); B. V. Padlyak, Univ. of Gdańsk (Poland); A. O. Matkovskii, National Univ. Lviv Polytechnic (Ukraine); A. Jankowska-Frydel, Univ. of Gdańsk (Poland); Z. Frukacz, Institute of Electronic Materials Technology (Poland)

- 69 **Optical properties of doped potassium gadolinium tungstate single crystals** [4412-12]
E. Michalski, J. Żmija, Z. Mierczyk, A. Majchrowski, K. Kopczyński, S. Cichowski,
J. Wojtanowski, Military Univ. of Technology (Poland)
- 74 **Optical properties of some borate single crystals** [4412-13]
A. Majchrowski, Military Univ. of Technology (Poland); T. Łukasiewicz, Institute of Electronic
Materials Technology (Poland); Z. Mierczyk, Military Univ. of Technology (Poland);
M. Malinowski, Warsaw Univ. of Technology (Poland)

SILICON: TECHNOLOGY AND CHARACTERIZATION

- 81 **Peculiarities of the thermal donor formation in Czochralski-grown silicon under high hydrostatic pressure** [4412-14]
V. V. Emtsev, Univ. of Amsterdam (Netherlands); V. V. Emtsev, G. A. Oganessian, A.F. Ioffe
Physico-Technical Institute (Russia); A. Misiuk, Institute of Electron Technology (Poland);
C. A. Londos, Univ. of Athens (Greece)
- 85 **Effect of silicon microstructure on stress-stimulated creation of thermal donors** [4412-15]
A. Misiuk, Institute of Electron Technology (Poland)
- 91 **Effect of high-pressure high-temperature treatment on neutron-irradiation-induced defects in Czochralski silicon** [4412-16]
C. A. Londos, L. G. Fytros, Univ. of Athens (Greece); A. Misiuk, Institute of Electron Technology
(Poland); J. Bąk-Misiuk, Institute of Physics (Poland); M. Pruszczyk, Institute of Electron
Technology (Poland); M. Potsidou, Univ. of Athens (Greece)
- 97 **Two-dimensional model of the intrinsic point defects behavior during Cz silicon crystal growth**
[4412-17]
A. I. Prostomolotov, N. A. Verezub, Institute for Problems in Mechanics (Russia)
- 104 **Study of material behavior in DAC: system Si-O (SiO_x) and compound $\text{Fe}_{78}\text{Mn}_{20}\text{Si}_2$** [4412-18]
B. M. Efros, N. V. Shishkova, Physics and Technology Institute (Ukraine); A. Misiuk, Institute
of Electron Technology (Poland)
- 110 **Investigation of system Si-O (SiO_x) behavior in DAC at submegabar pressure** [4412-19]
B. M. Efros, N. V. Shishkova, A. Prudnikov, Physics and Technology Institute (Ukraine);
A. Misiuk, Institute of Electron Technology (Poland); J. Bąk-Misiuk, Institute of Physics
(Poland); J. Härtwig, European Synchrotron Radiation Facility (France)
- 116 **Investigation of as-grown nitrogen-doped Czochralski silicon** [4412-20]
D. Yang, J. Lu, Y. Shen, D. Tian, X. Ma, L. Li, D. Que, Zhejiang Univ. (China)
- 120 **Effect of stress on defect transformation in hydrogen-implanted silicon and SOI structures**
[4412-21]
I. V. Antonova, V. P. Popov, Institute of Semiconductor Physics (Russia); J. Bąk-Misiuk,
J. Domagala, Institute of Physics (Poland); A. Misiuk, Institute of Electron Technology
(Poland); V. I. Obodnikov, A. K. Gutakovskii, Institute of Semiconductor Physics (Russia);
A. Romano-Rodriguez, Univ. of Barcelona (Spain)

CRYSTAL PHYSICS, ORDERING PROCESSES

- 126 **Molecular simulations of concentrated aqueous solutions: ionic equilibrium structures in solutions (Invited Paper)** [4412-22]
W. M. Bartczak, Technical Univ. of Łódź (Poland) and Univ. of Łódź (Poland); M. Zapalowski, K. Wolf, Technical Univ. of Łódź (Poland)
- 137 **Dynamics of diffusion-controlled recombination of ions in ionic solutions: limits of validity of the Debye-Smoluchowski equation** [4412-23]
K. Wolf, Technical Univ. of Łódź (Poland); W. M. Bartczak, Technical Univ. of Łódź (Poland) and Univ. of Łódź (Poland)
- 149 **Simple models for crystallization processes** [4412-24]
D. de Cogan, L. R. Martin, Univ. of East Anglia (UK)
- 156 **Transient surface supersaturation after crystal submersion: II** [4412-25]
M. Rak, Technical Univ. of Łódź (Poland)
- 161 **Theory of behavior of ionized hydrogen in GaSb crystal structure** [4412-26]
V. Šestáková, B. Štěpánek, J. Šesták, Institute of Physics (Czech Republic)
- 166 **Dynamics and thermodynamics of quantum crystals near the instability point in the self-consistent phonon theory** [4412-27]
C. Malinowska-Adamska, P. Słoma, J. Tomaszewski, Technical Univ. of Łódź (Poland)
- 172 **Calculations of third-order electronic susceptibility of alkali halides** [4412-28]
W. Kucharczyk, Technical Univ. of Łódź (Poland); F. de Landa Castillo-Alvarado, Instituto Politécnico Nacional (Mexico); P. Górski, R. Ledzion, Technical Univ. of Łódź (Poland)
- 177 **Gd³⁺-Yb³⁺ exchange interactions in LiYb_xY_{1-x}F₄ single crystals** [4412-29]
L. E. Misiak, Maria Curie-Skłodowska Univ. (Poland)
- 181 **Crystal lattice dynamics of various silicon-carbide polytypes** [4412-30]
S. Nowak, Technical Univ. at Radom (Poland)
- 187 **Theoretical model of carrier flow process on boundary of electrode-dye layer** [4412-31]
D. Wróbel, T. J. Hoffmann, Poznań Univ. of Technology (Poland)

STRUCTURAL, OPTICAL, AND ELECTRICAL CHARACTERIZATION OF CRYSTALLINE MATERIALS

- 191 **Semiconductor surface characterization by scanning probe microscopies (Invited Paper)** [4412-32]
M. Hietschold, A.-D. Müller, F. Müller, Chemnitz Univ. of Technology (Germany)
- 196 **Phase transitions in double tungstate in extremely low-dimensional and low-symmetry compounds with cooperative Jahn-Teller effect (Invited Paper)** [4412-33]
M. T. Borowiec, Institute of Physics (Poland)
- 203 **Investigation of thermal annealing by gamma irradiation at room temperature in LiNbO₃ crystals** [4412-34]
A. L. Bajor, Institute of Electronic Materials Technology (Poland); S. M. Kaczmarek, Military Univ. of Technology (Poland); I. Pracka, M. Świrkowicz, Institute of Electronic Materials Technology (Poland); T. Wrońska, Institute of Chemistry and Nuclear Technics (Poland)

- 211 **Monocrystals Ag_3SbS_3 : investigation of electrical characteristics** [4412-35]
G. Khlyap, State Pedagogical Univ. at Drohobych (Ukraine); V. Belosertseva, Kharkiv State Polytechnical Univ. (Ukraine); L. Panchenko, Sumy State Univ. (Ukraine); M. Andrukhiv, State Pedagogical Univ. at Drohobych (Ukraine)
- 216 **Charge traps and emission kinetics in LuAP:Ce** [4412-36]
J. Glodo, A. J. Wojtowicz, Nicholas Copernicus Univ. (Poland)
- 221 **Energy transfer processes in $(\text{Lu,Gd})\text{AlO}_3\text{:Ce}$** [4412-37]
A. J. Wojtowicz, Nicholas Copernicus Univ. (Poland); J. A. Mareš, Institute of Physics (Czech Republic)
- 226 **Thermal fixing of holographic gratings in nearly stoichiometric LiNbO_3 crystals** [4412-38]
G. Mandula, K. Lengyel, L. Kovács, Research Institute for Solid State Physics and Optics (Hungary); M. A. Ellabban, R. A. Rupp, M. Fally, Univ. of Vienna (Austria)
- 231 **High-temperature properties of the fcc metallic crystals in anharmonic approximation** [4412-39]
J. Tomaszewski, C. Malinowska-Adamska, P. Słoma, Technical Univ. of Łódź (Poland)
- 236 **Investigation of highly energetic transitions in some Pr^{3+} -doped fluoride and oxide crystals** [4412-40]
I. Sokółska, W. Trzebiatowski Institute of Low Temperature and Structure Research (Poland) and Univ. Hamburg (Germany); S. Kück, Univ. Hamburg (Germany); M. Bałuka, W. Trzebiatowski Institute of Low Temperature and Structure Research (Poland)
- 242 **Crystal field study of Gd^{3+} -doped $\text{La}_x\text{RE}_{1-x}\text{F}_3$ ($\text{RE} = \text{Ce,Pr,Nd}$) single crystals** [4412-41]
M. L. Paradowski, L. E. Misiak, W. Korczak, Z. Korczak, Maria Curie-Skłodowska Univ. (Poland)
- 246 **PIXE and magnetic investigations of $\text{La}_x\text{RE}_{1-x}\text{F}_3$ ($\text{RE} = \text{Ce,Nd}$) single crystals** [4412-42]
M. L. Paradowski, M. Kulik, W. Korczak, Z. Korczak, Maria Curie-Skłodowska Univ. (Poland)
- 250 **Nonlinear I-V characteristics and threshold switching in As-Te-In glasses** [4412-43]
J. T. Devaraju, Bangalore Univ. (India); B. H. Sharmila, Indian Institute of Science/Bangalore; K. V. Acharya, Bangalore Univ. (India); S. Asokan, E. S. R. Gopal, Indian Institute of Science/Bangalore
- 255 **Irradiation effect on the pinning potential of YBCO single crystal** [4412-44]
S. N. Barilo, V. I. Gatafskaya, G. V. Gatafskii, S. L. Kurockin, Institute of Solid State and Semiconductor Physics (Belarus)
- 259 **Lower critical fields in BKBO single crystals** [4412-45]
S. N. Barilo, V. I. Gatafskaya, S. V. Shiryayev, A. S. Shestac, Institute of Solid State and Semiconductor Physics (Belarus)
- 263 **Determining of the material parameters of $\text{Zn}_x\text{Cd}_y\text{Hg}_{1-x-y}\text{Te}$ by magnetophonon spectroscopy** [4412-46]
J. Cebulski, J. Polit, E. M. Sheregii, Pedagogical Univ. at Rzeszów (Poland)
- 268 **Magnetic ordering of Dy^{3+} ion in low-dimensional $\text{CsDy}(\text{WO}_4)_2$ double tungstate** [4412-47]
V. P. Dyakonov, Institute of Physics (Poland) and A.A. Galkin Donetsk Physico-Technical Institute (Ukraine); M. T. Borowiec, A. Jędrzejczak, Institute of Physics (Poland); E. Zubov, A.A. Galkin Donetsk Physico-Technical Institute (Ukraine); T. Zayarnyuk, H. Szymczak, Institute of Physics (Poland)

- 272 **Studies of manganites by magnetic resonance spectroscopy methods** [4412-48]
V. P. Dyakonov, Institute of Physics (Poland) and A.A. Galkin Donetsk Physico-Technical Institute (Ukraine); A. Prohorov, V. Shapovalov, V. Pashchenko, A.A. Galkin Donetsk Physico-Technical Institute (Ukraine); P. Aleshkevych, S. Piechota, H. Szymczak, Institute of Physics (Poland)
- 276 **Effect of pressure and magnetic field on the phase transitions in lanthanum-deficient manganites** [4412-49]
V. P. Dyakonov, Institute of Physics (Poland) and A.A. Galkin Donetsk Physico-Technical Institute (Ukraine); I. Fita, E. Zubov, V. Pashchenko, V. Mikhaylov, A.A. Galkin Donetsk Physico-Technical Institute (Ukraine); Yu. Bukhantsev, H. Szymczak, Institute of Physics (Poland)
- 280 **Optical properties of potassium erbium double-tungstate $\text{KEr}(\text{WO}_4)_2$** [4412-50]
T. Zayarnyuk, M. T. Borowiec, Institute of Physics (Poland); V. P. Dyakonov, Institute of Physics (Poland) and A.A. Galkin Donetsk Physico-Technical Institute (Ukraine); H. Szymczak, Institute of Physics (Poland); E. Zubov, Institute of Physics (Poland) and A.A. Galkin Donetsk Physico-Technical Institute (Ukraine); A. A. Pavlyuk, Institute of Inorganic Chemistry (Russia); M. Barański, Institute of Physics (Poland)
- 284 **Photoinduced optical effects in BiB_3O_6 glass** [4412-51]
I. V. Kityk, M. Makowska-Janusik, Pedagogical Univ. at Częstochowa (Poland); A. Majchrowski, Military Univ. of Technology (Poland)
- 289 **Influence of the growth conditions on the elastic properties of SrLaAlO_4 and SrLaGaO_4 crystals studied by Brillouin light scattering** [4412-52]
D. Kasprowicz, M. Drozdowski, Poznań Univ. of Technology (Poland); A. Wronkowska, Bydgoszcz Univ. of Technology and Agriculture (Poland); A. Pajęczkowska, Institute of Electronic Materials Technology (Poland)
- 295 **Temperature, absorption, and excitation study of the $\text{A}_{1-x}\text{B}_x\text{C}$ crystals by Raman scattering method** [4412-53]
M. Kozielski, M. Szybowicz, Poznań Univ. of Technology (Poland)
- 299 **Thermal ionization energy of Mg acceptors in GaN: effects of doping level and compensation** [4412-54]
B. Pődör, Research Institute for Technical Physics and Materials Science (Hungary)
- 304 **Elastic and elasto-optic properties of $\text{Zn}_{1-x}\text{Be}_x\text{Se}$ mixed crystals by Brillouin scattering method** [4412-55]
P. Ziobrowski, M. Szybowicz, M. Drozdowski, Poznań Univ. of Technology (Poland); F. Firszt, S. Łęgowski, J. Szatkowski, Nicholas Copernicus Univ. (Poland)
- 309 **Correlation of domain structure of TGS single crystals doped with serine and its dielectric properties: new constructed computer measuring system for quantity analysis of domain images** [4412-56]
W. Proszak, M. Trybus, Technical Univ. of Rzeszów (Poland)
- 314 **Excited-state absorption in the $\text{Cr}^{6+}\text{O}^{2-}$ center in $\text{Li}_2\text{B}_4\text{O}_7$ glass** [4412-57]
Cz. Koepke, K. Wiśniewski, Nicholas Copernicus Univ. (Poland); M. Grinberg, Univ. of Gdańsk (Poland)
- 318 **Modeling of the carrier mobility at the silicon oxynitride-silicon interface** [4412-58]
K. J. Pluciński, Military Univ. of Technology (Poland)

- 323 **Analysis of the transient response of MIS circuits using pseudo-wavelet approach** [4412-59]
K. J. Pluciński, Military Univ. of Technology (Poland)
- 331 **Sensitivity of surface acoustic wave devices** [4412-60]
J. Filipiak, K. Zubko, Military Univ. of Technology (Poland)

CHARACTERIZATION AND APPLICATION OF ELECTRO-OPTICAL MATERIALS

- 337 **Nonlinear optical properties in ZnSe crystals** [4412-61]
B. Derkowska, Univ. d'Angers (France) and Nicholas Copernicus Univ. (Poland); B. Sahraoui, X. Nguyen Phu, Univ. d'Angers (France); W. Bala, Nicholas Copernicus Univ. (Poland)
- 342 **Growth and characterization of single crystals of ternary chalcogenides for laser applications (Invited Paper)** [4412-62]
L. I. Isaenko, A. P. Yelissev, Institute of Monocrystals (Russia); J.-J. Zondy, Observatoire de Paris (France); G. M. Knippels, FOM-Institute for Plasma Physics (Netherlands); I. Thenot, Observatoire de Paris (France); S. Lobanov, Institute of Monocrystals (Russia)
- 351 **Radio- and VUV-excited luminescence of YAP:Ce, YAP:Pr, and YAG:Pr** [4412-63]
M. Wiśniewska, A. J. Wojtowicz, N. Copernicus Univ. (Poland); T. Łukasiewicz, Z. Frukacz, Z. Gałązka, Institute of Electronic Materials Technology (Poland); M. Malinowski, Warsaw Univ. of Technology (Poland)
- 357 **Crystal growth and optical properties of Co²⁺-doped SrLaGa₃O₇** [4412-64]
S. M. Kaczmarek, Military Univ. of Technology (Poland); M. Grinberg, Univ. of Gdańsk (Poland); M. Berkowski, P. Aleshkevych, J. Fink-Finowicki, H. Szymczak, Institute of Physics (Poland)
- 363 **Controlling of the charge states in laser crystals** [4412-65]
S. M. Kaczmarek, Military Univ. of Technology (Poland)
- 369 **Growth and dielectric properties of Ca₄GdO(BO₃)₃ single crystals** [4412-66]
A. Kłos, A. Pajęczkowska, Institute of Electronic Materials Technology (Poland); C. Pawlaczyk, E. Markiewicz, Institute of Molecular Physics (Poland)
- 375 **Czochralski growth and characterization of SrLaGa₃O₇:Ho³⁺ single crystals** [4412-67]
I. Pracka, Institute of Electronic Materials Technology (Poland); M. Malinowski, Institute of Microelectronics and Optoelectronics (Poland); M. Świrkowicz, J. Kisielewski, A. L. Bajor, A. Kłos, B. Kaczmarek, B. Surma, Institute of Electronic Materials Technology (Poland)
- 380 **Relaxation dynamics of excited states of Er³⁺ in YVO₄ single crystals** [4412-68]
S. Gołąb, G. Dominiak-Dzik, P. Solarz, Institute of Low Temperature and Structure Research (Poland); T. Łukasiewicz, M. Świrkowicz, Institute of Electronic Materials Technology (Poland); I. Sokólska, W. Ryba-Romanowski, Institute of Low Temperature and Structure Research (Poland)
- 385 **Stokes and anti-Stokes luminescence in LiTaO₃:Ho** [4412-69]
W. Ryba-Romanowski, S. Gołąb, I. Sokólska, G. Dominiak-Dzik, P. Solarz, Institute of Low Temperature and Structure Research (Poland); T. Łukasiewicz, M. Świrkowicz, Institute of Electronic Materials Technology (Poland)

- 389 **Optical properties of $\text{Li}_2\text{B}_4\text{O}_7$ glasses doped with rare-earth and transition-metal ions** [4412-70]
S. M. Kaczmarek, Military Univ. of Technology (Poland); Cz. Koepke, Nicholas Copernicus Univ. (Poland); M. Grinberg, Univ. of Gdańsk (Poland); A. Majchrowski, Military Univ. of Technology (Poland); K. Wiśniewski, Nicholas Copernicus Univ. (Poland); M. Czuba, Military Univ. of Technology (Poland)
- 396 **X-ray study of Nd:YAG on (111)-oriented Si obtained by pulsed laser deposition** [4412-71]
R. Rumianowski, Warsaw Univ. of Technology (Poland); R. S. Dygdała, F. Rozpłoch, A. J. Wojtowicz, M. Wiśniewska, S. Kulesza, Nicholas Copernicus Univ. (Poland)
- 400 **Effect of divergence of light wave and alignment of crystal on the response of electro-optic modulators** [4412-72]
M. Izdebski, W. Kucharczyk, Technical Univ. of Łódź (Poland)
- 406 **Investigations of YAG:Er³⁺, Yb³⁺ and YAG:Co²⁺ crystals for laser application** [4412-73]
Z. Mierczyk, K. Kopczyński, M. Kwaśny, Military Univ. of Technology (Poland); T. Łukasiewicz, Military Univ. of Technology (Poland) and Institute of Electronic Materials Technology (Poland); Z. Frukacz, Z. Gałązka, Institute of Electronic Materials Technology (Poland)
- 413 *Author Index*

Conference Committees

Scientific Committee

Antoni Rogalski –	<i>co - chair</i>
Józef Żmija –	<i>co - chair</i>
Jarosław Rutkowski –	<i>secretary</i>
Marek Berkowski –	<i>chair of bulk crystals growth session</i>
Wacław Bała –	<i>chair of epitaxial layer characterization session</i>
Mirosław Drozdowski –	<i>chair of bulk crystals characterization session</i>
Maciej Oszałdowski –	<i>chair of nanostructured materials session</i>

Committee Members

Jacek Baranowski	Witold Bartczak
Ryszard Ciach	Mirosław Drozdowski
Marian Herman	Jan Karniewicz
Andrzej Majchrowski	Jan Misiewicz
Cecylia Malinowska-Adamska	Andrzej Mycielski
Anna Pajączkowska	Keshra Sangwal
Eugen Sheregii	Henryk Szymczak
Marek Tłaczała	Zygmunt Wokulski
Jerzy Zieliński	

International Advisory Board

Jacek M. Baranowski (Poland)	Jan Misiewicz (Poland)
Donard de Cogan (U.K.)	Manijeh Razeghi (USA)
Mirosław Drozdowski (Poland)	Antoni Rogalski (Poland)
Pierre Gibart (France)	John N. Sherwood (U.K.)
Marian A. Herman (Poland)	Fiodor F. Sizov (Ukraine)
Francois Kajzar (France)	Serge Tatarenko (France)
Lester J. Kozlowski (USA)	Robert Triboulet (France)
Victor A. Kuznetsov (Russia)	Józef Żmija (Poland)
Cecylia Malinowska-Adamska (Poland)	

Organizing Committee

Jerzy Zieliński - chair

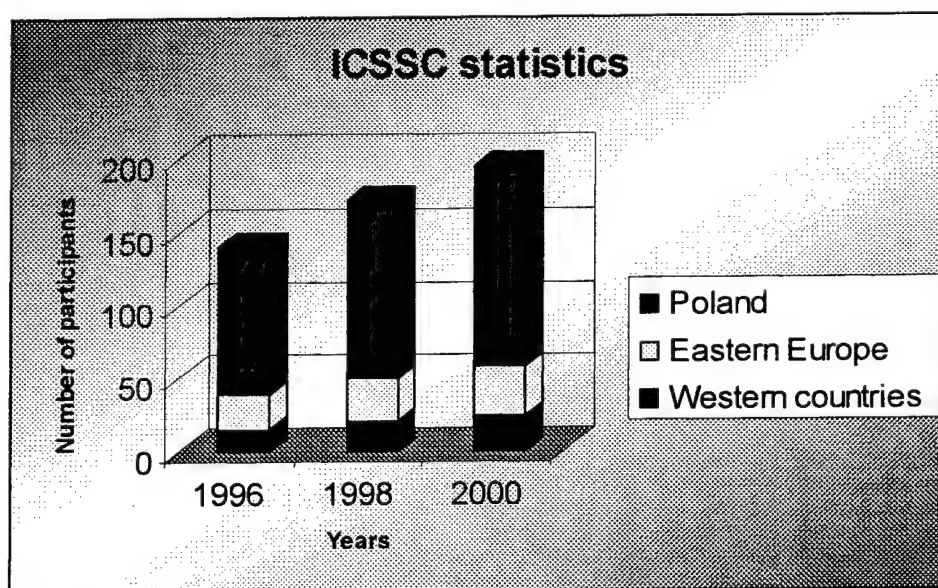
Committee Members

Krzysztof Adamiec	Andrzej Majchrowski
Ryszard Curyk	Jarosław Rutkowski
Leszek Kubiak	Danuta Staniszevska
Paweł Madejczyk	Jakub Wenus

Preface

The "Second International Conference on Solid State Crystals '2000 (ICSSC'2000) was held in Zakopane, Poland, from 9-13 October 2000. This second international event, following a series of conferences organized by the Military University of Technology in Warsaw, SPIE – The International Society for Optical Engineering, and Polish Society for Crystal Growth, appears now clearly as a well-established forum in the field of materials science. The conference was financially supported by the Committee for Scientific Research (KBN), European Office of Aerospace Research and Development, Institute of Physics Technical University of Łódź, and Institute of Physics Wrocław University of Technology.

The conference has attracted about 200 participants from 20 countries. The following diagram pictures the number of attendees of the three last editions, 1996, 1998 and 2000, showing the distribution of delegates depending on their countries of origin: Poland, Eastern countries and Western countries. As understandable, Polish participants are the majority. The conference had a huge role in consolidation of the Polish scientific community. It seems that the Polish researches in this field of science are very active despite the fact of serious financial shortcomings caused by the transformation period in Poland's economy. A strong delegation of Eastern countries attends this conference and ICSSC has now the privileged position of a well established forum of discussion and exchange of information between eastern and western delegates. A clear effort has to be undertaken to strengthen these two delegations, which requires more financial support to welcome people from eastern countries and likely more advertisement in western countries.



Some statistics allows a better identification of the subjects covered by this conference. About 200 communications (26 invited lectures, 34 oral presentations and 147 posters) have been dedicated to different families of materials.

The oxides were a major topic all along the conference, with 47 communications dealing with their non-linear properties, their photorefractive properties, with laser crystals, scintillators, frequency doubling, SAW devices, crystal growth,...etc.

30 communications have been devoted to III-Vs, with the growth of bulk crystals, of thin films, superlattices and nanoscale structures with the intention of making IR detectors (like InAs/GaInSb), green, blue, UV detectors and emitters (nitrides), nanoscale devices,...etc.

26 communications have been dedicated to II-VIs, among which 13 to HgCdTe IR detectors. The other II-VIs studied have been tellurides, mainly CdTe and CdZnTe, with their bulk growth, Schottky diodes and quantum dots, selenides, with ZnSe, (Zn,Mg)Se, (Zn,Ag)Se, Cd(S,Se), (Cd,Zn)Se, (Zn,Be)Se, (Zn,Mg)Se, sulfides with ZnS, Cd(Te,S), (Cd,Zn)S and oxides with ZnO.

25 communications dealt with the elements of Group IV: 19 communications devoted to Si, several of them dealing with porous silicon, 2 communications devoted to Ge, 4 to C, with fullerenes, fullerites, and nanotubes.

Two communications only were dedicated to SiC, one to TiC.

The infrared properties of IV-VI and II-IV-VI alloys were covered by PbSe, PbS, (Cd,Pb)Se and PbGeSnTe.

25 communications were dedicated to miscellaneous materials, ternary chalcogenides like AgGaS₂ or Se₂, LiInS₂ or Se₂, for laser applications, the As-Te-In glasses for their non linear properties, pyridium salts for their ferroelectric properties, Ag₂CdIn as a superionic material, the magnetic Tb(Co,Ga)₂ alloys, Ag₃SbS₃ for double beam reflection, some compounds with big iodo-copper anions for intense visible luminescence, Bi₂(S,Se)₃ alloys for their thermoelectric properties, amorphous Se for X-ray imaging, and several organic materials for applications in optoelectronics,...etc.

The most striking new features in the field of materials science have been recognized to be the incursion both of nanotechnologies, like electronics and optoelectronics at nanoscale with not only fascinating proposals but also marvelous realizations (single electron transistor, Wigner crystals, quantum dots with III-Vs and II-VIs,...) and of organic materials with now the demonstration of their potentialities in optoelectronics from short to long wavelengths.

This volume entitled "Epilayers and Heterostructures in Optoelectronics and Semiconductor Technology" contains the second part of papers presented at the ICSSC'2000. The papers are included in five sections:

- Thin layers and epitaxial growth
- Crystalline nanostructures and films, their formation and properties
- Structural, optical and electrical properties of thin layers
- Optoelectronic devices
- Organic materials for electronics.

Between the papers presented in this volume special attention should be paid on the following papers devoted to enabling technology for the new millenium (M. Razeghi), epitaxy on GaN single crystals (M. Leszczyński), III-Nitride optoelectronics (Y.S. Park), Wigner crystals (B. Pödör), properties of fullerenes (P. Byszewski), quantum well infrared focal plane arrays (S. Gunapala).

An exegesis of this conference cannot end without stressing how marvelous are the Tatra Mountains all around Zakopane. It is an ideal localization for a conference, with the possibility to be regenerated after the first intensive days of conference by marvelous excursions in the mountains. These excursions have been proved to participate efficiently in strengthening friendly relationships between delegates and in excellent atmosphere all over the conference.

Antoni Rogalski
Conference Chair

The scope of the ZnO growth

Robert Triboulet*,

CNRS, Laboratoire de Physique des Solides et de Cristallogénèse,
1, Place Aristide Briand, F 92195 Meudon Cedex, France

ABSTRACT

The main ZnO physical properties are reviewed and some of them compared to those of GaN. As a result of these attractive properties, the various applications it could be thought of for ZnO are summarized. A critical review is then proposed of the different techniques used for the growth of bulk ZnO crystals and of ZnO epitaxial films. The results are discussed from the assessment of their structural and electrical properties. The key issue of *p*-type doping is finally discussed in the light of the most recent results.

Keywords : ZnO physical properties, ZnO applications, ZnO bulk growth, ZnO epitaxial growth, ZnO doping

1. INTRODUCTION

ZnO can be considered as an 'old' semiconductor. It has been studied and used for a long time in a wide range of applications such as piezoelectric transducers, optical waveguides, acoustooptic media, conductive gas sensors, transparent conductive electrodes, varistors. It is now reactivated and becomes again topical for applications related not only to its optoelectronic possibilities in the UV range but also to its piezoelectric properties to develop SAW filters to be integrated in future analog circuits for portable electronic for which there is a strong need.

It is worth knowing that ZnO occupies already an enviable place in the industrial market. Tens of thousands tons of ZnO powder are industrially produced each year! They are used in the rubber industry as vulcanisation activator (~36 %), in the industry of ceramics as a flux (~26 %), in the chemical industry (desulphuration of gases, fabrication of stearates, phosphates..etc) (~20 %), as trace elements in the animal food (~12 %), in the paints (~3 %; 50 % in 1961!). The last ~3 % are used for different applications, in electronics (ferrites, varistors), ends of matches, pharmaceutic industry (fungicidal properties of ZnO for skin-problems, trace elements ..etc.).

ZnO powder is produced from the combustion of vapours coming from the distillation of metallic zinc, according to the so-called French process, or dry process. Using vapours coming from fractionated distillation, extra-pure oxide powders are produced, as illustrated from the chemical analysis data of two kinds of powder produced by two different companies:

- Quality 'pharmacy B', produced by Union Minière : Pb<20 ppm, Cd<10 ppm, Fe<5 ppm, Cu<1 ppm.
- Quality 'colloidal', produced by Silar SA : Pb<20 ppm, Cd<30 ppm, Fe<5 ppm, Cu<2 ppm, Mn<2 ppm.

The grain size can change according to the variety considered.

After summing up the main physical properties of ZnO, which is now attracting tremendous interest, the recent growth aspects of the compound, not only for making bulk crystals, but also epitaxial layers, will be addressed and critically reviewed. The doping issue will be also discussed in the light of the most recent results.

2. ZnO PHYSICAL PROPERTIES

If the field of wide band gap semiconductors has been clearly dominated by the nitride compounds during the last five years, the recent first International Workshop on ZnO (Dayton October 7-8 1999) and the Ninth International Conference on II-VI Compounds (Kyoto November 1-5 1999) have shown that the trend of the ten coming years could turn in favor of the semiconductor oxides because of their attractive physical properties.

*Further author information –

R.T. : Email : triboulet@cnrs-bellevue.fr; Telephone : (33-1) 45 07 50 88; Fax : (33-1) 45 07 58 41

In most of the applications aimed at by the nitrides, the oxides demonstrate fundamental advantages.

- ZnO has a band gap of 3.37 eV @ RT
- It presents a unique combination of piezoelectric ($e_{33} = 1.2 \text{ C/m}^2$, among the highest values of all semiconductors), conducting, thermal (thermal conductivity of $0.54 \text{ Wcm}^{-1}\text{K}^{-1}$, to compare with 0.5, for example, for GaAs) and optical properties
- It has the largest exciton binding energy of all II-VI and III-V semiconductors, 60 meV, allowing excitonic stimulated emission up to 550 K, as already demonstrated¹
- *P*-type conductivity, which remains a problematical issue for GaN, has been now reported for ZnO, as will be shown further, and paves the way to realization of junctions.
- Unlike GaN, high quality substrates are now produced by a variety of techniques, sublimation (40 mm diameter, by Eagle Picher), hydrothermal growth, vertical Bridgman under pressure, chemical vapor transport. This means that the ZnO homoepitaxy is now possible. As a result, layers of improved physical properties ought to be obtained, and the cleavage issue for making lasers, particularly difficult for GaN layers deposited on sapphire, should be made easier
- The ternary system CdO-ZnO-MgO covers a larger band gap range than nitrides with a smaller variation of the lattice parameter [3.24 to 3.26 Å from ZnCdO (2.8 eV) to ZnMgO (4 eV)]
- The ZnO drift mobility saturates at higher fields and at higher values than the GaN ones which is attractive for high frequency devices²
- ZnO is more radiation resistant (up to 2 MeV, $1.2 \times 10^{17} \text{ electrons/cm}^2$) than GaN
- ZnO UV detectors show very low dark current; their spectral response showing a maximum at the optimum wavelength of 350nm
- ZnO shows a strong two-photon absorption with high damage thresholds, which is very attractive for optical power limiting devices
- ZnO has a large shear modulus. The shear modulus has been identified to be a key material signature expressing the stability of the crystal³. The shear modulus of ZnO has been recently calculated by Vérie⁴ and found to be ~45.5 Gpa. By comparison, the shear modulus of ZnSe has been estimated to be 18.35, 32.60 for GaAs, 51.37 for Si.
- ZnO has finally the same crystallographic structure as GaN, with a lattice mismatch < 1.8%, and can then act as alternative substrate for GaN.

Beside GaN,

- ZnO is more radiation hard
- shows higher drift mobilities at higher electric fields
- has a higher exciton binding energy
- could be easier to convert to *p*-type, at higher concentrations
- its homoepitaxy is possible
- its film growth deposition temperatures are smaller (~ 400 °C)
- it is easier to cleave
- the CdO-ZnO-MgO system shows great potentialities, covering an energy range going from 2.8 eV to 4 eV with a weak variation of the lattice parameter
- zinc is more abundant, less expensive than gallium, and no toxic

Owing to these attractive assets, many applications can be thought of for ZnO. In addition to now classical applications (piezoelectric transducers, optical waveguides, acoustooptic media, conductive gas sensors, transparent conductive electrodes) the future perspectives of ZnO are hetero- and homo-epitaxial *p/n* junctions; LED's and lasers in blue and UV region; UV detectors for solar blind applications; high field electron devices; high power, high temperature electronics ; future wireless communication systems at frequencies beyond 5 GHz ; variable optoelectronic grating ; optical power limiting devices for high peak power pulses ; large diameter high quality substrates for GaN. It could furthermore be thought of also as an efficient scintillator.

Furthermore, a ferromagnetic phase transition, induced by a gas of electrons and holes, is expected from a theoretical work⁵ in the ZnMnO alloys at a Curie temperature higher than room temperature. This could lead to new physics and to the realization of devices based on the control of the spin state (spin electronics or spintronics) like quantum computers.

3. ZnO BULK GROWTH

Roughly four techniques are presently used to grow bulk ZnO crystals.

- In spite of its very high melting point of $\sim 1900^\circ\text{C}$ and of its high reactivity with any surrounding material but platinum, cm-sized ZnO crystals with rocking-curve FWHM of ~ 125 arcsec have been grown from the melt by the Bridgman method using Cermet's melt growth apparatus with water-cooled crucible under high oxygen pressure (50 atm)⁶. The perspective is to reach 2 inch diameter substrates.
- The hydrothermal method has been shown suitable for the growth of large ZnO crystals from $(\text{OH})^-$ solutions at temperatures $< 500^\circ\text{C}$ under high pressure (15 to 50 MPa) with a temperature difference $\Delta T \sim 3 - 40\text{K}$ and a growth rate in the range 0.05-0.3 mm/day⁷⁻¹⁰. More recently, high quality ZnO crystals, as demonstrated by X-ray rocking curves in the 40 arcsec range and sharp PL peaks, have been grown hydrothermally at 355°C with a ΔT of 10°C from NaOH/KOH solutions as the solvent, pressures of 18,000 to 22,000 psi (maximum pressure 1500 atm)¹¹. The crystals present a dislocation density $< 500\text{ cm}^{-2}$, a X-ray double diffraction FWHM ~ 130 arcsec and carrier mobilities $\sim 175\text{ cm}^2/\text{Vs}$ @ RT. The O and Zn surfaces of (0001) planes have been found to behave differently. GaN layers deposited at 750°C on such substrates show DDX FWHM of 735 arcsec. Using a KOH/LiOH solvent, ZnO bulk single crystals about 10 mm in dimension have been grown at temperatures less than 400°C at pressures ranging from 830 to 1110 MPa¹².

The advantages of the hydrothermal technique are a low growth temperature, a ΔT close to 0 at liquid/solid interface, an 'easily scalable' technique, the reduction of most of the impurities from source (except Li, incorporated in the crystals at 1-20 ppm). The disadvantages are the presence of intermediate products, the slow growth rates (~ 10 mils per day), the inert liner needed, the occasional incorporation of OH and H_2O , the lithium incorporation. The goal is an increase in the crystal size as well.

- Large diameter (2-inch diameter) boules have been recently reported to be grown at Eagle Picher at $1000-1200^\circ\text{C}$ by seeded physical vapor transport (SPVT) in a nearly closed horizontal tube using H_2 as a carrier gas and a small amount of water to maintain the proper stoichiometry¹³. The crystals are seeded at full diameter; the source/substrate distance is of about 3 inches; the stoichiometry is controlled from the presence of a residual water pressure; the growth rates are of about $40\text{ }\mu\text{m}$ per hour. The present diameter of the crystals is 40 mm; the etch pit (dislocation) density is of about 10^4 cm^{-2} ; the X-ray double diffraction rocking curve FWHM is of about 40 arcsec, with some scattering indicating the presence of residual strains. GDMS analysis reveals the purest material ever done by Eagle Picher. The crystals are of n -type with $n \sim 8 \times 10^{16}\text{ cm}^{-3}$ and $\mu \sim 150-350\text{ cm}^2/\text{Vs}$ @ RT. The homoepitaxial growth of ZnO on such substrates has been achieved on $<0001>$ Zn faces chemo-mechanically polished. The future goal is now the growth of 3 inch diameter substrates.

Furthermore, residual water, present in H_2 or Ar, has been shown to act as a sublimation activator of the vapor phase transport of ZnO^{14} .

- Smaller crystals have been obtained by chemical vapour transport (CVT) in closed tubes using such chemical transport agents as HCl, Cl_2 , NH_3 , NH_4Cl , HgCl_2 , H_2 , Br_2 , ZnCl_2 at source temperatures ranging from 800 to 1150°C and ΔT from 20 to $200^\circ\text{C}^{15-19}$. Centimeter-size single crystals with rocking curve FWHM ~ 28 arcsec have been recently obtained using C as a new transporting chemical agent²⁰.

Crystals of small size have been grown as well in open tube systems, either by oxidation of ZnI_2^{21} , ZnS , ZnSe^{22} , ZnBr_2^{23} and Zn^{24-26} or by hydrolysis of ZnF_2^{27} , $\text{ZnCl}_2^{28,29}$, ZnI_2^{30} . The oxidation or hydrolysis character of the reaction can depend on the temperature range used for a same source. The temperature of the growth region ranges generally in such experiments from 900 to 1350°C .

Such solvents as PbF_2^{31} and $\text{V}_2\text{O}_5/\text{P}_2\text{O}_5$ mixtures³² have been used for the flux growth of ZnO crystals. Using PbF_2 as the solvent in sealed Pt crucibles, ZnO crystals have been grown by THM³³. PbCl_2 has been found to be a very good solvent of ZnO as well, but showing also a great reactivity with any surrounding material but platinum³⁴. The same authors have found the Zn-In alloys to be good solvents of ZnO without reactivity with silica.

4. ZnO EPITAXIAL FILM GROWTH

ZnO thin polycrystalline films dedicated to the 'traditional' applications of ZnO, as specified above, are classically deposited by such techniques as sputtering, chemical vapor deposition, chemical spraying, electron cyclotron resonance plasma sputtering, sol-gel deposition, ion-beam assisted deposition, pulsed laser deposition etc.

More recently homoepitaxial and heteroepitaxial ZnO films dedicated to the 'new' ZnO applications for optoelectronic devices have been grown by four techniques :

- Classical ZnO sputtering has been achieved on (0001) sapphire substrates³⁵. A (0002) rocking-curve FWHM as low as 250 arcsec has been measured, but more generally of about 400 arcsec. The roughness was < 1nm (the best 0.1 nm). The resistivity ranged from 3 to $10^5 \Omega\text{cm}$ depending on the growth and cooling conditions. Under low pressure (3-150 mTorr) sputtering, rocking-curve FWHM ≤ 1080 arcsec³⁶ has been measured on sapphire substrates. Epitaxial ZnO films have been grown on Si(111) substrates by rf magnetron sputtering using a GaN buffer layer deposited by the same technique³⁷. The films show a crack-free morphology. RF magnetron sputtering has been used as well for the deposition of epitaxial ZnO films on diamond (111) planes at 260 °C³⁸ (smallest X-ray rocking-curve FWHM of 972 arcsec measured on the ZnO (0002) peak) and on LiNbO_3 (0001)³⁹ substrates at 550 °C (rocking-curve FWHM for the ZnO (0002) reflection ~ 1650 arcsec). The same kind of result was obtained on non-crystalline substrates (alumina and silica) using a two-step method in which a thin ZnO buffer layer was first deposited by magnetron sputtering, the epitaxial films being then deposited by CVD technique⁴⁰.
- ZnO, ZnMgO and ZnO/GaN films have been grown on sapphire substrates by pulsed laser deposition by Vispute et al.^{41,42}. The substrate temperature was 750 °C for ZnO/sapphire and 500-750 °C for ZnO/GaN/sapphire under an O_2 pressure of 10^{-5} - 10^{-4} Torr. The measured EPDs and rocking-curve FWHM were respectively $10^{10}/\text{cm}^2$ and ~ 612 arcsec on ZnO/sapphire and $10^8/\text{cm}^2$ and 180 arcsec on ZnO/GaN. Epitaxial ZnO thin films showing a FWHM rocking-curve ~ 600 arcsec have been grown on sapphire substrates using ultra-violet pulsed laser deposition at temperatures higher than 400 °C by Craciun et al.⁴³.
- MOCVD, generally on sapphire substrates, is carried out with separate inlets of the precursors to avoid pre-reactions, with DEZn for Zn and O_2 ^{44,45}, O_2 , N_2O or H_2O ⁴⁶ (with or without plasma), CO_2 ^{47,48} (with a plasma) or alcohol (butanol^{49,50}) as oxidizers, and Ar, He or N_2 as the carrier gas, in the temperature range 350-650 °C
 - either in a horizontal reactor^{49,50}
 - or in a vertical rotating disk reactor operated at low pressure with high speed rotation of the wafer carrier, with separated introduction of the precursors⁴⁴⁻⁴⁶, sometimes through a multi-nozzle shower⁴⁶. The possibility of obtaining both conductivity types, n and p , has been demonstrated using N_2O , NH_3 and N_2 (with and without plasma activation) for N doping⁴⁶.

A very few significant characteristics of the MOCVD grown ZnO layers are given. Only a value of 1500 arcsec has been reported for the FWHM of the (0002) diffraction peak⁴⁸. No electrical properties are reported for these MOCVD grown ZnO layers...

- MBE has been achieved by several groups for the growth of ZnO layers and related ternary alloys with Cd, Mg and Mn, according to two main variants :
 - Either laser-MBE (pulsed laser deposition, PLD, in ultra-high vacuum) on ScAlMgO_4 substrates⁵¹ or on sapphire for ZnO ⁵² and $\text{ZnO}/\text{Mg}_{1-x}\text{Zn}_x\text{O}$ quantum structures⁵³
 - Or by plasma-assisted MBE⁵⁴⁻⁶¹, with variants like radical source MBE⁶² (RS-MBE), electron cyclotron resonance assisted MBE⁶³ (ECR-assisted MBE), depending on the plasma cell used. ZnO films have been generally grown on sapphire substrates, using such buffer layers as MgO ^{54,58}, GaN ⁵⁵, or ZnS ⁵⁶ and on Si⁶². Such heterostructures like $\text{Mg}_{0.2}\text{Zn}_{0.8}\text{O}/\text{ZnO}/\text{Mg}_{0.2}\text{Zn}_{0.8}\text{O}$ and $\text{ZnO}/\text{ZnCdO}/\text{ZnO}$ on sapphire (0001), ScAlMgO_4 (0001) (SCAM) and ZnO/GaN substrates have been also grown⁶⁴. The growth temperature lies in the range 275-600 °C.

More details than in the MOCVD case are given concerning the structural and electronic properties of the layers. The following rocking-curve FWHM have been reported : 216 arcsec⁵⁷, 378 arcsec⁵¹, 576 arcsec⁶⁰, 1080 arcsec⁵⁹, 2016 arcsec⁶³ for ZnO directly deposited on Al_2O_3 , but 39 arcsec⁵¹ for ZnO(0002) on SCAM, and 13 arcsec⁵⁸ using a MgO buffer layer on sapphire. The layers grown without doping are always of n -type, with a carrier concentration closely related to their crystallographic perfection : electron concentration of $1.87 \times 10^{18} \text{ cm}^{-3}$ associated with a mobility of $10 \text{ cm}^2/\text{Vs}$ for ZnO layers grown on Si⁶¹, but $n = 10^{15} \text{ cm}^{-3}$, $\mu \sim 100 \text{ cm}^2/\text{Vs}$ for ZnO layers deposited on SCAM⁵¹ and $n = 2.1 \times 10^{16} \text{ cm}^{-3}$, $\mu \sim 98 \text{ cm}^2/\text{Vs}$ for ZnO layers deposited on $\text{MgO}/\text{Al}_2\text{O}_3$ ⁵⁸.

- Using Radical beam epitaxy (RBE), n -type, p -type ($p = 4 \times 10^{14} \text{ cm}^{-3}$, $\mu \sim 23 \text{ cm}^2/\text{Vs}$) or semi-insulating ZnO films have been produced at temperatures within 150-950 °C by bombardment of singlet $\text{O}(\downarrow\uparrow)$ radicals extracted from an oxygen plasma, using a magnetic filter, on substrates of any Zn chalcogenide (ZnTe , ZnSe , ZnS , ZnO)⁶⁵. No information about their structural properties.

5. DOPING

Whatever the growth method used, ZnO bulk crystals and films exhibit almost always strong *n*-type conductivity, with *n* lying generally in between 10^{17} and 10^{19} cm⁻³. It has been long assumed that the dominant donor was a native defect. From a recent first-principle investigation⁶⁶, it has been demonstrated that none of the dominant native defects, zinc and oxygen vacancies and ZnO antisites, has characteristics consistent with a high-concentration shallow donor. Furthermore, V_O has been identified from electron paramagnetic resonance studies as a deep donor⁶⁷. Hydrogen or a complex native defect-hydrogen has been suggested to be responsible for the strong donor behavior⁶⁶. We have analyzed by SIMS the residual concentration of hydrogen in ZnO bulk crystals grown by CVT using carbon as the chemical transport agent. Neither hydrogen nor residual carbon were found in these crystals which showed an electron concentration @ RT of $\sim 2 \times 10^{18}$ cm⁻³. The assignment of the residual native shallow donor in ZnO to Zn_i, as proposed by Look et al.⁶⁸, remains the best hypothesis.

The key issue for the ZnO and related alloys development remains *p*-type doping.

Minegishi et al.⁶⁹ reported for the first time the growth by chemical vapor deposition of *p*-type films realized by the simultaneous addition of NH₃ in the carrier hydrogen and excess Zn in the ZnO powder source. The RT hole concentration reached 1.5×10^{16} cm⁻³, with $\mu \sim 12$ cm²/Vs. But the resistivity remained too high (generally ~ 100 Ωcm) for making devices such as LEDs, and the results were poorly reproducible.

Later on, *p*-type electrical conduction has been achieved, according to a theoretical prediction⁷⁰, by Ga and N codoping of ZnO layers grown by pulsed laser deposition⁷¹. One sample only is reported to show an acceptor concentration of 4×10^{19} cm⁻³, with a very poor mobility of 7×10^{-2} cm²/Vs. The authors stress the fact that the *p*-type behavior seems to be very small and sensitive to experimental parameters.

A ZnO diode has been fabricated by using a laser-annealing doping technique to form a *p*-type ZnO layer on a *n*-type ZnO substrate⁷². A Zn-phosphide compound, used as a phosphorous source, was deposited on the ZnO wafer and subjected to excimer-laser pulses. But the authors indicate that an attempt to prove the *p*-type nature of the P-doped layer by Hall measurements was not successful. It has to be stressed that a highly damaged layer is generally found on surfaces as a result of laser annealing.

In a recent communication, hole carrier concentrations of 10^{18} - 10^{21} cm⁻³, associated with mobilities of 0.1-50 cm²/Vs and resistivities of 10 - 10^5 Ωcm have been reported in ZnO layers grown by pulsed layer deposition on GaAs substrates⁷³. The As atoms out-diffusing from the substrates into the ZnO layers were considered as the dopant elements. Their concentration were found to be in the range of upper 10^{17} to upper 10^{21} atoms/cm³ from SIMS measurements. No diodes have been so far fabricated from such layers. Furthermore, the electrical characteristics are said to "may have large uncertainties because contributions from the interference layers between the ZnO film and the GaAs substrate are not understood very well at this moment". In similar heterostructures, but with a ZnSe layer instead of ZnO on GaAs substrates, a highly *p*-type conductivity has been reported in the past⁷⁴. Raman spectroscopy measurements gave evidence of the presence of a *p*-type carrier gas with *p* ranging from 10^{18} to 10^{20} cm⁻³, which appeared as confined at the interface of ZnSe/GaAs⁷⁵⁻⁷⁷.

6. CONCLUSIONS

ZnO presents very attractive physical properties which have been reviewed and for some of them compared to those of GaN. As a result of these properties, the various applications which could be thought of for ZnO have been summarized. A critical review is then proposed of the different techniques used for the growth of bulk ZnO crystals and of ZnO epitaxial films. The results are discussed from the assessment of the structural and electrical properties of the crystals and films. Among the numerous communications related to the ZnO epitaxial growth, a very few of them report on layers of structural and electronic properties suitable for optoelectronic devices. *P*-type doping, discussed in the light of the most recent results, remains the key issue for the optoelectronic development of ZnO.

REFERENCES

1. D.M. Bagnall, Y.F. Chen, Z. Zhu, T. Yao, M.Y. Shen and T. Goto, "High temperature excitonic stimulated emission from ZnO epitaxial layers", *Appl. Phys. Lett.* **73**, pp. 1038-1040, 1998.
2. J.D. Albrecht, P.P. Ruden, S. Limpijumnong, W.R.L. Lambrecht and K.F. Brennan, "High field electron transport properties of bulk ZnO", *J. Appl. Phys.* **86**, pp. 6864-6867, 1999.
3. C.Vérié, "Covalency engineering through alloying with beryllium chalcogenides in wide band-gap II-VI crystals", *J. Electron. Mater.* **27**, 6, pp. 782-787, 1998.

4. C.Vérié, personal communication.
5. T. Dietl, H. Ohno, F. Matsukura, J. Cibert and D. Ferrand, "Zener Model Description of Ferromagnetism in Zinc-Blende Magnetic Semiconductors", *Science* **287**, pp 1019-1022, 2000.
6. G. Agarwal, J.E. Nause and D.N. Hill, "A new approach to growth of bulk ZnO crystals for wide bandgap applications", *Mat. Res. Soc. Symp. Proc.* **512**, pp. 41-46, 1998.
7. R.A. Laudise and A. Ballman, "Hydrothermal Synthesis of Zinc Oxide and Zinc Sulfide" *J. Phys. Chem.* **64**, pp. 688-691, 1960.
8. E.D. Kolb and R.A. Laudise, "Hydrothermally Grown ZnO Crystals of Low and Intermediate resistivity", *J. Am. Ceram. Soc.* **49**, pp. 302-305, 1966.
9. R.A. Laudise, E.D. Kolb and A.J. Caporaso, "Hydrothermal Growth of Large Sound Crystals of Zinc Oxide", *J. Am. Ceram. Soc.* **47**, pp. 9-12, 1964.
10. E.F. Venger, A.V. Melnichuk, L.Yu. Melnichuk and Yu.A. Pasechnik, "Anisotropy of the ZnO Single Crystal Reflectivity in the Region of Residual Rays", *phys. stat. sol. (b)* **188**, pp. 823-831, 1995.
11. M. Suscavage, M. Harris, D. Bliss, P. Yip, S-Q. Wang, D. Schwall, L. Bouthillette, J. Bailey, M. Callahan, D.C. Look, D.C. Reynolds, R.L. Jones, and C.W. Litton, 1999 *Mat. Res. Soc. Symp. Proc.* 537 to be published
12. T. Sekiguchi, S. Miyashita, K. Obara, T. Shishido and N. Sakagami, "Hydrothermal growth of ZnO single crystals and their optical characterization", *J. crystal Growth* **214/215**, pp. 72-76, 2000.
13. D.C. Look, D.C. Reynolds, J.R. Sizelove, R.L. Jones, C.W. Litton, G. Cantwell and W.C. Harsch, "Electrical properties of bulk ZnO", *Solid State Comm.* **105**, pp. 399- 401, 1998.
14. J-M. Ntep, M. Barbé, G. Cohen-Solal, F. Bailly, A. Lusson, and R. Triboulet, "ZnO growth by chemically assisted sublimation", *J. Crystal Growth* **184/185**, pp. 1026-1030, 1998.
15. M. Shiloh and J. Gutman, "Growth of ZnO single crystals by chemical vapour transport", *J. Crystal Growth* **11**, pp 105-109, 1971.
16. W. Piekarczyk, S. Gazda and T. Niemyski, "The growth of zinc oxide crystals by chemical transport method", *J. Crystal Growth* **12**, pp. 272-276, 1972.
17. K. Matsumoto, K. Konemura. and G. Shimaoka, "Crystal growth of ZnO by vapor transport in a closed tube using Zn and ZnCl₂ as transport agents", *J. Crystal Growth* **71**, pp. 99-103, 1985.
18. K. Matsumoto and G. Shimaoka, "Crystal growth of ZnO by chemical transport", *J. Crystal Growth* **86**, pp 410-414, 1988.
19. K. Matsumoto and K. Noda, "Crystal growth of ZnO by chemical transport using HgCl₂ as a transport agent", *J. Crystal Growth* **102**, pp. 137-140, 1990.
20. J-M. Ntep, , S. Said Hassani, A. Lusson, A. Tromson-Carli, D. Ballutaud, G. Didier and R. Triboulet, "ZnO growth by chemical vapour transport", *J. Crystal Growth*, **207**, pp. 30-34, 1999.
21. M. Hirose and I. Kubo, "Growth of ZnO Single Crystals by Oxidation of ZnI₂", *Jpn. J. Appl. Phys.* **8**, pp. 402, 1969.
22. Y.S. Park and D.C. Reynolds, "Growth of ZnO Single Crystals", *J. Appl. Phys.* **38**, pp. 56-760, 1967.
23. M. Hirose, Y. Furuya and I. Kubo, "Growth of ZnO Single crystal from ZnBr₂", *Jpn. J. Appl. Phys.* **9**, pp. 726-727, 1970.
24. E. Scharowsky, "Optical and electrical properties of ZnO single crystals with excess zinc", *Z. Phys.* **135**, pp. 318-330, 1953.
25. K.F. Nielsen, "Growth of ZnO single crystals by the vapor phase reaction method", *J. Crystal Growth* **3/4**, pp. 141-145, 1968.
26. K.J. Fischer, "Vapor phase growth of ZnO crystals in an open tube flow system", *J. Crystal Growth* **34**, pp. 139-144, 1976.
27. I. Kubo, "Crystal Growth of Zinc-oxide by Chemical Reaction of Zinc-fluoride with Air", *J. Phys. Soc. Jap.* **16**, pp. 2358-2359, 1961.
28. T. Takahasi, A. Ebina and A. Kamigawa, "Vapor Reaction Growth of ZnO Single Crystal", *Jpn. J. Appl. Phys.* **5**, pp 560-561, 1966.
29. E.A. Weaver, "Vapor phase growth of ZnO single crystals", *J. Crystal Growth* **1**, pp. 320-322, 1967.
30. M. Hirose and Y. Furuya, "Growth Mechanism of ZnO by Oxidation of ZnI₂", *Jpn. J. Appl. Phys.* **9**, pp 423-424, 1970.
31. K.F. Nielsen and E.F. Dearborn, "The growth of large single crystals of zinc oxide", *J. Phys. Chem.* **64**, pp 1762-1763, 1960.
32. B.M. Wanklyn, "The growth of ZnO crystals from phosphate and vanadate fluxes", *J. Crystal Growth* **7**, pp. 107-108, 1970.

33. G.A. Wolf and H.E. LaBelle Jr., "Growth of ZnO single crystals by a traveling solvent zone technique", *J. Am. Ceram. Soc.*, **48**, 8, pp. 441-442, 1965.
34. J.-M. Ntep, E. Dichi, B. Legendre, G. Didier and R. Triboulet, *Mater. Lett. to be published*
35. A.J. Drehman, L.O. Bouthillette, P.W. Yip, S.-Q. Wang, K. Vaccaro, S.M. Spaziani and C.L. Woods, oral communication in the International Workshop on ZnO, Dayton, USA October 7-8 1999.
36. S. Zhu, C.-H. Su, S.L. Lehoczky, M.A. George and P. McCarty, oral communication in the International Workshop on ZnO, Dayton, USA October 7-8 1999.
37. H.K. Kim, A. Nahhas, E. Kim and B. Lee, oral communication in the International Workshop on ZnO, Dayton, USA October 7-8 1999.
38. A. Hachigo, H. Nakahata, K. Higaki, S. Fujii and S.-I. Shikata, "Heteroepitaxial growth of ZnO films on diamond (111) plane by magnetron sputtering", *Appl. Phys. Lett.*, **65**, pp. 2556-2558, 1994.
39. K. Matsubara, P. Fons, A. Yamada, M. Watanabe and S. Niki, "Epitaxial growth of ZnO thin films on LiNbO₃ substrates", *Thin Solid Films*, **347**, pp. 238-240, 1999.
40. B.M. Ataev, I.K. Kamilov, A.M. Bagamadova, V.V. Mamedov, A.K. Omaev, M.Kh. Rabadanov, "Epitaxial ZnO films on non-crystalline substrates", *Mater. Sci. Engin.* **B68**, pp. 56-58, 1999.
41. R.D. Vispute, V. Talyansky, Z. Trajanovic, S. Choopun, M. Downes, P. Sharma, T. Venkatesan, M.C. Woods, R.T. Lareau, K.A. Jones and A.A. Iliadis, "High quality crystalline ZnO buffer layers on sapphire (001) by pulsed laser deposition for III-V nitrides", *Appl. Phys. Lett.* **70**, pp. 2735-2737, 1997.
42. R.D. Vispute, V. Talansky, S. Choopun, R.P. Sharma, T. Venkatesan, M. He, X. Tang, J.B. Halpern, M.G. Spencer, Y.X. Li, L.G. Salamanca-Riba, A.A. Iliadis and K.A. Jones, "Heteroepitaxy of ZnO on GaN and its implications for fabrication of hybrid optoelectronic devices", *Appl. Phys. Lett.* **73**, pp. 348-350, 1998.
43. V. Craciun, R.K. Singh, J. Perriere, J. Spear and D. Craciun, "Epitaxial ZnO Films Grown on Sapphire (001) by Ultraviolet-Assisted Pulsed Laser Deposition", *Journ. Electrochem. Soc.* **147**, pp. 1077-1079, 2000.
44. S. Liang, C.R. Gorla, N. Emanetoglu, Y. Liu, W.E. Mayo and Y. Lu, "Epitaxial Growth of (11-20) ZnO on (01-12) Al₂O₃ by Metalorganic Chemical Vapor Deposition", *J. Electron. Mater.* **27**, 11, pp. L72-L76, 1998.
45. C.R. Gorla, N.W. Emanetoglu, S. Liang, W.E. Mayo and Y. Lu, "Structural, optical, and surface acoustic wave properties of epitaxial ZnO films grown on (01-12) sapphire by metalorganic chemical vapor deposition", *J. Appl. Phys.* **85**, 5, pp. 2595-2602, 1999.
46. G.S. Tompa, L.G. Provost, C. Zhang and N. Glumac, "Rotating Disk Reactor-Low Pressure Metal Organic Chemical Vapor Deposition (MOCVD) Production of ZnO and Related Films", oral communication in the International Workshop on ZnO, Dayton, USA October 7-8 1999.
47. T. Sekiguchi, K. Haga and K. Inaba, "ZnO films grown under the oxygen-rich condition", *J. crystal Growth* **214/215**, pp. 68-71, 2000.
48. K. Haga, M. Kamidaira, T. Sekiguchi and H. Watanabe, "ZnO thin films prepared by remote plasma-enhanced CVD method", *J. crystal Growth* **214/215**, pp. 77-80, 2000.
49. C. Thiandoume, V. Sallet, R. Triboulet and O. Gorochoy, to be published
50. B. Hahn, G. Heindel, E. Pschorr-Schoberer, W. Gebhardt, "MOCVD layer growth of ZnO using DMZn and tertiary butanol", *Semicond. Sci. Technol.* **13**, 7, pp. 788 - 791, 1998.
51. K. Tamura, A. Ohtomo, K. Saikusa, Y. Osaka, T. Makino, Y. Segawa, M. Sumiya, S. Fuke, H. Koinuma and M. Kawasaki, "Epitaxial growth of ZnO films on lattice-matched ScAlMgO₄ (0001) substrates", *J. Crystal Growth* **214/215**, pp. 59-62, 2000.
52. M. Kawasaki, A. Ohtomo, H. Koinuma, Y. Sakurai, Y. Yoshida, Z.K. Tang, P. Yu, G.K.L. Wang and Y. Segawa, "Ultraviolet Excitonic Laser Action at Room Temperature in ZnO Nanocrystalline Epitaxial Films", *Mater. Sci. Forum* **264-268**, pp. 1459-1462, 1998.
53. A. Ohtomo and M. Kawasaki, "ZnO/Mg_xZn_{1-x}O Quantum Structures", oral communication in the International Workshop on ZnO, Dayton, USA October 7-8 1999.
54. Y. Chen, H.-J. Ko, S.-K. Hong, T. Yao and Y. Segawa, "Two-dimensional growth of ZnO films on sapphire (0001) with buffer layers", *J. crystal Growth* **214/215**, pp. 87-91, 2000.
55. S.-K. Hong, H.-J. Ko, Y. Chen, T. Hanada and T. Yao, "Evolution of initial layers of plasma-assisted MBE grown ZnO on (0001)GaN/sapphire", *J. crystal Growth* **214/215**, pp. 81-86, 2000.
56. A.B.M. A. Ashrafi, A. Ueta, A. Avramescu, H. Kumano, I. Suemune, Y.-W. Ok and T.-Y. Seong, "Growth and characterization of hypothetical zinc-blende ZnO films on GaAs (001) substrates with ZnS buffer layer", *Appl. Phys. Lett.* **76**, 5, pp. 550-552, 2000.

57. Y. Chen, D.M. Bagnall, Z. Zhu, T. Sekiuchi, K.-T. Park, K. Hiraga, T. Yao, S. Koyama, M.Y. Shen and T. Goto, "Growth of ZnO single crystal thin films on c-plane (0001) sapphire by plasma enhanced molecular beam epitaxy", *J. crystal Growth* **181**, pp. 165-169, 1997.
58. Y. Chen, H.-J. Ko, S.-K. Hong and T. Yao, "Layer-by-layer growth of ZnO epilayer on Al₂O₃(0001) by using a MgO buffer layer", *Appl. Phys. Lett.* **76**,5, pp. 559-561, 2000.
59. K. Sakurai, M. Kanehiro, K. Nakahara, T. Tanabe, S. Fujita and S. Fujita, "Effects of oxygen plasma condition on MBE growth of ZnO", *J. crystal Growth* **209**, pp. 522-525, 2000.
60. S. Yamauchi, H. Handa, A. Nagayama and T. Hariu, "Low temperature epitaxial growth of ZnO layer by plasma-assisted epitaxy", *Thin Solid Films* **345**, pp. 12-17, 1999.
61. S. Yamauchi, T. Ashigaa, A. Nagayama and T. Hariu, "Plasma-assisted epitaxial growth of ZnO layer on sapphire", *J. crystal Growth* **214/215**, pp. 63-67, 2000.
62. K. Iwata, P. Fons, S. Niki, A. Yamada, K. Matsubara, K. Nakahara, T. Tanabe and H. Takasu, "ZnO growth on Si by radical source MBE", *J. crystal Growth* **214/215**, pp. 50-54, 2000.
63. H.-B. Kang, K. Nakamura, K. Yoshida and K. Ishikawa, "Single-Crystalline ZnO Films Grown on (0001) Al₂O₃ Substrate by Electron Cyclotron Resonance-Assisted Molecular Beam Epitaxy", *Jpn. J. Appl. Phys.* **36**, pp. L933-L935, 1997.
64. Y. Chen, H.-J. Ko, S.-K. Hong, T. Sekiuchi, Y. Segawa and T. Yao, "Plasma assisted molecular beam epitaxy for ZnO based II-VI semiconductor oxides and their heterostructures", oral communication in the International Workshop on ZnO, Dayton, USA October 7-8 1999.
65. T. Khurlodava and T. Butkhuzi, "Optical and electrical properties of n- and p-type ZnO layers", oral communication in the International Workshop on ZnO, Dayton, USA October 7-8 1999.
66. A.F. Kohan, G. Ceder, D. Morgan and C.G. Van de Walle, "First-principles study of native point defects in ZnO", *Phys. Rev. B. materials physics., condens. matter mater. phys.*, **61**, 22, pp. 15019 – 15027, 2000.
67. P.H. Kasai, "Electron Spin Resonance Studies of Donors and Acceptors in ZnO", *Phys. Rev.* **130**, pp. 989-795, 1963.
68. D.C. Look, J.W. Hemsky and J.R. Sizelove, "Residual Native Shallow Donor in ZnO", *Phys. Rev. Lett.* **82**,12, pp. 2552-2555, 1999.
69. K. Minegishi, Y. Koiwai, Y. Kikuchi, K. Yano, M. Kasuga and A. Shimizu, "Growth of p-type Zinc Oxide Films by Chemical Vapor Deposition", *Jpn. J. Appl. Phys.* **36**, pp. L 1453-L 1455, 1997.
70. T. Yamamoto and H. Katayama-Yoshida, "Solution using a codoping method to unipolarity for the fabrication of p-type ZnO", *Jpn. j. Appl. Phys* **38**, 2B, pp. 166 – 169, 1999.
71. M. Joseph, H. Tabata and T. Kawai, "p-Type Electrical Conduction in ZnO Thin Films by Ga and N Codoping", *Jpn. J. Appl. Phys.* **38**, pp. L1205-L1207, 1999.
72. T. Aoki, Y. Hatanaka and D.C. Look, "ZnO diode fabricated by excimer-laser doping", *Appl. Phys. Lett.* **76**,22, pp. 3257-3258, 2000.
73. Y.R. Ryu, S. Zhu, D.C. Look, J.M. Wrobel, H.M. Jeong and H.W. White, "Synthesis of p-type ZnO films", *J. Crystal Growth* **216**, pp. 330-334, 2000.
74. N. Stuecheli and E. Bucher, "Low resistive p-type ZnSe a key for an efficient blue electroluminescent device", *J. Electron. Mater.* **18**,2, pp. 105-109, 1989.
75. O. Pagès, M.A. Renucci, O. Briot, N. Tempier and R.L. Aulombard, "J. Crystal growth **107**, pp. 670, 1991.
76. O. Pagès, M.A. Renucci, O. Briot, T. Cloitre and R.L. Aulombard, "Depth profiling of carriers in ZnSe/GaAs heterostructures by Raman spectroscopy", *J. Crystal Growth* **117**, pp. 569-572, 1992.
77. O. Pagès, M.A. Renucci, O. Briot and R.L. Aulombard, "Raman study of band bending at ZnSe/GaAs interfaces", *J. Appl. Phys.* **77**, 3, pp. 1241-1248, 1995.

The influence of mechanical stress on the growth of crystals

John N. Sherwood *

Department of Pure and Applied Chemistry
University of Strathclyde, Glasgow G1 1XL, Scotland, UK

ABSTRACT

A review is presented of the author's recent work on the influence of mechanical stress on the growth rate of materials. On the basis of the results, it is proposed that growth rate dispersion of secondary nuclei arises as a result of competition between stress reduction and dislocation enhancement of growth rates in the developing particles, with the former being the major influence at low particle sizes. The results are shown to account for the particle size and material dependence of the dispersion. Mechanistic studies suggest that the principal mechanism of stress reduction in growth rate is the influence of the applied stress on the surface free energy of the crystal. This effects both nucleation at the growth centre and the migration of growth steps across the crystal surface.

Keywords: Solution growth, growth inhibition, secondary nucleation, dislocations, lattice strain.

1. INTRODUCTION

The phenomenon of growth rate dispersion in crystals formed following secondary nucleation by attrition fragment in industrial crystallisers, causes considerable difficulties in the specification of operating parameters and the prediction of the size distribution of the product particles¹. Why such crystals should exhibit a wide range of growth rates from zero to some maximum value is not fully understood².

Studies of the problem suggest that the cause lies in the structure of the growing particle, all other parameters such as supersaturation, agitation, temperature, etc being controllable³⁻⁵.

Attrition can be regarded as a fracture process preceded by deformation. The nature of the deformation process will vary depending on the nature of the material. A brittle solid will deform elastically to fracture possibly retaining some degree of elastic strain. A plastic solid will undergo successively; elastic deformation, plastic deformation and finally fracture to yield a particle with an increased mechanically induced dislocation content compared with the original particle and possibly some residual strain. Additionally, as has been proposed previously⁶, the fracture particles may also contain varying numbers of dislocations due to the non-uniform distribution of growth dislocations in the original particle. In order to assess whether or not these varying properties do influence the growth process, we have examined the influence of stress on the growth of brittle and ductile materials in the macro- and micro-crystalline forms⁷⁻¹².

A suitable starting point for this review is the data obtained from our preliminary study of secondary nucleation in sodium chlorate⁷. This is presented in Figure 1 in a form that encapsulates some of the various features of growth rate dispersion. From this, we note that:

- a) growth rate dispersion is greatest at small sizes;
- b) it is at the lower end of the size range that zero growth rates are encountered; and
- c) the data points appear to converge to a more constant value at sizes approaching some critical size (in this case 100 – 150 μm)

A further consideration in the interpretation of Figure 1 is that examination of the growth of larger sized crystals of sodium chlorate (200-20,000 μm) has revealed an average growth rate of $3.5 \times 10^{-8} \text{ ms}^{-1}$ which provides an approximate convergence limit to the spread of points on Figure 1. This result is consistent with the general observations of a decrease in the range of growth rate dispersion with increasing particle size.

The obvious conclusion that can be derived from the data presented in Figure 1 is that we require to define the nature of processes that cause:

* Further author information

e-mail: J.N.Sherwood@strath.c.uk, Tel +44 141 548 2797, Fax +44 141 548 4822.

- growth rate enhancement to yield the growth rates in the upper part of the range, and
- growth rate suppression for growth rates below this level.

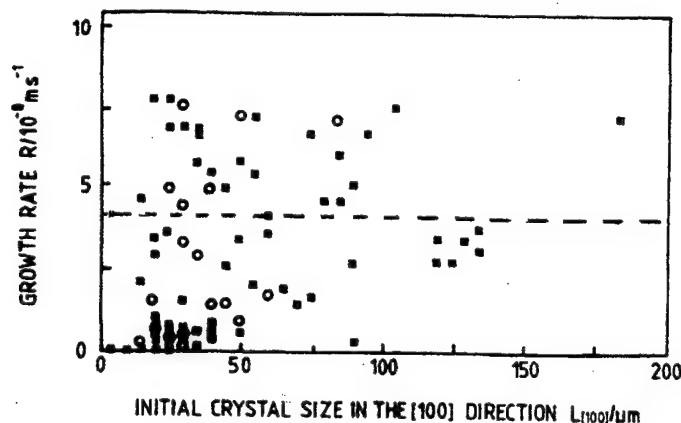


Fig. 1. The variation with initial crystal diameter of the rate of growth of sodium chlorate microcrystals in the [100] direction at supersaturation $\sigma = 0.35\%$. The dotted line represents the average growth rate ($3.5 \times 10^{-8} \text{ ms}^{-1}$) of larger crystals in the size range 200-20000 μm .

The latter should be capable of yielding zero growth rates under extreme conditions. The combination of the two effects should lead to a decrease in dispersion with increasing particle size to yield the average growth rate for the larger particles.

2. DISLOCATION ENHANCEMENT OF GROWTH RATES

The role of dislocations as growth sources is well defined through both the original theoretical work of Burton, Cabrera and Frank¹³ and those who followed them, also from the multitude of subsequent experimental examinations devised to test these theories. There are three potential sources of the growth dislocations that might influence the subsequent growth of an attrition particle.

- a) from the attrition nucleus and which develop into the new crystal;
- b) from the area of refacetting of the fractured interface. This area is always heavily strained and dislocations could form readily and propagate from this volume into the growing sector;
- c) by contact of the particle with other particles in solution during growth;
- d) by plastic deformation of the particle during the attrition process.

The first process has been defined to occur^{14,15} but we find that, all too often, dislocations in the seed terminate in the strain that is located at the newly developing interface⁹. Only under conditions of most careful regeneration can they be encouraged to persist. Even then, the numbers that do propagate are too low to make a major influence on the eventual growth rate of the developing crystal. We feel therefore that this potential source can be eliminated as a major contributor.

From our own work¹⁰, Fig. 2 defines the second process. Fig 2a shows an X-ray topograph¹⁶ of a $(0\bar{1}1)$ slice of a potash alum crystal which has been grown following cutting to show the development of both the interface and the lateral {100} growth sectors. The seed was immersed in a stirred, saturated solution following which the supersaturation was developed by lowering the temperature. Growth took place at the dark volumes XX' which represent the strain developed in the vicinity of the {100} interfaces during the refacetting process. Dislocations generate from this volume and propagate into the {100} sectors. Studies of the subsequent growth rates as a function of the number of dislocations developed yielded the variation shown in Fig. 2b. This confirms that variable numbers of growth dislocations can be generated on refacetting a fractured interface and that these lead to variation in growth rates.

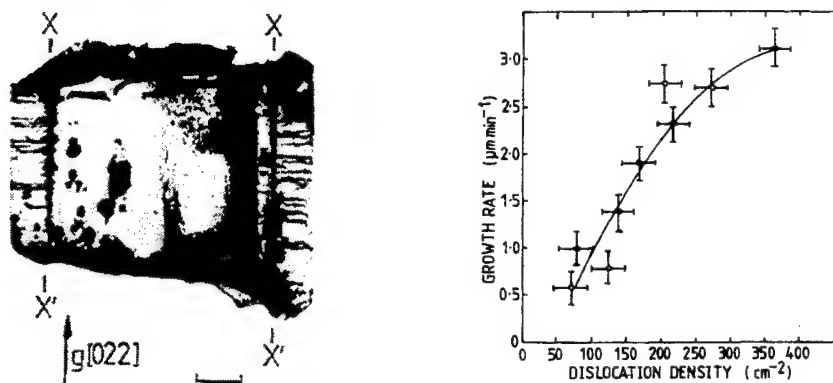


Fig. 2. X-ray topograph of a thin (011) slice of a potash alum crystal regrown to show the development of dislocations in the {100} sectors. The dark line XX' represents the strain developed at the refaceted interface. Dislocations can be seen to develop from this volume. Some of these become refracted into adjacent sectors as growth proceeds. Others continue to propagate towards the growing interface. The relationship between growth rate at constant supersaturation, $\sigma = 6.4\%$, and dislocation density for the {100} sectors of potash alum.

Equally important to dislocation enhancement is the consequence of collisions between the particles in solution. This process is particularly effective when smaller colliding particles adhere to the surface of a principal particle. The subsequent overgrowth can result in the formation of additional mismatch dislocations and lead to an overall enhancement of growth rates¹⁷. Alternatively, variable numbers of mechanical dislocations can be produced as a consequence of the degree of plastic deformation that results in the impacted and fractured crystal. In some circumstances, these can develop as growth dislocations and influence the growth rate¹².

It is obvious that the noted variations in growth rate could result from any of these sources and that they could yield a range of growth rates sufficiently variable to yield a wide dispersion. What we cannot assume, however, is that their absence would yield a zero growth rate. There are well-defined mechanisms of crystal growth which allow growth on dislocation-free crystals^{18,19}. Thus we can only expect that dislocation based processes will provide a dispersion which will range from some minimum to a maximum value. For the suppression of growth, and particularly zero growth we must look to the influence of lattice strain on the growth process.

3. STRAIN REDUCTION OF GROWTH RATES

3.1 Large Crystals (~ 1cm dimension)

In order to assess the influence of strain on crystal growth, large specimens were mounted in a growth cell furnished with a means of straining the crystal during the growth process¹². The result of this procedure is shown for the {100} habit faces of potash alum in Fig. 3.

This confirms that the growth rate decreases on straining and is recoverable on removing the stress. It can be also restored to the original growth rate by an increase in supersaturation. Hence the process is reversible provided that plastic deformation does not occur. Application of a high tensile stress resulted in a decrease in growth rate to zero.

Extension of the experiments to other materials showed, as might be expected, that the magnitude of the effect depended on the mechanical nature of the material⁸. Potash alum is a brittle material of low plasticity and tensile extension of this material yields the formation of only small numbers of mechanical dislocations. In contrast, and under similar conditions, sodium chlorate, which is even more brittle fractures before plastic deformation occurs, undergoes a more significant reduction in growth rate when the stress is applied²⁰.

This progression was underscored by further studies of sodium nitrate. On extension, this ductile material does not show the sudden changes in growth rate of the two previous materials. A more gradual change occurred which was followed by partial recovery as the material plastically deformed (Fig. 4).

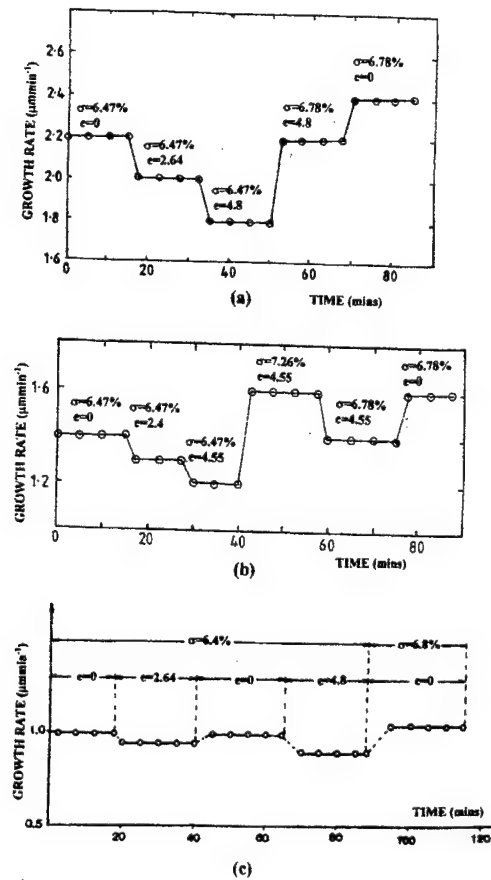


Fig. 3. The influence of tensile microstrain (e) and supersaturation (σ) on the growth rates of the (a) {100}, (b) {110}, (c) {111} faces of potash alum single crystals as a function of time.

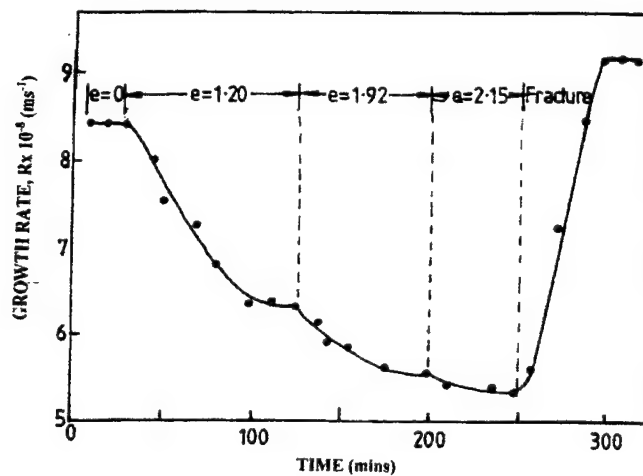
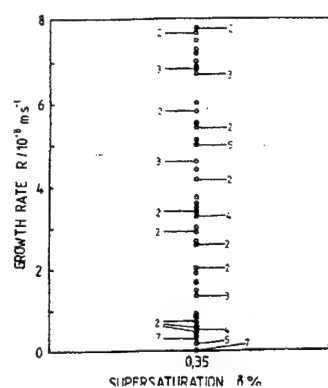
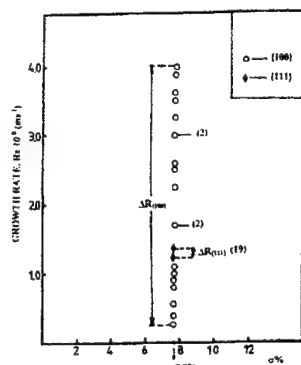
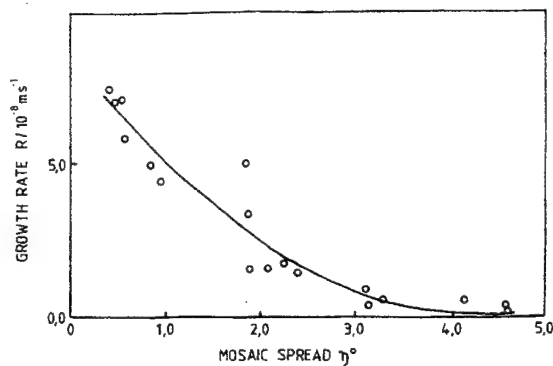


Fig. 4. The influence of successive applications of tensile microstrain (e) on the growth rate of sodium nitrate single crystals (σ = 0.4%)

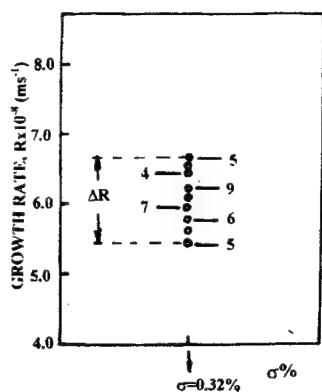
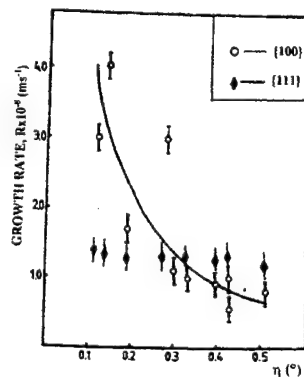
In summary, our studies of the influence of tensile strain on the growth rates of large crystals show a reduction of growth rate with increasing strain and zero growth under high strain conditions. They also indicate that the degree to which the reduction occurs is highly dependent on the brittle/plastic nature of the material.



(a)



(b)



(c)

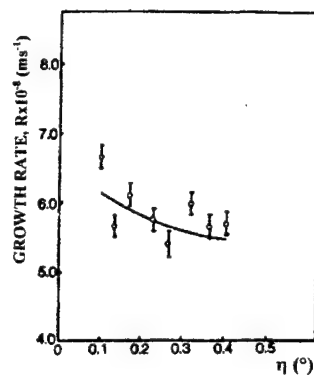


Fig. 5. Graphs showing the growth rate dispersion of microcrystals of Sodium chlorate, {100} faces, (b) Potash alum, {100} and {111} faces and (c) Sodium nitrate {104} faces at constant supersaturation (left hand column) together with graphs showing the relationship between the growth rates and integral strain in the particles (right hand column). The strain is expressed as mosaic spread η .

3.2 Microcrystals (~ 50-100 μm dimension)

The above variations refer to the behaviour of crystals some 200 times larger than those usually formed in industrial crystallisers. The question that must be answered is whether or not the same philosophy can be applied over the smaller size range more characteristic of the industrial product. Whilst there is no problem in assessing the growth rates of such crystals, it might be anticipated that the measurement of strain could present some difficulties. Happily, with the advent of large synchrotron sources producing polychromatic X-ray beams of high intensity, low divergence and high collimation, methods are now available^{4,21} for the assessment of the integral strain in very small crystals ($>100\ \mu\text{m}$) from the asterism which induced strain causes in Laue diffraction patterns²².

Measurements of growth rate dispersion on our three chosen materials are presented in Fig. 5, together with the relationships in each case between the growth rate and the mosaic spread of the crystal. There is a distinct correlation between the growth rates and the mosaic spread (induced strain). Immediately noticeable from these data is the fact that over the range, the degree of growth rate dispersion and the amount of induced strain varies in the order, sodium chlorate $>$ potash alum $>$ sodium nitrate. This reflects the increasing plasticity of the materials.

These distinctions mirror the experiments which were carried out on the larger crystals and serve to confirm that, although the size difference is large, the results of experiments on large crystals can be used to speculate on the behaviour of small crystals of these materials.

Thus, we confirm a significant influence of mechanical and growth induced lattice strain on the growth rates of crystals. That this is dependent on the mechanical characteristics of these materials is not surprising. When combined with the present and previous studies of the influence of dislocations on crystal growth, it offers an explanation of the range of growth rate dispersion including zero growth. It remains, however, to define the mechanistic basis of the process and to explain such factors as the size dependence of the effect.

4. MECHANISTIC STUDIES

In order to determine the mechanistic basis for the effect, it is necessary to have some means of defining in-situ a specific stress and, at the same time, to observe the nature and behaviour of growth sources on the crystal surface.

We have used two methods to develop such strain - radiation damage and the direct application of tensile stress to the crystal²³⁻²⁵. Simultaneously with the application of the stress, we have observed the form and development of the growth sources using an interferometric technique²⁶.

Both techniques for the introduction of strain to the samples show that the principle influence of strain is to slow the movement of the growth steps across the surface of the crystal. Within the space allotted it is not possible to present the detail of all experiments. The results of a typical tensile experiment are shown in Fig. 6. Using a more sophisticated version of the simple tensile stress system used in our earlier experiments²⁷ we have performed simultaneously stress/strain experiments during growth and interferometric examination of the crystal surface.

In Fig. 7 we present interferograms taken at various points during the straining of a paracetamol crystal²⁸. In Fig. 7 we show the overall dependence of growth rate on stress. The curvature observed fits well with the nature of the material. Paracetamol shows a well-defined plastic behaviour that has been shown to take place by slip of dislocation of the types $\{110\}$ $[001]$ and $\{111\}$ $[001]$ ³¹. Thus we would expect that the initial rapid development of elastic strain would give way to a slower relaxation in this factor as the plasticity develops. In parallel, there would be noted a fall off in the inhibition of the growth rate.

From the interferograms, it will be detected readily that there is an increase in the spacing of the interference fringes as the stress is increased. This corresponds to a decrease in the tangential velocity of the underlying growth steps. Similar results were obtained with both types of experiment; radiation induced strain and tensile induced strain and we can confidently claim that the principal influence of strain on the growth process is its influence on the initiation and development of the growth sources.

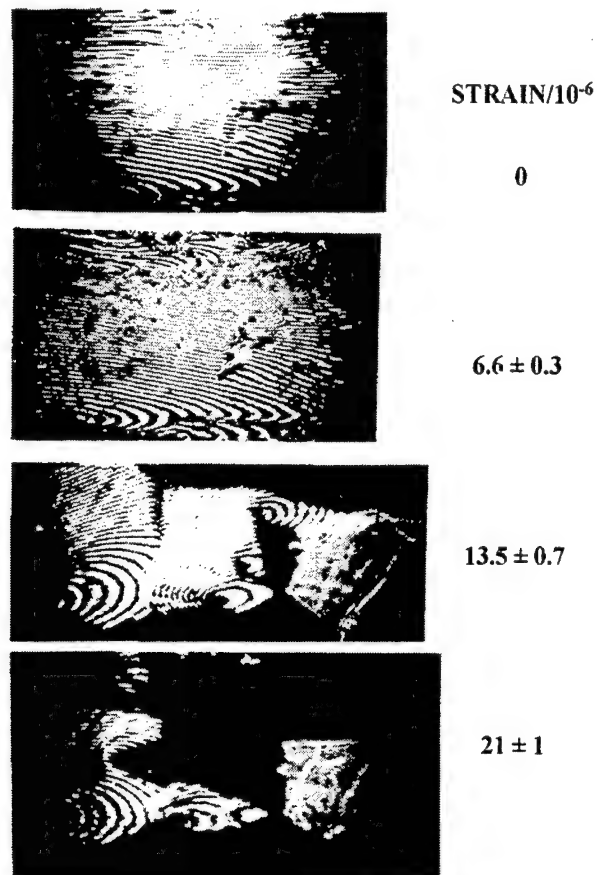


Fig. 6. Interferograms of the growth of a (001) surface of paracetamol as a function of applied tensile strain.

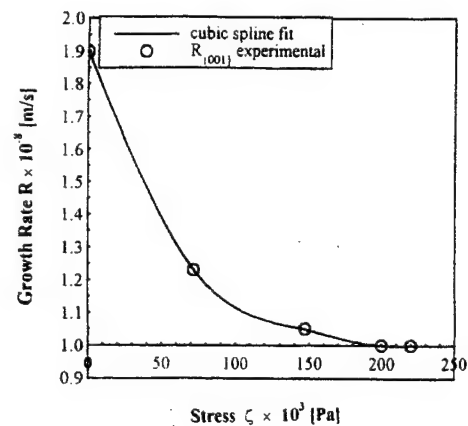


Fig. 7. The dependence of the growth rate of paracetamol (001) surfaces on applied tensile strain.

5. THEORETICAL BASIS

The development of the strain at the crystal surface could influence growth processes in two ways. Firstly, the surface-free

energy will increase, which can effect the nucleation of growth steps and their propagation over the surface. Secondly, the chemical potential of the surface (μ_s) will increase thus decreasing the driving force for crystallisation $\delta\mu = \mu_1 - \mu_s$ (μ_1 is the chemical potential of the liquid phase).

Let us consider first an active dislocation that emerges on the unstrained crystal surface. The dislocation core is surrounded by an elastically distorted (stressed) region of energy $\epsilon_{\text{disl}} \approx Gb^2/8\pi^{2/3}$, where G is the shear modulus, b is the modulus of the Burgers vector and r is the distance from the dislocation core to the point of observation. The elastic energy of one molecule is then $\Omega\epsilon_{\text{disl}}$, where Ω is the specific molecular volume. Chernov has shown⁵ that this elastic energy could be sufficient to increase significantly the chemical potential of the crystal over distances of the order of the radius of the critical nucleus. As a consequence, the local solubility around a dislocation, will increase by an amount defined as $\sigma_{\text{disl}} = \epsilon_{\text{disl}}\Omega/kT$. It follows from this expression that a necessary condition for keeping the dislocation active, in terms of nucleating growth steps, is that the absolute value of supersaturation acting in reality upon the central part of the spiral must be higher by $\Omega\epsilon_{\text{disl}}$ relative to the equilibrium state. In other words, the elastic energy hinders the nucleation of steps and helps dissolution at the dislocation core.

Applying the same philosophy to the more generally strained crystals, it is reasonable to assume that the elastic energy around the dislocations will be increased by a certain amount compared with that of the unstrained crystal. The greater the elastic strain, the higher the supersaturation required to render the dislocations active. This explains the passive role of dislocation sources in the strained crystals in the region of low supersaturation below the critical supersaturation. Instead, dissolution takes place, accompanied by the growth of unstrained portions of the crystals.

The second factor that defines the growth kinetics of strained crystals is the velocity of migration of steps over the crystal surface. This factor assumes an important role as soon as the face starts growing. Thus, the current evidence points to the influence of strain on growth step propagation as the principal cause of growth rate dispersion.

More work requires to be done to define the mechanistic basis for the influence of strain on growth. The present results do however point to the need for more detailed, direct studies of the influence of strain on both nucleation and growth step velocities. These can only come from the close examination of the influence of strain on the development of the growth centres on the crystal surface. To this end, in-situ atomic force microscopy studies of selected materials are proposed and will be reported in due course.

6. CONCLUSIONS

In conclusion, we feel confident that growth rate dispersion is primarily a consequence of stress reduction of the growth rate of small particles following fracture and refacetting. Effectively, we envisage a series of particles propagating at a narrow range of growth rates dependant on the dislocation density at the surfaces. These growth rates are then reduced by the inhibiting factor of any integral strain. At the smallest particle sizes the strain contribution is dominant with the result that zero (or very small) growth rates can be observed in highly strained crystals. Gradual increase in crystal size leads to the strained material being covered with unstrained material resulting in an increasing dominance of the dislocation contribution. As a result the lower limit to the growth rate dispersion rises with increasing particle size until the average growth rate is reached.

The upper boundary of the range of dispersion represents dominantly dislocation controlled growth. However the increase in particle size leads to a rapid decrease in dislocation density (the controlling factor) with a parallel fall-off in the growth rate to the average. Beyond the limit of convergence the strained core of the crystal is completely covered with unstrained material and the strain becomes ineffective. Within the upper size range of the small particles which form in industrial crystallizers and in crystals bigger than these the dislocation density remains fairly constant, as does the average growth rate.

The influence of stress is very much dependent on the mechanical properties of the material which defines the size range over which this model will operate. This concept offers the potential for the development of empirical models for the prediction of growth rate dispersion in a wider range of materials.

A more extended review of this work can be found in a recent article by the author and his principal co-worker Dr R. I. Ristic³⁰.

ACKNOWLEDGEMENTS

This work could not have been accomplished without the careful assistance of a number of people involved in the development of the concepts and equipment used in the experiments. We express our grateful thanks to these whose contributions are acknowledged in the many joint publications which are quoted below.

Our grateful thanks are also extended to those external bodies which provided the essential financial support to allow the

work to take place. These include the UK EPSRC, through a continuing series of research grants, Imperial Chemical Industries through their Joint Research Scheme and the pharmaceutical companies; Pfizer, Roche and Smithkline Beecham who jointly with the EPSRC, supported the latter stages of the work

REFERENCES

1. P.D.B. Bujac in *Industrial Crystallisation*, edited by J.W. Mullin p. 23, Plenum NY, 1976.
2. J. Nyvlt, O. Sohnel, M. Matuchova and M. Broul, *The Kinetics of Industrial Crystallisation* p. 105 Academia, Prague, 1985.
3. J. Garside, I. I. Rusli and M. A. Larson, *Am. Inst. Chem. Eng.*, **25**, p. 57, 1979.
4. C. Y. Sung, J. Estrin and G. Y. Youngquist, *Am. Inst. Chem. Eng.*, **19**, p. 957, 1973.
5. Chernov, *Contemporary Physics*, **30**, p. 251, 1989.
6. J. Garside, G. Webster, R.J. Davey and A.J. Ruddick in *Industrial Crystallisation*, edited by S. Jancic and E.J. de Jong, p.459, Elsevier, Amsterdam, 1984.
7. R.I. Ristic, J.N. Sherwood and K. Wojciechowski, *J. Crystal Growth*, **91**, p. 163, 1988.
8. R.I. Ristic, J.N. Sherwood and T. Shripathi in *Industrial Crystallisation*, edited by A. Mersmann, p. 349, 1990.
9. H.L. Bhat, J.N. Sherwood and T. Shripathi, *Chem. Eng. Sci.*, **42**, p. 609, 1987.
10. J.N. Sherwood and T. Shripathi, *J. Crystal Growth*, **88**, p. 358, 1988.
11. J.N. Sherwood and T. Shripathi, *Faraday Discuss.*, **95**, pp. 173-182, 1993.
12. R.I. Ristic, J.N. Sherwood and T. Shripathi, *J. Crystal Growth*, **179**, pp. 194-204, 1997.
13. W.K. Burton, N. Cabrera and F.C. Frank, *Philos. Trans. Roy. Soc.*, London, Ser.A, **243**, p. 299, 1953.
14. Yu. G. Kunetsov, A. A. Chernov, P. G. Vekilov and I. L. Smol'sky, *Soviet Phys. Crystallogr.*, **32**, p. 584, 1987.
15. A. Chernov, Yu G. Kuznetsov, I. L. Smol'sky and V. N. Rozhansky, *Soviet Phys. Crystallogr.*, **31**, p. 705, 1986.
16. A.R. Lang in *Modern Diffraction and Imaging Techniques*, edited by S. Amelinckx et al, p.407, N. Holland, Amsterdam, 1970.
17. H. Takiyama, N. Tezuka, M. Matsuoka, R.I. Ristic and J.N. Sherwood, *J. Crystal Growth*, **192**, pp. 439-447, 1988.
18. Y. Kuznetsov and A.A. Chernov, *Sov. Phys. Crystallogr.*, **31**, p. 709, 1988.
19. A.A. Chernov and A.I. Malkin, *J. Crystal Growth*, **92**, p. 432, 1988.
20. R.M. Hooper, K.J. Roberts and J.N. Sherwood, *J. Materials Sci.*, **18**, pp. 81-88, 1983.
21. R. Gerson, P. J. Halfpenny, S. Pizzini, R.I. Ristic, K. J. Roberts, D.B. Sheen, and J.N. Sherwood, "Characterisation of Materials" in *Materials Science and Technology*, edited by R. W. Cahn, P. Haasen and E. J. Kramer. Vol 2A (Volume Editor E. Lifshin), pp. 551-618, VCH, Weinheim, 1992.
22. M.M. Mitrovic, R.I. Ristic and I. Ciric, *Appl. Phys.*, **A51**, p. 374, 1990.
23. P.J. Halfpenny, R.I. Ristic, J.N. Sherwood and G.S. Simpson, *J. Mater. Chem.*, **3**, p. 407, 1993.
24. H.L. Bhat, A. Littlejohn, J.M.R. McAllister, J. Shaw, D.B. Sheen and J.N. Sherwood, *Mater. Sci. Monographs*, **286**, p. 707, 1985.
25. R.I. Ristic, B.Y. Shekunov and J.N. Sherwood, *J. Crystal Growth*, **179**, pp. 205-212, 1997.
26. A.A. Chernov, L.N. Rashkovich and A.A. Mkrtchan, *J. Crystal Growth*, **74**, p. 101, 1988.
27. Zikic, R.I. Ristic and J.N. Sherwood, *Rev. Sci. Instrum.*, **69**, pp. 2713-1719, 1998.
28. Zikic, R.I. Ristic and J.N. Sherwood, to be published, 2000.
29. J.P. Hirth and J. Lothe in *Theory of Dislocations*, p. 210, McGraw Hill, NY, 1968.
30. J.N. Sherwood and R.I. Ristic, *Chem. Eng. Sci.*, In Press, 2000.

Crystal growth of new functional materials for electro-optical applications

T.Fukuda*, K.Shimamura, A.Yoshikawa and E.G.Villora

Institute for Materials Research, Tohoku University, Sendai 980-8577, Japan

ABSTRACT

High quality fluoride and oxide single crystals for optical, piezoelectric and other applications have been grown by advanced crystal growth techniques. Corquitiite- and Perovskite-type fluoride single crystals – LiCaAlF_6 , LiSrAlF_6 , KMgF_3 and BaLiF_3 – have been grown for solid state UV laser applications, and as window materials for next generation optical lithography. $\text{La}_3\text{Nb}_{0.5}\text{Ga}_{5.5}\text{O}_{14}$ and $\text{La}_3\text{Ta}_{0.5}\text{Ga}_{5.5}\text{O}_{14}$ piezoelectric single crystals of size and quality comparable to $\text{La}_3\text{Ga}_5\text{SiO}_{14}$ (langasite), have been produced. The piezoelectric and device properties of the crystals were investigated. A search for new langasite-type materials was also performed. Promising new structural materials, $\text{Al}_2\text{O}_3/\text{RE}_3\text{Al}_5\text{O}_{12}$ (RE=rare earth) eutectic fibers, have been grown by the micro-pulling-down (μ -PD) technique. Undoped and doped β - Ga_2O_3 single crystals have been grown by the floating zone technique as promising transparent conductive oxides.

1. INTRODUCTION

The important role of oxide and fluoride crystals in various branches of science and technology demands a comprehensive and integrated treatment of the subject. We have carried out investigations focusing on the development of new materials for optical, piezoelectric and other applications, using advanced crystal growth techniques. Oxide crystals are of highest importance for modern electrical and electro-optical applications in several devices. Fluoride single crystals, because of their unique properties such as large band gap, also present many advantages as optical materials.

The recent crystal growth research described in this work involved the development of new, high-quality oxide and fluoride single crystals, and of novel crystal growth techniques. The growth of fluoride single crystals doped with Ce for ultra-violet (UV) laser applications is reviewed. Growth of new langasite ($\text{La}_3\text{Ga}_5\text{SiO}_{14}$) single crystals for piezoelectric applications, by the Czochralski (CZ) technique, is discussed. The micro-pulling-down (μ -PD) method and its application to the growth of structural materials are mentioned. Crystal growth of β - Ga_2O_3 for transparent conductive oxide (TCO) applications is also addressed.

2. FLUORIDES FOR UV OPTICAL APPLICATIONS

Coherent optical sources in the ultraviolet (UV) wavelength region are useful for many practical applications, such as medical procedures, semiconductor processing and remote sensing¹. Recently, Ce-doped LiCaAlF_6 (Ce:LiCAF) and LiSrAlF_6 (Ce:LiSAF) single crystals have been reported as leading candidates for tunable all-solid-state-lasers in the UV wavelength region^{2,3}. However, due to the limited size of the available crystals, it was difficult to obtain high energy output directly from a Ce:LiCAF laser. Furthermore, the growth of Ce:LiCAF itself was known to be difficult⁴.

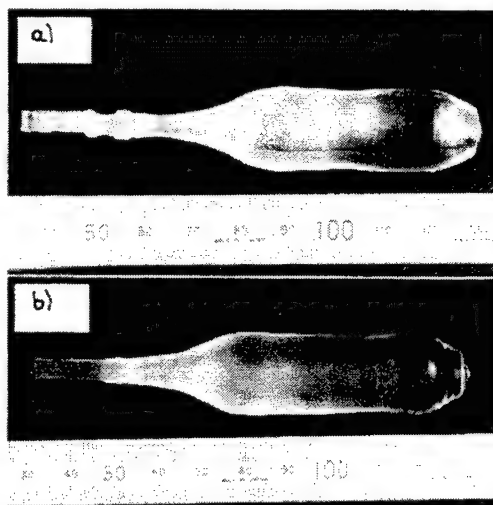


Fig.1 As-grown Ce-doped (a) LiCaAlF_6 and (b) LiSrAlF_6 single crystals.

* T.F.: Email: fukuda@lexus.imr.tohoku.ac.jp; Telephone: +81-22-215-2100; Fax: +81-22-215-2101
K.S.: Email: shimak@lexus.imr.tohoku.ac.jp; Telephone: +81-22-215-2103; Fax: +81-22-215-2104
A.Y.: Email: yoshikaw@lexus.imr.tohoku.ac.jp
E.G.V.: Email: villora@lexus.imr.tohoku.ac.jp

Crystal growth was performed in a CZ system with a resistive heater made of high-purity graphite. The starting material was prepared from commercially available AlF_3 , CaF_2 , SrF_2 , and LiF powders of high purity (>99.99%). The composition was 1 mol.% LiF and AlF_3 enriched from a stoichiometric one, in order to compensate for the vaporization of LiF and AlF_3 . As dopants, CeF_3 and NaF powders of high purity (>99.99%, Rare Metallic Co., Ltd.) were used. Na^+ was co-doped with Ce^{3+} in order to maintain the charge neutrality. The concentration of Ce^{3+} and Na^+ in the starting material was 1 mol.%. The pulling rate was 1 mm/h and the rotation rate was 10 rpm. Crystal growth was performed under high purity CF_4 gas (99.9999%).

Fig.1 shows as-grown Ce:LiCAF and Ce:LiSAF single crystals with dimensions of 18 mm in diameter and 60 mm in length. Cracks, bubbles and inclusions were not observed. Under the modified growth conditions, foreign substances on the surface of the grown crystal, as observed in ref.5, were not formed. However, Ce:LiSAF showed a tendency to crack perpendicular to the growth axis after several days. On the contrary, Ce:LiCAF did not show cracks at any time. Therefore, LiCAF was chosen for the growth of large diameter crystals. The effective distribution coefficient (k_{eff}) of Ce^{3+} in LiCAF and LiSAF has been determined to be 0.021 and 0.013, respectively. The k_{eff} of Ce^{3+} in LiCAF was larger than in LiSAF . This is because the ionic radius of Ce^{3+} under 6-fold coordination (1.01 Å) is closer to that of Ca^{2+} (1.00 Å) than to that of Sr^{2+} (1.18 Å)⁶, the ions thought to be replaced by Ce^{3+} ⁵.

Fig.2 shows an as-grown Ce:LiCAF single crystal of 2-inch diameter, free from cracks and inclusions. When crystals of this diameter were grown, the following two problems, not observed for crystals of 18 mm diameter, appeared: formation of inclusions, and cracks accompanied by the formation of an impurity phase at the bottom of the crystal.

Fig.3 shows a crystal which contains inclusions. It should be noticed that the formation of these inclusions was related to a change of the crystal diameter, for example at the shoulder part of the crystal. Once they appeared at the shoulder part, they did not disappear during crystal growth. In order to avoid these inclusions, the diameter at the shoulder part had to be controlled precisely and extended smoothly, without rapid change of the diameter. Although the absorption spectrum for the inclusion free region did not show any absorption peaks, that of the region with inclusions had one small absorption peak around 3600 cm^{-1} . Since this peak indicates the existence of OH^- , it is thought that H_2O based impurities were present in the inclusions.

Fig.4 shows an as-grown crystal with one large crack along the growth axis and a white substance at the bottom of the crystal. This large, flat crack appeared during cooling after growth, in cases when white material was present. This white substance usually formed when the solidification fraction exceeded 70 %. The XRD analysis showed that the white substance was composed of LiCAF and CaF_2 phases. This is because the melt composition shifted in the CaF_2 -enriched direction during growth, since the vaporization pressure of LiF and AlF_3 is very high⁷. CeF_3 and NaF might have accumulated in the residual melt due to the small k_{eff} . In order to avoid formation of this white substance, crystal growth was terminated at the solidification fraction 60 %, as for the crystal shown in Fig.2. For further improvement, optimization of melt composition should be carried out.

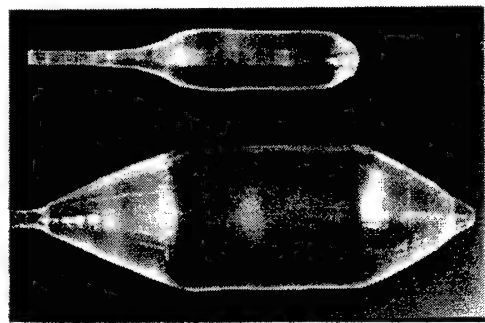


Fig.2 2 inch size Ce:Na:LiCaAlF_6 single crystal. compared with 1 inch crystal.

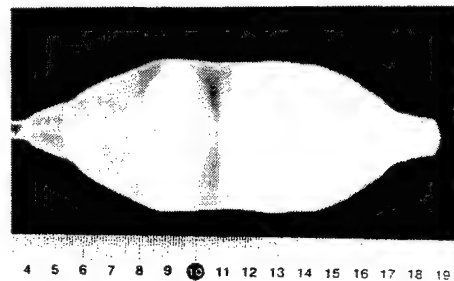


Fig.3 Ce:LiCaAlF_6 crystal with inclusions.

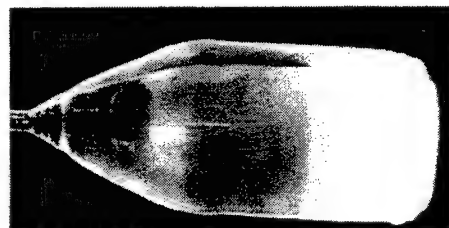


Fig.4 Ce:LiCaAlF_6 crystal with white substances.

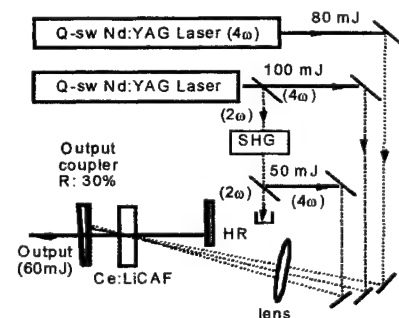


Fig.5 Ce:LiCaAlF_6 laser setup.

We have already demonstrated an output energy of 30 mJ from a UV solid-state Ce:LiCAF laser that operated at 290 nm at a repetition rate of 10 Hz^{5,8}. In order to obtain higher output energy, we increased the pumping energy. Fig.5 shows a setup for laser experiments. We obtained 60 mJ at 10 Hz, to our knowledge the highest performance so far reported for Ce:LiCAF.

Fig.6 shows the transmission edge of the LiCAF and LiSAF single crystals grown under Ar and CF₄ atmosphere. The transmission edge of LiCAF was measured to be at 112 nm and that of LiSAF 116 nm, the shortest reported to our knowledge. The absorption at around 125 nm observed from the crystals grown under Ar atmosphere, disappeared when crystals were grown under CF₄ atmosphere. These transmission characteristics of LiCAF and LiSAF show their high potential as optical window materials in the UV and VUV wavelength region.

Recently, there has been significant interest in using 157-nm laser sources in projection lithography as successors to 193-nm based system. One of the most serious problems in realizing a 157-nm based system is the development of suitable optical materials for lenses and other optical components. In particular, for an all-refractive design of 157-nm laser source, a second material other than CaF₂ is strongly required, because CaF₂ is the most promising material to be used. Primary candidates for a second material were LiF and MgF₂; however, they have several disadvantages such as a fragile and hygroscopic nature and large birefringence⁹.

We have identified KMgF₃ (KMF) as a new promising optical material for 157-nm based system. The reasons to focus on KMF are as follows: (1) It belongs to the cubic crystal system¹⁰, so theoretically it has no birefringence. (2) As it is composed of K and Mg cations, which have smaller atomic weight than Ca, it can be expected to have a shorter transmission edge than CaF₂. (3) As it melts congruently at a melting temperature of 1070 °C¹¹, it can more likely be grown to a large size. BaLiF₃ (BLF) can also be a promising candidate, since it belongs to the cubic crystal system¹² and it can transmit 157-nm.

Crystal growth was performed in the same CZ system as for LiCAF and LiSAF. The starting material was prepared from commercially available high purity powders (>99.99%). The pulling rate was 0.5 to 1.5 mm/h and the rotation rate was 15 rpm.

Fig.7 shows an as-grown KMF and BLF single crystals 20 mm in diameter and 90 mm in length, pulled at a rate of 1 mm/h. No cracks, bubbles or inclusions were observed. The thermal expansion coefficients of KMF and BLF along <111> was estimated to be $1.98 \times 10^{-5} \text{ K}^{-1}$ and $3.06 \times 10^{-5} \text{ K}^{-1}$, respectively, over the range 100 - 500 °C. The variations of birefringence among KMF-wafer, BLF-wafer and LiCAF-wafer were of order 10^{-7} , 10^{-5} , and 10^{-7} , respectively. Furthermore, the transmission edge of KMF and BLF single crystals was determined to be 115 nm and 120 nm. Fig.6 shows the transmission spectrum of KMF and BLF single crystals in VUV wavelength region, compared with LiCAF and LiSAF. These transmission characteristics of KMF and BLF single crystals shows its high potential as optical material in the UV and VUV wavelength region.

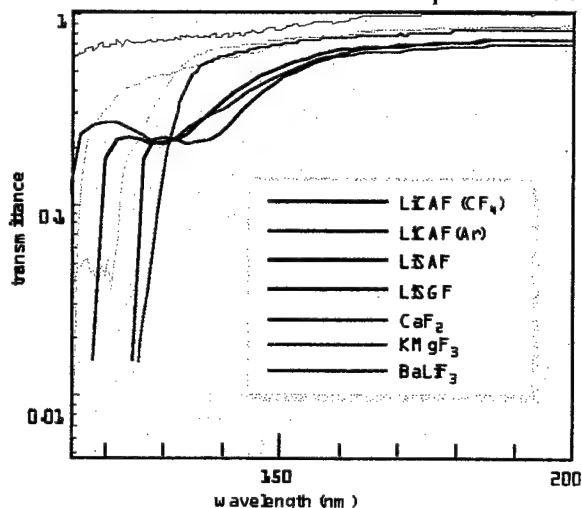


Fig.6 Transmission spectra of different fluoride single crystals.

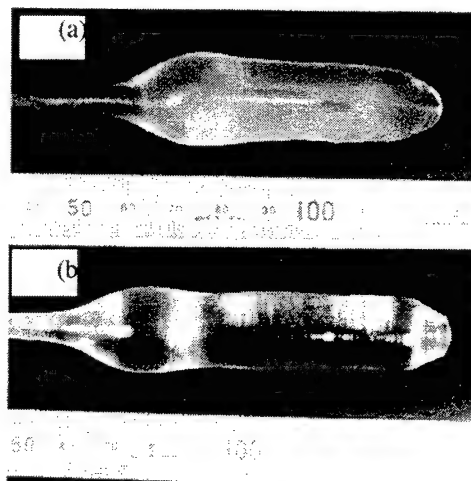


Fig.7 (a) KMgF₃ and (b) BaLiF₃ single crystals

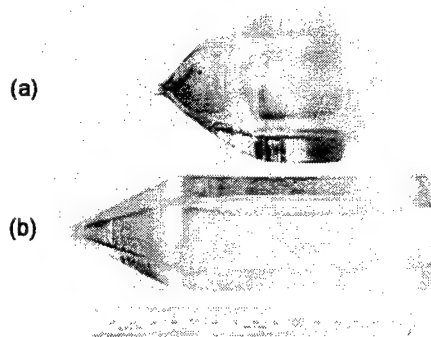


Fig.8 La₃Ta_{0.5}Ga_{5.5}O₁₄ single crystals (a) 3-inch (b) 2-inch diameter.

3. NEW LANGASITE SINGLE CRYSTALS FOR PIEZOELECTRIC APPLICATIONS

The recent progress of electronic technology requires new piezoelectric crystals having properties intermediate between those of quartz and LiTaO_3 (LT). Currently, Languisite ($\text{La}_3\text{Ga}_5\text{SiO}_{14}$; LGS) crystals have received attention as new candidates for piezoelectric applications^{13,14}.

The LGS crystal has the $\text{Ca}_3\text{Ga}_2\text{Ge}_4\text{O}_{14}$ -type structure with the space group P321. There are four kinds of cation sites in this structure, which can be described by the chemical formula, $\text{A}_3\text{BC}_3\text{D}_2\text{O}_{14}$. In this formula, A and B represent the decahedral (twisted Thomson cube) site coordinated by 8 oxygens, and the octahedral site coordinated by 6 oxygens, respectively. C and D represent tetrahedral sites coordinated by 4 oxygens. Different isovalent and aliovalent substitutions in a given structure are quite interesting in themselves, and could, perhaps, also result in useful structural and physical properties.

High-quality single crystals of LGS, and its aliovalent analogs $\text{La}_3\text{Nb}_{0.5}\text{Ga}_{5.5}\text{O}_{14}$ (LNG) and $\text{La}_3\text{Ta}_{0.5}\text{Ga}_{5.5}\text{O}_{14}$ (LTG), were grown by the conventional CZ technique¹⁵. Fig.8 shows the as-grown LTG single crystals of approximately 2 and 3 inches diameter. Pulling and rotation rates were 1mm/h and 10 rpm, respectively.

Lattice parameters of the grown crystals were found to be almost constant from shoulder to tail of the boules. Concentrations of each oxide, *i.e.* La_2O_3 , Ga_2O_3 , SiO_2 , Nb_2O_5 and Ta_2O_5 , were almost constant, within the estimated errors, throughout the crystallizing process. The uniformity of lattice parameter and chemical composition suggests that the stoichiometric composition is close to the congruently melting composition of the three compounds.

Synthesis of more than 70 chemical compositions were attempted. The incorporation of different A cations (Na^+ , Ba^{2+} , Sr^{2+} , Bi^{3+} , Nd^{3+} , etc) and B cations (Li^+ , Mg^{2+} , Ga^{3+} , Ti^{4+} , Sb^{5+} , Mo^{6+} , etc) into the A and B sites was studied, respectively. Materials which showed a langasite-type single phase were crystallized in fiber form by the μ -PD method, and subsequently their bulk crystals were also grown by the Cz technique. Bulk single crystals of $\text{Sr}_3\text{Ga}_2\text{Ge}_4\text{O}_{14}$, $\text{Na}_2\text{CaGe}_6\text{O}_{14}$, $\text{Pr}_3\text{Ga}_5\text{SiO}_{14}$ and $\text{La}_3\text{Al}_x\text{Ga}_{5-x}\text{SiO}_{14}$ were successfully produced by Cz technique. In Fig.9, $\text{La}_{3-x}\text{Sr}_x\text{Ta}_{0.5+x/2}\text{Ga}_{5.5-x/2}\text{O}_{14}$, $x=0.1554$ (LSTG) and $\text{Sr}_3\text{TaGa}_3\text{Si}_2\text{O}_{14}$ (STGS) single crystals are shown as examples.

Using LGS single crystals, we made monolithic-type filters (10.4 and 21.4 MHz) as seen in Fig.10. The electrical properties of these filters include low input and output impedance, small size and low attenuation, compared with those made of quartz (see Table I).

A 71MHz-wide passband SMD (Surface Mount Discrete-type) filter for the GSM (Global System for Mobile Communication) base station was also made, which exhibited superior properties. The main features of the electrical characteristics are listed below:

(1) Low input and output impedance ($940\Omega/0.5\text{pF}$, versus several $\text{k}\Omega$ for quartz filter);

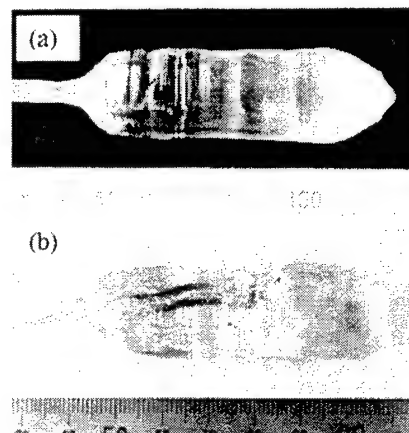


Fig.9 (a) $\text{La}_{3-x}\text{Sr}_x\text{Ta}_{0.5+x/2}\text{Ga}_{5.5-x/2}\text{O}_{14}$, $x=0.1554$ and (b) $\text{Sr}_3\text{TaGa}_3\text{Si}_2\text{O}_{14}$ single crystals

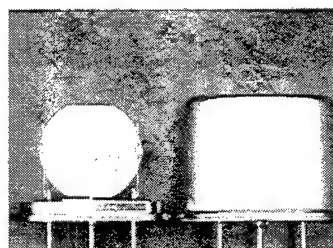


Fig.10 21.4MHz filter made of $\text{La}_3\text{Ga}_5\text{SiO}_{14}$ single crystal (size: $6.9 \times 5.8 \times 2.2 \text{ mm}^3$).

Table I Electrical properties of LGS monolithic-type filters compared with quartz ones.

Frequency (MHz)	Material	Passband Width (3 dB) (kHz)	Attenuation (dB)	Input-Output Impedance ($\text{k}\Omega$ // pF)
10.7	quartz	3 ± 1.5	2.5	$5.5 \text{ k} // -1.0$
	LGS	3 ± 1.5	2.0	$2.5 \text{ k} // 1.7$
21.4	quartz	3 ± 1.5	2.0	$2.0 \text{ k} // 0.5$
	LGS	3 ± 1.5	2.0	$8.0 \text{ k} // 4.0$
	LGS	3 ± 1.5	2.0	$1.3 \text{ k} // 1.7$

- (2) Interstage coupling requires only capacitors (For quartz filter, transfer is required);
 (3) Electrode gap may be wide (approximately 100mm, vs. several mm for quartz filter).

Table II Characteristics of LNG, LTG and LGS compared with those of LT and quartz.

	LiTaO ₃	LGS	LNG	LTG	quartz
phase transition	exist	none	none	none	exist
melting point (°C)	1650	1490	1470	1500	—
Mohs hardness	5.5	6~7	6~7	6~7	7
electromechanical coupling factor k (%)	43	15~25	~30	~30	7
Q-factor	5000	30,000~ 40,000	40,000~ 60,000	40,000~ 60,000	60,000~ 80,000
equivalent series resistance (Ω)	—	5~10	2~5	2~5	10~20
thermal stability (ppm) (-20~70°C)	200~400	~150	~150	~150	10~20

In Table II, the characteristics of LNG, LTG and LGS are given, along with those of LT and quartz. Since LNG, LTG and LGS have no phase transitions and have lower melting point and higher hardness, the possibility of growing high-quality crystals allowing easy processing is expected to be likely. Their electromechanical coupling factors k and thermal frequency stability are between those of LT and quartz. The above characteristics indicate that LGS-family crystals are more promising materials for piezoelectric devices than lithium tetraborate (Li₂B₄O₇) and berlinite single crystals, which have similar piezoelectric properties¹⁴.

Li₂B₄O₇ is easily soluble in all acids and bases, and easily deliquescent in air, while berlinite single crystals are difficult to grow to a large size.

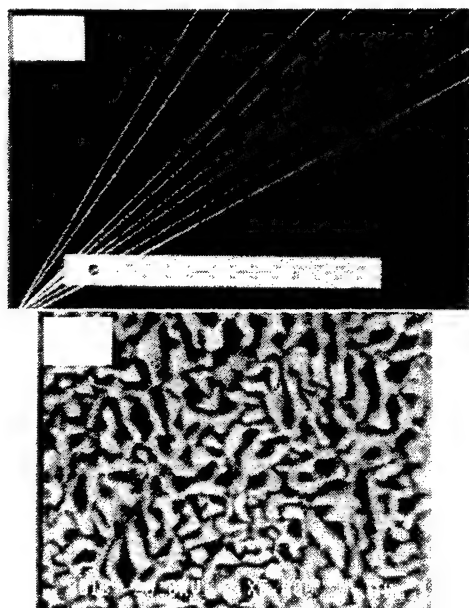


Fig.12 (a) Eutectic fibers and (b) back scattered electron image of Al₂O₃/Y₃Al₅O₁₂ fibers.

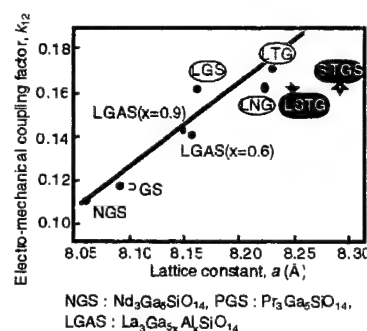


Fig.11 Electro-mechanical coupling factor vs. lattice constant.

Fig.11 shows the dependence of the electro-mechanical coupling factor, k_{12} , on the lattice parameter a in the langasite-type crystals. As can be seen from the figure, an increase in lattice parameter a leads to an increase of the electro-mechanical coupling factor, k_{12} . The electro-mechanical coupling factor of LTG is the largest of the langasite-type crystals studied. Therefore, we conclude that substitution of the B site is effective for improvement of the piezoelectric properties. This tendency serves as a guide for development of improved compounds of langasite-type structure.

4. FIBER CRYSTALS

Directionally solidified ceramic eutectics are drawing a strong interest because of their high structural stability up to the melting temperature. Recently, promising results were reported for Al₂O₃/Y₃Al₅O₁₂ (YAG)¹⁶⁻¹⁸ and Al₂O₃/GdAlO₃¹⁹ systems. However, because of processing difficulties, the experimental data for oxide eutectics are still limited and often uncertain.

We have applied the μ -PD method for the growth of Al₂O₃/YAG

eutectic fibers. The μ -PD method involves downward pulling of a crystalline fiber 0.1-2.0 mm in diameter through a capillary hole arranged in a crucible bottom. The μ -PD features two points important for eutectic growth: (i) a very high axial temperature gradient exists near the growth interface of the order of $3-5 \times 10^3$ °C/cm²⁰. It permits high pulling rates and assures a planar interface and process stability. Secondly, (ii) composition is always uniform along the fiber length, since melt convection is impossible inside the narrow capillary channel.

A high-temperature version of μ -PD employed an iridium crucible directly coupled to the RF power generator. A sapphire <0001> seed was used for growth of the eutectic fibers. The starting materials were 4N purity Al₂O₃ and Y₂O₃ in the molar ratio of 81.3 mol % Al₂O₃ to 18.7 mol % Y₂O₃²¹.

Eutectic fibers 0.25-1.00 mm in diameter and up to 500 mm in length were grown over a range of pulling rate 0.15 - 10.00 mm/min (see Fig.12). Samples of eutectic fibers grown under various pulling rates were examined using scanning electron microscopy (SEM). Several fibers were grown at a step-variable pulling rate starting from 0.15 and up to 10 mm/min. In all these experiments, the 'Chinese script' type structure was found to possess excellent reproducibility, whereas the cellular structure was not found at all. (The microstructure of eutectic sometimes forms the structure, which is resembles to Chinese character. Such microstructure is called 'Chinese-script type' microstructure.) The volume fraction of YAG was 0.45 ± 0.02 for all types of structure including inter-cell areas, which corresponds exactly to the theoretical value for the eutectic composition (0.44). The characteristic script size was found to be very uniform for each cross-section studied. Experimentally, the generally accepted relation $\lambda \sim v_p^{-1/2}$, where λ is interlamellar spacing of a conventional lamellar structure and v_p is the solidification rate, also applies to the script structure of the Al₂O₃/YAG system. The constant of proportionality was found to be 10, if λ has dimensions of mm and v_p mm per second. This value is large enough to allow effective microstructure control by changing solidification rate

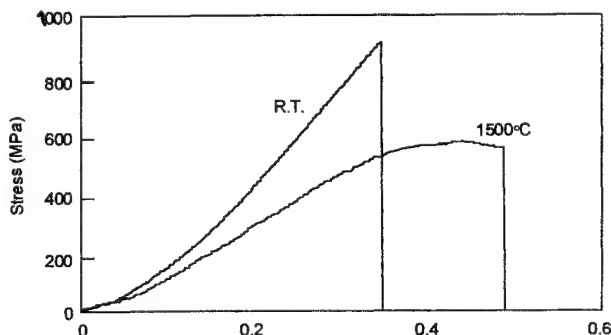


Fig.13 Tensile stress-displacement curves of Al₂O₃/Y₃Al₅O₁₂ eutectic fibers (grown in Ar gas atmosphere).

The composite has been shown to have high mechanical strength up to 1800 °C, excellent oxidation resistance, high thermal stability of microstructure and thermal shock stability (Fig.13). Al₂O₃/Tm₃Al₅O₁₂ showed a tensile strength of 620 MPa at 1500 °C in vacuum. This is the highest strength at this temperature to date.

5. β -Ga₂O₃ AS TRANSPARENT CONDUCTIVE OXIDE

β -Ga₂O₃ is transparent with a band gap of 4.8 eV, and belongs to the space group C2/m. It is intrinsically an insulator, but its n-type semiconduction when grown under reducing conditions is well known²². An undesired side effect is the resulting blue coloration, and thus degradation of the transmission, a fundamental property for window applications such as displays, solar cells, etc. Improvement of electrical conductivity through the addition of dopants while preserving the transparency of the pure β -Ga₂O₃ makes of this material a substitutive candidate for transparent conductive oxides (TCOs). Moreover, its shorter absorption edge will allow to extend the application fields of TCOs.

Powders of Ga₂O₃, WO₃ and HfO₂ of nominal 4N purity were mixed, sintered and grown to single crystals using the floating zone (FZ) technique with a double ellipsoid image furnace (ASGAL Co.:SS-10W). The growth was done under previously optimized conditions: growth rate of 5 mm/h, simultaneous rotation of feed and seed rods at 20 rpm in opposite directions, 500 ml/min. gas flow of different N₂/O₂ mixtures. The grown crystals had typical length of 3-4 cm, and diameter varying between 0.5 and 1 cm. For transmission and electrical measurements, crystals were cleaved in the (001) plane to obtain thin platelet-like samples, which exhibited flat, reflective surfaces.

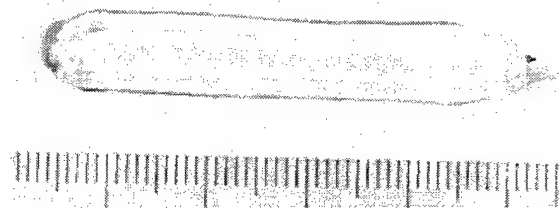


Fig.14. Nominally pure β -Ga₂O₃ single crystal grown under pure O₂ and a pressure of 2 atmosphere.

The optical and electrical properties of the as-grown crystals depended on the concentration of the dopants and on the

oxygen partial pressure. Crystal growth from nominally undoped feed rods under 1 atmosphere pressure was impossible due to the appearance and explosion of bubbles, which destabilized the molten zone. The formation of bubbles could be suppressed by the increase of pressure to 2 atmospheres (Fig.14), or by the incorporation of W or Hf as dopants. Fig.15 and Fig.16 show the crystals grown under pure O₂ and 1 atmosphere pressure, with a nominal composition of the feed rod of 6 mol.% WO₃ and 0.2 mol.% HfO₂, respectively. These crystals were visually homogeneous, transparent, colorless and without cracks or inclusions. Improved transmittance and conductivity could be also achieved, indicating the beneficial effects of the substitution of Ga³⁺ by W⁴⁺ or Hf⁴⁺ and the potential optimization of Ga₂O₃ properties for TCO applications.

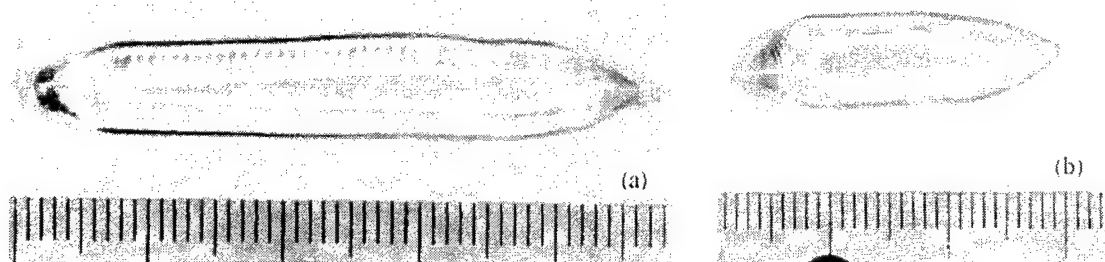


Fig. 15 (a) W-doped and (b) Hf-doped β -Ga₂O₃ single crystals grown under pure O₂, 1atm pressure.

6. CONCLUSIONS

Various new fluoride and oxide crystals were developed. Ce:LiCAF and Ce:LiSAF single crystals of 18 mm diameter were grown by the CZ technique under CF₄ atmosphere. Under the same growth conditions, Ce:LiCAF single crystals of 50 mm diameter (2 inch) were also grown up to a solidification fraction of 60 %. Laser output energy of 60 mJ was obtained. This demonstrates that Ce:LiCAF is a promising material for high-energy UV pulse generation. KMF and BLF single crystals of 20 mm diameter were also grown. LiCAF, LiSAF, KMF and BLF single crystals showed a transmission edge at 112 nm, 119 nm, 115 nm and 120 nm, respectively. These characteristics indicate the high potential of these crystals as optical materials. A series of new promising langasite-type materials were found. LGS, LNG and LTG single crystals with maximum size of 3 inches in diameter were successfully grown by the Czochralski technique. Prototype models of wide passband filters were prepared using these crystals. LGS, LNG and LTG single crystals showed to have superior piezoelectric properties compared to other compounds with properties intermediate between those of quartz and LT. By applying the high-temperature μ -PD technique, directionally-solidified eutectic Al₂O₃/REAG fibers were grown. Al₂O₃/Tm₂Al₂O₁₂ showed a tensile strength of 620 MPa at 1500 °C in vacuum. Undoped and doped β -Ga₂O₃ single crystals were grown by the FZ technique. The substitution of Ga³⁺ by W⁴⁺ or Hf⁴⁺ improved transmittance and conductivity, indicating the potential optimization of β -Ga₂O₃ properties for TCO applications.

ACKNOWLEDGMENT

The authors would like to acknowledge and thank to Associate Professor Dr.S.Durbin and the members of the Fukuda laboratory of the Institute for Materials Research, Tohoku University. They are also indebted to Mr.J.Sato (TDK Corporation), Mr.H.Kawanaka (Victor company of Japan, Ltd.), Mr.S.Murakami (KYOCERA Corporation) for their many contributions.

REFERENCES

1. N.Sarukura, M.A.Dubinskii, Z.Liu, V.V.Semashko, A.K.Naumov, S.L.Korableva, R.Y.Abdulsabirov, K.Edamatsu, Y.Suzuki, T.Itoh and Y.Segawa, *IEEE J. Selected Topics in Quantum Electronics*, **1** (1995) 792.
2. M.A.Dubinskii, V.V.Semashko, A.K.Naumov, R.Y.Abdulsabirov, and S.L.Korableva, *Laser Phys.* **3** (1993) 216.
3. C.D.Marshall, S.A.Payne, J.A.Speth, W.F.Krupke, G.J.Quarles, V.Castillo and B.H.T.Chai, *J. Opt. Soc. Am. B*, **11** (1994) 2054.
4. R.F.Belt and R.Uhrin, *J. Cryst. Growth*, **109** (1991) 340.
5. K.Shimamura, N.Mujilat, K.Nakano, S.L.Balochi, Z.Liu, H.Ohtake, N.Sarukura and T.Fukuda, *J. Cryst. Growth*, **197** (1999) 896.
6. R.D.Shannon, *Acta Cryst.* **A32** (1976) 751.

7. D.Klimm, P.Reiche, *Proceedings of International Symposium on Laser and Nonlinear Optical Materials*, 3-5 November 1997, 284.
8. Z.Liu, S.Izumida, H.Ohtake, N.Sarukura, K.Shimamura, N.Mujilatu, S.L.Balochi and T.Fukuda, *Jpn. J. Appl. Phys.*, **37** (1998) L1318.
9. T.M.Bloomstein, M.W.Hom, M.Rothschild, R.R.Kunz, S.T.Palmacol and R.B.Goodman, *J. Vac. Sci. Technol.*, **B 15** (1997) 2112.
10. Al.Darabont, C.Neamtu, S.I.Farcas and Gh.Borodi, *J. Cryst. Growth*, **169** (1996) 89.
11. R.C.DeVries and R.Roy, *J. Am. Chem. Soc.*, **75** (1953) 2481.
12. S.L.Balochi, K.Shimamura, K.Nakano, N.Mujilatu and T.Fukuda, *J. Cryst. Growth*, **200** (1999) 521.
13. I.M.Silvestrova, Yu.V.Pisarevsky, V.V.Bezdelkin, P.A.Senyushenkov, *Proc. 1993 IEEE International Frequency Control Symposium*, p.351.
14. J.Detaint, J.Schwartzel, A.Zarka, B.Capelle, J.P.Denis, E.philippot, *Proc. 1994 IEEE International Frequency Control Symposium*, p.58.
15. K.Shimamura, H.Takeda, T.Kohnno and T.Fukuda, *J. Cryst. Growth*, **163** (1996) 388.
16. T.A.Parthasarathy, T.I.Mah, L.E.Matson, *J. Am. Ceram. Sci.*, **76** (1993) 29.
17. Y.Waku, N.Nakagawa, H.Ohtsubo, Y.Ohsora, Y.Kohtoku, *J. Jpn. Inst. Metals*, **59** (1995) 71.
18. Y.Waku, H.Ohtsubo, N.Nakagawa, Y.Kohtoku, *J. Mater. Sci.*, **31** (1996) 4663.
19. Y.Waku, N.Nakagawa, T.Wakamoto, H.Ohtsubo, K.Shimizu, Y.Kohtoku, *Nature*, **389** (1997) 49.
20. S.Uda, J.Kon, J.Ichikawa, K.Inaba, K.Shimamura, T.Fukuda, *J. Cryst. Growth*, **179** (1997) 567.
21. D.Viechnicki, F.Schmid, *J. Mater. Sci.*, **4** (1969) 84.
22. N.Ueda, H.Hosono, R.Waseda and H.Kawazoe, *Appl. Phys. Lett.*, **70** (1997) 3591.

Possibilities and limitations of multioxides crystals growth

M. Berkowski, J. Fink-Finowicki, R. Aleksiyo

Institute of Physics Polish Academy of Sciences, Al. Lotników 32/46, Warsaw, Poland

ABSTRACT

The main methods of crystal growth from the melt the Czochralski and floating zone will be discussed and compared. Advantages, disadvantages and limitations of both methods as well as ways of solving some of the problems existing during growth of different types of multioxides crystals will be discussed.

The chemical composition of crystals grown by the Czochralski method very often differs from the stoichiometric composition. Such deviations were found and well documented in a few groups of materials for example in garnets. Since the deviation is not known for most of the crystals, a simple way to determine the optimum starting composition of the melt will be presented. In order to determine the composition of the melt one should take into account evaporation of a volatile component that dissociates at high temperatures during crystal growth.

Some problems related to the dopant distribution along the crystal growth direction in correlation with segregation coefficient for both methods will be discussed. To grow solid solution single crystals by the Czochralski method with a desired concentration of the admixture one has to know segregation coefficients of the components. A few examples of the dopant solubility limit in different crystal matrices will be presented.

1. INTRODUCTION

We will present and compare the Czochralski and floating zone methods that we use to grow single crystals. We intend to discuss advantages and disadvantages of both methods and ways of solving some of the arising problems. In particular we will show the problems involved with doping of the crystals, segregation of the dopants and methods of determining the dopant concentration in the crystals.

2. ADVANTAGES AND LIMITATIONS OF THE FLOATING ZONE METHOD

The compounds melting incongruently with a peritectic reaction, at the melting point decompose into the substance remaining in solid phase and the liquid with the composition corresponding to the peritectic point. Compounds of the composition only slightly differing from the peritectic point may still be crystallized by the Czochralski method if the process is started with the melt of the peritectic point composition. Then the composition of the melt will change from the peritectic to eutectic one during the crystal growth.

To the other important class of compounds belong systems in which the starting substances form solid solutions. It is obvious that the crystal and the melt composition change during the crystal growth by the Czochralski method.

The floating zone method allows one to crystallize not only congruently melting materials but also a lot of compounds exhibiting peritectic point reaction. In this method only a small part of the ceramic material is melted. The equilibrium state is reached very soon after beginning the process, yet the crystal and the melted rod have the same composition while the molten drop composition corresponds to the peritectic point. Thus in contrast to the Czochralski method, it may be applied to much wider range of materials. The segregation of the dopant is less important here and influences the dopant concentration only at the beginning and at the end of the crystal.

Also during growth of solid solution crystal by this method, equilibrium is soon reached with the same composition of the crystal and the ceramic rod, while the molten zone has another composition depending on segregation coefficient between components.

Since this method does not require any crucible, it may be used to grow crystals with higher melting temperatures. Thus, the problems of reaction between the melt and crucible are avoided. In principle, the crystallization may be carried out in any atmosphere even in air or oxygen consequently decreasing dissociation of the melt. It further extends the range of materials that may be crystallized, to those melting congruently but strongly dissociating.

The main disadvantage of the floating zone method results from the large temperature gradient along the crystal, from the growth region to the part previously crystallized. In consequence, the quality of the crystals is lower than those grown by the Czochralski method.

2.1. Critical concentration of the dopant

Complex compound $\text{BaMgAl}_{10}\text{O}_{17}$ (BAM) melts incongruently with the peritectic reaction and the melt composition at the peritectic point considerably differs from the BAM formula. It proved possible to grow pure and doped transparent BAM single crystals by the floating zone method.

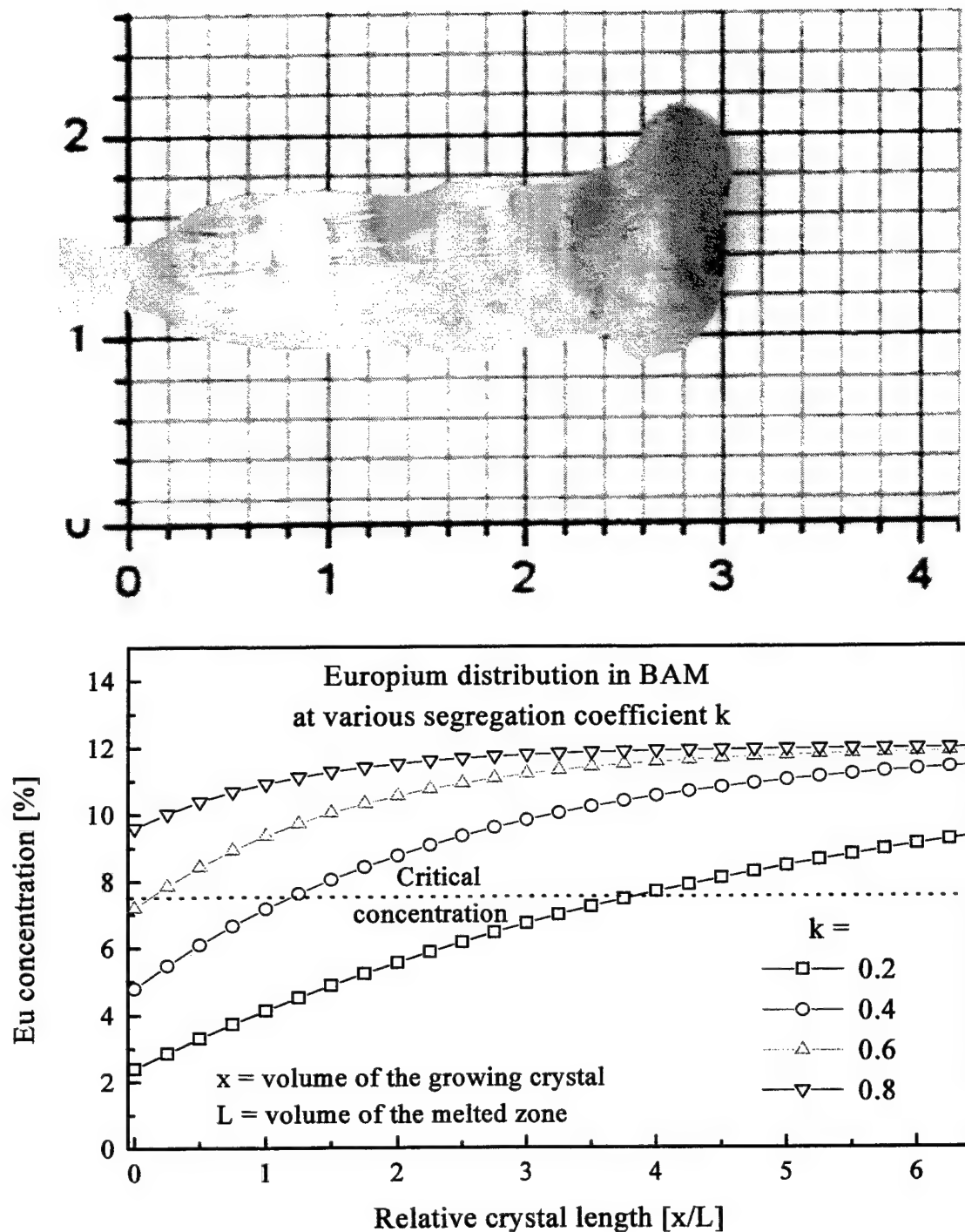


Fig. 1. Image of BAM:Eu crystal (top) and calculated distribution of europium in the crystal for various segregation coefficients k (bottom).

Determination of the segregation coefficient and influence of the dopant critical concentration on the crystal quality will be shown using the example of BAM:Eu crystal. The crystal has been grown from the sintered rod containing 12 at.% of Eu. The transparent part of the crystal extends over 24 mm; the end of the crystal is not transparent (Fig. 1 top). The concentration of Eu in the crystal determined by Electron Probe Microanalysis (EPMA) method at the beginning of the crystal -0 mm in the picture equals 2.4% Eu, it increases to 7.1% Eu near the end of the transparent part -22nd mm and reaches about 43% Eu in the non transparent polycrystalline part at 28th mm.

Dopant concentration in crystals C_s follows the equation:

$$C_s = C_0 - C_0(1-k)\exp(-kx/L) \quad (1)$$

where C_0 is starting concentration in the rod; k segregation coefficient; L volume of the molten drop and x volume of the crystallized part¹. Distribution of the dopant concentration calculated for various segregation coefficient k is shown in the lower panel of Fig. 1.

Using the plots of Fig. 1 the effective segregation coefficient has been determined to be $k_{\text{eff}}=0.2$. Distribution of Eu in the imaged crystal is shown in the graph by the open squares plot, the horizontal axes of both parts are adjusted. Because of very low segregation coefficient of Eu in BAM not all europium enters the growing crystal thus its concentration in the molten drop increases rapidly. Eu concentration in the growing crystal increases up to the critical concentration. At growth rate close to zero, the critical concentration limit is 8.6 %. In our case of 2 mm/h growth rate the critical concentration decreases to 7.6% that is the 24th mm in the picture. Above the critical concentration, material solidifies in a polycrystalline form shown in the right end of the top picture of Fig. 1.

The results have been verified in other process starting with the rod containing 8% Eu that allowed to grow transparent crystals.

3. ADVANTAGES AND LIMITATIONS OF THE CZOCHRALSKI METHOD

The main advantage of the Czochralski method is the possibility of fast growth of good quality large single crystals. Moreover, since the crystals are grown using oriented seeds they adopt required orientation. In the typical Czochralski arrangements using high frequency generators the metallic crucible heats the melt and the ceramic thermal shields. The need of crucibles seriously limits applicability of the Czochralski method. The platinum crucibles may be used to grow materials melting below 1500 °C and iridium ones below 2100 °C. The ceramic shields are also heated to high temperatures. Pure Al_2O_3 may be used as thermal insulator during crystallizing materials melting below 1750 °C because of the existing radial thermal gradients. Crystallization of higher melting temperature materials requires use of ZrO_2 , which withstand crystallization processes of materials melting below 2200 °C. The radial and vertical temperature gradients that exist during crystal growth by the Czochralski method are significantly lower than those in the floating zone method it leads to obtaining crystals with low density of defects.

3.1. Crystal growth rate

Typical crystal growth rates applied in the Czochralski method as well as in other single crystal growth methods from the melt range from several mm/h for simple oxides to less than 1 mm/h for complex oxides as well as heavily doped crystals and solid solutions. The crystal growth rate is limited by diffusion rate of: its component to the crystal/melt interface, intentionally introduced dopants and unintentional admixtures in opposite direction from the melt interface. When the composition of the melt is incorrect, e.g. contains an excess of components which plays a role similar to the dopant then growth rate must be reduced. When the growth rate is too high, a large concentration gradient of the admixtures (dopant, impurities or excessive amount of some components) is created in the melt, and consequently the melt neighboring to the crystal growth region becomes supercooled. As a result, a tendency to spontaneous nucleation appears in the melt in front of the growing crystal, that causes formation of various defects in the crystal.

The crystal growth process by the Czochralski method always begins on a thin seed crystal with convex crystal/melt interface. When the crystal diameter increases the growth rate in the central part of the interface also increases and is higher than the actual pulling rate. This increase in the growth rate is a function of the cone angle and the convexity of the crystal/melt interface. At this stage of the crystal growth process the pulling rate must be reduced in order to maintain the growth rate below the critical value.

3.2. Starting melt composition

The chemical composition of crystals grown by the Czochralski method very often slightly differs from the stoichiometric composition of the crystallized material. Such deviations were found and were well documented, for example in rare earth gallium garnets^{2,3}.

Determining the composition of the melt one should take into account the evaporation of a volatile component that dissociates at high temperatures. To such materials belong compounds containing Ga_2O_3 like rare earth gallium garnets and rare earth gallium perovskites.

For example GGG single crystal grown by the Czochralski method contains 61.85 mol.% of Ga_2O_3 instead of stoichiometric composition 62.5 mol.%. Optimal starting composition is between these two values (about 62.2 mol.%)²⁻⁴. Therefore, during crystal growth the melt becomes enriched in Ga_2O_3 when crystal is pulled from the melt. Fortunately, this enrichment is compensated by thermal dissociation and subsequent evaporation of Ga_2O_3 .

In case of some materials like gehlenites⁵ or crystals with the K_2NiF_4 structure⁶, growing good quality crystals from stoichiometric melts is very difficult or almost impossible. If one starts from stoichiometric composition only small part at the beginning of the crystal will be transparent. Since the deviation from the stoichiometric composition is not known for most of the crystals, it has to be determined.

The relative change in crystal composition along crystal growth direction determined by EPMA method varies in some direction, consequently the melt composition changes in the same direction. It means that the initial composition has to be changed in the opposite direction. This procedure has to be repeated until the crystal is transparent throughout its whole length and the concentration of elements measured on the slice along the crystal growth direction does not reveal significant changes.

3.3. Segregation coefficient

Segregation of the dopants is yet another disadvantage of the Czochralski method. It leads to a difference in composition between the crystal and the melt if the segregation coefficient differs from one. In order to pull single crystals with a specific desired dopant concentration, it is needed to know the segregation coefficient of the dopant in the particular melt.

We have determined the segregation between neodymium and lanthanum along growth direction of $\text{La}_{1-x}\text{Nd}_x\text{GaO}_3$ single crystals⁷. Concentration of components measured on slices cut from single crystals along the growth direction, versus parameter g describing the part of crystallized material is shown in Fig. 2. Concentration of admixture in mol.% along growth directions, versus parameter g describing the part of crystallized material follows⁸ the equation:

$$C_s(g) = k_{\text{eff}} C_0 (1-g)^{k_{\text{eff}}-1} \quad (2)$$

where: k_{eff} is the effective distribution coefficient; C_0 starting admixture concentration in the melt and g ratio of the crystal mass to the total starting mass in the crucible. The effective segregation coefficient of Nd in $\text{La}_{1-x}\text{Nd}_x\text{GaO}_3$ solid solutions is about 0.77 and is reciprocal to La segregation in NdGaO_3 ($k_{\text{eff}}=1.30$).

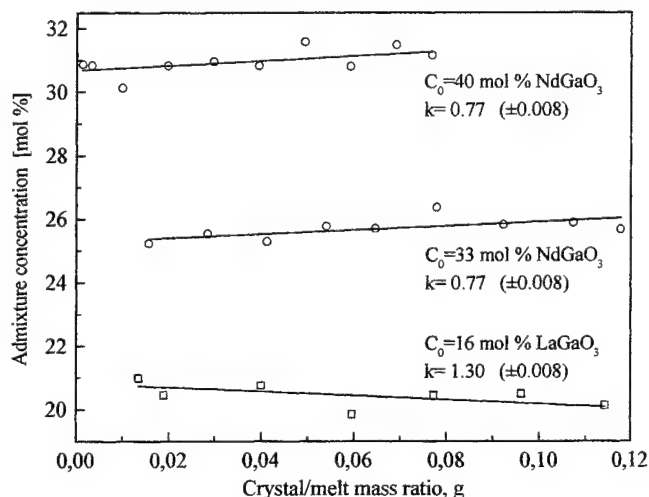


Figure 2. Determination of segregation coefficient in solid solutions crystals grown by the Czochralski method.

3.4. Phase transition temperature dependence

The orthorhombic to rhomboedral first order phase transition that occurs at 150 °C in pure LaGaO_3 ⁹ have been studied as a function of Nd and Pr concentration^{7, 10}. It has been found that the temperature of the first order phase transition increases linearly with the dopant concentration with the rate of 20.5 °C/mol.% Nd and 13.3 °C/mol.% Pr, respectively.

The temperature of the phase transition in $\text{La}_{1-x}\text{Nd}_x\text{GaO}_3$ and $\text{La}_{1-x}\text{Pr}_x\text{GaO}_3$ as function of the unit cell volume increases linearly while orthorhombic unit cell volume almost linearly decreases with Nd/Pr concentration x . It implies that transition temperature T_{tr} linearly rises with the unit cell volume V_{ort} . It is interesting that both plots are almost identical. We are unable to tell whether it is merely accidental coincidence or has any deeper meaning since the X-ray diffraction has been measured only at room temperatures. Analysis of deformation of the perovskite unit cell and gallium oxygen GaO_6 octahedron as a function of dopant concentration indicates that both La and Pr ions are too small to form the cubic lattice.

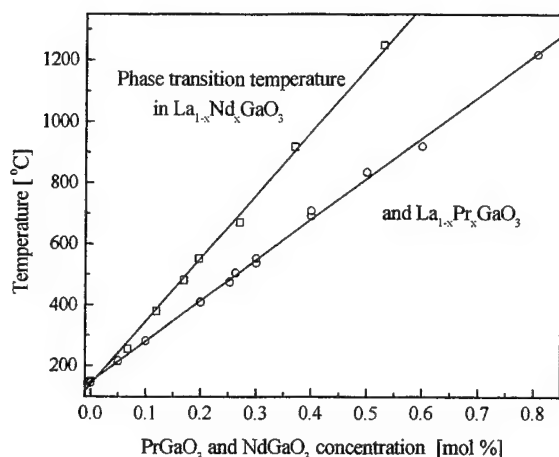


Figure 3. Phase transition temperature dependence in $\text{La}_{1-x}\text{Nd}_x\text{GaO}_3$ and $\text{La}_{1-x}\text{Pr}_x\text{GaO}_3$.

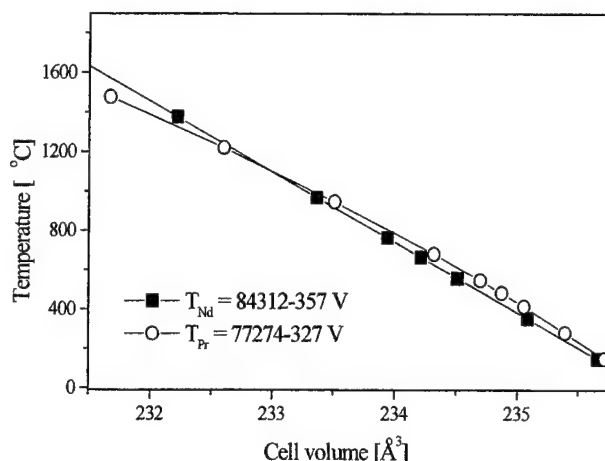


Figure 4. The phase transition temperature in $\text{La}_{1-x}\text{Nd}_x\text{GaO}_3$ and $\text{La}_{1-x}\text{Pr}_x\text{GaO}_3$ as function of the unit cell volume.

3.5. Rare earth ions and strontium in LaGaO_3

We have also investigated other isomorphous rare earth elements apart from Pr and Nd such as Sm, Eu and Er in LaGaO_3 single crystal and non-isomorphous doping by Sr. It has been found that only Pr and Nd galates form solid solutions in the whole concentration range with LaGaO_3 . The solubility limit decreases to around 20 at. % for Sm, about 1.6 at. % for Eu and only to around 0.4 at. % for Er. The solubility limit for non-isomorphous substitution of La by Sr is approximately 12 mol.% while up to about 1.5 mol.% the introduced admixture behaves as isomorphous substitution. From the determined segregation coefficient for Sr, Pr, Nd, Eu and Er in LaGaO_3 it has been found that the value of the segregation coefficient varies linearly with the substituting ions radii.

Substitution of La by Eu or Er also increases the first order phase transition temperature faster than Pr or Nd; substitution of La by Sr decreases the temperature of the phase transition. Preliminary measurements suggest that the rate of the phase transition temperature shift with dopant concentration may be also a linearly vary with the ionic radius of the substituting element.

3.6. Cubic perovskite solid solutions

Results previously published¹¹⁻¹⁵ and our investigations^{7, 10} prove that cubic perovskites that do not undergo any phase transitions should be searched for in the crystals based on strontium perovskites such as $\text{SrAl}_{0.5}\text{Ta}_{0.5}\text{O}_3$ (SAT) and $\text{SrAl}_{0.5}\text{Ta}_{0.5}\text{O}_3$ (SAN). The typical representative of this group of solid solutions is $(1-x)\text{SAT}:x\text{LA}$ ($\text{LA}=\text{LaAlO}_3$). We have performed preliminary crystal growth processes using floating zone and the Czochralski methods for $x = 0, 10, 20, 22, 25, 30, 50, 60$ and 66.6 mol.% of lanthanum aluminate concentration. The crystals adopt cubic structure at x up to 0.50 with the half of lattice constant varying from 3.895 to 3.845 Å (Fig. 6), while at $x=66.6$ the structure changes to rhombohedral.

To grow crystals by the Czochralski method we used $\langle 111 \rangle$ and $\langle 100 \rangle$ oriented seeds, pulling rate of 2 mm/h, rotation rate 20 rpm and used 40 mm diameter iridium crucible. The 18 mm in diameter crystals grown from the melt containing 22 mol.% and

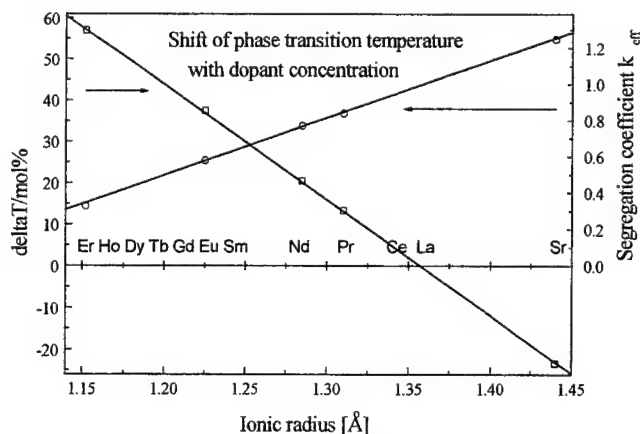


Figure 5. Segregation coefficient of Sr, Pr, Nd, Eu and Er in LaGaO_3 and shift of phase transition temperature with dopant concentration versus substituting ions radius.

more lanthanum aluminate were light yellow if the processes were carried out in pure nitrogen with oxygen level in the output gas below 500 ppm. The crystals adopt dark yellow color in case of insufficient thermal insulation or in case of unidentified reasons leading to higher oxygen concentration in the output gas. The crystals grown with starting composition of 20 mol.% and less of LA were dark, almost not transparent and they had tendency to unstable growth (e.g. spiral growth) increasing with lowering of LA concentration. Images of two crystals are presented in Fig. 7.

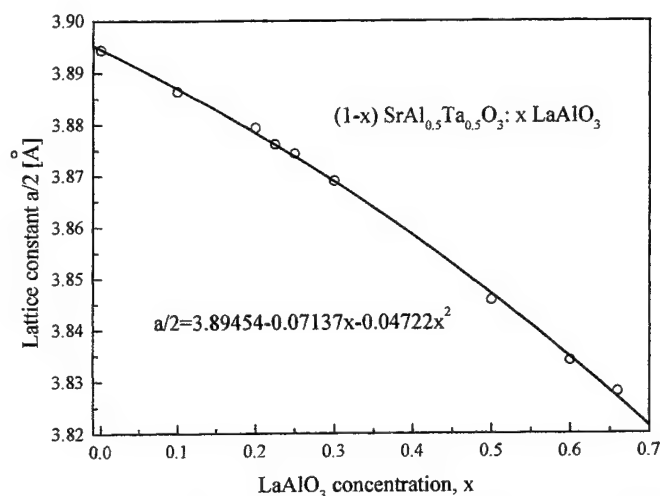


Figure 6. Dependence of the lattice constant on LaAlO₃ concentration in SrAl_{0.5}Ta_{0.5}O₃:LaAlO₃ solid solutions.

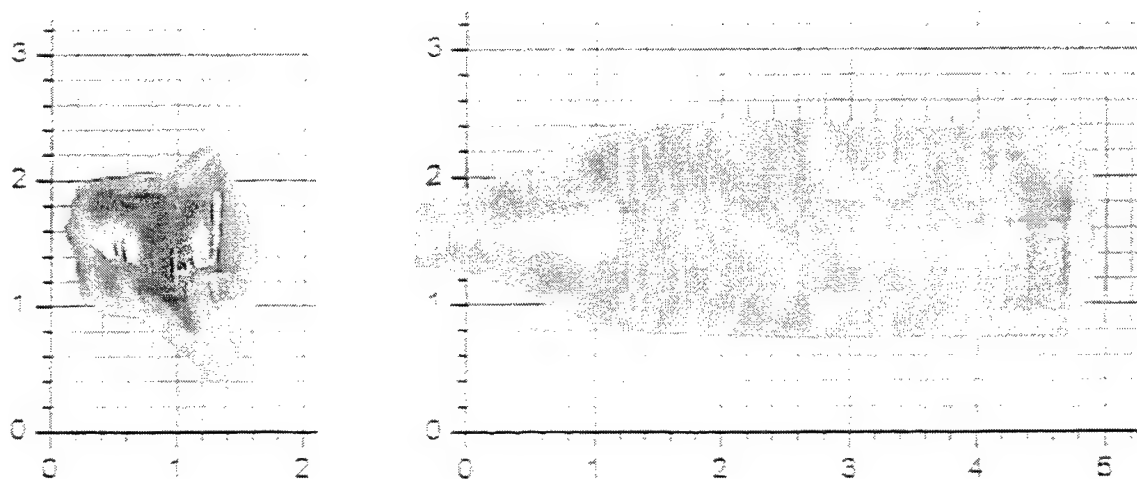


Fig. 7. Solid solution crystals $(1-x)\text{SrAl}_{0.5}\text{Ta}_{0.5}\text{O}_3 : x\text{LaAlO}_3$ grown by the Czochralski method, $x=0.2$ (left) and $x=0.25$ (right).

4. CONCLUSIONS

The Czochralski and floating zone methods have been compared and types of compounds that can be crystallized by either of them have been discussed. To the main problems influencing crystal quality discussed here belong temperature gradients, maximum crystal growth temperature, growth atmosphere, melt dissociation and dopant segregation.

The floating zone method allows one to crystallize also many compounds exhibiting peritectic point reaction. The crystallization may be carried out in any atmosphere even in air or oxygen thus decreases dissociation of the melt. Thus in comparison with the Czochralski method, it may be applied to much wider range of materials. The segregation of the dopant is less important here. Since this method does not require any crucible, it may be used to grow crystals with higher melting temperatures. In addition, the problems of reaction between the melt and crucible are avoided.

The main disadvantage of the floating zone method results from the large temperature gradient along the crystal. In consequence, the quality of the crystals is lower than of those grown by the Czochralski method.

ACKNOWLEDGEMENTS

The authors would like to express sincere thanks Dr. P. Byszewski, for his critical reading of the manuscript and fruitful discussions and Mrs Rusudan Kikalejshwili-Domuchowska for X-ray measurements. This work was supported by the Polish Committee for Scientific Research under grant No 7T08A01115 and by the Polish Science foundation, program Sezam.

REFERENCES

1. W. Pfann in "Zone melting", p.29 (John Wiley & Sons, New York 1966),
2. M. Allibert, C. Chatillon, J. Marschal, F. Lissalde, "Etude du diagramme de phase dans le systeme $Gd_2O_3 - Ga_2O_3$ ", *J. Cryst. Growth*, **23**, p.289, 1974,
3. C.D. Brandle, L.R. Barns, Crystal stoichiometry of Czochralski grown rare-earth gallium garnets" *J. Cryst. Growth*, **26**, p.169, 1974,
4. M. Makino, S. Nakamura, K. Matsumi, "Lattice parameter variations in Czochralski grown gadolinium gallium garnet single crystals" *Jpn. J. Appl. Phys.*, **15**, p.415, 1976,
5. W. Piekarczyk, M. Berkowski, G. Jasiolek, "The Czochralski growth of $BaLaGa_3O_7$ single crystals", *J. Cryst. Growth*, **71**, p.395, 1985,
6. M. Berkowski, "SrLaGaO₄ - SrLaAlO₄ Solid solutions: New promising substrate materials for HTSC", *J. of Alloys and Compounds*, **251**, 1, 1997,
7. M. Berkowski, J. Fink-Finowicki, W. Piekarczyk, L. Perchuc, P. Byszewski, L.O. Vasylechko, D.I. Savytskij, K. Mazur, J. Sass, E. Kowalska, J. Kapusniak, "Czochralski growth and structural investigations of $La_{1-x}Nd_xGaO_3$ solid solution single crystals", *J. Cryst. Growth*, **209**, p.75, 2000,
8. R.A. Laudise, The growth of single Crystals, p.74 (Prentice Hall, Englewood Cliffs. NJ. Russian Translation, Moscow, 1974,
9. H.M.O'Bryan, P.K.Gallagher, G.W.Berkstresser and C.D.Brandle, "Thermal analysis of rare earth gallates and aluminates", *J. Mater. Res.*, **5**, p.183, 1989,
10. M. Berkowski, J. Fink-Finowicki, P. Byszewski, R. Didusko, E. Kowalska, R. Alekseyko, W. Piekarczyk, L.O. Vasylechko, D.I. Savytskij, L. Perchuc, J. Kapusniak, "Growth and structural investigations of $La_{1-x}Pr_xGaO_3$ solid solution single crystals", will be published in *J. Cryst. Growth*, 2000,
11. C.D. Brandle and V.J. Fratello, "Preparation of perovskite oxides for high Tc superconductor substrates" *J. Mater. Res.* **5**, p.2160, 1990,
12. D. Mateika, H. Köhler, H. Laudan and E. Völkel, "Mixed - perovskite substrates for high-Tc superconductors" *J. Cryst. Growth* **109**, p.447, 1991,
13. R. Guo, A.S. Bhalla J. Sheen, F.W. Aigner, S. Erdei, E.C. Subbarao, L.E. Cross, "Strontium aluminum tantalum oxide and strontium aluminum niobium oxide as potential substrates for HTSC thin films" *J. Mater. Res.* **10**, p.18, 1995,
14. A. Bhalla, R. Guo, "Design of dielectric substrates for high Tc superconductor films" *Acta Phys. Polon.*, **92**, p.7, 1997,
15. K. Shimamura, H. Tabata, H. Takeda, V.V. Kochurikhin, T. Fukuda, "Growth and characterization of $(La,Sr)(Al,Ta)O_3$ single crystals as substrates for GaN epitaxial growth", *J. Cryst. Growth*, **194**, p.209, 1998.

Single-domain HTc superconducting materials synthesis: BaZrO₃ substrates as a tool for optimized systems

Benedicte Robertz^{*,a}, Frederic Boschini^a, Andre Rulmont^a, Marcel Ausloos^b and Rudi Cloots^a

SUPRAS, University of Liège,
^aChemistry Institute B6, ^bPhysics Institute B5,
Sart-Tilman, B-4000
LIEGE, Belgium

ABSTRACT

Large Dy-123 single-domains have been grown by the top-seeding melt-textured growth technique on yttrium oxide substrates. The main obstacles in fabricating such "single grain" 123 superconducting samples are discussed, i.e.

- (i) the dissolution of the seed during the melting and the peritectic cooling stages
- (ii) the nucleation of subsidiary 123 grains at the compact/substrate interface.

Such secondary nucleation process prevents the single grain from growing further. Solutions are suggested as for example by considering the use of a modified coating. BaZrO₃ displays a strong inertia in barium cuprate fluxes which suggests to use it as a very promising candidate for buffer layer in between the 123 compact and the furnace "environment". In order to provide such "high quality" sufficiently dense BaZrO₃ coatings, soft solution routes have been investigated. Advantages of these are a lower calcination temperature and the production of very homogeneous and fine monodisperse powders. The influence of the synthesis conditions on the properties of BaZrO₃ and on the sintering process is thus reported.

Keywords : superconductors, single domain, barium zirconate, syntheses, sintering

1.INTRODUCTION

Superconducting ceramics are promising materials for a wide variety of applications going from conductors to magnetic energy storage systems¹. YBa₂Cu₃O₇ is one member of this large family of compounds exhibiting a high magnetic irreversibility field at liquid nitrogen temperature. In fact, single domain melt textured YBa₂Cu₃O₇ has been shown to be able to trap significant magnetic induction (>2T) at liquid nitrogen temperature². As a consequence, these materials have clear potential for applications such as superconducting magnetic bearings³. The maximum induction which can be achieved in bulk superconductors is determined by the product of the critical current density and the radius over which the current flows. It is therefore limited by any weak links. The ability to fabricate HTS in large-grain form by a variety of melt processed techniques has overcome many of the problems associated with the weak intergrain links observed in polycrystalline specimens. The top seeding melt textured growth technique has been developed in order to grow large and well oriented single domain 123 monoliths⁴. The microstructure of the melt-processed 123 monoliths generally consists of pseudo-crystalline Y-123 matrix containing secondary phases, mostly 211, and other defects such as cracks, twins, stacking faults⁵. Another problem related to the microstructure of 123 monoliths is the following : the quality of the seed used in the top seeded melt textured growth process, i.e. a single crystal of Nd-123, can influence strongly the crystallinity of the grown 123 single domain. Three different modes for the 123 single-domain have been reported which are dependent on the degree of the dissolution of the single crystal seed⁶. In fact, although the processing temperature is lower than the peritectic decomposition of the Nd-123 single crystal seed, the single crystal dissolves completely or partially in the liquid formed by the incongruent melting of the Y-123 compact:

*Corresponding author e-mail address : B.Robertz@ulg.ac.be

1. When the seed dissolves completely, it no longer acts as a seed : a random growth process is observed leading to a polycrystalline material.
2. When the seed dissolves partially, the dissolved parts tend to resolidify which leads to more or less controlled growth of the Y-123 single domain at the seed, depending on the degree of dissolution.
3. A perfectly oriented single domain is obtained when the seed doesn't dissolve during the course of the reaction.

So, taking into account the main features of the microstructure of melt-textured grown YBCO materials, and keeping in mind the dissolution of the seed during the process, the main obstacles in fabricating a single grain 123 superconducting sample are the following:

1.a subsidiary misoriented 123 grain grown at the seed: generally due to a partial dissolution and resolidification of the seed during melting and peritectic cooling.

2.the nucleation of 123 grains at sample surface and at the compact/substrate interface.

Indeed, the substrate plays an important role in controlling the growth parameters of the 123 single-domain. As for example a high porosity of the substrate can induce porosity and microcracks formation in the 123 single-domain related to liquid losses during melting. In order to put into evidence the role of the substrate, different substrates have been used in this top seeding melt-textured growth process. Yttrium oxide has been used as a buffer layer. This oxide reacts with the solid phase above the solidification point of the 123 phase leading to the precipitation of very fine 211 particles at the compact/substrate interface⁷. The resulting locally high concentration of 211 particles reduces the supersaturating level necessary for the growth of 123 phase itself from the liquid. Secondary nucleation appears at the compact/substrate interface that prevents the single grain from growing further and does not grow to consume the entire sample volume. Solutions for the "substrate issue" have been proposed. Ytterbium oxide has been used as a buffer layer : in this case, the liquid containing ytterbium solidifies last during the peritectic cooling process due to the fact that the peritectic recombination temperature decreases with the size of the rare earth ion, and thus suppressing the 123 grain nucleation at the compact/substrate interface⁸. Another possibility is to use a barium zirconate coating. In fact lets remind that BaZrO₃ displays a strong inertia towards Ba-Cu-O fluxes making it the best material for single crystal growth⁹. Hence it should be considered as a promising candidate to be used as a buffer layer for the top-seeding melt textured growth process.

2.BARIUM ZIRCONATE AS A BUFFER LAYER FOR THE GROWTH OF HIGH QUALITY Y-123 SINGLE DOMAIN

The quality of the substrate used in the process is an important parameter for the controlled growth of a single domain. The morphology and properties of the ceramic powders have been shown to be dependent on the preparation mode. We have synthesized barium zirconate by three different techniques : solid state syntheses, precipitation and combustion techniques. The powders obtained have been compared from scanning electron microscope images. The different powders are then uniaxially pressed into pellets and sintered for 12 hours at 1400°C. The pellets are cut, a vertical section is inserted in resin and coated for SEM observation.

2.1. Solid state route

Barium zirconate is classically prepared by the classical solid state route starting from barium carbonate and zirconium oxide¹ in stoichiometric quantities (powder 1). The precursor powders are mixed in an agate mortar and calcined at 1200°C for 5 hours. A mixture of barium carbonate and basic zirconium carbonate hydrate has also been calcined (powder 2).

The solid state syntheses are known to present several drawbacks : high calcination temperatures, chemical inhomogeneity of the product; broad particle size distribution. This has been confirmed in both cases.

SEM images of both calcined powders showed a high degree of agglomeration. Powder 2 prepared starting from barium carbonate and basic zirconium carbonate presents a particular mode of agglomeration as can be seen on fig.1a. Agglomerates are made of smaller spherical-like agglomerates having a mean diameter of 2.5µ.

After sintering at 1400°C, the samples have undergone abnormal grain growth. Large polyhedral grains are observed. The pellets also show a high porosity.

The drawbacks related to the classical solid state synthesis have led to the development of soft solution methods for the preparation of ceramic powders. The methods tested for the preparation of barium zirconate are : calcination of an oxalato complex of barium-zirconium¹⁰, calcination of a mixed citrato complex¹¹, the controlled double jet precipitation¹², the precipitation in the presence of urea¹³, and a combustion method using oxalic dihydrazide as a fuel¹⁴. Preparation modes of the previous techniques can be found elsewhere.

2.2. Precipitation methods.

This group of methods includes precipitation and calcination of a mixed oxalato or citrato complex of barium-zirconium, the controlled double jet precipitation and the precipitation in the presence of urea. Powders obtained by these preparation

modes are characterized by a similar morphology after calcination. An electron micrograph of a powder prepared by calcination of an oxalato complex is presented for example in Fig.1b. The powders are constituted by spherical grains. The size distribution of the particles is homogeneous with a mean diameter of 0.2μ in this case. They show a small degree of agglomeration.

The microstructures observed after sintering are different for the four powders. The powders prepared by the oxalate and urea methods seem to be denser. For the oxalate method the small grains are still distinguishable. For the urea method some parts are almost pore free, a good coalescence has occurred and the particles are not distinguishable anymore. In other parts the formation of necks has only begun and polyhedral particles can be seen (Fig.2b). The powders prepared by the citrate method show an abnormal grain growth with large polyhedral grains. For powders prepared by the controlled double jet precipitation, no diffusion occurred. The temperature of 1400°C is not sufficient to induce sintering of the powders prepared by the controlled double jet precipitation. This temperature has to be increased or a sintering aid has to be added to the powder before sintering.

2.3. Combustion method

An organic fuel, namely oxalic dihydrazide $\text{NH}_2\text{NHCOCOCONHNH}_2$, is added to a mixture of the nitrates salts of barium and zirconium¹⁴. The solution is placed in a furnace and heated at a temperature sufficient to induce ignition of the mixture. In our case the ignition temperature is 400°C . The powder is calcined at 600°C for 12 hours.

The morphology of the calcined powder is totally different from what has been observed until now (Fig.1c). The grains have grown as cube with a size of the order of $1\mu^3$. Barium zirconate being a perfect cubic perovskite compound, the formation of cubic microcrystals is not astonishing. The conditions of obtention of barium zirconate by this combustion method are probably suitable to the growth of single microcrystals. The better cristallinity of the product has been confirmed using X-ray diffraction. The intensity is twice or thrice what is generally observed for barium zirconium oxide prepared by precipitation techniques.

After sintering, a denser pellet is obtained as in the case of the oxalate and urea methods. Some cubic particles are still present (Fig.2c).

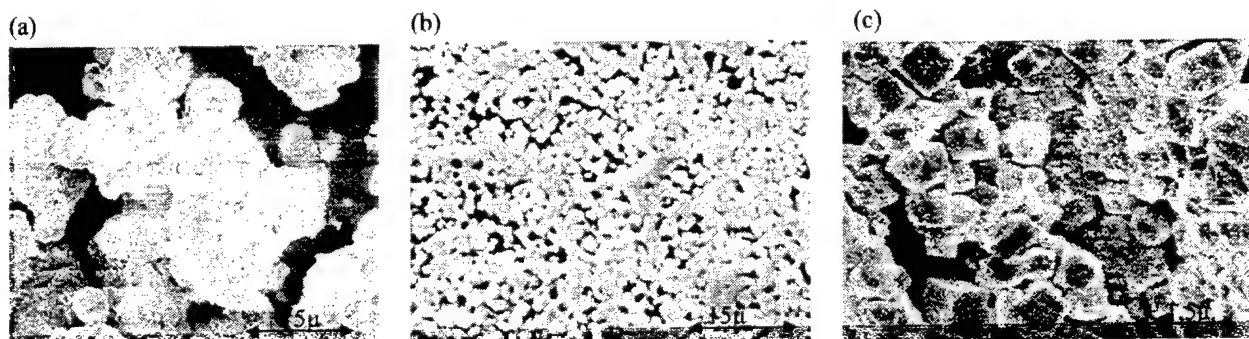


Fig.1 : Electron micrographs of the calcined powders. (a) BaCO_3 and ZrO_2 solid state synthesis, (b) calcination of an oxalato complex, (c) combustion using oxalic dihydrazide.

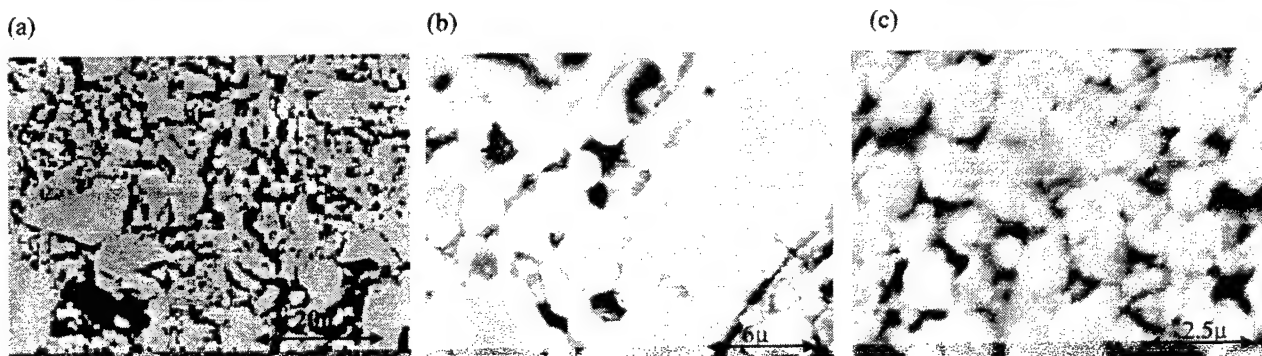


Fig.2 : Electron micrographs of pellets sintered at 1400°C for 12 hours. (a) BaCO_3 and ZrO_2 solid state synthesis, (b) precipitation using urea, (c) combustion using oxalic dihydrazide

The differences observed from the electron micrographs clearly demonstrate that the preparation mode strongly influences the sintering behavior. In order to determine which preparation mode leads to the densest substrate, porosity measurements have to be made.

4. INTERACTION BETWEEN THE SUBSTRATE AND THE COMPACT DY-123

The inertia of barium zirconate towards the fluxes of Ba-Cu-O has been demonstrated in our laboratory. Pellets of $\text{DyBa}_2\text{Cu}_3\text{O}_7$ powders were laid on two different substrates : Al_2O_3 and BaZrO_3 . The heat treatment was conducted simultaneously for the two samples. Al_2O_3 was used for comparison as it is well known to react with the fluxes.

The interaction layer between alumina and the 123-material is visible to the naked eye. A micrograph of a polished section analysed by optical microscopy is shown here. The interaction layer noted 1 represents 1/6 of the total sample height. The compound found at the interface is a mixed oxide of barium, dysprosium and aluminium. Its composition is close to $\text{Ba}_2\text{AlDyO}_5$.

The same experiment conducted on a BaZrO_3 substrate leads to a clear interface between compact and substrate. Yet the pellet of Dy-123 is attached to the substrate. This is due to the high porosity of the substrate used in this experiment inducing diffusion of the liquid phase formed during the peritectic reaction into the porous substrate. But no barium oxide nor zirconium oxide has been observed into the 123 material.



Fig.3. Optical micrograph of a Dy-123 pallet grown on alumina substrate.

5. CONCLUSIONS

The synthesis of large single domain 123-compounds requires a thorough control of the growth parameters. The quality of the substrate used in the top seeding melt textured method is one important parameter to avoid segregation of 211 particles at the compact/substrate interface which is deleterious to the growth of large single domains. Barium zirconate has gained much interest because of its inertia towards the Ba-Cu-O melts. The preparation mode of the BaZrO_3 directly influences the sintering behavior of the powders and subsequently the properties of the sintered substrate. Solid state synthesis should be abandoned to the profit of soft solution methods. None of the sintered material can be used as such for the growth of large single domains. Sintering aids have to be added in order to improve the final density and to control the morphology of the final product.

REFERENCES

1. M.Murakami, « Electromagnetic applications of melt-processed YBCO » in *Superconductivity and superconducting materials*, pp.627-636, Technal Srl., 1995
2. M.Murakami, « Melt-processing of high-temperature superconductors » in *Progress in Materials Science* **38**, pp.311-357, 1994
3. T.A.Combs, A.M.Campbell, I.Ganney, W.Lo, T.Twardowski and B.Dawson, «Superconductings bearings in fly wheels», *Mat.Sci.Engineering B* **53**, pp. 225-228, 1998
4. D.A.Cardwell, « Processing and properties of large grain (RE)BCO », *Mat.Sci.Engineering B* **53**, pp. 1-10, 1998

5. W.Lo, D.A.Cardwell, C.D. Dewhurst, H.T.Leung, J.C.L. Chow and Y.H. Shi, « Controlled processing and properties of large Pt-doped Y-Ba-Cu-O pseudocrystals for electromagnetic applications », *J.Mater.Res.* **12**, pp. 2889-2900, 1997
6. Y.A.Jee, G.W.Hong, C.J.Kim and T.H.Sang, « Dissolution of $\text{SmBa}_2\text{Cu}_3\text{O}_{7-y}$ seed crystals during top-seeded melt growth of $\text{YBa}_2\text{Cu}_3\text{O}_{7-y}$ », *Supercond.Sci.Technol.* **11**, pp. 650-658, 1998
7. R.Cloots, F.auguste, A.Rulmont, N.Vandewalle and M.Ausloos, « Directional solidification by appropriate chemically active single crystal seed : An alternative way of generating large superconducting 123 single domain », *J.Mater.Res.* **12**, pp. 3199-3202, 1997
8. C.J.Kim, Y.A.Jee, S.C.Kwon, T.H.Sung and G.W.Hong, « Control of YBCO growth at the compact substrate interface by bottom seeding and Yb_2O_3 coating in seeded melt-growth processed YBCO oxides using a MgO substrate. », *Physica C* **315**, pp.263-270, 1999
9. A.Erb, E.Walker and R.Flükiger, « BaZrO_3 : the solution for the crucible corrosion problem during the single crystal growth of high-Tc superconductors $\text{REBa}_2\text{Cu}_3\text{O}_{7-x}$; RE = Y, Pr », *Physica C* **245**, pp. 245-251, 1995
10. H.S.Potdar, S.B.Deshpande, P.D.Godbole and S.K.Date, « Synthesis of microcrystalline BaZrO_3 via molecular precursor route », *J. Mater. Res.* , **8**(5), pp. 948-950, 1993
11. M.Rajendran and M.Subba Rao, « Synthesis and characterization of barium bis(citrato)oxozirconate (IV) tetrahydrate : A new molecular precursor for fine particle BaZrO_3 », *J.Mater.Res.* **9**, pp. 2277-2284, 1994
12. Y-S. Her and E.Matijevic, « Preparation of well-defined colloidal barium titanate crystals by the controlled double jet precipitation », *J. Mater. Res.* **10**(12), pp. 3106-3114, 1995
13. E.E. Oren, E.Taspinar and A. Cüneyt Tas, « Precipitation of lead zirconate by homogeneous precipitation and calcination », *J. Am. Ceram. Soc.* **80**, pp. 2714-2716, 1997
14. K.R.Venkatachari, D.Huang, S.P.Ostrander, W.A.Schulze, G.C.Stangle, « A combustion synthesis process for synthesizing nonacrystalline zirconia », *J. Mater. Res.* **10**, pp. 748-755, 1995

Very high quality crystals of wide-gap II-VI semiconductors: What for?

A. Mycielski, A. Szadkowski, W. Kaliszek and B. Witkowska

Institute of Physics, Polish Academy of Sciences,
Al. Lotników 32/46, 02-668 Warszawa, Poland

ABSTRACT

A review of some of the most important applications of the wide-gap II-VI semiconductors is presented, the key parameters of the crystals for specific applications are emphasized, and the necessity of growing crystals of very high quality is substantiated. Modern methods of growth of high-quality wide-gap II-VI semiconductor crystals are shortly described. The results of the physical vapor transport method, chosen by the authors for ZnTe and CdZnTe crystals, are shown.

Keywords: wide-gap II-VI semiconductors; high-quality crystals; applications of II-VI semiconductors; technology of semiconductor crystals

1. INTRODUCTION

The physics of the wide-gap II-VI semiconductors has been developing during last fifty years, but technical applications are spreading fast only recently. The development of applications is determined by the progress in the technology of crystals. In this review we are going to show why in many applications of the semiconductor crystals the wide-gap II-VI semiconductor crystals are the best choice and that numerous applications require very high quality crystals. The quality requirements for particular applications will be emphasized. Finally, the leading technologies, which enable the growth of very high quality wide-gap II-VI semiconductor crystals, will be discussed with special attention paid to the technology chosen by the authors. Among important applications of the wide-gap II-VI semiconductor crystals one can name:

- X-ray and gamma-ray detectors.
 - Substrates for IR detector structures.
 - Photorefractive elements for optoelectronics.
 - Electro-modulators.
 - Optical isolators (CdMnTe).
 - Green diodes and lasers (ZnTe).
- In all these cases the quality of the crystals plays a crucial role.

2. SELECTED APPLICATIONS OF THE WIDE-GAP II-VI SEMICONDUCTOR CRYSTALS

2.1. X-ray and gamma-ray detectors

Semiconductor detectors of X and gamma radiation are used in many areas of life, science, and technology, like common X-ray diagnostics, nuclear medicine, national security, environment protection, physics of elementary particles and nuclear physics, astrophysics, cosmic-ray physics, material sciences and monitoring of the industrial processes, to mention only a few of them.

The semiconductor detector of X or gamma rays consists of a piece of *properly* chosen semiconductor crystal of *proper* quality with the electrodes for detecting currents. The names "X-rays" and "gamma-rays" describe different ranges of electromagnetic spectrum, i.e. — different ranges of photon energies. Usually we call the photons with energies 1keV - 100keV — "X-ray" photons, and the photons with energies above 100keV — "gamma-ray" photons.

Inside the crystal the photons interact with atoms, giving away all or part of their energy and the final result - the mobile charges - can be detected by the electric circuit. The first required step is the creation of at least one fast charged particle, which subsequently produces many free electrons (and/or holes) through ionization. Different processes of interaction, characterized by a different effectiveness of production of current carriers, dominate different ranges of the photon energy:

- 1keV - 400keV — photoelectric effect
- 400keV - 5MeV — Compton scattering
- 5MeV - 100MeV — creation of electron-positron pairs.

The generation of current carriers by photons due to these processes is proportional:

- to Z^n ($4 < n < 5$) — for photoelectric effect,
- to Z — for Compton scattering,
- to Z^2 — for creation of electron-positron pairs

It is obvious that the crystals for the detectors should have the average value of the atomic number Z as large as possible. For some crystals these values are: HgJ — 66; CdTe — 50; GaAs — 32; Ge — 32; Si — 14. One can see the advantage of choosing II-VI's - CdTe and HgJ.

In the detectors measuring the total intensity of radiation — the current for a given rate of generation of charge carriers (say - only electrons, for simplicity) — is proportional to the product of electron lifetime, electron mobility and the applied electric field. In the photon counting detectors (e.g. - spectrometers) — the magnitude of a current pulse for a given number of created charge carriers is proportional to the product of electron mobility and the applied electric field, and the electron lifetime must be long enough to ensure the effective charge collection. Large values of electron mobility, electron lifetime, and the maximum allowed electric field are required for reasonable sensitivity. If the mobility is to be high — the crystal must be pure, with low concentration of carrier scattering impurities and defects, no grain boundaries and twinning. If the lifetime is to be high — the concentration of defects and residual impurities acting as recombination centers must be low. High electric field may be applied only to a crystal of high resistivity if the noise caused by the thermally excited carriers is to be lower than the observed signals. High resistivity implies low concentration of defects (like vacancy related complexes in CdTe) and impurities, responsible for shallow levels. Compensation by the opposite type of impurities is not very good, as it decreases mobility. In the photon counting detectors — the high resistivity is necessary to avoid neutralization of the mobile space charge, during its transit, by the existing carriers. Usually the resistivities of the order of $10^{10} \Omega \cdot \text{cm}$ are required. Very often the detector crystals or the detector arrays are of quite a large size. For obvious reasons — the properties of the crystal must be uniform in the whole volume. When the ternary crystal is used, the homogeneous composition is required. Last but not least — the crystals for radiation detectors have to offer possibility of making reliable electric contacts.

High quality CdTe and $\text{Cd}_{1-x}\text{Zn}_x\text{Te}$ ($x < 0.2$) crystals find increasing application as the crystals for semiconductor detectors. The high average atomic number of CdTe was already mentioned. Zinc is added to increase the energy gap in order to achieve very high resistivity without the necessity of excess compensation. Vast information on semiconductor X-ray and gamma-ray detectors can be found e.g. in Refs. 1-6.

2.2 Substrates for IR-detector structures

Mercury-cadmium telluride ("MCT" or "CMT") is still the basic material for construction of IR-detectors and IR-detector structures. Usually $\text{Hg}_{0.8}\text{Cd}_{0.2}\text{Te}$ is used because its energy gap at room temperature matches the "atmospheric window" and the photon energy of the popular CO_2 laser. The detector structures are fabricated by Molecular Beam Epitaxy (MBE), Metal-Organic Chemical Vapour Deposition (MOCVD) or Liquid-Phase Epitaxy (LPE). High quality substrate crystals are required for all of these processes.

$\text{Cd}_{0.96}\text{Zn}_{0.04}\text{Te}$ has the same lattice constant as that of $\text{Hg}_{0.8}\text{Cd}_{0.2}\text{Te}$ and is used as the substrate for IR-detector structures based on $\text{Hg}_{0.8}\text{Cd}_{0.2}\text{Te}$. The substrate crystals must be single crystals with no grain boundaries and twins. Definite crystallographic orientation is required for the substrate surface. For example, the substrate surface parallel to the crystallographic plane (001) is used frequently for the MBE processes and (111) - for LPE. Extended defects in the substrate crystal spreading towards the interface give rise to defects detrimental to the detector layers. Density of dislocations in the substrate crystals must be kept below 10^4 cm^{-2} . The diffusion of impurities from the substrate crystal to the detector structure has to be excluded, as in some cases it results in the concentration of unwanted impurities inside the layer of the detector crystal much higher than that in the substrate. Thus, very high purity of the substrate is a must. It is often necessary to illuminate the detector structure through the substrate which has to be transparent for the IR radiation, so the concentration of any absorbing centres and the concentration of free carriers must be low. The high quality single crystals intended for substrates must be large enough to allow the substrate plates of the size of at least $20 \text{ mm} \times 20 \text{ mm}$ to be cut off. The last process in the preparation of the substrate plates is the preparation of the perfect ("epi-ready") surface, which is able to avoid

degradation (e.g. fast oxidation) in the period of time between the fabrication of the surface plate and the beginning of the epitaxy process. Many references to the papers dealing with the problems discussed above can be found e.g. in the article by Rogalski⁷.

2.3 Electro-modulators and photorefractive elements

The physical phenomenon which underlies the operation of these devices is the Pockels effect: the refraction coefficient of a crystal is modified by the electric field. In electro-modulators — an external field is applied. In photorefractive elements — the electric fields inside a crystal result from the rearrangement of the charges caused in turn by illumination with a certain pattern. The carriers are photoexcited from the localized states to the extended states and migrate towards nonilluminated regions, where they are captured into empty deep centers. Local space charge electric fields are formed and the refractive index is modulated locally by these fields.

For example — a photorefractive optical grating (consisting of stripes with different n) can be created inside a crystal containing suitable impurities by interference of the two laser beams resulting in stripes of strong illumination. The carriers excited inside the stripes migrate outside, where they are captured and the stripes of charges and fields are created. As the electric fields modulate the refractive index — the optical grating is formed.

The CdTe:V (and CdZnTe:V), GaAs:Cr, or InP:Fe are studied as promising photorefractive crystals. CdTe:V is good as a photorefractive material owing to its high (5.5) effective electro-optic coefficient. The figure of merit of a photorefractive material is the product of the electro-optic coefficient and the refractive index, n_0 . For cadmium telluride this product is twice as high as for the two other compounds mentioned. Very high quality of the crystal structure, absence of precipitates, and very low concentration of residual impurities are required for the CdTe:V or CdZnTe:V crystals meant to be used as photorefractive crystals, since the residual optical absorption must be below 0.1 cm^{-1} . High resistivity must be achieved by a reasonable compensation. High concentration of vanadium of $10^{17} \div 10^{18} \text{ cm}^{-3}$ must be accompanied by its homogeneous distribution. The basic knowledge of the photorefractive materials can be found in the book edited by Garmire and Kost⁸ and in the references cited therein. The topics specific to CdZnTe and CdTe can be found in the references to the articles of Triboulet et al⁹ and Marfaing et al¹⁰.

2.4 Optical isolators (CdMnTe)

The role of an optical isolator used for a laser is to allow the laser beam to go out but to forbid its coming back inside after external reflections. The Faraday rotation of the polarization plane of the electromagnetic wave inside a crystal in the magnetic field is utilized in the construction of an optical isolators. The crystals of a semimagnetic semiconductor $\text{Cd}_{1-x}\text{Mn}_x\text{Te}$, where the giant Faraday rotation¹¹ occurs for the wavelengths close to the free exciton line, are used for this purpose. For the IR-lasers working in the wavelength range $1 \div 1.5 \text{ }\mu\text{m}$ — the $\text{Cd}_{1-x}\text{Mn}_x\text{Te}$ crystals with $x \approx 0.1$ are suitable. The rotation of the polarization plane must be uniform for the whole volume of the crystal working as an optical isolator. Thus, the composition x must be uniform. As the scattering of light must be avoided, the single crystals of $\text{Cd}_{1-x}\text{Mn}_x\text{Te}$ must have no grain boundaries and twins, and very small amount of any precipitates. As the power of the laser beam going through the optical isolator is often very high, very low absorption coefficient, i.e. very low concentration of any absorbing species, is required.

2.5 Green diodes and lasers (ZnTe)

ZnTe with its room-temperature energy gap of 2.27 eV (546 nm) is considered to be the best candidate for manufacturing optoelectronic structures working in the green region of the spectrum. The pure green light emitting diodes based on phosphorus-doped p-type ZnTe plates were realized in Japan Energy Corporation by a simple thermal diffusion process. According to the authors¹², the success in overcoming the compensation effect in a II-VI material was due to the use of high quality p-type ZnTe single crystals with low dislocation densities of the level of 2000 cm^{-2} grown by the vertical gradient freezing (VGF) method and the suppression of the compensating point defects by low temperature annealing with the surface of the substrates covered by the deposited layer of aluminum (n-type dopant). The intrinsic p-n junctions were formed and the bright 550 nm electroluminescence from these p-n junctions was reproducibly observed at room temperature, with the lifetime exceeding 1000 hours. A more complex ZnTe structure produced by homoepitaxy on the ZnTe substrate is probably required for the construction of a green laser.

The poor quality of the heteroepitaxial (grown on alien substrates) layers of ZnTe results mainly from the lattice misfit, thermal misfit (different expansion coefficients), and from the diffusion of impurities from the substrate. Homoepitaxy of

ZnTe structures on ZnTe substrates is preferred! The ZnTe substrate crystals intended for manufacturing laser structures by homoepitaxy have to be large-size (50 mm in diameter) single crystals with perfect crystal structure, characterized by the FWHM (full width at half maximum) of the rocking curve below 20 arcsec, and the density of dislocations below $5 \times 10^3 \text{ cm}^{-2}$. Low-resistivity ($0.01 \div 0.1 \Omega \cdot \text{cm}$), p-type (e.g. phosphorus-doped) ZnTe substrate crystals are much-desired. As it has been shown in the text above — many important applications of the II-VI semiconductors require the crystals, which are of very high quality, at least with respect to some parameters. Before going to the technology of high quality crystals, it may be convenient to list the requirements appearing in the text above. A group, usually quite wide, of requirements from the following list applied to every discussed use of the II-VI semiconductor crystals.

- large single crystals — the diameters of about 50 mm
- no grain boundaries, no twins, perfect crystal structure, characterized by the FWHM of the rocking curve below 20 arc sec
- very high resistivity, above $10^{10} \Omega \cdot \text{cm}$
- very low resistivity, below $0.1 \Omega \cdot \text{cm}$
- uniform doping
- uniform distribution of intentional impurities
- low concentration of unintentional impurities
- homogeneous composition of the ternary compounds
- low concentration of point defects
- low density of dislocations, below $5 \times 10^3 \text{ cm}^{-2}$
- low concentration of precipitates
- "epi-ready" surface

3. THE TECHNOLOGIES OF HIGH-QUALITY II-VI SEMICONDUCTOR CRYSTALS

The technology of high-quality II-VI semiconductor crystals is difficult because of many unpleasant phenomena. Twinning may take place easily due to the temperature fluctuation during crystal growth. Softening quartz tubes become a source of contamination and hinder obtaining the crystals of large diameter. Dislocations are easily generated due to the stress from the container and the thermal stress during crystal growth. It is difficult to control the melt/solid interface shape as desired, because the heat released during solidification cannot be duly dissipated. These phenomena are the consequences of some parameters of the II-VI compounds, which are unfavourable for the technology: low stacking fault energy, high melting point, low critical resolved shear stress and low thermal conductivity.

Nowadays — the following methods of crystal growth are considered to be appropriate for the growth of high quality wide-gap II-VI semiconductor crystals:

- Modified Bridgman Methods
 - Travelling Heater Method
 - Cold Travelling Heater Method
 - Physical Vapour Transport
- We are going to describe shortly merits and demerits of those methods.

3.1 Modified Bridgman methods

A growth method called "vertical gradient freezing method" (VGF) has been described by Asahi et al.^{13,14} as applied to CdZnTe. VGF method is the Bridgman method modified in such a way that neither the furnace nor the ampoule containing the crystal are moved but the temperature profile of the furnace is continuously shifted by a proper electronic control of the temperature as a function of position and time in a multiple-zone furnace. The absence of the relative movement of the ampoule and furnace ensures more stable conditions at the crystallization front. The second modification was the use of a Cd reservoir outside the crucible made of pyrolytic boron nitride, in which the crystal was growing. Both the crucible and cadmium reservoir were sealed in one quartz ampoule, and the pressure of cadmium vapours in the crucible was controlled by the temperature of the cadmium reservoir (the temperature of the appropriate zone of the furnace) in order to regulate the stoichiometry of the melt. It was possible to achieve low concentration of cadmium vacancies. Because of the very low thermal conductivity, low growth rate of 1 mm/h was used.

The results were very promising - large (100 mm in diameter) single crystals were free of twins and grain boundaries, the density of dislocations was $4 \div 6 \times 10^4 \text{ cm}^{-2}$, the FWHM of the rocking curve — $8 \div 13 \text{ arcsec}$, resistivity — $30 \div 35 \Omega \cdot \text{cm}$, concentration of holes — $2.2 \times 10^{15} \text{ cm}^{-3}$, and their Hall mobility — $80 \div 100 \text{ cm}^2 \text{ V}^{-1} \text{ s}^{-1}$ for the whole ingot. The authors did

not discuss the segregation of zinc (composition homogeneity) along the ingot and the concentration of Te precipitates. The problem of zinc segregation is especially important for $\text{Cd}_{1-x}\text{Zn}_x\text{Te}$ crystals with $x > 0.1$. Such crystals are used for X-ray and gamma-ray detectors and optical modulators.

A very promising version of the VGF method has been applied to ZnTe by Seki, Sato, Oda and Matsuda^{15,16}. They used sapphire (Al_2O_3), with the surface parallel to the (0001) hexagonal crystallographic plane, as a hetero-seed for the growth of ZnTe. The sapphire does not dissolve in ZnTe and has a much higher melting point than ZnTe. There is a peculiar match between the crystal structures of sapphire and ZnTe - the (001) plane of ZnTe can be put on the (0001) plane of sapphire in such a way that some of the ZnTe atoms nearly hit the sapphire atoms. Just in this way ZnTe started to grow on the sapphire. The diameter of the growing crystals was up to 50 mm. The growth was performed either in stoichiometric conditions or as a growth from the tellurium-rich solution. The crystals grown in the stoichiometric conditions were of very high quality. In particular, the density of dislocations measured as etch pit density (EPD) was of 2000 cm^{-2} . In the crystals grown from the tellurium-rich solution the density of dislocations was higher — $10^5 \div 10^6 \text{ cm}^{-2}$, and a large amount of precipitates has been found, but the purity of crystals was better owing to the purifying effect of the solvent. The growth rate was 4.5 mm/day and 1 mm/day for the stoichiometric and non-stoichiometric growth, respectively.

The phenomenon which plagues the growth of the tellurium-based crystals by a Bridgman method or by any method of growth from the liquid phase is the precipitation of tellurium. According to Uchida et al.¹⁷ — the number of tellurium precipitates can be diminished only after crystallization, by the annealing of the crystal wafers in the cation vapor under controlled pressure. The wafers prepared in such a way have been successfully used in the manufacturing of the ZnTe-based green diode¹².

3.2. Travelling heater method

In the widely known "travelling heater method" (THM), developed by Triboulet and Didier¹⁸, the zone of hot liquid (tellurium in the tellurium-based crystals) travels slowly (a few millimeters per day) along a batch of previously synthesized polycrystalline material. High purity of the crystals grown by THM results from the refining effect of the travelling zone of liquid. The tellurium based crystals contain always tellurium precipitates. Usually it is difficult to obtain the whole cross-section of the ampoule filled with one single crystal.

3.3. Cold travelling heater method

In this method, elaborated by Triboulet, Pham Van and Didier¹⁹ for CdTe and ZnTe, the zone of liquid Te travels along a batch of elements (not a polycrystalline compound) in the form of pieces or powder. "The crossing of the solvent zone through this charge, at a temperature lower than the melting point of the compound, induces the fractional synthesis of the compound in Te solution, its growth and purification as well. Synthesis, growth and purification are thus achieved at low temperature, at the same time, in a simple and inexpensive furnace, in contrast to other processes." The best pair "growth temperature - growth rate" has been found to be 780°C — 2.5 mm/day for CdTe and 980°C — 3mm/day for ZnTe. The single crystals (large fragments of a rod, 20 mm in diameter) obtained with this method showed very high mobility of free carriers and low concentration of residual impurities but were apt to contain tellurium precipitates.

3.4. Physical vapour transport

The "physical vapour transport" (PVT) is a process, in which the previously synthesized compound ("source material") evaporates, goes to the region of a little lower temperature and condenses, causing the growth of the crystal. The advantage of all the vapor-phase methods of growth of the II-VI compounds is the low temperature, which is usually $250 \div 400^\circ\text{C}$ below the melting point. Thus, the tendency to twinning and contamination is greatly reduced. Another good point of these methods is the effect of "self purification". The impurities, which are less volatile than the crystallizing compound, remain at the place of the source material.

The contact between the growing crystal and the wall of the quartz ampoule poses very serious problems (contamination, stress etc.). The "contactless" PVT growth method has been elaborated for CdS by Markov and Davydov²⁰. Grasz et al.²¹⁻²³ have developed the "contactless" method for CdTe and ZnTe using a very peculiar procedure to achieve self-seeding at low supersaturation. The method is complex, requires a great operational skill, but results in the single crystals of very high quality.

The main disadvantage of the crystallization from the vapour phase is the slow pace of the process. Usually the rate of the crystal growth is below 10 mm per day.

4. THE HIGH-QUALITY CRYSTALS OF ZnTe AND CdZnTe GROWN BY THE AUTHORS

4.1. The method of growth

We have chosen^{24,25} the simple horizontal vapour transport method, described by Piper and Polich²⁶ in the first paper on the PVT technique. The process of crystallization proceeded in a closed horizontal quartz ampoule with a conical tip at the colder end. The temperature profile of the furnace was presented in one of our papers²⁷. The design of the furnace allowed us to observe the process of nucleation in the tip of the ampoule. Typical growth rate for good quality crystals was of $3 \div 10$ mm/day. The crystal rods 25 mm in diameter and $30 \div 50$ mm long were grown. Because the quality of the source material, which should be stoichiometric (very important!), pure, and free of trapped gases, turned out to be one of the fundamental factors influencing the process of growth and the quality of the crystals — the source material was the object of characterization nearly as extensive as that used for the final crystals.

4.2. Methods of characterization of the crystals

The quality of the crystal structure was checked by X-ray rocking curve measurements with a Philips High Resolution Diffractometer, by the reciprocal space mapping, by the etch pit density (EPD) measurements (to determine the density of dislocations) and by the measurement of the width of the free exciton structure in the reflection spectrum. The composition of the ternary $\text{Cd}_{1-x}\text{Zn}_x\text{Te}$ crystals was studied by the energy dispersive X-ray fluorescence (EDXRF) measurements, by the measurements (at 2 K) of the position of the free exciton structure in the reflection spectrum and of the position of the bound exciton line in the luminescence spectrum²⁸. The impurities were investigated by the luminescence, reflectivity, conductivity, and Hall effect measurements.

4.3. Results of characterization

The FWHM of the rocking curve was of about 17 arcsec for both $\text{Cd}_{0.89}\text{Zn}_{0.11}\text{Te}$ and ZnTe crystals. The EPD was in the range $5 \times 10^3 \div 10^4 \text{ cm}^{-2}$ for $\text{Cd}_{1-x}\text{Zn}_x\text{Te}$ crystals and about 10^4 cm^{-2} for ZnTe. The reciprocal space mapping of the crystals has shown that the stress (related to the chemical disorder) in the ternary crystals was very small. The distance between minimum and maximum of the free exciton structure in the reflectivity spectrum was only 1.5 meV for ZnTe crystals and the free exciton peak in luminescence was clearly seen in the vicinity of the free exciton structure in reflection.

The homogeneous composition of the CdZnTe crystals was a very important achievement. Very small decrease of the Zn content could be seen in the growth direction, but there was usually a "plateau" in the middle of the rod, indicating a large, homogeneous piece of crystal.

While the lines belonging to excitons bound to neutral acceptors: Ag_{Zn} and Li_{Zn} and the DAP band corresponding to Na-acceptors could be detected, the Cu-related DAP band and the characteristic oxygen-related band were below the detection limits. The concentration of Cu impurity was estimated to be well below 10^{15} cm^{-3} . At room temperature the crystals of ZnTe and $\text{Cd}_{1-x}\text{Zn}_x\text{Te}$ were of p-type. The concentration of holes in the $\text{Cd}_{1-x}\text{Zn}_x\text{Te}$ crystals was, for example, of 10^{16} cm^{-3} , according to Hall effect measurements (resistivity of about $10 \Omega \cdot \text{cm}$). The high resistivity CdZnTe crystals, transparent to the infrared light up to the wavelength of 20 micrometers, were prepared by annealing in Zn vapor ambient. The room temperature resistivity of the annealed crystals was $10^6 \div 10^7 \Omega \cdot \text{cm}$.

5. CONCLUSIONS

The wide-gap II-VI semiconductors begin to be extensively used in many important fields of technology because various properties of those crystals make them, for specific applications, superior to the other ones. But very often the great advantage of the application of those semiconductors can be revealed not before the crystals of very high quality can be grown. This is the reason why the technology of the *very high quality crystals* of the wide-gap II-VI semiconductors has to be developed.

ACKNOWLEDGEMENTS

The authors wish to express their gratitude: to Dr. L. Kowalczyk and Mr. W. Oksiński for luminescence measurements, to Dr. W. Dobrowolski for EDXRF measurements and to Dr. A. Zaręba for conductivity measurements.

This work was supported in part by the Committee for Scientific Research through grant No. 7 T08A 010 19

REFERENCES

1. T. E. Schlesinger and R. B. James (volume editors), *Semiconductors for room temperature nuclear detector applications. Semiconductors and semimetals. Vol. 43*, Academic Press, San Diego, 1995
2. A. A. Melnikov, A. S. Sigov, K. A. Vorotilov, A. A. Davydov, L. I. Topalova and N. V. Zhavoronkov, "Growth of CdZnTe single crystals for radiation detectors," *J. Cryst. Growth* **197** pp.666-669, 1999.
3. P. Fougeres, P. Siffert, M. Hage-Ali, J. M. Koebel and R. Regal, "CdTe and $Cd_{1-x}Zn_xTe$ for nuclear detectors: facts and fictions." *Nuclear Instruments & Methods in Physics Research Section A-Accelerators Spectrometers Detectors & Associated Equipment* **428**, pp. 38-44, 1999.
4. T. Kamae, "Developments in semiconductor detector technology and new applications-symposium summary." *Nuclear Instruments & Methods in Physics Research Section A-Accelerators Spectrometers Detectors & Associated Equipment* **436**, pp.297-303, 1999.
5. Z. He, W. Li, G. F. Knoll, D. K. Wehe and Y. F. Du, "Effects of charge sharing in 3-D position sensitive CdZnTe gamma-ray spectrometers." *Nuclear Instruments & Methods in Physics Research Section A-Accelerators Spectrometers Detectors & Associated Equipment* **439**, pp.619-624, 2000.
6. M. A. J. van Pamelén, C. Budtz-Jorgensen and I. Kuvvetli, "Development of CdZnTe X-ray detectors at DSRI." *Nuclear Instruments & Methods in Physics Research Section A-Accelerators Spectrometers Detectors & Associated Equipment* **439**, pp.625-633, 2000.
7. A. Rogalski, "Infrared thermal detectors versus photon detectors. II. Focal plane arrays." *Proceedings of SPIE - the International Society for Optical Engineering* **3179**, pp. 224-234, 1997.
8. E. Garmire and A. Kost (volume editors), *Nonlinear optics in semiconductors I. Semiconductors and semimetals. Vol. 58*, Academic Press, San Diego, 1999.
9. R. Triboulet, E. Rzepka, A. Aoudia, G. Martel and J-Y. Moisan, "Growth issues of CdZnTe crystals doped with transition elements for photorefractive applications." *Proceedings of SPIE - the International Society for Optical Engineering* **3178**, pp. 22-30, 1997.
10. Y. Marfaing, "State of the art and prospects of photorefractive CdTe." *J. Cryst. Growth* **197**, pp. 707-717, 1999.
11. J. A. Gaj, R. R. Galazka, M. Nawrocki, "Giant exciton Faraday rotation in $Cd_{1-x}Mn_xTe$ mixed crystals," *Solid State Communications* **25**, pp. 193-195, 1978.
12. K. Sato, M. Hanafusa, A. Noda, A. Arakawa, T. Asahi, M. Uchida and O. Oda, "Pure green light-emitting diodes based on high quality ZnTe substrates and a thermal diffusion process." *IEICE Transactions on Electronics* **E83-C**, pp. 579-584, 2000.
13. T. Asahi, O. Oda, Y. Taniguchi and A. Koyama, "Characterization of 100 mm diameter CdZnTe single crystals grown by the vertical gradient freezing method." *J. Cryst. Growth* **149**, pp. 23-29, 1995.
14. T. Asahi, O. Oda, Y. Taniguchi and A. Koyama, "Growth and characterization of 100 mm diameter CdZnTe single crystals by the vertical gradient freezing method." *J. Cryst. Growth* **161**, pp. 20-27, 1996.
15. Y. Seki, K. Sato and O. Oda, "Solution growth of ZnTe single crystals by the vertical Bridgman method using a hetero-seeding technique." *J. Cryst. Growth* **171**, pp.32-8, 1997.
16. K. Sato, Y. Seki, Y. Matsuda and O. Oda, "Recent developments in II-VI substrates." *J. Cryst. Growth* **197**, pp. 413-422, 1999.
17. M. Uchida, Y. Matsuda, T. Asahi, K. Sato and O. Oda, "Stoichiometry control of ZnTe single crystals by the vapor pressure-controlled wafer-annealing method." *J. Cryst. Growth* **216**, pp. 134-140, 2000.
18. R. Triboulet and G. Didier, "Growth of ZnTe by stoichiometric and off stoichiometric zone refining." *J. Cryst. Growth* **28**, pp. 29-35, 1975.
19. R. Triboulet, K. Pham Van and G. Didier, " 'Cold travelling heater method', a novel technique of synthesis, purification and growth of CdTe and ZnTe." *J. Cryst. Growth* **101**, pp. 216-220, 1990.
20. E. V. Markov, A. A. Davydov, "Sublimation of CdS crystals," *Izv. Akad. Nauk SSSR, Neorg. Mater* **7**, pp. 575-579, 1971
21. K. Graszka, U. Zuzga-Graszka, A. Jędrzejczak, R. R. Gałazka, J. Majewski, A. Szadkowski, E. Grodzicka, "A novel method of crystal growth by physical vapor transport and its application to CdTe," *J. Cryst. Growth* **123**, pp. 519-528, 1992
22. K. Graszka, "Bulk vapour growth of CdTe," *J. Cryst. Growth* **146**, pp. 65-68, 1995
23. K. Graszka, S. B. Trivedi, Z. Yu, S. W. Kutcher, W. Palosz, G. A. Brost, "Low supersaturation nucleation and contactless growth of photorefractive ZnTe crystals," *J. Cryst. Growth* **174**, pp. 719-725, 1997

24. A. Mycielski, E. Łusakowska, A. Szadkowski and L. Kowalczyk, "Low defect density, substrate quality crystals of the wide-gap II-VI compounds, obtained by physical vapour transport technique," *J. Cryst. Growth* **184/185**, pp. 1044-1047, 1998
25. A. Mycielski, A. Szadkowski, E. Łusakowska, L. Kowalczyk, J. Domagała, J. Bąk-Misiuk, Z. Wilamowski, "Parameters of substrates - single crystals of ZnTe and $\text{Cd}_{1-x}\text{Zn}_x\text{Te}$ ($x < 0.25$), obtained by physical vapor transport technique (PVT)." *J. Cryst. Growth* **197**, pp. 423-426, 1999
26. W. W. Piper and S. J. Polich, "Vapor-phase growth of single crystals of II-VI compounds," *J. Appl. Phys.* **32**, pp. 1278-1279, 1961
27. K. Grasa, E. Janik, A. Mycielski and J. Bąk-Misiuk, "The optimal temperature profile in crystal growth from the vapour," *J. Cryst. Growth* **146**, pp. 75-79, 1995
28. J. Gonzalez Hernandez, E. Lopez Cruz, D. D. Allred, W. P. Allred, "Photoluminescence studies in $\text{Zn}_x\text{Cd}_{1-x}\text{Te}$ single crystals," *J. Vac. Sci. Technol. A, Vac. Surf. Films* **8**, pp. 3255-3259, 1990

Annealing of GaSb single crystals in ionised hydrogen atmosphere

Bedřich Štěpánek, Věra Šestáková and Jaroslav Šesták

Institute of Physics, Semiconductor Department, Academy of Sciences of the Czech Republic,
Cukrovarnická 10, 162 00 Praha 6, Czech Republic

ABSTRACT

GaSb undoped wafer were annealed in flowing ionised hydrogen atmosphere at temperature range between 100 – 350°C for 1 – 50 hours. The free carrier concentration and resistivity were measured. It was found out that the wafers being treated at a temperature of 150°C for 24 hours reached the resistivity of about $10^2 - 10^3 \Omega \cdot \text{cm}$ and the free carrier concentration was lower than $1 \times 10^{15} \text{ cm}^{-3}$. However, the thickness of the passivated layer was only 0.4 – 0.6 μm .

1. INTRODUCTION

Gallium antimonide (GaSb) single crystals are promising candidates for a variety of military and civil applications in the 2 - 5 and 8 - 14 μm ranges, among others infrared (IR) imaging sensors for missile and surveillance systems (so-called focal plane arrays), fire detection and monitoring environmental pollution and other light diodes and lasers. In comparison with traditional GaAs, InSb, InP, for which the semi-insulating as well as conductive material is available, GaSb has a disadvantage: its conductivity that is usually very high due to the large amount of p-type natural defects in the lattice, which puts very serious limits on the construction of GaSb-based devices. To develop high-resistive GaSb, intensive optimisation of doping and growth conditions was undertaken^{1,2}. Doping by the following elements Cu, Zn, Cd, In, Si, Ge, Sn, N, As, S, Te, Mn was investigated^{3,4,5,6} systematically using the Czochralski method of growth without encapsulant in a hydrogen flowing atmosphere as well as by diffusion studies⁷. The limit of the doping concentration of each dopant was measured indicating the lowest solubility for S, N, Cu, and the highest for In, Ge, Te, As⁸. Extensive thermodynamic evaluation were also carried out and directed to analyse some binaries and ternaries, such Ga-Sb-S (Te, Cu), etc.^{3,4,5}.

However, in spite of big efforts, the desired low conductivity material was not obtained yet. Therefore a special and rather unique method has been developed using the passivation of active donors of n-type (Te-doped) crystals by protons during the inherent growth realised in the ionised hydrogen atmosphere generated in situ by deuterium lamp radiation^{9,10}. From a thermodynamic point of view the ionised hydrogen passives a part of donors and shifts equilibrium between passivated and active donors depending on the starting concentration of n- and p-dopants to the intrinsic-like position. The preparation of stable GaSb with sufficiently high resistivity would open unique perspectives in the construction of integrated IR-optoelectronic devices of a new generation.

A major drawback of GaSb substrates is their higher concentration of residual acceptors that reach, in the pure undoped GaSb single crystal, a value¹¹ of about $1.7 \times 10^{17} \text{ cm}^{-3}$. The acceptors are identified as $V_{\text{Ga}}\text{GaSb}$ complexes (where V is the vacancy) with a double ionised structure¹². The resulting resistivity of undoped GaSb single crystals is about $10^{-2} \Omega \cdot \text{cm}$. Many researchers have tried to reduce the residual acceptor concentration and to increase the resistivity of GaSb.

The achieved results of growth under the ionised hydrogen atmosphere were sufficiently stimulating to encourage us in opening the question of annealing of GaSb wafers in ionised hydrogen a to study influence of this treatment on change of free carrier concentration and resistivity.

2. EXPERIMENTAL AND DISCUSSION

Hydrogen passivation of different defects and impurities was studied in many III-V compounds^{13,14}. Polyakov et al¹⁵ treated GaSb samples either undoped or Zn- or Si-doped both in hydrogen and in deuterium atmosphere in the temperature range between 100 - 250°C and with the exposure times of 0.5 - 1 hour with interesting results. In the case of the undoped GaSb

the carrier concentration decreased as much as to the value of about $1 \times 10^{16} \text{ cm}^{-3}$ and the resistivity increased by one order of magnitude. Polyakov et al.'s method showed that this way is likely to successfully manage the preparation of least high-resistivity GaSb crystals with a low carrier concentration.

Using the Czochralski method without encapsulant in a hydrogen flowing atmosphere the undoped GaSb single crystals were grown having a carrier concentration of $(1.70 - 1.80) \times 10^{17} \text{ cm}^{-3}$ and a resistivity of $(6.50 - 6.70) \times 10^{-2} \Omega \cdot \text{cm}$. The crystal bowl was cut to the wafers with a thickness of 200 μm . The samples were treated in a quartz tube at temperatures of 100, 120, 150, 180, 200, 220, 250, 280 and 350°C for 1-50 hours. Hydrogen ionised by means of a deuterium lamp flew through this annealing reactor. After cooling the quartz ampoule, the carrier concentration and the resistivity were measured on the treated wafers in the first step by means of van der Pauw method. Then the layers of about 10 μm on both sides of the wafers were ground out and the electrical measurements were repeated.

It turned out that in the case of the temperature range 200 - 350°C (Fig.1.); the values of the measured parameters were the same, both before and after the temperature annealing. However, when the temperature was lower than 200°C, mainly at 150°C, and the duration of the annealing procedure exceeded 10 hours, the carrier concentration in the nonground wafers achieved the value of $(1.20 - 1.30) \times 10^{17} \text{ cm}^{-3}$ (i.e. about 40%). After grinding a 10 μm layer, the carrier concentration was the same as in the case of the untreated samples.

This method of measurement, however, is influenced by a high inaccuracy because the total volume of the samples was measured for only a small passivated layer. For this reason, the resistivity and free carrier concentration were studied by the spreading resistivity procedure. It has been found that in the case of the wafers being treated at a temperature of 150°C for 24 h, the thickness of the passivated layer was only 0.4 - 0.6 μm and its resistivity reached value of $10^2 - 10^3 \Omega \cdot \text{cm}$. The free carrier concentration was lower than $1 \times 10^{15} \text{ cm}^{-3}$ and with increasing time of temperature treatment the values of free carrier concentration does not change essentially. It seems the optimal duration to be about 20 - 30 hours only. However, such a thin layer of high-resistivity GaSb crystals would be difficult to fabricate because, on the one hand, the thickness of the layer was not uniform on the surface of the wafers and, on the other hand, the spreading of the resistivity was very inhomogeneous.

3. CONCLUSIONS

The results of electrical measurements show that the ionised hydrogen does effect the resistivity of GaSb. However, the effect of temperature is not fully clear (Fig.2.). We only suggest that the temperature influence, on the one hand, the diffusion of ionised hydrogen into GaSb material and, on the other hand, the evaporation of hydrogen from the crystal. The equilibrium could create between these effects and for this reason the temperature of 150°C seems to be the most suitable for obtaining GaSb with low free carrier concentration. Diffusion of ionised hydrogen into GaSb wafers play very important role in decrease of free carrier concentration during the temperature treatment and could be said that the diffusion is the limiting factor. Of course, higher temperature speed up the diffusivity, however, in the case of our procedure the ionised hydrogen also starts either to recombining to molecular hydrogen or evaporating from material. It seems that annealing in higher pressure of hydrogen could help to stimulate diffusion and prevent evaporation from GaSb.

Next study will be mainly oriented to look for new methods how to increase ionised hydrogen concentration in GaSb material and if it is still possible to work in the region of higher temperature, especially at melting point of GaSb (712°C), i.e. during crystal growth.

It is worth noting that we are in process to study this effect in more detail and to use special thermodynamic procedure.

ACKNOWLEDGEMENT

The work was supported by the Grant Agency of the Czech Republic Nr. 104/97/0589, Nr. 100/98/0024 and Nr. 203/98/1276. The authors would like to express their thanks to Mr. V.Charvat (Institute of Physics, Czech Republic) for his excellent co-operation and fruitful help.

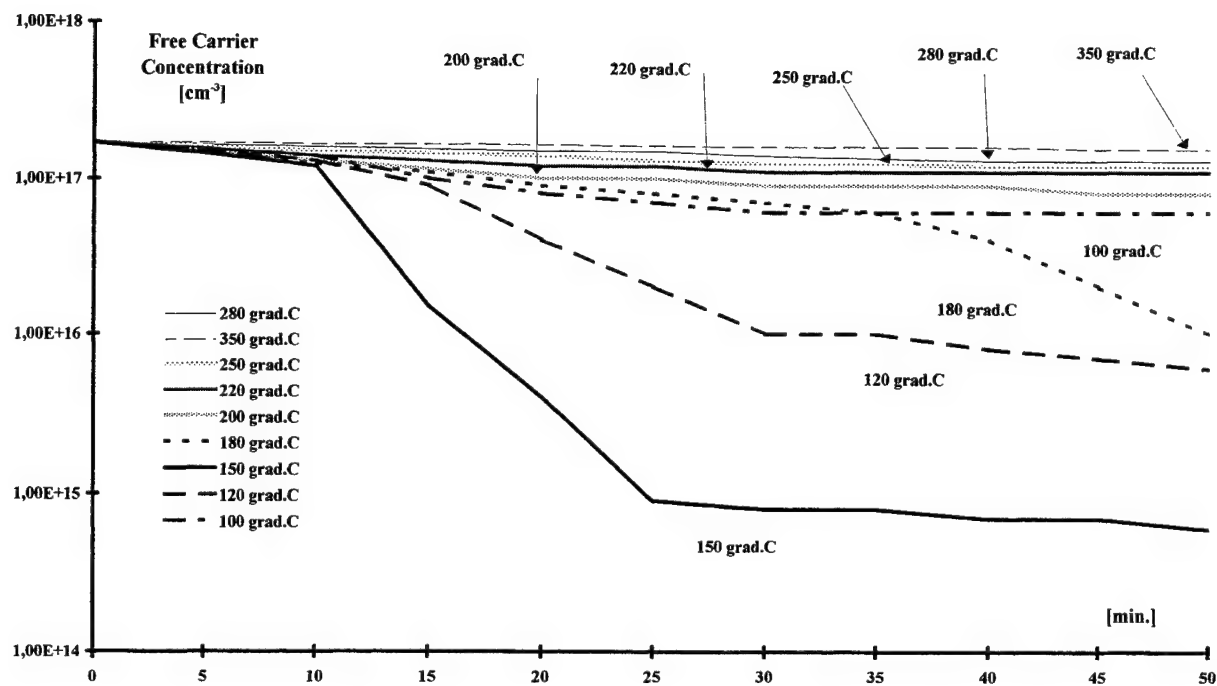


Fig. 1. Dependence of free carrier concentration on temperature and duration of annealing.

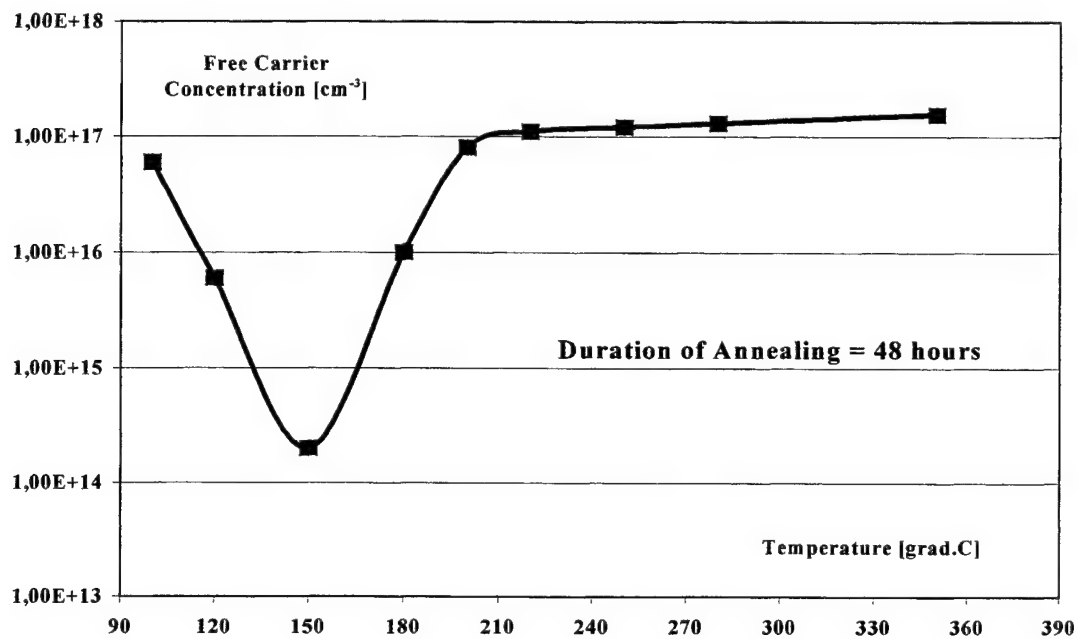


Fig. 2. Dependence of free carrier concentration on temperature of annealing of 48 hours.

REFERENCES

1. B.Štěpánek, V.Šestáková and J.Šesták, "Comparative analysis of GaSb single crystal growth techniques," *Inorganic Mater.* **29**, pp. 1071-1075, 1993.
2. V.Šestáková, B.Štěpánek and J.Šesták, "Various methods for the growth of GaSb single crystals," *J.Cryst. Growth* **165**, pp. 159-162, 1996
3. V.Šestáková, B.Štěpánek, J.Šesták, P.Hubík and V.Šmíd, "Thermodynamic aspects of (Te,S)-double-doped GaSb crystal growth," *Mater. Sci. Eng.* **B2**, pp. 14-18, 1993.
4. J.Šesták, J.Leitner, H.Yokokawa and B.Štěpánek, "Thermodynamics and phase equilibrium data in the S-Ga-Sb system auxiliary to the growth of doped GaSb single crystals," *Thermo. Acta* **245**, pp. 189-206, 1994.
5. J.Šesták, V.Šestáková and Z.Zivkovic, "Estimation of activity data for the Ga-Sb-S binaries regarding the doped GaSb semiconductor crystals," *Pure Appl.Chem.* **67**, pp. 1885-1889, 1995
6. V.Šestáková and B.Štěpánek, "Doping of GaSb single crystals with various elements." *J. Cryst. Growth* **146**, pp. 87-91, 1995.
7. J.Mimkes, V.Šestáková, K.M.Nassr, M.Lübbbers and B.Štěpánek, "Diffusion mobility and defect analysis in GaSb," *J. Cryst. Growth* **187**, pp. 355-362, 1998.
8. V.Šestáková, B.Štěpánek and J.Šesták, "Estimation of doping limit of some elements in GaSb single crystals," *Proc. of SPIE, Single Crystal Growth, Characterisation, and Applications* **3724**, pp. 125-129, 1999.
9. V.Šestáková, B.Štěpánek, J.J Mareš and J Šesták, "Decrease in free carrier concentration in GaSb crystals using an ionised hydrogen atmosphere," *Materials Chem. and Phys.* **45**, pp. 39-42, 1996.
10. B.Štěpánek, V.Šestáková and J.Šesták, "Growth of GaSb single crystals with low carrier concentration," *Proc. SPIE, Solid State Crystals: Growth and Characterisation* **3178**, pp. 64-67, 1996.
11. B.Štěpánek and V.Šestáková, "Czochralski grown concentration profiles in the undoped and Te-doped GaSb single crystals," *Thermochim. Acta* **209**, pp. 285-294, 1992.
12. Y.J.Van der Meulen, "Growth properties of GaSb: The structure of the residual acceptor centres," *Phys. Chem. Solids* **28**, pp. 25-32, 1967.
13. S.J.Pearson, J.W.Corbett and T.S.Shi, "Hydrogen in crystalline semiconductors," *Appl.Phys. A* **43**, pp. 153-195, 1987.
14. J.Chevallier and M.Aucouturier, "Influence of hydrogen atmosphere in III – V semiconductor crystals," *Ann.Rev. Mater.Sci.* **18**, pp. 219-268, 1988.
15. A.Y.Polyakov, S.J.Pearson, R.G.Wilson, R.Rai-Choudhury, R.J.Hillard, X.J.Hillard, X.J.Bao, M.Stam, A.G. Milnes, T.E.Schlesinger and J.Lopata, "Hydrogen treatment effect on shallow and deep centres in GaSb," *Appl. Phys.Lett.* **60**, pp. 1318-1320, 1992.

Growth and structure of strontium doped LaGaO₃

R. Alekseyko¹, M. Berkowski¹, J. Fink-Finowicki¹, P. Byszewski^{1,2},
R. Diduszko², E. Kowalska²

¹Institute of Physics Polish Academy of Sciences, Al. Lotników 32/46, 02-668 Warsaw, Poland

²Institute of Vacuum Technology, ul. Długa 44/50, 00-241 Warsaw, Poland

ABSTRACT

A series of La_{1-x}Sr_xGaO₃ solid solution single crystals with $x = 0, 0.04$ and 0.12 were grown by the Czochralski method and with $x = 0.01, 0.06$ and 0.1 by the floating zone method. The segregation coefficient of Sr in LaGaO₃ has been found to be $k_{\text{eff}}(\text{Sr}) = 1.25 (\pm 0.01)$. The crystals were grown from the melt with stoichiometric Ga₂O₃ amount at a growth rate ranging from 2.5 mm/h for pure LaGaO₃ to 1.2 mm/h for La_{0.88}Sr_{0.12}GaO₃.

The structure of these crystals was investigated by X-ray powder diffraction technique using CuK α radiation. The diffraction patterns were analyzed by Rietveld refinement method. Crystals with strontium concentrations from $x = 0$ to 0.1 crystallizes adopting Pbnm structure. It was found that deviation from the ideal perovskite structure decreases with rising strontium concentration, finally reaching centrosymmetric Ibmm structure at $x = 0.12$. Orthorhombic unit cell parameters c and b decreases whereas a increases with x .

Thermal analysis proved that the temperature of the first order phase transition observed in pure LaGaO₃ at 150 °C falls to 126 °C at $x = 0.01$ and remains almost constant at higher x .

Keywords: crystal growth, doping, Czochralski method, high temperature superconductor epitaksy.

1. INTRODUCTION

LaGaO₃ crystallizing in the space group Pbnm¹⁻³ would be an attractive substrate material for YBCO epitaxial films⁴, because of a small lattice mismatch and good chemical stability resulting from its relatively high melting point of 1710 °C were it not for the fact that a structural phase transition occurs at ~150 °C⁵. The phase transition is the most serious drawback of many lanthanide gallates and aluminates⁵ for it can cause formation of twins and roughness of the substrate surface⁶. We have previously investigated the La_{1-x}Nd_xGaO₃ La_{1-x}Pr_xGaO₃ systems^{7,8} and found crystals with the lattice parameters suitable as substrates for High Temperature Superconductors (HTSc) epitaxy.

The thermal analysis proved that the temperature of the first order phase transition observed in LaGaO₃ rises linearly with Nd and Pr concentration x at the rate of 20.5 °C/Nd mol % and 13.3 °C/Pr mol % respectively. Apart from Pr and Nd we have also investigated other isomorphous rare earth elements including Sm, Eu and Er in LaGaO₃ single crystal. Substitution of Sm, Eu and Er increases the phase transition temperature at the rate higher than Pr and Nd. It shows that the phase transition temperature increases at higher rate for smaller ions. This results suggest possibility of using larger ions like Sr that should decrease the phase transition temperature.

It is interesting to note that the volume of GaO₆ octahedron increases in both systems despite decrease of the unit cell volume. The ratio of the perovskite unit cell to the octahedron volume linearly decreases with x from 5.73 in LaGaO₃ to 5.55 in PrGaO₃ and 5.57 in pure NdGaO₃, while in the ideal perovskite lattice it equals 6. This ratio indicates that La, Pr and Nd ions are too small to form the cubic lattice but Sr might be sufficiently large in order to remove the distortion.

It has been found that only Pr and Nd galates form solid solutions in the whole concentration range with LaGaO₃. The solubility limit of other rare earth elements decreases rapidly with decreasing radii of ions smaller than La. Nonisomorphic substitution should be possible in a limited range of concentration lowering phase transition temperature and decreasing unit cell distortion.

2. GROWTH OF La_{1-x}Sr_xGaO₃ SINGLE CRYSTALS

A series of La_{1-x}Sr_xGaO₃ solid solution single crystals with $x = 0, 0.04, 0.12$ were grown by the Czochralski method and with $x = 0.01, 0.06, 0.1$ by the floating zone method. The growth processes by the floating zone method were carried out in the ambient atmosphere at 2mm/h growth rate using rods sintered at 1340 °C.

The floating zone method allows growing mixed crystals with constant concentration of the admixture along the growth direction, apart from the relatively short regions at the beginning and the end of the grown crystal. Thus, the crystals obtained by the floating zone method can be used not only for investigation but also as a reference with well defined composition for future comparison with crystals grown by the Czochralski method. Quality of the crystals grown by this method decreases with increasing strontium concentration; therefore we employed the Czochralski method to grow crystals with high Sr concentration.

In order to grow solid solution single crystals by the Czochralski method with a definite composition, the segregation coefficient of the admixture in the host lattice has to be known. The segregation coefficient can be derived from both ions concentration varying along the crystal in the growth direction. The details of the derivation procedure are described in⁷.

The admixture concentration in solid solution single crystals along the crystal growth directions was measured by the Electron Probe Microanalysis (EPMA) method. The accuracy of this method depends on the type of reference sample, therefore we used crystals grown by the floating zone method as the reference. The effective segregation coefficient of strontium in LaGaO_3 $k_{\text{eff}}(\text{Sr}) = 1.25 (\pm 0.01)$ was determined from the crystal grown by the Czochralski method from the melt containing 3.2 Sr at. %. Because of Sr segregation, the crystals contained 4 Sr at. %.

It has been found that the concentration of Ga_2O_3 in LaGaO_3 , $\text{La}_{1-x}\text{Sr}_x\text{GaO}_3$ single crystals grown by the Czochralski method is slightly lower than that corresponding to the stoichiometric composition. Consequently, if the process is started from the melt of stoichiometric composition, the concentration of Ga_2O_3 in the melt increases with time. The increase in Ga_2O_3 concentration is compensated to a substantial degree by thermal dissociation of Ga_2O_3 followed by evaporation of dissociation products. This process can be controlled by partial pressure of oxygen in the growth chamber atmosphere. The best crystals were grown when they were pulled from the melt with the stoichiometric Ga_2O_3 concentration in a nitrogen atmosphere containing 1 vol. % of oxygen, at the pulling rate from 2.5 mm/h (for pure LaGaO_3) to 1.2 mm/h (for $\text{La}_{0.88}\text{Sr}_{0.12}\text{GaO}_3$).

3. ANALYSES OF THE $\text{La}_{1-x}\text{Sr}_x\text{GaO}_3$ STRUCTURE

The structure of $\text{La}_{1-x}\text{Sr}_x\text{GaO}_3$ solid solution crystals was investigated by means of precise X-ray powder diffraction technique using $\text{Cu K}\alpha$ radiation. Since these crystals exhibit a distinct tendency to twinning, it is difficult², to prepare a single domain sample necessary for single crystal diffraction technique. We preferred to rely on the powder X-ray diffraction because twins does not interfere with this technique. The diffraction was measured in a $\theta/2\theta$ scanning mode in the angle range $19^\circ < 2\theta < 150^\circ$ with a step of 0.02° and averaging time of 10 s/step.

Table 1. Crystallographic data of $\text{La}_{1-x}\text{Sr}_x\text{GaO}_3$ solid solutions.

Atom sites	Parameters	$\text{La}_{1-x}\text{Sr}_x\text{GaO}_3$						
		Pbnm						Ibmm
		x=0	0.01	0.04	0.06	0.1	0.12	0.12
	a, Å	5.52469	5.52479	5.5248	5.52723	5.52872	5.529	5.52898
	b, Å	5.49259	5.49062	5.49062	5.4901	5.48911	5.48772	5.48771
	c, Å	7.7744	7.77121	7.7712	7.77095	7.77033	7.77032	7.77031
	V, Å ³	235.91	235.74	235.74	235.81	235.81	235.76	235.76
La(Sr) 4c	x	-0.0033	-0.00369	-0.00408	-0.00238	-0.00514	-0.003	-0.00363
	y	0.0176	0.01508	0.01526	0.01240	0.00906	0.00491	0
	z	0.25	0.25	0.25	0.25	0.25	0.25	0.25
Ga 4b	x	0.5	0.5	0.5	0.5	0.5	0.5	0.5
	y	0	0	0	0	0	0	0
	z	0	0	0	0	0	0	0
O1 4c	x	0.07070	0.07349	0.07306	0.09483	0.07114	0.10565	0.10874
	y	0.508	0.50046	0.50091	0.46691	0.49851	0.50316	0.5
	z	0.25	0.25	0.25	0.25	0.25	0.25	0.25
O2 8d	x	-0.28	-0.26771	-0.26814	-0.25538	-0.26412	-0.2738	0.25
	y	0.269	0.27154	0.27379	0.25741	0.28073	0.27099	0.25
	z	0.039	0.04167	0.04119	0.05817	0.02848	0.03222	0.02626

The diffraction patterns were analyzed by the Rietveld refinement method, using the DBWS-9006PC package⁹. This package allows one to take into account positional and thermal corrections, scaling factor, zero shift, background parameter, Bragg-peak profile parameter and extinction correction. The diffraction patterns were analyzed in $44^\circ < 2\theta < 150^\circ$ range only, in order to avoid experimental errors that might arise from misalignment of the samples particularly at low diffraction angles. There are 480 reflections within this angle range for Cu $K_{\alpha 1}$ and Cu $K_{\alpha 2}$ lines, number sufficient for Rietveld analyzes. The structure was measured for following compositions $x=0, 0.01, 0.04, 0.06, 0.1, 0.12$. The lattice structure has been analyzed in $Ibmm$ and $Pbnm$ space groups, parameters and atom positions in both structures are listed in Table 1.

The diffraction patterns in the angle range $44^\circ < 2\theta < 71^\circ$ for Sr concentration $x=0, 0.04, 0.06, 0.1, 0.12$ is shown in Fig. 1. The plots are shifted vertically for clarity. There is evident decrease of intensity of some reflections with odd sum of h, k, l indices. At $x=0.12$ these reflections disappear completely. That is characteristic for higher space group symmetry: $Ibmm$. Thus, it ought to be concluded that lattice of $Pbnm$ symmetry at $0 < x < 0.12$ adopts the $Ibmm$ space group at $x=0.12$.

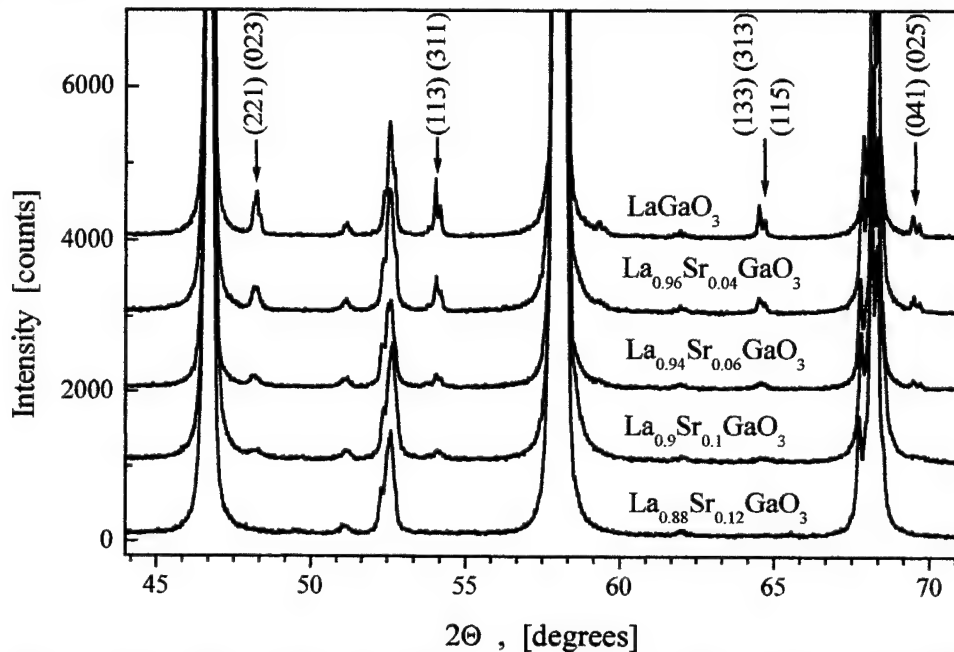


Figure 1. X-ray powder diffraction patterns of $La_{1-x}Sr_xGaO_3$ crystals. The plots are shifted vertically for clarity. The reflections characteristic for the $Pbnm$ symmetry are indexed.

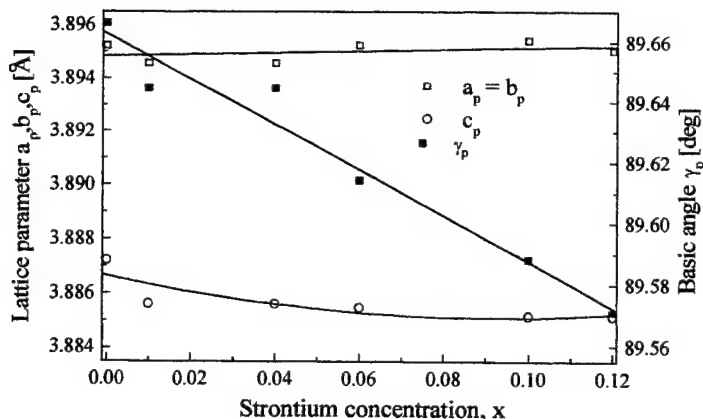


Figure 2. Perovskite-like unit cell parameters

The orthorhombic unit cell parameters a, b and c determined by Rietveld analyzes were used to calculate the parameters of a perovskite-like unit cell using the formulas: $a_p = \sqrt{(a^2 + b^2)} / 2$, $c_p = c/2$ and $\gamma_p = 2 * \arctg(b/a)$. The perovskite-like cell parameters of the $La_{1-x}Sr_xGaO_3$ crystals versus Sr concentration x are presented in Fig. 2. The lattice parameter a_p increases and c_p decreases with increasing Sr concentration though range of a_p change is smaller than of c_p , the angle γ_p at the base of the perovskite unit cell changes from 89.7° to 89.6° .

The projection of the unit cells along $<001>$ and $<010>$ directions of $La_{0.88}Sr_{0.12}GaO_3$ in $Ibmm$ and $Pbnm$ space groups are depicted in Fig. 3 in order to visualize the differences in

the atoms arrangement. There are evident differences between the unit cells: projections of the GaO_6 octahedra are rectangle in the Ibmm structure.

4. THERMAL ANALYSES

The temperature of the first order phase transitions was measured for following compositions $x=0, 0.01, 0.04, 0.1, 0.12$. The dependence of the first order phase transition temperature T_c on Sr concentration is presented in Fig. 4. The temperature changes nonlinearly with the composition, it may be assumed that in the range from $x=0$ to slightly above 0.01 the phase transition temperature changes at the rate of $-23.3^\circ\text{C}/\text{Sr mol \%}$, at higher concentrations $x \leq 0.12$ the rate decreases to about $2^\circ\text{C}/\text{Sr mol \%}$.

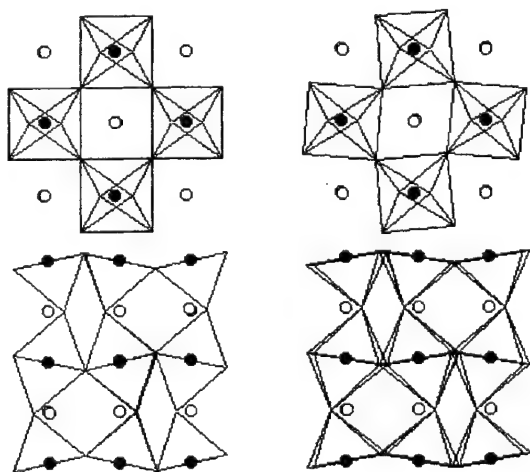


Figure 3. Projections along $\langle 001 \rangle$ (top) and $\langle 010 \rangle$ (bottom) of the unit cell in Ibmm (left) and Pbnm (right) space groups.

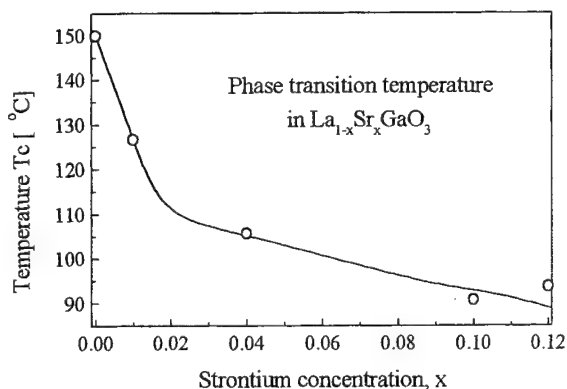


Figure 4. Phase transition temperature dependence on Sr concentration.

5. CONCLUSIONS

Large single crystals of $\text{La}_{1-x}\text{Sr}_x\text{GaO}_3$ solid solutions were grown by the Czochralski method in the concentration range from 0 to 0.12. The Sr segregation coefficient in LaGaO_3 has been determined to be $k_{\text{eff}}(\text{Sr}) \approx 1.25$. The solubility limit for nonisomorphic substitution of La by Sr is about 12 mol.% while up to about 1.5 mol.% the introduced admixture behaves as isomorphic substitute. The unit cell volume hardly changes with Sr concentration, it probably results from oxygen vacancies introduced by nonisomorphic doping.

It is interesting to note that with Sr concentration $x=0.12$ crystal adopts space group Ibmm not the expected Pbnm .

The first order phase transition temperature decreases linearly from $\sim 150^\circ\text{C}$ at the rate of approximately $23.3^\circ\text{C}/\text{Sr mol \%}$ in concentration range from $x=0$ to 0.01 and $2^\circ\text{C}/\text{Sr mol \%}$ in concentration range from $x=0.04$ to $x=0.12$.

The (110) oriented plane of the crystal with $x=0.04$ has the perovskite-like unit cell parameters $a_p = 3.8946 \text{ \AA}$ ($3 \cdot a_p = 11.6838 \text{ \AA}$) and $c_p = 3.8856 \text{ \AA}$ which are very close to the YBCO lattice constants $c = 11.6827 \text{ \AA}$ and $b = 3.8836 \text{ \AA}$ respectively.

ACKNOWLEDGEMENTS

This work was partially supported by the Polish Committee for Scientific Research under grant No 7T08A01115 and by the Polish Science Foundation, program Sezam.

REFERENCES

1. W. Marti, P. Fischer, F. Altorfer, H.J. Scheel, M. Tadin, "Crystal structures and phase transitions of orthorhombic and rhombohedral RGaO_3 ($\text{R}=\text{La, Pr, Nd}$) investigated by neutron powder diffraction", *J. Phys.: Condens. Matter* **6**, p. 127, 1994.

2. W. Marti, P. Fischer, J. Scheffer, F. Kubel, "Structure characterization with neutron powder data of LaGaO_3 based on X-ray single-crystal data: evidence for an inversion center", *Z. Kristallogr.* **211**, p. 891, 1996.
3. L.O. Vasylechko, A. Matkovskii, A. Suchocki, D. Savytskii, I. Syvorotka, "Crystal structure of LaGaO_3 and $(\text{La,Gd})\text{GaO}_3$ solid solutions", *J. Alloys and Compounds* **286**, p. 213, 1999.
4. R.L. Sandstrom, E.A. Giess, W.J. Gallagher, A. Segmüller, E.I. Cooper, M.F. Chisholm, A. Gupta, S. Shinole, R.B. Laibowitz, "Lanthanum gallate substrates for epitaxial high-temperature superconducting thin films", *Appl. Phys. Lett.*, **53**, p. 1874, 1988.
5. H.M. O'Bryan, P.K. Gallagher, G.W. Berkstresser and C.D. Brandle, "Thermal analysis of rare earth gallates and aluminates", *J. Mater. Res.* **5**, p. 183, 1990.
6. S. Miyazawa, "Surface roughening associated with $\sim 140^\circ\text{C}$ transition of a LaGaO_3 substrate for high T_c superconducting films", *Appl. Phys. Letters*, **55**, p. 2230, 1989.
7. M. Berkowski, J. Fink-Finowicki, W. Piekarczyk, L. Perchuć, P. Byszewski, L.O. Vasylechko, D.I. Savytskii K. Mazur, J. Sass, E. Kowalska, J. Kapuśniak, "Czochralski growth and structural investigations of $\text{La}_{1-x}\text{Nd}_x\text{GaO}_3$ solid solution single crystals", *J. Crystal Growth* **209**, p. 75, 2000.
8. M. Berkowski, J. Fink-Finowicki, P. Byszewski, R. Didusko, E. Kowalska, R. Alekseyko, W. Piekarczyk, , L.O. Vasylechko, D.I. Savytskii, L. Perchuć, J. Kapuśniak, "Growth and structural investigations of $\text{La}_{1-x}\text{Pr}_x\text{GaO}_3$ solid solution single crystals", *J. Crystal Growth*, accepted for publication, 2000.
9. A.Saktivel, R.A.Young, School of Physics, Georgia Inst. of Technology, Atlanta GA 30332; A.Saktivel, R.A.Young IUCr Int. Workshop on the Rietveld method, Petten, 1989.

Al-Cu-Co single quasicrystals obtained by the method of inclined front crystallisation

W. Bogdanowicz, Z. Bojarski

Institute of Physics and Chemistry of Metals, University of Silesia, 40-007 Katowice, Bankowa 12, Poland

ABSTRACT

An Al-Cu-Co alloy was obtained by the inclined front of crystallisation method (IFC). During crystallisation the alloy delaminated into three layers, two of which were single decagonal quasicrystals of different orientations and the third one was a mixture of two phases. The first quasicrystalline layer was formed in a peritectic reaction of an earlier created single crystalline layer of an approximant (phase of the B2 structure), the second – grew directly from liquid. With the use of X-ray topography it was found that the (00001) planes of both quasicrystals are rotated of about 1° against each other.

Keywords: Al-Cu-Co single quasicrystals, decagonal quasicrystals, peritectic reaction.

1. INTRODUCTION

Crystal structure of decagonal quasicrystalline phases consists in periodic arrangement of planes which have non-periodic order of atoms. In result the single quasicrystals of decagonal phases may show specific anisotropy of physical properties and thus arouse wide interest. Single quasicrystals of Al-based decagonal phases have been obtained from liquid phase for many years¹⁻³. However, the mechanism of their growth is not completely clear. The decagonal phase of the Al-Cu-Co alloy may be formed from liquid by peritectic reaction of B2 phase crystallised at higher temperatures, or it can grow directly from liquid⁴. Fig. 1 shows schematic pseudobinary cross-section of the Al-Cu-Co phase diagram suggested in⁴. At 1048°C in the L+B2+DQC three phase area there occurs a peritectic reaction $L+B2 \rightarrow DQC$ ^{4,5}.

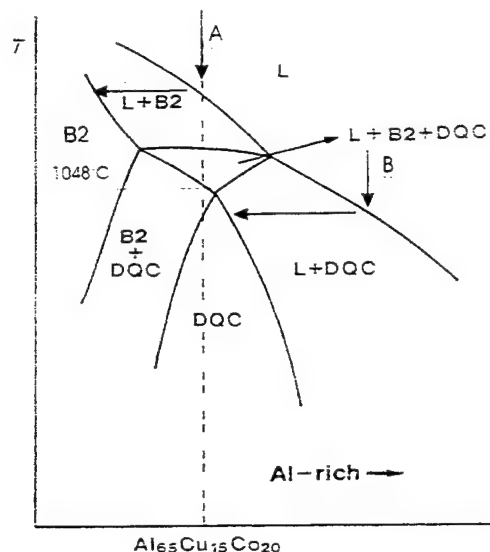


Fig.1 Schematic cross-section of the Al-Cu-Co phase diagram according to ref. [4].

If the alloy composition is close to Al₆₅Cu₁₅Co₂₀ than first the B2 phase crystallises and then the phase reacts with the rest of the liquid and forms the decagonal phase (A arrows at Fig. 1). The concentration of Al in the liquid increases. At

temperatures lower than 1048°C the decagonal phase crystallises directly from the liquid in the two phase L+DQC region (B arrows at Fig.1).

The aim of this work was to obtain a single quasicrystals of the Al-Cu-Co alloy formed in both ways i.e. by peritectic reaction and directly from liquid using the method of inclined front of crystallisation. Knowledge of differences in structure and defects gives an opportunity to determine the mechanism of the phase creation.

2. EXPERIMENTAL

The inclined front of crystallisation method⁶ was used to grow the material. The charge of composition of Al – 24%at.Cu – 11%atCo in form of plate of 15x4x0,5 mm was melted and than subjected to horizontal crystallisation. The shape of the charge (Fig. 2) was preserved during melting thanks to surface tension. The charge was obtained from elements of 5N purity. The metals were melted in an Al₂O₃ crucible in induction furnace under helium atmosphere. After homogenisation the melt was cast onto a brass plate cooled with liquid nitrogen. The charge composition measured with the use of atomic absorption spectroscopy was equal to the nominal composition.

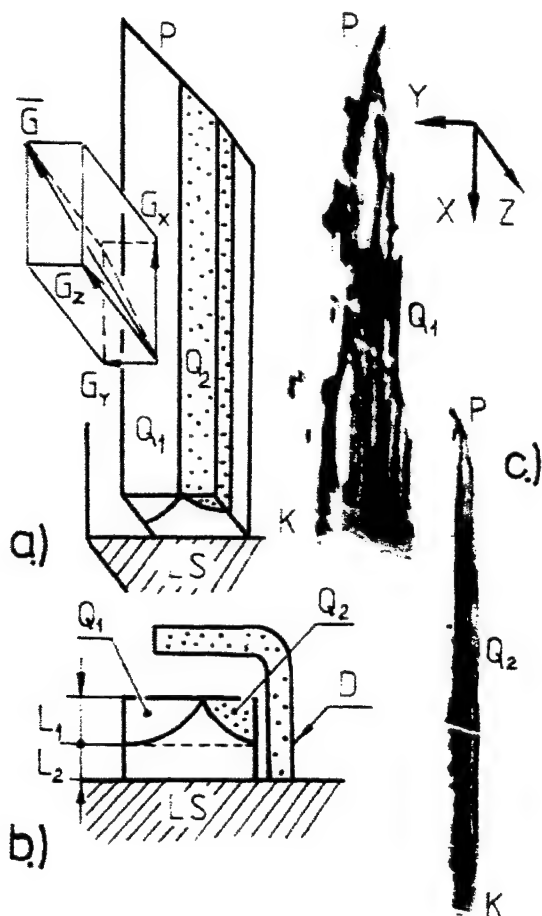


Fig.2. Diagram of the Al-Cu-Co specimen delamination after crystallisation by the IFC method (a, b) and topogram of the single crystalline L₁ layer (c). Radiation Cu_{Kα}, reflex 00001.

The decagonal DQC phase created in the peritectic L+B2→DQC reaction forms in between the two phases. The speed of the DQC phase volume growth, controlled by diffusion of atoms from the liquid to the B2 phase and from the B2 phase to the liquid, will decrease with the DQC phase growth.

In the IFC method⁶, inclination of the crystallisation front versus the crystallisation direction causes that the crystallisation (in the x direction, Fig. 2a) takes place at first in the upper layer of the charge (in the L₁ layer, Fig.1b). According to the phase diagram shown in Fig. 1, a layer of the B2 phase should be formed during this crystallisation. At lower temperatures

the lower layer (L_2 , Fig.2b), being still in the liquid state, can react with the upper layer and in a peritectic reaction form the decagonal phase. Due to directional heat abstraction the temperature of the peritectic reaction is reached first at the layer interface in the primary area of the specimen (P, Fig.2a), and when the reaction proceeds it moves towards the specimen end (K, Fig.2a). Thus the speed of the decagonal phase single quasicrystal growth in the X direction is much faster than in conventional methods of single crystal growth at which the crystallisation front is perpendicular to the growth direction.

The growth was carried out in the induction furnace with a horizontal graphite heating element in helium atmosphere. The charge of a shape shown in Fig. 2a was placed on a leucosapphire plate (the LS symbol, Fig 2a). The plate was then put on a shelf milled in the graphite heating element. The charge was covered by a graphite cover (D, Fig.2b) in such a way that it

covered only one side of the charge shown in Fig. 2a and 2b by the letter Q_2 . In result the temperature gradient \vec{G} was neither perpendicular nor parallel to the growth direction X i.e. none of its components G_x or G_y was equal zero (Fig. 2a). At first the temperature in the area of the specimen denominated as K (Fig. 2a) was 1430°C. Then it was decreased to 900°C with speed 100K/h. Then the specimen was kept for 3 h at stable temperature and the furnace was switched off and the helium flow was increased. In such a way the speed of temperature decrease from 900°C to room temperature was average 1800°K/h.

3. RESULTS AND DISCUSSION

Metallographic studies showed that after crystallisation the specimens (11 pieces) were delaminated. In the upper layer L_1 (Fig.2b) there were two plates of the quasicrystalline phase denominated by Q_1 and Q_2 . The lower layer L_2 consisted of a mixture of two phases.. Fig.2c shows a typical topogram of the single crystalline layer L_1 obtained with the use of Auleytner method of wide beam⁷. The topogram consists of two reflexes coming from the Q_1 and Q_2 plates. Both reflexes come from the (00001) planes of the decagonal phase. The disorientation angle between the two plate determined from the topogram is 59,4 minutes. For 11 studied specimens the angle value was from 18 to 95 minutes. The single L_1 layer was obtained by polishing the lower L_2 layer. The L_1 layer was powdered and an X-ray diffraction pattern was taken. It showed reflexes only from the decagonal phase (Fig. 3). From the L_1 layer a thin foils were also produces which were studied by TEM. These studies also showe presence of the decagonal phase (Fig.4).

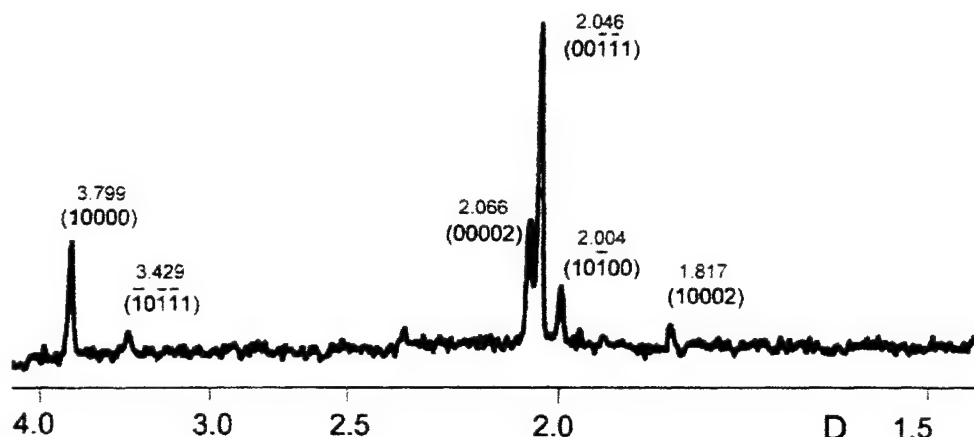


Fig.3. Powder X-ray diffraction pattern of the L_1 layer of the Al-Cu-Co alloy.
Radiation $Cu_{K\alpha}$.

The chemical composition averaged over five specimens and determined by the X-ray microanalysis was for the Q_1 specimen: Al-64,2 at%, Cu-18,5at%, Co-17,3at% and for the Q_2 specimen: Al-68,3at%, Cu-14,6at%, Co-17,2at%. Increased amount of Al in the Q_2 means that crystallisation of the Q_2 layer occurred at lower temperatures.

X-ray topograms of the both layers show contrast bands situated along the growth direction X. This is connected with a small non-homogeneity of the chemical composition occurring at the crystallisation front during the growth process as well as with internal stresses in the specimen. In the first area of the specimen Q_1 (symbol P, fig.2c) the contrast was more diffused than in the last area of the specimen (symbol K, fig.2c). It may be due to less stable conditions of the beginning of crystallisation controlled by diffusion of atoms between the L_1 and L_2 layers. The final part of the specimen Q_1

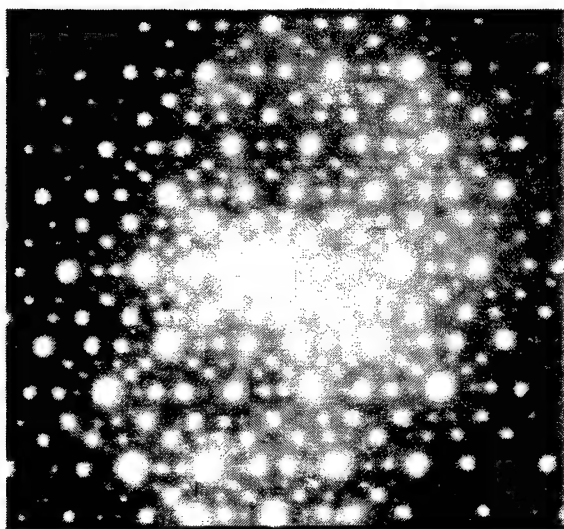


Fig.4. Electron diffraction pattern from the L_1 layer of the Al-Cu-Co alloy. [00001] orientation.

(symbol K, fig.2c) is less defected and the contrast is more sharp and at the end of the specimen the contrast bands do not occur. The topogram of the single crystal Q_2 layer almost do not show diffused band contrast which means that the specimen has less internal stresses than the Q_1 plate.

4. CONCLUSIONS

In result of IFC crystallisation with the temperature gradient asymmetric in regards to the direction of growth the single decagonal phase quasicrystals were obtained. They consisted of two plates. The disorientation angle between the plates was in average 57° . The first plate (Q_1 , Fig.2) most probably was formed in a peritectic reaction from a earlier crystallised B2 phase (Fig.1, arrow A.) and from the liquid phase. The second plate (Q_2 , Fig.2) crystallised at lower temperatures directly from the liquid phase and in result it contained more Al (arrow B, Fig.1).

ACKNOWLEDGEMENTS

This research was financed by the Polish Scientific Research Committee (Grant 7 T08A 026 15)

REFERENCES

1. I. R. Fisher, M. J. Kramer, Z. Islam, A. R. Ross, A. Kracher, T. Wiener, M. J. Sailer, A. I. Coldman, and P. C. Canfield, "On the growth of decagonal Al-Ni-Co quasicrystals from the ternary melt", *Philos. Mag. B* **79**, pp. 425-434, 1999.
2. T. A. Lograsso and D. W. Delaney, "Preparation of large single grains of the quasicrystalline icosahedral Al-Cu-Fe ψ phase", *J. Mater. Res.* **11**, pp. 2125-2127, 1996.
3. R. Kortan, F. A. Thiel, H. S. Chen, A. P. Tsai, A. Inoue, and T. Masumoto, "Stable tenfold faceted single-grain decagonal quasicrystals of $Al_{65}Cu_{15}Co_{20}$ ", *Phys. Rev. B* **40**, pp. 9397-9399, 1989.
4. X. Z. Liao, X. L. Ma, J. Z. Jin, K. H. Kuo, "Peritectic solidification of the stable Al.-Cu-Co decagonal quasicrystal", *J. Mater. Sci. Lett.* **11**, pp. 909-912, 1992.
5. B. Gruszko and Ch. Freiburg, "An $Al_{13}Co_4$ phase in the Al-Cu-Co alloy system", *J. Mater. Res.* **7**, 1100-1103, 1992.
6. W. Bogdanowicz, Z. Bojarski, " β_1 -SnSb single crystals obtained by the method of inclined front crystallization", *J. Crystal. Growth* **147**, pp. 369-381, 1995.
7. W. Bogdanowicz and A. Lehr, "Zastosowanie metody Auleytnera do badań struktury blokowej dużych monokryształów metali", *Arch. Nauki o Mater.* **3**, pp. 199-205, 1989.

Correlation of Cu and V_{Zn} concentration within the diffusion region of ZnSe monocrystals

Tadeusz Łukaszewicz

Department of Physics, Technical University of Białystok, Wiejska 45 A, 15-351 Białystok, Poland

ABSTRACT

In the paper both the diffusion of Cu ions in ZnSe monocrystals of $M_{1-y}X$ type as well as its influence on the concentration of cation vacancy have been investigated. For the purpose of the investigation the phenomenon of luminescence was used since the diffused impurity by acting on the native defects of the crystal was found to have caused the formation of complexes e.g. centres of luminescence. Thus we can have a few diffusion mechanisms.

Keywords: diffusion, luminescence, point defects.

1. INTRODUCTION

The introduction of a foreign atom F into the lattice of a compound MX has an extremely marked effect on its various physical properties, mainly electrical and optical ones. These changes caused by the formation of complexes between the atoms of the impurity and the native defects of the monocrystals. In such a situation it is essential to take into account a possible presence of several diffusion mechanisms. Namely, the diffusion of Cu in ZnSe monocrystals takes place by means of two mechanisms - the vacancy mechanism and interstitial mechanism of the collinear type¹. Between the diffused Cu concentration and the concentration of cation vacancy in ZnSe there exists a close relationship.

2. EXPERIMENTAL

All the ZnSe monocrystals studied in the present investigations were obtained from Military University of Technology in Warsaw. The samples of the monocrystals studied for the diffusion of Cu were pretreated in the vapour of the anion component. This pretreatment, on one hand, assured a considerable lowering of the number of interstitial atoms and Zn ions and, on the other hand, it increased the concentration of vacancies in the cation sublattice. The ZnSe monocrystals pretreated in such a way showed an actual deficiency of the metal thus forming a compound of $M_{1-y}X$ type.

Cu diffusion was carried out in sealed quartz ampules at the pressure of saturated selenium vapour. The doping source was a film of Cu vacuum-sprayed onto the surface of the samples investigated.

On the basis of the two-sample luminescence method measurements were made of the diffusion coefficients of Cu in ZnSe at temperatures: 773 K, 878 K and 973 K. The method is based on the fact that for a given crystal there is a precisely defined and always the same limiting concentration at which the luminescence appears. For two samples taken from the same crystal and subjected to diffusion under the same physical conditions but with different diffusion annealing times the luminescence front of the sample penetrates to a depth of x_1 in time t_1 and that of the other sample to a depth of x_2 in time t_2 . Then we obtain the following equation²:

$$D = \frac{|x_1^2 t_2 - x_2^2 t_1|}{2 t_1 t_2 \ln(t_2 / t_1)} \quad (1)$$

All the quantities on the right-hand side of (1) can be determined experimentally. Thus the above equation can be used for measurement of impurity diffusion coefficients in semiconductors in which the impurity produces luminescence centres.

3. RESULTS

The diffusion of Cu was carried out on samples of ZnSe which as a result of pretreatment were characterized by an actual deficiency of metal (Zn_{1-y}Se). The introduction of a cation impurity of a valency lower than that of the parent cations has such an effect that with an increase in the impurity concentration, a fall in the ion defect concentration and an increase in the electron defect concentration occur. The cation vacancy concentration, assuming that $[\text{Cu}'_{\text{Zn}}] \gg [\text{V}''_{\text{Zn}}]$, may be expressed by the equation¹

$$[\text{V}''_{\text{Zn}}] = \frac{\text{const}}{[\text{Cu}'_{\text{Zn}}]^2} p_{\text{Se}_2}^{1/2} \quad (2)$$

from which it is seen that the concentration of cation vacancies in a solid solution $\text{Cu}_2\text{Se-Zn}_{1-y}\text{Se}$ decreases with an increase of the concentration of ions Cu^+ .

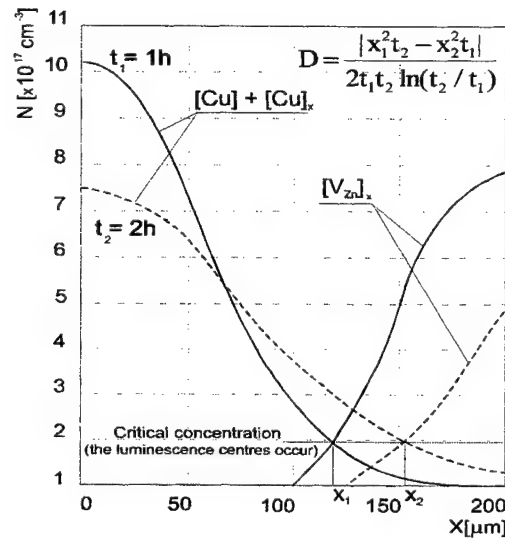


Fig.1. Cu and V_{Zn} concentration profiles for two ZnSe samples at 773 K, $D_{\text{Cu}} = (4.45 \pm 2.48) \cdot 10^{-9} \text{ cm}^2/\text{s}$

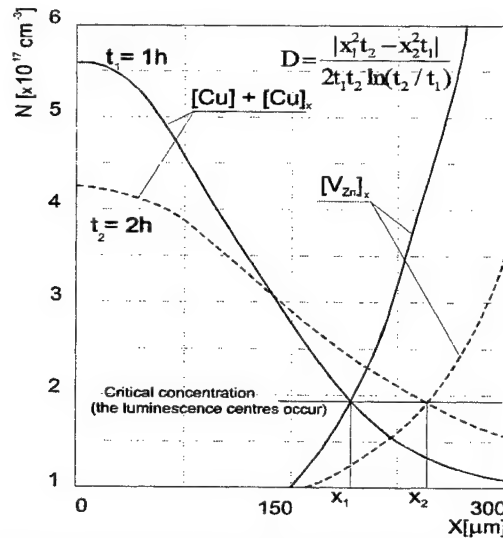


Fig.2. Cu and V_{Zn} concentration profiles for two ZnSe samples at 873 K, $D_{\text{Cu}} = (1.63 \pm 0.39) \cdot 10^{-8} \text{ cm}^2/\text{s}$

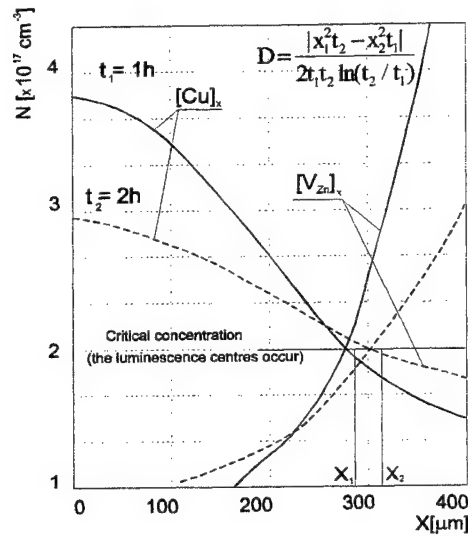


Fig.3. Cu and V_{Zn} concentration profiles for two ZnSe samples at 973 K, $D_{Cu} = (5.40 \pm 0.54) \cdot 10^{-8} \text{ cm}^2/\text{s}$

The relationship between concentration of cation vacancies and the concentration of Cu ions in diffused ZnSe sample may be considered in the following way. Let's assume the denotations below:

- $[Cu]$ - Cu concentration in the initial material,
- $[Cu]_x$ - Cu concentration at depth x in the sample after the diffusion process,
- $[Cu]_0$ - Cu concentration on the surface of sample after the diffusion process.

The concentration distribution of Cu in ZnSe sample is expressed by the following equation:

$$\frac{[Cu]_x - [Cu]}{[Cu]_0 - [Cu]} = \frac{h}{\sqrt{\pi D t}} \exp\left(-\frac{x^2}{4 D t}\right) \quad (3)$$

Based on equation (2) the relationship between the concentration of cation vacancies in the initial sample $[V_{Zn}]$ and that on the depth x from its surface after the diffusion process $[V_{Zn}]_x$ may be expressed as follows:

$$[V_{Zn}]_x = [V_{Zn}] \frac{[Cu]^2}{[Cu]_x^2} \quad (4)$$

On the basis of the measured values of Cu diffusion coefficients and knowing that: $h=1\mu\text{m}$, $[Cu]=1.0 \cdot 10^{17} \text{ cm}^{-3}$, $[Cu]_0=6.5 \cdot 10^{19} \text{ cm}^{-3}$ and $[V_{Zn}]=8.2 \cdot 10^{17} \text{ cm}^{-3}$, it was possible to create profiles of the distribution concentration for both the impurity $[Cu]_x$ and $[V_{Zn}]_x$ of the compound. The graphs of equations (3) and (4) were depicted in fig.1., fig.2. and fig.3. for ZnSe samples doping Cu at 773 K, 873 K and 973 K respectively. It can be seen that $[Cu]_x=f(x)$ and $[V_{Zn}]_x=f(x)$ curves intersect at such an impurity concentration that will form luminescence centres independent of the temperature process. Furthermore, the course of the curves suggests that the intersection point i.e. the point where the concentration of Cu activator equals the concentration of cation vacancies and where the luminescence front occurs, we have a transition from the region of higher conductivity to the compensated region of lower conductivity. This fact was proved strictly by Aven and Halsted³.

4. CONCLUSIONS

The result of the investigations and the analysis of the correlation of the concentrations of both Cu impurity and cation vacancies in the ZnSe diffusion region made it possible to conclude that Cu diffusion in the compound followed two distinct mechanisms: a vacancy mechanism at Cu concentration a little above $2 \cdot 10^{17} \text{ cm}^{-3}$ and an interstitial mechanism of collinear type at higher concentrations.

In the case under discussion in the present paper, Cu is diffused into a compound of the $M_{1-y}X$ type, i.e. a compound containing a high concentration of cation vacancies $[V''_{\text{Zn}}]$. It may, therefore, be assumed that the diffused Cu ions occupy these vacancies first and then together with other defects in the lattice (e.g. anion vacancies) form red luminescence centres. As we know (see (1)), increasing concentration of $[\text{Cu}'_{\text{Zn}}]$ lowers the concentration of cation vacancies. Therefore, after a critical concentration of the impurity is exceeded, an interstitial mechanism of diffusion begins to prevail over the vacancy mechanism.

ACKNOWLEDGEMENTS

The work was supported by KBN under the Technical University of Bialystok grant No W/IMF/2/97.

REFERENCES

1. T. Lukaszewicz, "The diffusion of Atoms and Luminescence Centres in II-VI Compounds", *Phys. Stat. Sol. (a)* **74**, pp. 307-312, 1982.
2. T. Lukaszewicz and J. Zmija, "A luminescence Modification of the Two-Sample Method for Studying Impurity Diffusion in $A^{\text{II}}\text{-}B^{\text{VI}}$ Semiconductors", *Phys. Stat. Sol. (a)* **62**, pp. 695-699, 1980.
3. M. Aven and R.E. Halsted, "Diffusion of Electrically and Optically Active Defect Centres in II-VI Compounds", *Phys. Rev.* **137**, pp. 228-234, 1965.

Chromium recharging processes in the $Y_3Al_5O_{12}$: Mg, Cr single crystal under the reducing and oxidizing annealing influence

S.B. Ubizskii^{a*}, S.S. Melnyk^a, B.V. Padlyak^b, A.O. Matkovskii^a, A. Jankowska-Frydel^b, Z. Frukacz^c

^aNational University "Lviv Polytechnic", 12, Bandera St., 79646, Lviv, Ukraine

^bInstitute of Experimental Physics, University of Gdańsk, 80-952 Gdańsk, Poland

^cInstitute of Electronic Materials Technology, 133 Wolczynska St., 01919, Warsaw, Poland

ABSTRACT

The influence of reducing and oxidizing annealing on optical absorption spectra of the yttrium aluminium garnet (YAG) single crystal co-doped with Mg and Cr is investigated using step-by-step isothermal and isochronous thermal treatment in H_2 or air flow. The changes in the spectra were analyzed using decomposition on elementary absorption bands of Gaussian shape. The separated absorption bands attributed to the Cr^{4+} ions occupying octahedral and tetrahedral sites in garnet lattice demonstrate different behaviour. The analysis allows to distinguish the electronic recharging process $Cr^{4+}_{[oct]} \leftrightarrow Cr^{3+}_{[oct]}$ taking place in the octahedral sites of garnet lattice and having lower activation energy from the chromium migration process $Cr^{4+}_{[tet]} \leftrightarrow Cr^{4+}_{[oct]}$ happening at higher temperatures or longer exposure. Estimations show that approximately 0.2% of total number of chromium ions occupied tetrahedral sites forming phototropic centers in the YAG: Mg, Cr crystal.

Keywords: yttrium aluminium garnet, Cr doping, thermal treatment, phototropic centers, optical characterization, electron paramagnetic resonance.

1. INTRODUCTION

An ability of the tetrahedrally coordinated Cr^{4+} ions to saturable absorption of the Nd-activated lasers' emission is widely used for passive Q-switching.¹⁻⁵ Owing to peculiarities of their luminescent properties these centers are used in tunable lasing in near infrared region as well.⁶⁻⁹ That's why processes of controllable formation of Cr^{4+} centers in tetrahedral sites of laser hosts are of top interest.

The Cr^{4+} centers formation in garnet host crystals is usually forced by simultaneous co-doping with Ca^{2+} or Mg^{2+} ions during the synthesis¹⁰⁻¹¹ that promotes their stabilisation due to the charge compensation. Formation of the Cr^{4+} centers during crystal growth is accompanied by their incorporation into both tetrahedral and octahedral sites of garnet structure while the main part of chromium occupies octahedral sites in three-valence state.¹⁰⁻¹² The dependence of amount of phototropic centers from Ca/Cr ratio was studied in¹⁰. Oxygen vacancies can also contribute to the charge compensation.^{11,12} Healing of anion vacancies by oxygen during post-growth annealing leads to the change of the chromium valence ($Cr^{3+} \rightarrow Cr^{4+}$) in crystals¹²⁻¹⁵ and particularly to increase of the phototropic centers concentration. The reducing and oxidation annealing can change the ratio of Cr^{4+}/Cr^{3+} but the details of this process was not studied and understood well due to complexity of processes with chromium participation in co-doped garnets. The present work is devoted to further studying peculiarities of the chromium recharging process and phototropic centers formation taking place in the yttrium-aluminium garnet ($Y_3Al_5O_{12}$) co-doped with Mg and Cr subjected to reducing annealing in the H_2 and oxidation annealing in the air flow.

2. EXPERIMENTAL

The yttrium-aluminium garnet single crystals co-doped with Cr and Mg (YAG: Mg, Cr) were investigated. The crystals of high chemical purity have been grown by Czochralski method along [111] direction in the ($N_2 + 3\% O_2$) atmosphere with

* S.B.U. (Correspondence): E-mail: crystal@polynet.lviv.ua; Fax: (380-322) 742-164; Phone: (380-322) 398-153

growth rate of 2 mm per hour. The samples were prepared in the form of plates with diameter of 10 mm and thickness of 1 mm by crystal cutting perpendicular to growth axis and their surfaces were polished up to optical quality.

The thermal treatment in both reducing and oxidising atmosphere has been performed gradually. The isothermal treatment of as-grown crystal in the hydrogen (H_2) flow at temperature $875^\circ C$ was fulfilled first with net time from 15 min to 8 hours. Then the reduced and as-grown samples were subjected to the isochronous annealing in air during 30 min at each temperature in the sequence at 700, 800, 940, 1020, 1200 and $1400^\circ C$. The annealing in air during 2 hour at $1400^\circ C$ also was performed in the end of an experiment.

Optical absorption spectra of the samples were calculated from transmission spectra, that was measured using "Specord M-40" (Carl Zeiss Jena) and "Lambda-2" (Perkin-Elmer) spectrophotometer in the spectral range $50000...8000\text{ cm}^{-1}$ at room temperature. An effect of thermal treatment was analysed using additional absorption (AA) spectra. The last were determined as an excess absorption of the sample under consideration relatively to the totally reduced one excepting the case of oxidising annealing of the as-grown samples when the AA spectrum was determined relative to the initial spectrum of the as-grown sample. Decomposition of the AA spectra of the samples using Gaussian-shaped lines was carried out. It was established that the six Gaussian lines describe satisfactorily the AA spectra in the $40000...12000\text{ cm}^{-1}$ range. Absorption band of the $Cr^{4+}_{[tet]}$ ions with maximum at 9400 cm^{-1} in the $13000...8000\text{ cm}^{-1}$ range was not taken into account because of its nature was established with enough reliability¹²⁻¹⁷ and it does not overlap another bands in the spectrum. After decomposition of all AA spectra the positions and widths of each line were averaged and fixed. Afterwards amplitudes of elementary absorption bands were determined repeatedly for each AA spectra.

Total concentration of chromium content was determined by the Cr^{3+} optical absorption band intensity in entirely reduced sample as well as by intensity of EPR spectrum. The sample made from the YAG:Cr³⁺ crystal without co-doping of Mg^{2+} was used as a reference sample. The Cr^{3+} concentration in it was determined by chemical analysis. Electron paramagnetic resonance (EPR) measurements were carried out at room temperature using commercial Radiopan SE/X-2543 (Poland) X-band ($\nu \approx 9.4\text{ GHz}$) spectrometer with 100 kHz magnetic field modulation. The concentration of Cr^{4+} ions in tetrahedral sites of YAG: Mg, Cr samples was estimated by intensity of detached absorption band with maximum at 9400 cm^{-1} in accordance with data presented in¹⁷.

3. RESULTS AND DISCUSSION

Absorption spectrum of the as-grown YAG: Mg, Cr crystal is presented by the curve 1 in Fig. 1a as well as its spectra after reducing (curve 2) and oxidising (curve 3) annealing. The characteristic changes of absorption spectra of YAG: Mg, Cr after reducing and oxidising are well coinciding with those observed in the past.¹³⁻¹⁵ The completely reduced sample got a green colour and its absorption contained two characteristic absorption bands only at 23040 and 16450 cm^{-1} connected with the Cr^{3+} transitions.¹⁸ That's why the additional absorption calculated relatively to spectrum of the completely reduced sample may be interpreted as the absorption of the chromium ions of higher valence.

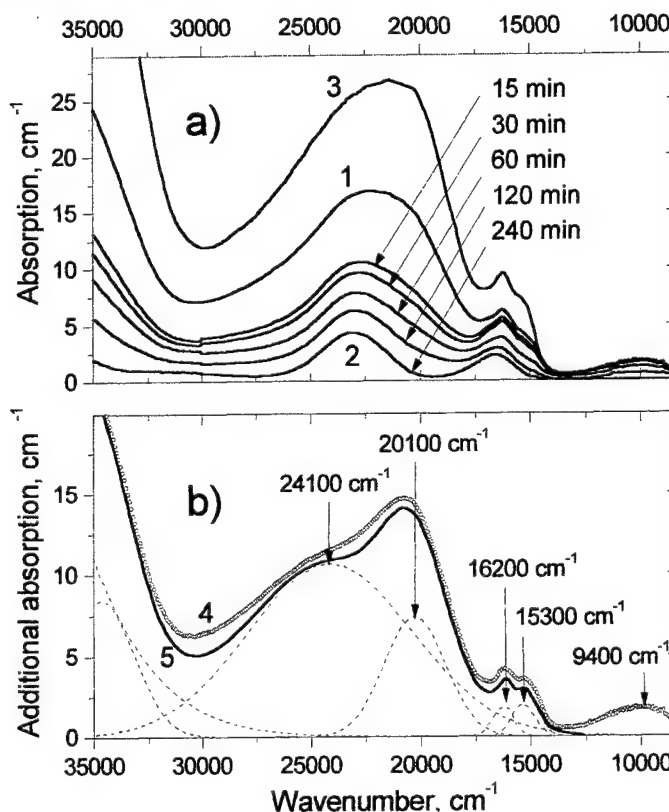
Change of the absorption spectrum during the isothermal reducing annealing in H_2 flow at $875^\circ C$ is also presented in Fig. 1a by the curves marked with arrows and are situated between curves 1 and 2. After four hours of reducing annealing no changes were observed further up to net time of annealing of 8 h. Absorption spectrum of the reduced sample was identical with the spectrum of satellite sample subjected to annealing in hydrogen flow during 10 h at $1200^\circ C$. The last confirms that reducing of the sample occurs practically completely after the 4-hour annealing in H_2 flow at $875^\circ C$. The spectrum changes happen in the opposite direction during the isochronous oxidising annealing in air of the preliminary reduced YAG: Mg, Cr sample. The spectrum of the preliminary reduced sample subjected to the oxidising annealing at $1400^\circ C$ during 2 h occurs practically coinciding with that of the as-grown sample after the same thermal treatment.

An example of the AA spectrum of the as-grown YAG: Mg, Cr crystal relatively to the completely reduced one is shown by the curve 4 in the Fig. 1b as well as its approximation (curve 5) by the sum of Gaussian-shaped absorption bands depicted by dashed lines. It can be seen from the Fig. 1b the set of six elementary bands describes satisfactorily the additional absorption spectrum in the $35000...13000\text{ cm}^{-1}$ range. Some of them can be interpreted on the base of a number of published results.^{10,12,15-17} The absorption bands with maxima at 16200 and 15300 cm^{-1} originate from transitions of tetrahedral Cr^{4+} ions^{15,16} as well as absorption in the near-IR region with maximum at 9400 cm^{-1} mentioned above. The absorption lines with maxima at 24100 and 20100 cm^{-1} form the non-elementar broad and intense band in the region $17000...30000\text{ cm}^{-1}$ whose nature is under discussion over more than ten years. Various suppositions were published on the base of the energy level scheme calculation as well of non-direct experimental observation. They connected this band with the octahedral Cr^{4+} intracenter transitions^{12,16} as well as with charge transfer transitions with participations of octahedral Cr^{4+} shells¹⁶ and charged oxygen vacancies¹⁵. The last possibility looks as improbable one because as it was shown in^{12,19} the oxygen vacancies exist in co-doped garnet as complexes $[Me^{2+}V_O]$ and are absorbing in UV region. The similar

evidences were found in ²⁰ where the strong absorption band likely connected with such complexes was observed in YAG: Mg, Cr epitaxial layers at 35710 cm⁻¹. That is why we shall consider the Cr⁴⁺ situated in octahedrons as more probably responsible for absorption at 20100 and 24100 cm⁻¹ in accordance to ^{12,16}.

In this connection it should be emphasised that the nature of UV absorption in the region with wavenumbers higher than 30000 cm⁻¹ is also not clear yet and is under discussion in literature. The Cr⁶⁺ ions, charged oxygen vacancies or complexes like [Me²⁺V_O] as well as uncontrollable impurities are considered as responsible for absorption in this region. ^{10,15,19}

Fig. 1. (a) Absorption spectra of the YAG: Mg, Cr crystal registered in as-grown sample (1), after reducing annealing in H₂ flow at 1200°C during 10 h (2) and after annealing in air at 1400°C during 2 h (3) samples (curves between 1 and 2 represent change of absorption spectrum of the YAG: Mg, Cr crystal during isothermal reducing in H₂ flow at 875°C); (b) Additional absorption of the as-grown crystal relative to reduced one: experimental data (4) and their approximation (5) by set of Gaussian lines (elementary lines are represented by dashed lines).



Dependencies of the absorption spectrum components' intensity during isothermal reducing annealing at 875°C is plotted in the Fig. 2 as normalised ones to the initial absorption of each Cr⁴⁺- connected band of as-grown YAG: Mg, Cr crystal.

It is clearly seen that two types of the bands' behaviour can be distinguished: the absorption bands conforming to the octahedral Cr⁴⁺ ions start to decrease immediately from beginning of annealing and is slowly continuing at least four hours. In contrast, the Cr⁴⁺_[tet] absorption bands begin much later (in second half of hour) and practically stop after 2 h of annealing.

It is natural to suggest that the changes happening just after start of annealing are connected with electronic processes of chromium ions recharging while the second stage can be explained by ion migration processes, which require higher energy (the same as temperature) or longer time for their activation. On the first stage the Cr⁴⁺ ions occupying octahedra can easily change their valence to "3+" according to reaction:

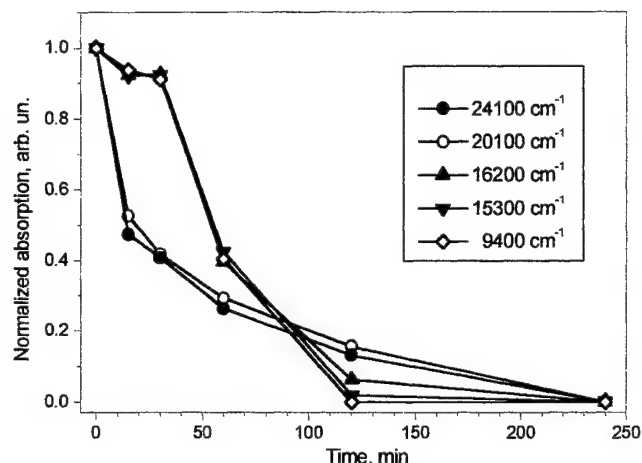


It does not need the ion migration and is caused by loss of oxygen on surface of the crystal that has to be compensated in order to save charge balance. The Cr⁴⁺ reducing process to the Cr³⁺ is impossible in tetrahedra because the Cr³⁺ ions are too big to occupy these sites. ^{12,16} When the ion migration is activated on the second stage the Cr⁴⁺ ions can move from the tetrahedra to octahedra:



where the reaction (1) can take place again.

Fig. 2. Dependence of normalised absorption of separate bands during isothermal reducing annealing of the as-grown YAG: Mg, Cr crystal in H_2 flow at $875^\circ C$.



Different behaviour of two groups of absorption bands is found also during isochronous oxidation annealing of both samples subjected to it – the preliminary reduced crystal and as-grown one. These dependencies are shown in Fig. 3a and 3b, respectively. The AA values presented in Fig. 3b are calculated relatively to the level of the as-grown crystal. In this case the reactions (1) and (2) happen in opposite direction and in opposite order. That's why the increase of the octahedral Cr^{4+} absorption starts just at relatively low temperatures. It is clearly observed in the temperature range below $800^\circ C$ for as-grown crystal and may be, probably, connected with recharging both the equilibrium oxygen vacancies being present in the crystal and the Cr^{3+} ions owing to oxidation reaction on the surface of crystal. The increase of phototropic centres takes place since the migration of chromium is activated by rise of temperature.

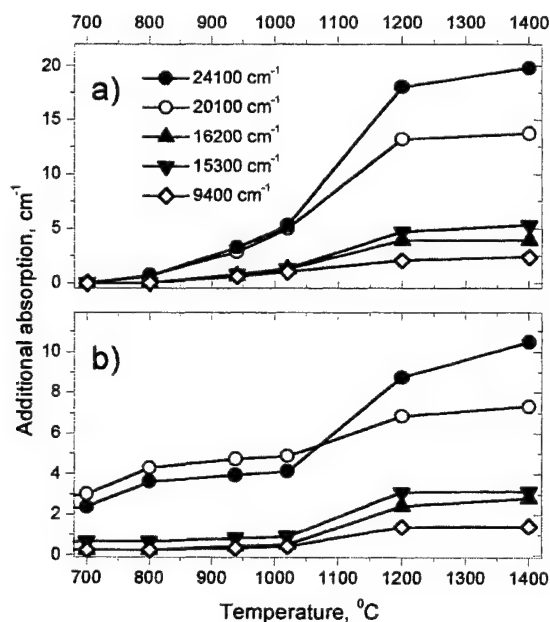


Fig. 3. Dependence of separate absorption bands' intensities during the 30 min isochronous annealing in the air for completely reduced YAG: Mg, Cr (a) and as-grown YAG: Mg, Cr (b) samples.

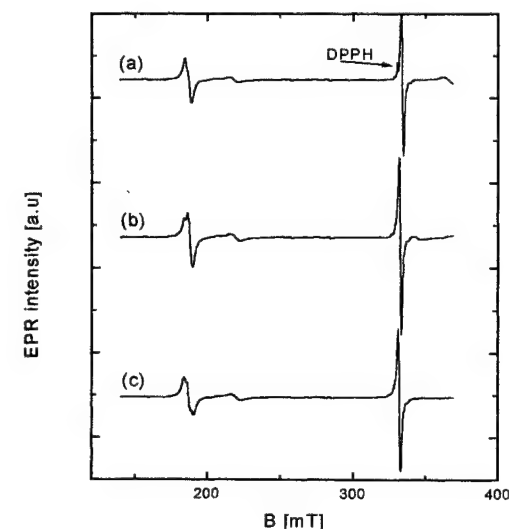


Fig. 4. EPR spectra of the Cr^{3+} ions in YAG: Mg, Cr single crystal, registered in magnetic field B parallel to the $[111]$ direction; (a) as-grown sample, (b) after annealing in the air at $1400^\circ C$, (c) after annealing in the H_2 atmosphere at $1000^\circ C$.

It may be noted that observed behaviour of separated absorption bands does not contradict to the interpretation of absorption spectrum of co-doped YAG: Mg, Cr given in ¹⁵ because in this case the changes of absorption under reducing

and oxidising annealing can be explained again by electronic recharging and ion migration processes. The first process results in this consideration in recharging of oxygen defects.

EPR spectra of the Cr^{3+} ions in the as-grown crystals as well as annealed ones show that Mg co-doping and annealing at oxygen or hydrogen do not change of the local symmetry and crystal field parameters of the Cr^{3+} impurity centres typical for $\text{YAG}:\text{Cr}^{3+}$ (Fig. 4). The Cr^{3+} concentrations were determined from intensities of EPR spectra for [111] crystal axis parallel to the magnetic field using DPPH standard ($N = 8 \cdot 10^{15}$ spins). It remains nearly constant within experimental error, independently of the annealing process of the Mg co-doped samples.

The Cr^{4+} concentration in tetrahedral sites was determined from intensity of absorption at $1.06 \mu\text{m}$. Estimations of the Cr^{3+} and Cr^{4+} concentrations in the $\text{YAG}:\text{Mg}, \text{Cr}$ crystal under investigation gave the following values: the concentration of Cr^{3+} in the completely reduced sample was equal to $2 \cdot 10^{20} \text{ cm}^{-3}$ while the concentration of phototropic $\text{Cr}^{4+}_{\text{tet}}$ centres after oxidation annealing became $4 \cdot 10^{17} \text{ cm}^{-3}$ that corresponds to 0.2 % of total number of the Cr ions. The small amount of Cr^{4+} ions participating in the observed processes does not allow to observe practically any changes in intensity of EPR signals of the Cr^{3+} ions after both reducing and oxidation annealing.

4. CONCLUSIONS

The processes of the chromium impurity centres transformation are investigated using decomposition analysis of absorption spectra of the $\text{YAG}:\text{Mg}, \text{Cr}$ single crystal subjected to reducing and oxidising graduated annealing.

Absorption bands separated by mean of spectrum decomposition clearly demonstrate two different behaviours during after-growth thermal treatment of crystal. The $\text{YAG}:\text{Mg}, \text{Cr}$ absorption changes in the $28000 \dots 17500 \text{ cm}^{-1}$ range are mainly determined by electronic recharging that can be interpreted as reaction $\text{Cr}^{4+}_{\text{tet}} \leftrightarrow \text{Cr}^{3+}_{\text{tet}}$ taking place in octahedral sites of garnet lattice and having lower activation energy. The chromium migration process $\text{Cr}^{4+}_{\text{tet}} \leftrightarrow \text{Cr}^{4+}_{\text{oct}}$ happening at higher temperatures or longer exposure is responsible for absorption changes in the $17500 \dots 8000 \text{ cm}^{-1}$ range.

Our estimation show that only about 0.2 % of total number of chromium impurity ions in the crystal under investigation can occupy tetrahedral sites forming phototropic centres and participate in the observed processes. The small amount of this part in comparison with total chromium content does not allow to observe by EPR any remarkable changes in local symmetry, crystal field parameters and microwave absorption intensity of the Cr^{3+} centres in octahedral sites of $\text{YAG}:\text{Mg}, \text{Cr}$ crystal subjected to reducing and oxidising annealing.

ACKNOWLEDGMENTS

This work have been partly supported by research project No. 2M/50-2000, No. 0501/01460 and "OPGEN" of the Ukrainian Ministry of Education and Science and Gdańsk University (grant No. BW/5200-0304-0). Authors express their gratitude to Igor Syvorotka and Igor Izhnin for fruitful discussion as well as to Alexander Izhnin, Borys Rejkin, Vasyl' Baluk for valuable assistance in this research.

REFERENCES

1. J.J. Zayhowski, "Q-switched operation of microchip lasers", *Opt. Lett.* **16**, pp. 575-577, 1991.
2. Y. Shimony, Y. Kalisky, B.H.T. Chai, "Quantitative studies of $\text{Cr}^{4+}:\text{YAG}$ as a saturable absorber for $\text{Nd}:\text{YAG}$ laser", *Optical Materials*, **4**, p. 547-551, 1995.
3. J.J. Zayhowski, "Microchip lasers", *Optical Materials*, **11**, pp. 255-267, 1999.
4. E. Molva, "Microchip lasers and their application in optical microsystems", *Optical Materials*, **11**, pp. 289-299, 1999.
5. J.J. Zayhowski, "Passively Q-switched Nd-YAG microchip lasers and applications", *J. Alloys and Compounds*, **303/304**, pp. 393-400, 2000.
6. N.B. Angert, N.I. Borodin, V.M. Garmash, V.A. Zhytniuk, A.G. Okhrimchuk, O.G. Sijuchenko, A.V. Shestakov, "Generation of impurity centers in the yttrium alluminate crystals in the wavelength region $1.35\text{--}1.45 \mu\text{m}$ ", *Quantum Electronics (Russia)*, **15**, No. 1, pp. 113-115, 1988.
7. G.M. Zverev, A.V. Shestakov, "Tunable lasers of near IR region based on oxide crystals", *Elektronnaja tekhnika. Ser. Lasernaja tekhnika i optoelektronika (Russia)*, No. 3(51), pp. 15-17, 1989.
8. N.I. Borodin, V.A. Zhitnyuk, A.G. Okhrimchuk, A.V. Shestakov, "Laser generation based on $\text{Y}_3\text{Al}_5\text{O}_{12}:\text{Cr}^{4+}$ in the wavelength region $1.34\text{--}1.6 \mu\text{m}$ ", *Izv. Akad. Nauk SSSR, Neorg. Mat. (Russia)*, Vol. **54**, No. 8, pp. 1500-1506, 1990.

9. H. Eilers, W.M. Dennis, W.M. Yen, S. Kück, K. Peterman, G. Huber, "Performance of Cr:YAG laser", *IEEE J. Quantum Electronics*, **29**, pp. 2508-2512, 1993.
10. A. Sugimoto, Y. Nobe, K. Yamagishi, "Crystal growth and optical characterization of Cr,Ca:Y₃Al₅O₁₂", *J. Cryst. Growth*, **140**, p. 349-354, 1994.
11. S.A. Markgraf, M.F. Pangborn, R. Dieckmann, "Influence of different divalent co-dopants on the Cr⁴⁺ content of Cr-doped Y₃Al₅O₁₂", *J. Crystal Growth*, **180**, pp. 81-84, 1997.
12. V.M. Garmash, N.I. Borodin, L.A. Ermakova, "Influence of impurities on formation of phototropic centers in the YAG: Mg, Cr crystals", *Electronnaja tekhnika. Ser. Lasernaja tekhnika i optoelektronika (Russia)*, No. 3 (51), pp. 20-25, 1989.
13. Z. Frukacz, T. Łukasiewicz, M. Malinowski, Z. Mierczyk, "Growth of Cr⁴⁺:YAG crystals for applications in laser technique", *Proc. SPIE*, **2373**, pp. 74-78, 1995.
14. Z. Mierczyk, Z. Frukacz, J. Kisielewski, "Influence of charge state of chromium ions on the bleaching dynamics of YAG:Cr⁴⁺ non-linear absorbers", *Proc. SPIE*, **3186**, pp. 180-183, 1997.
15. B. Henderson, H.G. Gallagher, T.P.J Han and M.A. Scott, "Optical spectroscopy and optimal crystal growth of some Cr⁴⁺-doped garnets", *J. Phys.:Condens. Matter*, **12**, pp. 1927-1938, 2000.
16. S. Kück, K. Petermann, U. Pohlmann and G. Huber, "Electronic and vibronic transitions of Cr⁴⁺-doped garnets Lu₃Al₅O₁₂, Y₃Al₅O₁₂, Y₃Ga₅O₁₂ and Gd₃Ga₅O₁₂", *J. Luminescence* **68**, pp. 1-14, 1996.
17. V.M. Garmash, V.A. Zhitnyuk, A.G. Okhrimchuk and A.V. Shestakov, "Spectral properties of the rare-earth garnet crystals containing impurities of chromium and magnesium", *Izv. Akad. Nauk SSSR, Neorg. Mat.* **26**, pp. 1700-1705, 1990.
18. A.O. Matkovskii, "Materials of quantum electronics"(in Ukrainian), Liga-Press, Lviv, 2000.
19. A.O. Matkovskii, D.Yu. Sugak, I.M. Bolesta, V.I. Vasylytsiv, L.E. Vitruk, Ya.M. Zakharko, O.N. Sevriukov, "Colour centers in the single crystals of gadolinium gallium garnet contained the Ca²⁺, Mg²⁺ ions", *Zhurnal prikladnoj spektroskopiji (Russia)*, **51**, pp. 542-545, 1989.
20. S.B. Ubizskii, I.M. Syvrotka, S.S. Melnyk, A.O. Matkovskii, K. Kopczynski, Z. Mierczyk, Z. Frukacz, "Growth and characterization of YAG:Cr⁴⁺ epitaxial films", *Proc. SPIE*, **3724**, pp. 353-357, 1998.

Optical properties of doped Potassium Gadolinium Tungstate single crystals

E. Michalski^a, J. Żmija^a, Z. Mierczyk^b, A. Majchrowski^{a,*}, K. Kopczyński^b, S. Cichowski^b,
and J. Wojtanowski^a

^a Institute of Applied Physics MUT, 00-908 Warsaw, ul. Kaliskiego 2, Poland

^b Institute of Optoelectronics MUT, 00-908 Warsaw, ul. Kaliskiego 2, Poland

ABSTRACT

Single crystals of double tungstates find applications as laser materials having very good parameters. One of the intensively investigated materials is $\text{KGd}(\text{WO}_4)_2$ doped with rare earth elements. Single crystals of $\text{KGd}(\text{WO}_4)_2$ were grown with the use of Top Seeded Solution Growth technique from $\text{K}_2\text{W}_2\text{O}_7$ solvent. The crystals have low absorption losses and show high lasing efficiency. Optical investigations of as grown KGW:Nd single crystals confirmed their good optical quality and high absorption coefficient near 810 nm, what in connection with strong luminescence near 1067 nm allows fabrication of diode pumped microchip lasers working both in CW and giant pulse regime. Absorption and luminescence spectra of Nd^{3+} doped KGW single crystals are presented. Laser action was obtained in form of 128.5 kHz train of 100 ns giant pulses due to $\text{YAG}:\text{Cr}^{4+}$ passive Q-switch.

keywords: potassium gadolinium tungstate, high temperature solution growth, diode pumped laser, microlaser.

1. INTRODUCTION

In recent years double tungstates have been intensively investigated^{1,2,3} due to their excellent properties allowing their applications in many optoelectronic devices. Especially solid state lasers with laser diode selective pumping establish a new class of lasers with particular properties. The spectral matching of diode radiation to the absorption bands of doped double tungstates makes it possible to obtain high pumping efficiency, single mode operation, and miniaturization of lasers. Two main double tungstates which find applications in diode pumped lasers fabrication are rare earth ions doped $\text{KGd}(\text{WO}_4)_2$ (KGW)⁴ and $\text{KY}(\text{WO}_4)_2$ (KYW)⁵ single crystals. Owing to the possibility of Gd or Y ions substitution with rare earth ions in a very broad range, one can create single crystals having properties suitable for chosen applications. In this paper we report on crystal growth and characterization of KGW:Nd single crystals containing different amounts of neodymium ions. Absorption and luminescence spectra of uniform KGW:Nd single crystals grown from high temperature solutions were measured.

2. KGW SINGLE CRYSTAL GROWTH

Monoclinic KGW with space group C2/c , as many other double tungstates, reveals high temperature irreversible phase transition at 1005°C.⁶ This property imposes necessity of crystallization of low temperature KGW phase from high temperature solutions which enable lowering the temperature of crystallization below the temperature of the phase transition. $\text{K}_2\text{W}_2\text{O}_7$, a well-known compound commonly used in crystallization of double tungstates containing potassium, was chosen as a solvent. $\text{K}_2\text{W}_2\text{O}_7$ has relatively low viscosity,⁴ what is very important factor in flux growth, and does not introduce any additional elements to the melt (so called self-flux). The solutions for crystallization were prepared by melting together proper amounts of K_2CO_3 p.a., WO_3 99.998%, Gd_2O_3 99.99%, and Nd_2O_3 99.99% to obtain 20 mol.% solution of $\text{KGd}_{1-x}\text{Nd}_x(\text{WO}_4)_2$ in $\text{K}_2\text{W}_2\text{O}_7$. Crystal growth was carried out from platinum crucibles on KGW seeds oriented in [010] direction under conditions of small temperature gradients (5°C/cm). Two-zone resistance furnace controlled by two independent Eurotherm 906S regulators/programmers was used in our experiments. High heat capacity of the furnace in connection with good temperature control (linear changes of temperature at a rate 0.1°C/hr) provided stable thermal conditions of crystallization.

* e-mail: amajchrowski@altair.geo.wat.waw.pl

Top Seeded Solution Growth (TSSG) technique in connection with pulling growing crystals up at a rate of 2 mm/day allowed to grow uniform KGW:Nd single crystals having, contrary to crystals grown without pulling in Ref. 4, only one crystallographic plane (010) on the bottom of the growing crystal. Owing to this the as grown crystals had uniform distribution of neodymium. Such uniformity was impossible to obtain when crystallization occurred on several crystallographic planes having different coefficients of dopant distribution. KGW:Nd single crystals containing 1, 3 and 8 at.% of neodymium were grown. In Fig.1 typical KGW:Nd single crystal grown by TSSG with flat (010) bottom is presented.

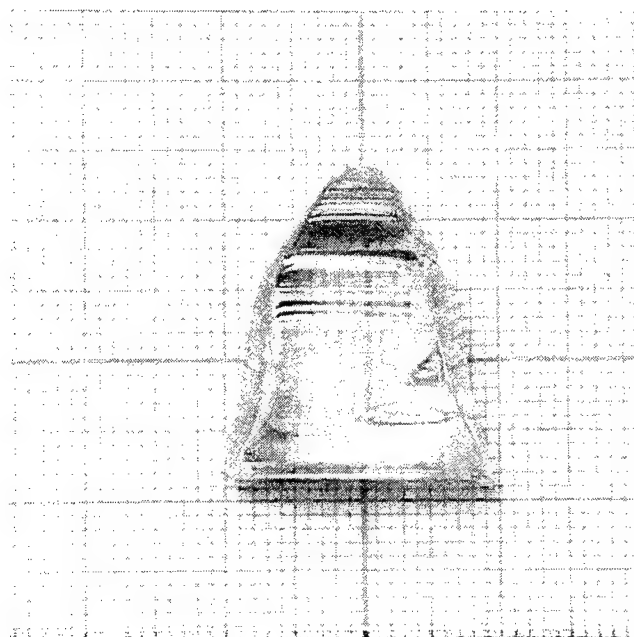


Fig. 1. As-grown [010] KGW:Nd single crystal having flat bottom. Scale in mm.

3. SPECTROSCOPIC INVESTIGATIONS

Plane-parallel plates 1 mm thick were cut from obtained single crystals of KGW:Nd, then graded, and polished. In order to determine absorption coefficient dependence on wavelength $k(\lambda)$ of the examined samples, the transmission measurements as a function of wavelength were performed. The measurements were carried out using the LAMBDA2 PERKIN ELMER spectrophotometer within the spectral range of 200÷1100 nm ($\Delta\lambda=1$ nm), the ACTA MVII BECKMAN spectrophotometer within the range of 1100÷1500 nm ($\Delta\lambda=1$ nm), and the Fourier PERKIN ELMER spectrophotometer 1725-X FT-IR within the range of 1.5÷25 μm ($\Delta 1/\lambda=1$ cm^{-1}). On the basis of the transmission $T(\lambda)$ measurements of the samples, an absorption coefficient was calculated with consideration of multiple reflections of radiation inside a sample. The spectral curves of the absorption coefficient for Nd^{3+} doped KGW crystals are shown in Fig. 2.

The measurements of luminescence spectra have been performed in the system with the H20 JOBIN YVON monochromator (focal length 200 mm). In the excitation channel the laser diode emitting at 808 nm was applied. Luminescence excited with laser radiation, after spectral splitting in H20 monochromator with holographic gratings, was registered by means of the LOCK-IN (STANFORD RESEARCH SR510) system with thermoelectrically cooled InGaAs detector. Three luminescence bands located at 900, 1067, 1350 nm were observed. The measurements of Nd^{3+} ions lifetime at the upper laser level (${}^4\text{F}_{3/2}$) for the samples of KGW:Nd crystals were made by means of direct method with pulse excitation. The investigated medium was excited with radiation pulse duration significantly shorter than the lifetime τ at the excited level. After excitation a population level decay occurs, the evidence of which is fluorescence decay that can be observed. As a source of 808 nm diagnostic pulses SDL2430 laser diode was used. The laser was supplied from the power supply SDL800, controlled by a pulses generator. Generated pulses of 8 μs duration and 0.66 kHz frequency. In the detection channel, perpendicular to the excitation channel, the silicon photodiode was applied and time characteristics of fluorescence decay were registered with the digital oscilloscope LeCROY 9350AM (500 MHz). The results of measurements of fluorescence decay time in the investigated samples are listed in Table 1.

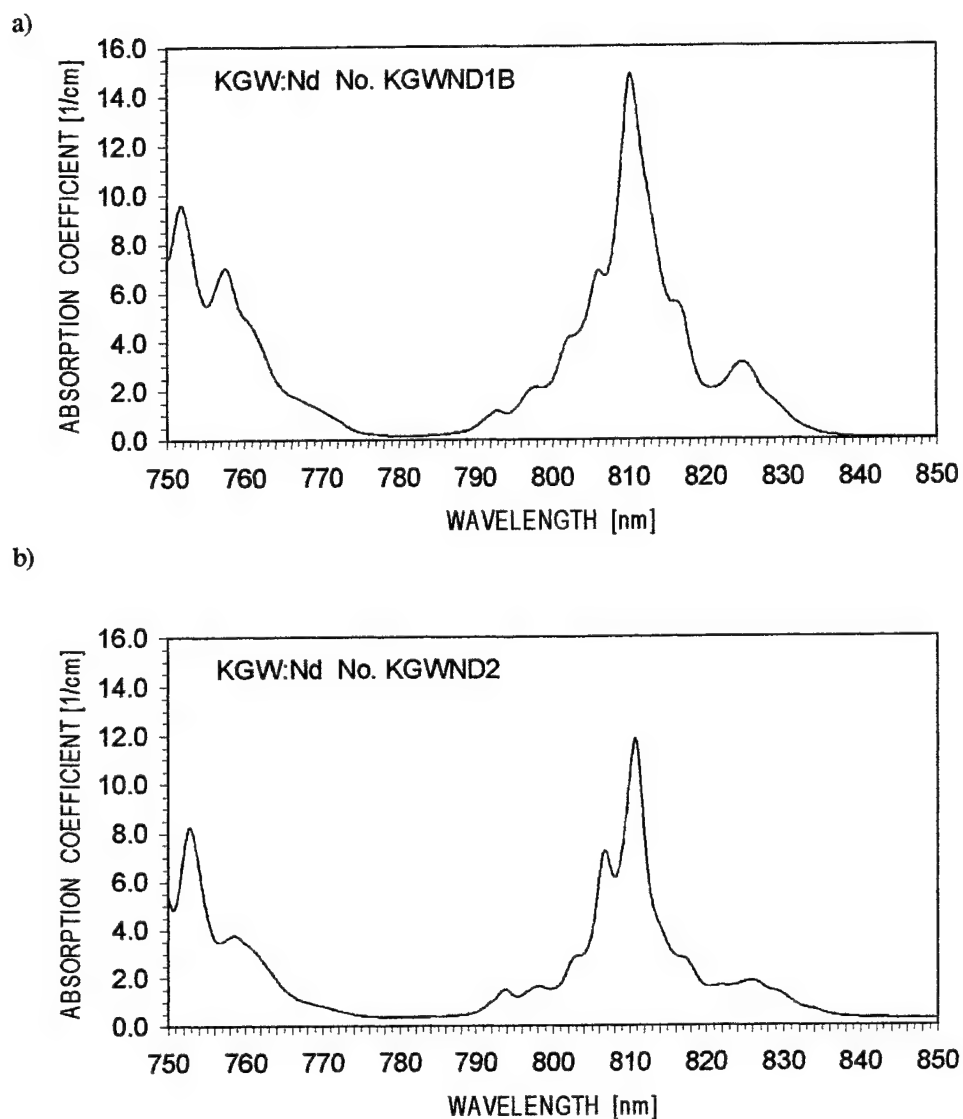


Fig. 2. Absorption spectra of neodymium doped KGW crystals
a) KGW:Nd³⁺ (8 at.% Nd³⁺), b) KGW:Nd³⁺ (3 at.% Nd³⁺).

Table 1. Results of measurements of fluorescence decay time (level $^4F_{3/2}$) in the investigated samples of KGW:Nd³⁺ crystals.

Crystal	Fluorescence decay time
KGW:Nd (8 at.% Nd ³⁺)	$101 \pm 2 \mu\text{s}$
KGW:Nd (5 at.% Nd ³⁺)	$115 \pm 2 \mu\text{s}$
KGW:Nd (3 at.% Nd ³⁺)	$128 \pm 2 \mu\text{s}$
KGW:Nd (1 at.% Nd ³⁺)	$132 \pm 2 \mu\text{s}$

4. LASER ACTION IN KGW:Nd

Investigations of longitudinally pumped microlasers generating at 1067 nm made of KGW:Nd with various Nd^{3+} ions concentration, were carried out. A schematic of the laser cavity is shown in Fig. 3. The results for KGW:Nd 3 at.% are presented in Fig. 4. Also the generation characteristics of longitudinally pumped microlasers with passive Q-modulation by CW SDL 2362 P3 laser diode were measured.

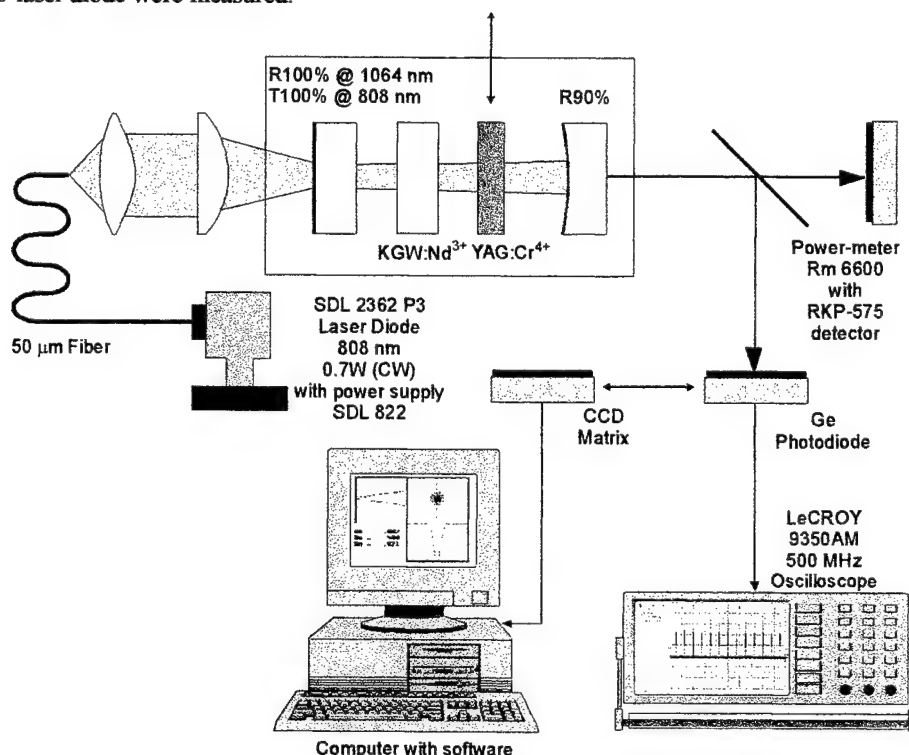


Fig. 3. Schematic of the YAG:Cr^{4+} Q-switched KGW:Nd^{3+} laser cavity

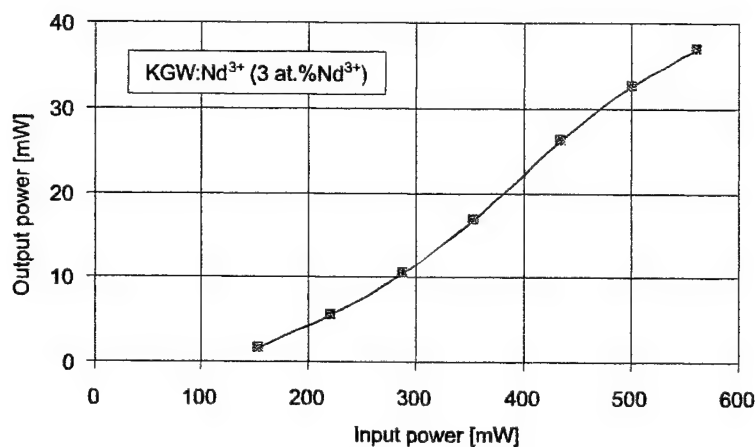


Fig. 4. Generation characteristics of KGW:Nd^{3+} diode pumped laser (output mirror $T=3.1\%$, $r=50$ mm)

The generation of a train of pulses with duration of 100 ns, frequency of 128.5 kHz and energy 9 μJ has been obtained (see Fig. 5). Q-switched pulses showed intensity and timing jitter depending on the positions of intracavity elements.

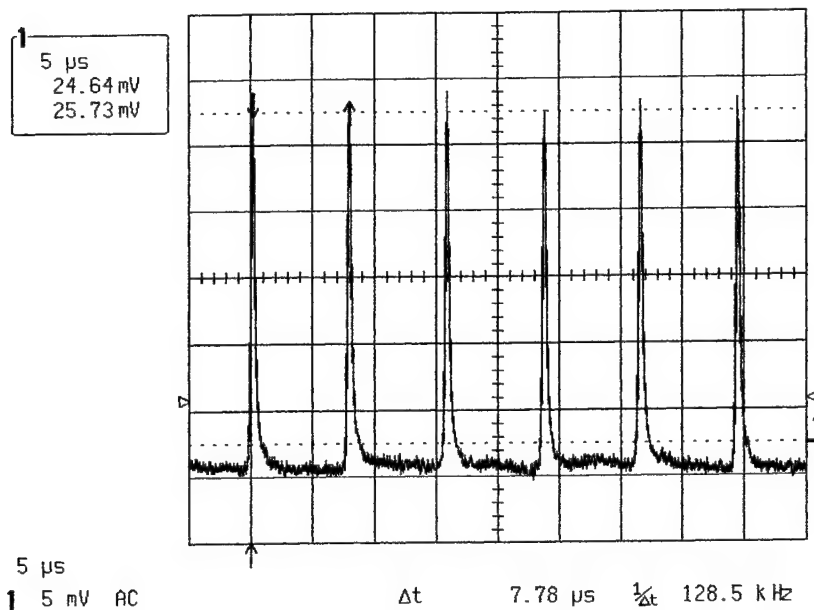


Fig. 5. Train of giant-pulses from YAG:Cr⁴⁺ passive Q-switched KGW:Nd laser (repetition rate 128.5 kHz, giant-pulse duration 100 ns)

5. CONCLUSIONS

The conditions of growth of KGW:Nd single crystals having various concentrations of dopant were determined. High Temperature Solution Growth technique was used. Investigations of optical and spectroscopic properties of the obtained crystals showed their good optical quality, so they can be applied in laser systems.

Due to advantageous spectroscopic parameters of KGW:Nd crystals and good thermal and mechanical resistance, those crystals were used both in CW as well as giant pulses train generation of the diode pumped microlasers.

ACKNOWLEDGEMENTS

This research was partially supported by Polish State Committee on Science (KBN) – project No. 0T 00A 013 17.

REFERENCES

1. M.C. Pujol, M. Rico, C. Zaldo, R. Solé, V. Nikolov, X. Solans, M. Aguiló and F. Diaz, "Crystalline structure and optical spectroscopy of Er³⁺-doped KGd(WO₄)₂ single crystals", *Applied Physics B*, **68**, pp. 187-197, 1999
2. A.A. Kaminskii, K. Ueda, H.E. Eichler, J. Findeisen, S.N. Bagayev, F.A. Kuznetsov, A.A. Pavlyuk, G. Boulon, and F. Gourgeois, "Monoclinic Tungstates K₂WO₄ and K₂WO₄ – New $\chi^{(3)}$ – Active Crystals for Laser Raman Shifters", *Jap. J. Appl. Phys.*, Vol. **37**, No. 8A, pp. L923-L926, 1998
3. M.T. Borowiec, A. Majchrowski, H. Szymczak, M. Załęski, and J. Żmija, "Structural Phase Transition in K_{1-x}Cs_xDy(WO₄)₂ Single Crystals", *Cryst. Res. Techn.*, **35**, pp. 1343-1346, 2000.
4. R. Solé, V. Nikolov, X. Ruiz, Jna. Gavalda, X. Solans, M. Aguiló, and F. Diaz, "Growth of β -KGd_{1-x}Nd_x(WO₄)₂ single crystals in K₂W₂O₇ solvents", *J. Crystal Growth*, **169**, pp. 600-603, 1996.
5. A.A. Kaminskii, L. Li, A.V. Butashin, V.S. Mironov, A.A. Pavlyuk, S.N. Bagayev, and K. Ueda, "New Crystalline Lasers on the Base of Monoclinic KR(WO₄)₂:Ln³⁺ Tungstates (R=Y and Gd)", *Optical Review*, Vol. **4**, No. **2**, pp. 309-315, 1997.
6. A.A. Pavlyuk, L.I. Yudanov, and O.G. Potapova, "Fazovye diagrammy sistem KGd(WO₄)₂-KNd(WO₄)₂, RbGd(WO₄)₂-RbNd(WO₄)₂ i wyraszczanie monokryształów KGd(WO₄)₂ i RbGd(WO₄)₂ aktywowanych neodymem", *Neorg. Mat.*, **33**, No. **1**, pp.72-75, 1997.

Optical properties of some borate single crystals

A. Majchrowski^{a*}, T. Łukasiewicz^b, Z. Mierczyk^c, M. Malinowski^d

a - Institute of Applied Physics MUT, ul. Kaliskiego 2, 00-908 Warsaw, Poland

b - Institute of Electronic Materials Technology, ul. Wólczyńska 133, 01-919 Warsaw, Poland

c - Institute of Optoelectronics MUT, ul. Kaliskiego 2, 00-908 Warsaw, Poland

d - Institute of Microelectronics and Optoelectronics PW, ul. Koszykowa 75, 00-662 Warsaw, Poland

ABSTRACT

This paper describes efforts taken in Institute of Applied Physics and Institute of Electronic Materials Technology to obtain several single crystals from borate family, namely $\text{CsLiB}_6\text{O}_{10}$ (CLBO), $\text{Ca}_4\text{GdO}(\text{BO}_3)_3$ (GdCOB), $\text{Li}_2\text{B}_4\text{O}_7$ (TBO), $\beta\text{-BaB}_2\text{O}_4$ (BBO), and $\text{YAl}_3(\text{BO}_3)_4$ (YAB), pure and doped with several ions. The main goal of this investigation was to develop technology of these new nonlinear optical materials to create possibility of their applications in higher harmonics generators and self-frequency doubling lasers. Depending on such properties of crystallized borate materials as incongruent melting or high temperature phase transitions, Czochralski technique or high temperature solution growth technique were used. The main aspects of crystallization of these materials as well as their optical properties are discussed.

keywords: borate single crystals, high temperature solution growth, Czochralski growth, nonlinear optical materials.

1. INTRODUCTION

Recent tremendous advances in the area of solid state lasers and nonlinear optics have been mainly driven by the development of new materials, having better properties than standard materials. Very important group of these new materials are borate single crystals, which possess excellent properties such as high damage threshold for laser radiation, high coefficients of second and higher harmonics generation, transparency far into ultraviolet, high optical quality, and good chemical and mechanical stability.

Borate crystals exist in many structural types due to three-fold (trigonal) or four-fold (tetrahedral) coordination of boron atoms in boron-oxide compounds.¹ Various anionic groups as basic structural units cause the existence of different structures of borates, what gives the possibility of selecting appropriate materials for chosen applications. Borates find many applications as substrates for Surface Acoustic Wave (SAW) devices, and dosimetric, nonlinear and lasing materials. The most interesting feature of borates are their nonlinear optical (NLO) properties. Powerful, tunable ultraviolet sources required for many applications (spectroscopy, data storage, remote sensing, medicine etc.) rely on frequency-doubling of lasers working in the visible range.

The wavelength range of solid state lasers has been greatly increased due to parametric conversion, nonlinear mixing, and higher harmonics generation. All these applications depend on the development of new NLO materials. As it was mentioned earlier borates have properties which fulfil conditions required for good NLO materials. According to Chen¹ the following anionic groups as basic structural units in borate crystals are of practical interest $(\text{BO}_3)^{3-}$, $(\text{BO}_4)^{5-}$, $(\text{B}_2\text{O}_5)^{4-}$, $(\text{B}_2\text{O}_7)^{6-}$, $(\text{B}_3\text{O}_6)^{3-}$, $(\text{B}_3\text{O}_7)^{5-}$, $(\text{B}_3\text{O}_8)^{7-}$, $(\text{B}_3\text{O}_9)^{9-}$, $(\text{B}_4\text{O}_9)^{6-}$ and $(\text{B}_5\text{O}_{10})^{5-}$. Chen's calculations have shown that planar anionic groups containing conjugated π -orbital systems (e.g. $(\text{B}_3\text{O}_6)^{3-}$) are more favorable to the appearance of large second-order susceptibilities (influencing SHG coefficients), compared with the non-planar tetrahedral groups. On the other hand absorption edges of the planar groups lie within the wavelength range of 190-200 nm, while those of non-planar groups move towards shorter wavelengths up to 160 nm. The discovery of $\beta\text{-BaB}_2\text{O}_4$ (BBO)² triggered intensive researches in the area of nonlinear borates. As a result a group of promising NLO materials has been found, among which the most interesting are: LiB_3O_5 (LBO),³ CsB_3O_5 (CBO),⁴ $\text{CsLiB}_6\text{O}_{10}$ (CLBO),⁵ $\text{KBe}_2\text{BO}_3\text{F}_2$ (KBBF),⁶ and $\text{Sr}_2\text{Be}_2\text{B}_2\text{O}_7$ (SBBO).⁷ They find applications in second harmonic generation, sum or difference frequency mixing and optical parametric oscillators. Borates are also very attractive as host materials for many dopants, due to possibility of substitution of some ions in host lattices by, for example neodymium or chromium ions. The substitution forms lasing materials with nonlinear behavior, what gives as a result self-frequency doubling materials.

* e-mail: amajchrowski@altair.geo.wat.waw.pl

The most promising of these materials are: $\text{Nd}_{1-x}\text{Y}_x\text{Al}_3(\text{BO}_3)_4$ (NYAB),⁸ $\text{YAl}_3(\text{BO}_3)_4:\text{Cr}$ (YAB:Cr),⁹ $\text{GdAl}_3(\text{BO}_3)_4:\text{Cr}$ (GAB:Cr)¹⁰ with huntite structure and $\text{Ca}_4\text{GdO}(\text{BO}_3)_3:\text{Nd}$ (GdCBO:Nd)¹¹ and $\text{Ca}_4\text{Y}(\text{BO}_3)_3:\text{Nd}$ (YCBO)¹² from oxoborates family. Y and Gd do not show absorption in the wavelength range interesting for NLO applications and can be easily substituted by lasing ions, in some cases up to 15%, without modification of the accentric host lattice. They are presently intensively investigated as candidates for self-frequency doubling laser crystals. The progress in borate crystals investigations is so great, that every month new borate crystals are reported. In a very detailed review, dealing with borate crystals, Becker¹³ gives information concerning more than 20 borate single crystals – and since that time new efficient NLO borates have been reported. This paper describes efforts of our group in the area of borate crystal growth and characterisation.

2. BORATE SINGLE CRYSTALS GROWTH

In Tables 1, and 2 some properties of chosen NLO and self-frequency doubling borates are given, respectively. $\text{K}_2\text{Al}_2\text{B}_2\text{O}_7$ ¹⁴ and BiB_3O_6 ¹⁵ are new NLO borates having good properties. BiB_3O_6 is specially promising material due to its very high SHG coefficient, although in our opinion it may suffer from rather small damage threshold.

Investigations of borates crystallisation have been carried out in our group for last decade. The first borate material obtained by us was $\text{Li}_2\text{B}_4\text{O}_7$ ¹⁶, at that time it was sought for its applications in SAW devices. Recently $\text{Li}_2\text{B}_4\text{O}_7$ has been found to have good NLO properties, namely very high damage threshold for laser radiation and generation of UV radiation due to fourth and fifth harmonics. Good quality $\text{Li}_2\text{B}_4\text{O}_7$ single crystals, free from twinning, were obtained by the Czochralski method.

Single crystals of $\beta\text{-BaB}_2\text{O}_4$, which up till now is one of the most frequently used NLO materials, were also obtained by our group. The material undergoes phase transition at 925°C, and we used both top seeded solution growth (TSSG)¹⁷ and Czochralski growth from supercooled stoichiometric melts¹⁸ to obtain low-temperature phase of BBO.

For last two years we have been investigated three relatively new borate single crystals, $\text{CsLiB}_6\text{O}_{10}$, $\text{Nd}_{1-x}\text{Y}_x\text{Al}_3(\text{BO}_3)_4$, and $\text{Ca}_4\text{GdO}(\text{BO}_3)_3:\text{Nd}$. Both TSSG and Czochralski technique were used, depending on properties of grown crystal. TSSG experiments were carried out in multi-zone resistance furnaces having high heat capacity. Precise temperature regulation, down to 0.01 K/hr linearly, was possible due to Eurotherm 906S regulators/programmers. Czochralski growth, depending on the melting point of the investigated material, was carried out using resistance or r.f. heating.

2.1. $\text{CsLiB}_6\text{O}_{10}$

CLBO is a congruently melting material (1118 K) with very high damage threshold for laser radiation. Both, TSSG technique using 5 mol.% of $\text{Cs}_2\text{O}:\text{Li}_2\text{O}$ (1:1 molar ratio) self-flux diminishing very high viscosity of the molten material, and Czochralski technique, were used in our experiments. The temperature during CLBO crystallisation was lowered linearly at the rates 0.01-0.1 K/hr. When TSSG was used crystals grew into the melt, in case of Czochralski method crystals were pulled up 2mm/day. The rotation rate did not exceed 5 rpm. Czochralski grown CLBO crystals were 20-30 mm in diameter and 50 mm long.

The transparency of investigated CLBO crystals was far into UV. We found that at 190 nm the transmission of 3.3 mm thick CLBO sample was 86%, what is in good agreement with literature – see Tab. 1. CLBO is slightly hygroscopic, but careful storage stops the harmful influence of moisture. Second harmonic generation for 1.06 μm YAG:Nd laser radiation was obtained in our CLBO crystals.

2.2. $\text{Nd}_{1-x}\text{Y}_x\text{Al}_3(\text{BO}_3)_4$

NYAB crystals combine both NLO and lasing properties. 1.06 μm laser oscillations in NYAB are then self-frequency doubled to 0.53 μm in the same crystal. NYAB melts incongruently, what imposes the necessity of TSSG from high temperature solutions. As flux $\text{K}_2\text{Mo}_3\text{O}_{10}$ was used. The starting composition was 20 mol.% of NYAB in $\text{K}_2\text{Mo}_3\text{O}_{10}$ with 5 at.% of neodymium in NYAB. The growth was carried out in multi-zone resistance furnaces in very low temperature gradients. The temperature was lowered at the rate 2.4 K/day in the range of 1323 – 1223 K. Growing crystals were rotated at the rate of 100 rpm. Typical growth lasted 3-4 weeks. As-grown crystals 1.5x1.5x1.0 cm have inclusions in the central parts but the outer parts of the crystals were transparent.

2.3. $\text{Ca}_4\text{GdO}(\text{BO}_3)_3:\text{Nd}$

GdCBO also possesses self-frequency doubling properties. The main advantage of GdCBO, comparing with NYAB, is relatively easy growth from stoichiometric melts – the material melts congruently at 1753 K. GdCBO single crystals, pure and doped with neodymium up to 7 at.%, have been grown by the Czochralski technique with use of MSR-2 puller equipped in r.f. generator. Crystals were grown on [010] seeds in pure nitrogen atmosphere. Single crystals up to 20 mm in diameter and 60 mm long, free of macroscopic defects were obtained.

3. SPECTROSCOPIC INVESTIGATIONS

Plane-parallel plates 1 mm thick were cut from obtained borate single crystals. In order to determine absorption coefficient dependence on wavelength $k(\lambda)$ of the examined samples, the transmission measurements as a function of wavelength were performed. The measurements were carried out using the LAMBDA2 PERKIN ELMER spectrophotometer within the spectral range of 200÷1100 nm ($\Delta\lambda=1$ nm), the ACTA MVII BECKMAN spectrophotometer within the range of 1100÷1500 nm ($\Delta\lambda=1$ nm), and the Fourier PERKIN ELMER spectrophotometer 1725-X FT-IR within the range of 1.5÷25 μm ($\Delta 1/\lambda=1$ cm^{-1}). On the basis of the transmission $T(\lambda)$ measurements of the samples, an absorption coefficient was calculated with consideration of multiple reflections of radiation inside a sample. The absorption spectra of investigated crystals are shown in Fig. 1 and Fig. 2.

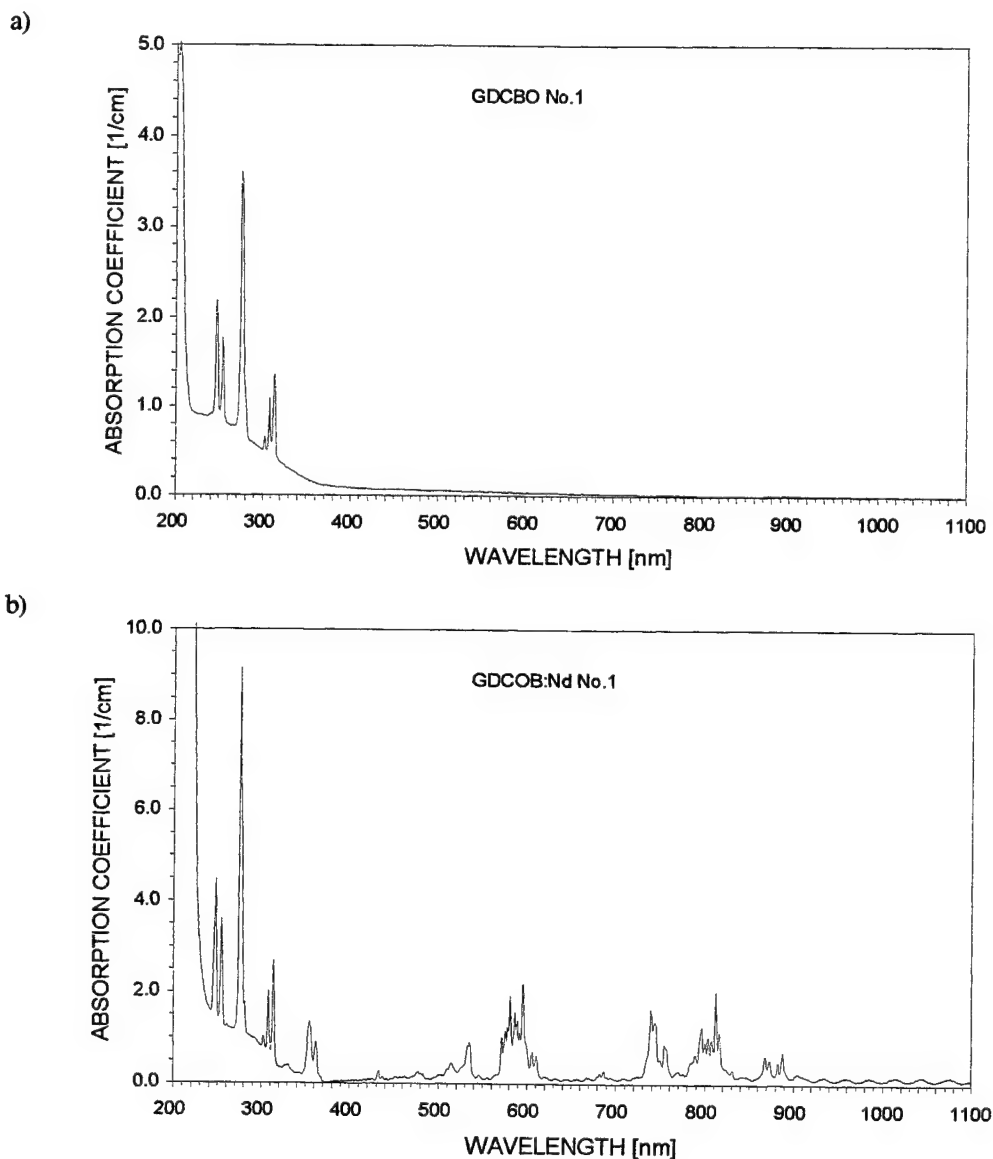


Fig. 1. Absorption spectra of undoped (a) and 3 at. % Nd^{3+} doped (b) GdCOB crystals

Tab. 1. Borates for SHG.^{13,14,15}

MATERIAL	SPACE GROUP	TRANSPARENCY nm	SHG COEFF. pm/V	DAMAGE THRESHOLD GW/cm ²	METHOD OF CRYSTALLISATION
β -BaB ₂ O ₄ (BBO)	R3c	190-2500	2.3	5 (10ns)	FLUX CZOCHRALSKI
LiB ₃ O ₅ (LBO)	Pna2 ₁	155-2600	0.85	>0.9 (9ns)	SELF-FLUX
CsLiB ₆ O ₁₀ (CLBO)	I42d	180-2750	0.95	26 (1ns)	SELF-FLUX CZOCHRALSKI
Li ₂ B ₄ O ₇ (LTB)	I4 ₁ cd	200-3500	0.55	40 (10ns)	CZOCHRALSKI BRIDGMAN
Sr ₂ Be ₂ B ₂ O ₇ (SBBO)	P6c2	160-3780	1.7	-	SELF-FLUX
K ₂ Al ₂ B ₂ O ₇ (KAB)	P321	180-	<SBBO	-	SELF-FLUX
BiB ₃ O ₆ (BiBO)	C2	250-2300	3.2	-	CZOCHRALSKI

Tab. 2. Self-frequency doubling borates.¹³

MATERIAL	SPACE GROUP	TRANSPARENCY nm	SHG COEFF. pm/V	METHOD OF CRYSTALLISATION
Nd _x Y _{1-x} Al ₃ (BO ₃) ₄ (NYAB)	R32	200-5000	1.28	FLUX
Ca ₄ GdO(BO ₃) ₃ :Nd (GdCBO:Nd)	Cm	320-2700	0.56	CZOCHRALSKI
Ca ₄ YO(BO ₃) ₃ :Nd (YCBO:Nd)	Cm	220-	1.1	CZOCHRALSKI

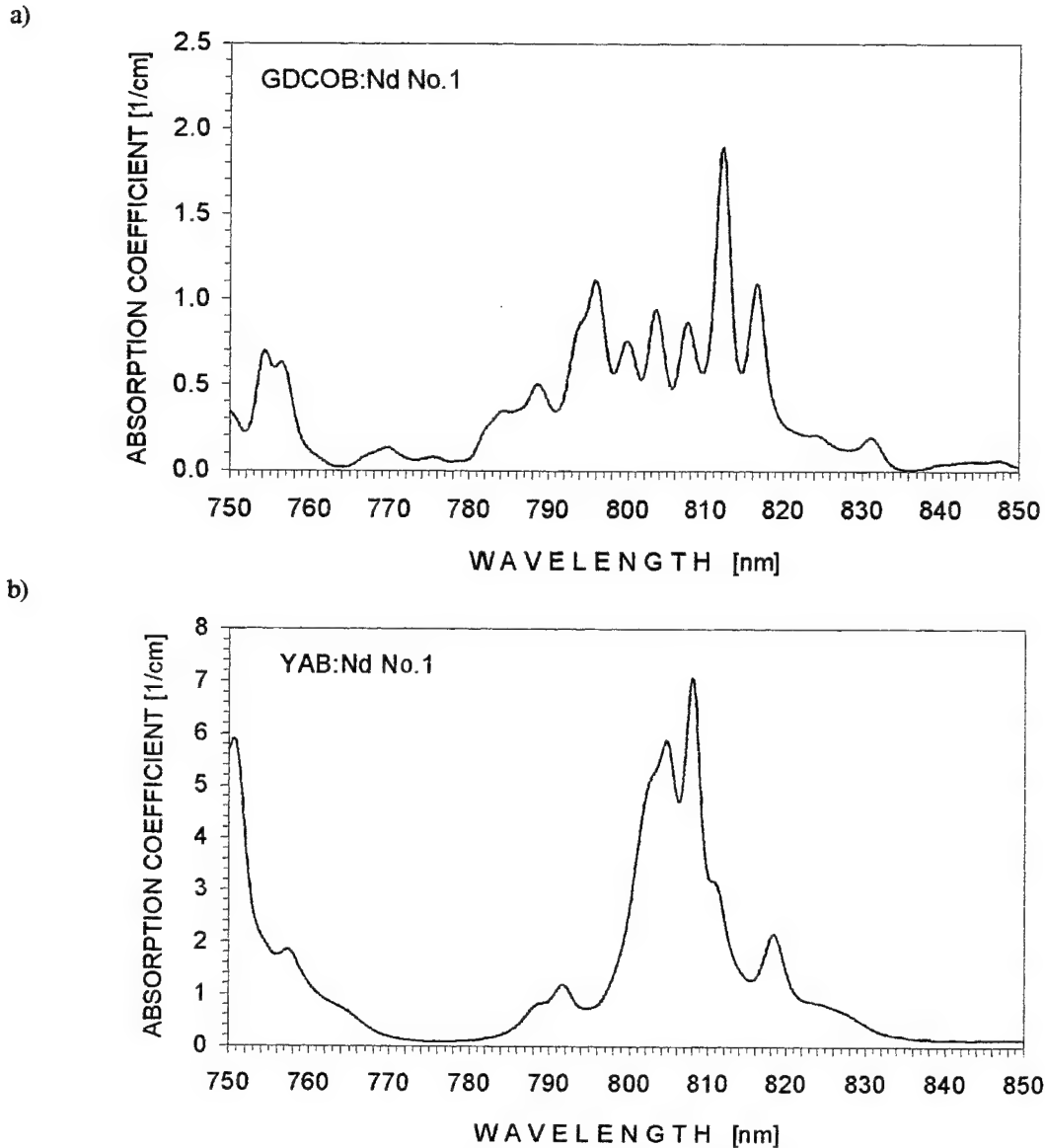


Fig. 2. Absorption spectra of neodymium doped borate crystals in 750÷850 nm region ($\Delta\lambda=0.1$ nm)
 a) GDCOB:Nd³⁺ (3 at.% Nd³⁺), b) YAB:Nd³⁺ (5 at.% Nd³⁺).

The measurements of luminescence spectra have been performed in the system with the H20 JOBIN YVON monochromator (focal length 200 mm). In the excitation channel the laser diode emitting at 808 nm was applied. Luminescence excited with laser radiation, after spectral splitting in H20 monochromator with holographic gratings, was registered by means of the LOCK-IN (STANFORD RESEARCH SR510) system with thermoelectrically cooled InGaAs detector. Luminescence spectra of neodymium doped borate crystals are presented in Fig. 3. The measurements of Nd^{3+} ions lifetime at the upper laser level ($^4\text{F}_{3/2}$) for the samples of neodymium doped borate crystals were made by means of direct method with pulse excitation.

The investigated medium was excited with radiation pulse duration significantly shorter than the lifetime τ at the excited level. After excitation a population level decay occurs, the evidence of which is fluorescence decay that can be observed. As a source of 808 nm diagnostic pulses SDL2430 laser diode was used. The laser was supplied from the power supply SDL800, controlled by a pulses generator. Generated pulses of 8 μs duration and 0.66 kHz frequency.

In the detection channel, perpendicular to the excitation channel, the silicon photodiode was applied and time characteristics of fluorescence decay were registered with the digital oscilloscope LeCROY 9350AM (500 MHz). The time-constant τ (fluorescence decay time) corresponds to the time after which the fluorescence intensity I reaches the I_0/e value. The results of measurements of fluorescence decay time in the investigated samples are listed in Table 3.

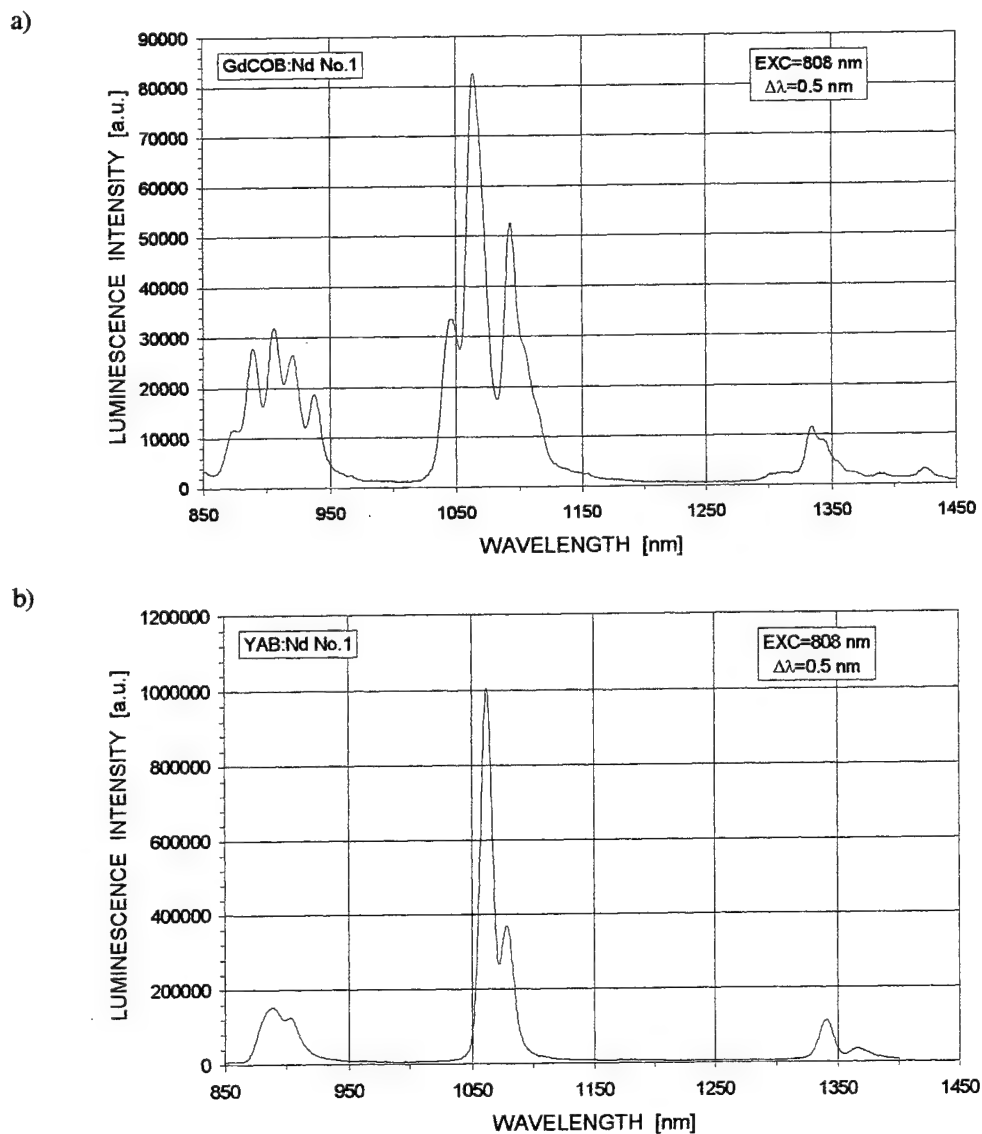


Fig. 3. Luminescence spectra of neodymium doped borate crystals
a) GdCOB:Nd³⁺ (3 at.% Nd³⁺), b) YAB:Nd³⁺ (5 at.% Nd³⁺).

Tab. 3. Results of measurements of fluorescence decay time (level $^4F_{3/2}$) in the investigated crystals.

Crystal	Fluorescence decay time
GdCOB:Nd (3 at.% Nd ³⁺)	$78 \pm 2 \mu\text{s}$
YAB:Nd (5 at.% Nd ³⁺)	$57 \pm 2 \mu\text{s}$

4. CONCLUSIONS

Nonlinear optical and lasing borates crystallisation, namely CLBO, NYAB, and GdCBO:Nd, was investigated. Top seeded solution growth and Czochralski method were used to grow borate crystals. Optical and spectroscopic properties of as-grown crystals show their applicability both in second harmonic generation (SHG), and in self-doubling frequency of laser radiation.

REFERENCES

1. C. Chen, Y. Wu and R. Li "The development of new NLO crystals in borate series", *J. Cryst. Growth*, **99**, pp. 790-798, 1990.
2. L.K. Cheng, W. Bosenberg, C.L. Tang, "Growth and characterization of low temperature phase barium metaborate crystals", *J. Cryst. Growth*, **89**, pp. 553-559, 1988.
3. C.T. Chen, Y. Wu, A. Jiang, B. Wu, G. You, R. Li, S. Lin, "New nonlinear-optical crystal LiB_3O_5 ", *J. Opt. Soc. Am.*, **B6**, pp. 616-621, 1989.
4. Y. Wu, T. Sasaki, S. Nakai, A. Yokotani, H. Tang, C. Cheng, "CsB₃O₅: a new nonlinear optical crystal", *Appl. Phys. Lett.*, **62**, pp. 2614-2615, 1993.
5. Y. Mori, I. Kuroda, T. Sasaki, S. Nakai, "Nonlinear optical properties of cesium lithium borate", *Jpn. J. Appl. Phys.*, **34**, pp. L296-L298, 1995.
6. L. Mei, Y. Wang, C. Chen, B. Wu, "Nonlinear optical materials based on $\text{MBe}_2\text{BO}_3\text{F}_2$ (M=Na, K)", *J. Appl. Phys.*, **74**, pp. 7014-7015, 1993.
7. C.L. Hill, X. Zhang, "Design and synthesis of an ultraviolet-transparent nonlinear optical crystal $\text{Sr}_2\text{Be}_2\text{B}_2\text{O}_7$ ", *Nature*, Vol. **373**, pp. 322-324, 1995.
8. T. Omatsu, Y. Kato, M. Shimosegawa, A. Hasegawa, I. Ogura, "Thermal effects in laser diode pumped self-frequency-doubled NYAB microchip laser", *Opt. Comm.*, **118**, pp. 302-308, 1995.
9. G.F. Wang, T. Han, H.G. Gallagher, B. Henderson, "Novel laser gain based on Cr^{3+} - doped mixed borates $\text{RX}_3(\text{BO}_3)_4$ ", *Appl. Phys. Lett.*, **67**, pp. 3906-3908, 1995.
10. M. Iwai, Y. Mori, T. Sasaki, S. Nakai, N. Sarakura, Z. Liu, Y. Segawa, "Growth and optical characterization of Cr:YAB and Cr:YGAB crystal for new tunable and self-frequency doubling laser", *Jpn. J. Appl. Phys.*, **34**, pp. 2338-2343, 1995.
11. G. Aka, A. Kahn-Haradi, D. Vivien, J.M. Benitez, F. Salin, J. Godard, "New nonlinear and neodymium laser self-frequency doubling crystal with congruent melting: GdCOB", *Eur. J. Solid State Inorg. Chem.*, **33**, pp. 727-732, 1996.
12. D. Xue, S. Zhang, "Structural analysis of nonlinearities of $\text{Ca}_4\text{ReO}(\text{BO}_3)_3$ (Re= La, Nd, Sm, Gd, Er, Y)", *Applied Physics a - Mat. Science and Processing*, **68**, pp. 57-61, 1999.
13. P. Becker, "Borate materials in nonlinear optics", *Adv. Mater.*, Vol. **10**, No. **13**, pp. 979-992, 1998.
14. Z.G. Hu, T. Higashiyama, M. Yoshimura, Y.K. Yap, Y. Mori, T. Sasaki, "A new nonlinear optical borate $\text{K}_2\text{Al}_2\text{B}_2\text{O}_7$ ", *Jpn. J. Appl. Phys.*, Vol. **37**, pp. L1093-1094, 1998.
15. H. Hellwig, J. Liebertz, L. Bohaty, "Exceptional large nonlinear optical coefficients in the monoclinic bismuth borate BiB_3O_6 ", *Solid State Commun.*, Vol. **109**, No. **4**, pp. 249-251, 1999.
16. T. Łukasiewicz and A. Majchrowski, "Czochralski growth of lithium tetraborate single crystals", *Materials Letters*, **11**, pp. 281-283, 1991.
17. A. Majchrowski, J. Żmija, "Growth, properties and applications of borate crystals", *Proc. SPIE*, Vol. **3178**, pp. 52-54, 1997.
18. T. Łukasiewicz, J. Kisielewski, Z. Łuczyński, J. Sass, " β -BaB₂O₄ single crystals obtained by Czochralski method", *Mat. Res. Soc. Symp. Proc.*, Vol. **329**, pp. 29-32, 1994.

Peculiarities of the thermal donor formation in Czochralski grown silicon under high hydrostatic pressure

Valentin V. Emtsev ^{a*}, Vadim V. Emtsev ^b, Gagik A. Oganessian ^b,
Andrzej Misiuk ^c, and Charalambos A. Londos ^d

^a Van der Waals-Zeeman Institute, University of Amsterdam, Valckenierstraat 65,
1018 XE Amsterdam, The Netherlands

^b Ioffe Physicotechnical Institute, Russian Academy of Sciences, 194021 St. Petersburg, Russia

^c Institute of Electron Technology, al. Lotników 32/46, 02-668 Warsaw, Poland

^d Solid State Section, Physics Department, The University of Athens,
Panepistimiopolis, Zografos, 157 84 Greece

ABSTRACT

Oxygen agglomeration processes leading to the formation of thermal donors in Czochralski grown silicon subjected to heat treatment at $T=450^{\circ}\text{C}$ at atmospheric pressure and a high hydrostatic pressure of $P=1$ GPa are studied. The samples investigated were doped with isoelectronic impurities of carbon and germanium. Both impurities are known to suppress the formation processes of thermal donors under normal conditions of heat treatment. It has been shown that the stress applied during heat treatment to Cz-Si with high concentrations of these impurities results in an enhanced formation of thermal donors. This effect is thought to be associated with increasing oxygen diffusivity under stress.

Keywords: silicon, isoelectronic impurity, hydrostatic pressure, oxygen aggregates, thermal donors.

1. INTRODUCTION

Czochralski grown silicon crystals (Cz-Si) contain high concentrations of oxygen, usually from $7 \cdot 10^{17} \text{ cm}^{-3}$ to $9 \cdot 10^{17} \text{ cm}^{-3}$. Because of a low solubility of oxygen in silicon below $T < 1000^{\circ}\text{C}$ oxygen impurity atoms form aggregates of different size upon annealing of silicon crystals at $T \geq 350^{\circ}\text{C}$. At relatively low temperatures of heat treatment at $T < 500^{\circ}\text{C}$ these agglomeration processes result in the appearance of Thermal Double Donors (TDD). This family of oxygen-related thermal donors consists of more than 16 centers whose shallow and deep energy states are in the ranges of $E_c - (40 \text{ to } 70) \text{ meV}$ and $E_c - (100 \text{ to } 160) \text{ meV}$, respectively. ¹⁻³ The donor centers mentioned are formed predominantly at $T < 500^{\circ}\text{C}$. Their maximal concentration in Cz-Si can be reached if heat treatment is performed at $T = 450^{\circ}\text{C}$.

Such isoelectronic impurities as carbon and germanium if present in high concentrations can strongly suppress the TDD formation. ^{1, 4-6} Pronounced effects of suppression are observed at impurity concentrations of $\geq 1 \cdot 10^{17} \text{ cm}^{-3}$ and $\geq 1 \cdot 10^{19} \text{ cm}^{-3}$ for carbon and germanium, respectively.

The aim of the present work is to shed new light on how the formation processes of thermal donors in Cz-Si:C and Cz-Si:Ge can be changed during heat treatment under high hydrostatic pressure. One could expect to observe some effects in view of strongly enhanced formation of oxygen-related thermal donors in normal Cz-Si subjected to annealing under stress. ^{7, 8}

* Further author information -

V.V.E. (correspondence): Email: emtsev@ioffe.rssi.ru; Telephone: (7812) 2479952; Fax: (7812) 2471017

V.V.E.: Email: emtsev@wins.uva.nl; Telephone: (3120) 5255628; Fax: (3120) 5255788

2. EXPERIMENTAL

Two wafers of Cz-Si doped with carbon and germanium were used. The initial materials were n-type. The concentrations of phosphorus were about $1 \cdot 10^{14} \text{ cm}^{-3}$ and $7 \cdot 10^{14} \text{ cm}^{-3}$ in the Cz-Si:C and Cz-Si:Ge, respectively.

The initial concentrations of oxygen in both wafers were about $7 \cdot 10^{17} \text{ cm}^{-3}$ using a conversion factor of $2.45 \cdot 10^{17} \text{ cm}^{-2}$ for the oxygen absorption band at 1108 cm^{-1} . The carbon and germanium concentrations were close to $1 \cdot 10^{17} \text{ cm}^{-3}$ and about $5 \cdot 10^{19} \text{ cm}^{-3}$ in the Cz-Si:C and Cz-Si:Ge, respectively. The wafer doped with germanium was carbon-lean, $N_{\text{CARBON}} < 5 \cdot 10^{16} \text{ cm}^{-3}$.

Square samples of $7 \times 7 \times 1 \text{ mm}^3$ were cut from these wafers. The electrical contacts were applied to samples in the Van der Pauw geometry. Samples were annealed at $T = 450^\circ\text{C}$ for $t = 10$ hours in pure argon under a hydrostatic pressure of $P = 1$ GPa. For comparison some reference samples were annealed under similar conditions at atmospheric pressure. After heat treatment a layer of about $50 \mu\text{m}$ were removed from sample surface by polishing and etching.

Hall effect measurements were taken with the aid of a computerized facility in the temperature range from $T = 20 \text{ K}$ to $T = 300 \text{ K}$.

3. Results

In Fig. 1 and Fig. 2 several $n(T)$ curves of the electron concentration *versus* reciprocal temperature are given for the initial and heat treated Cz-Si:Ge. It is known from the literature that the TDD formation in Cz-Si:Ge is retarded,^{4,6} despite the fact that in the presence of germanium the oxygen diffusivity increases.^{6,9} However, the TDDs are still a dominating family of thermal donors. Our data on the Cz-Si:Ge annealed at atmospheric pressure are in line with these findings. Actually, the initial formation rate of thermal donors in this material was found to be about $3 \cdot 10^{13} \text{ cm}^{-3} \cdot \text{h}^{-1}$. Without germanium the TDD formation rate in Cz-Si with similar oxygen contents is larger by a factor of two. The heat treatment of the same material for $t = 10$ hours under a pressure of $P = 1$ GPa resulted in a strong enhancement of the thermal donor

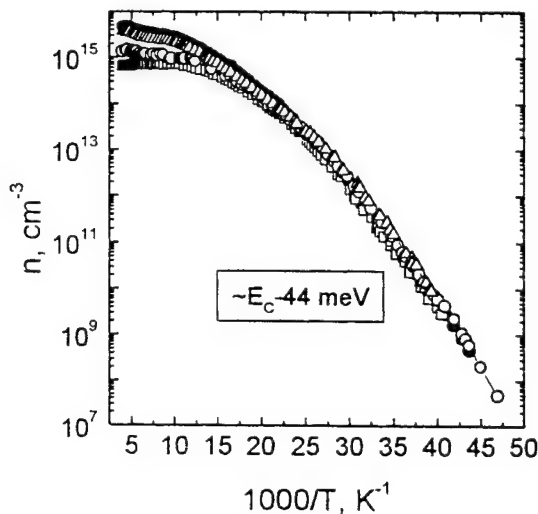


Fig. 1. Electron concentration *vs* reciprocal temperature in the Cz-Si:Ge heat treated at $T = 450^\circ\text{C}$ for $t = 10$ hours (open and black circles) and 120 hours (open triangles) under atmospheric pressure (open circles and triangles) and a hydrostatic pressure of $P = 1$ GPa (black circles). For comparison the $n(T)$ curve for the Cz-Si:Ge in the initial state is also shown (open squares). Activation energies of donor centers are given.

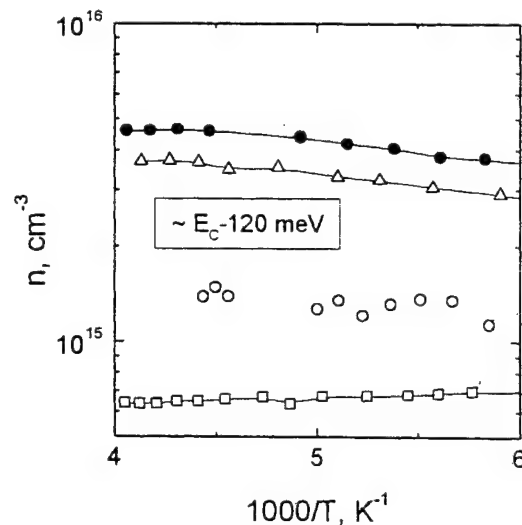


Fig. 2. Fragments of the $n(T)$ curves shown in Fig. 1.

formation (Fig. 2). As is seen, under such conditions of annealing the electron concentration at room temperature turned out to be larger than that after annealing of the same material for $t = 120$ hours at atmospheric pressure (Fig. 2). According to ⁵, the mechanism of TDD suppression in Cz-Si doped with germanium is mainly associated with decreasing capture radius of diffusing oxygen atoms by nucleation centers, precursors of forming TDDs. Both factors mentioned, increasing oxygen diffusivity and decreasing capture radius, are believed to be related to internal stress produced in Cz-Si:Ge by germanium atoms. In our case the high pressure applied to Cz-Si:Ge during heat treatment is thought to strongly enhance the oxygen diffusivity, thus changing the contributions of the factors considered. Optical measurements are now carried out to clarify this point.

Let us briefly discuss the role of carbon in heat-treated silicon. In Fig 3 and Fig. 4 several $n(T)$ curves are shown for the initial and annealed Cz-Si:C. A simple analysis of the $n(T)$ curves meets certain difficulties, since together with the TDDs other shallow donor centers also make their appearance during heat treatment at atmospheric pressure. This is not

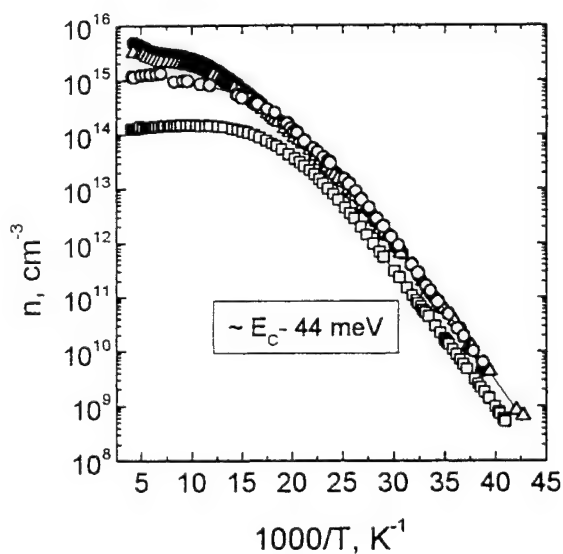


Fig. 3. Electron concentration vs reciprocal temperature in the Cz-Si:C heat treated at $T = 450^\circ\text{C}$ for $t = 10$ hours (open and black circles) and 60 hours (open triangles) under atmospheric pressure (open circles and triangles) and a hydrostatic pressure of $P = 1$ GPa (black circles). For comparison the $n(T)$ curve for the Cz-Si:Ge in the initial state is also shown (open squares). Activation energies of donor centers are given.

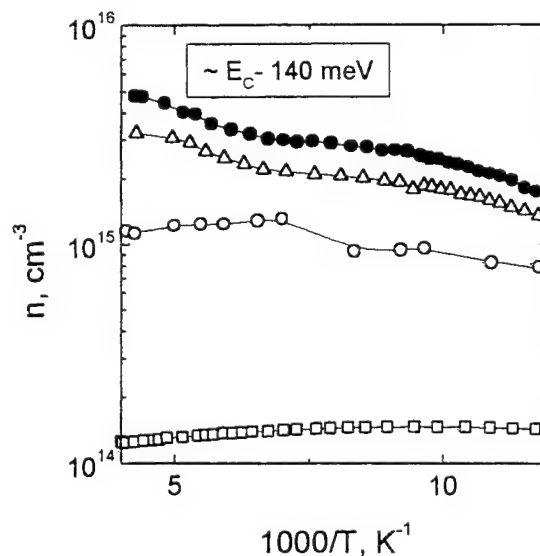


Fig. 4. Fragments of the $n(T)$ curves shown in Fig. 3.

surprising because of many quasichemical reactions of carbon with intrinsic defects and impurities, first of all oxygen.¹⁰ Besides, it is well known that as a result of oxygen agglomeration in Cz-Si self-interstitials are produced to relieve the strain around growing SiO_2 precipitates.¹ Interactions of substitutional and interstitial carbon atoms with oxygen can be responsible for the appearance of additional centers in annealed Cz-Si:C. Suppression of the TDD formation in the presence of carbon is thought to be due the overall strain relief in Cz-Si:C crystals associated with this dopant.¹ As a consequence, the driving force for oxygen agglomeration is weakened. The effect of hydrostatic pressure upon the formation processes of thermal donors in Cz-Si:C is similar to that observed in Cz-Si:Ge. In view of the different mechanisms of suppression of thermal donor formation in these materials one can conclude that their similar behavior under hydrostatic pressure is dictated by the same factor, mainly by increasing oxygen diffusivity under stress.

4. CONCLUSIONS

The formation processes of thermal donors in Cz-Si:C and Cz-Si:Ge annealed at $T = 450^\circ\text{C}$ under atmospheric and high pressure have been studied. Under normal conditions of heat treatment both isoelectronic impurities if present in large concentrations can retard markedly these processes. Heat treatment of Cz-Si:C and Cz-Si:Ge at $T = 450^\circ\text{C}$ under high pressure results in a strong enhancement of the thermal donor formation in both materials. The observed effect is thought to be due to increasing oxygen diffusivity under stress.

ACKNOWLEDGMENTS

The work was partly supported by the NATO project SA (HTECH CRG 974588).

REFERENCES

1. P. Wagner and J. Hage, "Thermal double donors in silicon," *Appl. Phys. A* **49**, pp. 123-138, 1989.
2. W. Götz, G. Pensl and W. Zulehner, "Observation of five additional thermal donor species TD12 to TD16 and regrowth of thermal donors at initial stages of the new donor formation in Czochralski grown silicon," *Phys. Rev. B* **46**, pp. 4312-4315, 1992.
3. B.J.H. Liesert, T. Gregorkiewicz and C.A.J. Ammerlaan, *Mater. Sci. Forum* **83-87**, pp. 404-404, 1992.
4. Yu.M. Babitskii, N.I. Gorbacheva, P.M. Grinshtein, M.A. Il'in, V.P. Kuznetsov, M.G. Mil'vidskii and B.M. Turovskii, "Formation kinetics of low-temperature oxygen-related donors in silicon with isoelectronic impurities," *Fiz. Tekh. Poluprovodn. [Sov. Phys. Semicond. (AIP)]* **22**, pp. 307-312, 1988.
5. D.I. Brinkevich, V.P. Markovich, L.I. Murin and V.V. Petrov, "Formation kinetics of thermal donors in Si <Ge,O>," *Fiz. Tekh. Poluprovodn. [Sov. Phys. Semicond. (AIP)]* **26**, pp. 682-690, 1992.
6. V.M. Babich, V.P. Baran, K.I. Zotov, V.L. Kiritsa and V.B. Koval'chuk, "Low-temperature diffusion of oxygen and formation of thermal donors in silicon doped with an isoelectronic impurity of germanium," *Fiz. Tekh. Poluprovodn. [Semiconductors (AIP)]* **29** pp. 58-64, 1995.
7. V.V. Emtsev, B.A. Andreev, A. Misiuk and K. Schmalz, *NATO ASI Series (3.High Technology)* **17** (1996) 345-353.
8. V.V. Emtsev, B.A. Andreev, A. Misiuk, W. Jung and K. Schmalz, "Oxygen aggregation in Czochralski grown silicon heat treated at 450°C under compressive stress," *Appl. Phys. Lett.* **71**, pp. 264-266, 1997.
9. A.K. Tipping, R.C. Newman, D.C. Newton and J.H. Tucker, "Enhanced oxygen diffusion in silicon at low temperatures," *Defects in Semicond. (Mater. Sci. Forum)* **10-12**, pp.887-892, 1986.
10. L.C. Kimerling, M.T. Asom, J.L. Benton, P.J. Drevinsky and C.E. Caefer, "Interstitial defect reactions in silicon," *Mater. Sci. Forum* **38-41**, pp. 141-150, 1989.

Effect of silicon microstructure on stress - stimulated creation of thermal donors

Andrzej Misiuk

Institute of Electron Technology, Al. Lotników 46, 02-668 Warsaw, Poland

ABSTRACT

Effect of intentionally created oxygen - related structural defects on generation of thermal donors, TD's, in Cz-Si treated at (670 K) 720 K under enhanced hydrostatic pressure of gas ambient, HP, up to 1.5 GPa (HT - HP treatment) was investigated. The as - grown Cz-Si samples with initial interstitial oxygen content up to $1.2 \times 10^{18} \text{ cm}^{-3}$, as well as that pre - annealed at 720 - 1020 K - 10^5 Pa for up to 170 h, indicate strongly HP - dependent increase of electron concentration in the conduction band after the HT - HP treatment at 720 K for 2 - 20 h. This confirms the stress - stimulated creation of TD's. HP - induced creation of TD's was much weaker after pre - annealing at 920 - 1020 K while not detected for the samples containing extended defects (created by 2 - steps pre - annealing at 10^5 Pa , the second step at 1230 - 1420 K). Qualitative explanation of observed phenomena was proposed.

Keywords: Cz-Si, microstructure, defects, thermal donors, annealing, hydrostatic pressure, oxygen interstitials.

1. INTRODUCTION

The nature of thermal donors in Czochralski silicon crystals, Cz-Si (the basic semiconductor for microelectronics), created in effect of annealing at 670 - 720 K (thermal donors, TD's) and at 870 - 1000 K (new donors, ND's) is still not fully understood. Enhanced hydrostatic pressure, HP, of neutral gas ambient at annealing (HT - HP treatment) of as - grown Cz-Si as well as of that pre - annealed at 720 K result in the much higher (even for an order of magnitude as compared to that observed for the samples annealed at 10^5 Pa) rate of TD's and ND's generation¹⁻⁷. The presence of HP - induced TD's and of ND's is also manifested by deep - level photoluminescence at about 1.08 eV detected at 2 K whereas the PL peak at 0.79 eV has been observed at room temperature⁸. Creation of thermal double donors⁹, TDD's, with ground state binding energies 42 - 57 meV was confirmed⁷ in the HP - treated Cz-Si samples by Fourier Transform Infrared Spectroscopy, FTIR. On the other hand, generation of shallow thermal donors with ionization energies of 30 - 40 meV was reported for such samples (interpretation of photoconductivity measurements)⁵.

One possible explanation of stress - stimulated creation of thermal donors is related to HP - induced activation of initially existing structural irregularities, that act at HT - HP as the nucleation centres for growth of oxygen clusters exhibiting donor activity^{4,7}. Just this presumption is investigated in the present work in more details.

The Cz-Si samples with oxygen interstitials, O_i , concentration, c_o , up to above $1.1 \times 10^{17} \text{ cm}^{-3}$ were subjected to one or two - steps pre - annealing at 10^5 Pa (atmospheric pressure) to cause oxygen precipitation and creation of different oxygen - related defects (what follows as well in decrease of c_o). Such pre - annealing results in creation of „additional” local irregularities in oxygen distribution. The as - grown (reference) and pre - annealed samples were next subjected to the HT - HP treatment at 670 / 720 K under hydrostatic pressure up to 1.5 GPa and their structural and electrical properties were determined.

2. EXPERIMENTAL

The (001) oriented 100 mm Cz-Si wafers from different suppliers, with c_o up to above $1.1 \times 10^{17} \text{ cm}^{-3}$ and of different conductivity (Table 1) were subjected to pre - annealing at $T = 720 - 1420 \text{ K}$ in nitrogen for up to 170 h, eventually followed by the next pre - annealing step at 1230 K or 1420 K, to create oxygen clusters and other oxygen - related defects. The samples of about $10 \times 10 \times 0.6 \text{ mm}^3$ dimension were cut from the pre - annealed wafers and treated

*A.M. (correspondence) Email: misiu@ite.waw.pl; Telephone: + 48 22 5487792; Fax: + 4822 8470631

Table 1. Typical investigated samples: designation, supplier, initial conductivity type, carrier concentration, N_i , and O_i concentration, c_o .

Sample designation	Supplier	Type	$N_i \times 10^{15}, \text{cm}^{-3}$	$c_o \times 10^{17}, \text{cm}^{-3}$
A	Silicon - IEMT	p	0.8	6.2
B	Silicon - IEMT	n	1.0	6.5
C	Silicon - IEMT	n	0.9	8.0
D	Silicon - IEMT	p	0.85	8.0
E	Silicon - IEMT	p	1.9	10.8 - 11.8
F	Russia	n	1.2	6.8
G	Russia	p	1.1	7.0
H	Wacker	n	1.0	9.2

at 670 K / 720 K under argon pressure up to 1.5 GPa for up to 20 h in high pressure furnace. Kind and density of defects created at pre - annealing were revealed by optical observation after selective etching in the Yang solution. After the HT - HP treatment about 20 μ thick sample surface layer was removed to prepare the samples for electrical (CV, four point probe methods), and FTIR (conversion factor equal to 2.45 was used to calculate c_o) measurements. Most results are reported for the samples treated at temperature 720 K, at which the TD's creation rate was the highest. In what follows the conditions of pre-annealing (T and time) are indicated in parenthesis after the sample symbol.

3. RESULTS

3.1 Effect of HT - HP treatment on carrier concentration in as - grown (reference) Cz-Si

Effect of HT - HP treatment on carrier concentration (related to creation of TD's) in as - grown (reference) Cz-Si samples is presented in Figs 1 and 2 (for sample designations see Table 1). $\Delta N_e = |N_{\text{HT-HP}} - N_i|$, where $N_{\text{HT-HP}}$ means the carrier (electron) concentration after the HT-HP treatment and N_i - the initial carrier concentration (see Table 1).

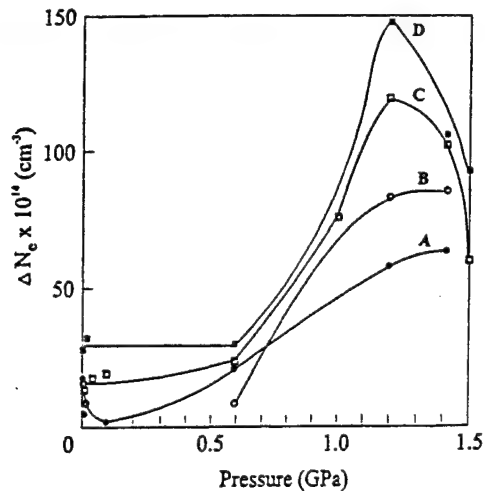


Fig. 1. Dependence of ΔN_e on HP for A, B, C, and D samples treated for 10 h at 720 K - HP.

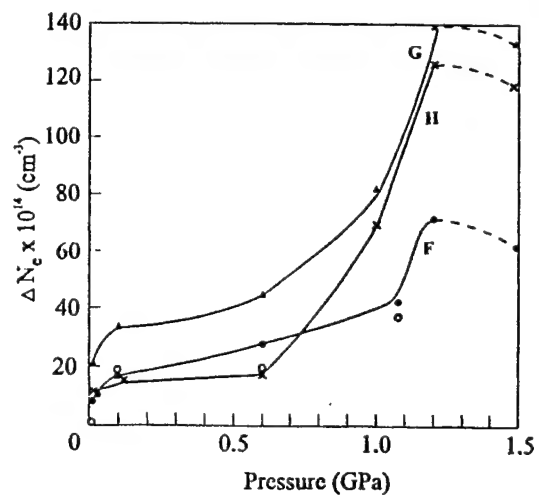


Fig. 2. ΔN_e for F, G and H samples treated at 720K- HP for 10 h, as determined by CV and Hall measurements (the last marked by o).

Table 2. ΔN_e ($\times 10^{15}$, cm^{-3}) after the treatments at 670 K - 1.2 GPa - 10 h and 720 K - 1.2 GPa - 10 h.

Sample:	A	B	C	E	F	G	H
$\Delta N_{e\ 670\text{K}}$	1.5	1.1	2	4.4	1.1	3.6	1.5
$\Delta N_{e\ 720\text{K}}$	6	8.5	11.6	16	7	13.5	12.5

The ΔN_e value peaks for HP equal to about 1.1 - 1.3 GPa for treatment time equal to 10 h (Figs 1, 2). The ΔN_e „peak” values measured for the samples treated at 670 K - 1.2 GPa and 720 K - 1.2 GPa for 10 h are compared in Table 2.

3. 2. Effect of pre - annealing on carrier concentration in Cz-Si treated at 670 / 720 K - HP

Interstitial oxygen concentration and density of defects, d , revealed in chosen pre - annealed (at 720 - 1000 K - 10^5 Pa) samples (of stacking faults, SF, precipitate dislocation complexes, PDC, and saucer pit defects, SPD) are presented in Table 3.

Table 3. Microstructure of some pre - annealed samples (before the treatment at 670 - 720 K - HP).

Sample	Pre-annealing [K, h]:	$c_o \times 10^{17}$, cm^{-3}	d_{SF} , cm^{-2}	d_{PDC} , cm^{-2}	d_{SPD} , cm^{-2}
E	720K-10h	11.3	-	2×10^3	2×10^5
E	720K-40h	10	-	4×10^3	5×10^3
G	720K-170h	6.8	-	-	5×10^4
E	920K-10h	11.7	-	4×10^2	3×10^3
E	920K-20h	11.8	4×10^2	-	3×10^3
E	720K-20h+820K-20h	9.8	2.5×10^6	2×10^2	2×10^2
E	1000K-20h	8.5	4×10^2	3×10^5	1×10^6

The ΔN_e values measured for the samples treated at 670 K - 1.2 GPa and 720 K - 1.2 GPa for 10 h are compared in Table 4. Effect of pre - annealing at 10^5 Pa on carrier concentration in Cz-Si treated at 720 K - 1.2 GPa for up to 20 h is presented in Fig 3.

The samples pre - annealed for prolonged time (for 40 h - sample E and for 170 h - sample G) at 720 K - 10^5 Pa (typical conditions for creation of TD's at ambient pressure) exhibit further rise of electron concentration in the conduction band if next treated at 670 - 720 K under HP (compare ΔN_e dependence on treatment time for samples G and E (720 K - 170 h). The same (but to a lesser extent) concerns the samples subjected to pre - annealing at 920 K and 1020 K for up to 40 h.

Dependencies of ΔN_e on HP for the C and E samples subjected to pre - annealing at 720 K, 920 K and 1000 K and afterwards treated at 720K - HP are presented in Fig. 4.

Changes of the interstitial oxygen concentration in effect of the treatment at 720 K / 870 K - HP are presented in Fig. 5. Results for treatment temperature equal to 870 K were presented to stress an effect of the treatment temperature on oxygen precipitation which also occurs during annealing / treatment.

Table 4. ΔN_e ($\times 10^{15}$, cm^{-3}) measured for samples subjected to pre - annealing and afterwards treated at 670 K - 1.2 GPa - 10 h and 720 K - 1.2 GPa - 10 h.

Sample:	C(720K-20h)	E(720 K-10h)	E(720K-40h)	E(920K-10h)	G(720K-170h)
$\Delta N_{e\ 670\text{K}}$	5.4	5.4	10.4	3.4	8.1
$\Delta N_{e\ 720\text{K}}$	7.6	17	18.6	20	11.3

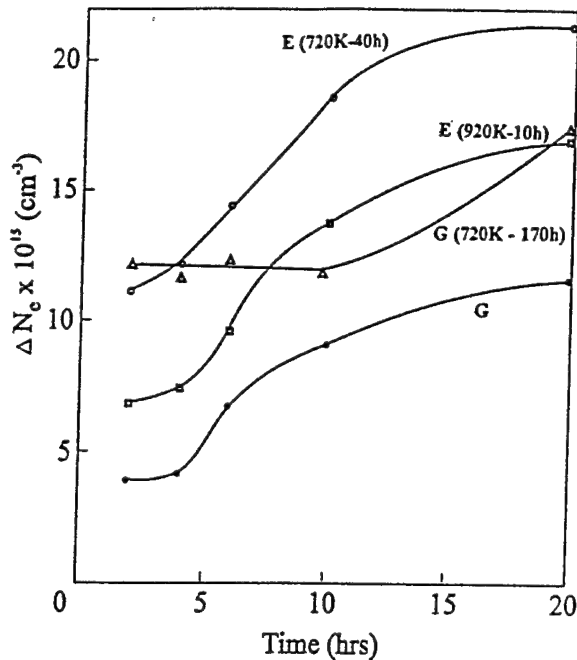


Fig. 3. ΔN_e dependence on time of treatment for pre-annealed E and G samples treated at 720 K - 1.2 GPa and for as - grown reference G sample.

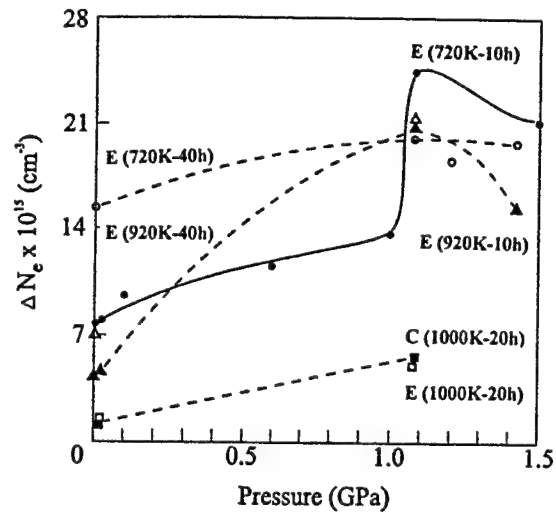


Fig. 4. ΔN_e dependence on HP for C and E samples pre-annealed at 720 K, 920 K and 1000 K and afterwards treated at 720 K - HP for 10 h.

The most „pressure - sensitive” (in respect of the highest values of ΔN_e) were the E samples with the highest content of interstitial oxygen, as - grown ($\Delta N_e = 1.58 \times 10^{16} \text{ cm}^{-3}$ after the treatment at 720 K - 1.2 GPa for 20 h), and that pre - annealed at 720 K - 10^5 Pa (Figs 3, 4). In effect of the HT - HP treatment an increase of electron concentration in the conduction band occurs with simultaneous decrease of the interstitial oxygen concentration (Table 3, Fig. 5, compare

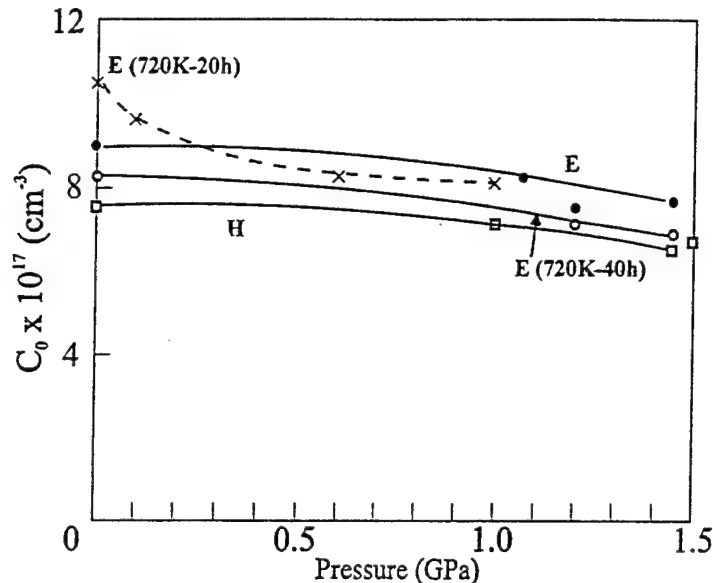


Fig. 5. Dependence of c_o on HP for E and H samples, as - grown and pre - annealed at 720 K and afterwards treated at 720 K / 870 K - HP for 10 h. Circles and squares concern samples treated at 720 K - HP, while crosses (dashed line) - of sample treated at 870 K - HP. Marks on the left axis correspond to HP = 10^7 Pa .

with Table 1). The HT - HP treatment results in HP - stimulated creation of TD's, even in the case of the G sample with comparatively high „initial” concentration of TD's, introduced by very prolonged (170 h) pre - annealing at 720K under atmospheric pressure (Fig. 3). Similar HP - induced increase of the TD's concentration was stated for the G samples subjected to pre - annealing at 720K - 10^5 Pa for 96 h.

The samples pre - annealed at 920 K and especially at 1000 - 1020 K indicate markedly lower rate of HP - induced TD's creation; the TD's concentration increases, however, with HP for the samples treated at 720 K - HP (Figs 3, 4). The samples subjected to comparatively short - time (2 - 4 h) pre - annealing at even higher temperatures (1320 K and 1420 K) still indicate distinct HP - induced increase of N_e . For example, the B sample pre - annealed at 1420 K - 10^5 Pa for 2 h (which resulted in creation of defects: $d_{SF} = 9 \times 10^3 \text{ cm}^{-2}$, $d_{SPD} = 1.3 \times 10^3 \text{ cm}^{-2}$) indicate $N_e = 7 \times 10^{14} \text{ cm}^{-3}$ after the treatment at 720 K - 10^7 Pa for 6 h and $N_e = 1.4 \times 10^{15} \text{ cm}^{-3}$ after the treatment at 720 K - 1 GPa for 6 h.

The Cz-Si samples subjected to two - steps pre - annealing (the last step at 1320 - 1420 K) and so with markedly higher concentration of oxygen - related defects and decreased content of oxygen remaining still in the interstitial positions, do not indicate dependence of carrier concentration on HP and so creation of TD's is negligible (Table 5).

Table 5. Effect of treatment at 720 K - HP on E samples subjected to 2 - steps pre - annealing. $N_p(0.03)$ means hole concentration after treatment at 720 K - 0.03 GPa and $N_p(1.1)$ - the same after treatment at 720 K - 1.08 GPa, both for 10 h. * means reference A sample (compare Table 1).

Pre-annealing [K, h]:	$c_o \times 10^{17}, \text{ cm}^{-3}$	$d_{SF}, \text{ cm}^{-2}$	$d_{PDC} + d_{SPD}, \text{ cm}^{-2}$	$N_p(0.03), \text{ cm}^{-3}$	$N_p(1.1), \text{ cm}^{-3}$
920K20h+1420K20h	6.3	-	2.5×10^6	2.6×10^{15}	2.3×10^{15}
920K20h+1320K20h	6.0	-	3×10^5	1.5×10^{15}	1.5×10^{15}
920K40h+1320K20h	5.4	1.5×10^6	3×10^3	1.6×10^{15}	1.6×10^{15}
1000K20h+1320K20h	3.2	2.5×10^6	1.5×10^6	1.5×10^{15}	1.5×10^{15}
A*(1000K - 20h)*	4.9*			$N_n = 1.6 \times 10^{14}*$	$N_n = 2.6 \times 10^{14}*$

4. DISCUSSION AND CONCLUSIONS

Cz-Si samples investigated in this study were subjected to pre - annealing at 720 - 1420 K, typical for creation of different oxygen - related defects, and to the HT - HP treatment at 670 - 720 K, typical for generating of TD's. Total pre - annealing time was up to 170 h, whereas duration of the HT - HP treatment - up to 20 h. The pressure - stimulated creation of thermal donors^{3,4} was confirmed in present work for the as - grown samples (Figs 1, 2).

The rate of creation of „HP - induced” TD's is dependent and, in the first approximation, proportional (Fig. 1) to the interstitial oxygen concentration^{2,7}. However, by comparing the ΔN_e dependence on HP for the initially n-type (B and C) and p-type samples (A and D) in pairs of the similar c_o value (A with B and C with D in Fig. 1, F with G in Fig. 2), as well as of the data in Table 2, one can conclude that ΔN_e is definitely dependent also on other, except the concentration of interstitial oxygen, factors. Most probably just different non - uniformity in the O_i distribution¹⁰⁻¹² and so the presence of cloud - like oxygen clusters are responsible for dependence of the TD's generation rate⁷ also on the sample origin as well as on particular sample batch (Figs 1 and 2, Table 2). Just the HP - induced activation of initially existing structural irregularities, that act at HT - HP as the nucleation centres for the growth of oxygen clusters exhibiting donor activity^{4,7} can be responsible for stress - stimulated creation of TD's⁷.

Pre - annealing of Cz-Si at 720 - 1020 K at atmospheric pressure resulted in creation of some structural defects (Table 3) as well as of „ambient - pressure” TD's and ND's. The treatment of such samples at 670 - 720 K - HP produced TD's in astonishingly high concentrations (Figs 3, 4, Table 4). It concerns even the sample pre - annealed for 170 h (the TD's concentration has been reported to be saturated or even decreasing with time of annealing¹³ in the case of prolonged annealing at 10^5 Pa). It suggests that the nature of the „HP - induced” TD's is different⁵ from that for TD's created at 10^5 Pa. Most possibly, both the „ambient - pressure” TD's and the „HP - induced” TD's are created simultaneously but at different proportions at 670 - 720 K - HP. The generation of „HP - induced” TD's seems to be clearly related to structural irregularities present in the HP - treated oxygen - containing Cz-Si samples. Pre-annealing of Cz-Si at 720 - 920 K seemingly does not result markedly in decrease of the concentration of such precursors of TD's (the markedly HP - induced increase of N_e was still observed in such materials - Figs 3, 4 and Table 4).

Pre - annealing at higher (starting from about 920 K) temperatures, and especially 2 - steps pre - annealing (resulting in creation of numerous extended defects - Table 5) follow in much decreased rate of creation of the „HP - induced” TD's (Fig. 4) or even in practical absence of their creation (Table 5). Decrease of interstitial oxygen concentration (Fig. 5) resulting from 2 - steps pre - annealing can not explain this effect because the sample A pre - annealed at 1000 K, with $c_o = 4.9 \times 10^{17} \text{ cm}^{-3}$ (Table 5) indicates creation of TD's while the samples with distinctly higher c_o ($5.4 - 6.3 \times 10^{17} \text{ cm}^{-3}$) but subjected to 2 - steps pre - annealing do not exhibit an effect of the HP - induced TD's generation.

It means that pre - annealing at about 1000 K and, especially that performed at 2 steps (the second step at 1230 - 1420 K), result in such changes of the state of O_i in Cz-Si that the HP - induced generation of TD's becomes to be practically suppressed. It is reasonable to suppose that the clouds / clusters of oxygen interstitials which are believed⁷ to be responsible for creation of HP - related TD's, are disappearing at $> 1000 \text{ K}$ because of O_i precipitation as well as of Ostwald ripening effect. Similar effect of suppressed generation of the „ambient pressure” TD's has also been reported for Cz-Si containing defects created by annealing at up to 1370 K under atmospheric pressure¹⁴.

Unambiguous determination of the nature of the „HP - induced” TD's deserves extended future research.

ACKNOWLEDGEMENTS

Author thanks Dr W.Jung, Dr T.Przyslawski, Mr T.Koska and Mr M.Prujszczyk from the Institute of Electron Technology as well as m. sc. H.B. Surma from IEMT, Warsaw for sample preparation and some measurements. This work has been supported in part by the Polish Committee for Scientific Research, grant no. 7T08A 05717.

REFERENCES

1. A.Misiuk, W.Jung and M.Wroblewski, „Stress-induced generation of thermal donors in near-surface layer of Czochralski grown silicon”, *Electron Technology* **29**, pp. 210 - 212, 1996.
2. A.Misiuk, W.Jung, „The effect of pressure on the generation of thermal donors in Czochralski grown silicon”, *phys.stat.sol. (b)* **198**, pp. 565 - 568, 1996.
3. A.Misiuk, „Uniform stress effect on nucleation of oxygen precipitates in Czochralski grown silicon”, in „*Early Stages of Oxygen Precipitation in Silicon*”, edited by R.Jones, pp. 485 - 492, Kluwer Academic Publishers, Dordrecht, 1996.
4. A.Misiuk, „Uniform stress effect on initial stages of oxygen precipitation in Czochralski grown silicon”, in *Solid State Crystals: Growth and Characterization*, edited by J.Zmija, A.Majchrowski, J.Rutkowski and J.Zielinski, *Proceed. SPIE*, Vol. **3178**, pp. 230 - 237, 1997.
5. V.V.Emtsev, B.A.Andreev, A.Misiuk, W.Jung and K.Schmalz, „Oxygen aggregation in Czochralski - grown silicon heat - treated at 450°C under compressive stress”, *Appl.Phys.Lett.* **72**, pp. 264 - 266, 1997.
6. A.Misiuk, G.P.Karwasz, M.Cazzanelli, W.Jung and L.Pavesi, „Effect of annealing under uniform stress on photoluminescence, electrical and structural properties of silicon”, in *MRS Materials Research Society Symp. Proceed. „Defects and Diffusion in Silicon Processing”*, edited by Tomas Dias de la Rubia, S.Coffa, P.A.Stolk and C.S.Rafferty, Vol. **469**, pp. 245 - 250, MRS Pittsburg, Pennsylvania, 1997.
7. A.Misiuk, W.Jung, B.Surma, J.Jun and M.Rozental, „Effect of stress induced defects on electrical properties of Czochralski grown silicon”, *Solid State Phen.* **57 - 58**, pp. 393 - 398, 1997.
8. A.Misiuk, H.B.Surma, „Photoluminescence studies of Czochralski grown silicon pressure - annealed at $\leq 1000 \text{ K}$ ”, in *International Conference on Solid State Crystals '98: Single Crystal Growth, Characterization, and Application*, Andrzej Majchrowski, Jerzy Zielinski, Editors, *Proceed. SPIE*, Vol. **3724**, pp. 239 - 243, 1999.
9. P.Wagner, J.Hage, „Thermal double donors in silicon”, *Appl.Phys.A* **49**, pp. 123 - 138, 1989.
10. A.Kornylo, A.Maksymov, M.Pashkovski, I.Savytskii, „Initial stage of oxygen precipitation in silicon”, *Solid State Phen.* **57 - 58**, pp. 165 - 170, 1997.
11. V.B.Neimash, E.A.Puzenko, A.N.Kabaldin, A.N.Kraichinskii, N.Kras'ko, „Nature of the nuclei for thermal donor formation (or another variant of accelerated oxygen diffusion)”, *Semiconductors* **33**, pp. 1279 - 1283, 1999.
12. P.A.Selishchev, „Accumulation dynamics of oxygen clusters in silicon and formation of their nonhomogeneous distribution”, *Semiconductor Physics, Quantum Electronics & Optoelectronics* **3**, pp. 19 - 21, 2000.
13. V.M.Babich, N.P.Baran, Yu.P.Dotsenko, K.I.Zotov, V.B.Kovalchuk, V.M.Maksimenko, „Investigation of thermal donors generated in Cz-Si crystals by prolonged annealing at temperatures below 550°C ”, *phys.stat.sol.(a)* **127**, pp. 405 - 414, 1991.
14. N.V.Vabishchevich, D.I.Brinkevich, V.S.Prosolovich, „Oxygen precipitates and suppression of thermodonor generation in silicon”, *Phys.Tekhn.Polupr.* **32**, pp. 712 - 713, 1998.

The effect of high pressure - high temperature treatment on neutron irradiation induced defects in Czochralski silicon

C.A. Londos^(a), L.G. Fytros^(a), A. Misiuk^(b), J. Bak-Misiuk^(c), M. Prujarczyk^(b) and M. Potsidou^(a)

(a) University of Athens, Physics Department, Solid State Section,
Panepistimiopolis, Zografos, Athens 157 84, Greece

(b) Institute of Electron Technology,
Al. Lotnikow 32/46, 02-668 Warszawa, Poland

(c) Institute of Physics, PAS, Al. Lotnikow 32/46, 02-668 Warszawa, Poland

ABSTRACT

Czochralski-grown (Cz-grown) silicon crystals of the same initial oxygen content ($8.33 \times 10^{17} \text{ cm}^{-3}$) were subjected to various high temperature - high pressure (HTHP) treatments for different time durations. Subsequently, the crystals were irradiated by fast neutrons at $\sim 50^\circ\text{C}$. One of the main defects form is VO pair (A-Center) usually identified in the Infrared (IR) Spectra by the 830cm^{-1} Localized Vibrational Mode (LVM) band. Upon annealing, this defect is converted to the VO_2 defect responsible for a LVM band at 887cm^{-1} . The purpose of this work is to study the effect of various combinations of HTHP treatment prior to irradiation on the annealing behaviour of the VO defect and particularly on its conversion to the VO_2 defect. We have concluded that the conversion of VO to VO_2 depends on the forms of oxygen impurity (i.e. oxygen aggregates, precipitates etc.) and on other defects created in the sample after the HTHP treatment, as for example dislocations and stacking faults.

Keywords: high temperature - high pressure treatments, annealing, neutron irradiation.

1. INTRODUCTION

Oxygen is one of the two main impurities (the other is Carbon) always present in Cz-grown Si and oxygen-related defects in Si have been studied for years¹. One family of such defects is a series of oxygen-vacancy complexes formed in silicon upon irradiation and subsequent thermal anneal. The first member of this series is the well-known A-center where an oxygen atom is positioned nearly substitutionally in a lattice vacant site. The neutral charge state of this defect gives rise to a LVM band at $\sim 830\text{cm}^{-1}$ which is its fingerprint in the IR-Spectra². Upon thermal anneal this defect is converted to VO_2 center. In this process, a migrating VO pair is captured by an oxygen interstitial atom to form a dioxygen-vacancy center giving rise to an IR band² around 887cm^{-1} . Further anneals lead to more complex centers generally labeled^{3,4} as V_nO_m complexes.

It is well-known in the literature that heat treatments of the silicon crystals prior to irradiation cause considerable changes in the annealing behaviour of the irradiation-induced defects. More specifically, it has been observed that, due to heat treatments at 600°C , the annealing temperature of A-center could be changed depending⁵ on the annealing duration as well as the initial oxygen content of the samples. It has been found that a critical value of the oxygen interstitial content, $[\text{O}]_{\text{crit}}$, exists about $7 \times 10^{17}\text{cm}^{-3}$ and samples with oxygen concentration above this value exhibit a substantial decrease of the annealing temperature of A-centers. The whole process has been explained^{5,6} as a result of the oxygen precipitation induced in the heat-treated samples with oxygen content larger than the critical one.

External stress, applied during the course of thermal treatment prior to irradiation, is another important parameter which is reasonably expected to affect the annealing behaviour of the radiation-induced defects. Enhanced hydrostatic pressure during gas ambient annealing is known to affect the formation of oxygen precipitates and of other

^(a) electronic mail address: hlontos@ccc.uoa.gr

defects created in Cz-Si, due to the stress related change of oxygen diffusivity rate^{7,8}, stress-stimulated creation⁹ of nucleation centers for oxygen precipitation, and stress-stimulated oxygen precipitation¹⁰ as well as of large differences in the compressibilities between Si and SiO₂ phases¹¹. Therefore the HTHP treatments prior to irradiation are obviously expected to affect the annealing behaviour of the radiation-induced defects and the purpose of the present paper is to examine the effect of various combinations of HTHP treatments on the evolution of VO defect and its conversion to VO₂ defect.

2. EXPERIMENTAL DETAILS

Six silicon samples of 15x10x2mm³ dimensions were cut from a commercially obtained Cz-grown wafer with initial oxygen interstitial concentration $\sim 8.33 \times 10^{17} \text{ cm}^{-3}$. The samples were subjected to a four stage treatment i) Firstly, they were subjected to HTHP treatments. More specifically, they were annealed under different hydrostatic pressures (1 bar[1 atm] up to 12Kbar in argon ambient), at temperatures in the range of (900-1027)^oC, for various time durations (3-10)h, (the conditions of the HTHP treatments of each sample are shown in the tables cited in section 3), ii) afterwards, they were irradiated by fast neutrons at a dose of $\sim 10^{17} \text{ n/cm}^2$, at T=50^oC, iii) after the irradiation, they were subjected to a heat treatment at 220^oC for 150h for the purpose of complete annealing of large clusters of defects and disordered regions, and iv) finally, to a thermal anneal at 420^oC for 4 hours to study the conversion of A-centers to VO₂ defects. Infrared spectroscopy measurements were performed after each stage of the above procedure.

3. EXPERIMENTAL RESULTS AND DISCUSSION

Fig. 1 shows the IR spectra, for each sample, after a HTHP treatment, after neutron irradiation, after the anneal at T=220^oC for t=150h and after the isothermal anneal at T=420^oC for t=4h. The curve (a) of Fig.1 (S₁) refers to a sample which has not been subjected to HTHP treatment and therefore the corresponding spectra prior to irradiation represent also the spectra of any of the six as received samples in the present experiment.

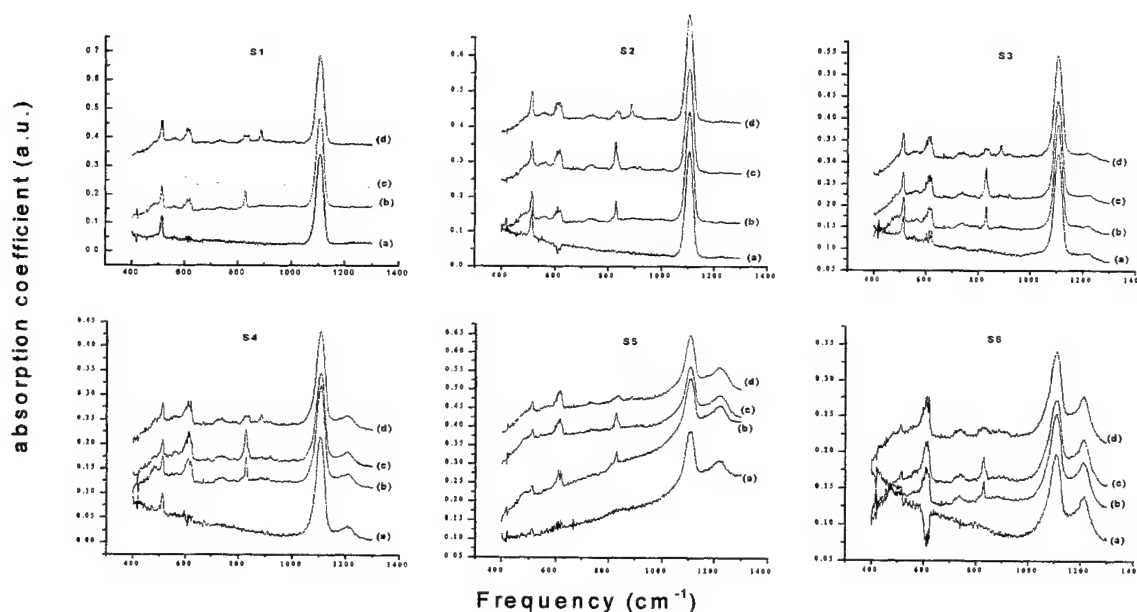


Fig. 1 IR Spectra for the investigated samples, (a) just after HTHP treatment, (b) after neutron irradiation, (c) after heat treatment at 220^oC, 1 bar, for t=150h, (d) after additional heat treatment at 420^oC, 1 bar, for t=4h

Tables I,II and III summarize all the results containing the changes of the parameters which are of interest in this work. Particularly, table I presents the variation of oxygen for each sample for the above four stages of the whole procedure. The concentration of oxygen was calculated from the Oi absorption band at 1106cm^{-1} . Table II presents the variations of oxygen precipitates for the four stages correspondingly as in table I. Table III presents VO variations after irradiation, after the heat treatment, $T=220^\circ\text{C}$, $t=150\text{h}$ and after the isothermal anneal ($T=420^\circ\text{C}$, $t=4\text{h}$) for each sample. It also presents the amplitudes of VO_2 defect appearing in the spectra after the ($T=420^\circ\text{C}$, $t=4\text{h}$) isothermal anneal.

Table I. The variations of the oxygen interstitial concentration of the samples in the course of the four stages of the experimental procedure.

	A	B	A-B	C	B-C	D	C-D	E	D-E
SAMPLE $T(^{\circ}\text{C}),P(\text{Kbar}),t(\text{h})$	$[\text{Oi}]\times 10^{17}$ initial	$[\text{Oi}]\times 10^{17}$ after HTHP (bef. irradi)	$(\Delta\text{Oi})_1$ $\times 10^{17}$	$[\text{Oi}]\times 10^{17}$ (after irradi)	$(\Delta\text{Oi})_2$ $\times 10^{17}$	$[\text{Oi}]\times 10^{17}$ before transition $\text{VO} \rightarrow \text{VO}_2$	$(\Delta\text{Oi})_3$ $\times 10^{17}$	$[\text{Oi}]\times 10^{17}$ after transition $\text{VO} \rightarrow \text{VO}_2$	$(\Delta\text{Oi})_4$ $\times 10^{17}$
S1 untreated	8.33	8.33	0	8.16	0.17	7.78	0.38	8.01	-0.23
S2 900,3,3	8.33	7.94	0.39	8.24	-0.30	7.71	0.53	7.86	-0.15
S3 900,12,5	8.33	6.28	2.05	6.40	-0.12	5.95	0.45	6.18	-0.23
S4 1027,12,5	8.33	5.33	3.00	5.24	0.09	4.82	0.42	5.10	-0.28
S5 900,12,10	8.33	4.17	4.16	4.25	-0.08	3.91	0.34	4.20	-0.29
S6 957,12,10	8.33	3.06	5.27	3.26	-0.20	3.02	0.24	3.17	-0.15

Table II. The variations of the oxygen precipitates strength of the samples in the course of the four stages of the experimental procedure.

	A	B	B-A	C	C-B	D	D-C
SAMPLE $T(^{\circ}\text{C}),P(\text{Kbar}),t(\text{h})$	$\text{O}_{\text{precip}} (\text{a.u.})$ before irradi.	$\text{O}_{\text{precip}} (\text{a.u.})$ after irradi	$\Delta\text{O}_{\text{precip}} (\text{a.u.})$	$\text{O}_{\text{precip}} (\text{a.u.})$ before transit.	$\Delta\text{O}_{\text{precip}} (\text{a.u.})$	$\text{O}_{\text{precip}} (\text{a.u.})$ after transit.	$\Delta\text{O}_{\text{precip}} (\text{a.u.})$
S1 untreated	—	—	—	—	—	—	—
S2 900,3,3	—	—	—	—	—	—	—
S3 900,12,5	0.01548	0.01503	-0.0004	0.01423	-0.0008	0.01610	0.00187
S4 1027,12,5	0.02077	0.0237	0.003	0.02630	0.0026	0.02581	-0.00049
S5 900,12,10	0.05491	0.06139	0.0065	0.06391	0.0025	0.06659	0.00268
S6 957,12,10	0.05946	0.06042	0.0009	0.06190	0.0014	0.06207	0.00017

Table III. The variation of the intensities of the VO and the VO₂ defects in the samples in the course of the last three stages of the procedure.

	A	B	B-A	C	C-B	D
SAMPLE T(°C),P(Kbar),t(h)	VO (a.u) after irradi.	VO (a.u) before trans.	Δ VO (a.u.)	VO (a.u) after trans.	Δ VO (a.u.)	VO ₂ (a.u) after trans.
S1 untreated	0.06025	0.0788	0.01855	0.0246	-0.0542	0.038
S2 900,3,3	0.05671	0.0771	0.02039	0.0227	-0.0544	0.037
S3 900,12,5	0.0505	0.0681	0.0176	0.0157	-0.0524	0.0228
S4 1027,12,5	0.04806	0.0612	0.01314	0.0151	-0.0461	0.0172
S5 900,12,10	0.03799	0.0424	0.0044	0.0149	-0.0275	0.0105
S6 957,12,10	0.02492	0.0304	0.00548	0.0106	-0.0198	0.0042

At first, we observe that the largest the change of the oxygen content of each sample due to the HTHP treatment, the larger the amplitude of the oxygen precipitation peak around 1220cm⁻¹. This could be somehow expected since most of the oxygen interstitial atoms that remove from the solution due to the above treatments precipitate. It is also known¹² that a fraction of oxygen atoms is trapped near oxygen precipitates during the treatment. We also observe (Table II) that neutron irradiation does not affect virtually the amplitude of the oxygen precipitation peak around 1220cm⁻¹ which alternatively means that the preformed irradiation did not result in dissolution of oxygen atoms from precipitates. This conclusion is in agreement with previous reports¹² concerning 3MeV electron irradiation. It is worth noting that after irradiation the oxygen content of the samples increases (apart for sample S₄, for which however, the oxygen variation seems to be within experimental error). Most possibly this occurs because oxygen atoms trapped near precipitates are liberated and the number of these oxygen atoms is larger than the number of oxygen interstitials participating in the formation of VO defects. Furthermore, we see that the larger the amplitude of the oxygen precipitate the smaller the VO amplitude which is something also expected since the initial oxygen concentration of the samples after the HTHP treatment is smaller.

It is known that in neutron-irradiated Si, large defect aggregates and disordered regions are formed which generally trap vacancies. These vacancies are released^{13,14} upon annealing at ~200°C. This release could be studied in Cz-grown Si indirectly, by monitoring the increase of A-centers since the liberated vacancies are readily captured by oxygen interstitial atoms. To this end, the samples were kept at T=220°C for t=150h. In the first 15h of this process the A-center peak amplitude in the spectra was increased substantially in all the samples and then stabilized. Thus, a time duration of about 15h is adequate for all the samples. However, the annealing at this temperature was extended to time durations up to 150h to investigate any other changes in the spectra, particularly in the peak amplitude of the VO and the O_i defects. No changes were observed for any sample. It is an indication that the HTHP treatment prior to irradiation does not affect the structure and the behaviour of the formed disordered regions. Table III contains the changes in the VO concentration of each sample occurring in the course of this annealing stage. The oxygen concentration of the samples was decreased (Table I) during the same stage as was expected due to the participation of oxygen atoms in the formation of VO defects. It is worth noting that during this stage the oxygen precipitation peak amplitude remained practically unaltered (Table II), an indication that oxygen atoms from precipitates do not participate in the above process, as it is reasonably expected for these low temperature anneals.

In the final stage of the whole process the samples were subjected to an isothermal anneal at T=420°C for t=4h. As it is seen from fig.1 and table III the conversion of VO to VO₂ is not the same in all the samples. This will be discussed below in connection with fig.2. Another observation is that in all the samples the oxygen content was increased. This strongly suggests that apart for the reaction $VO + O_i \rightarrow VO_2$ which characterizes the conversion VO to VO₂, another reaction occurs parallel which is the source of the additional oxygen atoms. This reaction is: $VO + Si_i \rightarrow O_i$ describing the destruction of VO by silicon self-interstitials. At this temperature both components of this reaction are mobile. The

self-interstitials interacting with A-centers are liberated from some traps in the crystal. Another possibility is that A-centers migrate to the traps containing self-interstitials which in turn can annihilate with A-centers.

Fig. 2 presents, for each sample, the remaining VO defects and the created VO₂ defects after the final stage, versus the difference (ΔO_i) of the total oxygen concentration. More specifically (ΔO_i) is the difference between the initial oxygen concentration, which is the same for all samples, and their concentration of each sample after the final ($T=420^\circ\text{C}$, $t=4\text{h}$) isothermal treatment. Notice that VO₂ exhibits a linear dependence on (ΔO_i) although the corresponding dependence of VO is more complicated and certainly not linear. This behavior of the VO₂ defect could be understood if one looks at the formation reaction $\text{VO} + \text{O}_i \rightarrow \text{VO}_2$ which entails a proportionality between the concentrations of VO₂ and

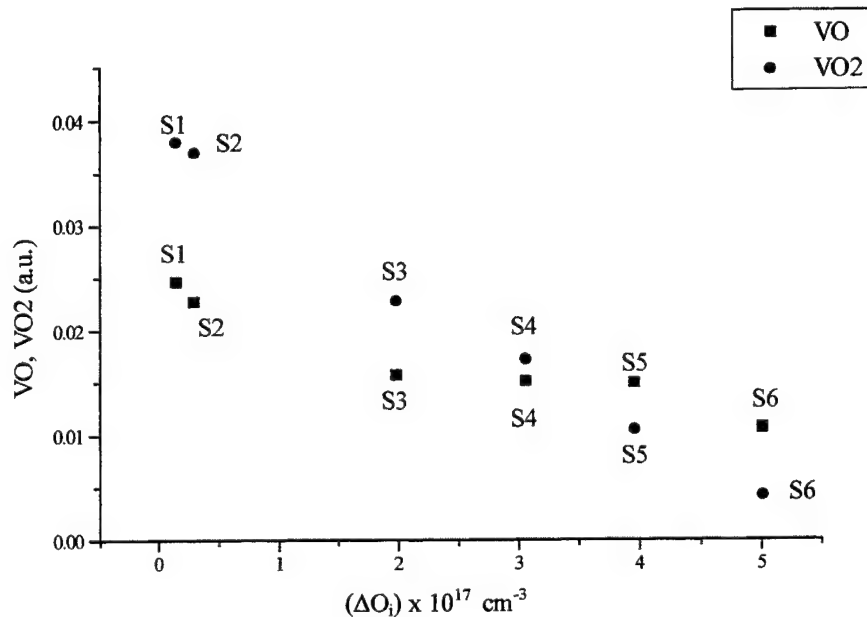


Fig. 2 The variation of the intensities of the VO and the VO₂ defects as a function of the total oxygen interstitial concentration change between the initial value and the final value after the four stages procedure.

O_i defects. According to this reaction, VO₂ concentration is also expected to be proportional to the concentration of the VO defect. However, this is not the case as it is seen, if one looks at columns (C-B) and D of Table III. In general, it is expected a difference in the behavior of VO and VO₂ defects, since VO participate^{(3),(4)} in parallel to other reactions as well, i.e. $\text{VO} + \text{V} \rightarrow \text{V}_2\text{O}$, $\text{VO} + \text{V}_2 \rightarrow \text{V}_3\text{O}$, etc. The fact now that the remaining VO defects, after the conversion of VO to VO₂, are not the same for all samples could be generally related to the effect of HTHP treatment. It indicates that the existed precipitated oxygen in the samples affects differently the conversion of VO to VO₂. Generally hydrostatic pressure P, temperature T and time t of anneal have their own special effect on the precipitation of oxygen. However, when all the parameters are combined it is very difficult to separate the contribution of each one and we have to analyze the results considering them acting externally as a whole. At first sight, it is reasonable to refer to the number of the remaining oxygen interstitials after the final stage of the whole procedure. This change is very important in our opinion and affects the behaviour of the VO and the VO₂ defects as it is indicating in fig.2. At least two parameters influence the conversion of the VO to the VO₂: i) the number of oxygen interstitials still available in the samples and ii) the presence of other defects (precipitates, dislocations, stacking faults) after HTHP, which are more numerous for the samples subjected to HTHP treatments with larger amount of oxygen precipitates (i.e. treatments at 957°C). Notice that after HTHP treatments with $T=1027^\circ\text{C}$ the induced oxygen precipitation is much less pronounced.

4. CONCLUSIONS

Cz-grown silicon samples of the same initial oxygen content have been subjected to various HTHP treatments and then irradiated by fast neutrons for the purpose of investigating the effect of these treatments on the conversion of the VO centers to the VO₂ defects. We have found that the HTHP pre-treatment affects the amount of the VO defects converted to the VO₂ defects. The phenomenon is attributed to the production of oxygen precipitates affecting the available oxygen interstitials participating in the formation reaction of VO₂ defect and also to the creation of various defects due to the HTHP treatment, as for example dislocation and stacking faults, which have also an impact on the above reaction.

ACKNOWLEDGEMENTS

The authors thank Mr. T.Koska from IET Warsaw, Poland, for his help during sample preparation and processing. This work was supported by the Polish Committee for Scientific Research (grant no. 7T08A 057 17) at 1999-2000 and by the NATO HTECH CRG974588 grant.

REFERENCES

1. A.Borghesi, B.Pivac, A.Sassella, A.Stella, "Oxygen precipitation in silicon," *J.Appl.Phys.* **77**, pp.4169-4244, 1995.
2. J.W. Corbett, G.D. Watkins and R.S. McDoland, "New oxygen infrared bands in annealed irradiated silicon," *Phys.Rev.* **135A**, pp.1381-1385, 1964.
3. Y.Lee, J. Covelli and J.W.Corbett, "Oxygen vibrational band in irradiated silicon," *Phys Lett.* **60A**, pp.55-57, 1997
4. N.V.Sarlis, C.A. Londos and L.G. Fytros, "Origin of infrared bands in neutron irradiated silicon," *J.Appl.Phys.* **81**, pp.1645-1650, 1997.
5. K. Schmalz, K.Tittlebach, V.V.Emtsev and Yu.N.Daluda, "Effects of oxygen clustering at 600°C on the annealing of A-centers in Cz-silicon," *phys.stat.sol (a)* **116**, pp.K37-K42, 1989.
6. V.V Emtsev, G.A. Oganessian and K. Schmelz, "Peculiarities in the defect behaviour in heat-treated Cz-Si with a low and high oxygen content," *Solid State Phenomena* **32-33**, pp.173-180, 1993.
7. J.Dzelme, I.Ertsinsh, B.Zapol, A.Misiuk, "Structure and diffusion of oxygen and silicon interstitials in silicon" *J.Alloys Comp.* **286**, pp.254-257, 1999.
8. V.V.Emtsev, B.A.Andreev, A.Misiuk, W.Jung and K.Schmalz, "Oxygen aggregation in Czochralski-grown silicon heat treated at 450°C under compressive stress," *Appl.Phys.Lett.* **71**, pp.264-266, 1997.
9. A.Misiuk, W.Jung, B.Surma, J.Jun, M.Rozental, "Effects of stress induced defects on electrical properties of Czochralski grown silicon," *Solid State Phen.* **57-58**, pp.393-398, 1997.
10. A.Misiuk, B.Surma, J.Hartwig, "Stress-induced oxygen precipitation in Cz-Si," *Mater.Sci.Eng. B* **36**, pp.30-32, 1996.
11. A. Misiuk, L.I. Datsenko, B. Surma and V.P. Popov, "Oxygen precipitation in Cz-Si under uniform stress," in ESSDERC'94 Proc. of the 24th European Solid State Device Research Conference, pp.243-246, Edinburgh, 1994.
12. I.V.Antonova, V.P.Popov, L.I.Fedina, S.S.Shaimeev and A.Misiuk, "A DLTS study of the evolution of oxygen precipitates in Si at high temperatures and high pressure," *Semiconductors* **30**, pp.760-764, 1996.
13. L. S. Berman, V. B. Voronkov, V. A. Koslov and A. D. Remengyuk, "Mechanism of divacancy annealing in proton-irradiated silicon" *Sov.Phys.Semicond.* **26**, pp.847-848, 1992.
14. H.Stein, "Atomic displacement effects in neutron transmutation doping," in *2nd International Conference on Neutron Transmutation Doping in Semiconductors*, edited by J.M.Meese, pp.229-248, Plenum Press, New York, 1979.

Two-dimensional model of the intrinsic point defects behaviour during Cz silicon crystals growth

Anatolii I. Prostomolotov, Natalia A. Verezub

Institute for Problems in Mechanics RAS, 117526 Moscow, pr. Vernadskogo 101, Russia

ABSTRACT

Two-dimensional mathematical model of the intrinsic point defects recombination during Cz growth of dislocation-free silicon single crystals is developed. The results of its verification are compared with the data of the one-dimensional model supposing the "fast" vacancies and interstitials recombination near the liquid-solid interface. For various growth conditions and with using of the calculated two-dimensional temperature fields in Cz silicon crystals the resulting distributions of these intrinsic point defects in a crystal are analyzed.

Keywords: two-dimensional (2D) model; Czochralski (Cz) crystal growth, calculation; silicon; intrinsic point defects (IPD); vacancy; interstitial; recombination.

1. INTRODUCTION

Diffusive and convective transport of the intrinsic point defects (IPD) and its recombination in a growing crystal near a liquid-solid interface (LSI) causes the main influence on peculiarity of a defect formation in dislocation-free silicon single crystals (formation of voids and oxygen particles, congestions of interstitials)^{1,2}. At present the model of the defect formation in dislocation-free single crystals working effectively is based on the one-dimensional approximation supposing the "fast" IPD recombination and using transformation of two basic transfer equations to one equation by replacement of variables².

However in the two-dimensional case it is more reasonable to solve the initial system of two equations, applying the standard Newton algorithm linearizing two equations with the subsequent approximation and the numerical solution by the finite elements method³. In addition there is a possibility of calculation in regions with curved boundaries by taking into account the curved LSI shape and by using the temperature and temperature gradients distributions calculated by using the global thermal Cz model⁴. In given work this approach was developed.

For verification of the two-dimensional algorithm the case of the one-dimensional (given analytically) temperature field in a crystal was applied, because in this case the concentration of IPD fields are known on basis of the one-dimensional modeling^{2,5}. The input parameters influence on the residual vacancies and interstitials concentrations and on the recombination threshold are investigated. In particular ξ_{crit} value is studied according to the known transition criterion from the "interstitials" growth mode to the "vacancy" one (here $\xi = V_p/G$ and V_p is the pulling rate, G is the axial temperature gradient at LSI). The further calculations are carried out for a two-dimensional temperature field, appropriate to growing of silicon single crystals of 150 mm in diameter. Two-dimensional fields of the IPD concentrations are calculated at various growth stages (30, 50 and 80% of length of the cylindrical grown crystal part) and for various pull rates.

2. FORMULATION OF THE PROBLEM

The crystals growth from a melt by Cz method is carried out in the high-temperature hot zone, which thermal efficiency depends on a design of thermal shields and properties of chosen thermoinsulating materials. Besides, hot zone should satisfy technological conditions of perfect crystal growth. In ref [4] the conjugate mathematical model for the investigation of heat transfer processes in hot zone for the Cz method was developed. In the radiative-conductive approximation temperature fields and the distribution of G for consecutive growth stages of silicon single crystals of 150 mm in diameter were

Further author information –

A.I.P.: Email: prosto@stk.mmtel.ru; Telephone: (095) 434-4153; Fax: (095) 938-2048

N.A.V.: Email: verezub@ipmnet.ru

investigated. Calculations of heat transfer processes were carried out for 10 consecutive growth stages depending on volume of a cylindrical part of a growing crystal (in percentage): the beginning of a cylindrical part, then the stages corresponding to the increase of crystal volume on every 10%. The regularities of axial temperature gradients and ξ values change at the LSI were obtained which can be used for theoretical estimations of the IPD recombination processes in silicon. In fig. 1 the frame of a hot zone and isotherms are shown for the 50%-s crystal growing stage.

During Cz silicon crystal growth the vacancies and interstitials transfer is realized by the convective diffusion. We neglect

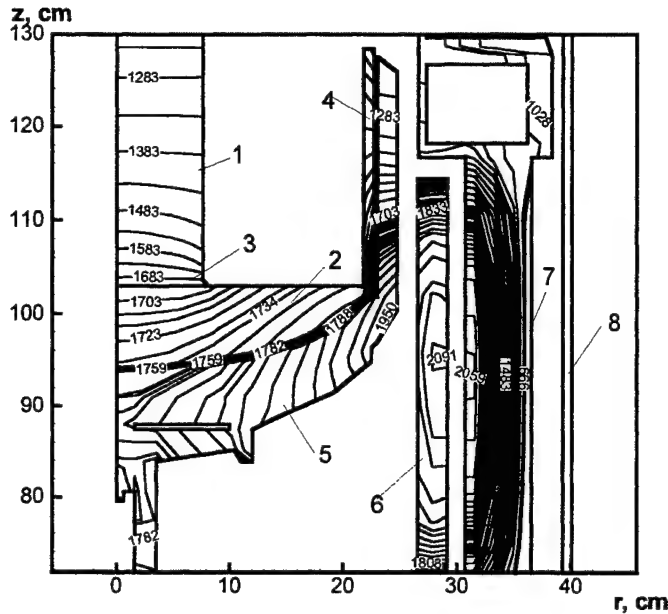


Fig.1. Temperature distribution in the hot zone for the 50%-s crystal growing stage: 1 – single crystal, 2 – melt, 3 – liquid-solid interface, 4 – crucible, 5 – susceptor, 6 – resistive heater, 7 – thermal shields, 8 – water-cooled tank.

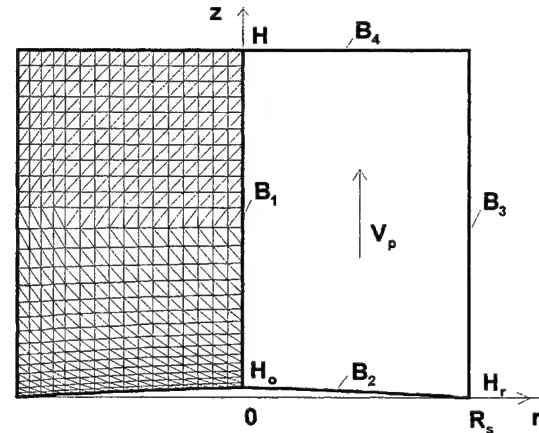


Fig.2. Scheme of the calculation region (on the right) and according mesh of 6-nodes triangular finite elements (on the left). Here: B₁ - symmetry axis, B₂ - LSI, B₃ is crystal surface, B₄ is top boundary of a recombination.

the thermodiffusion. The stationary equations system for calculation of the vacancies $C_v(r, z)$ and interstitials $C_i(r, z)$ concentrations has the following form:

$$V_p \frac{\partial C_v}{\partial z} = \text{div}(D_v \nabla C_v) - \omega \quad (1),$$

$$V_p \frac{\partial C_i}{\partial z} = \text{div}(D_i \nabla C_i) - \omega \quad (2)$$

Coefficients of diffusions (D_v, D_i) and equilibrium concentrations of vacancies and interstitials (C_{ve}, C_{ie}) are set by using its values (C_{vm}, C_{im}) at the melting temperature (T_m) as follows:

$$D_v(T) = D_{vm} \exp(-E_{vD}/kT + E_{vD}/kT_m), \quad D_i(T) = D_{im} \exp(-E_{iD}/kT + E_{iD}/kT_m),$$

$$C_{ve}(T) = C_{vm} \exp(-E_v/kT + E_v/kT_m), \quad C_{ie}(T) = C_{im} \exp(-E_i/kT + E_i/kT_m)$$

Here $\omega = K_{vi}(C_v C_i - C_{ve} C_{ie})$, the recombination factor $K_{vi} = A_{vi}(D_v + D_i) \exp(-E_{rec}/kT)$ and $A_{vi} = 4\pi r_{cap}$ (r_{cap} - radius and E_{rec} - recombination energy); E_{vD}, E_{iD} - energies of vacancies and interstitials diffusion activation, and E_v, E_i -

energies of vacancies and interstitials equilibrium activation. In these formulas the constants are used: silicon melting temperature $T_m = 1683K$ and Boltzman constant $k = 8.625 \times 10^{-5}$ eV/K.

The experimental value of a transition $-\xi_{crit} = 0.132$ mm²/Kmin from vacancies to interstitials growth mode corresponds to the following parameters⁵:

$$D_{vm} = 4.0 \times 10^{-5} \text{ cm}^2/\text{s}, E_{vD} = 0.35 \text{ eV}, D_{im} = 5.25 \times 10^{-4} \text{ cm}^2/\text{s}, E_{iD} = 0.20 \text{ eV}; \quad (3)$$

$$C_{vm} = 7.2 \times 10^{14} \text{ cm}^{-3}, E_v = 4.5 \text{ eV}, C_{im} = 5.2 \times 10^{14} \text{ cm}^{-3}, E_i = 4.6 \text{ eV}.$$

The value of recombination energy barrier E_{rec} is not known. At its choice the satisfaction to "fast" recombination condition is required. This condition is satisfied, if $E_{rec} = 1.5$ eV is set. Radius of recombination r_{cap} is equal to 3.0×10^{-8} cm. The scheme of calculation region is given on Fig. 2. Accordingly boundary conditions are set as follows:

$$\frac{\partial C^{(i)}}{\partial n} = 0 \text{ at } B_1, B_4 \text{ boundaries, } C^{(i)} = C_e^{(i)} \text{ at } B_2, B_3 \text{ boundaries.}$$

Here $C^{(i)}$ corresponds to the actual values of C_v, C_i and $C_e^{(i)}$ are appropriate equilibrium concentrations. For calculations a geometry and sizes of a recombination region were chosen as following values: $H = 115.2$ cm and $H_r = H_o = 103.7$ cm, according to the size of global thermal Cz model.

The stationary equations (1) - (2) are solved iteratively by a finite element method (FEM) in the Galerkin's formulation. The approximation of unknown concentrations C_v and C_i is represented as decomposition on square-law basic functions on 6-nodes triangular elements (fig. 2). Preliminary a residual for each equation is linearized by Newton's method. FEM equations system is solved by a frontal method. As a whole the algorithm of the solution of the discrete FEM equations, earlier developed for global thermal model is kept⁴.

3. COMPARISON WITH ONE-DIMENSIONAL MODEL

For the test based on the data of one-dimensional recombination model the temperature field in a crystal was set as only depending upon z :

$$\frac{1}{T(z)} = \frac{1}{T_m} + \frac{G \cdot z}{T_m^2},$$

and at a lateral crystal surface the boundary condition was set as follows: $\frac{\partial C^{(i)}}{\partial n} = 0$.

Here G is axial gradient of temperature at LSI. In this case calculation results on based of 2D-model should correspond to one-dimensional data^{2,5}.

The comparison of V_p/G critical value at G changes in range of 30-300 K/cm and at V_p pull rate variation near (v-i) - transition threshold shows, that the transition occurs at constant value of $(V_p/G)_{crit} = 0.132$ mm²/Kmin, that precisely corresponds to the data⁵.

In a case of 2D model a value of K_{vi} at T_m was equal $\approx 2 \times 10^{-19}$ cm³/s and for this value a "fast" recombination condition of $C_{ve}C_{ie} = C_vC_i$ is satisfied with rather high accuracy. Also a value of a residual C_{vs} concentration for a vacancies mode ($G = 120$ K/cm, $V_p = 1.61$ mm/min) was equal to $C_{vs} = 3.9 \times 10^{12}$ cm⁻³. According to ref [5] this value is a little lower: $C_{vs} = 2.8 \times 10^{12}$ cm⁻³. The small divergence can be caused by distinction in approximation of the basic equations, because in ref [2,5] the "fast" recombination condition is used for transformation of (1) - (2) system to one equation. Opposite, in given 2D- model the initial (1)-(2) system is solved and the "fast" recombination condition follows from the calculations. Thus, it is possible to consider, that for an one-dimensional temperature field the received results rather well correspond to 1D-data.

4. IPD BEHAVIOUR IN TWO-DIMENSIONAL THERMAL FIELD

In a case of 2D thermal field the boundary C_v, C_i concentrations are set as $C_v = C_{ve}$ and $C_i = C_{ie}$ at a lateral crystal surface. Input 2D thermal fields are set according to results of calculations by a global thermal model⁴ for different crystal growth stages. In this case the radial inhomogeneities of an axial temperature gradient G at LSI plays the important role. Therefore determining its are two values of ξ : $\xi_o = V_p/G_o$ - at an axis and $\xi_R = V_p/G_R$ - at a lateral crystal surface. Its ratio with ξ_{crit} determines the recombination results and a growth mode: vacancy (v), interstitials (i) or mixed (v-i). For the latter case

a so-called OSF-ring is created in a crystal³. Radius of this ring is determined experimentally and this characteristic plays an important role at IPD distribution verification.

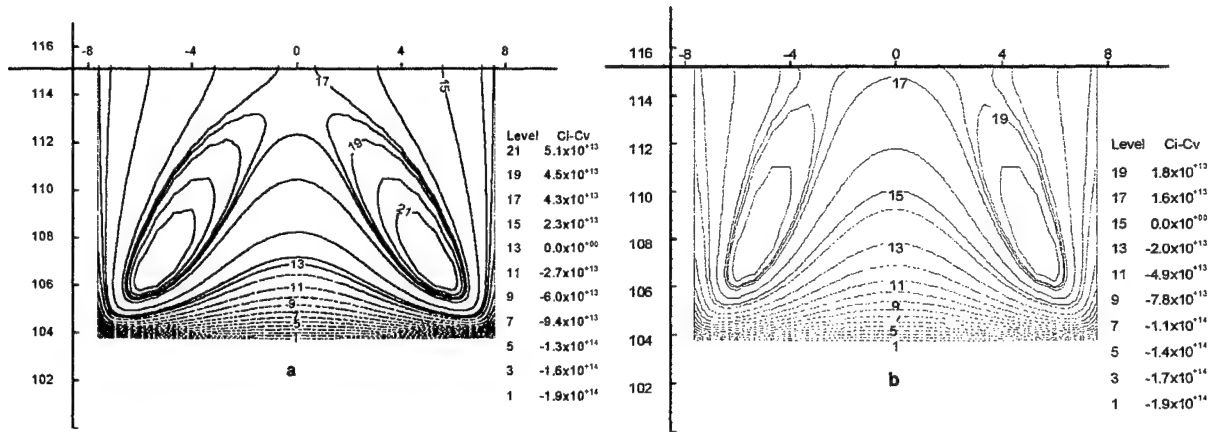


Fig.3. Isolines of the IPD concentration difference ($C = C_i - C_v$ [cm⁻³]) for various crystal growth stages at the interstitial growth mode: a - 30% body, $V_p = 0.39$ mm/min; b - 50%, $V_p = 0.37$ mm/min.

According to (3) the parameters of 2D model correspond to $\xi_{crit} = 0.132$ mm²/Kmin. However for 2D thermal field a value of ξ_{crit} requires an additional check. For this purpose the appropriate parametrical calculations were carried out, in which the pull rate V_p and values of temperature gradients (G_o and G_R) were varied at various crystal growth stages. In a number of calculations (50- and 80%-s' growth stages) the value of ξ_{crit} was checked by means of V_p change for conditions according to an identical temperature field in a crystal, i.e. without the appropriate recalculation of a thermal field on global thermal model.

For 30% and 50% growth stages the appropriate values $V_p = 0.39$ and 0.37 mm/min and the axial temperature gradients are 35 and 30 K/cm at an axis, 51 and 42 K/cm at a crystal edge. At 30 % stage: $\xi_o = 0.111$, $\xi_R = 0.077$, and at 50 %: $\xi_o = 0.126$, $\xi_R = 0.088$ mm²/Kmin, i.e. at B_4 boundary is realized the interstitials mode (fig. 3a,b), because $\xi < \xi_{crit}$.

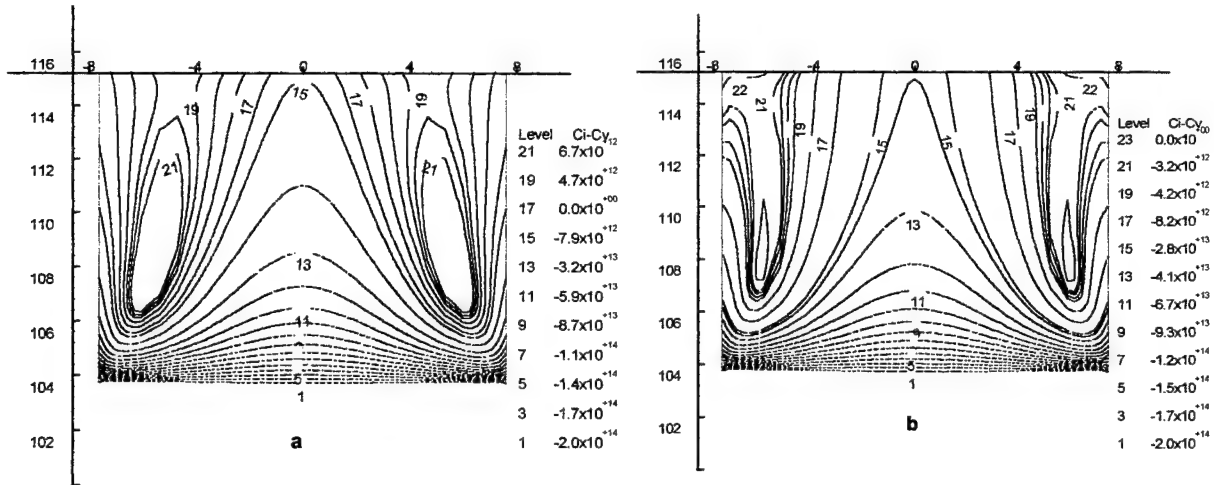


Fig.4. Isolines of the IPD concentration difference for the 50%-s growing stage and pull rates according to the mixed ($v-i$) and vacancy (v) growth modes: a - $V_p = 0.42$ mm/min; b - 0.47 mm/min.

All calculations were carried out at the initial conditions according to equilibrium concentration values of vacancies and interstitials in calculation region. For the chosen parameters (3) the equilibrium vacancies concentration exceed the equilibrium interstitials concentration. Therefore for initial iterations the prevalence of vacancies concentration is observed. For the subsequent iterations an action of the interstitials source in a region of the greatest temperature gradients (near LSI and a crystal edge) leads to a visible effect. It results in characteristic elliptical shapes of concentration isolines $C = C_i - C_v$. On fig. 4a,b the vacancies and interstitials distributions are shown at pull rates, which are a little larger, than in the previous case for the 50%-s growth stage: $V_p = 0.42$ and 0.47 mm/min. In this case thermal data corresponds to former value $V_p = 0.37$ mm/min, and the change of pull rate is taken into account only in the recombination equations (1)-(2).

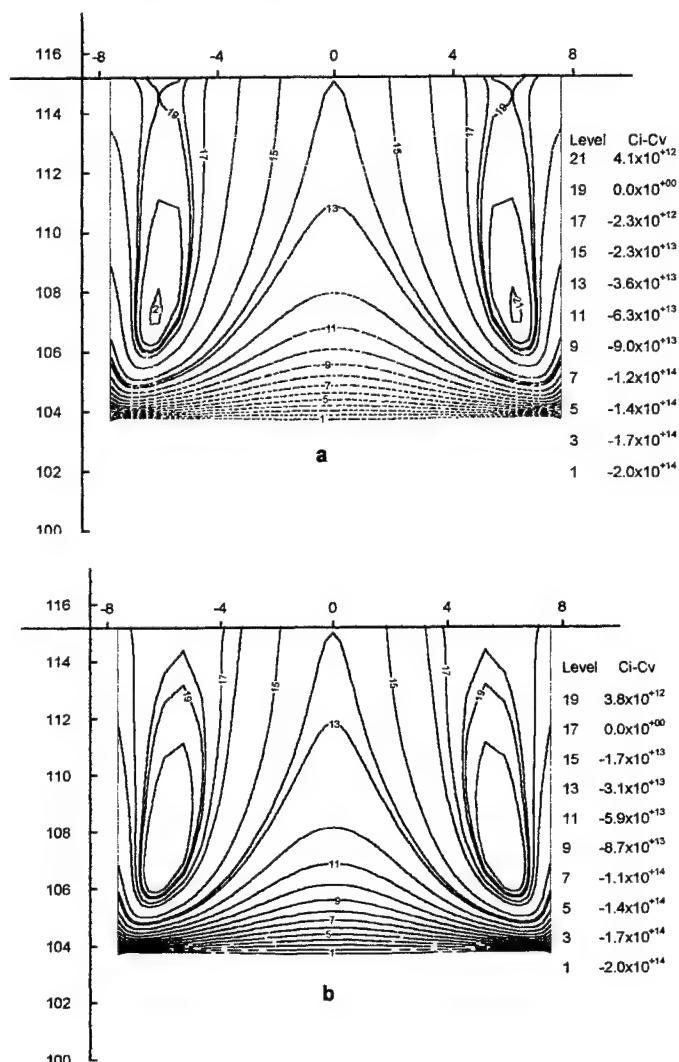


Fig.5. Isolines of the IPD concentration difference for various crystal growth stages at $V_p = 0.50$ mm/min corresponding to the following growth modes:
a - transition from the mixed (v-i) to the vacancy (v) mode at the 50%-s stage;
b - formation of the mixed (v-i) mode at the 80%-s stage.

The growth of V_p increases ξ : $\xi_o = 0.143$, $\xi_R = 0.100$ and $\xi_o = 0.159$, $\xi_R = 0.112$ mm²/Kmin, accordingly. In particular at $V_p = 0.42$ mm/min is created a mixed v-i mode, which turns into a vacancies mode at increasing of pull rate till 0.47 mm/min.

Let's notice, that ξ_R remains smaller than ξ_{crit} .

Strictly speaking, a pull rate change causes the changes of a temperature field in a crystal. These changes may be accounted for 50% growth stage at $V_p = 0.50$ mm/min. The axial temperature gradient increases then to 32 K/cm at the center and to 46 K/cm at the crystal edge. It gives next values: $\xi_o = 0.159$ and $\xi_R = 0.110$ mm²/Kmin. The interstitials region extends essentially such that the vacancies distribution is divided from a top boundary (fig. 5a).

Similar changes occur at increase of pull rate for the 80%-s growth stage. At $V_p = 0.35$ mm/min the appropriate axial gradients at the axis and at the crystal edge are equal $G_0 = 22$ and $G_R = 48$ K/cm, and $\xi_0 = 0.110$ and $\xi_R = 0.073$ mm²/Kmin. It may be a confirmation of an interstitials growth mode.

However at larger pull rate - $V_p = 0.50$ mm/min, the values ξ grow so that there is mixed v-i mode ($\xi_0 = 0.157$, $\xi_R = 0.104$ mm²/Kmin). Respective calculation results are shown in fig. 5b.

The main results of solution of this stationary recombination problem are the radial distribution of residual concentrations of vacancies $C_v(r)$ and interstitials atoms $C_i(r)$ at the top boundary of calculation region B_4 (Fig. 2). These data are necessary for further plotting of summarizing 2D distributions of residual IPD defects in the crystal (which are plotted on based of calculated data for 10 and more growth stages).

Here for comparison the radial output distributions $C_v(r)$ and $C_i(r)$ on the top boundary of recombination region are given in fig. 6 for the 50% growth stage and two pull rate values, according to interstitials ($V_p = 0.37$ mm/min) and mixed v-i ($V_p = 0.50$ mm/min) modes. The analysis of the graphs at $r = 0$ shows, that in the interstitial mode C_i exceeds C_v concentration essentially. The similar graphs for mixed (v-i) mode show significant growth of vacancies concentration and practically complete disappearance of interstitial atoms at the axis.

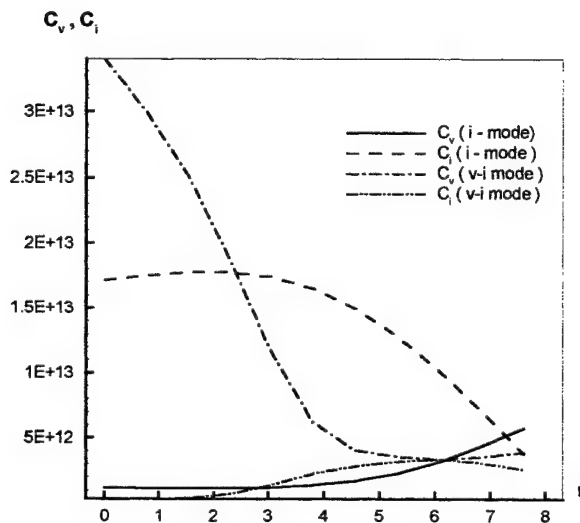


Fig.6. Radial distributions of C_v and C_i concentrations on the top boundary ($z = H$) corresponding to pull rate variations at the 50%-s crystal growing stage. Here: the interstitial (i) mode is at $V_p = 0.37$ mm/min, and the mixed (v-i) mode arises at $V_p = 0.50$ mm/min.

5. CONCLUSIONS

Considered 2D model develops the previous 1D model of IPD behaviour near the LSI during Cz silicon crystal growth. The assumption of the "fast" vacancies and interstitials recombination taken into account at a choice of parameters by using of 1D data was confirmed numerically. The values of the residual IPD concentrations (after a recombination) were verified too.

Using 2D global thermal Cz model for calculations of 2D thermal growth history gives the possibility of IPD behaviour modeling adequately at various changes of thermal shields in a hot zone and for different pull rates. In particular this model gives possibility for investigation of important 2D effects such as OSF ring in dislocation-free silicon single crystals caused by radial temperature gradients.

ACKNOWLEDGEMENTS

The authors thank M.G. Milvidskii, V.V. Voronkov and R. Falster for advices and useful discussion of results of given work.

REFERENCES

1. M.G. Milvidskii and V.B. Osvenskii, *Structural Defects in Single Crystals of Semiconductors*, p. 256, Metallurgy, Moscow, 1984 (in Russian).
2. V.V. Voronkov, "The mechanism of swirl defects formation in silicon," *J. Crystal Growth*, **59**, pp. 625-643, 1982.
3. T. Sinno, R.A. Brown, W.A. Ammon and E. Dornberger, "Point defect dynamics and the oxidation-induced stacking-fault ring in Czochralski-grown silicon crystals," *J. Electrochem. Soc.* **145**, pp. 302-318, 1998.
4. A.I. Prostomolotov and N.A. Verezub, "Global mathematical model of heat transfer in Czochralski silicon crystal growth," in *Single Crystal Growth, Strength Problem, and Heat Mass Transfer*, edited by V.P. Ginkin, **Vol. 2**, pp. 398-409, Ins. For Physics and Power Engineering, Obninsk, 2000.
5. V.V. Voronkov and R. Falster, "Vacancy and self-interstitial concentration incorporated into growing silicon crystals," *J. Appl. Phys.* **86**, pp. 5975-5982, 1999.

Study of material behavior in DAC: system Si-O (SiO_x) and compound $\text{Fe}_{78}\text{Mn}_{20}\text{Si}_2$

Borys M. Efros^{a*}, Natalya V. Shishkova^a, Andrzej Misiuk^b

^aPhys.& Tech. Institute, NASc, 72, R.Luxemburg St., 83114, Donetsk, Ukraine

^bInstitute of Electron Technology, Warsaw, Poland

ABSTRACT

For the last ten years or so, the gasketed diamond anvil cell (DAC) has become the standard tool for the generation of high pressures. Compared with the classic hydraulic piston-cylinder devices, a DAC is three to four orders of magnitude less massive, and will generate static pressures one to two orders of magnitude higher than previous devices.

In this paper, we attempt to give an understanding of the gasket behavior which will be helpful to the worker requiring routine and reliable use of a DAC in the submegabar pressure range.

Keywords: diamond anvil cell, gasket, material behavior, phase and structure transitions.

1. INTRODUCTION

The diamond anvil cell (DAC) became a widely used tool due to the application of the ruby method for pressure determination and the possibility of obtaining quasi-static high pressure.^{1,2} But for the compression of solids the non-uniformity of pressure is accompanied by the efficiency reduction of a high pressure apparatus due to the elastic deformation of the anvils at higher pressure. In practice, the methods of quasi-static pressure generation by applying deformable metal gasket containers for a sample, ruby gauge and pressure-transmitting media help to eliminate the above mentioned drawbacks. At the same time the pressure generation in a DAC with a metal gasket depends substantially on the gasket geometry and character of the elastic-plastic deformation of the gasket material.

2. THE MATHEMATICAL MODEL OF GASKET BEHAVIOR IN DAC

One of the basis parameters of pressure character in a gasket operating volume is the degree of reduction of the initial gasket thickness under axial load. Experimental data on the pressure value $P_{r=0}$ (acting upon the gasket center) in dependence on the T301 steel gasket thickness h μm are presented in Fig. 1.

The experimental curve $P_{r=0}(h)$ shows three basis types of stress-strain state within the central gasket part under compression between the anvils: the elastic-plastic deformation state (pressure range 0 - ~5 GPa); the plastic flow state (~ 5 - ~ 40 GPa); the volumetric triaxial compression state (≥ 40 GPa).

The analytical solving of the stress-pressure-strain distribution problem (in the gasket) is quite difficult. That is why we consider the gasket operation, when it is used for pressure generation, by approximate methods. Pressure in the gasket within the elastic deformation area may be calculated according to the relation given by Prins⁴:

* Further author information-

B.M.E.(correspondence): Email: efros@hpress.dipt.donetsk.ua

N.V.Sh.:Email: shishkov@kinetic.ac.donetsk.ua; Telephone, Fax: 380 (622) 557462

A.M.:Email: misiuk@ite.waw.pl

$$P = - \int_{h_0}^h \frac{dh}{Ch}, \quad (1)$$

where C is the materials compressibility, h_0 is the initial gasket thickness. With the axial load increase on the diamond anvils the gasket material starts to deform. Thus the pressure acting upon the gasket center within the plastic flow area may be calculated by the formula given by Prins ⁴:

$$P_{r=0} = \sigma_z (e^{2\mu b/h} - 1), \quad (2)$$

where σ_z is the axial stress (initial pressure) at which plastic flow of the gasket material occurs, μ is the friction coefficient, b is the radius of the operation butt end of the anvil. For a further increase in load the flow of the gasket material from the center to the periphery stops and the pressure at the gasket center under uniform compression is calculated by an equation like Eq.(1):

$$P_{r=0} = - \int_{h'_0}^h \frac{dh}{Ch}, \quad (3)$$

where h'_0 is the efficient initial gasket thickness after the plastic flow stoppage.

The analytical dependencies of $P_{r=0}(h)$ describing all the main stress-strain state areas are calculated for the parameter values of the T301 steel gasket and for the anvils of the octah: dron type of diamond single crystals: $C = 0.69 \times 10^{-5}$ MPa; $h_0 = 250$ μm ; $h'_0 = 50$ μm ; $\sigma_z = 1000$ MPa; $\mu = 0.25$; $b = 300$ μm ; (Fig. 1, curves 2, 3, 6). The values of h_{cr} and P_{max} are calculated as follows: $h_{cr} = (2\mu/\alpha)b$, $P_{max} = \sigma_z(e^\alpha - 1)$, where α is a parameter determined by the properties of the gasket material. In our case $h_{cr} = 40$ μm , $P_{max} = 41$ GPa, $\alpha = 3.75$. It may be seen from a comparison of the experimental dependence with the theoretical curves $P_{r=0}(h)$, Fig. 1, that the application of the given analytical expressions describing the behavior of the deformable gasket gives rise to serious objections because of the discordance between the analytical dependence $P_{r=0}(h)$, Fig. 1, curve 3, and the experimental curve, Fig. 1, curve 1, during the elastic-plastic deformation of the gasket.

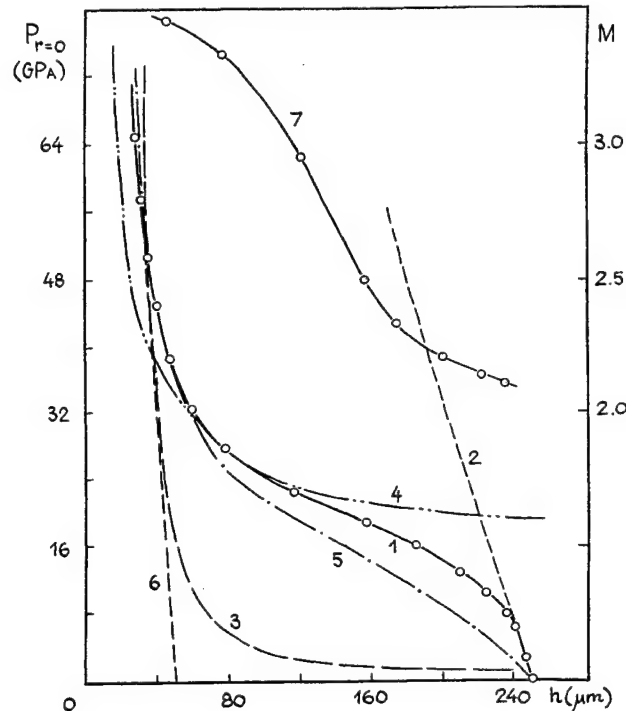


Fig.1. Relation between pressure $P_{r=0}$ (1-6) on the gasket axis and multiplication coefficient M (7) and the deformable gasket thickness h : 1- experiment; 2-6 -calculation

Efros^{5,6} have suggested that other analytical expressions describing the gasket behavior should be used for the generation of pressure in the DAC. According to model 1, the mean pressure p of the gasket-sample may be evaluated by the relation given by Samanta⁷:

$$\frac{\bar{p}}{2k} = 1 + \frac{1 + \sec \theta}{2} \left[\left(1 + \frac{2b}{h} \operatorname{tg} \theta \right) \times \ln \left(1 + \frac{h}{2b} \operatorname{ctg} \theta \right) - 1 \right] + \frac{b}{3h} + \frac{\operatorname{tg} \theta}{2} + \frac{h}{b} + \frac{\sec \theta \cos \theta}{2}, \quad (6)$$

where k is the shear yield strength of the gasket material, θ is the shape variation angle of the diametrical gasket cross-section ($\theta = 36 - 40^\circ$), b is the operating butt end radius of the anvil.

According to the model 2, suggested by Ilyushin⁸, we may evaluate the unit pressure p generated in the gasket-container as

$$p = \begin{cases} 1 + q + \frac{2}{\sqrt{3}h} (r - a) & \text{at } a \leq r \leq r_0 \\ 1 + m + \frac{2}{\sqrt{3}h} (b - r) & \text{at } r_0 \leq r \leq b \end{cases},$$

where a is the gasket operating cell radius, q is the operating cell pressure (at $a = 0$, $q = P_{r=0}$), $r_0 = \frac{1}{4} \sqrt{3} h (m -$

$\bar{q}) \frac{1}{2} (b + a)$ is the radius of a circle along which the pressure is maximum, $\bar{q} = q/\sigma_s$, b is the operating butt end radius of the anvil, m is a parameter representing the support from that part of the gasket which is out of the anvil.

The dependences of $P_{r=0}(h)$ calculated by model 1 and 2 describe the behavior of the T301 steel gasket (Fig. 1, curves 4 and 5). Comparison of the experimental dependence $P_{r=0}(h)$, Fig. 1, curve 1, with the theoretical curves, Fig. 1, curves 4 and 5, shows the existence of discordance, though it is smaller than that obtained by the relations suggested by Prins⁴ (Fig. 1, curve 3).

The following parameters most easily monitored during operation of the DAC are the force Q applied to the cell, the pressure P generated, the gasket operating cell radius a and thickness h . The dependence $P(Q)$ (the dependencies $a(P)$ and $h(P)$) turns out to be very useful as a diagnostic tool, and so we calculate it here by model 2 (Fig. 2 and 3). For each experiment to be carried out in a DAC, the geometry and properties of gasket may be selected differently according to the pressure range required. The sample size, and the number of pressure cycles required.

3. HIGH PRESSURE EFFECT ON PHASE AND STRUCTURE TRANSITIONS

High pressure structural studies are important not only to test various physical theories and thereby improve our theoretical understanding of solids, or to map out phase diagrams in pressure, volume, temperature- space, but in terms of producing new, and possible better materials as well.

DAC has revolutionised high pressure experiment in the pressure range above $P \approx 1$ GPa. The DAC can be used either with a hole or without one in gasket between the diamond anvils.

3.1. The gasket-container: system Si-O

Extensive experimental studies of the group-IV elements Si and Ge have been made in recent years. Motivations have included the rich variety of phase transitions. Si shows the following phase-transition sequence in the pressure range 0-50 GPa⁹⁻¹¹: cubic diamond to β -Sn at 11 GPa; β -Sn to simple hexagonal (SH) at 13-16 GPa; SH to an intermediate phase at 34 GPa and finally to hexagonal close packed (HCP) above 40 GPa.

In spite of considerable efforts done in above area, the structural systematic of the group-IV and related semiconductors still demands to be clarified. Moreover, practically nothing is known about possible effects of dopants or impurities on pressure-induced phase transitions, even in the case of the best investigated material, silicon. However, also from the last

published data on the phase behaviour of Si nanocrystallites coated with SiO_2 it follows that such dopant-related effects are highly probable to exist. A considerable increase of the transition pressure (from 11 GPa to approximately 22 GPa) in the diamond to β -Sn phase transition has been observed in Si nanocrystals as compared to the case of bulk Si. This increase in the transition pressure is ascribed to a low density of defect nucleation sites for phase transformation in Si nanocrystals as compared to that in the bulk material. A quite opposite situation (large concentration of the mentioned nucleation sites) would exist in case of heavy doped materials. A representative example would be the system Si - O (SiO_x): Czochralski grown silicon, Cz-Si, in which oxygen atoms are typically present in form of interstitials O_i , with a concentration up to more than 10^{18} cm^{-3} . These atoms are clustering/transforming at higher temperatures (pressures) creating different oxygen-related defects, also clusters and precipitates with a SiO_{2-x} composition.¹² One can reasonable assume that such "secondary defects" would create a lot of additional nucleation sites, so promoting the pressure-induced diamond - to - β -Sn phase transition. The increase of defect concentration in the HP - (HT) treated Cz-Si samples with initially present SiO_{2-x} precipitates can be considered as a proof of HP-induced massive creation of defects on before-created oxygen-related defects.^{13,14}

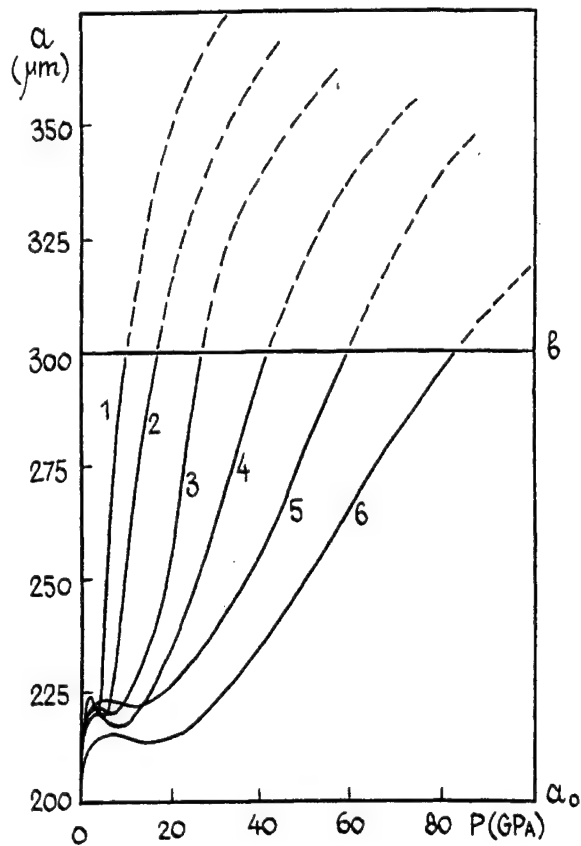


Fig.2

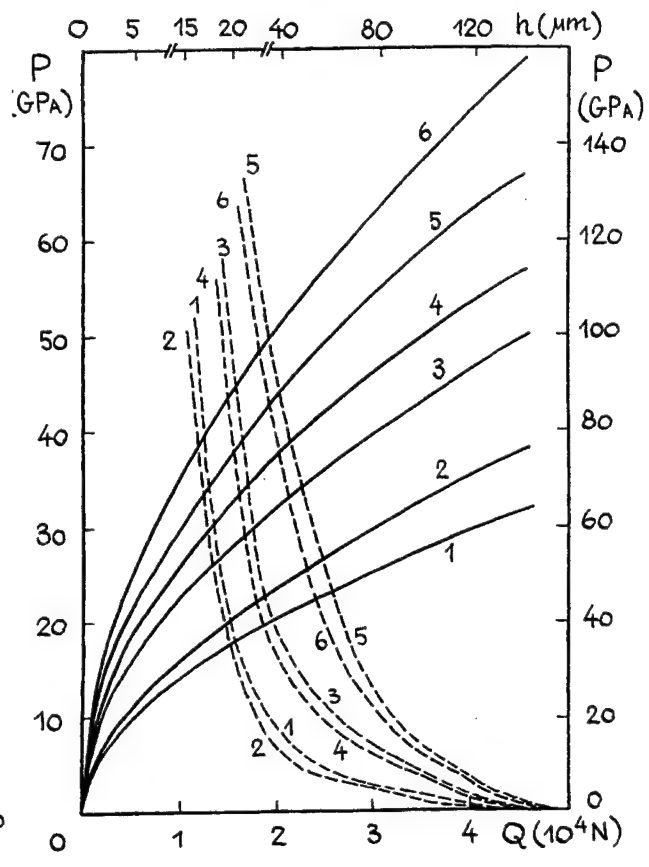


Fig.3

Fig.2. Pressure P - force Q and pressure P - thickness h plots for different values of yield stress $YS_{0.2}$ and radius of gasket hole a_0 ($h_0 = 150 \mu\text{m}$ and $b = 300 \mu\text{m}$): 1 - $YS_{0.2} = 200 \text{ MPa}$, $a_0 = 200 \mu\text{m}$; 2 - 200 MPa , $150 \mu\text{m}$; 3 - 500 MPa , $200 \mu\text{m}$; 4 - 500 MPa , $150 \mu\text{m}$; 5 - 1000 MPa , $200 \mu\text{m}$; 6 - 1000 MPa , $150 \mu\text{m}$

Fig. 3. Radius of gasket hole a - pressure P plots for different values of yield stress $YS_{0.2}$ and initial thickness of gasket h_0 ($a_0 = 200 \mu\text{m}$ and $b = 300 \mu\text{m}$): 1 - $YS_{0.2} = 200 \text{ MPa}$, $h_0 = 200 \mu\text{m}$; 2 - 200 MPa , $150 \mu\text{m}$; 3 - 500 MPa , $200 \mu\text{m}$; 4 - 500 MPa , $150 \mu\text{m}$; 5 - 1000 MPa , $200 \mu\text{m}$; 6 - 1000 MPa , $150 \mu\text{m}$

3.2. The gasket-sample: compound $\text{Fe}_{78}\text{Mn}_{20}\text{Si}_2$

The characteristic feature of studied compound is the development of strain/baric-induced martensitic transitions $(\gamma+\varepsilon) \rightarrow \varepsilon', \alpha'$.¹⁵

At investigation of the structure for compound $\text{Fe}_{78}\text{Mn}_{20}\text{Si}_2$ in dependence on the gasket compression degree ε one can differ two types of the substructure (Fig.4). The first (I) is characterised by thin plates of HCP ε -phase in FCC γ -matrix along two or three-intersection plane $\{111\}_\gamma$ (Fig. 4,b). The second (II) is characterised by availability of large plates of ε -phase usually along one plane from the system $\{111\}_\varepsilon$ in which BCC α' -crystals of lath shape are arranged, having alike orientation or forming structural complex "frame"- type (Fig.4c). Increasing of the degree ε by the *DAC* technique as well as decreasing of the radius in the region of compression of a gasket-sample of compound $\text{Fe}_{78}\text{Mn}_{20}\text{Si}_2$ results in the growth of type I-structure. Besides, in the deformed substructure $\varepsilon > 30\%$ together with reduction of α' -phase as a result of suppression of martensitic transition $(\gamma+\varepsilon) \rightarrow \alpha'$ and with appearance of new plates of ε' -phase as a result of shift of the dynamic balance $\gamma \leftrightarrow \varepsilon$ in direction of activation of $(\gamma+\varepsilon) \rightarrow \varepsilon'$ -transition at loading in *DAC* we revealed also twins of deformation in ε -phase of types: $\{1012\}_\varepsilon$ and $\{1011\}_\varepsilon$.

Thus the obtained results prove that the specific features of the stressed state (η factor, where $\eta = \sigma/T$, where $\sigma = -P$, T -tangential stress) at which the loading in *DAC* of metastable materials is carried out can considerably influence on processes of phase and structure transitions and thus cause as a result the desirable level of physico-mechanical properties of materials¹⁶. The considered dependencies for the factor of the stressed state $\eta(\varepsilon)$ at deformation under pressure of compound $\text{Fe}_{78}\text{Mn}_{20}\text{Si}_2$ by the *DAC* method makes it possible to consider that the intensity of martensitic $(\gamma+\varepsilon) \rightarrow \varepsilon, \alpha'$ -transitions is determined by two competing processes: increase of degree ε ($(\gamma+\varepsilon) \rightarrow \varepsilon, \alpha'$ -transitions) and decrease of the factor η ($\eta < 0$) (increase P) ($(\gamma+\varepsilon) \rightarrow \varepsilon$ and $(\gamma+\varepsilon) \leftarrow \alpha'$ -transitions) (Fig.5).

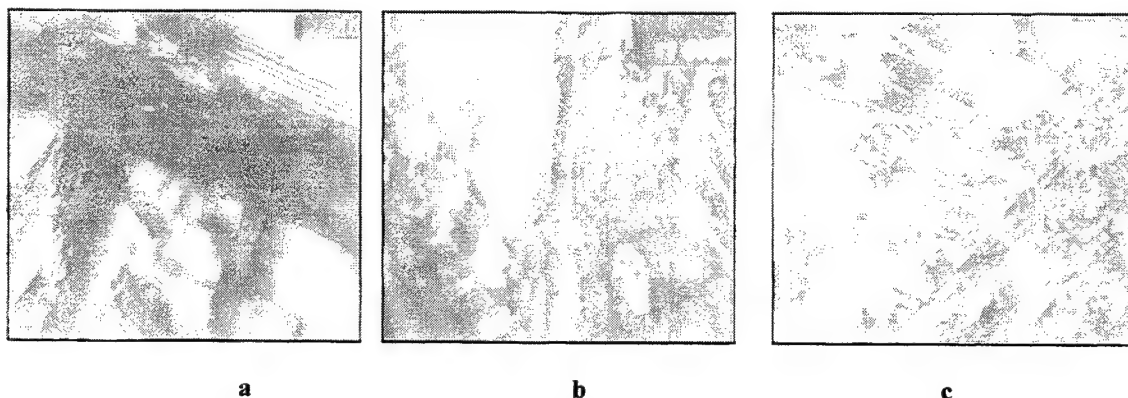


Fig. 4. Structural changes of gasket compound $\text{Fe}_{78}\text{Mn}_{20}\text{Si}_2$ at *DAC* loading ($\times 27000$): a - $\varepsilon \approx 0\%$, $P_{r=0} \approx 0.1$ MPa; b - 75%, 28 GPa ($r = 0$); c - 75%, 28 GPa ($r = b$)

4. CONCLUSION

The preliminary analysis carried out on the stress-strain of the metal gasket being used in the *DAC* shows the exceptional importance of the stage of gasket material plastic flow in generating high pressure. Besides, the study of this problem helps not only to characterize the optimum conditions of high pressure generation, but also to obtain information on the phase and structure transformations and rheologic properties of solids (gasket-sample and gasket-container) under high pressure.

The obtained experimental and theoretical results makes it possible to choose the optimum of gasket parameters and properties for the deformable containers, thus providing the submegabar pressure generation functions and the support of the diamond anvils peripheral area.

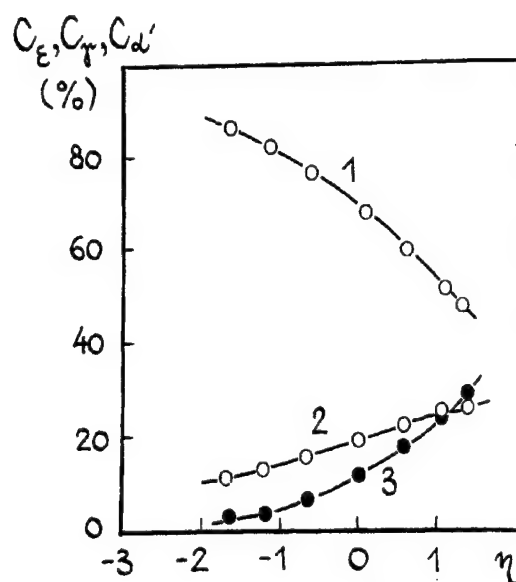


Fig.5. Phase composition in the compound $\text{Fe}_{78}\text{Mn}_{20}\text{Si}_2$ in dependence on the index η : 1 - C_ϵ ; 2 - C_γ ; 3 - $C_{\alpha'}$

REFERENCES

1. Block and G. Piermarini, "The diamond cell stimulates high-pressure research", *Phys. Today* **29**, N9, pp. 44-55, 1976.
2. B. Beresnev and B. Efros, "Pressure generation in a diamond anvil apparatus", *Physica B* **139&140**, pp. 910-915, 1986.
3. B. Beresnev and B. Efros, "Application of metallic gaskets in apparatus with diamond anvils for generation super high pressures", *High Pressure and Technology* **15**, pp. 39-43, 1984.
4. J. Prins, "Cessation of flow between bridgman anvils", *High Temp.-High Press.* **15** N1, pp. 21-26, 1983.
5. B. Efros, "Investigation of plastic flow of materials used for deformable containers in high pressure apparatus with diamond anvils at the megabar range of pressure", in *Physics and Physicochemistry of Highly Condensed Matter*, XXIIInd of the EHPRG (11-14 September) Aussois, France, p. 22, 1984.
6. B. Efros, "Study of plastic flow for metallic gaskets in super high pressure apparatus" *High Pressure and Technology* **21**, N9, pp. 44-55, 1986.
7. S.K. Samanta, "The application of the upper bound theorem to the prediction of indenting and compressing loads", *Acta Polytech. Scand.* **38**, p.35, 1962.
8. A. Ilyushin, "Flow theory questions for plastic matter on the surfaces", *Appl.Math. & Mech.* **8**, N3, pp. 265-289, 1954.
9. H. Olijnyk, W.B. Holzapfel, "Phase transitions in Si, Ge and Sn under pressure", *J. Phys.*, **45**, C8, pp. 153-159, 1984.
10. A. Jayaraman, "Ultrahigh pressure", *Rev.Sci. Instrum.*, **57**, N6, pp. 1013-1031, 1986.
11. S. Duclos, Y. Vohra and A. Ruoff, "HCP-to-FCC transition in silicon at 78 GPa and studies to 100GPa", *Phys.Rev.Letters*, **58**, pp. 775-777, 1987.
12. A. Misiuk, B. Surma, and J. Haertwig, "Stress- induced oxygen precipitation in Cz-Si", *Mater. Sci. Eng.* **B36**, pp. 30-36, 1996.
13. A. Misiuk, J. Haertwig, J. Bak-Misiuk, M. Tkacz, *Zeszyty Naukowe Uniwersytetu Jagiellonskiego*, **39**, p. 37 1998.
14. A. Prudnikov, A. Misiuk, J. Haertwig, B. Efros, J. Bak - Misiuk, "Influence of oxygen dopant in silicon on pressure-induced phase transition", in *High Pressures, VI Intern. Conf.* (15-19 September) Donetsk, Ukraine, p. 20, 2000.
15. B. Efros, N. Shishkova and S. Gladkovskii, "Phase composition, structure and properties of metastable heterophase materials at deformation under superhigh pressure", *High Pressure and Technology* **5**, N 1, pp. 26-36, 1996.
16. B. Efros, N. Shishkova and S. Gladkovskii, "Phase transitions in high-manganese compounds at deformation in diamond anvils", *Metallofiz. Noveishie Tekhnol.* **22**, N 2 pp.85-93, 2000.

Investigation of system Si – O (SiO_x) behavior in DAC at submegabar pressure

Borys M. Efros^{a*}, Natalya V. Shishkova^a, Anatolii Prudnikov^a,
Andrzej Misiuk^b, J. Bak-Misiuk^c, Juergen. Härtwig^d

^aPhys.& Tech. Institute, NASc, 72, R.Luxemburg, 83114, Donetsk, Ukraine

^bInstitute of Electron Technology, Warsaw, Poland

^cInstitute of Physics, PASC, Warsaw, Poland

^dEuropean Synchrotron Radiation Facility, Grenoble, France

ABSTRACT

Extensive experiment studies of the IV elements have been made in recent years. Motivations have included the rich variety of phase and structural transitions.

Different SiO_{2-x} defects can be created in Czochralski grown silicon, Cz-Si, by appropriate pre-annealing at atmospheric pressure (10^5 Pa). Some data concerning the effect of enhanced hydrostatic pressure on creation of defects in the Si- SiO_{2-x} system have been reported for defects-containing Cz-Si subjected to cyclic hydrostatic pressure treatment.

An attempt to observe the mentioned hydrostatic pressure-induced effect of massive creation of "new" defects in Cz-Si with oxygen-related defects was undertaken in this work.

The increase of defect concentration in the hydrostatic pressure-treated Cz-Si samples with initially present SiO_{2-x} precipitates can be considered as a proof of hydrostatic pressure-induced massive creation of defects on before-created oxygen-related defects. However, in the case of some DAC-treated samples, a misfit dislocation network was not directly proved to be created because of too small sample in comparison to the resolution of the spectroscopy and X-ray methods.

Keywords: diamond anvil cell, Czochralski sample, submegabar pressure.

1.INTRODUCTION

The fundamental nature and technological importance of elemental and binary semiconductors have made their high-pressure properties one of the most active areas of research, especially since the advent of the diamond-anvil cell (DAC) technique about 30 years ago. In spite of considerable effort done in above area, the structural systematic of the group-IV and related semiconductors still demands to be clarified. Moreover, practically nothing is known about possible effects of dopants or impurities on pressure-induced phase transitions, even in the case of the best-investigated material, silicon.

An effect of defect creation in the misfitting particle/matrix system has been investigated for about 25 years. Because of importance of silicon as the model semiconductor and basic material for microelectronics, the case of SiO_2 precipitates in Si bulk is of special interest.

Different SiO_{2-x} defects can be created in Czochralski grown silicon (Cz-Si) by appropriate pre-annealing at atmospheric pressure (10^5 Pa). Some data concerning the effect of enhanced hydrostatic pressure (HP) on creation of defects in the Si- SiO_{2-x} system have been reported¹ for defects-containing Cz-Si subjected to the cyclic HP treatment at ≤ 2.5 GPa, much below the pressure of the diamond – to β -tin phase transition (at about 11 GPa).

An attempt to observe the mentioned HP-induced effect of massive creation of "new" defects in Cz-Si with oxygen-related defects was undertaken in this work. An effect of short-time HP-treatment (at HP up to 1.35 GPa) of the OPs-containing Cz-Si samples at temperatures just below the melting point of silicon (≈ 1680 K) was also investigated.

*Further author information

B.M.E.(correspondence): Email efros@hpress.dipt.donetsk.ua

N.V.Sh.: Email: shishkov@kinetic.ac.donetsk.ua

A.M.:Email:misiuk@ite.waw.pl

2. EXPERIMENTAL

Cz-Si samples were cut from commercially available Cz-Si *p*-type wafers of about 600 μm thickness. The oxygen interstitial concentration (c_0) determined by Fourier Transform Infrared Spectrometry (FTIR) was $\leq 11 \cdot 10^{17} \text{ cm}^{-3}$. One sample, designated as *S*, with $c_0 = 11 \cdot 10^{17} \text{ cm}^{-3}$ was pre-annealed at 1000 K for 20 h to create small oxygen clusters with a total density of $1.3 \cdot 10^6 \text{ cm}^{-2}$ – sample *S1*. In effect of pre-annealing, the c_0 value decreased to $8.5 \cdot 10^{17} \text{ cm}^{-3}$.

Another sample was pre-annealed at 1000 K for 20 h and, additionally, at 1320 K for 20 h – to create larger defects (OPs with a density $2.1 \cdot 10^4 \text{ cm}^{-2}$ and stacking faults) – sample *S2*. In effect of such pre-annealing the c_0 value decreased to $6.1 \cdot 10^{17} \text{ cm}^{-3}$.

By chemical etching, foils with thickness of 50 μm were prepared from the *S1* and *S2* samples. The foils were pressurized for 20-36 hours at 8.5-10.5 GPa at room temperature in DAC, using an H_2O - methanol solution.

The DAC design and the pressure measuring device are described in work ². In the DAC, a sample hole of radius a_0 is formed in the centre of the gasket, and contains a pressure-transmitting fluid, ideally with shear strength $k = 0$. While increasing pressure (Fig. 1), the cell seals by virtue of the normal pressure between the gasket and anvil being greater than the hydrostatic pressure by an amount equal to the shear strength in a thick gasket, and greater still in a thin gasket (Fig. 2). For each experiment to be carried out in a DAC, the gasket may be selected differently according to the pressure range required, the sample size, and the number of pressure cycles required. A thick gasket may be chosen to give a larger sample space, or a more linear force *Q*-pressure *P* curve, and less hysteresis between increasing and decreasing pressure. A thin gasket, on the other hand, will allow higher pressures to be reached, and can give better control at low pressure since the gasket seals at forces much below those necessary to give any pressure in the fluid. However, in either case, the run should be stopped if the gasket hole shows signs of enlarging, or the force-pressure plot becomes sub-linear.

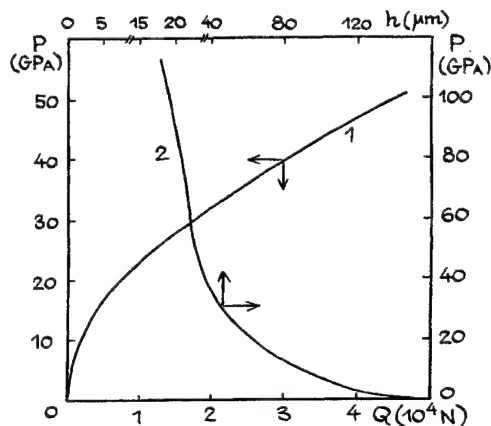


Fig.1.

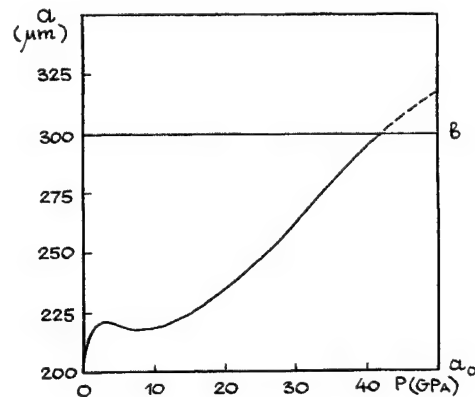


Fig.2

Fig. 1. Pressure *P* -force *Q* (1) and pressure *P* – thickness *h* (2) plots for value of stress yielding $YS_{0.2} = 500 \text{ MPa}$ and radius of gasket hole $a_0 = 200 \mu\text{m}$ (initial thickness of gasket $h_0 = 150 \mu\text{m}$ and radius of diamond anvil $b = 300 \mu\text{m}$)

Fig. 2. Radius of gasket hole *a* - pressure *P* plot for value of yielding stress $YS_{0.2} = 500 \text{ MPa}$ and initial thickness of gasket $h_0 = 150 \mu\text{m}$ (initial radius of gasket hole $a_0 = 200 \mu\text{m}$ and radius of diamond anvil $b = 300 \mu\text{m}$)

The deformable gasket material was 301 stainless steel; the disk-shaped gaskets (diameter $D = 4 \text{ mm}$, thickness $h_0 = 150 \mu\text{m}$) after pre-strengthening treatment were tested in screw-lever DAC at pressures *P* up to 15 GPa. Pressure was determined with the help of the shift of R_1 and R_2 ruby luminescence lines using the relation given in work ³:

$$P = 380.8 \cdot \left[\left(\Delta\lambda / 694.2 + 1^5 \right) - 1 \right] \quad (1)$$

where $\Delta\lambda = \lambda_p - \lambda_0$ is the difference in position between R-ruby luminescence lines at pressure P (GPa) and at atmospheric pressure (nm).

Other 600 μm thick, S2 and S3 samples (for S3 initial c_0 was $8 \cdot 10^{17} \text{ cm}^{-3}$, S3 was pre-annealed at 720 K for 96 h) were HP-treated for 5 min at 1550-1620 K in a high-pressure furnace.

After HP-treatment, the X-ray topographs were obtained at the Topography Beamline (ID19) of the ESRF. White beam topography was used for the DAC-treated thin S1 and S2 samples, and double crystal topography – for the furnace-treated “thick” S2 and S3 samples. Complementary X-ray and FTIR measurements were performed to check structure perfection of the samples.

3. RESULTS AND DISCUSSION

The description of defect formation model at the particle/matrix boundary at HP has been presented e.g. in work ⁴. For a precipitate completely embedded in a matrix, it is necessary to exploit the concept of a misfit (ε) between the matrix and precipitate material. A misfitting precipitate may lose part of its elastic energy when a dislocation is emitted from an interface between the precipitate and the matrix. There are two criteria for estimation of ε and of precipitate size (d) for which dislocation loops can be generated. The first criterion (A) defines the smallest misfit for which the local shear stress at a precipitate boundary can exceed the theoretical shear strength of the matrix. In this case the stress at a precipitate surface and, hence, the critical misfit (ε_{cr}) does not depend on d . The ε_{cr} value for criterion A would be close to $5 \cdot 10^{-2}$ according to paper ⁴.

The second criterion (B) defines the critical misfit from the energy of the system decreases if a dislocation loop is generated at a precipitate boundary, the ε_{cr} value decreases for higher d . Its value would be closed to 10^{-3} for $d \approx 1 \mu\text{m}$, and to about 10^{-2} for $d \approx 100 \text{ nm}$.⁵ The criterion B applies for generation of dislocations at incoherent precipitates.

“Initial” misfit (ε_0) is present usually at the Si matrix/oxygen precipitate (OP) boundary because of much larger OP volume as compared to that of Si as well as of different thermal expansion of Si and SiO_{2-x} .

HP would influence on ε at the mentioned boundary because of much higher compressibility γ ($\gamma = 1/K$, where K – the bulk modulus) of SiO_2 as compared to that of Si ($K_{\text{SiO}_2} = 40 \text{ GPa}$, $K_{\text{Si}} = 98 \text{ GPa}$). For a spherical embedded particle, the misfit can be estimated from Eq. 2 ^{5,6}:

$$\varepsilon = \varepsilon_0 + \frac{K_p}{3K_p + 4G_{\text{Si}}} \cdot \left[\Delta T \cdot (\beta_p - \beta_{\text{Si}}) + HP \cdot \left(\frac{1}{K_{\text{Si}}} - \frac{1}{K_p} \right) \right] \quad (2)$$

where: K – bulk modulus,
 G – shear modulus,
 β – volume thermal expansion coefficient,
 $\Delta T = T_{\text{exp}} - 300 \text{ K}$, T_{exp} – temperature for which ε is calculated.
The bottom indexes in Eq. 2 denote the precipitate/matrix.

An estimation (Eq. 2) gives, for SiO_2 – Si system at 10 GPa, the misfit value equals to about $1.3 \cdot 10^{-2}$ (close to the value for criterion A, may be even reaching it under assumption that OPs are composed of stoichiometric SiO_2).

So, at sufficiently high HP one can expect massive creation of dislocations and other defects on each, even coherent, particle. Of course, nonstoichiometry of the OP composition (in comparison to stoichiometric SiO_2) must be taken into account.

White beam topographs of the DAC-treated samples showed elongated, very weak Laue spots (Fig. 3).

This can be considered as a sign of asterism which has its origin in the HP-induced transformation of Si single crystals to crystals with grains. From this effect it was possible to estimate the mosaic spread of the single grains and orientational

distribution of the grains. It appears that these mosaic spreads were of the order of 2-6 arc min for individual grains and of 12-30 arc min for the grain distribution (Table 1).

In the case of *S1* sample (with high density of small oxygen clusters), a strong sample fragmentation after the *DAC* treatment at 10.5 GPa was observed. The treatment of the *S1* sample at 8.5 GPa caused much minor structure changes (Fig.3 and Table 1).

In the case of *S2* sample with larger *OPs*, such fragmentation was observed just after the treatment at 9 GPa. This can be considered as some kind of proof that, at sufficiently high pressure (dependent on *d*), the presence of defects in Cz-Si resulted in massive *HP*-induced creation of additional defects because of reaching the "criterion *B* value" of ϵ_{cr} , or, possibly, even the ϵ_{cr} value according to the criterion *A*.

Table 1. Estimation of mosaic spread half-width within individual grain and those of grains within whole crystal

Sample	DAC treatment, GPa	Mosaic spreads, arc min	
		Individual grain	Grain distribution
<i>S1</i>	8.5	2	12
	10.5	4-8	25-30
<i>S2</i>	9.0	2-6	20-30

It must be stressed, however, that it would be impossible to investigate Cz-Si in this respect at higher *HP* because at about 11 GPa a phase transition occurs in Si.⁶ Possibility of some kind of phase transformation at about 10 GPa in amorphous SiO₂ must also be accounted for paper.⁷ In this last case the Si matrix would be untouched, whereas the mentioned phase transformation in SiO₂ (in fact SiO_{2-x}, because *OPs* are typically of substoichiometric composition) would contribute to structural changes at the *OP*/Si boundary.

In the case of experiments at enhanced temperatures (*HT*) (at which ϵ_{cr} is expected to be achieved at lower *HP* than that at about 300 K), there exists some uncertainty in interpretation of results. It follows, between others, from stress-enhanced oxygen precipitation⁸, dissolution of *OPs* at the *HT*⁹ and from structural transformations during sample cooling. So, only short-time *HP-HT* experiments can lead to conclusive results.

Indications of *HP*-induced creation of additional defects were found for the samples treated at parameters: > 1550 K – 1 GPa for 5 min (Fig. 4).

The *A* and *B* topographs (of the sample *S2*) are quite similar. However, as it follows from supplementary measurements, the *S2* sample structure was more "disturbed" when annealed at higher *HP* (Table 2).

Table 2. Effect of *HP* on c_0 , on static Debye-Waller factor, L_{660} ¹⁰ and on anomalous X-ray transmission (*Ia*) for *S* (as-grown) and *S2* samples treated at 1580 K for 5 min

Sample	<i>HP</i> , Pa	$c_0 \cdot 10^{17}$, cm ⁻³	$L \cdot 10^3$	<i>Ia</i> [arb. units]
<i>S</i>	10 ⁵	8.6		110
<i>S</i>	10 ⁹	8.6		120
<i>S2</i>	10 ⁵	8.6	26	78
<i>S2</i>	10 ⁹	7.9	33	67

It can be explained as an effect of "fulfillment" of the conditions for creation of additional defects at the largest defects/matrix boundary (*OPs* with different sizes were present in the Si matrix).

In the case of *S3* samples with small oxygen clusters (created by pre-annealing at 720 K), the effect of *HP* was even stronger. The treatment at 10⁵ Pa resulted in creation of individual large dislocation loops (probably an effect of oxygen

precipitation on some structural irregularities during sample cooling), whereas in the samples treated at 1.35 GPa, numerous "additional" defects were observed.

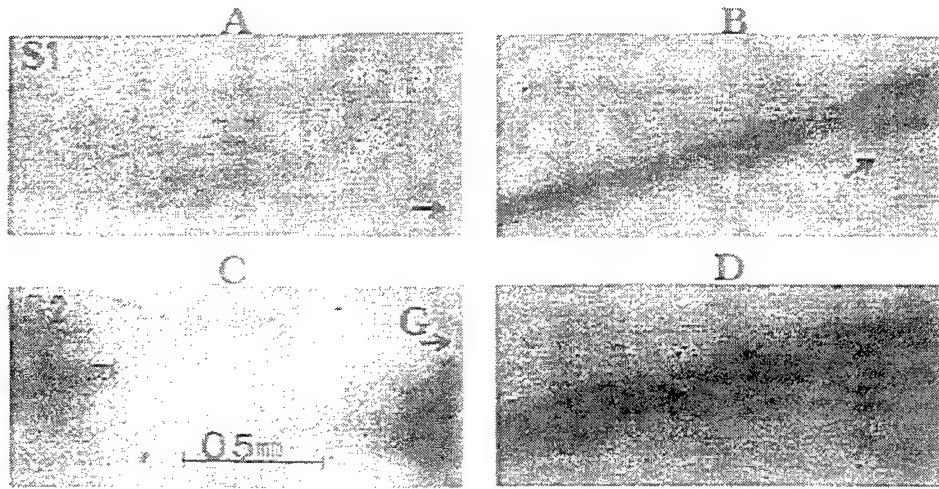


Fig. 3. White beam Laue topographs of 50 μm thick *S1* and *S2* samples: *A* – *S1* sample *DAC*-treated at 8.5 GPa; *B* – *S1* sample *DAC*-treated at 10.5 GPa; *C* – non-treated *S2* sample; *D* – *S2* sample *DAC*-treated at 9 GPa; *G* – diffraction vector

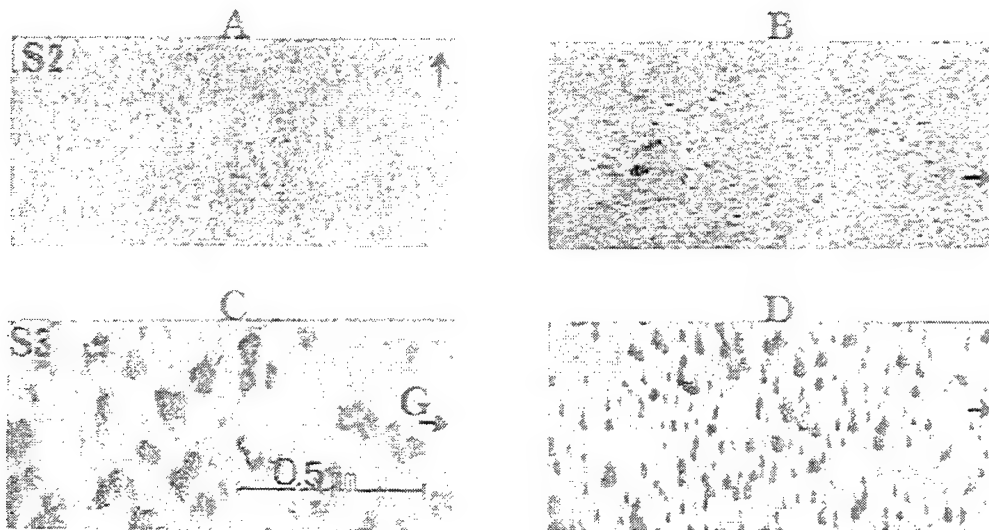


Fig. 4. 111 topographs ($\lambda \approx 0.04 \text{ nm}$) of 600 μm thick *S2* and *S3* samples subjected to *HP* treatment for 5 min. Treatment conditions: *S2* sample was annealed at 1580 K - 10^7 Pa (*A*) and at 1580 K - 1 GPa (*B*); *S3* sample – at 1550 K - 10^5 Pa (*C*) and at 1550 K - 1.35 GPa (*D*)

4. CONCLUSIONS

The increase of defect concentration in the *HP* – (*HT*) treated Cz-Si samples with initially present SiO_{2-x} precipitates can be considered as a proof of *HP*-induced massive creation of defects on before-created oxygen-related defects. However, in the case of *DAC*-treated *S1* and *S2* samples, a misfit dislocation network was not directly proven to be created because of too small sample dimension (all dimensions of about 50 μm) in comparison to the resolution (of the order of a micrometer) of the applied X-ray (synchrotron) method.

Also results obtained at *HP* – *HT* experiments must be considered with caution, because part of structural transformations can occur during sample cooling (the cooling rate of about 2 Ks^{-1}). For this reason, it would be desirable to perform “direct” observations of the *HP*-induced phenomena by further *in situ* experiments, using *DAC* mounted directly on the *ESRF* beam line.

ACKNOWLEDGEMENTS

The authors are grateful to Dr J.Jun from the High Pressure Research Centre, PAS, Warsaw and m.sc. A.Panas from the Institute of Electron Technology, Warsaw for their help during preparation of investigated samples.

This work was supported in part at 1999 - 2000 by Polish Committee for Scientific Research, grant no. 7T08A 057 17.

REFERENCES

1. Misiuk A., Wolf J., Datsenko L., Adamczewska J., Bak-Misiuk J., "Microscopic model of phenomena at SiO_x/Si boundary in strained Cz-Si single crystals", *Nukleonika*, **39**, 281-286, 1994.
2. Beresnev B.I., Efros B.M., *Physica* **139&140**, pp 910-915, 1986.
3. Mao H., Bell P., "High pressure Physics: Sustained static generation of 1.36 to 1,72 megabars" *Science* **200**, pp.1145-147, 1978.
4. Jung J. "High-pressure-induced defect formation in silicon singlecrystals.II.Mechanism of stress-field formation at precipitates", *Phil. Mag. A*, **50**, 257-274, 1984.
5. Bak-Misiuk J., Misiuk A., Klima K., Kucharski K., Skibska M., in *Proc. 8th Intern. School "Defects in Crystals"*, ed.E.Mizera., SzcZyrk, Poland, Publ. World Scientific, pp. 359-367, 1988
6. Olijnyk H., Holzapfel W.B., "Phase transitions in Si, Ge and Sn under pressure", *J. Phys.*, **45**, C8-153-159, 1984.
7. Polian A., Grimsditch M., "Room-temperature densification of α -SiO₂ versus pressure", *Phys. Rev. B*, **41**, pp.6086-87, 1990.
8. Misiuk A., Surma B., Hartwig J., "Stress induced oxygen precipitation in Cz-Si", *Mater.Sci. Eng., Mater. Sci. Eng.*, **B36**, pp. 30-32, 1996.
9. Datsenko L., Khrupa V., Krasulya S., Misiuk A., Hartwig J., Surma "Structural perfection of Czochralski grown silicon crystals annealed above 1500 K under hydrostatic pressure", *Acta Phys. Pol. A*, **91**, pp. 929-933, 1997.

Investigation of as-grown nitrogen-doped Czochralski silicon

Deren Yang*, Jinggang Lu, Yijun Shen, Daxi Tian, Xiangyang Ma, Liben Li, Duanlin Que

State Key Laboratory of Silicon Material Science, Zhejiang University,
Hangzhou 310027, People's Republic of China

ABSTRACT

Two Czochralski (CZ) silicon ingots, named NCZ and ACZ silicon, were grown under the same procedure in nitrogen and an argon atmosphere respectively. The experiments reveal that nitrogen was doped into the silicon ingot and N-O complexes were generated during the crystal growth, while it was grown in a nitrogen atmosphere. The nitrogen concentration profile in the NCZ silicon ingot indicates that the nitrogen concentration in the wafer edges was less than that in the center. It is also found that the as-grown oxygen-thermal donors were almost same. Furthermore, it is discovered that the profile of phosphorus concentration in NCZ silicon was also the same as that in ACZ silicon. It is considered that compared with argon atmosphere, nitrogen atmosphere has no influence on the evaporation rates of phosphorus from melting silicon.

Keywords: nitrogen doping, oxygen, silicon.

1. INTRODUCTION

In recent years, nitrogen behavior in single crystal silicon has been intensively studied. In general, nitrogen is used as a protective gas or a carrier gas in manufacture processes of very large scale integration (VLSI). It is well known that nitrogen atoms exist in silicon as pairs.¹ It has been found that nitrogen in silicon can suppress microdefects, and lock dislocations to increase mechanical strength.^{2,3} Due to the contamination of quartz crucible Oxygen is main impurity in CZ silicon. It has been widely reported that thermal donors(TDs), which affect the electrical stability of silicon material and devices, are produced in CZ silicon annealed in the temperature range 300-550°C.⁴ It was also reported that nitrogen in CZ silicon can slightly suppress the generation of thermal donors⁵, and interact with oxygen atoms to form nitrogen-oxygen (N-O) complexes which are a kind of donors. However, few papers about the properties of nitrogen in as-grown silicon has been published^{6,7}.

In our experiment, we introduced nitrogen into silicon by growing silicon ingot in a nitrogen ambience. Compared with ACZ, the influences of nitrogen ambience on the introduction of nitrogen, the generation of as-grown thermal donors and Phosphorus evaporation rates from melting silicon has been investigated. It was found the nitrogen was induced into silicon ingot and the N-O complexes were generated during crystal growth. It is considered that nitrogen atmosphere has no influence on the thermal donors, the evaporation rates of phosphorus and the concentration profile phosphorus in silicon ingot.

2. EXPERIMENT

The n-type <111> NCZ and ACZ silicon ingots were grown under the same procedure in nitrogen and an argon atmosphere, respectively. And the same amount of phosphor dopant was used. Samples were cut from different sections at the same positions for the two ingots. All samples were 2.0mm in thickness. From head to tail, the ACZ samples are numbered as A0-A3 and the NCZ samples N0-N3.

The samples were checked by a Fourier transform infrared spectrometer (FTIR) at room temperature. A high pure float zone silicon in which the concentration of oxygen, nitrogen and carbon is less than the detection limit of FTIR. The absorption lines at 1107 cm⁻¹ and 963 cm⁻¹ were used to determine the concentration of oxygen and nitrogen, respectively.

* Further author information

Email: mseyang@diel.zju.edu.cn

The calibration factor for oxygen is $3.14 \times 10^{17} \text{ cm}^{-2}$ and $1.82 \times 10^{17} \text{ cm}^{-2}$ for nitrogen. Furthermore, the samples were annealed at 650°C for 30 min. and 900°C for 2 h to eliminate as-grown TDs and N-O complexes, respectively. Before and after annealing, the resistivity of the samples was measured. A four-point probe technique was used to measure the resistivity of samples. The resistivity was then converted into the carrier concentration according to the ASTM F723-88 standard.

3. RESULTS AND DISCUSSION

3.1. Nitrogen and N-O complex in as-grown nitrogen doped silicon

Nitrogen pairs were found in the tail end of NCZ silicon ingot. Fig.1 shows the FTIR spectrum of NCZ silicon sample from the tail position. It can be seen that the local vibration mode (LVM) absorption line of nitrogen pairs at 963 cm^{-1} was observed. This indicates that nitrogen impurity was introduced into the NCZ silicon ingot. In the NCZ samples from the head position, no relative line at 963 cm^{-1} was detected. It is clear that nitrogen was mainly induced into the tail position, but not the head position. Because the segregation coefficient of nitrogen in silicon is very low (about 1×10^{-4}), it is easily understood that nitrogen concentration in the tail position is higher than that in the head position.

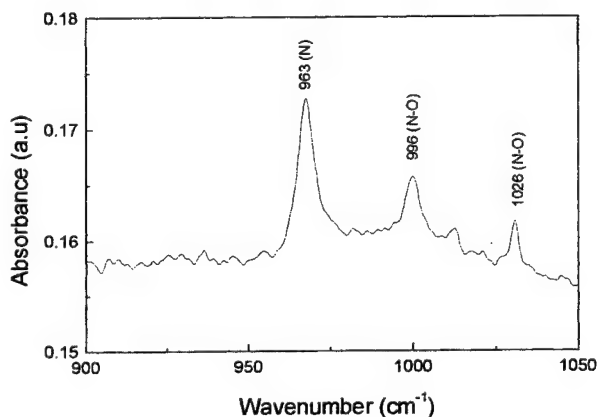


Fig.1. FTIR spectrum of NCZ silicon sample from the tail position.

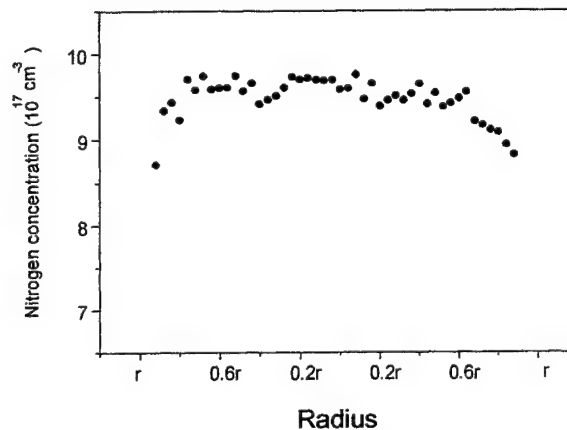


Fig. 2. Nitrogen concentration profile along with the radius of NCZ silicon sample from the tail position.

Meanwhile, the lines at 996 and 1026 cm^{-1} , which were recognized to be LVM of N-O complexes⁷, were observed in Fig. 1. This illustrates that N-O complexes were generated in the tail position of the NCZ silicon ingot during the crystal growth. Again, no LVM lines of N-O complexes in the head position were detected. During cooling processes of crystal, silicon ingots were kept at high temperatures in the furnaces. This means that silicon ingots suffered from heat treatments at different high temperatures. It is considered that during cooling process, nitrogen with higher concentration in the tail position can interact with oxygen to produce the N-O complexes, which existed in as-grown silicon.

Fig. 2 shows the radius profile of nitrogen concentration in the NCZ silicon sample from the tail position. The nitrogen concentration in the edges was less than that in the center. This profile was depended on the condition of crystal growth.

3.2. Effect of nitrogen atmosphere on TDs concentration in as-grown silicon

The samples of NCZ and ACZ silicon were annealed at 650°C for 30 minutes. It is well known that such a heat treatment has been applied to eliminate TDs. After annealing, as-grown TDs in the NCZ and ACZ silicon were annihilated, but the concentration of N-O complex donors in NCZ silicon changed very small.⁸ So we can deduce that the variations of carrier concentration before and after annealing is just owing to the as-grown TDs being annihilated in the annealing process. The as-grown TDs in the NCZ and ACZ silicon is shown in Fig. 3.

It is obvious that the as-grown TDs concentration in the NCZ silicon was the same as that in the ACZ silicon. It was reported that TDs in NCZ silicon annealed at 450°C for 1 h were suppressed⁵. In this experiments, the NCZ silicon ingot was suffered from different annealing in the temperature range of 350 - 550°C . Moreover, the as-grown TDs concentration was up to $1 \times 10^{15} \text{ cm}^{-3}$, which was very higher the possible concentration of N_2O complexes. The TDs concentration is

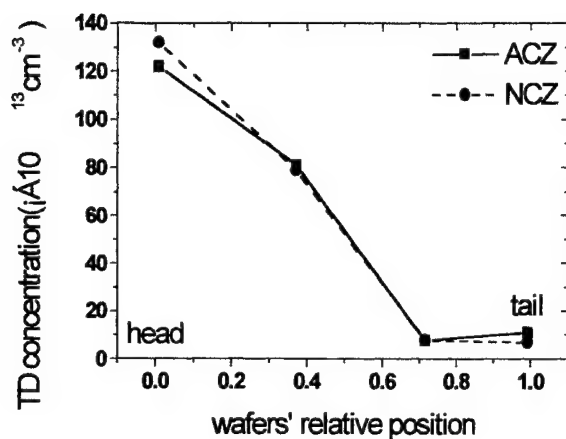


Fig 3. TDs concentration in as-grown silicon.

determined by oxygen concentration and thermal history, which is associated with the sample positions in silicon ingot, but not nitrogen. It was found in the experiments that the oxygen concentration in the different positions of NCZ silicon ingot was similar to that of ACZ silicon ingot. Thus, the concentration of as-grown TDs in both the ingots was almost same (Fig. 3)

3.3. Effect of nitrogen atmosphere on the rates in which P and SiO evaporate from melting silicon

After NCZ and CZ silicon samples were annealed at 900°C for 2 hours, as-grown thermal donors and N-O complexes (only

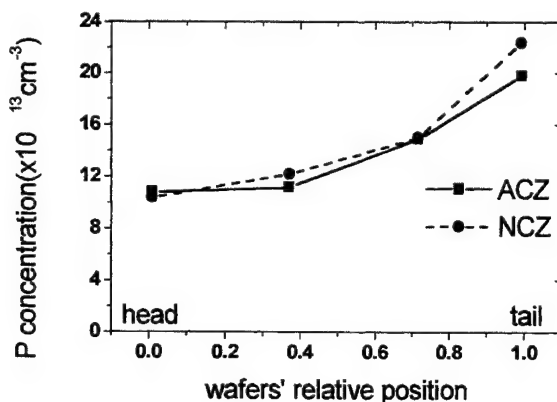


Fig.4. Phosphor concentration in ACZ and NCZ silicon.

in NCZ silicon) were totally annihilated⁸. And then the carriers in silicon came exactly from the dopant--phosphorus. Fig 4. shows the phosphorous concentration in ACZ and NCZ silicon ingots. We can find the concentration profiles of phosphorus are very similar between ACZ and NCZ silicon. That means that compared with argon atmosphere, pulling crystal in a nitrogen atmosphere has no influences on the evaporation rates of phosphorus from melting silicon.

4. CONCLUSIONS

Two CZ silicon ingots were grown in nitrogen and an argon atmosphere, respectively. It is found that in comparison with argon atmosphere, nitrogen was introduced into NCZ silicon ingot, and N-O complexes were formed during the crystal

growth. Nitrogen atmosphere has no influence on TDs concentration in as-grown silicon and the evaporation rates of phosphorus from melting silicon.

ACKNOWLEDGEMENT

The authors would like to acknowledge the financial support of the Chinese National Natural Science Foundation and Chinese RFDP.

REFERENCES

1. R. Jones, S. Oberg, F. Berg Rasmussen and B. Bech Nielsen, "Identification of the dominant nitrogen defect in silicon," *Phys. Rev. Lett.* 72 (12), pp.1882-1885, 1994.
2. Koji Sumino, Ichiro Yonenaga, Masato Imai and Takao Abe, "Effects of nitrogen on dislocation behavior and mechanical strength in silicon crystal," *J. Appl. Phys.* 54 (9), pp. 5016-5020, 1983.
3. Huanming Lu, Deren Yang, Liben Li, Zhizhen Ye and Duanlin Que, "Thermal warpage of Czochralski silicon wafers grown under a nitrogen ambience," *Phys. Stat. Sol. (A)*169, pp. 193-198, 1998.
4. C. S. Fuller and R. A. Logan, "Effect of heat treatment upon the electrical properties of silicon crystal," *J. Appl. Phys.* 28, pp.1427-1436, 1957.
5. Deren Yang, Duanlin Que and Koji Sumino, "Nitrogen effects on thermal donor and shallow thermal donor in silicon," *J. Appl. Phys.* 77(2), pp. 943-944, 1995.
6. Masashi Suezawa, Koji Sumino, Hirofumi Harada and Takao Abe, "Nitrogen-oxygen complexes as shallow donors in silicon crystal," *Jpn. J. Appl. Phys.* Vol25, No. 10, L859-L861, 1986.
7. P. Wagner, R. Oeder and W. Zulehner, "Nitrogen-oxygen complexes in Czochralski-silicon," *Appl. Phys.* A46, pp. 73-76, 1988.
8. Deren Yang, Ruixing Fan, Liben Li, Duanlin Que and Koji Sumino, "Effect of nitrogen-oxygen complex on electrical properties of Czochralski silicon," *Appl. Phys. Lett.* 68, pp.487-489, 1996.

Effect of stress on defect transformation in hydrogen implanted silicon and SOI structures

I.V.Antonova^{a*}, V.P.Popov^a, J.Bak-Misiuk^b, J.Domagala^b, A.Misiuk^c, V.I.Obodnikov^a,
A.K.Gutakovskii^a, A.Romano-Rodriguez^d

^aInstitute of Semiconductor Physics, RAS, 630090 Novosibirsk, Russia

^bInstitute of Physics Polish Academy of Sciences, Al. Lotnikow 46, 02-668 Warsaw, Poland

^cInstitute of Electron Technology, Al. Lotnikow 46, 02-668 Warsaw, Poland

^dBarcelona University, Marti i Frangues 1, E-08028 Barcelona, Spain

ABSTRACT

Transformation of defects in hydrogen implanted silicon and silicon-on-insulator structures caused by external pressure of argon ambient (up to 1.5 GPa) at the stage of defect removal in implanted material and high temperature annealing SOI structures is reported. The results are compared to these for crystals annealed at argon atmosphere of ambient pressure. Formation of the new phase crystallites was found in SOI structures annealed at high temperature in conditions of high pressure (1.2 GPa). Small insulations were also observed in hydrogen implanted silicon, which can be patterns of the new phase. Two reasons can cause phase transformation in the top silicon layer of as-bonded SOI structures: high hydrogen concentration and high local strain.

Keywords: silicon, hydrogen implantation, silicon-on-insulator, high pressure, new phase

1. INTRODUCTION

Hydrogen implantation is known to be used for Silicon-On-Insulator (SOI) structure fabrication by Smart-Cut or similar technologies¹⁻³. This SOI technology includes the bonding of hydrogen implanted wafer with another substrate at relatively low temperatures (400 - 600°C) and demands the high temperature (1100°C) annealing of SOI to improve structural and electrical properties^{1,3}. Furthermore, silicon layers oversaturated with hydrogen are seemed to be perspective for optical applications⁴. The utilisation of high pressure (HP) at the stage of high temperature (HT) treatments can affect defect transformation⁵⁻⁷. As it was found in⁵ HP-HT treatments cause the increase in concentration of oxygen precipitates and decrease in their sizes in Cz-Si, the increase in thermal donor concentration in hydrogen implanted silicon⁶ and decrease in dislocation density in oxygen implanted crystals⁷. The aim of the present efforts was to investigate the transformation of defects and structure in Si:H and SOI structures caused by annealing at external pressure.

2. EXPERIMENTAL

The Czochralski- and Floating Zone grown silicon with (100) and (111) orientation were used as initial crystals. Hydrogen implantations (H_2^+) were carried out with the energy of 130 keV in the dose range of $4 - 6 \times 10^{16} \text{ cm}^{-2}$. The ion projected range is equal to 0.52 μm . SOI structures were fabricated by bonding at the temperature of 450°C and with the final annealing at 1100°C for 1 hour. The thicknesses of layers of the SOI structure were about 0.48 μm for the top silicon layer and 0.4 μm for the buried oxide. Hydrostatic pressure of argon ambient up to 1.5 GPa was used at the stage of defect removal in implanted material and high temperature annealing SOI structures. The results are compared to those for crystals annealed at argon atmosphere of ambient pressure (AP).

X-ray investigations were performed using a High-resolution diffractometer in a double and triple configuration. Rocking curve and reciprocal space maps were recorded after HP-HT and AP-HT treatments. A high-resolution experimental set-up was realised by employing a four-crystal Ge (220) Bartels-type monochromator in the primary beam

* I.V.A. (correspondence): E-mail: antonova@isp.nsc.ru, Telephone: 7-383-2-33-24-93; Fax 7-383-2-33-27-71

V.P.P.: E-mail: popov@isp.nsc.ru

J.B.-M.: E-mail: bakmi@ifpan.edu.pl

and a channel-cut double-reflection Ge (220) analyser in the diffracted beam. Secondary ion- mass spectroscopy (SIMS) (Cameca Riber, sputtering by Cs^+ ions), electron diffraction, and transmission electron microscopy (TEM and HREM) were also used for investigation. Electrical measurements with using of high-frequency capacity-voltage (CV) technique were done for Si:H and SOI samples. CV measurements were done with using a mercury probe.

3. RESULTS

The hydrogen depth distributions in implanted silicon annealed at different temperatures and pressures are presented in Fig.1. Some delay in hydrogen out-diffusion is observed in the case of HP treatments. But the hydrogen sheet concentration in the last case is higher than that in AP treated sample by approximately 10-20%. The AP annealing of Si:H samples at 1100°C for 1 hour leads to decrease in hydrogen concentration lower than limit of SIMS sensitivity, whereas HP treated Si:H samples still conserve some hydrogen atoms.

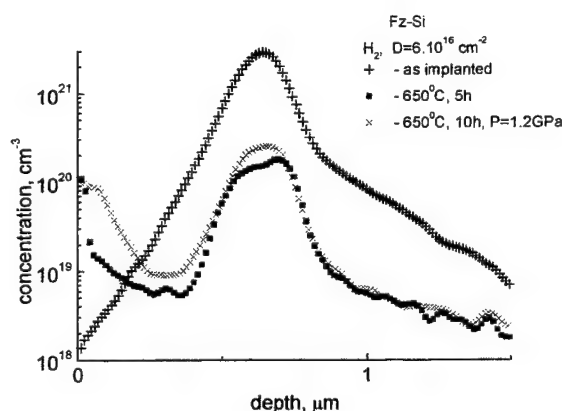


Fig.1 Hydrogen profiles obtained by SIMS for samples annealed at different temperatures and pressures.

The hydrogen profiles for as-bonded and annealed SOI structures are presented in Fig.2. As-bonded SOI contains the high hydrogen concentration in the top silicon layer (about $1.6 \times 10^{16} \text{ cm}^{-2}$). Practically complete removal of hydrogen from SOI structure was found for the sample annealed at 1100°C at AP for 0.5 hour. A slightly higher hydrogen concentration (~10%) in the top silicon layer and Si/SiO₂ interface was observed for the sample annealed at 1100°C in HP conditions.

Figure 3 presents the cross-section of hydrogen implanted samples (Si:H) and samples annealed at the temperature of 450°C at ambient and high pressure. The HP effect, which one can observe in Fig.3 is a suppression of formation of large cracks at the depth of maximum destruction of defects produced by ions. If for samples annealed at 450°C some small and very narrow (about 10 nm) cavities are observed than for samples annealed at $T \geq 650^\circ\text{C}$ cavities are not practically seen. The second interesting moment is that visible defects are expanded towards the surface in the case of HP-HT treatments. The size of these defects becomes smaller but they occupy the main part of the layer from surface to ion projected range (R_p). On the contrary the end-range defects have a lower density in the case of HP-HT treatments.

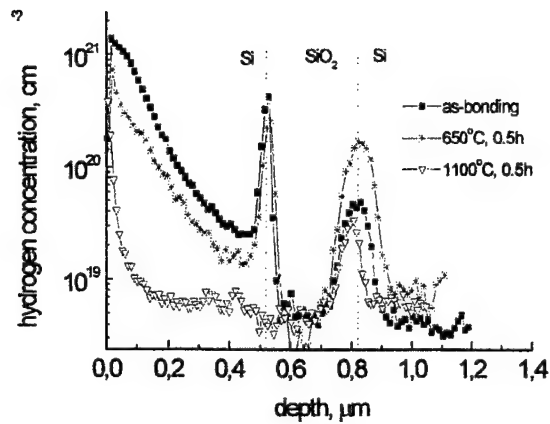


Fig.2 Depth hydrogen distribution for as-bonded SOI structure and annealed one

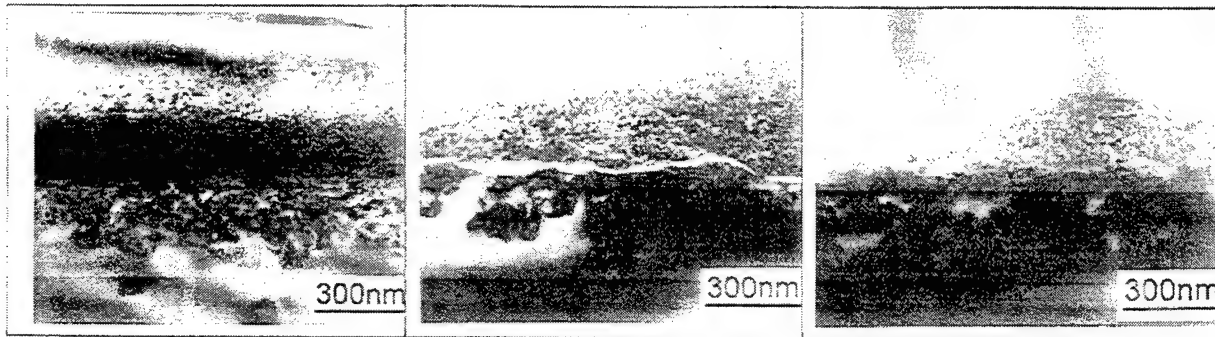


Fig.3 Cross section of hydrogen implanted sample (left), and samples annealed at 450°C for 2 hours at atmospheric pressure (middle) and 1.2 GPa (right).



Fig.4 Cross section with atomic resolution (HREM) of hydrogen implanted sample (crack) annealed at 650°C for 2 hours at 1.2 GPa.

Some incorporations can be seen near the cavities in HP treated samples (Fig.4). These incorporations have very small summary volume, and the measurement of electron diffraction for this sample gives the usual diffraction pattern as for a single crystal silicon.

The rocking curve full widths at half maximum (FWHM) for ω scans in double mode for Si:H samples are given in Table 1. Enhanced pressure of argon ambient during treatment at 1100°C results in high FWHM in comparison with AP annealed samples. The reciprocal space maps for HP-HT treated Si:H samples shows the high diffuse scattering intensity. These facts indicate development of mosaic structure (high defect concentration) after HP-HT treatments.

The rocking curves in double configuration (ω -scan) and $2\theta/\omega$ -scan of the (004) reflection for the SOI structures annealed at 1100°C for 1 hour at different pressures are presented in Figs. 5a-d. The peaks from the top silicon layer and the substrate are separated in the ω -scan (Fig. 5a,b). This separation of peaks is connected to the strain in the SOI top layer and also with the tilt between the layer and the substrate. The $2\theta/\omega$ -scan for the AP annealed SOI indicates the presence of the thickness fringes. The thickness value calculated from the fringes is equal to that obtained by different methods. Lack of the thickness-related fringes in the HP treated SOI (Fig. 5d) is probably caused by unhomogeneity of top silicon layer. The FWHM values for the top silicon layers of the SOI structures and substrates are given in Table 1. The FWHM value for the Si substrate did not differ from that of a typical silicon wafer. Broadening of the rocking curve for top silicon film in a double and triple configuration may be caused by the fluctuation of the lattice constant (caused by thickness effect, presence of defects, local strains, new phase, and so on). The calculated FWHM broadening for the 0.4 μm thick top Si layer, caused by the thickness effect, is equal to about 25 arcsec. As it is seen from Table 1, the FWHM value for the silicon layer of the AP annealed SOI structures is higher than that of the typical silicon single crystal even considering for thickness effect. In the case of HP treated SOI the FWHM value is very high.

Table 1 FWHM obtained in double and triple beam configurations and strain values for investigated samples.

Sample	FWHM Double conf.		FWHM Triple conf.		Strain
Si:H as-implanted	27		-		-
Si:H, 1100C, AP	15		-		-
Si:H, 1200C, 1.5GPa	23		-		-
	film	substrate	film	substrate	
SOI, as-bonded	135	15	80	9	5×10^{-4}
SOI, 1100C, AP	60	15	48	9	2×10^{-5}
SOI, 1100C, 1.2GPa	125	15	108	9	1.5×10^{-4}

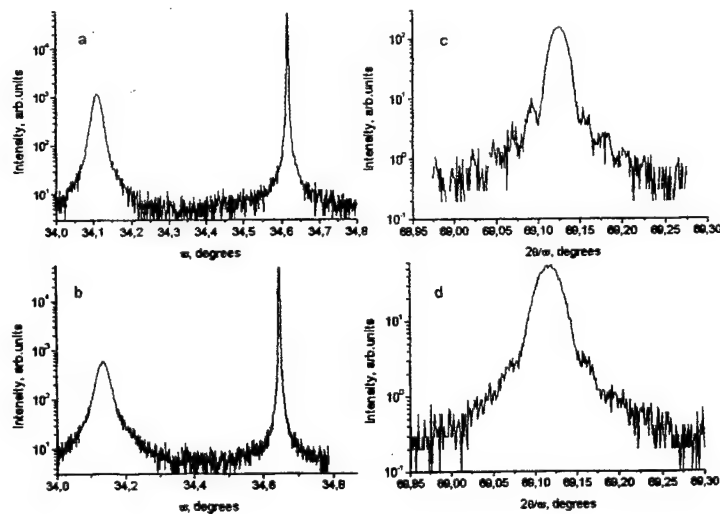


Fig.5. ω -scan of the 004 reflection in double configuration (a,b) and $2\theta/\omega$ -scan (c,d), from the SOI structures annealed at 1100°C for 1 hour at atmospheric pressure (a,c) and 1.2 GPa (b,d). Left and right peaks in ω -scans correspond to the top silicon layer and substrate, respectively.

If AP annealed SOI subjects to additional treatment at HP the perfection of the silicon top layer does not change.

The strain in the top silicon layer (defined as the relative change of the (004) plane spacing for the top Si layer with respect to that for the substrate) is determined as $\frac{\Delta a}{a} = \frac{a_L - a_S}{a_S}$, where a_L and a_S are the lattice constants for the top Si layer and the substrate, respectively. The $\frac{\Delta a}{a}$ values measured from the rocking curves of the same reflection for $\varphi = 0^\circ$ and 180° (φ denotes a rotation of the sample around the axis perpendicular to the sample surface) for the SOI samples are also given in Table 1. The strain value is high in the as-bonded SOI structure and in HP treated one.

Electron diffraction patterns and dark field TEM images for SOI structures annealed at different pressure are presented in Fig.6. AP annealing of SOI structure leads to a single crystalline top silicon layer. Mosaic-like structure is observed in TEM images. Additional annealing at HP of the AP treated SOI does not change defect structure. In the case of HP treated SOI the formation of new phase crystallites was found. Electron diffraction pattern reveals additional reflexes and twinning of reflexes.



Fig.6 Dark field TEM micrograph and electron diffraction pattern from the (001) oriented top silicon layer of SOI structures annealed at atmospheric pressure (left) and at 1.2 GPa (right). The micrograph size is $1\mu\text{m} \times 0.75\mu\text{m}$.

CV measurement shows that the top silicon layer in as-bounded SOI structures has n-type of conductivity with concentration about $(2-3) \times 10^{17} \text{ cm}^{-3}$. For SOI annealed at 1100°C in AP condition the electron concentration is equal to $(3-5) \times 10^{15} \text{ cm}^{-3}$. The silicon layer of HP treated SOI is a high resistive layer, which can not be measured by CV technique.

4. DISCUSSION

HP treated Si:H samples and SOI show a very different structure as compared to AP annealed ones. The most pronounced changes are observed in SOI. According to data presented in Fig.6, the patterns of a new phase are formed in the top silicon layer. Phase transformation is obviously the reason of high FWHM value and strain for this structure. The small insulations observed for Si:H samples can also be patterns of a new phase or twins. They are too small for real identification.

Stable hexagonal-wurtzite silicon crystallites up to $20\mu\text{m}$ were found to form in a-Si:H layer directly deposited at low pressure using ultraviolet laser ablation [8], in a silicon oxide deposition process with NN_2O -Silane plasma [9], or in CVD silicon [10]. In all cases there were layers which contained high hydrogen concentration. Presence of hydrogen in our structures can stimulate phase transformation. In as-bounded SOI effect can be intensified by high local strain presented in the top silicon layer due to the roughness of the Si/SiO₂ interface: the layer and the substrate were not contacting at all points of the interface with the same strength resulting in incomplete adhesion. The insulations observed in Si:H samples are also formed in the place of maximal local strain in hydrogen implanted sample – at the border of the cavity.

The AP-HT annealing of SOI leads to homogeneous adhesion on bonded interface and practically complete removal of hydrogen from the top silicon layer. As a result, the additional HP-HT treatment of AP annealed SOI does not cause phase transformation.

5.CONCLUSIONS

Formation of the new phase crystallites was found in SOI structures annealed at high temperature in conditions of high pressure (1.2 GPa). The significantly low pronounced effect is observed in Si:H samples. Two reasons can cause phase transformation in the top silicon layer of as-bonded SOI structures: high hydrogen concentration and high local strain.

ACKNOWLEDGEMENTS

This work was supported in part by Polish Committee for Scientific Research (grant N 8T11B 009 13) and in part by International Science and Technical Centre (grant N 563).

REFERENCES

1. M.Bruel, "Appliction of Hydrogen Ion Beams to Silicon On Insulator Material Technology", *NIM*, **B108**, pp.313-319, 1996.
2. Y.A.Li, R.W.Bower, "Surface Roughness of Hydrogen Ion Cut Low Temperature Bonded Thin Film Layers", *Jpn. J. Appl. Phys.*, **39**, pp. 275-276, 2000.
3. V.P.Popov, I.V.Antonova, V.F.Stas, L.V.Mironova, E.P.Neustroev, A.K.Gutakovskii, A.A.Franzusov, G.N.Feofanov, "Structural and Electrical Properties of Silicon On Insulator Structures Manufactured on FZ-and Cz-Silicon by Smart-Cut Technology", in *Perspectives, Science and Technologies for Novel Silicon on Insulator Devices*, P.L.F.Hemment at al. (eds.), pp. 47-54, 2000 Kluwer Academic Publisher, Netherlands.
4. E.Edelberg, S.Bergh, R.Naone, M.Hall, E.S.Aydil, "Luminescence from Plasma deposited Silicon Films", *J.Appl.Phys.*, **81**, pp.2410-2417, 1997.
5. I.V.Antonova, A.Misiuk, V.P.Popov, A.E.Plotnikov, B.Surma, "Nucleation and formation of oxygen precipitates in Gz grown silicon annealed under uniform stress conditions", *Phys.B*, **253**, pp.131-137, 1998.
6. E.P.Neustroev, I.V.Antonova, V.P.Popov, V.F.Stas, V.I.Obodnikov, "Donor center formation in hydrogen implanted silicon", *Phys.B*, **270**, pp.1-5, 1999.
7. A.Misiuk, J.Jun, B.Surma, I.V.Antonova, A.Romano-Rodriquez, M.Lopez, "Luminescence Properties of Oxygen-Containing Silicon Annealed at Enhanced Argon Pressure", *Phys. Stat. Solidy B*, **211**, pp.233-238, 1999.
8. Y.Zhang, Z.Igbal, S.Vijayalakshmi, H.Grebel, "Stable Hexagonal-Wurtzite Silicon Phase by Laser Ablation", *Appl.Phys.Lett.*, **75**, pp.2758-2760, 1999.
9. J.Bandet, B.Despax, M.Caumont, L.Date, "Raman Analysis of Wurtzite Silicon Islands in Silicon Oxide Deposited in N₂O-SiH₄ Plasma Process", *Jpn.J.Appl.Phys.*, **39**, pp.L141-L142, 2000
10. H.Cerla, "High-Resolution Electron Microscopy of Diamond Hexagonal Silicon in Low Pressure Chemical Vapor Deposited Polycrystalline Silicon", *J.Mater. Res.*, **6**, pp.2324-2328, 1991.

Molecular simulations of concentrated aqueous solutions: Ionic equilibrium structures in solutions

Witold M. Bartczak^{a,b}, Michał Zapałowski^a and Krystyna Wolf^c

^a Institute of Applied Radiation Chemistry, Technical University of Łódź, Wróblewskiego 15, Łódź

^b Chair of Theoretical Chemistry, University of Łódź, Pomorska 149/153, Łódź, Poland

^c Institute of Physics, Technical University of Łódź, Wólczańska 219, Łódź, Poland

ABSTRACT

The computer simulation methods have been applied to study the structure of aqueous solutions of simple ionic salts in the region of very high concentrations. The calculations of ionic structures in solutions were performed for NaOH, NaCl, LiCl and MgCl₂ solutions. The concentrations ranged from 0.2 M to saturated solutions, in some cases as much as 19 M.

A particularly careful analysis was devoted to the topology of the ionic structures in solution. Up to now, most of the research on ionic solutions was devoted to studies of the ionic hydration shells. However, beyond the Debye – Huckel range of very low concentrations, very little is known about the interionic spatial correlations. Certain theories predict the existence of ionic quasi-lattices in the region of high concentrations.

In the present work we used the Molecular Dynamics method combined with such statistical tools as the radial distribution functions, Voronoi tessellations, the running and O'Keeffe coordination numbers, *etc.*, in order to analyze the ionic structures. The radial distribution functions of three types: the cation – anion, cation – cation and the anion – anion type were calculated for each solution. The functions are typical for the quasi-crystalline order within the first 2 – 3 ionic coordination layers around a selected ion. The order is particularly pronounced for the anion – cation RDF's.

The distributions of the sphericity factor of the Voronoi polyhedra were calculated for the ionic substructures in the configurations produced by the Molecular Dynamics simulation. The increase of the ion concentration causes evolution of these distributions towards increased signatures of predominant geometries of the Voronoi polyhedra. This, together with the results for RDF's, provides a strong conjecture for existence of the ordered structures of ions in concentrated solutions.

Keywords: ionic solutions, lattice theory, computer simulation.

1. INTRODUCTION

The structure of ionic solutions - both the local structure of the solvation layers around the ions and the topology of the ion distributions in solution - is of primary importance for our understanding of nucleation phenomena and growth of crystals from the solutions. Unfortunately the aqueous solutions of electrolytes represent a complicated case and can not be described by any analytical theory in the full range of concentrations. For low concentrations of ions there is a number of theoretical models that work reasonably well: among others the Debye-Hückel theory, the hyper-netted chain theory, the mean spherical theory (see ^{1, 2} for references). All these theories converge to the same result - the limiting laws of the Debye-Hückel theory - when the ion concentration decreases to zero. On the other hand, at the range of high concentrations the validity of the models deteriorates very quickly and another theory should be introduced. Such a theory, based on the lattice-like topology of the ionic structures, has been mentioned and discussed many times in the literature. The consequent formulation of the theory has been provided by Frank and Thompson ³. The most complete version of the lattice theory of concentrated electrolytes was given in a series of papers by Ruff and coworkers ^{4, 5, 6}. The model proposed by Ruff is can be

described as follows. (1) The ions are distributed in a lattice - like arrangement. The positions of the ions are allowed to deviate randomly from the lattice sites. (2) The ions are immersed in a structureless continuous dielectric and their coulombic interactions are scaled down with the average dielectric constant which may be taken as a function of interionic separation distance. The medium around the ions has a dielectric gradient which acts as a repulsive force between the ions at short separation distances.

Comparisons of calculated and observed data for the dielectric constant, activity coefficients and partial molar enthalpy of several 1-1 and 1-2 electrolytes show fairly good agreement in entire concentration range ^{4,5}. It has been shown ⁶ that in the limit of dilute systems, the deviations of the ion distribution from the lattice positions grow and the lattice theory converges to the Debye-Hückel theory.

In the modern investigations of liquids and liquid solutions the computer experiments play the important role occupying in a way an intermediate place between theory and experiment. In the case of very complicated problems, that are impossible to treat in an analytical way, the simulations correspond to the theory. On the other hand, for simpler and more tractable problems, the simulations can be used as a check against existing analytical theories. Hence, we propose to check the lattice theory of concentrated strong electrolytes by comparing it with the results of the computer experiment for these media.

The computer simulation method has been frequently used, with remarkable success, to predict the structure and physico-chemical properties of aqueous electrolyte solutions. The first simulations were performed by Heininger as early as 1974. We refer to the review papers ^{7,8} as the source of references. However, with very few exceptions like *e.g.* ⁹, most of the calculations concerned the solvation structures of the ions, that is the geometrical arrangements of water molecules in the vicinity of the cations and anions. The ion - ion correlations were either neglected or shown by the radial correlation functions. The investigation of the geometry of the ion arrangements is very difficult. In order to obtain reliable results one has to include in the simulation box at least a hundred of ions and proportional number of water molecules that results from relative concentrations. This increases the quantity of atomic objects in the simulation box to almost intractable number and such calculations have become possible only recently due to the increase of the speed of available computers.

2. COMPUTER SIMULATION METHOD

2.1. Simulation details.

The simulations have been performed by the Molecular Dynamics method ¹⁰ using the flexible model of water. The box contained 400-2000 water molecules and the number of ions that results from the concentration of the solution and the size of the box (16-160 ions). The simulation box was assumed in the cubic form with the size ranging between 2.5 and 4.1 nm, depending on the ion concentration. The calculations were performed for NaCl and MgCl₂ solutions with concentrations ranging from 0.2 to about 5.0M as well as for LiCl and NaOH solutions with concentrations from 0.5 to 19.0M.

The ion-ion interaction was assumed as a sum of the Coulomb potential and the Lennard-Jones interactions. The interaction parameters were taken from the Universal Force Field version 1.02 and the shifted force method for non-coulombic interactions has been applied. The periodic boundary conditions have been employed with the Ewald summation for calculations of the long-range electrostatic forces. A typical simulation run included three stages: (a) the initial, equilibration phase of $1 \div 2 \times 10^4$ time steps with the temperature scaling, (b) the control phase of 1×10^4 time steps and (c) the proper simulation of $4 \div 8.5 \times 10^4$ time steps. The elapsed time of the proper simulation reached 40÷85 ps and the temperature oscillated near 300 K. The analysis of the ionic structures was performed using the radial distribution functions (RDF) and stochastic Voronoi polyhedra.

2.2. Analysis of radial distribution functions and Voronoi polyhedra.

The local structure of a disordered medium can be described by a set of distribution functions for atomic positions. The pair distribution function $g_2(r_i, r_j)$ (usually calculated as a function $g(r)$ of radial distance only and called the radial distribution function, RDF) is most often used. The value of $g(r)$ at a given r represents the density of probability of finding

a pair of atoms separated by the distance r relative to the probability expected for an uniform distribution of atoms with the same density. The formula for calculating $g(r)$ is given by:

$$g(r) = (V/N)^2 \langle \sum_{ij, i \neq j} \delta(r - r_{ij}) \rangle \quad (1)$$

where N is the number of particles in volume V , δ denotes the Dirac delta, the brackets $\langle \rangle$ denote the averaging over the ensemble of the particles, the sums over i and j run over the different pairs of the particles in the simulation box.

For a multicomponent system the radial distribution function can be defined for each type of the atom pair. For an AB mixture the following functions: g_{AA} , g_{AB} , g_{BB} can be defined. In the present paper we calculate the RDF's describing spatial correlations between ions: the cation - anion RDF, cation - cation RDF and anion - anion RDF. It is commonly assumed¹⁰ that the region of the distances from 0 through the first maximum up to the first minimum of the RDF corresponds to the first neighbourhood of the central atom, the region from the first minimum to the second minimum corresponds to the second neighbours, etc. The integrals of the RDF within the limits given above correspond to the number of the nearest neighbours of the central atom, the second nearest neighbours, etc.

Stochastic Voronoi polyhedra seem to be a very convenient tool for the description of the long range order in disordered systems¹¹. The definition of the Voronoi polyhedron is illustrated in Figure 1. For a selected atom, referred to as the "central atom", we define the Voronoi polygon as the set of the points that are closer to the "central atom" than to any of the "medium atoms" of the disordered system. To find the Voronoi polygon we join the "central atom" and all the "medium atoms", then at the points halving the distances we draw perpendicular planes and select the minimal convex polyhedron constructed from these planes. Thus, the Voronoi polyhedron can be considered as a generalization of the well-known Wigner - Seitz symmetric cells to the disordered systems.

In an ideal crystal all the Voronoi polyhedra are identical and take on highly symmetrical forms. When the ion positions deviate from the lattice sites we observe rapidly increasing variety of the shapes of the Voronoi polyhedra. Some of the polyhedra acquire or loose one or more faces. Thus, we can construct the distribution of the number of faces of the Voronoi polyhedra drawn for the disordered set of points. The sets that are close to the crystalline order exhibit the distributions that are sharply peaked around the number of faces predominating in the system. In the limiting case of the perfect crystal, the distribution is a Dirac delta function placed at the number of faces which corresponds to the number of the first neighbours in the crystal lattice.

Figure 1 shows the Voronoi polyhedra plotted for a series of cubic lattices with the increasing random deviations of the atom positions from the lattice sites. The left upper part shows the polyhedron for an ideal lattice. The upper right part of the figure shows a typical polyhedron for the cubic lattice when atoms are allowed 20 % deviation from the lattice sites. The lower right part shows a typical polyhedron drawn for one of the configurations obtained in the course of simulation of 13 M LiCl solution. It is worth noting that the upper right and lower right polyhedron are very similar one to another. These polyhedrons can be compared with the polyhedron of the lower left part of the Figure drawn for completely random set of points. We observed that even minor deviations from the ideal lattice, of the order of 1%, produce polyhedrons with a wide range of the shapes. The distributions for the distorted crystals are however clearly different than the distribution for the random system.

It was demonstrated that analysis of non-sphericity (or anisotropy) factor of the Voronoi polyhedra is suitable to the study of the structure of disordered systems. The anisotropy parameter is given by:

$$\alpha = \frac{A^3}{36\pi V^2} \quad (2)$$

where A and V are the surface and volume of the Voronoi polyhedron. For a sphere α equals to 1, for the bcc, fcc and simple cubic lattices it equals to 1.33, 1.35 and 1.91, respectively. In limiting case of the perfect crystal, the distribution of α is the delta Dirac function. The sets of points that are close to the crystalline order exhibit sharply peaked distribution. For less-ordered systems the distribution is much broader and exhibits a bell-shaped form. The distributions of the anisotropy factors of the Voronoi polyhedra were calculated for the NaOH and MgCl₂ solutions with different concentrations. The distributions are shown in Figure 6 together with the distribution for a random set of points.

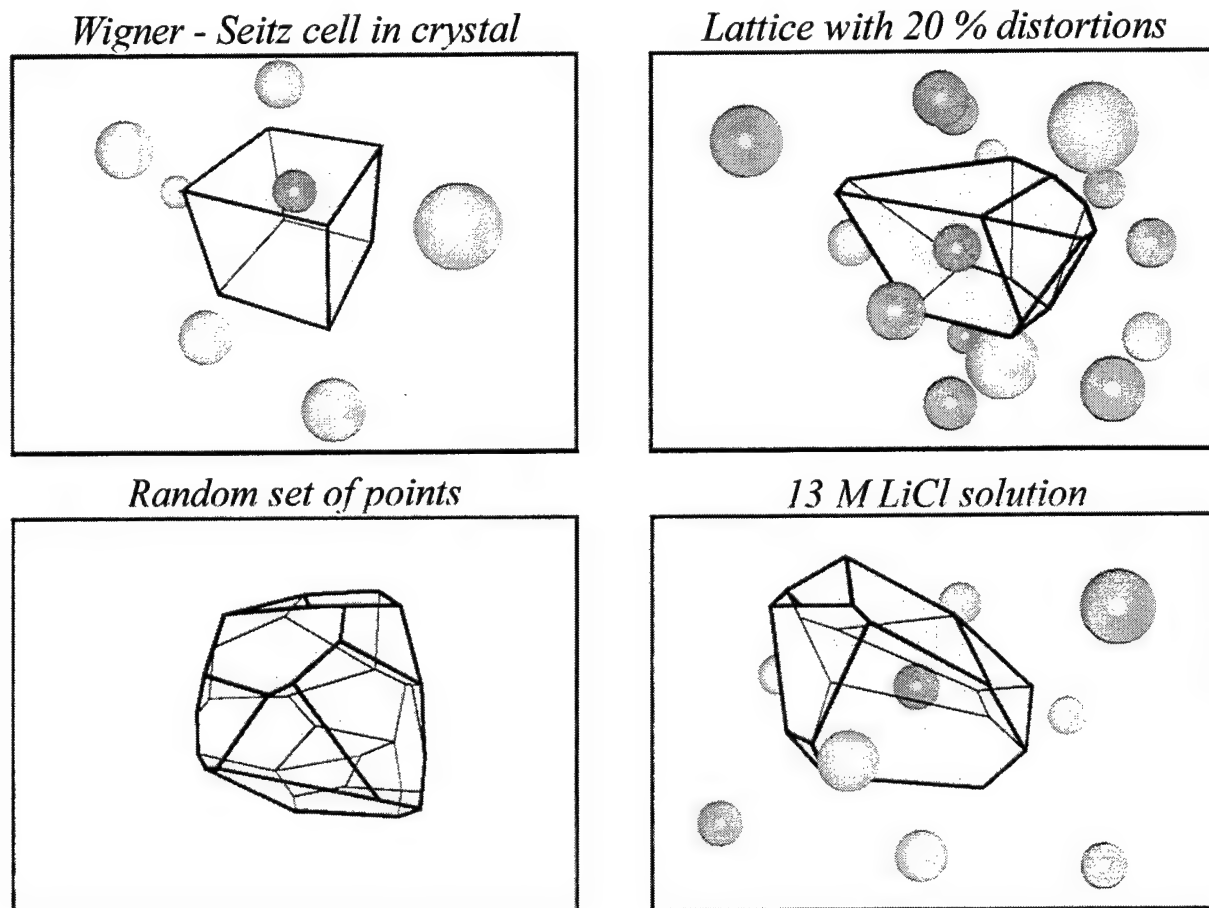


Fig.1. Voronoi polyhedra plotted for a series of systems with increasing random deviations of the atom positions from the lattice sites. The left upper part: the polyhedron (Wigner-Seitz cell) for an ideal cubic lattice. The upper right part: a typical polyhedron for the cubic lattice when atoms are allowed 20 % deviation from the lattice sites. The lower right part: shows a typical polyhedron drawn for one of the configurations obtained in the course of simulation of 13 M LiCl solution. The lower left part: a polyhedron drawn for random set of points.

3.RESULTS AND DISCUSSION

3.1. Radial distribution functions

The ion - ion pair distribution functions are plotted in the following arrangement: Figure 2 corresponds to NaOH solutions with concentrations 0.5 M, 3.0 M, 6.0 M and 19.0 M; Figure 3 to NaCl solutions with concentrations 0.3 M, 0.9 M, 2.8 M and 5.1 M; Figure 4 to LiCl solutions with concentrations 0.5 M, 5.0 M, 11.9 M and 14.0 M; Figure 5 to MgCl₂ solutions with concentrations 0.2 M, 1.1 M, 2.4 M and 4.9 M. The highest concentrations of the series are close to the saturation point. Each figure is composed of the upper, middle and lower part representing the cation - anion distributions, the cation - cation distributions and the anion - anion distributions, respectively. The distributions are additionally labeled in the figures.

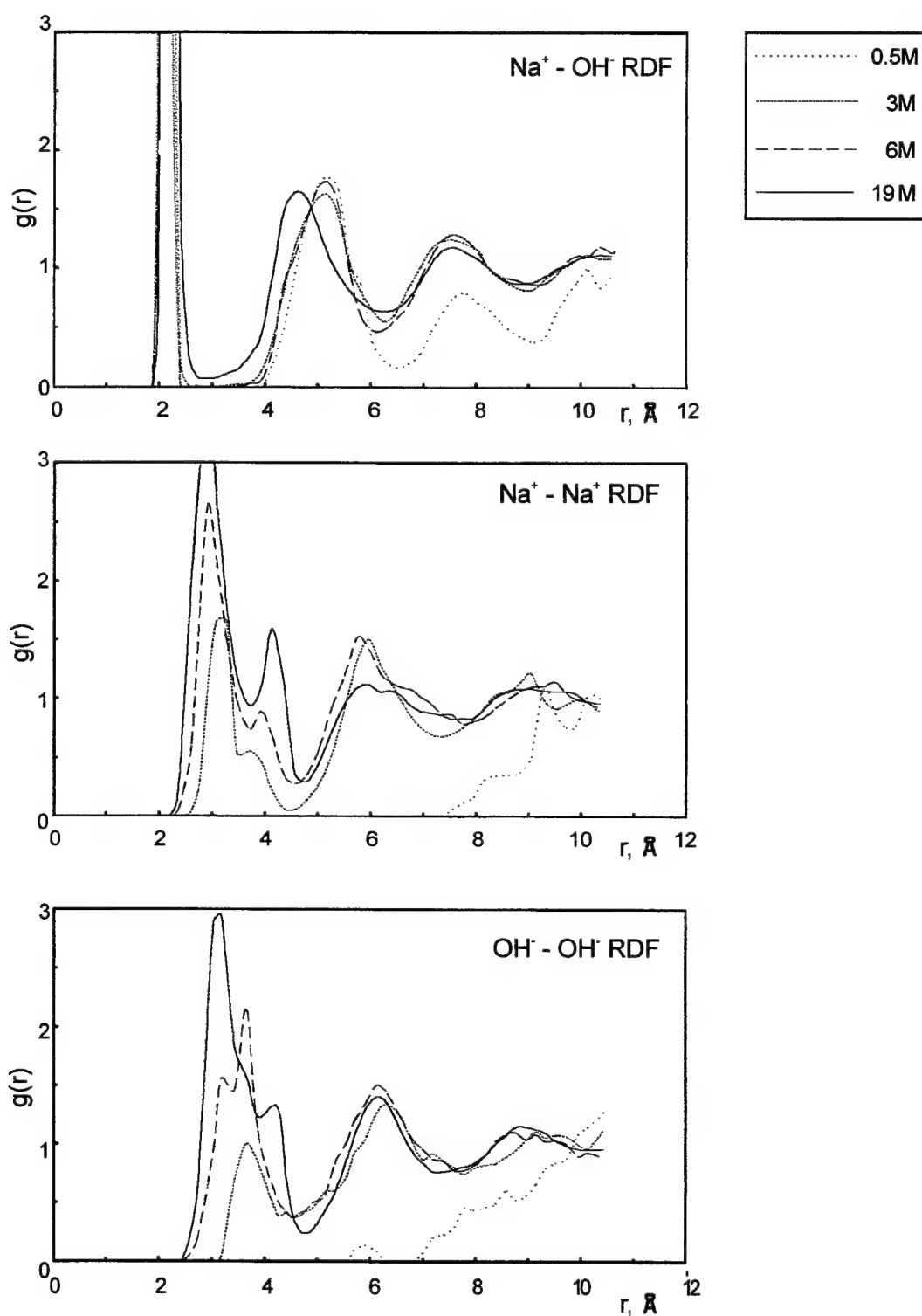


Fig.2. The ion – ion radial distribution functions for NaOH solutions with concentrations: 0.5 M, 3 M, 6 M and 19 M. The upper figure shows the $\text{Na}^+ - \text{OH}^-$ RDF, the figure in the middle shows the $\text{Na}^+ - \text{Na}^+$ RDF and the lower figure shows the $\text{OH}^- - \text{OH}^-$ RDF.

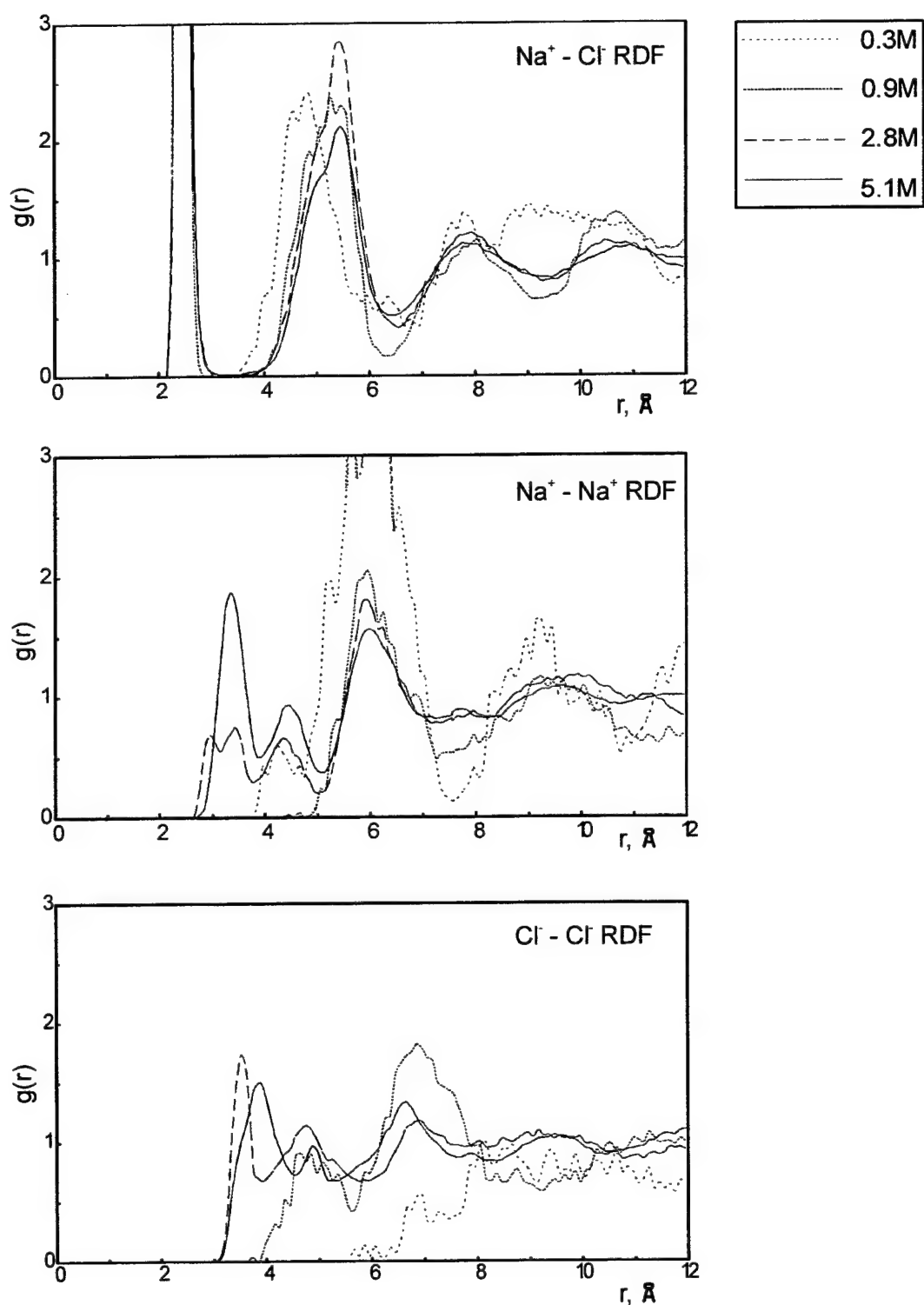


Fig.3. The ion – ion radial distribution functions for NaCl solutions with concentrations: 0.3 M, 0.9 M, 2.8 M and 5.1 M. The upper figure shows the $\text{Na}^+ - \text{Cl}^-$ RDF, the figure in the middle shows the $\text{Na}^+ - \text{Na}^+$ RDF and the lower figure shows the $\text{Cl}^- - \text{Cl}^-$ RDF.

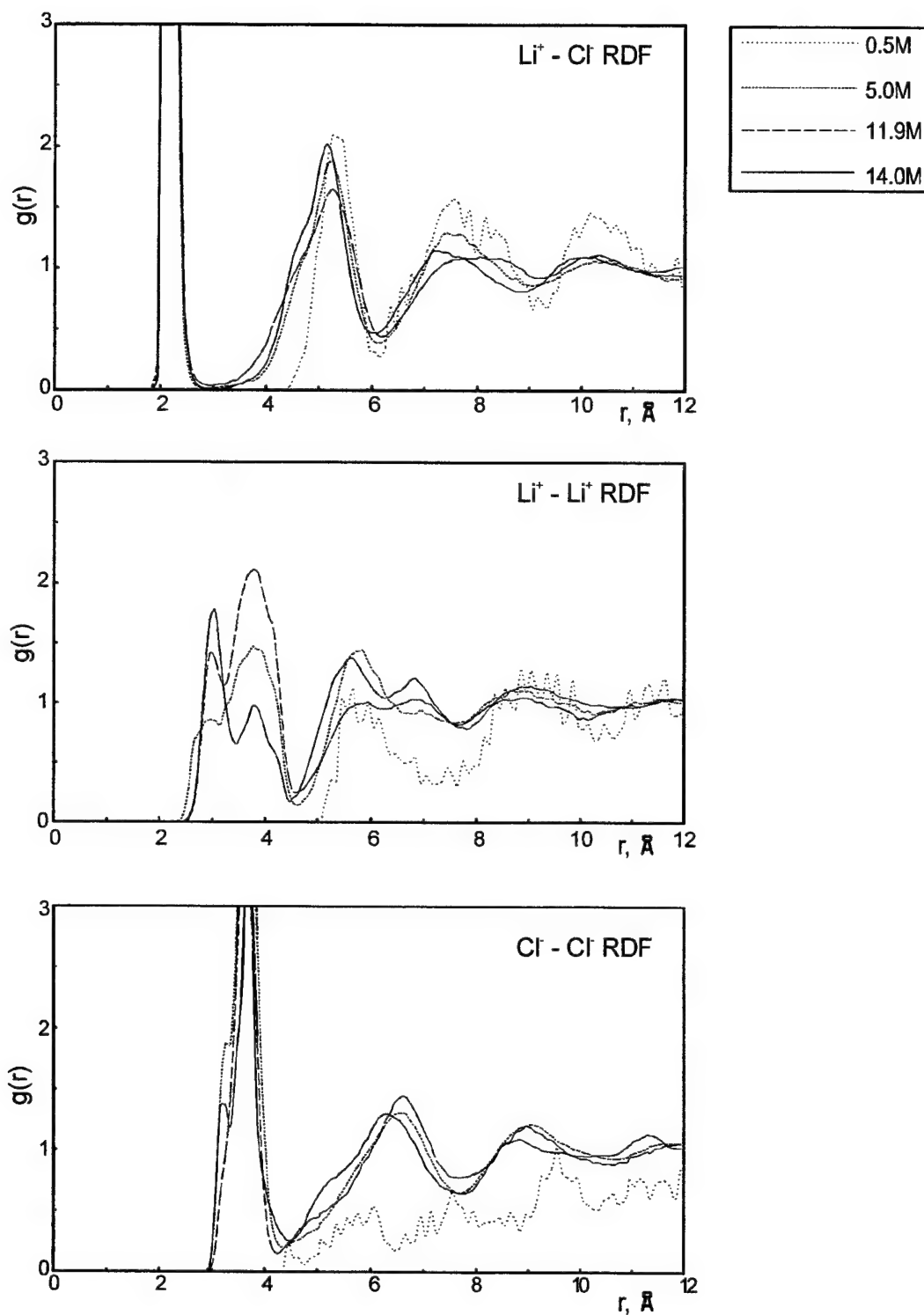


Fig. 4. The ion - ion radial distribution functions for LiCl solutions with concentrations: 0.5 M, 5.0 M, 11.9 M and 14.0 M. The upper figure shows the $\text{Li}^+ - \text{Cl}^-$ RDF, the figure in the middle shows the $\text{Li}^+ - \text{Li}^+$ RDF and the lower figure shows the $\text{Cl}^- - \text{Cl}^-$ RDF.

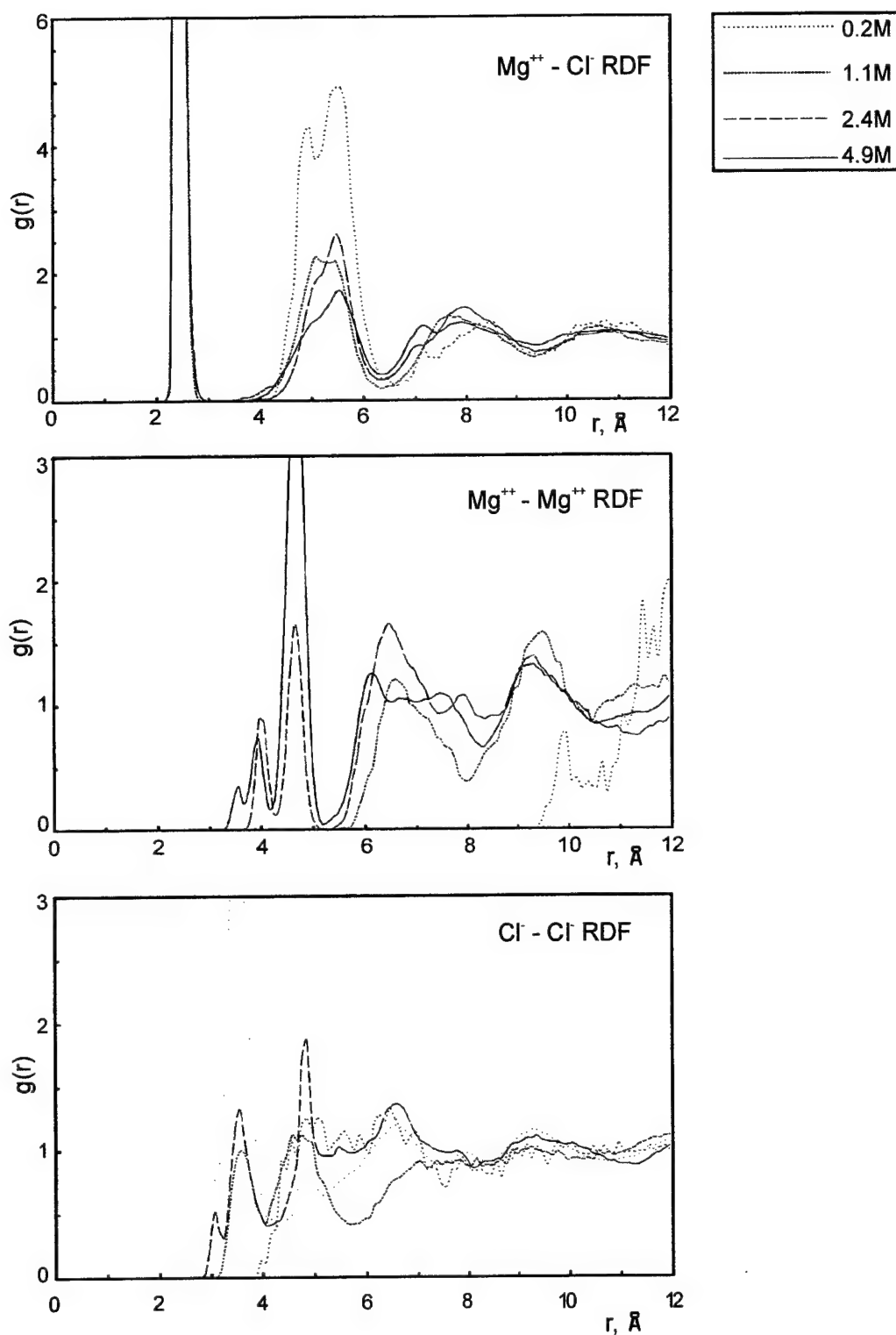


Fig. 5. The ion – ion radial distribution functions for MgCl_2 solutions with concentrations: 0.2 M, 1.1 M, 2.4 M and 4.9 M. The upper figure shows the $\text{Mg}^{2+} - \text{Cl}^-$ RDF, the figure in the middle shows the $\text{Mg}^{2+} - \text{Mg}^{2+}$ RDF and the lower figure shows the $\text{Cl}^- - \text{Cl}^-$ RDF.

The pair distribution function gives only a spherically averaged information about the system structure and the nonspherical ionic associations are sometimes masked. However, in the case of the concentrated NaOH, NaCl and LiCl solutions the presence of the ionic aggregates can be easily observed. We describe the correlations exhibited in Figure 2 (the NaOH case) in a more detailed way.

The cation – cation RDF (Fig. 2, middle part) significantly changes with the increase of the NaOH concentration. In the solution with the lowest concentration the positions of sodium ions are not correlated. In the case of 3 M solution there are three peaks visible at 3.2, 6.0 and 9.0 Å. The first peak corresponds to two Na⁺ ions separated by a H₂O molecule. The position of the first maximum moves to 3.1, 3.0, 2.95 and 2.9 Å in 6 M, 10 M, 14 M and 19 M solutions, respectively. Beginning from the 6M NaOH solution, the cation – cation RDF's exhibit peak typical to the crystal-like arrangement at 4.2 Å, corresponding to two sodium ions separated by two hydroxyl ions. Similar tendency could be observed for the anion – anion RDF plots. There are no correlations in 0.5 M solution, in 3 M (and more concentrated) solutions the maxima at 3.1, 6.3 and 8.9 Å are appearing as the number separated and Na⁺ separated ion pairs increases. The cation – anion pair distribution functions show three peaks at 2.1 Å, about 5 Å and 7.6 Å. The position of the second peak changes from 5.2 to 4.7 Å with the increase of the concentration. These data suggest that with the increase of the concentration the hydrated ions probably merge into ion-pair solvated complexes. Further increase of the concentration leads to appearance of multi-ionic structures and, finally, solvated crystals. The plots of the RDFs undoubtedly suggest the presence of higher ionic aggregates in concentrated NaOH solutions and, for the highest concentrations, the appearance of hydrated lattice-like structures.

Similar conclusions result from the analysis of the ion – ion radial distribution functions for NaCl and LiCl solutions (Figures 3 and 4, respectively).

Figure 5 represents somewhat different case: magnesium chloride, which is non-symmetric solution. All the RDF's change significantly with the increase of the MgCl₂ concentration. Let us begin with the Mg²⁺ - Mg²⁺ correlations. In the solution with the lowest concentration, 0.2 M, the positions of magnesium ions are not correlated. In the case of 1.1 M solution we observe two peaks at relatively large distances, 6.8 Å and 9.3 Å. From the concentration 2.4 M MgCl₂ upwards, the cation – cation RDFs exhibit peaks typical to the crystal-like arrangement at 4.0 Å and 4.8 Å, corresponding to two Mg²⁺ ions in contact through the Cl⁻ bridge and H₂O bridge, respectively. Similar tendency is observed for the Cl⁻ - Cl⁻ RDF. We do not observe any anion – anion correlations in 0.2 M solution. From the concentration 1.1 M upwards, the RDFs exhibit the maxima at 3.8 Å, 4.9 Å which correspond to the solvent separated and Mg²⁺ separated anion pairs. The cation – anion RDFs show three peaks at 2.3 Å, around 5.3 Å and 7.2 Å but the peak at the lowest distance does not appear in the 1.1 M solution. The structure of the Mg²⁺ - Cl⁻ RDF at the highest concentrations resembles typical RDFs for crystalline media. The evolution of the RDFs with the increase of the MgCl₂ concentration clearly reflects the process of merging of the solvated ions into solvated ion-pair complexes and further into multi-ion structures.

3.2. Voronoi polyhedra

Studies of the radial distribution functions have been completed by the calculations of the Voronoi polyhedra for the cation – anion coordination in the NaOH and MgCl₂ solutions. For a given cation (Na⁺ or Mg²⁺) we build the Voronoi polyhedron taking into account all the anions in the system. The calculation is repeated for all the cations in the simulation box and then repeated for a large number of the ion configurations in the simulation box recorded in the course of the simulation. The system of the polyhedra was then analysed with the aim to estimate a degree of order in the ionic structures. From many possible versions of such analysis (e.g. plotting the distributions of the number of walls of the polyhedra, calculating the effective coordination numbers, etc.) we include in the present paper the distributions of the anisotropy factor of the polyhedra and their evolution with the increase of the ion concentration.

Figure 6 shows the α -parameter distributions for the NaOH solutions with the concentrations 0.5 M, 10 M and 19 M (upper part of the figure) and for the MgCl₂ solutions with the concentrations 0.2 M, 2.4 M and 4.9 M (lower part). The distribution for the random system of the Lennard – Jones particles is given also in the figures. For very low concentrations (not shown in the figures) the α distributions resemble the distributions for the random system. Then, with the increase of the concentration the simulated distributions steadily evolve towards the distributions for the distorted fcc or bcc lattices. Figure 6 provides thus an additional support for the presence of multi-ion ordered structures in concentrated solutions.

Distribution of anisotropy factor α of Voronoi polyhedra

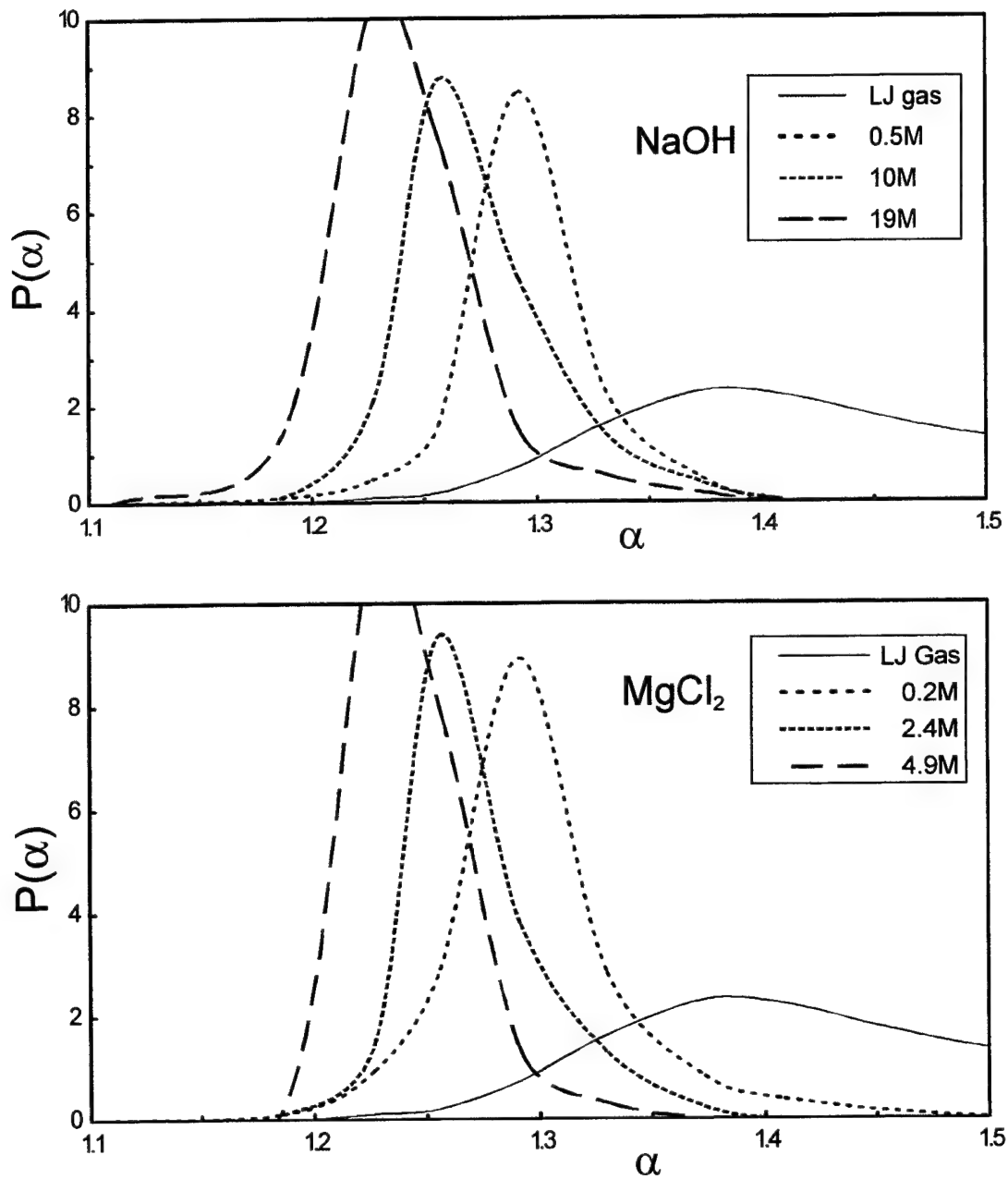


Fig. 6. Distributions of the anisotropy parameter α for the NaOH solutions with the concentrations 0.5 M, 10 M and 19 M (upper part of the figure) and for the MgCl₂ solutions with the concentrations 0.2 M, 2.4 M and 4.9 M (lower part). The distribution for the random system of the Lennard – Jones particles is given also in the figures.

4. CONCLUSIONS

The results of the simulations of the concentrated ionic solutions allow us to formulate the following conclusion. For a wide range of concentrations, from 1 M to 20 M, the geometry of the ionic configurations is significantly different from the geometry of a random set of points.

This conclusion is based on the analysis of the ion - ion radial distribution functions and on the comparison of the characteristics (such as distribution of the anisotropy coefficient or the distribution of the number of faces) of the Voronoi polyhedra constructed around the ions in the simulation box to the distribution calculated for the random tessellation of space. The Voronoi polyhedra for the simulated ion configurations in solutions have similar characteristics as the polyhedra drawn for the slightly distorted regular lattices of ions.

On a basis of these results, we can put forward a conjecture that regions or domains of the quasi-crystalline order of ions exist in the concentrated solutions. The quasi-crystalline order is more evident for lower part of the concentration range, between 1 M and 5-6 M. For the highest concentrations, the structure of the ionic configurations was determined not only by the ion - ion interactions but, perhaps even predominantly, by the interactions between the ions and the solvent molecules which belong at the same time to more than one solvation sphere. Finally, the increase of the charge of the cation, like Mg^{2+} , results in a more pronounced quasi-crystalline order. It seems that the results of the simulations of the concentrated ionic solutions support to a large extent the lattice theory of concentrated electrolytes.

ACKNOWLEDGMENTS

This work has been supported by the Government of the Republic of Poland as the KBN Grant 3 T09A 029 17

REFERENCES

1. R. W. Gurney, *Ionic Processes in Solution*, Dover, New York, 1963.
2. *Physical Chemistry. An Advanced Treatise. Vol. VIII: Liquid State*, ed. D. Henderson, Academic Press, New York, 1971
3. H. S. Franck, P. T. Thomson, in: *The Structure of Electrolytic Solutions*, ed. W. J. Hamer, J. Wiley, New York, 1959.
4. I. Ruff, "Theory of Concentrated Solutions of Strong Electrolytes. I. Some Thermodynamic Quantities of a Lattice-Like Network of Ions Surrounded by a Dielectric Gradient", *J. Chem. Soc. Faraday Trans. II*, **73**, 1858-1877 (1977).
5. I. Ruff, "Theory of Concentrated Solutions of Strong Electrolytes. II. Thermodynamic Properties of Mixed Electrolytes. Theoretical Basis of the Harned Rule", *J. Chem. Soc. Faraday Trans. II*, **75**, 1-11 (1979).
6. I. Ruff, G. Palinkas, K. Gombos "On the Transition from the Lattice-Like Structure of Electrolytes to the Debye-Hückel Limit", *J. Chem. Soc. Faraday Trans. II*, **77**, 189-1201 (1981).
7. K. Heinzinger, "Computer Simulations of Aqueous Electrolyte Solutions", *Physica*, **131B**, 196-2216 (1985).
8. K. Heinzinger, in: *Computer Modelling of Fluids, Polymers and Solids*, eds. R. A. Catlow, S. C. Parker, M. P. Allen, Kluwer Academic Publishers, Dordrecht, 1990, pp.357-394.
9. Y. Tamura, K. Tanaka, E. Spohr, K. Heinzinger, "Structural and Dynamical properties of an $LiCl \cdot 3H_2O$ Solution", *Z. Naturforsch.*, **43a**, 1103-1110 (1988).
10. M. P. Allen, D. J. Tildesley, *Computer Simulations of Liquids*, Clarendon Press, Oxford, 1994.
11. A. Okabe, B. Boots, K. Suigihara, *Spatial Tessellations*, J. Wiley, New York, 1992.

Dynamics of diffusion-controlled recombination of ions in ionic solutions. Limits of validity of the Debye - Smoluchowski equation

Krystyna Wolf^a and Witold M. Bartczak^{b,c}

^a Institute of Physics, Technical University of Łódź, Wólczńska 219, Łódź, Poland

^b Institute of Applied Radiation Chemistry, Technical University of Łódź, Wróblewskiego 15, Łódź

^c Chair of Theoretical Chemistry, University of Łódź, Pomorska 149/153, Łódź, Poland

ABSTRACT

The diffusion and recombination process in an ensemble of isolated single pairs of opposite charges is usually described by the Debye - Smoluchowski equation. The present work is an overview of a series of computer simulations of diffusion and recombination of ions in solution performed with the aim to determine the limits of validity of the Debye - Smoluchowski equation.

In the first part of the project, the calculations were performed for the media with the short mean free path (MFP) of the free movement of ions between scattering events, *i.e.*, for the conditions of the diffusion model of the ion transport. Results were obtained on the probability of ion survival as a function of time and the probability of ion escape from recombination at infinite time. The recombination processes in the clusters of non-separable ion pairs and the bulk recombination of ions in solution were simulated. The deviations of the multi-pair kinetics and escape probability from the corresponding results of the calculations performed on a basis of the Debye-Smoluchowski theory are significant but we found that the Debye-Smoluchowski recombination rate constant can be applied for all concentrations of ions.

We also consider the effects of restricted geometry and anisotropy of the medium on the kinetics of the recombination of oppositely charged species in each other's field and the escape probability. This model roughly corresponds to the electron - cation recombination in organic crystals.

The results for short MFP's were then compared with the results of the calculations of the electron - cation recombination in the systems characterized by long MFP of electron between the scattering events. It was found that for long mean free paths, above 10-20 % of Onsager distance in the medium ($R_c = e^2 / 4\pi\epsilon\epsilon_0 kT$, $\epsilon\epsilon_0$ is the dielectric permittivity of the medium, e - electron charge, $k_B T$ - the thermal energy), the recombination theory based on the Debye - Smoluchowski equation is no longer valid, even for isolated ion pairs.

Keywords: diffusion, ion recombination, rate constant, ionic solutions, computer simulation.

1. INTRODUCTION

The present theoretical basis for diffusion-controlled recombination of ions is provided by the Debye - Smoluchowski (DS) equation^{2,3} (see¹ for a source of references)

$$\partial C / \partial t = \nabla \{ D [\nabla C + (C / k_B T) \nabla U] \} \quad (1)$$

where $C(r, t)$ denotes the density of ions as a function of their spatial coordinates and time, V is the interaction potential between ions, D is the sum of the diffusion coefficients of cations and anions, k_B and T - the Boltzmann constant and temperature, respectively.

Unfortunately, this equation describes in fact only a single pair of interacting particles in space. If the interaction potential V corresponds to the Coulomb interaction $-e^2/4\pi\epsilon\epsilon_0$ in a dielectric continuum with the permittivity $\epsilon\epsilon_0$, then we can write the specific version of the equation for ions. In radial coordinates we obtain

$$\partial C/\partial t = D\{\partial^2 C/\partial r^2 + (2/r + R_c/r^2) \partial C/\partial r\} \quad (2)$$

with the boundary conditions at the encounter radius R in the form of either

$$C(R, t) = 0 \quad \text{or} \quad (3)$$

$$k_R C(R, t) = 4\pi R^2 D (\partial C/\partial r) \big|_{r=R} \quad (4)$$

where the former is known as the Smoluchowski condition and the latter as the radiation boundary condition, with k_R the reaction rate at encounter. The parameter R_c is called the Onsager radius and is defined as the distance at which the energy of the Coulomb interaction in dielectric continuum becomes equal to the thermal energy $k_B T$:

$$R_c = e^2/4\pi\epsilon\epsilon_0 k_B T \quad (5)$$

The DS equation looks deceptively simple. Its approximate solutions are known already quite long time (see ¹ for a review) but the full state-of-art solution for $C(r, t)$ has been published by Hong and Noolandi ⁴. When the spatial variable from $C(r, t)$ is integrated out, we obtain $P(t)$, the survival probability of an ion pair as a function of time. Proper averaging of $P(t)$ over the initial spatial arrangements of charged species leads to a time dependent quantity that can be compared with the macroscopic recombination kinetics. The limiting value of the spatial integral of $C(r, t)$, at infinite time, represents the probability that an ion escapes recombination and is known as the ion escape probability. The (simplified) formula given by Onsager ^{1,4} is as follows

$$P_{esc} = \{exp(-R_c/R_0) - exp(-R_c/R)\} / \{1 - exp(-R_c/R)\} \approx exp(-R_c/R_0) \quad (6)$$

where R_0 is the initial distance between the counterions.

The DS equation has been derived for charged species with a short mean free path (MFP) between consecutive collisions with the molecules of an isotropic medium, i.e. for ionic species or for excess electrons with a relatively low mobility. Therefore, incorrect results may be obtained when the DS equation is applied to a physical system for which one or more of these assumptions is violated. In this paper we consider the following major causes of breakdown of the DS equation:

- (1) Presence of multiple ion pairs (which leads to breakdown of the scaling properties of the DS equation);
- (2) Anisotropy of diffusion tensor
- (3) Long mean free paths of mobile charges and velocity-dependent scattering mechanism of mobile charges

The present work is an overview of a series of computer simulations of diffusion and recombination of ions in the systems containing isolated ion pairs or a number of nonseparable ion pairs, the systems with short or long MFP, and the systems with significant anisotropy of diffusion coefficients.

2. COMPUTER SIMULATION METHOD

The method which has been selected for calculations of the diffusion processes belongs to the class of the Stochastic Dynamics methods (Allen and Tildesley ¹²). The method ignores the neutral particles of the medium and treats them as a dielectric continuum - only the ions in the sample are treated on the molecular level. The influence of the neutral molecules is simulated by the random walk of the ions. This method has been successfully used to simulate the ion recombination in the ionization tracks of high-energy particles in nonpolar media ^{6, 7, 13}. This section will be devoted to a more detailed description of the computer simulation programs.

2.1. The diffusion type of transport of charged species (short MFP)

The initial positions of the ions are represented by a set of numbers in the computer memory. Different rules of the ion distribution in the systems can be applied - from fully random distribution of ions, through simulation of the Boltzmann

distribution, to regular geometrical arrangements of the ions. The simulation method does not account for the actual velocity of the ions nor the movement of the neutral molecules of the medium. We assume that the frequency of collisions of an ion with the medium molecules is so high and its mean free path between the collisions is so short that the ion velocity is a random variable. The influence of the medium molecules on a given ion is modelled by the random walk (Brownian movement) of an ion in continuous medium. The random vectors are obtained from the random number generator and they are properly scaled using the Einstein relation - the mean value of the squared distance in the Brownian motion is proportional to the time of motion and the proportionality coefficient is calculated from the experimental diffusion coefficient $\langle(\Delta r)^2\rangle = 6D\Delta t$. The ion drift vectors in electric field are obtained by solving the electrodynamic equations of motion using experimental mobilities of the ions. It is of course possible to include any type of external field affecting the movement of ions.

2.2. The transport of charged species with long MFP

The initial conditions in the long MFP case include also the velocities of the electrons which are sampled from the Maxwell - Boltzmann distribution for an assumed temperature. The random directions of the electron velocities are assumed. The simulation method does not account for the actual velocity of the positive ions nor the movement of the neutral molecules of the medium.

New positions of the cations and electrons are calculated in discrete time steps using the two-timescale technique. The long time step Δt_c is selected for cations. Due to high electron mobility, the position of an electron can change quite significantly during the cation time step. The short time step Δt_e is selected for a given electron in the following procedure. First, an actual value of the electron path λ is sampled from the exponential distribution of λ . Having selected the time step Δt_e , the trajectory of a given electron is calculated by the numerical solution of the electrodynamic equations of motion (for a classical particle). At the end of the trajectory the mobile charge is scattered. The scattering mechanism was based on the assumption of complete randomization of velocity of the electron on collision. The model seems to be oversimplified, particularly in the case of elastic scattering and the correlations. On the other hand, the assumption of the full randomization of the electron momentum makes possible the direct comparisons between the diffusion transport and the long MFP cases and systematic investigation of the recombination kinetics and the escape probability as functions of the MFP length.

For the both cases, short and long MFP, new positions of the ions are calculated in discrete time steps. If any ion pair fulfills the assumed recombination criteria the algorithm simulates the ion recombination - the ions disappear from the file of the "living" ions and their positions are no longer modified. The program records the time from the beginning of the simulation run which will serve to construct the kinetics of the recombination process.

The simulation runs until a prescribed number of time steps (usually 10^4 or 10^5 time steps) or is terminated in the case of disappearance of all the ions in the simulated sample. The program starts again for a new geometrical configuration of ions and is repeated for a large number of the configurations. To obtain a good statistics of the recorded data and smooth kinetic curves, as much as about 10^6 ions are necessary, and even more in certain specific cases like the investigation of the long-time effects.

3. RESULTS AND DISCUSSION

3.1. Recombination in ensembles of clusters of nonseparable ion pairs - short MFP case.

There are numerous examples of multiple ion-pair systems. The ionic solutions which undergo some form of ionic reaction, ion pairing or nucleation make an obvious example. Typical concentrations of ions, from 10^{-4} M to 10 M, cause any reduction of the system to a collection of isolated ion pairs to be rather far from physical reality. Another example of the ensembles of nonseparable ion pairs is provided by the ionizing radiation. A high-energy particle when passing through condensed medium leaves in its wake clusters of ion pairs - 2, 3, 4 or even more ion pairs. In the case of heavy particles, like the α particles, we observe the columns of ionization. The ion pairs can not be separated and treated as the isolated entities. In the study of the chemical effects of high-energy radiation the consideration of the nonhomogeneous spatial distribution of the chemically active transients in the track plays an important role and considerable attention has been given to this problem, notably for the case of water and nonpolar liquids.

The recombination processes in spurs with more than one ion pair were studied by several authors. For the hydrocarbon systems characterized by short free paths of charged species, Bartczak and Hummel^{6,7} proposed a random flight simulation. They found that the multipair effects may lead to substantial changes in the recombination kinetics, the ion escape

probability at infinite time as well as the singlet/triplet ratio among the recombination products^{8,9}. Extensive studies of the multipair effects in different systems were performed by Green and coworkers (see^{10,11} and references therein).

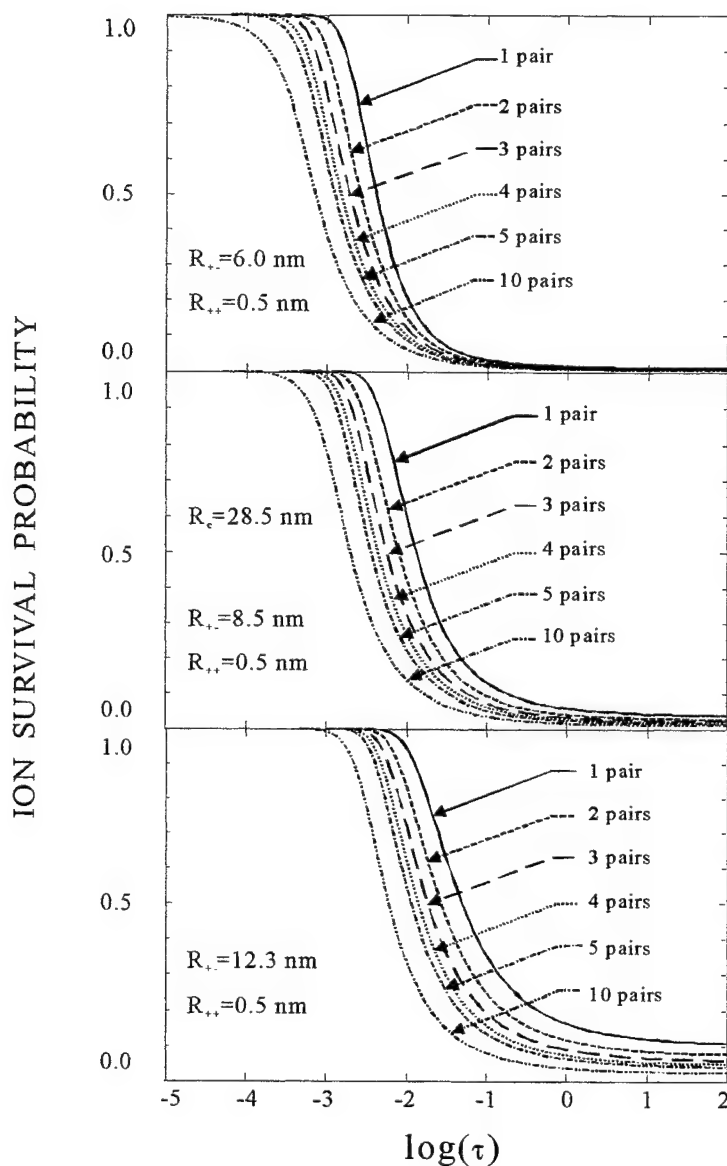


Fig. 1. The ion survival probability as a function of the logarithm of time for single-pair (full curve) and for multi-pair systems. The calculations correspond to the short MFP or diffusion model. The broken curves correspond to clusters initially composed of 2, 3, 4, 5 and 10 ion pairs, respectively. The initial distance between cations of different pairs is $R_{++}=0.5$ nm, the initial distance between cation and anion of the same pair is: $R_{+-}=6.0$ nm (upper figure), $R_{+-}=8.5$ nm (middle part) and $R_{+-}=12.3$ nm (lower figure). The diffusion coefficients for cations and for anions are $D_+ = D_- = 1.26 \times 10^{-9}$ m²/s, the Onsager radius is $R_c=28.5$ nm, the reaction radius $R=1.0$ nm. The time is expressed as a dimensionless parameter $\tau=Dt/R_c$.

The simulation of the ion recombination processes has been performed for systems of isolated clusters of ions, containing 1,2, 3, 4, 5 and 10 nonseparable ion pairs^{6,7} (later it was extended to large systems, such as ionization tracks¹³). An example of the results of the simulation, in the form of the time evolution of the ion survival probability, is given in Figure 1. The calculations allow us to compare the recombination kinetics calculated for the single pairs (the solution of the Debye-Smoluchowski equation) with those calculated for the multiple-pair clusters. The initial distance between the cation and the anion of a pair is assumed as $R_{+-}=6.0$ nm, 8.5 nm and 12.3 nm for the upper, middle and lower part of the figure, respectively. In the case of the clusters composed of more than one ion pair, the cations are placed on a straight line, $R_{++}=0.5$ nm apart, and the anion from a given pair is selected in random direction around its geminate cation. We performed the test calculations for different geometrical arrangements of the cations and the results were very similar. The calculations correspond to the ions in a nonpolar medium, with the dielectric permittivity $\epsilon=2$ and the Onsager radius $R_c=28.5$ nm.

The figure proves that the multiple-pair effects in the diffusion equation are indeed significant. The full line on the right hand side of the series of the kinetic curves represents the single-pair solution of the DS equation. One can see that even the recombination of ions in two-pair clusters shows some deviations from the single-pair model. When we refer to the kinetics obtained for the 10-pair clusters, the kinetics of the process is shifted by a time decade (the abscissa is expressed in the logarithmic scale) with respect to the DS kinetics.

Figure 2 shows the dependence of the ion escape probability on the initial cation - anion distance for single pairs (full line calculated from the Onsager formula) and for the clusters of 2, 3, 4, 5 and 10 ion pairs. The abscissa is defined as the inverse distance $1/R_{+-}$, the scale of the ordinate is logarithmic. In this coordinate system the Onsager dependence is linear. The dashed and dotted curves represent the best fitting to the results for 2,3,4,5 pairs. For these clusters, the curvature of the fitted curves is very slight. The fitting for the 10-pair clusters shows more significant deviation from linearity. The ion escape probability for the clusters of more than one ion pair is lower than the Onsager probability. It is important to underline that this rule is true only for short distance between the cations, $R_{++}=0.5$ nm, for which the calculations of Fig. 2 have been performed.

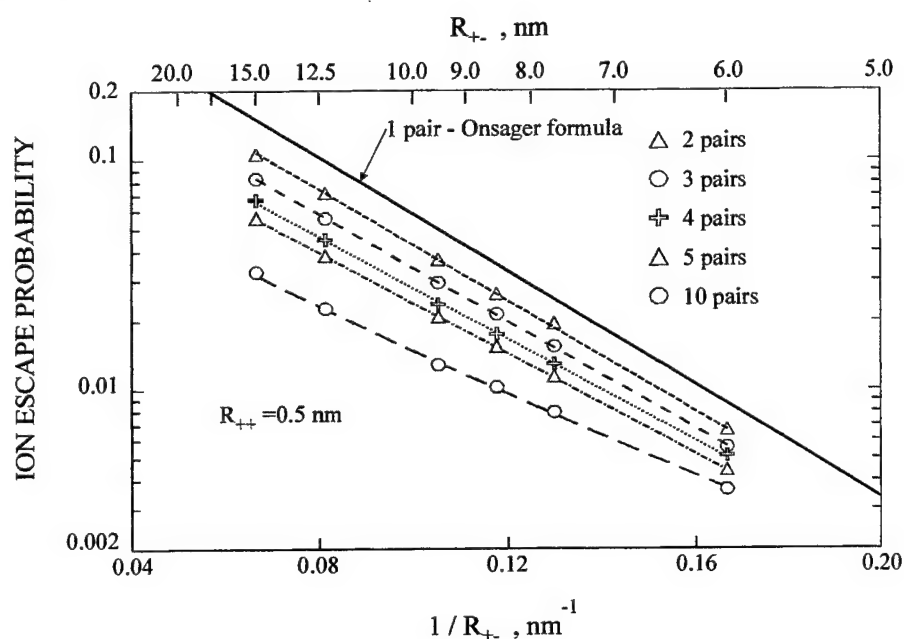


Fig. 2. The P_{esc} for the diffusion model as a function of the initial cation-anion distance for ions in groups of 2, 3, 4, 5 and 10 ion pairs with the separation of $R_{++}=0.5$ nm between cations and for single pairs (full line, calculated from the Onsager formula). The parameters are: the reaction radius $R=1.0$ nm, $R_c=28.5$ nm. The distance R_{+-} is given as the upper abscissa, $1/R_{+-}$ is given as the lower abscissa.

Interesting example which shows the potential of the simulation method in analysis of ion diffusion process is given below. Two important scaling properties of the DS equation can be mentioned: i) the time evolution of the ion density and its spatial integral, *i.e.* the ion survival probability, depends on the sum of the diffusion coefficients $D_+ + D_-$ but does not depend on the individual coefficients; ii) the probability P_{esc} that an ion escapes recombination after infinite time does not depend on the diffusion coefficients of the cations and anions at all.

Using the computer simulation method we calculated the ion survival and the ion escape probability as a function of time in the systems composed of independent clusters of pairs, from $N=1$ to 10 pairs. The sum of the diffusion coefficients is, for all the simulations, $D_+ + D_- = 2D = 2.528 \times 10^{-9} \text{ m}^2/\text{s}$. The calculation of the ion escape probability as a function of N was performed for three cases: for immobile anions $D_-=0$ and mobile cations, for the same mobilities of cations and anions $D_+=D_-=D$ and for immobile cations $D_+=0$. The recombination kinetics is different for these cases, in contrast with the first scaling property of the DS equation. We observe quite significant difference between the extremal cases of the escape probability P_{esc} : $D_+=0$, and $D_-=0$. The ions in the $D_+=2D$ case recombine faster at the initial phase of the process but the ion decay slows down at long times and its asymptotics, *i.e.* the escape probability, is higher than the $D_+=0$ result.

3.3. Kinetics and rate constant of bulk recombination of ions in solutions

It is assumed (ref.¹, p.59) that for high ionic concentrations the rate of recombination decreases below the Debye-Smoluchowski limiting rate

$$k_{DS} = 4\pi R_c D / \{1 - \exp(-R_c/R)\} \approx 4\pi R_c D \quad (7)$$

towards the rate typical for neutral molecules:

$$k_S = 4\pi R D. \quad (8)$$

The conjecture is reasoned out as follows. In the system of many ionic charges, the charges of an individual pair are in a sense neutralized. When two ions are alone in space the Coulomb field dominates the diffusion processes but in the system of a large number of charges the ions should behave like almost neutral molecules and their effective radius of influence is reduced from a large Onsager radius R_c to a much smaller radius comparable with the encounter radius R . In the case of hydrocarbons we can expect quite substantial reduction of the rate constant at high concentrations (by a factor of 100). For polar solutions the reduction of the rate constant is not so spectacular, but even in the case of aqueous solutions we can expect the reduction by a factor of 2-3.

The recombination kinetics described so far is calculated for the multiple-pair but finite systems. In order to simulate infinite systems the periodic boundary conditions have been introduced. We place a certain number of ions in the simulation box. If we assume a given size of the box then the number of ions is calculated from the concentration. The central box is then repeated periodically in all three directions: x , y , z . The typical size of the box differs from 10 nm to 20 nm and usually contains few hundred independent ions. The infinite size of the system causes also another problem. The Coulomb forces are of infinite range and the ions from even very far boxes interact with the ions from the central box. Therefore the field acting on a given ion has to be calculated by summing up the contributions from infinite number of ions. The Ewald method has been used to calculate these forces in our simulations. The method is explained in the Allen and Tildesley book¹².

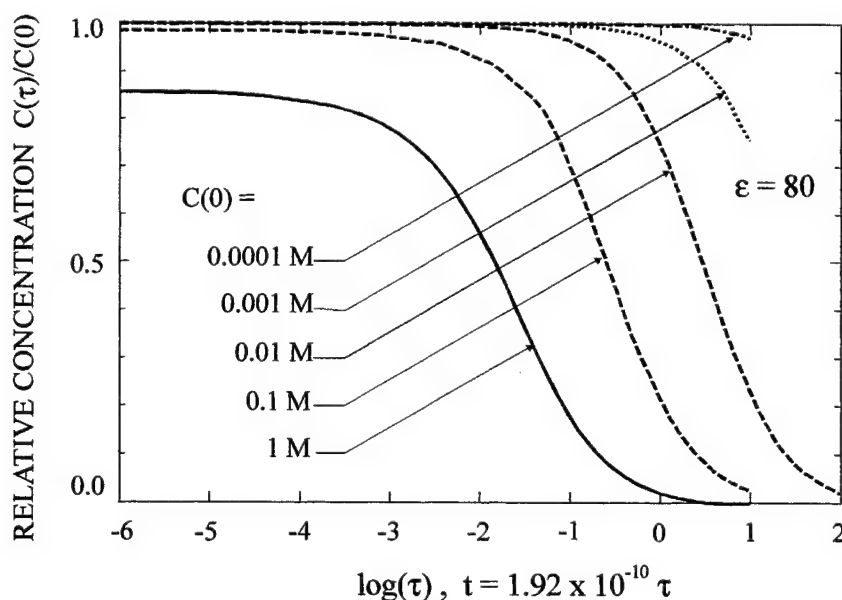


Fig. 3. The ion survival probability as a function of the logarithm of the dimensionless time τ obtained by the computer simulation of the diffusion and recombination of ions in solutions with the dielectric constant $\epsilon=80$ and for the ion concentrations 10^{-4} M, 10^{-3} M, 10^{-2} M, 10^{-1} M, 1 M.

Figure 3 shows the evolution of the relative concentration of ions for the ion recombination in ionic solutions, for a series of initial concentrations: 10^{-4} M, 10^{-3} M, 10^{-2} M, 10^{-1} M, 1 M. The simulation was performed for the dielectric constant $\epsilon=80$, which corresponds to an aqueous solution. The figure shows the recombination kinetics as a function of the dimensionless time τ , which is defined as $\tau=Dt/R_c^2$ and, for the assumed parameters, we have the relation between the real time and the dimensionless time that is given in the figure. The time axis is expressed as the logarithmic scale. The time scale spans over eight time decades.

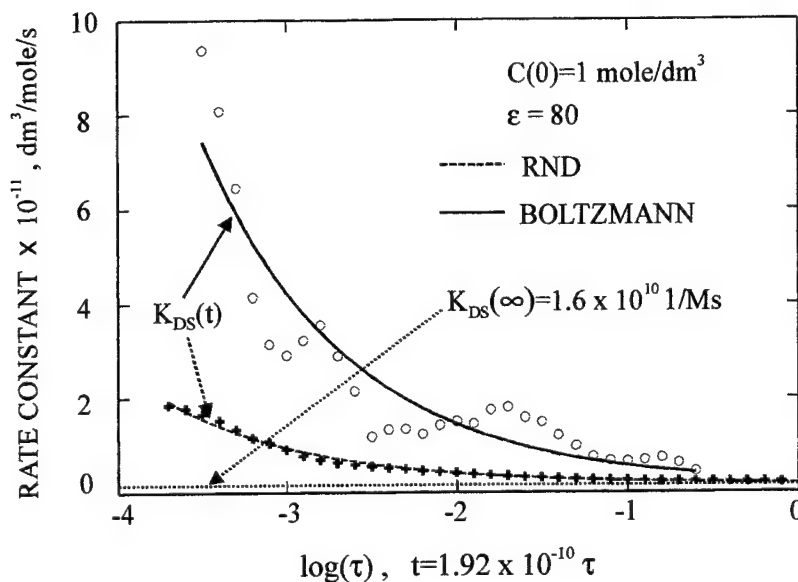


Fig. 4. The results of the rate coefficient calculations for the ion concentration $C=1$ M in an aqueous solution ($\epsilon=80$).

The circles and crosses show the rate coefficient of recombination as a function of the logarithm of (dimensionless) time calculated by direct differentiation of the simulated kinetics of Fig. 3. The circles correspond to the Boltzmann initial distribution of cation – anion distances, the crosses correspond to a random configuration of ions. The full and dashed curve show the time dependence rate that results from the Debye-Smoluchowski model for the Boltzmann and random condition, respectively, and the dotted horizontal line is the stationary rate constant.

The reaction rate constant has been calculated by direct differentiation of the ion survival probability $P(\tau)$ over the time τ . The results of the rate constant calculation are given in Figure 4. These results show the time dependence of the rate constant. The circles show the simulated rate coefficient for the Boltzmann initial distribution of the cation – anion distances and the crosses for the random configuration of ions. The Debye-Smoluchowski rate constant (calculated from the full time - dependent formula) is shown also in the figure as the full line for the Boltzmann condition and the dashed curve for the random condition. The asymptotic value of the rate is $k_{DS} = 1.614 \times 10^{10}$ l/mole/s, more than two times higher than the rate for neutral molecules $k_s = 4\pi RD = 0.747 \times 10^{10}$ l/mole/s (the encounter reaction radius has been assumed as 0.4 nm). The simulated rate reaches the steady state value in the last decade. The rate is 2.05×10^{10} l/mole/s.

Figures 5 and 6 summarize the results of the rate constant calculations. In Figure 5 the rate constants are shown as a function of the initial concentration of ions in the solution, $C(0)$. Two sets of the rate constants are given: for $\epsilon=10$ and $\epsilon=80$. The corresponding horizontal lines show the values of the steady-state Debye-Smoluchowski rate constant. In Figure 6 the rate constants are given as function of the dielectric permittivity of the solution ϵ . The simulated results (squares) for $C(0)=0.01$ M, for which the interionic distance is on average about 4.4 nm, are compared with the theoretical Debye-Smoluchowski rates (full curve) and with the rate for the neutral molecules (horizontal dotted line).

Commenting upon the results of these calculations, we found rather interesting and unexpected behaviour of the diffusion-controlled recombination processes in concentrated ionic systems. According to qualitative conjectures, it was expected that the rate constant will decrease with the increase of the ion concentration, from the Debye-Smoluchowski limiting rate for the isolated pairs to the rate constant $k_s=4\pi RD$ typical for neutral molecules (represented in Figures 5 and 6 by the horizontal dashed line). However, the picture obtained from the simulations is different. Roughly, we can summarize it as follows: the ions of the reacting ion pair are not influenced by all the other charges of the system and their reaction rate does not depend on the overall density of charge. The discussion of these results from the point of view of experimental measurements of the rate constant of ionic reactions is given in ^{17, 19}. Marciniak and Rozwadowski ¹⁸ investigated the reaction rate constants for the recombination of the positively charged organic ions (derivatives of pyridine) with a series of singly and multiply charged ions with the concentration of between 10^{-3} and 10^{-2} mole/l. They obtained the rate constants about 1.3×10^{10} l/mol/s whereas the rate constants for similar reactions but with neutral molecules were about 4×10^9 l/mol/s, more than 3 times lower. These results are in very good agreement with our simulation results.

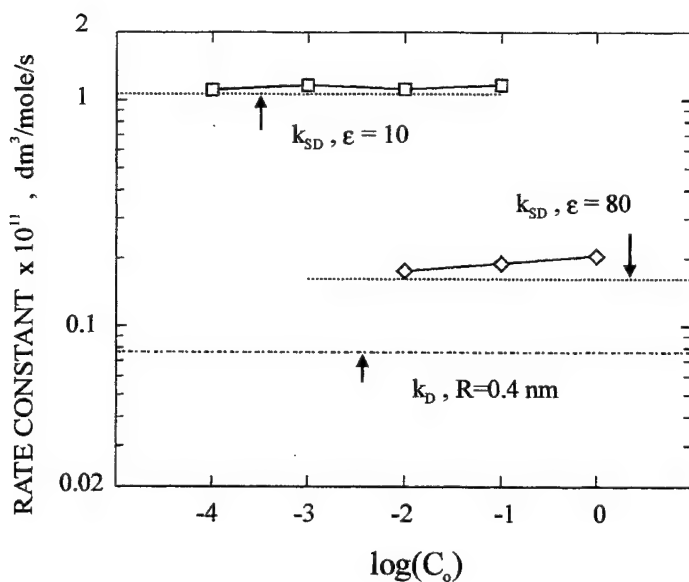


Fig 5. The compilation of the rate constants from the simulations of the homogeneous recombination. The steady state rate constant is given as a function of the initial ion concentration in the solution. The squares show the results for slightly polar solutions ($\epsilon=10$), the diamonds correspond to aqueous solutions ($\epsilon=80$). The horizontal dotted lines in the vicinity of the simulated rate constants show the values of the theoretical, single-pair rate k_{DS} . The dashed line at the bottom of the figure shows the value of the rate constant for the neutral particles reacting at encounter.

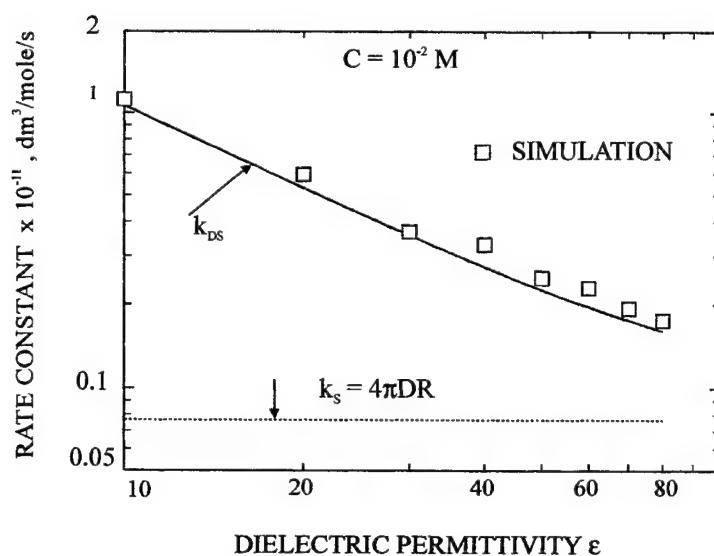


Fig 6. The rate constant of the ion recombination in the solutions with the initial concentration $C(0)=10^{-2}$ M calculated as a function of the dielectric permittivity of the solution. The results of the simulation are shown as the squares, the single-pair Debye-Smoluchowski rate constant is shown as the full curve, the rate constant for neutral molecules with $R=0.4$ nm is represented by the horizontal dotted line.

3.4. The charge recombination in the systems characterized by anisotropy of diffusion coefficient

Studies of the migration of the charged species induced by high-energy radiation in various solid systems have been carried out recently¹⁵. In some cases the kinetics of the charge recombination is complicated by the fact that the mobility of the charged species differs in different directions. For example, in crystalline polyethylene a large anisotropy has been observed, the mobility having been found to be at least a factor of 100 larger in the direction of the chain than perpendicular to it¹⁶. In various "conducting" polymers the charge migration takes place along the chain and in phtalocyanine and porphyrin aggregates along the columnar stacks.

For the computer experiments discussed in this chapter¹⁴ we assume that the medium is characterized by the diffusion coefficient D_z in the z -direction and the diffusion coefficient $D_x=D_y=D$ in the direction perpendicular to the z -axis. The degree of anisotropy is represented by the coefficient $\delta=D_z/D$. The diffusion tensor is thus assumed in the diagonal form, without any off-diagonal components. The diagonal elements D_z and $D_x=D_y$ can differ as much as by factor of 10 in our calculations, although in molecular crystals the ratio δ does not exceed the value of 2-3. In the present calculations we assume δ as a free parameter and we perform the simulations for selected values of δ from the range 1 - 10. When the calculations have to be compared with the isotropic case, we calculate the effective diffusion coefficient, D_{eff} , defined as the cube root of the determinant of the diffusion tensor, $D_{eff}=D(\delta)^{1/3}$.

Figure 7 shows the kinetics of the ion recombination. The probability of the ion survival against recombination up to time t is plotted as a function of the logarithm of the dimensionless time $\tau=Dt/R_c^2$, $D=D_{eff+}+D_{eff-}$, and D_{eff} is the cube root of the determinant of the respective diffusion tensor. The kinetics in Fig. 8 were calculated for relatively high anisotropy coefficient $\delta=10$. Different curves in the figure correspond to different angles θ between the z -axis (i.e. the direction of the fast movement) and the axis defined by the cation and anion of the pair. The calculations were performed for the angles: 0° (the pair axis aligned with the z -axis), 30° , 60° , 90° (the pair axis perpendicular to the direction of the fast movement). These calculations are represented by the broken or dotted curves. The thick full line gives the results of the calculations for the averaged kinetics: the negative ion was produced on a sphere in a random direction around the positive ion. In all the cases the initial cation - anion distance was fixed: the initial distance was $R_{+-}=7.7$ nm. Finally, the thin continuous curve shows the corresponding kinetics in isotropic media. The diffusion coefficients are: for cations $D_{+z}=\delta D_+$, $D_{+x}=D_+$, $D_{+y}=D_+=2.527 \times 10^{-10}$ m²/s, for anions $D_{-z}=\delta D_-$, $D_{-x}=D_-$, $D_{-y}=D_-=2.527 \times 10^{-8}$ m²/s. The medium parameters correspond to a nonpolar medium with the Onsager radius $R_c=30$ nm.

The recombination kinetics for different angles θ are significantly different one from another even for low anisotropy. For the anisotropy coefficient $\delta=10$ the curves for $\theta=0^\circ$ and $\theta=90^\circ$ are shifted by more than a time decade. The recombination at low angles θ is the fastest and the escape probability is the lowest. In the contrary, for high θ the recombination process is slower and the escape probability very high. For $\delta=2$ the escape probability at $\theta=90^\circ$ is almost 4 times higher than the probability at $\theta=0^\circ$, for $\delta=10$ the ratio of the escape probabilities can be as high as 30 - 40. The angle averaged kinetics of recombination has no longer typical shape of the diffusion-controlled kinetics but extends over large number of time decades and becomes similar to the dispersion-type kinetics with time-dependent rate constant.

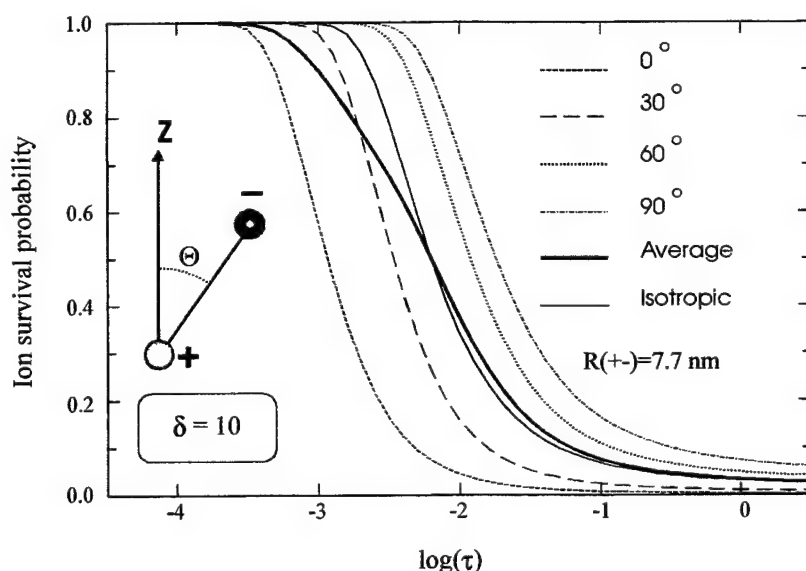


Fig. 7. The ion survival probability as a function of logarithm of (dimensionless) time for the systems with axial anisotropy. The anisotropy coefficient $\delta=10$. The series of broken curves correspond to the following angles θ between the z -axis of the coordinate system and the position vector of the anion relative to the position of the cation of a pair: $\theta=0^\circ$, 30° , 60° and 90° . The thick continuous line shows the kinetics averaged over the angle θ , the thin line is the isotropic kinetics.

3.5. Kinetics and escape probability for different lengths of MFP - recombination of isolated ion pairs.

Electron mobility μ in chain or cyclic hydrocarbons is low: in *n*-pentane and *n*-hexane at room temperatures is $1.4 \times 10^{-5} \text{ m}^2/\text{Vs}$ and $0.9 \times 10^{-5} \text{ m}^2/\text{Vs}$, respectively, in cyclohexane $3.5 \times 10^{-5} \text{ m}^2/\text{Vs}$ (see for instance ⁵). There is however a class of liquids where an excess electron has much higher mobility: tetramethylsilane ($\mu=1 \times 10^{-2} \text{ m}^2/\text{Vs}$ at 296 K), methane ($\mu=3.73 \times 10^{-2} \text{ m}^2/\text{Vs}$ at 120 K), argon ($\mu=4.9 \times 10^{-2} \text{ m}^2/\text{Vs}$ at 87 K), etc. Using Langevin relation (see ref. ⁵) between the electron MFP λ and the mobility μ : $\mu=\lambda (e/3k_B T) U_{ms}$ (where U_{ms} is the root mean square velocity of thermalized electron calculated from the Maxwellian distribution) we obtain the MFP for electron in *n*-pentane or *n*-hexane of the order of $1 \times 10^{-2} \text{ nm}$ but in tetramethylsilane the MFP is 6.05 nm, in methane 22.5 nm and in argon 29.6 nm. The latter MFP's are similar to the Onsager distance in these media.

In the case of a large MFP the electron may pass, keeping to an orbital trajectory, at a very short distance from a positive ion, without recombining, and move away from the cation again. Experimental evidence for this phenomenon is given by the decrease of the recombination rate k_r for high mobility systems, e.g. liquid methane. Also the increase of the yield of escaped charges in such systems as liquid methane, neopentane and tetramethylsilane in comparison with low mobility liquids may be an indication of this phenomenon. An excellent review of the experimental and theoretical results on ion recombination in the systems characterized by long mean free path of electrons is given by Schmidt ⁵. The calculations (see refs. ^{5, 20}, for a source of references) have proven that when the MFP of electrons is increasing towards the values of the order of the Onsager length R_c in a given medium, the theory of transport and recombination of charges that is based on the DS equation does not describe properly the recombination kinetics, ion escape probabilities nor rate constant of recombination. In the case of the geminate recombination, the escape probability at infinite time becomes higher than the probability that results from the Onsager formula, much higher for MFP of the order of R_c . The rate constant for electron - cation recombination in high-mobility liquids k_r is lower than the DS rate $k_{DS}=4\pi D R_c$. There is no explicit calculation of the electron - cation geminate recombination process in the system of more than one e⁻-cation pair. This is particularly important in the experiments where the electron - cation pairs were produced by ionizing radiation and a large part of the ionization appears in the form of clusters of nonseparable ion pairs.

In order to compare the results for long MFP with the calculations performed for short MFP and low mobility electrons, the first series of the simulations has been performed for single pairs electron - cation. The results of the calculations of the kinetics of recombination are presented in Figure 8. The kinetic curves are plotted versus logarithm of the dimensionless time τ defined as $\tau=Dt/R_c^2$ where $D=e\mu/k_B T$ is the diffusion coefficient of the electrons (the diffusion coefficient of the cations is negligible as compared to D).

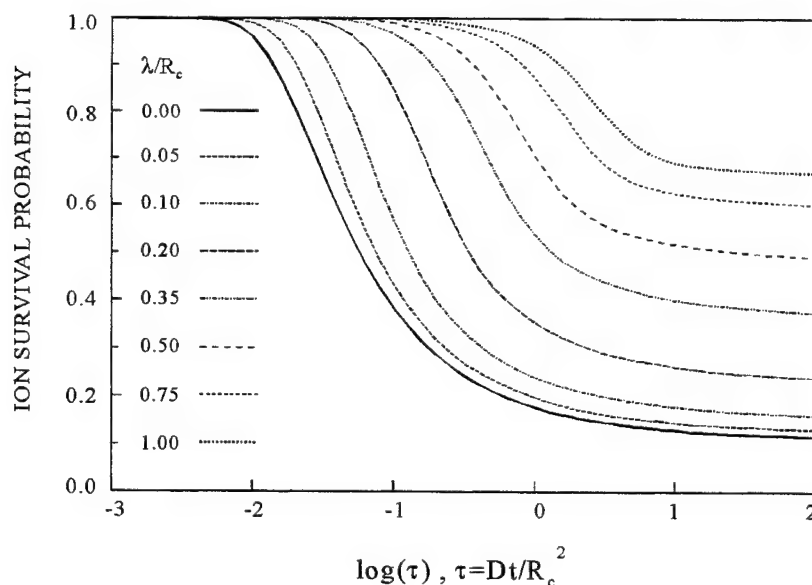


Fig. 8. The probability of electron survival up to the time t plotted as a function of the logarithm of $\tau=Dt/R_c^2$. The calculations were performed for single ion pairs. The different curves correspond to different length of the mean free paths (MFP) of electron: from $\lambda=0$ (the infinitely short MFP or the DS case), for $\lambda=0.05R_c$, $0.10R_c$, $0.20R_c$, $0.35R_c$, $0.50R_c$, $0.75R_c$ to $\lambda=1.0R_c$, where $R_c=28.5 \text{ nm}$ is the Onsager radius. The cation - electron initial distance is $R_+=0.45R_c$.

The full curve is calculated on a basis of the diffusion model and represents the DS kinetics of the ion recombination for isolated ion pairs in a nonpolar medium with $R_c=28.5$ nm. Physically, this kinetics corresponds to the electrons with mobility of the order of $5 \times 10^{-8} \text{ m}^2/\text{Vs}$, i.e. the mobility of the classical ions. The remaining kinetic curves correspond to the mean free path of the electrons of $0.05R_c$, $0.10R_c$, $0.20R_c$, $0.35R_c$, $0.50R_c$, $0.75R_c$ and $1.00R_c$ or to the electron mobilities from $2.4 \times 10^{-3} \text{ m}^2/\text{Vs}$ to $4.7 \times 10^{-2} \text{ m}^2/\text{Vs}$ for $0.05R_c$ and $1.00R_c$, respectively. It is worth to note a dramatic difference between the DS kinetics and the kinetics for the MFP $\lambda=1.00R_c=28.5$ nm. The results for the MFP $\lambda=0.20R_c$ are also very much different from the diffusion-controlled limiting case. The DS kinetics may be, with acceptable errors, applied only to the case of $\lambda=0.05R_c=1.43$ nm and this seems to be the limit of applicability of the DS equation.

Figure 9 shows the results of the calculations of the probability that an electron - cation pair ultimately escapes recombination. The probability is plotted as a function of the initial cation - electron separation R_{+} . The results were obtained from the long-time parts of the kinetic curves by fitting the kinetics to the function τ^α and taking the limit $\tau \rightarrow \infty$. A series of calculations were performed for the following values of the MFP λ : $0.05R_c$, $0.10R_c$, $0.20R_c$, $0.35R_c$, $0.50R_c$, $0.75R_c$, $1.00R_c$, labeled in the figure. The curve marked with "+" and the label ONS was calculated from the Onsager formula for the diffusion-controlled case: $P_{esc} = \exp(-R_c/R_{+})$. Similarly as in the case of the kinetic curves of Figure 1, we can see dramatic differences between the Onsager escape probability and the probability for the MFP $\lambda > 0.05R_c$. The increase of the escape probability above the Onsager limit exceeds an order of magnitude.

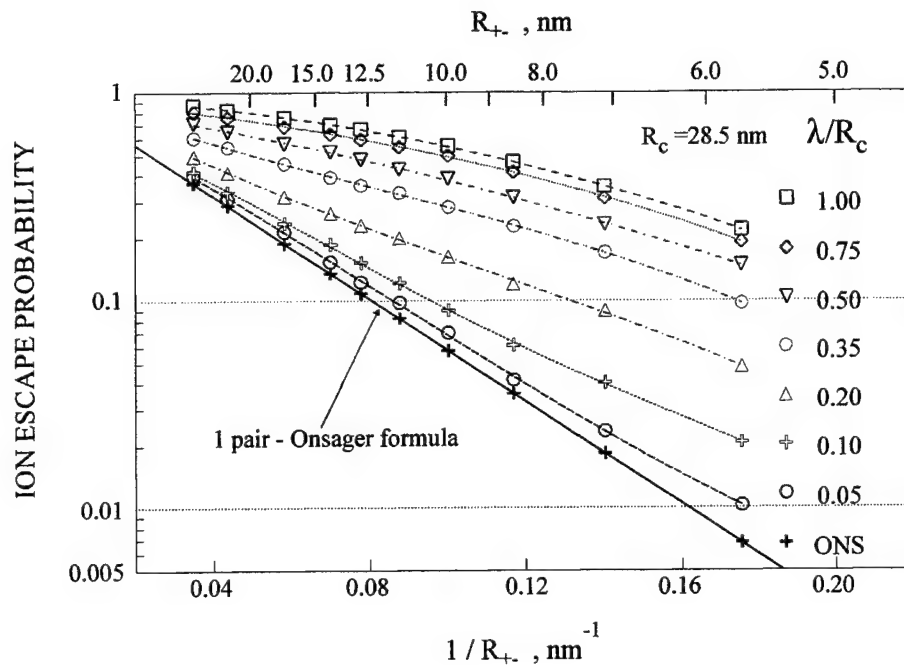


Fig. 9. The escape probability as a function of the inverse of the initial cation - electron distance R_{+} . The calculations were performed for single ion pairs. The different curves correspond to different lengths of the mean free paths (MFP) of electron: from $\lambda=0$ (the Onsager case, marked ONS), for $\lambda=0.05R_c$, $0.1R_c$, $0.2R_c$, $0.35R_c$, $0.5R_c$, $0.75R_c$ to $1.R_c$.

4. CONCLUSIONS

The limits of validity of the Debye - Smoluchowski equation applied to diffusion-controlled recombination of charges were investigated by means of the computer simulation method.

The scale of the deviations of the kinetics of the recombination process in the multi-pair clusters from the kinetics for the isolated pairs was estimated. The deviations of the multi-pair kinetics and escape probability from the corresponding single-pair results are significant. The kinetic curve for recombination in multi-pair clusters may be shifted by more than time decade from the DS kinetics and the escape probability can be lower by an order of magnitude than the Onsager probability for the same set of parameters. However, in the case of the bulk recombination of ions in solution, in spite of the significant difference of the simulated kinetics and the DS kinetics, the steady-state rate constants of recombination are quite close to the k_{DS} rate, even for very high concentration of ions.

Some differences between the simulated kinetics and the DS kinetics were also noted for the systems with marked anisotropy of the diffusion tensor.

For the processes with long mean free path of charges the scale of deviations is much higher. If the length of the electron MFP exceeds, say, $0.05R_c$, the deviations of the recombination kinetics and the escape probability from the respective values obtained on a basis of the diffusion mechanism are so large, that neither the DS equation nor the Onsager formula can be applied to describe the recombination between positive and negative charges.

ACKNOWLEDGMENTS

This work has been supported by the Government of the Republic of Poland as the KBN Grant 3 T09A 029 17

REFERENCES

1. S. A. Rice, *Diffusion-Limited Reactions*, Elsevier, Amsterdam, 1985.
2. M. Smoluchowski, "Versuch einer mathematischen Theorie der Koagulationskinetik kolloider Lösungen", *Z. Phys. Chem.* **92**, 129-168, 1917.
3. P. Debye, "Reaction rates in ionic solutions", *J. Electrochem. Soc.* **82**, 265-272, 1942.
4. K. M. Hong and J. Noolandi, "Solution of the Smoluchowski equation with a Coulomb potential. I. General results", *J. Chem. Phys.* **68**, 5163-5181, 1978.
5. W. F. Schmidt, *Liquid state electronics*, CRC Press, Boca Raton, 1997.
6. W. M. Bartczak and A. Hummel, "Monte Carlo calculations of diffusion controlled ion recombination for single and multiple pairs", *Radiat. Phys. Chem.* **27**, 71-72, 1986.
7. W. M. Bartczak and A. Hummel, "Computer simulation of ion recombinations in irradiated nonpolar liquids", *J. Chem. Phys.* **87**, 5222-5228, 1987.
8. W. M. Bartczak and A. Hummel, "Formation of singlet and triplet excited states on charge recombination in tracks of high-energy electrons in nonpolar liquids. A computer simulation study", *Chem. Phys. Lett.* **208**, 232-236, 1993.
9. W. M. Bartczak, M. Tachiya and A. Hummel, "Triplet formation in the ion recombination in irradiated liquids", *Radiat. Phys. Chem.* **36**, 195-198, 1990.
10. P. Clifford, N. J. B. Green and M. J. Pilling, "Stochastic models of diffusion-controlled ionic reactions in radiation-induced spurs. 1. High-permittivity solvents", *J. Phys. Chem.* **91**, 4417-4422, 1987.
11. N. J. B. Green, M. J. Pilling, S. M. Pimblott and P. Clifford, "Stochastic models of diffusion-controlled ionic reactions in radiation-induced spurs. 2. Low-permittivity solvents", *J. Phys. Chem.* **93**, 8025-8031, 1989.
12. M. P. Allen and D. J. Tildesley, *Computer Simulation of Liquids*, Clarendon, Oxford, 1987.
13. W. M. Bartczak and A. Hummel, "Computer simulation study of spatial distribution of the ions and electrons in tracks of high-energy electrons and the effect on the charge recombination", *J. Phys. Chem.* **97**, 1253-1255, 1993.
14. C. Kočka and W. M. Bartczak, "Effects of restricted geometry and anisotropy of the medium on the kinetics of the recombination of oppositely charged species in each other's field and the escape probability, studied by computer simulation", *Radiat. Phys. Chem.*, to be published.
15. S. M. Pimblott, A. Mozumder and N. J. B. Green, "Geminate ion recombination in anisotropic media. Effects of initial distribution and external field", *J. Chem. Phys.*, **90**, 6595-6602, 1989.
16. G. P. Van der Laan, *Charge Transport in π - and σ -Conjugated Polymers*, PhD Thesis, Delft University of Technology, Delft, 1996.
17. K. Wolf, J. Karniewicz and W. M. Bartczak, "Early Stages of Diffusion-Controlled Recombination and Aggregation of Ions in Supersaturated Ionic Solutions. A Computer Simulation Study", *Bull. Polish Acad. Sci. Chemistry*, **41**, 199-216, 1993.
18. B. Marciniak and J. Rozwadowski, "Quenching of excited singlet state of N-(9-methylpurin-6-yl)pyridinium cation by sulfur-containing amino acids and carboxylic acids in aqueous solution", *J. Photochemistry and Photobiol., A*, **101**, 163-169, 1996.
19. W. M. Bartczak, K. Wolf and A. Hummel, "Computer Simulation Studies of Recombination of Ions in Multi Ion-Pair Ensembles. I. Diffusion-Controlled Processes", *Computers and Chemistry*, **22**, 71-78, 1998.
20. W. M. Bartczak and A. Hummel, "Computer Simulation Studies of Recombination of Ions in Multi Ion-Pair Ensembles. II. Processes Characterized by Long Mean Free Paths of Charged Species", *Computers and Chemistry*, **22**, 79-87, 1998.

Simple models for crystallisation processes

D. de Cogan* and L.R. Martin

School of Information Systems, University of East Anglia, Norwich NR4 7TJ (UK)

ABSTRACT

Cellular Automaton (CA) modelling, the repeated application of simple rules can result in very complex behaviour and is being increasingly used to simulate physical processes. This paper outlines the technique with special emphasis on ordered states and order/disorder transitions.

keywords: Cellular Automata, Game of Life, Transmission Line Matrix (TLM), crystallisation, phase transitions

1. INTRODUCTION

At previous crystal conferences in Zakopane presentations have been made about the benefits of TLM, a numerical modelling technique which at one extreme can be interpreted in terms of electromagnetic theory^{1,2,3}. At the other extreme it can be considered as the repeated application of a set of rules; an example of a cellular automaton (CA). This paper introduces some basic concepts of general CA modelling in one and two dimensions. Even a cursory inspection of the subject⁴ reveals a bewildering expanse of interesting avenues. However, as will be demonstrated here, there has been much recent work on classification and this helps to reduce the apparent problems associated with disparity of formalism and dialect. In addition to introducing the subject, this paper presents details of work we have done in this area and discusses some of the wider work on crystallinity and phase transitions. We will start with a presentation of some interesting/amusing, but nevertheless useful two-dimensional CAs. We will then revert to one-dimension and demonstrate some of the CA aspects of one-dimensional TLM algorithms for diffusion. We follow this with a discussion on Wolfram's classification system and consider several specific cases. Finally, we will return to two-dimensional CAs and discuss recent developments in terms of the classification of CAs which distinguishes between those that lead to crystalline states, non-crystalline states and chaotic states.

2. SOME TWO-DIMENSIONAL CELLULAR AUTOMATA

2.1. Game of Life

'Life' was invented by J.H. Conway and was popularised by Martin Gardner in the Scientific American^{5,6}. It involves a rectangular mesh where grid-points are either alive (state '1') or dead (state '0'). The population of any point at the next generation is determined only by the state of the 8 nearest neighbours at the present generation (see figure 1).

There are three possible transitions in 'Life':

<i>Birth</i>	If $kP(x,y) = 0$ then $k+1P(x,y) = 1$ if <u>three</u> of the neighbours are currently alive.
<i>Survival</i>	If $kP(x,y) = 1$ then $k+1P(x,y) = 1$ if two or three neighbours are currently alive.
<i>Death (by crowding)</i>	If $kP(x,y) = 1$ then $k+1P(x,y) = 0$ if four or more neighbours are alive.
<i>Death (by isolation)</i>	If $kP(x,y) = 1$ then $k+1P(x,y) = 0$ if one or no neighbours are alive.

* Author contact information-

de Cogan (correspondence): Email: ddc@sys.uea.ac.uk; Telephone: +44 (0)1603 592567; Fax: +44 (0)1603 592345

Life is totally deterministic but we generally have to run a simulation to see what any but the most trivial starting configurations will yield as the simulation progresses.

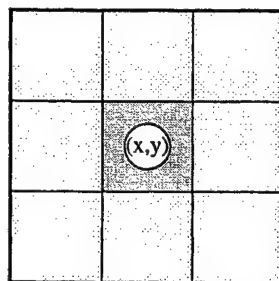


Figure 1. The eight nearest neighbours in Conway's 'Game of Life'

2.2. Forest fires

The 'Forest Fire' CA uses a square lattice but differs from the last case in that it has a stochastic element. Grid-points have three possible states: Red denotes a burning tree, White (blank) is either a dead tree or an empty site and Green is a living tree. The rules are as follows:

If $P(x,y) = \text{Red}$ then $P_{k+1}(x,y) = \text{White}$ (the tree has burnt).

If $P(x,y) = \text{Green}$ then $P_{k+1}(x,y) = \text{Red}$, if one of the eight neighbours is currently Red

If $P(x,y) = \text{White}$ then $P_{k+1}(x,y) \rightarrow \text{Green}$ with probability p (growth)

If $P(x,y) = \text{Green}$ then $P_{k+1}(x,y) \rightarrow \text{Red}$ with probability f (fire initiated by lightning)

Values of $p = 0.3$ and $f = 6 \times 10^{-5}$ give very convincing results⁴.

2.3. Others

Examples of CAs with different levels of random element that are discussed by Chopard and Droz⁴ include *percolation*, *Ising spin* modelling and *road traffic* simulation.

3. TLM ALGORITHM FOR ONE-DIMENSIONAL DIFFUSION AS A CA PROCESS

The basics of Transmission Line Matrix (TLM) for diffusion can be found in a variety of references which are summarised by de Cogan⁷. It has two basic steps, *Scatter* and *Connect*. The *Scatter* process has two rules *Reflect* and *Transmit*. *Reflect* multiplies any data impulse which is incident on a spatial node by the reflection coefficient, ρ and reverses its direction of motion. *Transmit* multiplies any incoming pulse by the transmission coefficient $\tau = (1-\rho)$ and retains the direction of motion. These determine the magnitude and destination of the pulses for the *Connect* process which determines the total population distribution at the next generation. The resulting scatter algebra can be summarised for a unit pulse incident at position (x) from the left:

$$\text{Reflect} \quad \hat{\rho}[(x)] \rightarrow \rho[(x-1)]$$

$$\text{Transmit} \quad \hat{\tau}[(x)] \rightarrow \tau[(x+1)]$$

$$\text{Thus, } \hat{\rho}\hat{\rho}[(x)] \rightarrow \rho^2[(x-1+1)], \text{ i.e. } \rho^2[(x)]$$

The process is not commutative: $\hat{\rho}\hat{\tau}[(x)]$ (working outwards) $\rightarrow \rho\tau[(x+1-1)]$, i.e. $\rho\tau[(x)]$, while $\hat{\tau}\hat{\rho}[(x)] \rightarrow \tau\rho[(x-1-1)]$ or $\tau\rho[(x-2)]$. This is similar to the CA which can be used to model the behaviour of falling sand in an hour-glass. When $\rho = \tau$ this is identical to Galton's 'Quincunx' which was an early experimental method of demonstrating that such processes yield a Gaussian distribution⁸.

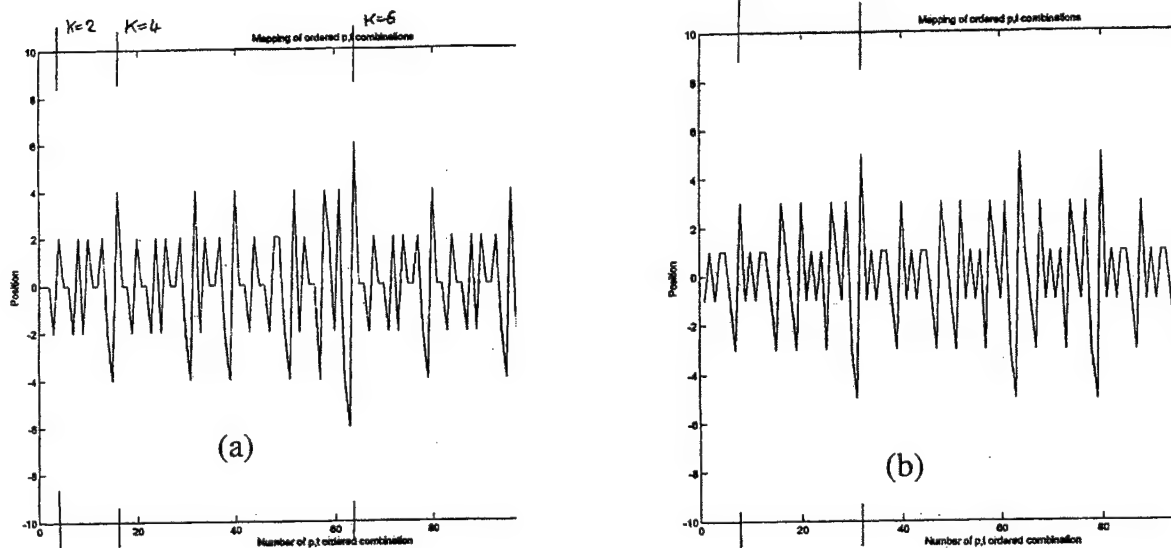


Figure 3 Displacement of successive elements in a p, τ binary sequence of length 2^k plotted against number in sequence (a) for $(k=2, 4, 6)$, (b) for $(k=3, 5)$.

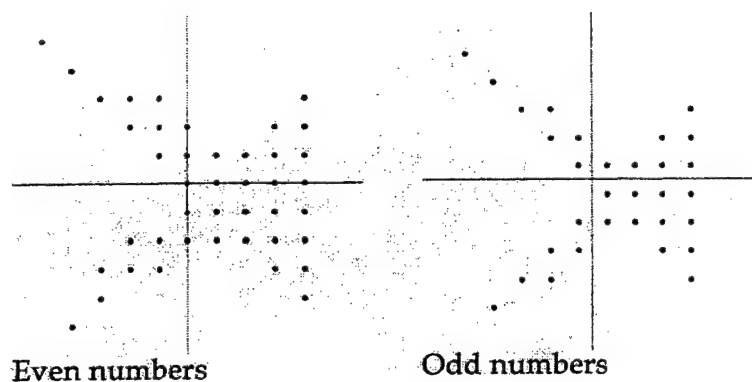


Figure 3 Displacement of successive elements in a p, τ binary sequence of length 2^k plotted as position of $(s+1)$ th in sequence (vertical axis) versus position of (s) th (horizontal axis) for even and odd length sequences.

If we assume that the diffusion process described by TLM is an arrangement by which data-pulses, starting at the source take all possible paths then we can describe the situation three time-steps after the start of our simulation by means of a three-bit binary sequence of scattering operators $\hat{p}\hat{p}\hat{p}[(x)]$, $\hat{p}\hat{p}\hat{\tau}[(x)]$, $\hat{p}\hat{\tau}\hat{p}[(x)]$, $\hat{p}\hat{\tau}\hat{\tau}[(x)]$, $\hat{\tau}\hat{p}\hat{p}[(x)]$, $\hat{\tau}\hat{p}\hat{\tau}[(x)]$, $\hat{\tau}\hat{\tau}\hat{p}[(x)]$, and $\hat{\tau}\hat{\tau}\hat{\tau}[(x)]$. Similarly, the scattering algebra can be used to determine the final position due to the sixteen four-bit binary operations after the fourth time-step. If we can take a large binary sequence and estimate the final positions of successive components then it can be seen from figure 2 that there is a high degree of correlation. This can also be investigated using a technique borrowed from phase-space plots in chaos theory. A plot of P_{s+1} , the position of the $(s+1)$ th component in the sequence vs P_s , the position of the (s) th component yields some very interesting, and as yet, unexplained results, which are shown for odd and even sequences in figure 3.

4. WOLFRAM'S CLASSIFICATION SYSTEM FOR ONE-DIMENSIONAL CAs

The few examples cited above give some indication of the complexity of the subject. Stephen Wolfram⁹ made a systematic study of one-dimensional CAs and recognised that if there are k states involving r nearest neighbours then the total number of distinct rules is:

$$k^{k^{2r-1}}$$

Thus, if there are two states (1,0) and if the outcome at position (x) is determined by two nearest neighbours ($x+1$) and ($x-1$) then there are 2^8 rules. Wolfram used the same binary approach as we have used in the previous section and these are shown for some rules in the tables below. The top row represents the current states of ($x-1$), (x) and ($x+1$). The bottom row in each shows the state at (x) at the next time as a result of applying the particular rule.

k	(111)	(110)	(101)	(100)	(011)	(010)	(001)	(000)
k+1	0	0	1	1	0	0	1	0

If we take the sequence 00110010 as a binary number then it represents decimal 50. Wolfram termed this as 'Rule 50'. The exclusive OR rule where the population at (x) is one at the next generation only if ($x+1$) or ($x-1$) is one is given in the table below and it can be seen why this is termed 'Rule 90'. Chopard and Droz⁴ discuss how rule 184 mimics a surface growth process.

k	(111)	(110)	(101)	(100)	(011)	(010)	(001)	(000)
k+1	0	1	0	1	1	0	1	0

Although there is the question of non-decidability (just as in nature) these rules can be divided into clearly empirical classes.

1. After a finite number of steps the system tends towards a unique homogeneous state (i.e. tends towards a limit point). *Rule 40* is an example of this.
2. The system develops periodic regions for almost all initial states (i.e. tends towards a limit cycle). *Rule 56* is an example of this.
3. Characterised by aperiodic or chaotic patterns, e.g. *Rule 18* (i.e. strange attractor).
4. Rules in this class yield persistent complex structures for a large class of initial states, the behaviour can only be determined by explicit simulation (e.g. *Rule 110*).

5. MORPHOLOGICAL STUDIES OF RULE 90

We were interested in *Rule 90* for two reasons. A single initial excitation in the middle of a string of zeros yields the beautiful Sierpinski gasket with its self-similar properties (figure 4).

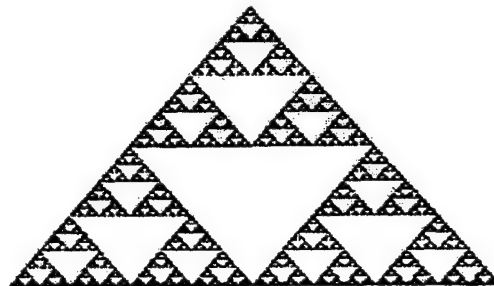
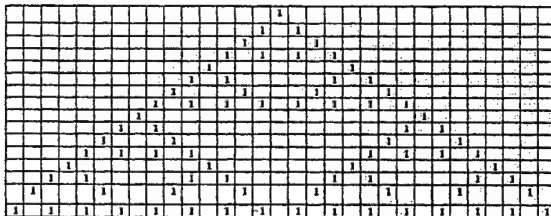


Figure 4 Wolfram's *Rule 90* for different numbers of iterations after a single initial excitation (Sierpinski Gasket)

The second reason for our interest was the fact that an excitation consisting of a random sequence of ones and zeros seems to 'develop' a level of order. We used techniques borrowed from image processing to identify the relative sizes of triangles. The situation is very simple in the Sierpinski gasket. The smallest triangles have 2 ones along each side. We call these class 2 triangles. The next smallest triangles are class 4 (they have 4 ones along each side), the next is class 8 and then class 16. There are no triangles with odd numbers of ones along each side. The total number of class 2 triangles at generation, k (where $k > 1$) is 3^{k-2} . Class 4 triangles do not appear until $k = 3$. Thereafter they increase as 3^{k-3} . The analysis can be extended to higher classes. Any real simulation of a Sierpinski gasket is bounded by the size of the chosen array and the boundary conditions which are applied (zero boundary, unit boundary, mirror boundary, wrap-around boundary) will affect the population of triangles. The effect of bounding can be to have the concentration of triangles of a given class tend towards a steady state. Knowing the relationship between equilibria and entropy we investigated the time variation of different classes of triangles which evolve from random initial excitations. The model spaces were large and we examined only a central region so as to eliminate boundary effects within the number of iterations used. In no case were we able to identify a time-dependent change in the number of triangles of a given class. We are forced to assume that within the limits of our numerical experiments there was no persistent change in the state of order of the system.

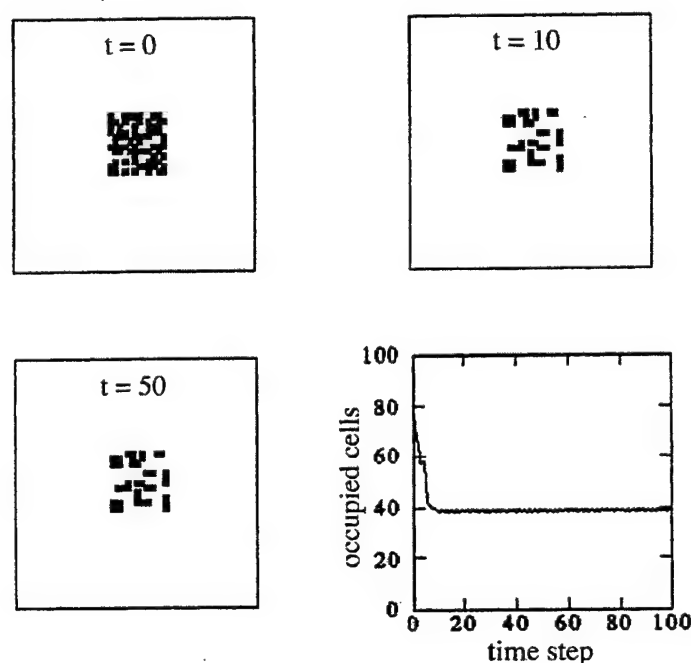


Figure 5 Population versus time for a rule which outputs zero except for $g(0,3)$, $g(1,1)$ and $g(1,2)$ which output 1.

6. CLASSIFICATIONS OF SIMPLE TWO-DIMENSIONAL CAS

Suzudo¹⁰ has extended the classification techniques to two-dimensions but his analysis may be difficult to assimilate on account of differences in formalism. He defines a generalised CA function, f which acts on the present population of states ${}_k a$ to generate ${}_{k+1}a(x,y)$, the value of $a(x,y)$ at the $(k+1)$ th generation.

$${}_{k+1}a(x,y) = f[{}_k a(x-1,y), {}_k a(x+1,y), {}_k a(x,y-1), {}_k a(x,y+1), {}_k a(x,y)]$$

He starts by insisting that $f(0,0,0,0,0) = 0$, ones are not generated from empty space. He then defines a function, g , where it is the sum of the neighbouring population that is important. (in the case of *Life* we are summing over the eight neighbours)

$$a(x,y) = g[a(x,y), a(x+1,y) + a(x-1,y) + a(x,y-1) + a(x,y+1)]$$

The condition $g(0,1)$ says that $a(x,y) = 0$ and at least one of its neighbours = 1.

$g(0,1) = 1$ is a 'Deposition' process and is the two-dimensional equivalent of Wolfram's *Rule 90*. This is an important rule, otherwise occupied cells may disappear or become localised (see figure 5). However, there are other rules where we can get the opposite effect, namely localised empty cells.

We can use the reverse of $g(0,1) = 1$, namely $g(1,3) = 0$ which causes empty states to advance into occupied territory. This is a 'Dissolution' or erosion process. A combination of $g(0,1)$ and $g(1,3)$ can be used to prevent localisation by occupied or empty cells. Figure 6 is an example of such a mixing process that can lead to 'crystallisation'.

Suzudo then introduces the concepts of spatial and temporal entropy, which we will designate as S_s and S_t which are arranged to be zero for ordered states and unity for disordered states. S_s can be plotted against S_t for all possible rules after a given evolution time and it is possible to distinguish those rules which lead to chaotic evolutions. They have large values of both entropies. Even after 2000 time-steps there is a significant clustering of rules with small S_t i.e. less than 0.1. This allows us to distinguish between rules that ultimately lead to a chaotic (liquid) state and those that will lead to a solid state. In order to distinguish between crystalline and amorphous states we need another parameter.

The Suzudo μ parameter is defined as $\mu = \frac{2^s - m}{2^s}$ (m = number of rule entries which update the cell with no change)

This can be related to the λ parameter of Langton¹¹ which gives the percentage of non-zero transitions in the CA transition table and is closely related to the Wolfram classes rules. The process of crystallisation really only applies to class 3 rules. Accordingly, we can divide the λ , μ space into six classification areas as shown schematically in figure 7.

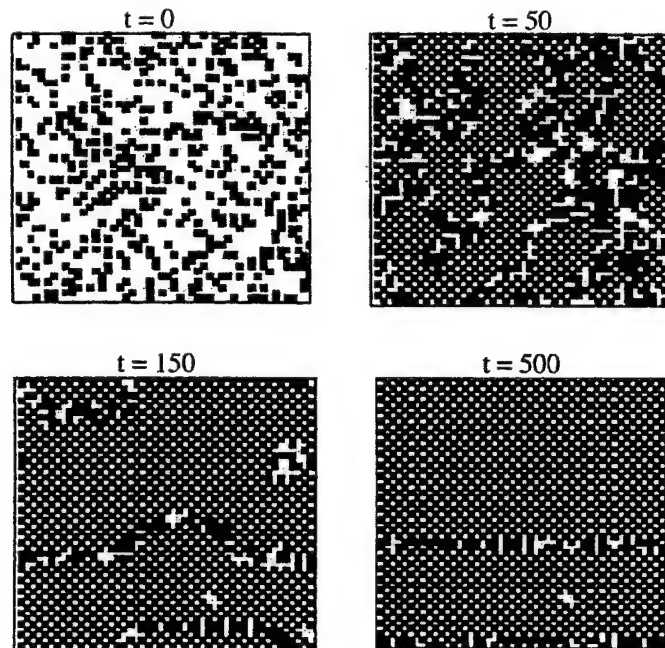


Figure 6 Evolution towards a crystalline state: $g(0,3) = 1$ and $(g(1,3) = 0$ or $g(1,4) = 0)$.

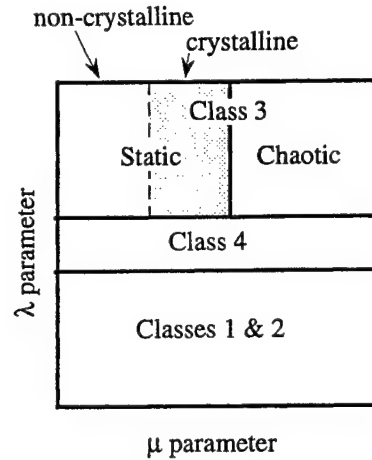


Figure 7 Crystalline/non-crystalline transitions in $\lambda\mu$ space (μ can be considered as the CA equivalent of temperature).

7. CONCLUSIONS

This paper has given some indication of the complexity that can be achieved from the repeated application of simple rules. In spite of the fact that the number of rules is limited by the number of states and the number of neighbourhood sites it is possible to distinguish different behavioural classes, and states of order/disorder. Rules which lead to an ordered state have much in common with the normal processes of crystallisation, even the inclusion of persistent 'defects'. There has been relatively little work on three-dimensional CAs. It may be that in numerical terms the prospect appears to be daunting, but with only two states and six nearest neighbours, there are less rules than in *Life*. The challenge to create a CA which emulates real crystallisation processes remains.

REFERENCES

1. D. de Cogan, A. Chakrabarti and R.W. Harvey, *TLM algorithms for Laplace and Poisson fields in semiconductor transport* SPIE Proceedings Vol. 2373, pp 198 - 206 (1995)
2. D. de Cogan, A. Chakrabarti and C.P. Kenny, *Recent advances in TLM algorithms for semiconductor transport* SPIE Proceedings Vol. 3179, pp 274 - 286 (1997)
3. D. de Cogan, *The application of Transmission Line Matrix techniques to the modelling of solid state problems* SPIE Proceedings Vol. 3724, pp 183- 192 (1999)
4. B. Chopard and M. Droz, *Cellular Automata modelling of physical systems*, Cambridge University Press 1998
5. M. Gardner, *Mathematical Games* Scientific American **224** (1971) Feb. p 112, March p 106, April p 114
6. M. Gardner, *Mathematical Games* Scientific American **226** (1972) Jan. p 104
7. D. de Cogan, *Transmission Line Matrix (TLM) techniques for diffusion applications*, Gordon and Breach 1998 (ISBN 90 5699 129 9)
8. see *Dictionary of Scientific Biography* (New York 1970).
see also (<http://www.cimm.jcu.edu.au/hist/stats/galton/galton16.htm>)
9. S. Wolfram, *Statistics of cellular automata* Rev. Mod. Physics **55** (1983) 601 - 644
10. T. Suzudo, *Crystallisation of two-dimensional cellular automata* Complexity International **6** (2000) 1 - 8 (ISSN 1320-0862)
11. C.G. Langton, *Computation at the edge of chaos: phase transitions and emergent computation* Physica **42** (1990) 12 - 37

Transient surface supersaturation after crystal submersion (II)

Mirosława Rak*

Institute of Physics, Technical University of Łódź, ul. Wólczńska 219, 93-005 Łódź, Poland

ABSTRACT

In our earlier papers [M. Rak, Proc. SPIE 3178 (1997) 108 and M. Rak et al., J. Cryst. Growth 197 (1999) 944], we solved the time-dependent equation of Burton, Cabrera and Frank (BCF) for transient state conditions occurring immediately after submersion of a crystal surface in supersaturated solution. As a result, the expression for the transient surface supersaturation was found and discussed. In this paper we present an approximation of that expression. The approximation enables a simple estimation of the time required to attain the steady-state value of the surface supersaturation.

Keywords: time-dependent BCF equation, surface supersaturation, surface diffusion theory of crystal growth, solution growth.

1. INTRODUCTION

In our previous papers^{1, 2} we studied, using the surface diffusion theory^{3, 4} of Burton, Cabrera and Frank (BCF), the transient surface supersaturation σ_s occurring immediately after submersion of crystal face in supersaturated solution. For this purpose, we solved^{1, 2} the BCF time-dependent equation:

$$\frac{\partial^2 n}{\partial x^2} + \frac{n_e}{\lambda^2} (1 + \sigma) - \frac{n}{\lambda^2} = \frac{\tau}{\lambda^2} \frac{\partial n}{\partial t} \quad (1)$$

where $n \equiv n(x, t)$ is the local concentration of growth units at the surface; n_e is the equilibrium concentration of growth units at the surface; σ is the relative supersaturation just above the surface and very far from a step, so it is the same as the bulk supersaturation; λ is the mean diffusion distance of the growth unit adsorbed on the surface and τ denotes the relaxation time for leaving the surface adsorption layer. The relaxation time τ is related to the activation free energy ΔG for desorption by Eyrings' formalism³:

$$\tau = \frac{h}{k_B T} \exp\left(\frac{\Delta G}{k_B T}\right), \quad (2)$$

where h is Planck's constant, k_B is the Boltzmann constant and T denotes temperature.

To formulate the initial condition, we assumed^{1, 2} that, as soon as the crystal face is submerged in the supersaturated solution, the surface supersaturation σ_s is equal to the bulk supersaturation σ :

$$\sigma_s(x, 0) = \sigma, \quad (3)$$

where the surface supersaturation $\sigma_s \equiv \sigma_s(x, t)$ is defined as:

$$\sigma_s = \frac{n - n_e}{n_e}. \quad (4)$$

Eq. (1) was solved^{1, 2} for a parallel sequence of equidistant steps and the origin of the coordinate system chosen in the centre of the step terrace. The positions $x = \pm x_0/2$ (where x_0 denotes the interstep distance) corresponding to the step edges were assumed^{1, 2} to remain unchanged during the transient state. Furthermore, the boundary conditions assumed^{1, 2} symmetrical diffusion fields around steps and equilibrium concentration n of growth units at the step edges. Taking into account Eq. (4), the solution for Eq. (1) with initial condition (3) was found^{1, 2} in the following form:

*Further author information –
M.R.: Email: mirarak@ck-sg.p.lodz.pl

$$\sigma_s(x, t) = \sigma \left\{ 1 - \frac{\cosh(x/2\lambda)}{\cosh(x_0/2\lambda)} + \right. \quad (5)$$

$$\left. - 4\pi \sum_{k=1}^{\infty} (-1)^k \frac{(2k-1) \cos[\pi(2k-1)x/x_0]}{\pi^2(2k-1)^2 + (x_0/\lambda)^2} \exp \left[- \frac{\pi^2(\lambda/x_0)^2(2k-1)^2 + 1}{\tau} t \right] \right\},$$

The analysis of the transient surface supersaturation, expressed by Eq. (5), revealed^{1,2} that the time t_s required to attain the steady-state value of σ_s does not depend on the bulk supersaturation σ , but it increases with increasing relative interstep distance x_0/λ . Furthermore, the longest period of time t_{s0} is necessary to reach the steady-state value of σ_s at the centre of the step terrace ($x = 0$) and therefore this point is of particular interest.

The aim of this paper is to present an approximation of Eq. (5) which enables a simple estimation of the time t_s required to attain the steady-state value of surface supersaturation after submersion of crystal face in the supersaturated solution.

2. APPROXIMATION OF EQ. (5)

In order to find an approximation of Eq. (5) we follow in the way similar to that presented in one of our earlier papers⁵. Therefore, we use the effective time t_{eff} defined⁵ as:

$$t_{\text{eff}} = \tau \left[1 - \frac{\cosh(x/\lambda)}{\cosh(x_0/2\lambda)} \right]. \quad (6)$$

In the summation term of Eq. (5), we now replace the power $[\pi^2(\lambda/x_0)^2(2k-1)^2 + 1]t/\tau$ by t_{eff}/τ , which leads to an approximation:

$$4\pi \sum_{k=1}^{\infty} (-1)^k \frac{(2k-1) \cos[\pi(2k-1)x/x_0]}{\pi^2(2k-1)^2 + (x_0/\lambda)^2} \exp \left[- \frac{\pi^2(\lambda/x_0)^2(2k-1)^2 + 1}{\tau} t \right] \approx$$

$$\approx 4\pi \exp \left(- \frac{t}{t_{\text{eff}}} \right) \sum_{k=1}^{\infty} (-1)^k \frac{(2k-1) \cos[\pi(2k-1)x/x_0]}{\pi^2(2k-1)^2 + (x_0/\lambda)^2}. \quad (7)$$

Taking into account that the solution given by Eq. (5) fulfils the initial condition [Eq. (3)], we find:

$$-4\pi \sum_{k=1}^{\infty} (-1)^k \frac{(2k-1) \cos[\pi(2k-1)x/x_0]}{\pi^2(2k-1)^2 + (x_0/\lambda)^2} = \frac{\cosh(x/\lambda)}{\cosh(x_0/2\lambda)} \quad (8)$$

This result is also obtainable using the Fourier expansion corresponding to the function $\cosh(x/\lambda)/\cosh(x_0/2\lambda)$ in the interval $(-x_0/2, x_0/2)$. Upon substituting Eq. (8) into Eq. (7), we have an approximation of Eq. (5) in the following form:

$$\sigma_s^A(x, t) = \sigma \left[\frac{t_{\text{eff}}}{\tau} + \left(1 - \frac{t_{\text{eff}}}{\tau} \right) \exp \left(- \frac{t}{t_{\text{eff}}} \right) \right], \quad (9)$$

where t_{eff} is expressed by Eq. (6). The approximation given by Eq. (9) and the solution found previously [Eq. (5)] take the same initial and steady-state values. In addition to this, Eq. (9) fulfils the boundary conditions assumed for solving the BCF time-dependent equation.

3. DISCUSSION

In order to illustrate the solution given by Eq. (5) and its approximation [Eq. (9)], we perform calculations for bulk supersaturations sufficiently low to predict the BCF spiral growth mechanism. The relative interstep distance x_0/λ present in Eqs. (5) and (6) can be found using one of the known approximations of the interstep distance (see e.g. Ref⁶). However, since this distance depends not only on supersaturation but also on the edge free energy and the number of cooperating spirals, we assume several values of x_0/λ ($x_0/\lambda = 2, 3, 4, 5$) to show the influence of x_0/λ on behaviour of the surface

supersaturation. In Fig. 1 the surface supersaturation σ_{s0} at the centre of step terrace ($x = 0$) is shown as a function of the relative time t/τ .

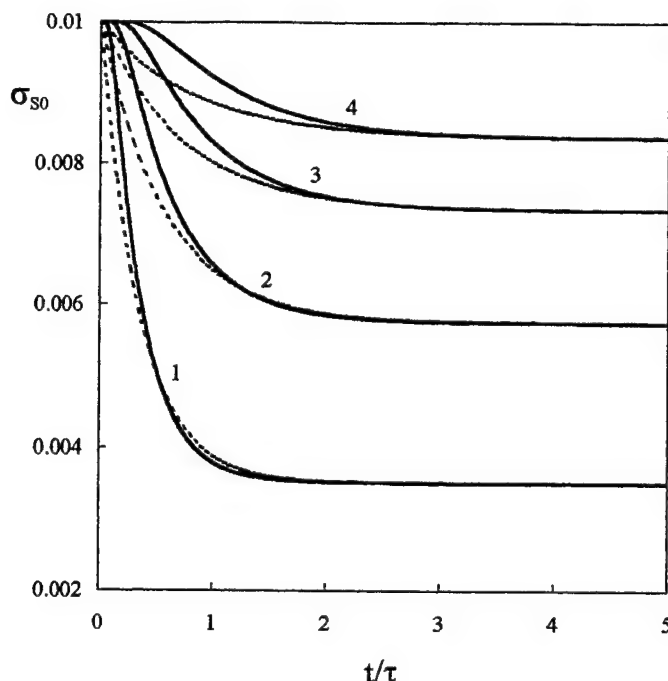


Fig. 1. Surface supersaturation σ_{s0} at the centre of the step terrace ($x = 0$) versus relative time t/τ for bulk supersaturation $\sigma = 0.01$. Curves 1, 2, 3 and 4 correspond to the relative interstep distance $x_0/\lambda = 2, 3, 4$ and 5, respectively. Full and dashed lines correspond to Eq. (5) and (9), respectively.

The full and dashed lines correspond to σ_{s0} calculated from Eq. (5) and σ_{s0}^A calculated from Eq. (9), respectively. It can be seen in Fig. 1 that, at small values of t/τ , the function $\sigma_{s0}(t)$ differs from the exponential function $\sigma_{s0}^A(t)$. The difference is more considerable for greater values of the relative distance x_0/λ . The slope $(\partial\sigma_s/\partial t)_{t=0}$ of the curve $\sigma_s(t)$ at $t = 0$ is equal to zero, which means that at $t = 0$, the surface supersaturation σ_s remains constant (cf. full lines in Fig. 1). This result is obvious from physical point of view. At $t = 0$, the behaviour of the surface supersaturation is determined by the exchange of growth units between the crystal surface and the solution bulk. The net flux j_v of growth units exchanged with the bulk of the solution is equal^{3,4} to:

$$j_v = \frac{n_s(\sigma - \sigma_s)}{\tau} \quad (10)$$

However, just after submersion of the crystal face in supersaturated solution, the surface supersaturation σ_s is equal to bulk supersaturation σ [cf. Eq. (3)]. In consequence, at $t = 0$, the net flux j_v is equal to zero and σ_s remains constant at $t = 0$. At $t > 0$, the surface supersaturation is reduced by the surface flux of growth units going to the step edges.

In Fig. 2 the surface supersaturations σ_s and σ_s^A are shown, for $x_0/\lambda = 3$ and various values of t/τ , as a function of the relative distance x/x_0 from the step centre. It can be noticed that with increasing distance x/x_0 from the step centre, the difference between σ_s and σ_s^A diminishes and for $x = (0.2 \div 0.3)x_0$ reaches zero. Then it changes its sign and with increasing x , the absolute value of the difference increases. Consequently, for $x = (0.2 \div 0.3)x_0$, values of σ_s and σ_s^A are very close to each other.

Although the behaviour of the functions $\sigma_s(t)$ and $\sigma_s^A(t)$ is different at the beginning of the transient state, these both

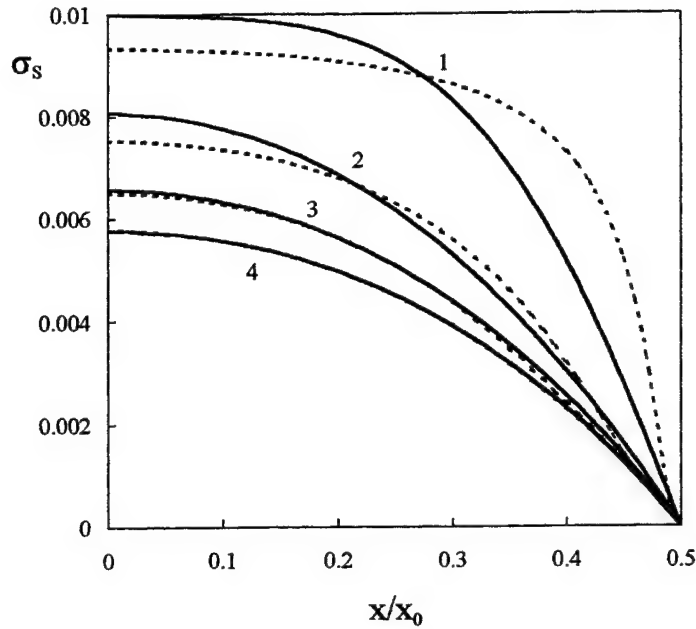


Fig. 2. Surface supersaturation σ_s versus relative distance x/x_0 from the terrace centre, plotted for $x_0/\lambda = 3$, $\sigma = 0.01$ and various values of the relative time t/τ . Curves 1, 2, 3 and 4 correspond to $t/\tau = 0.1, 0.5, 1$ and 3 , respectively. Full and dashed lines correspond to Eq. (5) and (9), respectively.

functions attain their steady-state value at the same time (cf. Fig. 1). Therefore, the time t_s required to attain the steady-state value of the surface supersaturation can be estimated with the use of Eq. (9). In transient state analysis, it is usually assumed that the steady-state is attained when the transient part of the equation is not greater than 0.01 of its initial value. Consequently, the exponential term in Eq. (9) can be neglected when it is not greater than 0.01 of its value at $t = 0$. This means that the time t_s necessary to attain the steady-state value of the surface supersaturation can be estimated as:

$$t_s \approx 4.6 t_{\text{eff}}, \quad (11)$$

where t_{eff} is given by Eq. (6). Values of the characteristic time t_{s0} (for $x = 0$) and the time t_s for $x = 0.25x_0$, obtained using Eq. (11), are presented in Table 1.

Table 1. Values of the relative time t_s/τ obtained using Eq. (11) and those following from Eq. (5), for various values of x_0/λ . Results for $x/x_0 = 0$ and $x/x_0 = 0.25$.

$x/x_0 = 0$	x_0/λ	t_{eff}/τ Eq.(6)	t_s/τ Eq.(11)	t_s/τ
	2	0.35	1.62	1.43
	3	0.57	2.64	2.41
	4	0.73	3.38	3.22
	5	0.84	3.85	3.87
	6	0.90	4.14	4.41
	7	0.94	4.32	4.89
	8	0.96	4.43	5.32

$x/x_0 = 0.25$	x_0/λ	t_{eff}/τ Eq.(6)	t_s/τ Eq.(11)	t_s/τ
	2	0.27	1.24	1.29
	3	0.45	2.07	2.12
	4	0.59	2.71	2.74
	5	0.69	3.18	3.17
	6	0.77	3.53	3.47
	7	0.82	3.78	3.70
	8	0.86	3.97	3.88

In this table, we also show values of the characteristic time t_{s0} and the time t_s calculated from Eq. (5). To calculate the times t_{s0} and t_s from Eq. (5) we also assumed that the transient part (summation term) in Eq. (5) can be neglected when it is not greater than 0.01 of its initial value. It follows from the results presented in Table 1 that, in the centre of step terrace ($x = 0$), the simple expression (11) may be used for estimation of the characteristic time t_{s0} only at not too large values of the interstep distance ($x_0/\lambda \leq 7$). At large x_0/λ , values of t_{s0} estimated using Eq. (11) are too low in comparison with those following from Eq. (5). It can also be noted that at the point $x=0.25x_0$, where the difference between σ_s and σ_s^A is negligible (cf. Fig. 2), the difference between values of t_s estimated using Eq. (11) and those following from Eq. (5) is also negligible.

4. CONCLUSIONS

The present study shows that for not too large interstep distances x_0/λ , the time t_s necessary to attain the steady-state value of the surface supersaturation σ_s is approximately equal to $4.6 t_{eff}$, where t_{eff} is expressed by Eq. (6). This simple estimation demonstrates that the time t_s does not depend on value of bulk supersaturation but it increases with increasing interstep distance x_0/λ and with increasing distance from the step edge. It should also be pointed out that the time t_s is directly proportional to the relaxation time τ for leaving the surface adsorption layer. This means that the time t_s , required to attain the steady-state value of σ_s , is related to the activation free energy ΔG for desorption, and temperature of the solution [cf. Eq. (2)].

5. LIST OF SYMBOLS

ΔG	Activation free energy for desorption.
j_v	Net flux of growth units exchanged with the solution bulk.
h	Planck's constant.
k_B	Boltzmann constant.
n	[$\equiv n(x,t)$] Local concentration of growth units at the surface.
n_e	Equilibrium concentration of growth units at the surface.
T	Temperature.
t	Time.
t_{eff}	Effective time defined by Eq. (6).
t_s	Time required to attain the steady-state value of σ_s .
t_{s0}	Characteristic time, required to attain the steady-state value of the surface supersaturation σ_{s0} .
x	Distance from the step centre.
x_0	Interstep distance.
λ	Mean diffusion distance of the growth unit adsorbed on the surface.
σ	Relative supersaturation just above the surface and very far from a step, so it is the same as the bulk supersaturation.
σ_s	[$\equiv \sigma_s(x,t)$] Surface supersaturation expressed by Eq. (5)
σ_s^A	[$\equiv \sigma_s^A(x,t)$] Surface supersaturation σ_s approximated by Eq. (9).
σ_{s0}	Surface supersaturation σ_s at the centre of the step terrace ($x=0$).
σ_{s0}^A	Surface supersaturation σ_{s0} approximated by Eq. (9).
τ	Relaxation time for leaving the surface adsorption layer.

REFERENCES

1. M. Rak, "Transient surface supersaturation (I)", in *Solid State Crystals: Growth and Characterization*, edited by J. Žmija, A. Majchrowski, J. Rutkowski and J. Zieliński, Proc. SPIE 3178, pp. 108-115, 1997.
2. M. Rak, X. Gui and D. de Cogan, "Transient analysis of surface supersaturation after crystal face submersion using the analytical and transmission-line matrix (TLM) methods", *J. Crystal Growth* 197, pp. 944-954, 1999.
3. W. K. Burton, N. Cabrera and F. C. Frank, "The growth of crystals and the equilibrium structure of their surfaces", *Phil. Trans. Roy. Soc. A243*, pp. 298-358, 1951.
4. P. Bennema and G. H. Gilmer, "Kinetics of crystal growth", in *Crystal Growth: An Introduction*, edited by P. Hartman, pp. 263-327, North-Holland, Amsterdam, 1971.
5. M. Rak, "Transient behaviour of surface supersaturation caused by variation in bulk supersaturation", *Surf. Scie.* 442, pp. 149-160, 1999.
6. M. Rak, "Influence of the back-stress effect on the interstep distance and on the surface supersaturation", *J. Crystal Growth* 193, pp. 189-196, 1998.

Theory of behavior of ionized hydrogen in GaSb crystal structure

Věra Šestáková, Bedřich Štěpánek and Jaroslav Šesták

Institute of Physics, Semiconductor Department, Academy of Sciences of the Czech Republic,
Cukrovarnická 10, 162 00 Praha 6, Czech Republic

ABSTRACT

Using the thermodynamical studies it seems proved that ionized hydrogen acts as amphoteric dopant of GaSb. It is splitting to H^+ (acceptor) and H^- (donor) and between these two kinds certain equilibrium is created depending on the concentration of acceptor's and donor's impurities in the GaSb material. There is an inclination of such a crystal to maintain the GaSb structure to be isoelectric. This behavior has been studied on undoped and slightly Te-doped GaSb single crystals grown by use of the Czochralski method without encapsulant under a flow of ionized hydrogen. For comparison the studies were repeated under a flow of molecular hydrogen.

Keywords: ionized hydrogen, GaSb crystal structure, residual acceptors, free carrier concentration.

1. INTRODUCTION

Systematic work lasting for more than three decades has been devoted mainly to the role of residual concentration of natural acceptors which is a limiting factor of the device application of gallium antimonide (GaSb)¹. The residual acceptors of the concentration of about $1.7 \times 10^{17} \text{ cm}^{-3}$ were identified as vacancy (V) complexes $V_{Ga}Ga_{Sb}^{2,3}$. Many attempts have been made to reduce their content in GaSb. Crystal growth from the nonstoichiometric melt⁴ was one of the most successful methods. This result supported our interest in opening the question of the GaSb single crystal growth from the melt with a reduced content of residual acceptors.

Hydrogen passivation of different defects and impurities was studied in many III-V compounds^{5,6}. Polyakov et al.^{7,8} treated GaSb samples either undoped or Zn- or Si-doped both in hydrogen and deuterium atmosphere in the temperature range between 100 and 250°C and with the exposure times of 0.5 - 1 h. Their results were very interesting. The carrier concentration in the case of undoped GaSb decreased as much as to the value of about $1 \times 10^{16} \text{ cm}^{-3}$ and the resistivity increased by one order of magnitude.

Polyakov et al.'s method showed that this way was likely to successfully manage the preparation of at least high-resistivity GaSb single crystals with a low concentration of residual acceptors.

We tried to use our undoped GaSb single crystal (grown in molecular hydrogen atmosphere) having a carrier concentration of $(1.70 - 1.80) \times 10^{17} \text{ cm}^{-3}$ and a resistivity of $(6.50 - 6.70) \times 10^{-2} \Omega \cdot \text{cm}$. The wafer from this crystal were cut to a thickness of 200 μm . The samples were treated in a quartz tube at temperatures of 350, 280, 250, 200 and 150°C for 1 - 24 h. Hydrogen ionized by means of a deuterium lamp flew through this annealing reactor. After cooling the quartz ampoule, the carrier concentration and the resistivity were measured on the treated wafers in the first step using the van der Pauw method. Then the layers of about 10 μm on both sides of the wafers were ground out and the electrical measurements were repeated.

It turned out that in the case of the temperature range of 250 - 350°C, the values of the measured parameters were the same, both before the temperature annealing and after this treatment. However, when the temperature was lower, i.e. from 200°C and mainly 150°C, and the duration of the annealing procedure exceeded 10 h, the carrier concentration in the nonground wafers achieved the value of $(1.20 - 1.30) \times 10^{17} \text{ cm}^{-3}$ (i.e. about 40%). After grinding a 10 μm layer, the carrier concentration was the same as in the case of the untreated samples. The resistivity changed only by 15%; i.e. it reached the values of $(7.60 - 7.70) \cdot 10^{-2} \Omega \cdot \text{cm}$.

This method of measurement is influenced by a high inaccuracy because the total volume of the samples was measured while only a small layer was passivated. For this reason, the resistivity and the free carrier concentration were

studied by the spreading resistivity procedure. It has been found that in the case of the wafers being treated at a temperature of 150°C for 24 h, the thickness of the passivated layer was only 0.4 - 0.6 μm and its resistivity reached a value of $10^2 - 10^3 \Omega\cdot\text{cm}$. The free carrier concentration was lower than $1 \times 10^{15} \text{ cm}^{-3}$. However, such a thin layer of high-resistivity GaSb single crystals would be difficult to fabricate because, on the one hand, the thickness of the layer was not uniform on the surface of the wafer and, on the other hand, the spreading of the resistivity was very inhomogeneous.

2. EXPERIMENTAL

For the reason mentioned above, we tried to prepare bulk crystal in such an atmosphere that would make possible to study the influence and stability of ionized hydrogen flow on free carrier concentration and resistivity of as-grown single crystals. The GaSb crystals were grown in our laboratory using the Czochralski method without encapsulant under the hydrogen atmosphere that suppressed the creation of an oxide scum on the melt surface⁹. A polycrystalline material made by the firm Spurrmetalle Freiburg (Germany) was used as the starting material for our investigation. Before the growth, the polycrystalline GaSb was cleaned by grinding and etching in a solution of acids ($6 \text{ HNO}_3 + 2 \text{ HF} + 1 \text{ CH}_3\text{COOH}$) followed by distilled water rinses, and then placed in a quartz crucible. For the reason of evaporation of antimony during the whole growth process, a small amount of antimony (0.1 wt.%) was added into the melt to prevent the non-stoichiometric growth of crystals. It was found that about $1 \times 10^{-3} \text{ mol}$ of antimony could be lost in gas form from the apparatus owing to the flowing hydrogen atmosphere¹⁰. Dopant (tellurium) was used in an elementary form and was added during the preparation of the polycrystalline material. The apparatus with the starting material was closed and rinsed out by very pure hydrogen during 24 hours in order to removing oxygen. From a very good quality undoped GaSb single crystal, the seed was cut at a length of about 5 cm having the dimensions 4 mm x 4 mm with an orientation of $\langle 111 \rangle_b$ (Sb) to the melt.

The axial temperature gradients close to the solidification interface were about 35 $\text{grad}\cdot\text{cm}^{-1}$, that is very low in comparison with other methods; for example, with the liquid encapsulated Czochralski (LEC) they reached up to 200 $\text{grad}\cdot\text{cm}^{-1}$. The horizontal gradient on the solid/liquid interface was almost flat. The pulling rate was 12 $\text{mm}\cdot\text{h}^{-1}$ with a rotation of the seed of about 20 - 25 rpm.

During the crystal growth two different kinds of atmosphere were used:

- a) very pure "atomic" hydrogen (ionized by deuterium lamp)
- b) very pure "molecular" hydrogen (for comparison)

The length of these crystals was about 60 mm and a diameter of about 20 - 25 mm.

For the investigation of electrical properties and dislocation density the GaSb crystals were cut along the growth direction to prepare samples of about $\sim 1 \text{ mm}$ thick. Both faces of wafers were mechanically polished using an alumina suspension on a thick glass plate. Afterwards the wafers were rinsed in water, in acetone and finally in distilled water several times. The free carrier concentration, mobility and resistivity of each crystal were measured using the van der Pauw method at room temperature, with an accuracy of about $\pm 8\%$.

3. RESULTS AND DISCUSSION

The crystals were grown from the same starting material containing always the same residual impurities. Undoped crystals grown under the molecular hydrogen atmosphere showed the starting carrier concentration (in the top part of crystals) of $1.7 \times 10^{17} \text{ cm}^{-3}$. This concentration along the growth direction has decreased down to $0.8 \times 10^{17} \text{ cm}^{-3}$. This effect is caused by the increasing concentration of the n-type impurities in the starting melt because their distribution coefficients are lower than 1. The concentration of n-type impurities in our material was higher than the concentration of p-type elements and therefore during the growth, the compensation of natural acceptors occurred².

It appears from these measurements, that the growth under ionized hydrogen atmosphere influences the electrical behavior of GaSb. However, the certain asymmetry in acceptor and donor passivation in GaSb material appears. In comparison with Polyakov's opinion⁷ we assume that the passivation of donors is higher than the passivation of acceptors, what should be confirmed in increasing of resistivity and of almost the same value of the free carrier concentration. For this reason we tried to prepare GaSb single crystals lightly doped with tellurium ($3.12 \times 10^{17} \text{ atoms}\cdot\text{cm}^{-3}$).

The concentration of tellurium in the top parts of crystals, calculated using the Pfann equation, shows the value of 1.0×10^{17} atoms. cm^{-3} and consequently the free carriers concentration is theoretically 0.7×10^{17} cm^{-3} (p-type). It is necessary to notice that the crystals were always pulled up so far that no melt was remaining any, i.e. up to $x = 1$ (x is the solidifying fraction). The bottom part ($0.98 > x > 1$) of crystals is always cut off. Thus, the crystals are ready to the measurements in the range of $0 < x < 0.98$. According to our previous studies of the GaSb crystals grown under molecular hydrogen atmosphere², the bottom fraction ($x = 0.98$) has showed that the tellurium concentration was about $(3.5 - 4.5) \times 10^{17}$ atoms. cm^{-3} , i.e. these parts of the crystals were always n-type with the free carriers concentration of the value of $(1.8 - 2.8) \times 10^{17}$ cm^{-3} (the starting concentration of tellurium in the melt was also 3.12×10^{17} atoms. cm^{-3}). However, the GaSb crystals doped with tellurium (the starting concentration of tellurium in the melt was the same, 3.12×10^{17} atoms. cm^{-3}) grown under the ionized hydrogen atmosphere showed quite different electrical properties from crystals pulled under the molecular hydrogen atmosphere. The free carrier concentration at the top of a crystal was 1.79×10^{16} cm^{-3} and resistivity $0.951 \Omega\cdot\text{cm}$ and at the end of the crystal 2.26×10^{16} cm^{-3} and $0.705 \Omega\cdot\text{cm}$. The whole crystal bowl showed p-type conductivity.

It is worth mentioning that the values of the free carrier concentration and resistivity were almost the same in a whole crystal in both directions, i.e. in the longitudinal and transversal directions to the growth axis. The homogeneity of the electrical properties was surprisingly quite good.

Electrical results show different values in both cases of used atmosphere (molecular and ionized hydrogen). According to the thermodynamical studies and calculations of the distribution of free carrier concentration in GaSb crystals, we prepared two figures that could very well describe behavior of ionized hydrogen in GaSb structure (see Fig.1. and Fig.2.).

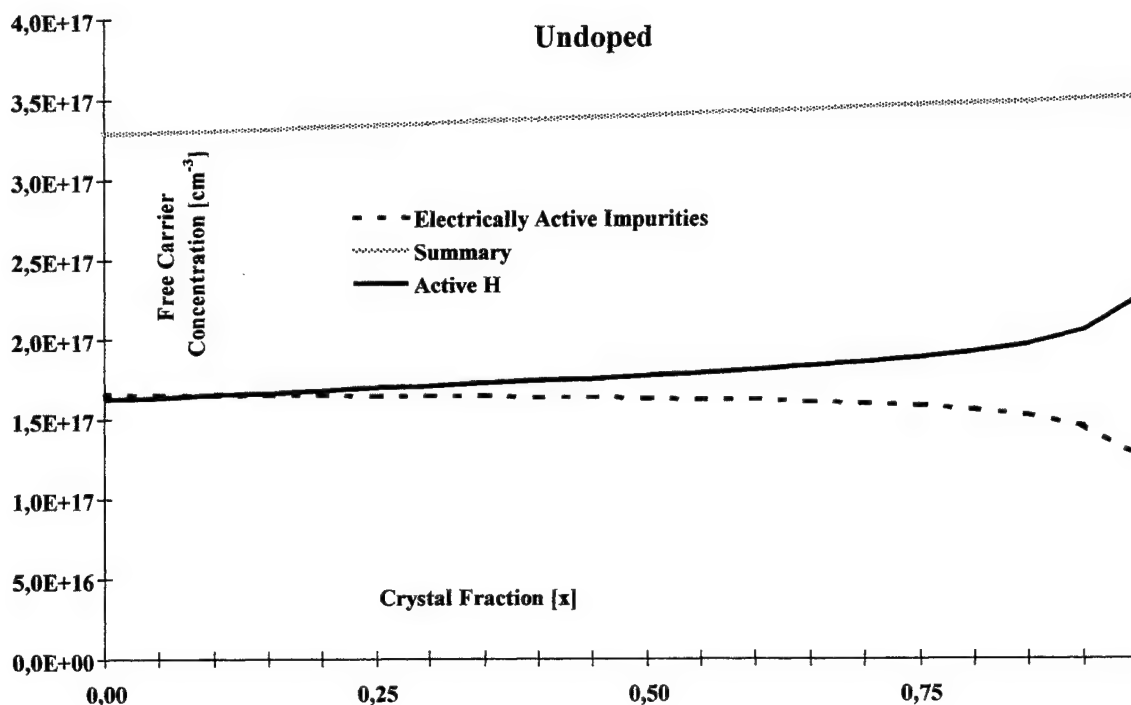


Fig. 1. Free carrier concentration distribution along to the growth axis in undoped GaSb single crystals grown using the Czochralski method in molecular and ionized hydrogen atmosphere.

As one can see on the figures 1 and 2, the concentration profiles of free carriers along the growth axis of the crystals grown in ionized hydrogen atmosphere (IHA crystals) are different in comparison with the profiles of the crystals

grown in molecular hydrogen atmosphere (MHA crystals). While MHA crystal profiles have logarithmic shape and could be very well described by Pfann equation, the IHA crystal profiles are almost exacting linear. It is visible for undoped and also for Te-doped GaSb. In the case of MHA crystals, the free carrier concentration has a decreasing tendency because the concentration of donors increases (it is also valid for undoped GaSb because the concentration of n-type impurities is higher than p-type ones in the starting GaSb material). However, IHA undoped and low Te-doped crystals have a slightly increasing profile. We follow our theory suggesting the preferably passivation of donors than acceptors.

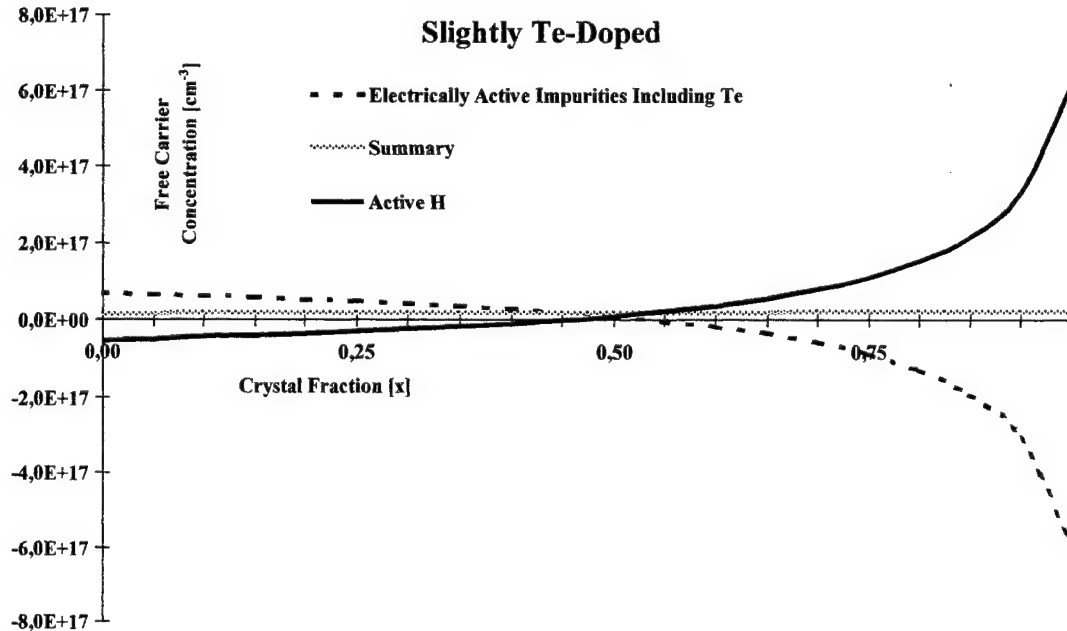


Fig. 2. Free carrier concentration distribution along to the growth axis in slightly Te-doped GaSb single crystals grown using the Czochralski method in molecular and ionized hydrogen atmosphere.

While molecular hydrogen during the growth procedure acts as an electrically neutral component and only reduces present oxides (Ga_2O_3 , etc.) and surplus oxygen, ionized hydrogen could be taken into consideration as an electrically active element. For this assumption the fact gives evidence that atomic gases always show higher activity in principle than molecular ones do. However, ionized hydrogen could be split to two different so-called dopants - acceptors as H^+ and donors as H^- . According to the free carrier concentration profiles along the crystal growth axis we assume an explanation that ionized hydrogen in GaSb is mainly an acceptor with a level close to the valence band edge. Calculating theoretically the active concentration of H^+ in crystals by using the Pfann equation, the distribution coefficient could be $k_{\text{eff}} = 0.15$ and then in the case of undoped GaSb crystals, the resulting free carrier concentration profile is a summary of the active concentration of impurities in the starting GaSb material and of the increasing concentration of H^+ . Seeing free carrier concentration profiles in slightly Te-doped GaSb, it seems that the behavior of ionized hydrogen is different. However, these results give us more detailed explanation how active hydrogen acts in GaSb structure.

Ionized hydrogen is split to H^+ and H^- active "dopants" which act as acceptors and/or donors. Between these two kinds certain equilibrium could be created in dependence on the concentration of acceptor's and donor's impurities in the GaSb material. There is an inclination in such a crystal to maintain the GaSb structure to be isoelectric. The suggested effect can be described by the following equations:

$$[\text{H}^+] \approx C_n \quad \text{and} \quad [\text{H}^-] \approx C_p, \quad \text{or} \quad (1)$$

$$k_1 \cdot \frac{[H^+]}{[H^-]} \approx k_2 \cdot \frac{C_n}{C_p}, \text{ while} \quad (2)$$

$$[H^+] + [H^-] = K_H \quad (3)$$

where C_p and C_n are acceptor's, resp. donor's concentration, and k_1 and k_2 are constants. K_H is a maximal concentration of ionized hydrogen in GaSb structure and reaches a value⁷ about of $10^{17} - 10^{18}$ atoms.cm⁻³. The ionized hydrogen seems to be an amphoteric material such as silicon. Concentration of H^+ increases with the concentration of donors, and vice versa, however, this splitting of active hydrogen to H^+ and H^- is limited by its total concentration.

The mathematical evaluation of this equilibrium should be next step of our study using thermodynamical methods to be able to effectively decrease free carrier concentration and to increase resistivity of GaSb single crystals.

4. CONCLUSION

The growth of GaSb single crystals under a flow of ionized hydrogen leads to lower free carrier concentration because of passivation of residual impurities (including dopants) and/or structural defects. It seems that the incorporated ionized hydrogen is splitting to H^+ and H^- active agents that could be characterized as acceptors and donors. Their concentrations depend on content of acceptor's and donor's dopants (impurities, structural defects, etc.) in the GaSb crystals. For a satisfactory growth of crystals with the free carrier concentration lower than 10^{15} cm⁻³ (which is the desired goal of scientists working with GaSb substrates) it is necessary to deal with a whole series of crystals with various concentrations of tellurium in the starting melt. According to our preliminary calculation, the optimal concentration should be (6 - 8) 10^{17} atoms.cm⁻³ of tellurium and such prepared crystals should show the free carrier concentration of about 10^{14} cm⁻³ along the whole crystal bowl. However, the total concentration of incorporated ionized hydrogen could be equivalent to the concentration of the whole impurities in GaSb material.

ACKNOWLEDGEMENT

The work was supported by the Grant Agency of the Czech Republic Nr. 104/97/0589, Nr. 100/98/0024 and Nr. 203/98/1276. The authors would like to express their thanks to Mr. V.Charvat (Institute of Physics, Czech Republic) for his excellent co-operation and fruitful help.

REFERENCES

1. H.Welker, "Über neue halbleitende Verbindungen II," *Z.Naturforsch.* **8a**, pp. 248-251, 1953.
2. B.Štěpánek and V.Šestáková, "Czochralski grown concentration profiles in the undoped and Te-doped GaSb single crystals," *Thermochim. Acta* **209**, pp. 285-294, 1992.
3. Y.J.Van der Meulen, "Growth properties of GaSb: The structure of the residual acceptor centers," *J.Phys.Chem.Solids* **28**, pp. 25-32, 1967.
4. D.Effer and P.J.Etter, "Growth of GaSb from non-stoichiometric melt," *J.Phys.Chem.Solids* **25**, pp. 451-460, 1964.
5. S.J.Pearton, J.W.Corbett and T.S.Shi, "Hydrogen in crystalline semiconductors," *Appl.Phys. A* **43**, pp. 153-195, 1987.
6. J.Chevallier and M.Aucouturier, "Influence of hydrogen atmosphere in III-V semiconductor crystals," *Ann.Rev.Mater.Sci.* **18**, pp. 219-268, 1988.
7. A.Y.Polyakov, S.J.Pearton, R.G.Wilson, R.Rai-Choudhury, R.J.Hillard, X.J.Bao, M.Stam, A.G.Milnes, T.E.Schlesinger and J.Lopata, "Hydrogen treatment effect on shallow and deep centers in GaSb," *Appl.Phys.Lett.* **60**, pp. 1318-1320, 1992.
8. A.Y.Polyakov, M.Stam, A.G.Milnes, R.G.Wilson, Z.Q.Fang, P.Rai-Choudhury and R.J.Hillard, "High-resistivity GaSb grown by molecular-beam epitaxy," *J.Appl.Phys.* **72**, pp. 1316-1319, 1992.
9. V.Šestáková, B.Štěpánek, J.J.Mareš and J.Šesták, "Decrease in free carrier concentration in GaSb crystals using an ionized hydrogen atmosphere," *Materials Chemistry and Physics* **45**, pp. 39-42, 1996.
10. F.Moravec, V.Šestáková, B.Štěpánek and V.Charvat, "Crystal growth and dislocation structure of gallium antimonide," *Cryst.Res. Technol.* **24**, pp. 275-281, 1989.

Dynamics and thermodynamics of quantum crystals near the instability point in the self-consistent phonon theory

Cecylia Malinowska-Adamska, Piotr Słoma, and Janusz Tomaszewski

Institute of Physics, Technical University of Łódź
Wólczńska 219, 93-005 Łódź, Poland

ABSTRACT

Formally one can distinguish between the thermodynamic stability conditions (the free energy of the lattice should have a minimum with respect to small variations mechanical or otherwise) and the dynamical ones (the phonon spectrum of the lattice should be positively defined). These last conditions are easily formulated in the self-consistent phonon theory (SCPT) based on the thermodynamic double-time Green's function method. According to it the dynamic instability temperature T_s for a simple Bravais lattice defines the temperature at which the bound crystalline state of atoms vanishes that really means that the phonon frequencies become complex at sufficiently high temperatures $T \leq T_s$.

Using the reduced second order approximation of the SCPT the dynamics of crystal lattice and the thermodynamical properties of the quantum crystals in the vicinity of the instability point are investigated. The results of calculations of the pressure dependence of the instability temperature, melting criterion, internal and free energy, free Gibbs energy as well as selected dynamic properties obtained with the help of the generalized form of the Buckingham, the Lennard-Jones and the Morse self-consistent potentials are given and compared with experimental data of solid h.c.p. ^4He and f.c.c. ^{20}Ne .

Comparison of the theoretical and experimental results allows us to state that the limiting temperatures of the dynamical stability obtained for the above-mentioned models pair potentials always appear to be the upper estimations of the real melting temperature.

Keywords: self-consistent phonon theory, quantum crystals, stability condition of solid helium and neon.

1. INTRODUCTION

In a series of papers^{1,2} Plakida and Siklós have developed the self-consistent phonon theory (SCPT) of highly anharmonic crystals. This theory has been considered for some models of crystals³⁻⁶. In this paper, using the SCPT in the reduced second order approximation (RSOA) the dynamic and thermodynamic properties of quantum crystals in the vicinity of the instability point are investigated.

As it appears in the RSOA the limiting temperature of dynamical stability T_s^{dyn} may be obtained through a detailed analysis of the solvability of the self-consistent (s.c.) equation for the mean square relative displacement of neighbouring atoms:

$$\langle u^2(l) \rangle = \left\langle \left[\bar{l}(\bar{u}_i - \bar{u}_0) \right]^2 \right\rangle / l^2, \quad (1)$$

where \bar{u}_0 and \bar{u}_i are the displacements of neighbouring atoms from their equilibrium positions and $l = l(T, p)$ is their separation. $\langle u^2(l) \rangle = \langle u^2(T, p) \rangle$ depends on the explicit form of the s.c. potential for the pairwise atomic interactions $\tilde{\varphi}(l)$. In particular, for the high temperature limit²:

$$\langle u^2(l) \rangle \approx \frac{6\theta}{zf(T, p)} \left\{ [1 - 0.11C_1(T, p)]^{-1} + C_2(T, p) \right\} \quad (2)$$

where: $\theta = k_B T$, $C_1(T, p) = \theta g^2(T, p) / f^3(T, p)$, $C_2(T, p) = \hbar^2 f(T, p) / 3M\theta^2$.

$f(T, p) = \partial^2 \tilde{\varphi} / \partial l^2$ and $g(T, p) = \partial^3 \tilde{\varphi} / \partial l^3$ are the anharmonic force constants. z , \hbar , k_B and M are the number of nearest neighbours, Planck constant divided by 2π , the Boltzmann constant and mass of atom, respectively.

The equation (2) has a different number of real solutions depending on the values of temperature T and pressure p . As it was shown by Siklós and Aksienov⁷ for any given p , below a critical pressure p_c , and for $T \leq T_s^{dyn}$ the lowest solution is the only physical one and corresponds to a stable crystal state.

In this paper we study the problem of lattice stability of quantum crystals (solid h.c.p. ^4He and f.c.c. ^{20}Ne). Apart from the pressure variations of T_s^{dyn} we also investigate the behaviour of selected dynamic and thermodynamic properties of these crystals near the limit of stability. The detailed calculations are performed for the following s.c. potentials:

- exponential-power (exp, m) Buckingham (B)

$$\tilde{\varphi}_B(l) = \frac{\alpha m}{\alpha - m} D_0 \left\{ \frac{1}{\alpha} \exp(\alpha x_1) - \sum_{k=0}^{\infty} \frac{1}{k!} y^k A_m^{(2k)} x^{m+2k} \right\}, \quad (3)$$

- purely power (n, m) Lennard-Jones (LJ)

$$\tilde{\varphi}_{LJ}(l) = \frac{nm}{n-m} D_0 \sum_{k=0}^{\infty} \frac{1}{k!} y^k \left[A_n^{(2k)} x^{n+2k} - A_m^{(2k)} x^{m+2k} \right], \quad (4)$$

- purely exponential (exp, exp) Morse (M)

$$\tilde{\varphi}_M(l) = \frac{\alpha\beta}{\alpha - \beta} D_0 \left\{ \frac{1}{\alpha} \exp(\alpha x_1) - \frac{1}{\beta} \exp(\beta x_2) \right\}, \quad (5)$$

The symbols used in (3) to (5) have the following meaning:

$$x = \frac{r_0}{l}, \quad x_1 = \left(1 - \frac{l}{r_0} + \alpha y \right), \quad x_2 = \left(1 - \frac{l}{r_0} + \beta y \right), \quad y = \langle u^2(l) \rangle / 2r_0^2,$$

$$A_{p'}^{(q)} = \begin{cases} \frac{1}{p'} & \text{for } q = 0 \\ \frac{1}{p'} p'(p'+1) \dots (p'+q-1) & \text{for } q = 1, 2, \dots \end{cases}$$

n, m, α and β are the dimensionless parameters describing the slope of the potentials curves, r_0 and D_0 define the potential minimum and are, respectively, the equilibrium distance of two isolated atoms and the energy of their dissociation. In order to obtain the numerical values of these parameters we take the zero point experimental data for the nearest-neighbours separation l_0 , the energy of sublimation E_0 and the isothermal compressibility K_0 together with the relationships connecting these quantities with the interatomic interaction function.⁶

2. DYNAMIC AND THERMODYNAMIC FUNCTIONS OF STRONGLY ANHARMONIC QUANTUM CRYSTALS.

To discuss the dynamics and thermodynamics of the model we should calculate the pressure variation of the renormalization parameter y , the limiting temperature of dynamic stability T_s^{dyn} , the anharmonic force constants $f(T, p)$ and $g(T, p)$ as well as the internal energy E , the binding energy of lattice atoms D , the enthalpy H , the free energy F and the free Gibbs energy G . By taking into account only the renormalized cubic anharmonic interaction, we obtain the same expressions for above mentioned functions as in the conventional perturbation theory but with renormalized frequencies.² The general analytical forms for them are presented collectively in our previous paper⁸ and are used in this paper in order to characterize the physical properties of h.c.p. helium and f.c.c. neon in numerical form with the help of the RSOA. The calculations are extended from low to high pressures.

3. NUMERICAL RESULTS.

Using the values of potential energy parameters given in Table 1 for the Buckingham (Eq.(3)), Lennard-Jones (Eq.(4)) and the Morse (Eq.(5)) s.c. functions we have found for the quantum crystals the pressure variations of the limiting temperature of dynamic stability T_s^{dyn} (Table 2). Numerical values of T_s^{dyn} are listed in Table 2 together with experimental data of the melting temperature T_m for comparison.

Table 1. Optimal values of the Buckingham (*B*), Lennard-Jones (*LJ*) and Morse (*M*) potential energy parameters of solid helium and neon calculated with the help of experimental data for the zero-point nearest-neighbour distance l_0 , energy of sublimation E_0 and isothermal compressibility K_0 .⁹

Solids	Experimental data	Potential functions	Parameters					
			D_0 (10^{-23} J/atom)	r_0 (nm)	α	β	n	m
⁴ He h.c.p.	$l_0=0.36378$ nm	(<i>B</i>)	9.2250	0.2892	4.2	-	-	6.0
	$E_0=-0.07976 \cdot 10^{-21}$ J/atom	(<i>LJ</i>)	10.5325	0.2860	-	-	10.2	5.1
	$K_0=3.29 \cdot 10^{-8}$ Pa ⁻¹	(<i>M</i>)	9.3440	0.2692	6.0	3.0	-	-
²⁰ Ne f.c.c.	$l_0=0.31560$ nm	(<i>B</i>)	76.5	0.3001	19.0	-	-	6.0
	$E_0=3.115 \cdot 10^{-21}$ J/atom	(<i>LJ</i>)	77.5	0.2990	-	-	18.50	6.0
	$K_0=0.09 \cdot 10^{-8}$ Pa ⁻¹	(<i>M</i>)	73.8	0.3025	14.1	6.1	-	-

Table 2. Pressure variations of the limiting temperature of the dynamical T_s^{dyn} stability of solid helium and neon in the RSOA. Experimental values of the melting temperature $T_m^{10,11}$ are given for comparison. The meaning of symbols is as in Table 1.

p	T_m	T_s^{dyn} (K) for ⁴ He			p	T_m	T_s^{dyn} (K) for ²⁰ Ne		
(MPa)	(K)	(B)	(LJ)	(M)	(MPa)	(K)	(B)	(LJ)	(M)
	(Ex)					(Ex)			
3.222	1.86	10.9	8.2	8.7	0	24.6	25.9	26.8	26.0
4.164	2.13	11.8	8.8	9.9	10	26.0	27.5	28.6	27.5
5.248	2.41	12.6	10.7	11.0	20	27.5	29.1	30.4	29.0
6.414	2.69	13.5	12.2	12.0	32	29.2		32.8	
7.842	3.00	14.3	13.2	13.1	40	30.3	32.4	x	32.1
9.646	3.37	15.4	14.6	14.2	50	31.7	34.1	x	33.6
11.774	3.80	16.7	15.7	15.3	58	32.9	35.4	x	
12.256	4.27	18.3	17.7	16.6	63	33.6	x	x	x

Within the investigations of the lattice stability we have also computed the pressure variations of the modified melting criterion defined as the ratio $x = \sqrt{\langle u^2 \rangle} / l_s$ (l_s – the equilibrium interatomic spacing at $T = T_s^{dyn}$) (Table 3). It should be noted that this coefficient is, in the RSOA, the equivalent of the classical Lindemann criterion¹².

The most characteristic results of our investigations of the dynamics and thermodynamics of the quantum crystals are given and compared with the available experimental data^{10,11,13} in Tables 3-6.

Table 3. The effect of pressure on the distance between neighbouring atoms l , renormalization parameter y , melting criterion x and the anharmonic force constants f and g of solid helium. Experimental (l_{exp}) values of l at $T=0K^{10}$ are shown for comparison. The meaning of symbols is as in table 2.

4He h.c.p.		(B)					(LJ)					(M)				
p	l_{exp}	l	y	x	f	g	l	y	x	f	g	l	y	x	f	g
(MPa)	($10^{10}m$)	($10^{10}m$)	-	-	(N/m)	($10^{10}Pa$)	($10^{10}m$)	-	-	(N/m)	($10^{10}Pa$)	($10^{10}m$)	-	-	(N/m)	($10^{10}Pa$)
3.222	3.6378	3.6376	0.0314	0.1992	0.031	-0.139	3.6380	0.0336	0.2039	0.045	-0.271	3.6386	0.0439	0.2193	0.015	0.048
4.164	3.6080	3.6023	0.0298	0.1959	0.033	-0.147	3.6083	0.0316	0.1996	0.048	-0.285	3.5517	0.0410	0.2171	0.017	0.052
5.248	3.5777	3.5662	0.0282	0.1927	0.035	-0.156	3.5776	0.0298	0.1953	0.050	-0.301	3.4750	0.0385	0.2150	0.019	0.057
6.414	3.5468	3.5317	0.0269	0.1898	0.037	-0.165	3.5482	0.0281	0.1914	0.054	-0.318	3.4095	0.0365	0.2132	0.020	0.062
7.842	3.5155	3.4944	0.0254	0.1867	0.040	-0.177	3.5161	0.0264	0.1872	0.057	-0.338	3.3445	0.0345	0.2114	0.022	0.067
9.646	3.4835	3.4534	0.0240	0.1834	0.043	-0.190	3.4806	0.0247	0.1827	0.062	-0.364	3.2782	0.0325	0.2095	0.024	0.072
11.774	3.4509	3.4117	0.0226	0.1801	0.047	-0.206	3.4442	0.0230	0.1784	0.067	-0.393	3.2147	0.0307	0.2076	0.027	0.079
14.256	3.4178	3.3699	0.0212	0.1769	0.051	-0.223	3.4076	0.0215	0.1714	0.073	-0.426	3.1541	0.0291	0.2058	0.029	0.085

Table 4. Pressure variations of the internal energy E , binding energy D , enthalpy H , free Gibbs energy G and the free energy F (all quantities in units of 10^{-21} J/atom) of 4He obtained in the RSOA. Experimental data (E_{exp}) for E at $T=0K^{10}$ are given for comparison. The meaning of symbols is as in Table 2.

4He		(B)					(LJ)				
p	E_{exp}	E	D	H	G	F	E	D	H	G	F
(MPa)											
3.222	-0.07976	-0.07970	-0.04956	0.02996	-0.06539	-0.17505	-0.07964	-0.05927	0.03006	-0.28662	-0.39632
4.164	-0.07672	-0.07087	-0.04978	0.06678	-0.02093	-0.15858	-0.07772	-0.05937	0.06061	-0.23163	-0.36997
5.248	-0.07286	-0.06114	-0.05009	0.10718	0.02653	-0.14180	-0.07415	-0.05955	0.09578	-0.17369	-0.34364
6.414	-0.06803	-0.05111	-0.05046	0.14868	0.07414	-0.12565	-0.06922	-0.05981	0.13337	-0.11629	-0.31888
7.842	-0.06210	-0.03928	-0.05094	0.19734	0.12881	-0.10782	-0.06216	-0.06015	0.17890	-0.05118	-0.29224
9.646	-0.05492	-0.02498	-0.05155	0.25594	0.19338	-0.08754	-0.05228	-0.06062	0.23532	0.02477	-0.26283
11.774	-0.04581	-0.00881	-0.05225	0.32180	0.26472	-0.06589	-0.03984	-0.06118	0.30033	0.10772	-0.23245
14.256	-0.03533	0.00928	-0.05302	0.39505	0.34295	-0.04282	-0.02479	-0.06182	0.37410	0.19774	-0.20115

4He		(M)				
p	E_{exp}	E	D	H	G	F
(MPa)						
3.222	-0.07976	-0.07970	-0.04238	0.03006	0.00622	-0.10354
4.164	-0.07672	-0.07933	-0.04467	0.05261	0.03139	-0.10055
5.248	-0.07286	-0.07726	-0.04672	0.07849	0.05949	-0.09626
6.414	-0.06803	-0.07390	-0.04848	0.10586	0.08867	-0.09109
7.842	-0.06210	-0.06882	-0.05024	0.13864	0.12315	-0.08431
9.646	-0.05492	-0.06153	-0.05203	0.17876	0.16493	-0.07536
11.774	-0.04581	-0.05219	-0.05374	0.22440	0.21206	-0.06453
14.256	-0.03533	-0.04074	-0.05536	0.27559	0.26458	-0.05174

Table 5. The effect of pressure on the distance between neighbouring atoms l , renormalization parameter γ , melting criterion x and the anharmonic force constants f and g of solid neon. The meaning of symbols is as in Table 2.

^{20}Ne	(B)					(LJ)					(M)				
p	l	γ	x	f	g	l	γ	x	f	g	l	γ	x	f	g
(MPa)	(10^{10}m)	-	-	(N/m)	(10^{10}Pa)	(10^{10}m)	-	-	(N/m)	(10^{10}Pa)	(10^{10}m)	-	-	(N/m)	(10^{10}Pa)
0	3.1562	0.0020	0.0607	0.707	-5.955	3.1563	0.0020	0.0600	0.774	-7.276	3.1562	0.0021	0.0628	0.577	-3.851
10	3.1471	0.0020	0.0601	0.741	-6.198	3.1472	0.0019	0.0593	0.812	-7.582	3.1470	0.0021	0.0622	0.603	-3.991
20	3.1388	0.0019	0.0595	0.774	-6.432	3.1388	0.0019	0.0587	0.848	-7.879	3.1385	0.0020	0.0617	0.628	-4.127
32	3.1296	0.0019	0.0588	0.812	-6.706	3.1296	0.0018	0.0580	0.891	-8.225	3.1290	0.0020	0.0611	0.657	-4.286
40	3.1238	0.0018	0.0584	0.837	-6.883	x	x	x	x	x	3.1230	0.0020	0.0607	0.677	-4.389
50	3.1171	0.0018	0.0579	0.868	-7.101	x	x	x	x	x	3.1159	0.0019	0.0602	0.700	-4.515
58	3.1119	0.0018	0.0575	0.892	-7.272	x	x	x	x	x	3.1105	0.0019	0.0599	0.719	-4.615
63	x	x	x	x	x	x	x	x	x	x	3.1073	0.0019	0.0597	0.730	-4.676

Table 6. Pressure variations of the internal energy E , binding energy D , enthalpy H , free Gibbs energy G and the free energy F (all quantities in units of 10^{-21} J/atom) of ^{20}Ne obtained in the RSOA. The meaning of symbols is as in Table 2.

^{20}Ne	(B)					(LJ)				
p	E	D	H	G	F	E	D	H	G	F
(MPa)										
0	-3.11548	-0.61877	-3.11548	-3.12680	-3.12680	-3.11417	-0.62026	-3.11417	-3.13319	-3.13319
10	-3.11860	-0.62232	-2.89820	-2.90859	-3.12899	-3.11847	-0.62414	-2.89805	-2.91575	-3.13617
20	-3.11968	-0.62552	-2.68236	-2.69193	-3.12925	-3.12062	-0.62765	-2.68329	-2.69983	-3.13716
32	-3.11870	-0.62900	-2.42513	-2.43385	-3.12742	-3.12085	-0.63145	-2.42725	-2.44258	-3.13618
40	-3.11688	-0.63114	-2.25468	-2.26288	-3.12508	x	x	x	x	x
50	-3.11347	-0.63362	-2.04270	-2.05032	-3.12108	x	x	x	x	x
58	-3.10991	-0.63547	-1.87396	-1.88114	-3.11710	x	x	x	x	x
63	x	x	x	x	x	x	x	x	x	x

^{20}Ne	(M)				
p	E	D	H	G	F
(MPa)					
0	-3.11568	-0.61358	-3.11568	-3.11855	-3.11855
10	-3.11684	-0.61637	-2.89645	-2.89889	-3.11927
20	-3.11609	-0.61891	-2.67888	-2.68094	-3.11815
32	-3.11305	-0.62168	-2.41986	-2.42151	-3.11470
40	-3.10989	-0.62338	-2.24835	-2.24977	-3.11130
50	-3.10482	-0.62538	-2.03522	-2.03636	-3.10596
58	-3.09996	-0.62687	-1.86567	-1.86660	-3.10089
63	-3.09658	-0.62777	-1.76011	-1.76063	-3.09740

The results of our investigations are collected in numerical forms, instead of the graphs, in order to complete the full experimental and theoretical characteristics of the properties of solid helium and neon.

4. CONCLUSIONS

With the reduced, second order approximation² we have presented numerical calculations of the pressure variations of the limiting temperature of stability T_s^{dyn} (Table 2) and selected dynamic (Table 3 and 5) and thermodynamic properties (Table 4 and 6) of solid helium and neon. The calculations are performed in terms of the (exp,m) Buckingham, the (n,m) Lennard-Jones and the (exp,exp) Morse self-consistent potentials as interatomic potentials models in quantum solids.

The detailed analysis of the numerical values for T_s^{dyn} , (defined as the temperature at which the lattice as a bound state of the atoms due to the attractive part of the interatomic potential becomes unstable with respect to the collective excitations-self-consistency phonons²) show that ones are always the upper estimation of the real melting temperature – the better when the pressure is low and the pair potential hard. On the other hand the high-pressure results for the dynamical and thermodynamical quantities are generally better when the potential is soft. In connection with this we are convinced that, for further investigations of the quantum crystals, it is worthwhile taking all the three potentials but the RSOA of the lattice dynamics should be expanded by taking into account not only nearest-neighbour interactions but increasing over four the number of “important” terms in the potential energy decomposition. Work in this direction is in progress.

REFERENCES

1. N.M.Plakida, T.Siklós, „Theory of anharmonic crystals”, *Phys. Stat. Sol.*, **33**, pp. 103-112 and pp. 113-123, 1969; **39**, pp. 171-180, 1970.
2. N.M.Plakida, T.Siklós, „Lattice dynamics and stability of anharmonic crystals”, *Acta Phys. Hung.* **45**(1), pp. 37-74 1978.
3. C.Malinowska-Adamska, I.Maciejewska, J.Tomaszewski, „Study of rare gas solids in the self-consistent phonon theory”, *Acta Phys. Hung.* **71**, pp. 179-200, 1992.
4. C.Malinowska-Adamska, P.Słoma, J.Tomaszewski, „Application of the Lennard-Jones (n,m) potential function to quantum crystals in the self-consistent phonon theory”, *Phys. Stat. Sol.*, **(b) 200**, pp. 451-462, 1997.
5. J.Tomaszewski, C.Malinowska-Adamska, „Self-consistent description of the lattice destabilisation phenomenon for the heavier rare gas solids”, *Proceedings of SPIE, Solid State Crystals: Single Crystal Growth, Characterization and Applications*, Vol. **3724**, pp. 177-182, 1999.
6. C.Malinowska-Adamska, P.Słoma, J.Tomaszewski, „Self-consistent calculations of the thermodynamic and elastic properties of heavier rare gas solids near the lattice instability point”, *Phys. Stat. Sol.*, **(b) 219**, pp. 229-240, 2000.
7. T.Siklós, V.L.Aksienov, „Thermodynamics of strongly anharmonic crystals”, *Phys. Stat. Sol.*, **(b) 50**, pp. 171-178, 1972.
8. C.Malinowska-Adamska, „Interatomic interaction and physical properties of quantum crystals in the self-consistent phonon theory”, *Proceedings of SPIE, Single Crystal Growth, Characterization and Applications*, Vol. **3724**, pp. 94-103, 1999.
9. P.Słoma, C.Malinowska-Adamska, J.Tomaszewski, „Self-consistent interatomic interaction in quantum crystals”, *ibid.* pp. 171-176.
10. D.O.Edwards and R.C.Pandorf, „Heat capacity and other properties of hexagonal close-packed helium-4”, *Phys. Rev.*, **140** (3A), A816-A825, 1965.
11. G.L.Pollack, „The solid state of rare gases”, *Rev. Modern Physics*, **36**, pp. 748-791, 1964.
12. C.Malinowska-Adamska, „Self-consistent calculations of the melting criterion based on lattice instability”, *Phys. Stat. Sol.*, **(b) 143**, pp. 63-71, 1987.
13. D.N.Batchelder, D.L.Losse and R.O.Simmons, „Measurements of lattice constant thermal expansion and isothermal compressibility of neon single crystals”, *Phys. Rev.*, **162**, pp. 767-775, 1967.

Calculations of third-order electronic susceptibility of alkali halides

Włodzimierz Kucharczyk^{a*}, Fray de Landa Castillo-Alvorado^b,
Piotr Górski^a and Rafał Ledzion^a

^aInstitute of Physics, Technical University of Łódź,
ul. Wólczańska 219, 93-005 Łódź, Poland,

^bEscuela Superior de Física y Matemáticas, Instituto Politécnico
National, Edificio 6 UPLAM, Delegado G.A. Madero,
07738 Mexico District Federal, Mexico

ABSTRACT

Hyper-Raman scattering by the zone-centre optical phonons in some alkali halides is investigated. In our calculations we relate the electrooptic part of the hyper-Raman tensor to the third-order optical susceptibility and the electric field associated with the LO phonons. The results obtained for those alkali halides for which the third-order optical susceptibility has not been measured yet, show that the electrooptic and lattice contributions to the hyper-Raman scattering are comparable. In all crystals considered, we found the cubic anisotropy of the electrooptic part of the hyper-Raman tensor to be not strongly exhibited.

Keywords: Nonlinear susceptibilities, nonlinear refractive index, hyper-Raman scattering, electrooptic effects, alkali halides

1. INTRODUCTION

The bond polarizability model has been employed previously for various crystals, including alkali halides and crystals composed of different bonds, either to nonlinear effects of purely electronic origin or to phenomena due to nonlinear interactions of electric fields with the crystal lattice. For example, the method has been applied to second-¹⁻³ and third-harmonic generation⁴⁻⁶, and the linear^{7,8} and quadratic electrooptic coefficients.⁹ Recently, studies of hyper-Raman scattering in alkali halides by the zone-centre optical phonons¹⁰ and calculations of the nonlinear refractive of alkali halides have been presented as well.¹¹

The aim of this work is to present calculations of the electronic third-order nonlinear susceptibility of alkali halides and to discuss the contribution of the nonlinear susceptibility to the hyper-Raman scattering of the crystals.

2. METHOD

Our calculations utilize the approach based on the idea of interionic excitations. These are often described in terms of the one-gap Penn model.¹² In the model, the optical susceptibility can be related to the transition from the valence band to an exciton state or to the conduction band. One notes that the interionic description is not necessary limited to covalent compounds. In alkali halides the highest valence band is formed from the p-electrons of the anions and the lowest conduction band from the s-electrons of the cations.¹³

Within the Phillips-Van Vechten theory^{14,15}, the effective energy gap E_g of the Penn model can be decomposed into heteropolar C and homopolar E_h contributions. In the long-wavelength limit, the linear optical susceptibility $\chi(\infty)$ is given by

$$\chi(\infty) = \frac{(\hbar\omega_p)^2}{(C^2 + E_h^2)}. \quad (1)$$

In this, ω_p is the plasma frequency of the free-valance electron gas defined as

* W.K. (correspondence): Email: kucharcz@ck-sg.p.lodz.pl; Telephone: +48 42 6313669; Fax: +48 42 6313639

$$(\hbar\omega_p)^2 = \frac{N_e e^2 A D}{4 \pi m}, \quad (2)$$

where A and D are correction factors of order unity, N_e is the density of the valence electrons, and e and m are the electron charge and mass, respectively. The Phillips-Van Vechten theory introduces the so-called spectroscopic scale of ionicity^{14,15}, as measured by the parameter f_i

$$f_i = \frac{C^2}{C^2 + E_h^2}. \quad (3)$$

The heteropolar contribution is related to the ionic binding and in the $A^I B^{VII}$ compounds can be expressed by

$$C = b e^2 \left(\frac{1}{r_\alpha} - \frac{7}{r_\beta} \right) \exp \left(- \frac{k_s R}{2} \right), \quad (4)$$

where r_α and r_β are the cation and anion radii, respectively, $R = r_\alpha + r_\beta$ is the bond length, k_s is the Thomas-Fermi screening wave number and the parameter b accounts for the deficiency of the model in describing the screening by free electrons. Following Levine¹, we expressed E_h as

$$E_h = A_h R^{-s} \left(\frac{(R - 2r_c)^{2s}}{r_{\alpha c}^{2s} + r_{\beta c}^{2s}} \right)^{\frac{1}{2}}, \quad (5)$$

where A_h and s are constants, $r_{\alpha c} = r_\alpha - 0.175R$, $r_{\beta c} = r_\beta - 0.175R$ and $r_c = 0.175R$.

Although the approach describes the optical susceptibility in terms of the interionic excitations, Phillips and Van Vechten have introduced an additional coefficient D into the Eq. (2) to account for excitations of core electrons.^{14,15} Accordingly, Weber¹⁶ decomposed the linear susceptibility of alkali halides into two parts due to different microscopic phenomena

$$\chi_{ij} = \chi'_{ij} + \chi''_{ij}, \quad (6)$$

where the term χ'_{ij} describes that part of the optical susceptibility which is interionic and can be related to the bond polarizability. The contribution χ''_{ij} stems from excitations of the cation cores and represents the intraionic part of χ_{ij} . According to the bond polarizability approach (see, for example, in Refs 1,4), the macroscopic linear optical susceptibility χ'_{ij} can be expressed by

$$\chi'_{ij} = \frac{1}{V} \sum_n \beta_n^{L,T} \alpha_{ni} \alpha_{nj}. \quad (7)$$

Here, $\beta_n^{L,T}$ is the longitudinal or transverse component of the axially symmetric bond polarizability tensor, defined in a way which includes local field effects, α_{ni} is the relevant direction cosine, and the summation is taken over all bonds in the volume V. The bond polarizability model provides a simple link between the crystal structure and magnitude of nonlinear optical susceptibilities. In terms of the bond polarizability model these are described by higher-order bond polarizabilities. Dispersion in the linear and second-order bond polarizabilities of alkali halides has been discussed in Ref. 17.

Employing Eqs (1)-(7), two independent components of the third-order optical susceptibility tensor of the rock salt-structure crystals can be expressed as⁶

$$\chi_{1111} = \frac{(\chi')^3 R^4 (F_e^L + 2c^3 F_e^T)}{(4\pi)^2 q_{\text{eff}}^2 (1+2c)^3}, \quad (8)$$

and

$$\chi_{1122} = \frac{2(\chi')^3 R^4 c^3 F_e^T}{8\pi^2 q_{\text{eff}}^2 (1+2c)^3}, \quad (9)$$

where $c = \beta^T / \beta^L$ describes the anisotropy of the linear bond polarizability tensor, q_{eff} is the effective bond charge, and $F_e^{L,T}$ defined as

$$F_e^{L,T} = \frac{R^2}{2\beta^{L,T}} \left(\frac{\partial^2 \beta^{L,T}}{\partial (\Delta r_{\text{eff}}^{L,T})^2} \right)_R, \quad (10)$$

represents the electronic contribution to the longitudinal or transverse component of the third-order bond polarizability tensor.

Except for the effective bond charge, all parameters which appear in Eqs (8) and (9) can be easily obtained from experimental data. The way of deriving the numerical values of components β^L and β^T and, therefore, c from the interionic part of the linear optical susceptibility, has been proposed in Ref. 16. In our calculations, we employed the effective bond charge determined by taking into account the relationship between the charge and the ionicity of the crystals.^{18,19}

3. HYPER-RAMAN SCATTERING IN ALKALI HALIDES

In centrosymmetric crystals like alkali halides, the second-order nonlinear susceptibility $\chi_{ijk}^{(2)}$ is allowed on the bond level. When the local changes in the symmetry due to the lattice vibrations are neglected, contributions of all bonds in the unit cell cancel themselves and $\chi_{ijk}^{(2)}$ vanishes on the macroscopic level.¹⁰ However, when phonons locally brake the inversion symmetry, an observation of scattering of light in the vicinity of the second harmonic of the incident light, i.e. hyper-Raman scattering, is possible.^{20,21}

In the halite-type alkali halides, of-resonance, the HR tensor $R_{\alpha\beta\gamma}$ of the zone-center TO and LO phonons is given by derivatives of the susceptibility $\chi_{ijk}^{(2)}$ with respect to the relative displacement u of the alkali metal and halogen sublattices and the macroscopic electric field E associated with the LO phonon^{20,21}

$$\begin{aligned} R_{\alpha\beta\gamma}^{TO} &= \frac{\partial \chi_{\alpha\beta\gamma}^{(2)}}{\partial u_\delta}, \\ R_{\alpha\beta\gamma}^{LO} &= \frac{\partial \chi_{\alpha\beta\gamma}^{(2)}}{\partial u_\delta} + R_{\alpha\beta\gamma}^{eo}. \end{aligned} \quad (11)$$

In this, the second term in the expression for $R_{\alpha\beta\gamma}^{LO}$ is related to the electro-optic contribution to HR scattering by the LO mode, namely

$$R_{\alpha\beta\gamma}^{eo} = -\frac{4\pi e_s N (\epsilon(\infty) + 2)}{3 \epsilon(\infty)} \left(\frac{\partial \chi_{\alpha\beta\gamma}^{(2)}}{\partial E_\delta} \right)_R, \quad (12)$$

where e_s is the Szegedi effective charge, $\epsilon(\infty)$ is the long-wave value of the electronic dielectric constant, N is the density of ion pairs and $\partial \chi_{\alpha\beta\gamma}^{(2)} / \partial E_\delta = 3 \chi_{\alpha\delta\beta\gamma}^{(3)}$, with $\chi_{\alpha\delta\beta\gamma}^{(3)}$ being the third harmonic generation susceptibility. Within the Kleinmann symmetry approximation, the zone-centre HR tensor of the crystals possess 12 non-zero and 2 independent components R_{xxxx} and R_{xxyy} for $\alpha=\delta=x$ and $\beta=\gamma=y$, and $\alpha=\delta=\beta=\gamma=x$, respectively.²¹

The hyper-Raman-spectra of some alkali halides have been measured by Vogt and Presting at room temperature. Two hyper-Raman lines corresponding to the transverse-optic (TO) and longitudinal-optic (LO) phonons at the center of the Brillouin zone were observed. Different configurations have been considered.²⁰ The first one was the configuration $x(yx)z$ where the scattering is due to the hyper-Raman tensor elements R_{xxyy}^{TO} and R_{xxyy}^{eo} . The spectral hyper-Raman efficiencies $S_{TO}(\Omega)$ and $S_{LO}(\Omega)$ can be given by²⁰

$$S_{TO}(\Omega) = \frac{h I_L}{4\pi \eta c N^2} [\Omega c]^4 [n(\omega) + 1] \frac{|R_{xxyy}^{TO}|^2}{Z^2} \text{Im}[\epsilon(\omega)], \quad (13)$$

$$S_{LO}(\Omega) = \frac{h I_L \epsilon(\omega)^2}{4\pi \eta c (ZN)^2} [\Omega c]^4 [n(\omega) + 1] \left| R_{xxyy}^{TO} + \frac{R_{xxyy}^{eo}}{N} \right|^2 \text{Im} \left[\frac{-1}{\epsilon(\omega)} \right]. \quad (14)$$

In Eqs (13) and (14), $\Omega=2\omega_L-\omega$ is the frequency of the scattered light, N is the number of primitive cells per unit volume, I_L is the laser intensity, Z is the transverse effective ionic charge, $[n(\omega)+1]$ is the Bose occupation factor and η is the refractive index. From Eqs (13) and (14) one obtains²⁰

$$S_{TO}(\Omega) = \frac{\pi}{\eta c} \left[\frac{\Omega}{c} \right]^4 \frac{h}{2 N M \omega_{TO}} [n(\omega) + 1] |R_{xxyy}^{TO}|^2 I_L, \quad (15)$$

where M is the reduced mass of the vibrating ions. Analogously, the expression for S_{LO} can be obtained by replacing ω_{TO} by ω_{LO} and the hyper-Raman tensor element R_{xxyy}^{TO} by R_{xxyy}^{eo} .²⁰ The values $|R_{xxxx}^{TO}| / |R_{xxyy}^{TO}|$ have been experimentally determined by switching between the scattering configurations $x(yy)z$ and $x(yx)z$. To obtain more information about the relative values of

the hyper-Raman components, in Ref. 20 the intensities of the LO-phonon lines in the scattering configurations $x(yy^*)z^*$ and $x(yx)z^*$, $y^* \equiv [001]$ and $z^* \equiv [011]$ were compared. The ratio of the corresponding hyper-Raman efficiencies

$$\frac{S_{LO}[x(yy^*)z^*]}{S_{LO}[x(yx)z^*]} = \frac{1}{4} \left[\frac{R_{xxxx}^{LO}}{R_{yyxx}^{LO}} - 1 \right]^2, \quad (16)$$

along with Eqs (13) and (14), allowed the experimental values of $|R_{xxxy}^{LO}/R_{xxxy}^{TO}|$, $|R_{xxxx}^{LO}/R_{xxxy}^{LO}|$, $|R_{xxxx}^{LO}/R_{xxxx}^{TO}|$ and next $|R_{xxxy}^{TO}|$ to be determined.²⁰ The values presented in Refs 10,20 show that the magnitude of the lattice contributions to R_{xxxx}^{TO} and R_{xxxy}^{TO} are of the order of magnitude of 10^{-14} esu.

4. RESULTS

The electrooptic contributions to the HR tensor of alkali halides derived in this work by employing Eqs (8) - (10) and (12) are listed in Table 1. The values obtained correspond to the long-wavelength limit, what is an intrinsic feature of the approach. In

Table1. Calculated values of the electrooptic contribution to the HR tensor of alkali halides.
Like previously published results^{10,19,20}, our values are given in 10^{-14} esu.

Crystal	R_{xxxx}^{eo}	R_{xxxy}^{eo}	$R_{xxxx}^{eo} / R_{xxxy}^{eo}$
LiCl	1.79	0.50	3.55
LiBr	2.46	0.73	3.35
LiI	2.90	1.45	2.90
NaI	2.23	0.93	2.40
KF	0.60	0.18	3.39
KI	1.32	0.52	2.56
RbF	1.12	0.38	2.95
RbCl	0.77	0.24	3.16
RbBr	0.86	0.27	3.25
RbI	1.17	0.41	2.84

our calculations we employed values of χ'_{ij} , χ''_{ij} , and f_i as listed in Ref. 22, along with the ionic radii corresponding to the minimum of electron density between cation and anion.²³ The long-wavelength values of the linear refractive index were taken from Refs 24,25. In our work we adopted calibration scale for the third-order optical susceptibility recommended in Ref. 26. This scale is roughly midway between the lowest²⁷ and the highest²⁸ proposed scales. To compare the values of the electrooptic contribution to the HR tensor calculated or measured at different frequencies, the dispersion in the third-order optical susceptibility should be taken into account. This can be done by using the generalized Miller rule or some others semi-empirical formulas (see, for example, Refs 11,29).

5. CONCLUSION

The ratio $R_{xxxx}^{eo} / R_{xxxy}^{eo}$ is close to 3, as it should be in isotropic materials. This proves that in the alkali halides the cubic anisotropy of the electrooptic contribution to the HR tensor is not strongly exhibited. When comparing our results with the previous experimental and theoretical results^{10,20,21} one observes that the lattice and electro-optic contribution to HR scattering are of comparable magnitudes.

REFERENCES

1. B.F. Levine, "Bond-charge calculation of nonlinear optical susceptibilities for various crystal structures", *Phys. Rev. B*7, pp. 2600-2626, 1973

2. D.F. Xue and S.Y. Zhang, "Comparison of nonlinear optical susceptibilities of KNbO_3 and LiNbO_3 ", *J. Phys. Chem. Solids*, **58**, pp. 1399-1402, 1997
3. D.F. Xue and S.Y. Zhang, "Calculation of nonlinear optical coefficients of orthorhombic $\text{Re}_2(\text{MoO}_4)_3$ crystals", *J. Phys. Chem. Solids* **59**, pp. 1337-1341, 1998
4. D.S. Chemla, R.F. Begley and R.L. Byer, "Experimental and theoretical studies of third-harmonic generation in the chalcopyrite CdGeAs_2 ", *IEEE J. Quantum Electron.* **QE-10**, pp. 71-81, 1974
5. V.G. Tsirelson, O.V. Korolkova, I.S. Rez and R.P. Ozerov, "Extended model of bond charges and its application in calculation of optical properties of crystals with different types of chemical bonds", *Phys. Stat. Sol. (b)* **122**, pp. 599-612, 1984
6. W. Kucharczyk, "The anisotropy of the cubic susceptibility in alkali halides as related to electro-optic and elasto-optic phenomena", *J. Phys. C: Solid State Phys.* **21**, pp. L985-L988, 1988
7. C. Shih and A. Yariv, "A theoretical model of the linear electro-optic effect", *J. Phys. C: Solid State Phys.* **15**, pp. 825-846, 1982
8. D.F. Xue and S.Y. Zhang, "Bond-charge calculation of electro-optic coefficients of diatomic crystals", *J. Solid State Chem.* **130**, pp. 54-57, 1997
9. W. Kucharczyk, "A bond-charge calculation of the quadratic electro-optic effect in LiF ", *J. Phys. C: Solid State Phys.* **20**, pp. 1875-1880, 1987
10. W. Kucharczyk and F.L. Castillo Alvarado, "Calculations of hyper-Raman tensor components of alkali halides", *J. Phys.: Condens. Matter* **11**, pp. 305-309, 1999
11. W. Kucharczyk, F.L. Castillo Alvarado, P. Górski and R. Ledzion "Calculations of nonlinear refractive index of alkali halides", *Opt. Quant. Electron.* **32**, in print, 2000
12. Penn D.R., "Wave-number-dependent dielectric function of semiconductors", *Phys. Rev.* **128**, pp. 2093-2097, 1962
13. S.T. Pantelides "Mechanisms that determine the electronic dielectric constants of ionic crystals", *Phys. Rev. Lett.* **35**, pp. 250-254, 1975
14. J.C. Phillips, "Ionicity of the chemical bond in crystals", *Rev. Mod. Phys.* **42**, pp. 317-356, 1970
15. J.A. Van Vechten "Quantum dielectric theory of electronegativity in covalent systems. I. Electronic dielectric constant", *Phys. Rev.* **182**, pp. 891-905, 1969
16. H.-J. Weber, "An empirical model of optical susceptibilities of crystals. I. Refractivity in alkali halides", *Z. Kristallogr.* **177**, pp. 185-199, 1986
17. W. Kucharczyk, "Dispersion in the linear and second-order bond polarizabilities of alkali halides", *phys. stat. sol. (b)* **182**, pp. 477-484, 1994
18. W. Kucharczyk, "Relationship between bond charge and the Szegedi effective charge in alkali halides", *J. Phys. Chem. Solids* **56**, pp. 871-876, 1995
19. W. Kucharczyk, F.L. Castillo Alvarado, P. Górski and R. Ledzion, "The effective bond charge in alkali halides - Another manifestation of the crystals ionicity", *J. Phys. Chem. Solids*, in print
20. H. Vogt and H. Presting, "Hyper-Raman scattering from alkali halides", *Phys. Rev. B*, **31**, pp. 6731-6738, 1985
21. H. Vogt, "Shell model description of hyper-Raman scattering from alkali metal halides", *J. Raman Spectrosc.* **21**, pp. 813-818, 1990
22. W. Kucharczyk, "The first-and second-order strain derivatives of electronic dielectric constants in alkali halides", *J. Phys. Chem. Solids* **55**, pp. 237-242, 1994
23. W. Kucharczyk, "Ionic sizes and strain derivative of electronic susceptibility in alkali halides", *Physica B* **172**, pp. 473-490, 1991
24. R.P. Lowndes and D.H. Martin, "Dielectric dispersion and the structures of ionic lattices", *Proc. R. Soc. A* **308**, pp. 473-496, 1969
25. M.E. Lines, "Bond orbital theory of linear and nonlinear electronic response in ionic crystals. II. Nonlinear response", *Phys. Rev. B* **41**, pp. 3383-3390, 1990
26. Landolt-Börnstein: *Numerical Data and Functional Relationships in Science and Technology*, New Series, Group III vol. 18, pp. 456-464, Springer Verlag, Berlin-Heidelberg-New York, 1984
27. R. Adair, L.L. Chase and S.A. Payne, "Nonlinear refractive index of optical crystals", *Phys. Rev. B* **39**, pp. 3337-3500, 1989
28. W.L. Smith, J.H. Bechtel and N. Bloembergen, "Dielectric-breakdown threshold and nonlinear-refractive index measurements with picosecond laser pulses", *Phys. Rev. B* **12**, pp. 706-714, 1975
29. P. Górski, M. Kin and W. Kucharczyk, "On the application of a generalized form of Miller's δ coefficient to nonlinear refractive indices in partially ionic crystals", *J. Phys. D: Appl. Phys.* **30**, pp. 1111-1114, 1997

Gd³⁺-Yb³⁺ exchange interactions in LiYb_xY_{1-x}F₄ single crystals

Lucjan E. Misiak

Department of Experimental Physics, Maria Curie-Skłodowska University, Place Marii Curie-Skłodowskiej 1, 20-031 Lublin, Poland.

ABSTRACT

The evaluated Gd³⁺-Yb³⁺ exchange interactions over the nearest and the next-nearest neighbors in LiYb_xY_{1-x}F₄ are found to increase in parabolic manner with x , the concentration of Yb³⁺ ions. The Gd³⁺-Yb³⁺ exchange interactions are sensitive to x in the range $x = 0.6 - 1.0$, while they are almost constant in the range $x = 0.1 - 0.5$. The estimated Gd³⁺-Yb³⁺ exchange interaction constants ($J = J_{nn} + J_{nnn}$) are in the range 0.5 – 2.8 GHz for x from 0.1 to 1, respectively. These exchange interaction constants are increased with lowering temperature. The results are comparable to those of estimated using the molecular-field model. The average Gd³⁺-Yb³⁺ pair exchange interaction constant is determined to be 0.33 GHz in paramagnetically diluted LiYb_xY_{1-x}F₄ crystals.

Keywords: lithium rare-earth fluorides, electron paramagnetic resonance (EPR), exchange interactions, spin-hamiltonian parameters, exchange interaction constant.

1. INTRODUCTION

LiYF₄ is the most-used fluoride laser host crystal, generally doped with trivalent rare-earth ions.¹ The LiYF₄ crystals are also used for preparation of infrared and laser windows,² to convert infrared excitation to green emission,³ as well as neutron scintillation detectors.⁴ The LiYb_xY_{1-x}F₄ crystals have scheelite (CaWO₄) structure with the space group I4₁/a (C_{4h}^6) and the S₄ local symmetry at Y³⁺ or Yb³⁺ sites, the same as those of LiYF₄ and LiYbF₄.^{5,6} The LiY_{1-x}Yb_xF₄ ($x = 0 - 1$) single crystals doped with Gd³⁺ were grown from the melt by a modified Bridgmann-Stockbarger method.⁶

X-band (~9.5 GHz) EPR studies of Gd³⁺-doped LiYF₄ and LiYbF₄ have been reported.^{7,8} A detailed X-band EPR study has been performed in Gd³⁺-doped LiYb_xY_{1-x}F₄ crystals, for various values of x and at variable temperatures, in the range 4.2 - 290 K.⁹ Further, the molecular-field model¹⁰ was used to estimate the Gd³⁺-Yb³⁺ exchange interactions at 4.2 K. For the host crystals with $x > 0.1$, it was not possible to record EPR spectra at temperatures much lower than room temperature, because of increasing line broadening. Detailed Gd³⁺ EPR-linewidth studies have also been reported.¹¹

The EPR spectrum of Yb³⁺ ions was not at all observed, due to the rather short spin-lattice relaxation time of Yb³⁺, which broadens out the Yb³⁺ EPR lines substantially at temperatures above 4.2 K; Yb³⁺ EPR spectrum was observed only for the host crystals with $x < 0.2$. This consisted of a broad line corresponding to the 69% non-magnetic, even-mass isotopes in natural ytterbium with nuclear spin $I = 0$ (¹⁶⁸Yb, ¹⁷⁰Yb, ¹⁷²Yb, ¹⁷⁴Yb and ¹⁷⁶Yb), at about 4960 G, without any superhyperfine structure. (The Yb³⁺ superhyperfine structure was observed¹² in LiYF₄ host crystal, doped by Yb³⁺ ions (0.1 at. %) at X-band, for the magnetic field orientation only within 2° from the c axis.) The spectrum of ¹⁷¹Yb ($I = 1/2$), with nonzero nuclear magnetic moment in scheelite crystal hosts occurs at X-band in the magnetic field range 8.5 – 10 kG.¹³ In LiYb_{0.1}Y_{0.9}F₄ crystal at 4.2 K only one line was observed at about 9.5 kG.⁹

The nearest-neighbor (nn) Gd³⁺ pair spectrum in EuCl₃ have been recorded¹⁴ for the direction of \mathbf{H} along the c crystal axis, and the next-nearest neighbor (nnn) Gd³⁺ pair spectrum with \mathbf{H} parallel to the calculated nnn bond direction. In LiYb_xY_{1-x}F₄ crystals, the pair spectrum was not at all observed, neither for \mathbf{H} parallel to the c axis, nor for \mathbf{H} in the XY plane, which contains the bond direction of the nnn Gd³⁺ pair. This can be explained to be due to the rather small concentration of the Gd³⁺ ions (0.1 - 0.2 mole %) in LiYb_xY_{1-x}F₄,⁹ compared to that in EuCl₃ (0.5 - 1.0 mole % of Gd³⁺).¹⁴ The g shift of Gd³⁺ ion in a paramagnetic LiYb_xY_{1-x}F₄ host, from that in the isostructural diamagnetic LiYF₄ host, is dependent upon the magnetic interactions of the Gd³⁺ ion with the Yb³⁺ paramagnetic neighbors. These exchange interactions can be estimated from the g shift values of the Gd³⁺ ion in the isostructural paramagnetic and diamagnetic hosts.^{8,14}

2. ESTIMATION OF Gd^{3+} - Yb^{3+} EXCHANGE INTERACTIONS

The exchange-interaction constant due to the nearest and next-nearest Gd^{3+} - Yb^{3+} neighbors in the paramagnetic hosts $LiYb_xY_{1-x}F_4$ can be evaluated using the shift of the isotropic part of the single-ion g -tensor of a Gd^{3+} ion, from that in the isostructural diamagnetic host ($LiYF_4$):^{8,14}

$$(\delta g_{zz} + \delta g_{xx}) = (g_{zz} + 2g_{xx})_p - (g_{zz} + 2g_{xx})_d = -\frac{96}{\Delta_{av}}(J_{nn} + J_{nnn}). \quad (1)$$

In eq. (1), J_{nn} and J_{nnn} are respectively the exchange-interaction constants of Gd^{3+} with the nearest and next-nearest Yb^{3+} neighbors, the subscripts p and d refer to the isostructural paramagnetic and diamagnetic hosts $LiYb_xY_{1-x}F_4$ and $LiYF_4$, respectively, and Δ_{av} is an average energy difference between the first excited levels and the ground state of Yb^{3+} . The multilevel spacings, Δ_{av} , of these levels from the ground state can be taken into account by averaging.¹⁵

$$\Delta_{av} = \frac{\sum_i \Delta_i \exp(-\Delta_i/k_B T)}{\sum_i \exp(-\Delta_i/k_B T)}. \quad (2)$$

The uncertainty, caused by the averaging, is less than that associated with the experimental measurements.¹⁵ The separations (Δ_i) of the energies between the ground level and the next-three excited states of Yb^{3+} ion in $LiYF_4$ crystal¹⁶ are determined to be 212, 364, 455 cm^{-1} , respectively. The average energy separation, to be used in eq. (1) is 294 cm^{-1} . (The other higher-lying levels do not contribute as they are separated from the ground state by large energies,¹⁶ e.g., $\sim 10^4$ cm^{-1} .)

2.1. Estimation of g_{zz} and g_{xx}

The spin hamiltonian for the Gd^{3+} ion, occupying a site of local symmetry S_4 in the tetragonal $LiYb_xY_{1-x}F_4$ host lattice, can be found elsewhere.⁹ For the estimation of the Gd^{3+} - Yb^{3+} exchange-interaction constant it is necessary to have very accurate values of g_{zz} and g_{xx} . These values were usually obtained from least-squares fitting of all the spin Hamiltonian parameters in which a large number of EPR line positions (obtained for several orientations of the external magnetic field) were simultaneously fitted.⁹ More precise values of g -factor can be calculated by the use of the experimentally observed line positions for the $1/2 \leftrightarrow -1/2$ transition (for $H \parallel Z$ and $H \parallel X$). The calculation to second order using perturbation method, gives¹⁷

$$g\beta H^{(2)} = h\nu + E \left[\frac{90}{(1-y^2)} - \frac{120}{(1-y^2)} \right], \quad (3)$$

where,

$$y = b_2^0 / g\beta H^{(2)}, \quad E = (b_2^0)^2 / 18g\beta H^{(2)}.$$

One can calculate from eq. (3) for $LiYb_xY_{1-x}F_4$:

$$g_{zz} = h\nu / \beta H_z^{(2)} \quad \text{and} \quad g_{xx} = h\nu / \beta H^{(2)}(1-A), \quad (4)$$

where,

$$A = \frac{9(b_2^0)^2}{72g_{xx}^2\beta^2(H^{(2)})^2} \left\{ \frac{90}{1 - \left[\frac{9(b_2^0)^2}{4g_{xx}^2\beta^2(H^{(2)})^2} \right]} - \frac{120}{1 - \left[\frac{(b_2^0)^2}{4g_{xx}^2\beta^2(H^{(2)})^2} \right]} \right\}. \quad (5)$$

This A value at room temperature can be estimated fairly reasonably by using the g_{xx} and b_2^0 values, specific to each $LiYb_xY_{1-x}F_4$ host, determined from least-squares fitting. Thus, when the determined values of A for the various hosts are used in eq. (4) for the evaluation of g_{xx} , they do not cause significantly large errors. The values of g_{zz} and g_{xx} , so computed from eq. (4) for the various hosts, are listed in table 1.

2.2. Estimation of the Gd^{3+} - Yb^{3+} exchange interaction constant

The values of the exchange-interaction constant (J), computed using the g shift in eq. (1) are given in table 1. It is seen from Fig. 1 that, as the amount of paramagnetic Yb^{3+} ions increases for x in the range 0.1 - 1.0, the Gd^{3+} - Yb^{3+} exchange-interaction constant J also increases in parabolic manner.

Table 1. The room-temperature values of g_{zz} , g_{xx} , A , and J (the exchange-interaction constant) in Gd^{3+} -doped $LiYb_xY_{1-x}F_4$ single crystals. The x is the mole fraction of Yb^{3+} ions, z is the number of nearest and next-nearest neighbors and J_p ($= J/z$) is the average Gd^{3+} - Yb^{3+} pair exchange-interaction constant.

x	0.0	0.1	0.2	0.3	0.4	0.5	0.6	0.8	0.9	1.0
g_{zz}	1.9956(5)	1.9953(5)	1.9947(5)	1.9947(5)	1.9941(5)	1.9935(11)	1.9920(11)	1.9864(11)	1.9788(11)	1.9738(11)
g_{xx}	1.9908(8)	1.9885(8)	1.9866(8)	1.9894(8)	1.9860(8)	1.9855(14)	1.9862(14)	1.9882(14)	1.9863(14)	1.9864(14)
A	-0.1165	-0.1173	-0.1188	-0.1171	-0.1188	-0.1186	-0.1185	-0.1161	-0.1165	-0.1169
J (GHz)		0.5(0.30)	0.9(0.30)	0.4(0.3)	1.0(0.3)	1.2(0.6)	1.2(0.6)	1.3(0.6)	2.4(0.6)	2.8(0.6)
z	0	1	2	2	3	4	5	6	7	8
J_p (GHz)		0.5	0.45	0.20	0.33	0.30	0.24	0.22	0.34	0.35

In $LiYbF_4$ the number of each of the nearest-neighbors and the next-nearest neighbors (z) is four.⁵ As for the $LiYb_xY_{1-x}F_4$ single crystals, the number of z can be scaled in proportion to x , to estimate the average number of Yb^{3+} neighbors to a Gd^{3+} ion, and further to calculate the average pair exchange-interaction constant J_p ($= J/z$). The values of J_p , so calculated, are included in table 1. It is seen that all the J_p values are the same (on average 33 GHz), within errors of estimation.

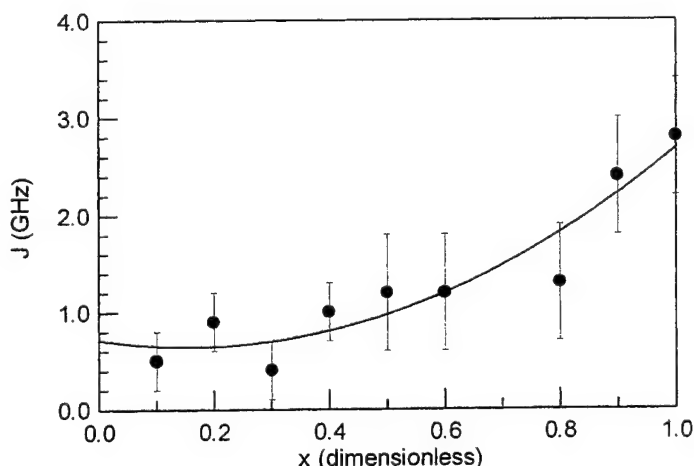


Fig. 1. The exchange-interaction constant (J) as a function of the mole fraction of Yb^{3+} ions (x) in Gd^{3+} -doped $LiYb_xY_{1-x}F_4$ single crystals.

3. DISCUSSION AND COMPARISON OF RESULTS

The calculation of Gd^{3+} - Yb^{3+} exchange interactions was made previously, using the molecular-field model for $LiYb_{0.1}Y_{0.9}F_4$ at 4.2 K,⁹ because this is the only crystal containing Yb^{3+} ions, which exhibits well-resolved spectrum at liquid-helium temperature. The values of the Gd^{3+} - Yb^{3+} exchange-interaction constants J , at 4.2 K, were calculated to be 3.8 GHz from the molecular-field model⁹ and 4.9 GHz in the present calculations. These two values can be considered to be in reasonably good agreement, taking into account the experimental errors and the approximations made in the calculation of J . The value of J was estimated to be 6.24 GHz and 2.32 GHz at 77 K and at room temperature, respectively, for Gd^{3+} - Eu^{3+} exchange interactions in $Eu(OH)_3$ single crystal.¹⁵ The room-temperature value of Gd^{3+} - Eu^{3+} exchange interactions (2.32 GHz) is not much different from that of 2.8 GHz, the Gd^{3+} - Yb^{3+} exchange interactions in $LiYbF_4$ at room temperature. From the values of Gd^{3+} - Yb^{3+} exchange interaction constants at room temperature and at 4.2 K in $LiYb_{0.1}Y_{0.9}F_4$, and those of estimated for Gd^{3+} - Eu^{3+} exchange interactions in $Eu(OH)_3$,¹⁵ it is seen that the strength of the exchange interactions increases with decreasing temperature in these hosts. As the temperature decreases, the distances between the ions in the lattice become smaller, thereby enhancing the exchange-interaction constant. This is to be expected, because the exchange interaction constant is determined to be dependent upon an interionic distance R as R^{-12} ,¹⁸ or as $e^{-3.55R}$,¹⁹ the latter provides a better agreement to the experimental values of exchange interactions. The exchange interactions between the Gd^{3+} - Yb^{3+} ions in $LiYb_xY_{1-x}F_4$ are effected mostly through the ligand F^- ions.

4. CONCLUSIONS

The Gd^{3+} - Yb^{3+} exchange-interaction constant J ($= J_{nn} + J_{nnn}$), as estimated for Gd^{3+} -doped $LiYb_xY_{1-x}F_4$ single crystals, are in the range 0.5 - 2.8 GHz at room temperature. On the other hand, at liquid-helium temperature, the calculated value of J for $LiYb_{0.1}Y_{0.9}F_4$ is 4.9 GHz. Thus, the exchange-interaction constant is strongly dependent upon temperature, and upon the mole fraction x (in the range $x = 0.5 - 1.0$). However, J is almost independent of the mole fraction (x) for $x < 0.5$. The average Gd^{3+} - Yb^{3+} pair exchange interaction constant in paramagnetically diluted $LiYb_xY_{1-x}F_4$ crystals is determined to be 0.33 GHz.

The values of the Gd^{3+} - Yb^{3+} exchange-interaction constants as estimated in $LiYb_xY_{1-x}F_4$, are consistent with those of evaluated using the molecular-field model⁹ and are comparable in magnitude to those for Gd^{3+} - Eu^{3+} exchange constant in $Eu(OH)_3$ host.¹⁵ Reasonable agreement between the exchange-interaction constants in $LiYb_xY_{1-x}F_4$ as estimated presently with those of estimated using the molecular-field model, is expected, since the latter is an approximation of the former.

REFERENCES

1. E. P. Chicklis, C. S. Naiman, R. C. Folweiler, D. R. Gabbe, H. P. Jensen and A. Linz, "High efficiency room-temperature 2.06 μm laser using sensitized Ho^{3+} : YLF," *Appl. Phys. Lett.* **19**, pp. 119-121, 1971.
2. N. C. Fernelius, G. S. Coble, D. V. Dempsey, J. A. Detrio, J. A. Fox, P. R. Gearson, G. T. Johnston and D. B. O'Quinn, "Multiwavelength laser rate calorimetry on various infrared window materials," in *Emerging Optical Materials, Proc. SPIE Int. Soc. Opt. Eng.* **297**, pp. 137-142, SPIE - The International Society for Optical Engineering, San Diego, 1981.
3. R. K. Watts and W. C. Holton, "Infrared to green conversion in $LiYF_4$: Yb, Ho," *Solid State Commun.* **9**, pp. 137-139, 1971.
4. A. R. Spowart, "Evaluation of $LiYF_4$ as a neutron scintillation detector," *J. Phys. D* **16**, pp. 1819-1822, 1983.
5. R. E. Thoma, G. D. Brunton, R. A. Penneman and T. K. Keenan, "Equilibrium relations and crystal structure of lithium fluorolanthanate phases," *Inorg. Chem.* **9**, pp. 1096-1101, 1970.
6. L. E. Misiak, P. Mikolajczak and M. Subotowicz, "Lithium rare-earth fluoride crystal growth and thermal variation of lattice constants," *Phys. Stat. Sol. A* **97**, pp. 353-359, 1986.
7. Y. Vailis, J. Y. Buzaré and J. Y. Gesland, "Zero-field splittings of Gd^{3+} in $LiYF_4$ determined by EPR," *Solid State Commun.* **45**, pp. 1093-1098, 1983.
8. S. K. Misra, M. Kahrizi, P. Mikolajczak and L. E. Misiak, "EPR of Gd^{3+} -doped single crystals of $LiYF_4$ and $LiYbF_4$: Gd^{3+} - Yb^{3+} exchange constant," *Phys. Rev. B* **32**, pp. 4738-4741, 1985.
9. L. E. Misiak, S. K. Misra and P. Mikolajczak, "EPR of Gd^{3+} -doped single crystals of $LiYb_xY_{1-x}F_4$," *Phys. Rev. B* **38**, pp. 8673-8682, 1988.
10. M. R. St. John and R. J. Myers, "Electron-paramagnetic-resonance spectra of ions substituted into transition-metal ion lattices," *Phys. Rev. B* **13**, pp. 1006-1016, 1976.
11. L. E. Misiak, S. K. Misra and U. Orhun, "Study of temperature variation of EPR linewidth of Gd^{3+} -doped $LiYb_xY_{1-x}F_4$ single crystals," *Phys. Stat. Sol. B* **154**, pp. 249-258, 1989.
12. J. P. Sattler and J. Némarch, "Electron-paramagnetic-resonance spectra of Nd^{3+} , Dy^{3+} , Er^{3+} , and Yb^{3+} in lithium yttrium fluoride," *Phys. Rev. B* **4**, pp. 1-5, 1971.
13. J. P. Sattler and J. Némarch, "Unusual electron paramagnetic resonance hyperfine spectra of Yb^{3+} in scheelites," *Phys. Rev. B* **1**, pp. 4256-4261, 1970.
14. R. J. Birgeneau, M. T. Hutchings and W. P. Wolf, "Magnetic interactions between rare-earth ions in insulators. II. Electron-paramagnetic-resonance measurements of Gd^{3+} pair and Gd^{3+} - Eu^{3+} interaction constants in $EuCl_3$," *Phys. Rev.* **179**, pp. 275-288, 1969.
15. V. M. Malhotra and H. A. Buckmaster, "A study of the host lattice effect in the lanthanide hydroxides. 34 GHz Gd^{3+} impurity ion EPR spectra at 77 and 294 K," *Can. J. Phys.* **60**, pp. 1573-1588, 1982.
16. J. E. Miller and E. J. Sharp, "Optical properties and energy transfer in $LiYF_4$: Nd^{3+} , Yb^{3+} ," *J. Appl. Phys.* **41**, pp. 4718-4722, 1970.
17. S. K. Misra, "Evaluation of spin hamiltonian parameters from ESR data of single crystals," *Mag. Reson. Rev.* **10**, pp. 285-331, 1986.
18. K. N. Shrivastava and V. Jaccarino, "Variation of superexchange with interatomic distance. I. The T_{2g} system V^{++} -F- V^{++} ," *Phys. Rev. B* **13**, pp. 299-303, 1976.
19. S. K. Misra and S. Z. Korczak, "EPR of Mn^{2+} in the Tutton salts $M(NH_4)_2(SO_4)_2 \cdot 6H_2O$ ($M = Cd, Co, Ni$): Mn^{2+} - Ni^{2+} exchange interactions," *Phys. Rev. B* **35**, pp. 4625-4632, 1987.

Crystal lattice dynamics of various silicon-carbide polytypes

Stanisław Nowak

Technical University, Radom, Poland

ABSTRACT

A valence force field model with an added ionic interaction is applied to an explanation of phonon dispersion curves in 6H-SiC. The phonon dispersion curves in 3C-, 2H-, and 4H-SiC are calculated within the same model. Our results are compared with the published results of *ab initio* calculations. One can suppose that the present model may be applied for other polytypes of SiC. A phonon contribution to Helmholtz energy is determined for the simplest four polytypes. The results indicate a stability of hexagonal polytypes in relation to the cubic one at high temperatures.

Keywords: lattice dynamics, valence force field model, silicon carbide polytypes.

1. INTRODUCTION

Silicon carbide (SiC) is an interesting semiconducting material. It exists in numerous different structures called polytypes, built up by stacking identical SiC layers in different stacking sequences. In all structures every atom is tetrahedrally surrounded by four atoms of the other species. Some physical properties of SiC are strongly dependent on the crystal structure. The band gap varies from 2.42 eV in 3C-SiC to 3.33 eV in 2H-SiC. The mechanical and thermal stability of SiC is unique. These features imply the prospects for applications in various electronic and optoelectronic devices. Before SiC is generally applied in electronic devices, many technological problems have to be solved. Therefore, the insight into the basic physical properties of SiC is of great interest.

The physical properties of SiC are studied intensively. A great part of these investigations concentrates on the electronic structure of the pure and doped material, as well as on its optical properties. The results of these studies are summarised in a review article by Choyke and Devaty¹. The crystal lattice dynamics investigation is important for the understanding of the phonon related properties and the polytypism of SiC. Feldman et al.^{2,3} have reported the results of Raman spectroscopy of SiC. They have determined the dispersion relation for the direction of phonon wavevector parallel to the trigonal symmetry axis. Olego and Cardona^{4,5} have reported the dependence on temperature and pressure of the optical phonons observed in Raman spectra. The absence of the dispersion relation for low symmetry directions has been stimulating theoretical studies. Progress of the density functional theory has enabled the calculation of the crystal structure of different polytypes and the dispersion relations for the simplest polytypes of SiC. Cheng et al.⁶ and Käckell et al.⁷ have determined the distortion of the hexagonal polytypes structure. Cheng et al.⁸ have calculated some phonon frequencies using the frozen phonon method. On the basis of these calculations and the Feldman's experimental results, they have determined a shell model of the cubic SiC lattice dynamics. They have studied the problem of SiC polytypism^{9,10}, too. Karch et al.^{11,12,13} have calculated the phonon dispersion relations in two simplest polytypes using the density functional perturbation theory (DFPT). Hofmann et al.¹⁴ have presented a bond charge model of SiC lattice dynamics, determined on the basis of Feldman data and Karch calculations. Van Elsbergen et al.¹⁵ have reported the results of surface phonon investigation by means of a high energy resolution electron spectroscopy.

New experimental results have been reported in 1998. Dorner et al.¹⁶ have measured the dispersion relations in 6H polytype by an inelastic neutrons scattering. They have determined the dispersion relation for two mutually perpendicular symmetry directions: along line Δ (Γ -A) and along line Σ (Γ -M). The results for line Δ confirmed the data of Feldman et al.³. The 36 nondegenerate phonon branches exist for line Σ , but the measurements of scattering have been performed in the plane of mirror symmetry, therefore 12 branches have been invisible. The results for the line Σ form a complicated structure of dispersion curves. No model of the dynamics has been presented. The authors have made the transformation of the dispersion curves of 3C-SiC to 6H-SiC structure, but the agreement with the experimental results is poor.

The aim of the present paper is to explain the dispersion relations in 6H-SiC. A phenomenological model of valence force field is used. The chemical bonds in SiC are treated as heteropolar covalent bonds, therefore the Madelung energy is included. This model operates with 11 parameters. These parameters are fitted by a least squares method. It is assumed that the interatomic interactions are identical in all SiC polytypes. The dispersion curves and phonon spectra of four

simplest polytypes are determined. The phonon contribution to Helmholtz energy is calculated in the harmonic approximation on the basis of these results.

2. SILICON CARBIDE POLYTYPES

It is well known that close packed spheres form a face centred cubic structure or a hexagonal close packed structure. The repetition period contains three layers in the fcc structure and two layers in the hcp structure. More complicated structures exist with a longer period of repetition. The phenomenon of forming different crystal structures by stacking identical layers in different sequences is called the polytypism¹⁷.

SiC crystals are built from layers of Si and C atoms. The stacking of SiC layers in different sequences causes the polytypism. The simplest polytype, called 3C, has the cubic structure of sphalerite. The polytype 2H has the hexagonal structure of wurtzite. The primitive unit cells of 3C and 2H polytypes contain one and two SiC molecules respectively. The hexagonal polytypes 4H and 6H unit cells contain four and six molecules respectively. Many other hexagonal polytypes denoted by the symbol nH, and rhombohedral polytypes denoted by symbol nR, exist. Their structure is more complicated. The Landolt-Börnstein Tables¹⁸ contain the crystallographic data for many polytypes of SiC with the explanation of structure. The ratio of lattice constants c/a is equal to $\sqrt{8/3}$ for the 2H structure if the nearest neighbours of each atom form a regular tetrahedron, like in the cubic 3C structure. The ratio c/a is equal to integer multiplicity of this value for other hexagonal polytypes. The lattice constants of four examined polytypes are given in Table 1. One can see that the divergence from the perfect symmetry is very small.

Table 1. Lattice parameters of SiC polytypes at room temperature and distances between nearest neighbours and valence angles

Polytype	a [Å]	c [Å]	Ratio c/a		Bond lengths R_0	Valence angles α
			in real structure	in perfect structure		
3C	4.3596	-	-	-	1.888	109.47°
2H	3.0763	5.0480	1.6409	1.633	1.885	109.38°
					1.893	109.56°
4H	3.073	10.053	3.2714	3.266	1.882	109.44°
					1.885	109.50°
6H	3.0806	15.1173	4.9073	4.899	1.887	109.44°
					1.889	109.50°

3. VALENCE FORCE FIELD MODEL OF INTERATOMIC INTERACTION IN SILICON CARBIDE

The valence force field method (VFFM) of crystal lattice dynamics has been formulated by McMurphy et al.¹⁹. The bond lengths and interbond angles are used as valence co-ordinates. The potential energy of crystal lattice is expressed in terms of valence co-ordinates changes. VFFM operates with a set of parameters, called valence force constants (VFC).

It is assumed that the short range interaction in SiC originates in the covalent bonds between nearest neighbours. This interaction is expressed in the VFFM. The long range interaction is ionic in nature and expressed in the form of Madelung energy of rigid ions interaction. This interaction is described by the parameter q^2 , where q denotes the absolute value of the ion charge. The set of VFC used for description of SiC lattice potential energy is listed in Table 2. The perfect symmetry of crystal, with the lattice constants c equal to $(24)^{1/2}a$, is assumed. This assumption is quite well realised. The phonon dispersion curves of 6H-SiC¹⁶ are used to determine q^2 and the VFC values by the least squares method. The value of ion charge determined in this way equals

$$q = 1.028 \pm 0.010 \text{ e.}$$

The VFC values are presented in Table 2. The value of the first VFC is determined from the condition of equilibrium between Coulomb forces and the repulsive covalent force. One can deduce, from the values of some parameters, that the carbon atoms are negatively charged and silicon atoms are positively charged. It agrees with the ab initio calculations of Karch et al.¹¹.

Table 2. Valence force constants of 6H-SiC with the explanation. R_0 is the equilibrium distance between nearest neighbours.

VFC	Explanation	Value [N/m]
$R_0^{-1} \cdot (\partial \Phi / \partial R)$	R = distance between nearest neighbours	-15.24 ± 0.29
$\partial^2 \Phi / \partial R^2$	R = distance between nearest neighbours	269.42 ± 8.37
$R_0^{-2} \cdot (\partial^2 \Phi / \partial \alpha^2)$	α = C-Si-C angle	9.55 ± 2.75
$R_0^{-2} \cdot (\partial^2 \Phi / \partial \alpha^2)$	α = Si-C-Si angle	21.66 ± 5.66
$\partial^2 \Phi / \partial R' \partial R''$	R', R'' = lengths of Si-C bonds with common Si	-15.17 ± 2.83
$\partial^2 \Phi / \partial R' \partial R''$	R', R'' = lengths of Si-C bonds with common C	34.99 ± 3.62
$R_0^{-1} \cdot (\partial^2 \Phi / \partial R \partial \alpha)$	α = angle C-Si-C, R = one leg of α	11.33 ± 0.87
$R_0^{-1} \cdot (\partial^2 \Phi / \partial R \partial \alpha)$	α = angle Si-C-Si, R = one leg of α	5.18 ± 0.78
$R_0^{-2} \cdot (\partial^2 \Phi / \partial \alpha' \partial \alpha'')$	α', α'' = angles Si-C-Si, C-Si-C with common leg but not common apex; all atoms are coplanar and the bonds form zigzag structure	1.59 ± 0.31
$R_0^{-2} \cdot (\partial^2 \Phi / \partial \alpha' \partial \alpha'')$	α', α'' = angles C-Si-C with common leg and apex	-2.48 ± 1.15
$R_0^{-2} \cdot (\partial^2 \Phi / \partial \alpha' \partial \alpha'')$	α', α'' = angles Si-C-Si with common leg and apex	2.30 ± 2.32

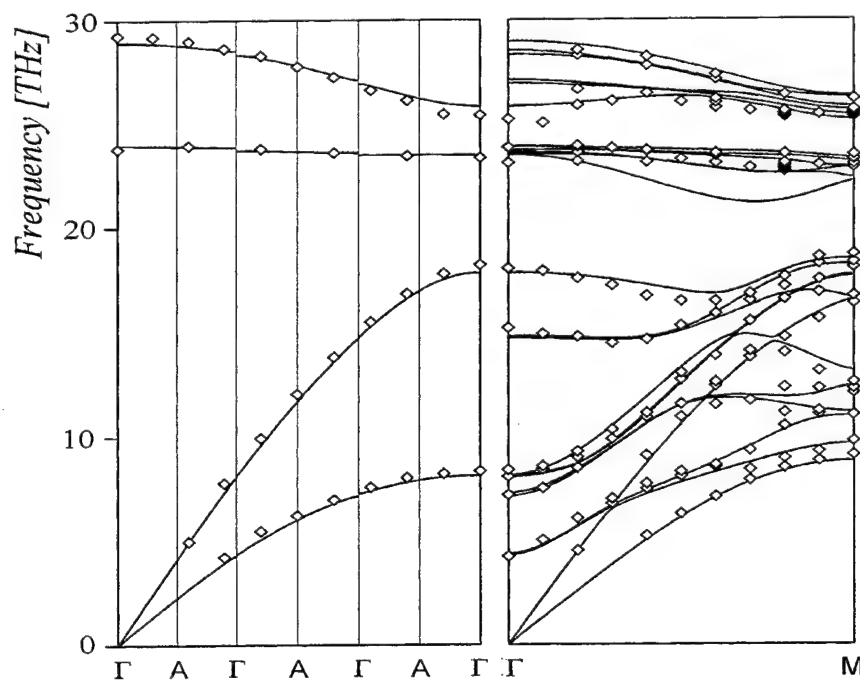


Fig.1. Phonon dispersion curves in 6H-SiC. Diamonds represent the experimental points determined by Dörner et al.¹⁶. The dispersion relations in the hexagonal direction are shown in an extended zones scheme. The curves for phonons measured experimentally are only shown for the ΓM direction.

Dörner et al.¹⁶ have divided the measured phonons into three groups. The phonons with frequency below 19 THz are called "acoustic", the ones with frequency between 20 and 24 THz are called "transverse optical", and with frequency above 25 THz are called "longitudinal optical". Figure 1 presents the experimental points of Dörner et al.¹⁶, and the phonon dispersion relation calculated within VFFM. The data for the line Δ (Γ -A) are shown in an extended zones scheme. One can see from the right part of this figure that the splitting of the "transverse optical" branches is very small and cannot be resolved experimentally. The "optical" phonons for the line Σ (Γ -M) are excluded from the estimation of VFC, but the agreement of the dispersion curves with the experimental points is satisfactory, excepting one curve for "transverse optical phonons".

The dispersion curves calculated for the line Δ (Γ -A) have discontinuities at two "inner" Γ -points. These gaps have been determined by Feldman et al.². The agreement of calculated and measured gaps is within 10%-50% accuracy. This agreement is satisfactory, taking into account that experimental errors are of the same order.

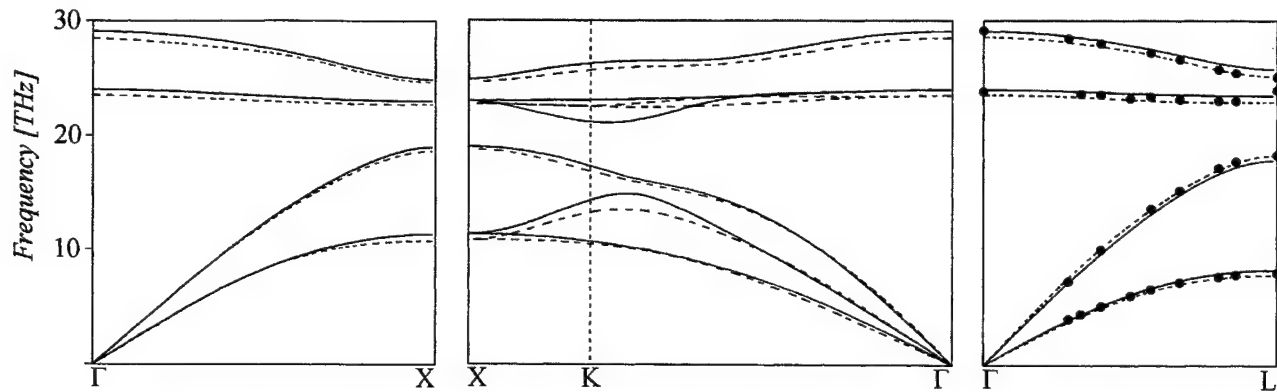


Fig.2. Phonon dispersion relation in 3C-SiC: solid lines - determined within VFFM, dashed lines - determined from DFPT by Karch et al¹¹. Circles represent the experimental data of Feldman et al³.

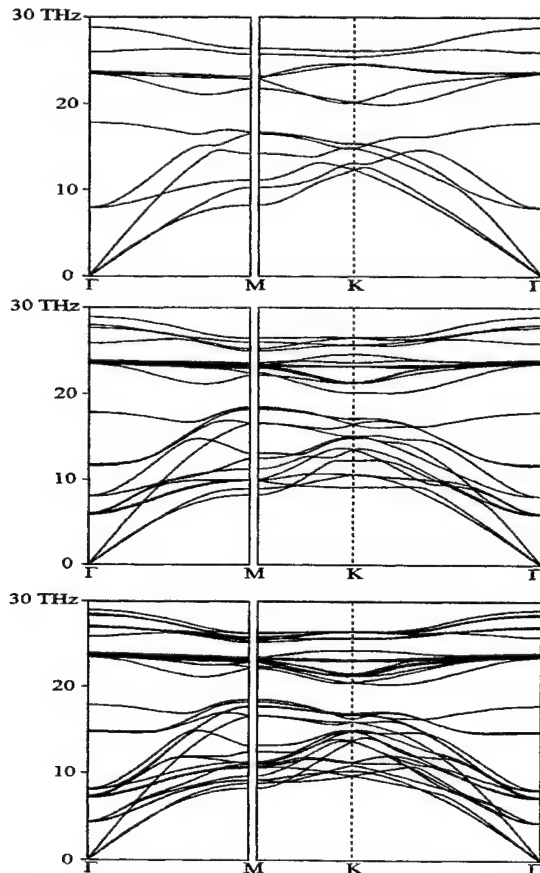


Fig.3. The phonon dispersion relations for hexagonal polytypes: 2H (upper), 4H (middle), 6H (down). The lines Γ M and Γ KM are perpendicular to hexagonal axis and mutually one to another.

The presented VFFM contains eleven independent VFC. The shell model⁸ and the bond charge model¹⁴ of 3C-SiC dynamics contain ten parameters each. The bond charge model of 6H-SiC dynamics¹⁴ contains sixteen parameters. It is clear that the number of the present model parameters is reasonable.

A comparison of the different SiC polytypes structure suggests that in all polytypes the chemical bonds and the interatomic interaction are identical. Therefore, it is assumed that in other polytypes the crystal lattice potential has the form of VFFM with the same values of VFC. The phonon dispersion curves for 3C-, 2H-, and 4H-SiC polytypes are calculated. The results are shown in Fig.2 and Fig.3.

The experimental results of Feldman³, the results of DFPT calculation¹¹ and dispersion relation determined within VFFM for 3C-SiC are presented in Fig.2. One can see that all the presented results are in satisfactory agreement.

The dispersion relation along the line Δ (Γ -A) in all hexagonal polytypes, presented in the extended zones scheme, is similar to the dispersion relation along the line Δ (Γ -L) for the 3C-SiC. Figure 3 presents the dispersion relations along lines Σ (Γ -M) and Γ (Γ -K-M) for three simplest hexagonal polytypes. Karch and et.¹¹ have calculated, by means of DFPT, the dispersion relations in 2H-SiC along line Γ . Those results agree with ours very well.

Figure 4 presents the frequency dependence of the phonon density of states for four SiC polytypes under examination. One can see that the phonon spectra are similar, but some small differences are noticeable. The spectrum of 3C can be divided into the "acoustic", "transverse optical" and "longitudinal optical" phonons. The "transverse" and "longitudinal optical" phonons in the spectra of hexagonal polytypes are inseparable.

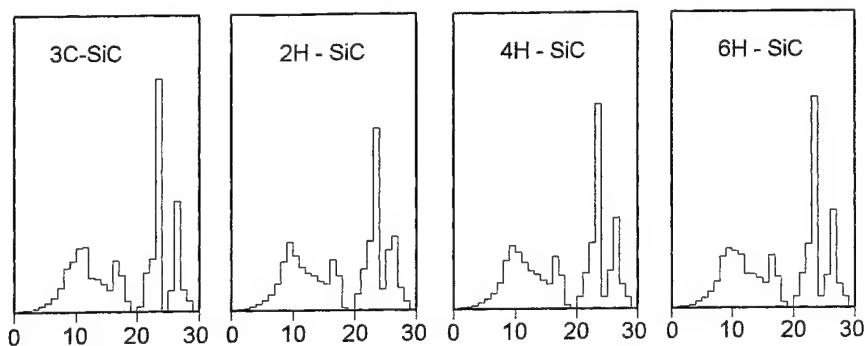


Fig.4. Phonon density of states for different polytypes of SiC

4. PHONON CONTRIBUTION TO FREE ENERGY AND POLYTYPISM

We have determined the crystal lattice dynamics of SiC, therefore we are able to calculate the different thermodynamic quantities related to phonons within the harmonic approximation. The free energy is important in understanding the polytypism phenomenon. It is calculated according to the formula²⁰:

$$F_{ph} = \sum_{q,j} \left[\frac{1}{2} h \cdot \nu_{q,j} + k_B T \cdot \ln \left(1 - e^{-\frac{h \cdot \nu_{q,j}}{k_B T}} \right) \right]$$

All the calculations are performed using the lattice constants from Table 1. The temperature dependence of the 3C-SiC phonon free energy is presented in the Fig.5. Similar dependencies can be drawn for other polytypes, the differences are very small. Fig.6 presents the phonon free energy of hexagonal polytypes relative to cubic polytype, i.e. $F_{ph}(nH, T) - F_{ph}(3C, T)$.

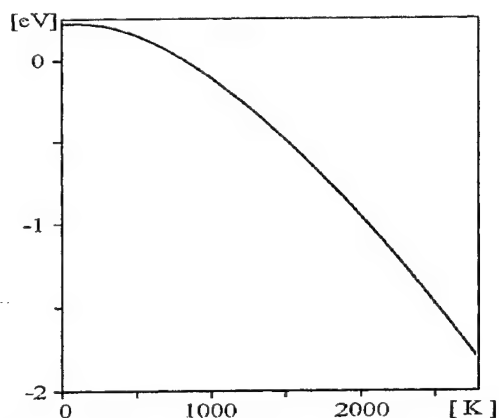


Fig.5. Phonon free energy of cubic silicon carbide (per one molecule SiC)

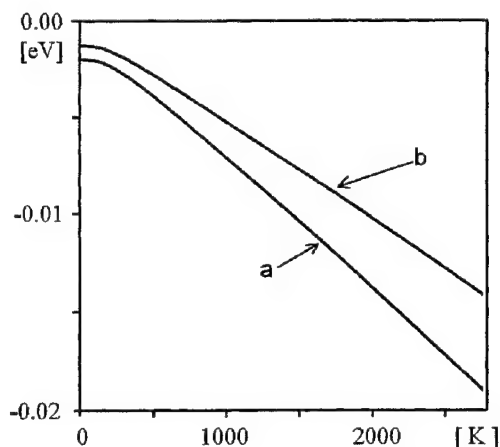


Fig.6. Phonon free energy of hexagonal polytypes relative to the cubic one in electronvolts per one molecule. The curve denoted with the letter *a* stands for 2H, the curve with the letter *b* for 4H and 6H polytypes

Over one hundred SiC polytypes are known¹⁷. The polytype with the lowest free energy is stable (at low pressure). To solve the problem, one has to take into account other contributions to the free energy. According to results of Käckell et. al. calculation⁷ the cohesive energy of 2H polytype is the lowest, which means that the electronic free energy is the highest. Our results suggest that at low temperatures the 2H-SiC is in the nonequilibrium state. The wurtzite structure

of SiC is preferred at very high temperatures only. The sphalerite structure of SiC is preferred at low temperatures, according to the analysis of Käckell and our data. The polytypes 6H is stable at middle temperatures. Unfortunately, this conclusion is uncertain within the precision of these calculations. The free energy differences of various polytypes are smaller than the thermal energies at the crystal growth. Therefore, the nonequilibrium effects related to growth can play an important role.

5. CONCLUSIONS

The VFFM has been successfully applied to the calculation of phonon dispersion relations in 6H-SiC. The same potential of interatomic interaction describes the dispersion relations in 2H- and 3C-SiC. The presented agreement between the results of ab initio calculations for 3C and 2H polytypes and our results proves the identity of interatomic interaction in all examined polytypes of SiC. DFPT has a great potential but is restricted to simple structures at present. Thus, a marriage of experiment, ab initio methods and phenomenological models is very useful. The phonon contribution to the free energy stabilises the 6H-SiC structure at middle and high temperatures.

REFERENCES

1. W.J. Choyke and R.P. Devaty, "Progress in the study of optical and related properties of SiC since 1992", *Diamond and Related Materials* **6**, pp.1243-1248,1997.
2. D.W. Feldman, J.H. Parker, W.J. Choyke and L. Patrick, "Raman scattering in 6H SiC", *Phys.Rev.***170**,pp.698-704,1968.
3. D.W. Feldman, J.H. Parker, W.J. Choyke and L. Patrick, "Phonon dispersion curves by Raman scattering in SiC, polytypes 3C,4H,6H,15R, and 21R", *Phys.Rev.***173**,pp.787-793,1968.
4. D. Olego and M. Cardona, "Temperature dependence of the optical phonons and transverse effective charge in 3C-SiC", *Phys.Rev.***B25**,pp.3889-3896,1982.
5. D. Olego, M. Cardona and P. Vogl, "Pressure dependence of the optical phonons and transverse effective charge in 3C-SiC", *Phys.Rev.***B25**,pp.3878-3888,1982.
6. C. Cheng, V. Heine and R.J. Needs, "Atomic relaxation in silicon carbide polytypes", *J.Phys.:Condens. Matter* **2**,pp.5115-5134,1990.
7. P. Käckell, B. Wenzien and F. Bechstedt, "Influence of atomic relaxation on the structural properties of SiC polytypes from ab initio calculations", *Phys.Rev.* **B50**,pp.17037-17046,1994.
8. C. Cheng, K. Kunc and V. Heine, "Shell-model interpolation of frozen phonons in cubic silicon carbide", *Phys.Rev.* **B39**,pp.5892-5898,1989.
9. C. Cheng, R.J. Needs and V. Heine, "Inter-layer interactions and the origin of SiC polytypes", *J.Phys.C:Solid State Phys.***21**,pp.1049-1063,1988.
10. C. Cheng, V. Heine and I.L. Jones, "Silicon carbide polytypes as equilibrium structures", *J.Phys.:Condens. Matter* **2**,pp.5097-5113,1990.
11. K. Karch, P. Pavone, W. Windl, O. Schütt and D. Strauch, "Ab initio calculation of structural and lattice-dynamical properties of silicon carbide", *Phys.Rev.* **B50**,pp.17054-17063,1994.
12. K. Karch, F. Bechstedt, P. Pavone and D. Strauch, "Pressure-dependent properties of SiC polytypes", *Phys.Rev.***B53**, pp.13400-13413,1996.
13. K. Karch, P. Pavone, A.P. Meyer, F. Bechstedt and D. Strauch, "First-principles study of thermal properties of 3C SiC", *Physica* **B219&220**, pp.448-450,1996.
14. M. Hofmann, A. Zywiets, K. Karch, F. Bechstedt, "Lattice dynamics of SiC polytypes within the bond-charge model", *Phys.Rev.* **B50**,pp.13401-13411,1994.
15. V. van Elsbergen, H. Nienhaus and W. Mönch, "Dynamical properties of 3C-, 4H-, and 6H-SiC surfaces", *Applied Surface Science* **123/124**,pp.38-42,1998.
16. B. Dorner, H. Schober, A. Wonhas, M. Schmitt and D. Strauch, "The phonon dispersion in 6H-SiC investigated by inelastic neutron scattering", *Eur.Phys.J.* **B5**,pp.839-846,1998.
17. G.C. Trigunayat and G.K. Chadha, "Progress in the study of polytypism in crystals", *Phys.Stat.Sol.* **A4**,pp.9-42,1971.
18. Landolt-Börnstein: Numerical Data and Functional Relationship in Science and Technology, Vol.III/17a, pp.132-142.
19. H.L. McMurry, A.W. Solbrig, J.K. Boyter and C. Noble, "The use of valence force potentials in calculating crystal vibrations", *J.Phys.Chem.Solids* **28**,pp.2359-2368,1967.
20. Duane C. Wallace, *Thermodynamics of Crystals*, Chapter 4.16, Dover Publications, Mineola New York,1998.

Theoretical model of carrier flow process on boundary of electrode-dye layer

Danuta Wróbel* and Tadeusz J. Hoffmann**

*Institute of Physics, Poznan University of Technology, Piotrowo 3, 60-965 Poznań, Poland

**Institute of Applied Mechanics, Poznan University of Technology, 60-965 Poznań, Poland

ABSTRACT

The aim of this paper is better understanding of the process of carrier flow generation on the boundary of electrode-dye layer in a photoelectrochemical cell for application in solar energy conversion. Such a boundary of two semispaces is a theoretical two-dimensional model of a photoelectrochemical cell which consists of electrodes and a layer of organic dye molecules in which electron transport process can take place. The semispaces are described in their own microcanonical distributions.

We will consider the process of carrier flow generation on the boundary of electrode-dye layer by means of formalism of thermodynamical quantum statistics. We have obtained the statistical average value of the function of electromagnetic field at the given temperature and in approximation of the low temperature.

Key words: photocurrent creation, photoelectrochemical cell, extended electrodynamics, quantum statistics.

1. INTRODUCTION

Semiconducting-metal photoelectrochemical cell with the organic dye molecules is widely studied because of its potential application as a device in solar energy conversion.¹ A sandwich-like photoelectrochemical cell is usually constructed with two thin transparent electrodes (semiconductor and metal) with the molecular material (natural pigments or synthetic organic dyes in proper solution) embedded between them. In this system the photoactive dye layer deposited on a semiconducting electrode is used to absorb incident light. Incident light excites dye molecules and electron can be injected to the electrode on the boundary of electrode-dye layer. The semiconducting and the dye layer serve as an electron acceptor and electron donor, respectively²⁻⁶. In such a cell photocurrent can be created in closed circuit under light illumination²⁻⁶.

Several groups have reported theoretical approach for seeking the mechanisms of the electron transfer reaction in various models⁷⁻¹². One of the first theoretical treatments in searching for the mechanisms of oxidation - reduction reactions in solvent medium was proposed by Marcus⁹ and then theories concerning mechanisms of electron transfer were developed by other authors¹⁰⁻¹⁴. In our description we use the extended phenomenological electrodynamics theory^{7,8}. In our model the current density vector could be represented by two, tangential and normal components which get jump on the boundary of two semiconducting layers. It has been shown that the current density components are dependent on the ratio of electric permittivity and conductivity of the semiconducting electrode and the dye layer. Thus the charge carrier flow can vary efficiently with the material parameters of the interfacial system.

Our previous papers dealt with the problem of photogenerated electron transfer from photoexcited dye molecule to the semiconducting electrode with the use of the classical thermodynamical statistics¹⁵ and in view of hamiltonian formalism by using quantum description¹⁶. It has been shown that with the theoretical model of electromagnetic energy transfer in a photoelectrochemical cell presented as two semispaces (an electrode and a dye layer) and described in terms of the extended phenomenological electrodynamics the electromagnetic incident and refractive waves can be modelled as the harmonic oscillators on the boundary of these two semispaces.

In this paper we will consider the process of carrier flow generation on the boundary of electrode-dye layer for application in solar energy conversion in a photoelectrochemical cell by means of formalism of thermodynamical quantum statistics.

**e-mail: Tadeusz.Hoffmann@put.poznan.pl

2. RESULTS AND DISCUSSION

For our description we will consider the 2 dimensional (2D) system (in the x_2, x_3 plane) consisting of the thin layer of semiconducting electrode (semispace 1) and the layer of photoexcited dye molecules (semispace 2) as we have done in our previous paper⁷. The dye layer is located very closely to the semiconducting electrode. The right-handed Cartesian coordinate system is taken in such a way that the plane which separates the semiconducting semispace 1 and the dye semispace 2 is represented by the equation $x_3 = 0$. The positive direction of the x_3 axis goes inside the semispace 1⁷.

One supposes, that the two semispaces are characterised by the proper material constants: ϵ, μ, σ , (for semispace 1) and ϵ', μ', σ' (for semispace 2). These parameters describe electric permittivity, magnetic permeability and conductivity, respectively, in classical electrodynamics and also describe the modelling constants: $A, A', C, C', I, I', J, J', K, K'$ and N, N' in the extended electrodynamics description. According to the results of our paper⁷ the classical theory of the refraction of the optic wave describes the components of the field functions: b_1, d_2, d_3 , and b_1', d_2', d_3' in two semispaces, respectively.

On the basis of the formalism of the extended electrodynamics the hamiltonian has a form: in semispace 1:

$$H = \frac{1}{2} \dot{b}_1^2 + \frac{1}{2} J(\dot{d}_2^2 + \dot{d}_3^2) - \frac{1}{2} A(b_{1,2}^2 + b_{1,3}^2) - \frac{1}{2} C(d_{2,3}^2 + d_{3,2}^2) + C d_{2,3} d_{3,2} + \frac{1}{2} K b_1^2 + \frac{1}{2} N(d_2^2 + d_3^2), \quad (1)$$

where: $\dot{b} = \frac{\partial b}{\partial t}$ and $b_{i,k} = \frac{\partial b_i}{\partial x_k}$.

In the semispace 2 in the equation (1) all quantities have indices "prim".

In the hamiltonian formalism the variables are the functions of b_1, b_1' and the magnetic induction B_1, B_1' are the canonical momenta. The hamiltonian [eq. (1)] in the representation of these functions has the form:

$$H = \frac{B_1^2}{2I} + \frac{1}{2} b_1^2 [q^2 A + K + \eta^2 (N\epsilon\mu - q^2 J)], \quad (2)$$

where: q is the wave number of the incident wave and $\eta = \frac{A}{2J}\epsilon$.

According to the taken formalism for the canonical hamiltonian equation for semispace 1 one obtains:

$$\begin{aligned} \dot{b}_1 &= B_1 \\ \dot{B}_1 &= b_1 [q^2 A + K + \eta^2 (N\epsilon\mu - q^2 J)], \end{aligned} \quad (3)$$

For the semispace 2 the analogue equations are obtained and all quantities have indices „prim“, as previously.

From the formal viewpoint equations (3) are the equations for the harmonic oscillators. With this solution the phenomenon of the refraction of the electromagnetic wave and the generation of the electron transfer on the boundary of two semispaces has been brought to the model of interaction of two continuous harmonic oscillators in the hamiltonian formalism. Energy transfer across the boundary of two semispaces can be described as an interaction between these oscillators.

The quantum description of this problem will be got when the operators and the Poisson comutators replace all physical quantities and brackets, respectively. The hamiltonian equations of motion are transferred to the proper quantum equations¹⁷. The energetic levels are then determined as the eigenvalues of the hamiltonian. In quantum description the hamiltonian [eq. (2)] for the semispace 1 will have the form:

$$\hat{H} = \frac{\hat{B}_1^2}{2I} + \frac{1}{2} F \hat{b}_1^2, \quad (4)$$

where:

$$F = q^2 A + K + \eta^2 (N\epsilon\mu - q^2 J).$$

For semispace 2 all quantities have indices „prim”.

The hamiltonian (4) has a form which is characteristic for quantum version of the harmonic oscillator what allows to write the standard equation of the eigenvalues for energy:

$$E_n = (n + \frac{1}{2})h\Omega, \quad n = 0, 1, 2, \dots \quad (5)$$

with: h – Planck's constant and

$$\Omega = \left[\frac{q^2 A + K + \eta^2 (N\epsilon\mu - q^2 J)}{I} \right]^{\frac{1}{2}}.$$

The eigenvalues of energy [eq. (5)] determine the admitted energetic levels in the two semispaces. Energy of photon absorbed by dye molecules (semispace 2) is utilised for the excitation of electrons and their transfer to the conductivity band of the semiconductor (semispace 1).

In quantum theory the Heisenberg uncertainty principle plays an essential role in relation between co-ordinates and canonical momenta. In our previous paper ¹⁶ we have first established the allowed energetic levels of a system as the classical levels of the harmonic oscillator taking the Heisenberg principle into account. In the theory of the oscillator the probability of these energetic states which are described by the proper eigenfunction can be determined ¹⁸. On the basis of that the distribution of the probability for dynamic function of the oscillator or of canonical momenta can be determined in statistical sense. The energy states E_n of the oscillator are non-degenerated and the oscillator is modelled as the isolated system at the temperature T . The probability of the state with the energy E_n is given by the expression ¹⁸:

$$W_n = \exp \left[\frac{\Psi - E_n}{kT} \right], \quad (6)$$

where: k is Boltzmann's constant and

$$\Psi = -kT \ln \left[\sum_{n=1}^{\infty} \exp \left(-\frac{E_n}{kT} \right) \right].$$

The probability [eq. (6)] for the oscillator is given in a form of the gaussian distribution:

$$W(b_s) = \left(\frac{I\Omega}{h\pi} \operatorname{tg} h \frac{h\Omega}{2kT} \right)^{1/2} \exp \left[-\frac{I\Omega}{h} b_s^2 \operatorname{tg} h \frac{h\Omega}{2kT} \right]. \quad (7)$$

The statistical average of the field function b_s can be estimated from Ref. [18]:

$$\bar{b}_s^2 = \frac{h}{\Omega} \left\{ \frac{1}{2} + \frac{1}{\left[\exp \left(\frac{h\Omega}{kT} \right) - 1 \right]} \right\}. \quad (8)$$

If $\frac{h\Omega}{kT} \gg 1$ (what is interpreted as low temperature approximation) eq. (8) can be obtained in a form:

$$\bar{b}_s^2 = \frac{h}{\Omega} \left[\frac{1}{2} + \exp \left(-\frac{h\Omega}{kT} \right) \right]. \quad (9)$$

Hence, we have obtained the statistical average value of the function of electromagnetic field at the temperature T . The value of magnetic induction (canonical momentum in the extended electrodynamics formalism ⁷) must be determined in such a way to fulfil the Heisenberg uncertainty principle. The determination of the field function and of canonical momentum will give full description of the system under consideration.

3. CONCLUSIONS

In the paper we have used the thermodynamic quantum statistic theory of the harmonic oscillator for description of the optic wave of electromagnetic field in the given model of the photoelectrochemical cell with the dye. It was possible on the ground of the results obtained in the previous papers ^{7,15,16}.

Marcus approach ⁹⁻¹¹ does not exactly explain the observed increasing of the electron transfer rate with decreasing temperature in reaction centre, which can be treated as a microscopic photovoltaic device on the molecular level. In this paper we have obtained the statistical average of the value of the field function of the optic wave at the given temperature and in the approximation of the low temperature. In the light of Marcus theory and mentioned discrepancy between the experimental and theoretical electron transfer rate values our results seem to be important since they show the possibility of modelling of electron transfer process on the boundary of semiconducting and dye layer in the photoelectrochemical cell at room and low temperatures. The presented thermodynamic description can be used in the study of interaction between the electron donor-acceptor pair and it will be the subject of the forthcoming paper.

ACKNOWLEDGEMENTS

The paper was supported by Poznan University of Technology, grants DPB 62-168/00 (DW) and PB 21-891/99 (TJH).

REFERENCES

1. *Molecular Electronics, Biosensors, Biocomputers*, (ed. F.T. Hong) Plenum Press, New York, London, 1989.
2. D. Wróbel, J. Goc and R.M. Ion, *J. Mol. Structure*, 450 (1998) 239.
3. W.I. Gruszecki, D. Szymczuk and A. Small, *Bioelectrochem. Bioenerg.*, 29 (1993) 357.
4. K. Akiyama, S. Nishikawa, S. Ueyama and S. Isoda, *Jpn. J. Appl. Phys.*, 34, (1995) 3942.
5. A.N. Macpherson, P.A. Liddel, S. Lin, L. Noss, G.R. Seely, J.M. De Graciano, A.L. Moore, T.A. Moore and D. Gust, *J. Am. Chem. Soc.*, 117 (1995) 7202.
6. T. Wakamatsu, K. Saito, Y. Sakakibara and H. Yokohama, *Jpn. J. Appl. Phys.* 34 (1995) 1467.
7. T.J. Hoffmann and D. Wróbel, *J. Mol. Structure*, 450 (1998) 155.
8. T.J. Hoffmann, *J. Techn. Phys.* 32 (1991) 3.
9. R.A. Marcus, *J. Chem. Phys.*, 24 (1956) 966.
10. A. Marcus, *J. Chem. Phys.*, 43 (1965) 679.
11. R.A. Marcus and R. Almeida, *J. Phys. Chem.*, 94 (1990) 2973.
12. A.D. Joran, B.A. Leland, P.M. Felker, A.H. Zewail, J.J. Hopfield and P.B. Dervan, *Nature (London)* 327 (1987) 508.
13. R. Kubo and Y. Toyozawa, *Prog. Theor. Phys.*, 13 (1955) 160.
14. W.W. Parson and A. Warshel, in: *Anoxogenic Photosynthetic Bacteria*, Kluwer Academic Publishers, 1995 ch. 25.
15. Wróbel and T.J. Hoffmann, *J. Mol. Structure*, 2000 (in press).
16. T.J. Hoffmann and D. Wróbel, *SPIE*, 3725 (1999) 174.
17. L.I. Schiff, *Quantum Mechanics*, McGraw-Hill Book Company, New York, St Louis, San Francisco, Toronto, London 1968.
18. M.A. Leontowicz, *Fizyka statystyczna*, Państwowe Wydawnictwo Naukowe PWN, Warszawa, 1957.

Semiconductor surface characterization by scanning probe microscopies

Michael Hietschold^{*1}, Anne-D. Müller and Falk Müller

Solid Surfaces Analysis Group, Institute of Physics, Chemnitz University of Technology,
D-09107 Chemnitz, Germany

ABSTRACT

Besides the well-known 3-dimensional surface topography, scanning probe methods give access to a whole world of local physical information on solid surfaces. Here, we demonstrate opportunities given by scanning tunnelling spectroscopy (STS) and scanning electrical force microscopy/spectroscopy (SEFM/SEFS). In this paper, we compare the wide-spread UHV-STM/STS technique with ambient SEFM/SEFS. After short description of the methods, some applications to semiconductor surfaces are discussed. Possibly SEFS has a great potential for local electronic spectroscopy in near future.

Keywords: Scanning probe microscopies; Semiconductor surfaces; Local electronic spectroscopy

1. INTRODUCTION

Scanning probe microscopies have fastly developed to standard methods in solid surface microscopy and analysis. When the scanning tunneling microscope (STM) was invented in 1981¹ there has been started a rapid development of near-field microscopies allowing extremely high spatial resolution and approaching also highly-resolved mappings of various surface properties. The most famous representatives of these microscopies are the STM and the atomic force microscope (AFM)². The common feature typical to all of these methods is a sharp probing tip which is approached to a very short distance to the surface and raster scanned within this distance across the surface. Due to tip-sample interaction local physical properties of the sample surface can be imaged. For a more detailed representation we refer to^{3,4}.

In this paper, we restrict us to applications concerning semiconductors, especially the Si(111) surface, to demonstrate the opportunities offered by the scanning probe methods. Actually the whole world of semiconductor materials and structures studied meanwhile has lead to a hardly to overview amount of publications.

2. SCANNING TUNNELING MICROSCOPY AND SPECTROSCOPY

In scanning tunneling microscopy a sharp metallic tip is approached to the sample till to a distance typically smaller than 1 nm. If a bias is applied between tip and sample there occurs an electrical current due to the quantum mechanical tunnel effect which allows electrons to overcome the narrow gap between both electrodes. This current I_T depends according to

$$I_T \propto \exp(\text{const.} \cdot \sqrt{\Psi} z)$$

extremely sensitive on the width z of this gap (Ψ – energetic “height” of the potential barrier made of the gap). In the constant current mode a feedback circuit controls the movement of the tip during the raster scan in such a way that the tunnel current remains constant. For a homogeneous sample, the tip then follows the surface profile with very high accuracy which can even reach atomic dimensions.

¹ Further author information –

M.H. (correspondence): Email: hietschold@physik.tu-chemnitz.de; Telephone: (+49)-371-531-3203;

Fax: (+49)-371-531-3077

F.M.: Email: fmueLLer@physik.tu-chemnitz.de

Si(111)7x7 was the first surface imaged with atomic resolution in real space⁵. Fig.1 shows an image of this surface with the characteristic rhombohedral surface unit cell marked by 4 corner holes. In combination with theoretical simulations the detailed atomic arrangement in this complex surface reconstruction could be determined⁶. This image demonstrates also the advantage of imaging in real space: detailed surface structure including local defects is visible. (An disadvantage is, on the other hand, that only a very small area of the surface is investigated and one has carefully to proof all generalizations made from such images.)

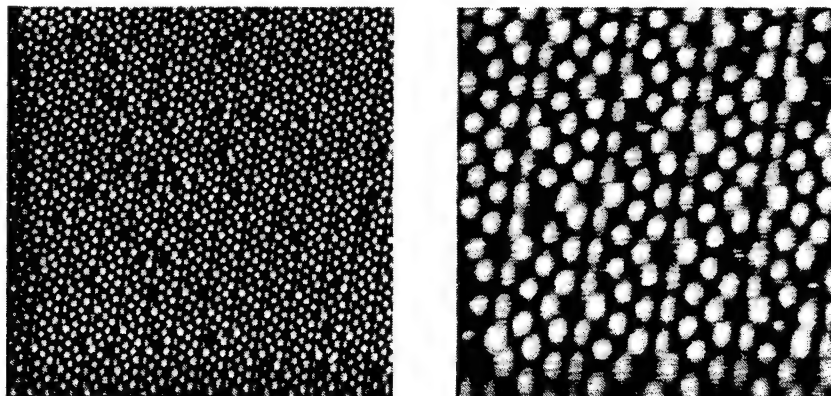


Fig. 1: STM images of a 7x7 reconstructed Si(111)-surface.

Besides pure surfaces, adsorbate structures, processes of epitaxial growth, influence of technological surface treatment, and device structures can be imaged.

In many cases, one obtains slightly different images from semiconductor surfaces at different applied voltages U . This is due to the imaging of different electronic states. Applying a positive bias (sample on positive potential) unoccupied states of the sample are imaged whereas applying a negative bias (sample on negative potential) allows the investigation of occupied sample states. Actually the constant current mode image reflects contours of constant local density of states (LDOS). In the case of Si(111)7x7 for positive U appears the image already seen in Fig. 1 whereas at negative U an asymmetric unit cell is observed⁶.

Local spectroscopy (STS) is performed by measuring $I(U)$ characteristics over fixed positions on the sample surface. These characteristics allow directly a local imaging of energy gaps and Schottky barriers. A more elaborate analysis shows that actually $d \ln I / dU$ reflects the LDOS⁷.

STM/STS is a pure surface method. It visualizes surface bands instead of bulk bands, reflects band bending at the surface, and is influenced also by the tip (the electric field in the tunnel gap influences the surface bands).

Extensions of STM include scanning tunneling potentiometry (STP)⁸ and ballistic electron emission microscopy (BEEM)⁹ which allow mapping of lateral surface potential and local subsurface Schottky-barrier heights, respectively.

3. ATOMIC FORCE MICROSCOPY AND SCANNING ELECTRICAL FORCE MICROSCOPY AND SPECTROSCOPY

Atomic force microscopy allows direct imaging without electrical current. In this case a sensitive miniaturized tip-cantilever system is scanned across the surface. In the contact modus there is a very small distance between tip and sample atoms leading to a repulsive interaction. Keeping the interaction force constant (via the cantilever deflection) one can image the sample surface topography till to atomic resolution.

For clean semiconductor surfaces as Si(111) atomic resolution in UHV is relatively difficult due to strong interaction of the cantilever with the dangling bonds. It could be achieved¹⁰ only in the non-contact modus. In this modus of operation¹¹, the cantilever is externally excited to oscillations near to its eigenfrequency. Approaching the sample surface the tip reaches the

range of attractive van der Waals interaction. The corresponding force gradient influences the effective spring constant and so the eigenfrequency of the cantilever. Experimentally this leads to a change of the stationary oscillation amplitude and phase. Imaging is performed by keeping one of this quantities constant.

In general the AFM allows nm-resolution imaging of surfaces and devices. An essential advantage with respect to scanning electron microscopy is that really three-dimensional images are obtained. Additional contrast may be included using lateral (frictional) forces¹².

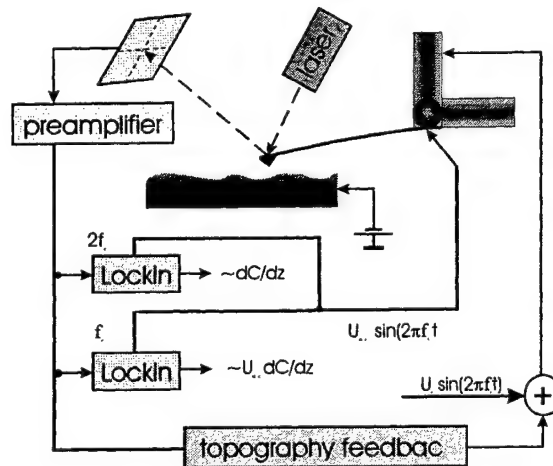


Fig. 2: Principle of SEFM operation.

Scanning electrical force microscopy (SEFM)^{13,14} is based on non-contact atomic force microscopy. Fig. 2 demonstrates the principle of operation. An additional modulated bias is applied between the conducting cantilever-tip and the sample

$$U = U_{dc} + U_{ac} \sin \omega t .$$

The additional electrostatic force between cantilever-tip and sample is

$$F_{el} = -\frac{1}{2} \frac{\partial C U^2}{\partial z}$$

$$= -\frac{1}{2} \frac{\partial C}{\partial z} \left[\left(U_{dc}^2 + \frac{1}{2} U_{ac}^2 \right) + 2 U_{dc} U_{ac} \sin \omega t - \frac{1}{2} U_{ac}^2 \cos 2\omega t \right]$$

It contains components independent of time and such oscillating with frequencies ω and 2ω but only the first of them depends on U_{dc} . According to

$$x(t) = \frac{1}{k} F(t)$$

(k – spring constant of the cantilever) these components can be obtained from the complex cantilever movement (which always includes the movement due to the external mechanical excitation from the usual non-contact mode too) by use of lock-in technique. The additional information which can be obtained from the oscillating components concerns the potential drop across the sample surface (via U_{dc}) and the vertical component of the local capacitance gradient of the tip-sample system. According to this analysis SEFM allows a simultaneous mapping of topography and local electrical properties.

The interpretation turns out to be quite complex. This is due to the complex character of $\delta C/\delta z$. We remember the expression of a parallel plate capacitor

$$C = Q/U = \epsilon_0 \epsilon A / d.$$

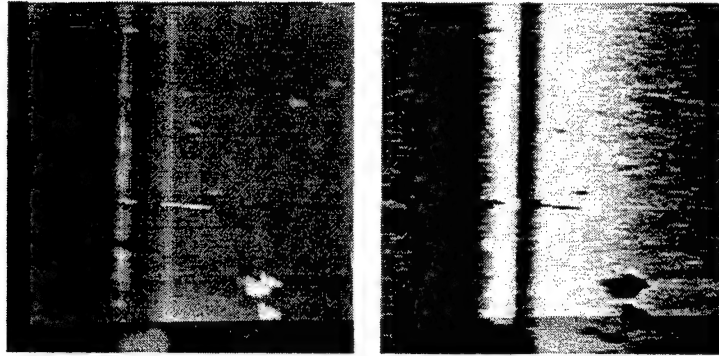


Fig. 3: Cross-section trough a poly-silicon resistor. Left: Topography. Right: Capacitance. Scan range: $3 \mu\text{m} \times 3 \mu\text{m}$. $U_{ac} = 5 \text{ V}$. $f_c = 49 \text{ kHz}$. $f_r = 67 \text{ kHz}$.

First of all, topographic features are reflected in C via the variation of the effective area A when the tip is positioned above a valley (relatively large A) or above a hill (relatively small A). This makes interpretation of images from samples with topographic profiles quite difficult. Plane sample surfaces and especially polished cross-sections are much better suited for SEFM investigations^{14,15}. Fig. 3 shows a cross-section through a poly-Si resistor. In this case, the contrast from the 2ω signal reflects local variations in carrier density (that means in the induced charge Q) between the poly-Si channel, the insulating layer and the Si substrate.

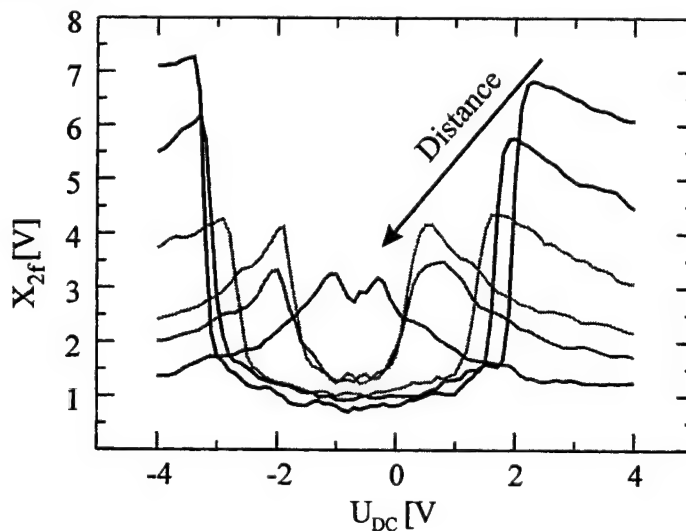


Fig. 4: $C(U_{dc})$ -characteristics on a hydrogenated silicon (100)-surface detected in several distances.

There can also be measured local characteristics $C(U_{dc})$ with U_{ac} as a constant parameter¹⁶. Fig. 4 shows such characteristics for a hydrogenated Si(100) surface. There is a step-like increase of $\delta C/\delta z$ at some threshold voltage which increases with U_{ac} , that means with increasing field strength. This phenomenon reflects the gap and the band bending on the surface which consists of the original bending at the sample and the additional bending due to the local electric field between tip and sample.

We would like to draw attention to the fact that such characteristics can be measured at ambient conditions which is in contrast to STS which allows electronic structure investigations only in UHV.

4. CONCLUSIONS

We have demonstrated the broad field of applications accessible by using various scanning probe methods in semiconductor research and technology. The local character of information available allows high-resolution mapping of surface topography supplemented in some cases by detailed physical properties of the (tip-) sample (system). The full potential offered by these methods has not yet been exhausted.

ACKNOWLEDGEMENTS

This work has been supported by Deutsche Forschungsgemeinschaft (DFG) INK 2.

REFERENCES

1. G.Binnig, H.Rohrer, Ch.Gerber, E.Weibel, "Tunneling through a controllable vacuum gap", *Appl.Phys.Lett.* **40**, pp. 178-180, 1982.
2. G.Binnig, C.F.Quate, Ch.Gerber, "Atomic Force Microscopy", *Phys.Rev.Lett.* **56**, pp. 930-933, 1986.
3. H.-J.Guentherodt, R.Wiesendanger, *Scanning Tunneling Microscopy*, Vol. I-III, Springer Verlag
4. M.Hietschold, *Einführung in die Raster-Sonden-Mikroskopie-Verfahren*, B.G.Teubner (will appear in 2001).
5. G.Binnig, H.Rohrer, Ch.Gerber, E.Weibel, "7x7 Reconstruction on Si(111) Resolved in Real Space", *Phys.Rev.Lett.* **50**, pp. 120-123, 1983.
6. R.M.Tromp, R.J.Hamers, J.E.Demuth, "Atomic and electronic contributions to Si(111)-(7x7) scanning-tunneling-microscopy images", *Phys.Rev.* **B 34**, pp. 1388-1391, 1986.
7. R.M.Feenstra, J.A.Strosio, A.P.Fein, "Tunneling Spectroscopy of the Si(111)2x1 Surface", *Surf.Sci.* **181**, 295-306, 1987.
8. P.Muralt, D.W.Pohl, "Scanning tunneling potentiometry", *Appl.Phys.Lett.* **48**, 514-516, 1986..
9. W.J.Kaiser, L.D.Bell, "Direct Investigation of Subsurface Interface Electronic Structure by Ballistic-Electron-Emission Microscopy", *Phys.Rev.Lett.* **60**, 1406-1409, 1988.
10. F.J.Giessibl, "Atomic-Resolution of the Silicon (111)-(7x7) Surface by Atomic-Force Microscopy", *Science* **267**, pp. 68-71, 1995.
11. Y.Martin, C.C.Williams, H.K.Wickramasinghe, "Atomic force microscope - force mapping and profiling on a sub 100-μ scale", *J.Appl.Phys.* **61**, 4723-4729, 1987.
12. J.Colchero, O.Marti, J.Mlynek, A.Humbert, C.Henry, C.Chapon, "Palladium Clusters on Mica - A Study by Scanning Force Microscopy", *J.Vac.Sci.Technol.* **B 9**, 794-797, 1991.
M.Hirano, K.Stinjo, R.Kaneko, Y.Mirata, "Anisotropy of Frictional Forces in Muscovite Mica", *Phys.Rev.Lett.* **67**, 2642-2645, 1991.
13. Y.Leng, C.C.Williams, "Charge Mapping with the Electrostatic Force Microscope", *Proc.SPIE* **1855**, pp. 35-39, 1993.
14. M.Hietschold, F.Müller, A.-D.Müller, H.J.Engelmann, E.Zschech, "Investigations of local electrical surface characteristics by dynamical scanning force microscopy", *Fresenius J.Anal. Chem.* **365**, 96-98, 1999.
15. F.Müller, A.-D.Müller, M.Hietschold, S.Kämmer, "Detecting electrical forces in noncontact atomic force microscopy", *Meas.Sci.Technol.* **9**, 734-738, 1998.
16. F.Müller, A.-D.Müller, S.Peschel, M.Bäumle, G.Schmid, "Local C(U) Spectroscopy on Chemically Bounded Au₅₅ Clusters", *Surf.Int.Anal.* **27**, 530-532, 1999.

The phase transitions in double tungstate - in extremely low-dimensional and low-symmetry compounds with cooperative Jahn-Teller effect

Mieczysław Tadeusz Borowiec*

Institute of Physics, Polish Academy of Sciences
al.Lotników 32/46, 02-668 Warsaw, Poland

ABSTRACT

The rare earth double tungstates are of special interest because of manifestation of cooperative Jahn-Teller effect (CJTE) for low-dimensional and low-symmetry (monoclinic) crystallographic structure. The structural phase transition (SPT) as a result of the CJTE is unique one among large numbers of various SPT in solids. In the alkali-dysprosium double tungstates $\text{ADy}(\text{WO}_4)_2$ ($A = \text{K, Rb, Cs}$) in spite of monoclinic symmetry the SPT of CJTE type are realized because the presence of Dy^{3+} ions with closely spaced energy levels.

In alkali-dysprosium double tungstates the magnetically ordered structures possessing a number of features connected with low-dimensional interactions of Dy^{3+} ions were observed. Studies of specific heat in magnetic field and of magnetic susceptibility led to conclusion that the magnetic phase transitions (MPT) from paramagnetic to antiferromagnetic state take place at subkelvin temperature region.

Both MPT and SPT are very sensitive to magnetic field. In case of SPT this confirms its CJTE nature and allows to determine the type of the elastic ordering (SPT from para- to antiferroelastic states are observed). The external magnetic field induced the transitions from antiferro- to ferromagnetic states.

The alkali-dysprosium double tungstates belong to the more general class of magneto-elastics with interrelation between magnetic and elastic ordering.

Keywords: rare earth double tungstate; cooperative Jahn-Teller effect, structural phase transition, magnetic phase transition, elastic ordering, magnetic ordering

1. INTRODUCTION

Phase transitions, including structural phase transitions (SPT), are among the most pervasive phenomena in nature. They are intriguing because of the SPT manifest connections and interactions in a substance that determine the structure and properties of its stable states. The SPT, whether spontaneous or induced, can be used to establish the basic laws governing the formation of phase states and symmetry in real crystalline materials. Accordingly, the studies of SPT as a result of the cooperative Jahn-Teller effect (CJTE) are of major importance. As a rule, the SPT of the cooperative Jahn-Teller type (SPT CJTE) takes place in high symmetry compounds¹. This kind of phase transitions is not very common for rare earth compounds. Particularly SPT CJTE has never been observed in rare-earth low-dimensional materials.

The dysprosium double tungstates with general formula $\text{ADy}(\text{WO}_4)_2$ (ADyW), where A is alkali metal ion, with low-symmetry (monoclinic) and with low-dimensional structures in the form of chain-layered atomic constructions are currently intensively studied²⁻²⁹. Scientific interest in these compounds is mainly connected with the SPT CJTE which occurs in them at low temperature of order of several kelvins and with the complex magnetic ordering at subkelvins region.

One of the main purposes of this paper was to determine the character and mechanism of elastic ordering in ADyW compounds (where $A = \text{K, Rb, Cs}$). Studies of magnetic properties of the ADyW crystals are of interest because of the interrelation between magnetic and elastic ordering realized in these magneto-elastics. Main goal of these studies was to investigate peculiarities of magnetic ordering and character of spin-spin interactions in low-dimensional magnets as well as to establish the magnetic structure of the ground state.

*MTB - e-mail: borow@ifpan.edu.pl; mkpbor@it.com.pl

Elastic and magnetic ordering in the alkali-dysprosium double tungstates ADyW has been studied by means of several independent experimental methods, namely: specific heat (from 0.2 K); specific heat in magnetic field; index of refraction; optical absorption spectroscopy of electronic states (from 1.1K); photoluminescence, Raman scattering; optical absorption spectroscopy of phonon states; Electron Spin Resonance (ESR); magnetization; magnetization under pressure, magnetic susceptibility (from 0.6 K); neutron scattering (from 0.04 K) in wide interval of temperatures ($T = 40$ mK - 300 K) and magnetic fields (up to 3 T) including also studies under pressure up to 1.2 GPa. (the pressure for elastics plays the same role as the magnetic field for magnetics or the electric field for electrics). The details of used experimental methods are described in large number of papers²⁻²⁹.

2. EXPERIMENTAL TECHNIQUES

The double tungstates of the general formula $ARe(WO_4)_2$, where A is an alkaline ion, Re - rare-earth ion, undergo irreversible structural phase transitions at temperatures slightly below their melting points. This phenomenon does not allow obtaining low temperature phases of these compounds by means of the Czochralski technique despite their congruent melting. To lower the temperature of crystallization below the temperature of the phase transition High Temperature Solution Growth (HTSG) technique is used. The single crystals of $ADy(WO_4)_2$, where $A = K, Rb$, were grown by the TSSG technique on $[110]$ oriented $KDy(WO_4)_2$ seeds (in some paper this technique is called the modified Czochralski method), which were obtained by means of spontaneous crystallization from solutions of $KDy(WO_4)_2$ in $K_2W_2O_7$ as solvent. The single crystals grow in form of cylinder bounded by $\{110\}$ and $\{011\}$ prisms and by $\{100\}$, $\{010\}$, and $\{001\}$ pinacoids. The dimensions of the homogeneous single crystals reached about $20 \times 20 \times 60$ mm for $KDy(WO_4)_2$ and about $6 \times 6 \times 10$ mm for $RbDy(WO_4)_2$. The microcrystals of $CsDy(WO_4)_2$ grown by the method of spontaneous crystallization reached of about 300 μm in diameter. The $CsDy(WO_4)_2$ microcrystals were pressed to form of pellets. Density is equal: $7.47 g/cm^3$ for $KDy(WO_4)_2$ and $7.79 g/cm^3$ for $RbDy(WO_4)_2$. The Mohs hardness (pinacoid $\{100\}$) was approximately five. The energy gap is of about 3.8 eV. The color of single crystals is connected with optical absorption of rare earth ions: for the $ADy(WO_4)_2$ is light yellow, for the $ARe(WO_4)_2$ is pink.

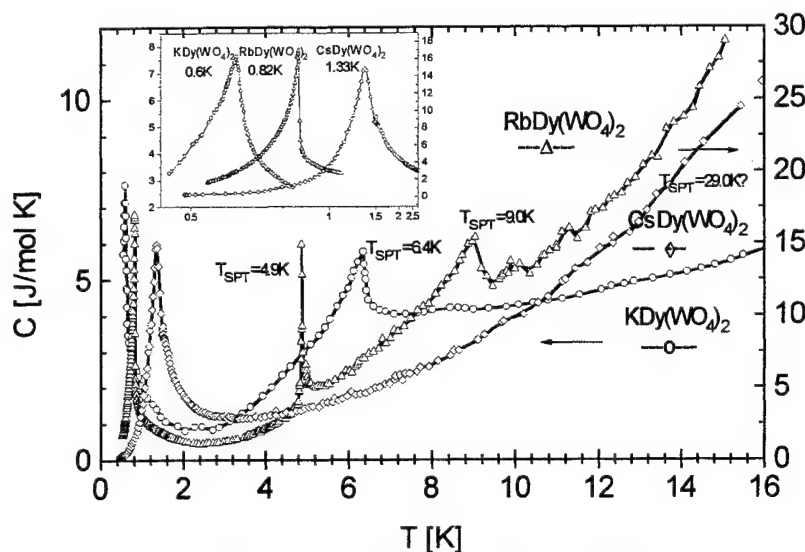


Fig. 1. The specific heat for $ADy(WO_4)_2$, where $A = K, Rb, Cs$.

The alkali-dysprosium double tungstates crystallize at room temperature in $\alpha-KY(WO_4)_2$ structure and they are characterized by the space group $C_{2h}^6 = C2/c$ ³⁰. The unit cell contains four formula units. The lattice parameters are $a = 8.05 \text{ \AA}$; 8.14 \AA , $b = 10.32 \text{ \AA}$; 10.45 \AA , $c = 7.52 \text{ \AA}$; 7.57 \AA , $\beta = 94^\circ 13'$; $94^\circ 34'$ for $KDy(WO_4)_2$ and $RbDy(WO_4)_2$ respectively. The structure is characteristic for several others rare earth double tungstates and belongs to the chain-layered systems. The unit cell consists of layers of $(DyW_2O_8)^-$ spaced parallel to the ac plane and separated by layers of K^+ ions. Eight oxygen ions surrounding the dysprosium ion form a dodecahedron in which two oxygen ions are spaced at a greater distance from the rare earth ion than the other six. The dodecahedrons of oxygen are located in chains parallel to a axis. The oxygen and tungstate ions are located at common positions. The dysprosium and alkali metal ions are placed on C_2 point symmetry site.

The chain-layered crystallographic structure is a reason of anisotropy of many physical properties (for example mechanical anisotropy observed in processes of cutting and polishing of single crystals). In the system characterized by $C_{2h}^6 = C2/c$ the symmetry point exists. For systems with this symmetry point any Jahn-Teller distortions cannot lead to state with spontaneous electrical polarization but they can lead to state with spontaneous deformation of lattice. That means the alkali-dysprosium double tungstates can be elastics (ferro- or antiferroelastics) but they cannot be electrics (ferro- or antiferroelectrics).

The cooperative Jahn-Teller effect is a phase transition which is driven by the interaction between the electronic states of one of the constituent species of ions in a solid and the collective lattice vibrations (phonons). The phase transition may be of first or second order and in both these cases a symmetry-lowering distortion of the crystal lattice is involved. As a result the splitting of all electron energy levels is observed. This short description of the cooperative Jahn-Teller effect indicates that we must consider thermodynamical properties (for example specific heat) to find a phase transition, and then (next) the electron states, the lattice vibrations and finally we must find a change of the space symmetry (point or translational; the phase transition is proper if point symmetry is changed and it is improper if only translational symmetry changes).

3. SELECTED EXPERIMENTAL RESULTS

3.1. Specific heat

Fig. 1 presents globally the results of specific heat measurements in zero magnetic field for the ADyW crystals, where A= K, Rb, Cs. The subkelvins region is presented in details in the insert of Fig. 1. Several anomalies can be observed. For the $\text{KDy}(\text{WO}_4)_2$ crystal the temperature dependence of specific heat $C(T)$ has a broad maximum with peak at $T_{\text{SPT}} = 6.38$ K. For the $\text{RbDy}(\text{WO}_4)_2$ crystal the zero-field specific heat as a function of temperature $C(T)$ was found to exhibit the peculiarities at the following temperatures: 4.9 K; 9.0 K and about 18 K. The results of measurements of specific heat in the $\text{CsDy}(\text{WO}_4)_2$ powder pellets have shown that anomaly takes place at $T = 29$ K. All above anomalies were attributed to the structural phase transitions. In subkelvins region the anomalies at 0.6 K, 0.82 K and 1.34 K for KDyW , RbDyW , CsDyW , respectively are clearly seen. These anomalies are shown to be related to the magnetic phase transitions.

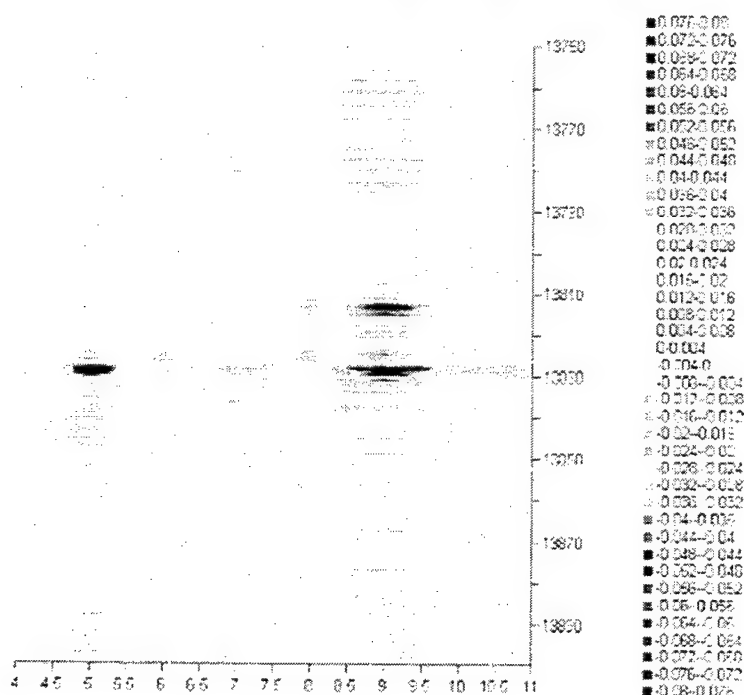


Fig. 2 Derivative of optical absorption coefficient for $\text{RbDy}(\text{WO}_4)_2$ (as example) in arbitrary selected spectral region 13750cm^{-1} - 13900cm^{-1} (optical transition from ${}^6\text{H}_{15/2}$ to ${}^6\text{H}_{1/2}$ and ${}^6\text{F}_{3/2}$) at temperature from 4.0K to 11K in maep representation.

The ground multiplet ${}^6\text{H}_{15/2}$ in crystal field of low monoclinic symmetry is split into 8 Kramers doublets. The energy separations between the lowest Kramers doublets of ground multiplet are following 10 cm^{-1} , 135 cm^{-1} and 350 cm^{-1} . Specially important is the system of two lowest Kramers doublets separated by only 10 cm^{-1} . This two level system is nearly degenerated.

What happens with electronic states of dysprosium ions, and in consequence with optical absorption, at temperature of structural phase transitions? For potassium and rubidium dysprosium double tungstates some small changes

3.2. Optical spectroscopy of electron states

Because of low symmetry (C_{2h}^6 - C_{2v}^2) of the $\text{ADy}(\text{WO}_4)_2$ single crystals its optical properties are highly anisotropic. In particular, the alkali-dysprosium double tungstates belong to the optical class of biaxial crystals. The orientations of optical axes (main axes of indicatrix) and the crystallographic axes are different with one exception of the optical axis y which is identical with the crystallographic axis b. The angle between the optical axis x and the crystallographic axis a is of order of 20 degrees.

The trichroism (pleochroism) of $\text{ADy}(\text{WO}_4)_2$ was found experimentally, that means the optical absorption is characterized by three different, independent spectra attributed to three optical axes (so called main optical spectra). The spectra are composed of several groups of narrow lines in the same spectral regions (and in the same order) similarly to the spectrum of free dysprosium ion. The absorption spectra are attributed to the electronic transitions between ground state and excited states of Dy^{3+} ion with f^9 electron configuration.

were found, but enough small, that in usual representation of optical absorption curves they would be difficult to observe. In contrary to usual representation, Fig. 2 presents derivative of optical absorption coefficient on temperature for $\text{RbDy}(\text{WO}_4)_2$ single crystals as example. It is clearly seen in Fig. 2, that in this representation of optical absorption there can be found spectacular changes on temperature strongly correlated to the anomalies in specific heat at 4.9 K and 9.0 K. Similar results can be obtained for potassium dysprosium double tungstates at 6.4 K. The explanation of the optical result is following: at temperatures of structural phase transitions the energy separations between two nearly degenerated lowest Kramers doublets increase: for KDyW of about $2\text{--}3\text{ cm}^{-1}$ (at 6.4 K), for RbDyW of about $1\text{--}2\text{ cm}^{-1}$ (at 4.9 K) and 1 cm^{-1} (at 9.0 K). Change of energy separations between two lowest Kramers doublets is the biggest for mixed single crystals with cesium: for $\text{Cs}_x\text{K}_{1-x}\text{DyW}$ the change is of about 4 cm^{-1} (for SPT at 14.0 K and 19.0 K for $x=0.05$ and $x=0.1$ respectively). The increase of separation between two lowest Kramers doublet strongly indicates on mechanism of Jahn-Teller effect type.

3.3. ESR

The smooth change of g -factors with temperature in the KDyW crystal has been observed in the vicinity of the SPT (for example, g_z is equal to 3.13 at $T > 12\text{ K}$ and 1.98 at 4.2 K). The transition region has sufficiently wide temperature interval of about 8 K. The ESR linewidth increases from 0.17 T (at $T > 12\text{ K}$) to maximum value of 0.24 T at $T_{\text{SPT}} = 7\text{ K}$. A narrowing of resonance line to 0.19 T takes place at $T = 4.2\text{ K}$. Similar behavior has been observed in the RbDyW crystal. The g -tensor components change considerably from: $g_z = 2.5$; $g_x \approx 0$; $g_y = 1.41$ for $T > 12\text{ K}$ to: $g_z = 1.53$; $g_x \approx 0$; $g_y = 1.2$ for $T < 7\text{ K}$. The ESR linewidth increases from 130 mT for $T > 12\text{ K}$ up to maximum value of 190 mT at $T_{\text{SPT}} \approx 9\text{ K}$ and then it decreases monotonously to 150 mT at 5 K.

The change of gyroscopy factor at temperature of the structural phase transition, the width of ESR line of specific shape near the SPT are simple interpreted in frame of change of energy separation between two lowest Kramers doublets. That means the interpretation of ESR results are in full agreement with the interpretation of the optical absorption results.

Partially summarizing, at SPT the changes of electronic state are observed, the electron ground state energy has lower energy below the temperature of the SPT. To confirm of manifestation of the cooperative Jahn-Teller effect one should consider now the behavior of the atomic system.

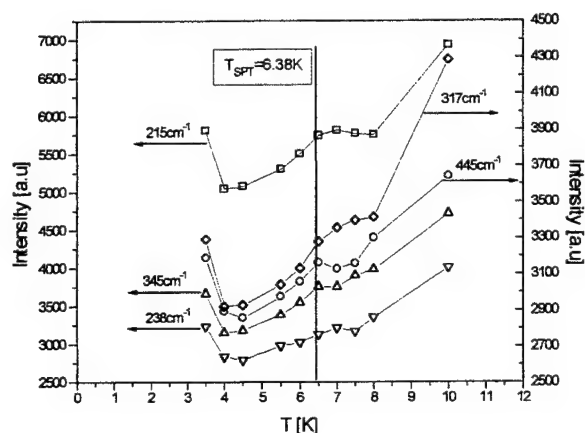


Fig. 3 The Raman scattering results for XX polarization for selected phonon modes in function of temperature.

3.5. Elastic ordering

The information about the type of elastic ordering bases on the experimental results of specific heat in magnetic field. Generally magnetic field diminishes the structural phase transitions. Interpretation of dependences on magnetic field in the frame of molecular field theory, with interaction between Jahn-Teller active ions in formalism of pseudo-spin³², with magnetic field and magnetoelastics coupling included to the formalism indicates that for all dysprosium double tungstates the antiferroelastic ordering is realized.

3.4. Raman scattering

Raman scattering is unusual complicated. However, the good explanation (at room temperature) made by Hanuza³¹ is known in world literature. The phonon modes, mainly these ones, which are connected with dysprosium ions in Hanuza interpretation, behaves anomaly at temperature of structural phase transition - Fig. 3. The irregularities of the behavior of the atomic system which were searched for and found strongly suggest that the structural phase transitions observed in specific heat are related to the cooperative Jahn-Teller effect.

Now the summary is following: the anomalies in specific heat, strongly correlated with lowering of energy of the electron state and the irregularities in behavior of the atomic systems suggests: our SPTs are type of the cooperative Jahn-Teller effect.

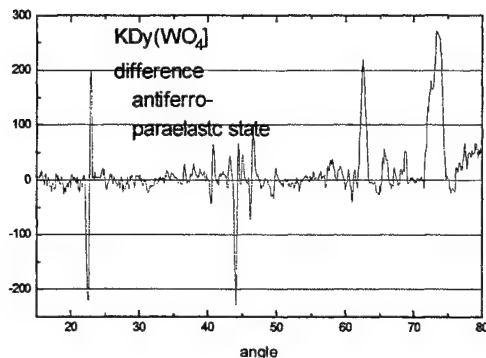


Fig. 4 The neutron scattering results for powdered potassium dysprosium double tungstate

3.7. Magnetic phase transitions

The magnetic phase transitions (MPT) in alkali-dysprosium double tungstates have been studied using the temperature dependence of the specific heat $C(T)$ measured in magnetic field and the results of the magnetization and magnetic susceptibility experiments. The results indicate that the alkali-dysprosium double tungstates ADyW crystals are good paramagnets with strong anisotropy of magnetic properties up to helium temperatures.

The main feature of $C(T)$ dependences at subkelvin temperature is an anomaly connected with the magnetic ordering of Dy^{3+} ions with the peak at $T_N = 0.6$ K; 0.82 K; 1.34 K, respectively for the KDyW, RbDyW, CsDyW. The $C(T)$ dependences above and below T_N were analyzed using the theoretical models for both 3D Ising and 2D Ising lattices and XY model. Data of the analysis give no single-valued answer as to what model well describes the specific behavior near T_N . The temperature dependences of the specific heat at $T > T_N$ can not be well described by 2D and 3D Ising models. The $C(T)$ dependences below T_N are in reasonable agreement with 2D Ising model. The behavior of the specific heat at $T > 1.5T_N$ correlates with theoretical $C(T)$ dependence for 2D Ising model better than for 3D one.

In magnetic field the $C(T)$ peaks shift to lower temperatures. The $C(H, T)$ dependences strongly depend on magnetic field orientation. For example for KDyW crystals the decreasing of T_N by 0.04 K takes place in field of 240 mT along the c -axis while field $H = 60$ mT applied along the a -axis is enough to obtain the same shift. The experimental and theoretical $H - T_N$ diagrams also show that T_N depends strongly on magnetic field direction. The experimental phase boundary between the magnetic (antiferromagnetic) and paramagnetic phases is in a reasonable agreement with the theoretical $T_N(H)$ dependence for 2D Ising antiferromagnet that suggest the magnetic ordering of Dy^{3+} sublattice has a two-dimensional character. The comparison of the calculation with the experiment data shows that a part of the expected $Rln2$ entropy is missing. The experimental value of the effective exchange parameter was obtained. Both the sign of J/k and the character of the temperature dependence of the specific heat in a magnetic field indicate the antiferromagnetic character of the Dy^{3+} ions interactions. The experimental J/k value was shown to correlate with theoretical value for 2D Ising model better than for 3D one.

4. CONCLUSIONS

The rare earth double tungstates are unique one among large numbers of various SPT in solids because of manifestation of cooperative Jahn-Teller effect (CJTE) as the reason of structural phase transition for low-dimensional and low-symmetry (monoclinic) crystallographic structure. To this time, the structural phase transitions (SPT) of the cooperative Jahn-Teller type from paraelastic to antiferroelastic state were observed at 6.38K, 4.9K and 9.0K, ~29K for KDyW, RbDyW and CsDyW, respectively.

In the tungstates (K,Rb,Cs)DyW in spite of monoclinic symmetry the SPT of CJTE type are realized because the presence of Dy^{3+} ions with closely spaced energy levels. According to our conceptions they are accompanied by the distortions of ligand environment of Dy^{3+} ions as a result of effective interaction of rare-earth ions. The interactions of rare earth ions change the distance between two lowest Kramer's doublets of Dy^{3+} ions. The following values of increase of the energy distance were noticed: of about 2.5 cm^{-1} , 2 cm^{-1} (4.9K) and 1 cm^{-1} (9.0K), 4 cm^{-1} (from of about 10 cm^{-1}) for KDyW, RbDyW and $K_{0.9}Cs_{0.1}DyW$, respectively.

In rare earth double tungstates the magnetically ordered structures possessing a number of features connected with low-dimension interactions of Dy^{3+} ions were observed at very low temperatures (because of a weak exchange interactions and of essential role of dipole-dipole coupling). Studies of specific heat in magnetic field and of magnetic susceptibility led to conclusion

3.6. Neutron structural investigations

Fig. 4 presents the preliminary results of the neutron scattering for powder of potassium dysprosium double tungstate. Figure presents the difference between the neutron scattering for antiferroelastic and paraelastic states. The difference is composed from shifts of some lines and additional lines for higher angles. However, because of high coefficient of neutron absorption of dysprosium ions the errors are enough high that the results must be confirm with used the independent or high sensitivity method. But it is clear that results present additional information about the symmetry of the atomic system and they will be very important to understand of mechanism of the SPT in double tungstates.

that the magnetic phase transitions from paramagnetic to antiferromagnetic state take place at 0.6K, 0.82K and 1.34K for KDyW, RbDyW, CsDyW, respectively.

Table 1. Phase transitions of $ADy(WO_4)_2$, where A= K, Rb, Cs

double tungstates	magnetic phase transition	structural phase transitions
$KDy(WO_4)_2$	0.60 K	6.38 K
$RbDy(WO_4)_2$	0.82 K	4.9 K; 9.0 K; ~18 K?
$CsDy(WO_4)_2$	1.34 K	29 K?
$K_{0.95}Cs_{0.05}Dy(WO_4)_2$		14.0 K
$K_{0.9}Cs_{0.1}Dy(WO_4)_2$		19.0 K

The temperature dependence of specific heat near the magnetic phase transition (MPT) can not be properly described in frames 2D and 3D models. The phase H-T diagram of RbDyW has a complicated shape indicative of the occurrence of different magnetic phases in magnetic field H parallel to c-axis. This allows to suppose that a complicated (two sublattice and more) structure with exchange interactions of different signs along various axes as well as with different orientation of magnetic moments in various sublattices can be realized.

Both MPT and SPT transitions are very sensitive to magnetic field. In case of SPT this confirms its CJTE nature. The external magnetic field induced the transitions from antiferro- to ferromagnetic states

ACKNOWLEDGEMENTS

The presented results were obtained in frame of broad cooperation of higher than thirty coworkers from the six polish and foreign institutes. Our studies based on two projects of the Polish Committee on Science (KBN): „Magnetic and elastic ordering of low dimensional systems” (No 2 P02B 071 08) and „Cooperative phenomenons in Jahn-Teller rare earth single crystals with low symmetry” (No. 2 P03B 141 18) directed by author. The neutronographic investigations were made in frame of project of Hahn-Meitner Institute in Berlin PHY 01-692, PHY-01-738 titled „Structural and magnetic phase transition of potassium- and rubidium-dysprosium double tungstates” directed by dr. Andreas Hoser (now dr. Michael Hofmann) and by author.

Author is very grateful to Professor Henryk Szymczak and Professor Vladimir Dyakonov for valuable discussions and cooperation and to Professor Józef Zmija and dr. Andrzej Majchrowski for technological studies and mastery of growth of new crystalline materials.

Author thanks also the Polish Committee on Science for its partial support of this research (project No. 2P03B 141 18).

REFERENCES

1. M.D.Kaplan, B.G.Vekhter, *Cooperative Phenomena in Jahn-Teller crystals*, Plenum Press, New York, London, 1995
2. G.A.Gehring, K.A.Gehring "Cooperative Jahn-Teller effects", *Rep.Prog.Phys.* **38**, 1-89, 1974
3. M.T.Borowiec, V.P.Dyakonov, A.Jędrzejczak, V.I.Markowicz, H.Szymczak, "Low temperature specific heat of the tungstate $KDy(WO_4)_2$ ", *Phys.Solid.State* **38(7)**, pp.1229-1232, 1996.
4. M.T.Borowiec, V.P.Dyakonov, A.Nabiałek, A.A.Pavlyuk, S.Piechota, A.D.Prochorov, H.Szymczak, "Jahn-Teller type structural transition in $KDy(WO_4)_2$ ", *Sol.St.Comm.* **102(8)**, pp.627-630, 1997.
5. M.T.Borowiec, V.P.Dyakonov, A.Nabiałek, A.A.Pavlyuk, S.Piechota, A.D.Prochorov, H.Szymczak, "ESR study of low temperature phase transition in $KDy(WO_4)_2$ ", *Physica B* **240(1-2)**, pp.21-25, 1997.
6. M.T.Borowiec, A.Jędrzejczak, A.Nabiałek, S.Piechota, H.Szymczak, M.Załęski, V.P.Dyakonov, V.I.Markovich, A.D.Prochorov, A.A.Pavlyuk, "The Jahn-Teller type structural phase transition for dysprosium-potassium double tungstate", *Proc. SPIE* **3178**, pp.270-272, 1997.
7. M.T.Borowiec, V.P.Dyakonov, E.E.Zubov, E.N.Khatsko, H.Szymczak, "Magnetic properties of $KDy(WO_4)_2$ monoclinic magnet", *J.de Physique I* **7(12)**, pp.1639-1644, 1997.
8. M.T.Borowiec, V.P.Dyakonov, A.Jędrzejczak, V.I.Markovich, A.A.Pavlyuk, H.Szymczak, E.E.Zubov, M.Załęski, "Magnetic ordering of Dy^{3+} ions in $RbDy(WO_4)_2$ single crystal", *J.Low Temp.Phys.* **110(5-6)**, pp.1003-1011, 1998.
9. V.P.Dyakonov, V.I.Markovich, V.L.Kovarskii, A.V.Markovich, M.T.Borowiec, A.Jędrzejczak, H.Szymczak, "Low-temperature structural phase transition in a monoclinic $KDy(WO_4)_2$ crystal", *Phys. Solid State* **40(4)**, pp.691-698, 1998.
10. M.T.Borowiec, V.P.Dyakonov, A.Jędrzejczak, V.I.Markovich, A.A.Pavlyuk, H.Szymczak, E.E.Zubov, M.Załęski, "Magnetic phase transition in $KDy(WO_4)_2$ single crystal", *Phys.Lett. A* **243(1-2)**, pp.85-90, 1998.
11. M.T.Borowiec, V.P.Dyakonov, V.I.Kamenev, A.Nabiałek, A.D.Prochorov, H.Szymczak, M.Załęski, "Low temperature structural phase transition in monoclinic $RbDy(WO_4)_2$ crystal", *Acta Phys.Polon. A* **94(1)**, pp.71-77, 1998.
12. M.T.Borowiec, V.P.Dyakonov, V.I.Kamenev, I.N.Krygin, S.Piechota, A.D.Prochorov, H.Szymczak, "Pressure effect on the Gd^{3+} ion ground state in the $KY(WO_4)_2 + 0.5\%Gd$ crystal", *Phys.Stat.Solidi B* **209**, pp.443-448, 1998.

12. A.Szewczyk, M.U.Gutowska, K.Piotrowski, M.Gutowski, M.T.Borowiec, V.P.Dyakonov, V.L.Kovarskii, H.Szymczak, L.Gładczuk, "Specific Heat and the Cooperative Jahn-Teller effect in $\text{KDy}(\text{WO}_4)_2$ ", *J.Phys. Cond. Matter* **10(47)**, pp. 10539-10548, 1998.
13. M.T.Borowiec, A.Majchrowski, H.Szymczak, M.Załęski, J.Żmija, "Structural Phase Transitions in $\text{K}_{1-x}\text{Cs}_x\text{Dy}(\text{WO}_4)_2$ ", XXth International Conference on Crystal Growth, Jerusalem 1998.
14. V.P.Dyakonov, M.T.Borowiec, A.Jędrzejczak, V.I.Markovich, H.Szymczak, E.E.Zubov, M.Załęski, "Magnetic ordering of Dy^{3+} ions in $\text{ADy}(\text{WO}_4)_2$ single crystals", series Phys.Chem.Sol. 1998, pp.80-83, ed. M.Kazimierski, Proc. XIth Seminar on Phase Transitions and Critical Phenomena, May 4-7, 1998, Wrocław, Polanica Zdrój.
15. M.T.Borowiec, V.P.Dyakonov, A.Jędrzejczak, V.I.Markovich, A.D.Prokhorov, H.Szymczak, M.Załęski, "Elastic ordering in double tungstates", series Phys.Chem.Sol. 1998, pp.71-74, ed. M.Kazimierski, Proc. XIth Seminar on Phase Transitions and Critical Phenomena, May 4-7, 1998, Wrocław, Polanica Zdrój.
16. V.P.Dyakonov, V.I.Markovich, V.L.Kovarskii, A.V.Markovich, M.T.Borowiec, A.Jędrzejczak, H.Szymczak, "The effect of a magnetic field on Jahn-Teller ordering in the monoclinic crystal $\text{RbDy}(\text{WO}_4)_2$ ", *Phys. Solid State* **40(12)**, pp. 2017-20, 1998.
17. M.T.Borowiec, H.Szymczak, M.Załęski, V.P.Dyakonov, A.Majchrowski, J.Żmija, M.Ceremuga, "Optical properties of $\text{ADy}(\text{WO}_4)_2$ single crystal ($A=\text{K,Rb,Cs}$)", *Proc. SPIE* **3724**, pp.292-295, 1999.
18. M.T.Borowiec, M.Załęski, V.P.Dyakonov, A.Majchrowski, H.Szymczak, J.Żmija "Pleochroism (trichroism) of dysprosium-alkali metal double tungstates", *Proc. SPIE* **3724**, pp.283-287, 1999
19. M.T.Borowiec, H.Szymczak, M.Załęski, P.Kaczor, L.Adamowicz, J.Strzeszewski, A.Watterich, L.Kovacs, "Raman and IR spectroscopy investigations of double tungstates", *Proc. SPIE* **3724**, pp.288-291, 1999.
20. M.T.Borowiec, V.P.Dyakonov, I.M.Fita, A.Nabiałek, A.A.Pavlyuk, H.Szymczak, M.Załęski, E.E.Zubov, "Magnetization of the $\text{KDy}(\text{WO}_4)_2$ single crystal in paramagnetic phase", *Proc. SPIE* **3724**, pp.318-322, 1999.
21. M.T.Borowiec, V.P.Dyakonov, I.M.Fita, A.Nabiałek, A.A.Pavlyuk, A.Szewczyk, H.Szymczak, M.Załęski, E.E.Zubov, "Magnetic structure of ground state of the $\text{KDy}(\text{WO}_4)_2$ single crystal", *JMMM* **195**, pp.119-124, 1999.
22. M.T.Borowiec, A.Hoser, „Structural and magnetic phase transition of potassium- and rubidium-dysprosium double tungstates”, *BENSC Experimental Reports* 1998, p.42, 1999; *BENSC Experimental Reports* 1999, p.44, 2000.
23. V.P.Dyakonov, E.E.Zubov, A.A.Pavlyuk, M.T.Borowiec, H.Szymczak, "Magnetic structure of a $\text{RbDy}(\text{WO}_4)_2$ single crystal", *Phys. Solid State* **41(4)**, pp.605-609, 1999.
24. V.P.Dyakonov, V.I.Markovich, V.L.Kovarskii, A.V.Markovich, M.T.Borowiec, A.Jędrzejczak, H.Szymczak, "Characteristic features of the magnetic ordering of Dy^{3+} ions in a monoclinic $\text{RbDy}(\text{WO}_4)_2$ single crystal", *Phys. Solid State* **41(3)**, pp.440-444, 1999.
25. M.T.Borowiec, V.P.Dyakonov, A.D.Prokhorov, H.Szymczak, "Peculiarities of EPR spectrum in the $\text{KY}(\text{WO}_4)_2 + \text{Dy}^{3+}$ single crystal", *Phys.Rev. B* **92(9)**, pp.5834-5838, 2000.
26. M.T.Borowiec, A.Majchrowski, H.Szymczak, M.Załęski, J.Żmija, „Structural Phase Transition in $\text{K}_{1-x}\text{Cs}_x\text{Dy}(\text{WO}_4)_2$ Single Crystals”, *Cryst.Res Technol.* **35(11-12)**, pp.1343-1346, 2000.
27. V.P.Dyakonov, M.T.Borowiec, A.Jędrzejczak, E.E.Zubov, T.Zayarnyuk, H.Szymczak, „Magnetic ordering of Dy^{3+} ion in low-dimensional $\text{CsDy}(\text{WO}_4)_2$ double tungstates”, ICSSC 2000, Zakopane.
28. T.Zayarnyuk, M.T.Borowiec, V.P.Dyakonov, H.Szymczak, E.E.Zubov, A.A.Pavlyuk, M.Barański, „Optical properties of potassium erbium double tungstate $\text{KEr}(\text{WO}_4)_2$ ”, ICSSC 2000, Zakopane.
29. A.Majchrowski, E.Michalski, J.Żmija, M.T.Borowiec, V.P.Dyakonov, H.Szymczak, T.Zayarnyuk, M.Barański, „Growth and properties of potassium holmium double tungstate $\text{KHo}(\text{WO}_4)_2$ ”, ICSSC 2000, Zakopane (abstract only).
30. S.V.Borisov, R.F.Klevtsova, "Kristalicheskaya struktura $\text{KY}(\text{WO}_4)_2$ ", *Kristallografija* **13(2)**, pp. 517-519, 1968
31. E.N.Ipatova, R.F.Klevtsova, L.P.Soloveva "Crystal structure of the double rubidium dysprosium tungstate $\text{RbDy}(\text{WO}_4)_2$ ", *Sov. Phys.-Crystallogr. (USA)*. **21(6)**, pp. 648-651, 1976.
32. P.V.Klevtsov, L.P.Kozeeva, R.F.Klevtsova, "Kristallograficheskie izuchenie kalii-ittriievkh volframata i molibdata", *Izv. AN SSSR Neorg.Mater.* **4(7)**, pp. 1147-1151, 1968.
33. J. Hanuza, „Vibrtational characteristics of oxygen bonds in $\text{KDy}(\text{WO}_4)_2$ single crystal”, *Acta Phys.Pol. A* **70(5)**, pp.585-602, 1986.
34. R.B.Stinchcombe, „Pseudo-spin approach to structural phase transitions”, in *Electron-Phonon Interactions and Phase Transitions*, ed. T.Riste, Plenum Press, New York and London, pp.209-244.
35. M.T.Borowiec, bibliographical database "The Double Tungstates and Double Molibdates", WWW page on Internet adress: <http://info.ifpan.edu.pl/PERSONAL/borow/baza.htm>.

Investigation of thermal annealing by gamma irradiation at room temperature in LiNbO_3 crystals

Andrzej L. Bajor^a, Sławomir M. Kaczmarek^b, Izabella Pracka^a, Marek Świrkowicz^a and Teresa Wrońska^c

^aInstitute of Electronic Materials Technology, ul. Wólczyńska 133, 01-919 Warsaw, Poland

^bInstitute of Optoelectronics, Military University of Technology, Kaliskiego 2, 00-908 Warsaw, Poland

^cInstitute of Chemistry and Nuclear Technics, ul. Dorodna 16, 03-195 Warsaw, Poland

ABSTRACT

An interesting phenomenon of thermal annealing in gamma irradiated undoped, and photorefractive Cu- and Fe-doped, Z-oriented LiNbO_3 crystals has been observed. Prior and after each gamma irradiation the crystals were thermally annealed in the air at 800°C for a couple of hours. Optical homogeneity was investigated on the entire areas of LiNbO_3 wafers by measuring distributions of birefringence, the principal azimuth, transmission, and parameters associated with birefringence dispersion, and also by measurements of additional absorption in a few wafers' points. It has been rather unexpectedly observed that the classical thermal annealing can lead to a decrease in optical homogeneity in the majority of cases. It is attributed to generation of an internal electric field by the pyroelectric effect, and to the electrooptic effect involved thereafter. On the other hand, the secondary electrons generated by gamma irradiation are believed to increase the optical homogeneity by increasing the crystal's conductivity and dissipating this field. A uniform temperature heating across the wafer generated by this irradiation is also a helpful factor in this gamma-annealing. It has been found that this effect at room temperature is small for gamma irradiation of 10^5 Gy, while increasing the doses to 10^6 Gy and 10^7 Gy can profit in a considerable reduction of the optical inhomogeneity. A certain influence of Cu-doping on this effect has also been observed.

Keywords: thermal annealing, gamma irradiation, doping, electrooptic phenomenon, Birefringence Dispersion Coefficient (BDC).

1. INTRODUCTION

Lithium niobate (LiNbO_3) is a promising photorefractive material and is also used e.g. for manufacturing polarizers, electrooptic modulators or acoustooptic devices. Its optical homogeneity is then of primary importance in many practical applications. In this work we investigate the influence of gamma irradiation (1.2 MeV, ^{60}Co source, source yield 1.5 Gy/s) on undoped, and photorefractive Cu- and Fe-doped crystals grown by the Czochralski method from the congruent melt. The influence of gamma irradiation on the optical properties of crystals or devices can be expected in several specific cases including nuclear power stations and laboratories or extraterrestrial environment. One might then have expected rather parasitic effects associated with this radiation. However, it was rather unexpectedly observed that thermal annealing applied after each gamma irradiation resulted in a certain increase in the optical inhomogeneity, whereas the gamma irradiation was found to be a fruitful factor in cancelling this effect. One may then suspect that a certain temperature gradients in the samples during the annealing and cooling processes can result in an internal electric field due to the pyroelectric effect, and, therefore, to some parasitic birefringence caused by this field through the electrooptic phenomenon. When such samples are next homogeneously irradiated by gamma rays the secondary electrons generated by this radiation are helpful for relaxation of this electric field. Since samples are also uniformly heated by this radiation it should also imply a positive effect on canceling this parasitic birefringence.

2. EXPERIMENT

The investigated samples (Cu-doped at 0.05, 0.06, and 0.07 at. %, respectively; and undoped) were cut perpendicularly to the Z-growth direction, being also the direction of their optical axis. They were next mechanically both-sides polished to the thicknesses of 2.1 mm. Also three Fe-doped samples (0.1 at. %, 3.1 mm thick) were cut parallelly to the Y-growth

direction, and perpendicularly to Z. The samples after checking their optical homogeneity were thermally annealed, next they were gamma irradiated at 10^5 Gy, again thermally annealed, again gamma irradiated at 1.065×10^6 Gy, and after the consecutive thermal annealing they were finally gamma irradiated at 10^7 Gy. Prior and after each such operation the samples were checked for their optical homogeneity. The three optical methods have been used : an automated polarimeter (refs. [1,2]) having the capacity of measuring the three maps on the entire sample area (birefringence, the principal azimuth (one of the principal residual stresses in the case of birefringence induced by residual stresses), and transmission), an automated spectropolarimeter (refs. [3-5]) utilizing a novel technique of mapping of parameters associated with the birefringence optical dispersion, and optical spectroscopic measurements of the so-called additional absorption. In the latter case the additional absorption was measured in a few (usually five) sample points, and an average or the most typical result has been taken into consideration. UV-VIS Lambda 900 and Fourier transform IR 1705 Perkin Elmer spectrophotometers have been used in these measurement, as described e.g. in ref. [6]. The values of additional absorption ΔK were calculated according to formula

$$\Delta K(\lambda) = \frac{1}{d} \ln \frac{T_1}{T_2} \quad (1)$$

where λ is wavelength, d is sample thickness, and T_1 and T_2 are the transmissions of the sample measured before and after gamma irradiation, respectively.

Due to the shortage of space in this paper on the following maps (figs. 1 to 8) one can note only the results for one sample only (no. 4, Cu-doped at 0.06 at. %) achieved with the use of the automated spectropolarimeter, since it has been found to be the most characteristic for this experiment. The remaining results of the birefringence, principal azimuth, and transmission mapping are supporting those shown on these maps for this sample. However, since the technique of mapping of parameters associated with birefringence dispersion is quite a new one, a few words have to be said on it here.

It can be shown (e.g. in ref. [3]) that the so-called **Birefringence Dispersion Coefficient (BDC)** in sample cut out from an isotropic crystal, or, alternatively, cut perpendicularly to the Z-optical axis in an anisotropic crystal, is a function of the stress-optic coefficients C_i , i.e.

$$\text{BDC}(\lambda_i) = \frac{\Delta n(\lambda_i)}{\Delta n(\lambda_{i+1})} = \frac{C_i}{C_{i+1}} \quad (2)$$

where Δn is birefringence, and the wavelength increment $\lambda_{i+1} - \lambda_i$ was adjusted to 10 nm in this experiment. The stress-optic coefficients of the crystal are defined by the direct relation of birefringence to (residual) stresses σ

$$\Delta n_i = C_{ij} \sigma_j \quad (3)$$

where the matrix notation like that used e.g. in ref. [7] has been applied. In contrary to such parameters like the piezooptic(al) π_{ij} , or elastooptic(al) p_{ij} coefficients, which have been usually measured by many investigators for describing the elastooptic properties of crystals, the piezooptic coefficients C_{ij} , closely related to π_{ij} , and being a good alternative for them (using C_{ij} one does not need to know or measure the refractive index of the ordinary ray) have been, however, mentioned only in a few papers on optics (e.g. refs. [8,9]). It can be also shown (ref. [5]) that the so-called **Relative Differential Birefringence Dispersion (RDBD)** (unshown in this work, since its maps and their cross-sections are close in shape to the BDC's ones) is another important function (relative dispersion) of the stress-optic coefficient :

$$\text{RDBD}(\lambda_i) = \frac{\Delta n(\lambda_i) - \Delta n(\lambda_{i+1})}{\Delta n(\lambda_i)(\lambda_{i+1} - \lambda_i)} = \frac{1 - \frac{1}{\text{BDC}(\lambda_i)}}{\lambda_{i+1} - \lambda_i} = \frac{1}{C_i} \frac{dC}{d\lambda} \Big|_{\lambda_i} \quad (4)$$

In fig. 1 one can see the BDC map for the investigated sample after it had been gamma irradiated at 1×10^5 Gy. The map has been calculated for $\lambda_i = 760$ nm using eq. (2), and so has been the following maps and cross-sections shown in this work. The BDC horizontal cross-section of the map in fig. 1 is shown in fig. 2. All the horizontal and also vertical cross-

ITME Birefringence Dispersion
Coefficient
in LiNbO₃ Cu/4/97
Date : 1999- 9-15 P-U : 3597.0

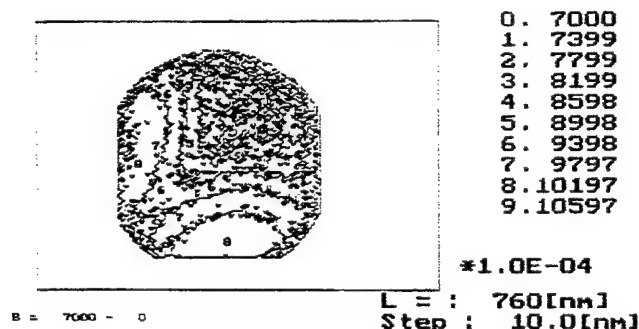


Fig. 1. BDC distribution in Cu (0.06 at. %) doped, Z-cut LiNbO₃ after gamma irradiation at 1×10^5 Gy.

ITME Birefringence Dispersion
Coefficient
in LiNbO₃ Cu/4/97
Date : 1999-11-26 P-U : 2820.0
L = : 760[nm]

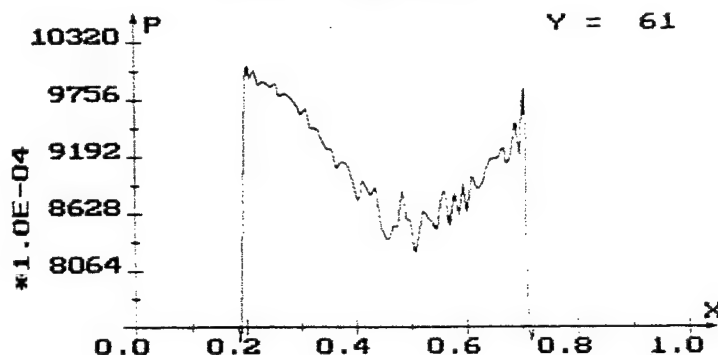


Fig.2. Horizontal cross-section of the map shown in fig. 1.

sections are plotted along the diameter of the quasicircular sample. In figs. 3 and 4 one can see for comparison the horizontal and vertical cross-sections, respectively, of the BDC map (unshown here) after the sample had been thermally annealed at 800°C for 4 hours. Such BDC horizontal and vertical cross-sections for the sample gamma irradiated at 1.065×10^6 Gy are shown in figs. 5 and 6, whereas only the BDC horizontal cross-sections of this sample again thermally annealed, and next gamma irradiated at 1×10^7 Gy are shown in figs. 7 and 8, respectively.

As it clearly comes out from fig. 3 the thermal annealing of this sample after gamma irradiation at 1×10^5 Gy had only a minor influence on optical homogeneity of this sample. The reason is an insignificant influence of this dose on the optical homogeneity of the sample that prior to this irradiation had been also thermally annealed. However, the dramatic and positive changes in the BDC distribution can be seen after the sample had been next gamma irradiated at 1.065×10^6 Gy (figs. 5 and 6 compared to figs. 3 and 4, respectively). The horizontal BDC cross-section shown in fig. 5 is almost flat, and so is also approximately flat the respective vertical cross-section (fig. 6). The rocking curves that can be seen in the

vertical cross-sections come solely from the background, not from the sample. Also the rocking curves seen on the left, and on the right hand side, respectively, in the horizontal cross-sections come out from some reflections at the border of the sample and its holder.

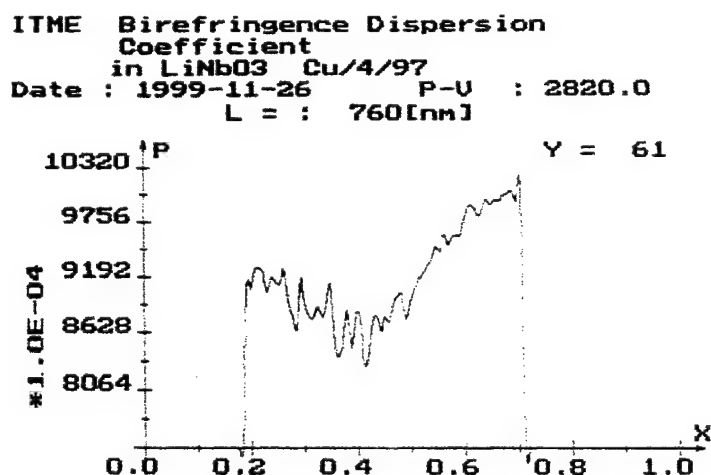


Fig. 3. Horizontal cross-section of the BDC map (unshown in this work) for the sample thermally annealed after gamma irradiation at 10^5 Gy.

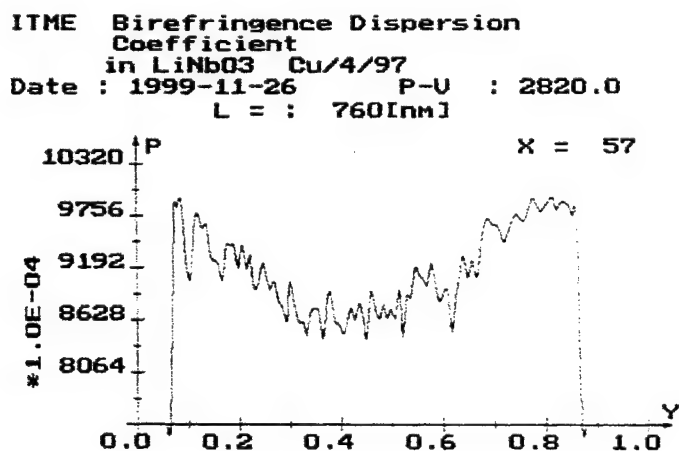


Fig. 4. Vertical cross-section of the BDC map (unshown in this work) for the sample thermally annealed after gamma irradiation at 10^5 Gy.

By comparing fig. 7 and fig. 5 one can observe a considerable decrease in the optical homogeneity when the sample had been thermally annealed after gamma irradiation at 1.06×10^6 Gy. A certain, but small, increase in this homogeneity has been observed (fig. 8) when this sample was again gamma irradiated for a long time at 1×10^7 Gy.

From these results it is evident that thermal annealing leads to degradation of the optical homogeneity in LiNbO₃ crystals, what, at first sight, seems to be something unusual in materials engineering. On the other hand, however, gamma irradiation of the thermally annealed samples has been found to be a positive factor in cancelling parasitic birefringence induced by this thermal treatment. Similar results have been observed for another LiNbO₃ samples. These results are also in good agreement with measurements carried out in the automated polarimeter (unshown here), and with measurements of the additional absorption (fig. 9). Changes in absorption of the sample shown in this figure are considerable in the

visible part of the spectrum (up to about 600 nm). The largest changes are associated with the thermal annealing after gamma irradiation at 10^6 Gy (curve no. 5), and at 10^7 Gy (curve no. 6). This thermal annealing has only a minor influence on the additional absorption after the sample had been gamma irradiated at 10^5 Gy (curve no. 4). A clear positive influence on the additional

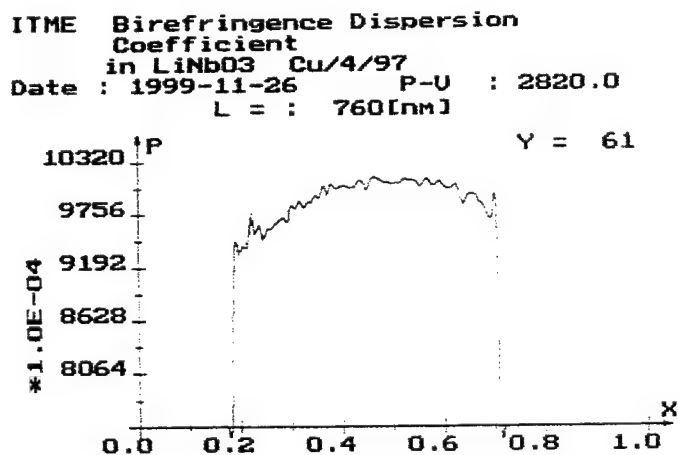


Fig. 5. Horizontal cross-section of the BDC map (unshown in this work) for the sample gamma irradiated at 1.065×10^6 Gy.

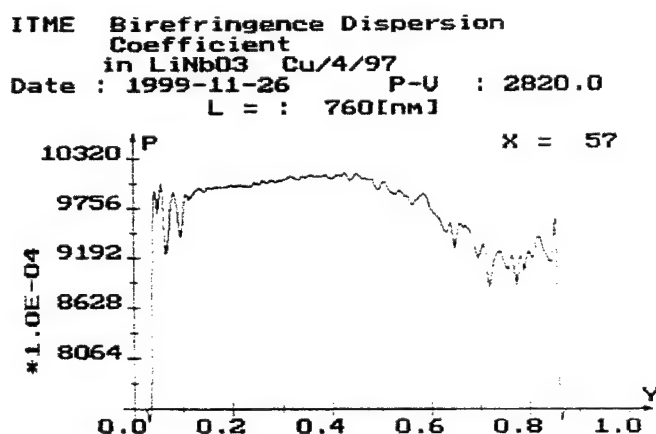


Fig. 6. Vertical cross-section of the BDC map (unshown in this work) for the sample gamma irradiated at 1.065×10^6 Gy.

absorption from gamma irradiation is also evident in this figure when the sample had been gamma irradiated at 10^6 Gy (curve no. 2), and later irradiated at 10^7 Gy (curve no. 3). The results of these spectroscopic measurements are at least in good qualitative agreement with that achieved by using the (spectro)polarimeters. It is worth noting that the results of the polarimetric measurements in the wavelength region above 600 nm are corresponding with those obtained for shorter wavelengths by the spectroscopic investigations. It means that these measurements are complementary to each other.

It has been also found that the sample doped with 0.07 at. % of Cu seems to be more influenced by gamma irradiation than that doped with smaller amounts of copper. Also a larger influence of gamma irradiation on Cu-doped, than on Fe-doped or undoped samples can be deduced from the results of these investigations. However, this last conclusion needs a further and stronger evidence.

3. SUMMARY AND CONCLUSION

In this work we have shown that the classical thermal annealing, i.e. the annealing of the wafers in a furnace at high temperature, can lead to a certain decrease in the optical homogeneity, while gamma irradiation is a helpful factor in restoring this homogeneity. Thus we can talk about the "thermal annealing by gamma irradiation" because this irradiation also involves a certain temperature increase above the room temperature in the irradiated wafers.

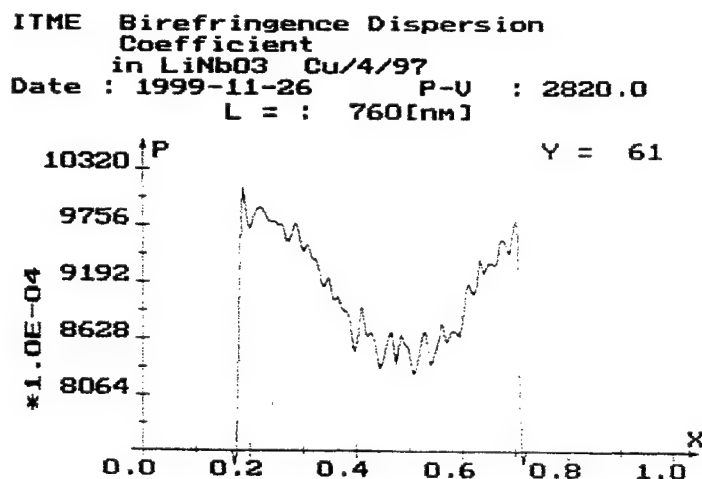


Fig. 7. Horizontal cross-section of the BDC map (unshown in this work) for the sample thermally annealed after gamma irradiation at 1.065×10^6 Gy.

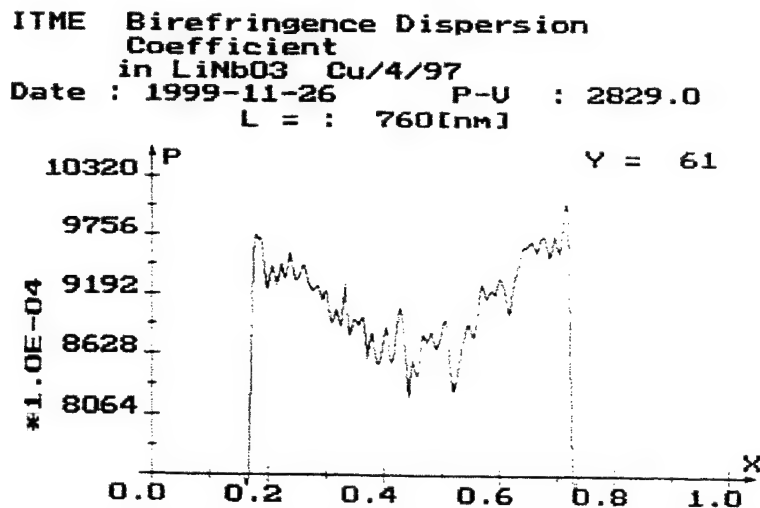


Fig. 8. Horizontal cross-section of the BDC map (unshown in this work) for the sample gamma irradiated at 1×10^7 Gy.

The mechanism of this phenomenon seems to be the electric fields induced in the wafers by the pyroelectric effect, and the electrooptic effect involved thereafter. However, in general case this mechanism is very complicated, and only a simplified qualitative, and to some extent - also a quantitative interpretation is given here.

When the Z-cut LiNbO₃ wafer, like in this work, is thermally annealed in the furnace, the critical steps of this operation seem to be the proper annealing itself, and next cooling of the wafer down to the room temperature. The electric field duly involved in these operations should be parallel to the Z-axis, and since the light beam is also parallel to this Z (optical) axis in this experiment, it ideally should then have no influence on the birefringence data at all. However, one can easily

imagine that firstly, there is always a certain temperature distribution (a few °C) on the wafer area during the annealing itself, and, secondly, that a certain, but very small, spread distribution of the cooling rate on this area may be also expected in the cooling process. These two effects may result in a certain inhomogeneous distribution of the electric charges on both sides of the wafer, thus generating also some electric field in the X and Y directions. The relaxation of this field while cooling is small. For example, the time constant of this relaxation at 80°C is approx. equal to two hours (ref. [10]), and is of course rapidly increasing with decrease of temperature. It means that in the cooling process (about 24 hours) only a fraction of this electric field can be dissipated. When cooled down to the room temperature, the process of charge relaxation goes on, but extremely slow.

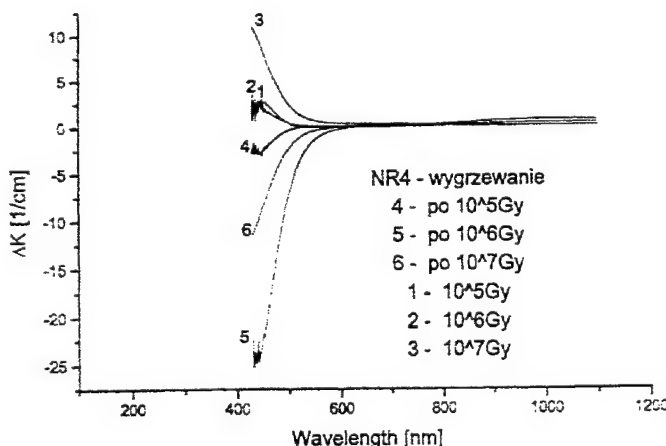


Fig. 9. Additional absorption in Cu (0.06 at. %) doped, Z-cut LiNbO₃ wafer prior and after the thermal annealing or gamma irradiations.

The magnitude of the electrooptic effect can be estimated from a simple formula $\Delta n = n_o^3 r_{22} E$, where n_o is refractive index of the ordinary ray, r_{22} is electrooptic coefficient in this configuration (Z-cut wafer, light beam parallel to Z, the electric field E perpendicular to Z). Providing a static electric field, like in this example, and 760 nm wavelength from the following data: $n_o = 2.26$ (ref. [11]), and $r_{22} = 6.8 \times 10^{-10}$ cm/V (ref. [12]), one can calculate the constant $n_o^3 r_{22}$ to be 7.85×10^{-9} cm/V. It means then that even such a weak electric field, like e.g. 10^4 V/cm acting in the wafer plane, can result in a parasitic birefringence of 7.85×10^{-5} , i.e. the birefringence comparable to that induced by the residual stresses. Usually, the electric fields generated by the pyroelectric effect in LiNbO₃ are estimated to be within the range of 10^5 - 10^8 V/cm. Since in the crossed polarizers configuration of the used polarimeter one could always observe the so-called isoclinic cross associated with principal directions of the residual stresses, it might have been concluded that the additional birefringence due to the pyroelectric and electrooptic effects was weaker than that originally induced by these stresses. Most probably the electric fields generated in our samples at room temperature were then in the vicinity of 10^3 - 10^4 V/cm.

The effect of cancelling of the electric field by gamma irradiation is primarily associated with a rapid increase in conductivity of the wafers due to the secondary electrons generated by this radiation. Also increase of the wafer's temperature, being the secondary effect of gamma irradiation, and uniformity of this temperature distribution on wafer area, is another helpful factor for migration of the charges and for dissipation of the electric field components parallel to the wafer area.

It was observed that these effect have been significantly large for gamma irradiation at the level of 1.065×10^6 Gy. This figure, or maybe a little smaller one, might then have seem to be something like a threshold in this effect, since the positive influence of gamma irradiation at the level of 1×10^7 Gy has not been so pronounced as that achieved at 1.065×10^6 Gy. The exact magnitude of this threshold is, however, rather difficult to be precisely estimated in these long lasting irradiation experiments.

REFERENCES

1. A.L. Bajor, "Automated polarimeter-microscope for optical mapping of birefringence, azimuths, and transmission in large area wafers. Part I. Theory of the measurement", *Rev. Sci. Instrum.* **66**, pp. 2977-2990, 1995.
2. A.L. Bajor, M.J. Kukla, T. Pi_tkowski, L. Sałbut, A. Spik, and A. Szwedowski, "ibid. Part II. Measurement setup and results", *Rev. Sci. Instrum.* **66**, pp. 2991-2995, 1995.
3. A.L. Bajor, "Birefringence dispersion inhomogeneity testing in optical materials by imaging polarimetry", in *Optics and Optoelectronics. Theory, Devices and Applications*, edited by O.P. Nijhawan, A.K. Gupta, A.K. Musla, and K. Singh, **Vol. 2**, pp. 1312-1316, Narosa Publ. House, New Delhi, Madras, Bombay, Calcutta, London, 1998.
4. A.L. Bajor, "Testing of optical materials by birefringence dispersion mapping", in press SPIE, 2000.
5. A.L. Bajor, "Birefringence dispersion mapping - a new technique for testing of optical inhomogeneity in crystalline materials", in press SPIE, 2000.
6. I. Pracka, A.L. Bajor, S.M. Kaczmarek, M. Świrkowicz, B. Kaczmarek, J. Kisielewski, and T. Łukasiewicz, "Growth and characterization of LiNbO₃ single crystals doped with Cu and Fe ions", *Cryst. Res. Technol.* **34**, pp. 627- 634, 1999.
7. J.F. Nye, *Physical properties of crystals. Their representation by tensors and matrices*, Clarendon Press, Oxford, 1957.
8. P.K. Ajmera, B. Huner, A.K. Dutta, and C.S. Hartley, "Simulation and observation of infrared piezobirefringent images in diametrically compressed semiconductor discs", *Appl. Opt.* **27**, pp. 752-757, 1988.
9. A.K. Dutta, P.K. Ajmera, and B. Huner, "Piezobirefringence effects in GaAs discs subjected to diametrical compression", *J. Appl. Phys.* **65**, pp. 5230-5232, 1989.
10. A.A. Blistanov, E.V. Makarevska, V.V. Geraskin, O. Kamalov, and M.M. Koblova, "The influence of doping on optical quality and on electric conductivity of LiNbO₃", *Sol. State Phys. (Sov.)*, **20**, pp. 9-12, 1978.
11. D.F. Nelson, and R.M. Mikulyak, "Refractive indices of congruently melting LiNbO₃", *J. Appl. Phys.* **45**, pp. 3688-3689, 1974.
12. A. Yariv, and P. Yeh, *Optical Waves in Crystals*, Wiley-Interscience, New York, 1984.

Monocrystals Ag_3SbS_3 : Investigation of electrical characteristics

G.Khlyap^{a*}, V.Belosertseva^b, L.Panchenko^c, M.Andrukhiv^a

^a State Pedagogical University, 24 Franko str., Drohobych 82100, UKRAINE

^b Kharkiv State Politechnical University, 21 Frunze str., 61002 Kharkiv, UKRAINE

^c Sumy State University, 2 R.- Korsakov str., Sumy 244007, UKRAINE

ABSTRACT

Electrical characteristics (current-voltage and capacitance-voltage) of metal-semiconductor structure based on monocrystals Ag_3SbS_3 are reported. Studies carried out at the room temperature were shown space-charge limited (SCL) current caused by the peculiarities of Ag_3SbS_3 crystallographic structure: velocity saturation mode and ballistic regime were observed. Results of the numerical modeling of experimental data are also presented.

Keywords: Ag_3SbS_3 monocrystal, I-V and C-V measurements, SCL-current, numerical modeling.

1. INTRODUCTION

Recently, the attention of researchers has been attracted by chalcogenide semiconductor systems $\text{A}^1\text{B}^5\text{C}^6$. The compound Ag_3SbS_3 (pyrargyrite) is of particular interest. Due its high electrooptical effect, significant double-beam refraction and transparency in the wave length 0.6-14 μm , this material is very important for many technical applications. However, the electrical characteristics of the compound and structures based on this material have been poorly studied so far. The article reports first results of electric studies of barrier structure metal-semiconductor based on $\text{p-Ag}_3\text{SbS}_3$ compound.

2. Ag_3SbS_3 MONOCRYSTALS STRUCTURE

This compound belongs to the crystallographic group $\text{R}\bar{3}\text{C}$ (C_{3v}^6); $Z=6$; $a = 11.04 \text{ \AA}$, $c = 8.72 \text{ \AA}$. The rhombohedron cell forms the structure basis: $a = 7.01 \text{ \AA}$, $\alpha = 104^\circ 04'$ with trigonal pyramids SbS_3 at the apex and in the centre of the rhombohedron¹. Fig. 1 plots the scheme of pyrargyrite elemental cell. One of the peculiarities of the crystallographic structure is the availability of infinite spiral-like chains $\dots\text{S} - \text{Ag} - \text{S} \dots$ formed along Z axis.

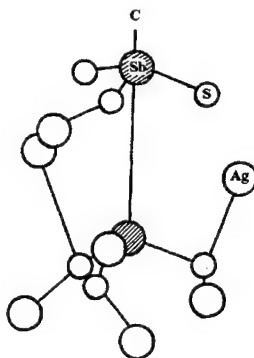


Fig.1. Crystallographic elemental cell of Ag_3SbS_3 .

Further author information –
G.K.(correspondence): Email: gal@dr.lv.ukrtel.net

3. RESULTS of ELECTRICAL STUDIES

Electrical measurements (current-voltage and capacitance-voltage) were carried out on the monocrystalline samples of the structure In/p-Ag₃SbS₃ ($E_g=2.05$ eV at 300 K, $\rho \approx 10^5$ - $10^6 \Omega \cdot \text{cm}$) of electric area $A_d = 2$ - 5 mm^2 . All the studies described below were performed at the room temperature; the investigated samples had not been underwent an additional treatment, In-contacts were prepared by fusion under normal atmospheric conditions.

Figure 2 presents the main results of electric studies.

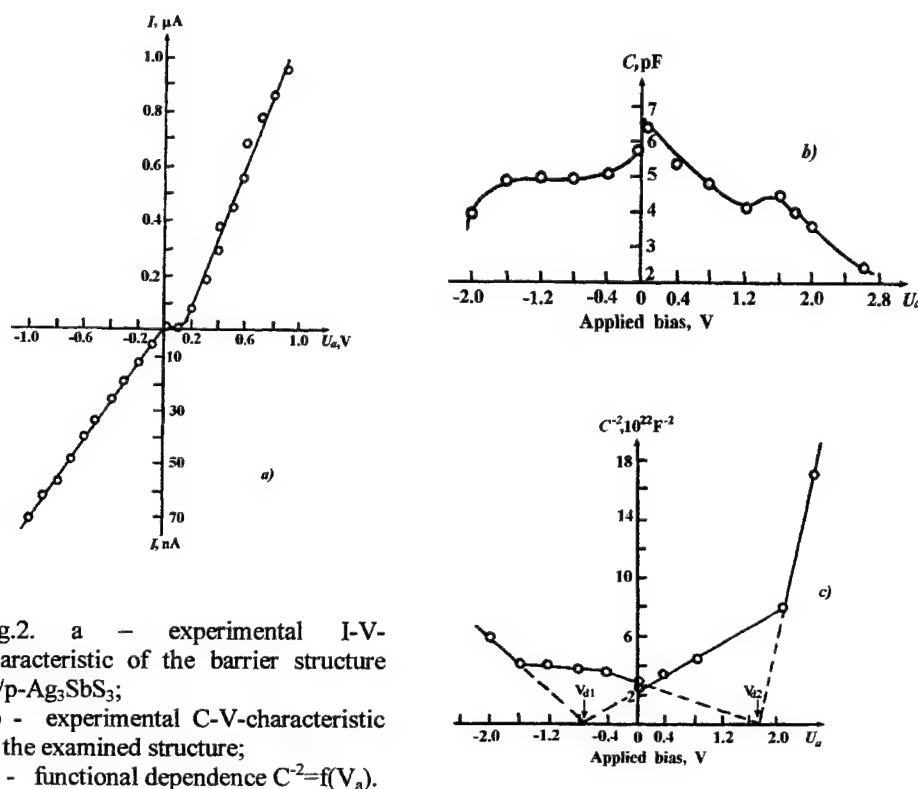


Fig.2. a - experimental I-V-characteristic of the barrier structure In/p-Ag₃SbS₃;
b - experimental C-V-characteristic of the examined structure;
c - functional dependence $C^{-2}=f(V_a)$.

Current-voltage (I-V) characteristics were measured under applied bias $V_a = 0 \div 1$ V (Fig.2, a). As one can see, the experimental functional dependence $I(V_a)$ is seemed to be typical for the diode structures: the exponential section ($0 \div 1 \mu\text{A}$) is qualitatively described by the expression:

$$I = f(m.p., V_a) \exp(eW/nkT), \quad (1)$$

where $f(m.p., V_a)$ is a complete function depending on the parameters of Ag₃SbS₃ monocrystals and applied voltage, W is an energy parameter (see below), n is a non-ideality factor of I-V forward section; the sublinear section ($0 \div 70 \text{ nA}$) is observed under the opposite direction of applied voltage.

The capacitance-voltage (C-V) dependencies studied under the testing signal frequency $f = 1 \text{ kHz}$ are plotted in Fig. 2, b. It is obvious that the C-V-characteristic of In/p-Ag₃SbS₃ structure is similar to one of the double-saturation barrier structures with graded distribution of impurities in the base. The function $C^{-2} = f(V_a)$ (Fig. 2, c) is linear and demonstrates two barriers 0.8 eV and 1.6 eV in "forward" direction and 0.86 eV and 1.62 eV under reverse bias (the total applied voltage was about 2 V which is closed to the bandgap of Ag₃SbS₃).

More detailed analysis of current-voltage characteristics has showed the availability of complete mechanism of charge carriers transfer.

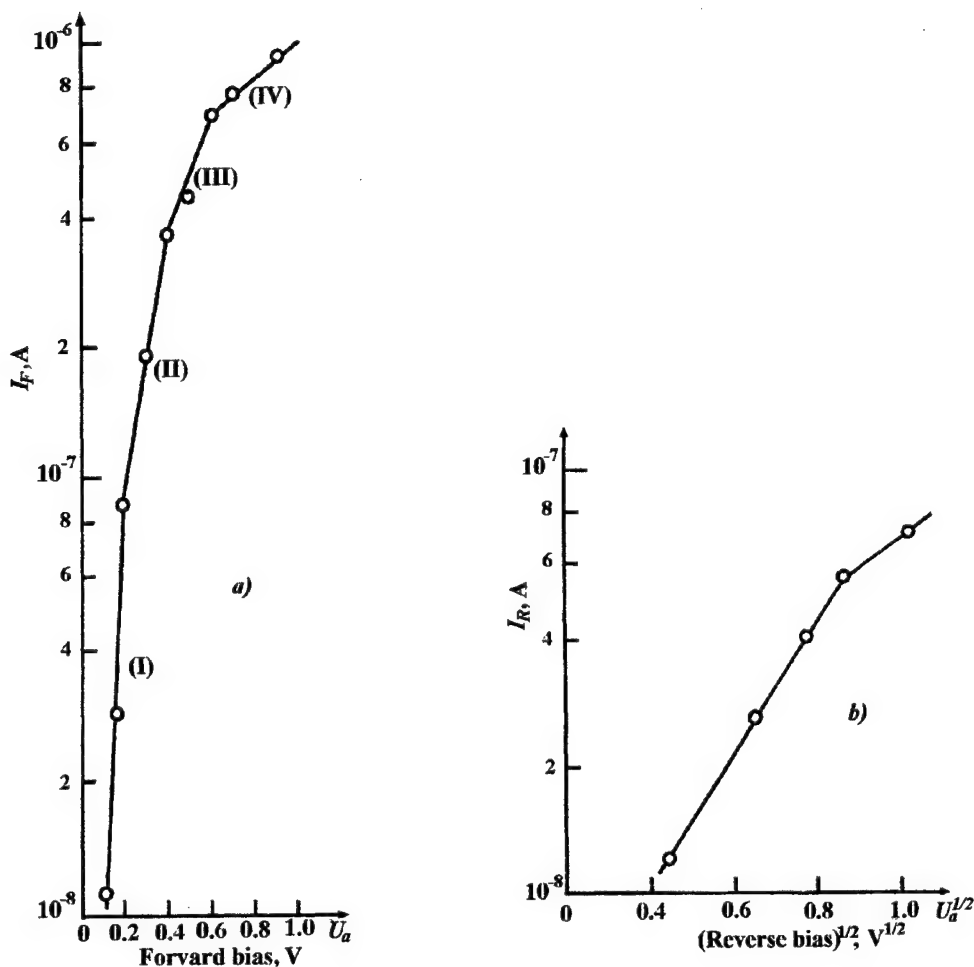


Fig. 3. Semi- (plot a) and double- (plot b) logarithmic graphs built according to the experimental data.

In particular, the exponential section of the I-V-characteristic (Fig. 3, a) shows tunneling current dominated under applied bias up to 0.6 V (sections I and II, $n = 19.1$ and 6.3 , respectively); as the applied voltage increases up to 0.8 V, charge carriers tunneling changes by tunneling-recombination processes (section III, $n \approx 2.75$) and at V_a close to 1 V diffusion process starts to dominate (section IV, $n \approx 0.8$).

Fig. 3, b plots the reverse section of the I-V-characteristic in coordinates $I = f(V_a^{1/2})$ and also shows that tunneling processes are dominant in current transfer at the whole range of applied voltage. The flex point at $V_{TR,rev} = 0.84$ V (the so-called threshold voltage under the reverse bias) points out the mild break-down indicated an sufficient increase of charge carriers immediately taking part in current transfer.

4. NUMERICAL SIMULATION OF EXPERIMENTAL CURRENT-VOLTAGE CHARACTERISTICS

Numerical modeling of the experimental results is an effective tool of nondestructive monitoring of the studied material properties. In our case such an analysis is performed according to the method described in²⁻³.

Experimental current-voltage characteristics point out the space-charge limited (SCL) current prevalent in the carriers transport in the examined structure. Two modes of the charge carriers transfer are observed experimentally:

$$I = \frac{2\epsilon_0\epsilon v_{sat}A}{L^2} V_a, \quad (2)$$

under the applied bias > 0.7 V, in the range of applied voltage from 0 to 0.6 V the expression described the current is given below:

$$I = \frac{9\epsilon_0\epsilon A\mu V_a^2}{8L^3}, \quad (3)$$

and the reverse section of the experimental I-V-characteristic is presented by the equation of ballistic mode of majority charge carriers transport:

$$I = \frac{4\epsilon_0\epsilon A}{9L^2} \left(\frac{2e}{m_h^*} \right)^{1/2} V_a^{3/2}, \quad (4)$$

where A , L , V_a , v_{sat} , μ are the sample area, its length, applied bias, saturation velocity (expression (4) produced by the solution of eqs (1) and (3)) and the charge carriers mobility, respectively.

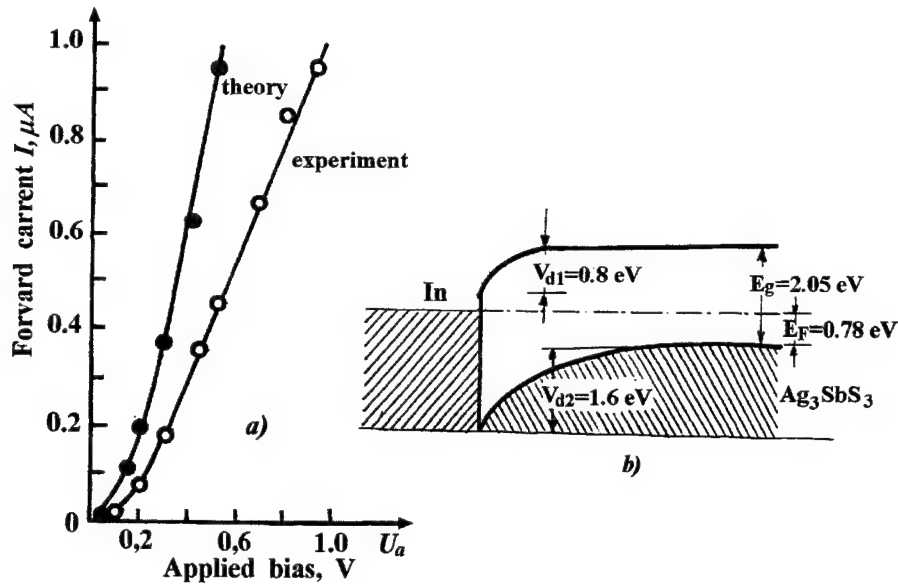


Fig. 4. a – numerically simulated and experimental forward current-voltage characteristics of the barrier structure In/p-Ag₃SbS₃; b- static energy band diagram. T=290 K.

$$V_{sat} = \sqrt{\frac{8eV_{TR}}{81m_h^*}}. \quad (5)$$

Numerical simulation was carried out for the forward I-V-dependence because the peculiarities of the crystallographic structure of Ag_3SbS_3 indicates on considerable effect of intrinsic intercrystalline barriers. The reverse current-voltage dependence is influenced not only by the processes described above, but also by silver oxide formed on the pyrrargyrite monocrystal surface revealed by Ag_3SbS_3 Auger-profiling of elemental composition⁴.

The modeled forward current-voltage characteristic (5) considering the majority charge carriers tunneling in the monocrystal bulk is shown in Fig. 4, a. Here d is a distance between ajointed chains ...-S -Ag - S... in Ag_3SbS_3 monocrystal, m_h^* is holes effective mass, V_d is diffusion potential determined by the capacitance-voltage measurements.

$$I_{ther} = \left(\frac{2\epsilon_0\epsilon V_{sat}A}{l^2} V_a + \frac{9\epsilon_0\epsilon A\mu}{8L^3} V_a^2 \right) \exp\left(\frac{-4d(2m_h^*)^{1/2}}{3\hbar} \right) \exp\left(\frac{-E_g}{kT} \right) \exp\left(\frac{V_a - V_d}{nkT} \right) \quad (6)$$

A good agreement is observed in the range of voltage 0 – 150 mV and a quantity coincidence is shown as the applied voltage increases. The discrepancy of simulated and experimental results can be explained by the additional influence of leakage current and the minority charge carriers tunneling in the subcontact region and surface oxide layer.

5. CONCLUSIONS

Electric investigations of metal-semiconductor structure based on monocrystal p- Ag_3SbS_3 carried out at the room temperature were shown barrier characteristics typical for the double saturation diode-like structures. The space-charge limited (SCL) current is observed in the whole range of applied voltage. The results obtained experimentally indicate that the electrical behavior of the examined structure is influenced by the peculiarities of the crystallographic structure of Ag_3SbS_3 monocrystals as well as by the AgO layer formed on Ag_3SbS_3 surface.

REFERENCES

1. P. Engel and W. Nowacki, "Die Verfeinerung der Kristallstruktur von Proustite (Ag_3AsS_3) and Pyrrargyrite (Ag_3SbS_3)", *Neues Jahrb. Mineralogie*, No.6, pp.191-195, 1966.
2. E. Hernandez, "Space-Charged-Limited Current Effects in p-Type $CuIn_{0.8}Ga_{0.2}Se_2/In$ Schottky Barriers", *Cryst. Res. Technol.*, 33, pp.285-289, 1998.
3. N. G. Kwok, "Complete Guide to Semiconductor Devices", pp. 564-565, McGraw Hill, New York, 1995.
4. V. Belosertseva, V. Basakutsa and L. Panchenko, "Structure and Crystallization of Ag_3SbS_3 layers obtained by Pulse Laser Evaporation", *Cryst. Res. Technol.*, 34, pp. 677-682, 1999.

Charge traps and emission kinetics in LuAP:Ce

J. Glodo* and A. J. Wojtowicz

Institute of Physics, N. Copernicus University, Grudziądzka 5/7, PL 87-100 Toruń, Poland

ABSTRACT

In this contribution we demonstrate the influence of shallow charge traps on emission kinetics of $\text{LuAlO}_3:\text{Ce}^{3+}$ (LuAP:Ce) scintillator. Shallow traps through their interference with the recombination process not only introduce into the emission time profiles long components (afterglow) but also can change the rising and decaying parts of time profiles. The lifetime of excited Ce^{3+} ion in LuAP crystal is ~ 18 ns, while the excitation at 78 nm leads to the emission described by 21.5 and 1.22 ns decay and rise time constants, respectively. Furthermore, temperature dependence of time profile shapes is observed. The analysis of emission kinetics measured against temperature shows that observed features can be explained in terms of a trap described by the following parameters: $E = 0.142$ eV and $s = 6.087 \times 10^{10} \text{ s}^{-1}$.

Keywords: recombination, traps, emission kinetics, scintillators, phosphors, LuAP:Ce

1. INTRODUCTION

In recent studies of a number of scintillating materials it has been shown that scintillation parameters such as efficiency and speed can strongly depend on shallow charge traps^{1,2,4}. The simple kinetic model based on existence of a number of electron traps and one recombination center (Ce^{3+}) allows for an easy explanation of temperature dependence of these parameters¹ and differences in scintillation properties between very similar materials ($\text{YAlO}_3:\text{Ce}$ and $\text{LuAlO}_3:\text{Ce}$)².

In this contribution we will focus on the effects of shallow charge traps on emission kinetics of LuAP:Ce. We will show that temperature dependence of measured time profiles can be explained by a shallow trap interfering with the recombination process.

2. CRYSTALS AND EXPERIMENT

The investigated samples of LuAP:Ce were grown by means of the Czochralski technique by Litton Airtron. Although the Ce content in the melt varied from 0.25 to 2.00 wt%, in the material it is approximately 10 times smaller.

The measurements of time profiles were performed at the SUPERLUMI station of HASYLAB³. The sample was excited with the pulsed synchrotron radiation of the 236 nm and 78 nm wavelengths. The resulting Ce^{3+} emission was analyzed at the 360 nm wavelength. The instrumental time response of the set-up is below 1 ns.

3. THEORY

Recently it has been shown that the recombination process of free charge carriers created by high energy excitation can take two different routes^{1,2}. The first route is the direct one, when the carriers recombine at the Ce^{3+} ion 'immediately' (in time shorter than the time resolution of the set-up, < 1 ns). In this case the time evolution of Ce^{3+} emission does not differ from that of directly excited Ce^{3+} ion. Thus the time profile of emission ideally follows a single exponential decay with the time constant equal to radiative lifetime of excited Ce^{3+} ion - τ_{Ce} (usually due to set-up, there also is detectable rise of a signal described by a time constant τ_n). The second route, so called delayed one, as it has been shown, involves charge traps. In that case, although the emission originates from Ce^{3+} ions as well, its time evolution follows a different pattern and depends on the mean lifetime of the involved traps (τ_{trap}). In the simplest case of one trap the time profile can be described by the following formula:

* JG: E-mail: jglodo@phys.uni.torun.pl; AJW: E-mail: andywojt@phys.uni.torun.pl; Fax: 48-56-6225397;

$$I(t) = I_0 \left\{ \frac{a}{\tau_{Ce} - \tau_n} \left[\exp\left(-\frac{t}{\tau_{Ce}}\right) - \exp\left(-\frac{t}{\tau_n}\right) \right] + \right. \quad (1a)$$

$$\left. \frac{b}{\tau_{Ce} - \tau_{trap}} \left[\exp\left(-\frac{t}{\tau_{Ce}}\right) - \exp\left(-\frac{t}{\tau_{trap}}\right) \right] \right\}, \quad (1b)$$

where τ_n is rise time of direct component ($\tau_n \ll \tau_{Ce}$), I_0 the total measured light, a and b branching coefficients. The first term (1a) corresponds to the direct component, whereas the second term (1b) describes the delayed component. The ratio of these two sorts of components is specified by the branching coefficients a (direct) and b (delayed).

It is important to note that in equation 1b the rise time will be equal to the shorter of the two time constants (τ_{trap} , τ_{Ce}) while the decay time to the longer one. Since the τ_{trap} varies with temperature therefore it is the key parameter in equation (1). Moreover τ_{trap} is a function of trap parameters (the activation energy E and frequency factor s):

$$\tau_{trap} = \left[s \exp\left(-\frac{E}{kT}\right) \right]^{-1}, \quad (2)$$

where k is the Boltzmann constant. This relation shows that by changing the temperature of the sample and studying the consequent variations of the time profile shapes (characterized in terms of decay and rise constants) it is possible to estimate the values of E and s . It can be easily seen if the equation (2) is rewritten in the following form:

$$\ln(\tau_{trap}) = \frac{E}{k} \frac{1}{T} - \ln(s), \quad (3)$$

that is equivalent to the linear equation of $y = \alpha x + \beta$. Using the equation (3) we can plot $\ln(\tau_{trap})$ vs. T^{-1} and easily solve for the energy depth E and frequency factor s .

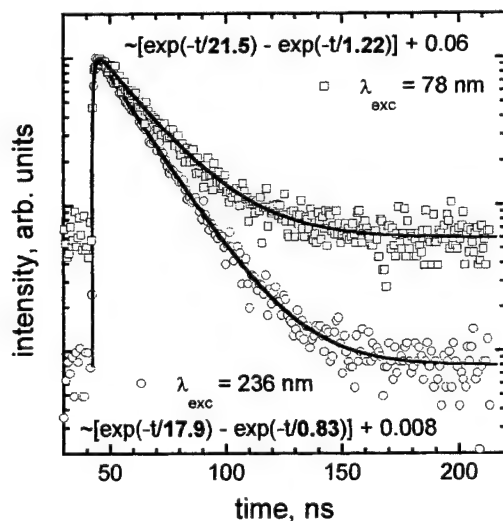


Fig. 1. Time profiles of LuAP:Ce 360 nm emission at 298 K. The experimental points measured under 78 and 236 nm excitation wavelength are shown by squares and dots, respectively. Note the differences in the backgrounds and time constants of two profiles. The solid lines represent fits to the points.

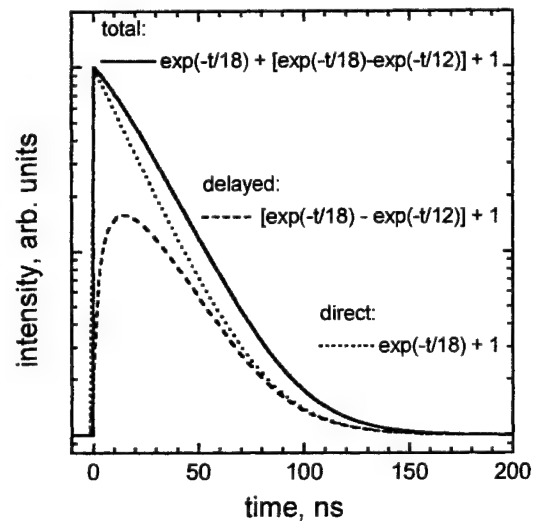


Fig. 2. Theoretical time profile calculated from the one-trap model. The dotted and dashed lines represent respectively the direct and delayed components. The solid line shows the sum of total. The delayed component modifies the profile as observed in experiment, see Fig. 1.

4. RESULTS AND DISCUSSION

In figure 1 we show two time profiles (TP) measured under 236 nm (dots) and 78 nm (squares) excitation at 298 K. The 236 nm light excites the Ce^{3+} ions directly (4f-5d transition) whereas the 78 nm light first more likely creates free charge carriers that excite the Ce^{3+} ions in the process of recombination (78 nm ~ 15.9 eV $>$ 8 eV the band gap of LuAP). As we can see in the figure the difference in the excitation results in different time profile shapes. The most visible change is in the background level which in the case of the 78 nm TP is much higher (~ 10 times). This can be easily explained by the presence in 78 nm TP of at least one component that decays with the long time constant (much longer than the time scale of the measurement, ~ 200 ns). Such components are usually related to deeper traps (afterglow).

But more peculiar difference is that the decay time constants derived from fits are not the same. (A function used to fit both TPs had the following form: $\sim [\exp(-t/\tau_D) - \exp(-t/\tau_R)]$, where τ_D and τ_R denote the decay and rise time constants respectively.) Emission measured under the 236 nm excitation decays at 17.9 ns time constant, while under the 78 nm excitation at 21.5 ns. There also is a difference in rise time constants, 0.83 ns and 1.22 ns respectively, although in the case of emission under 236 nm excitation this constant has no physical meaning as it is introduced by the experimental set-up. Similar decay and rise time constants have been reported by Dujardin *et al.*⁵

Since the observed emission comes from the same Ce^{3+} ions the difference of almost 20% in the τ_D value is at first hard to understand. Similar discrepancies have already been observed and explained in YAP:Ce^1 or $\text{BaF}_2\text{:Ce}^4$. The authors showed that such a lengthening of decay time constant in case of high energy excitation (γ) is due to shallow traps and takes place when the mean lifetime of carriers in traps is on the order of radiative lifetime of an activator (at a given range of temperatures). Such an effect can be easily seen in figure 2 where curves calculated according to equation (1) are plotted. The dotted line represents the direct component (equation (1a), $\tau_{\text{Ce}} = 18$ ns, $\tau_n = 0.7$ ns, $a = 75\%$), the dashed line the delayed component (equation (1b), $\tau_{\text{trap}} = 12$ ns, $b = 25\%$) and the solid line the total. Presence of the delayed component modifies the shape of the total curve in a way that in the first approximation it reminds a single exponential

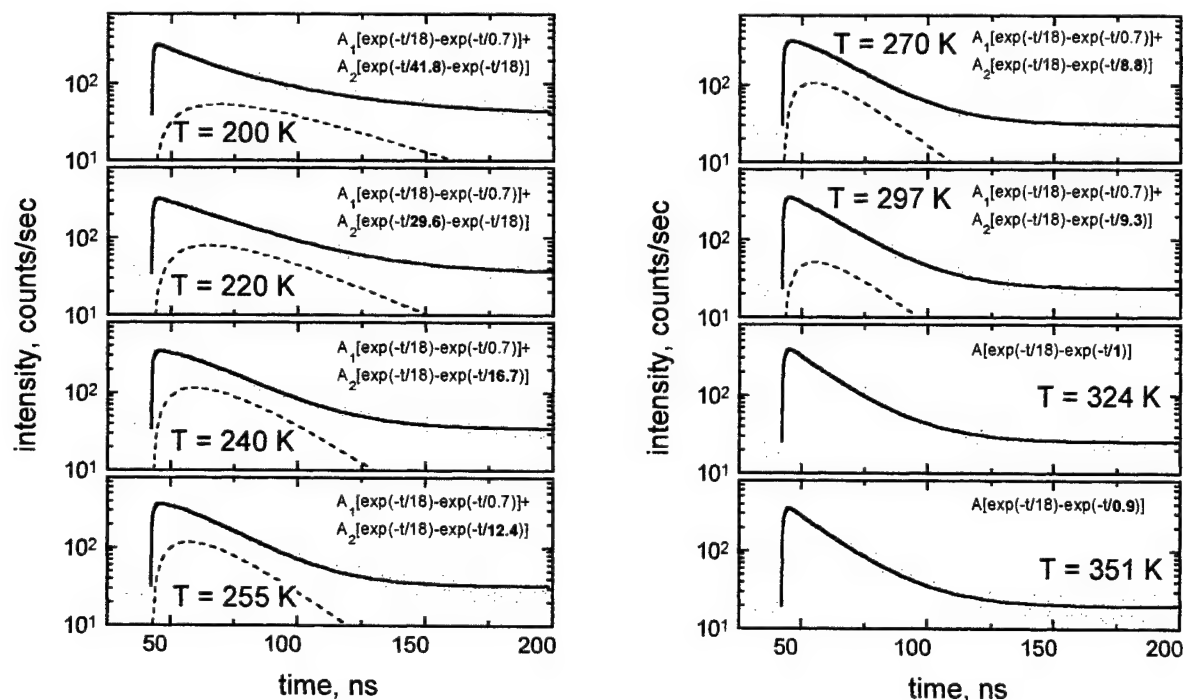


Fig. 3. Selected time profiles of LuAP:Ce 360 nm emission under the 78 nm excitation wavelength at different temperatures. Points are experimental data. The solid lines are fits calculated from equation (1) or in the case of 324 - 351 K traces equation (1b). The dashed lines represent the delayed component, see equation (1b). Note the changes in the delayed component with temperature.

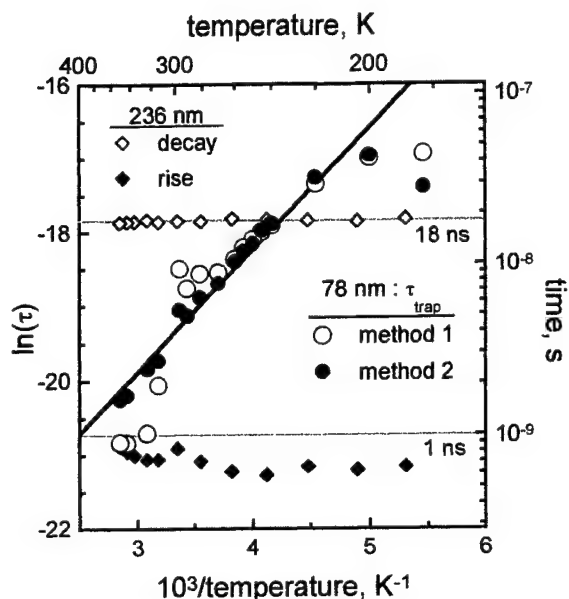


Fig. 4. Arrhenius type plot of decay and rise time constants derived from fits to the measured time profiles under 236 nm (diamonds) and 78 nm (dots) excitation. The solid line was calculated to parameters obtained from a fit (equation (3)) to the points (black dots). Acquired trap parameters are: $E = 0.142$ eV and $s = 6.087 \times 10^{10} \text{ s}^{-1}$.

obtained τ_{trap} values are put on an Arrhenius type plot, figure 4, it is easy to see that most of the points (open dots) lie along a line or at higher temperatures oscillate around this line. The alignment of these points can be improved if we

decay. The time constant of such a decay is not equal to τ_{Ce} but is rather a function of both: τ_{Ce} and τ_{trap} , and in this case has the value of ~ 21 ns.

If the observed lengthening is indeed caused by a shallow trap the shape of the measured TPs should change with temperature as τ_{trap} does, see equation (2). In fact, conducted experiments show that TP shapes are temperature dependent. Examples of obtained traces are shown in figure 3 (points). Lines represent curves calculated with parameters extracted from fits to experimental points. In case of most traces a fitting function in the form of equation (1) was used (the sum of two components: direct and delayed). Additionally, as we assumed that the direct component is analogous to the emission of directly excited Ce^{3+} ion (at 236 nm) the time constants τ_{Ce} and τ_n were held fixed at 18 and 0.8 ns, respectively. Thus the only free fit parameters were: τ_{trap} , amplitudes I_0 , a and b , and the background level. Only for the last three traces (324, 344, 353 K), as the τ_{trap} approached the value of τ_n and both components could be easily described as one, the fitting function in the form of equation (1b) was used. Obtained fit results are summarized in table 1 (method 1) and a plot of temperature changes of τ_{trap} is shown in figure 4 (open dots).

The fit results show that at lower temperatures τ_{trap} is relatively long (> 18 ns) and describes the decaying part of the delayed component (in figure 3 shown by dashed lines). As the temperature rises the τ_{trap} shortens and at 240 K the situation changes; τ_{trap} becomes shorter than 18 ns and from now on describes the rising part of the delayed component. If the

Table 1. Parameters derived from fits to emission time profiles of LuAP:Ce measured under 78 nm excitation. A fitting function was in the form of equation (1). Method 1: the τ_{Ce} and τ_n time constants were held fixed at 18 and 0.7 ns, respectively. Method 2: additionally the product $I_0 \times a$ was assumed constant. Negative values of b parameter indicate that τ_{trap} describes decaying part of the time profile instead of rising one, as it appears in equation (1). Note that τ_{trap} shortens with the rise of temperature.

method 1								method 2							
T	bg	a	b	τ_{trap}	bg	b	τ_{trap}	T	bg	a	b	τ_{trap}	bg	b	τ_{trap}
K	-	%	%	<i>ns</i>	-	%	<i>ns</i>	K	-	%	%	<i>ns</i>	-	%	<i>ns</i>
183	50	66	-34	43.9	55.7	-34	28.2	270	30.6	61	39	8.8	31.3	43	7.6
200	39.5	57	-43	41.8	38.7	-44	43.2	282	28.4	66	34	8.7	29.7	40	6.3
220	35.0	53	-47	29.6	33.3	-49	32.2	291	27.0	71	29	7.1	28.0	36	4.9
240	34.3	50	50	16.7	34.0	48	17.1	297	23.6	77	23	9.3	24.9	30	5.3
245	33.7	51	49	15.4	33.5	48	15.7	314	26.0	58	42	1.94	25.7	30	2.7
250	33.9	54	46	13.8	34.5	47	13.1	324	25.1	0	100	1.02	24.5	28	2.4
255	32.1	54	46	12.4	32.5	47	11.8	344	21.4	0	100	0.89	21.3	23	1.7
260	32.1	55	45	10.6	32.4	45	10.2	351	19.5	0	100	0.90	19.4	20	1.6

assume while fitting the measured traces that the intensity of direct component does not change with temperature (i.e. $I_0 \times a$ product constant). Time constants (table 1, method 2) acquired from such fits are shown in figure 4 by black dots.

Because the τ_{trap} values depend not only on temperature but also on the trap parameters E and s , it is possible to estimate these parameters from a fit to the points (black dots) shown in figure 4, see equation (3). In a result of such a fit (in figure 4 solid line) the following values were obtained: $E = 0.142$ eV and $s = 6.087 \times 10^{10} \text{ s}^{-1}$.

The expected maximum of a glow curve calculated to obtained parameters is located at 60 K. Although the experimental glow curve⁶ measured in this range of temperatures does not exhibit any strong signal (the main glow peak is at 180 K) there are relatively small peaks at around 55 and 90 K. Moreover, a trap of similar depth ($E = 0.205$ eV) has already been deduced from the analysis of scintillation light yield².

5. CONCLUSIONS

The experimental results and interpretation presented in this contribution indicate that apparent deviation of the decay time constant of Ce^{3+} emission in LuAP:Ce under the 78 nm excitation from the radiative lifetime of Ce^{3+} ion is artificial and can be explained by a shallow trap interfering with the recombination process. The analysis of time profiles measured against the temperature shows that trap responsible for the observed features has the following parameters: $E = 0.142$ eV and $s = 6.087 \times 10^{10} \text{ s}^{-1}$.

ACKNOWLEDGMENTS

This work was supported by the Polish Committee of Scientific Research, KBN (grant No 2P03B04914), by the TMR-Contract ERBFMGECT950059 of the European Community, by the U.S. Department of Energy (grant No DE-FG-02-90-ER61033). We are also very grateful to Prof. G. Zimmerer and Dr. M. Kirm of HASYLAB, Hamburg, Germany, for their hospitality and help in VUV experiments at SUPERLUMI station.

REFERENCES

1. A. J. Wojtowicz, J. Glodo, A. Lempicki and C. Brecher, "Recombination and Scintillation processes in $\text{YAlO}_3\text{:Ce}$ ", *J. Phys.: Condens. Matter* **10**, pp. 8401-8415, 1998.
2. A. J. Wojtowicz, J. Glodo, W. Drozdowski, K. R. Przegietka, "Electron traps and scintillation mechanism in $\text{YAlO}_3\text{:Ce}$ and $\text{LuAlO}_3\text{:Ce}$ scintillators", *J. Lumin.* **79**, pp. 275-291, 1998.
3. G. Zimmerer, "Status report on luminescence investigations with synchrotron radiation at HASYLAB", *Nucl. Instr. Meth. Phys. Res. A* **308**, pp. 178-186, 1991.
4. J. Glodo, P. Szupryczynski and A.J. Wojtowicz, "Thermoluminescence and scintillation time profiles of $\text{BaF}_2\text{:Ce}$ ", *Acta Physica Polonica A* **95**, pp. 259-268, 1999.
5. C. Dujardin, C. Pedrini, J. C. Gacon, A. G. Petrosyan, A. N. Belsky and A. N. Vasil'ev, "Luminescence properties and scintillation mechanisms of cerium- and praseodymium-doped lutetium orthoaluminate", *J. Phys.: Condens. Matter* **9**, pp. 5229-5243, 1997.
6. A. Lempicki, J. Glodo, "Ce doped scintillators: LSO and LuAP", *Nucl. Instr. Meth. A* **416**, pp. 333-344, 1998.

Energy transfer processes in (Lu,Gd)AlO₃:Ce

Andrzej J. Wojtowicz ^{a*} and Jiri A. Mareš ^b

^a Institute of Physics, N. Copernicus University, Grudziądzka 5, 87-100 Toruń, Poland

^b Institute of Physics, Academy of Sciences of the Czech Republic, Cukrovarnická 10,
16253 Prague 6, Czech Republic

ABSTRACT

In this paper we present initial results of studies on energy transfer processes in Ce-activated Lu, Y and Gd aluminum perovskite crystals that contribute to production of scintillation light in these new scintillator materials. In particular we report and analyze emission spectra, excitation spectra, and emission time profiles under pulsed synchrotron excitation in the wavelength range of 50-300 nm.

The emission spectra of Lu_{0.65}Gd_{0.35}AlO₃:Ce and Lu_{0.2}Y_{0.8}AlO₃:Ce display a characteristic double band that is due to the spin-orbit split *d-f* transition of Ce³⁺ with no indication of Gd³⁺ *f-f* emissions in the Gd-containing crystal. Nevertheless the "time-gated" and "integrated" excitation spectra of Ce-emission of this crystal in addition to the *f-d* Ce³⁺ bands reveal some additional fine features, absent in the Y-containing crystal, that are evidently related to the *f-f* transitions at Gd³⁺ ions. We also observe that the Ce-emission time profile measured under direct Ce-excitation displays fast decaying component while the Gd-tuned excitation produces slow profiles that resemble those observed under gamma or X-ray excitation.

These results directly prove that slow scintillation components characteristic of the Lu_xGd_{1-x}AlO₃:Ce scintillator are due to transfer of energy that was originally deposited by the ionizing radiation in the Gd-sublattice of the crystal.

Keywords: YAlO₃, LuAlO₃, GdAlO₃, cerium, scintillators, VUV spectroscopy, luminescence, time profiles, energy transfer

1. INTRODUCTION

The yttrium aluminum perovskite activated by Ce (YAlO₃:Ce, abbr. YAP:Ce) is a well established commercial scintillator material that has found a number of important applications.^{1,2} Its heavier lutetium isostructural analog, LuAlO₃:Ce (abbr. LuAP:Ce), is a promising new addition to scintillator materials considered for modern applications involving detection of ionizing radiation such as high energy and nuclear physics and nuclear medicine (positron-emission-tomography, PET).³ The Czochralski-grown monocrystals of LuAP:Ce were first evaluated in a garnet-free perovskite phase by Lempicki et al. in 1994.⁴ More detailed studies revealed that the dominant mechanism of energy transfer from the host to the Ce³⁺ ions in both Y and Lu-perovskites involves consecutive capture of electrons and holes at Ce³⁺ sites followed by recombination and Ce-emission (scintillation).^{5,6} It has also been established that traps strongly influence the basic scintillation characteristics of these materials such as scintillation light yield and scintillation time profiles (rise and decay times).⁷

Although LuAP:Ce is a reasonably efficient and fast scintillator (scintillation light yield ~11,300 photons/MeV, scintillation decay time ~17 ns)⁸ it is very expensive and notoriously difficult to grow. Initial studies seem to suggest that some addition of Y or Gd helps to stabilize the perovskite phase with only a moderate loss in scintillation light yield and speed⁹ but scintillation mechanisms (in particular host-to-ion energy transfer processes) in such materials have not been investigated. Therefore, as a part of a larger effort in Europe in the framework of the Crystal Clear Collaboration sponsored by CERN and aimed at perovskite scintillator materials,^{3,9,10,11} we have conducted vacuum ultraviolet (VUV) studies of mixed Lu, Y and Gd aluminum perovskite crystals at Superlumi station of Hasylab, Hamburg, Germany. In this paper we report our recent results in this area.

* Further author information:

AJW (correspondence): Email: andywojt@phys.uni.torun.pl, Telephone: +48 56 6113239, fax: +48 56 6225397

JAM: Email: amares@fzu.cz, Telephone: +420 2 24311137, Fax: +420 2 3123184

2. CRYSTALS AND EXPERIMENTAL SET-UPS

The reference $\text{LuAlO}_3\text{:Ce}$ sample was cut from the boule provided by M. Randles (Synoptics Div., Litton Airtron Corp., Charlotte, NC). The crystals were pulled from the melt (Czochralski method) on iridium wire in an atmosphere of N_2 . The Ce-concentration in the melt was 0.25 mole% but the actual concentration found by mass spectroscopy analysis was only 200 ppmw.

The mixed $\text{Lu}_x\text{Y}_{1-x}\text{AlO}_3\text{:Ce}$ and $\text{Lu}_x\text{Gd}_{1-x}\text{AlO}_3\text{:Ce}$ crystals were grown by Crytur Ltd (Palackého 175, 51119 Turnov, Czech Republic) by Czochralski method. The Ce-concentration in these crystals was much higher than in the reference LuAP sample at 0.1 to 0.3 at.%. More details about these crystals and their basic properties was given by Chval et al.⁹

The VUV experiments presented in this paper include measurements of luminescence spectra, excitation spectra and emission time profiles obtained under pulsed VUV excitation from the synchrotron radiation have been conducted at Superlumi station of Hasylab, Hamburg, Germany. A detailed description of Superlumi's experimental facilities given by Zimmerer¹² is also available on-line.¹³

3. EXPERIMENTAL RESULTS

In Fig. 1 we show uncorrected emission (resolution 3 nm) and excitation (resolution 1.6 nm) spectra of two samples of mixed crystals, $\text{Lu}_{0.65}\text{Gd}_{0.35}\text{AP:Ce}$ and $\text{Lu}_{0.2}\text{Y}_{0.8}\text{AP:Ce}$. For comparison we have also included the spectrum measured for the reference sample (LuAP:Ce). Since the emission spectra of these three samples are nearly the same only the (Lu,Gd)AP spectrum is shown in the figure. Note that unlike the LuAP spectrum the spectra of mixed crystals show strong saturation distortions typical of highly doped samples. Nevertheless some variations observed in these spectra at the VUV wavelength range may be indicative of different host-to-ion energy transfer processes.

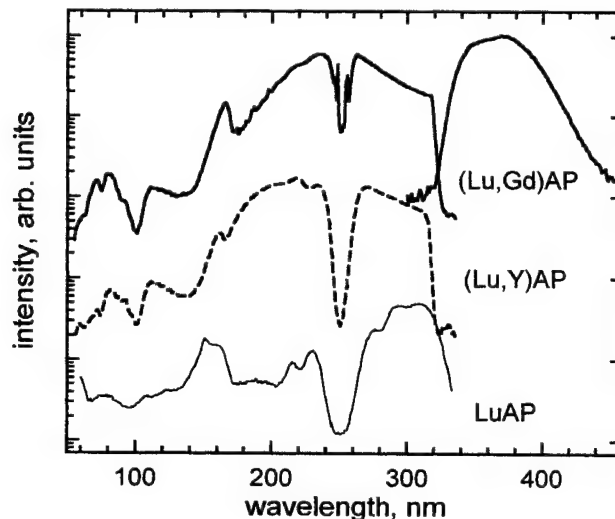


Fig. 1. Uncorrected emission and excitation spectra of Ce-doped Lu/Gd, Lu/Y and Lu aluminum perovskite crystals at 8 K. The emission spectrum was measured with the excitation wavelength set at 255 nm. The excitation spectra were measured with the emission wavelength set at 370 nm. Note the sharp features at about 250 nm in the (Lu,Gd)AP spectrum. The room temperature spectrum (not shown) displays almost no sharp line features because of thermal broadening.

The peaks in the vicinity of the bandgap energy (at 150 to 160 nm) have been previously associated with energy transfer mechanisms that enable the material to scintillate efficiently.¹⁴ Although the structure in the VUV part of the spectra does not reflect any true physical processes of energy transfer (the spectra were not corrected) the short wavelength pulsed excitations below 100 nm have been demonstrated to produce luminescence time profiles modified by trap mediated recombination of charge carriers via the Ce^{3+} ions.^{15,16} In this paper, however, we will concentrate on different processes

that are responsible for some fine features clearly visible in the excitation spectrum of (Lu,Gd)AP:Ce (e.g. at about 250 nm, see Fig. 1) but are conspicuously absent in LuAP:Ce and (Lu,Y)AP:Ce.

In Fig. 2 we present two excitation spectra of the Ce^{3+} emission in (Lu,Gd)AP:Ce (thick and thin solid lines) designated “(Lu,Gd)AP integrated” and “(Lu,Gd)AP:Ce time gated” and, for comparison, the spectrum of (Lu,Y)AP:Ce (thin dashed line). The “integrated” spectrum was measured with the emission signal accumulated during the time between the consecutive synchrotron pulses (192 ns) while the “time gated” spectrum was measured within a 40 ns time window triggered by a synchrotron pulse with no delay.

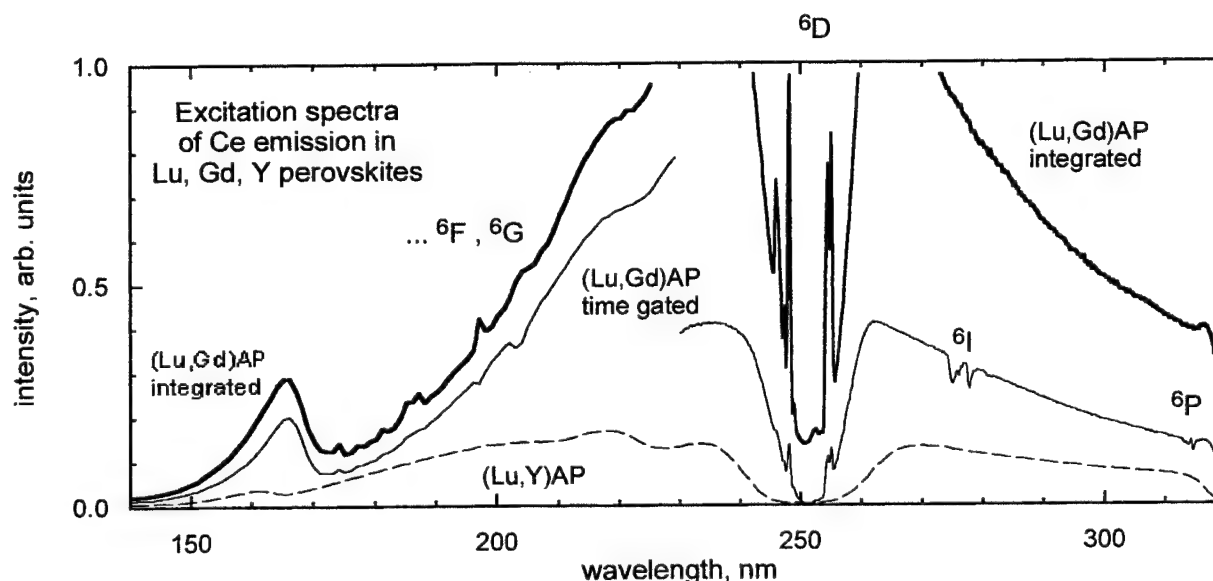


Fig. 2. Uncorrected excitation spectra of the Ce-doped Lu, Gd and Y aluminum perovskite crystals at 8 K. The emission wavelength was set at 370 nm. The spectral resolution was about 0.3 nm. Note the difference in appearance of sharp features between “time gated” and “integrated” curves. For designation of the curves see text.

The fine features observed in the spectra shown in Fig. 2 take a form of sharp lines (at about 245 and 255 nm) and/or “dents” (at 275 and 315 nm). Shorter wavelength features at about 203, 195, 185 nm take a form of lines (in the “integrated” spectrum) and/or “dents” (in the “time gated” spectrum). These lines were also observed in the absorption spectrum of (Lu,Gd):AP:Ce and GdAP:Ce crystals.^{9,10} Clearly, all these features can be associated with the Gd $f-f$ transitions starting at $^8\text{S}_{7/2}$ and terminating at various levels of the ^6P , ^6I , ^6D , ^6G , and ^6F terms of the Gd^{3+} ion.^{9,10,17,18} Note that energy levels of the lanthanide 3+ ions in VUV have only recently been measured and calculated theoretically.¹⁸ In Table 1 we summarize the energies of all the Gd-related spectral features that we were able to resolve in the excitation spectra of the Ce emission in (Lu,Gd)AP.

Table 1.
Summary of Gd^{3+} transition energies in (Lu,Gd)AP.

Terms	^6P	^6I	^6D	$^6\text{G}, ^6\text{F}...$
Observed energies (cm^{-1})	31,780 31,870	36,000 36,360	39,200 39,300 39,600 40,200 40,300 40,400 40,600	49,100 50,800 53,500 54,000 55,200 56,500

Finally in Fig. 3 we show time profiles of Ce^{3+} emission from (Lu,Gd)AP:Ce under pulsed synchrotron excitation of two different wavelengths; 255 nm (coincident with the wavelength of the sharp line in the excitation spectrum, see Fig. 2) and 260 nm. The temperature was 10 K. Note much larger contribution of slow components in the time profile obtained under the 255 nm excitation (into the Gd^{3+} line).

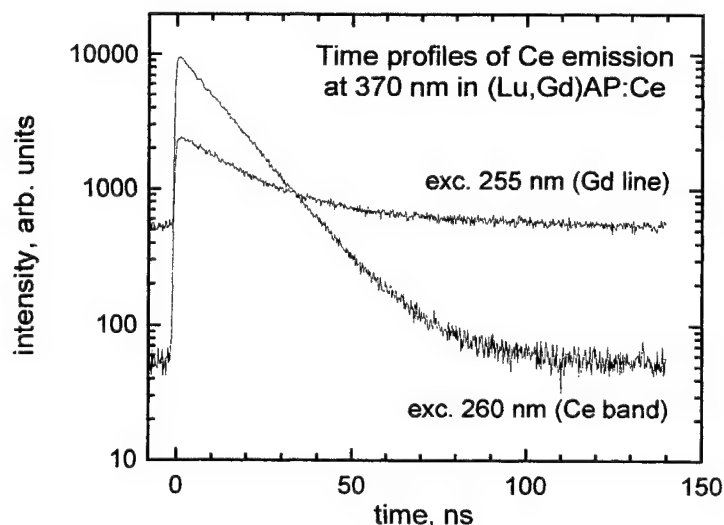


Fig. 3. Time profiles of Ce-emission in (Lu,Gd)AP:Ce under pulsed synchrotron excitations of 255 and 260 nm at 10 K. The emission wavelength was set at 370 nm.

It is interesting to note that larger contributions of slower components in the scintillation time profile (gamma excitation) in GdAP:Ce in comparison to YAP:Ce and (Lu,Y)AP:Ce have been reported earlier by Mares et al.¹¹ This suggests that direct excitation into Gd absorption lines mimicks processes that are active in the Gd-containing material excited by ionizing radiation such as gamma or x-rays.

4. DISCUSSION

The appearance of Gd-related features in the excitation spectra of Ce-emission in (Lu,Gd)AP:Ce (lines and dents) can easily be explained by assuming that energy absorbed by Gd^{3+} ions is transferred, with some delay, to Ce^{3+} ions.⁹ Note that the emission spectrum under the 255 nm (39,200 cm^{-1}) excitation into one of the well resolved Gd^{3+} peaks shows exclusively the well known poorly resolved double band characteristic of the spin-orbit split $d-f$ transition at Ce^{3+} ion (see Fig. 1). For excitation wavelengths, for which direct Ce^{3+} excitation is weak (240 to 260 nm), the Gd^{3+} ions provide additional channels by which energy (otherwise lost) is collected and transferred to Ce^{3+} ions (hence “lines”). On the contrary, for excitation wavelengths for which direct Ce^{3+} excitation is efficient (e.g. 265 to 320 nm), Gd^{3+} ions compete with Ce^{3+} ions changing the distribution of intensity between slower and faster components in the time profiles of the Ce^{3+} emission (see Fig. 3). In the short (40 ns) time window this process effectively lowers the intensity of the Ce^{3+} emission (hence “dents” in the “time gated” spectrum). Since no “dents” are observed in the “integrated” spectrum we conclude that efficiency of the Gd-Ce transfer must be very high.

5. CONCLUSION

The resonant excitation into Gd^{3+} absorption lines by synchrotron radiation in mixed (Lu,Gd)AP:Ce reveals the existence of additional channel by which the energy can be transferred to Ce^{3+} ions. Since the Gd-subsystem provides significant fraction of the stopping power of the mixed (Lu,Gd)AP crystal this channel must be important for scintillation performance of the material. Despite the prominence of the direct charge carrier capture and recombination at Ce^{3+} ions in perovskites other processes, such as the one studied in this paper, may prove important in these systems.

ACKNOWLEDGMENTS

This work was supported by the Polish Committee of Scientific Research, KBN (grant 2P03B04914), by the Swiss National Science Foundation (project 7IP 051218, growth of the mixed (Lu,Y)AP:Ce and (Lu,Gd)AP:Ce crystals by Crytur Ltd, Czech Republic) and by the TMR-Contract ERBFMGECT950059 of the European Community. We thank our colleagues from the Crystal Clear Collaboration for many fruitful discussions. We are grateful to R. Brunka, W. Drozdowski, P. Niezgoda and M. Wisniewska who took part in experiments at Superlumi station of Hasylab, Hamburg, Germany. The financial support of Hasylab and Polish Academy of Sciences and hospitality of Prof. G. Zimmerer and Dr M. Kirm of Hasylab is also gratefully acknowledged.

REFERENCES

1. M.J. Weber, "Optical spectra of Ce^{3+} and Ce^{3+} -sensitized fluorescence in YAlO_3 ", *J. Appl. Phys.*, **44**, pp. 3205-3208, 1973.
2. W.P. Trower, "Cerium-doped yttrium aluminum perovskite (YAP): properties of commercial crystals", in *Materials Research Society Symposium Proceedings: Scintillator and Phosphor Materials*, edited by M.J. Weber, P. Lecoq, R.C. Ruchti, C. Woody, W.M. Yen, R. Zhu, vol. **348**, pp. 131-136, Materials Research Society, Pittsburgh, 1994.
3. Crystal Clear Collaboration, CERN/DRDC P27/91-95, Project RD-18.
4. A. Lempicki, M.H. Randles, D. Wisniewski, M. Balcerzyk, C. Brecher, and A.J. Wojtowicz, "LuAlO₃:Ce and other aluminate scintillators", *IEEE Trans. Nucl. Sci.* **42**, pp. 280-284, 1995.
5. A.J. Wojtowicz, J. Glodo, W. Drozdowski, K. R. Przegliska, "Electron traps and scintillation mechanism in YAlO₃:Ce and LuAlO₃:Ce scintillators", *J. Lumin.* **79**, pp. 275-291, 1998.
6. A.J. Wojtowicz, J. Glodo, A. Lempicki and C. Brecher, "Recombination and scintillation processes in YAlO₃:Ce", *J. Phys.: Condens. Matter*, **10**, pp. 8401-8415, 1998.
7. A.J. Wojtowicz, "Some aspects of solid state radioluminescence", *Acta Phys. Pol. A* **95**, pp. 165-178, 1999.
8. M. Moszynski, M. Kapusta, M. Mayhugh, D. Wolski, S.O. Flyckt, "Absolute light output of scintillators", *IEEE Trans. Nucl. Sci.* **44**, pp. 1052-1061, 1997.
9. J. Chval, D. Clement, J. Giba, J. Hybler, J.-F. Loude, J.A. Mares, E. Mihokova, C. Morel, K. Nejezchleb, M. Nikl, A. Vedda, H. Zaidi, "Development of new mixed $\text{Lu}_x(\text{RE}^{3+})_{1-x}\text{AlO}_3$ scintillators ($\text{RE}^{3+}=\text{Y}^{3+}$ or Gd^{3+}): comparison with other Ce-doped or intrinsic scintillating crystals", *Nucl. Instr. and Meth. Phys. Res.*, **A 443** pp. 331-341, 2000.
10. J.A. Mares, C. Pedrini, B. Moine, K. Blazek and J. Kvapil, "Optical studies of Ce^{3+} -doped gadolinium aluminum perovskite single crystals", *Chem. Phys. Lett.*, **206**, 9-14, 1993.
11. J.A. Mares, N. Cechova, M. Nikl, J. Kvapil, R. Kratky, J. Pospisil, "Cerium-doped $\text{RE}^{3+}\text{AlO}_3$ perovskite scintillators: Spectroscopy and radiation induced defects", *J. Alloys and Comp.*, **275-277**, pp. 200-204, 1998.
12. G. Zimmerer, "Status report on luminescence investigations with synchrotron radiation at Hasylab", *Nucl. Instr. Meth. Phys. Res.*, **A 308**, pp. 178-186, 1991.
13. http://www-hasylab.desy.de/facility/experimental_stations/stations/, see the I-beamline.
14. D. Wisniewski, A.J. Wojtowicz, A. Lempicki, "Spectroscopy and scintillation mechanism in LuAlO₃:Ce", *J. Lumin.* **72-74**, pp. 789-791, 1997.
15. A.J. Wojtowicz, W. Drozdowski, J. Glodo, P. Szupryczynski and D. Wisniewski, "VUV studies of radiative recombination in rare earth activated wide bandgap materials, LuAlO₃:Ce", in *Hasylab Annual Report '98*, Hamburg, 1999; also available on-line: http://www.hasylab-desy.de/science/annual_reports/1998/index.html
16. J. Glodo, A.J. Wojtowicz, "Investigation of electron traps in YAP:Ce", in *Hasylab Annual Report '98*, Hamburg, 1999; also available on-line: http://www.hasylab-desy.de/science/annual_reports/1998/index.html
17. G.H. Dieke, *Spectra and Energy Levels of Rare Earth Ions in Crystals*, Wiley Interscience, New York, 1968.
18. R.T. Wegh, H. Donker, A. Meijerink, R.J. Lamminmäki, and J. Hölsä, "Vacuum-ultraviolet spectroscopy and quantum cutting for Gd^{3+} in LiYF_4 ", *Phys. Rev.* **B56**, pp. 13841-13848, 1997.

Thermal fixing of holographic gratings in nearly stoichiometric LiNbO_3 crystals

Gábor Mandula^a, Krisztián Lengyel^a, László Kovács^{a*}, Mostafa A. Ellabban^b, Romano A. Rupp^b,
and Martin Fally^b

^a Crystal Physics Laboratory, Research Institute for Solid State Physics and Optics, Hungarian Academy of Sciences, H-1121 Budapest, Konkoly-Thege M. út 29-33, Hungary

^b Institute of Experimental Physics, Vienna University, A-1090 Vienna, Strudlhofgasse 4, Austria

ABSTRACT

The thermal decay of holographic gratings recorded using the conventional two-wave mixing technique has been studied in congruent and nearly stoichiometric LiNbO_3 crystals doped with Mn. The activation energies of this process have been determined in the 70-130 °C range for congruent and 20-80 °C range for nearly stoichiometric crystals, the obtained values being 1.06 ± 0.03 and 1.10 ± 0.03 eV, respectively. The kinetics of the OH^- absorption spectrum has also been studied in undoped nearly stoichiometric LiNbO_3 between 40-120 °C. The time dependence of the band intensities can be characterized by exponential time constants obeying the Arrhenius-law. The average activation energy, $E_a \approx 1.1 \pm 0.1$ eV is in good agreement with those obtained from the thermal decay indicating that the hologram fixing process in nearly stoichiometric LiNbO_3 is governed by proton migration.

Keywords: hologram fixing, thermal decay, activation energy, proton migration, OH^- absorption.

1. INTRODUCTION

The light-induced refractive index change, the so called photorefractive effect has been discovered in LiNbO_3 ¹. This effect can be used for recording volume phase holograms in the crystal. A thermal fixing procedure has also been developed to reduce the degradation of recorded holograms during read-out². It is assumed that in the annealing step thermally activated ionic movement compensates for the electronic space-charge field, while a subsequent homogeneous illumination at room temperature develops the stable refractive index pattern. It has been shown that hydrogen ions are responsible for the fixing in $\text{LiNbO}_3:\text{Fe}^3$ and in crystals having high OH^- concentrations⁴. In both cases congruent crystals were studied. It is known, however, that a number of physical properties including the photorefractive effect and OH^- absorption depends on the crystal composition. In the present work the relation between the thermal fixing process and the hydroxyl ion absorption will be studied in nearly stoichiometric LiNbO_3 crystals.

2. EXPERIMENTAL

Congruent ($\text{Li/Nb}=0.945$) and nearly stoichiometric LiNbO_3 crystals were grown by the Czochralski and the top-seeded solution growth methods, respectively, in the Crystal Physics Laboratory, Budapest. The crystals used for holographic recording were doped with 10^{-3} mol/mol Mn. Before each recording phase the samples were heated to 140 °C and illuminated by intense homogeneous white light for 40 minutes to erase the possible gratings remaining from the previous experiment. Then a typical two-wave mixing experiment was applied to record a grating ($\Lambda \approx 2 \mu\text{m}$) in the crystal at room temperature using the 488 nm radiation of an Ar-ion laser. The diffraction efficiency of the grating was read out by a low intensity 633 nm He-Ne laser. After the recording process the sample was heated to fixed temperatures and the thermal decay of the diffraction efficiency was measured. The temperature ranges were chosen to obtain time constants between 1 minute and 100 hours. Accordingly, the temperature ranges used for these measurements were 70-130 °C for the congruent and 20-80 °C for the nearly stoichiometric crystals.

* Further author information
L.K. (correspondence): Email: lkovacs@szfki.hu

An undoped nearly stoichiometric LiNbO_3 crystal was used for detailed IR absorption measurements performed using a Jasco FT/IR-300E spectrometer. The composition of the undoped sample was determined to be $\text{Li/Nb} \approx 0.988$ ⁵ by UV absorption edge measurement. The composition of the nearly stoichiometric Mn-doped crystal was estimated to be the same as that of the undoped crystal, since the shape of the OH^- absorption bands, which strongly depends on the composition⁶, is practically identical in both crystals. A z-cut sample was placed in a Specac heated transmission cell, the temperature of which could be controlled between room temperature and 250 °C with a precision of about 1 °C. Following a standard one-hour annealing procedure at 250 °C, the evolution of the OH^- absorption spectra was measured at selected temperatures between 40-120 °C. About 50-100 scans were collected and averaged in about 5 minutes for each spectrum recorded with a resolution of 1 cm^{-1} .

3. RESULTS AND DISCUSSION

3.1. Thermal fixing

Undoped LiNbO_3 crystals show only weak light-induced refractive index change. The photorefractive effect can be enhanced by transition metal dopants; for this purpose a scarcely studied dopant, manganese, has been selected both for the congruent and the nearly stoichiometric crystal. After having created a periodic space charge field in these Mn-doped crystals, the relaxation of the diffraction efficiency was monitored at the chosen annealing temperatures. During this fixing process mobile ions compensate for the electronic space charge field, resulting in the decay of the diffraction efficiency. A typical time decay curve is shown in Figure 1 for the nearly stoichiometric crystal at 50 °C. The refractive index change, Δn has been calculated from the diffraction efficiency, η by using the formula

$$\eta = \sin^2 (\pi d \Delta n / \lambda \cos \theta) \quad (1)$$

where λ is the wavelength of the reading beam, θ is the angle of incidence within the crystal, and d is the thickness of the crystal. The time dependence of the refractive index change was fitted by the following equation:

$$\Delta n(t) = \Delta n_s \exp(-t/\tau) \quad (2)$$

where Δn_s is the saturation value of the refractive index change, and τ is the time constant of the relaxation process. In a thermally activated process τ follows the Arrhenius-law, i.e. the logarithm of the time constant yields a straight line as a function of reciprocal temperature. Figure 2 shows these lines both for congruent and nearly stoichiometric crystals. From the slope of the lines the activation energy of the process has been evaluated. The calculations lead to $E_a = 1.06 \pm 0.03$ eV, and $E_a = 1.10 \pm 0.03$ eV for the congruent, and the nearly stoichiometric crystals, respectively. So the activation energies of the thermal fixing process were found to be the same within experimental error for Mn-doped LiNbO_3 crystals having rather different compositions. These values agree perfectly with those obtained for congruent LiNbO_3 crystals in an early paper of Staebler and Amodei⁷. It has to be mentioned, however, that later a wide range of activation energies from 0.9 to 1.4 eV has been found both for hologram decay and ionic conductivity in LiNbO_3 depending on the hydroxyl impurity concentration, the range of temperature used in the experiments, the oxidation state and the dopant concentration as pointed out in Ref. 8 and references therein.

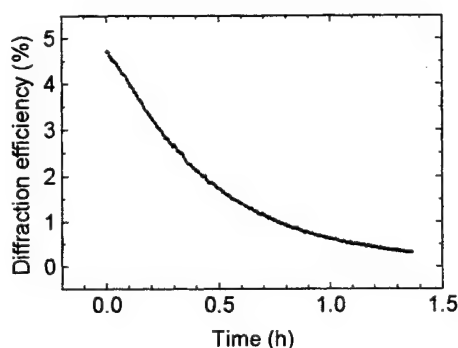


Figure 1. Evolution of the diffraction efficiency at 50 °C in a nearly stoichiometric Mn-doped LiNbO_3 crystal after recording of the grating at 20 °C.

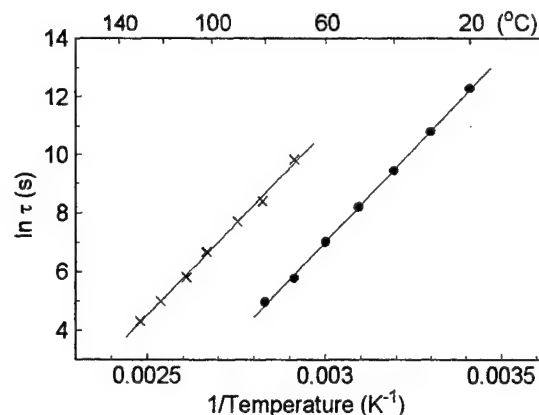


Figure 2. The Arrhenius-plot of the decay time constants for congruent (crosses) and nearly stoichiometric (dots) LiNbO_3 crystals.

The similar activation energy values obtained for hologram decay and ionic conductivity, the latter being linearly proportional to the hydrogen content of the crystal^{9,10,11}, suggested that hydroxyl ions or protons are the thermally activated ions responsible for the fixing process. Direct evidence for the proton mobility during fixing was only given in congruent $\text{LiNbO}_3\text{:Fe}^{3+}$ and in crystals having high OH^- concentrations⁴. In the next section we will show that the proton mobility can be demonstrated in the nearly stoichiometric crystal by a new method, i.e. by monitoring the temperature dependence of the OH^- band shape.

3.2. OH^- absorption

The absorption spectrum of the hydroxyl stretch mode in congruent LiNbO_3 is broad and complex. In the nearly stoichiometric crystal, however, the band components corresponding to different defect sites are narrower than in congruent LiNbO_3 ⁶, which makes the decomposition much more reliable. It has already been reported that the spectrum can be satisfactorily described by the assumption of four components¹². Figure 3 shows the decomposition of the OH^- band of an undoped nearly stoichiometric LiNbO_3 crystal into four Lorentzian components having wavenumbers 3465, 3472, 3479, and 3488 cm^{-1} . By careful analysis of the OH^- spectra we have observed that the intensity of the absorption band components at a given temperature changes with time, conserving the total area under the band constant. The intensities are assumed to be proportional to the proton concentrations in the corresponding defect sites. Therefore we may conclude that the protons migrate among the different sites until they reach a thermodynamic equilibrium, and they do not diffuse out of the crystal.

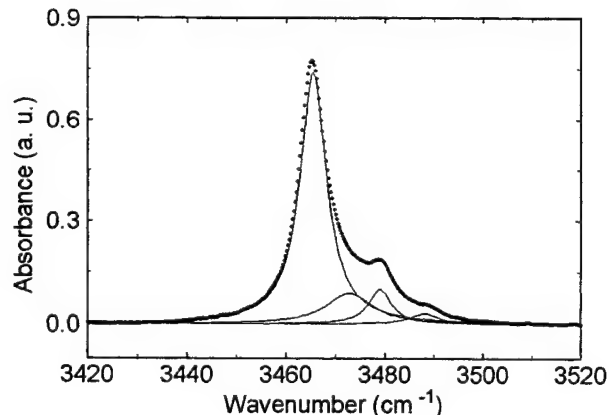


Figure 3. Decomposition of the OH^- stretching vibrational band in a nearly stoichiometric LiNbO_3 crystal. Dots represent the experimental spectrum, continuous lines are the fitted Lorentzian components.

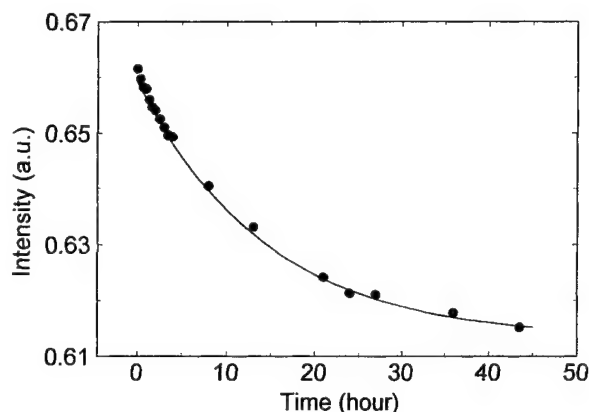


Figure 4. Intensity of the 3465 cm^{-1} OH^- band component as a function of time at 110°C . An exponential decay curve (continuous line) was fitted to the experimental points (dots) resulting in a time constant of about 14.4 hours.

The applied initial one-hour annealings at 250°C were sufficient to achieve a reproducible starting state for subsequent measurements. In fact, during this heat treatment no change of the OH^- absorption band shape could be observed, indicating that at this temperature the protons reach the thermodynamic equilibrium rather quickly. Following this standard procedure the temperature was set to a selected value between 40 – 120°C and the measurements of spectral evolution were started by recording the spectral changes for about 25–160 hours depending on the temperature. The decomposition of the spectra is described in detail elsewhere¹³. The intensities of the four Lorentzians were plotted for each temperature as a function of time. After a relatively fast change observable mainly at lower temperatures (40 – 80°C) a much slower process becomes dominant. During this slow process the intensity of the 3465 and 3479 cm^{-1} bands decreased, while that of the 3472 and 3488 cm^{-1} bands increased. The temporal dependence of the intensities can be characterized by a time constant obtained by fitting an exponential function to the data. As an example Figure 4 shows the decrease of the intensity of the 3465 cm^{-1} component as a function of time at 110°C , yielding a time constant of about 14.4 hours. Since the change of the band intensities is also a thermally activated process one may plot the time constants versus the reciprocal temperature, and similarly to the hologram decay, an Arrhenius-type behaviour is expected. Indeed, the time constants between 80 – 120°C obey the Arrhenius-law for each component. The activation energies for the four components listed above are 1.34 ± 0.08 , 1.0 ± 0.2 , 0.9 ± 0.1 , and $1.04 \pm 0.08\text{ eV}$, respectively. Although the error bars are relatively large for some of the components, the average activation energy calculated to be $E_{\text{av}} \approx 1.1 \pm 0.1\text{ eV}$ is in good agreement with those determined from the thermal fixing experiments. This agreement supports the assumption that the hologram fixing process is governed by protonic migration in the nearly stoichiometric crystal.

4. CONCLUSIONS

We have shown that the thermal activation energy of the dark decay of the holographic grating recorded using the two-wave mixing technique in congruent and nearly stoichiometric Mn-doped LiNbO_3 crystals is 1.06 ± 0.03 and $1.1 \pm 0.03\text{ eV}$, respectively. This agreement indicates that the crystal composition has no remarkable effect on the thermal fixing process in $\text{LiNbO}_3\text{:Mn}$. On the other hand, it has been demonstrated that the shape of the OH^- stretching vibrational band in LiNbO_3 changes with time until the moving protons reach a thermodynamic equilibrium at a given temperature. A careful analysis of the OH^- band shape at different temperatures allowed us to determine the activation energy of the proton migration ($E_{\text{av}} = 1.1 \pm 0.1\text{ eV}$). The agreement between the activation energy of the thermal decay and the protonic migration suggests that the protons are responsible for the thermal fixing process in nearly stoichiometric LiNbO_3 crystals as well.

ACKNOWLEDGEMENTS

This work was supported by the Hungarian Scientific Research Fund (OTKA Nos. T26088, T23092, T34262), and also by the Ministry of Education (Hungary) and the Bundesministerium für Auswärtige Angelegenheiten (Austria) in the framework of the Hungarian-Austrian Intergovernmental S & T Cooperation Programme (A2/1998).

REFERENCES

1. A. Ashkin, G. D. Boyd, J. M. Dziedzic, R. G. Smith, A. A. Ballmann, J. J. Levinstein, and K. Nassau, "Optically-induced refractive index inhomogeneities in LiNbO_3 and LiTaO_3 ," *Appl. Phys. Lett.* **9**, pp. 72-74, 1966.
2. J. J. Amodei, and D. L. Staebler, "Holographic pattern fixing in electro-optic crystals," *Appl. Phys. Lett.* **18**, pp. 540-542, 1971.
3. H. Vormann, G. Weber, S. Kapphan, and E. Krätzig, "Hydrogen as origin of thermal fixing in $\text{LiNbO}_3\text{:Fe}$," *Solid State Commun.* **40**, pp. 543-545, 1981.
4. K. Buse, S. Breer, K. Peithmann, S. Kapphan, M. Gao, and E. Krätzig, "Origin of thermal fixing in photorefractive lithium niobate crystals," *Phys. Rev. B* **56**, pp. 1225-1235, 1997.
5. L. Kovács, G. Ruschhaupt, K. Polgár, G. Corradi, and M. Wöhlecke, "Composition dependence of the ultraviolet absorption edge in lithium niobate," *Appl. Phys. Lett.* **70**, pp. 2801-2803, 1997.
6. K. Polgár, Á. Péter, L. Kovács, G. Corradi, and Zs. Szaller, "Growth of stoichiometric LiNbO_3 single crystals by top seeded solution growth method," *J. Cryst. Growth* **177**, pp. 211-216, 1997.
7. D. L. Staebler and J. J. Amodei, "Thermally fixed holograms in LiNbO_3 ," *Ferroelectrics*, **3**, pp. 107-113, 1972.
8. A. Yariv, S. S. Orlov, and G. A. Rakuljic, "Holographic storage dynamics in lithium niobate: theory and experiment," *J. Opt. Soc. Am. B*, **13**, pp. 2513-2523, 1996.
9. W. Bollmann and H.-J. Stöhr, "Incorporation and mobility of OH^- ions in LiNbO_3 crystals," *phys. stat. sol. (a)* **39**, pp. 477-484, 1977.
10. L. Kovács, I. Földvári, and K. Polgár, "Characterization of LiNbO_3 crystals resistant to laser damage," *Acta Phys. Hung.* **61**, pp. 223-226, 1987.
11. S. Klauer, M. Wöhlecke, and S. Kapphan, "Influence of H-D isotopic substitution on the protonic conductivity of LiNbO_3 ," *Phys. Rev. B*, **45**, pp. 2786-2799, 1992.
12. L. Kovács, M. Wöhlecke, A. Jovanovic, K. Polgár, and S. Kapphan, "Infrared absorption study of the OH^- vibrational band in LiNbO_3 crystals," *J. Phys. Chem. Solids*, **52**, pp. 797-803, 1991.
13. K. Lengyel, L. Kovács, G. Mandula, and R. Rupp, "Kinetics of OH^- ions in nearly stoichiometric LiNbO_3 crystals," *Ferroelectrics*, in print.

High temperature properties of the fcc metallic crystals in the anharmonic approximation

Janusz Tomaszewski, Cecylia Malinowska-Adamska, Piotr Słoma

Institute of Physics, Technical University of Łódź
Wólczańska 219, 93-005 Łódź, Poland

ABSTRACT

The reduced second-order approximation of the self-consistent phonon theory was applied some years ago for cubic metallic crystals whose interatomic interactions were approximated by the Morse and Lennard-Jones pair potential functions. Unfortunately, the parameters of these potentials were generally obtained with the help of semi-classical method basing on the classical static relationships between ground-state properties of a crystal and its interatomic potential, and the zero-point vibrations were taken into account only by certain corrections to the experimental data. Moreover, the further self-consistent calculations were being carried out semi-analytically which required some simplifications. In this paper we can reject them because all essential calculations are being carried out numerically. In the studies at high-temperature properties of selected fcc metallic crystals (Cu, Ag, Au) we take as a model of interatomic interactions the (α, m) Buckingham, (n, m) Lennard-Jones and (α, β) Morse pair potentials with the parameters determined self-consistently with the help of the experimental data for the zero-point lattice constant, cohesive energy and isothermal compressibility. Our new theoretical results for pressure variations of the limiting temperatures of dynamical and thermodynamical stability and for the stability criteria are collected and compared with available experimental data.

Keywords: self-consistent phonon theory, noble metals, stability of crystal lattices

1. INTRODUCTION

About 30 years ago Plakida and Siklós formulated¹ the self-consistent phonon theory (SCPT) using the double-time Green's functions method. The reduced second-order approximation of this theory (RSOSCP) enables to study the dynamical and thermodynamical properties of the fcc crystal lattices with central interatomic interactions, with special regard to the high anharmonicity region, that is at high temperatures close to the melting point and also in the case of the so-called quantum crystals for which even the zero-temperature is too high to use the quasi-harmonic treatment. In our previous papers we tried to describe self-consistently the physical properties of the rare gas solids (RGS) - both the heavier² and the lighter-quantum³ ones. As a model of the interatomic interactions we used three pairwise potentials:

- (α, m) Buckingham (B)

$$\varphi_B(r) = \frac{\alpha \cdot m}{\alpha - m} \cdot D_0 \cdot \left\{ \frac{1}{\alpha} \cdot \exp \left[\alpha \cdot \left(1 - \frac{r}{r_0} \right) \right] - \frac{1}{m} \cdot \left(\frac{r_0}{r} \right)^m \right\}, \quad r \geq r_{ext}, \quad (1)$$

- (n, m) Lennard-Jones (LJ)

$$\varphi_{LJ}(r) = \frac{n \cdot m}{n - m} \cdot D_0 \cdot \left[\frac{1}{n} \cdot \left(\frac{r_0}{r} \right)^n - \frac{1}{m} \cdot \left(\frac{r_0}{r} \right)^m \right], \quad n > m, \quad (2)$$

- (α, β) Morse (M)

$$\varphi_M(r) = \frac{\alpha \cdot \beta}{\alpha - \beta} \cdot D_0 \cdot \left\{ \frac{1}{\alpha} \cdot \exp \left[\alpha \cdot \left(1 - \frac{r}{r_0} \right) \right] - \frac{1}{\beta} \cdot \exp \left[\beta \cdot \left(1 - \frac{r}{r_0} \right) \right] \right\}, \quad \alpha > \beta, \quad (3)$$

where n , m , α and β are the dimensionless parameters describing the slope of the potential curve, r_0 and D_0 define the potential minimum and are, respectively, the equilibrium distance of two isolated atoms and the energy of their dissociation.

In this paper we try to apply the RSOSCPT, in connection with the three mentioned potentials, to the noble metal crystals (NMC): copper, silver and gold. As for metals there is no simple expression like the r^{-6} law of attraction in the RGS, so we must use just these generalised 4-parameters versions of the traditional 2- or 3-parameters potentials: ($\alpha, 6$) Buckingham, (12,6) Lennard-Jones and ($\alpha, \alpha/2$) Morse.

The physical properties of the NMC were already being studied on the basis of the RSOSCPT in terms of the ($\alpha, \alpha/2$) Morse⁴ and (n,m) Lennard-Jones⁵ potentials but the potential parameters were obtained from the ground-state crystal properties with the help of the static relations^{2,3} and so with neglect of the zero-point vibrations effect. In this paper we calculate the potential parameters self-consistently (dynamically) fitting them to the experimental data⁶ for the zero-point cohesive energy, lattice constant and compressibility. Instead of the 4-th condition we assume correctness of the theoretical values of the parameter α in the repulsive Born-Mayer potential, evaluated by Hafemeister⁷ with the help of the exchange charge model (ECM). It is also possible to take for α some of the experimental values reported by Hafemeister⁷.

2. THE BASIS OF THE SELF-CONSISTENT CALCULATIONS

The self-consistent method of treating the lattice dynamics consists in replacing the pairwise static potential with its dynamical self-consistent version according to the following renormalization scheme:

$$\tilde{\varphi}(r) = \sum_{k=0}^{\infty} \frac{1}{k!} \cdot y^k \cdot r_0^{2k} \cdot \varphi^{(2k)}(r), \quad (4)$$

where $y = \overline{u^2} / 2r_0^2$ is the renormalization parameter,

$\overline{u^2}$ is the mean-square relative displacement of the neighbouring atoms, which depends on the temperature range and is always very complicated function of the self-consistent potential and its derivatives¹.

It is worth-while to point out here that, as it was shown by Plakida, Siklós and Aksienov^{1,8}, all the physical quantities connected with crystal lattice can be expressed as functions of $y(l)$, $\tilde{\varphi}(l)$, $\tilde{\varphi}''(l)$ and $\tilde{\varphi}'''(l)$, where l is the equilibrium interatomic separation derived from the equilibrium condition:

$$p = -(z \cdot l / 6 \cdot v) \cdot \tilde{\varphi}'(l), \quad (5)$$

where p is the external pressure, z and v are the number of nearest neighbours and the specific volume, respectively.

The self-consistent system of equations (4-5) possesses an implicit form with respect to the renormalization parameter and so it can be solved only approximately - for instance numerically. It is worth-while to point out here that the analysis of solvability of this system enables us to find the limiting temperature of the dynamical stability of crystal lattice - defined by Plakida and Siklós as the temperature at which the theoretical phonon frequencies become complex. From the other hand, the limiting temperature of the thermodynamical stability can be obtained with the help of the thermo-mechanical and elastic conditions derived from the principle of minimal free Gibbs energy. We don't go here into details because the problem of theoretical description of lattice stability was extensively discussed in our previous paper⁹.

In the present study we make use of the self-consistent treatment in order to characterise the boundary of stability region of the NMC lattices.

3. NUMERICAL RESULTS AND CONCLUSIONS

Using the self-consistent relationships connecting the dynamical and thermodynamical quantities with the interatomic interaction function we have found the optimal values of the parameters n , m , α , β , r_0 and D_0 of the (α, m) Buckingham, (n,m) Lennard-Jones and (α, β) potentials for the NMC fitting them to the zero-point experimental data⁶ for the nearest-neighbours mean separation l_0 , the heat of sublimation L_0 and the isothermal bulk modulus B_0 . We have decided to create for each crystal and potential two series of parameters. Namely, it is possible to take for the repulsive parameter α in the Buckingham and Morse potentials either the theoretical value (obtained by Hafemeister⁷ with the help of the exchange charge model) or the experimental one (from among a few experimental values reported by Hafemeister⁷ we choose every time the lowest one which differs the most from the ECM result). The mentioned zero-point experimental data and the results of calculations of the potential parameters (two series) are collected in Tables 1 and 2, respectively. Let us notice that the ratios n/m and α/β are always higher than 2. Additionally n and m differ distinctly from 12 and 6, respectively. D_0 and r_0 are almost the same for all the potentials.

Table 1. The experimental data⁶ for the nearest-neighbours mean separation l_0 , the heat of sublimation L_0 and the isothermal bulk modulus B_0 used in calculations of the pair potential parameters.

l_0 [10^{-10} m]			L_0 [10^{-21} J/atom]			B_0 [GPa]		
Cu	Ag	Au	Cu	Ag	Au	Cu	Ag	Au
2.549	2.876	2.875	561.4	471.9	611.6	133.3	100.0	166.7

Table 2. Optimal values of the parameters of the Buckingham (B), Lennard-Jones (LJ) and Morse (M) pair potentials for the noble metal crystals: copper, silver, gold. The two sets of parameters were obtained for $\alpha = \alpha_{\text{theor}}$ (*) and $\alpha = \alpha_{\text{exp}}$ (**).

Solid	Potential	n	m	α	β	r_0 [10^{-10} m]	D_0 [10^{-21} J]
Cu	B*	-	2.88	10.17	-	2.542	94.51
	B**	-	1.73	15.97	-	2.539	94.51
	LJ*	8.8	2.88	-	-	2.541	94.51
	LJ**	14.85	1.73	-	-	2.539	94.51
	M*	-	-	10.17	2.47	2.542	94.51
	M**	-	-	15.97	1.60	2.540	94.51
Ag	B*	-	3.19	11.53	-	2.870	79.3
	B**	-	2.05	17.07	-	2.869	79.3
	LJ*	10.15	3.19	-	-	2.870	79.3
	LJ**	16.0	2.05	-	-	2.868	79.3
	M*	-	-	11.53	2.8	2.870	79.3
	M**	-	-	17.07	1.91	2.869	79.3
Au	B*	-	4.18	11.49	-	2.872	102.5
	B**	-	2.62	17.09	-	2.871	102.5
	LJ*	9.93	4.18	-	-	2.871	102.5
	LJ**	15.9	2.62	-	-	2.871	102.5
	M*	-	-	11.49	3.6	2.872	102.5
	M**	-	-	17.09	2.43	2.871	102.5

Having at disposal the potential parameters we could carry out the analysis of solvability of the self-consistent system of equations (4-5) with respect to the renormalization parameter for different temperatures and pressures. As a result we have found for all the noble metal crystal lattices the pressure variations of the limiting temperature of the dynamical stability for the three models of interatomic interactions. The next step was to study the behaviour of the thermodynamical quantities within the dynamical stability region. We were especially interested in the high-temperature properties of the isothermal bulk modulus and the isothermal elastic constants c_{11} , $(c_{11} - c_{12})/2$ and c_{44} , which for the thermodynamically stable cubic structure should be positively defined. The temperature over which these conditions (at least one of them) are violated is in fact the limiting temperature of the thermodynamical stability. The results of calculations of the limiting temperatures of the dynamical and thermodynamical stability of crystal lattices of noble metals are collected in Table 3 together with the experimental data¹⁰ for the melting temperature.

Table 3. Pressure variations of the limiting temperatures of the dynamical T_s^{dyn} and thermodynamical T_s^{tdm} stability of the noble metal crystals obtained in the RSOSCPT for the Buckingham, Lennard-Jones and Morse model potentials. Experimental values of the melting temperature T_m^{10} are shown for comparison. All results in Kelvin scale

Cu	0 GPa		1 GPa		2 GPa		3 GPa		4 GPa	
	T_s^{dyn}	T_s^{tdm}	T_s^{dyn}	T_s^{tdm}	T_s^{dyn}	T_s^{tdm}	T_s^{dyn}	T_s^{tdm}	T_s^{dyn}	T_s^{tdm}
B*	3083	3077	3376	3345	3700	3614	4079	3886	-	4158
B**	1999	1920	2227	2088	2485	2256	-	2423	-	2589
LJ*	2626	2600	2826	2779	3030	2956	3237	3131	3448	3303
LJ**	1702	1633	1853	1755	2010	1875	2175	1992	-	2109
M*	3477	3469	3783	3750	4115	4031	4485	4314	-	4597
M**	2360	2218	2611	2391	2892	2562	-	2733	-	2902
T_m (Exp)	1356		1397		1435		1473		1501	

Ag	0 GPa		1 GPa		2 GPa		3 GPa		4 GPa	
	T_S^{dyn}	T_S^{tdm}	T_S^{dyn}	T_S^{tdm}	T_S^{dyn}	T_S^{tdm}	T_S^{dyn}	T_S^{tdm}	T_S^{dyn}	T_S^{tdm}
B*	2609	2603	2972	2931	3391	3263	-	3596	-	3931
B**	1807	1746	2105	1968	2466	2189	-	2410	-	2629
LJ*	2281	2259	2543	2493	2813	2723	3091	2949	-	3171
LJ**	1569	1511	1774	1676	1988	1838	-	1996	-	2153
M*	2917	2911	3294	3253	3717	3598	-	3943	-	4289
M**	2097	1994	2417	2222	2790	2447	-	2671	-	2894
T_m (Exp)	1234		1288		1353		1401		1485	

Au	0 GPa		1 GPa		2 GPa		3 GPa		4 GPa	
	T_S^{dyn}	T_S^{tdm}	T_S^{dyn}	T_S^{tdm}	T_S^{dyn}	T_S^{tdm}	T_S^{dyn}	T_S^{tdm}	T_S^{dyn}	T_S^{tdm}
B*	3742	3742	4061	4053	4402	4368	4773	4685	5196	5006
B**	2687	2632	2954	2850	3243	3068	3563	3286	-	3504
LJ*	3341	3327	3594	3561	3852	3793	4116	4024	4387	4253
LJ**	2386	2322	2584	2489	2787	2654	2995	2818	3210	2979
M*	4079	4079	4406	4401	4752	4727	5124	5055	5530	5386
M**	3045	2959	3327	3183	3629	3407	3958	3630	4333	3853
T_m (Exp)	1338		1393		1447		1502		1562	

As we see, the thermodynamical stability conditions nearly always prevail over the dynamical ones - especially for high pressures and harder potentials (like the (n,m) Lennard-Jones). Moreover, the RSOSCPT provides a disappearance of the dynamical instability (but not the thermodynamical one) at sufficiently high pressures - the external forces become then strong enough to localise atomic vibrations for any given temperature. Consistently with the expectations both T_S^{dyn} and T_S^{tdm} are always greater than the real melting temperature T_m and the difference is the lowest in the case of the (n,m) Lennard-Jones (LJ**) potential with the attraction parameter m taken from the ($\alpha=\alpha_{ECM}$, m) Buckingham potential.

Within the investigations of the destabilisation phenomenon in the NMC we have studied the pressure variations of the ratio $\kappa = \left(\overline{u^2}\right)^{1/2} / l$, of the mean amplitude of relative thermal vibrations of neighbouring atoms to the equilibrium interatomic spacing, calculated at the limit of stability (κ_S^{dyn} , κ_S^{tdm}) (Table 4).

Table 4. Pressure variations of the dynamical and thermodynamical stability criteria of the noble metal crystals obtained in the RSOSCPT for the Buckingham, Lennard-Jones and Morse model potentials. The meaning of symbols is as in Table 2.

Cu	0 GPa		1 GPa		2 GPa		3 GPa		4 GPa	
	κ_S^{dyn}	κ_S^{tdm}	κ_S^{dyn}	κ_S^{tdm}	κ_S^{dyn}	κ_S^{tdm}	κ_S^{dyn}	κ_S^{tdm}	κ_S^{dyn}	κ_S^{tdm}
B*	0.1467	0.1441	0.1538	0.1461	0.1628	0.1476	0.1775	0.1492	-	0.1506
B**	0.1250	0.1093	0.1314	0.1103	0.1413	0.1112	-	0.1121	-	0.1128
LJ*	0.1286	0.1224	0.1312	0.1230	0.1346	0.1236	0.1376	0.1242	0.1406	0.1247
LJ**	0.1070	0.0949	0.1097	0.0953	0.1143	0.0957	0.1206	0.0959	-	0.0962
M*	0.1529	0.1497	0.1589	0.1516	0.1658	0.1530	0.1751	0.1545	-	0.1558
M**	0.1326	0.1132	0.1384	0.1141	0.1473	0.1148	-	0.1155	-	0.1162

Ag	0 GPa		1 GPa		2 GPa		3 GPa		4 GPa	
	κ_S^{dyn}	κ_S^{tdm}	κ_S^{dyn}	κ_S^{tdm}	κ_S^{dyn}	κ_S^{tdm}	κ_S^{dyn}	κ_S^{tdm}	κ_S^{dyn}	κ_S^{tdm}
B*	0.1332	0.1300	0.1423	0.1324	0.1547	0.1345	-	0.1363	-	0.1379
B**	0.1150	0.1024	0.1254	0.1037	0.1461	0.1049	-	0.1060	-	0.1069
LJ*	0.1181	0.1126	0.1222	0.1136	0.1268	0.1144	0.1313	0.1151	-	0.1157
LJ**	0.1002	0.0897	0.1050	0.0903	0.1104	0.0908	-	0.0911	-	0.0915
M*	0.1373	0.1348	0.1456	0.1370	0.1557	0.1390	-	0.1406	-	0.1422
M**	0.1218	0.1058	0.1305	0.1070	0.1429	0.1080	-	0.1089	-	0.1097

Au	0 GPa		1 GPa		2 GPa		3 GPa		4 GPa	
	κ_S^{dyn}	κ_S^{tdm}	κ_S^{dyn}	κ_S^{tdm}	κ_S^{dyn}	κ_S^{tdm}	κ_S^{dyn}	κ_S^{tdm}	κ_S^{dyn}	κ_S^{tdm}
B*	0.1240	0.1240	0.1297	0.1267	0.1354	0.1283	0.1421	0.1296	0.1538	0.1309
B**	0.1094	0.1001	0.1149	0.1010	0.1219	0.1019	0.1296	0.1027	-	0.1034
LJ*	0.1135	0.1099	0.1167	0.1106	0.1191	0.1112	0.1218	0.1119	0.1255	0.1125
LJ**	0.0979	0.0887	0.1001	0.0891	0.1029	0.0895	0.1058	0.0898	0.1095	0.0901
M*	0.1278	0.1278	0.1329	0.1306	0.1374	0.1321	0.1436	0.1334	0.1512	0.1346
M**	0.1146	0.1033	0.1194	0.1041	0.1248	0.1049	0.1316	0.1056	0.1435	0.1063

As it appears the thermodynamical stability criterion κ_S^{tdm} is nearly independent of pressure if crystal and the model potential are fixed while the dynamical stability criterion κ_S^{dyn} rises rapidly with pressure in all cases. The last fact means that the dynamical destabilisation becomes more and more difficult when the external pressure increases and so at higher pressures the melting phenomenon is rather caused by the order-disorder transition.

4. CONCLUSIONS

Summarising, we would like to stress, that the RSOSCPT provides a disintegration of the noble metal crystal lattices as an effect of extreme thermal vibrations of lattice atoms. The theoretical limiting temperatures of the dynamical and thermodynamical stability are always the upper estimations of the real melting temperature. The quality of this estimation is generally better in the case of the thermodynamical treatment and harder potential functions. If it about the two series of potential parameters, the results obtained with the help of parameters α and m derived from experiment are better than in the case of the parameters obtained purely theoretically with the help of the exchange charge model. It is worth-while to point out here that there exists no theoretical prediction for the value of $T_S - T_m$, and the only proper method of determining the melting temperature is the method based on the analysis of the equation of state and the thermodynamical potentials simultaneously for solid and liquid. Anyway, we must be aware of the fact that the reduced second-order approximation of the SCPT is formulated only for central, nearest-neighbours interactions and so it should be improved. In addition the real interactions in the metallic crystals are in significant part non-central and so we should rather evaluate the repulsive parameter α using the additional experimental data and if we want to describe the interactions theoretically a many-body, non-central force must be considered.

REFERENCES

1. N.M. Plakida, T. Siklós, "Theory of anharmonic crystals", *Phys. Stat. Sol.* **33**, pp. 103-112 and 113-123, 1969; **39**, pp. 171-180, 1970.
2. C. Malinowska-Adamska, P. Słoma, J. Tomaszewski, "Self-consistent calculations of the thermodynamic and elastic properties of heavier rare gas solids near the lattice instability point", *Phys. Stat. Sol.* **(b)219**, pp. 229-240, 2000.
3. C. Malinowska-Adamska, P. Słoma, J. Tomaszewski, "Application of the Lennard-Jones (n,m) potential function to quantum crystals in the self-consistent phonon theory", *Phys. Stat. Sol.* **(b)200**, pp. 451-462, 1997.
4. C. Malinowska-Adamska, "Self-consistent calculations of the lattice dynamics and thermodynamics of anharmonic noble metals", *Phys. Stat. Sol.* **(b)120**, pp. 601-610, 1983.
5. C. Malinowska-Adamska, "The effect of pressure on the thermodynamic properties of crystals near the lattice instability point", *Phys. Stat. Sol.* **(b)151**, pp. 53-60, 1989.
6. Shu Zhen, G.J. Davies, "Calculation of the Lennard-Jones n-m potential energy parameters for metals", *Phys. Stat. Sol.* **(a)78**, pp. 595-605, 1983.
7. D.W. Hafemeister, "Calculation of the ion-ion repulsive interaction in the rare gas solids and in the noble metals", *J. Phys. Chem. Solids* **30**, pp. 117-128, 1969.
8. N.M. Plakida, V.L. Aksienov, "Elastic constants and stability of anharmonic crystals", *Solid State Physics* **15**, pp. 2575- 2582, 1973 (in Russian).
9. J. Tomaszewski, C. Malinowska-Adamska, "Self-consistent description of the lattice destabilisation phenomenon for the heavier rare gas solids", *Proc. SPIE* **3724**, pp. 177-182, 1999.
10. L.H. Cohen, W. Klement, Jr., G.C. Kennedy, "Melting of copper, silver and gold at high pressures", *Phys. Rev.* **145**, pp. 519-525, 1966.

Investigation of high-energetic transitions in some Pr^{3+} -doped fluoride and oxide crystals

I. Sokólska^{a,b,*}, S. Kück^b and M. Bałuka^a

^a W.Trzebiatowski Institute of Low Temperature and Structure Research,
Polish Academy of Sciences, Okólna Street 2, P.O. Box 1410, Wrocław, Poland

^b Institut für Laser-Physik, Universität Hamburg, Jungiusstrasse 9a, 20355 HH, Germany,

ABSTRACT

The excitation and emission spectra obtained for $\text{Pr}^{3+}:\text{YAlO}_3$, $\text{Pr}^{3+}:\text{LiYF}_4$ and $\text{K}_5\text{PrLi}_2\text{F}_{10}$ crystals by means of high-energetic excitation with synchrotron radiation (HASYLAB, DESY Hamburg, Germany) are presented. In the emission spectra broad, overlapping bands in UV range are present. Their positions, bandwidths as well as the short emission decay times suggest, that emission from levels of 4f5d configuration dominate in all of the crystals investigated.

Keywords: Pr^{3+} , optical properties, synchrotron radiation excitation, 5d-4f interconfigurational transitions

1. INTRODUCTION

In recent years an interest in high-energetic intraconfigurational transitions within 4fⁿ electron configuration as well as in interconfigurational 4fⁿ-4fⁿ⁻¹5d transitions has significantly increased due to expected possible applications. Investigations of the 4fⁿ-4fⁿ⁻¹ transitions follow an old idea of achieving simultaneously more than one emitted photon of luminescence in the visible (VIS) range after excitation with a high energetic photon in the ultraviolet (UV) range¹⁻³. Various matrices singly or doubly doped with RE ions (first of all with Pr, Gd, Tm, Tb) have been recently studied [e.g. in ref. 4-7] with hope to find systems where processes of this type (called "cascade emission", "quantum cutting" or "down-conversion") take place with a high quantum efficiency. Such materials could then be used as phosphors for mercury-free UV lamps or other light sources. The interconfigurational 4fⁿ⁻¹5d - 4fⁿ transitions are parity-allowed and characterised by short emission lifetimes and broad emission bands of high intensity located in the UV range⁸⁻¹². It is expected that they can be used for tunable solid state lasers, as laser oscillation based on 4fⁿ⁻¹5d - 4fⁿ transition was yet realised in Ce^{3+} crystals¹³.

For trivalent praseodymium both types of transitions can take place, depending on the host matrix and energetic location of the ¹S₀ multiplet of the 4f² electron configuration (ca. 46500 cm⁻¹) relative to the states of the 4f5d electron configuration. In some materials the excitation into the ¹S₀ multiplet brings about a cascade emission due to the two-step intraconfigurational 4f²-4f² transitions: ¹S₀→¹I₆ (ca. 410 nm) followed by ³P₀→³H₄ (ca. 485 nm)^{1,2,6}. The presence of such a two-photon emission in Pr^{3+} -doped materials is possible only if the ¹S₀ multiplet is located energetically lower than the lowest state of the 4f5d configuration. It is expected to be observed mainly in fluoride crystals, where the high electronegativity of F⁻ ion induces a weak crystal field splitting of the 4f5d configuration. The efficiency of this two-photon emission depends strongly on the ion-host interactions (nonradiative relaxation rates) and highly efficient Pr-doped materials for application based on photon cascade emission have not been found yet.

In the majority of the materials investigated so far, the ¹S₀ multiplet is located within the energetically extended 4f5d states and the high-energetic excitation brings about the emission due to the 4f5d → 4f transitions. Spectroscopic investigations of transitions involving 4f5d levels of Pr^{3+} have been so far carried out for a number of materials (e.g. $\text{Y}_3\text{Al}_5\text{O}_{12}$ ¹²⁻¹⁴, YAlO_3 ^{12,15}, CaF_2 , LiYF_4 ^{16,17}) by means of either synchrotron radiation or excited state absorption and two-step excitation techniques or by using the UV excitation lamps. Due to the experimental limitations in the spectral range of high energies, the results obtained are not always consistent, complete and clear. Thus, the comparison of data obtained by various techniques and for various Pr^{3+} materials extends the knowledge about the energy level structure and processes investigated.

In this work we present the spectroscopic results obtained for three single crystals: YAlO_3 , LiYF_4 , $\text{K}_5\text{PrLi}_2\text{F}_{10}$ containing Pr^{3+} after high-energetic excitation by synchrotron radiation. The investigation was performed in order to get

*
I.S. (correspondence): Email: i.sokolska@int.pan.wroc.pl; Fax No. +48 71 3441029
S.K.: Email: kueck@physnet.uni-hamburg.de

better characterisation of the energy structure of Pr^{3+} ions in YAlO_3 and LiYF_4 crystals, yet partly investigated^{9,12,15} and to determine the position of higher-lying Pr^{3+} energy levels in $\text{K}_5\text{PrLi}_2\text{F}_{10}$ crystal.

2. EXPERIMENTAL

The $\text{YAlO}_3:\text{Pr}^{3+}$ (YAP) and $\text{LiYF}_4:\text{Pr}^{3+}$ (YLF) crystals investigated in this work were grown by the Czochralski method and contained 0.75at% and 3at% Pr, respectively. The $\text{K}_5\text{PrLi}_2\text{F}_{10}$ (KPLF) stoichiometric crystal was grown by the Bridgman method¹⁸. The investigations were carried out at the SUPERLUMI station of HASYLAB (Hamburger Synchrotron Laboratorium) at DESY (Deutsches Elektronen-Synchrotron) synchrotron centre in Hamburg. The experiments were performed at low temperatures (ca. 10K) and at room temperature (RT). The spectral range of the excitation measurements was 50-350 nm (24.7 eV-3.5 eV) with a resolution of the primary monochromator of 0.3 nm. The sensitivity of the set-up used for excitation measurements was corrected by comparison with the sodium salicylate spectrum measured as a standard. The emission spectra were measured in the 200-300 nm and 300-600 nm spectral ranges by using two different monochromators with the resolution of approximately 3nm. The presented emission spectra are not corrected with respect to the sensitivity of the set-up used. The kinetics of the emission decays were measured by standard single-photon counting method. The determination of the decay of the emission is limited by the period between the synchrotron bunches and decay times longer than 200 ns were not possible to be recorded.

3. RESULTS AND DISCUSSION

The optical properties of Pr^{3+} ions in the investigated YAP, YLF and KPLF crystals were previously investigated in spectral ranges of typical spectroscopic methods (e.g. in ref. [19], [20] and [18,21], respectively). In the absorption spectra the narrow bands due to the f-f transitions from the $^3\text{H}_4$ multiplet to the multiplets up to the $^3\text{P}_2$ are observed (see Fig. 1, energy levels scheme). As an example, the absorption spectrum of the KPLF crystal recorded at RT is presented in Fig. 2.

The positions of the high-lying states, that is of the $^1\text{S}_0$ multiplet or states of the 4f5d electron configuration, usually can not be determined from absorption spectra due to either absorption edge of the crystal host or to the too high absorption cross sections of f-d transitions or/and presence of other intense bands (charge transfer, crystal defects, impurities). In the presented absorption spectrum of KPLF the rise of absorption for wavelength lower than 300 nm is probable due to some defects or charge-transfer transition within the host, as it is observed also for the $\text{K}_5\text{LaLi}_2\text{F}_{10}$ crystal¹⁸. Under excitation into

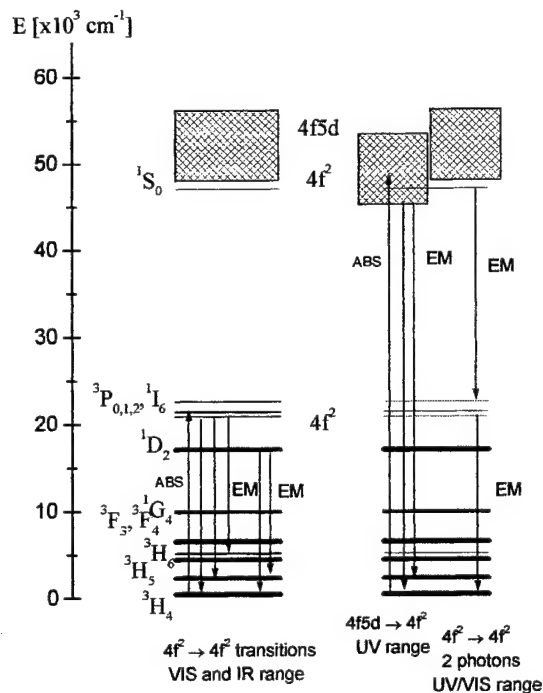


Fig. 1. Energy level scheme of Pr^{3+} -ion

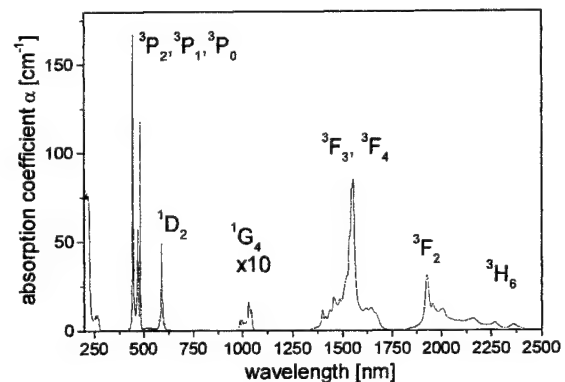


Fig. 2. Absorption spectrum (300K) of the $\text{K}_5\text{PrLi}_2\text{F}_{10}$ crystal

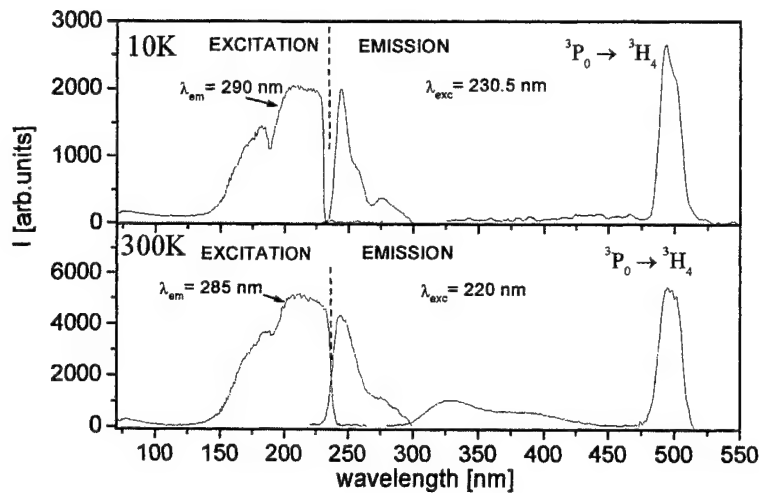


Fig. 3. Excitation and emission spectra of YAlO_3 crystal

states of $4f^2$ electron configuration up to the 3P_1 group (up to about 22500cm^{-1}) an emission from the 3P_0 or/and from the 1D_2 multiplets to the lower-lying multiplets is observed in the blue, green and red spectral ranges. The lifetimes of the luminescent 3P_0 multiplet for YAP, YLF and KPLF are at RT about $12\text{ }\mu\text{s}^{19}$, $43\text{ }\mu\text{s}^{16}$ and $0.7\text{ }\mu\text{s}^{20}$, respectively. In the Figs. 3-7 the excitation and emission spectra of the Pr^{3+} recorded in a spectral range from 50 nm to 350 nm and from 200 nm up to 600 nm, respectively, are shown. In the excitation spectra dominate the broad slightly structured bands in the range between about 120 nm to about 225 nm. These bands are assigned to the transitions from Pr^{3+} ground state of $4f^2$ configuration (3H_4) to the states of Pr^{3+} $4f5d$ configuration. Because of the large radial extension of the d-orbitals, transitions involving those states are crystal field sensitive, broad and vibronic in character. In the emission spectra obtained after excitation within the $4f5d$ states some broad bands in UV and VIS range are present, which are assigned as due to the $5d-4f$ transitions. The band at about 480 nm is assigned to the $^3P_0 \rightarrow ^3H_4$ transition. Although this band is not so narrow as expected for $4f-4f$ transition (due to the low resolution by the measurement), its position practically independent on the crystal host and the long decay time of this emission support this assignment.

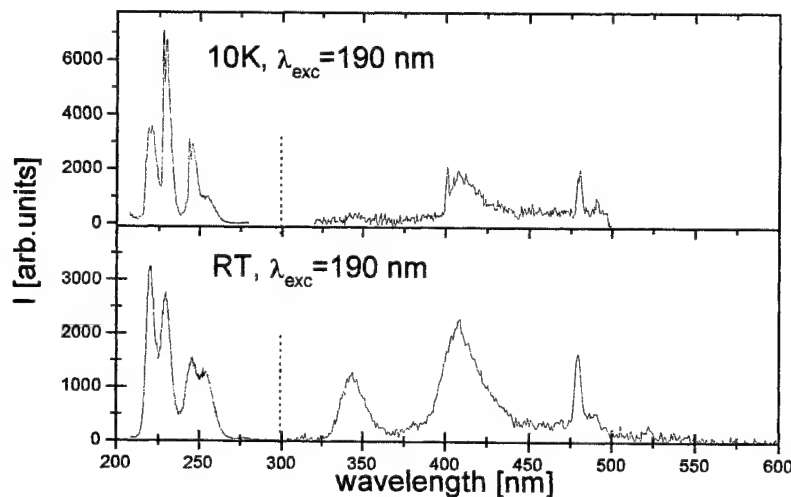


Fig. 4. Emission spectra of the $\text{Pr}^{3+}:\text{LiYF}_4$ crystal

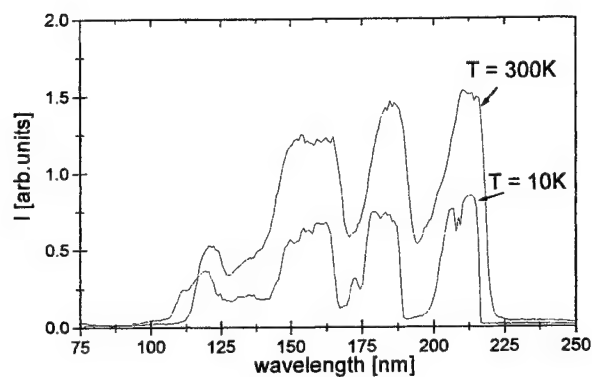


Fig. 5. Excitation spectra of the $\text{Pr}^{3+}:\text{LiYF}_4$ crystal, $\lambda_{\text{em}}=410$ nm

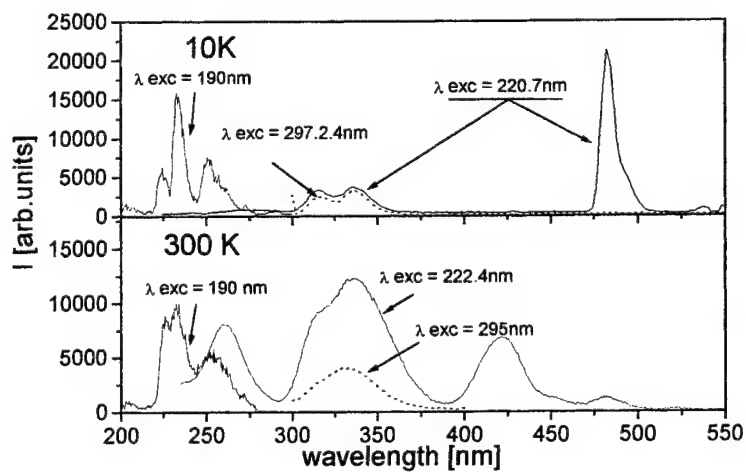


Fig. 6. Emission spectra of the $\text{K}_5\text{PrLi}_2\text{F}_{10}$ crystal

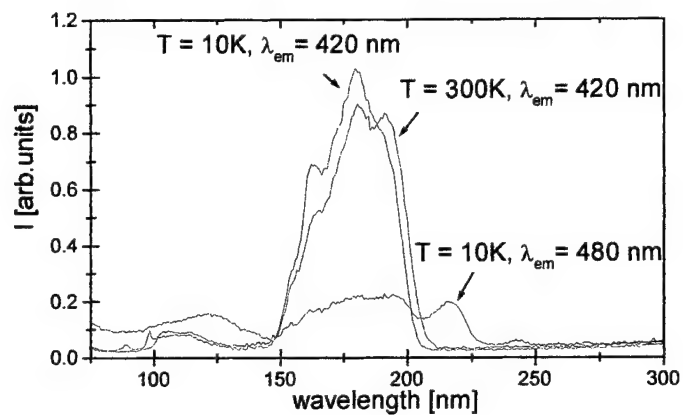


Fig. 7. Excitation spectra of the $\text{K}_5\text{PrLi}_2\text{F}_{10}$ crystal

The mean energies of main absorption and emission transitions observed in the spectra of the crystals investigated are summarised in Table 1. In neither absorption nor emission spectra there are hints for presence of transitions involving the 1S_0 multiplet. The f-f transitions due to the presence of the 1S_0 level would result in a weak and relative sharp peak in an excitation spectrum. However, no such peaks are observed for energies below states of 4f5d configuration in the presented spectra. In the emission spectra the bands due to the emission from 1S_0 multiplet ($^1S_0 \rightarrow ^1I_6$) should be located at about 410 nm and have a relative long lifetime. In our emission spectra we observe a strong band around 400 nm in the case of YLF and KPLF crystals and a weak one in the case of YAP crystal. However, these bands are relatively broad, are accompanied by other bands ascribed to the transitions from the 4f5d states, have practically the same decay characteristics and their energetic position can be ascribed to transitions from 4f5d levels to the 1D_2 or 3P_0 multiplets, respectively (see Table 1). Thus, we assume, that for all investigated crystals the 1S_0 level is located above the lowest levels of 4f5d states.

Crystal	Excitation energies/ λ [cm ⁻¹]/[nm]	Transition	Emission energies/ λ [cm ⁻¹]/[nm]	Lifetime	Transition
Pr:YAlO ₃	46 500/ 215	$^3H_4(4f^2) \rightarrow 4f5d(I)$	40 780/ 245	7-9 ns	$4f5d(I) \rightarrow ^3H_4(4f^2)$
	55 500/ 180	$^3H_4(4f^2) \rightarrow 4f5d(II)$	38 820/ 258	"	$4f5d(I) \rightarrow ^3H_5(4f^2)$
			36 280/ 275	"	$4f5d(I) \rightarrow ^3H_6(4f^2)$
			33 000/ 290	"	$4f5d(I) \rightarrow ^3F_{3,4}(4f^2)$
			25 640/ 390	"	$4f5d(I) \rightarrow ^1D_2(4f^2)$
			23 530/ 425	"	$4f5d(I) \rightarrow ^1D_2(4f^2)$
			20 400/ 490	long (μ s)	$^3P_0(4f^2) \rightarrow ^3H_4(4f^2)$
Pr:YLiF ₄	46 500/ 215	$^3H_4(4f^2) \rightarrow 4f5d(I)$	45 450/ 220.0	17-20 ns	$4f5d(I) \rightarrow ^3H_4(4f^2)$
	48 300/ 207	$^3H_4(4f^2) \rightarrow 4f5d(I)$	45 290/ 220.8	"	
	53 700/ 186	$^3H_4(4f^2) \rightarrow 4f5d(I)$	43 890/ 227.8	"	$4f5d(I) \rightarrow ^3H_5(4f^2)$
	57 940/ 173	$^3H_4(4f^2) \rightarrow 4f5d(I)$	43 515/ 229.8	"	
	61 730/ 162	$^3H_4(4f^2) \rightarrow 4f5d(II)$	41 050/ 243.6	"	$4f5d(I) \rightarrow ^3H_6, ^3F_2(4f^2)$
	86 960/ 115	excitons/ host	40 683/ 245.8	"	
			39 180/ 255.2	"	$4f5d(I) \rightarrow ^3F_{3,4}(4f^2)$
			35 650/ 280	"	$4f5d(I) \rightarrow ^1G_4(4f^2)$
			29 070/ 344	"	$4f5d(I) \rightarrow ^1D_2(4f^2)$
			24 930/ 401	"	$4f5d(I) \rightarrow ^3P_0(4f^2)$
K ₅ PrLi ₂ F ₁₀	41 150/ 243	charge transfer/defects	44 640/ 224	9-11 ns	$4f5d(I) \rightarrow ^3H_4(4f^2)$
	46 300/ 216	charge transfer/defects	43 100/ 232	"	$4f5d(I) \rightarrow ^3H_5(4f^2)$
	52 630/ 190	$^3H_4(4f^2) \rightarrow 4f5d(I)$	39 930/ 250	"	$4f5d(I) \rightarrow ^3H_6, ^3F_2(4f^2)$
	61 300/ 163	$^3H_4(4f^2) \rightarrow 4f5d(I)$	38 460/ 260	"	$4f5d(I) \rightarrow ^3F_{3,4}(4f^2)$
	64 510/ 163	$^3H_4(4f^2) \rightarrow 4f5d(II)$	29 655/ 337	~30 ns	defects/charge transfer
	81 960/ 122	excitons/ host	23 750/ 421	9-11 ns	$4f5d(I) \rightarrow ^3P_0(4f^2)$
			22 200/ 450	"	$4f5d(I) \rightarrow ^3P_2(4f^2)$
			20 800/ 480	long (μ s)	$^3P_0(4f^2) \rightarrow ^3H_4(4f^2)$

Table 1. Energies and wavelengths of transitions observed in excitation and emission spectra of the crystals investigated, emission decay times and assignment of transitions observed in the spectra.

The band appearing in the excitation spectra in the high energy region (100-150 nm) is usually characteristic of the transfer of the band to band energy to the luminescent dopant (host-sensitised or exciton luminescence). If the energy corresponds to the fundamental absorption edge of the crystal a photon of this energy can be absorbed by the host and create an electron in the conduction band and a hole in the valence band. The charge carriers can migrate separately within the lattice or together as an exciton till they reach the recombination centre. If the carriers are trapped by the dopant RE ion as a recombination centre, a part of the recombination energy can be emitted in the radiative transition. The host-sensitised luminescence is of significant intensity for some systems only. In the case of crystals investigated by us, the excitation bands at about 120 nm for YLF and for KPLF can be most probably due to the host-sensitisation of emission. The position of this band for YLF is in agreement with the position of fundamental absorption determined also by other techniques⁹. For KPLF the fundamental absorption was not known yet.

4. CONCLUSIONS

We have investigated the transitions involving the 4f5d states of Pr^{3+} ions in $\text{YAlO}_3:\text{Pr}^{3+}$ (YAP), $\text{LiYF}_4:\text{Pr}^{3+}$ (YLF) and $\text{K}_5\text{PrLi}_2\text{F}_{10}$ (KPLF) crystals. In both excitation and emission spectra of the crystals investigated the broad and intense bands due to interconfigurational 4f5d-4f transitions appear, suggesting that the $^1\text{S}_0$ multiplet of Pr^{3+} is located above the lowest levels of 4f5d states. Thus, the cascade emission does not take place in those materials. The lifetimes of emission from the 4f5d states are short, of the order of 10 ns for YAP and KPLF and about 20 ns for YLF. This is a desirable feature for possible laser oscillation in this range, as it implies high oscillator strengths and high stimulated emission cross sections.

ACKNOWLEDGEMENTS

This work was done within the frame of the DFG Graduiertenkolleg No. 463 of the University of Hamburg and HASYLAB Project No.II-99-065.

REFERENCES

1. D.L.Dexter "Possibility of Luminescence Quantum Yield Greater than Unity", *Physical Review* **108**, p. 630, 1957.
2. W.Piper, J.A.DeLuca and F.S.Ham, "Cascade fluorescent decay in Pr^{3+} -doped fluorides: Achievement of a quantum yield greater than unity for emission of visible light" *Journal of Luminescence* **8**, p. 344, 1974.
3. J.L.Sommerdijk, A.Bril and A.W.de Jager "Luminescence of Pr^{3+} -activated fluorides" *Journal of Luminescence* **8**, p. 341, 1974, and "Two photon luminescence with ultraviolet excitation of trivalent praseodymium" *Journal of Luminescence* **9**, p. 288, 1974.
4. R.T.Wegh, H.Donker, A.Meijerink, R.J.Lamminmäki and J.Hölsä "Vacuum-ultraviolet spectroscopy and quantum cutting for Gd^{3+} in LiYF_4 ", *Physical Review B*, **56**, p. 13841, 1997.
5. A.R. Gharavi and G.L.McPherson "Ultraviolet emissions from Gd^{3+} ions excited by energy transfer from pairs of photoexcited Er^{3+} ions: upconversion luminescence from CsMgCl_3 crystals doped with Gd^{3+} and Er^{3+} " *Journal of Optical Society of America B* **11**, p. 913, 1994.
6. A.M.Srivastava and W.W.Beers "Luminescence of Pr^{3+} in $\text{SrAl}_{12}\text{O}_{19}$: Observation of two photon luminescence in oxide lattice" *Journal of Luminescence* **71**, p. 285, 1997.
7. E.Bayer, J.Leppert, B.C.Grabmaier and G.Blasse "Time-resolved spectroscopy and energy transfer in Pr^{3+} -doped $\text{Gd}_2(\text{SO}_4)_3 \cdot 8\text{H}_2\text{O}$ " *Applied Physics A* **61**, p. 177, 1995.
8. R.T.Wegh and A.Meijerink "Spin-allowed and spin-forbidden $4f^0-4f^{n-1}5d$ transitions for heavy lanthanides in fluoride hosts" *Physical Review B* **60**, p. 10820, 1999.
9. J.C.Krupa and M.Queffelec, "UV and VUV optical excitations in wide band gap materials doped with rare earth ions: 4f-4d transitions" *Journal of Alloys and Compounds* **250**, p. 287, 1997.
10. J.Becker, J.Y.Gesland, N.Yu. Kirikova, J.C.Krupa, V.N.Makhov, M.Runne, M.Queffelec, T.V.Uvarova and G.Zimmerer "Fast VUV emission of rare earth ions (Nd^{3+} , Er^{3+} , Tm^{3+}) in wide bandgap crystals, *Journal of Luminescence* **78**, p. 91, 1998.
11. A.N.Belsky, P-Chevallier, J.Y.Gesland, N.Yu.Kirikova, J.C.Krupa, V.N.Makhov, P.Martin, P.A.Orekhanov and M.Queffelec "Emission properties of Nd^{3+} in several fluoride crystals" *Journal of Luminescence* **72-74**, p. 146, 1997.
12. E.G.Gumanskaya, M.V.Korzhik, S.A.Smirnova, V.B.Pawlenko and A.A.Fedorov "Interconfiguration luminescence of Pr^{3+} ions in $\text{Y}_3\text{Al}_5\text{O}_{12}$ and YAlO_3 single crystals" *Optics and Spectroscopy* **72**, p. 86, 1992.
13. J.Ehrlich, P.F.Moulton and R.M.Osgood Jr, "Optically pumped Ce:LaF₃ laser at 286nm" *Optics Letters* **5**, p. 339, 1980.
14. J.Ganem, W.M.Dennis and W.M.Yen "One-color sequential pumping of the 4f5d bands in Pr-doped yttrium aluminium garnet" *Journal of Luminescence* **54**, p. 79, 1992.
15. S.Nicolas, M.Laroche, S.Girard, R.Moncorge, Y.Guyou, M.F.Joubert, E.Descroix and A.G.Petrosyan "4f² to 4f5d excited state absorption in $\text{Pr}^{3+}:\text{YAlO}_3$ " *Journal of Physics and Condensed Matter*, **11**, p. 7937, 1999.
16. M.Laroche, A.Braud, S.Girard, J.L.Doualan, R.Moncorge, M.Thuau and L.D.Merkle "Spectroscopic investigation of the 4f5d energy levels of Pr^{3+} in fluoride crystals by excited-state absorption and two-step measurements" *Journal of Optical Society of America B* **16**, p. 2269, 1999.
17. J.K.Lawson and S.A.Payne "Excited-state absorption of Pr^{3+} -doped fluoride crystals" *Optical Materials* **2**, p. 225, 1993.
18. G.Dominiak-Dzik, I.Sokólska, S.Gołąb and M.Bałuka "Preliminary report on growth, structure and optical properties of $\text{K}_5\text{LaLi}_2\text{F}_{10}:\text{Ln}^{3+}$ ($\text{Ln}^{3+} = \text{Pr}^{3+}, \text{Nd}^{3+}, \text{Er}^{3+}$) crystals" *Journal of Alloys and Compounds* **300-301**, p. 254, 2000.
19. A.A.Kaminskii, A.G.Petrosyan, K.L.Ovanesyan and M.I.Chertanov "Stimulated emission of Pr^{3+} ions in YAlO_3 crystals" *Physica status solidi (a)* **77**, p. 173, 1983.
20. I. Sokólska, S.Gołąb, M. Bałuka and W. Ryba-Romanowski "Quenching of Pr^{3+} emission in single crystals of $\text{K}_5\text{Pr}_x\text{La}_{1-x}\text{Li}_2\text{F}_{10}$ " *Journal of Luminescence* **91**, p. 79, 2000.

Crystal field study of Gd^{3+} -doped $La_xRE_{1-x}F_3$ (RE = Ce, Pr, Nd) single crystals

Mieczysław L. Paradowski*, Lucjan E. Misiak, Wiesława Korczak, and Zbigniew Korczak

Institute of Physics, Maria Curie-Skłodowska University, Place Marii Curie-Skłodowskiej 1,
20-031 Lublin, Poland

ABSTRACT

The mixed $La_xRE_{1-x}F_3$ (RE = Ce, Pr, Nd) single crystals doped with Gd^{3+} (0.1 mol%) were grown by a modified Bridgmann-Stockbarger method. The crystal field was investigated using electron paramagnetic resonance technique. The angular dependencies of Gd^{3+} ($^8S_{7/2}$, f^7) line positions with magnetic field oriented in (001) plane were measured in the temperature range 4.2 – 295 K. The surroundings of Gd^{3+} ions were investigated analyzing spin-hamiltonian parameters in the light of the superposition model. The small distortion of the D_{3d}^4 trigonal symmetry has been observed in LaF_3 , $La_{0.9}Ce_{0.1}F_3$ and $La_{0.9}Nd_{0.1}F_3$ below 150 K. The local structure deformation of the site symmetry of Gd^{3+} ions induced by temperature starts at about 150 K becoming larger at 4.2 K. In PrF_3 the distortion was not observed in the temperature range 4.2 – 295 K. The results were compared with those of Gd^{3+} -doped $LiYF_4$ crystals.

Keywords: rare-earth trifluorides, electron paramagnetic resonance (EPR), spin-hamiltonian parameters, zero-field splitting, distortions, magnetic ordering.

1. INTRODUCTION

The $La_xRE_{1-x}F_3$ (RE = Ce, Pr, Nd) single crystals are utilized as laser materials and radiation hard scintillators for calorimetry at future colliders.¹⁻⁴ The mixed $La_xCe_{1-x}F_3$ single crystals can also be used as the filters for the vacuum ultraviolet.⁵ The single crystals doped with Gd^{3+} (0.1 mol%) were grown by a modified Bridgmann-Stockbarger method described elsewhere.^{6,7} The $^8S_{7/2}$ ground term of the Gd^{3+} ion in these single crystals is split by the crystalline electric field into four Kramers doublets. It is important to know how the crystal field splits this term at various temperatures. The small distortion from the D_{3d}^4 trigonal space group, caused by the strong influence of the crystalline field, was observed in $La_xCe_{1-x}F_3$ and $La_xNd_{1-x}F_3$ single crystals using magnetic susceptibility method.^{8,9} A small change of the crystal field in $La_{0.9}Nd_{0.1}F_3$ with lowering temperature, as a result of temperature induced distortion of the crystal lattice (which caused a change in site symmetry of Gd^{3+} ions from C_{2v} at 77 K towards C_2 at 4.2 K) was observed in our most recent works.^{7,10,11}

The purpose of the present paper is to study the crystal field in all samples at different temperatures using Electron Paramagnetic Resonance (EPR) technique and superposition model, because they are very sensitive to the distortion of the crystal lattice. Therefore surroundings of Gd^{3+} ions in the trigonal symmetry D_{3d}^4 with a hexamolecular unit cell were investigated. The spin-hamiltonian parameters (SHP) are analyzed in the light of the superposition model. Previously we studied local deformation in $La_{0.9}Nd_{0.1}F_3$ single crystal.^{7,11} Further, we extended the EPR measurements to temperatures covering the range 4.2 – 295 K in all chosen samples. The negative g shift of Gd^{3+} -doped $La_{0.9}Ce_{0.1}F_3$ and $La_{0.9}Nd_{0.1}F_3$ from that in the isostructural diamagnetic host LaF_3 indicates the antiferromagnetical ordering of Gd^{3+} -Ce³⁺ and Gd^{3+} -Nd³⁺ pairs.

2. CRYSTAL FIELD STUDY

The crystal field study has been performed by analyzing SHP's for Gd^{3+} -doped LaF_3 , $La_{0.9}Ce_{0.1}F_3$, $La_{0.9}Nd_{0.1}F_3$ and PrF_3 single crystals in the temperature range 4.2 – 295 K, using the superposition model.^{7,11} The above samples are the only crystals studied in detail for which well-resolved EPR spectra can be recorded down to liquid-helium temperature. Details of EPR measurements can be found elsewhere.¹¹ typical example of the spectrum and magnetic splitting of four Kramers

* Corresponding author: Email: mlpar@tytan.umcs.lublin.pl; Telephone: +48-81-5376281; Fax: +48-81-5376191

doublets are presented in Fig. 1. The zero-field splitting (ZFS) of Gd^{3+} is defined as $\Delta E = E(\pm 7/2) - E(\pm 1/2)$ at magnetic field $B = 0$. The ZFS was determined on the basis of nine SHP's and plotted in Fig. 2. It can be seen that ZFS depends on the temperature as a parabolic function. The ZFS reaches maximum value at about 150 K for LaF_3 , $La_{0.9}Ce_{0.1}F_3$ and $La_{0.9}Nd_{0.1}F_3$, whereas for PrF_3 the ZFS is increasing monotonically with lowering temperature down to 4.2 K.¹² In order to explain such behavior of ZFS, the intrinsic parameter b_2 ($m = 0$) should be taken into consideration.¹¹ The ZFS and SHP varied linearly with the intrinsic parameter as determined from the superposition model. The intrinsic parameters b_2 for Gd^{3+} -doped samples in the temperature range 4.2 – 295 K are plotted in Fig. 3. The b_2 reaches minimum of negative values at about 150 K for LaF_3 , $La_{0.9}Ce_{0.1}F_3$ and $La_{0.9}Nd_{0.1}F_3$, whereas for PrF_3 and $LiYF_4$ its negative values are continuously decreasing with decreasing temperature. The intrinsic parameter depends only on R_0 (the minimum distance between $Gd^{3+} - F^-$ ions corresponding to the 2-3 F^- pairs^{7,11}). The R_0 's depend on temperature similar to lattice constants⁶ and reach minimum value at liquid-nitrogen temperature for Gd^{3+} -doped LaF_3 , $La_{0.9}Ce_{0.1}F_3$ and $La_{0.9}Nd_{0.1}F_3$ (Fig. 4). On the other hand, for PrF_3 and $LiYF_4$ the R_0 is decreasing with decreasing temperature from 295 K to 4.2 K. Since the intrinsic parameter depends only on the R_0 , it can be plotted versus R_0 (Fig. 5). The slightly change of R_0 with decreasing temperature causes drastic increase of b_2 in the temperature range below 150 K. Such behavior of the intrinsic parameter explains changes of SHP and ZFS. On the other hand, in PrF_3 and $LiYF_4$ there are not any drastic changes of the intrinsic parameter b_2 with R_0 . Generally, the behavior is due to monotonic decrease of R_0 with temperature down to liquid-helium. We think that different behavior of the investigated samples is caused by critical temperature of the intrinsic parameter. The critical temperature of the intrinsic parameter does not depend on the structure of crystal lattice but individual character of lattice – the site symmetry of Gd^{3+} ion that is changed with temperature, as a result of temperature induced distortion of crystal lattice.

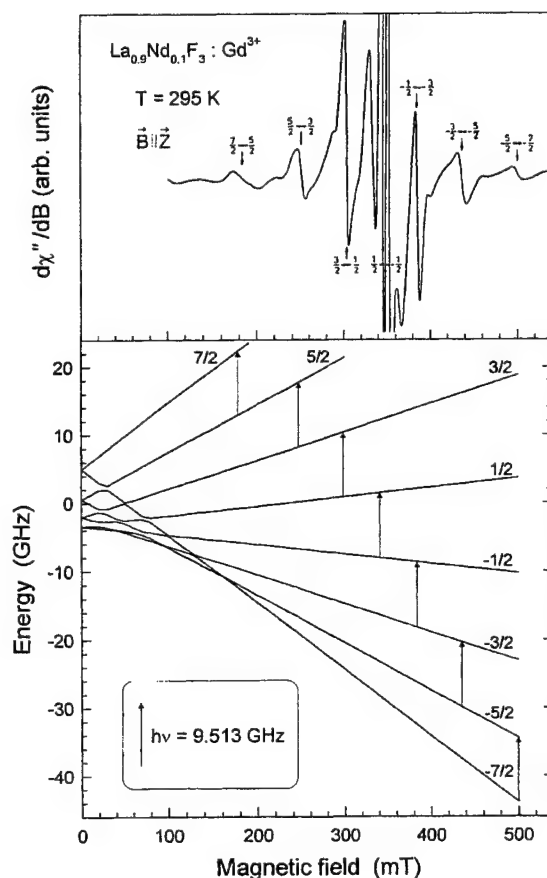


Fig. 1. EPR spectrum and energy levels of Gd^{3+} -doped $La_{0.9}Nd_{0.1}F_3$ single crystal at $T = 295$ K with $B \parallel Z$ (a -axis).

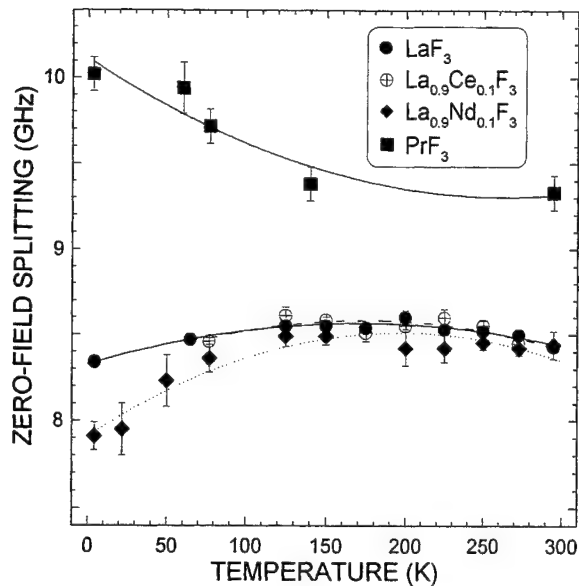


Fig.2. Temperature dependence of ZFS for Gd^{3+} -doped LaF_3 , $La_{0.9}Ce_{0.1}F_3$, $La_{0.9}Nd_{0.1}F_3$ and PrF_3 single crystals.

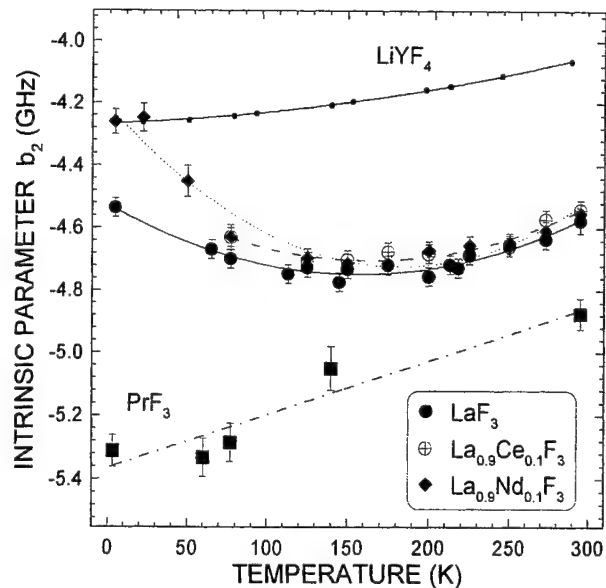


Fig. 3. Temperature dependence of the intrinsic parameter b_2 for Gd^{3+} -doped LaF_3 , $La_{0.9}Ce_{0.1}F_3$, $La_{0.9}Nd_{0.1}F_3$, PrF_3 and $LiYF_4$ ¹² single crystals.

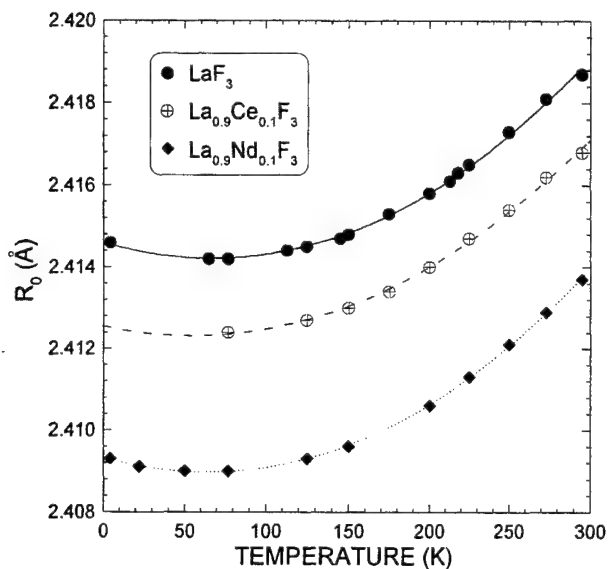


Fig. 4. Temperature dependence of the minimum distance R_0 between $Gd^{3+} - F^-$ ions corresponding to the 2-3 F^- pairs^{7,11} in LaF_3 , $La_{0.9}Ce_{0.1}F_3$, $La_{0.9}Nd_{0.1}F_3$ single crystals.

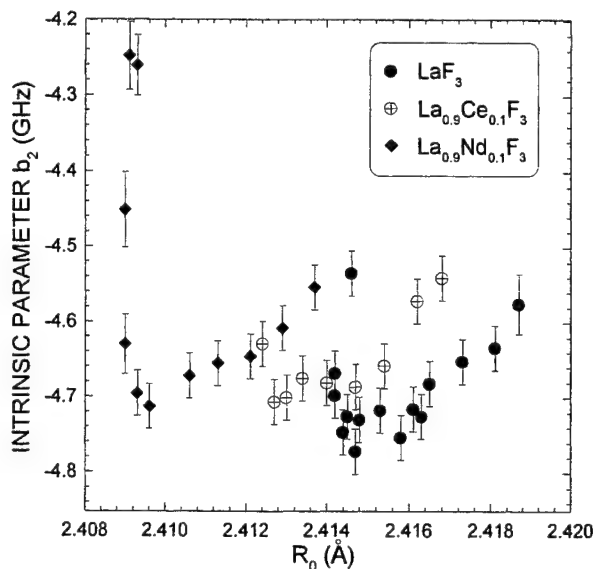


Fig. 5. The plot of the intrinsic parameter versus R_0 for Gd^{3+} -doped LaF_3 , $La_{0.9}Ce_{0.1}F_3$ and $La_{0.9}Nd_{0.1}F_3$ single crystals.

3. CONCLUSIONS

New insight into the intrinsic parameter b_2 has been performed using superposition model. The critical temperature for intrinsic parameter has been proposed. The intrinsic parameter is very sensitive to the distortion of the site symmetry of Gd^{3+} ions. Although the variation of the distortion is small, it has a drastic effect on the intrinsic parameter b_2 . The small distortion of the D_{3d}^4 trigonal symmetry has been observed in LaF_3 , $La_{0.9}Ce_{0.1}F_3$ and $La_{0.9}Nd_{0.1}F_3$ below 150 K. Further, the distortion of the local site symmetry of Gd^{3+} ions from C_{2v} towards C_2 starts at 150 K and continuously increases with temperature decreasing down to 4.2 K, whereas in PrF_3 the distortion was not observed in the temperature range 4.2 – 295 K.

REFERENCES

1. E. Auffray et al., "Extensive studies on CeF_3 crystals, a good candidate for electromagnetic calorimetry at future accelerators" *Nucl. Instrum. Methods Phys. Res. A* **383**, pp. 367-390, 1996.
2. P. Dorenbos, J.T.M. De Haas and C.W.E. Van Eijk, "The intensity of the 173 nm emission of $LaF_3 : Nd^{3+}$ scintillation crystals" *J. Lumin.* **69**, pp. 229-233, 1996.
3. A. A. Kaminskii and H.R. Verdun, "New room-temperature diode-laser-pumped CW lasers based on Nd^{3+} -ion doped crystals" *Phys. Stat. Sol. A* **129**, pp. K119-124, 1992.
4. D. Neogy and T. Purohit, "The behavior of active centers in a laser host" *Phys. Stat. Sol. B* **131**, pp. 329-338, 1985.
5. L. R. Elias, R. Flach and W. M. Yen, "Variable bandwidth transmission filter for the vacuum ultraviolet: $La_{1-x}Ce_xF_3$ " *Appl. Optics* **12**, pp. 138-139, 1973.
6. W. Korczak and P. Mikołajczak, "Crystal growth and temperature variation of the lattice parameters in LaF_3 , CeF_3 , PrF_3 and NdF_3 " *J. Crystal Growth* **61**, pp. 601-605, 1983.
7. M. L. Paradowski, W. Korczak, L.E. Misiak and Z. Korczak, "Growth and investigation of $La_xRE_{1-x}F_3$ ($RE = Ce, Pr, Nd$) single crystals," in *International Conference on Solid State Crystals '98: Single Crystal Growth, Characterization, and Applications*, edited by A. Majchrowski and J. Zieliński, Vol. **3724**, pp. 47-51, SPIE – The International Society for Optical Engineering, Washington, 1999.
8. M. L. Paradowski, A. W. Pacyna, A. Bombik, W. Korczak and S. Z. Korczak, "Magnetic susceptibility of $La_xCe_{1-x}F_3$ single crystals" *J. Magn. Magn. Mater.* **212**, pp. 381-388, 2000.
9. M. L. Paradowski, A. W. Pacyna, A. Bombik, W. Korczak and S. Z. Korczak, "Magnetic susceptibility of $La_xNd_{1-x}F_3$ single crystals" *J. Magn. Magn. Mater.* **166**, pp. 231-236, 1997.
10. M. L. Paradowski and L.E. Misiak, "EPR study of Gd^{3+} in $La_{0.9}Nd_{0.1}F_3$ single crystal" *Nukleonika* **42**, pp. 543-550, 1997.
11. M. L. Paradowski and L.E. Misiak, "EPR of Gd^{3+} -doped $La_{0.9}Nd_{0.1}F_3$ crystal: spin-phonon interactions and spin-lattice relaxations" *Acta Phys. Pol. A* **95**, pp. 367-380, 1999.
12. L. E. Misiak, S. K. Misra and P. Mikołajczak, "EPR of Gd^{3+} -doped single crystals of $LiY_{1-x}Yb_xF_4$ " *Phys. Rev. B* **38**, pp. 8673-8682, 1988.

PIXE and magnetic investigations of $\text{La}_x\text{RE}_{1-x}\text{F}_3$ (RE = Ce, Nd) single crystals

Mieczysław L. Paradowski*, Mirosław Kulik, Wiesława Korczak
and Zbigniew Korczak

Institute of Physics, Maria Curie-Skłodowska University, Place Marii Curie-Skłodowskiej 1,
20-031 Lublin, Poland

ABSTRACT

The mixed $\text{La}_x\text{RE}_{1-x}\text{F}_3$ (RE = Ce, Nd) single crystals doped with Gd^{3+} (0.1 mol%) were grown by a modified Bridgmann-Stockbarger method. The PIXE (Proton Induced X ray Emission) method was used to the determination of a composition x of this material. The value of x for these samples does not differ more than 2.5 % and 7.5 % in $\text{La}_x\text{Ce}_{1-x}\text{F}_3$ and $\text{La}_x\text{Nd}_{1-x}\text{F}_3$ respectively, from the assumed one. In addition, concentrations of the doped rare earth atoms were controlled by XRF (X-Ray Fluorescence) method. The abundance of other than Gd^{3+} rare earth impurities was estimated to be below 0.058 at. %.

The magnetic susceptibility of the single crystals was measured in the temperature range 4 – 300 K, in a magnetic field $B = 0.2$ T applied in the crystallographic plane (001) perpendicular to the c -axis (along the a -axis), using the Faraday method. The magnetic susceptibility measurements confirm the lack of Ce^{3+} and Nd^{3+} clusters in the diluted crystals. The effective spins of hosts Ce^{3+} and Nd^{3+} are equal to 1/2 in the temperature range 4 – 300 K.

Keywords: rare-earth trifluorides, PIXE (Proton Induced X ray Emission), magnetic susceptibility, effective spin.

1. INTRODUCTION

The $\text{La}_x\text{RE}_{1-x}\text{F}_3$ (RE = Ce, Nd) single crystals doped with Gd^{3+} (0.1 mol%) were grown by a modified Bridgmann-Stockbarger method described elsewhere.^{1,2} Previously we studied defects and distortions of crystal cells in the same samples.^{2,3} Applying any technology to grow single crystals by cooling slowly the initially homogeneous liquid material (e.g. Bridgmann-Stockbarger method) one obtains a samples of different composition along the direction of crystallization. So it is important to know exactly a composition x of the investigated single crystals, which could be different from nominal one. Therefore we used the PIXE (Proton Induced X ray Emission) method in order to confirm the composition x . In addition the value x of the investigated samples was controlled using the XRF (X Ray Fluorescence) method. It is also important to know how the magnetic Ce^{3+} and Nd^{3+} ions are distributed on the lattice of the single crystals diluted with diamagnetic La^{3+} ions. For this purpose we used magnetic susceptibility method.

2. PIXE INVESTIGATION

The PIXE method was used to the determination of a composition x of the crystals. In this experiment X ray was induced by beam of 2.5 MeV protons from Van de Graaf accelerator in JINR, Dubna. The Si (Li) X ray detector with an energy resolution about 220 eV at 6.4 keV was used in that measurements. Typical PIXE spectra of the some investigated samples are presented in Figs. 1 and 2. Relationship between the concentration of RE (Rare Earth) was found by dividing of the corresponding squares for $K - X$ ray peaks, assuming equality of inducing efficiency and detection one. The composition x of the investigated samples does not differ more than 2.5 % and 7.5 % in $\text{La}_x\text{Ce}_{1-x}\text{F}_3$ and $\text{La}_x\text{Nd}_{1-x}\text{F}_3$ respectively, from the assumed one. In addition the composition x of the investigated samples was controlled using the XRF method. The abundance of other than Gd^{3+} rare earth impurities was estimated to be below 0.058 at. %. The results are summarised in Tables 1 and 2.

* Corresponding author: Email: mlpar@tytan.umcs.lublin.pl; Telephone: +48-81-5376281; Fax: +48-81-5376191

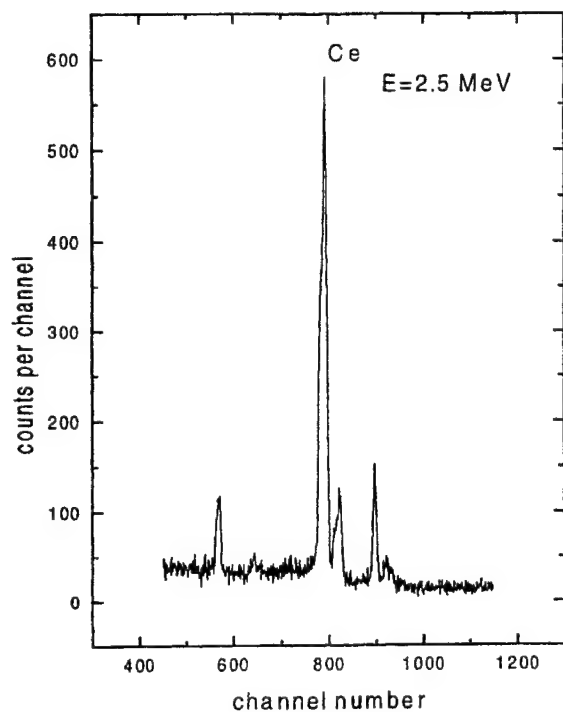


Fig.1. PIXE spectrum of the $\text{La}_{0.8}\text{Ce}_{0.2}\text{F}_3$ single crystal

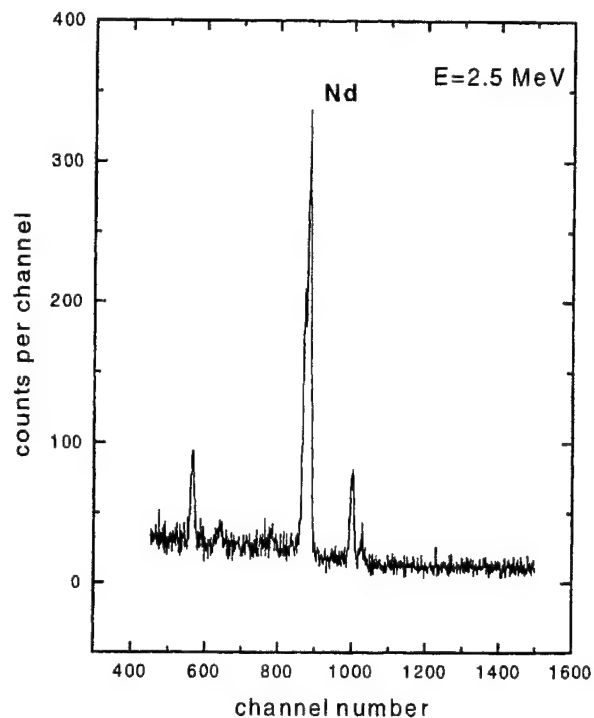


Fig.2. PIXE spectrum of the $\text{La}_{0.01}\text{Nd}_{0.99}\text{F}_3$ single crystal

Table 1. The composition of $\text{La}_x\text{Ce}_{1-x}\text{F}_3$ single crystals determined by PIXE method.

x	La (at.%)	Ce (at.%)
0.00	0.000	100.000
0.50	51.125	48.875
0.60	59.200	40.800
0.80	79.700	20.300
0.90	89.750	10.250
0.95	94.900	5.100
1.00	100.000	0.000

Table 2. The composition of $\text{La}_x\text{Nd}_{1-x}\text{F}_3$ single crystals obtained with the help of PIXE method.

x	La (at.%)	Nd (at.%)
0.00	0.000	100.000
0.01	1.075	98.925
0.02	2.100	97.900
0.05	5.225	94.775
0.10	10.400	89.600
0.90	89.600	10.400
0.95	94.825	5.175
0.98	97.935	2.065
0.99	98.970	1.030
1.00	100.000	0.000

3. MAGNETIC INVESTIGATIONS

The magnetic susceptibility of the $\text{La}_x\text{RE}_{1-x}\text{F}_3$ ($\text{RE} = \text{Ce}, \text{Nd}$) single crystals was measured in the temperature range from 4 K to 300 K using the Faraday method. In this experiment the magnetic field $B = 0.2$ T was applied in the crystallographic plane (001) perpendicular to the c -axis (along the a -axis). At these temperatures the single crystals remain paramagnetic for the all values of x in the range from 0 to 1.^{4,5} The crystal field effects and dipolar interactions between RE^{3+} ions influence significantly the magnetic susceptibility. The magnetic susceptibility of the investigated samples follows a Curie-Weiss law in the temperature range 100 – 300 K. The Curie-Weiss law parameters were given in our earlier works.^{4,5} Therefore the Curie constant C and the paramagnetic Curie temperature θ_p can be plotted as a function of x . The plots are presented in Figs. 3a and 3b. The Curie constant C and Curie-Weiss temperature θ_p scale linearly with x . It argues that the distribution of the magnetic Ce^{3+} and Nd^{3+} ions on the lattice is truly random – Ce^{3+} and Nd^{3+} host ions do not form the clusters. In addition magnetic study of the crystals revealed that the effective spins of hosts Ce^{3+} and Nd^{3+} are equal to 1/2 in the temperature range 4 – 300 K.^{2,4,5}

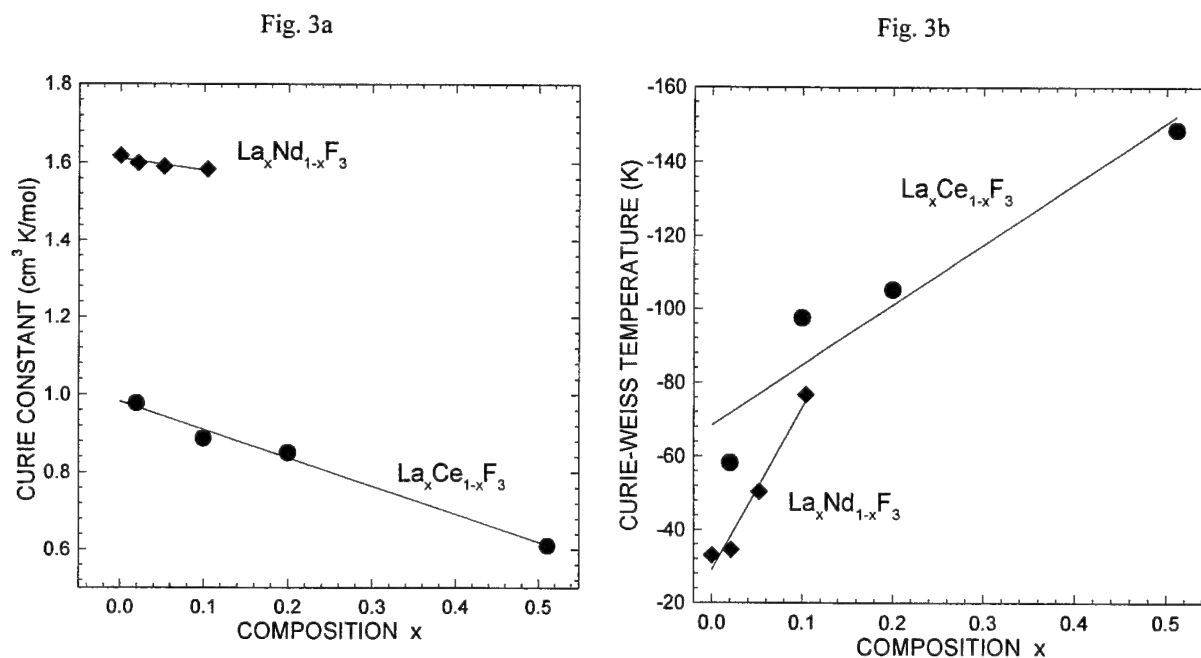


Fig. 3. The dependence of the Curie constant C and the Curie-Weiss temperature θ_p on composition x .

4. CONCLUSIONS

We have examined the composition x and the distribution of the magnetic Ce and Nd ions on the crystal lattice of the mixed $\text{La}_x\text{RE}_{1-x}\text{F}_3$ ($\text{RE} = \text{Ce}, \text{Nd}$) single crystals. The results confirm the good agreement with the earlier predictions of the composition and distribution of the magnetic Ce and Nd ions.

It can also be concluded that the effective spins of hosts Ce^{3+} and Nd^{3+} ions are equal to 1/2 in the investigated temperature range from 4 K to 300 K.

ACKNOWLEDGEMENTS

The authors would like to express their thanks to Dr A.P. Kobzev from Joint Institute for Nuclear Research, Dubna, Russia for the help with the investigations of PIXE, and also Mr. T. Wójcicki (Institute of Chemistry, Maria Curie-Skłodowska University, Lublin) for XRF analysis of the samples.

REFERENCES

1. W. Korczak and P. Mikołajczak, "Crystal growth and temperature variation of the lattice parameters in LaF_3 , CeF_3 , PrF_3 and NdF_3 ," *J. Crystal Growth* **61**, pp. 601-605, 1983.
2. M. L. Paradowski, W. Korczak, L.E. Misiak and Z. Korczak, "Growth and investigation of $\text{La}_x\text{RE}_{1-x}\text{F}_3$ (RE = Ce, Pr, Nd) single crystals," in *International Conference on Solid State Crystals '98: Single Crystal Growth, Characterization, and Applications*, edited by A. Majchrowski and J. Zieliński, Proceedings of SPIE Vol. **3724**, pp. 47-51, SPIE – The International Society for Optical Engineering, Washington, 1999.
3. M. L. Paradowski and L.E. Misiak, "EPR of Gd^{3+} -doped $\text{La}_{0.9}\text{Nd}_{0.1}\text{F}_3$ crystal: spin-phonon interactions and spin-lattice relaxations" *Acta Phys. Pol. A* **95**, pp. 367-380, 1999.
4. M. L. Paradowski, A. W. Pacyna, A. Bombik, W. Korczak and S. Z. Korczak, "Magnetic susceptibility of $\text{La}_x\text{Ce}_{1-x}\text{F}_3$ single crystals" *J. Magn. Magn. Mater.* **212**, pp. 381-388, 2000.
5. M. L. Paradowski, A. W. Pacyna, A. Bombik, W. Korczak and S. Z. Korczak, "Magnetic susceptibility of $\text{La}_x\text{Nd}_{1-x}\text{F}_3$ single crystals" *J. Magn. Magn. Mater.* **166**, pp. 231-236, 1997.

Non-linear I-V characteristics and threshold switching in As-Te-In glasses

Devaraju J T^a, Sharmila B H^b, Acharya K V^a, Asokan S^{b*} and Gopal E S R^c

^aDepartment of Electronics, Bangalore University, Bangalore 560056, India

^bDepartment of Instrumentation, Indian Institute of Science, Bangalore
560012, India

^cDepartment of Physics, Indian Institute of Science, Bangalore 560012, India

ABSTRACT

Non-linear I-V behaviour and electrical switching exhibited by chalcogenide glassy semiconductors, find applications in variety of areas including information storage and power control. In this work, semiconducting chalcogenide $\text{As}_{40}\text{Te}_{60-x}\text{In}_x$ glasses ($7.5 \leq x \leq 16.5$) have been prepared by melt quenching technique. The current-voltage and electrical switching behaviour of these glasses have been studied using a custom-built PC based system. The results obtained clearly indicate that all the glasses studied exhibit current controlled negative resistance behaviour, which leads to the low resistance state. The switching to the low resistance state is found to be reversible (threshold behaviour) and the samples revert back to the high resistance state on reducing the current. Threshold switching over such a wide range of compositions has been observed only in very few systems so far. The most interesting outcome of the present studies is the variation of the switching voltage with composition. It is observed that there is an increase in the switching voltage (threshold voltage) V_t with the increase in indium concentration in the composition range $7.5 \leq x \leq 12.5$. Further, the composition dependence of switching field is found to exhibit a distinct change in slope at $x=12.5$ (mechanical threshold) and V_t continues to increase with x until $x=13.5$. Around $x=13.5$, the trend is reversed and V_t starts decreasing with x . A minimum in V_t is seen around the composition $x=14.3$, which corresponds to the chemical threshold of the As-Te-In system. Beyond $x=14.3$, switching voltage is found to increase with composition again. The present results are consistent with earlier observations, which indicate the composition dependence of switching voltages of chalcogenide glasses are influenced by chemical ordering and rigidity percolation.

1. INTRODUCTION

Electrical switching in chalcogenide glasses was first observed by Ovshinsky,¹ when an appropriate electric field known as the threshold or the critical field (E_t) is applied, the glass switches from a semiconducting OFF state to a conducting ON state. Chalcogenide glasses, which exhibit switching, are classified into memory (irreversible) or threshold (reversible) types. Threshold-switching glasses revert to the OFF state upon the removal of the switching field, whereas memory switches remain locked to the ON state.

The relation between the electrical switching and the network topological thresholds of chalcogenide glasses, has been a topic of interest in the recent times.²⁻⁴ Theoretical investigations have revealed the existence of two topological effects namely, Rigidity Percolation and Chemical Ordering in chalcogenide glasses. The rigidity percolation deals with dimensionality and rigidity of a glassy network and is decided by the average co-ordination number $\langle r \rangle$ of the glass. The constraint theory of Phillips and Thorpe⁵ proposes that in a chalcogenide network glass, at an average critical co-ordination $\langle r_c \rangle$, a mechanical equilibrium is established. At $\langle r_c \rangle$, the degrees of freedom per atom and the number of constraints acting on it become equal.^{6,7} Chalcogenide network glasses with $\langle r \rangle < \langle r_c \rangle$ are under constrained and are elastically floppy, whereas glasses with $\langle r \rangle > \langle r_c \rangle$ are over constrained and rigid. The composition corresponding to $\langle r_c \rangle$ is known as the Rigidity Percolation Threshold (RPT) or mechanical threshold (MT) of the glass. For a glassy network with purely covalent bonding, rigidity percolation occurs at a mean co-ordination number $\langle r_c \rangle = 2.4$. However, it is pointed out that if ionic interactions are taken into account, the percolation threshold may shift to higher $\langle r \rangle$ values.^{8,9}

At a composition known as the chemical threshold (CT), a chalcogenide glass is considered to be chemically ordered consisting of only heteropolar bonds.¹⁰ The chemical threshold is expected to occur at a mean co-ordination $\langle r \rangle = 2.67$.¹¹

Anomalies in various properties of chalcogenide glasses have been observed at the Rigidity Percolation and Chemical thresholds.¹²⁻¹⁷ In this work, an attempt is made to understand the effect of topological thresholds on the switching behaviour of As-Te-In glasses.

2. EXPERIMENTAL

Bulk semiconducting $\text{As}_{40}\text{Te}_{60-x}\text{In}_x$ ($7.5 \leq x \leq 16.5$; $2.55 \leq \langle r \rangle \leq 2.73$), glasses have been prepared by melt quenching method. The amorphous nature of the quenched samples is confirmed by X-ray diffraction. The I-V characteristic of these glasses is studied using a custom built PC based system.¹⁸ Samples polished to different thickness are mounted between a flat plate and a point contact electrode using a spring loading mechanism. A constant current is passed through the sample and the voltage developed across the sample and corresponding current through the sample is measured.

3. RESULTS AND DISCUSSION

Figure 1-2 shows the current-voltage characteristics of all composition studied in the composition tie line $\text{As}_{40}\text{Te}_{60-x}\text{In}_x$ glasses for 0.28mm thick samples. It can be seen from figure 1-2 that all the $\text{As}_{40}\text{Te}_{60-x}\text{In}_x$ glasses exhibit non-linear I-V characteristics and switching above a critical voltage V_t . Further, the samples revert back to the high resistance OFF state on reducing the current (threshold switching behaviour).

Figure 3 shows the variation of the switching (threshold) voltage V_t as a function of composition (x)/average co-ordination number ($\langle r \rangle$) for $\text{As}_{40}\text{Te}_{60-x}\text{In}_x$ glasses for 0.28mm thick samples. It can be seen from figure 3 that V_t increases linearly with increase in indium content in the range $2.55 \leq \langle r \rangle \leq 2.65$ ($7.5 \leq x \leq 12.5$). At $\langle r \rangle = 2.65$ ($x=12.5$), a sharp slope change (lower to higher) is seen in the $\langle r \rangle$ dependence of V_t . Above $\langle r \rangle = 2.65$, V_t continues to increase, until a reversal in trend is observed around $\langle r \rangle = 2.67$ ($x=13.5$). Subsequently, V_t decreases with $\langle r \rangle$, reaching a minimum around $\langle r \rangle = 2.69$ ($x=14.3$). Beyond $\langle r \rangle = 2.69$, V_t increases with composition again.

In chalcogenide glasses, the composition dependence of switching voltage/field is determined by factors such as co-ordination of the additive element, rigidity percolation, chemical ordering, etc. Metallic dopants usually take up 4-fold co-ordination in chalcogenide glasses¹⁹ and based on a co-ordination of four for indium, it can be concluded that the network connectivity and rigidity increases with indium concentration. The increase in the switching voltages with $\langle r \rangle$ in the range 2.55–2.65, can be associated with the increase in network connectivity and rigidity percolation. Further, the mean co-ordination $\langle r \rangle = 2.65$ at which a slope change is seen in V_t is likely to correspond to the RPT of the As-Te-In system. A similar increase in V_t and the slope change in the composition dependence of V_t at RPT, have been observed earlier in many other chalcogenide.^{2,3,20}

Usually, non-covalent interactions in a covalent network¹¹ shift the rigidity percolation threshold from its ideal value of 2.4, to higher values of $\langle r \rangle$. The four fold or higher co-ordination of metallic atoms in a chalcogenide network demands partially ionic bonding, which explains the shifting in the RPT to $\langle r \rangle = 2.65$ in As-Te-In samples.

Above $\langle r \rangle = 2.65$, the switching voltages of As-Te-In glasses can be expected to exhibit a continued increase with $\langle r \rangle$. The observed turn-around in the switching voltage of As-Te-In glasses around $\langle r \rangle = 2.67$ occurs due to the onset of chemical ordering. With increasing chemical order, the charge carriers are likely to be less localised. The increased conductivity aids switching, leading to a reduction in switching voltage. Further, the minimum seen in the threshold fields of As-Te-In samples at the mean co-ordination number $\langle r \rangle = 2.69$ can be taken as an indication of a possible chemical threshold at the corresponding composition. A local minimum in V_t at CT has been reported earlier in other systems such as Ge-As-Te.³

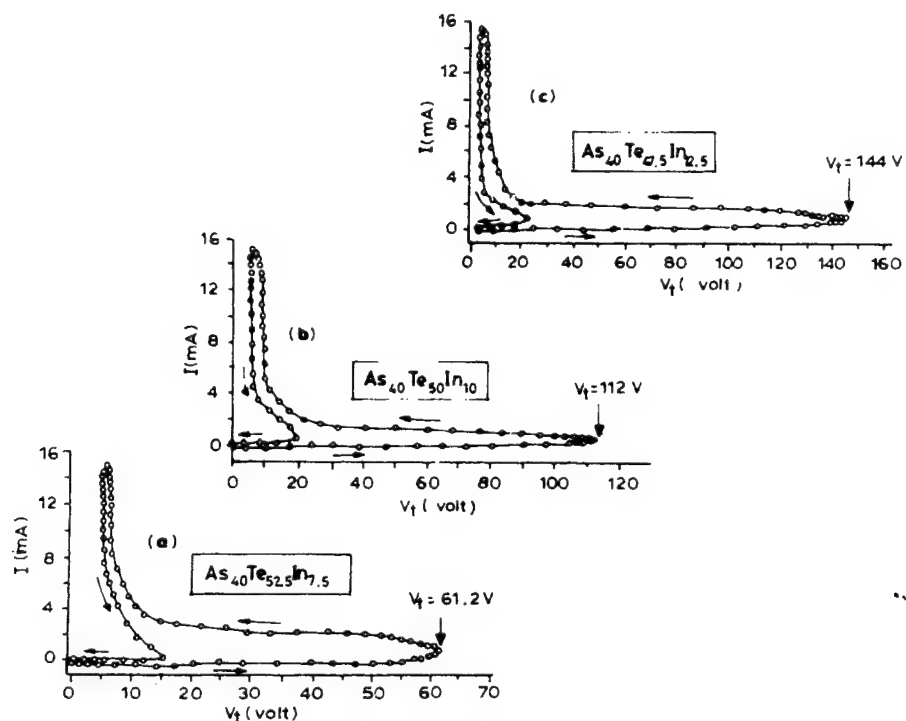


Figure 1. I - V characteristics of $\text{As}_{40}\text{Te}_{60-x}\text{In}_x$ glasses with (a) $x=7.5$, (b) $x=10$ and (c) $x=12.5$.

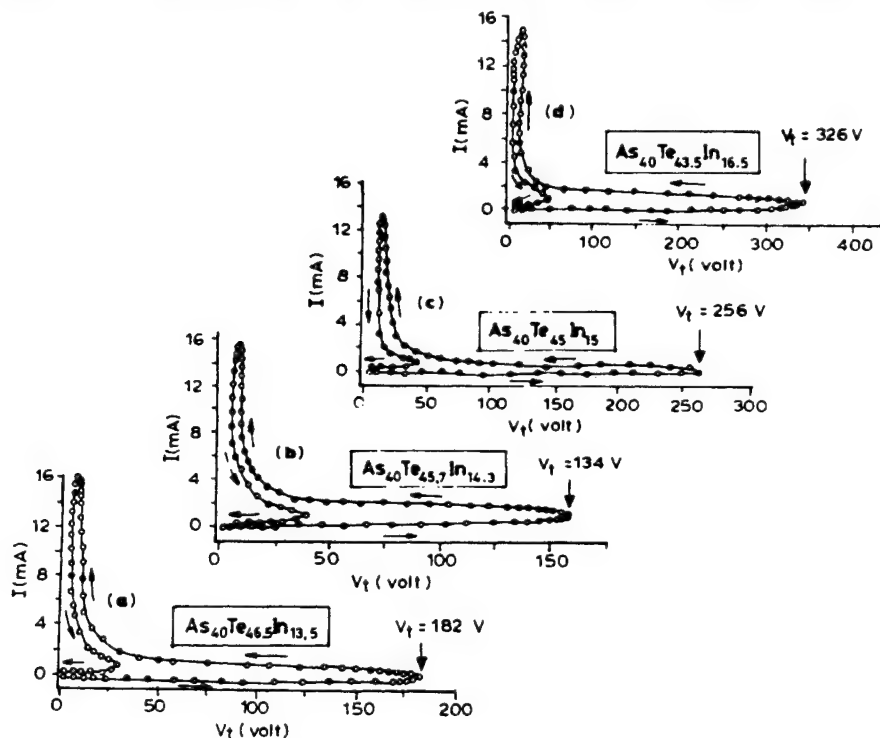


Figure 2. I - V characteristics of $\text{As}_{40}\text{Te}_{60-x}\text{In}_x$ glasses with (a) $x=13.5$, (b) $x=14.3$, (c) $x=15$ and (d) $x=16.5$.

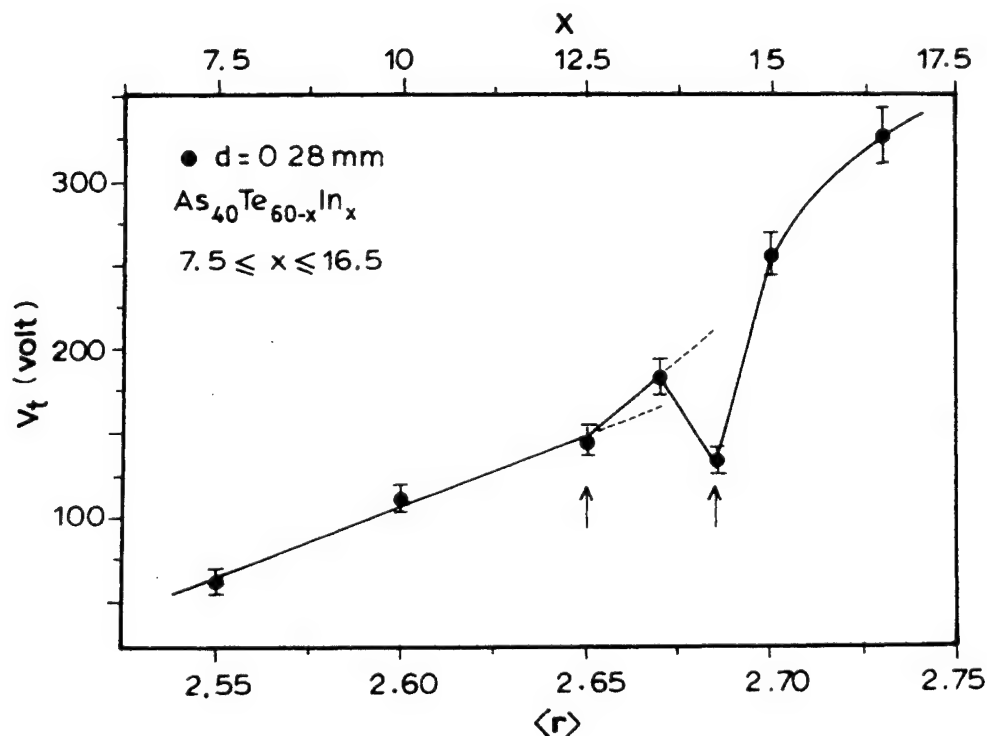


Figure. 3. The compositional dependence of switching voltages of $\text{As}_{40}\text{Te}_{60-x}\text{In}_x$ ($7.5 < x < 16.5$) glasses.

4. CONCLUSION

Bulk $\text{As}_{40}\text{Te}_{60-x}\text{In}_x$ glasses ($7.5 \leq x \leq 16.5$) have been found to exhibit threshold switching over a wide range of composition. The composition dependence of switching fields with indium concentration bears the signatures of rigidity percolation and chemical ordering at $\langle r \rangle = 2.65$ and $\langle r \rangle = 2.69$ respectively.

REFERENCES

1. S. R. Ovshinsky, "Reversible electrical switching phenomena in disordered structures," *Phys. Rev. Lett.* **21**, pp.1450-1453, 1968.
2. S. S. K. Titus, R. Chatterjee, S. Asokan and A. Kumar, "Electrical switching and short-range order in As-Te glasses," *Phys. Rev. B* **48**, pp.14650-14652, 1993.
3. R. Aravinda Narayanan, S. Asokan and A. Kumar, "Evidence concerning the effect of topology on electrical switching in chalcogenide network glasses," *Phys. Rev. B* **54**, pp.4413-4415, 1996.
4. R. Aravinda Narayanan, S. Asokan and A. Kumar, "Influence of chemical disorder on electrical switching in chalcogenide glasses," *Phys. Rev. B* **2000**, (Submitted).

5. J. C. Phillips and M. F. Thorpe, "Constraint theory, vector percolation and glass formation," *Solid St. Commun.* **53**, pp.699-702, 1985.
6. H. He and M. F. Thorpe, "Elastic properties of glasses," *Phys. Rev. Lett.* **54**, pp.2107-2110, 1985.
7. P. Boolchand and M. F. Thorpe, "Glass-forming tendency, percolation of rigidity, and onefold-coordinated atoms in covalent networks," *Phys. Rev. B* **50**, pp.10366-10368, 1994.
8. K. Tanaka, "Structural phase transitions in chalcogenide glasses," *Phys. Rev. B* **39**, pp.1270-1279, 1989.
9. K. Tanaka, "Layer structure in chalcogenide glasses," *J. Non-Cryst. Solids*, **103**, pp.149-150, 1988.
10. G. L  covsky and T. M. Hayes, "Short-range order in amorphous semiconductor," in *Amorphous Semiconductors*, edited by M. H. Brodsky, vol. 36, pp.215-250, Springer-Verlag, Berlin, Heidelberg, Newyork, 1979.
11. R. Aravinda Narayanan and A. Kumar, " Unified approach to the constraint counting theory of glasses," *Phys. Rev. B* **60**, pp.11859-11862, 1999.
12. S. Asokan, M. V. N. Prasad, G. Parthasarthy and E. S. R. Gopal, "Mechanical and chemical threshold in IV-VI chalcogenide glasses," *Phys. Rev. Lett.* **62**, pp.808-810, 1989.
13. S. Mahadevan, A. Giridhar and A. K. Singh, "Volumetric effect of topological in chalcogenide glass system," *J. Non-Cryst. Solids*, **169**, pp.133-142, 1993.
14. A. K. Varshneya, A. N. Sreeram and D. R. Swiler, "A review of the average coordination number concept in multicomponent chalcogenide glass system," *Phys. Chem. Glasses*, **34**, pp.179-192, 1993.
15. U. Senapati and A. K. Varshneya, "configurational arrangements in chalcogenide glasses: a new perspective on Phillips,' constraint theory," *J. Non-Cryst. Solids*, **185**, pp.289-296, 1995.
16. B. Uebbing and A. J. Sievers, "Role of network topology on the vibrational lifetime of an H₂O molecule in the Ge-As-Se Glass series," *Phys. Rev. Lett.*, **76**, pp.932-935, 1996.
17. X. Feng, W. J. Bresser and P. Boolchand, "Direct evidence for stiffness threshold in chalcogenide glasses," *Phys. Rev. Lett.*, **78**, pp.4422-4425, 1997.
18. R. Chatterjee, K. V. Acharya, S. Asokan and S. S. K Titus, "A PC-based system for studying current-controlled electrical switching in solids," *Rev. Sci. Instrum.* **65**, pp.2382-2387, 1994.
19. K. Ramesh, S. Asokan, K. S. Sangunni and E. S. R. Gopal, "Glass formation in germanium telluride glasses containing metallic additives," *J. Phys. Chem. Solids*, **61**, pp.95-101, 2000.
20. C. Nagaraja Murthy, "Development of an electrical switching analyzer and investigation on the switching behaviour of certain telluride glassy semiconductors," *Ph.D. Thesis, Indian Institute of Science Bangalore*, 1999.

Irradiation effect on the pinning potential of YBCO single crystal

Sergei N. Barilo, Valentina I. Gatalskaya*, Gennadii V. Gatalskii, and Sergei L. Kurochkin

Institute of Solid State and Semiconductor Physics, National Academy of Sciences,
Minsk, P. Brovki st., 17, 220072 Belarus

ABSTRACT

The results of the magnetization measurements of single crystal of $\text{YBa}_2\text{Cu}_3\text{O}_y$ with $T_c = 91$ K are adduced. The temperature, field and time dependencies of the remnant magnetization $M_r(T, B, t)$ were obtained using VSM method for the temperature range from 4.2 K to 75 K for H||c configuration. The single crystal has been irradiated by the fast electrons ($E = 4$ MeV) with fluences up to $2 \cdot 10^{18} \text{ cm}^{-2}$. The relaxation of $M_r(t)$ obeys to the logarithmic law for the time interval $t = 1$ h for whole temperature range except the $\sim 30 - 50$ K interval for starting and irradiated states. After irradiation the J_c decrease despite the flux creep reduction. The irradiation become less effective at high temperatures. The results are discussed in frame of conventional flux creep theory and of the interaction model of radiation defects with the background ones.

Keywords: the high- T_c superconductivity, $\text{YBa}_2\text{Cu}_3\text{O}_y$ single crystal, the magnetization relaxation, the pinning potential, irradiation.

1. INTRODUCTION

The introduction of radiation defects has proved to be a very useful method changing of the critical current density J_c in high- T_c superconductors. Besides J_c , the flux creep in high- T_c superconducting materials is very important with respect to potential applications. It is known that these superconductors are characterized by rather weak flux pinning by lattice defects and, ergo, by the strong relaxation rate of remnant magnetization even at low temperatures due to the flux motion across low energy pinning barrier U_{eff} . To use irradiation experiments permit to introduce the defects in a controlled manner. In our earlier work¹ we studied the isothermal magnetization at different temperatures in $\text{YBa}_2\text{Cu}_3\text{O}_y$ single crystal including the irradiated state. It was shown that at the temperatures above ~ 20 K the single crystal displayed nonmonotonous change of the difference $\Delta M(B)$ between rising and decreasing magnetization values in an external magnetic field. This so-called fishtail effect disappears at temperatures above ~ 70 K. The origin of this phenomenon is not yet clear² (and also the references therein). The investigation on the flux creep process, no doubt, can be complete our understanding of such anomalous behavior of $\text{YBa}_2\text{Cu}_3\text{O}_y$ single crystal. The purpose of the present work is determine the relaxation rate of the magnetization and, ergo, the pinning potential U_{eff} in $\text{YBa}_2\text{Cu}_3\text{O}_y$ single crystal in a wide temperature region before and after irradiation.

2. EXPERIMENTAL

The single crystal of $\text{YBa}_2\text{Cu}_3\text{O}_y$ was grown from flux melt.³ The value of T_c is equal to 91 K and $\Delta T_c \sim 1$ K determined from ac magnetic susceptibility at ZFC with $B = 5$ G. Magnetic hysteresis loops were obtained using automated vibrational magnetometer at external magnetic fields up to 6 T over temperature range from 4.2 K to ~ 75 K. All measurements have been performed with the magnetic field oriented parallel to c-axis to avoid the strong intrinsic flux pinning existing for the experimental geometry when the magnetic field is parallel CuO layers (H||c) as was shown by us for thick films of $\text{YBa}_2\text{Cu}_3\text{O}_y$.⁴ For each measurement run the crystal was heated to ~ 100 K, and prior to cooling was held in zero field. for some minutes. The magnetic field was increased up to the necessary value, then the field was switched on and the relaxation of remnant magnetization $M_r(t)$ has been recorded for $t \approx 1$ h after the field reached zero. The time dependence of remnant magnetization was analyzed according to next relation⁵:

* V. I. G. (corresponding author): E-mail: bars@ifftp.bas-net.by; Telephone: 375(017)2841547; Fax: 375(017)2840888.

$$dM/d\ln t = -kT/(M_r U_{\text{eff}}), \quad (1)$$

where U_{eff} is the activation energy of the flux creep or the pinning potential, which can be found from the slopes of curves M/M_r versus $\ln t$.

Then the single crystal was irradiated by the fast electrons with energy 4 MeV and fluences up to $\sim 2 \cdot 10^{18} \text{ cm}^{-2}$ at room temperature; afterwards, the hysteresis loops and magnetization decay under irradiation were re-measured.

3. RESULTS AND DISCUSSION

Since the width of the magnetization curve is proportional to the critical current density J_c (Bean model), this quantity was calculated using the standard expression $J_c = 30 \Delta M/d$, where d is the average width size of sample. The J_c values are $\sim 10^6 \text{ A} \cdot \text{cm}^{-2}$ at 4.2 K for $B = 0.5 \text{ T}$. With rising magnetic field J_c monotonously decreases and J_c (4.2 K, 5 T) amounts to $3 \cdot 10^5 \text{ A} \cdot \text{cm}^{-2}$. But at higher temperatures ($\geq 20 \text{ K}$) the pronounced additional peak H_p appears in the high field range and J_c (70 K) value, for example, at 1.5 T is three times larger than that at $\sim 0.5 \text{ T}$. The values of J_c at fixed temperatures ($20 \div 70 \text{ K}$) reach to maximum at $H_p = 4 \div 1.5 \text{ T}$.

As already known⁵, the remnant magnetization value M_r , obtained in the limiting hysteresis loop regime in accordance with Bean model, is proportional to the critical current density in the sample. If the temperature dependence $M_r(T)$ is determined by the flux creep, the value of $M_r(T)$ decreases linearly as the temperature rises:

$$M_r(T)/M_r(0) \approx J_c/J_0 \approx 1 - (T/U_{\text{eff}})\ln(t/\tau), \quad (2)$$

where t is the time of the first measurement, τ is a microscopic attempt time of order 10^{-6} to 10^{-12} s .⁶

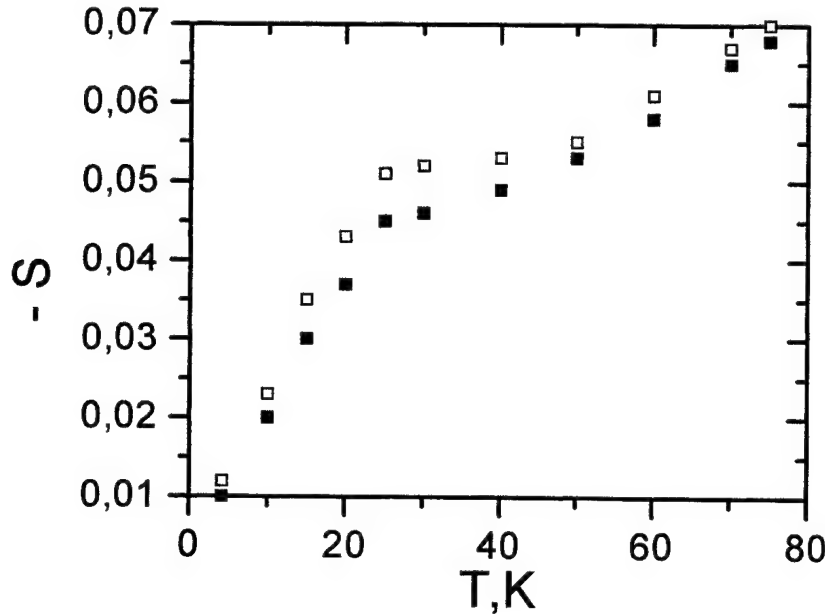


Fig. 1. The temperature dependence of the normalized magnetization relaxation rate for $\text{YBa}_2\text{Cu}_3\text{O}_y$ single crystal in starting (light symbols) and irradiated (dark symbols) states.

At low temperatures the magnetization was found to relax logarithmically with time (for $t \geq 10 \text{ s}$), indicating that the sample was in critical state. The normalized magnetization relaxation rate $S = (1/M_0)dM(t)/d\ln t \equiv T/U_{\text{eff}}$ where M_0 is the

initial magnetization, is very important characteristic describing the creep process in high- T_c superconductors. Fig. 1 (light symbols) shows the temperature dependence for the normalized magnetization relaxation rate ($-S$) in single crystal before irradiation. The values of ($-S$) equal to ~ 0.012 at 4.2 K starts increasing with the temperature and reach ~ 0.051 at 25K, but the $M(t)$ decay in time deviates from logarithmic law on the some plateau of $-S(T)$ dependence at $\sim 30\text{K} - 45\text{K}$, where the nearly constant value of ($-S$) is kept. The increasing of the relaxation rate is observed again at higher temperatures (fig. 1, light symbols). It is worth to note that nearly at such temperatures we have found an anomalous increase of hysteresis loops with field.¹

The value of magnetization decay can be calculated from⁵:

$$S = (1/M)(dM/d\ln t)|_t = -1/[(U_{\text{eff}}/kT) - \ln(t/\tau)]. \quad (3)$$

Assuming $t = 60\text{ s}$ we found $-1/S + 18 \leq U_{\text{eff}}/kT \leq -1/S + 32$ depending on the choice of τ . The values of $-S$ for $\text{YBa}_2\text{Cu}_3\text{O}_y$ single crystal are small, and $U_{\text{eff}}(T)$, ergo, is slightly depend of the choice of τ , at least, for low temperatures.

The Fig. 2 (light symbols) shows a temperature dependence of $U_{\text{eff}}(T)$ in starting state. As seen from our data, the U_{eff} barrier equal to $\sim 30\text{ meV}$ at 4.2 K reaches to $\sim 90\text{ meV}$ at 75 K.

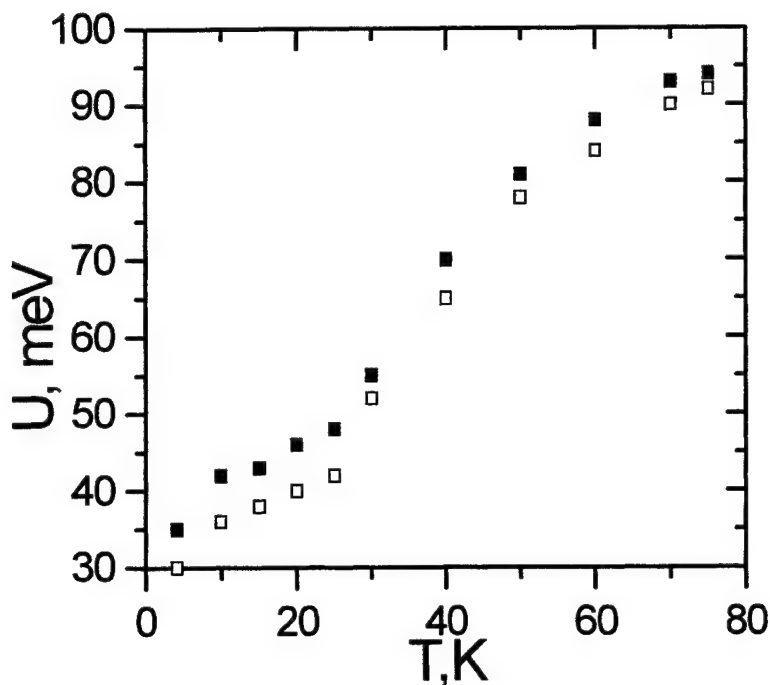


Fig. 2. The temperature dependence of the pinning potential for $\text{YBa}_2\text{Cu}_3\text{O}_y$ single crystal in starting (light symbols) and irradiated (dark symbols) states.

After electron irradiation with fluences up to $\sim 2 \cdot 10^{18}\text{ cm}^{-2}$ the critical temperature of the sample has decreased by $\sim 1\text{ K}$. This T_c deterioration is attributed mainly to displacement in the oxygen sublattice^{1,4}. The J_c decrease was observed in irradiated sample and $J_c(4.2\text{ K}, 0.5\text{ T})$ become $8 \cdot 10^5\text{ A} \cdot \text{cm}^{-2}$. After irradiation the fishtail features display less noticeable (for the same temperature interval above $\sim 20\text{ K}$), at the time no fishtail was observed at low temperatures. Remarkably that in irradiated single crystal the reduction of the flux creep was observed in spite of a J_c decrease (Fig. 1, dark symbols). The flux creep rate is reduced at any temperature up to $\sim 75\text{ K}$, but this reduction of ($-S$) is more effective at temperatures below

~ 30 K than at higher temperatures. Correspondingly, the activation energy U_{eff} increases after irradiation, especially at low temperatures, and the values of U_{eff} enhance up to ~ 35 meV at 4.2 K and ~ 93 meV at 70 K (Fig. 2, dark symbols).

In work² it was proposed that the anomalous magnetization behavior in high- T_c superconductor $\text{YBa}_2\text{Cu}_3\text{O}_y$ was resulted from the existence of two kinds of pinning centers with different T_c . The fishtail effect can be due to the flux pinning by the ordered oxygen-deficient domains in the sample with T_c and H_{c2} lower than the matrix. When the field and temperature pass over the critical parameters of such domain, the superconducting domain becomes normal and its pinning forces (and ergo J_c) rise with field. At higher fields the J_c values decrease because of the possible weakening of the pinning forces with rising field. But besides this „static” origin there is a „dynamic” cause⁵ of fishtail effect connected with change of the magnetization relaxation rate. Note that the fishtail effect in $\text{YBa}_2\text{Cu}_3\text{O}_y$ single crystal starts at temperatures ≥ 25 K when the „plateau” of the magnetization relaxation rate is displayed.

As seen from present study, after irradiation the J_c decrease in the sample is combined with the noticeable reduction of flux creep (especially at low temperatures). In other words, corresponding enhancement of the pinning potential in irradiated state (fig. 2) can not be absolute cause of the J_c rise. It should be mentioned the obtained values of the pinning potentials consist of the certain pinning potentials connected with the different sorts of pinning centers, therefore there is the effective pinning potential. The increase of J_c might be due to rise of the number of pinning centers or to arise of the new pinning centers with not certainly deep potential barriers. In works^{7, 8}, for example, obtained results for $\text{YBa}_2\text{Cu}_3\text{O}_y$ single crystals and epitaxial films after neutron irradiation were explained within the conventional flux creep theory,⁵ namely, $J_c \sim U/(N \cdot l \cdot b)$, where N is the number of vortices in a flux bundle, b and U are the main width and depth of potential, respectively, and l is the average distance between pinning sites. The decrease of J_c in $\text{YBa}_2\text{Cu}_3\text{O}_y$ single crystal along with the reduction of flux creep rate observed by us after electron irradiation may be attributed to the possible increase of b as was shown in⁸ for neutron irradiated $\text{YBa}_2\text{Cu}_3\text{O}_y$ single crystal. The increase of U_{eff} after irradiation can be due to introduce more strong pinning centers than the background defects which are already effective before the irradiation. The weakening of the fishtail effect in irradiated state as compared to the initial state is assumed to be connected with defects including oxygen vacancies with vortices at the boundaries of two phases.¹

4. CONCLUSION

The measurements of remnant magnetization relaxation in single crystal of $\text{YBa}_2\text{Cu}_3\text{O}_y$ with $T_c = 91$ K have been performed at 4.2 – 75 K. The M_r decay is found to decrease logarithmically with time except of the domain 30 ÷ 45 K. After irradiation by fast electrons with $E = 4$ MeV with fluences up to $2 \cdot 10^{18} \text{ cm}^{-2}$ the relaxation rate reduced in spite of J_c decrease. The results can be explained in terms of the flux creep theory with taking into account the interaction radiation defects and background ones.

REFERENCES

1. V. I. Gatal'skaya, G. V. Gatal'skii, P. V. Grizkov, L. A. Kurochkin and S. L. Kurochkin, „The investigation on the fishtail in irradiated YBCO single crystal”, *Izv. RAS, ser. phys.* **59**, pp. 164 – 166, 1995.
2. J. L. Vargas and D. C. Larbalestier, „Flux pinning by ordered-deficient phases in nearly stoichiometric $\text{YBa}_2\text{Cu}_3\text{O}_{7-\delta}$ single crystal”, *Appl. Phys. Lett.* **60**, pp. 1741 – 1743, 1992.
3. S. N. Barilo, A. P. Ges, S. A. Guretzkii, D. I. Zhigunov, A. A. Ignatenko, A. N. Igumentsev, L. A. Kurnevich and A. M. Luginets, „Growth and study of bulk $\text{YBa}_2\text{Cu}_3\text{O}_{7-\delta}$ single crystals”, *Physica* **185 – 189C**, pp. 459 – 460, 1991.
4. V. I. Gatal'skaya, G. V. Gatal'skii, P. V. Grizkov, L. A. Kurochkin and S. L. Kurochkin, „Critical current enhancement and flux creep in irradiated YBCO thick films”, *Phys. Stat. Sol. (a)* **140**, pp. 527 – 531, 1993.
5. G. Blatter, M. V. Feigel'man, V. B. Geshkenbein and V. M. Vinokur, „Vortices in high-temperature superconductors”, *Rev. Mod. Phys.* **66**, p. 1125 – 1338, 1994.
6. A. P. Malozemoff, T. K. Worthington, R. M. Yandofski and Y. Yeshurun, „Towards the theoretical understanding of high-temperature superconductivity”, edited by S. Lundquist, E. Tosatti, M. Tosir and Y. Lu, World-Scientific, Singapore, 1988.
7. W. Schindler, „Reduction of flux creep in spite of a J_c decrease in $\text{YBa}_2\text{Cu}_3\text{O}_{7-\delta}$ after neutron irradiation”, *J. Appl. Phys.* **70**, pp. 1877 – 1879, 1991.
8. Schindler, P. van Haelt, G. Saemann-Ischenko, G. Kumm, K. Winzer, B. Holzapfel, B. Roas, W. Gieres and H. Gerstenberg, „Critical current density and pinning potential in $\text{YBa}_2\text{Cu}_3\text{O}_{7-\delta}$ single crystals and epitaxial thin films after fast neutron irradiation”, *Supercond. Sci. Technol.* **5**, pp. S129 – 132, 1992.

Lower critical fields in BKBO single crystals

Sergei N. Barilo, Valentina I. Gatafskaya*, Sergei V. Shiryayev, and Anatolii S. Shestac

Institute of Solid State and Semiconductor Physics, National Academy of Sciences,
Minsk, P. Brovki st., 17, 220072 Belarus

ABSTRACT

We performed dc-magnetization measurements in low magnetic fields on single crystals of $\text{Ba}_{1-x}\text{K}_x\text{BiO}_y$ (BKBO) with the different potassium content. The single crystals reveal the superconducting transition at 29 – 31 K. It is shown that the lower critical fields H_{c1} in crystals amount to 104 Oe ($x = 0.34$), 126 ($x = 0.37$) and 112 Oe ($x = 0.4$). The values of the penetration depth $\lambda(0)$ are equal to 2530 Å, 2430 Å and 2670 Å for $x = 0.34$, 0.37, and 0.4, respectively.

Keywords: superconductivity, BKBO, single crystals, lower critical field, the penetration depth.

1. INTRODUCTION

The BKBO high- T_c system shows promising features for the possible application in the devices based on Josephson electronics because of its relatively long coherence length ($\xi = 45 - 70$ Å).^{1,2} It is important to note that the most successful superconductor – insulator – superconductor (SIS) and superconductor – insulator – normal conductor (SNS) structures using BKBO have been already obtained (see, p. ex.,³ and the references therein). On other hand, BKBO with $T_c \approx 30$ K is intermediate system between high- T_c and usual superconductors, and at present the origin of superconductivity in the copperless bismutate materials is not fully understood. It is necessary to know the critical parameters of BKBO both for the understanding of the mechanism of superconductivity and for the creating superconducting devices. The critical fields, the lower critical field, H_{c1} and the upper critical field, H_{c2} are important characteristics of the type-II superconductors providing us the information in order to evaluate the main characteristic lengths, the coherence length, ξ and the penetration depth, λ . Both critical fields can be determined from magnetization measurements. The purpose of present work is to measure the lower critical field H_{c1} in single crystals of $\text{Ba}_{1-x}\text{K}_x\text{BiO}_y$ with different potassium content. The data on these characteristics obtained for ceramic, polycrystalline or single crystals are markedly contradictory. The values of $H_{c1}(0)$ obtained only for single crystals and ranging from 100 Oe to 300 ÷ 420 Oe indicate that the sample to sample variations are usual both for single crystals and polycrystalline materials. The determination of this fundamental parameter and comparison with results obtained on BKBO in previous works are the aims of our work.

2. EXPERIMENTAL

The single crystals of $\text{Ba}_{1-x}\text{K}_x\text{BiO}_y$ with $x = 0.34 \div 0.4$ were grown using the electrochemical deposition method from KOH flux melt.⁸ The potassium concentration in the samples was determined by using a calibration curve for pseudocubic cell according to the approximation formula reported by S. Pei et al.⁹ obtained by neutron diffraction experiments. The high quality of single crystals with potassium content $x = 0.34$; 0.37; 0.4 was confirmed by X-ray diffraction analysis.¹⁰ The sample of practically cubic shape with average size ~ 1 mm³ were cut from the central part of as-grown large single crystals. All faces of the samples are oriented (100) surfaces. The critical temperature values T_c were obtained at fields ~ 5 (Oe) and were equal to 30 K ($x = 0.34$), 29 K ($x = 0.37$) and 31 K ($x = 0.4$). The transition width ΔT did not exceed 2 – 3 K. The magnetization measurements were taken using an automatic vibrating sample magnetometer with the sensitivity of 10^{-6} emu over the temperature range from 4.2 K to $\sim T_c$. For all measurements we waited about 20 min at the temperature of sample above T_c , subsequently we cooled the crystal at zero field down to temperature where performed a virgin magnetization curve. The $M(H)$ curves were recorded at continuously varying magnetic fields up to ~ 1 kOe of an Al-solenoid.

* V. I. G. (corresponding author): E-mail: bars@iftp.bas-net.by; Telephone: 375(017)2841547; Fax: 375(017)2840888.

More than ten different methods exist for measuring lower critical field H_{c1} .¹¹ For present work we choose the standard method¹² which consists of determining H_{c1} from the first deviation of $M(H)$ from linear behavior at $H_a = H_{c1}(1 - n)$, where H_a is external magnetic field, n is the demagnetization factor.

Typical magnetization data for BKBO single crystals are shown in Fig. 1 (single crystal with $x = 0.37$). Also shown is a straight line fit to the low-field diamagnetic regime. The values of H_{c1} were obtained from the field at which the flux first enters the sample by correcting for demagnetizing effects obtained from the initial slope of the magnetization curve assuming $M/H = -1/[4\pi(1 - n)]$. The value of n , deduced from the initial slope of the curve $M(H)$ is in good agreement with the calculated value based on the sample dimensions: $n \approx 0.56$ for single crystal with $x = 0.37$.

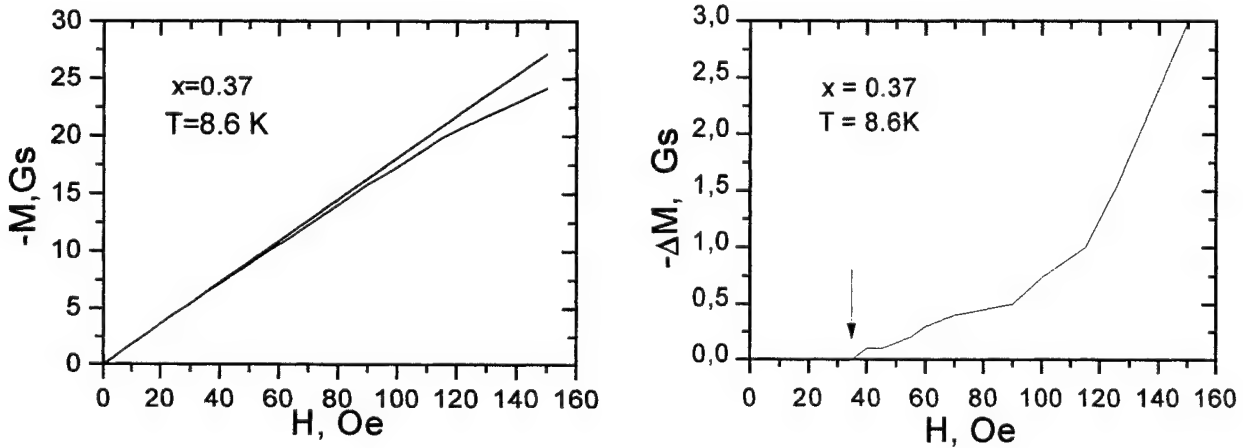


Fig. 1. Magnetization data $M(8.6 \text{ K}, H)$ for a $\text{Ba}_{1-x}\text{K}_x\text{BiO}_y$ single crystal with $x = 0.37$. The straight line is a least-squares fit to the first ten data points (perfect screening).

Fig. 2. The deviation $\Delta M(8.6 \text{ K}, H)$ from linear behavior (perfect screening) as in Fig. 1. The value for the lower critical field, H_{c1} was estimated as the field where ΔM starts to deviate from zero. The arrow denotes H_{c1} uncorrected for demagnetization factor.

In order to observe the deviation from linearity (perfect screening) of $M(H)$ we use the plot the curve (Fig. 2) corresponding to the curve in Fig. 1 after the linear fit extrapolation of the low-data was subtracted. The transition from the Meissner state ($B = 0$) to the mixed state ($B > 0$) is easily seen, and the entry field H_{c1} was determined as the field at which the deviation ΔM from perfect screening starts to deviate from zero. The arrow at Fig. 2 indicates the H_{c1} at 8.6 K uncorrected for demagnetization factor for single crystal with $x = 0.37$. Similar magnetization-versus-field data were also obtained for determination of the first entry field, H_{c1} values corrected for demagnetization factors are plotted versus temperature in Fig. 3 for single crystals with $x = 0.37$. The line depicting $H_{c1}(T)$ dependence was obtained using the expression:

$$H_{c1}(T) = \phi_0 / [4\pi(\lambda(T))^2] \cdot \ln[\lambda(T) / (\phi_0 / 2\pi H_{c2}(T))^{1/2}]$$

where ϕ_0 is the flux quantum, $\lambda(T)$ is the penetration depth.

Note that Werthamer, Helfand and Hohenberg (WHH) or linear extrapolations are usually assuming for the evaluation of temperature dependence of upper critical field, $H_{c2}(T)$, but we rely on the values of $H_{c2}(T)$, obtained from the direct magnetic measurements. The $H_{c2}(T)$ dependence was determined by means QUANTUM DESIGN MPMS-5 SQUID near T_c at the magnetic fields up to 5 T¹³ and at lower temperatures by the NHMFL cantilever force magnetometer at fields up to 33 T.¹⁴ The results for $x = 0.37$, e. g., can be described by relation $H_{c2}(T) = 46.2 - 2.8T + 0.04T^2$. The values of $\lambda(T)$ determined from the reversible magnetization data¹³ with the superconducting volume correction ($f = 0.8$) were used for the approximation of $H_{c1}(T)$ dependence. We obtained for the penetration depth $\lambda(0) = 2430$ Å and $H_{c1}(0) = 126$ (Oe).

Similar measurements and calculations were performed for other single crystals of BKBO (with $x = 0.34$ and 0.4). We can summarize the data by $H_{c1}(0) = 104$ Oe and $\lambda(0) = 2530$ Å for $x = 0.34$, and $H_{c1}(0) = 112$ Oe and $\lambda(0) = 2670$ Å for $x = 0.4$.

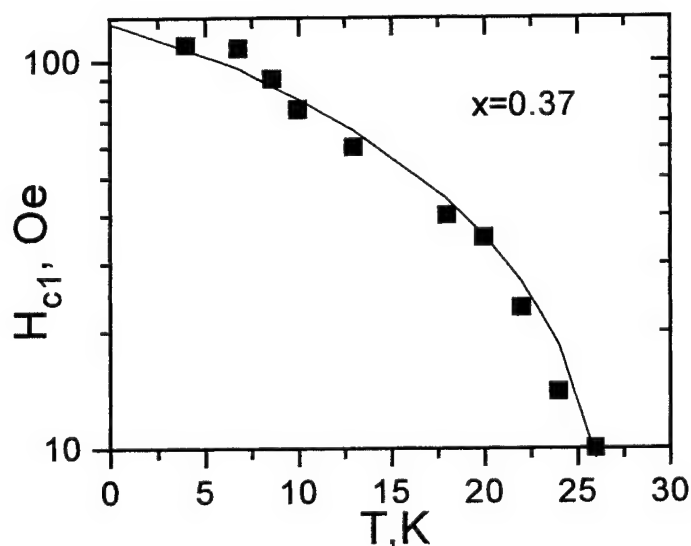


Fig. 3. The temperature dependence of lower critical field for single crystal with $x = 0.37$. The solid line represent fit of the data to theoretical expression as described in the text.

Analysis of the results of magnetization measurements on the three single crystals of BKBO shows that we find significantly lower values of H_{c1} compared to the values obtained in ^{5,7}. Qualitatively our data are in agreement with data ⁴.

3. CONCLUSION

We report measurements of the field of first magnetic flux entry and determined values of the lower critical field $H_{c1}(T)$ on the three single crystals of BKBO with the different potassium content. The obtained $H_{c1}(0)$ values amount to 104 Oe ($x = 0.34$), 126 ($x = 0.37$) and 112 Oe ($x = 0.4$).

ACKNOWLEDGEMENTS

Work was partly supported by the INTAS under grant N 97-1371.

REFERENCES

1. R. A. Schweinfurth, C. E. Platt, M. K. Teepe and D. J. Van Harlingen, „Electrical and magnetic transport properties of laser-deposited $Ba_{1-x}K_xBiO_3$ thin films”, *Appl. Phys. Lett.* **61**, pp. 480 – 482, 1992.
2. E. S. Hellman, E. H. Hartword and E. M. Gyorgy, „Epitaxial $Ba_{1-x}K_xBiO_3$ films on MgO: Nucleation, cracking, and critical currents”, *Appl. Phys. Lett.* **58**, pp. 1335 – 1337, 1991.
3. M. Inoue, Sh. Imaeda, Y. Tsukino, A. Fujimaki, Y. Takai and H. Hayakawa, „Planar-type $Ba_{1-x}K_xBiO_3$ Josephson tunnel junctions prepared on $SrTiO_3$ bicrystal substrates”, *Appl. Phys. Lett.* **65**, pp. 243 – 245, 1994.
4. Z. J. Huang, H. H. Fang, Y. Y. Hue, P. H. Hor, C. W. Chu, M. L. Norton and H. Y. Tang, „Study of the magnetic properties of single-crystal $Ba_{0.6}K_{0.4}BiO_3$ ”, *Physica (Utrecht)* **180C**, pp. 331 – 336, 1991.
5. G. T. Seidler, T. F. Rosenbaum, P. D. Han, D. A. Payne and B. W. Veal, „Critical fields and flux pinning in single

- crystal $\text{Ba}_{1-x}\text{K}_x\text{BiO}_3$ ", *Physica (Utrecht)* **195C**, pp. 373 – 378, 1992.
6. V. I. Gatal'skaya, G. V. Gatal'skii, L. A. Kurochkin, S. L. Kurochkin and S. V. Shiryayev, „Critical current, magnetic irreversibility line, and relaxation in electron irradiated single crystal of $\text{Ba}_{0.6}\text{K}_{0.4}\text{BiO}_3$ ”, *Phys. stat. sol. (a)* **143**, pp. 123 – 129, 1994.
 7. P. Kumar, D. Hall and R. G. Goodrich, „Thermodynamic of the superconducting phase transition in $\text{Ba}_{0.6}\text{K}_{0.4}\text{BiO}_3$ ”, *Phys. Rev. Lett.* **82**, pp. 4532 – 4535, 1999.
 8. S. N. Barilo, D. I. Zhigunov, L. A. Kurochkin, A. V. Pushkarev and S. V. Shiryayev, „The growth and study of superconducting single crystals of $\text{Ba}_{1-x}\text{K}_x\text{BiO}_3$ system”, *Superconductivity* **5**, pp. 1084 – 1089, 1992.
 9. Sh. Pei, J. D. Jorgensen, B. Dabrowski, D. G. Hinks, D. R. Richards, A. W. Mitchell, J. M. Newsam, S. K. Sinha, D. Vaknin and A. J. Jacobson, „Structural phase diagram of the $\text{Ba}_{1-x}\text{K}_x\text{BiO}_3$ system”, *Phys. Rev.* **41B**, pp. 4126 – 4141, 1990.
 10. S. N. Barilo, N. M. Olekhovich, N. S. Orlova, A. V. Pushkarev, A. N. Salak and S. V. Shiryayev, „X-ray study of the structure and thermal properties of $\text{Ba}_{1-x}\text{K}_x\text{BiO}_3$ at different temperatures”, *Cryst. Res. Technol.* **31**, pp. 107 – 117, 1996.
 11. V. Buntar and H. W. Weber, „Superconducting properties of fullerenes in the the mixed state”, *Fizika nizkikh temperatur* **22**, pp. 231 – 242, 1996.
 12. A. Umezawa, G. W. Grabtree, J. Z. Liu, T. J. Moran, S. K. Malik, L. H. Nunez, W. L. Knok and C. H. Sowers, „Anisotropy of the lower critical field, magnetic penetration depth, and equilibrium shielding current in single-crystal $\text{YBa}_2\text{Cu}_3\text{O}_{7-\delta}$ ”, *Phys. Rev.* **38B**, pp. 2843 – 2846, 1988.
 13. S. N. Barilo, S. V. Shiryayev, V. I. Gatal'skaya, J. W. Lynn, M. Baran, H. Szymczak, R. Szymczak, D. Dew-Hughes, „Scaling of magnetization and some basic parameters of $\text{Ba}_{1-x}\text{K}_x\text{BiO}_3$ superconductors near T_c ”, *Phys. Rev.* **58B**, pp. 12355 – 12367, 1998.
 14. S. N. Barilo, D. Hall, V. I. Gatal'skaya, T. V. Smirnova, S. V. Shiryayev and J. E. Crow, „H – T – J phase diagram and pinning mechanism in $\text{Ba}_{0.63}\text{K}_{0.37}\text{BiO}_{3-y}$ single crystal”, *Physica B* (submitted).

Determining of the material parameters of $\text{Zn}_x\text{Cd}_y\text{Hg}_{1-x-y}\text{Te}$ by the magnetophonon spectroscopy

J. Cebulski*, J. Polit and E. M. Sheregii

Institute of Physics Pedagogical University, 35-310 Rzeszów, Rejtana 16A Poland

ABSTRACT

The phonon and electron subsystems were studied in quaternary solid solutions of $\text{Zn}_x\text{Cd}_y\text{Hg}_{1-x-y}\text{Te}$ (ZMCT) by means of Raman scattering and Magnetophonon Resonance. The Raman spectra of several compositions confirm the three-mode behaviour of phonon spectra. The cluster mode has also been observed. Four kinds of LO-phonons (of HgTe-like, CdTe-like and ZnTe-like sublattices and ZnTe-clusters) participate in the electron-phonon interaction. Four types of one-phonon Magnetophonon Resonances and two types of Magnetophonon Resonances on the difference of phonon frequencies have been observed.

Keywords: magnetophonon resonance, semiconductors

1. INTRODUCTION

Random homogenous substitutions of matrix cations by another metal atoms in the solid solution lattices with common anion (as is the case in GaAs-AlAs or HgTe-CdTe) is known to cause a continuous reconstruction of the electronic structure and the phonon spectra with composition variation. It may be assumed that the introduction of a third cation will enable us to obtain a supplementary degree of freedom in the control of material parameters. It has an additional advantage in the case of HgTe-CdTe (MCT), because the introduction of Zn-atoms stabilises the weak Hg-Te bonds in crystal lattice of this solid solution, whereas the presence of Cd-atoms destabilises them¹⁻³. The introduction of the fourth component Zn causes not only a simple extension of the physical properties of MCT, but also new phenomena, connected with multimodeness of the crystal lattice. 'Multimodeness' is an issue of primary significance in the study of four-component solid solutions. ZMCT has three sublattices (ZnTe-like, CdTe-like and HgTe-like). Therefore, a three-mode behaviour of the phonon spectrum in this solid solution may be predicted. Other possibilities also exist⁴.

The present article discusses of ZMCT structures investigated of ZMCT by means of Magnetophonon Resonance (MPR) experiments, a powerful tool for the investigation of electron and hole spectra⁵.

A series of films of ZMCT obtained by liquid-phase epitaxy on CdTe substrates have been studied. The thickness of homogeneous layers is $d = 4\mu\text{m}$. The temperature dependencies of electroconductivity and Hall coefficient measured in those structures have shown an activated behaviour. The quality of epitaxial layers investigated by MPR is comparable with the corresponding high quality MCT alloys with the same energy gap (near 180 - 300 meV). The mobility of electrons in those layers is sufficiently high to observe the MPR. It is important to note that the parameters of these samples have not changed over the period of three years, whereas MCT samples are characterised by the temporal degradation of parameters.

2. EXPERIMENTAL RESULTS

MPR was observed on three samples: IV, V and VI. The measurements were performed in pulsed magnetic fields. The second derivation of transverse magnetoresistance $d^2\rho_{xx}(B)/dB^2$ as a function of a magnetic field B was registered up to 6.5 T at different temperatures within the range of 77 - 200 K. The most detailed investigations were performed for sample IV. The experimental records obtained for this specimen at different temperatures are shown in Fig. 1.

When the temperature was increased above 124 K, a group of strong peaks (a wide maximum) appears in the range from 2.0 to 3.8 T; the corresponding harmonics were at 1.0 - 1.9 T and 0.6 - 0.9 T. The peak $a1^+$ is the strongest and the most distinguishable for the range $124\text{ K} \leq T \leq 158\text{ K}$, whereas peak $a1^-$ is most distinguishable at $T > 158\text{ K}$.

These peaks are correspondent to their harmonics $a2$, $a3$ and $a4$, are observed in the fields approximately equal to $1/2 B_0$, $1/3 B_0$ and $1/4 B_0$, respectively (B_0 - resonance magnetic field for peak $a1^+$).

* cebulski@atena.univ.rzeszow.pl; tel.: 048 017 8625628 ext. 1554, fax: 048 017 8527951

In this manner three other series of peaks can be determined - *b*, *c* and *k*. Therefore, the structure of wide maximums - which are clearly visible on experimental curves in Fig.1 at temperatures above 124 K - corresponds to four series of peaks. These series are connected with four kinds of phonons.

A similar investigation has been conducted for specimens V and VI, for which *x+y* is significantly larger and, correspondingly, the effective mass of electrons is also greater. Consequently, the whole system of resonances is shifted to higher magnetic fields.

From these general considerations it follows that the series *a* is caused by the absorption of LO-phonons of HgTe-like sublattice, since these phonons have the lowest energy and they are present in the greatest numbers in the lattice of ZMCT. However, the energy of the LO-phonons which can participate in electron-phonon interaction in this lattice have to be determined for the correct interpretation of MPR-s data.

The LO-phonon frequencies for HgTe-like, CdTe-like, ZnTe-like sublattices as well as ZnTe-binary clusters were determined from Raman Spectra and far-infrared reflection spectra in our previous paper ⁶. The frequencies and energies of LO-phonon for measured samples are given in Table 1.

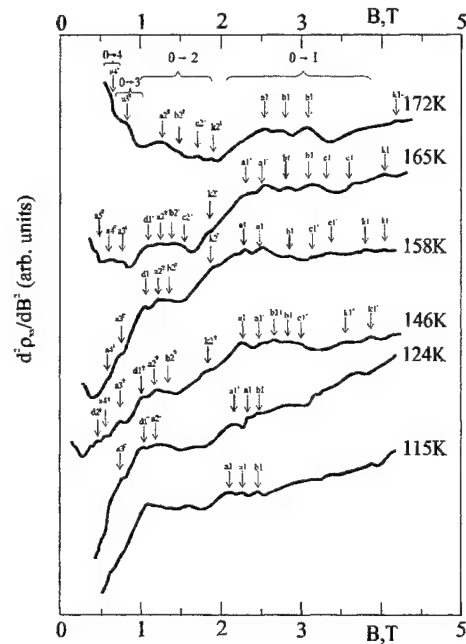


Fig. 1 Experimental records of $d^2\rho_{xx}(B)/dB^2$ obtained for sample IV at different temperatures.

Table 1. Values LO(Γ)-phonons frequencies and energies for compositions IV,V and VI.

composition	HgTe-like mode	CdTe-like Mode	ZnTe-like Mode	ZnTe-cluster
IV $\omega_{LO}, \text{cm}^{-1}$	137	156.0	171.5	198.0
$\hbar\omega_{LO}, \text{meV}$	17.0	19.3	21.3	24.6
V $\omega_{LO}, \text{cm}^{-1}$	136.0	156.0	174.0	198.0
$\hbar\omega_{LO}, \text{meV}$	16.8	19.3	21.7	24.6
VI $\omega_{LO}, \text{cm}^{-1}$	136.0	156.0	175.0	198.0
$\hbar\omega_{LO}, \text{meV}$	16.8	19.3	21.9	24.6

It follows from the considerations above that peaks $a1^+$ and $a1^-$ - the strongest and the most distinguishable at $T > 124$ K on experimental curves in Fig. 2 - 4 and characterised by harmonics at corresponding magnetic fields - are caused by electron transitions $0^+ - 1^+$ and $0^- - 1^-$ accompanied by absorption of LO-phonons of HgTe-like sublattice. Our further interpretation of MPR-spectra is based on this assumption which enables us to estimate to the first approximation the parameters of the band structure using the energy value of LO-phonon of HgTe-like sublattice from Table 1 and experimental positions in magnetic field of peaks $a1^+$ and $a1^-$.

3. THE BAND STRUCTURE PARAMETERS

The band structure parameters have been calculated according to R. Aggrawal's version ⁷ of the Pidgeon-Brown model ⁸. This method is based on the three-level Kane's model ⁹.

The experience has shown that the choice of the values of the Luttinger valence-band parameters γ_1^L , γ_2^L , γ_3^L and K^L is crucial to the determination of the band structure parameters for MCT ¹⁰⁻¹² using the relations between them given below:

$$\gamma_1^L = \frac{E_P}{3E_g} + 2.5, \quad \gamma_2^L = \gamma_3^L = \frac{E_P}{6E_g}. \quad (1)$$

It has been assumed that $E_p = 18.0$ eV and $\Delta = 1.0$ eV¹⁰ and they do not depend on the temperature and composition. According to¹³, the next parameter K^L should be represented as follows:

$$K^L = \gamma_3^L - \frac{1}{3}\gamma_1^L + \frac{2}{3}\gamma_2^L - \frac{2}{3} - \frac{5}{4}\delta_{\text{exch}}, \quad (2)$$

where δ_{exch} stands for the correction for the nonlocality of the potential and is equal to 0.4 for MCT¹³. As for the parameter F , representing the interaction of the conduction band with the upper bands, we have used the value $F = -0.5$ determined by Weiler et al.¹⁰. We have assumed that this parameter is also not dependent on the temperature and composition.

4. THE DETERMINING PROCEDURE OF THE BAND STRUCTURE PARAMETERS

In order to calculate the theoretical positions of MPR-s peaks, we applied the best fit procedure to the experimental positions of peaks $a1^+$ and $a1^-$ and thus obtained the value of energy $E_g = 190$ meV at obtained temperature: $T = 146$ K. The next step of the calculation procedure is to fit the theoretical positions of all the observed peaks a -series to the experimental ones at a given temperature. The best fittings are shown in Fig. 2 for $T = 146$ K and Fig. 3 for $T = 165$ K, where electron transitions corresponding to resonance peaks of series a are shown by solid lines. We can state a good agreement between experimental and theoretical positions of resonances (the average discrepancy for eight peaks of series a^+ and a^- on the curve at 146 K is equal to approximately 1.5%). The thus - obtained band parameters for $T = 146$ K and 165 K are shown in Table 2.

Now, it is possible to interpret the other series of peaks, namely: b , c and k . Since the positions of peaks $b1^+$, $c1^+$ and $k1^+$ are characterised by an increase in magnetic field, these peaks may be expected to be caused by electron transitions $0^+ - 1^+$ with the assisted absorption of LO-phonons of, consequently, increasing frequencies. This sequence of increasing frequencies corresponds to the LO-phonons in CdTe-like, ZnTe-like sublattices and ZnTe-clusters. The theoretical positions of MPR for all series were calculated using the aforementioned band-structure parameters and phonon energies (Table 1).

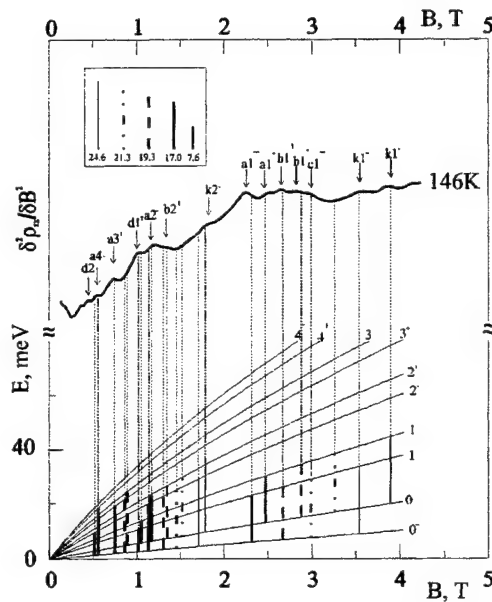


Fig 2. Experimental record of $d^2\rho_{xx}(B)/dB^2$ obtained for sample IV at temperature 146 K. The electron transitions between Landau levels corresponding to the observed MPR's are shown lower. The inset shows the appropriated phonon energies or difference of phonon energies (the values are given in meV).

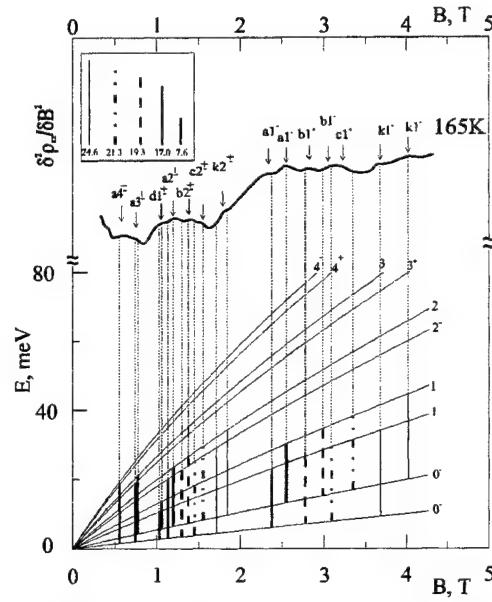


Fig. 3 Experimental record of $d^2\rho_{xx}(B)/dB^2$ obtained for sample IV at temperature 165 K. The electron transitions between Landau levels corresponding observed MPR's are shown lower. The inset shows the appropriated phonon energies or difference of phonon energies (the values are given in meV).

Table 2. The band-structure parameters values for sample IV-VI.

Parameters	sample IV 146 K	sample IV 165 K	Sample V 106 K	sample VI 99 K
E_g , meV	192	205	320	350
E_p , meV	18000	18000	18000	18000
γ_1^L	33.75	31.7	21.25	19.64
$\gamma_2^L = \gamma_3^L$	15.62	14.6	9.38	8.57
K^L	13.62	12.6	7.38	6.57
F	-0.5	-0.5	-0.5	-0.5
Δ , meV	1000	1000	1000	1000

The overall representation of the electron transitions which interpret the observed MPR peaks may be found in Fig.2, 3. It shows that the suggested interpretation of MPR's peaks based on the application of four kinds of LO-phonons is in good agreement with the experimentally observed structures of the resonance curves. Simultaneously, the quantitative agreement between calculated positions of corresponding electron transitions in the magnetic field and observed peaks of four series is within the range of about 1.5% (measurement accuracy of resonance fields is ~3%). The comparison of the two curves (the first one at 146 K and the second at 165 K) reveals that the increase in the temperature is accompanied with the increase of amplitudes of the peaks $a1'$ and $a2'$. This observation is also made for the peaks of another series caused by electron transitions between 0^- and N^- Landau levels. It is obvious enough that the increase of temperature causes the increase of the electron occupation of 0^- Landau level and the increase in the amplitude of the aforementioned peaks. Nevertheless, the peaks of series d in the small magnetic fields are hardly visible at temperatures higher than 124 K (for sample IV).

The same method of the band-structure parameters calculation and the interpretation of MPR's peaks using phonon energies as represented in Table 1 is applied to the samples V and VI. The values of the band -structure parameters determined for these samples from MPR data are represented in Table 2.

5. CONCLUSIONS

Temperature dependence of energy gap $E_g(T)$ and effective mass of the conductivity electrons $m_c(T)$ calculated with help of the temperature shift of MPR peaks for two samples ZnCdHgTe (II and V) are presented in Fig. 5 and 6. It is shown that increasing of ZnTe contains in solid solutions leads to decreasing of value of the coefficient dE_g/dT . That means it is possible to obtain ZnCdHgTe solid solutions with nondependent on temperature band-structure parameters.

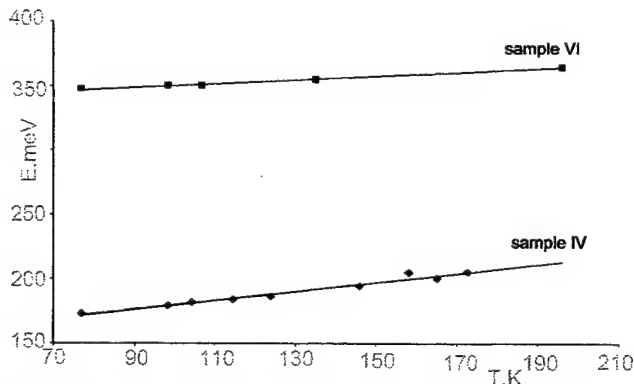


Fig 4. The temperature dependence of the energy gaps.

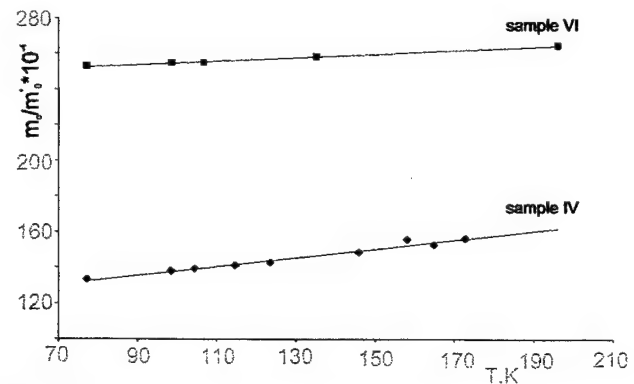


Fig 5 The temperature dependence of the effective masses.

REFERENCES

1. A.Sher, A.-B. Chen, W.E. Spicer, and C.-K. Shih, "Effects Influencing the Structural Integrity of Semiconductors and Their Alloys", *J. Vac. Sci. Technol. A* **3** 105-111, 1985
1. R. Triboulet, "(Hg, Zn)Te a new material for IR detection" *J. Crystal Growth*, **86**, pp 79-86, 1988.
2. N.L. Bazhenov, A.M. Andrushiv, V.I.Ivanov-Omskii "Carrier Lifetime in $Zn_xCd_yHg_{1-x-y}Te$: Calculation and experiment," *Infrared. Phys.* **34** pp. 357-364 1993.
3. D.W.Taylor in Optical properties of mixed crystals 1988 ed R.J. Elliott and I.P. Ipatova vol.23 of Modern Problems in Condensed Matter Sciences ed V.M. Agranovich and A.A. Maradudin (North-Holland Publ.) pp.35- 131
4. R.J.Nicholas, *Prog. Quantum Electron.* **10** 1 1985.
5. J. Polit, E.M. Sheregii, E. Szczecinska, J. Szczecinski, V.I. Ivanov-Omskii, "Raman Scattering and FarInfrared Reflection - Absorption Spectra of the Four-Component Solid Solution $Zn_xCd_yHg_{1-x-y}Te$ " *phys.stat.sol.(b)* **208**, pp. 21-30, 1998.
6. R.L. Aggarwal, "Modulated Interband Magnetooptics in Semiconductors and Semimetals" ed R.K. Willardson, A.C. BeerY. Vol.9) pp.169-185 (Academic Press, New York) 1972
7. C.R. Pidgeon, R.N. Brown, "Interband Magnetoabsorption and Farady Rotation", *Phys. Rev.* **146**, pp 575-583, 1966
8. O.Kane "Band structure indium antimonide" *J. Phys. Chem Solids* **1** pp. 249-261 1957.
9. M.H. Weiler, R.L. Aggarwal and B. Lax, "Interband Magnetorelectance in Semiconducting $Hg_{1-x}Cd_xTe$ Alloys", *Phys. Rev. B* **16**, pp. 3603-3607, 1977.
10. Y. Guldner, C. Rigaux, A. Mycielski and Y. Couder, "Magneto-optical Investigation $Hg_{1-x}Cd_xTe$ ", *phys. stat. sol. (b)* **81** pp. 615-627, 1977 ; *ibid* **82**, pp. 149-161, 1977.
11. Yu. O Ugrin., E.M Sheregii., I.M Gorbatiuk., I.M. Rarenko, "Ob. anomalnoj temperaturnoj zavisimost sziriny zapreszczonoy zony w CdHgTe", *Fiz. Tverdogo Tela* **32**, pp. 43-48 1990.
12. B.L. Gelmont, R.P. Seisyan, A.L. Efros, "Otklonienia ot modeli Kana, swiazanyje z nielokalnostiu potencjala s uzkoj zapreszczonoy zonoj", *Fiz. Techk. Poluprovod* **16**, pp. 776- 781, 1982.
13. E.M. Sheregii, J. Polit, J. Cebulski, A.M.Andrushiv, "Influence of temperature on Magnetophonon Resonances in Four-Component Solid Solution $Zn_xCd_yHg_{1-x-y}Te$ " *phys. stat. sol. (b)* **192**, pp. 121-127 1995.

Magnetic ordering of Dy^{3+} ion in low-dimensional $\text{CsDy}(\text{WO}_4)_2$ double tungstate

V.P.Dyakonov ^{1,2*}, M.T.Borowiec ^{1*}, A.Jędrzejczak ¹, E.Zubov ², T.Zayarnyuk ¹, H.Szymczak ¹

¹ Institute of Physics, al. Lotników 32/46, 02-668 Warsaw, Poland

² A.A.Galkin Donetsk Physico-Technical Institute, 72 R.Luxemburg Str., 340114 Donetsk, Ukraine

ABSTRACT

Magnetic ordering of Dy^{3+} ion in low-dimensional magnet $\text{CsDy}(\text{WO}_4)_2$ (CsDyW) has been first studied by means of measurements of the low temperature specific heat over a temperature range of 0.5-23 K. The ordering temperature (T_N) of the Dy^{3+} sublattice was established to be 1.34 K. The experimental data indicate on the antiferromagnetic (AFM) character of Dy^{3+} ions interactions. The magnetic behavior above and below T_N is discussed in the framework of different theoretical models.

Keywords: rare-earth tungstate; specific heat; antiferromagnetic ordering; low-dimensional magnet.

1. INTRODUCTION

Investigations of the alkaline (M) - rare-earth (Re) double tungstates $\text{MRe}(\text{WO}_4)_2$ are of a special interest because of a possible realization of both magnetic and structural phase transitions in them. The existence of rare-earth ions with closely spaced energy levels in these low-symmetry compounds results in the occurrence of structural phase transitions connected with the manifestation of the cooperative Jahn-Teller effect. Indeed, such structural phase transitions (SPT) have been recorded in a monoclinic $\text{KDy}(\text{WO}_4)_2$ ($T_{\text{spi}} = 6.38$ K) and $\text{RbDy}(\text{WO}_4)_2$ ($T_{\text{spi}} = 4.9$ and 9.0 K) single crystals. The double tungstates are also considered to be a model system to check the conceptions of the low-dimensional magnetism. These studies are also strongly stimulated by possible applications of these materials as active component in solid state lasers. It is shown [1] that there is possibility of application of rubidium-dysprosium double tungstate as a cooling agent in an adiabatic demagnetization method for obtaining very low temperatures.

The interconnection and mutual influence of spin-spin and Jahn-Teller interactions in low-dimensional compound is expected to lead to interesting peculiarities of magnetic ordering in crystals having Jahn-Teller ion. The magnetic phase transitions (MPT) in related $\text{KDy}(\text{WO}_4)_2$ and $\text{RbDy}(\text{WO}_4)_2$ compounds were observed at $T = 0.6$ and 0.8 K ^{1,2} respectively. The presented below measurements of the $\text{CsDy}(\text{WO}_4)_2$ ceramic are a continuation of studies of magnetic ordered state peculiarities in the dysprosium double tungstates.

In this paper the results of specific heat measurements in the $\text{CsDy}(\text{WO}_4)_2$ compound near temperature of the magnetic phase transition are presented. The presence of equivalent Dy^{3+} ions in the $\text{CsDy}(\text{WO}_4)_2$ lattice makes this compound to be very convenient for magnetic studies. The measurements were performed as a function of temperature and magnetic field intensity. The obtained results are used for both determination of the magnetic phase transition temperature and elucidation of character of the magnetic ordering.

It should be added that the investigations of magnetic and thermodynamic properties in the cesium - dysprosium double tungstate were not carried out until now.

2. SAMPLES AND EXPERIMENTAL

The double cesium-dysprosium tungstate $\text{CsDy}(\text{WO}_4)_2$ has monoclinic symmetry of crystalline lattice at room temperature. The lattice parameters are: $a = 8.14$ Å, $b = 10.45$ Å, $c = 7.569$ Å. The monoclinic angle is equal to $94^\circ 33'$. The elementary cell contains four structural units. The Dy^{3+} ion is surrounded by eight oxygen atoms and has local symmetry C_2 ³. Detailed measurements of the $\text{CsDy}(\text{WO}_4)_2$ structure at low temperatures have not been carried out yet.

* V.D. - e-mail : dyakon@ifpan.edu.pl

MTB - e-mail: borow@ifpan.edu.pl; mkpbor@it.com.pl

The specific heat measurements have been carried out using a computer controlled quasi-adiabatic calorimeter over a temperature range 0.5-23 K. For these experiments a ^3He cryostat was used. The sample in the form of powder of $\text{CsDy}(\text{WO}_4)_2$ formed into a tablet by pressing with small amount of GE 7031 glue was mounted on a sapphire plate with diameter of 20 mm and thickness of 0.3 mm using Apiezon N vacuum grease (strictly, in our experiment we measure heat capacity of mixture with GE 7031 glue because we do not able, on reasonable way, to separate part connected with this small amount of glue). The sapphire plate (sample holder) was parallel to the vertical axis of the experimental setup and to the magnetic field direction. The four-probe method was used in the experiments to measure the resistance of thermometers and heater. The temperature of the sample was determined by two small-sized RuO_2 thermometers on Al_2O_3 ceramic. The small power heat pulses have been used to supply an increase of the temperature between initial and final temperature levels. The temperature difference between these levels near magnetic phase transition was about 1-1.5 mK. The temperature run of every experimental point was measured within 40-60 s.

3. RESULTS

3.1. Zero field heat capacity

The zero-field specific heat as a function of temperature for $\text{CsDy}(\text{WO}_4)_2$ is displayed in Fig. 1. As it is seen, the specific heat has the peak at $T = 1.34$ K. A nonsymmetrical shape of the $C(T)$ anomaly near T_C is obviously due to that the specific heat temperature dependence has a different character below and above T_N . The $C(T)$ dependence is similar to the low temperature behavior of specific heat in both potassium-dysprosium $\text{KDy}(\text{WO}_4)_2$ and rubidium-dysprosium $\text{RbDy}(\text{WO}_4)_2$ tungstates. This dependence has clearly defined λ -type shape and its value at T_N is considerably reduced in comparison with $\text{KDy}(\text{WO}_4)_2$ and $\text{RbDy}(\text{WO}_4)_2$ compounds. In above compounds the peak of $C(T)$ dependence has been explained as being due to the antiferromagnetic ordering of the Dy^{3+} sublattice. By analogy and on the base of the below presented results we assume that in $\text{CsDy}(\text{WO}_4)_2$ the $C(T)$ anomaly is also connected with AFM phase transition.

One can say with reasonable confidence

that the $C(T)$ dependence characterizes the magnetic contribution to the total specific heat because the contributions to $C(T)$ from both lattice and crystal field splitting are negligible in the considered temperature range. The estimation of the contribution of the crystal field splitting to the total specific heat of $\text{CsDy}(\text{WO}_4)_2$ at low temperatures has shown that it is less than 1%. The Debye temperature in these compounds is high and the contribution of phonons is very small. The $\text{CsDy}(\text{WO}_4)_2$ is an insulator and the conduction electrons do not contribute to the specific heat. In the temperature region 1.5-2.5 K, the experimental data are well described by the quadratic dependence, namely, $C_m / R = 0.365 / T^2$ which characterizes the magnetic contribution to the specific heat. Therefore, the $C(T)$ dependence at $H = 0$, shown in Fig. 1, mainly characterizes the magnetic specific heat.

We have analyzed the data of $C(T)$ dependence above and below T_N and have estimated the Dy^{3+} ions exchange parameters (J/k) using the theoretical models for both simple cubic (3D Ising) and quadratic (2D Ising) lattices as well as the analysis of the magnetic specific heat behavior at $T > T_N$. In the case of the Ising model, the value of T_N was taken from experiment and the effective spin $S = 1/2$ was used.

The measurements of the $C(T)$ dependence and the high temperature analysis have been carried out in a temperature range up to 3.5 K only. This is due to the influence of the tail of the Jahn-Teller transition on the $C(T)$ data at higher temperatures (the temperature behavior of the magnetic susceptibility at $T > 5$ K indicates the approach to a structural phase transition which was observed at 29 K).

Using the high temperature expansion for a specific heat within the frame of the 3D Ising model we used the relationship between critical temperature and exchange interaction parameter of the form $2T_N/zJ = -0.752$ where $z = 6$ is the

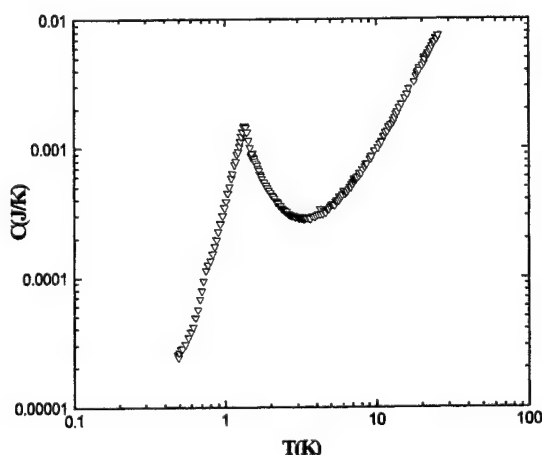


Fig. 1. Temperature dependence of the $\text{CsDy}(\text{WO}_4)_2$ specific heat near magnetic phase transition.

coordination number of the simple cubic lattice. The T_N and paramagnetic temperature θ are related by the expression: $T_N = 0.752\theta$ where $\theta = 2/3S(S+1)zJ$. The value of J is obtained to be equal to -0.336 K.

We have compared the experimental $C(T)$ dependence with the theoretical one for 2D antiferromagnet, too. The value of the exchange interaction parameter determined from equation of $J/k = T_N (\ln\sqrt{2} - 1)$ is equal to -1.18 K. Note that in this case the we used the relationship between critical temperature and exchange interaction parameter of the form $2T_N/zJ = -0.567$ where $z = 4$.

The behavior of specific heat correlates reasonably with theoretical $C(T)$ dependence for 2D Ising model below T_N , whereas at $T > T_N$ it can be well described by neither 2D or 3D Ising. The behavior of $C(T)$ at $T > 1.5 T_N$ correlates with theoretical $C(T)$ dependence for 2D Ising model better than for 3D one.

The high temperature $C(T)$ dependence is fitted also by $1/T^2$ law, namely, $4C_M T^2 / R = zJ^2 / k^2$ ($z=4$). The exchange parameter determined by such procedure is equal to $J/k = -1.298$ K. Note that the experimental J/k is in reasonable agreement with J/k one obtained for 2D Ising model only.

The J/k parameters are effective and consist of two contributions which result from the exchange and dipole-dipole interactions. Taking into account the low temperature of magnetic phase transition, it can be assumed that the exchange interaction is weak and the contribution of dipole-dipole interactions to spin-spin interactions may be essential. Unfortunately, the absence of data on the low temperature structure of $\text{CsDy}(\text{WO}_4)_2$ does not allow to calculate exactly the dipole-dipole contribution of the Dy - Dy interactions.

An important parameter determining the character of magnetic phase transition is the critical index. It can be determined from the behavior of the specific heat in the critical region. The slope of the specific heat versus reduced temperature curve in a log-log plot close to T_N directly determines the critical index. As it is well known, the critical behavior of the specific heat in the limit $T \rightarrow T_N$ above and below T_N is characterized by the critical exponents in the following equations :

$$\begin{aligned} C/R &\propto A (1 - T/T_N)^{-\alpha} \text{ for } (T < T_N); \\ C/R &\propto A (1 - T_N/T)^{-\alpha'} \text{ for } (T > T_N). \end{aligned}$$

The values α and α' are known for the 3D Ising model ($\alpha=\alpha'=1/8$), while for 2D Ising model the critical exponents are close to zero. The analysis have shown that the critical exponents for $\text{CsDy}(\text{WO}_4)_2$ are close to zero that corresponds to the theoretical value expected for the 2D Ising system.

It is interesting to estimate how much entropy is released at and above the magnetic transition ($T = 0.5-3.5$ K). At $T > 4$ K calculations present definite difficulties because it is necessary to take into account both the lattice specific heat and the contribution connected with a structural transition. The temperature dependence of the magnetic entropy of $\text{CsDy}(\text{WO}_4)_2$ near T_N has been obtained by integrating the specific heat

$$\Delta S_{\text{mag}}(T) = \int_0^T (C(T)/T) dT.$$

Above T_N the entropy should approach the value $R \ln 2$ in accordance with the molar entropy of the electronic doublet of the ground state of the Dy^{3+} ion. In our case, the entropy is only 40% of $R \ln 2$ at T_N and 70% of $R \ln 2$ at 4 K. Note that for $T > 4$ K the contributions from the lattice and structural phase transition ($T_{\text{sp}} = 29$ K) appear in $C(T)$ dependence (Fig. 1) and correspondingly in $S(T)$ value which can only decrease ΔS_{mag} .

The observed behavior of ΔS_{mag} is due to the characteristic features of the magnetic ordering of $\text{CsDy}(\text{WO}_4)_2$. At structural phase transition, in the sample two or more crystallographic sublattices can appear. At AFM ordering, below the Neel temperature additional separation into two or more magnetic sublattices occurs in each crystallographic sublattices. In the $\text{CsDy}(\text{WO}_4)_2$ compound, the AFM interactions are dominant and the crystal separates into four magnetic sublattices at $T < T_N$. In the case when the sample can separate into a large number of sublattices, actually into clusters, the value of ΔS_{mag} is not expected to reach $R \ln 2$.

3.2. Magnetic field heat capacity

We have also studied the magnetic field effect on the specific heat in $\text{CsDy}(\text{WO}_4)_2$ compound. As can be seen in Fig. 2, the $C(T)$ dependence in magnetic field show that the interactions of Dy^{3+} ions have an antiferromagnetic character because the peak of the specific heat shifts to lower temperatures and the magnitude of the maximum of specific heat decreases with increasing magnetic field. The magnetic phase $H-T_N$ diagram constructed using the T_N values corresponding to the specific heat maximum (Fig. 2) characterizes the metamagnetic transition from antiferromagnetic (AFM) to the paramagnetic (PM) phase.. The experimental phase boundary of AFM to PM state was compared to the theoretical $T_N(H)$ dependence for the Ising antiferromagnet. The latter was calculated by the high temperature expansion method describing

the shift of the anomaly of the magnetic susceptibility in a magnetic field by the following equation :

$$T_N(H) = T_N(0) \{1 - (H / H_{cr})^2\}^\zeta,$$

where H_{cr} is the transition field at $T = 0$ K, $\zeta = 0.87$ and 0.35 for square and simple cubic lattices, respectively. For the $\text{CsDy}(\text{WO}_4)_2$ compound, the experimental $T_N(H)$ dependence agrees better with the above expression for $\zeta = 0.87$. This also suggests that the magnetic ordering of Dy^{3+} sublattice has the two-dimensional character.

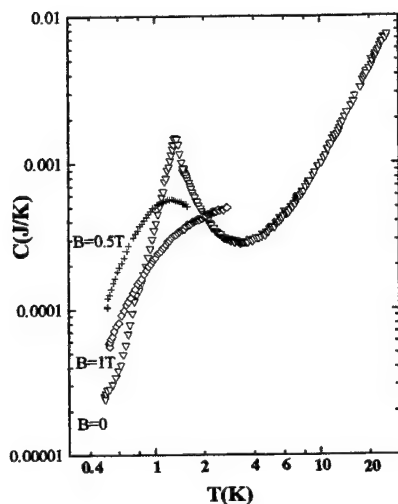


Fig. 2. Temperature dependence of the $\text{CsDy}(\text{WO}_4)_2$ specific heat near magnetic phase transition for various magnetic field strengths.

dependence of the specific heat is indicative of the antiferromagnetic character of Dy ions interactions. The experimental phase boundary between the antiferromagnetic and paramagnetic phases is in a reasonable agreement with the theoretical $T_N(H)$ dependence for 2D Ising antiferromagnet. The experimental value of the effective exchange parameter was obtained to be equal to $J/k = -1.298$ K. Both the sign of J/k and the character of the temperature dependence of the specific heat in a magnetic field indicate the antiferromagnetic character of the Dy^{3+} ions interactions. The J/k parameter was estimated by various methods. The experimental J/k value was shown to correlate with theoretical value for 2D Ising model better than for 3D one.

5. CONCLUSIONS

The magnetic ordering of Dy ions in the $\text{CsDy}(\text{WO}_4)_2$ has been studied for the first time at very low temperatures $0.5 < T < 23$ K. The Neel temperature was determined to be equal to 1.34 K. The peculiarities of magnetic ordering of Dy^{3+} ions was discussed. Data of the above analysis give no single-valued answer as to what model well describes the specific behavior near T_N . The temperature dependence of the specific heat at $T > T_N$ can not be well described by 2D and 3D Ising models. The $C(T)$ dependence below T_N is in reasonable agreement with 2D Ising model. The behavior of the specific heat at $T > 1.5T_N$ correlates with theoretical $C(T)$ dependence for 2D Ising model better than for 3D one. The comparison of the calculation with the experiment data shows that a part of the expected $R \ln 2$ entropy is missing. The magnetic field

ACKNOWLEDGMENTS

This work was partially supported by Polish State Committee on Science (KBN) (project No. 2 P03B 141 18).

REFERENCES

1. M.T. Borowiec, V.P. Dyakonov, A. Jędrzejczak, V.I. Markovich, A.A. Pavlyuk, H. Szymczak, E. Zubov, M. Załęski, "Magnetic ordering of Dy^{3+} ions in $\text{RbDy}(\text{WO}_4)_2$ single crystal", *J. Low Temp. Phys.* **Vol.110**, p.p. 1003-1011, 1998.
2. M.T. Borowiec, V.P. Dyakonov, A. Jędrzejczak, V.I. Markovich, A.A. Pavlyuk, H. Szymczak, E. Zubov, M. Załęski, "Magnetic phase transition in $\text{KDy}(\text{WO}_4)_2$ single crystal", *Phys. Lett. A* **Vol.243**, pp 85-90, 1998.
3. P.V. Klevtsov, R.F. Klevtsova, *J. Strukt. Chem.* **Vol.18**, pp.339, 1978.

Studies of manganites by magnetic resonance spectroscopy methods

V. Dyakonov^{a,b,*}, A. Prohorov^b, V. Shapovalov^b, V. Pashchenko^b, P. Aleshkevych^a,
S. Piechota^a, H. Szymczak^a

^aInstitute of Physics, PAS, 02-668 Warsaw, Poland

²A.A.Galkin Donetsk Physico-Technical Institute, 340114, Donetsk, Ukraine

ABSTRACT

In this work, we present the studies of manganites with superfluous manganese content performed by the magnetic resonance spectroscopy methods. The ferromagnetic resonance (FMR) has been measured on the $(\text{La}_{0.7}\text{Ca}_{0.3})_{1-x}\text{Mn}_{1+x}\text{O}_3$ films. The symmetrical FMR line in paramagnetic phase has the Dysonian-like shape below T_C . The FMR linewidth increases abruptly near the transition temperature. By comparing resonance fields oriented parallel and perpendicular to the film plane, the easy axis of magnetization was determined to be perpendicular to the film plane. In the perpendicular magnetic field, the spin-wave resonance (SWR) spectrum consisting of seventeenth of spin - wave modes has been observed in the $\text{La}_{0.7}\text{Mn}_{1.3}\text{O}_3$ film. Two of them observed on the high-field side of SWR spectrum are connected to a surface modes. The others are the bulk nonuniform spin-wave modes. Based on a study of temperature and angular dependencies of SWR and FMR spectra, the spin-wave stiffness, g-factor and exchange constant were established. An analysis of the ^{55}Mn NMR spectrum in $\text{La}_{0.6}\text{Sr}_{0.2}\text{Mn}_{1.2}\text{Cr}_{0.2}\text{O}_3$ has shown that a wide asymmetrical line can be uniquely expanded into four components with different resonance frequencies. There are manganese ions, which ionization states are close to $(3+)$ and $(4+)$, as well as the Mn ions with intermediate valence resulted from the high-frequency electron exchange.

Keywords: resonance, FMR, NMR, spin-wave and surface modes, manganites, epitaxial films.

1. INTRODUCTION

In the last years, the investigations of monocrystal single-layer and multi-layer films of manganites with the general formula $\text{La}_{1-x}\text{Ca}_x\text{MnO}_3$ demonstrating the effect of colossal magnetoresistance (CMR) is of an active interest. This is due to both their remarkable magnetic and transport properties and a potential application of the CMR effect¹.

The character of spin ordering at the transition to the ferromagnetic state was shown to influence on mobility of charge carriers and, correspondingly, on the electronic transport. Therefore, in studying of the magnetic properties of manganites, it is important to investigate the spin dynamics as it is intimately connected with charge motion between Mn^{3+} and Mn^{4+} ions. One of methods of spin dynamics study is ferromagnetic (FMR) and spin wave (SWR) resonance. The SWR spectrum can be excited in a ferromagnetic thin film if it exhibits appropriate boundary conditions. The pinning mechanism is responsible for excitation of the SWR spectra². If measurements of the bulk spin wave resonance in thin manganites films have been carried out, the observation of the surface spin-wave modes has not been reported yet.

In the $(\text{La}_{0.7}\text{Ca}_{0.3})_{1-x}\text{Mn}_{1+x}\text{O}_3$ compounds studied the cation deficiency responsible for the existence of mixed-valent $\text{Mn}^{3+} / \text{Mn}^{4+}$ ions is due to the provision of superfluous Mn content. The substitution La^{3+} with Mn induces the metal - insulator transition and the charge carriers due to this doping mediate the ferromagnetic interactions between the localized Mn spins³. The substitution of Mn with Cr ion is also of some interest because the Cr ion can exist in various ionization and magnetic states.

The main purpose of present paper to report the effect of superfluous manganese content on peculiarities of the FMR, SWR and NMR spectra in the manganites studied.

* Further author information-

V.Dyakonov (correspondence): E-mail : dyakon@ifpan.edu.pl

2. SAMPLE PREPARATION AND CHARACTERIZATION

The FMR samples studied are the $(\text{La}_{0.7}\text{Ca}_{0.3})_{1-x}\text{Mn}_{1+x}\text{O}_3$ films epitaxially deposited onto the LaAlO_3 substrate using both DC-magnetron sputtering and pulsed-laser deposition. The DC sputtering of the $\text{La}_{0.7}\text{Mn}_{1.3}\text{O}_3$ films was realised in a 10 mTorr $\text{Ar}:\text{O}_2 = 4:1$ atmosphere. Temperature of the substrate surface was 600°C. In order to achieve a homogeneous films, the last were post-deposition annealed at 600°C for additional 30 min in oxygen flow. In the pulsed-laser deposition method, a 248 nm KrF excimer laser was used to deposit the films from stoichiometric targets. Deposition were carried out at oxygen pressure of 300 mTorr. The films were deposited on a substrate at temperature of 780 K. The films thickness measured by optical interferometry method was about 1000 - 3500 Å. According to the X-ray structural analysis, the films are single-phase and have perovskite structure with the lattice constant of 3.907 Å. The ceramic samples have been sintered using the standard technological method⁴. The obtained chemical composition for the $(\text{La}_{0.7}\text{Ca}_{0.3})_{1-x}\text{Mn}_{1+x}\text{O}_3$ compounds is assumed to conserve for films with an uncertainty of about 10 %.

The resonance measurements for in-plane and out-of plane magnetic field geometry were performed using a X-band reflection spectrometer operating at fixed frequency (about 9.235 GHz) in conjunction with a variable temperature flowing gas cryostat. Rotation of the sample was realized in the cavity in plane normal to the film plane with DC magnetic field changing its angle from the film normal to the film plane. The applied magnetic field was changed from 0 to 1.1 T. A HFF field was perpendicular to external magnetic field and was parallel to the film plane. Sample temperature was varied in steps from room temperature to liquid-helium temperature. The measurements of the ^{55}Mn NMR spectra determined using the two - impulse spin echo method have been carried out over a temperature of 77- 300 K.

3. EXPERIMENTAL RESULTS

3.1. Ferromagnetic resonance in the $(\text{La}_{0.7}\text{Ca}_{0.3})_{1-x}\text{Mn}_{1+x}\text{O}_3$ films

A typical FMR spectra for parallel and perpendicular to the film plane fields display one intensive peak identified

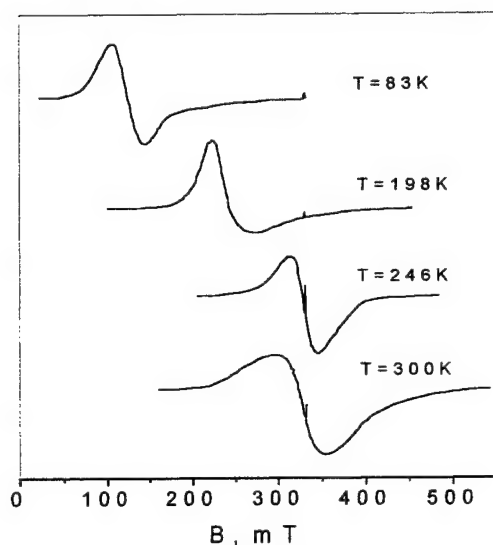


Fig.1 FMR spectrum in the parallel magnetic field geometry for different temperatures.

with the uniform precession FMR mode (Fig. 1). Almost symmetric FMR lines shape was observed in paramagnetic phase. Below T_C , the FMR signal shape becomes asymmetric (Dysonian-like) one. The resonance field H_{res} as a function of temperature for both the parallel ($H_{//}$) and perpendicular (H_{\perp}) configurations of the applied magnetic field is well described by the equations for the resonance frequency : $\omega = \gamma (H_{\perp} - H_{eff})$ and $\omega = \gamma [H_{//} (H_{//} + H_{eff})]^{1/2}$, respectively, where $H_{eff} = 4\pi M_{eff} - 2H_A$. From experiment, we have $H_{\perp} > H_{//}$. That is why in our case the anisotropy of easy-plane type is realized. It should be noted that the value of the effective magnetization $4\pi M_{eff}$ obtained from FMR is in satisfactory agreement with the SQUID data³. The anisotropy of H_{res} field was detected at $T < T_C$ when external field was scanned in the film plane. The anisotropy of linewidth was also fixed: ΔH_{pp} varies from 35 mT when $H // [110]$ to 85 mT for $H // [100]$.

The peak-to-peak linewidth increases sharply reaching the maximum value in the vicinity of T_C . A large peak in the linewidth near the transition temperature is a typical feature of manganite samples with magnetoresistive effect. One possible cause of such ΔH_{pp} behavior can be assumed to be an existence of AFM clusters near defects.

3.2. Spin-wave resonance in the $\text{La}_{0.7}\text{Mn}_{1.3}\text{O}_3$ films

According to the results of measurements for magnetic field perpendicular to the film plane, a resonance spectrum consists of eleven well-resolved lines (Fig. 2). Two of them on the high-field side we identify as the acoustic surface modes, SM_1 and SM_2 , while the others are the bulk nonuniform spin-wave modes. The following experimental facts give evidence for conclusion of surface character of SM_1 and SM_2 modes :

- (i) the resonance field of the modes is above the uniform-mode field position;
- (ii) the intensity of the modes is smaller than the next-lower field mode ($n = 1$);

(iii) the angle dependence of these modes is consistent with the predictions of surface-inhomogeneity model⁵.

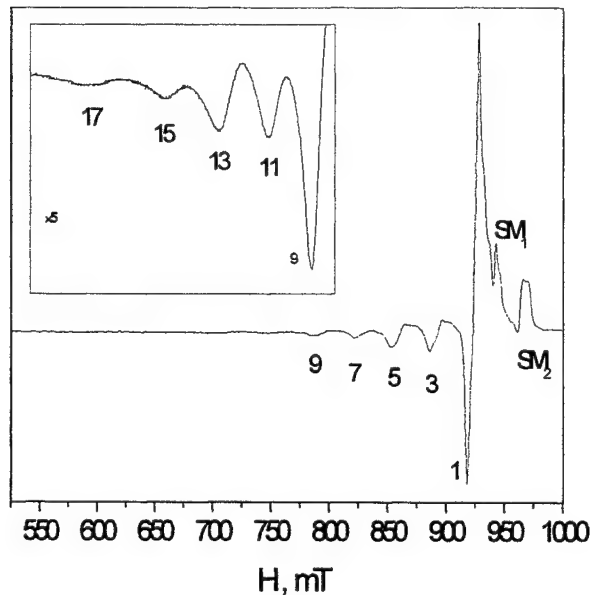


Fig.2 Spin-wave resonance spectrum in the perpendicular magnetic field at 100 K. The inset shows the higher number modes increased by a factor of five.

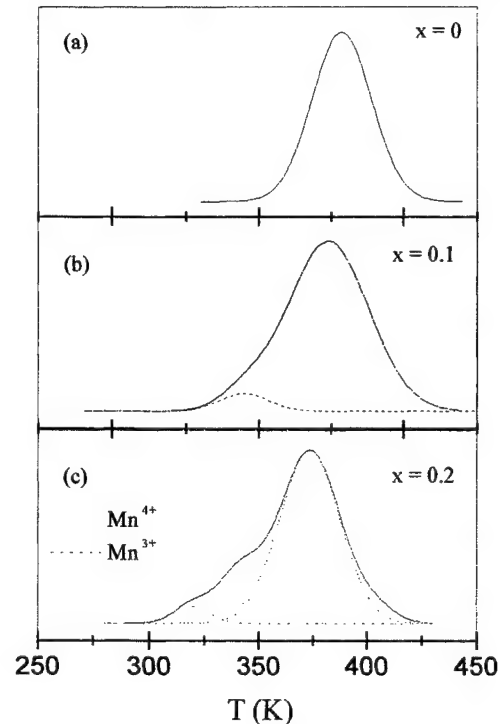


Fig.3 The ^{55}Mn NMR spectra in the $\text{La}_{0.6}\text{Sr}_{0.2}\text{Mn}_{1.2-x}\text{Cr}_x\text{O}_3$ compounds at 77 K.

Unusual transformation of the SWR spectrum is observed with decreasing temperature. Unlike nine lines of SWR observed below 165 K, the fifteenth and seventeenth modes occur only below $T = 143$ K and disappear at 48 and 87 K, respectively. Thus, the maximum number of detected modes is observed over a temperature range of 87 - 143 K.

Other interesting feature was detected in the temperature dependence of SWR linewidths. The linewidths of the higher-order modes ($n = 13, 15$ and 17) have nonmonotonic low temperature behaviour, namely, a decrease of $n=11$ mode linewidth is accompanied by occurrence of $n = 13$ mode. Similar behavior is observed for $n = 15$ mode.

According to an angular dependence of the mode positions, with deviation of field from perpendicular orientation, the resonance modes of SWR start to disappear. There exists a critical angle $\varphi_{cr} \approx 14^\circ$ between static magnetic field and the normal to the film ($90 \pm \varphi_{cr}$). For angles $\varphi < \varphi_{cr}$, a well-resolved multi-peaks SWR spectrum is detected, whereas for $\varphi > \varphi_{cr}$ the spectrum contains in general only one resonance absorption line. At critical angle, the surface and first spin-wave modes transform into the uniform mode. The uniform mode exists only in the region $0 < \varphi < \varphi_{cr}$.

Using the experimental data, we have made some quantitative estimations of the spin-wave stiffness constant, g -factor, saturation magnetization and exchange interaction parameter. Their values were obtained to be equal to $150 \text{ meV}\text{\AA}^2$, 1.96, 560 Oe and 32 K, respectively.

3.3. ^{55}Mn NMR in $\text{La}_{0.6}\text{Sr}_{0.2}\text{Mn}_{1.2-x}\text{Cr}_x\text{O}_3$ compounds

For the $\text{La}_{0.6}\text{Sr}_{0.2}\text{Mn}_{1.2}\text{O}_3$ sample ($x=0$), the NMR spectrum is a simple symmetric line (Fig. 3a) with the resonance frequency (379 MHz) intermediate between the frequencies characteristic for NMR lines of manganese ions in the trivalent state (400-430 MHz) and in the tetravalent state (319 MHz). The presence of one wide line in the spectrum indicates an electronic exchange between multivalent manganese ions with frequency considerably higher than the ^{55}Mn NMR frequency. It can be assumed that a surplus of Mn ions are in distorted A-sites in the divalent state. However, the NMR line in the region of 500-600 MHz typical of Mn^{2+} ions was not observed at 77 K. The ^{55}Mn NMR spectra in $\text{La}_{0.6}\text{Sr}_{0.2}\text{Mn}_{1.2-x}\text{Cr}_x\text{O}_3$ perovskites with $x > 0$ become more complicated and are asymmetrically shifted to lower frequency. An analysis has shown that its wide line can be expended into four lines centered around 319, 342, 373 and 404 MHz

(Fig. 3c). These components arise due to both different ionization states of the manganese ions and a non-equivalence of their crystallographic surrounding. The Cr^{3+} ions are most likely to substitute trivalent Mn ions in octahedral B positions. It is confirmed by a decrease of the NMR frequency of the Mn ions with increasing Cr content. In this case, the Cr ions partly suppresses an electron exchange between the Mn ions and the value T_C . As a result, the Mn ions with localized 3d-electrons are created. These are trivalent and tetravalent manganese ions with NMR lines centered at 319 and 404 MHz, respectively. The NMR line at 342 MHz should be related to manganese ions with intermediate valency.

4. CONCLUSIONS

1. We report a systematic study of FMR, SWR and NMR spectra in the La-deficient manganites with superfluous manganese content.

2. An anisotropy of FMR spectra determined from temperature and angular dependencies of both resonance field and linewidth is due to film-substrate strain effect. The large peak in the linewidth detected below the transition temperature is due to intrinsic phase separation when the film consists mainly of a FM matrix and embedded in the matrix AFM filamentary microdomains.

3. In epitaxial $\text{La}_{0.7}\text{Mn}_{1.3}\text{O}_3$ film the spin-wave resonance consisting of a seventeenth of standing spin-wave modes in the perpendicular magnetic field geometry has been observed. Two of them are the surface modes, while the others are the bulk spin-wave modes. The mode separation with angle observed in this study suggests that the boundary conditions are angular dependent. An unusual transformation of the spin-wave spectrum, namely, the disappearance of highest resonance modes with decreasing temperature have been found. Based on the temperature and angular dependencies data of SWR spectra, the spin-wave stiffness, exchange constant, g-factor value and saturation magnetization were estimated.

4. Numerical analysis of a wide asymmetrical line of the ^{55}Mn NMR spectrum in the $\text{La}_{0.6}\text{Sr}_{0.2}\text{MnCr}_{0.2}\text{O}_3$ compound enables its unique decomposition into four components with different resonance frequencies. These lines are due to both different valence states of the manganese ions and non-equivalence of their crystallographic surrounding in real structure. The NMR studies have shown that the Cr doping leads to a decrease of double exchange between manganese ions of different valencies.

ACKNOWLEDGMENTS

This work was partially supported by the Polish Government Agency KBN under contract N 2 P03B 139 18.

REFERENCES

1. J.M.D. Coey, M. Viret and S. von Molnar, "Mixed-valence manganite", *Adv. Phys.* **48**, p.p. 167-293, 1999.
2. C. Kittel, "Excitation of spin waves in a ferromagnet by a uniform rf field", *Phys. Rev.* **110**, p. p. 1295-1297, 1958.
3. V.N. Krivoruchko, S.I. Khartsev, A.D. Prohorov, V.I. Kamenev, R. Szymczak, M. Baran and M. Berkowski, "Transport and magnetic properties of DC magnetron sputtered $\text{Ln}_{0.7}\text{Mn}_{1.3}\text{O}_{3-x}$ thin films", *JMMM* **207**, p.p. 168 – 179, 1999.
4. V.P. Pashchenko, A.A. Andreev, A.A. Shemyakov, V.K. Prokopenko, E.G. Darovskikh, O.P. Cherenkov and A.D. Loiko, "Crystall lattice defects and properties of magnetoresistive manganite – lanthanum oxides with perovskite structure", *Inorg. Mater.* **34**, p.p. 62 – 69, 1998 (in Russian).
5. H. Puzzkarski, "Quantum theory of spin wave resonance in thin ferromagnetic films; Part I. Spin wave in thin films", *Acta Phys. Polonica A* **38**, p.p. 217 - 238, 1970.
6. H. Puzzkarski, "Quantum theory of spin wave resonance in thin ferromagnetic films; Part II. Spin wave resonance spectrum", *Acta Phys. Polonica A* **38**, p.p. 899 - 914, 1970.

Effect of pressure and magnetic field on the phase transitions in lanthanum-deficient manganites

V. Dyakonov^{a,b*}, I. Fita^b, E. Zubov^b, V. Pashchenko^b, V. Mikhaylov^b, Yu. Bukhantsev^a, H. Szymczak^a

^aInstitute of Physics, PAS, 02-668 Warsaw, Poland

^bA.A.Galkin Donetsk Physico-Technical Institute, 340114, Donetsk, Ukraine

ABSTRACT

We report on the pressure, field and temperature dependencies of magnetization and resistance in manganites of $(\text{La}_{1-x}\text{Ca}_x)_{1-y}\text{Mn}_{1+y}\text{O}_3$ type. The $M(T)$ dependencies is established to exhibit the following peculiarities: the first is connected with the paramagnet (PM) -ferromagnet (FM) transition at 267 K; the peak of $M(T)$ dependence at 263 K is presumably due to an existence of AFM clusters; an anomaly in magnetization (as well as in susceptibility) is connected with the FM - canted phase transition at 42 K and the large irreversibility in the field-cooled and zero field-cooled magnetization. As field is increased above 200 Oe, the sign of the $M(T)$ anomaly changes, namely, the $M(T)$ magnetization increases with increasing field at 42 K. The character of $M(T)$ dependencies does not change under pressure. However, both the Curie temperature, T_C , and the resistance peak (T_{maxR}) corresponding to metal-insulator transition shift in the direction of high temperatures with increasing pressure. A pressure stabilizes the ferromagnetic metallic phase. The temperature of the FM - canting phase transition does not change under pressure. The magnetoresistance effect increases by 15% under pressure of 12.6 kbar. The linear increasing of T_C with the derivatives of $dT_C/dP \approx +1.5 \text{ K / kbar}$ in $(\text{La}_{0.7}\text{Ca}_{0.3})_{0.8}\text{Mn}_{1.2}\text{O}_3$ and $dT_C/dP \approx +1.9 \text{ K / kbar}$ in $\text{La}_{0.6}\text{Mn}_{1.4}\text{O}_3$ ceramics was observed at pressure up to 10 kbar. The $T_{\text{maxR}}(P)$ dependencies display a nonmonothonic behaviour with a peculiarity at $P = 5 \text{ kbar}$.

Keywords: pressure, magnetic transition, magnetization, resistance, manganite, canted phase.

1. INTRODUCTION

The hole-doped manganites $\text{La}_{1-x}\text{A}_x\text{MnO}_3$ where La is the lanthanide and A is the alkaline-earth ion were in fact extensively studied in the 1950s for their remarkable magnetic and electrical behaviour. Among the perovskites, the La-Ca-Mn-O system has been explored mostly these last years owing to both the colossal magnetoresistance (CMR) effect and occurrence both ferromagnetic (FM) and metal-insulator (MI) transitions at rather high temperatures. The $\text{La}_{1-x}\text{Ca}_x\text{MnO}_3$ compounds with $0.1 \leq x \leq 0.3$ transform from an antiferromagnetic (AFM) insulator to a FM metal. In these compounds AFM and FM interactions are competing to give the complicated magnetic structures when not only FM and AFM, but canted structure (for certain compositions and temperatures) can be exist.

The magnetic behavior of the lanthanum-manganese oxides is determined by several factors such as the kind of cation (trivalent or divalent or monovalent) substitution for La and the percentage of the n-valent doped ions. The substitution of the Mn ions by other transition metal ions gives also rise to important modifications in the magnetic properties.

In this paper, to modify the $\text{Mn}^{3+} / \text{Mn}^{4+}$ ratio less traditional method, namely, the method connected with the provision of superfluous manganese content was used. As a result of Mn-doping, the optimum conditions for the double exchange interaction also take place what corresponds to the higher temperature of FM and MI transitions.

It should be noted that the magnetic properties of the La-deficient compounds have so extensively been not investigated including under high pressure. Therefore, the main purpose of this paper is to report the effect of magnetic field and pressure on the character of magnetic phase transitions in the perovskites with superfluous manganese content of $(\text{La}_{0.7}\text{Ca}_{0.3})_{1-x}\text{Mn}_{1+x}\text{O}_3$ type. These experiments is expected to provide new information to understand magnetic properties of these materials.

*Further author information –

V. Dyakonov (correspondence); E-mail : dyakon@ifpan.edu.pl

2. SAMPLE PREPARATION AND CHARACTERIZATION

The $(\text{La}_{0.7}\text{Ca}_{0.3})_{1-x}\text{Mn}_{1.2+x}\text{O}_3$ samples were prepared by a ceramic technology using the double synthesizing annealing (at 900 - 950° C) and sintering in air at 1150° C with the subsequent slow cooling. All specimens were examined by X-ray diffraction with $\text{CuK}\alpha$ radiation. The room temperature X-ray diffraction patterns show that the samples are single-phase with close to cubic structure (the lattice parameter of $a = 3.8674 \text{ \AA}$). The Mn-doping does not change the structural symmetry and leads to a decrease in the a parameter in comparison with the parent oxide $\text{La}_{0.7}\text{Ca}_{0.3}\text{MnO}_3$. Magnetization, $M(T,H)$, measurements were performed using a vibrating sample magnetometer over a temperature range of 4.2-300 K. The zero-field-cooled (ZFC) and field-cooled (FC) magnetization was measured in magnetic fields from 2 to 10 kOe. Real and imaginary parts of the ac susceptibility were measured employing a mutual induction method with an excitation field $h_{ac} = 5.0 \text{ Oe}$ at various frequencies. The magnetic measurements were carried out on pressed powder pellets of cylindrical shape ($d = 3 \text{ mm}$, $l = 6 \text{ mm}$). Resistance of the epitaxial films as a function of temperature, pressure and magnetic field was measured using the conventional Dc four-probe method. For magnetic measurements under hydrostatic pressure (10 GPa) was used the specially constructed microcontainer of the piston-cylinder type ($d_{int} = 1.4 \text{ mm}$, $d_{ext} = 4 \text{ mm}$, $l = 60 \text{ mm}$). Similar container ($d_{int} = 6 \text{ mm}$, $d_{ext} = 30 \text{ mm}$, $l = 120 \text{ mm}$) was used for study of transport properties up to 21 kbar. The pressure was tested at low temperature measuring the T_C change of Sn-probe placed near the sample inside the channel of pressure cell.

3. RESULTS

3.1. Effect of magnetic field on the phase transitions in $(\text{La}_{0.7}\text{Ca}_{0.3})_{0.8}\text{Mn}_{1.2}\text{O}_3$ manganite

The measurements of zero field cooled (ZFC) magnetization were performed after cooling of the sample from room temperature to 4.2 K in zero magnetic field, and then warming at the given magnetic field. The field cooled (FC) magnetization of the sample cooled was measured during slow cooling in the applied magnetic field from 300 to 4.2 K. It was observed that the low-temperature magnetization depends on the sample cooling conditions. In Fig. 1, the temperature dependencies of M_{ZFC} and M_{FC} magnetization measured in fields of 100 and 500 Oe are presented. A spontaneous magnetization appears below $T = 270 \text{ K}$. The FM - paramagnetic (PM) phase transition determined as an inflection point of the M vs T curve occurs at $T_C \approx 263$ and 258 K , respectively. These values are above T_C of related compound $\text{La}_{0.7}\text{Ca}_{0.3}\text{MnO}_3$ which is equal to 245K. The FC curve indicates that the ferromagnetism extends slowly below 250 K. It should be noted a clear irreversibility of $M_{FC}(T)$ and $M_{ZFC}(T)$ magnetization. A difference between $M_{FC}(T)$ and $M_{ZFC}(T)$ curves is almost constant at temperatures below 250 K.

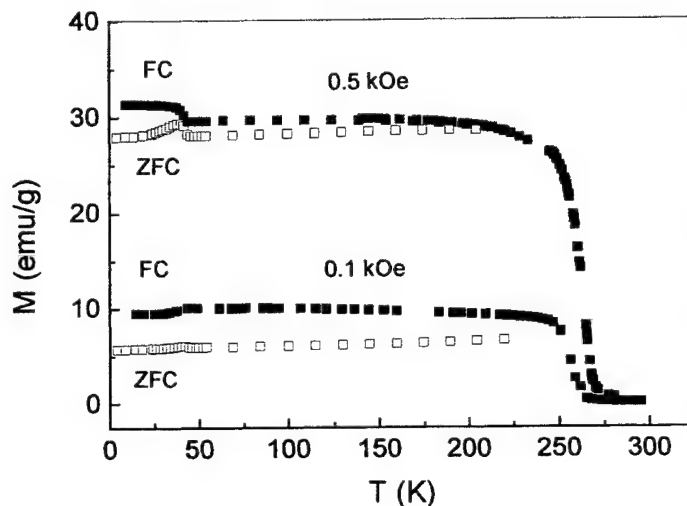


Fig.1. The temperature dependence of magnetization at 0.1 and 0.5 kOe.

interplanar superexchange energy and kinetic energy of electrons in FM planes at very low temperatures is apparently responsible for this magnetization behaviour. In magnetic fields more than 200 Oe (up to 1 T), the FC magnetization increases at $\sim 42 \text{ K}$. The ZFC magnetization shows a similar behavior at these fields. When the field is increased, a hysteresis between ZFC and FC magnetization becomes less pronounced than that in low fields. The magnetization isotherms have the typical FM character. An increase of the Mn content above the stoichiometric one leads to a decrease in magnetization of sample.

The temperature dependence of in-phase, $\chi'(T)$, susceptibility indicates that the FM state rapidly develops below 270 K and depends slightly on temperature below 250 K. The out-of-phase, $\chi''(T)$, susceptibility abruptly increases reaching a maximum at about 260 K and rapidly decreases to zero. The temperature of maximum in the $\chi''(T)$ susceptibility coincides

The ZFC and FC magnetization drop appears in magnetic fields of $H < 200 \text{ Oe}$ at $\sim 42 \text{ K}$. Thus, a part of the spins is excluded from participation in an establishment of the FM long-range ordering. The competition of AFM

with inflection point of the $\chi'(T)$ and $M(T)$ curves which corresponds to the PM-FM phase transition. The ac susceptibility versus temperature, $\chi'(T)$, has a jump at ~ 42 K which coincides with anomaly in the ZFC and FC magnetization at the same temperature indicating a change in magnetic ordered state of the compound studied. It should be noted that the $\chi'(T)$ and $\chi''(T)$ susceptibilities display no frequency dependence up to 2000 Hz.

Thus, an observable $M(T,H)$ dependencies reflect peculiarities connected with both ferromagnetic ordering and phase transition at 42 K as well as the large irreversibility in the FC and ZFC magnetization.

An absence of the frequency and field dependencies in ac susceptibility as well as a cusp in ZFC magnetization indicates that the large irreversibility in the FC and ZFC magnetization has no relation to spin-glass states. The ZFC magnetization remains almost constant between 4.2 and 250 K that can be connected with freezing of some magnetic domains below T_C when the sample is cooled at zero or very low fields. It may be supposed that the large irreversibility arises due to the blocking of cluster magnetic moment which complicate a movement of domain walls at magnetization process and promote a manifestation of relaxation effects. When the compound is cooled under an applied field, the latter help some weakly interacting domains to overcome the freezing and to flip to the direction of magnetic field. In result, a more and more domains will tend to align along field which gives a larger magnetization values and a hysteresis between ZFC and FC magnetization becomes less pronounced than that in low fields.

Analysis of the low temperature peculiarities in $M(T,H)$ and $\chi(T)$ dependencies suggests that these are most probably a result of a FM to canted spin state transition taking into account also that, in theory, an average magnetization of canted spin structure is approximately less on 10 -15 % than one in FM saturated structures as it is observed in experiment.

The magnetization behaviour below 42 K strongly depends on value of an applied magnetic field. Therefore, we also do not exclude that the peculiarities of $M(T,H)$ and $\chi(T)$ dependencies at very low temperature in magnetic field can be connected with the AFM ordering of Mn in the 2+ valence state, which according to the NMR data presents in the $\text{La}^{3+}\text{A}^{2+}\text{MnO}_3$ systems and is likely to locate in the $(\text{Mn}^{2+} - \text{Mn}^{4+})$ clusters. Therefore, the changes in sign of the ZFC and FC magnetization with increasing magnetic field indicate that these are related to a change in the spin configuration and are most probably a result of both the FM to canted phase transition and the presence of AFM ordered $(\text{Mn}^{2+} - \text{Mn}^{4+})$ clusters.

3.2. Pressure effect on the phase transition and resistance in $(\text{La}_{0.7}\text{Ca}_{0.3})_{1-x}\text{Mn}_{1+x}\text{O}_3$ manganites

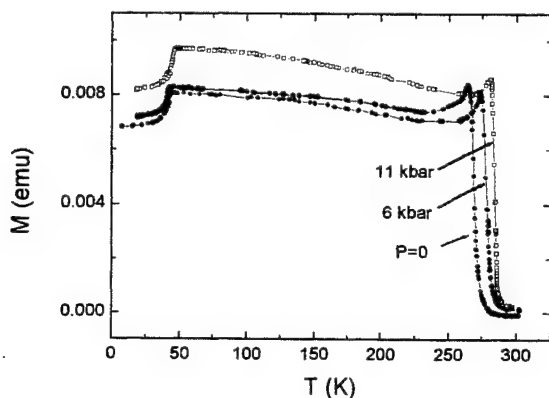


Fig. 2. Effect of the pressure on temperature dependence of magnetization.

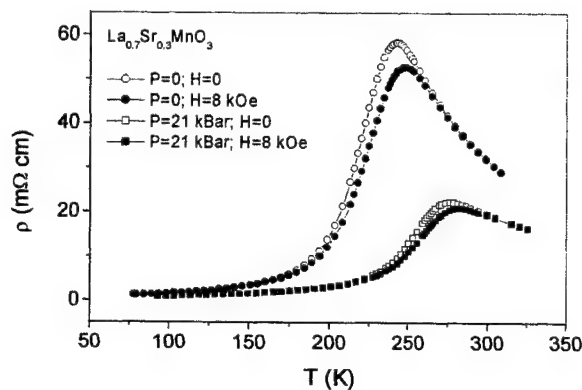


Fig. 3. The pressure and magnetic field effects on the temperature dependence of resistivity.

In Fig. 2, the temperature dependencies of M_{FC} magnetization in $(\text{La}_{0.7}\text{Ca}_{0.3})_{0.8}\text{Mn}_{1.2}\text{O}_3$ at different pressures are presented. It is seen that the character of $M(T)$ dependencies does not change under pressure. The temperature of the FM - canted phase transition also does not change practically with increasing pressure. However, the Curie temperature, T_C , shifts in the direction of high temperatures with increasing pressure. Analogous the pressure effect on the temperature of the PM - FM phase transition is observed in $\text{La}_{0.6}\text{Mn}_{1.4}\text{O}_3$. This testifies about increase of the double exchange interaction between multivalency ions. The linear increasing of T_C with the derivatives of $dT_C / dP \approx +1.5$ K / kbar in $(\text{La}_{0.7}\text{Ca}_{0.3})_{0.8}\text{Mn}_{1.2}\text{O}_3$ and $dT_C / dP \approx +1.9$ K / kbar in $\text{La}_{0.6}\text{Mn}_{1.4}\text{O}_3$ ceramics was observed at pressure up to 10 kbar.

Fig. 3. presents the $R(T)$ dependence for the epitaxial $\text{La}_{0.7}\text{Sr}_{0.3}\text{MnO}_3$ film at pressure $P = 0$ and 21 kbar. It is seen that the resistance peak corresponding to metal-insulator transition shifts towards higher temperatures with increasing

pressure. A pressure stabilizes and expands the ferromagnetic metallic phase. Under pressure and in magnetic field, the value of $R(T,H)$ decreases in comparison with one at $P = 0$ in zero field. Thus, the pressure and magnetic field effect on resistance of the film is analogous. At low and very high temperatures, the pressure does not influence practically on magnetoresistive effect ($\Delta R/R$). The magnetoresistance effect increases by 15% under pressure of 12.6 kbar near the phase transition temperature only. The pressure dependencies $T_{\max R}(P)$ at $H = 0$ and 4.2 kOe is detected to display a nonmonotonous behaviour with a peculiarity at $P = 5$ kbar. It can be evidence of an existence of the structural phase transition. To date, there do not exist the publications on the structural phase transitions in these materials under the pressure.

4. CONCLUSIONS

In this paper, the magnetic phase transitions and transport properties in compounds with superfluous manganese content has been studied in magnetic fields and under pressure. The dc magnetization and ac susceptibility in the $\text{La}_{0.56}\text{Ca}_{0.24}\text{Mn}_{1.2}\text{O}_3$ ceramic were investigated. It was shown that, despite the constant La / Ca ratio, there are essential changes in the magnetic properties of the system as the Mn content is increased above the stoichiometric one. Magnetization of the sample studied decreases and the Curie temperature increases. Peculiarities in $M(T,H)$ and $\chi(T)$ dependencies observed at temperatures of $T_C \approx 260$ and 42 K are connected with a PM to FM phase transition and a FM to canted spin state transition, respectively. A presence of AFM clusters, in parallel with an canted spin state, is responsible for the change of sign in magnetization in applied fields of $H > 200$ Oe below 42 K. An absence of the frequency and field dependencies in ac susceptibility as well as a cusp in ZFC magnetization allow to propose that the large irreversibility in the FC and ZFC magnetization arises due to the random freezing of domain walls. The character of $M(T)$ dependencies does not change under pressure. However, both the Curie temperature, T_C , and the resistance peak corresponding to metal-insulator transition shift in the direction of high temperatures with increasing pressure. A pressure stabilizes and expands the ferromagnetic metallic phase. The temperature of the FM - canting phase transition does not change practically with increasing pressure. The maximal increase of the magnetoresistance effect by 15% under pressure of 12.6 kbar takes place near the phase transition temperature. The linear increasing of T_C with the derivatives of $dT_C/dP \approx +1.5$ K / kbar in $(\text{La}_{0.7}\text{Ca}_{0.3})_{0.8}\text{Mn}_{1.2}\text{O}_3$ and $dT_C/dP \approx +1.9$ K / kbar in $\text{La}_{0.6}\text{Mn}_{1.4}\text{O}_3$ ceramics was observed in the interval pressure up to 10 kbar.

ACKNOWLEDGMENTS

This work was partially supported by the Polish Government Agency KBN under contract N 2 P03B 139 18.

Optical properties of potassium erbium double tungstate $\text{KEr}(\text{WO}_4)_2$

T.Zayarnyuk^{1*}, M.T.Borowiec^{1*}, V.Dyakonov^{1,2}, H.Szymczak¹, E.Zubov^{1,2}, A.Pavlyuk³, M.Barański¹

¹Institute of Physics, Polish Academy of Sciences, al.Lotników 32/46, 02-668 Warsaw, Poland

²A.A.Galkin Donetsk Physico-Technical Institute, 340114 Donetsk, Ukraine

³Institute of Inorganic Chemistry, 630095 Novosibirsk, Russia

ABSTRACT

Results of spectroscopic investigations of crystalline potassium-erbium double tungstate $\text{KEr}(\text{WO}_4)_2$ are reported. The single crystals of $\text{KEr}(\text{WO}_4)_2$ were grown by Top Seeded Solution Growth (TSSG) technique. They belong to the chain-layered group of materials crystallizing in monoclinic syngony (space group C_2^6-C2/c). The investigations were carried out in the broad spectral and temperature range (temperature range from 1.1K up to room temperature and the spectral range from 6000 cm^{-1} to 25000 cm^{-1}). It was found that the potassium erbium double tungstate belong to the class of the biaxial crystals and it is a pleochroic. The main optical absorption spectra are determined.

Keywords: rare-earth double tungstate; pleochroism, optical absorption spectra, biaxial crystals, index of refraction

1. INTRODUCTION

Investigations of physical properties of the rare earth-alkali metal double tungstates are of interest both from scientific and practical point of view. Their studies are strongly stimulated first of all by possible applications of these compounds as active materials in solid state lasers¹. Another very important possible application of rare earth double tungstates is using them as cooling agents in an adiabatic demagnetization method for obtaining very low temperatures². From scientific point of view main considered problems are possible phase transitions as well structural as magnetic ones and the interaction between rare earth ions responsible for phase transitions. Dysprosium alkali metal double tungstates are currently a topic of intensive study³. These compounds are interesting by virtue of structural phase transitions that take place in them in the presence of complex magnetic ordering at subkelvins region⁴. The studies of the structural phase transition caused by the cooperative Jahn-Teller effect (CJTE) are of the significant interest. They are directed to establish the mechanism responsible for phase states and symmetry in real crystals. The detailed study of the structural phase transitions of the CJTE type shows that these occur in compounds composed of ions having two closely spaced energetic levels as a ground state.

In this paper we present optical properties of $\text{KEr}(\text{WO}_4)_2$. The spectra of erbium ions (Er^{3+}) in crystals give information on the optical and other physical properties. The potassium-erbium double tungstate crystallises in $\alpha\text{-KY}(\text{WO}_4)_2$ structure in monoclinic space group C_2^6-C2/c ⁵ with cell parameters $a=8.03\text{ \AA}$, $b=10.29\text{ \AA}$, $c=7.51\text{ \AA}$, $\beta=94^\circ$ ⁵. The structure is characteristic for several others rare earth double tungstates and belongs to the chain-layered systems. The erbium ion is surrounded by eight oxygen ions and it is placed on C_2 point symmetry site. Because of low symmetry of the $\text{KEr}(\text{WO}_4)_2$ single crystals many physical properties are highly anisotropic. For C_2^6 symmetry double refraction and pleochroism are expected.

2. EXPERIMENTAL TECHNIQUES

The double tungstates of the general formula $\text{MRe}(\text{WO}_4)_2$, where M is an alkaline ion, Re - rare-earth ion, undergo irreversible structural phase transitions at temperatures slightly below their melting points. This phenomenon does not allow obtaining low temperature phases of these compounds by means of the Czochralski technique despite their congruent melting. To lower the temperature of crystallisation below the temperature of the phase transition High Temperature Solution Growth (HTSG) technique is used. In case of $\text{KEr}(\text{WO}_4)_2$ single crystal growth $\text{K}_2\text{W}_2\text{O}_7$ was used as a solvent due

*MTB - e-mail: borow@ifpan.edu.pl; mkpbor@it.com.pl

TZ - e-mail: zayar@ifpan.edu.pl

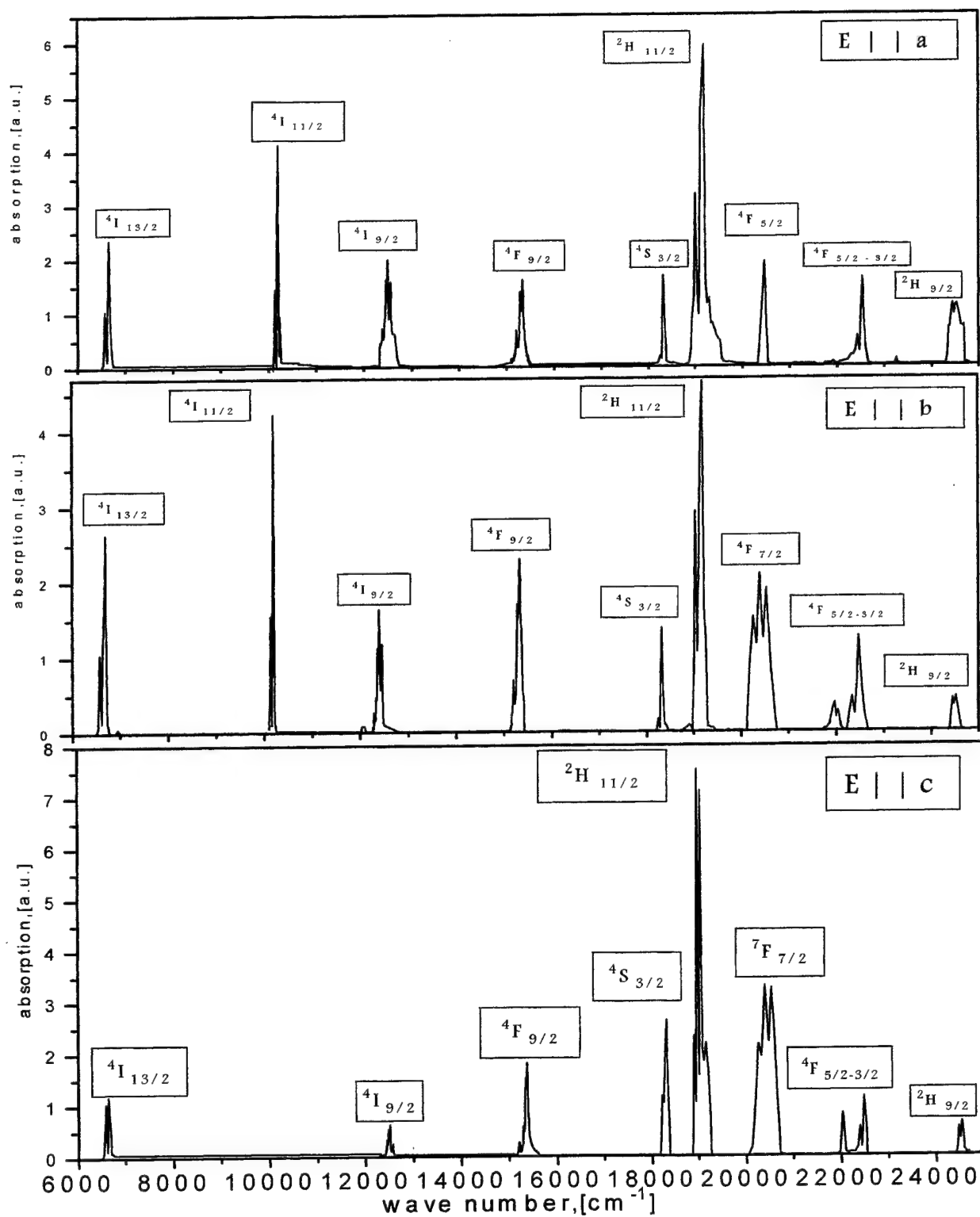


Fig1. The main optical absorption spectra of $\text{KEr}(\text{WO}_4)_2$ are connected with $4f^{11}$ electron configuration of Er^{3+} ions. Ground state multiplet for Er^{3+} ions is $4I_{13/2}$. The next multiplets are $4I_{3/2}$, $4I_{11/2}$, $4I_{9/2}$, $4F_{9/2}$, $4S_{3/2}$, $2H_{11/2}$, $4F_{5/2}$, $4F_{3/2}$, $2F_{5/2}$, $2H_{9/2}$. Figure presents optical transitions to all above excited multiplets at temperature 1.1 K.

to its low viscosity and good solubility of double tungstates. The single crystals were grown by the TSSG technique on oriented $\text{KEr}(\text{WO}_4)_2$ seeds, which were obtained by means of spontaneous crystallisation from solutions of $\text{KEr}(\text{WO}_4)_2$ in $\text{K}_2\text{W}_2\text{O}_7$. For optical investigations the single crystals of $\text{KEr}(\text{WO}_4)_2$ were cut and polished to form of plates with different orientation of flat surface. The orientation of plates was established by the X-ray diffraction method.

Optical spectra were determined in two different cryogenic systems working globally in temperature range between 1.1 K and 500 K from which the range between 1.1 K to 300 K was used. First cryogenic system based on the Oxford Instrument Cryostat CF1104 working from 3.5 K to 500 K with programmable controller ITC4 necessary to set the temperature sweep and hold parameters. The second one was composed mainly from the cryostat of own production, reducing temperature down to 1.1 K.

The optical signal was measured by phase-sensitive method using the Princeton Applied Research (PAR) Lock-In Amplifier - model 5209. Two monochromator systems were used. One working mainly in VIS spectral region based on Carl Zeiss Jena double grating monochromator Model GDM 1000. Second one working also in NIR spectral region up to 6 μm was made from Carl Zeiss Jena monochromator Model SPM2 with changeable different dispersion elements (set of prisms and gratings). To detection of light three different detectors were used - for VIS region two different photomultipliers with the S20 spectra response photocathode and with the GaAs-photocathode and for NIR region the PbS detector. In summary the optical spectra were measured in broad spectral range from 6000 cm^{-1} to 25000 cm^{-1} . The full experimental systems were controlled by the computer DTC-8 with suitable hardware and software.

3. EXPERIMENTAL RESULTS AND DISCUSSION

Because of low symmetry ($C_{2h}^{62}-C2/c$) of the $\text{KEr}(\text{WO}_4)_2$ single crystal also its optical properties are highly anisotropic. In particular, the potassium erbium double tungstate belongs to the optical class of biaxial crystals. Using optical methods, the orientations of optical axes (main axes of indicatrix) at 300 K have been found. The optical (a, b, and c) and the crystallographic (x, y and z) axes are different with one exception of the optical axis b which is identical with the crystallographic axis y. The angles between the optical axes a and c and the crystallographic axes x and z were determined experimentally (the angle between the optical axis a and the crystallographic axis x is equal 17°). Using microscopy method the main refractive indexes have been measured at 300 K. The experimentally obtained values are following: $n_a = 2.881 \pm 0.084$, $n_b = 1.205 \pm 0.011$, $n_c = 4.438 \pm 0.040$.

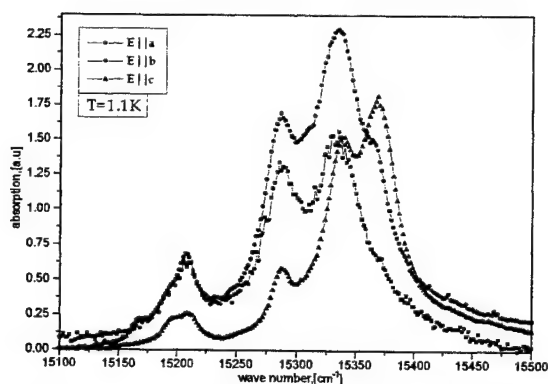


Fig. 2. The main optical absorption spectra of $\text{KEr}(\text{WO}_4)_2$ at temperature 1.1 K in the region 15100 cm^{-1} -15500 cm^{-1} .

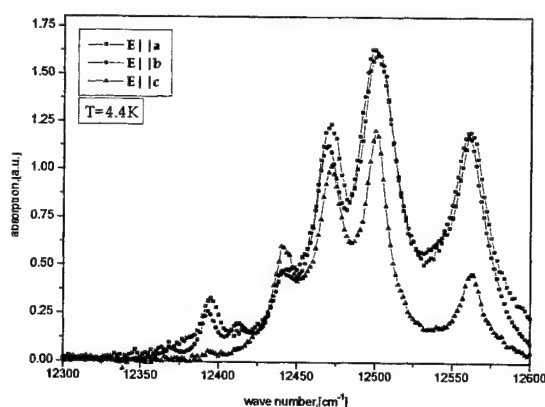


Fig. 3. The main optical absorption spectra of $\text{KEr}(\text{WO}_4)_2$ at temperature 4.4 K in the region 12300 cm^{-1} -12600 cm^{-1} .

The investigations of absorption spectrum of $\text{KEr}(\text{WO}_4)_2$ single crystals were performed in a wide spectral range (6000 cm^{-1} - 25000 cm^{-1}) at temperature from 1.1 K up to 300 K. The trichroism of $\text{KEr}(\text{WO}_4)_2$ was found experimentally, that means the optical absorption is characterized by three different, independent spectra attributed to three optical axes (so called main optical spectra). Fig. 1 presents three main optical spectra at temperature 1.1 K for electrical vector of linearly polarized light parallel to a, b, c optical axes, respectively. The presented spectra are composed of several groups of narrow lines in the same spectral regions (and in the same order) similarly to the spectrum of free Er^{3+} ion⁶. The

differences in intensities and number of lines between individual main spectra in particular spectral regions should be underlined. It is a simple manifestation of pleochroic (trichroic) properties of the erbium-potassium double tungstate.

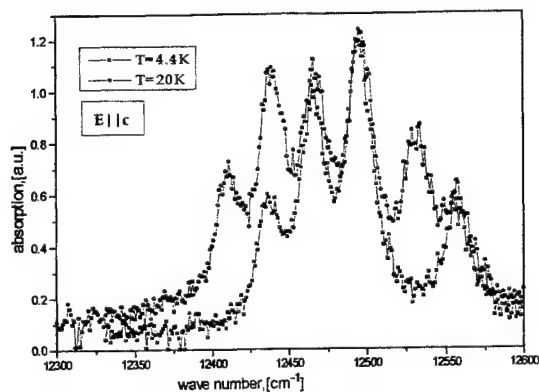


Fig. 4. The main optical absorption spectra of $\text{KEr}(\text{WO}_4)_2$ at temperature 4.4 K and 20 K in the region 12300 cm^{-1} - 12600 cm^{-1} .

Figs. 2 and 3 present main optical absorption spectra in details for two arbitrary selected spectral regions: from 15100 cm^{-1} to 15500 cm^{-1} and from 12300 cm^{-1} to 12600 cm^{-1} . In the Fig. 2 it is clearly seen that observed three main spectra are different.

With temperature increase the optical spectra become more complicated. There are observed thermal satellites on low energy side - for example in the Fig. 3 in the region of about 12440 cm^{-1} . Fig. 4 presents the comparison of the optical spectra with strongly resolved thermal satellites at higher temperatures (the spectra at 4.4 K and 20 K). The presence of the observed thermal satellites up to 300 K allows to divide all satellites into three groups with different energy distances to high-energy lines. The lowest experimentally found distance between thermal satellites and high-energy lines is equal to about 27 cm^{-1} .

The above presented main optical absorption spectra of $\text{KEr}(\text{WO}_4)_2$ are connected with $4f^{11}$ electron configuration of Er^{3+} ions. Ground state multiplet for Er^{3+} ions is $^4I_{15/2}$. The next multiplets for free Er^{3+} ions are $^4I_{13/2}$, $^4I_{11/2}$, $^4I_{9/2}$, $^4F_{9/2}$, $^4S_{3/2}$, $^2H_{11/2}$, $^4F_{5/2}$, $^4F_{3/2}$, $^2F_{5/2}$, $^2H_{9/2}$. From the Fig. 1 it was found that they are observed the optical transitions to all above excited multiplets. In low symmetry crystal field the ground multiplet $^4I_{15/2}$ is split in 8 Kramers doublets. The above described thermal dependences of spectra allow to estimate the energy distance between two lowest Kramers doublet to be about 27 cm^{-1} .

4. CONCLUSIONS

The double tungstate $\text{KEr}(\text{WO}_4)_2$ has unusual optical properties and it is both biaxial (double refraction) and trichroic (pleochroism). The observed spectra are connected with f^1 configuration of Er^{3+} ions. The ground term for Er^{3+} ion is $^4I_{15/2}$. In low symmetry crystal field this term is split into 8 Kramers doublets. The observed temperature dependences of optical absorption spectra are explained in terms of the transitions from first, second and third excited states.

ACKNOWLEDGMENTS

This work was partially supported by Polish State Committee on Science (KBN) (project No. 2 PO3B 141 18).

REFERENCES

1. A.L.Kaminski, A.V.Butashin, V.S.Mironow, A.A.Pavlyuk, S.N.Bagaev, K.L.Ueda, „New crystalline on the base of monoclinic $\text{KR}(\text{WO}_4)_2 : \text{Ln}^{3+}$ tungstates”, *Optical Review* Vol.4, pp.309-315, 1997.
2. M.T.Borowiec, V.P.Dyakonov, A.Jędrzejczak, V.I.Markovich, A.A.Pavlyuk, H.Szymczak, E.Zubov, M.Załęski, "Magnetic ordering of Dy^{3+} ions in $\text{RbDy}(\text{WO}_4)_2$ single crystal", *J. Low Temp. Phys.* Vol.110, pp.1003-1011, 1998.
3. M.T.Borowiec, A.Jędrzejczak, H.Szymczak, V.P.Dyakonov, V.I.Markovich, A.A.Pavlyuk, "Low temperature specific heat of the tungstate $\text{KDy}(\text{WO}_4)_2$ ", *Phys. Solid State (USA)*, Vol.38, pp.1229-1232, 1996; M.T.Borowiec, V.Diakonov, A.Nabialek, A.Pavlyuk, S.Piechota, A.Prochorov, H.Szymczak, "ESR study of low temperature phase transition in $\text{KDy}(\text{WO}_4)_2$ ", *Physica B* Vol.240(1-2), pp.21-25, 1997; M.T.Borowiec, V.Dyakonov, V.Kamenev, A.Nabialek, A.Prokhorov, H.Szymczak, M.Załęski, "Low temperature structural phase transition in monoclinic $\text{RbDy}(\text{WO}_4)_2$ crystal", *Acta Phys.Polon. A* Vol.94, pp.71-77, 1998.
4. M.T.Borowiec, V.P.Dyakonov, A.Jędrzejczak, V.I.Markovich, A.A.Pavlyuk, H.Szymczak, E.Zubov, M.Załęski, "Magnetic phase transition in $\text{KDy}(\text{WO}_4)_2$ single crystal", *Phys. Lett. A* Vol.243, pp.85-90, 1998.
5. B.M.Ayupov, V.I.Potasova, A.A.Pavlyuk, L.Yu.Kharchenko, „Optical properties of some binary alkaline-rare-earth tungstates with the structure $\alpha\text{-KY}(\text{WO}_4)_2$ ”, *Izv. AN SSSR, Neorg. Mat.* Vol.22, pp.1156-1160, 1986.
6. for example M.A.Elyashevich, *Spektry redkikh zemel*, Gosudarstvennoe Izdatelstvo Tekhniko-Teoreticheskoi Literatury, Moskva 1953

Photoinduced optical effects in BiB_3O_6 glass

I.V. Kityk^a, M. Makowska-Janusik^a, A. Majchrowski^b

^a Solid State Department WSP, 42 217 Częstochowa, Al. Armii Krajowej 13/15, Poland

^b Institute of Applied Physics MUT, 00-908 Warsaw, ul. Kaliskiego 2, Poland

ABSTRACT

A new borate material, BiB_3O_6 (BiBO), has been reported to have extremely high nonlinear optical (NLO) coefficient. In our investigations we obtained both glass and single crystals of BiBO. Owing to its composition, the material is very viscous when molten. This factor causes serious problems both during synthesis and crystallization of BiBO. In this paper only properties of BiBO glass are reported. We found that for the increase of the long-range ordering the photoinduced optical second harmonic generation (SHG) shows a maximum, which is shifted towards the lower photoinducing power with the increase of the temperature. Maximal value of SHG was about 0.081 pm/V at 1.06 μm radiation from YAG:Nd laser ($W=30\text{MW}$, $\tau=35\text{ps}$).

keywords: borate glass, bismuth borate, nonlinear optical properties.

1. INTRODUCTION

In recent years borates have been intensively investigated due to their excellent nonlinear optical and laser properties. Among the newly synthesized borate single crystals, it is necessary to point out the following: BiBO,¹ YCOB,² KAB,³ and CLBO.⁴ Crystalline BiBO was reported by Liebertz et al.¹ to have extremely high NLO coefficient for SHG of 3.2 pm/V. This value is larger than that of widely used NLO crystals such as $\beta\text{-BaB}_2\text{O}_4$ (BBO)⁵ or KTiOPO_4 (KTP).⁶

In our investigations both BiBO crystals and glass were produced. In this paper we report only on photoinduced optical effects in BiBO glass, the NLO properties of BiBO single crystals will be published elsewhere. Molten borates are characterized by very large viscosity and its steep temperature dependence.⁷ Some molten borates have viscosity approaching 10^3 poise near their temperature of crystallization. The segregation of melt constituents on the melt-crystal interface is very slow and even the slightest changes of the melt temperature can deteriorate the growth conditions, what in consequence gives crystals with poor quality. Additionally such melts show strong tendency to glass formation, so it is very difficult to initiate their crystallization. On the other hand this property of molten borates makes obtaining them in form of glass relatively easy. Decreasing the temperature of molten borates below the melting point causes rapid increase of melt viscosity, what reduces the atomic mobility in the melt. The nucleation of crystallization centres in such melts is very slow and as a consequence glass formation is observed.

The starting material was synthesized from stoichiometric amounts of B_2O_3 and Bi_2O_3 in a platinum crucible. To obtain material with known composition boron oxide was molten first to remove water which is easily absorbed by this compound. In next step, after finding the mass of molten B_2O_3 appropriate amount of Bi_2O_3 was added to the crucible. Owing to high viscosity of molten BiBO it was very difficult to obtain homogeneous melt which had to be stirred with the use of a platinum mixer at 850°C. The process lasted several days until the melt became totally transparent. BiBO glass was produced by rapid cooling of the melt to temperatures below 600°C, then rods of different diameters were formed from the viscous melt.

For investigations we have chosen the specimens with different degree of crystallinity. The degree of crystallinity was evaluated as a ratio of intensity of the first crystalline maximum to the total amorphous-like background. The corresponding parameter was introduced by direct ratio of the first X-ray maximum to the total amorphous-like background.

2. MEASUREMENT PROCEDURE

The output optical SHG light intensities were detected using FEU-79 (FEU-39) photomultipliers. The measurements were carried out in the single-pulse regime, with a pulse frequency repetition of 12 Hz with the tunable pulse duration within 1.0 ps. From expression $T \approx 1 - \beta I_p$, where β is the two-photon absorption (TPA) coefficient, l is the thickness of specimen (about 0.5 mm), T -intensity dependent transparency, we have determined the TPA coefficient. The nonlinear TPA was extracted from the intensity-dependent transparency measurements. Simultaneously we have subtracted an influence of linear absorption (220 cm^{-1} , $\lambda=530\text{ nm}$) and of Fresnel reflection 0.04. The averaging statistics over the sample surface was performed in order to average a space nonuniformity in the optical constant distribution.

During the evaluations of time delayed nonlinear optical response we performed measurements of the light intensities at ω and 2ω laser frequencies with the time step of about 0.06 ps. This was ensured using the electronic boxcar (GENETIC12 M) used in the time-synchronized pump-probe conditions. The calculations of the nonlinear optical susceptibility were done from the expression:

$$I(2\omega, t) = \frac{2\mu_0^{3/2} \varepsilon_0^{3/2} \omega^2 \chi_{ijk}^2 I(\omega, t - \tau)^2 d^2}{\pi R_0^2 n(2\omega) n(\omega)^2} \left[\frac{\sin(d\Delta k(t)/2)}{d\Delta k(t)/2} \right]^2 \quad (1)$$

Here R_0 is a radius of the pumping beam which possesses gaussian-like form; $n(2\omega)$ and $n(\omega)$ – refractive indices for the pumping and PISHG doubled frequencies during the photo-pumping; χ_{ijk} – components of the second order nonlinear optical susceptibility determined for different angles of incident light.

To exclude an influence of the hyper-Raman scattering, we have performed the additional investigations of the scattered light up to 3000 cm^{-1} , starting from the wavelength light of 530 nm. Three hyper-Raman maxima between 1200 cm^{-1} and 1800 cm^{-1} were observed with the intensities at least 13 times weaker than the probing phototransparent signal. In the case of the Raman and hyper-Raman measurements we have used argon laser at 522 nm Ar^+ laser line and Spex Triplemate spectrometer. A position-sensitive photomultiplier calibrated using helium-neon gaseous mixture discharge was used to detect the scattered light quanta.

Photoinduced changes of the investigated specimens were done by light of the Q-switched Ti-sapphire laser. The pulses of this laser were multiplied by frequency and their power was varied within the 0.1 – 12 MW, the corresponding pulse duration was changed within the 2- 65 ps. As a probing second harmonic generation source the pulses of the YAG-Nd laser with wavelength $1.06 \mu\text{m}$ and pulse duration 2 ps were used. The output second harmonic generation ($\lambda=0.53 \mu\text{m}$) and pumping ($\lambda=1.06 \mu\text{m}$) signals were spectrally separated by grating monochromator SPM-3. The detection of the corresponding signals was performed by 450 ps boxcar connected with the PDP computer.

From the Fig. 1 one can clearly see that increasing photoinducing power E and disordering (otherwise connected with degree of crystallinity dc) stimulate the enhanced value of the SHG. This indicates an additional enhancement of the output SHG signal due to the disordered non-centrosymmetric voids.

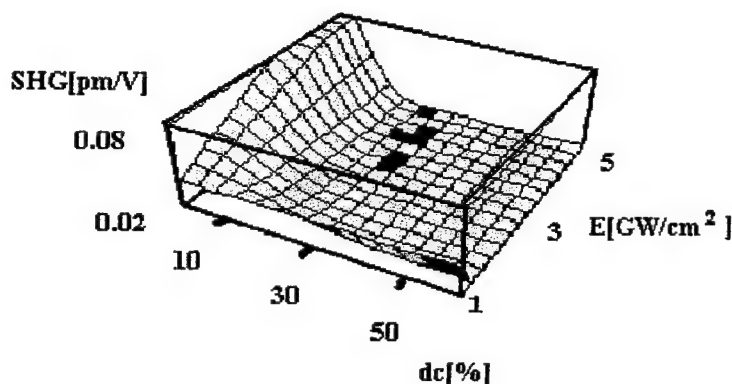


Fig. 1. Dependence of the SHG versus the photoinducing power E and degree of crystallinity dc .

Special interest causes influence of scalar hydrostatic pressure effectively varying the inter-atomic bonds. From Fig. 2 one can see that increasing hydrostatic pressure suppresses the output TPA signal. At the same time the decreasing temperature favours increasing TPA. These values are described by the fourth rank tensors and in this case dominant contribution gives randomly oriented vacancies. This fact is very important for possibility of operation by the output TPA in the partially disordered materials due to varying dc.

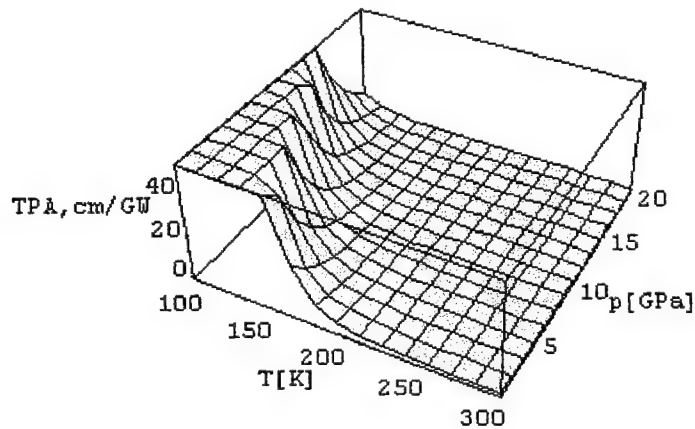


Fig. 2. Temperature dependence of the TPA versus the hydrostatic pressure and temperature. All the measurements were done for the $dc = 12\%$.

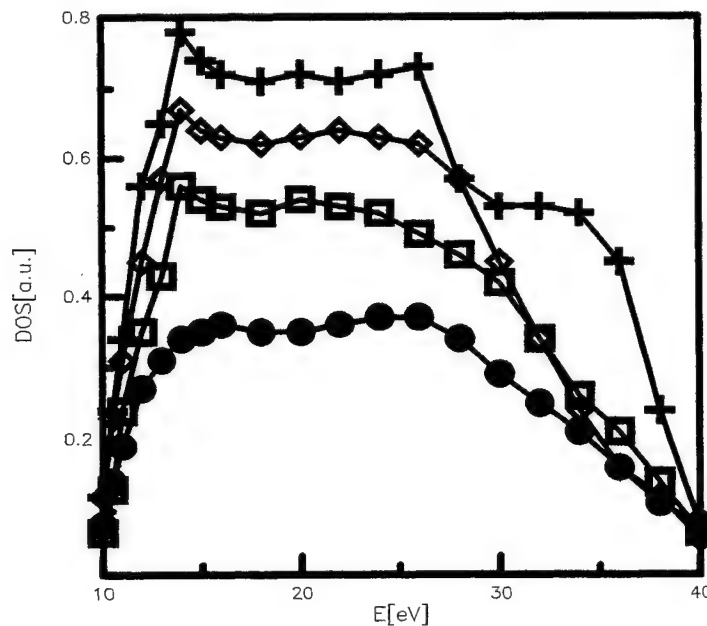


Fig. 3. Dependence of the density of states of BiBO glass on energy for the different degree of crystallinity: • -5%; □ - 12%; ◊ -24%; + - 38%.

From Fig. 3 one can see additional redistribution of the density of states for the amorphous-like glasses of different ordering obtained from X-ray photoelectron spectroscopy. One can clearly see that enhanced disorder substantially decreases total density of states. In order to explain the observed phenomena we have done theoretical simulations using the molecular dynamics simulation and solid state calculations. Generally the method is similar to the described in the Ref. 8.

Calculations of the band electronic structure have been performed taking into account electron-phonon interactions. The calculations have been carried out using *ab initio* norm-conserving pseudopotential method within a Local Density Approximation (LDA). The degree of crystallinity has been taken into account using an extended quasi-Brillouin zone. We have separated contribution of the electron and phonon subsystems, effectively contributing to the nonlinear optical susceptibilities. The phonon modes (within the BiBO glasses) have been calculated using a harmonic approximation, i.e.:

$$d^2\Psi_k/dQ_k^2 + [4\pi^2 \mu_k \hbar^{-2} \Omega_k^2] \Psi_k = 0 \quad (2)$$

where Ψ_k is a phonon-like wave function corresponding to k -th normal coordinate Q_k within the BiBO crystallites, renormalized by surrounding long-range amorphous-like background; μ_k denotes a reduced mass of ions in the k -th phonon mode. Second derivatives of the effective crystalline potential (renormalized by surrounding amorphous-like background) play a dominant role in the observed phonon modes.

An eigen-energy of the k -th phonon mode can be written in the following standard form:

$$\Omega_k(v_k) = 2\Omega_{k0}(v_k + 1/2) \quad (3)$$

where $\Omega_{k0} = \hbar/(f_k/\mu_k)^{1/2}/2$ is an eigen-energy for the zero-point quasi-phonons and $v_k = 0, 1, 2, \dots$ are phonon quantum numbers associated with the following wave functions:

$$\Psi_k(Q_k) = (2\Omega_{k0}/\pi)^{1/4} (2^{v_k}/v_k!)^{1/2} \exp(-\Omega_{k0} Q_k^2) H_{v_k}((2\Omega_{k0})^{1/2} Q_k) \quad (4)$$

where $H_v(x)$ is a Hermite polynomial.

In order to model the vacancy-induced changes, it should be noticed that the electron-phonon interactions should be considered, particularly for the low-frequency phonon modes that could be in a frequency resonance with vacancy resonances. Calculations of the electron-phonon anharmonic potential have been carried out (this can be seen in absorption spectra) in a nonlinear approximation, i.e.:

$$V_{e-ph}(r_i) = e^2 \sum_{ms} M_{ms}^{-1/2} [Z_{ms}(r_s - u_{ms}) |r_s - u_{ms}|^{-3} - \sum_{m's'} Z_{m's'}(r_s - u_{m's'}) |r_s - u_{m's'}|^{-3}] \quad (5)$$

where M_{ms} and eZ_{ms} is effective ionic mass and charge for corresponding ions numbered by m and s , respectively. The intra- as well as inter-crystalline interactions have been taken into account. Moreover, two effective wavevectors have been introduced. The first one, traditionally corresponding to the ordered crystallite units and the second one, quasi-wavevector that is built on the effective molecular sphere originating from the amorphous-like disorder. Influence of the interface region (between the effective BiBO nanocrystallites and the glass-like background) has been extracted by performing a derivative procedure that eliminates possible potential jumps on the crystallite borders. The $u_{ms,m's'}$ vector is a relative displacement of two ions from their equilibrium positions r_s and $r_{s'}$. A probability of a one-phonon transition induced by the phonon of a frequency Ω_k is equal to:

$$\Xi(\Omega_k) = 4(\hbar/2\pi)^{-2} c^{-3} \hbar^{-1} g^{-1}(r_i) (E_{el} - \Omega_k)^2 \Theta(\Omega_k) \quad (6)$$

where H is a sum of the η and ξ level widths, E_{el} is an electron transition energy, Ω_k denotes a phonon energy and $g(r_i)$ is a degeneration degree of the corresponding electron energy levels. The parameter $\Theta(\Omega_k)$ is equal to:

$$\Theta(\Omega_k) = \sum_{\eta} g(\eta) \sum_{\xi} g(\xi) \{ \sum_{\varphi} \langle \eta, \eta_{\Omega} | V_{e-ph}(r_i) | \varphi, \eta_{\Omega+1} \rangle \langle \varphi | d | \xi \rangle (E_{\xi} - E_{\eta} + \Omega_k)^{-1} + \sum_{\varphi} \langle \eta | d | \varphi \rangle \langle \varphi, \eta_{\Omega} | V_{e-ph}(r_i) | \xi, \eta_{\Omega-1} \rangle (E_{\xi} - E_{\eta} - \Omega_k)^{-1} \}^2_{\theta} \quad (7)$$

here η and ξ are lower and upper electron energy levels, respectively; φ denotes a virtual electron state, d is an electric dipole moment for a given spectral transition. The summation is performed over all degenerated initial and final states. Orthogonalization to the highly delocalized states has been carried out by the orthogonalisation procedure of the Legendre polynomials. The symbol θ denotes averaging over all occupied phonon states for phonons with frequency Ω_k . The symmetric phonon modes included in the electron-phonon interaction (see Eq. 5) are renormalized by the normal coordinates that leads to:

$$\Theta(\Omega_k) = C_{\eta\xi} \gamma(r_{\lambda}^{\Delta}) C_{\eta\xi} \gamma(r_{\lambda}^{\Delta'}) \text{Im } G_{\Delta\Delta'} \gamma(r_{\lambda}^{\Delta}, \Omega_k^2) \quad (8)$$

where $G_{\Delta\Delta}^{\gamma\gamma'}(r_{\lambda}^{\Delta})$ is a Green function (γ and γ' are numbers of interacting coordination spheres) defined as:

$$G_{\Delta\Delta}^{\gamma\gamma'}(r_{\lambda}^{\Delta}) = \sum_{\varphi} \{ \langle \eta | V_{e-ph}(\mathbf{r}_i) | \varphi \rangle \langle \varphi | \mathbf{d} | \xi \rangle + \langle \eta | \mathbf{d} | \varphi \rangle \langle \varphi | V_{e-ph}(\mathbf{r}_i) | \xi \rangle \} (E_{\xi} - E_{\eta})^{-1} \quad (9)$$

The Green function calculations were carried out for a perfect BBO lattice renormalized by glass-like environment with taking into account effective nanocrystallite sizes and by performing the summations over 125 \mathbf{k} -points in the irreducible part of the quasi-Brillouin zone. The resulting expression is given below:

$$G_{\Delta\Delta}^{\gamma\gamma'}(r_{\lambda}^{\Delta}, \Omega_k^2) = \sum_{\alpha} K_{\Delta}^{\gamma'}(r_{\lambda}^{\Delta}) K_{\Delta}^{\gamma}(r_{\lambda}^{\Delta}) (\Omega_k^2 - \Omega_{\alpha}^2 - i\delta)^{-1} \quad (10)$$

where the coordinates $K_{\Delta}^{\gamma}(r_{\lambda}^{\Delta})$ were obtained for a given quasi-phonon type by means of the electron states averaging. The vacancy-induced lattice perturbation of the Green function has been done using a deformation localization that allows us to use a Dyson relation:

$$G_{\Delta\Delta}^{\gamma\gamma'}(1) = G_{\Delta\Delta}^{\gamma\gamma'}(0) + G_{\Delta\Delta}^{\gamma\gamma'}(0) U G_{\Delta\Delta}^{\gamma\gamma'}(1) \quad (11)$$

where $G_{\Delta\Delta}^{\gamma\gamma'}(0)$ and $G_{\Delta\Delta}^{\gamma\gamma'}(1)$ is the Green function for an ideal and vacancy-perturbed system, respectively. Coming out from the equation (11), we have obtained the effective electron-phonon wavefunctions for calculations of the intra-the-cluster electrostatic potential and corresponding phonon modes before and after applying the acoustical waves. Afterwards the interaction of the defects with appropriate phonon modes has been taken into account. The changes of effective electrostatic potential contours and of effective low-frequency vacancy modes under influence of external photoinducing field show that the applied photoinducing field essentially changes the electrostatic potential distribution. The appearance of additional non-centrosymmetry in the electrostatic potential distribution is a main requirement to enhance of the second-order nonlinear optical properties, particularly of the SHG, and such an effect is unambiguously seen in this case. Comparison of the calculations made before and after applying of photoinducing field indicates on essential charge density redistribution before illumination and after the illumination. The branches corresponding to the acentric symmetry are responsible for the SHG and the centrosymmetric ones for the TPA.

3. CONCLUSIONS

In conclusion it is necessary to underline that:

Experimentally and theoretically was revealed an occurrence of the non-centrosymmetry due to the disappearance of long-range ordering in the BiBO glass.

Increased non-crystallinity stimulates an enhanced SHG.

Two-photon absorption is critically dependent on the hydrostatic pressure.

Band energy structure calculations confirm essential redistribution of the valence electronic states during the photoinducing illumination.

REFERENCES

1. H. Hellwig, J. Liebertz, L. Bohaty, "Exceptional large nonlinear optical coefficients in the monoclinic bismuth borate BiB_3O_6 (BIBO)", *Solid State Comm.*, **109**, No.4, pp. 249-251, 1999.
2. D. Xue, S. Zhang, "Structural analysis of nonlinearities of $\text{Ca}_4\text{ReO}(\text{BO}_3)_3$ (Re= La, Nd, Sm, Gd, Er, Y)", *Applied Physics a - Mat. Science and Processing*, **68**, pp. 57-61, 1999.
3. Z.G. Hu, T. Higashiyama, M. Yoshimura, Y.K. Yap, Y. Mori, T. Sasaki, "A new nonlinear optical borate $\text{K}_2\text{Al}_2\text{B}_2\text{O}_7$ ", *Jpn. J. Appl. Phys.*, Vol. **37**, pp. L1093-1094, 1998.
4. Y. Mori, I. Kuroda, T. Sasaki, S. Nakai, "Nonlinear optical properties of cesium lithium borate", *Jpn. J. Appl. Phys.*, **34**, pp. L296-L298, 1995.
5. L.K. Cheng, W. Bosenberg, C.L. Tang, "Growth and characterization of low temperature phase barium metaborate crystals", *J. Cryst. Growth*, **89**, pp. 553-559, 1988.
6. J.D. Bierlein, and H. Vanherzeele, "Potassium titanyl phosphate: properties and new applications", *J. Opt. Soc. Am.B*, Vol. **6**, No. **4**, pp. 622-633, 1989.
7. J. Liebertz, "Crystal growth from melts of high viscosity", *Prog. Crystal Growth and Charact.*, **6**, pp. 361-369, 1983.
8. I.V. Kityk, and B. Sahraoui, "Photo induced two-photon absorption, and second harmonic generation in As_2Te_3 - CaCl_2 - PbCl_2 glasses". *Physical Review(USA)*. V. **60**, No. **1**, pp. 942-949, 1999.

The influence of the growth conditions on the elastic properties of SrLaAlO₄ and SrLaGaO₄ crystals studied by Brillouin light scattering

D. Kasprowicz¹, M. Drozdowski¹, A. Wronkowska², A. Pajęczkowska³

¹Faculty of Technical Physics, Poznań University of Technology, Poznań, Poland

²Institute of Mathematics and Physics, University of Technology and Agriculture, Bydgoszcz, Poland

³Institute of Electronic Materials Technology, Warszawa, Poland

ABSTRACT

Study of the optic and elastic properties of SrLaAlO₄ and SrLaGaO₄ crystals are presented. The investigated crystals were grown by Czochralski method. The elastic constants of SrLaAlO₄ and SrLaGaO₄ crystals at room temperature have been determined by Brillouin scattering method. Refractive indices have been measured independently by ellipsometry technique. The results are discussed in terms of the oxygen point defects, which can be created in the lattices of SrLaAlO₄ and SrLaGaO₄ crystals during the growth process.

Keywords: oxides, point defects, Brillouin scattering, ellipsometry

1. INTRODUCTION

SrLaAlO₄ (SLA) and SrLaGaO₄ (SLG) are applied as substrates for high temperature superconducting thin films. SLA and SLG compounds crystallize in the perovskite – like, tetragonal KNiF₄ – type structure of I4/mmm space group. The structure of the crystal is built up of translationally equivalent layers formed by AlO₆ (GaO₆) octahedra and between the layers the Sr²⁺ and La³⁺ ions are randomly distributed in the sites of C_{4v} symmetry. There are two non-equivalent positions of oxygen atoms in the unit cell. The oxygen O2 is situated along the c-axis above Al³⁺(Ga³⁺) ion and the oxygen O1 situated in a-b plane.¹ The physical properties of SLA and SLG crystals have been studied intensively using different experimental method.²⁻⁵ It was reported that the structure of SLG crystal is disturbed by the existence of the oxygen point defects which appear during the growth process.⁶⁻¹⁰ In this paper we presents results concerning the influence of growing atmosphere on the optic and elastic properties of SLA and SLG crystals. The values of refractive indices n_o , n_e , elastic constants $C_{11} = C_{22}$, C_{33} , C_{44} , $C_{55} = C_{66}$, C_{12} , $C_{13} = C_{23}$ of SLA and SLG crystals, which were grown in different atmosphere, are compared. Cross sections of the phase velocities v for longitudinal (L) and transverse (T₁ and T₂) acoustic waves propagating in (001) plane of SLA and SLG crystals are presented. The results are discussed in terms of the oxygen point defects, which can be created in the lattices of SLA and SLG crystals during the growth process.

2. EXPERIMENT

SLA and SLG crystals used in our experiment were grown by Czochralski method at the nonstoichiometric proportion. The light yellow SLA and SLG crystals were grown in nitrogen atmosphere at the oxygen pressure of $4 \cdot 10^{-5}$ atm. The green color SLA and SLG crystals were obtained at the oxygen pressure higher than $5 \cdot 10^{-3}$ atm.⁶ Samples of very good optical quality were cut in appropriate directions according to the imposed selection rules. For our measurements we used samples of sizes: 5mm x 4mm x 3mm, with faces perpendicular to the [100], [010], [001], [110], [101] directions. The Brillouin polarized spectra were taken in the standard 90° scattering geometry at room temperature. As a source of light we used $\lambda = 488$ nm line of an argon – ion laser operating on a single – mode. The scattered light was analyzed through a piezoelectrically driven Fabry – Perot interferometer. The overall finesse (free spectral range divided by the instrumental full width at half maximum of the incident light) achieved was not less than 50.

Refractive indices of SLA and SLG crystals were obtained by applying variable angle ellipsometry. The ellipsometric azimuths ψ and Δ were determined at room temperature as a function of incidence angle ϕ for wavelength $\lambda = 488$ nm. The ellipsometer used was an automatic instrument of the rotating analyzer type from J. A. Woollam Company. The measurements were performed for ϕ ranging from 60° to 70° at an angular resolution of 0.1°. The accuracy of angle of incidence was $\pm 0.005^\circ$.

3. RESULTS

The elastic stiffness tensor of SLA and SLG has six nonzero and non equal components: $C_{11} = C_{22}$, C_{33} , C_{44} , $C_{55} = C_{66}$, C_{12} , $C_{13} = C_{23}$.¹¹ In order to determine elastic constants from Brillouin scattering spectra suitable scattering geometry have to be chosen.¹² Using different scattering geometry we were able to study the propagation of the longitudinal (L) and transverse (T_1 and T_2) acoustic waves. The velocities v of a proper acoustic waves were calculated using Brillouin equation:

$$\Delta v_B = \frac{v}{\lambda} \sqrt{n_i^2 + n_s^2 - 2n_i n_s \cos \theta} \quad (1)$$

where: λ is the wavelength of the incident light, n_i , n_s are refractive indices for the incident and scattered light, respectively and θ is the scattering angle, Δv_B is the Brillouin shift. The elastic constants are calculated from the solution the equation of the motion which is given by:

$$|C_{ijkl} q_j q_k - \rho v^2 \delta_{ij}| = 0 \quad (2)$$

where: q_j , q_k are the direction cosines of the acoustic wave propagation, C_{ijkl} are the elastic constants and ρ is the density of crystal. The direction of phonons q and corresponding ρv^2 as a function of the elastic constants for longitudinal (L) and transverse (T_1 and T_2) acoustic waves are summarized in the Table 1.

Table 1. The direction q , expression for ρv^2 as a function of the elastic constants C_{ij} and values of velocities v for longitudinal (L) and transverse (T_1 and T_2) acoustic waves propagating in yellow and green SLA and SLG crystals. The density $\rho = 5.924 \text{ g/cm}^3$ for SLA and $\rho = 6.389 \text{ g/cm}^3$ for SLG.

q	mod	ρv^2	SLA yellow v [m/s]	SLA green v [m/s]	SLG yellow v [m/s]	SLG green v [m/s]
[110]	T_2	C_{44}	4000	4010	3670	3770
$[\bar{1}10]$	T_2	C_{44}	4000	4010	3650	3780
[110]	L	$\frac{C_{11} + C_{12} + 2C_{66}}{2}$	7120	7130	6340	6420
[101]	T_2	$\frac{C_{44} + C_{66}}{2}$	4260	4300	3790	3820
$[\bar{1}01]$	T_2	$\frac{C_{44} + C_{66}}{2}$	4260	4280	3780	3810
[011]	T_2	$\frac{C_{44} + C_{66}}{2}$	4330	4270	3790	3810
$[0\bar{1}1]$	T_2	$\frac{C_{44} + C_{66}}{2}$	4240	4260	3790	3870
[101]	L	$\frac{(C_{11} + C_{33} + 2C_{44}) + \sqrt{(C_{11} - C_{33})^2 + 4(C_{13} + C_{44})}}{4}$	6750	6800	6460	6540
[011]	L	$\frac{(C_{11} + C_{33} + 2C_{44}) + \sqrt{(C_{11} - C_{33})^2 + 4(C_{13} + C_{44})}}{4}$	6770	6820	6570	6460
[100]	L	C_{11}	6630	6540	6130	6350
[001]	L	C_{33}	6620	6660	6300	6320

The refractive indices of yellow and green SLA and SLG which are needed for the calculation of the elastic constants using Brillouin scattering have been determined by applying variable angle ellipsometry. It is an optical technique based on analyzing the polarization changes caused by reflection of light at the interface between two dielectric media. The components of the electric field \mathbf{E} parallel (E^p) and perpendicular (E^s) to the plane of incidence are reflected and transmitted to a different degree resulting in polarization dependent reflection and transmission coefficients $r^{p,s}$ and $t^{p,s}$, respectively, which are described by Fresnel's equations.¹³ The basic quantity measured is the complex reflection ratio defined as:

$$\mu = \frac{r^p}{r^s} \quad (3)$$

that can be expressed through the ellipsometric azimuths ψ and Δ in the following form:

$$\mu = \tan\psi \exp(i\Delta) \quad (4)$$

where $i = \sqrt{-1}$. In the last equation $\tan\psi$ contains ratio of the electric field amplitudes of the incident and reflected light beams, and Δ is the reflection induced difference in phase change between the two field components. Since ellipsometric azimuths are dependent on a wavelength λ , and angle of incidence of light, ϕ , such a measurement can be used for characterization of the optical properties of the entire system. By ellipsometry it is possible to directly determine, for a given photon energy, the complex refractive index $N = n - ik$ of an isotropic material with a perfectly smooth surface. In the case of an anisotropic sample, for uniaxial crystal, two measurements of ellipsometric parameters for the high symmetry orientations of the optic axis with respect to the plane of incidence are necessary to calculate the principal components of the dielectric tensor.¹³⁻¹⁴ In general, reflection of light from anisotropic or chiral media is determined by the four reflection amplitude coefficients (r^{pp} , r^{ss} , r^{ps} , and r^{sp}).

An alternative method of finding the ordinary n_o and extraordinary n_e indices of refraction of uniaxial crystal is based on the identification of an analogous the Brewster angle or pseudo-Brewster angle when the sample is absorbing the applied radiation. It means that p-polarized light is not reflected at the Brewster angle of incidence ϕ_B , thus giving $\psi = 0$ ($r^{pp} = 0$). Only special orientations of uniaxial crystals are known for which an explicit formula exists for the angle ϕ_p , at which no p-polarized light is reflected when the incident light has the p-polarization.¹⁵ When the optic axis (c-axis) is normal to the plane of incidence the polarizing angle ϕ_p is equal to the Brewster angle for an isotropic medium of refractive index n_o by

$$\tan\phi_p = \frac{n_o}{n} \quad (5)$$

where n is the refractive index of ambient. The extraordinary index of refraction can be found using the following formula:

$$n_e = \sqrt{\frac{(n_o^2 - 1) \tan^2\phi_p}{n_o^2} + 1} \quad (6)$$

which applies for the case when the optic axis lies in the plane of incidence parallel to the interface and the measurements are made in air.

In this experiment the polarizing angles ϕ_p and ϕ'_p were derived from $\psi(\phi)$ $\Delta(\phi)$ curves for high-symmetry orientation of the crystal samples with c-axis perpendicular and parallel to the plane of incidence, respectively. They were determined as the angles of incidence for which $\psi = 0$ (or it has minimum) whereas $\Delta = \pi/2$. In this way, it is possible to find the Brewster angles with accuracy limits not exceeding $\pm 0.05^\circ$. The extinction coefficients k_o and k_e were determined using the ellipsometric azimuths measured for the high-symmetry orientations of c-axis with respect to the plane of incidence.

In Table 2 we present values of refractive indices n_o and n_e together with extinction coefficients k_o and k_e of yellow and green SLA and SLG crystals. The accuracy of refractive indices estimated is ± 0.0025 .

The values of elastic constants C_{ij} of yellow and green SLA and SLG crystals determined at RT by Brillouin scattering are listed in the Table 3. The accuracy in the estimation of elastic constants is no more than 2%.

The phase velocities of longitudinal (L) and transverse (T_1 and T_2) elastic waves propagating in (001) plane for SLA and SLG crystals have been calculated using C_{ij} constants. Cross sections of the phase velocities of the elastic waves propagating in (001) plane for yellow and green SLA and SLG crystals are shown in Fig.1 and Fig.2.

Table 2. The values of refractive indices n_o and n_e , extinction coefficients k_o and k_e of yellow and green SLA and SLG crystals.

crystal	n_o	n_e	k_o	k_e
SLA – yellow	1.9754	1.9960	0.093	0.102
SLA – green	1.9685	1.9912	0.121	0.153
SLG – yellow	2.0189	2.0530	0.118	0.130
SLG – green	2.0010	2.0416	0.144	0.172

Table 3. Elastic constants C_{ij} of yellow and green SLA and SLG crystals at RT (in 10^{10} N/m²)

crystal	C_{11}	C_{12}	C_{13}	C_{33}	C_{44}	C_{66}
SLA – yellow	25.73	10.25	9.18	25.93	9.45	12.06
SLA – green	25.31	10.55	9.96	26.30	9.51	12.20
SLG – yellow	24.04	8.61	11.67	25.32	8.94	9.37
SLG – green	25.73	7.97	10.80	25.49	9.09	9.51

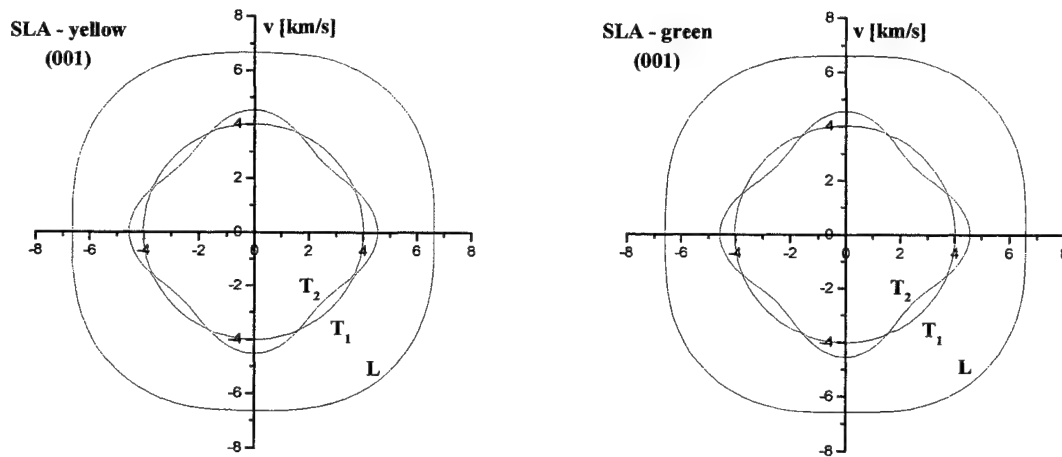


Fig. 1. Cross sections of the phase velocities v (km/s) for longitudinal (L) and transverse (T_1 and T_2) acoustic waves propagating in (001) plane for yellow and green SLA crystals.

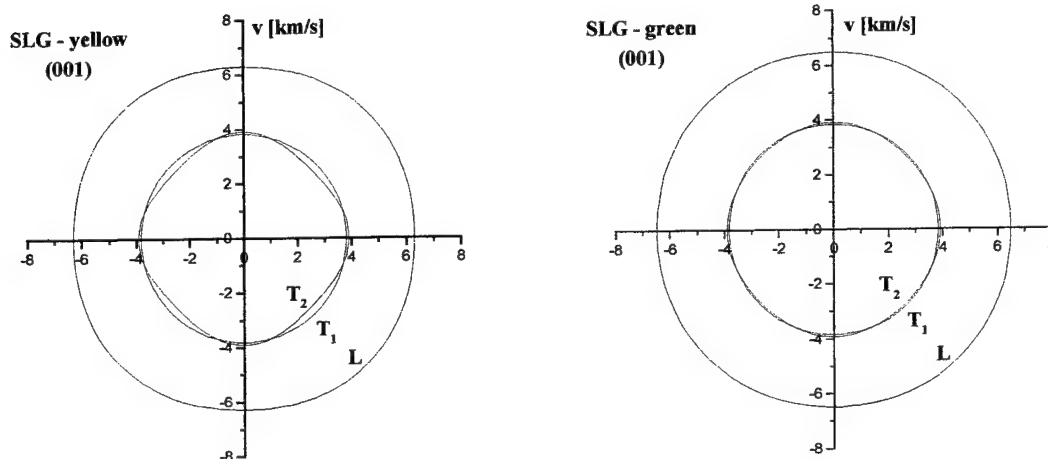


Fig.2. Cross sections of the phase velocities v (km/s) for longitudinal (L) and transverse (T_1 and T_2) acoustic waves propagating in (001) plane for yellow and green SLG crystals.

4. CONCLUSIONS

Both, SLA and SLG single crystals are characterized by larger the n_e than n_o values for wavelength $\lambda = 488$ nm. The refractive indices of green colored samples are lower than those determined for yellow colored ones. As it can be seen from Fig.1. the propagation of the longitudinal (L) and transverse (T_1 and T_2) acoustic waves in (001) plane is typical for tetragonal symmetry both, for yellow and green SLA crystals. However, we observe the disturbed propagation of the longitudinal (L) and transverse (T_1 and T_2) acoustic waves propagating in (001) plane for yellow and green SLG crystals Fig.2. Moreover, for green SLG crystal the degeneracy of the transverse (T_1 and T_2) modes along the [100] and [010] directions occurs. The observed anomaly in the acoustic waves propagation for yellow and green SLA and SLG crystals is probably associated with the displacement of the oxygen ions from their original positions in the crystal lattice. This phenomena can lead to the distortion of the oxygen octahedral, which finally leads to a lower symmetry of the crystal structure from the tetragonal $I4/mmm$. Moreover, the concentration of oxygen defects depends on the oxygen pressure during the growth process which is visible as the increase some of the elastic constants (Table 3) for green SLG crystals. The results obtained are consistent with our previous study of the elastic and elasto-optic properties.

ACKNOWLEDGEMENTS

Authors wish to thank Department of Physics and Measurement Technology Linköping University and individually Prof. Hans Arwin for permission of use their automatic ellipsometer and measurement assistance. This work has been sponsored by the Research Program PB-64-003/2000/BW

REFERENCES

1. J. F. Britten, H. A. Dabkowska, A. D. Dabkowski, J. E. Greedan, J. L. Campbell, W. J. Teesdale, *Acta Cryst.* **C51**, pp.1975, 1995.
2. A. Pajęczkowska, A. Glubokov, „Synthesis, growth and characterization of tetragonal $ABCO_4$ crystals.”, *Prog. Cryst. Growth and Charact.*, **36**, pp. 123-162, 1998.
3. A. Glubokov, R. Jabłoński, W. Ryba-Romanowski, J. Sass, A. Pajęczkowska, R. Uecker, P. Reiche, „On the preparation and crystal growth of $SrLaAlO_4$ ”, *J. Cryst. Growth.*, **147**, pp. 123-129, 1995.
4. S. Kamba, E. Buixaderas, A. Pajęczkowska, “Polarized Infrared Reflectivity Spectra of $SrLaAlO_4$ and $SrGaAlO_4$ single crystals.” *Phys.Stat. Sol. (a)*, **168**, pp. 317-324, 1998.
5. M. Drozdowski, A. Pajęczkowska, D. Kasprowicz, P. Ziobrowski, A. Kłos, „Study of the elastic properties of $SrLaAlO_4$ and $SrGaAlO_4$ single crystals by Brillouin light scattering.”, *Cryst. Res. Technol.*, **31**, pp. 361-364, 1996.

6. A. Pajączkowska, A. Kłos, D. Kasprowicz, M. Drozdowski, „Influence of oxygen on the growth of some oxide crystals.”, *J. Cryst. Growth.*, **198/199**, pp. 440-443, 1999.
7. W. Ryba-Romanowski, S. Gołąb, I. Sokólska, W. A. Pisarski, G. Dominiak-Dzik, A. Pajączkowska, M. Berkowski, „Anisotropy of optical properties of SrLaAlO_4 and $\text{SrLaAlO}_4\text{:Nd}$ ”, *J. Alloys. Comp.*, **217**, pp. 263-267, 1995.
8. M. Drozdowski, J. Domagała, M. Kozielski, M. Szybowicz, A. Pajączkowska, „Temperature study of lattice constants and Raman scattering of SrGaAlO_4 single crystal.”, *Sol. St. Commun.*, **96**, pp. 785-788, 1995.
9. M. Kozielski, A. Jezierski, D. Kasprowicz, M. Szybowicz, “Band structure of $\text{SrLaAlO}_{3+\delta}$ and $\text{SrLaAlO}_{3+\delta}$.”, *Cryst. Res. Technol.*, **34**, pp. 715-718, 1999.
10. D. Kasprowicz, M. Drozdowski, A. Pajączkowska, P. Ziobrowski, A. Kłos, „Anisotropy of the elastooptic properties of SLA and SLG crystals studied by Brillouin scattering.”, *Cryst. Res. Technol.*, **34**, pp. 703-707, 1999.
11. J. F. Nye, *Physical Properties of Crystals*, Oxford, Clarendon Press, 1957.
12. R. Vacher and L. Boyer, „Brillouin scattering: A tool for the measurement of elastic and photoelastic constants.”, *Phys. Rev.*, **B6**, pp. 639-673, 1972.
13. R. M. A. Azzam, N. M. Bashara, *Ellipsometry and polarized light*, North-Holland, Amsterdam-New York-Oxford, 1977.
14. A. G. Pahomov, B. J. Posylnyi, A. F. Konstantinova, *Ellipsometria – metod issledovania povierchnostii*, Nauka, Novosibirsk, 1983.
15. J. Lekner, “Reflection by uniaxial crystals: polarizing angle and Brewster angle.”, *J. Opt. Soc. Am.*, **A 16**, pp. 2763, 1999.

Temperature, absorption and excitation study of the $A_{1-x}B_xC$ crystals by Raman scattering method

M. Kozielski, M. Szybowicz

Faculty of Technical Physics, Poznan University of Technology,
Piotrowo 3, 60-965 Poznań, Poland

ABSTRACT

Recently, wide gap II-VI mixed crystals are studied for their application in technology of blue-green laser diodes. The mixed crystals were grown using the modified pressure Bridgman method.

The temperature, absorption and excitation study of $Zn_{1-x}A_xSe$ mixed crystals using Raman scattering method is reported. Measurements have been performed for crystals with $x = 0.07$ for $A = Mg$ content and $x = 0.09$ for $A = Be$ content. The Raman scattering spectra were obtained for different temperatures and different excitation wavelengths.

From the Raman spectra the longitudinal optical (LO) and transverse optical (TO) modes which correspond to $ZnSe$ -, $MgSe$ - and $BeSe$ -like single crystals were distinguished. For all used excitation wavelengths and different temperatures the integrated intensities of LO and TO modes using a curve-fitting method have been calculated.

Keywords: Raman scattering, mixed crystals, optical phonons.

1. INTRODUCTION

Recently, the physical properties of wide-gap II-VI mixed crystals have been extensively studied using different experimental techniques.^{1,2} These crystals are of significant interest for their potential applications in technology of blue semiconductor lasers. In order to construct such a devices, the proper band structure modulation has to be obtained. This may be achieved with the use of ternary alloys. The mixed crystals based on II-VI compounds offer direct band gap through the entire visible spectral range up to the ultraviolet.

In this paper the study of the vibrational modes in $Zn_{1-x}Mg_xSe$ and $Zn_{1-x}Be_xSe$ mixed crystals using Raman scattering method are reported. Semiconductor crystals were measured at room temperature (RT) and liquid nitrogen temperature (LNT), for various excitation wavelengths. We have also estimated the temperature dependence of the integrated intensity ratio $I_{LO}^{ZnSe} / I_{TO}^{ZnSe}$ for both crystals and for different excitation lines. Some results concerning Raman investigations performed at RT and LNT for $Zn_{1-x}Mg_xSe$ and $Zn_{1-x}Be_xSe$ have been recently published.^{3,4,5}

2. EXPERIMENT

The $Zn_{1-x}Mg_xSe$ and $Zn_{1-x}Be_xSe$ crystals were grown by the modified Bridgman method described in details elsewhere.⁶ The mixed crystals composition was determined by electron microprobe ($Zn_{1-x}Mg_xSe$) and chemical wet ($Zn_{1-x}Be_xSe$) analysis. The measurements were performed for mixed crystals in the composition $x = 0.07$ for $Zn_{1-x}Mg_xSe$ and $x = 0.09$ for $Zn_{1-x}Be_xSe$. The samples used in Raman scattering experiment were ground and polished to the optical quality. The Raman measurements were performed with the use of the helium cryostat (Optistat^{CF} static continuous flow cryostat). The Raman spectra were measured for various excitations wavelength (458 nm, 477 nm, 488 nm, 497 nm and 515 nm). The scattered radiation was analysed with a double-grating monochromator and detected by a cooled EMI photomultiplier, followed by a photon counting system. The experimental setup permitted the band positions of Raman spectra to be estimated with an accuracy of $\pm 2 \text{ cm}^{-1}$.

3. RESULTS AND DISCUSSION

Vibrational Raman spectra of $\text{Zn}_{1-x}\text{Mg}_x\text{Se}$ and $\text{Zn}_{1-x}\text{Be}_x\text{Se}$ for various excitation wavelengths obtained at room temperature are presented in Fig. 1. The typical spectrum consists of ZnSe-like and MgSe-like modes for $\text{Zn}_{1-x}\text{Mg}_x\text{Se}$ crystals, and ZnSe-like and BeSe-like modes for $\text{Zn}_{1-x}\text{Be}_x\text{Se}$ crystals. Both crystals being under study show a typical two-mod behaviour. This problem was described in details in our previous works.^{7,8}

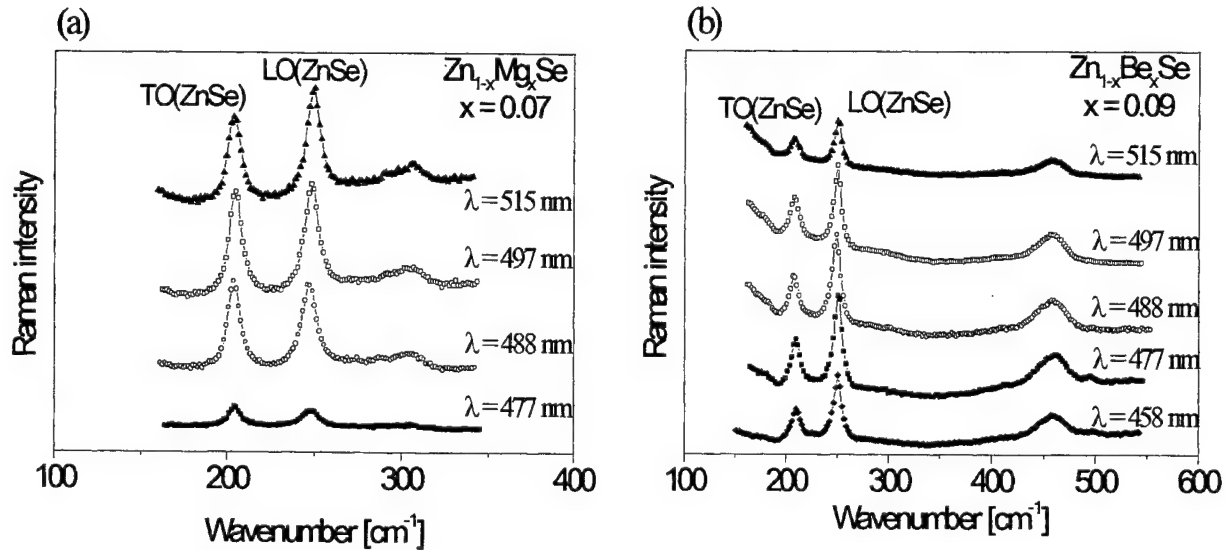


Fig. 1. The Raman spectra of $\text{Zn}_{1-x}\text{Mg}_x\text{Se}$ and $\text{Zn}_{1-x}\text{Be}_x\text{Se}$ crystals obtained for different excitation lines at room temperature.

As it can be seen from Fig. 1a for $\text{Zn}_{1-x}\text{Mg}_x\text{Se}$ crystals the increase of excitation wavelength induces increasing of $\text{LO}_{\text{ZnSe-like}}$ and $\text{TO}_{\text{ZnSe-like}}$ Raman integrated intensities. For excitation wavelength $\lambda_{\text{exc}} = 515$ nm the integrated intensity of LO mode is larger than TO mode. For $\lambda_{\text{exc}} = 477$ nm the integrated intensity of $\text{LO}_{\text{ZnSe-like}}$ mode is smaller than $\text{TO}_{\text{ZnSe-like}}$ mode. In the case of $\text{Zn}_{1-x}\text{Mg}_x\text{Se}$ crystal integrated intensities of LO and TO modes corresponding to ZnSe-like mode increase with increasing of the excitation wavelength. There is no Raman spectra observed at room temperature for excitation wavelength $\lambda_{\text{exc}} = 458$ nm.

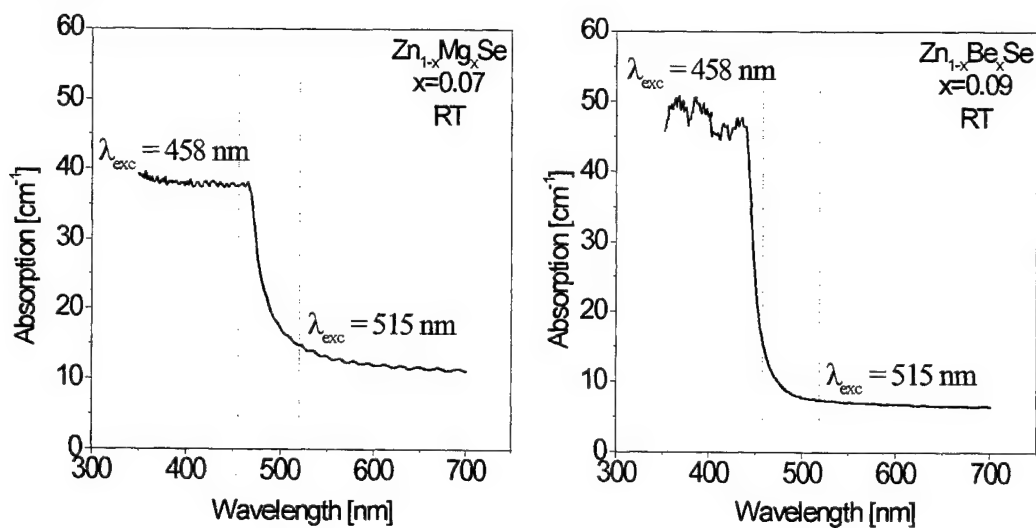


Fig. 2. The absorption of $\text{Zn}_{1-x}\text{Mg}_x\text{Se}$ and $\text{Zn}_{1-x}\text{Be}_x\text{Se}$ crystals as a function of excitation wavelength at room temperature.

The increase of the intensity of Raman bands versus excitation wavelength can be reasoned by considering the dependence of the light absorption in the crystals (see Fig. 2a). As it can be seen from Fig. 2a there is no possibility to observe the Raman spectrum for excitation line 458 nm due to great absorption in the crystal for this wavelength. With the increase of the excitation wavelength the absorption in the crystal decreases and in consequence the integrated intensity of Raman bands increases.

There is different behaviour of the intensity of the LO and TO modes for $\text{Zn}_{1-x}\text{Be}_x\text{Se}$ and $\text{Zn}_{1-x}\text{Mg}_x\text{Se}$ crystals. The Fig. 2b shows that at room temperature the intensity of the $\text{LO}_{\text{ZnSe-like}}$ and $\text{TO}_{\text{ZnSe-like}}$ modes for $\text{Zn}_{1-x}\text{Be}_x\text{Se}$ crystals have almost the same value for various excitation lines. The biggest intensity is observed for excitation wavelength $\lambda_{\text{exc}} = 477$ nm and the lowest intensity for line $\lambda_{\text{exc}} = 515$ nm. For $\text{Zn}_{1-x}\text{Be}_x\text{Se}$ crystals the excitation line $\lambda_{\text{exc}} = 477$ nm is not situated on absorption edge (see Fig. 2b). At it can be seen from Fig. 2b the excitation line $\lambda_{\text{exc}} = 515$ nm is located at small absorption range, causing the lower intensity the LO and TO modes in the Raman spectrum.

We have also analysed the behaviour of integrated intensities of the $\text{LO}_{\text{ZnSe-like}}$ and $\text{TO}_{\text{ZnSe-like}}$ modes as a function of temperature and excitation wavelength. The estimated temperature dependence of the integral intensity ratio $I_{\text{LO}}^{\text{ZnSe}} / I_{\text{TO}}^{\text{ZnSe}}$ as a function of excitation wavelength is presented in Fig. 3.

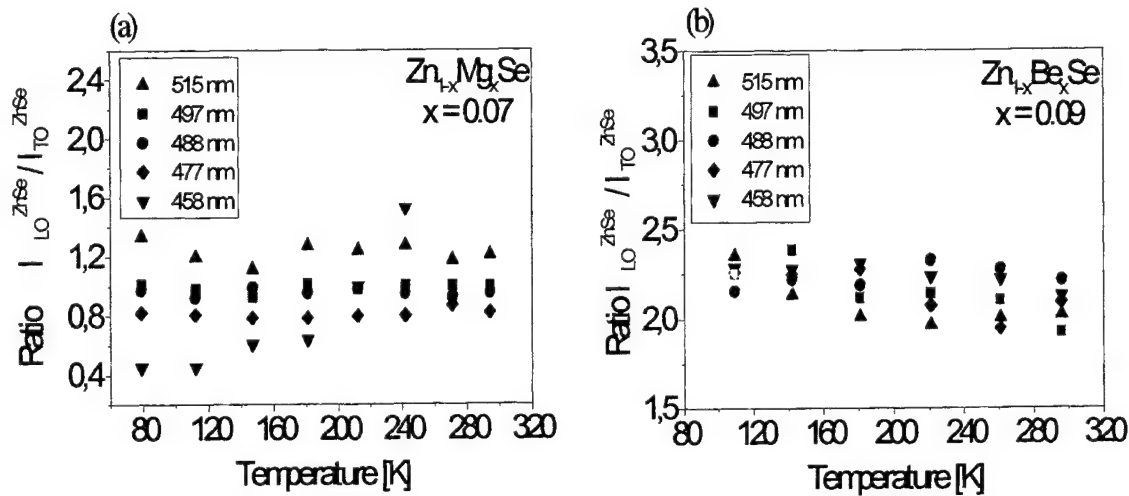


Fig. 3. The temperature dependence of the integral intensity ratio $I_{\text{LO}}^{\text{ZnSe}} / I_{\text{TO}}^{\text{ZnSe}}$ for $\text{Zn}_{1-x}\text{Mg}_x\text{Se}$ and $\text{Zn}_{1-x}\text{Be}_x\text{Se}$ crystals obtained for different excitation wavelength.

As it can be seen from Fig. 3a for $\text{Zn}_{1-x}\text{Mg}_x\text{Se}$ crystals the Raman spectra for excitation line $\lambda_{\text{exc}} = 458$ nm appears at 241 K. For these crystals the integrated intensity ratio $I_{\text{LO}}^{\text{ZnSe}} / I_{\text{TO}}^{\text{ZnSe}}$ for excitation lines: 477 nm, 488 nm, 497 nm and 515 nm through the temperature range is constant. Figure 3a also shows that with the increase of excitation wavelength the integrated intensity ratio $I_{\text{LO}}^{\text{ZnSe}} / I_{\text{TO}}^{\text{ZnSe}}$ increases. However, for $\lambda_{\text{exc}} = 458$ nm we observe an increase of the integrated intensity ratio $I_{\text{LO}}^{\text{ZnSe}} / I_{\text{TO}}^{\text{ZnSe}}$ while the temperature is increasing. For $\text{Zn}_{1-x}\text{Be}_x\text{Se}$ crystals the temperature dependence of the integrated intensity ratio $I_{\text{LO}}^{\text{ZnSe}} / I_{\text{TO}}^{\text{ZnSe}}$ for all excitation lines is constant (see Fig. 3b).

3. CONCLUSIONS

The Raman study of $\text{Zn}_{1-x}\text{Mg}_x\text{Se}$ and $\text{Zn}_{1-x}\text{Be}_x\text{Se}$ mixed crystals has been performed for various temperatures and different excitation wavelengths. The temperature dependence of the integrated intensity ratio $I_{\text{LO}}^{\text{ZnSe}} / I_{\text{TO}}^{\text{ZnSe}}$ for ZnSe-like modes should be considered in terms of the absorption for these crystals. The increase in the value of $I_{\text{LO}}^{\text{ZnSe}} / I_{\text{TO}}^{\text{ZnSe}}$ with increasing of the excitation wavelength can be attributed to the different penetration depth in the crystal. Interaction of the LO phonon field with the surface electric field causes the increase of the intensity ratio $I_{\text{LO}}^{\text{ZnSe}} / I_{\text{TO}}^{\text{ZnSe}}$.

ACKNOWLEDGEMENTS

We would like to acknowledge the help of Professor H. Męczyńska with co-workers from Institute of Physics N. Copernicus University for providing the Zn(Mg/Be)Se single crystals. This work was supported in part by the Research Project TB-64-001/2000/DS of Poznan University of Technology.

REFERENCES

1. F. Firszt, H. Męczyńska, B. Sekulska, J. Szatkowski, W. Paszkowicz, J. Kachniarz, *Semicond. Sci. Technol.* **10**, pp.197, 1995.
2. P.D. Lao, Y. Guo, G. Siu, S.C. Chen, *Phys. Rev.* **B 48**, pp. 11701, 1993.
3. F. Firszt, S. Łęgowski, H. Męczyńska, J. Szatkowski, T. Isshiki, M. Shiojiri, M. Kozielski, M. Szybowicz, W. Paszkowicz, *SPIE* **3178**, pp. 213, 1996.
4. M. Kozielski, M. Szybowicz, F. Firszt, S. Łęgowski, H. Męczyńska, J. Szatkowski, W. Paszkowicz, *Cryst. Res. Technol.* **34**, pp. 699, 1999.
5. F. Firszt, S. Łęgowski, H. Męczyńska, J. Szatkowski, W. Paszkowicz, K. Godwod, J. Domagała, M. Kozielski, M. Szybowicz, M. Marczak, *Proceedings of the 2nd International Symposium on Blue Laser and Light Emitting Diodes, Chiba 1998*.
6. F. Firszt, H. Męczyńska, S. Łęgowski, J. Szatkowski, U. Falke, M. Hietschold, *SPIE* **3178**, pp. 205, 1997.
7. M. Kozielski, M. Szybowicz, F. Firszt, S. Łęgowski, H. Męczyńska, B. Sekulska, J. Szatkowski, *Acta Phys. Pol.* **A 90**, pp. 1040, 1996.
8. M. Szybowicz, M. Kozielski, F. Firszt, S. Łęgowski, H. Męczyńska, J. Szatkowski, W. Paszkowicz, *Optoelectronics Review* **7(2)**, pp. 103, 1999.

Thermal ionization energy of Mg acceptors in GaN: Effects of doping level and compensation

B. Pődör

Hungarian Academy of Sciences,
Research Institute for Technical Physics and Materials Science, Budapest, Hungary

ABSTRACT

It is shown that the thermal ionization energy of Mg acceptors in GaN, as determined by temperature dependent Hall effect measurements, exhibits the usual dependence on the concentration of ionized impurities, as seen in many other semiconductors. The observed difference in the thermal and optical ionization energies of Mg acceptors can be quantitatively understood based on a simple electrostatic interaction model.

Keywords: thermal ionization energy, gallium nitride (GaN), Mg acceptors.

1. INTRODUCTION

Gallium nitride (GaN) is a promising direct wide band gap semiconductor for potential applications in visible and near-UV optoelectronics and in high temperature electronic devices (for recent reviews see e.g. references¹⁻⁴). In fact the invention of blue semiconductor lasers made from gallium nitride has been one of the key technological breakthroughs of the decade. One of the key steps forward in the long way to the realization of these promises was the achievement of controlled p-type doping using Mg as an acceptor by Amano et al.⁵ and later by Nakamura et al.⁶ One of the basic characteristics of an acceptor dopant is its ionization energy. The ionization energy of the Mg acceptor as determined by optical (low temperature photoluminescence) methods is 224 ± 4 meV.⁷ However reported values of thermal ionization energies for the Mg acceptor are considerably lower, with values scattered in the range from 125 meV to 170 meV based on temperature dependent Hall effect measurements (see e.g. reference³), and about 155 to 165 meV based on the temperature dependence of the intensity of donor-acceptor pair emission.^{8,9} These large differences are usually ascribed to the ubiquitous concentration dependence of the thermal ionization energy of impurity centres in semiconductors, however, up to now a systematic quantitative analysis has not yet been attempted. For device applications, however, the thermal ionization energy of the dopant is the relevant parameter, because it controls the degree of ionization of the dopant centres, and in this way it determines the available free charge carrier density, dopant efficiency, etc. Because of this it is important to understand these significant differences.

Here I present a quantitative analysis and interpretation of the observed differences in the thermal and optical ionization energies of Mg acceptors in GaN on the basis of the available models for the concentration and compensation degree dependence of thermal ionization energies of impurity centres. It is proposed that these differences can be satisfactorily described using a simple electrostatic interaction model originally due to Pearson and Bardeen¹⁰ and Debye and Conwell,¹¹ and later discussed and generalized by Monecke et al.,¹² and by the present author.¹³⁻¹⁵

2. MODELS FOR THE CONCENTRATION DEPENDENCE OF THE THERMAL IONIZATION ENERGY

Since the pioneering work of Pearson and Bardeen¹⁰ it has been well known that the thermal activation energy of the impurities decreases with increasing concentration of the impurity centres. Various models^{10-12,15} lead to the following generic expression for the dependence of the thermal ionization energy on the majority impurity concentration (acceptors in p-type materials, to be definitive) and on the compensation degree:

* H-1525 Budapest, P.O.B. 49, Hungary. Fax: +36-1-392-2235, E-mail: podor@mfa.kfki.hu

$$E_A = E_A(N_A, K) = E_{A0} - f(K) \frac{e^2}{4\pi\epsilon_r\epsilon_0} N_A^{1/3} \quad (1)$$

here E_{A0} is the ionization energy of acceptors at infinite dilution, N_A is the acceptor concentration, K is the compensation degree ($K = N_D/N_A$), ϵ_0 is the dielectric permittivity of the vacuum, and ϵ_r is the static dielectric constant of the host semiconductor. $f(K)$ is a (dimensionless) function, the exact form of which depends on the details of the concrete mechanism leading to the reduction of the thermal ionization energy. E_{A0} can be identified with the optical ionization energy as determined e. g. from PL measurements.

Several theoretical models are supporting the form of the dependence of E_A on various parameters especially on N_A and K as given by Eq. (1). These include among others the model based on the concept of electrostatic interaction between the free carriers and the oppositely charged impurity centres originally proposed by Pearson and Bardeen¹⁰ and modified by Debye and Conwell,¹¹ a similar model incorporating also the effects of the relaxation of the distribution of carriers on the impurity centres due to Monecke et al.,¹² and another model based on the concept of random potential fluctuations and quantum overlap effects changing the energy spectrum of impurities, proposed by Lien and Shklovskii¹⁶ (see also references^{17,18}). All lead to Eq. (1) but with different functional forms of $f(K)$. Notably, according to Pearson and Bardeen¹⁰ $f(K) = 1$, according to Debye and Conwell¹¹ $f(K) = 1.646(4\pi/3)^{1/3} = 2.6533K^{1/3}$, according to Monecke et al.¹² $f(K) = \Gamma(2/3)(4\pi/3)^{1/3} = 2.1828K^{1/3}$, and according to Lien and Shklovskii¹⁶ $f(K)$ is a more complicated function with the value of 1 at $K = 0$, the value increasing slowly up to about 1.4 for $K = 0.4 - 0.6$, and dropping more sharply for $K > 0.8$, and even changing sign above $K = 0.93$.

3. ANALYSIS OF THE HALL DATA ON p-GaN:Mg AND DISCUSSION

Using the Hall data for GaN:Mg collected from references¹⁹⁻²⁸ I calculated $f(K)_{\text{exp}}$ i.e. the "experimental" values of the function in Eq. (1) for various samples. In order to have a meaningful comparison the hole concentration versus reciprocal temperature curves were reanalyzed using the standard partially compensated single acceptor model:

$$\frac{p(p + N_D)}{N_A - N_A - p} = \frac{1}{\beta} N_v \exp\left(-\frac{E_A}{kT}\right) \quad (2)$$

with $N_v = 4.829 \times 10^{15} (\text{m}^*/m_0)^{3/2} T^{3/2}$. The adjustable parameters were the acceptor concentration N_A , the donor concentration N_D , and the thermal ionization energy of the acceptors E_A . The values used for the constants were as follows: for the impurity level spin degeneracy β , a value of 4 was chosen, and the density-of-states effective mass of holes in the valence band was assumed to be $m^*/m_0 = 0.8$.

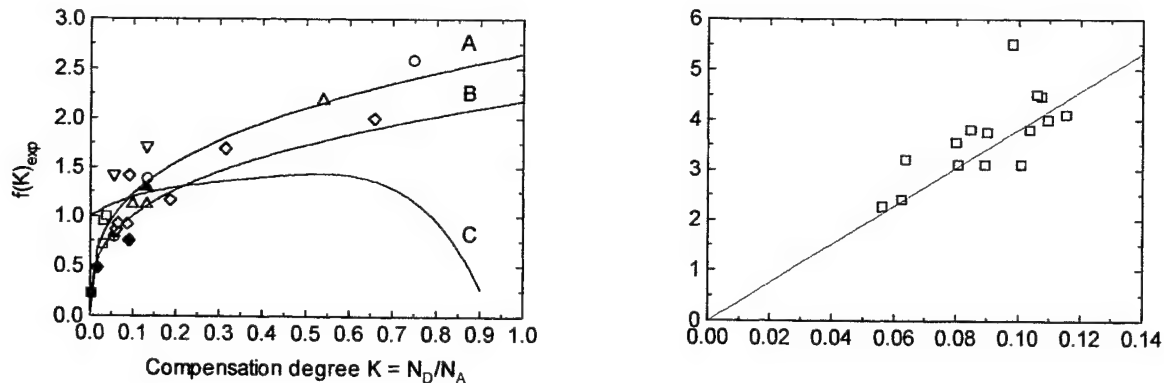


Fig. 1. Theoretical and "experimental" curves of the function $f(K)$ versus K . Data collected and reanalyzed from the literature.¹⁹⁻²⁷ Theoretical curves: A - according to Debye and Conwell,¹¹ B - according to Monecke et al.,¹² C - according to Lien and Shklovskii.¹⁶

Fig. 2. Plot of the values of α versus the reciprocal dielectric constant for various semiconductors. The straight line corresponds to $\alpha\epsilon_T = 38.2 \times 10^{-5}$ meVcm. Data and plot from Pöör, ^{13,14} the GaN datum point is the present result.

The results obtained for $f(K)$ versus K are presented in Fig. 1 together with the theoretical curves for the models of Debye and Conwell,¹¹ Monecke et al.,¹² and Lien and Shklovskii.¹⁶ In evaluating $f(K)$ from Eq. (1) the acceptor ionization energy at infinite dilution was taken as $E_{A0} = 224$ meV, and the relative dielectric constant as $\epsilon_T = 9.6$. Notwithstanding the relatively big scatter, the data follow a common trend, i. e. the values of $f(K)_{\text{exp}}$ deduced from the Hall curves reported in the literature increase monotonously with increasing K , and the actual values of the function $f(K)_{\text{exp}}$ seem to be somewhat better described by the model due to Debye and Conwell¹¹ than by the model of Monecke et al.,¹² without any fitting parameter. It is to be noted that in the limit of $K = 0$ the deduced values of $f(K)_{\text{exp}}$ tend to zero. The theoretical curve based on the model of Lien and Shklovskii¹⁶ is clearly at variance with the data analysed here. In the range of intermediate compensation ($K = 0.3$ to 0.6) the values of $f(K)_{\text{exp}}$ lie significantly higher than the curve corresponding to this model, and at high compensation degrees this difference reaches a factor of 2 to 3. Similar behaviour of the function $f(K)$ in various semiconductor-impurity systems has already been noted by Zabrodskii and Timofeev¹⁸ and by the present author¹⁵ too.

If we suppose the *a priori* applicability of the electrostatic interaction model of Debye and Conwell to the experimental data, as the validity of this assumption is being corroborated by the results of analysis of a great amount of data,¹⁰⁻¹⁴ then using the relationship $N_D = KN_A$ Eq. (1) can be rewritten as

$$E_A = E_{A0} - \frac{e^2}{4\pi\epsilon_T\epsilon_0} N_D^{1/3} = E_{A0} - \alpha N_D^{1/3} \quad (3)$$

with a theoretical value of $\alpha = 38.2 \times 10^{-5}/\epsilon_T$ (meVcm). Using the model of Monecke et al.¹² the constant would be $\alpha = 31.4 \times 10^{-5}/\epsilon_T$ (meVcm).

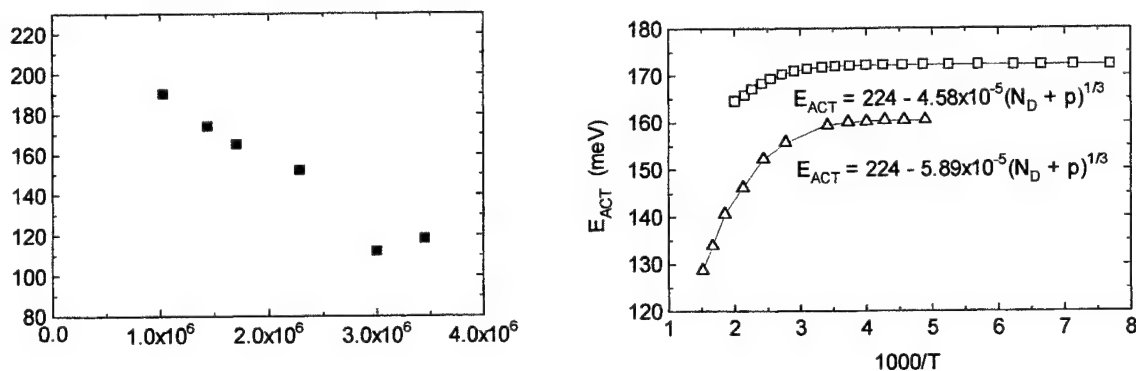


Fig. 3. Plot of the thermal activation energy of Mg acceptors in GaN versus the cubic root of the compensating impurity (donor) concentration. Up triangles, solid circles, down triangles, squares, circles, solid squares - data from the literature.^{19,21,22,26,27,28} The straight line represents the least-squares fit to the data.

Fig. 4. Acceptor activation energies deduced using a model incorporating the dependence of the activation energy on the concentration of ionized acceptors: $N_{Ai} = N_D + p$. Triangles - data from Nakayama et al.,²¹ squares - data from Götz et al.,²³ reanalyzed with $E_{A0} = 224$ meV.

This model suggests that the value of α for various impurities in the same semiconductor host should be equal, and the values of α for different semiconductors should scale with the reciprocal of the dielectric constants. An analysis of the available large amount of data for group IV, III-V, II-VI and II-IV-V₂ semiconductors confirms this statement.^{13,14} Fig. 2, after ^{13,14} summarizes these results. Empirically it was found that $\alpha = (40 \pm 5) \times 10^{-5}/\epsilon_T$ meVcm, which corresponds to the theoretical value for the model of Debye and Conwell.¹¹ Fig. 3. presents the data for GaN:Mg plotted according to Eq.

(2). Least-squares fit yields $E_A = (217 \pm 8) - (3.14 \pm 0.40) \times 10^{-5} N_D^{1/3}$ (energy in meV, concentration in cm^{-3}). The energy intercept agrees within error with the optical ionization energy, the fitted value of the slope α however, as can be seen in Fig. 2, is lower than the theoretical value for the model of Debye and Conwell,¹¹ and is close to that expected for the model of Monecke et al.¹² However, if the fit is performed with a fixed intercept $E_{A0} = 224$ meV, a greater value of α is obtained, which is close to the value expected on the basis of the model of Debye and Conwell.¹¹

The usual interpretation attached to Eq. (3) is that the thermal ionization energy decreases linearly with the cubic root of the ionized acceptor (majority impurities in p-type material) concentration because, at least at low temperatures where $p \ll N_A$, $N_{Ai} \approx N_D$. However, in general $N_{Ai} = N_D + p$, therefore in the strict sense of the electrostatic interaction models (like of Debye and Conwell¹¹ and of Monecke et al.¹²) in Eq. (3) $N_{Ai} = N_D + p$ should figure instead of N_D .²⁹ With this refinement instead of Eq. (3) we have

$$E_A = E_{A0} - \alpha N_{Ai}^{1/3} = E_{A0} - \alpha (N_D + p)^{1/3} \quad (4)$$

implying that the "effective" thermal ionization energy itself depends on the temperature through the temperature dependence of the carrier concentration p . Typical results of Hall curve fits, taking into account the implicit temperature dependence of the thermal activation energy as given by Eq. (4), are presented in Fig. 4. In these fits $E_{A0} = 224$ meV, a constant, was assumed. As might be expected from Eq. (4), the fitted activation energies exhibit a substantial decrease at higher temperatures, and concomitantly and somewhat surprisingly, the fitted values of the constant α are 20-40 per cent higher than those obtained from the conventional analysis, and also from the electrostatic interaction model.¹¹

4. CONCLUSIONS

The observed differences in the thermal and optical ionization energies of Mg acceptors in GaN were analyzed on the basis of the available models for the concentration and compensation degree dependence of thermal ionization energies of impurity centres. It was established that these differences can be satisfactorily described using a simple electrostatic interaction model originally due to Pearson and Bardeen and Debye and Conwell.

ACKNOWLEDGEMENTS

This work was supported from grant No. 030395 from the Hungarian National Research Fund (OTKA).

REFERENCES

1. S. Strite and H. Morkoc, "GaN, AlN, and InN: a review," *J. Vac. Sci. Technol. B* **10**, pp. 1237-1266, 1992.
2. S. Strite, M. E. Lin and H. Morkoc, "Progress and prospects for GaN and the III-V nitride semiconductors," *Thin Solid Films* **231**, pp. 197-210, 1993.
3. J. W. Orton and C. T. Foxon, "Group III-nitride semiconductors for short wavelength light emitting diodes," *Rep. Prog. Phys.* **61**, pp. 1-75, 1998.
4. S. J. Pearton, J. C. Zolper, R. J. Shul and F. Ren, "GaN: Processing, defects, and devices," *J. Appl. Phys.* **86**, pp. 1-78, 1999.
5. H. Amano, H. Kito, K. Hiramitsu and I. Akasaki, "P-type conduction in Mg-doped GaN treated with low-energy electron beam irradiation," *Jpn. J. Appl. Phys.* **28**, L2112-L2114, 1989.
6. S. Nakamura, T. Mukai, M. Senoh and N. Iwasa, "Thermal annealing effects on p-type Mg-doped GaN films," *Jpn. J. Appl. Phys.* **31**, pp. L139-L142, 1992.
7. M. A. L. Johnson, Zh. Yu, C. Boney, W. C. Hughes, J. W. Cook, J. F. Schetzina, H. Zhao, B. J. *III-V Nitrides, Materials Research Society Symposium Proceedings*, edited by F. A. Ponce, T. D. Moustakas, I. Akasaki and B. A. Monemar, **Vol. 449**, pp. 215-220, MRS, Pittsburgh, 1997.
8. I. Akasaki, H. Amano, M. Kito and K. Hiramitsu, "Photoluminescence of Mg-doped p-type GaN and electroluminescence of GaN p-n junction LED," *J. Lumin.* **48/49**, pp. 666-670, 1991.
9. I. Akasaki and H. Amano, "MOVPE growth of high quality $\text{Al}_x\text{Ga}_{1-x}\text{N}/\text{Ga}_y\text{In}_{1-y}\text{N}$ heterostructures for short wavelength light emitter," in *Materials Research Society Symposium Proceedings*, **Vol. 339**, pp. 443-451, MRS, Pittsburgh, 1994.

10. G. L. Pearson and J. Bardeen, "Electrical properties of the silicon and silicon alloys containing boron and phosphorus," *Phys. Rev.* **75**, pp. 865-883, 1949.
11. P. P. Debye and E. M. Conwell, "Electrical properties of n-type germanium," *Phys. Rev.* **93**, pp. 693-706, 1954.
12. J. Monecke, W. Siegel, E. Ziegler and G. Kühnel, "On the concentration dependence of the thermal impurity-to-band activation energies in semiconductors," *phys. stat. sol. (b)* **103**, pp. 269-279, 1981.
13. B. Pödör, "On the concentration dependence of the thermal ionization energy of impurities in InP," *Semicond. Sci. Technol.* **2**, pp. 177-178, 1987.
14. B. Pödör, "On the concentration dependence of the thermal ionization energy of impurities in semiconductors," *Proceedings of the 2nd International Institute on New Developments in Semiconductor Physics, August 30 - September 4, 1987, Szeged, Lecture Notes in Physics*, edited by G. Ferenczi and F. Beleznyay, **Vol. 301**, pp. 55-60, Springer Verlag, Berlin, 1988.
15. B. Pödör, "On the concentration and composition dependence of the acceptor energy in $\text{Al}_x\text{Ga}_{1-x}\text{As:Ge}$ ($x \leq 0.40$)," *phys. stat. sol. (a)* **119**, pp. K135-K139, 1979.
16. N. V. Lien and B. I. Shklovskii, "Level of percolation in weakly doped semiconductors," *Fiz. Tekh. Poluprov.* **13**, pp. 1763-1770, 1979.
17. B. I. Shklovskii and A. L. Efros, *Electronic Properties of Doped Semiconductors*, Springer-Verlag, Berlin, 1984.
18. A. G. Zabrodskii and M. P. Timofeev, "On the effect of random field on thermal energy of ionization in lightly doped semiconductors," *Fiz. Tekh. Poluprov.* **21**, pp. 2217-2219, 1987.
19. T. Tanaka, A. Watanabe, H. Amano, Y. Kobayashi, I. Akasaki, S. Yamazaki, and M. Koike, "P-type conduction in Mg-doped GaN and $\text{Al}_{0.08}\text{Ga}_{0.92}\text{N}$ grown by metalorganic vapor phase epitaxy," *Appl. Phys. Lett.* **65**, pp. 593-594, 1994.
20. W. Götz, N. M. Johnson, J. Walker, D. P. Bour, H. Amano and I. Akasaki, "Hydrogen passivation of Mg acceptors in GaN grown by metalorganic chemical vapor deposition," *Appl. Phys. Lett.* **67**, pp. 2666-2668, 1995.
21. H. Nakayama, P. Hacke, M. R. H. Khan, T. Detchprohm, K. Hiramitsu and N. Sawaki, "Electrical transport properties of p-GaN," *Jpn. J. Appl. Phys.* **35**, pp. L282-L284, 1996.
22. W. Götz, N. M. Johnson, J. Walker, D. P. Bour and R. A. Street, "Activation of acceptors in Mg-doped GaN grown by metalorganic chemical vapor deposition," *Appl. Phys. Lett.* **68**, 667-669, 1996.
23. W. Götz, N. M. Johnson, D. P. Bour, C. Chen, H. Lin, C. Kuo and W. Ilmer, "Shallow and deep level defects in GaN," in *Gallium Nitride and Related Materials, Materials Research Society Symposium Proceedings*, edited by F. A. Ponce, R. D. Dupuis, S. Nakamura and J. A. Edmond, **Vol. 395**, pp. 443-454, MRS, Pittsburgh, 1996.
24. Y. Ohuchi, K. Tadatomo, H. Nakayama, N. Kaneda, T. Detchprohm, K. Hiramitsu and N. Sawaki, "New dopant precursors for n-type and p-type GaN," *J. Cryst. Growth* **170**, pp. 325-328, 1997.
25. W. Kim, A. E. Botchkarev, A. Salvador, G. Popovici, H. Tang and H. Morkoc, "On the incorporation of Mg and the role of oxygen, silicon, and hydrogen in GaN prepared by reactive molecular beam epitaxy," *J. Appl. Phys.* **82**, pp. 219-226, 1997.
26. B. Suchanek, M. Palczewska, M. Pakula, J. Baranowski and M. Kaminska, "Electrical and ESR studies of GaN layers grown by metal organic chemical vapour deposition," *Acta Phys. Polonica A* **92**, pp. 1001-1004, 1997.
27. M. S. Brandt, P. Herbst, H. Angerer, O. Ambacher, and M. Stutzmann, "Thermopower investigation on n- and p-type GaN," *Phys. Rev. B* **58**, 7786-7791, 1998.
28. P. Kozody, H. Xing, S. P. DenBaars, U. K. Mishra, A. Saxler, R. Perrin, S. Elhamri and W. C. Mitchell, "Heavy doping effects in Mg-doped GaN," *J. Appl. Phys.* **87**, pp. 1832-1835, 2000.
29. W. Siegel, G. Kühnel, H. Koi and W. Gerlach, "Electrical properties of n-type and p-type InP grown by the synthesis, solute diffusion technique," *phys. stat. sol. (a)* **95**, pp. 309-316, 1986.

Study of the elastic and elastooptic properties of $\text{Zn}_{1-x}\text{Be}_x\text{Se}$ mixed crystals by Brillouin scattering method

P. Ziobrowski ^{a*}, M. Szybowicz ^a, M. Drozdowski ^a, F. Firszt ^b, S. Łęgowski ^b, J. Szatkowski ^b

^aFaculty of Technical Physics, Poznan University of Technology, Piotrowo 3, 60-965 Poznań, Poland

^bInstitute of Physics, N. Copernicus University, Grudziądzka 5, 87 - 100 Toruń, Poland

ABSTRACT

In this paper we report experimental results concerning the elastic and elastooptic properties of $\text{Zn}_{1-x}\text{Be}_x\text{Se}$ mixed crystals grown by high pressure Bridgman technique. Using Brillouin scattering method some of the elastic and elastooptic constants of $\text{Zn}_{1-x}\text{Be}_x\text{Se}$ crystals with different Be content have been determined at room temperature. It has been revealed that the elastic and elastooptic properties strongly depend on the content of Be.

Keywords: II-VI mixed crystals, $\text{Zn}_{1-x}\text{Be}_x\text{Se}$, elastic and elastooptic properties, Brillouin scattering.

1. INTRODUCTION

There has been a considerable interest in the physical properties of wide gap II-VI mixed crystals containing Mg or Be. $\text{Zn}_{1-x}\text{Be}_x\text{Se}$ solid solution is promising material for construction blue-green laser diodes.^{1,2} These compounds are interesting in the context of control of band gap energies, lattice constants as well as elastic and elastooptic properties. $\text{Zn}_{1-x}\text{Be}_x\text{Se}$ mixed crystals have regular structure, belonging to the T_d^2 space group at room temperature. Recently, some of the physical properties of $\text{Zn}_{1-x}\text{Be}_x\text{Se}$ crystals have been studied using different experimental techniques, such as Raman spectroscopy, photoluminescence and photoacoustic investigations.³⁻⁸ In this paper we report the preliminary study of the elastic and elastooptic properties of $\text{Zn}_{1-x}\text{Be}_x\text{Se}$ mixed crystals with different Be content using Brillouin scattering method.

2. EXPERIMENT

$\text{Zn}_{1-x}\text{Be}_x\text{Se}$ crystals were grown from the melt by the modified high pressure Bridgman method described in details elsewhere.⁹ Their composition was determined by chemical wet analysis. The samples used in Brillouin scattering experiment were ground and mechanically polished to the optical quality. They were cut to the sizes of 3mm x 4mm x 5mm, with faces perpendicular to the [100], [010] and [001] directions.

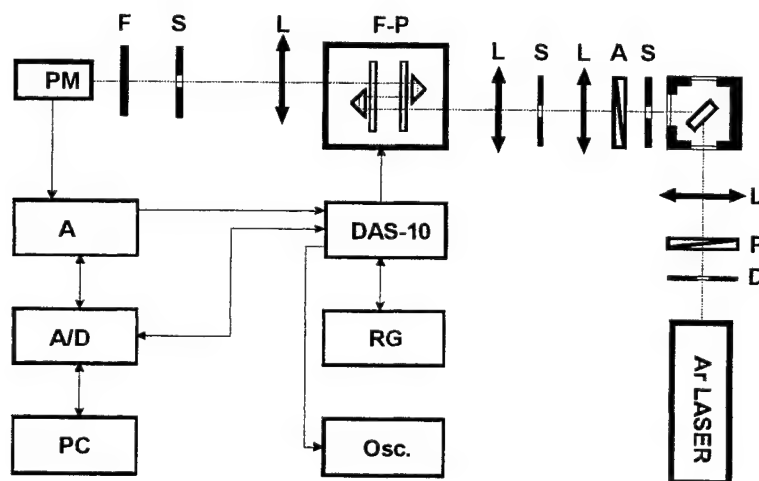


Fig. 1. Schematic picture of the spectrometer used in Brillouin experiment.

The Brillouin polarized spectra were measured at RT using experimental procedure described elsewhere.¹⁰ The schematic picture of the experimental set-up is presented in Fig. 1. An Ar ion laser operating on the 488nm line was used as a source of light. It provided 100mW of cw power during operation on a single mode. The scattered radiation was observed at right angle to the incident beam. As a standard we have employed quartz for which the Rayleigh ratio R_{st} of the longitudinal phonon propagating along [100] direction is known from the literature.¹¹ The calculation of the Brillouin lines parameters has been performed using curve fitting method. To ensure greater certainty, we made a minimum of 5 separate recordings for each scattering geometry. The estimated error of C_{ij} does not exceed 1% and 5% in the case of p_{ij} .

3. RESULTS AND DISCUSSION

Using Brillouin scattering method we have studied the elastic and elastooptic properties of $Zn_{1-x}Be_xSe$ mixed crystals with different Be content. The scattering geometries used in Brillouin experiment are described in Table 1. For our study we have chosen the longitudinal (L) and transverse (T_2) acoustic phonons propagating in $[01\bar{1}]$ direction.

The data which served as a basis for the determination some of the elastic and elastooptic constants of $Zn_{1-x}Be_xSe$ mixed crystals are listed in Table 2. The phase velocity for longitudinal and transverse acoustic modes deduced from Brillouin spectra are also presented in Table 2.

The typical Brillouin spectra of $Zn_{1-x}Be_xSe$ mixed crystals with different Be content obtained for longitudinal (L) and transverse (T_2) acoustic phonons propagating in $q=[01\bar{1}]$ direction at room temperature are presented in Fig. 2.

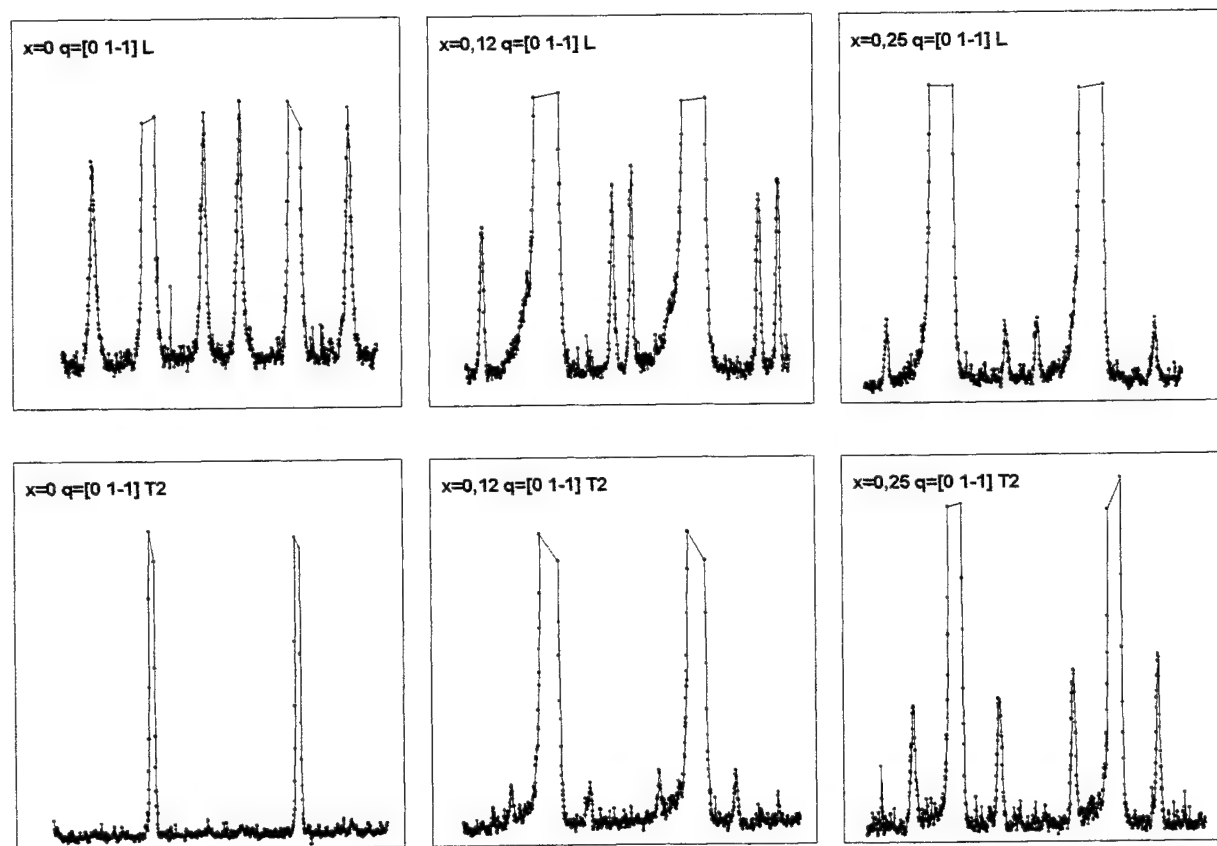


Fig. 2. The Brillouin spectra of $Zn_{1-x}Be_xSe$ mixed crystals with different Be content obtained for the acoustic phonon propagating in $[01\bar{1}]$ direction.

Table 1. Scattering geometries used in Brillouin experiment

$k_i = [001]$ $k_s = [010]$	q	L $u = [01\bar{1}]/\sqrt{2}$ $\rho V^2 = (C_{11} + C_{12} + 2C_{44})/2$	T_2 $u = [100]$ $\rho V^2 = C_{44}$
$d_i = [001]$ $d_s = [001]$	$[01\bar{1}]/\sqrt{2}$	p_{12}^2	0
$d_i = [001]$ $d_s = [110]/\sqrt{2}$	$[01\bar{1}]/\sqrt{2}$	0	$p_{44}^2/2$

Table 2. The data which served as a basis for determination some of the elastic and elastooptic constants of $Zn_{1-x}Be_xSe$ mixed crystals.

X	ρ [g/cm ³]	N	V_L [m/s]	V_{T_2} [m/s]
0	5.269	2.784	4422	2418
0.12	5.194	2.760	4557	2727
0.25	5.102	2.734	4179	2851

3.1. Study of the elastic properties

$Zn_{1-x}Be_xSe$ mixed crystals crystallize in the regular structure (T_d^2 space group). They have three independent elastic constants: $C_{11} = C_{22} = C_{33}$, $C_{44} = C_{55} = C_{66}$, $C_{12} = C_{13} = C_{23}$.¹²

Velocities V_j of the transverse and longitudinal acoustic phonons propagating along $[01\bar{1}]$ direction in $Zn_{1-x}Be_xSe$ mixed crystals with different Be content were determined first. These velocities were deduced from the measured frequency shift $\Delta\omega_B$ using the Brillouin equation, which in the case of 90° scattering geometry takes the form:

$$\Delta\omega_B = V_j \omega_i [(n^i)^2 + (n^s)^2 - 2n^i n^s \cos \Theta]^{1/2} / c \quad (1)$$

where ω_i is the frequency of the incident light, n^i and n^s are the refractive indices for the incident and scattered light, respectively and Θ is the angle between the incident and scattered beams.

The velocities were then used to estimate the elastic constants C_{ij} . The elastic constants can be determined from the solution of the equation of motion, which is given by:

$$|C_{ijk1} q_j q_k - \rho V^2 \delta_{i1}| = 0 \quad (2)$$

Here q_j , q_k are the direction cosines of the phonon wave-vector q , ρ is the density of the crystal and C_{ijk1} are the elastic constants.

Our study enabled us to estimate the values of the $(C_{11} + C_{12} + 2C_{44})/2$ and C_{44} elastic constants. Obtained results are presented in Fig 3a. It can be seen that the elastic properties of $Zn_{1-x}Be_xSe$ mixed crystals strongly depend on Be content. The value of the $(C_{11} + C_{12} + 2C_{44})/2$ decreases, while the value of C_{44} elastic constant increases with the increase of Be content.

3.2. Study of the elastooptic properties

$Zn_{1-x}Be_xSe$ mixed crystals belonging to the regular structure (T_d^2 space group) have three independent elastooptic constants: $p_{11} = p_{22} = p_{33}$, $p_{44} = p_{55} = p_{66}$, $p_{12} = p_{13} = p_{23}$.¹² In order to determine the elastooptic properties of $Zn_{1-x}Be_xSe$ mixed crystals with different Be content, we used a substitution technique proposed by Cummins and Shoen¹¹, and developed by Nelson and Lax.¹³ In this method the Brillouin spectrum of the crystal under study is compared to that of a standard scatterer whose

Rayleigh ratio R_{st} is known. If I is the observed (integrated) intensity of the Brillouin line in the sample spectrum while I_{st} is the intensity of the Brillouin line in the spectrum of the standard scatterer, the Rayleigh ratio R of the sample is given by:

$$R = R_{st} (I / I_{st}) = R_{st} J \quad (3)$$

Using Nelson and Lax's approach¹³, the formula for Rayleigh ratio can be written as:

$$R = (\pi^2 kT / 2 \lambda^4) BCF \quad (4)$$

where, for 90-degree scattering geometry, C is given by :

$$C = (n^i n^s)^3 \cos \delta^i \cos \delta^s / \rho V^2 \quad (5)$$

and F is given by :

$$F = |d_m^s p_{mnkl} d_n^i u_k q_l|^2 \quad (6)$$

In Eqs (4) - (6): B is geometric factor which is assumed to be equal for the unknown sample and the standard, $\delta^{i,s}$ is the angle between the Poynting vector and the wave-vector of the incident/scattered beam, d_m^s , d_n^i describe the polarization vector of the scattered and incident waves, respectively, $n^{i,s}$ is the appropriate refractive index, p is the effective elastooptic tensor, u_k is the component of the atomic displacement vector and q_l is the component of the phonon wave-vector.

The appropriate elastooptic constant p_{ij} can be determined from equation:

$$F / F_{st} = J C_{st} / C \quad (7)$$

From our study the values of p_{12} and p_{44} elastooptic constants were determined. The obtained results are presented in Fig. 3b. It can be seen that in the investigated range of composition the elastooptic properties of $Zn_{1-x}Be_xSe$ mixed crystals depend on Be content noticeably. The value of the p_{12} decreases, while the value of p_{44} elastooptic constant increases with the increase of Be content.

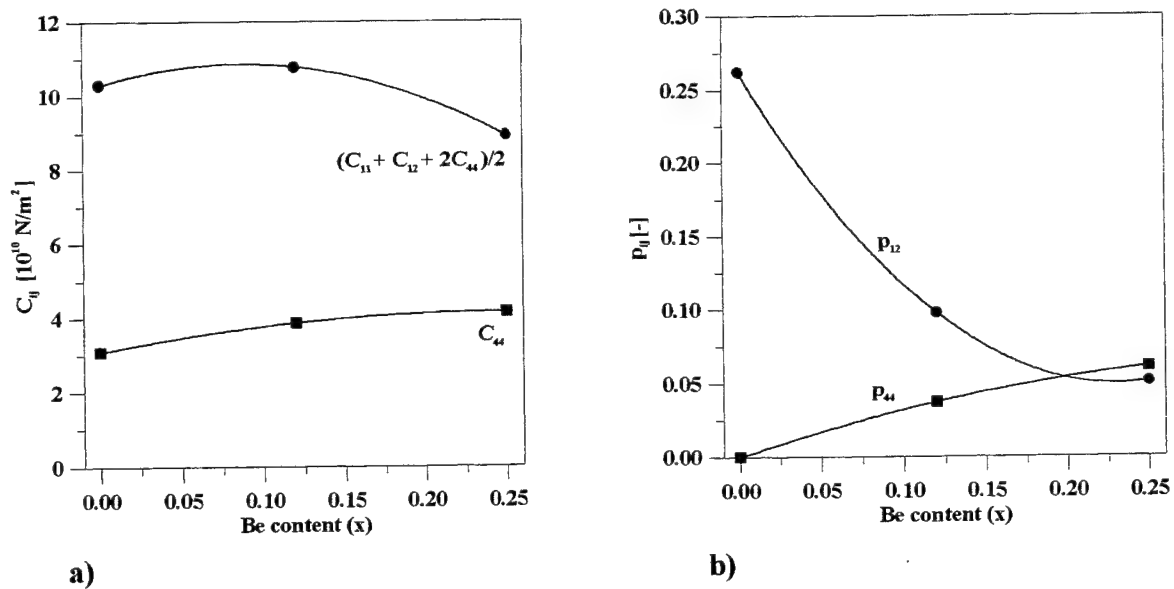


Fig. 3. The dependence of the : a) - $(C_{11} + C_{12} + 2C_{44})/2$ and C_{44} elastic constants and b) - p_{12} and p_{44} elastooptic constants for $Zn_{1-x}Be_xSe$ mixed crystals as a function of Be content obtained for acoustic phonon propagating in direction $[01\bar{1}]$ at room temperature.

4. CONCLUSIONS

Using Brillouin scattering measurements some of the elastic and elastooptic constants have been determined. It has been revealed, that the elastic and elastooptic properties of $\text{Zn}_{1-x}\text{Be}_x\text{Se}$ crystals strongly depend on Be content. However, the nature of this phenomenon is still not well recognized. Its qualification needs further Brillouin scattering study and this is now in progress.

ACKNOWLEDGEMENTS

The authors would like to thank MSc. Barbara Sekulska from Institute of Physics N. Copernicus University for technical assistance.

This work was supported in part by the Research Project TB-64-001/2000/DS of Poznań University of Technology and grant nr 321-F of N. Copernicus University.

REFERENCES

1. G. Landwehr, F. Fischer, T. Baron, T. Litz, A. Waag, K. Schül, H. Lugauer, T. Gerhard, M. Keim and U. Lunz, "Recent Results on Beryllium Chalcogenides", *Phys. stat. sol. (b)* **202**, pp. 645-655, 1997.
2. S.O. Ferreira, H. Sitter, W. Fashinger, R. Krump and G. Brunthaler, "Type I - type II band offset transition of the ZnMgSe-ZnTe system" *J. Cryst. Growth* **146**, pp. 418-421, 1995.
3. M. Kozielski, M. Szybowicz, F. Firszt, S. Łęgowski, H. Męczyńska, J. Szatkowski, W. Paszkowicz, "Study of the $\text{A}_{1-x}\text{B}_x\text{C}$ Mixed Crystals by Raman Scattering," *Cryst. Res. Technol.* **34**, pp. 699-702, 1999.
4. M. Szybowicz, M. Kozielski, F. Firszt, S. Łęgowski, H. Męczyńska, J. Szatkowski, W. Paszkowicz, "Study of $\text{Zn}_{1-x}\text{Mg}_x\text{Se}$ and $\text{Zn}_{1-x}\text{Be}_x\text{Se}$ semiconducting crystals by Raman scattering," *Opto-Electr. Rev.* **7**, pp. 103-106, 1999.
5. F. Firszt, S. Łęgowski, H. Męczyńska, J. Szatkowski, W. Paszkowicz, K. Godwod, J. Domagała, M. Kozielski, M. Szybowicz, M. Marczak, "Structure, Luminescence and Lattice Hardening of Be-rich $\text{Zn}_{1-x}\text{Be}_x\text{Se}$ Bulk Crystals" Proceedings of the 2nd International Symposium on Blue Laser and Light Emitting Diodes, Chiba, Japan 1998.
6. F. Firszt, S. Łęgowski, H. Męczyńska, B. Sekulska, J. Szatkowski, J. Zakrzewski, and W. Paszkowicz "Photoluminescence and photoacoustic investigations of beryllium and magnesium containing wide-gap II-VI mixed crystals" *Acta Phys. Polon.* **A95**, pp. 991-996 1989.
7. I.F. Chang, S.S. Mitra, "Long wavelength optical phonons in mixed crystals," *Adv. Phys.* **20**, pp. 359-403, 1971.
8. M. Kozielski, M. Szybowicz, "Temperature and excitation study of the $\text{A}_{1-x}\text{B}_x\text{C}$ crystals by Raman scattering method", *Proc. Fifth International Conference on Intermolecular Interactions in Matter 1999*, pp. 144 -147, Eds. K. Sangwal, E. Jartych and W. Polak, Politechnika Lubelska, Lublin, 1999.
9. J. Szatkowski, F. Firszt, H. Męczyńska and S. Łęgowski, "Electrical and optical properties of ZnSe:Mg crystals," *Acta Phys. Pol.* **A84**, pp. 531-534, 1993.
10. M. Drozdowski, P. Ziobrowski, K. Łapsa, M. Kozielski and W. Bala, "Study of elastic properties of n-ZnSe single crystals by Brillouin scattering", *Proc. SPIE Vol.* **2373**, pp. 277-282, 1995.
11. H.Z. Cummins and P.E. Schoen, in "Laser Handbook", ed. by F.T. Arecchi and E.D. Schultz-Dubois, North-Holland, Amsterdam, 1972.
12. J.F. Nye, in "Physical Properties of Crystals", Clarendon Press, Oxford, 1957.
13. D.F. Nelson and M. Lax, "Theory of the photoelastic interaction," *Phys. Rev. B*, **3**, pp. 2778-2779, 1971.
14. F.C. Peiris, S. Lee, U. Bindley and J.K. Furdyna, "ZnMgSe/ZnCdSe and ZnMgSe/ZnSeTe distributed Bragg reflectors grown by molecular beam epitaxy," *J. Appl. Physics*, **86**, pp. 719-724, 1999.
15. M. Gonzales-Diaz, P. Rodrigues-Hernandez and A. Munoz, "Elastic constants and electronic structure of beryllium chalcogenides BeS, BeSe, and BrTe from first-principles calculations," *Phys. Rev. B*, **55**, pp. 14043-14046, 1997.

Correlation of domain structure of TGS single crystals doped with serine with its dielectric properties – new constructed computer measuring system for quantity analysis of domain images

W.Proszak, M. Trybus

Technical University in Rzeszów, Physics Institute

ABSTRACT

This paper presents works over correlation between parameters of domain structure and pyroelectric current in IR sensors based on TGS (Triglicyne sulphate). In the frames of realised works new single-crystal of TGS doped with amino acid – serine was grown. Computer measuring system making possible registration of domain structure images of non-linear dielectrics was designed and executed. We worked out measuring and analysis algorithms of domain images. Software making possible calculations and analysis of parameters of observed structures was created and static measurements of domain structure within different growth pyramids were performed. Correlation between parameters of domain structure, quantity of admixture and temperature characteristics of pyroelectric coefficient was found..

Keywords: ferroelectrics, pyroelectrics, domain structure, tgs

1. INTRODUCTION

Process of releasing of an electric charge as a consequence of temperature changes of ferroelectric sample is well-known phenomenon called pyroelectricity. Till present days one produced many materials showing pyroelectric proprieties. One of the best material often examined and practically applied in IR detection is group of ferroelectrics with hydrogen - bond. This group of materials includes also Tryglicyne Sulphate (TGS).

One of the most essential features of the detectors based on TGS single crystals are as follows; detectors are active elements of detection circuits where an electric response is proportional to changes of temperature, detectors show a capacitive character and high sensitivity, low noises, high speed of a detection without necessity of cooling. Additionally this material makes possible easy creation of the large detection areas at relatively low costs of a production. One of not numerous but very essential defect of this material is practically impossible repeatability of electric parameters. From this reason the works of our team were concentrated on an elaboration of method making possible fast identification of basic electric parameters of samples in the aspect of its utilisation as active elements of pyroelectric sensors.

2. CRYSTAL GROWTH AND DOPING

Single crystals of TGS are grown from water solutions using a static method of the water evaporation. Pure TGS is obtained by mixing aminoacetic and sulphuric acids in proper amounts. The received solution is left for autonomous crystallisation. In order to obtain an investigative material of high purity, received crystals are taken off from the solution and after dissolving in distilled water such solution is filtered and left for renewed crystallisation. Such procedure is repeated several times. So received pure solution of TGS is admixed with a dopant in proper concentration 10% or 40%. So the received solution is put in special glass vessel in to thermostat. Here in the temperature of 35°C (ferroelectric phase) after partial vaporisation of a water on the bottom of vessel spontaneous crystallisation occurs. Small single crystals are taken off from

the solution and they become seeds for the final single crystals growth. Crystal growth takes place in temperature of 35°C in a specially designed vessel. Seed is fastened in handle, which is set in rotatory movement with the stabilised speed.

3. PREPARATION OF THE SAMPLES

Samples are cleaved out on (010) surface, which is perpendicular to the ferroelectric axis of a single crystal, profiting from natural cleavage plane or cut out by a wire saw, after determining of the cleavage plane. Thus obtained samples are mechanically treated in order to obtain thickness about 1mm. Polishing of samples is performed with use of fine-grained abrasive paper, during the last phase of polishing, a sample is polished on the moist blotting-paper. So prepared samples are rejuvenated by overheating to the temperature of 45°C for 24 hours. (2) Rejuvenating process is passed in order to destroy domain structure being a result of mechanical treatment. Rejuvenated samples are then left at room temperature for about 100 hours. We may assume that after 100 hours domain structure stops to change in a consequence of balance reached between free energy of the crystal and an energy of forming of the domain walls. So its structure is similar to the structure, which occurs during a normal work of the pyroelectric detector. So prepared samples are ready for an investigation of domain structure. In order to develop domain images, samples are etched using a solution of ammoniac water and then covered by the liquid crystal (3).

4. OBSERVATIONS OF THE DOMAIN STRUCTURE

Ferroelectric domain is an area of homogenous polarisation of the crystal. Well ordered orientation changes an optical properties of the samples' area. For that reason it is possible to observe domain structure with use of polarising microscope. In case of too little contrast of the domain images a thin layer of liquid crystal is deposited on the sample's surface. Measuring equipment (4) consists of the polarising microscope coupled with CCD camera and a computer with the frame grabbing card on the board – fig. 1.

Designed software enables the various analysis of images, including calculation of the domain amount within observed area, perimeter of a particular domain and its surface. There is also a analyses of domain images, thanks to possibility of recording of images on magnetic carrier (video tape or hard disc of the computer) possibility to investigate the processes of changes of domain structure and to make comparative

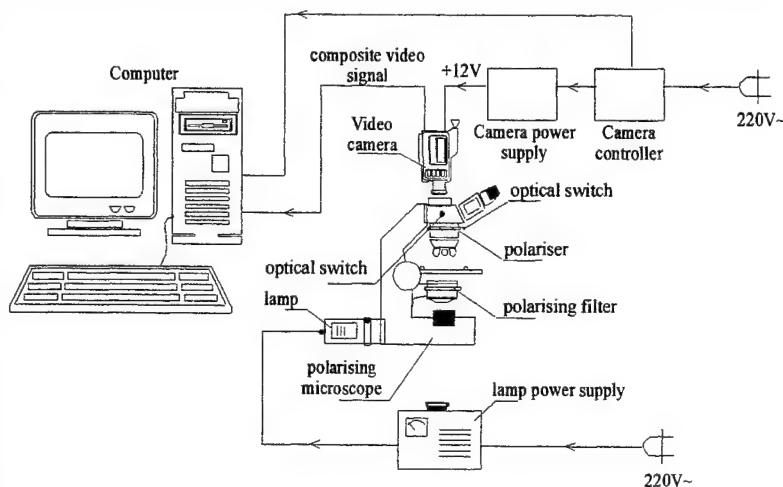


Fig. 1. Measuring system for domain structure researches

5. MEASURING ALGORITHM

Sample is placed in a polarising microscope. Camera records images of the domain structure in five statistically selected areas of sample's surface on its both sides. Basing on ten images registered in this manner, computer analysis of domain structure parameters was performed. Designed software makes possible registration domains' amount, its area and perimeter of domain walls.

Each area within eyeshot identified by the programme as domain was analysed and ordering parameter W_{sp} was determined for it. For each domain we measured its surface area (P_i) and perimeter (O_i). The ratio P_i/O_i means half of the regular circle radius ($R/2$). Figure of circle was chosen because a shape of the domain influences energy of domain wall and in case of the circle this energy is minimal (circle like and lenticular domains have smallest energy). Thus parameter R may be treated as a radius of domain standardised to the circle shape. Then we calculated an area of standardised domain and the ratio between measured area P_i and calculated area. Results of the calculations for each domain are stored and on the base of it an average value of W_{sp} parameter for the whole sample is being calculated.

$$W_{sp} = 1 / n \left[\sum_1^n \left(\frac{P_i}{\pi \left(\frac{2 P_i}{O_i} \right)^2} \right) \right] \quad (1)$$

Where: P_i - surface area of domain, O_i - perimeter of domain, N - quantity of domains

Basing on W_{sp} calculations, the samples are classified to one of five groups. Measurements of temperature characteristics of the pyroelectric coefficient are performed for each group.

We assumed the following boundary values of W_{sp} parameter:

Group	W_{sp}
p(5)	>7
p(4)	7-5
p(3)	5-3
p(2)	3-2
p(1)	2-1

Thus in the group of samples p(5) we find samples with domain structure of a large size and well developed borders, whereas in the group p(1) samples with small domains of lenticular and a circle like shapes.

6. MEASUREMENTS OF PYROELECTRIC COEFFICIENT

Pyroelectric coefficient is measured with use of static method, by a measurement of the pyroelectric current of short circuited sample. Sample with the attached electrodes is fastened in measuring - handle, which is then placed in a thermostat. Temperature and pyroelectric current values are registered simultaneously with the selected constant time interval.

From the theory of pyroelectrics yields, that pyroelectric effect does not step out independent. Other phenomena related with a temperature gradient within the sample take a place. The most essential disturbing factor is a piezoelectric effect. In order to eliminate this factor and other disturbances measurements of pyroelectric coefficient are conducted with very small increase of temperature and investigated sample is possibly the thinnest. An additional disturbing factor is a temperature inertia of the sample - handle set. Too fast measurements may result in deformation of the temperature characteristic of pyroelectric coefficient and its shift in the direction of higher temperatures.

6.1 Results of measurements

Two kinds of new ferroelectric single crystals were grown. TGS doped with 10% serine (TGSS10) and TGS doped with 40% serine (TGSS40). The spectroscopy researches confirmed a building in admixtures in single crystals' structure. We performed the described above procedures related with growing and mechanical treatment for both kinds of single crystals. Optical investigations and the electric measurements were conducted according to described measuring - algorithm.

Domain structure of TGSS10 and TGSS40 differs significantly each other (fig.1 and fig.2). An average value of Wsp parameter for all samples is 2.21 for TGSS10 and 4.63 for TGSS40. Respectively higher value of Wsp parameter the higher is difference between shape of domains and regular circles/lens. It means, that a dopant blocks process of a creation of the domain structure. This process is responsible for higher value of crystals' internal energy because process of creation of domain walls runs until depolarisation energy is in balance with energy of domain walls.

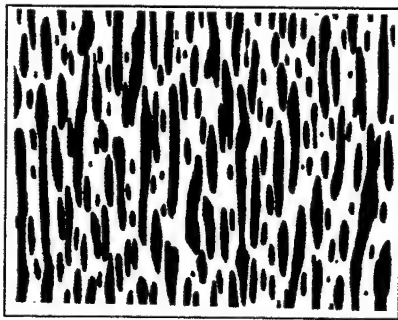


Fig. 1 Domain structure of TGSS10

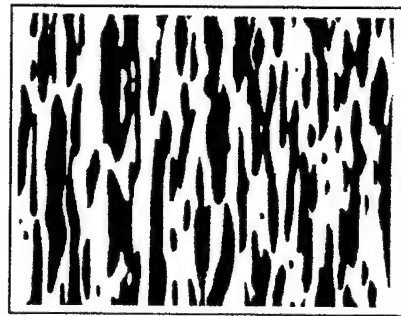


Fig. 2 Domain structure of TGSS40

Measurements of the pyroelectric coefficient showed, that samples made of TGSS10 and TGSS40 show in every group p(1)-p(5) similar values of pyroelectric coefficient and similar shapes of its characteristics fig. 3, fig. 4 - maximum of coefficient value grows together with a value of Wsp coefficient. However in case of TGSS10 width of pyroelectric peak is smaller and increase of its value is sharper within the same temperature range. Also this material shows longer linear part of characteristics of pyroelectric coefficient versus a temperature, what has an essential meaning relating an application in the detection circuits. In case of both materials basing on Wsp parameter calculation we may estimate a height of the pyroelectric peak and length of a linear part of pyroelectric current characteristics.

7. CONCLUSIONS

The received results encourage to the researches focused on working out algorithm of correlation of Wsp parameter with the other electric parameters of the samples, that are very essential from the point of view of its application in detectors of infra-red radiation. At the present moment our works are focused on the quantitative relations between Wsp parameter, and electric parameters of the samples enabling more precise estimation of electric parameters of the samples on a base of an optical measurements.

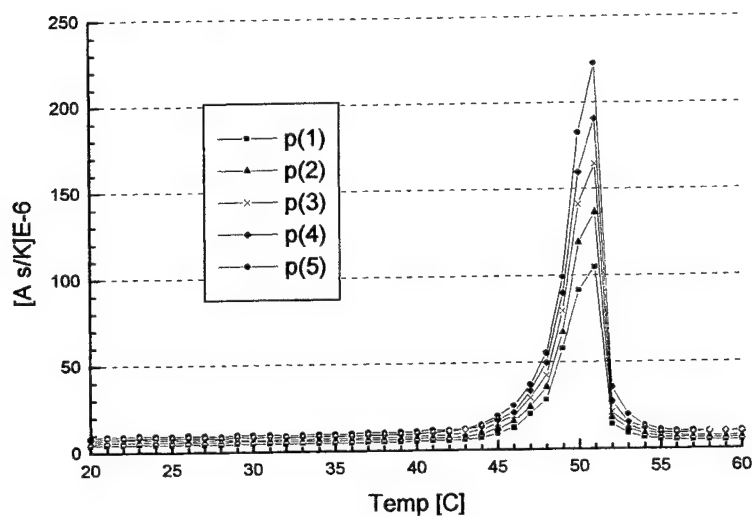


Fig. 3 Temperature characteristics of pyroelectric coefficient TGSS10

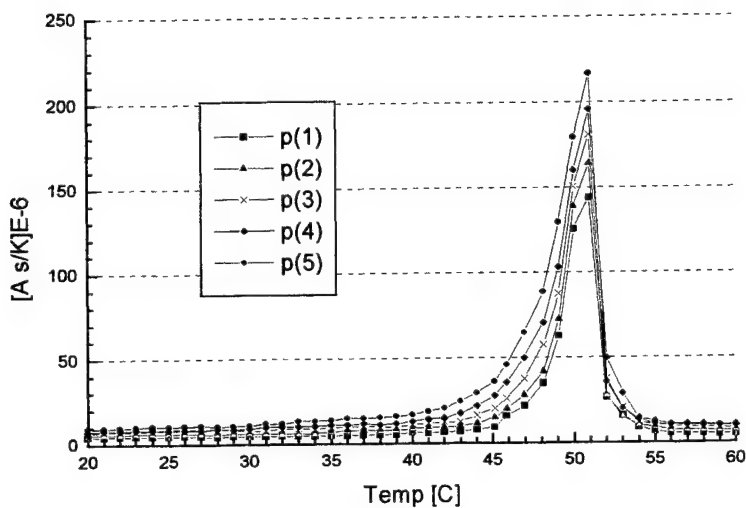


Fig. 4 Temperature characteristics of pyroelectric coefficient TGSS40

REFERENCES

1. J. Stankowska, "Correlation Between Domain Structure and Dielectric Properties of TGS", *Ferroelectrics* vol. 22 pp 423, 1978
2. J. Stankowska, And. Czarnecka, "Investigation of the Ageing Process And Domain Structure of TGS Group Crystals", *Ferroelectrics* Vol. 98 pp 95-103, 1989
3. T. Ozaki, "Polarities of Ferroelectric 180 Degrees Domains Observed Using Liquid Toner Method in an Uncoated TGS Crystal", *J. Appl. Phys.* Vol 80 pp 453, 1985

Excited state absorption of the $\text{Cr}^{6+}\text{O}^{2-}$ center in $\text{Li}_2\text{B}_4\text{O}_7$ glass

Czesław Koepke^{a*}, Krzysztof Wiśniewski^a, and Marek Grinberg^b

^aInstitute of Physics, N. Copernicus University, Grudziądzka 5/7
87-100 Toruń, Poland

^bInstitute of Experimental Physics, University of Gdańsk, Wita Stwosza 57
80-952 Gdańsk, Poland

ABSTRACT

We present excited state absorption (ESA) measurements of the $\text{Cr}:\text{Li}_2\text{B}_4\text{O}_7$ glass ($\text{Cr}:\text{LBO}$ -glass) along with preliminary interpretation. The most distinct feature in the ESA characteristics is connected with the presence of chromium in its hexavalent (d^0) valence states. The Cr^{6+} ions appear to contribute in the deexcitation processes and their evidence can be seen in the ESA spectra under excitation wavelength at 308 nm. We interpret the ESA spectra detected with UV excitation in terms of transitions in the framework of Cr^{5+}O^- center which forms after charge-transfer-type absorption in $[\text{CrO}_4]^{2-}$ group. We assume the presence of the double-electron state of the $3d^2 2p^4$ electronic configuration together with crystal field-split states of the $3d^1 2p^5$ configuration, both allow to reproduce the obtained ESA spectra.

Keywords: absorption (ESA), $\text{Cr}:\text{Li}_2\text{B}_4\text{O}_7$ glass

1. INTRODUCTION

Lithium tetraborate ($\text{Li}_2\text{B}_4\text{O}_7$) is a well known material, which found numerous optoelectronic applications¹⁻³ but so far it has not yet been used as a primary laser host or gain medium. This is because of the tight packing of LBO single crystal lattice and the relatively large sizes of the dopant ions that are of interest, for example Cr^{3+} ions. In glass matrix situation is different because the glasses have more loose and relaxed structures and are more "dopant friendly" allowing much higher concentrations doping than in crystals. The optical spectroscopy of the Cr^{3+} ions in the LBO glass has been described in detail in several papers⁴⁻⁶. In this contribution, after making sure that Cr^{3+} in the LBO glass is rather poor candidate for lasing medium (because of the high strength of the ESA transitions)⁷, we focus our attention on other chromium ions: Cr^{6+} that, take important part in the deexcitation process. Their presence produces the highest distinct peak in the absorption spectrum, situated around 360 nm, hence in our investigation we used the UV excitation by the XeCl excimer laser working at 308 nm.

2. EXPERIMENTAL

The excited state absorption (ESA) spectra were measured using a setup which utilized a RD-EXC-150/25 XeCl excimer laser (308 nm) as a source of excitation, a Hamamatsu Xe flash lamp as a source of probe beam and ORIEL InstaSpec II photodiode array detector coupled to MultiSpec 1/8 m spectrograph in the detection branch. The setup operated in pulsed regime and transverse geometry⁸. The 308 nm line excites the $\text{Cr}:\text{LBO}$ glass within the highest absorption peak which can be ascribed to the following charge transfer transition in the frame of $[\text{CrO}_4]^{2-}$ group: $\text{Cr}^{6+}\text{O}^{2-} (3d^0 2p^6) \rightarrow \text{Cr}^{5+}\text{O}^- (3d^1 2p^5)$,⁹⁻¹¹

3. RESULTS AND DISCUSSION

The ESA spectrum of the $\text{Cr}:\text{LBO}$ glass sample is presented in figure 1. As it is seen, there is no chance to fit this ESA spectrum by a single Gaussian function, whereas two Gaussians {one relatively narrow (2800 cm^{-1}) and another much broader (8200 cm^{-1})} fit the spectrum perfectly. This strongly suggests that the observed ESA under UV excitation consists of transitions to two distinctly defined excited states.

* Further author information -

Cz. K. (correspondence): Email: koepke@phys.uni.torun.pl, Telephone: (48-56) 611-3239

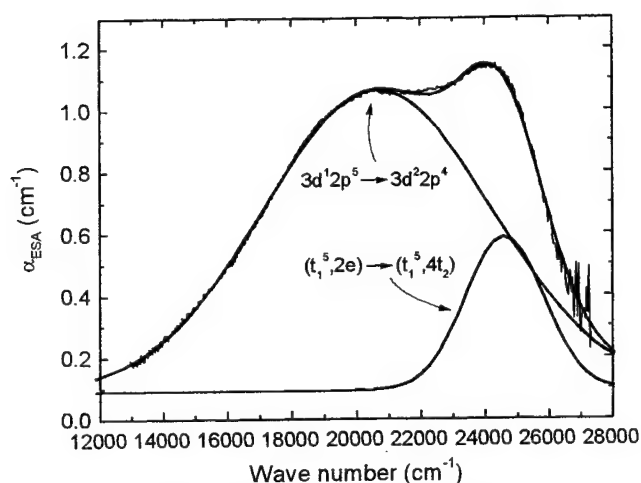


Fig. 1 Experimental ESA spectrum obtained for 308 nm excitation, fit by two Gaussians, and assignation of the contributing ESA bands.

Table I Parameters used to creation of the SCC diagram explaining the ESA spectra shown in Fig. 1. κ is the elastic constant and Γ_i are the half-widths corresponding to the respective relaxation energies

Parameter	Energy (cm ⁻¹)
κ	8000
$\eta\omega$	250
$\eta\omega'$	400
kT	200
CT_1	27933
CT_2	42500
Γ_1	4450
Γ_2	8200
Γ_3	2800
ESA_1	20520
ESA_2	24600

The single configuration coordinate (SCC) diagram can be used to reproduce a characteristic ESA spectrum comparable to that obtained with 308 nm excitation (figure 1). To achieve this, certain assumption has to be made, namely - the existence of additional excited electronic manifold, strongly coupled to the lattice, not detectable in the ground state absorption (GSA) spectrum. Such a state can be related to the $3d^22p^4$ electronic configuration of the central ion - ligand system. The $3d^22p^4$ excited electronic configuration originates from the consecutive excitation of two electrons from the valence band (made mostly of ligands orbitals) to the d orbitals of the central ion.

The resulting SCC diagram calculated using the parameters given in Table I is presented in figure 2 together with definitions of energies taken from the experiment. It shows two positions of the state $|3\rangle$ ($3d^22p^4$) (dashed and solid) corresponding to two qualitatively different situations described in the caption. We believe that the real situation is closer to that represented by solid line parabola of the state $|3\rangle$ ($3d^22p^4$) because such a positioning of the state $|3\rangle$ explains lack of emission from the higher excited state as well as other ESA bands when exciting the $Cr^{6+}O^{2-}$ center.

Considering the nature of the electronic configurations which the SCC diagram is constructed from, one should remember that $Cr^{6+}O^{2-}$ center is a typical d^0 complex (of approximated T_d symmetry). Then it is possible to write formally the electronic configuration of the central ion-ligand system as $3d^02p^6$.¹¹ The exemplary molecular orbital diagram for tetrahedral MX_4 complex¹²⁻¹⁴ is illustrated in figure 3. It is noted that the highest occupied bonding orbital t_1 of the ground state of such a complex is composed exclusively from ligand p_π orbitals. The higher, nonbonding molecular orbital $2e$ is of d type and consists mostly d orbital of the central ion, whereas the next antibonding orbital $4t_2$ is a typical mixed orbital consisting d orbital of the central ion but also p_σ orbitals of the ligands. This is why the parabola corresponding to $(t_1^5, 4t_2)$ symmetry is shifted with respect to the $(t_1^5, 2e)$ parabola (different charge distributions and consequently different couplings to the lattice). The ground state absorption (CT_1) is due to one of the t_1 electrons, making a transition to the $2e$ orbital and leaving a hole in the bonds. Because the transition occurs practically from the ligands to central-ion d orbital, this is what is usually called "charge transfer transition", resulting in a distinct charge redistribution. This is consistent with the right-hand shift of the first excited state parabola. There is also another absorption, CT_2 , which is involved with a transition of one of the t_1 electrons to $4t_2$ orbital with suitably smaller charge redistribution. Thus the CT transition transforms the center $Cr^{6+}O^{2-}$ to $Cr^{5+}O^-$ center of $3d^12p^5$ configuration.¹¹ The larger energy ESA transition (ESA_2) is from d-type $2e$ to more diffused $4t_2$ orbital of mixed d-p type. This is also charge redistribution (simplifying: from central ion back to ligands) which results in the $(t_1^5, 4t_2)$ parabola shifted back in respect to shift of the $(t_1^5, 2e)$ parabola, almost to the same position as the ground state parabola. The smaller energy ESA transition

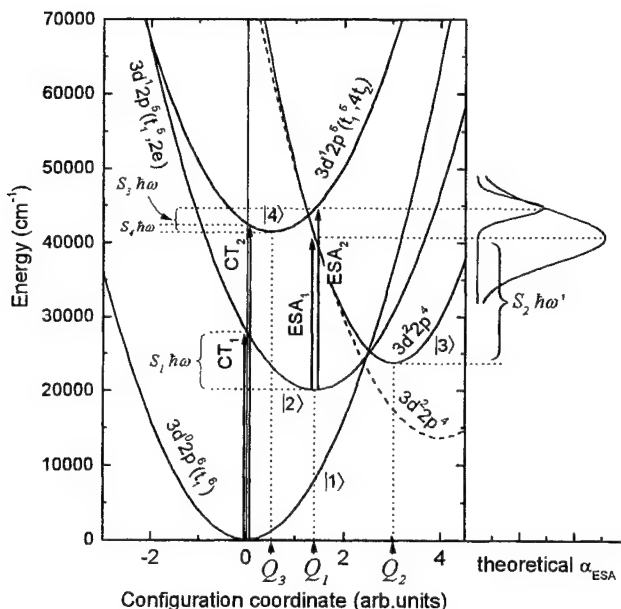


Fig. 2 SCC diagram quantitatively reproducing the ESA spectrum obtained with 308 nm excitation. Right side of the figure shows two Gaussian ESA spectra (of the widths corresponding to the respective relaxation energies) whose composition fits the experiment. The dashed parabola corresponds to the $3d^2 2p^4$ state of linear coupling to the lattice i.e. with the same phonon energy as all remaining states ($\eta\omega = 250 \text{ cm}^{-1}$). The solid parabola of the $3d^2 2p^4$ state corresponds to the different phonon energy $\eta\omega' = 400 \text{ cm}^{-1}$.

(ESA₁) occurs also from the state of $(t_1^5, 2e)$ configuration but to the state of quite different electronic configuration, namely $3d^2 2p^4$.

The model discussed above and the goodness of the fit to experimental data suggested the manifold involved of the $3d^2 2p^4$ electronic configuration.

4. CONCLUSION

In the Cr:LBO glass an important role in the deexcitation process is played by charge transfer absorption in the frame of $[\text{CrO}_4]^{2-}$ group. Excitation into the charge transfer peak, situated at 362 nm, does not lead to apparent emission but, instead, to intensive excited state absorption. The spectrum of this absorption can be fully explained in terms of the excitation of the d⁰-type complex: $[\text{CrO}_4]^{2-}$. This excitation gives rise to creation of the Cr^{5+}O^- center of $3d^1 2p^5$ electronic configuration of two terms split in the crystal field: $2e$ and $4t_2$. Transition between them is a source of shorter wavelength component of the ESA spectrum. Longer wavelength, broadband component of the ESA spectrum is caused by double-electron state of $3d^2 2p^4$ configuration ($\text{Cr}^{4+}\text{O}_2^-$ center) which forms after two consecutive transfers of the ligand electrons onto the central ion. This double-electron state plays a role of terminal ESA state.

ACKNOWLEDGMENTS

This work was supported by the State Committee for Scientific Research (KBN) under grants numbers: 2 P03B 117 16 and 2 P03B 063 16. Authors are grateful to Dr. A. Majchrowski of Military University of Technology, Warsaw, Poland, for growing and supplying the samples.

REFERENCES

1. R. Komatsu, T. Sugawara, K. Sassa, N. Sakura, Z. Liu, S. Izumida, Y. Segawa, S. Uda, T. Fukuda, and K. Yamanouchi, "Growth and ultraviolet application of $\text{Li}_2\text{B}_4\text{O}_7$ crystals: generation of the fourth and fifth harmonics of $\text{Nd}:\text{Y}_3\text{Al}_5\text{O}_{12}$ lasers", *Appl. Phys. Lett.* **70**, 3492-3494, 1997
2. A. Ciocan, J. Uebbing, and K. Niemax, "Analytical application of the microwave induced plasma used with laser ablation of solid samples", *Spectrochimica Acta B*, **47B**, 611-617, 1992
3. J. Gasiot, P. Braunlich, and J.P. Fillard, "Laser heating in thermoluminescence dosimetry", *J. Appl. Phys.* **53**, 5200-5209, 1982
4. F. Rasheed, K.P. O'Donnell, B. Henderson, and D.B. Hollis, "Disorder and the optical spectroscopy of Cr^{3+} -doped glasses: II. Glasses with high and low ligand fields", *J. Phys.: Condens. Matter* **3**, 3825-3840, 1991
5. B. Henderson, M. Yamaga, Y. Gao, and K.P. O'Donnell, "Disorder and nonradiative decay of Cr^{3+} -doped glasses", *Phys. Rev. B* **46**, 652-661, 1992

-
- The diagram illustrates the energy levels and orbital interactions for a complex. On the left, the metal atom orbitals are shown: 3d, 4s, and 4p. On the right, the ligand atom orbitals are shown: $t_1\pi$, $t_2\sigma_p$, $e\pi$, $t_2\pi$, $a_1\sigma_p$, $t_2\sigma_s$, and $a_1\sigma_s$. The central part shows the complex orbitals: $3a_1$, $5t_2$, $4t_2$, $2e$, $3t_2$, $2t_2$, $1e$, $1t_2$, and $1a_1$. The diagram also indicates the formation of bonding and antibonding molecular orbitals, with labels for GSA (Grouped Symmetry Adapted) and ESA (Energy Symmetry Adapted) orbitals.

Modeling of the carrier mobility at the silicon oxynitride-silicon interface

K.J. Pluciński

Military University of Technology, Warsaw, Poland

ABSTRACT

The main issue which is yet to be resolved in further developing the Surface Channel MOSFETs (SCMOSFETs) is understanding and eliminating deterioration of the carrier mobility at the insulator-semiconductor interface. The main factor causing this deterioration is hole and electron trapping-detrapping. One of the ways recently suggested of minimizing hole and electron trapping-detrapping at the Si-SiO₂ interface involves replacing the SiO₂ by silicon oxynitride (SiON). However degradation of MOSFETs, which have oxynitrides as gate dielectric, caused by trapping of hot electrons from the channel, is still found.

1. INTRODUCTION

The electrophysical parameters of the insulator-semiconductor interface are needed in order to determine the parameters of the transport carriers in the channel, and in particular the main parameters for models of MIS devices – carrier mobility in the inversion layer. The latter has been the subject of intensive investigation since the 1960s.

Two fundamental problems in this field are (a) developing the technology for measuring the structures, and (b) interpreting the results of these measurements.

- a) accuracy of modern methods for identifying mobility is largely dependent on accuracy in determining flat-band voltage U_{FB} . Accuracy in determining U_{FB} is, in turn, dependent on accuracy in determining such interface parameters as doping profile, the energy distribution of the traps and work function difference;
- b) up to now it was believed that effective carrier mobility must be modeled by taking into account Coulomb, phonon and roughness scattering of the insulator-semiconductor interface with the help of the Mathiesen' rule, according to which these mechanisms are independent.

However measurements show that electron and hole mobility in the inversion layer are dependent on charge concentration both in the inversion layer and in the depletion region, but do not depend on their combination, which is not in keeping with the Mathiesen rule.

The main reasons for this divergence are that the influence of the interface structure on carrier transport is not taken into account, and over-simplifications occur.

Two examples of the latter are:

- i) existing models of mobility are based in essence on a relaxation approximation of in the BTE;
- ii) quantum effects in the inversion equation are not taken into account in these models.

Both these approximations cease to apply in the channel sizes currently obtainable and in the case of large dependent concentrations at the surface.

Therefore among the fundamental problems which need to be resolved in order to develop a model for transport mobility in the SCMIS transistor channel are the following:

- i) the development of methods to solve BTE without any approximations;
- ii) identification of a doping profile at the interface with a level of efficiency enabling their implementation.

Mechanisms for carrier transport, in particular, for scattering and for generation-recombination are clearly dependent on the structure of the insulator – semiconductor interface.

The structure of this interface is determined in the first instance by the mechanisms for the formation of the isolation layer. As a result of recently research into these mechanisms, significant progress towards the construction of a physical and chemical model has been achieved. Agreement of several parameters of this model with the parameters of an electrophysical model, which were determined using the modified conductance method was found. This confirms the desirability of carrying out further work in integrating both approaches (the physical – chemical and the electro-physical) in order to model this interface.

In the oxydation procedure one key process is the transportation of atoms and particles.

The oxynitrides have both advantages over SiO_2 (improved hot-electron immunity, higher charge to breakdown and suppressed boron diffusion) as well as shortcomings (degradation of MOSFETs with oxynitride as gate dielectric is still observed; considerably more interface states created for oxynitrides per injected hole than with SiO_2 , more vulnerable to hole bombardment). Classical electric methods of investigations of mobility related phenomena are restricted because the relatively low mobility of the trapping carriers limits electroconductivity¹⁻¹³. In order to assess the possible explanations both for these phenomena and for the nature of the defects, which have been proposed, a study of the electronic structure of a MOS system, using silicon oxynitrides as gate oxide, based on a first-principle molecular dynamic method, was carried out. A satisfactory explanation for the above-mentioned issues is crucial for constructing a model of carrier mobility. We present a method which employs a band energy approach with molecular dynamic cluster optimization, the latter taking into account various structural modifications related to the non-stoichiometry of nanoclusters. We simulated the influence of chemical composition on the trapping properties of defects in silicon oxynitride. Clusters with different numbers of oxygen and nitrogen atoms in the second coordination sphere were considered.

By calculating the differences between the total energy of clusters in different charge states, we determined the energy gain for hole or electron trapping in the case of different types of defects, and the dependency of this gain on composition and cluster size. Thermal delocalization of the energy level of traps was calculated. On the basis of these results, we propose models for the trapping (localization) and detrapping (delocalization) of electrons on different kinds of defects in SiO_xN_y and Si_3N_4 . Mechanisms for creating different kind of defects, e.g. Linking two-fold coordinated nitrogen atoms with an unpaired electron, are proposed.

In order to determine the parameters of the oxynitride-Si system, non-linear optical methods, in particular photoinducing second harmonic generation (PISHG) were used.

2. ENERGY BAND STRUCTURE

The films were deposited by thermal low pressure chemical vapor deposition (LPCVD) on a silicon(111) substrate. The entire process was carried out using an ultra high vacuum chamber with pressure of about (4×10^{-8}) bar. The silicon(111) substrate is heated by radiation from a tungsten lamp. Such equipment enables acceleration of the evaporation process.

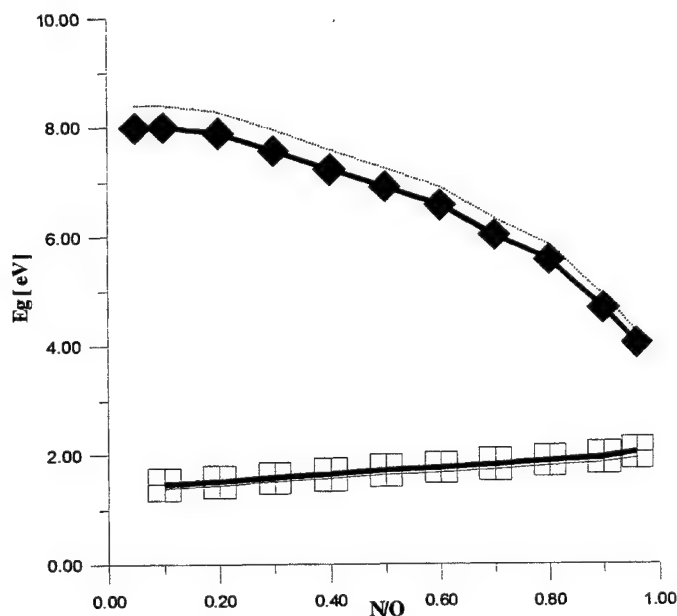


Fig. 1. Dependence of the energy gap E_g and refractive index n on the N/O ratio. \blacklozenge - E_g measured; \square - n measured.

High-purity gases (chlorosilane - SiH_2Cl_2 , ammonia - NH_3 , and nitrogen monoxide - N_2O), the contents of which can be controlled with precision up to 0.2%, are used as a source for this process. The N/O ratio is changed by continuously varying the $\text{N}_2\text{O}/\text{NH}_3$ source/gas ratio. The growth rate, which is dependent on the N/O ratio, is selected in accordance with the Habraken rule. On the basis of the calculations carried out, the dependence of the band energy structure on the parameters of the oxynitride-silicon (SiON-Si) system was calculated. In Fig. 1 the calculated dependence of the energy gap E_g and refractive index n on the N/O ratio is presented, as well as the corresponding results of measurements¹⁵. One can see that the band energy gap decreases with a decreasing of nitrogen content. Good agreement between the calculated and experimentally evaluated parameters validates the adopted model of simulation.

In Figure 2 calculated dependence of the energy gap on the N/O ratio and film thickness is presented¹⁶. One can see that both the N/O ratio, as well as the film thickness, form modulated-like dependencies.

These dependencies reflect, as it were, a kind of "competition" between long-range bulk-like crystalline ordering, two-dimensional intersurface disorder and electron-phonon near-the-surface non-centrosymmetry. Analysis showed that the dependencies on film thickness of both the top of the valence band (VB), as well as of the bottom of the conduction band (CB), are non-periodic. The dependence on film thickness was found to be entirely different for the VB and the CB. This reflects the different influence of electron-phonon anharmonicity on the models considered, and the role of electron-phonon interactions on long-range ordering

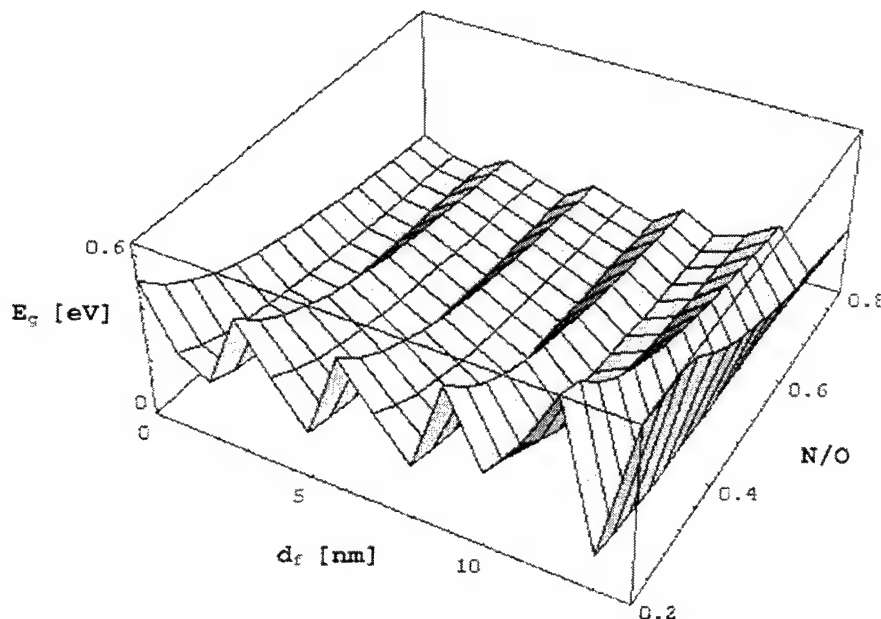


Fig. 2. Dependence of the band structure on N/O ratio and film thickness d_f .

3. GEOMETRY STRUCTURE

The results of molecular dynamic simulations of the O-Si and N-Si distances in relation to the N/O ratio and film thickness, carried out using the method described above are presented in Figure 3.¹⁶ It can be seen that an increase in film thickness leads to an increase in the oxygen-silicon distance of between 0.16 and 0.28 nm. For an N/O ratio of approximately 0.015, the oxygen-silicon distance achieves its maximum at a thickness of about 28 nm. A further increase in the N/O ratio leads to a shift of the observed maximum positions towards the lower thickness (up to 16.5 nm for an N/O of about 1.0). The existence of maxima would also seem to reflect a kind of 'competition' between long-range ordering of the silicon crystalline surface, and random amorphous-like disordering due to the substitution of the nitrogen and oxygen in the silicon

positions. Oxygen and nitrogen cause opposite changes in the charge density distribution, and, therefore, in the interface electrostatic potential distribution near the oxynitride-silicon $\langle 111 \rangle$ (SiON-Si $\langle 111 \rangle$) interface. The dependence on film thickness for the nitrogen-silicon (N-Si) distances is significantly different from that for oxygen-silicon (O-Si) distances. In the first place, one can see in Figure 8 two thickness maxima. The first has a value of about 0.21 nm for a film thickness range of 10-16 nm, the second of about 0.28 nm within the thickness range 18 nm-24 nm. The appearance of the two maxima suggests the existence of two possible minima of the local cluster total energy for the nitrogen-silicon (N-Si) distances, in contrast to the oxygen-silicon (O-Si) distances.

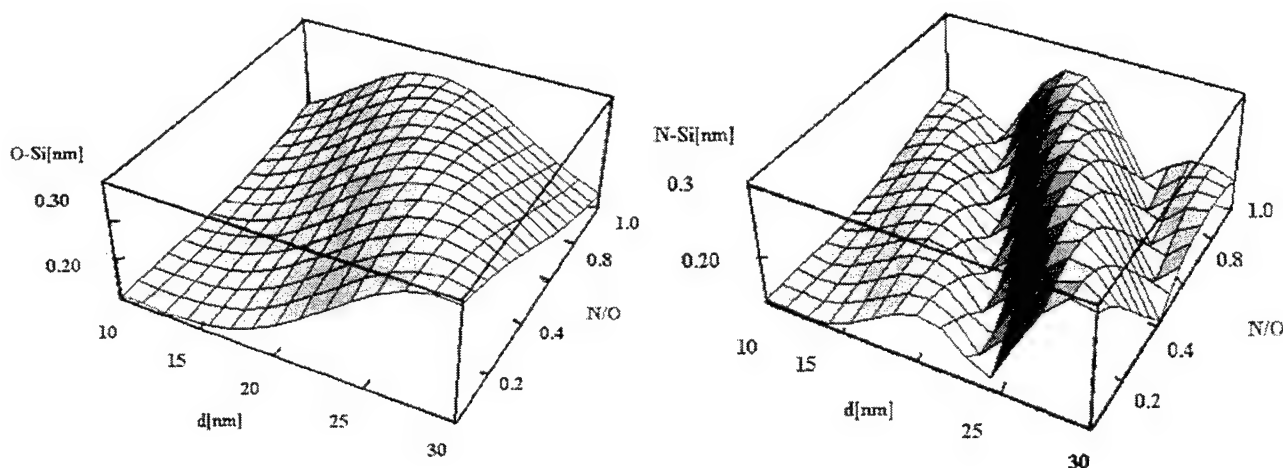


Fig. 3. Molecular dynamics geometry optimization of the O-Si and N-Si distances versus the film thickness d and the N/O ratio.

4. CONCLUSIONS

Nitridation leads to an increase in concentration of interface states and $1/f$ noise. This is seen particularly in the case of nitridation in NH_3 where trapping centers are introduced through the hydrogen, and with oxides formed in an N_2O atmosphere, due to deterioration in the structure of the interface layer as a result of an initial increase in the speed of formation. A significant decrease in carrier mobility for lower strengths of the electric field has also been found in MOS transistors with an n channel as a result of nitrogen implantation before oxydation. On the other hand, no increase in carrier mobility was observed for higher electric fields. However where formation occurred in an N_2O atmosphere, there was no significant decrease in mobility for lower strengths of the fields, while there was a detectable increase in mobility for higher fields. In the case of SiON layers formed through a PECVD (plasma enhanced chemical vapor deposition) procedure, a significant decrease in mobility for lower strengths and a detectable increase for higher strengths have been established, together with lower hot-hole immunity, in comparison with SiO_2 of the interface SiON-Si layer.

In the carrying out the present work I found a number of discrepancies in the explanation for the above-mentioned specific observations regarding the influence of nitrogen on the properties of the SiON-Si system. These discrepancies make it practically impossible to give a uniform description of carrier transport in transistor channels with SiON gate isolation. A model of the influence of nitrogen on the properties of M-SiON-Si structures, based on an investigation both of the energy structure, as well as of the geometry structure, of the SiON-Si interface region is needed. In order to determine the influence of nitrogen on the properties of the SiON layers and on the properties of the interface SiON-Si layers, the ratio of the nitrogen concentration to that of oxygen (N/O) must be established, together with influence of nitrogen atoms on the geometry structure (for example, the distances N-Si and O-Si) and the energy structure of both the SiON, as well as the interface SiON-Si layer.

ACKNOWLEDGEMENTS

The study was supported by the Polish State Committee for Scientific Research through grant No KBN-8-T11B 026 14.

REFERENCES

1. Avid Kamgar, J.T. Clemens, A. Ghetti, C.T. Liu and E.J. Lloyd, "Reduced Electron Mobility due to Nitrogen Implant Prior to the Gate Oxide Growth", *IEEE El. Dev. Lett.*, **v.21**, No. 5, pp. 227-229, 2000.
2. Hnyang Yang, Hiro Niimi, Jeff W. Keister, Gerald Lucovsky, and Jack E. Rowe, "The effects of Interfacial Sub-Oxide Transition Regions and Monolayer Level Nitridation on Tunneling Currents in Silicon Devices", *IEEE El. Dev. Lett.*, **v.21**, No. 2, pp. 76-78, 2000.
3. H. Niimi and G. Lucovsky, "Monolayer - level controlled incorporation of nitrogen in ultra-thin gate dielectrics using remote plasma processing: formation of stacked 'N-O-N' gate dielectrics", *J. Vac. Sci. Technol. B*, **v. 17**, pp.1250-1257, 1999
4. F. J. Guarin, Stewart E. Rauch, Giuseppe La Rosa, and Kevin Bresford, "Improvement in Hot Carrier Lifetime as a Function of N₂ Ion Implantation Before Gate Oxide Growth in Deep Submicron NMOS Devices", *IEEE El. Dev. Lett.*, **v.20**, No. 12, pp. 602-604, 1999
5. M.F. Li, Y.D. He, S.G. Ma, B.J. Cho, K.F. Lo, and M.Z. Xu, "Role of Hole Fluence in Gate Oxide Breakdown", *IEEE El. Dev. Lett.*, **v.20**, No. 11, pp. 586-588, 1999.
6. Wen-Chin Lee, Tsu-Jae King, Chenming Hu, "Observation of Reduced Boron Penetration and Gate Depletion for Poly-Si_{0.8}Ge_{0.2} Gated PMOS Devices", *IEEE El. Dev. Lett.*, **v.20**, No. 1, pp. 9-11, 1999.
7. Jin-Woo Lee, Nae-In Lee, and Chul-Hi Han, "Stability of Short-Channel Polysilicon Thin-Film Transistors with ECR N₂O-Plasma Gate Oxide", *IEEE El. Dev. Lett.*, **v.20**, No. 1, pp. 12-14, 1999.
8. Nae-In Lee, Jin-Woo Lee, Hyong-Sub Kim, and Chul-Hi Han, "High-Performance EEPROM's Using N- and P-channel Polysilicon Thin-Film Transistors with Electron Cyclotron Resonance N₂O-Plasma Oxide", *IEEE El. Dev. Lett.*, **v.20**, No.1, pp. 15-17, 1999.
9. Mukesh Khare, X.W. Wang, T.P. Ma, "Transconductance in Nitride-Gate or Oxynitride-Gate Transistors", *IEEE El. Dev. Lett.*, **v.20**, No. 1, pp. 57-59, 1999.
10. P. Masson, Jean-Luc Autran, J. Brini, "On the Tunneling Component of Charge Pumping Current in Ultrathin Gate Oxide MOSFET's", *IEEE El. Dev. Lett.*, **v.20**, No. 2, pp. 92-94, 1999.
11. Y. Wu and G. Lucovsky, "Ultrathin Nitride/Oxide (N/O) Gate Dielectric for p⁺-Polysilicon Gated PMOSFET's Prepared by a Combined Remote Plasma Enhanced CVD/Thermal Oxidation Process", *IEEE El. Dev. Lett.*, **v.19**, No. 10, pp. 367-369, 1998.
12. Y. Shi, X. Wang, and T.P. Ma, "Tunneling Leakage Current in Ultrathin (<4 nm) Nitride/Oxide Stack Dielectrics", *IEEE El. Dev. Lett.*, **v.19**, No. 10, pp. 388-390, 1998.
13. P.T. Lai, Jing-Ping Xu, and Y.C. Cheng, "Improvement on 1/f Noise Properties of Nitrided n-MOSFET's by Backsurface Argon Bombardment", *IEEE El. Dev. Lett.*, **v.20**, No. 4, pp. 149-151, 1999.
14. Y. Okada and P.J. Tobin, "Hot-Carrier Degradation of LDD MOSFET's with Gate Oxynitride Grown in N₂O", *IEEE El. Dev. Lett.*, **v.15**, No. 7, pp. 233-235, 1994.
15. K.J. Pluciński, I.V. Kityk, "Elliptically - polarized light - induced second harmonic generation in SiN_xO_y", *Journal of Non-Crystalline Solids*, **v. 26**, pp. 143-154, 2000
16. K.J. Pluciński, I.V. Kityk, M. Makowska-Janusik, A. Mefleh, H. Kaddouri, and S. Benet, "Photoinduced Optical Second Harmonic Generation of SiNO Films Deposited on Si<111. Substrate", *Journal of Applied Physics*, **v. 87**, N 8

Analysis of the transient response of MIS circuits using pseudo-wavelet approach

K.J. Pluciński*

Military University of Technology, 2 Kaliski Str., 00-908 Warsaw, Poland,

ABSTRACT

This paper deals with the possibilities offered by the wavelet transform used in the analysis of the transient response of MIS circuits. This approach has certain advantages over the classical finite element or finite difference-based algorithms when applied to drift-diffusion (Roosebroeck's) model.

1. INTRODUCTION

The transient response of MIS circuits is determined by the transient response of the concentration of carriers in MIS structures, for example in the channel of the MIS transistors.

At the most fundamental level the flow of the charge carriers is described by transport equations derived from quantum mechanics, semiclassical or classic models. The common feature of these equations is the employment of a phase space density function $f(x,v,t)$ of the spatial variable $x \in \Omega$, velocity variable $v \in \mathbb{R}^3$, and the time variable $t \in (0, \infty)$. A widely used transport equation is the Boltzmann equation^{1,3}:

$$\partial_t f + v \cdot \nabla_x f - \nabla U \cdot \nabla_v f = (\partial_t f)_c \quad (1)$$

where $U(x,t)$ is the electrostatic potential:

$$\Delta U = \int f dv - C \quad (2)$$

C is the doping profile and the term $(\partial_t f)_c$ is the collision operator.

The simulations by solving to the Boltzmann equation are known to be very time-consuming, so they cannot be employed for fast circuit simulations.

A frequently employed method to make the Boltzmann equation more tractable was found to be the 'moment method' approach.

By this method the hydrodynamic model is derived which in turn is reduced to drift-diffusion equations, e.g. van Roosbroeck model which consist of:

Poisson's equation:

$$\varepsilon \Delta U = \rho \quad (3)$$

continuity equation for electrons:

$$\frac{\partial n}{\partial t} = \frac{1}{q} \operatorname{div} J_n - R(n, p) \quad (4)$$

* E-mail: kpluc@wel.wat.waw.pl

continuity equation for holes:

$$\frac{\partial p}{\partial t} = \frac{1}{q} \operatorname{div} J_p + R(n, p) \quad (5)$$

where J_n is the electron current density:

$$J_n = q\mu_n(U_T \nabla n - n \nabla U) \quad (6)$$

J_p is the hole current density:

$$J_p = q\mu_p(U_T \nabla p + p \nabla U) \quad (7)$$

ρ is the charge concentration:

$$\rho = q(n - p - C) \quad (8)$$

$R(n, p, x)$ is the net generation-recombination rate, $\mu_n = \mu_n(n, \nabla U, C, x)$ and $\mu_p = \mu_p(p, \nabla U, C, x)$ are the mobilities of electrons and holes, respectively, $C = C(x)$ is the doping profile, U_T is the thermal voltage, $\epsilon(x)$ is the electric permittivity and q is the elementary charge.

That drift-diffusion model constitutes up to now the core of state-of-the-art semiconductor device simulation programs. In conclusion, the mathematical description of the transient process in MIS circuits is based on the nonlinear partial differential equations for electrons and holes, which are coupled together through the Poisson equation. The crucial element in realisation of the algorithm is effectiveness of this coupling.

2. SOME NOTES ON POISSON EQUATION

The potential distribution is described using the equation:

$$\frac{d^2 u}{dx^2} = \frac{Q(u, x)}{\epsilon},$$

where:

(9)

$$\begin{aligned} Q(u, x) &= Q_1(u) + qN(x); \\ N(x) &= N_0 + N_1(x); \\ Q_1(u) &= -q(a_1 \exp(-\alpha u) - a_2 \exp(\alpha u)); \\ N_0 &= (a_1 - a_2); \end{aligned}$$

u is the potential, Q – the charge density, ϵ – the dielectric susceptibility, q – the elementary charge; a_1, a_2 – are dependent on doping N , $\alpha = q/kT$ [1/V], k – is the Boltzmann constant [qV/K], T is the temperature in Kelvin. Introducing the

following variables in potential units: $A_1 = \frac{qa_1}{\epsilon} l^2$; $A_2 = \frac{qa_2}{\epsilon} l^2$ and the dimensionless variable $y = x/l$ we can rewrite (1) in a somewhat different form

$$\begin{aligned} \frac{d^2 u}{dy^2} - \Omega(u)u &= \hat{N}(y); \\ \Omega(u) &= \frac{\hat{Q}(u)}{u}; \\ \lim_{u \rightarrow 0^+} [\Omega(u)] &= \alpha(A_1 + A_2) \begin{cases} < 0 & \text{when } q < 0 \\ > 0 & \text{when } q > 0 \end{cases} \end{aligned} \quad (10)$$

Equation (14) is thus the Helmholtz equation, where the boundary problem is unambiguously solvable for $q > 0$ (where an electron charge is the elementary charge), and cannot be solved unambiguously for $q < 0$ (where a pozyton charge is an elementary charge). The function $\Omega(u)$ is presented in diagram 1.

2.1. The conditions for applying the finite differences method

Equation (2), for a network with constant step h , takes the following form:

$$u_{i-1} - (2 + h^2 \Omega_i)u_i + u_{i+1} = h^2 \hat{N}_i; \quad (11)$$

By varying (3) we get:

$$\delta u_{i-1} - \left(2 + h^2 \Omega_i + h^2 \frac{\partial \Omega_i}{\partial u_i} u_i \right) \delta u_i + \delta u_{i+1} = 0$$

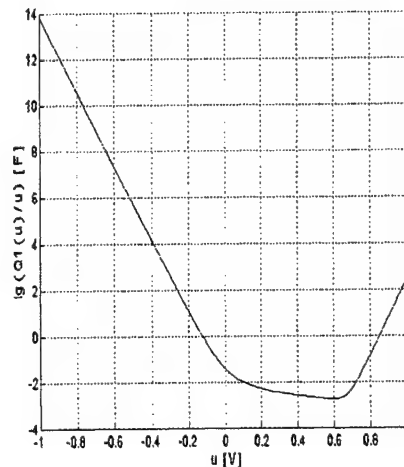


Fig. 1. The dependence of $\Omega(u) l^2 / \varepsilon$ on u , where $q > 0$

In order to ensure that the solution to equation (2.1) was stable under the Dirichlet border condition, that is, where $\delta u_1 = \delta u_I = 0$, it is sufficient

that $\min(|\delta u_{i-1}|, |\delta u_{i+1}|) < |\delta u_i|$. This, in turn, causes the dependence $R \equiv \Omega + \frac{\partial \Omega}{\partial u} u > 0$ for each u . Due to the

large gradients of u in the vicinity $y=0$, we can apply the 'expansion of coordinates' method to (1.1), by using the transformation

$$y = \frac{(a+1)^z - 1}{a}; z = \frac{\log(ay+1)}{\log(a+1)} \quad (12)$$

The coefficient (a) is calculated as the limit of the series presented in the following way:

$$a_{n+1} = a_n - \frac{W_n}{W_n^{diff}} \quad (13)$$

Where:

$$W_n = V_0 \frac{(a_n+1)^{dz} - 1}{a_n} - 0.001(U_L);$$

$$W_n^{diff} = V_0 \frac{(a_n+1)^{dz} \times (a_n dz / (1+a_n) - 1) + 1}{a_n^2};$$

V₀ is the beginning value.

Equation (2) with variable "z" can be written as follows:

$$\begin{aligned} \frac{d^2 u}{dz^2} - \log(a+1) \frac{du}{dz} = \\ = \left[\frac{(a+1)^z \log(a+1)}{a} \right]^2 \\ \left[\hat{Q}(u) + \hat{N} \left(\frac{(a+1)^z - 1}{a} \right) \right] \equiv Q^{(z)}(u, z) \end{aligned} \quad (14)$$

The dependence $\log_{10}(dz/dy)$ on y is given in Fig. 2.

Equation (6) can be solved on a uniform network with constant step (dz) in view of the small difference in du/dz over the entire specimen investigated.

An important feature of this method is its accuracy, of evaluation according to the following formula

$$M = \frac{u_x|_{x=l} - u_x|_{x=0}}{\int_0^l Q(x, u(x)) dx} \varepsilon \quad (15)$$

2.2. The shot method

Equation (10) is replaced by the system:

$$\begin{aligned} \frac{du}{dy} = v; \frac{dv}{dy} = \hat{Q}(u) + \hat{N}(y); \\ u|_{y=0} = U_L; v|_{y=0} = IV_0 \end{aligned} \quad (16)$$

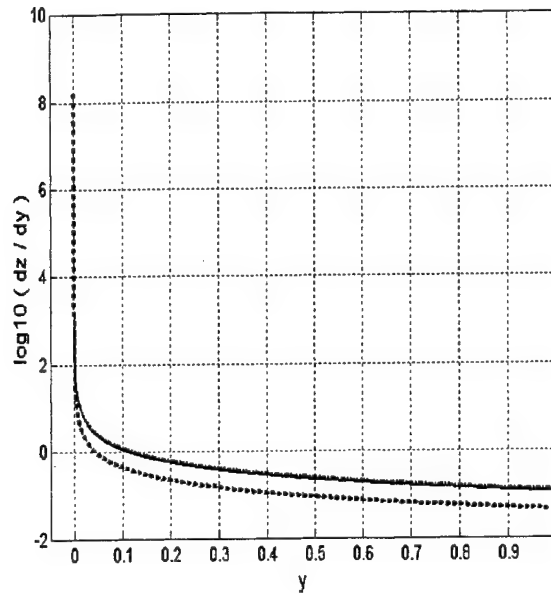


Fig. 2. Dependence $\log_{10}(dz/dy)$ on y . For $U_L = [-1, -0.3, 1]$ [V] the line style: [„- - -”, „—”, „• • •”] respectively are used.

The conditions for the stability of the shot method are examined. To this end, we create variation equations in the surrounding $[u^*(y), v^*(y)]$ fulfilling the beginning conditions

$$\begin{aligned} \frac{d}{dy} \delta u &= \delta v; & \frac{d}{dy} \delta v &= \left. \frac{\partial \hat{Q}}{\partial u} \right|_{u=u^*} \delta u; \\ \delta u(0) &= \varepsilon_u; & \delta v(0) &= \varepsilon_v. \end{aligned} \quad (17)$$

where $\varepsilon_u, \varepsilon_v$ - relate to the modules. Equation (3.2) is written in the matrix form:

$$\begin{aligned} \frac{d}{dy} \begin{bmatrix} \delta u \\ \delta v \end{bmatrix} &= \begin{bmatrix} 0 & 1 \\ \left. \frac{\partial \hat{Q}}{\partial u} \right|_{u=u^*} & 0 \end{bmatrix} \begin{bmatrix} \delta u \\ \delta v \end{bmatrix}; \\ \begin{bmatrix} \delta u \\ \delta v \end{bmatrix}_{y=0} &= \begin{bmatrix} \varepsilon_u \\ \varepsilon_v \end{bmatrix}; \end{aligned} \quad (18)$$

The necessary condition for stability of the

trajectory $[u^*(y), v^*(y)]$ is that the real part

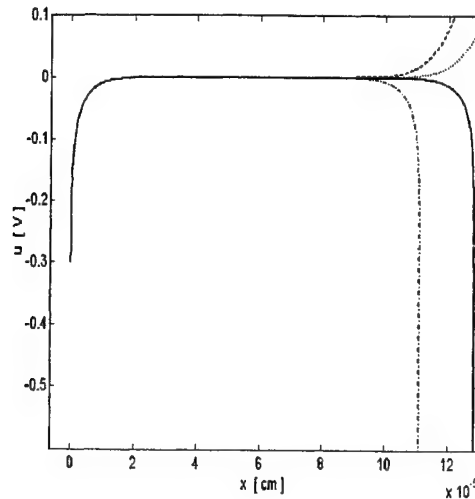


Fig. 3. The instability of the trajectory in the shot method

of the eigenvalue of the matrix are not positive. Since the eigenvalues can be expressed:

$$\begin{aligned} \rho_{1,2} &= \pm \sqrt{\left. \frac{\partial \hat{Q}}{\partial u} \right|_{u=u^*}} \\ &= \pm \sqrt{\alpha [A_1 \exp(-\alpha u^*) + A_2 \exp(\alpha u^*)]} \end{aligned} \quad (19)$$

in the shot method, any trajectory is unstable, if its elementary charge is an electron.

3. PSEUDOWAVELETS APPROACH

Equation (4) take the form: $u_t = Lu + Nf(u)$, where L and N are linear differential operators and $f(u)$ is a nonlinear function. A generic feature of the solution of such equations is that they behave in a smooth, non-oscillatory and shock-like manner. According to analysis based on the solution of the drift-diffusion model, in which the above-mentioned equations are coupled through elliptic Poisson equation, the transient response of the carriers, when pulsed from accumulation into inversion, can be divided into three periods: dielectric relaxation time, depletion time and equilibration time. During dielectric relaxation time, the surface concentration of the majority carriers sharply decreases (in some cases by about 8 orders in 1 ns). During depletion time it becomes constant and during equilibration time it slowly increases to equilibrium value.

In the approach presented the solution $u(x,t)$ and the operators L and N were projected onto a wavelet base. The vanishing moments of the base functions are the reason for the sparsity of the representation of both the solution and operators. This sparsity makes it possible to develop fast, adaptive algorithms for applying operators to functions and for calculating the functions in the wavelet base.

These algorithms use the fact that wavelet expansions may be viewed as a localized Fourier analysis with a multiresolution structure that adapts automatically to both the smooth and shock-like behavior of the solution. In smooth regions, few wavelet coefficients are needed, and in singular regions the large variation in the solution requires more wavelet coefficients. This approach make it possible to combine many finite-differences, (pseudo-) spectral and adaptive grid methods into a collection of efficient, generic algorithms, named adaptive pseudo-wavelet algorithms. The approach was applied to transient responses in some MIS circuits, and numerical results are presented.

The approach takes advantage of the efficient representation of functions and operators in wavelet bases, and updates the solution by implementing recently developed adaptive algorithms. These algorithms are adaptive since they update the solution using its representation in a wavelet basis, which concentrates significant coefficients near singular behavior.

We used the semigroup method to replace the nonlinear partial differential equation with a nonlinear integral equation. The transient response of the MIS circuits has both shock-like as well as smooth parts. An algorithm based on a pseudo-wavelet approach, which is automatically adaptive to both smooth and shock-like behavior of the solution, was applied to analyze this response. This approach makes it possible to combine many finite-differences, spectral and front-tracking grid methods into a collection of efficient, generic algorithms.

4. RESULTS

Changes of incremental of hole density as a function of time in cross sections placed at different distances (x) from the interface are presented in Fig. 4. At the interface and at $x=0.1\mu\text{m}$ increments are negative. At $x=1\mu\text{m}$ the increments at the beginning of the transient process are negative and then, during the equilibration period, are positive.

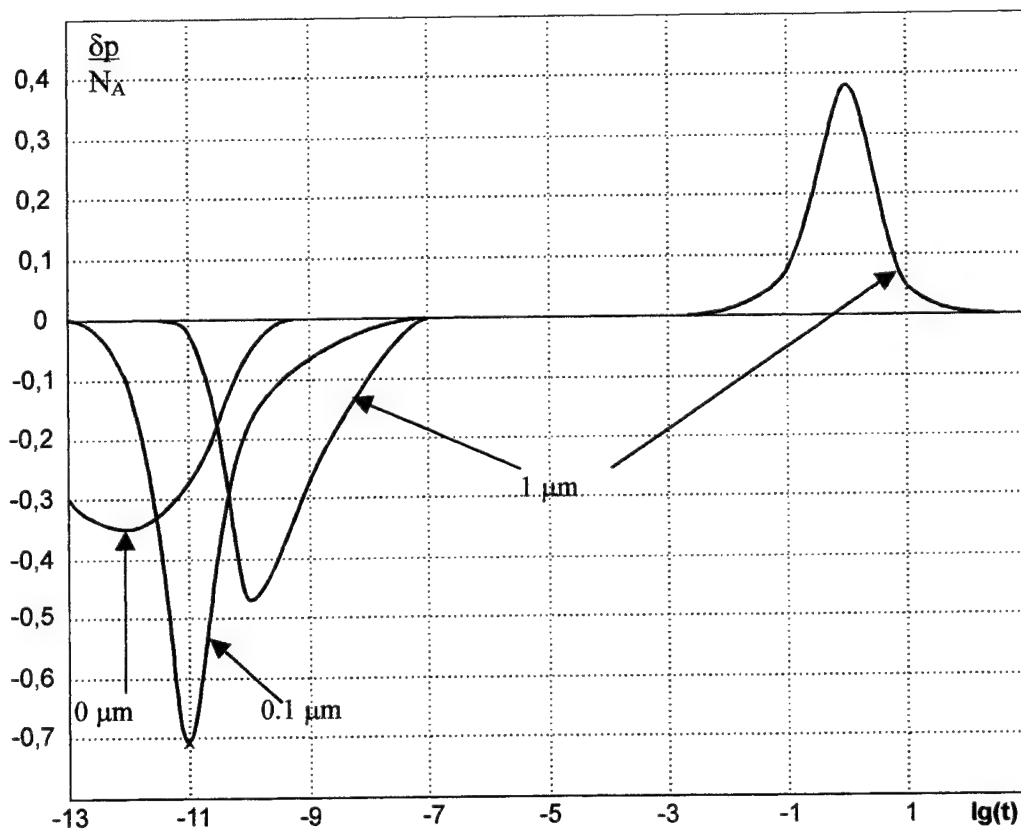


Fig. 4. Dependence of the hole charge increment on time.

The inversion layer buildup is presented in Fig. 5, where the move of the zero current density point as a function of time is depicted. As the gradient of the concentration of carriers in inversion layer rises, also rises the drift and diffusion components of the total current. This is very crucial when calculation are based on finite differences. Wavelets approach enable to overcome these difficulty.

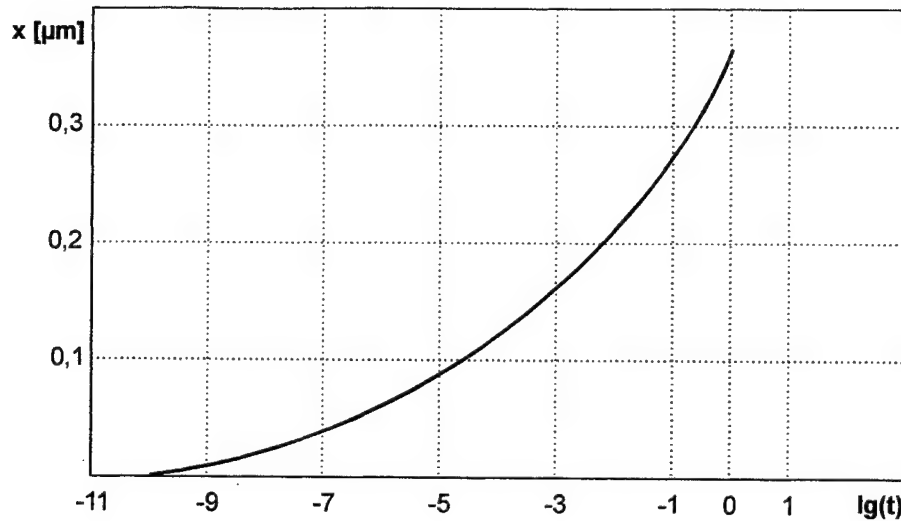


Fig. 5. Time-dimension trajectory of the zero-point current.

5. CONCLUSIONS

The regions of stability of the finite difference algorithm for Poisson equation were determined. Approach based on combined finite-differences, spectral and front-tracking grid methods into a collection of efficient, generic algorithm was investigated. Application of the wavelet approach increase the efficiency of the algorithm, especially in the equilibration period, when coupling of the drift diffusion equations through Poisson equation is very tight.

ACKNOWLEDGEMENTS

The study was supported by the Polish State Committee for Scientific Research through grant No KBN-8-T11B 026 14.

REFERENCES

1. G. Beylkin and J.M. Meiser, "An Adaptive Pseudo-Wavelet Approach for Solving Nonlinear Partial Differential Equations", in *Multiscale Wavelet Methods for PDEs*, Academic Press 1997.
2. P. Joly, Y. Maday, and V. Perrier, "A Dynamic Adaptive Concept Based on Wavelet Packet Best Bases: Application to Convection Diffusion Partial Differential Equations", in *Multiscale Wavelet Methods for PDEs*, Academic Press 1997.
3. T.W. Collins and J.N. Churchill, "Exact modelling of the transient response of an MOS capacitor", *IEEE Tr.El.Dev.*, v. ED-23, p.90

Sensitivity of surface acoustic waves devices

Jerzy Filipiak ^a, Konrad Zubko ^b

Institute of Applied Physics, Military University of Technology, Warsaw, Poland
Kaliskiego Str. 2, 00-908 Warsaw

ABSTRACT

The Surface Acoustic Waves (SAW) devices are widely used as filters, delay lines, resonators and gas sensors. It is possible to use it as mechanical force. The paper describes sensitivity of acceleration sensor based on SAW using the Rayleigh wave propagation. Since characteristic of acceleration SAW sensors are largely determined by piezoelectric materials, it is very important to select substrate with required characteristics. Researches and numerical modeling based on simply sensor model include piezoelectric beam with unilateral free end. An aggregated mass is connected to the one. The dimension and aggregated mass are various. In this case a buckling stress and sensitivity are changed. Sensitivity in main and perpendicular axis are compare for three sensors based on SiO₂, LiNbO₃, Li₂B₄O₇. Influences of phase velocity, electro-mechanical coupling constant and density on sensitivity are investigated. Some mechanical parameters (Young's modulus, dynamic strength) of the substrates in dynamic work mode are researched using sensor model and Rayleigh model of vibrations without vibration damping. The model is useful because it simply determines dependencies between sensor parameters and substrate parameters. Differences between measured and evaluated quantities are less then 5%. Researches based on sensor models, which fulfilled mechanical specifications similarly to aircraft navigation.

Keywords: surface acoustics waves, piezoelectric crystals, acceleration sensors

1. INTRODUCTION

Reacting to the force or to the field's force is the common feature of mechanical dimension's sensors. The acceleration sensor is characterized by the simplest construction ^{1, 12}. There are the results of researches for the sensors, which are made as ST quartz cantilever beam, shown in that work. The converter used as SAW generator with the sensitivity of 74 MHz which changes the waves by the beam's stress, is located on the beam's surface, near the fixed area. The length of its dilatory line realized with standard of 50 ohm amounts about 30 mm. The beam was 30 – 70 mm long, 3 mm wide, 1mm across. The proportion (ratio) of aggregated mass based on the free end of the beam is from 0 to 10 times. That 's the various resonance differences of beams and other various stress located in the fixing area of the generator.

Sensor's sensitivity is a parameter, which has an influence on its range of use ^{4,5}. The ideal sensor would react only to integrand force parallel to the axis of its sensitivity. Real sensors show the sensitivity also for integrand force in perpendicular axis square with the axis of main sensitivity. It reduces the accuracy of measurements. For sensors made in that way the ratio of sensitivity in the main axis is marked to the sensitivity in inclined axis.

Further author information -

a) Jerzy Filipiak email: filipj@glob.wic.wat.waw.pl, phone 48 22 685 96 04

b) Konrad Zubko email: zubkonrad@mach3.polbox.pl, phone 48 22 685 48 51

Military University of Technology

<http://www.wat.waw.pl/>

Institute of Applied Physics

<http://altair.wic.wat.waw.pl/instytutu/ift/>

2. THE BEAM MODEL

To define force describing the work of beam which are possible to use the Rayleigh model is used ³. That method requires the approximation of anisotropical mechanical ratio of the crystal, which has the cut by isotropic chosen ². After defining the parameters of the substitute system (Eq. 1), such as mass, energy and damping, the range of beam's work in the function of amplitude and frequency of sinusoidal force was named.

Parameters of the substitute Rayleigh system: mass, elasticity, damping and equation of motion:

(1)

$$m = 0.23 \rho b h l + m_s$$

$$k = \frac{3E}{l^3} \frac{b h^3}{12}$$

$$c = \frac{2\lambda}{T} m$$

$$F \sin pt = m \frac{d^2 x(t)}{dt^2} + c \frac{dx(t)}{dt} + kx(t)$$

where m_s - aggregated mass; ρ - mass density; b - width; h - height; l - length; E - Young modulus; λ - logarithmic damping

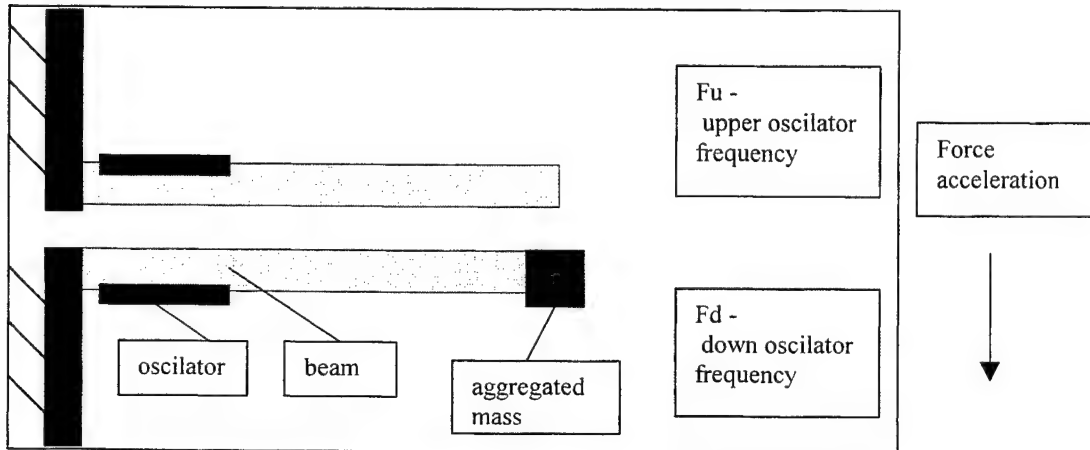


Fig. 1. Schematic view of piezoelectric beam mounted in sensor.

3. THE METHOD OF SENSITIVITY RATIO IN INCLINED AXIS TO MAIN SENSOR AXIS

The method to define the sensitivity ratio is based on:

- taking the angular SAW sensor characteristic;
- comparing the characteristics for two kinds of fixing in the starting point, the generator is supposed to be on the top and on the bottom of the beam.

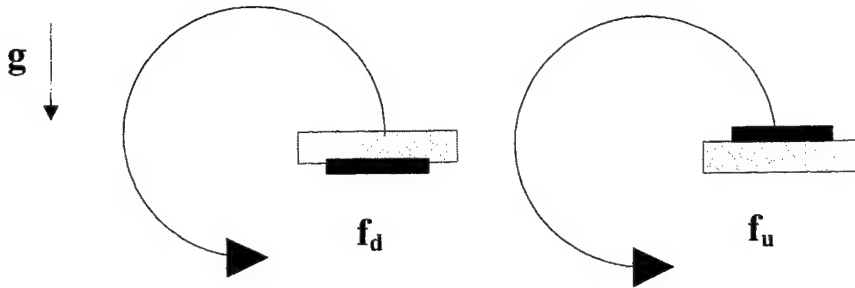


Fig. 2. View of sensor rotation in the field of Earth acceleration.

In such experiments the acceleration of gravity was defined as a force and it was treated as a constant and congeneric one^{1,7}. The sensors⁹ were rotated round the surface fixed by the axis of main sensitivity and one of the inclined sensitivities (longitudinal or transversal). Two kinds of fixing in the starting point were based on locating with the generator on the top and on the bottom of the beam. Received dependencies are different only because of the sign next to the coefficient of sensitivity in the main axis. Indicating the sum and difference of those expressions, there were received the dependencies containing only coefficients of the sensitivity in main or perpendicular axis. Change of oscillator frequency forced by various angles¹⁰

$$\begin{aligned}\Delta f_u(\alpha) &= A \sin(\alpha) + B \cos(\alpha) \\ \Delta f_d(\alpha) &= -A \sin(\alpha) + B \cos(\alpha)\end{aligned}\quad (2)$$

where: A - sensitivity in main axis, B - sensitivity in perpendicular axis, hence analytic sum and difference of (2)

$$\begin{aligned}f(-)(\alpha) &= 2A \sin(\alpha) \\ f(+)(\alpha) &= 2B \cos(\alpha)\end{aligned}\quad (3)$$

The difficulties of these analyses of experimental figures were based on the unacquaintance of the starting spatial orientation's angle. It consisted of beam orientation mistake in the sensor's cover, and also the mistake of sensor's fixing in the direction of the rotating surface. It causes the necessity of numerical corrections of that angle to fix its analytical dependencies to the results of the experiment as well as it is possible. Dividing the values received analytically (α) by the values subsequent to analytical functions (β) the constant value of sensor's sensitivity coefficient in that axis is received. The figures 3 shows the method.

The discrete areas connected with dividing the dimensions close to 0. Their breadth is connected with the quality of numerical device, however the symmetricalness of the decomposition is the evidence of well designated starting position of the angle.

The simplified method is based on fixing the sensitivity of SAW generator's work only in two ending positions¹. Considering faults which are possible to make while fixing the spatial orientation of the sample and also considering relatively small difference read out values that method is less accurate. On the other hand it is very useful under the circumstances of dynamic force where the sensor fixing stability while lasting the experiment, is required. Sensor sensitivity in axis is connected with the cover of SAW converter (generator's frequency, its dimension). Whereas the sensitivity ratio is now a parameter characterizing the material of basement^{8,9, 12}.

4. RESULTS

The researches were made for the amount of 16 SAW ST quartz sensors with various resonance frequency under static force circumstances. The accuracy of defining than spatial orientation's angle was about 2 grades. The average of defined sensitivity ratio was about 0,11 and its max mistake was about 3%.

For the second axis that dimension was smaller than 0,001. In consideration of fulfilled measuring devices it has not been able to show it more accurate. The researches were repeated for some dynamic forces using that simplified method. It confirmed the results of static researches. Those results including the sensitivity in main axis have been tabulated comparing to the results of D. Hauden's work.

Tab. 1 Results of the D. Hauden and this work

Quartz ST [D. Hauden]	parameters	Quartz ST
200	length [mm]	70
10	width[mm]	5
0,5	thin[mm]	0,5
2,6	agg. mass [g]	0,5
1	(agg. mass)/(beam mass)	1
105	osc. frequency [MHz]	76
1387	sensitivities in main axis (Hz/g)	~ 2000
$2,38 \times 10^{-6}$	sensitivities transverse/main	> 0.001
$5,82 \times 10^{-3}$	sensitivities compression/main	0.1
5	cantilever beam res. freq. [Hz]	38
17,5	cantilever beam max. stress [MPa]	2,1

5. CONCLUSIONS

Defined value of sensitivity ratio is bigger than the figures shown in the sensor's catalogue (0 – 5%). The divergence may be caused by the fact that the figures refer to the devices containing the electronic system of characteristic correction inside. Researched sensitivities in the main axis is 2000+/-30 Hz/g and the material parameter sensitivities ratio transverse/main is 0.1 +/- 0.01. Secound sensitivities ratio is less then 0.001, but it was not possible to research it more accuracy in the fact of used measurement devices. It depends on quality of made SAW acceleration sensor.

The discussion about the difference according to D. Hauden's work can not be provided, because there are not enough sensor descriptions, which are examined in his work. However the sensitivity definition in transversal axis which is less significant than the sensitivity in longitudinal axis is the thing which is common for both of works.

To reduce the sensitivity in prependericual axis it is proposed to use two sensors in the same device, which are different from each other in the location of the generator on both sides of the beam.

The differential frequency of such a system theoretically depends only on the sensitivity in the main axis. Various parameters of the beams 30 – 70 mm long, 3 mm wide, 1mm across. The proportion (ratio) of aggregated mass based on the free end of the beam is from 0 to 10 times. That 's the various resonance differences of beams and other various stress (crytical is about 60 MPa) located in the fixing area of the generator are showed Fig 3.

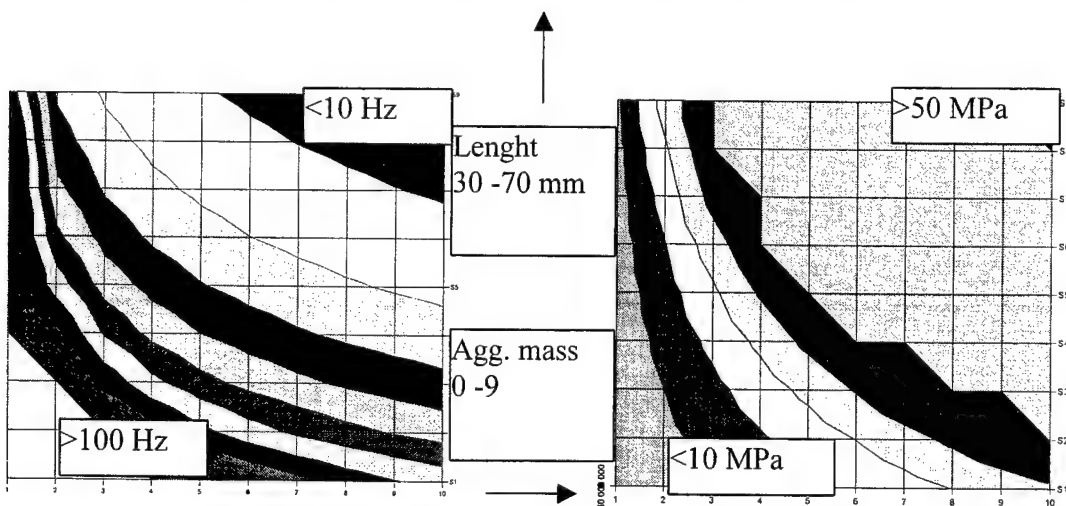


Fig. 3 a ,b. Resonance frequency (belt is 10 Hz) and buckling stress (belt is 10 MPa) in quartz ST beam.

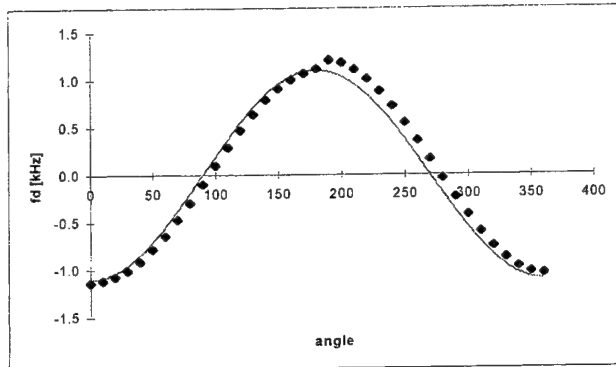
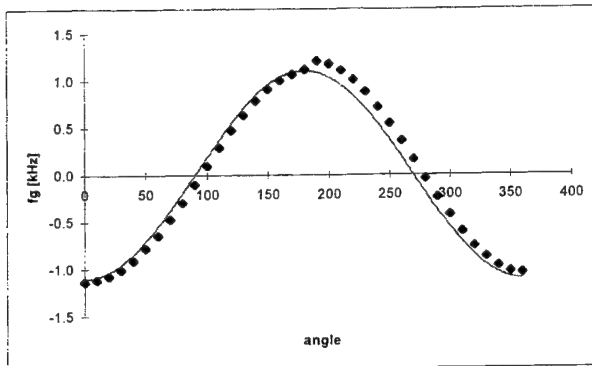


Fig. 4 a, b. Points - (experimental values) change of oscillator frequency (f_u and f_d), line (theoretical) $-\sin(\beta)$ function

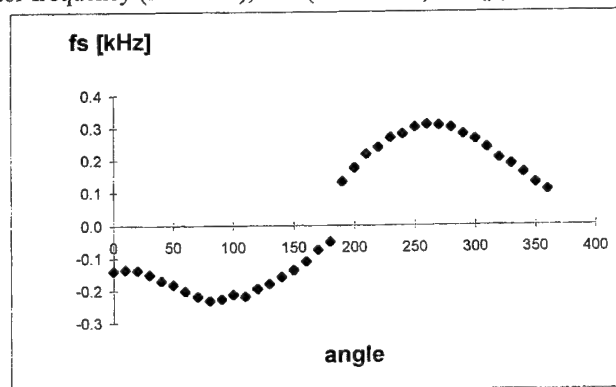
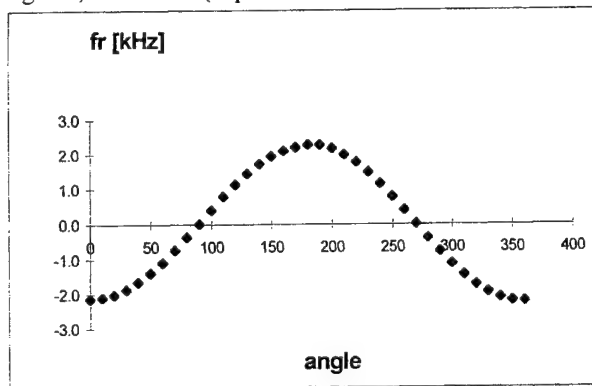


Fig. 4 c, d. Experimental $f_{(-)}(\alpha) = 2A\sin(\alpha)$ and $f_{(+)}(\alpha) = 2B\cos(\alpha)$ from Eq. 3

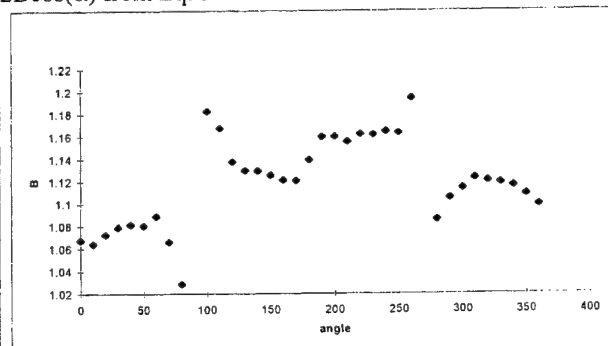
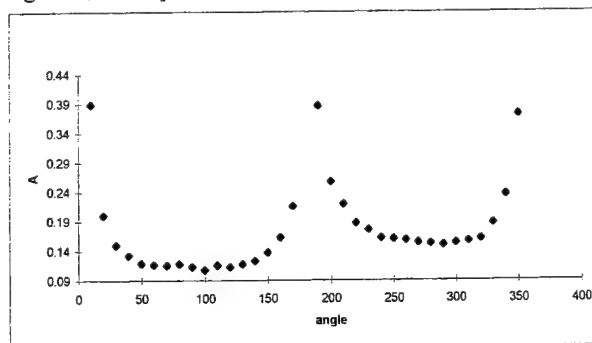


Fig. 4 e, f. Results of the $2A\sin(\alpha)/\sin(\beta)$ and $2B\cos(\alpha)/\cos(\beta)$ operations

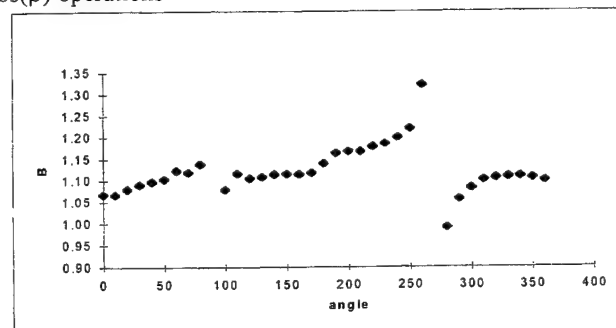
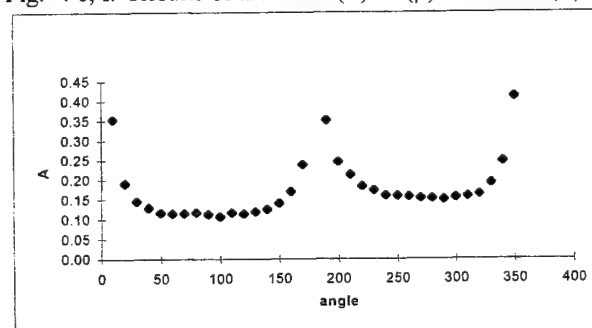


Fig. 4 g, h. Results of the $2A\sin(\alpha)/\sin(\beta+1)$ and $2B\cos(\alpha)/\cos(\beta+1)$ operations

ACKNOWLEDGMENTS

Researches were supported by Polish State Committee for Scientific Research (KBN), under projects:

- 8 T10C 037 08 "Acceleration sensors based on SAW"
- 7 T08A 047 17 "Possibilities of using piezoelectric substratum LBO (lithium tetraborate) for mechanical sensors based on SAW "
- Military University of Technology, research program no 169 "SAW devices"

REFERENCES

1. D. Hauden, "Elastic waves for miniaturized piezoelectric sensors: applications to physical quantity measurements and chemical detection", *Archives of Acoustics*, vol. **16** no **1**, pp. 8 - 15, 1991
2. J. F. Nye, *Physical properties of crystals, their representation by tensors and matrices*, ch. 5, PWN, Warsaw, 1962
3. S. Kaliski, *Waves and vibrations*, ch. 1, Elsevier and PWN, Warsaw, 1992
4. Litton Industries *Guidance and control systems*, catalog 10/1996
5. Sawtek Incorporated *Product catalog 1997*, <http://www.sawtek.com>
6. J. Filipiak, C. Kopycki, "Surface acoustic waves for the detection of small vibrations" *Sensors and Actuators*, **2435**, pp. 109-112, 1998
7. C. Kopycki, J. Filipiak, Modeling of SAW sensors sensitivity based on multiple transit signals in a delay line, *International Conference on Solid State Crystals*, pp. 229 - 232 Jurata 1998
8. J. Filipiak, L. Solarz, J. Ostrowski, C. Kopycki "Lithium niobate as the substratum for the SAW acceleration sensor", *Solid State Crystals in Optoelectronics and Semiconductors Technology*, Proceedings SPIE 1997 - The International Society for Optical Engineering, 3179, pp. 256-260.
9. J. Filipiak, L. Solarz, C. Kopycki, K. Zubko, "Linear acceleration sensor on Surface Acoustics Waves", proceedings of the Navigation Symposium, Air Force Institute of Technology, pp. 68-74, Warsaw 1998,
10. J. Filipiak, K. Zubko "Two dimension acceleration sensor on Surface Acoustic Waves" *proceedings of the 28 Winter School on Molecular and Quantum Acoustics*, pp. 53-56, Ustron 1999
11. K. Zubko "Lithium Tetraborate properties as a substrate for SAW acceleration sensor" *proceedings of the 28 Winter School on Molecular and Quantum Acoustics*, p. 50, Wisla 2000
12. R. Shear "Piezoelectric sensors for OEM applications", <http://www.sensorsmag.com/articles/0299/oem0299/main.shtml>

Nonlinear optical properties in ZnSe crystals

Beata Derkowska^{a, b}, Bouchta Sahraoui^a, Xuan Nguyen Phu^a, and Wacław Bala^b

^aLaboratoire des Propriétés Optiques des Matériaux et Applications (POMA), EP CNRS 130 Université d'Angers, 2 Bd. Lavoisier, 49045, Angers Cedex 01, France

^bInstitute of Physics, Nicholas Copernicus University, Grudziadzka 5, 87-100 Torun, Poland

ABSTRACT

The two photon absorption (TPA) coefficient (β) and third order nonlinear optical susceptibility ($\chi^{(3)}$) of ZnSe crystals were investigated using the transmission and degenerate four wave mixing (DFWM) methods. The experimental results show that imaginary part of third order nonlinear optical susceptibility ($\chi^{(3)}$) decrease with increase of free carriers (n) and the absolute value of third order nonlinear optical susceptibility increase with increase of free electron concentration (n).

Keywords: degenerate four wave mixing, optical nonlinearities, third order nonlinear optical susceptibility, two photon absorption, crystals

1. INTRODUCTION

Wide band gap A^{II}B^{VI} compounds are very attractive materials for optoelectronics devices, such as light emitting diodes, surface emitting lasers, waveguides and modulators¹, in the visible or ultraviolet region of the spectrum. In particular, ZnSe, as a semiconductor with a direct band gap of 2.67 eV at room temperature, is an important material for use in optoelectronics applications.

Knowledge of the optical properties of ZnSe crystals is especially important in the searching and analysis of laser structures and waveguiding devices in the whole visible field.

In this work, we present an experimental investigation of optical nonlinearity in ZnSe crystals using the nonlinear transmission and degenerate four wave mixing (DFWM) methods².

2. EXPERIMENTAL

The DFWM response of the crystals was measured with a mode-locked Q-switched Nd:YAG laser with 30 ps pulses width, 1 Hz repetition rate, and 532 nm wavelength. We assume that the intensity of the laser beam at the input face of the sample is the Gaussian distribution in space and time. Measurements were performed at room temperature. Intentionally undoped ZnSe crystals were grown from the melt by the modified high-pressure Bridgman method under an argon over pressure of 11 MPa using ZnSe powder as a starting material. The crystals were cut into 1 mm thick plates parallel to (111) crystallographic plane. The obtained samples have been annealed in liquid zinc at different temperatures between 830° and 920°. After this process, the samples were mechanically polished and chemically etched. The final thickness of the ZnSe crystals was about 0.73 mm. The measurements of resistivity, Hall mobility and carrier concentration were performed with the Van der Pauw method using indium dots as the contacts. The investigated monocrystal ZnSe belong to point group $\bar{4}3m$ for which spatial symmetry imposes restrictions on the form of the fourth-rank electric susceptibility tensor.

3. RESULTS AND DISCUSSION

In general third order nonlinear optical susceptibility ($\chi^{(3)}$) is considered to be a complex quantity: $\chi^{(3)} = \chi^{(3)'} + i\chi^{(3)''}$, where the real part of third order nonlinear optical susceptibility ($\chi^{(3)'}$) describe the nonlinear refractive index change

which will be extracted from degenerate four wave mixing (DFWM) measurements, and the imaginary part of third order nonlinear optical susceptibility ($\chi^{(3)}$) is related to the two photon absorption (TPA) coefficient (β) calculated from transmission measurement.

The knowledge of the two photon absorption (TPA) spectrum of semiconductors is important for development of all-optical switching elements, because TPA imposes a fundamental limitation on the performance of such devices³. The TPA takes place when the laser photon energy ($h\nu$) is larger than half the energy band gap and lower than the energy band gap of crystal ($E_g/2 < h\nu < E_g$). The relation between the laser photon energy and energy band gap of the investigated crystals allows us to determine the TPA coefficient (β) for ZnSe crystals⁴.

We used the nonlinear transmission measurements to obtain the TPA coefficient (β) related to the imaginary parts of the third order nonlinear optical susceptibility ($\chi^{(3)}$).

The experimental result for ZnSe crystal is presented in Fig. 1. As can be seen, the solid line shows the best fit with theoretical formula (1) to the experimental data. We can notice that all samples studied reveal a strong nonlinear absorption decreasing with an increase of the free electron concentration.

$$T = \frac{I_T(L)}{I_1(0)} = \frac{\alpha \exp(-\alpha L)}{\alpha + \beta I_1(1 - \exp(-\alpha L))} \quad (1)$$

where I_1 is the incident intensity, I_T is the transmitted intensity, α is the linear absorption coefficient, L is the thickness of the crystal and β is the TPA coefficient.

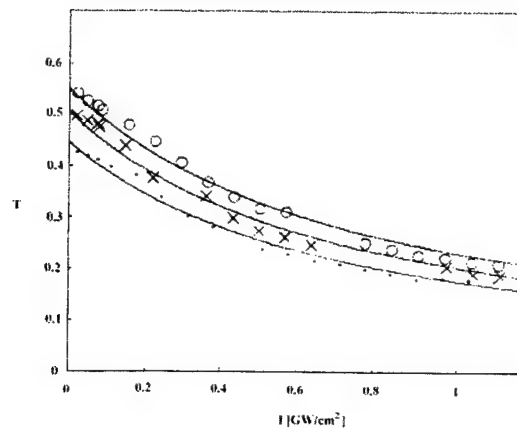


Fig. 1. The transmission as a function of the incident intensity I_1 at 532 nm. The (.), (x) and (o) represent the experimental data for n-type ZnSe crystals annealed in the temperatures 870°C, 890°C, 920°C, respectively.

We assumed Gaussian distribution of the laser intensity I_1 and took into account Fresnel reflection, which reduced the laser intensity in the crystal by the factor $(1-R)^2$, where $R = \left(\frac{1-n}{1+n}\right)^2$ is the reflection coefficient of the air-semiconductor interface³. The values of TPA coefficient (β) extracted from dependencies of Fig. 1 and theoretical formula (1) are presented in Table 1. We can see that for the crystal the straight line of Fig. 1 intercepts the ordinate axis and their value is lower than the unity. So it intercepts the ordinate axis at values of $\exp(-\alpha L)$ corresponding to the values of the linear absorption coefficient (α) listed in Table 1. We can also observe that the linear absorption (α) coefficient decreases as the free electron concentration increases. The linear absorption is due, among other reason, to the impurity levels in the band gap. The imaginary part of $\chi^{(3)}$ for ZnSe crystals was calculated by the equation (2) and is presented in Table 1:

$$\chi^{<3>} = \frac{n^2 c \lambda}{48 \pi^3} \beta \quad (2)$$

where n is the refractive index and $\chi^{<3>}$ is the imaginary part of third order nonlinear optical susceptibility.

Table 1: The values of linear absorption (α) and nonlinear absorption (β) coefficients, the absolute value and imaginary parts of third order nonlinear optical susceptibility ($\chi^{<3>}$) for ZnSe for different free carriers concentration (n) and different temperatures (T)

Table. 1.

Crystals	T [°C]	$n \cdot 10^{-15}$ [cm ⁻³]	α [cm ⁻¹]	β [cm/GW]	$Im(\chi^{<3>})$ [esu]	$ \chi^{<3>} $ [esu]
ZnSe-1	870	74	5	14.9	$1.1 \cdot 10^{-11}$	$5.7 \cdot 10^{-12}$
ZnSe-2	890	130	3.3	13.7	$1.07 \cdot 10^{-11}$	$6.2 \cdot 10^{-12}$
ZnSe-3	920	290	2.1	12.3	$0.96 \cdot 10^{-11}$	$7.1 \cdot 10^{-12}$
ZnSe	-	-	-	5.5 ^[7]	$0.64 \cdot 10^{-11}$ ^[8]	$1.8 \cdot 10^{-12}$ ^[8]

The absolute value of $\chi^{<3>}$ for ZnSe crystals was estimated using DFWM method. In the DFWM measurement (Fig.2), two counter-propagating strong pump beams (<1> and <2>) are incident on the sample with a third weaker probe beam (<3>), which incidents at the angle θ ($\theta = 12^\circ$) with respect to the pump beams. The pump beams interfere inside the sample to form the refractive index grating from which the third beam diffracts to form a conjugate signal (designated by <4>) that retraces the probe path⁵. The incident beams of the same frequency (ω) are temporally and spatially overlap in the sample and their intensities satisfy the relations: $I_1(z=0) = I_2(z=L)$ and $I_3 = 6 \cdot 10^{-2} I_1$. All the DFWM measurements were taken using the parallel (xxxx) configuration. The phase conjugate signal was detected by a photo-multiplier tube (PM). A portion of the input beam was picked off and measured by a photodiode (V_c) to monitor the input energy. The photodiode and conjugate signals were averaged and displayed by a Tektronix TDS 3054 Digital Phosphor Oscilloscope.

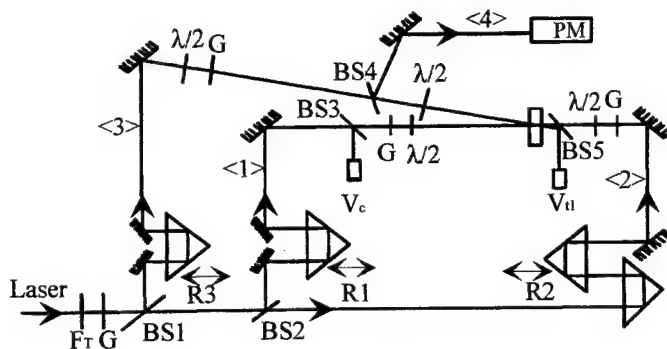


Fig. 2. The experimental set-up of DFWM method: <1> and <2> - pump beams; <3> - probe beam; <4> - fourth beam; S - sample; F_T - neutral filter; R_1 , R_2 , R_3 - delay lines; G - glan prism; V_c , V_t - control photodiodes; PM - photo-multiplier tube.

The experimental and theoretical results of DFWM reflectivity (R) are presented in Fig. 3. The DFWM reflectivity (R) was calculated from the propagation equation of the four interacting beams deduced from the Maxwell equations using slowly varying amplitude approximations and took into account linear and nonlinear absorption and the transformation from the crystallographic axis to laboratory axis. The DFWM reflectivity (R) can be expressed as follows⁶:

$$R = \frac{I_4(0)}{I_3(0)} = \frac{K^2}{\left[q \coth(qL) - \frac{\phi}{2} \right]^2} \quad (3)$$

$$\text{where } q^2 = \left(\frac{\phi}{2} \right)^2 - K^2, \text{ and } K^2 = \left(\frac{48\pi^3}{n^2 c \lambda} \right)^2 (\chi'^2 + \chi''^2) I_1 I_2, \quad \phi = -\alpha - 2\beta(I_1 + I_2).$$

χ' and χ'' are the real and imaginary parts of third order nonlinear optical susceptibility ($\chi^{<3>}$), respectively.

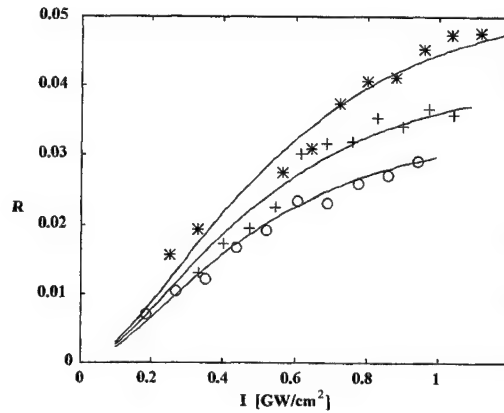


Fig. 3. DFWM reflectivity (R) as a function of the incident intensity I_1 . The (*), (+) and (o) represent the experimental data for n-type ZnSe crystals annealed in the temperatures 920°C, 890°C, 870°C, respectively.

As can be seen in Fig. 3, the solid line shows the fit with theoretical formula (3) to the experimental data. The values of absolute value of $\chi^{<3>}$ estimated from the dependencies of Fig. 3 and theoretical formula (3) are presented in Table 1. We obtain that the absolute value of third order nonlinear optical susceptibility ($\chi^{<3>}$) tends to increase with electron concentration (n). However the relative changes of the real part of third order nonlinear optical susceptibility ($\chi^{<3>}$) with electron concentration remain smaller than those of the imaginary part of third order nonlinear optical susceptibility ($\chi^{<3>}$).

4. CONCLUSIONS

We evaluated the TPA coefficient (β) and calculated the imaginary part of $\chi^{<3>}$ from the nonlinear transmission at 532 nm. It is found that the nonlinear absorption and the imaginary part of $\chi^{<3>}$ decreases with increasing of free carriers (n). We also evaluated the absolute value of $\chi^{<3>}$ for studied crystals using DFWM method. The absolute value of $\chi^{<3>}$ increases with increase of free electron concentration. We observe that the linear absorption coefficient α decreases as free electron concentration increases. Heat treatment of crystals improves their structure due to the elimination of some impurity levels in the band gap, which causes a decrease in linear absorption in ZnSe. The experimental values of the TPA coefficient (β) for ZnSe crystals presented in this work are about two-three times higher than for polycrystals of ZnSe ($\beta = 5.5[\text{cm/GW}]$, $\beta = 5.8[\text{cm/GW}]$)⁷. Also the experimental values of $\chi^{<3>}$ in our work are about two times larger than for polycrystals of ZnSe ($\text{Im}(\chi^{<3>}) = 0.64 \cdot 10^{-11} [\text{esu}]$ and $\text{Re}(\chi^{<3>}) = 1.8 \cdot 10^{-11} [\text{esu}]$)⁸.

ACKNOWLEDGEMENT

The authors are grateful to F. Firszt for heating sample.

REFERENCES

1. E. Snoeks, T. Marshall, J. Petruzzello, M.D. Pashley, L.L. Chao, and G.S. Cargill, "Diffusion lengths of carriers in *n*- and *p*-type ZnMgSSe cladding layers of green laser diodes", *J. Appl. Phys.* 84, pp. 3611-3616, 1998
2. R.W. Boyd, *Nonlinear optics* Academic Press Inc., 1992
3. J.A. Bolger, A.K. Kar, B.S. Wherrett, R.DeSalvo, D.C.Hutchings, and D.J.Hagan, "Nondegenerate two-photon absorption spectra of ZnSe, ZnS and ZnO", *Optics Comm.* 97, pp. 203-209, 1993
4. K.R. Allakhverdiev, "Two-photon absorption in layered TlGaSe₂, TlInS₂, TlGaS₂ and GaSe crystals", *Solid State Comm.* 111, pp. 253-257, 1999
5. A.A. Said, M. Sheik-Bahae, D.J. Hagan, E.J. Canto-Said, Y.Y. Wu, J. Young, T.H. Wei, and E.W. Van Stryland, "Nonlinearities in semiconductors for optical limiting", SPIE, Vol. 1307 Electro-Optical Materials for Switches, Coatings, Sensor Optics, and Detectors, pp. 294-301, 1990
6. B. Sahraoui, G. Rivoire, and W. Bala, "Influence of doping and annealing temperature in n-type semiconductors ZnSe and ZnSe:Ag on two-photon absorption and third-order susceptibility", *J. Luminescence* 72/74, pp. 829-831, 1997
7. D.C. Hutchings, and E.W. Van Stryland, "Nondegenerate two-photon absorption in zinc-blende semiconductors", *J. Opt. Soc. Am. B* 9, pp. 2065-2074, 1992
8. Y. Guo, L. Yang, A.D. Walser, and R. Dorsinville, "Experimental observation of all-optical deflection using forward degenerate four-wave mixing in ZnSe", *Optics Comm.* 119, pp. 139-142, 1995

Growth and characterization of single crystals of ternary chalcogenides for laser applications

Ludmila Isaenko^{a*}, Alexander Yelissev^a, Jean-Jacques Zondy^b, Guido Knippels^c, I. Thenot^b, Sergei Lobanov^a

^a Design & Technological Institute of Monocrystals, 43 Russkaya str., Novosibirsk 630058, Russia

^b Laboratoire Primaire du Temps et des Fréquences, Bureau National de Métrologie, Observatoire de Paris, 61 avenue de l'Observatoire, 75014 Paris, France

^c FOM-Institute for Plasma Physics 'Rijnhuizen', Edisonbaan 14, 3439 MN, Nieuwegein, The Netherlands

ABSTRACT

Bulk single crystals up to 20 mm in diameter and 40 mm long for LiInS_2 and up to 10 mm, 20 mm, respectively, for LiInSe_2 have been grown. Their color changed from colorless to rose for the first one and from yellow to dark red for the other. All crystals have wurtzite-type lattice (Pna2₁ space group), lattice parameters were determined. A band gap was found to be 3.72 and 3.57 eV for LiInS_2 and 3.02, 2.86 eV for LiInSe_2 at 80 and 300K respectively. Color variations are due to point defects, first of all to interstitial sulfur, resulting in additional wide absorption bands in the shortwave part of transparency range. For LiInS_2 the SHG phase matching conditions were found to be similar for samples of different color and some difference from Boyd's predictions of 1973 was shown: for XY plane $\Delta\phi \sim +3^\circ$ at 2.6 μm and $\Delta\phi \sim -3$ to -5° at 4–5 μm . Nonlinear susceptibility for LiInS_2 was estimated: $d_{\text{eff}}(\text{XY}) \sim 3.4 \text{ pm/V}$ relative to Boyd's value as 10.6 pm/V. A proper illumination gives a photoinduced change of LiInSe_2 color from dark red to yellow as a result of changes in point defects charge state.

Keywords: lithium indium sulfide/selenide, absorption, color, nonlinear susceptibility, band gap, lattice parameters

1. INTRODUCTION

The mid-IR spectral range is of large importance because the overwhelming majority of chemical compounds has specific vibrational/rotational spectra and their detection and identification make it possible to solve various fundamental and applied tasks in molecular spectroscopy, atmospheric sensing, optical metrology, medicine etc.. To date the most widespread techniques to produce the coherent widely tunable radiation with wavelengths up to 20 μm are based on difference frequency generation of two near-IR lasers in infrared nonlinear optical (NLO) crystals and on use of optical parametric oscillators (OPO). Very few good NLO crystals including GaSe and a set of ternary chalcogenides as AgGaS_2 , AgGaSe_2 et al have been recently used for cw optical parametric oscillator¹ but each of them has its own shortcomings. For GaSe it is a problem with mechanical treatment including finishing, while silver ternary chalcogenides have an insufficient nonlinear susceptibility and low thermal conductivity.

An active search for new promising nonlinear crystals is in progress. The Li-containing ternary chalcogenides such as LiInS_2 and LiInSe_2 are considered as promising ones for generation of coherent radiation in the mid-IR region thanks to their transparency in a wide region from the 0.4 μm for LiInS_2 and 0.6 μm for LiInSe_2 to 12 microns in the mid-IR and relatively high nonlinear susceptibility. The latter was estimated using a wedge technique: d_{33} was shown to be about 18 pm/V for LiInS_2 ² which is 1.5 times higher than that for the wide-spread AgGaS_2 . Moreover there are several additional reasons that make the Li-based crystals very attractive for non-linear optics:

1. The Ag-ion replacement by the lighter Li-ion results in an increase in the frequencies of crystal lattice vibrations and of the Debye temperature. It intensifies the U-processes in phonon-phonon interactions and increases the thermal

L.I. (correspondence) E-mail: lisa@lea.nsk.su, Telephone/Fax: 7(383-2) 333-843

A.Y.: E-mail: elis@mail.nsk.ru

J.-J.Z.: E-mail: Jean-Jacques.Zondy@obspm.fr

G.K. E-mail: Knippels@rijnh.nl

conductivity, which in turn, are accompanied by an increase of the optical damage threshold.

2. LiInS_2 and its analogues crystallise in an mm2 space-group, like KTP, and are related to pyro-electrics and maybe ferro-electrics, where a periodic domain structure can be created and quasi-phase-matching operation (QPM) can be realised. This will allow us to considerably widen the spectral range of generated frequencies and to increase the non-linear conversion efficiency.
3. LiInS_2 crystals have the largest energy gap (3.59 eV at 300 K) among NLO crystals used for the mid-IR, which reduces the effect of two-photon absorption when pumping this crystal by the most widely used diode laser or a Nd:YAG laser.
4. The wurtzite type crystal lattice different from a chalcopyrite one of AgGaS_2 , AgGaSe_2 and ZnGeP_2 type allows us to avoid the difference in sign of the thermal expansion coefficients along different and resulting creation of typical stresses and {112} micro-twin defects. Therefore, these crystals are expected to benefit from several different available crystal growth technologies. The more rarefied wurtzite-type crystal structure facilitates doping when adjusting the phase-matching (PM) conditions.

Although the first LiInS_2 crystals appeared in the 70th, a high chemical activity of lithium and a considerable volatility of some components, resulting in considerable variation of composition and in turn of their chemical and physical properties prevented from growing bulk crystals of good quality. Only recently a technique for obtaining large crystals up to several cubic centimetres in volume was worked out and a detailed study of these crystals was continued³. The as grown LiInS_2 crystals were found to be colorless or slightly yellow while after annealing in sulfur vapour the samples became reddish. A special testing on thin samples gave identical band gap value for all samples independent of color: $E_g=3.72$ and 3.57 at 80 and 300 K, respectively³, while coloration is a result of point defects presence. The annealed samples demonstrated two dominating absorption bands at 480 nm (EIIb,c) and 540 nm (EIIa). An additional band at 740 nm (EIIa), which was found in some samples, did not affect the colour. An intense band at 360 nm in as grown LiInS_2 samples disappeared after annealing in sulfur and was related to sulfur vacancy, V_s . Chemical analysis showed that composition of all studied LiInS_2 crystals was close to a stoichiometric one although a lithium deficit and an indium excess was present. Thus a part of indium ions substitutes lithium and this antisite defect, In_{Li} , was supposed to be responsible for a broad absorption band at 380 nm and an intense blue photoluminescence which both are characteristic for all LiInS_2 samples studied³. In the present paper the identity of crystal structure in all LiInS_2 samples was confirmed using a single crystal X-ray diffraction analysis while the lattice parameters varied slightly. On the other hand the phase-matching conditions for second harmonic generation (SHG) were experimentally determined using a set of available laser systems and they were found to be similar for colourless and reddish samples, although there is a difference between them both and a theoretical curve built in accord with Boyd's data of 1973². Changes in colour were found to be much stronger in LiInSe_2 : in contrast to previous data⁴ the as grown LiInSe_2 samples were found to be yellow while after annealing in Se vapour their colour changes to dark red. Nevertheless combined X-ray diffraction study and optical spectroscopy showed that in LiInSe_2 these effects are also due to point defects.

2. EXPERIMENTAL DETAILS

2.1 Crystal growth

The bulk LiInS_2 and LiInSe_2 crystals were grown by the Bridgman-Stockbarger technique in vertical set-ups with counter-pressure on (001) and (010) seeds. The starting reagents were with 99,999% for S, Se and In, and 99.9% for Li nominal purity. Sulfur was additionally purified by sublimation in dynamic or static vacuum while metals were cleaned by repeated zonal melting and directed crystallization. Partial attention was paid to ratios between starting Li, In, S, Se elements. A correction of the stoichiometric $\text{Li:In:S(Se)}=1:1:2$ ratios was made taking into account different stability of the elements to weight loss during the runs because of volatilization and interaction between melt and container walls. To avoid Li interaction with silica ampoule a synthesis was performed in a special polished graphite crucible located inside silica ampoule. Some sulfur losses took place because of its interaction with graphite walls. An additional post-growth thermal treatment in S (Se) vapor at temperature close to melting point was made to remove the small opaque inclusions of different phases. Since vapor composition and partial pressure of gaseous species were unknown the optimized conditions for high quality crystal obtaining were empirically found. Using X-ray diffraction technique rectangular optical elements of certain orientation relative to crystallographic axes were cut from boules and their opposite working faces were polished for optical measurements.

2.2 X-ray diffraction study

The crystal structure determination for different LiInS_2 and LiInSe_2 samples was performed using CAD4 diffractometer along with the SHELXL97 structure determination/refinement program.

2.3 Optical spectroscopy

Optical transmission spectra were recorded in a whole transparency region using Shimadzu UV-3101 PC UV/VIS-NIR and Bomem FTIR spectrometer. For measurements in polarised light the film polarizers were used. A sample with parallel opposite faces was located inside metal vacuum cryostat, cooled by liquid nitrogen, which provided 90 to 600 K temperature variation.

2.4 Nonlinear experiments

Three different set-ups were used as IR sources of fundamental radiation for investigation of SHG process in LiInS_2 crystals:

- **IR source 1, which covers 1.8 to 2.6 μm spectral range.** The pump source is a LiNbO_3 nanosecond OPO pumped by a 15-ns pulsed Nd:YAG laser with 10 Hz repetition rate providing a typical output pulse energy of over 700mJ. This infrared OPO is continuously tunable from 1.8 to 2.6 μm , with a pulse duration $\tau = 10$ ns and a 100-mJ output (signal + idler) energy. After pump and signal rejections, a fraction of the idler beam, which varied from 0.5 to 5mJ was used as the fundamental wave for SHG. The beam profile at the crystal is a flat spot with diameter $2w = 3\text{mm}$. The idler wavelength λ ranges from 2.35 to 2.6 μm and has a full spectral width $\Delta\nu = 0.7$ nm, well below the quasi lambda non-critical spectral PM bandwidth ($\Delta\lambda \sim 49\text{nm}$). At the exit of the sample, the fundamental wave is reflected by a specific set of filters with a calibrated transmission at the harmonic. The uncoated sample is mounted on a computer-controlled motorized rotation stage which rotation axis has been set at 45° from the vertical to the table, in order to project the vertically polarized pump wave into two components (along Z and in the XY plane). The harmonic pulse energy is measured with a pyroelectric detector and the pump wavelength is determined (to $\pm 2\text{nm}$) by a scanning monochromator (2m focal length) and an InAs photodetector.
- **IR source 2 (2.8-12 μm).** A 1 kHz 800 nm, 800 μJ pulse from a Ti:sapphire laser was used to pump a parametric generator/ amplifier OPG/OPA system (TOPAS, Light conversion). The latter generated tunable signal (1.2-1.6 μm) and idler (1.6-2.1 μm) waves, which are then difference-frequency mixed in a AgGaS_2 crystal to give tunable infrared from 2.8-12 microns. The IR pulse duration is 250-300 fs and the spectral width is $50\text{--}70\text{ cm}^{-1}$. Typical pulse energies in the infrared are about 5-10 μJ .

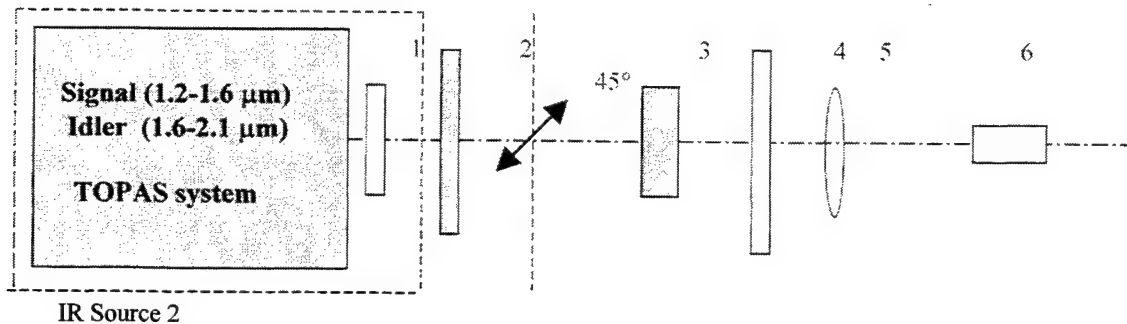


Fig.1 A scheme of nonlinear measurements with Ti-sapphire laser pumped OPG/OPA system as an IR source of fundamental radiation (Source 2). 1- an AgGaS_2 nonlinear element for mixing signal and idler components; 2- a long wave pass filter ($T > 2.5\text{ }\mu\text{m}$); 3- a LiInS_2 NLO element under investigation, rotated around horizontal axis; 4- a glass filter, separating a SH radiation; 5- a BaF_2 lens and 6- a MCT detector for SH radiation. An arrow shows fundamental wave polarisation for the II type PM case.

- **IR source 3 (4.5-40 μm):** A short-wavelength free-electron laser of the FELIX facility in Nieuwegein, the Netherlands. Pulse energies are around 10-20 μJ per pulse. The picosecond micropulses are grouped in a train of 5 μs duration (macropulse) with a micropulse spacing of 40 ns (or 1 ns). The macropulses are repeated at 10 Hz. The micropulse duration can be tuned from 200 fs to about 2 ps, while maintaining a fourier-transform limited spectrum.

2. RESULTS AND DISCUSSION

The as grown bulk crystals were up to 20 mm in diameter and 40 mm long for LiInS_2 and up to 10 mm, 20 mm, respectively, for LiInSe_2 . A preliminary testing using conoscopic techniques showed that all grown samples are single crystals. As grown LiInS_2 samples were colorless or yellowish while annealing changed their color to reddish. As grown LiInSe_2 crystals were yellow and annealing changed their color to dark red. Both changes in crystal structure and point defects can be responsible for color changes. In multicomponent compounds the phase diagram can be of very complicated structure and an area of homogeneity related to a certain phase is sometimes only about 1 w.% in width. In such case one can have another crystal structure after annealing in proper vapors and just this effect is used to remove the small inclusions inside bulk AgGaS_2 and AgGaSe_2 crystals. A nonlinear susceptibility is determined by the lattice structure and it is important to become sure that structure is the same in all crystals. Thus it is necessary to understand what is the origin of color changes in LiInS_2 and LiInSe_2 crystals. Four different structurally sensitive techniques were used:

1. An X-ray diffraction technique (Table 1);
2. The transmission spectra were recorded for especially performed plates about 0.1 mm thick, a form of fundamental absorption edge was analyzed and a band gap width, E_g , was measured; a longwave edge of the transparency region is also structurally sensitive since it is determined by specific vibrations in the lattice.
3. The attempts to change the color under proper illumination were made: in the case of point defects it is possible to change their charge state and thus to affect the color.
4. A second harmonic generation: the phase-matching conditions is a structurally sensitive parameter and it changes considerably at structure transformation.

Table 1 Lattice parameters for LiInS_2 and LiInSe_2 single crystals of different color

Formula	LiInS_2 (C1)	LiInS_2 (C2)	LiInS_2 (C3)	LiInSe_2	LiInSe_2	LiInSe_2
Color	Colorless	Yellowish	Rose	Yellow	Rose	Dark red
Space group	$\text{Pna}2_1$	$\text{Pna}2_1$	$\text{Pna}2_1$	$\text{Pna}2_1$	$\text{Pna}2_1$	$\text{Pna}2_1$
$a, \text{\AA}$	6.8744(8)	6.8915(7)	6.8930(4)	7.1917(8)	7.1939(8)	7.1934(10)
$b, \text{\AA}$	8.0332(14)	8.0563(10)	8.0578(4)	8.4116(10)	8.4163(10)	8.4159(11)
$c, \text{\AA}$	6.4624(9)	6.4784(5)	6.4816(3)	6.7926(8)	6.7926(8)	6.7971(9)
$V, \text{\AA}^3$	356.88(9)	359.68(6)	360.00	410.90(8)	411.27(8)	411.49(9)

3.1 LiInS_2

Absorption spectra for LiInS_2 crystals for EIIa polarisation, in which all bands, mentioned in ref.^{3,4} appear, are given in Fig.2a. One can see the main bands at 480, 540 and 740 nm, which are responsible for variations in crystal color from colorless to rose³. All crystals studied have the same form of the fundamental absorption edge which can be described by a relation of the form $ah\nu = A(h\nu - E_g)^{1/2}$. Such relation is valid for allowable direct transitions between the simple parabolic bands^{3,4}, the band gap values are $E_g = 3.72$ eV at 80 K and 3.57 eV at 300 K. Form and position of the longwave absorption edge are also identical. The X-ray data, obtained for all samples, give the same space group as $\text{Pna}2_1$ and the lattice parameters are similar (Table 1, first three columns). UV illumination was noticed to decrease a rose color of annealed LiInS_2 crystals, while He-Ne laser red radiation removed a grey color (photoinduced effects will be reported elsewhere). Thus, a complex of techniques shows that a color of different LiInS_2 samples is due not to structural difference but to variations in concentration and charge state of certain point defects in the crystal lattice.

The phase-matching properties of LiInS_2 have been studied earlier by Boyd *et al.*². They showed that the most efficient processes are type-II (eoe) phase-matched in the (a, b) plane, for which SHG occurs between the two angular noncritical wavelengths (along a -axis) of 2.32 μm and 5.88 μm . Using a one-pole Sellmeier equations fitted by Ch.Ebbers, we cut a 5x5x5 mm³ element at $\varphi = 66.1^\circ$ in the $(X, Y) = (b, a)$ plane. Note that, for standardization sake, our assignment for the crystallographic axes is $(XYZ) = (bac)$ such that $n_x < n_y < n_z$, differing thus with the one used in ref [2], $(XYZ) = (abc)$.

When the Kleinman symmetry conditions is assumed ($d_{32} = d_{24}$, $d_{31} = d_{15}$), the effective

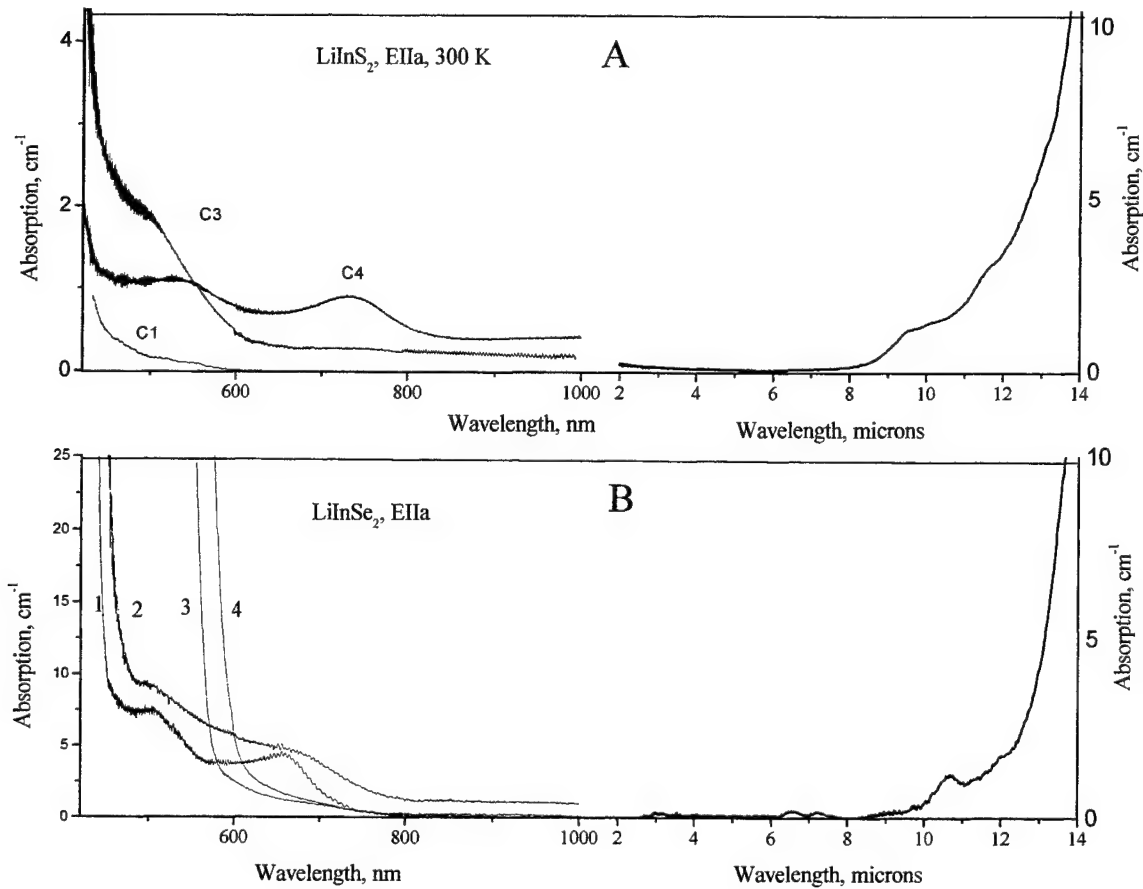


Fig.2 Absorption spectra for LiInS_2 (A) and LiInSe_2 (B) samples 1 mm thick. In Fig 2A C1 and C4 are LiInS_2 samples are colorless and gray-reddish as grown crystals, while C3 was annealed in sulfur vapor [3]. In Fig.B spectra 1,2 were obtained for yellow as grown LiInSe_2 and 3,4 correspond to dark red sample. Spectra 1,3 and 2,4 were recorded at 80 K and 300K, respectively. Spectra C3, C4 and 2 in Figures A and B, respectively are shifted upwards for clarity.

nonlinear coefficient for an (eoe) interaction in the XY plane is $d_{\text{eff}}^{\text{II}}(\varphi, \theta = 90^\circ) = d_{32} \sin^2 \varphi + d_{31} \cos^2 \varphi$. From the calibrated (using GaAs) wedge technique measurements at $10.6\mu\text{m}$ and $1.06\mu\text{m}$ (LiInS_2 cannot phase-match SHG for these wavelengths), Boyd *et al* found that d_{31} and d_{32} have the same sign with $d_{31} = 15 \text{ pm/V}$, $d_{32} = 9.7 \text{ pm/V}$, $d_{33} = 18 \text{ pm/V}$ (using $d_{14}(\text{GaAs}) = 134 \text{ pm/V}$ [2]). This would give $d_{\text{eff}}^{\text{II}} = 10.6 \text{ pm/V}$ for our SHG of $2.5 \mu\text{m}$.

Fig. 3 shows the dependence of the SH pulse energy as a function of the fundamental pulse energy, obtained in experiments with IR source 1 in 2.3 to $2.7 \mu\text{m}$ region. The Figure displays the expected quadratic dependence in the regime of low conversion efficiency (the maximum conversion $E(2\omega)/E(\omega)$ does not exceed 1%). From a fit to a quadratic law, one can deduce an energy conversion coefficient of $\Gamma = E(2\omega)/[E(\omega)]^2 = 2\text{J}^{-1}$. Assuming the same pulse duration at ω and 2ω the plane-wave conversion formula leads to a preliminary rough determination of $d_{\text{eff}} \approx 3.4 \text{ pm/V}$, about 3 times smaller than the expected value deduced from non-phase-matched SHG [3]. In Fig. 4, we show the recorded angular bandwidth of the phase-matching, as a function of the internal angle which yields $\Delta\varphi = (0.8 \pm 0.1)^\circ$ at a phase mismatch

$\Delta kL/2 = \pm 0.443\pi$ (FWHM). Superimposed to it we have plotted the plane-wave theoretical $\text{sinc}^2(\Delta kL/2)$ curve deduced from the indices of Boyd, which yields $\Delta\phi_B = 0.9^\circ$. The agreement is excellent for the crystal length (5 mm) used, which indicates a good crystal homogeneity over the whole volume⁵.

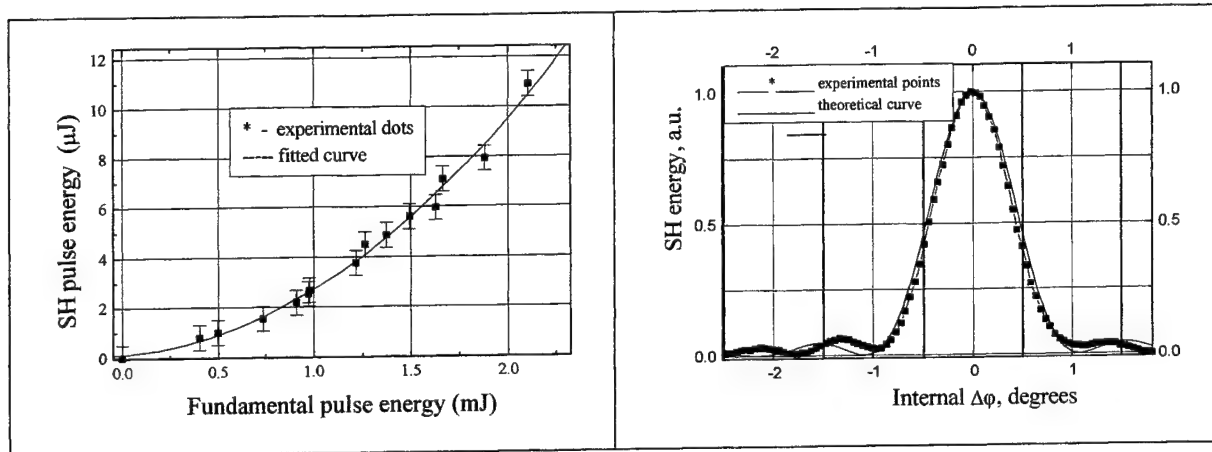


Fig.3 SH pulse energy corrected for blocking filters loss and Fresnel reflections loss on the crystal facets versus fundamental energy at $\lambda = (2841 \pm 2)\text{nm}$. The measured internal phase-matching angle is $\phi = 72.4^\circ$.

Fig.4 Internal angular acceptance bandwidth at nearly normal incidence at $\lambda = 2611\text{nm}$ ($\phi = 66.3^\circ$). The symbol curve is experimental data with $\Delta\phi = 0.8^\circ$ compared to the grey theoretical curve with $\Delta\phi = 0.9^\circ$ computed with ref.[2]. The sample size is $5 \times 5 \times 5\text{ mm}^3$.

The theoretical curve for phase-matching conditions was built using the refractive indices from² and fitting equation as $n^2 = A + B/(C + \lambda^2) + D\lambda^2$ with A, B, C, D, values from Table 2⁶. In Fig.5 the phase matching experimental data obtained using different IR sources 1 to 3 are compared with theoretical curve in a wide spectral region where the SH generation was predicted in ref². In the insert especially results for a shortwave region are given: one can see a good correlation in the form between theoretical and experimental curves although one can see an angle offset of $\sim 3^\circ$ (or a wavelength shift of $\sim 50\text{nm}$). A cross at $\lambda = 2.31\text{ }\mu\text{m}$ corresponds to noncritical phase matching (NPM) at $\Theta = 90^\circ$ and $\phi = 90^\circ$ (along Y or a axis), which was demonstrated by Ch.Ebbers in 1999⁶. At longer waves a good enough correlation between experimental PM curves for yellow, as grown and rose, annealed LiInS_2 samples although for them both an angle offset of ~ 3 to 5° from theoretical curve was found (Fig.5). One can infer that the Boyd's data give a good prediction on the birefringence value of LiInS_2 but need to be refined.

Table 2 Sellmeier parameters for LiInS_2 ⁶.

	α or Y	β or X	γ or Z or 2 fold axis
A	4.418222	4.559534	4.59206
B	0.1254461	0.1403701	0.1410887
C	-0.0657432	-0.69233	-0.069287
D	-0.0028850	-0.0028731	0.0030589

Optical damage threshold was measured using a free electron laser operating at 1 GHz with a beam focused to a Gaussian waist of $410\text{ }\mu\text{m}$ with an irradiated area of about $1.3 \times 10^{-2}\text{ cm}^2$. The macropulse energy is 14.5 mJ, so the fluence is about 1.1 J/cm^2 . The peak power in this case is 3.6 μJ per micropulse in 750 fs leading to 4.8 MW. Thus a peak intensity, corresponding to optical damage threshold of a rose, annealed LiInS_2 element, was estimated to be about $4.8\text{ MW}/1.3 \times 10^{-2}\text{ cm}^2 = 370\text{ MW/cm}^2$, while for a yellow sample it is about 20 % lower.

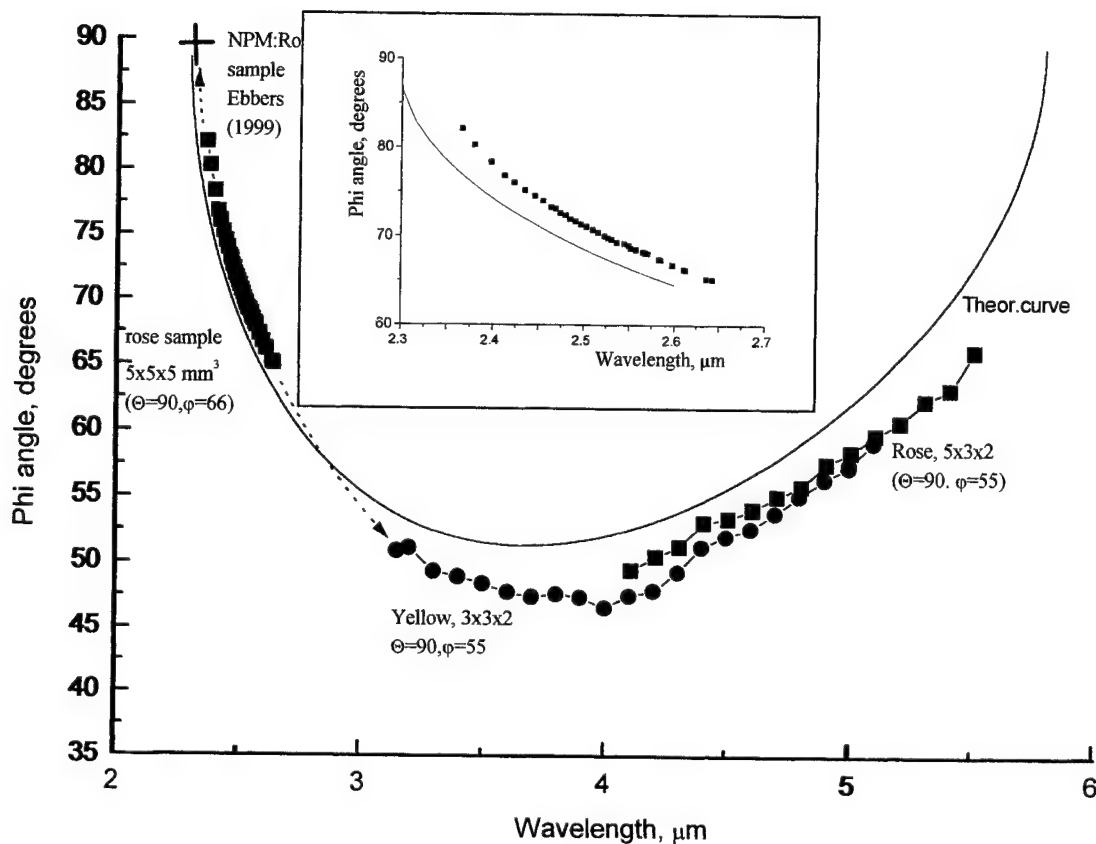


Fig. 5 Wavelength dependence of the internal phase-matching angles for different LiInSe_2 samples in comparison with a theoretical curve built basing on data from [2]:

at 2.31 μm and in 2.38 to 2.7 μm range –for a rose, annealed sample, 5x5x5 mm^3 in size;

in 3 to 5.0 μm range - for a yellow, as grown LiInSe_2 3x3x2 mm^3 in size;

in 4.2 to 5.5 μm – also for a rose, annealed sample 5x3x2 mm^3 in size.

In the insert: data for a shortwave range represented in extended scale.

3.2 LiInSe_2

To date from previous luminescence, resistance, absorption and diffuse reflectance measurements the energy of the fundamental absorption edge of LiInSe_2 is not established reliably and falls into the range of 1.6-2.0 eV⁷. Thus LiInSe_2 are expected to have a red color and nobody grew yellow bulk crystals. We studied carefully absorption spectra of LiInSe_2 samples, both as grown and annealed in selenium vapor. Absorption spectra for different in color LiInSe_2 crystals 1 mm thick are given in Fig.2B. One can see a sharp α decrease in the shortwave region : at ~ 450 nm and ~ 590 nm for yellow samples and dark red samples, respectively. Two additional broad absorption bands can be seen at 500 and 660 nm for yellow samples. When LiInSe_2 is heated from 80 K to room temperature the shortwave absorption edge, measured at 15 cm^{-1} level, is shifted 16 nm (0.096 eV) for yellow LiInSe_2 and ~ 23 nm (0.087 eV) for a dark red one. As the next step we decreased the crystal thickness to $d=100$ μm . In contrast to LiInSe_2 thin crystals had also different color: the annealed sample remained red. Indeed, in absorption spectra (Fig. 6) one can see a considerably different spectra again : only yellow pronounced bend near 540 nm is present. Analysis of the form of absorption spectra shows that they can be approximated by a straight line when $(\alpha \cdot h\nu)^2$ is plotted versus photon energy $h\nu$ (Fig.7). As for LiInSe_2 this case corresponds to allowed direct transition between simple parabolic bands⁴ and band gap values E_g are 2.86 and 2.87 eV for EIIa and EIIb at 300 K, while at 80 K the same values are 3.01 and 3.04 eV. Illumination by a visible light with $\lambda \sim 400$ -500 nm from 1kW Xe lamp

through MDR2 diffraction monochromator was found to remove a red color of annealed LiInSe_2 crystals and to make them yellow. Thus it is obvious that a red color of LiInSe_2 crystals is due to some kind of point defects (maybe interstitial selenium Se_i). This conclusion is in a good agreement with X-ray data (Table 1) which show that all LiInSe_2 crystals studied have identical structure (space group $\text{Pna}2_1$, wurtzite-type lattice) as well as with the fact that a longwave edge of the transparency spectrum also does not depend on crystal color (dominating vibrations are the same in crystal studied).

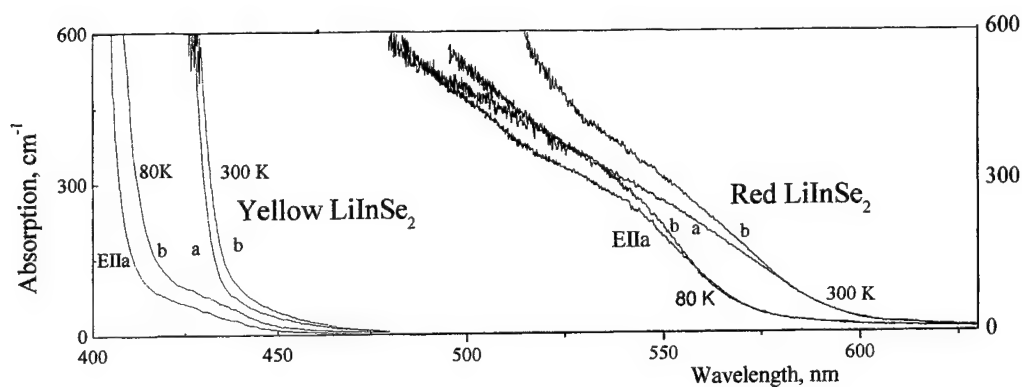


Fig. 6 Absorption spectra of LiInSe_2 plates 100 μm thick, cut from yellow and dark red samples. Spectra were recorded at 80 and 300 K for EIIa and EIIb polarizations.

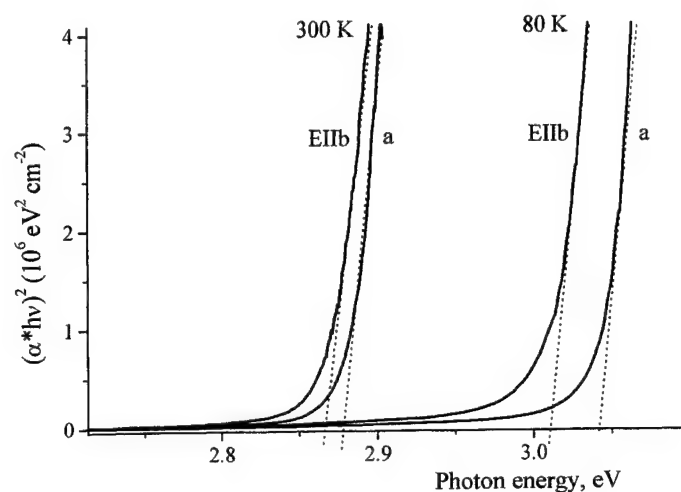


Fig. 7 Absorption spectra for yellow LiInSe_2 plate 100 μm thick, represented in $(\alpha^* \hbar \nu)^2 = f(\hbar \nu)$ coordinates.

The results of present report confirm that both yellow and dark red LiInSe_2 crystals have the same wurtzite-type structure and are suitable for nonlinear optics. The determined E_g values ~ 3 eV show that this crystal has the largest band gap among ternary selenium-containing compounds, indeed. To date the most important properties such as a nonlinear susceptibility and phase matching conditions are still unknown. In analogy with other compounds one can suppose that a nonlinear susceptibility is at least two times higher than that of its sulfur analogue, LiInS_2 . Determination of these parameters is of great importance and the work is in progress.

4. CONCLUSIONS

1. Bulk single crystals up to 20 mm in diameter and 40 mm long for LiInS_2 and up to 10 mm, 20 mm, respectively, for LiInSe_2 were obtained. Their color changed from colorless to rose for the first one and from yellow to dark red for the other. All crystals have a wurtzite-type lattice ($\text{Pna}2_1$ space group), lattice parameters were determined.
2. Color variations are due to point defects, first of all interstitial sulfur, resulting in additional wide absorption bands in the shortwave part of transparency range. For LiInS_2 the SHG phase matching conditions were found to be similar for samples of different color and some difference from Boyd's predictions of 1973 was shown: for XY plane $\Delta\phi \sim +3^\circ$ at 2.6 μm and $\Delta\phi \sim -3$ to -5° at 4-5 μm . Nonlinear susceptibility for LiInS_2 was estimated: $d_{\text{eff}}(\text{XY}) \sim 3.4 \text{ pm/V}$ relative to Boyd's value as 10.6 pm/V. The optical damage threshold was estimated to be $\sim 350 \text{ MW/cm}^2$ for given regime.
3. Both yellow and dark red LiInSe_2 crystals have the same wurtzite-type structure. Difference in color is due to point defects and resulting intense absorption bands near the fundamental absorption edge. A proper illumination gives a photoinduced change of LiInSe_2 color from dark red to yellow as a result of changes in charge state of point defects. A band gap for LiInSe_2 was found to be 3.02 and 2.86 eV at 80 and 300K, respectively.

ACKNOWLEDGEMENTS

This research is partly supported by a European Community INCO-COPERNICUS program (contract No ERBIC15-CT98 0814) and CRDF (grant RE2-2222, proposal 6410). The authors would like to express their thanks to Ph.Kupecek and G.Mennerat for support in nonlinear experiments.

REFERENCES

1. A.Douillet, J.-J.Zondy, A.Yelisseyev, S.Lobanov, L.Isaenko, "Stability and frequency tuning of thermally loaded continuous-wave AgGaS_2 optical parametric oscillators" *J.Opt.Soc.Amer.* **B16** 1998.
2. G. D. Boyd, H.M. Kasper, and J.H. Mo Fee, "Linear and nonlinear optical properties of LiInS_2 " *J. Appl. Phys.* **44** pp. 2809, 1973.
3. L.Isaenko, I.Vasilyeva, A.Yelisseyev, S.Lobanov, V.Malakhov, L.Dovlitova, J.-J.Zondy, I.Kavun, "Growth and Characterization of LiInS_2 single crystals", *J.Cryst.Growth*, **218**, N 2-4 pp.313, 2000.
4. K.Kuryama, T.Kato, "Optical band gap and photoluminescence studies in blue-band region of Zn-doped LiInS_2 single crystals" *Solid St Comm.* **89**, pp.959 1994.
5. A.Yelisseyev, L.Isaenko, S Lobanov, J.-J.Zondy, A.Douillet, I.Thenot, Ph.Kupecek, G.Mennerat, J.Mangin, S.Fossier, S.Salaun, "New ternary sulfide for Double application in laser schemes", *Proc.ASSL 2000 Int.Conf.*, Davos, Switzerland, 2000 (in press).
6. Ch.Ebbers, "Summary of known nonlinear properties of LiInS_2 ", preprint UCRL-ID-116744 Feb. 1994, LLNL, Livermore, USA.
7. H.J.Beister, S.Ves, W.Hohle, K.Syassen, G.Kuhn, "Structural phase transitions and optical absorption of LiInSe_2 under pressure, *Phys.Rev. B*, **43**, pp. 9635, 1991.

Radio- and VUV – excited luminescence of YAP:Ce, YAP:Pr and YAG:Pr

M. Wiśniewska ^a, A. J. Wojtowicz ^{a*}, T. Łukasiewicz ^b, Z. Frukacz ^b, Z. Gałązka ^b, M. Malinowski ^c

^aInstitute of Physics, N. Copernicus University, Grudziądzka 5, 87-100 Toruń, Poland

^bInstitute of Electronic Materials Technology, Wólczyńska 133, 01-919 Warsaw, Poland

^cInstitute of Micro- and Optoelectronics, Warsaw University of Technology, Koszykowa 7, 00-662 Warsaw, Poland

ABSTRACT

In this Communication we report initial results of studies on X-ray and VUV excited luminescence of YAP and YAG crystals activated with Pr^{3+} , and YAP activated with Ce^{3+} . Excitation and luminescence spectra of Pr^{3+} and Ce^{3+} *d-f* and Pr^{3+} *f-f* emissions and luminescence time profiles under pulsed synchrotron excitation are presented and analysed in order to identify and characterize various host-to-ion energy transfer channels. The results support the notion that direct and trap mediated capture and recombination of holes and electrons via Pr^{3+} or Ce^{3+} ions provide the dominant mechanism of radioluminescence production in both YAP and YAG crystals.

Keywords: YAG:Pr, YAP:Pr, YAP:Ce, radioluminescence, energy transfer, recombination, VUV spectroscopy

1. INTRODUCTION

Potential applications in opto- and microelectronics of systems consisting of wide bandgap materials activated with rare earth (RE) ions belong to such diverse areas as lighting and display phosphors, radiation detectors, light emitting diodes and solid state lasers. Some of these systems show fast and efficient UV *d-f* emission and/or a rich *4f* energy structure that sustains various co-operative interactions leading to efficient up- and down-conversion. In particular two ions, Pr^{3+} and Ce^{3+} , in a number of solid state hosts, became prime objects of research in the field of ionizing radiation detector and solid state laser materials.

Two host materials, YAG and YAP, have a long history of successful applications in the field of solid state laser materials (YAG:Nd^{1,2} and YAP:Nd^{2,3}). Laser properties of Pr^{3+} activated YAG and YAP crystals have also been studied and laser action was achieved in both of these materials.^{4,5} Scintillation properties of YAG and YAP activated with Ce^{3+} and Pr^{3+} have been studied for some time.^{6,19} In particular YAP:Ce is a well established commercial scintillator material that has found many applications⁷ such as a small animal PET camera,⁸ a prototype gamma camera based on a position sensitive photomultiplier tube (high resolution single photon emission computed tomography or HIRESPCT,⁹, dosimeters, scintimamography cameras,¹⁰ and pulse shape discrimination for Astro-E Hard X-ray Detector. Nevertheless the peculiar scintillation properties of YAP:Ce, such as the longer than radiative scintillation decay time constant and large variations of the scintillation light yield with temperature, have only recently been explained in the frame of the model involving charge carrier capture and recombination mediated by traps.¹¹

The synchrotron radiation has been extensively used in research aimed at scintillation mechanisms in RE-activated solid state materials.¹² In particular energy transfer processes that occur in such materials can be conveniently studied by selecting a proper wavelength of the exciting synchrotron radiation. In this Communication we report results of studies on X-ray and synchrotron radiation excited luminescence of YAG and YAP crystals activated with Pr^{3+} and Ce^{3+} .

MW (correspondence): Email: barska@phys.uni.torun.pl; Telephone+48 56 6113239, fax: +48 56 6225397

* AJW: Email: andywojt@phys.uni.torun.pl; Telephone: +48 56 6113239, fax: +48 56 6225397

2. MATERIALS AND EXPERIMENTS

All samples used in this study were cut from the boules grown by the Czochralski method at Institute of Electronic Materials Technology in Warsaw, Poland. X-ray excited luminescence spectra were measured at Institute of Physics of N. Copernicus University in Torun, Poland. The X-ray tube with the copper anode operated at 35kV was used as an excitation source. The luminescence spectra, luminescence excitation spectra and emission time profiles under pulsed synchrotron excitation in the wavelength range of 50-300 nm were measured using experimental facilities of Superlumi station at Hasylab in Hamburg, Germany.¹³

3. EXPERIMENTAL RESULTS AND DISCUSSION

In Fig. 1 we present radioluminescence spectra of YAP:Ce (a), YAG:Pr (b), and YAP:Pr (c) measured at room temperature. The spectra are dominated by the well known broad bands at 365nm (a), 325nm, 380nm (b), and 240nm and 280nm (c) due to $d-f$ transitions at Ce^{3+} (a) and Pr^{3+} (b, c) ions. As observed before the positions of $d-f$ emission bands depend not only on the activating ion but also on the host material. In particular a much stronger crystal field in YAG is responsible for a red shift of the Pr^{3+} -emission in this material. An additional unexpected feature of the YAG:Pr³⁺ radioluminescence spectrum is an intense sharp line peaking at around 315nm. Although this line has not been observed before it is easy to miss in the low resolution measurement. The origin of this line is not yet clear; the two possible interpretations that have been advanced include a transition between the 1S_0 and 1I_6 levels of the Pr^{3+} ion and an uncontrolled impurity emission (the most likely candidate being the Gd^{3+} ion).¹⁴ Other sharp longer wavelength lines (at about 490 nm, traces b and c in Fig. 1) are due to $f-f$ transitions originating at the 3P_1 and terminating at the 3H_1 levels of the Pr^{3+} ion.¹⁵ In addition to $d-f$ emission bands there are also much weaker bands at about 260-300nm. These bands represent so-called "host" emissions that are prominent in undoped YAG and YAP crystals¹⁶ but are strongly reduced by Ce^{3+} and Pr^{3+} doping. Note that although the "host"-to- Pr^{3+} centers radiative and nonradiative energy transfers are unlikely in YAP:Pr (Pr^{3+} absorption bands and "host" emission bands do not overlap) the radioluminescence intensity is comparable in YAP:Pr and YAP:Ce. This is consistent with recombination as the dominant mechanism of scintillation and radioluminescence light production as proposed in the case of Ce doped materials.^{11,16,17}

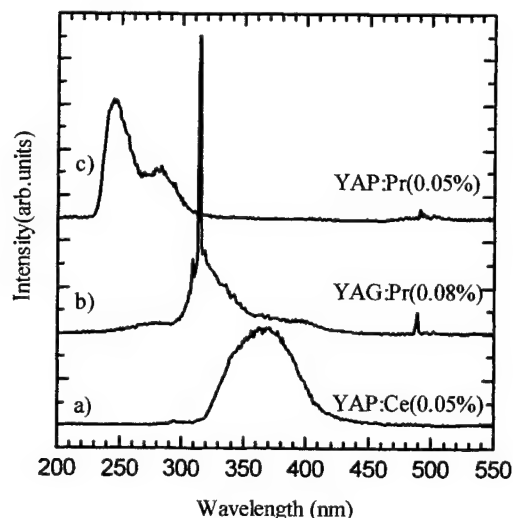


Fig. 1. Radioluminescence spectra of: a) YAP:Ce (0.05%), b) YAG:Pr (0.08%) and c) YAP:Pr (0.05%). The temperature was 300 K (RT). The origin of the sharp emission line at about 315 nm in YAG:Pr is not clear (see text).

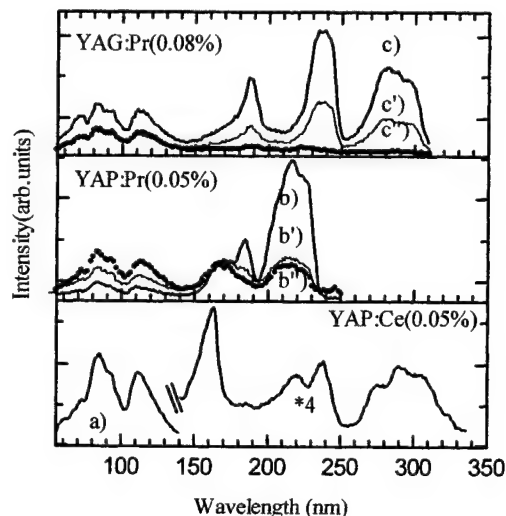


Fig. 2. Luminescence excitation spectra of YAP:Ce (a), YAP:Pr (b-b'') YAG:Pr (c-c''). The emission wavelengths and temperatures: a) 369 nm, RT; b) 280 nm, RT; b'') 490 nm, 10 K; c) 324 nm, RT; c'') 490 nm, 10 K. Note the much higher VUV sensitivity of the Ce-doped YAP.

While radioluminescence spectra usually reflect the dominant mode of radiative decay of relevant electronic excitations of the material, photoluminescence spectra oftentimes show a strong dependence upon the wavelength of the excitation light and temperature, indicating the existence of thermally activated and competing energy transfer channels to various emitting centres. In Fig. 2 we present Ce^{3+} $d-f$ and Pr^{3+} $d-f$ and $f-f$ emission excitation spectra measured at room and cryogenic temperatures in YAP and YAG. The spectra are not corrected and, in particular, the “structure” in the VUV below 140 nm is due to spectral characteristics of the set-up and does not reflect any true physical processes.

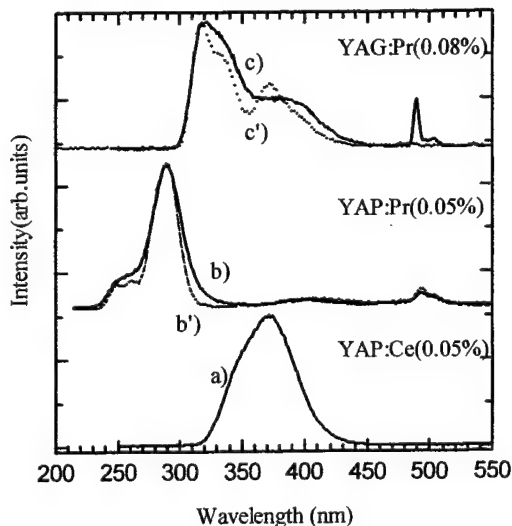


Fig. 3 Luminescence spectra. Excitation into $f-d$ absorption bands. a) RT, $\lambda_{\text{exc}} = 240$ nm, b) RT, $\lambda_{\text{exc}} = 210$ nm, b') 10 K, $\lambda_{\text{exc}} = 210$ nm, c) RT, $\lambda_{\text{exc}} = 235$ nm, c') 10 K, $\lambda_{\text{exc}} = 235$ nm.

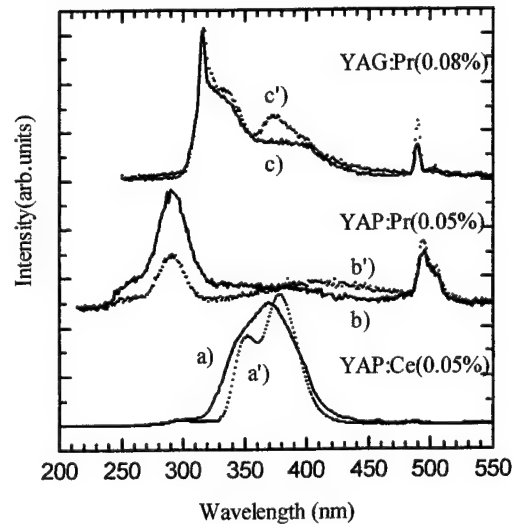


Fig. 4 Luminescence spectra. VUV excitation at 85 nm. YAP:Ce (a, a'), YAP:Pr (b, b'), and YAG:Pr (c, c'). The temperature was: RT (a-c) and 8 K (a'-c'). Note that the contribution of $f-f$ emission is different than in Fig. 3.

The bands that dominate the spectra are typical of $f-d$ transitions of Ce^{3+} and Pr^{3+} ions.¹⁶ So, the trace a reveals the two well known $f-d$ bands of Ce^{3+} at 240 and 310 nm. The traces b and c (excitation spectra of Pr^{3+} $d-f$ emission in YAP and YAG) are dominated by two broad bands peaking at 185 and 214 nm in YAP, and at 238 and 290 nm in YAG. These bands correspond to the $^3\text{H}_4 \rightarrow 4f5d$ transitions of Pr^{3+} .^{18,19}

At vacuum ultraviolet (VUV) wavelengths below 200 nm the spectra reveal also the so-called “host” peaks at about 160 nm (YAP) and 185 nm (YAG) and a “structure” at VUV below 140 nm. The “host” peaks and the high sensitivity at VUV wavelengths have previously been associated with the occurrence of energy transfer mechanisms that enable the material to scintillate efficiently. Excitation spectra of Ce^{3+} and Pr^{3+} $d-f$ emissions had been also measured at 10 K but since there were no important differences the spectra are not presented here.

The $4f^2$ electron configuration of Pr^{3+} exhibits a rich energy level structure that supports numerous $f-f$ transitions. Some of these transitions in the visible have been extensively studied in the past using resonance or shorter wavelength visible excitation. As shown in Fig. 2 a far UV and VUV wavelength excitation can also be used to excite a visible 490 nm $f-f$ emission. Traces b' and c' represent spectra measured at room temperature for YAP and YAG crystals, respectively. Traces b'' and c'' represent the same spectra measured at 10 K.

Interestingly, for both YAP and YAG, the Pr^{3+} 490 nm $f-f$ emission can be efficiently excited by wavelengths that belong to $f-d$ bands, “host” peaks and VUV tail as in the case of the $d-f$ emission, although their relative contributions vary with temperature. The mere presence of $f-d$ bands proves that the $^3\text{P}_j$ level is fed by the energy transfer from the Pr^{3+} $4f5d$ levels. Nevertheless relatively higher contributions of the “host” peak and VUV tail clearly show that the $^3\text{P}_j$ levels are also populated by an additional energy transfer from the host material with no mediation of $4f5d$ levels. We note also that there is a distinct difference between spectra taken at different temperatures. While at room temperature the spectrum is

dominated by intraionic $f-d$ transitions, the “host” peak and VUV tail dominate the low temperature spectrum. The relative contributions of the “direct” (intraionic) and “host-related” energy transfer channels vary with temperature.

In Figs. 3 and 4 we present luminescence spectra under UV and VUV excitations. The spectra of YAP:Ce, YAG:Pr and YAP:Pr in Fig. 3 were obtained under the UV excitation into $f-d$ absorption bands at room and cryogenic temperatures. We note that the spectra are dominated by the strong broad $d-f$ bands as in the case of X-ray excitation (Fig. 1) although there is, obviously, no indication of “host” emissions. In addition to Pr^{3+} $d-f$ emission bands there also are strong (or weak) lines representing $f-f$ emission at about 490 nm in agreement with the excitation spectra presented in Fig. 2. In particular there is almost no $f-f$ emission at 490 nm at 10 K in YAG:Pr (see the trace c') while in YAP:Pr the ratio of $d-f$ and $f-f$ emissions does not vary with temperature (compare traces b and b'). The origin of the weak broad band at around 400 nm (traces b and b') will be discussed later.

In Fig. 4 we present luminescence spectra under the 85 nm VUV excitation measured at room and cryogenic (8 K) temperatures. With the sole exception of the 8 K spectrum of YAP:Pr (trace b) the spectra are dominated by $d-f$ emission bands. The 8 K and 300 K spectra of YAP:Ce³⁺ are fairly typical showing the characteristic spin-orbit split Ce³⁺ doublet ($^2F_{5/2}$, $^2F_{7/2}$) (traces a and a'). In the case of Pr^{3+} doped YAG and YAP the trends observed under $f-d$ excitation are reversed; the ratio of $d-f$ and $f-f$ emissions is almost independent of temperature in YAG:Pr while in YAP:Pr at low temperature the contribution of $f-f$ emission to the spectrum is unusually large (trace b'). To summarize we note that VUV excitation promotes Pr^{3+} $f-f$ emission at 490 nm while at higher temperature the relative contribution of $d-f$ emissions increases. The VUV excitation also promotes an additional wide emission band localized at the wavelengths between 300 and 500 nm (“host” emissions). The shape and even the peak wavelength of this band varies with temperature suggesting that in fact it may well be not a single band but a combination of two or more bands. The origin of these emissions is not firmly established but it is quite likely to be due to radiative decay of an exciton trapped on some kind of a defect or impurity. In the case of YAG:Pr³⁺ a “host” emission is hidden under much stronger and overlapping Pr^{3+} $d-f$ emission bands.

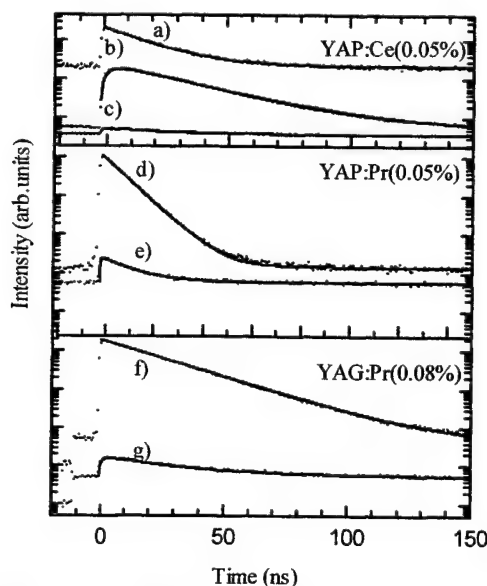


Fig.5 Emission time profiles of YAP:Ce (a-c), YAP:Pr(d-e), and YAG:Pr (f-g). Solid lines represent fits to one- or two-exponential expressions. a) 10 K, $\lambda_{exc}=240nm$, $\lambda_{em}=369nm$, $I(t)=0.2exp(-t/17.4)+0.02$; b) RT, $\lambda_{exc}=85nm$, $\lambda_{em}=369nm$, $I(t)=2.6exp(-t/30)-2.3exp(-t/3.2)+0.05$; c) 7 K, $\lambda_{exc}=85nm$, $\lambda_{em}=369nm$, $I(t)=0.16exp(-t/29)-0.1exp(-t/1.0)+0.37$; d) 10 K, $\lambda_{exc}=210nm$, $\lambda_{em}=280nm$, $I(t)=1.16exp(-t/7.6)+0.002$; e) 10 K, $\lambda_{exc}=85nm$, $\lambda_{em}=280nm$, $I(t)=0.02exp(-t/12.4)-0.02exp(t/0.3)+0.006$; f) 10 K, $\lambda_{exc}=240nm$, $\lambda_{em}=324nm$, $I(t)=1.9exp(-t/23)+0.004$; h) 280 K, $\lambda_{exc}=85nm$, $\lambda_{em}=324nm$, $I(t)=0.12exp(-t/30)-0.12exp(-t/1.1)+0.05$

Finally, in Fig. 5 we show the emission time profiles obtained under various wavelength VUV and UV excitations. Traces (a, d, g) represent pulse shapes of the Ce^{3+} and Pr^{3+} d - f emissions in YAP:Ce, YAP:Pr, and YAG:Pr, respectively, measured at 10K under direct excitation into f - d absorption bands. Thin solid lines show single-exponential fits to experimental points that yielded the following decay time constants: ~ 23 ns (YAG:Pr $^{3+}$), ~ 7.6 ns (YAP:Pr $^{3+}$), and ~ 17 ns (YAP:Ce $^{3+}$). These decay time constants are probably very close to the corresponding radiative lifetimes. Note that the Pr^{3+} radiative lifetime is much shorter in YAP than in YAG, and that the Ce^{3+} radiative lifetime in YAP falls between the two lifetimes of Pr^{3+} (in YAP and YAG). This is consistent with the well known dependence of the Einstein coefficient A on the emission wavelength.²⁰

The time profiles of the Ce^{3+} and Pr^{3+} d - f emissions in YAP:Ce, YAP:Pr, and YAG:Pr were also measured at room temperature but, since they are less likely to truly reflect the radiative lifetimes we have chosen not to present them here. The decays were, nevertheless, single-exponential, although the decay time constants assumed different values. In YAP these values increased to 8.3 ns (Pr $^{3+}$) and 18.8 ns (Ce $^{3+}$); the most likely reason of this effect being the radiation trapping caused by the increased overlap between emission and absorption bands at elevated temperatures. Similar behaviour was found for many materials.²¹

Interestingly we observe a different behaviour in YAG:Pr $^{3+}$, where a decay time constant decreases with temperature reaching 14.5 ns at 300K. A likely reason is increased thermal quenching caused by a relatively low d - f energy gap ($\sim 10,000$ cm $^{-1}$)¹⁸ Another explanation involves thermally activated autoionization of an electron occupying the highly lying $4f5d$ levels of Pr $^{3+}$ ions that overlap the conduction band of YAG.²² Autoionized electrons are then unable to return to the $5d$ levels and the only deexcitation route for the exciton bound to the Pr $^{3+}$ ion is radiative or nonradiative energy transfer to the f - f energy levels. As a consequence there is an increased f - f emission at higher temperatures, as observed (see Fig. 3, traces c and c').

In order to study the host-to-activator ion energy transfer the time profiles of d - f emission under the VUV excitation at various temperatures were measured. Traces c and b represent time profiles of the Ce^{3+} d - f emission measured under the 85 nm excitation at 7 and 300 K, respectively. These profiles display longer decay times (at about 29 ns) and higher backgrounds (the background of the 7 K profile being about 7 times higher). Interestingly both profiles show also rise times of about 1 and 3 ns at 7 and 300 K, respectively. Temperature dependent decay and rise times in YAP:Ce and LuAP:Ce have been studied before and interpreted in the frame of a model including recombination center (Ce $^{3+}$) and electron traps.²³

We note the similar behaviour for Pr $^{3+}$ doped YAP and YAG. In both materials the decay time constants are longer for VUV excitation and at higher temperatures (10 to 12.5 ns increase between 10 and 300 K for YAP and 23 to 32 ns increase for YAG). We also observe longer rise times and higher backgrounds. To give an example we present traces e and h for YAP and YAG, respectively. More experimental data and a detailed quantitative analyses of these results will be presented elsewhere.

4. CONCLUSIONS

The effect of conversion of a single γ or X-ray photon in a scintillator material is well reproduced by excitation of the material by a large number of VUV photons since both lead to a large number of free electrons and holes. It has been firmly well established that in a number of Ce-activated modern scintillator materials it is the recombination of charge carriers via the Ce^{3+} ions that provides the dominant mechanism of scintillation light production. In this Communication we find that also Pr activation in YAG and YAP leads to effects that are readily explained in the frame of the same model. These effects include high VUV sensitivity, presence of the "host" peaks in the excitation spectra, longer and temperature dependent decay and rise times, and higher background in time profiles. The process of charge carrier recombination via Pr $^{3+}$ is more complex than in the case of Ce-activation because higher lying levels that are due both to $4f5d$ and $4f^2$ configurations are active. Although VUV-excitation of Pr-activated YAG and YAP leads to emission dominated by the Pr $^{3+}$ d - f emission the Pr $^{3+}$ f - f emission is also observed. We find that in addition to nonradiative or radiative $4f5d \rightarrow 4f^2$ energy transfer also a direct recombination of e-h pairs via $4f^2$ Pr $^{3+}$ levels provides an efficient mechanism of light production in these materials.

ACKNOWLEDGEMENTS

This work was supported by the Polish Committee of Scientific Research, KBN (grants 2P03B04914 and 8T11B02917) and by the TMR-Contract ERBFMGECT950059 of the European Community. We are grateful to R. Brunka, W. Drozdowski, P. Niezgoda and P. Szupryczynski who took part in experiments at Superlumi station of Hasylab, Hamburg, Germany. The financial support of Hasylab and Polish Academy of Sciences and hospitality of Prof. G Zimmerer and Dr M. Kirm of Hasylab is also gratefully acknowledged.

REFERENCES

1. M Bass, M.J. Weber. "Nd,Cr:YAlO₃ laser tailored for high-energy Q-switched operation". *Applied Physics Letters*, **17**, pp.395-8, 1970.
2. H.M. Kretschmann, F. Heine, V.G. Ostroumov, G. Huber, "High-power diode-pumped continuous-wave Nd³⁺ lasers at wavelengths near 1.44 μ m". *Optics Letters*, **22**, pp.466-8, 1997
3. M.J. Weber, M. Bass, K. Andringa, R.R. Monchamp, E. Comperchio, "Czochralski growth and properties of YAlO₃ laser crystals", *Applied Physics Letters*, **15**, pp.342-5, 1969
4. M. Malinowski, M.F. Joubert, B. Jacquier. "Simultaneous laser action at blue and orange wavelengths in YAG:Pr³⁺" *Physica Status Solidi A*, **140**, pp.K49-52, 1993
5. Z. Mierczyk, S. Kaczmarek, Kopczynski K, Fruckacz Z, Pracka I, Lukasiewicz T. "Spectroscopic and laser properties of different materials doped with Pr³⁺ ions.", *Acta Physica Polonica A*, **90** pp.407-10, 1996.
6. C. Pedrini, D. Bouttet, C. Dujardin, B. Moine, I. Dafinei, P. Lecoq, M. Koselja, K. Blazek. "Fast fluorescence and scintillation of Pr-doped yttrium aluminium perovskite", *Optical Materials*, **3** pp.81-7, 1994
7. W.P. Trower, "Cerium-doped yttrium aluminium perovskite (YAP): properties of commercial crystals", in Materials Research Society Symposium Proceedings: Scintillator and Phosphor Materials, edited by M.J Weber, P.Lecoq, R.C. Ruchti, C. Woody, W.M. Yen, R. Zhu, **348**, pp 131-136, Materials Research Society Pittsburgh, 1994
8. F. de Notaristefani, R. Pani, F. Scopinaro, L.M. Barone, K. Blazek, G. De Vincentis, T. Malatesta, P. Maly, R. Pellegrini, A. Pergola, A. Soluri, F. Vittori. "First results from a YAP:Ce gamma camera for small animal studies." *IEEE Trans. Nucl. Sci.*, **43**, pp.3264-71, 1996
9. K. Blazek, P. Maly, F. de Notaristefani, R. Pani, R. Pellegrini, A. Pergola, F. Scopinaro, A. Soluri, "YAP multi-crystal gamma camera prototype", *IEEE Trans. Nucl. Sci.* **42**, pp. 1474-1482, 1995,
10. D. Steinbach, S. Majewski, M. Williams, B. Kross, A.G. Weisenberger, R. Wojcik. "Development of a small field of view scintimammography camera based on a YAP crystal array and a position sensitive PMT". 1996 *IEEE Nucl. Sci. Symposium Conference Record (Cat. No.96CH35974)*. *IEEE*, **2**, pp.1251-6, 1996, New York, NY, USA
11. A.J. Wojtowicz, J. Glodo, A. Lempicki, C. Brechcer, "Recombination and scintillation processes in YAlO₃:Ce", *J.Phys.: Condens. Matter*, **10**, pp.8401-8415, 1998
12. A.J. Wojtowicz, W.Drozdowski, J. Glodo, P. Szupryczyński, and D.Wisniewski "VUV studies of radiative recombination in rare earth activated wide bandgap materials: LuAlO₃:Ce" in *Hasylab Annual Report '98*, Hamburg, Hamburg 1999; also available on-line: http://www.hasylab-desy.de/science/annual_reports/1998/index.html
13. G. Zimmerer, "Status report on luminescence investigations with synchrotron radiation at Hasylab", *Nucl. Instr. Meth.Phys.Res.*, **A308**, pp 178-186, 1991
14. A.J. Wojtowicz, M. Wisniewska, M. Malinowski, "Sharp line and broad band UV emissions from Pr-activated YAG", in *Hasylab Annual Report '99*, Hamburg, Hamburg 1999; also available on-line: http://www.hasylab-desy.de/science/annual_reports/1998/index.html
15. M. Malinowski, C. Garapon, M.F. Joubert and B. Jacquier, "One- and two-photon spectroscopy of Pr³⁺-doped YAlO₃", *J.Phys.:Condens. Matter*, **7**, pp. 199-211, 1995
16. D. Wisniewski, W. Drozdowski, A.J. Wojtowicz, A.Lempicki, P.Dorenbos, J.T.M.De Haas,et.al. "Spectroscopy and thermoluminescence of LuAlO₃:Ce" *Acta Physica Polonica A*, **90**, pp.377-383, 1996
17. A.J. Wojtowicz, J. Glodo, W. Drozdowski, K.R. Przegietka 1998, "Electron Traps and Scintillation Mechanism in YAlO₃:Ce and LuAlO₃:Ce Scintillators", *J. Luminescence* **79**, pp.275-291, 1998
18. M.J. Weber, "Nonradiative decay from 5d States of rare earths in crystals", *Solid State Communications*, **12**, pp.741-744, 1973
19. E.G. Gumayskaya, M.V. Korzhik, S.A. Smirnova, V.B. Pavlenko and A.A. Fedorov "Interconfiguration luminescence of Pr³⁺ ions in Y₃Al₅O₁₂ and YAlO₃ single crystals", *Opt. Spectros.(USSR)* **72**(1), pp.86-88, 1995
20. B. Henderson and G. F. Imbusch, *Optical Spectroscopy of Inorganic Solids* p.173, Oxford: Clarendon Press, 1989
21. A.J. Wojtowicz, M. Balcerzyk, E. Berman, and A. Lempicki "Optical Spectroscopy and Scintillation Mechanisms of CexLa1-xF3", *Phys. Rev. B*, **49** pp.14880-14895, 1994
22. G.Wittmann, R.M. Macfarlane "Photon-gated photoconductivity of Pr³⁺:YAG", *Optics Letters*, **21**, pp.426-429, 1996
23. A. Lempicki, A.J. Wojtowicz "Fundamental limitations of scintillators", *J. Luminesc.* **60&61**, pp.942-947, 1994

Crystal growth and optical properties of Co^{2+} doped $\text{SrLaGa}_3\text{O}_7$

S.M. Kaczmarek^a M. Grinberg^b M. Berkowski^c P. Aleshkevych^c J. Fink-Finowicki^c H. Szymczak^c

^a Institute of Optoelectronics, Military University of Technology, 2 Kalisky Str., 00-908 Warsaw, Poland

^b Institute of Experimental Physics, University of Gdańsk, Wita Stwosza 57, 80-952 Gdańsk, Poland

^c Institute of Physics, Polish Academy of Sciences, 32/46 Lotników 32/46 Str., 02-668 Warsaw, Poland

ABSTRACT

Cobalt doped $\text{SrLaGa}_3\text{O}_7$ single crystals have been grown by the Czochralski method in a nitrogen atmosphere and by a floating zone method with optical heating in air. Starting concentrations of Co in the melt were: 0.15, 0.3, 2 and 3 mol.% with respect to Ga by the Czochralski method whereas 2 and 4 mol.% by the floating zone method. We have presented absorption spectra as well as EPR spectra related to octahedrally coordinated Co^{2+} ion in $\text{SrLaGa}_3\text{O}_7$. It shows EPR spectra with a spin of $S=1/2$, $g_{\parallel}=2.26\pm0.04$, $g_{\perp}=4.7\pm0.2$ and three different octahedral positions in SLGO lattice.

Keywords: crystal growth, Electron Spin Resonance, absorption spectra, gallate crystals, thermal annealing.

1. INTRODUCTION

$\text{SrLaGa}_3\text{O}_7$ (SLGO) belongs to the family of binary gallates of alkaline and rare earth metals. Crystal of these compounds have the tetragonal gehlenite ($\text{Ca}_2\text{ASi}_2\text{SiO}_7$) structure (space group: $P-42_1m_1$, D_{2d}^3). Unit cell parameters of SLGO crystals are: $a = 0.8058 \text{ nm}$ and $c = 0.5333 \text{ nm}$.

Single crystals of gehlenites such as $\text{BaLaGa}_3\text{O}_7$ (BLGO)¹, $\text{SrLaGa}_3\text{O}_7$ (SLGO)^{2,3} and $\text{SrGdGa}_3\text{O}_7$ (SGGO) were manufactured for potential laser and display applications as matrix materials. They were doped with neodymium⁴, praseodymium⁵ and chromium⁶. Although SLGO crystals doped with various rare-earth ions have been investigated^{2-5,7-9}, there is no detailed report on the optical properties of SLGO doped with Co^{2+} ions.

In the present paper the behaviour of Co ion intentionally introduced into the crystal lattice is investigated by means of optical and EPR techniques.

2. EXPERIMENTAL

2.1. Single crystal growth of SLGO:Co^{2+}

Single crystals of $\text{SrLaGa}_3\text{O}_7$ doped with cobalt (SLGO:Co) have been grown using the Czochralski method in a nitrogen atmosphere and the floating zone method with optical heating in air. Starting compositions of SLGO matrix slightly differ (about 0.8 mol.%) from the stoichiometric one in the direction to SrGa_2O_4 rich. Starting concentrations of Co in the melt were: 0.15, 0.3, 2 and 3 mol.% with respect to Ga in the Czochralski method whereas 2 and 4 mol.% in the floating zone method. The floating zone method was employed in order to determine the maximum dopant concentration at which obtained crystals are still transparent. Since the crystal obtained by the floating zone method from the melt containing 4 mol.% of Co was nontransparent, we decided to limit the dopant concentration for the Czochralski method to 3 mol.%.

Single crystals obtained by the Czochralski method were pulled from a 40 mm diameter iridium crucible in nitrogen atmosphere containing 1 vol.% of oxygen in the $\langle 001 \rangle$ direction on oriented seed crystals. The pulling rate was decreased in the range from 2.2 mm/h to 1 mm/h as the cobalt concentration in the melt was increased.

High purity carbonate, SrCO_3 (4N5) and oxides La_2O_3 (5N), Ga_2O_3 (5N) and Co_3O_4 (3N) were used as starting materials. They were annealed or dried before weighing. Starting melt composition was calculated on the basis of congruent melting composition $\text{Sr}_{1.04}\text{La}_{0.935}\text{Ga}_{3.02}\text{O}_{7.8}$. Concentrations of cobalt admixture in starting melts with reference to gallium were equal to 0.15 mol.% (P1), 0.3 mol.% (P2), 2 mol.% (P3) and 3 mol.% (P4). A convex crystal-melt interface was kept during the whole crystal growth process. Single crystals with the diameter of 20 mm and length up to 60 mm were obtained.

*Further author information

S. M. K. (correspondence): Email: skaczmar@wat.waw.pl.; Telephone: (022) 6859019

They had a blue color the intensity of which increased with increasing dopant concentration. In the core region a precipitation extending along the crystal growth direction with a diameter of around 1 mm appeared in the crystal with the highest cobalt concentration (P4). Such precipitation's were not observed in crystals with lower dopant concentrations (P1-P3).

2.2. Absorption measurements

To study of optical properties of the SLGO:Co single crystals, polished in both sides, parallel-plate samples of thickness from 0.3 to 1 mm were prepared. The absorption spectra were taken at 300 K in the spectral range between 190 - 25 000 nm using LAMBDA-900 PERKIN-ELMER and FTIR 1725 PERKIN-ELMER spectrophotometers. We have not noticed the emission related to Co in the visible and near infrared region. In this paper we present the absorption spectra of P3 sample. Changes in the absorption of P3 sample were also investigated after annealing treatment at 1050°C in the air for 16h.

2.3. ESR measurements

The samples for measurement had dimension of $2.5 \times 2.5 \times 2 \text{ mm}^3$. The experiments were performed with X-band spectrometer for frequency $f = 9.25 \text{ GHz}$. During measurements the samples were mounted in a helium gas-flow Oxford Instruments cryostat. The samples temperature was varied in the range 4K to 13 K. The samples were glued to a rotating sample holder for the measurements of the angular variation of the EPR spectra. In this paper we present the ESR spectra of both P1 and P3 samples.

3. RESULTS

3.1. Absorption measurements

The octahedral crystal field acting on Co^{2+} ion substituting Sr^{2+} splits the sevenfold degenerate ^4F state into an orbital triplet $^4\text{T}_1$, followed by another orbital triplet $^4\text{T}_2$ and an orbital singlet $^4\text{A}_2$ ¹⁰. The next higher state of the free Co^{2+} ion has the $^4\text{T}_1(^4\text{P})$ configuration. The spin-orbit interaction and low symmetry field split the twelve fold degenerate $^4\text{T}_1$ level into a number of Kramer's doublets. Co^{2+} in the octahedral field has been investigated in various lattice long time ago¹¹. Thus still there are many questions that are not clear and therefore have to be discussed. Especially it concerns the spin-orbit and electron - lattice interactions, the effects that are responsible for the specific absorption band shape.

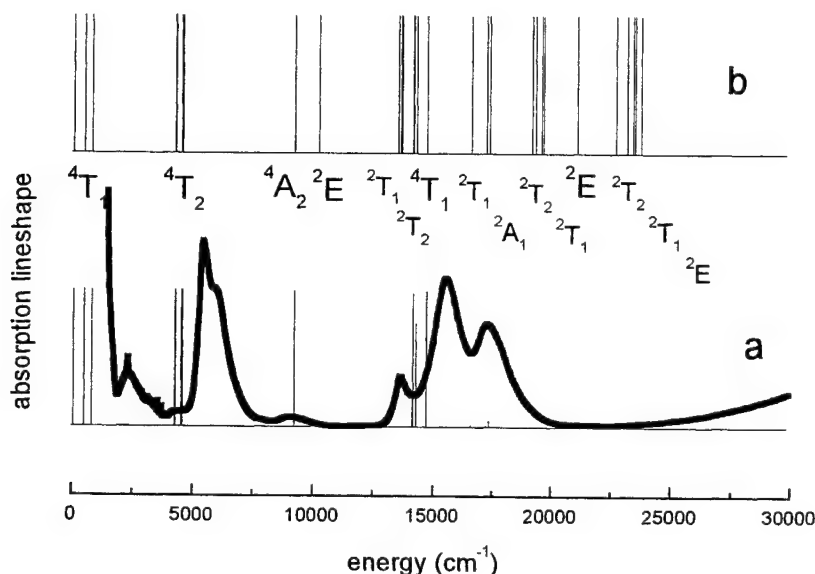


Fig. 1. Absorption line shape of P3 crystal.

Absorption line shape of the $\text{SrLaGa}_3\text{O}_7:\text{Co}$ is presented in Fig. 1.a. The line shape has been obtained from the absorption spectrum by dividing the absorption by photon energy¹². The main features of spectrum consist of a double band in the IR region ($5000\text{--}7500\text{ cm}^{-1}$) and triple band in the visible region ($12500\text{--}20000\text{ cm}^{-1}$). The latter absorption band is responsible for blue color of the sample. We notice also the strong absorption in the far IR, and in the UV region (not indicated in figure).

One can analyze the spectrum of Co^{2+} (octahedrally coordinated $3d^7$ system) using crystal field approach¹³, that describes the energetic structure of the ion by the crystal field strength parameter $10Dq$, the Racah parameters B and C , and the spin-orbit coupling ζ . In Fig 1.b we present the energetic structure of octahedrally coordinated Co^{2+} , which was calculated for $10Dq = 4750\text{ cm}^{-1}$, $B = 720\text{ cm}^{-1}$, $C = 3170\text{ cm}^{-1}$ and spin-orbit coupling constant $\zeta = 400\text{ cm}^{-1}$. It seems that values of parameters listed above reproduce quite well the energy of ${}^4T_1 \rightarrow {}^4A_2$ absorption band. On the other hand one can see that calculated energy of the 4T_2 multiplet is smaller than the energy of respective ${}^4T_1 \rightarrow {}^4T_2$ absorption band. Up to some extent the situation is similar as far as the ${}^4T_1 \rightarrow {}^4T_1$ transition is considered. Such a deviation is attributed to the strong Jahn-Teller coupling of the ground state. It was discussed elsewhere¹⁴ that for such a system the real crystal field strength $10Dq$ can be different than the energy of absorption band.

One notices that the ground state of the system is well defined spin-orbit and Jahn-Teller splitted the 4T_1 multiplet. Considering the relative intensities of the absorption bands our spectra are consistent with the spin-selection rule that allows only the quartet-quartet transitions and forbids the transitions from the ground state to the excited doublets. In Fig. 1.a the solid vertical line heights are proportional to the percentage of quartet in given state. It is seen that one well reproduces the transitions from the ground state to the 4T_2 and 4T_1 states. Also the strength and position of the spin-allowed ${}^4T_1 \rightarrow {}^4A_2$ transition seems to be well fitted. In fact the triple structure between 12500 cm^{-1} and 20000 cm^{-1} is related to the mixed states: 4T_1 quartet and 2T_1 , 2T_2 , 2T_1 and 2A_1 doublets. The strong spin-orbit coupling that interacts together with the strong Jahn-Teller effect produces the specific feature of the absorption lineshape. Thus it is difficult to attribute the absorption peaks to the specific crystal field states unambiguously.

3.2. Additional absorption after annealing treatment. Co^{3+} absorption

Fig. 2. presents absorption of P3 single crystal before (1) and after (2) annealing in oxygen for 16 h in the air. As it can be seen additional absorption band centered at about 1200 nm arises in the second case, which leads to decrease in the intensity of Co^{2+} absorption. This band may be connected with ${}^5T_2 \rightarrow {}^5E$ transition of Co^{3+} ion in octahedral coordination.

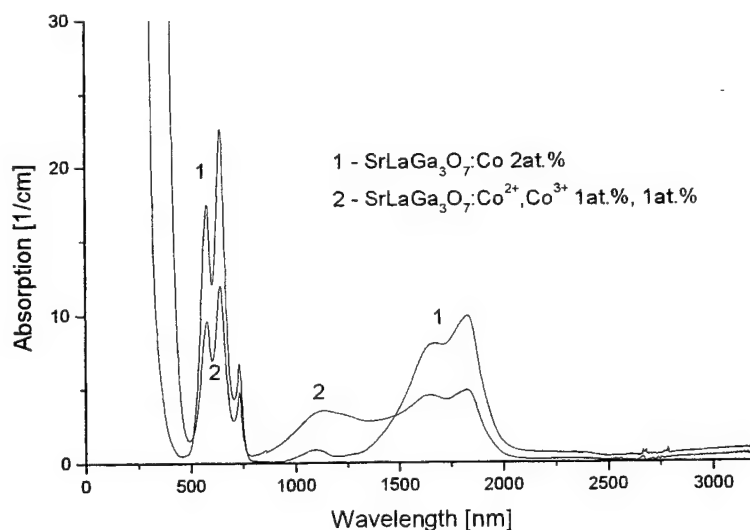


Fig. 2. Absorption of P3 crystal before (1) and after (2) annealing in the air for 16 h.

If we assume that annealing leads to ionization of Co^{2+} at octahedral positions of Sr^{2+} then at first approximation $10Dq$ for Co^{3+} system should be equal to $10Dq$ of Co^{2+} one. But obtaining due to ionization Co^{3+} ions have got smaller ionic radii (0.525 as compare to 0.65 of Co^{2+} ¹⁵) and the strength of Coulomb interaction between central ion and ligands is much more greater, so $10Dq$ is also greater, about $10Dq = 6606\text{ cm}^{-1}$. Moreover, one can take into account also that in the 5T_2

ground state there arises strong lattice relaxation. So additional absorption at about 1200 nm may be correlated to $^5T_2 \rightarrow ^5E$ transition of Co^{3+} ion.

3.3. ESR spectra and their analysis

The ESR spectra were observed at temperatures from 4.2K to 12.4 K. No ESR lines that could be attributed to Co^{2+} pairs was observed. The spectrum consists of eight hyperfine structure components due to Co^{59} nuclear spin $I=7/2$. Fig. 3 shows typical ESR spectra of Co^{2+} for the magnetic fields applied perpendicular and parallel to the c-axis direction and for two applied concentrations of Co^{2+} ions 0.15at.% and 2at.%. The group of the observed lines is interpreted as a consequence of the transition between the lowest Kramers doublet ($M_s = \pm 1/2$) levels.

The observed resonance signal is very anisotropic. The positions of experimental lines can be described by the spin-Hamiltonian of tetragonal symmetry with an effective spin $S=1/2$:

$$\hat{H} = g_{\parallel} \mu_B H_z \hat{S}_z + g_{\perp} \mu_B (H_x \hat{S}_x + H_y \hat{S}_y) \quad (1)$$

where: μ_B – Bohr magneton, $g_{\parallel}=2.26 \pm 0.04$, $g_{\perp}=4.7 \pm 0.2$, H – magnetic field and S – electron spin. The obtained ESR data do not indicate presence of Co^{3+} ions.

Fig. 4. presents angle dependencies of ESR lines. As it is seen there are three different lines distinguishable corresponding to the three octahedral nonequivalent positions of Co^{2+} ions in SLGO lattice one of them being Sr positions. It is possible that some of Co^{2+} ions locates at tetrahedral Ga^{3+} positions (for this case fine structure from $3/2$ spin should be observed and g factor should be equal to about 2). But we observed only a weak one signal in the range of $g = 2$.

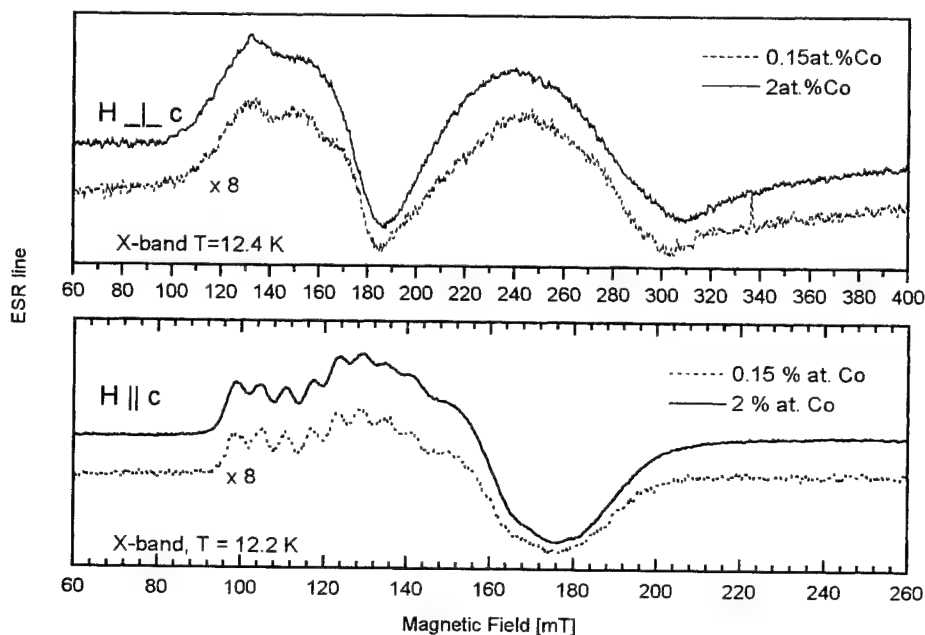


Fig. 3. Typical ESR lines of $SrLaGa_3O_7:Co$ single crystal for two cases $H \perp c$ and $H \parallel c$ and two values of Co^{2+} concentration 0.15at.% and 2at.%.

Intensity of ESR lines changes after annealing of the crystal in the air in such a way that relative intensity of ESR line is smaller one. This confirms supposition about ionization process during annealing treatment of SLGO:Co sample.

4. CONCLUSIONS

Analysis of the absorption spectrum of Co doped $\text{SrLaGa}_3\text{O}_7$ in the framework of the crystal field approach and EPR measurements allow to conclude that we deal with octahedrally coordinated Co^{2+} ions, that replace the Sr in the lattice.

Analysis of the EPR spectrum confirm results obtained by optical measurements that there arise only Co^{2+} ions in SLGO:Co single crystals and indicate three different octahedral positions of the ions one of which is Sr^{2+} .

Annealing at 1050°C in the air for 16h may perform about 50% Co^{2+} ions to Co^{3+} state. The coordination of Co^{3+} ions seems to be also octahedral.

It may be supposed that the quality (absence of the precipitation in the core region) of highly doped crystals will considerably improve if the above fact will be taken into account when calculating the starting composition of the melt. This will make an optimization of the starting melt composition possible.

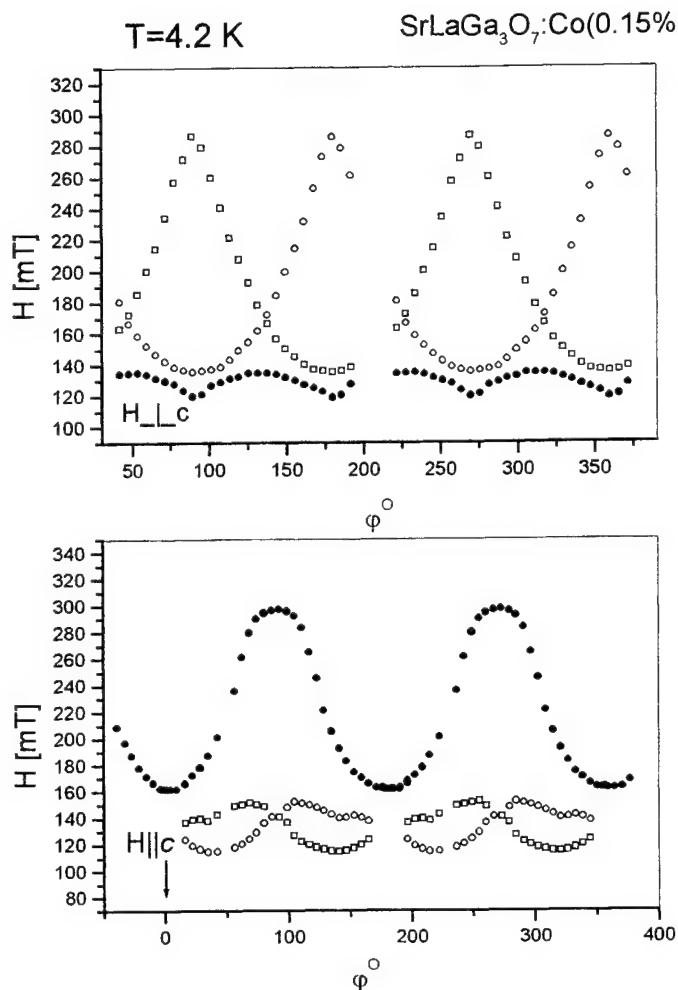


Fig. 4. Angular dependencies of ESR lines of SLGO:Co (P3) single crystal for two perpendicular directions.

ACKNOWLEDGEMENTS

Authors thank to dr M. Palczewska from ITME Warsaw for some ESR investigations. This paper is partly supported by Grant of Polish Committee for Scientific Research no 2P03 B003 13.

REFERENCES

1. M. Berkowski, M. Borowiec, K. Pataj, W. Piekarczyk and W. Wardzyński, "Absorption and birefringence of $\text{BaLaGa}_3\text{O}_7$ single crystals", *Physica B* **123**, pp 231, 1984.
2. A.A. Kaminskii, E.L. Belokoneva, B.V. Mill, S.E. Sarkisov and K. Kurbanov, *Phys. Stat. Sol. (a)* **97**, pp. 279, 1986.
3. W. Ryba-Romanowski, S. Gołąb, G. Dominiak-Dzik and M. Berkowski, "Effect of substitution of barium by strontium on optical properties of neodymium doped XLaGa_3O_7 ($\text{X}=\text{Ba}, \text{Sr}$)", *Mat. Sci. & Eng.*, **B 15**, pp. 217, 1992.
4. I. Pracka, W. Giersz, M. Świrkowicz, A. Pajęczkowska, S. M. Kaczmarek, Z. Mierczyk and K. Kopczyński, "The Czochralski growth of $\text{SrLaGa}_3\text{O}_7$ single crystals and their optical and lasing properties", *Mat. Sci. & Eng.*, **B26**, pp. 201, 1994.
5. S. M. Kaczmarek, Z. Mierczyk, K. Kopczyński, Z. Frukacz, I. Pracka and T. Łukasiewicz, "Pr Doped YAG and SLGO Laser Rods", *Proc. SPIE*, **Vol. 2772**, pp. 139, 1995.
6. S.M. Kaczmarek, M. Berkowski and R. Jabłoński, "Recharging processes of chromium ions in $\text{Cr: SrGdGa}_3\text{O}_7$ and $\text{Cr: SrLaGa}_3\text{O}_7$ single crystals", *Cryst. Res. Technol.* **34**, pp. 1023, 1999.
7. S. Kubota, M. Izumi, H. Yamane and M. Shimada, *J. Alloys & Comp.* **283**, pp. 95, 1999.
8. M. Malinowski, I. Pracka, P. Myziak, R. Piramidowicz and W. Wolinski, "Spectroscopy of Dy^{3+} doped $\text{SrLaGa}_3\text{O}_7$ crystals", *J. Lumin.*, 72-74, pp 224, 1997.
9. B. Simondi-Teisseire, B. Viana, A.M. Lejus and D. Vivien, *J. Lumin.* 72-74, pp. 971, 1997.
10. A. Abragam and B. Bleaney, *Electron Paramagnetic Resonance of Transition Ions*, Clarendon Press, Oxford, 1970.
11. J. Ferguson, D.L. Wood and K. Knox, *J. Chem. Phys.* **39**, pp. 881, 1963.
12. B. Henderson and G.F. Imbusch, *Optical Spectroscopy of Inorganic Solids*, Oxford University Press, Oxford, 1989.
13. S. Sugano, Y. Tanabe and H. Kamimura, *Multiplets of Transition Metal Ions in Crystal*, Academic press, New York 1970.
14. M. Grinberg, S.M. Kaczmarek, M. Berkowski, T. Tsuboi, "Jahn -Teller effect in the $\text{SrLaGa}_3\text{O}_7:\text{Co}^{2+}$ system", *J. of Cond. Matter*, in press.
15. R.D. Shannon, C.T. Prewitt, *Acta Cryst.*, **B25**, pp. 925, 1969; R.D. Shannon, *Acta Cryst.*, **A32**, pp. 751, 1976.

Controlling of the charge states in laser crystals

S.M. Kaczmarek

Institute of Optoelectronics, Military University of Technology, 2 Kaliski Str., 00-908 Warsaw, Poland

ABSTRACT

In this paper changes in active and lattice ions valence were investigated in some laser materials such as: Cr: Y₃Al₅O₁₂, Cr:LiNbO₃ and Cr:Li₂B₄O₇ glass, Ti:Al₂O₃ and Ti:LaGaO₃, Co:SrLaGa₃O₇ and Co:Li₂B₄O₇ glass, Eu, Dy: Li₂B₄O₇ glass, Ho:LiTaO₃, Nd:YVO₄, Nd: SrLaGa₃O₇ and Pr: SrLaGa₃O₇ after annealing in oxidizing and reducing atmospheres, ionizing with gamma, electrons and protons. After γ -irradiation 446 nm emission is observed for Ti:LaGaO₃ single crystal due to $^2E \rightarrow ^2T_2$ transition of Ti³⁺.

Keywords: laser crystals, γ -irradiation, Cr doped crystals

1. INTRODUCTION

In the past decade, the renewal in the search of new laser materials covering wide spectrum from ultraviolet to infrared has been very strong and the demand of various applications in many areas is increased. In many lasing materials there arise, however, not only intentional active dopant but also dopants with other valence states. As an example one can take into account Cr doped crystals. In some of them there may exist chromium in: 2+, 3+, 4+, 5+ and 6+ states. The last state is very unstable and exist in oxide complexes only, e.g. Cr⁶⁺O₄ (e.g. in Li₂B₄O₇ glasses), while other are stable and influence laser characteristics of different materials¹⁻².

Generally annealing in the air (in normal pressure) leads to the increase in valence of uncontrolled or active impurity (Cr³⁺:Y₃Al₅O₁₂, Nd³⁺:Y₃Al₅O₁₂), while gamma, electron and proton irradiation (or annealing in reducing atmosphere), due to ion recombination with secondary or primary electrons (or reduction), leads to the decrease in valence (Cr⁴⁺:Y₃Al₅O₁₂)³. There are some ions, although which are ionized by gamma, electrons and protons (Co²⁺:SrLaGa₃O₇, Cr³⁺:Y₃Al₅O₁₂). It depends on a previous treatment (starting defect structure), local symmetry of an ion and crystal field.

In this paper we show changes in optical properties of some laser materials observed after ionizing radiation or annealing treatment and their possible influence on performance of opto-electronic devices.

2. EXPERIMENTAL

The following crystals were investigated: Y₃Al₅O₁₂ (YAG), SrLaGa₃O₇ (SLGO), LiNbO₃ (LN), LiTaO₃ (LT), LaGaO₃, Al₂O₃ and Li₂B₄O₇ (LBO) glass. They were obtained in the Institute of Electronic Materials Technology, Institute of Physics of the Polish Academy of Sciences and Institute of Physics Military University of Technology in Warsaw. The as grown crystals and glasses were cut and polished into samples with approximate dimensions: about 10 mm in length and 1 mm thick.

Using various ⁶⁰Co sources the samples were irradiated by γ -rays in the Institute of Chemistry and Nuclear Technology (ICNT) in Warsaw, Poland. For the electron irradiation a 300 keV or 1 MeV beams from the Van de Graaf accelerator of the ICNT were used, while for irradiation with 21 MeV protons a beam from compact isochronous proton cyclotron installed in the Sołtan Institute of Nuclear Studies, Świerk, was applied.

The dose of γ -irradiation was varied from 10² to 10⁷ Gy, fluency of electrons was varied from 10¹⁴ to 5*10¹⁶ particles/cm², and protons fluencies from 5*10¹² to 10¹⁶ particles/cm² were applied.

Annealing was performed in three regimes: (i) thermal relaxation by annealing in the air at 400°C for YAG and at 800°C for LN and LT, for 3 hours in order to remove radiation defects, (ii) annealing in the range 1100-1400°C for 3 h in air (an oxidizing atmosphere) in order to change the defect structure of a crystal, and (iii) annealing in a mixture of hydrogen and nitrogen (a reducing atmosphere) at 1200°C for 0.5-2 h.

Optical transmission spectra were recorded before and after each irradiation or thermal treatment of the samples using LAMBDA-900 PERKIN-ELMER, and FTIR 1725 PERKIN-ELMER spectrophotometers. The induced additional absorption (AA) was calculated from the formula:

$$\Delta K = 1/\ln(T_1/T_2) \quad (1)$$

*Further author information

S. M. K. (correspondence): Email: skaczmar@wat.waw.pl.; Telephone: (022) 6859019

where K is the absorption, d is the sample thickness, and T_1 and T_2 are the optical transmissions of a sample before and after irradiation or annealing treatment, respectively.

Photoluminescence was recorded using PERKIN-ELMER spectrofluorimeter. Radioluminescence spectra were measured in the range 200-850 nm using excitation with X-rays (DRON, 35 kV / 25 mA) and Spectrograph: ARC SpectraPro-500i (Hol-UV 1200 gr/mm grating, 0.5 mm slits), PMT: Hamamatsu R928 (1000 V).

The dimensions of samples for ESR investigation were the following 3.5x3.5x2 mm. They were investigated in the Bruker ESP300 ESR spectrometer (X-band). The spectrometer was equipped with helium flow cryostat type ESR900 Oxford Instruments. The ESR investigations were performed in the temperature range from 4 to 35 K and microwave power from 0.002 to 200 mW.

3. RESULTS

Fig. 1 shows the absorption (K) – curves 1 and 3 and changes in the absorption (ΔK) (curve 2) for Cr^{4+} (Cr^{4+} : YAG crystal, curve 1) and Cr^{3+} doped YAG crystals (curve 3 - after annealing of Cr^{4+} : YAG crystal in reducing atmosphere). The “as-grown” Cr^{4+} : YAG crystal was black in color, while the Cr^{3+} : YAG one was green. As it is seen from absorption curves both crystals contain a dopant of second type (Cr^{4+} : YAG crystal contains also Cr^{3+} and Cr^{3+} : YAG crystal contains also Cr^{4+}). The dashed lines mark the positions of absorption bands characteristic for a given type of the active dopant.

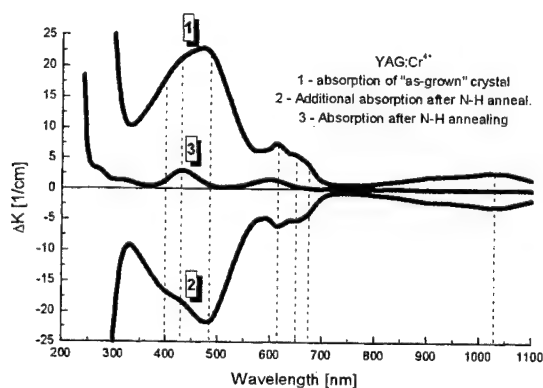


Fig. 1. Absorption coefficient of YAG single crystal doped with chromium 4+ and 3+

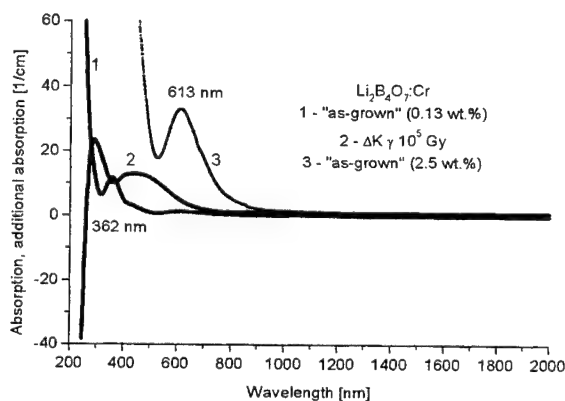


Fig. 2. Absorption (1, 3) and additional absorption (2) of Cr doped (0.15wt.% - 3+ and 6+ - and 2.5wt.% - 3+) $\text{Li}_2\text{B}_4\text{O}_7$ glass

Thus, annealing of the crystal in reducing atmosphere (curve 3), leads to a decrease in concentration of Cr^{4+} ions, due to reduction ($\text{Cr}^{4+} \rightarrow \text{Cr}^{3+}$).

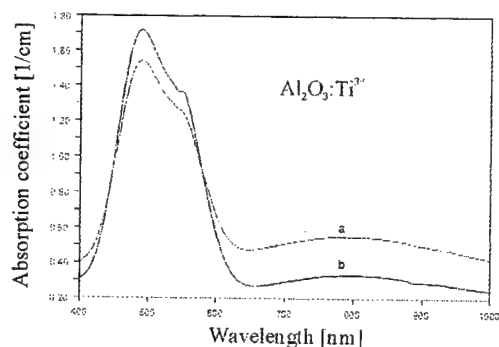


Fig. 3. Absorption coefficient of $\text{Al}_2\text{O}_3:\text{Ti}$ (3+, 4+)

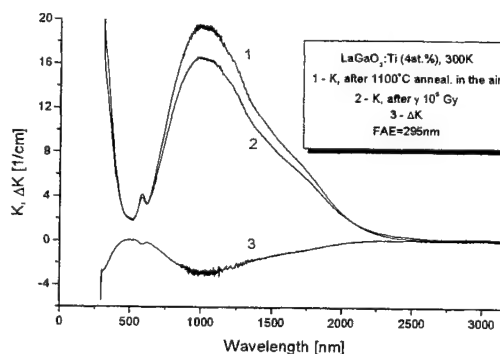
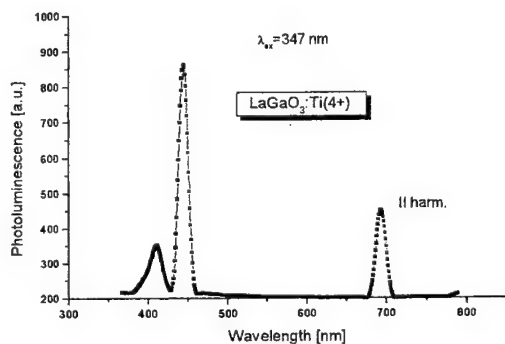


Fig. 4. Absorption coefficient of $\text{LaGaO}_3:\text{Ti}$ (3+, 4+) before (1) and after (2) γ -irradiation with a dose of 10^5 Gy and additional absorption (3)

In the 0.15wt% chromium doped LBO glass (Fig. 2, curve 1) we observe Cr^{3+} and Cr^{6+} ions spectra⁴. Fundamental absorption edge of the glass is equal to 245 nm and lattice absorption origin at 2700 nm. The Cr^{3+} ion has two absorption bands centered at about 430 and 614 nm due to d-d transition: the former was attributed to the spin-allowed but parity forbidden $^4\text{A}_2 \rightarrow ^4\text{T}_1$ transition and the latter to the spin-allowed but parity-forbidden $^4\text{A}_2 \rightarrow ^4\text{T}_2$ transition. The Cr^{6+} ion has strong absorption band centered at 358 nm and a weak one at 318 nm. It seems that these bands refer to Cr^{6+}O_4 complex of 3d^0 configuration rather than to Cr^{6+} ion². Curve 2 shows additional absorption of the glass after 10^5 Gy γ -rays. There are seen at least two bands in the additional absorption centered at about 297 and 450 nm. Curve 3 shows the absorption of highly doped with Cr (2.5wt.%) $\text{Li}_2\text{B}_4\text{O}_7$ glass. One can see that in case of high doping only 614 nm band due to $^4\text{A}_2 \rightarrow ^4\text{T}_2$ transition in Cr^{3+} ions is present.

a).



b).

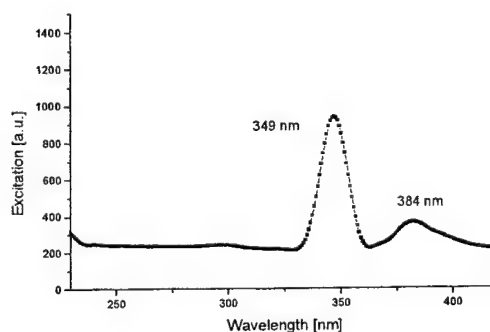


Fig. 5. Photoluminescence (a) of $\text{LaGaO}_3:\text{Ti}(3+,4+)$ single crystal after gamma irradiation with a dose of 10^5 Gy, $\lambda_{\text{ex}} = 347$ nm, and excitation spectrum (b) of 446 nm emission.

Fig. 3 present results of absorption measurements for $\text{Ti}:\text{Al}_2\text{O}_3$ single crystal before (a) and after (b) annealing in reducing atmosphere. As one can see figure of merit (FOM) is two times greater for the annealed crystal than for "as-grown"⁵. It means that annealing in reducing atmosphere leads simply to change in titanium valence $\text{Ti}^{4+} \rightarrow \text{Ti}^{3+}$ without other changes characteristic for the ions diffusion. In Fig. 4 one can see absorption of mainly Ti^{4+} doped LaGaO_3 single crystal (curve 1). In this case annealing in oxidizing atmosphere also leads to valence change of titanium ions. It is seen especially in the change of crystal coloration (from light green to almost transparent). Irradiation with gamma quanta changes amount of Ti^{4+} ions as can be seen in curves 2 and 3. But not only. As is seen from Fig. 4 some lightening of the crystal in the UV range is observed.

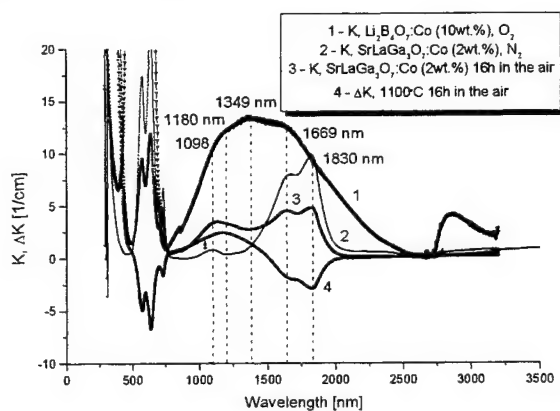


Fig. 6. Absorption coefficient of LBO glass and $\text{SrLaGa}_3\text{O}_7$ single crystal doped with cobalt 2+ and 3+

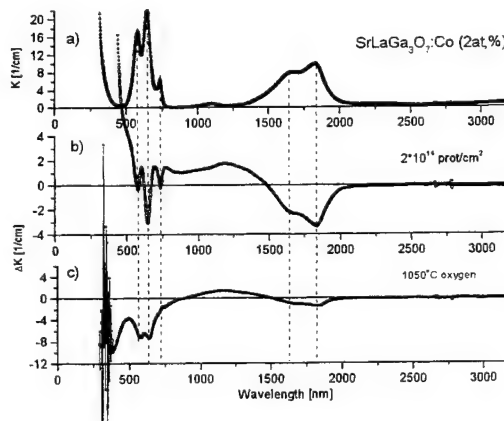


Fig. 7. Absorption (a) and additional absorption of $\text{SrLaGa}_3\text{O}_7:\text{Co}$ single crystal after $2 \cdot 10^{14}$ protons/cm² (b) and subsequent annealing at 1050°C in the oxygen (c)

This lightening leads to arising of some emission in the visible range of emission spectrum (382, 414 and 446 nm bands excited with bands peaked at 304, 339, 374 nm, respectively, Fig. 5). The emission is probably due to ${}^2E \rightarrow {}^2T_2$ transition of Ti^{3+} ions ⁶.

In Fig. 6 absorption of LBO glass doped with cobalt in oxidizing atmosphere (1) as compare to Co:SLGO obtained in reducing atmosphere (2) is shown. In the first case Co^{2+} and Co^{3+} ions are seen in the absorption spectrum. In second one Co^{3+} ions arise only after annealing of the crystal in the oxygen (3). Additional absorption curve (4) indicate probable absorption peak of ${}^5T_2 \rightarrow {}^5E$ transition inside Co^{3+} ion of octahedral coordination. In this case ⁷ change in a valence takes place due to ionization $Co^{2+} \rightarrow Co^{3+}$. This fact is confirmed by Fig. 6, where absorption (a), additional absorption after proton irradiation (b) and subsequent additional absorption after annealing in the oxygen are presented.

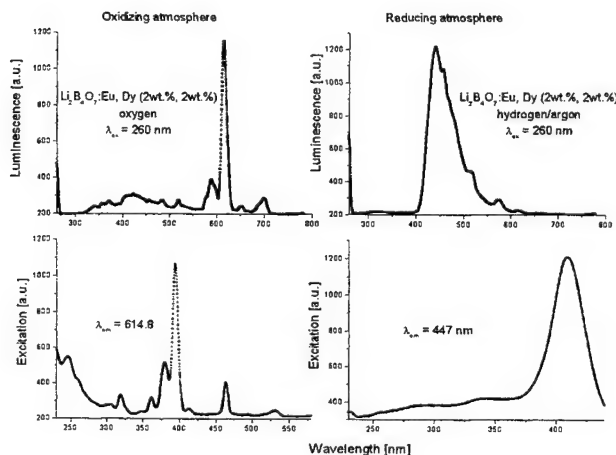


Fig. 8. Photoluminescence and excitation of LBO glass obtained at different growth atmospheres

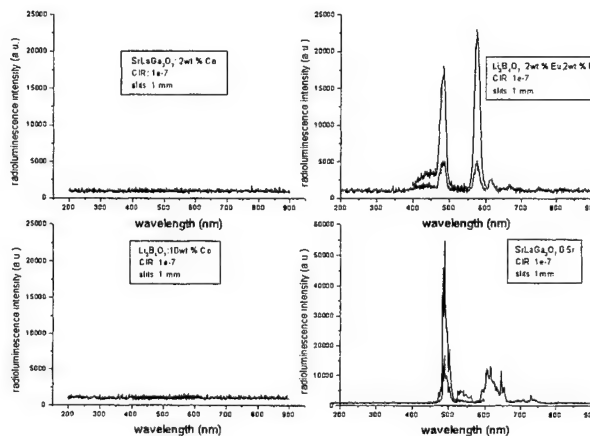


Fig. 9. Radioluminescence of LBO glass and $SrLaGa_3O_7$ single crystal doped with Co, Eu, Dy and Pr

Fig. 8 shows results of excitation-emission measurements for Eu and Dy doped LBO glass in two cases: oxidizing and reducing growth atmosphere. As one can see dependently on the type of atmosphere Eu^{2+} or Eu^{3+} doping takes place. Fig. 9 presents radioluminescence measurements for LBO glass doped with Co and Eu, Dy (reducing atmosphere) and SLGO single crystal doped with Co and Pr. As one can see Co ions does not give any emission in the range up to 900 nm for both cases, moreover, emission of Eu, Dy: LBO glass has other shape than photoluminescence for the glass seen in Fig. 7. It means that not only active dopant concentration has influence on sample emission. Very important factor is also effectivity of energy transfer from lattice to active dopant ion. In the case of Pr: SLGO single crystal the latter is very high.

In Fig. 10 one can see ESR spectra of Cr, Mn: LN single crystal also influenced by gamma and electron irradiation. As is seen only electron irradiation changes Mn valence ionizing it to Mn^{3+} state. Mn was uncontrolled dopant in the crystal. In Fig. 11 radiation defect seen as additional ESR spectrum is presented. As it was shown elsewhere ⁸ this defect is connected with $Ga^{3+} \rightarrow Ga^{2+}$ transition of lattice ion.

Fig. 12 shows absorption (1) and additional absorption (2-4) for Ho: LT single crystal after γ -irradiation (2), subsequent annealing at 800°C (3) and annealing in reducing atmosphere (4) at 1200°C. As is seen, some part (about 10%) of Ho ions changes valence under γ -irradiation⁹. This change is reversible after annealing in the air. Annealing in hydrogen does not give univocal changes.

Fig. 13 presents result of the annealing of Nd:YVO₄ single crystal in reducing H₂ atmosphere. As one can see structural transition take place to Nd:YVO₃ crystal where vanadium is of 3+ valence as compare to previous 5+, according to ref [10]. This is one more case (see Fig. 11), where lattice ion changed your valence. Similar situation took place also for LN single crystal underwent to gamma or proton irradiation when Nb⁴⁺ ion pairs are observed¹¹.

4. DISCUSSION

Chromium and magnesium doped YAG crystal (Fig. 1) reveals the simultaneous presence of 3+ and 4+ chromium ions the amount of which may be changed by proper annealing process.

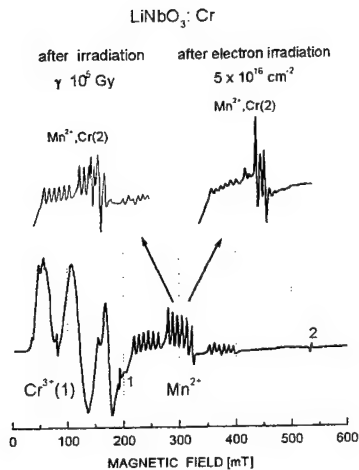


Fig. 10. ESR spectra of LiNbO_3 single crystal doped Cr^{3+} and Mn^{2+} before and after gamma (10^5 Gy) and electron ($5 \times 10^{16} \text{ cm}^{-2}$) irradiation

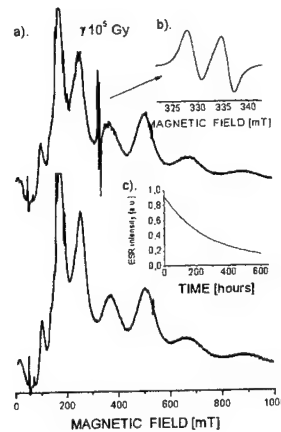


Fig. 11. ESR spectra of $\text{SrLaGa}_3\text{O}_7:\text{Nd}$ single crystal before and after γ -irradiation (a), additional ESR line (b) and time quenching (c)

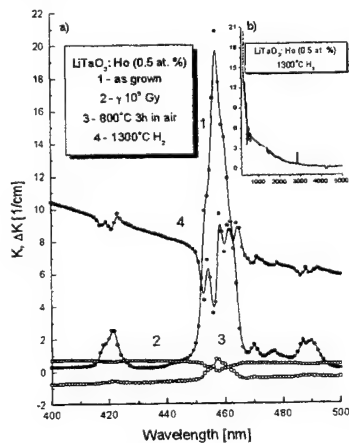


Fig. 12. Absorption (1a) and additional absorption after gamma irradiation (2a), subsequent annealing at 800°C in the air (3a) and annealing in hydrogen at 1300°C (4a and b) of LiTaO_3 single crystal doped with Ho (0.5at.%)

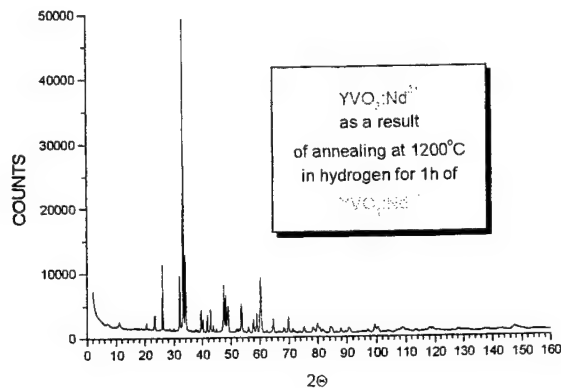


Fig. 13. Structural transition in $\text{YVO}_4:\text{Nd}^{3+}$ single crystal under H_2 annealing

Chromium doped lithium tetraborate glass (Fig. 2) (low doping) shows classical $3+$ absorption and, for 362 nm absorption of Cr^{6+}O_4 complex. After gamma irradiation this complex disintegrates for Cr^{3+} and Cr^{4+} . The same glass highly doped with chromium reveal only 613 nm absorption. Analyzing low and high doping in case of $\text{Li}_2\text{B}_4\text{O}_7$ glass one can state that there exists compositional dependence of the valence states of Cr ions in the glasses. In ² it was stated that the contents of Cr^{3+} and Cr^{6+} vary systematically with basicity in the silicate and borate glasses.

Titanium doping of the both crystals (Fig. 3-5) simultaneously shows the presence of $3+$ and $4+$ ions the relevant amount of which may be changed by proper annealing procedure. Gamma irradiation may lead to significant change of emission properties of $\text{LaGaO}_3:\text{Ti}$ single crystal.

SLGO:Co "as-grown" single crystal (Fig. 6-7) seems to be doped with $2+$ cobalt only but it is possible to change a half of these ions to $3+$ state by ionizing with gamma, electrons, protons or annealing in oxidizing atmosphere. Opposite to

it wide absorption bands seen in the visible as well as IR parts of the absorption spectrum of LBO:Co glass suggest the presence of both Co^{2+} and Co^{3+} ions simultaneously.

Luminescence and radioluminescence spectra of LBO:Eu glass (Fig. 8-9) confirm dependence of europium valence on the atmosphere of growth. Moreover, radioluminescence spectra indicate high efficiency of energy transfer from lattice ions to active dopants in case of Eu, Dy: LBO glass and Pr: SLGO single crystal and low one in the case of Co: LBO glass and Co: SLGO single crystal.

Different type of radiation in other way acts on the investigated crystals leading to recombination and/or ionization phenomena or Frenkel defects. Especially change in a valence of uncontrolled but optically active dopant (Mn) takes place (Fig. 10) and sometimes change in a valence of lattice ion (Ga) (Fig. 11).

Simple recombination with Compton electrons was observed for Ho: LT irradiated with gamma quanta (Fig. 12) giving increase in amount of Ho^{2+} ions. The change of valence was confirmed by annealing treatment. In case of YVO_4 crystal doped with Nd (Fig. 13) annealing in reducing atmosphere leads to a structural transition observed in raw powder diffraction pattern.

5. CONCLUSIONS

Generally, annealing in the air leads to an increase in valence of uncontrolled or active impurity (Cr^{3+} :YAG), while γ , electron or proton irradiation (or annealing in reducing atmosphere) (Cr^{4+} :YAG), due to ion recombination with secondary Compton or delta electrons (or reduction), leads to a decrease in valence (Fig. 1). However there are some ions, which are ionized by gamma quanta (Cr^{3+} :YAG, Co^{2+} :SLGO) due to the Compton interaction. In particular case recharging depends on a previous treatment, local symmetry of ion, and crystal field. Protons can also interact similarly as gamma rays. The only difference in the mechanisms of their interaction with oxide crystals is the source of secondary electrons or, ionization mechanism.

Different treatments (annealing in reducing or oxidizing atmospheres, irradiation) produce different characteristic defects. They may be CC's, such as F^+ , F^- , F^{2+} , F^{2-} , polarons, trapped holes, AA bands attributed to recharged active dopants (Co^{2+} , Pr^{3+} , Ho^{3+} , Cr^{3+} , Eu^{2+} , Ti^{3+}), uncontrolled ions (Mn^{2+} , Fe^{3+} , Fe^{2+}) or lattice ions (Ga^{2+} , Nb^{4+} , V^{3+}).

ACKNOWLEDGMENTS

Author want deeply acknowledge to prof. T. Łukasiewicz, prof. M. Berkowski and dr A. Majchrowski for crystals to investigations.

REFERENCES

1. M. Casalboni, V. Ciafardonne, G. Giuli, B. Izzi, E. Paris and P. Proposito, "An optical study of silicate glass containing Cr^{3+} and Cr^{6+} ions", *J. Phys.: Condens. Matter* **8**, pp. 9059-9069, 1996.
2. T. Murata, M. Torisaka, H. Takebe and K. Morinaga, "Compositional dependence of the valency state of Cr ions in oxide glasses", *J. Non-Cryst. Solids* **220**, pp. 139-146, 1997.
3. S.M. Kaczmarek, M. Berkowski, Z. Moroz, S. Warchol, "Effect of annealing and irradiation on the optical properties of oxide crystals", *Acta Phys. Pol. A*, **96**, pp. 417-427, 1999.
4. S.M. Kaczmarek, "Influence of external radiation and thermal fields on optical properties of laser materials", pp. 50-52, *Proc. of The Second Int. Symp. on Laser, Scintillator and Nonlinear Optical Materials*, May 28-31, Lyon, 2000.
5. Z. Mierczyk, S.M. Kaczmarek, M. Kwaśny, "Spectral properties of titanium sapphire $\text{Al}_2\text{O}_3:\text{Ti}^{3+}$ ", *Biul. WAT*, **5**, pp. 67-75, 1993.
6. N. Kodama, M. Yamaga, "Crystal characterization and optical spectroscopy of Ti^{3+} -doped CaGdAlO_4 crystals", *Phys. Rev. B* **57**, pp. 811-817, 1998.
7. S.M. Kaczmarek, M. Grinberg, M. Berkowski, P. Aleshkevych, J. Fink-Finowicki, H. Szymczak, "Crystal growth and optical properties of Co^{2+} doped $\text{SrLaGa}_3\text{O}_7$ ", this conference
8. S. M. Kaczmarek, R. Jabłoński, I. Pracka, G. Boulon, T. Łukasiewicz, Z. Moroz and S. Warchol, "Radiation Defects in $\text{SrLaGa}_3\text{O}_7$ Crystals Doped With Rare-Earth Elements", *Nucl. Instr. and Meth. Section B*, **142**, pp. 515-522, 1998.
9. S.M. Kaczmarek, M. Świrkowicz, R. Jabłoński, M. Kwaśny, T. Łukasiewicz, "Growth and characterization of rare-earth and transition metal ions doped LiTaO_3 single crystals", *J. Alloys and Comp.*, **300/301**, pp. 322-328, 2000.
10. S.M. Kaczmarek, R. Jabłoński, M. Świrkowicz, T. Łukasiewicz, "Paramagnetic Centers in YVO_4 single crystals", pp. 153-157, *Proceedings of International Conference on Intermolecular Interactions with Matter*, Lublin, 1999.
11. S.M. Kaczmarek, "Influence of gamma and proton radiations on optical properties of lithium niobate single crystals doped with Cu, Fe and Cr ions", pp. 198-200, *Proc. of The Second Int. Symp. on Laser, Scintillator and Nonlinear Optical Materials*, May 28-31, Lyon, 2000.

On growth and dielectric properties of $\text{Ca}_4\text{GdO}(\text{BO}_3)_3$ single crystals

Andrzej Kłos^a, Anna Pajęczkowska^{a*}, Czesław Pawlaczyk^{b*}, Ewa Markiewicz^b

^aInstitute of Electronic Materials Technology, Warszawa, Wólczyńska 133

^bInstitute of Molecular Physics, Polish Academy of Science, Poznań, Smoluchowskiego 17

ABSTRACT

Single crystals of $\text{Ca}_4\text{GdO}(\text{BO}_3)_3$ (CGBO) have been grown from a melt by the Czochralski pulling method making use [010] seed orientation. Defects, like dislocation were investigated. Chemical methods were developed on various planes of crystals, in order to reveal the nature and the distribution of these defects. Dielectric measurements in frequency range 20 Hz – 13 MHz in three main crystallographic directions were carried out. The values of elastic and piezoelectric coefficients were calculated for the first mode of piezoelectric vibration in each direction.

Keywords: Oxides, growth, defects, dielectric.

1. INTRODUCTION

In the recent years there has been a great interest in non-linear optical materials that allow producing a visible laser beam by second harmonic generation (SHG).

Calcium gadolinium oxoborate $\text{Ca}_4\text{GdO}(\text{BO}_3)_3$ (CGBO) is a new efficient non-linear optical crystal^{1,2}, belonging to the rare earth calcium borate group with general composition $\text{Ca}_4\text{RB}_3\text{O}_{10}$ ($\text{R} = \text{La} - \text{Lu}, \text{Y}$). The compound melts congruently at 1480°C ¹ and the crystal has high hardness (6.5), is nonhygroscopic, chemically stable and easy to polish. Additionally, it exhibits large transparency region and high damage threshold³.

1.1. Crystal structure

Norrestam et al.⁴ synthesised a series of calcium oxoborate compounds with $\text{R} = \text{La}, \text{Nd}, \text{Sm}, \text{Gd}, \text{Y}$ by high - temperature solid state reaction. Iliukhin et al.⁵ grow crystals by the flux method with $\text{R} = \text{Gd}, \text{Tb}, \text{Lu}$ ions and measured the crystal structure of $\text{LnCa}_4\text{O}(\text{BO}_3)_3$ by X-ray diffraction methods. CGBO structure is related to the fluoroborate and fluoroapatite. The unit cell parameters are $a = 0.8104(1)$, $b = 1.6030(3)$, $c = 0.35584(3)$ nm and $\beta = 101.250^\circ$. The space group is monoclinic noncentrosymmetric Cm. The CGBO crystal is biaxial what means that the optical axis (X,Y,Z) are not in coincidence with the crystallographic axis (a, b, c). There are two types of Ca^{2+} ion occupy distorted octahedral sites. All octahedra share corners with BO_3 triangles to form a three-dimensional network. There are two kinds of boron site, B(1) and B(2), with threefold coordination. Three planar borate units lie approximately parallel to the (001) plane. The Gd^{3+} ions are located in the crystallographic mirror plane. The environment of Gd^{3+} is a distorted octahedron with Cs site symmetry. Four oxygen ions are shared with the BO_3 groups. The existence of a probable disorder between calcium and gadolinium atoms in the two octahedral positions is expected⁵.

2. GROWTH OF CGBO SINGLE CRYSTALS

The CGBO compound was prepared by solid state reaction, with CaCO_3 of 4N purity and Gd_2O_3 and B_2O_3 of 5N purity. B_2O_3 was prepared in the special way to III-V technology and contains water no higher than 70 ppm. The mixture was heated at 950°C , cooled and ground, and then heated again at 1150°C , for 20 h, respectively. Crystals were grown by the Czochralski method. The synthesised charge was melted in iridium crucible and the seed of orientation [010] was introduced into crucible, at the top, and kept in contact with the melt. The growth processes were computers monitored by a weight-and-diameter system and without the computer system by visual diameter control. A nitrogen atmosphere was provided during growth. The typical growth rate was about 1 mm/h and crystal was rotated at 10-25 rpm. The crystals obtained in this way are colourless, with a good optical quality, not hygroscopic, and chemically stable. The CGBO single crystal presents good mechanical properties, permitting easy polishing.

*Further author information –

A.P.: Email: itme3@atos.warman.com.pl

C.P.: Email: czpawl@ifmpan.poznan.pl

3. CHEMICAL ETCHING

To investigate a quality of CGBO single crystals chemical etch methods were developed on planes of cube cut out along the three monoclinic axes [010] from three regions of crystal (top, central and bottom). The dislocations were detected on all planes of cube, however, they were observed very well on (100) and (010) planes (see Fig.1) and less on (001) flat. The dislocations were revealed by etching in 4% HCl at room temperature.

The (010) oriented plates showed similar amount of etches pits at the outer part of plates. Etch pits density decrease from $6 \cdot 10^4 \text{ cm}^{-2}$ at the top of the crystal to $8 \cdot 10^3 \text{ cm}^{-2}$ at the central part of the cone. However at the inner part of the crystal the etch pits density is about $1 \cdot 10^3 \text{ cm}^{-2}$.

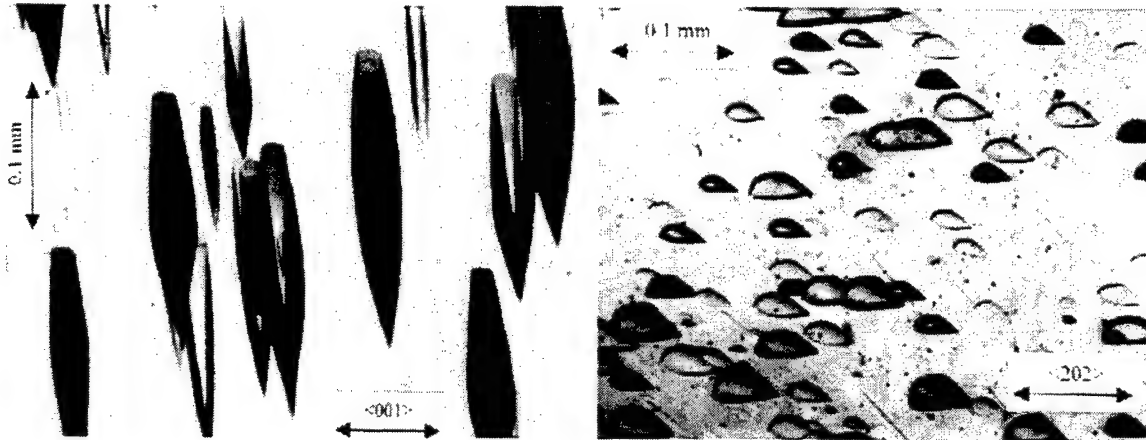


Fig.1. Etch pits pattern developed on the (100) plane (left) and (010) plane (right).

4. DIELECTRIC MEASUREMENTS

The dielectric measurements in frequency from 20 Hz to 13 MHz range were carried out using a HP4284A RCL meter and HP4192A impedance analyser. The temperature was stabilised in the range from 10K to 450K using an Oxford Instruments cryostat CF 1204.

The measurements were performed for samples cut out in the three main crystallographic directions [100], [010], [001]. The temperature dependence of permittivity and dielectric losses is show in the Fig.2. From this one can conclude that the crystal is very good isolator with maximum electric permittivity along the monoclinic axis [010] ($\epsilon' = 12$) and a very small dielectric losses ($\text{tg}\delta \leq 0,01$).

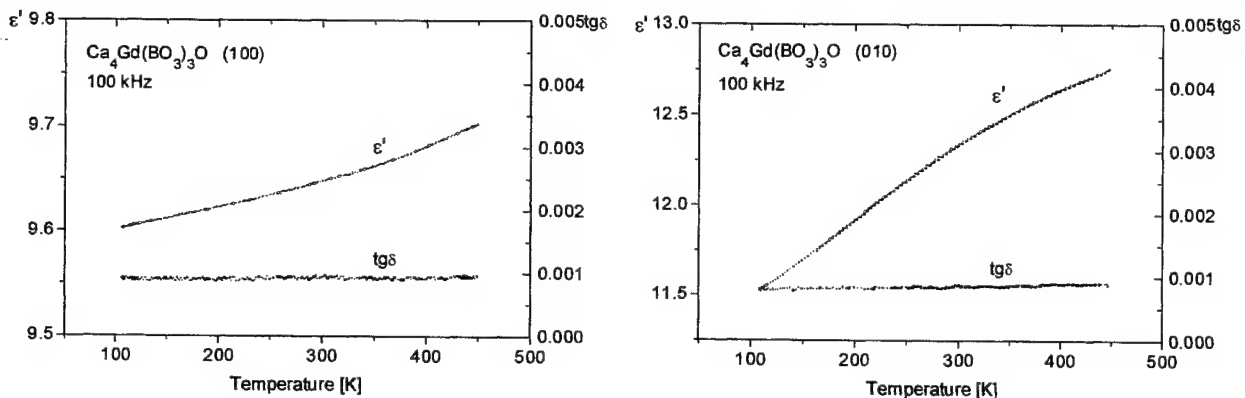


Fig.2. The temperature dependence of permittivity and dielectric losses in two main crystallographic directions.

In the Fig.3 the frequency dependencies of both parts ϵ' and ϵ'' of the permittivity are shown. Resonance dependencies are observed at frequencies near 1MHz. The number of resonance peaks reflects the number of piezoelectric vibration modes of the sample. In the (100) oriented sample e.g. a tripled of basic modes is observed. The experimental points for basic tripled can be well fitted with dielectric function for the sum of three harmonic oscillators:

$$\epsilon^*(f) = \sum_i \frac{A_i f_{ri}^2}{f_{ri}^2 - f^2 - jf\Gamma_i}, \quad (1)$$

where f denotes measuring frequency, A_i , f_{ri} and Γ_i - amplitude, resonance frequency and damping constant of the i -th oscillator, respectively. The values of parameters A , f_r and Γ obtained from the fit are also given in the Fig.3c. Moreover, at higher frequencies non-odd harmonic vibrations can be observed. The ratios of the harmonic/basic frequencies amount ..., 5, 3, 1, as expected in the case of piezoelectric resonance (see Fig. 3d).

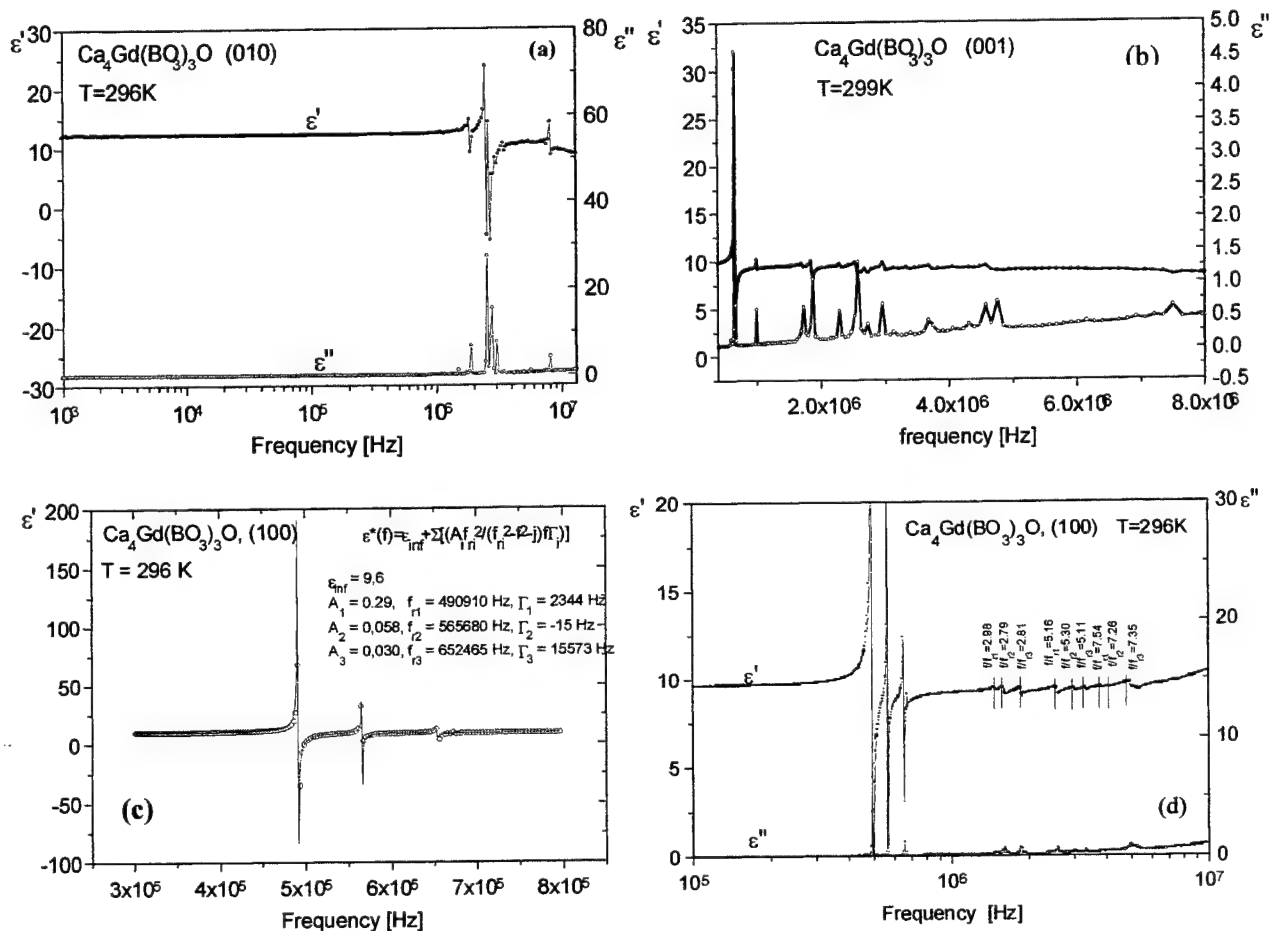


Fig.3. The frequency dependencies of the permittivity in the three crystallographic directions.

The electric equivalent circuit method⁶ was used to calculate elastic and piezoelectric coefficients. The circuit is given in Fig. 4.

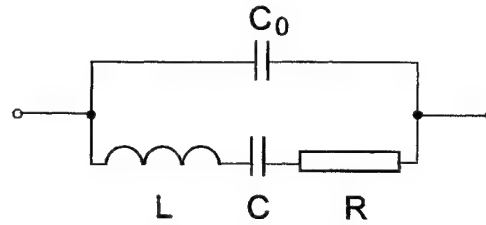


Fig. 4. The RLCC₀ electric equivalent circuit.

The R, L, C and C₀ values are associated with the above coefficients^{7,8} in the following way:
electromechanical coupling factor k_{ij} :

$$k_{ij}^2 = \frac{1}{8} \pi^2 \frac{C}{C_0} \quad (2)$$

dielectric permittivity under constant tension ϵ_{ij}^T :

$$\epsilon_{ij}^T = \frac{C_0 t}{A} \quad (3)$$

where: A is the area of the sample,
t is the thickness of the sample

elastic compliance coefficient under constant field s_{ij}^E :

$$\frac{1}{s_{ij}^E} = \frac{1}{\pi^2} t^2 \omega_s^2 \rho \quad (4)$$

piezoelectric coefficient d_{ij} :

$$d_{ij}^2 = k_{ij} \epsilon_{ij}^T s_{ij}^E \quad (5)$$

The values of above coefficients were calculated for the first mode of piezoelectric vibration in each direction. They are summarised in the Table 1. The measurement results showed that CGOB crystals exhibit the best piezoelectric properties along the monoclinic axis [010]. The piezoelectric coefficients along this axis shows 1.6 - 2 time more value than along the others. Elastic compliance of CGOB crystal is the least one related to the monoclinic axis because the reciprocal of the elastic compliance coefficient under constant field $\frac{1}{s_{22}^E}$ reaches the largest value.

Table1. Elastic and piezoelectric coefficients.

parameter	value	unit
$\epsilon_{11}^T / \epsilon_0$	8.92	
$\epsilon_{22}^T / \epsilon_0$	5.18	
$\epsilon_{33}^T / \epsilon_0$	10.92	
$\frac{1}{s_{11}^E}$	1.76×10^9	N/m ²
$\frac{1}{s_{22}^E}$	55.37×10^9	N/m ²
$\frac{1}{s_{33}^E}$	3.14×10^9	N/m ²
d_{11}	3.84×10^{-11}	C/N
d_{22}	6.32×10^{-12}	C/N
d_{33}	3.04×10^{-11}	C/N

The measurement results showed that CGOB crystals exhibit the best piezoelectric properties along the monoclinic axis [010]. The piezoelectric coefficients along this axis shows 1.6 - 2 time more value than along the others. Elastic compliance of CGOB crystal is the least one related to the monoclinic axis because the reciprocal of the elastic compliance coefficient under constant field $\frac{1}{s_{22}^E}$ reaches the largest value.

5. CONCLUSIONS

CGOB single crystals obtained by the Czochralski method are colourless, with a good optical quality. The investigated crystals were partially defected showing dislocations and stacking faults along the crystal growth direction [010]. The etch pits density at the central part of crystal on the {010} face was $1 \cdot 10^3 \text{ cm}^{-2}$.

Dielectric measurements carried out in frequency range 20 Hz - 13 MHz and in temperature range up to 450K in the three main crystallographic directions [100], [010], [001] showed, that CGBO crystal is a very good isolator with dielectric losses $\text{tg}\delta < 0.01$ stable with temperature and frequency. Resonance dependency was found at frequencies near 1MHz. CGBO single crystal exhibits the best piezoelectric properties along the monoclinic [010] axis.

ACKNOWLEDGEMENTS

This work was supported by the Polish Committee for Scientific Research under grant No 8T11B00716.

REFERENCES

1. G. Aka, A. Kahn-Harari, D. Vivien, F. Salin, J. Godard, J. M. Benitez, Eur. "A new non-linear and neodymium laser self-frequency doubling crystal with congruent melting : $\text{GdCa}_4\text{O}(\text{BO}_3)_3$ (GdCBO)" *J. Solid State. Inorg. Chem.* **33** pp. 727- 736, 1996.
2. D. Vivien, F. Mougel, G. Aka, A. Kahn-Harari, D. Pelenc, "Neodymium-activated $\text{Ca}_4\text{GdB}_3\text{O}_{10}$ (Nd : GdCOB): A multifunctional material exhibiting both laser and optical properties", *Laser Phys.* **8**, pp. 759-763 (1998).
3. H. Furuya, M. Yoshimura, M. Kobayashi, K. Murase, Y. Mori, T. Sasaki, "Crystal growth and characterization of $\text{Gd}_x\text{Y}_{1-x}\text{Ca}_4\text{O}(\text{BO}_3)_3$ ", *J. Cryst. Growth* **198/199**, pp. 560-563, 1999.
4. R. Norrestam, M. Nygren, J. O. Bovin, "Structural investigations of new calcium-rare earth (R) oxyborates with the composition $\text{Ca}_4\text{RO}(\text{BO}_3)_3$ " *Chem. Mater.* **4** pp. 737-743, 1992.
5. A. B. Iliukhin, B. F. Dzhurinskii, "Kristalicheskiye struktury dvoynych oxyboratow $\text{LnCa}_4\text{O}(\text{BO}_3)_3$ (Ln =Gd, Tb, Lu) i $\text{Eu}_2\text{CaO}(\text{BO}_3)_2$ " *Russ. J. Inorg. Chem.* **38**, pp. 917-920, 1993.
6. E. Markiewicz, J. Kurek and Cz. Pawlaczyk, "Simple Electric Equivalent Circuit Method to Determine Piezoelectric and Elastic Properties of Piezoelectric Polymer Film", *IEEE Transactions on Dielectric and Electrical Insulation*, **6**, pp. 304 - 308, 1999.
7. D.A. Berlincour, D.R. Curran and H. Jaffe, "Piezoelectric and Piezomagnetic Materials and Their Function in Transducers in Physical Acoustic", W.P. Mason (ed), Academic Press Inc., New York, Vol. 1, part A, pp. 182 - 189, 1964.
8. W.P. Mason, "Piezoelectric Crystals and Their Application to Ultrasonic", D. Van Nostra, New York, 1950.

The Czochralski growth and characterization of $\text{SrLaGa}_3\text{O}_7: \text{Ho}^{3+}$ single crystals

I. Pracka^a, M. Malinowski^b, M. Świrkowicz^a, J. Kisielewski^a, A. Bajor^a, A. Kłos^a, B. Kaczmarek^a,
B. Surma^a

^aInstitute of Electronic Materials Technology, 133 Wólczyńska Street, 01-919 Warsaw, Poland

^bInstitute of Microelectronics and Optoelectronics, ul Koszykowa 75, 00-662 Warsaw, Poland

ABSTRACT

Rare – earth (Nd, Pr, Dy) doped $\text{SrLaGa}_3\text{O}_7$ single crystals are promising laser materials. Also crystals doped with Ho^{3+} ions could be used as efficient laser in visible and near infrared regions. Laser materials, generating in visible and infrared regions, can be used for optical data recording in microphotolithography and in medicine.

$\text{SrLaGa}_3\text{O}_7$ single crystals doped with 0.3, 1.5 and 2 at % of Ho^{3+} , respectively were grown by the Czochralski method with use of iridium crucible and afterheater. According to EPMA measurements distribution coefficient of Ho^{3+} in $\text{SrLaGa}_3\text{O}_7$ was estimated to be $k \approx 0.22$. Optical absorption spectra in visible and infrared regions were measured at 300 K and 12 K, respectively.

Optical quality of single crystals was checked by the use of computerized imaging spectropolarimeter and polariscopic measurements. Temperature dependence of capacitance and conductivity for different dopant concentrations were also measured.

Keywords: crystal growth, oxide compounds, laser materials, doping.

1. INTRODUCTION

Recently, solid-state laser materials, which generate in blue and UV regions are of great interest due to their potential applications for optical data storage, in microphotolithography and medicine. Moreover, lasers with up-conversion mechanism pumped with gallium arsenide infra-red diode lasers can transfer energy to shorter wavelengths (visible).

According to the energy level scheme of Ho^{3+} ion it can be concluded that there are metastable energy levels which correspond to emission transitions in the region from near infrared to ultraviolet.

It is known that Ho^{3+} ion is responsible for emission near 2 and $2.9\mu\text{m}$ regions^{1,2} which correspond to transitions between $^5\text{I}_2$ and $^5\text{I}_6$ Stark excited levels and the ground level $^5\text{I}_8$.

There are many works on Ho^{3+} ion behavior in different host materials, and especially in fluorides and in glasses. In the case of oxide materials only for YAG³ and YAP and YSGG⁴ energy level positions of the Ho^{3+} ion were determined and up-conversion excitations were investigated for different dopant concentrations.

$\text{SrLaGa}_3\text{O}_7$ single crystals exhibit advantageous spectroscopic properties, and first of all low probability of non-radiative transitions, and therefore, long fluorescence lifetime of the excited states.

In this work the grow conditions in the Czochralski technique of $\text{SrLaGa}_3\text{O}_7$ single crystals doped with Ho^{3+} ions have been elaborated and optical and spectroscopic properties of the obtained crystals have been determined.

2. EXPERIMENTAL

The charge material was prepared starting from SrCO_3 , La_2O_3 , Ga_2O_3 , and Ho_2O_3 (at least 4N purity) according to the formula $\text{Sr}_{1.04}\text{La}_{0.92}\text{Ho}_{0.03}\text{Ga}_{3.02}\text{O}_7$ (for 0.3at. % Ho^{3+} concentration in the charge). Ho was substituted for La in the charge. The following dopant concentrations were introduced into the charge 0.3, 1.5 and 2 at. %.

Single crystals were grown by the Czochralski method with the use of MSR-2 equipment (Metals Research Limited, England). Thermal system with iridium crucible of 50mm in diameter and height, respectively, and the passive iridium afterheater of 50mm in diameter was used.

The following growth conditions have been applied:

- pulling rate 1 – 2mm/h,
- rotation rate 30 – 40 rpm,
- growth direction [001],
- atmosphere: N₂.

Single crystals 20mm in diameter, with length up to 70mm were obtained.

The optical quality of crystals was determined by the polariscopic and polarimetric methods. Computer controlled imaging spectropolarimeter was used for studying of birefringence. The absorption spectra at temperatures 12 and 300K were measured using the Bruker IFS 113V FT-IR spectrometer.

Electrical conductivity and capacitance were measured as a function of temperature for undoped and holmium doped specimens (with 0.3, 1.5 and 2 at. %). Hewlett Packard LCR Meter type HP 4263B was used. The measurements were performed in resistivity furnace in air atmosphere at $f=1\text{kHz}$.

3. OPTICAL INVESTIGATIONS

For optical measurements samples were cut perpendicularly to the growth direction [001] and were both sides optically polished. Absorption spectra at temperatures of 12K and 300K were measured with a Bruker IFS 113V FT-IR spectrometer. They are shown in Figs.1 and 2.

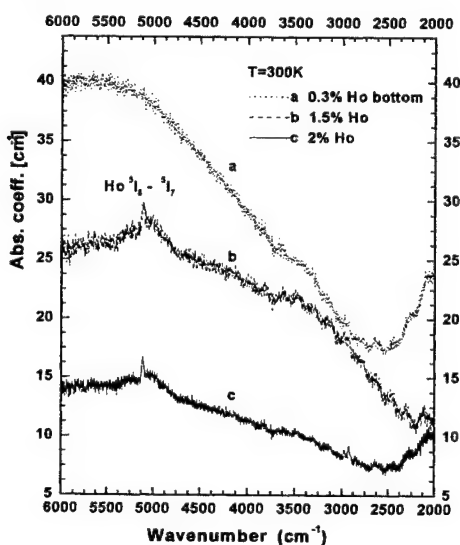


Fig.1.

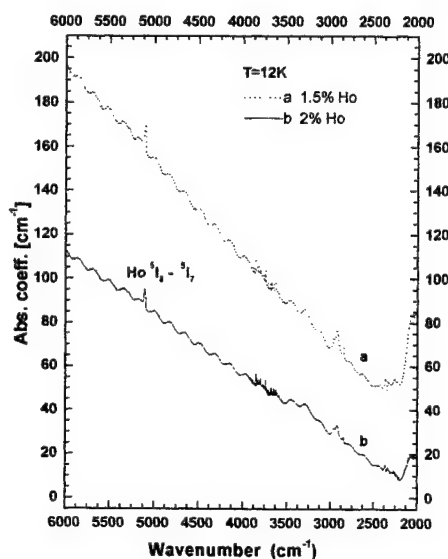


Fig.2.

Fig.1 and Fig.2. Absorption coefficient vs. wavenumber for SrLaGa₃O₇:Ho at temperatures of T=300K (Fig.1) and T=12K (Fig.2).

The crystal and wafers have been checked for their optical properties in the macroscale in the plane and circular polariscopes, an automated polarimeter capable of measuring the three maps on wafer area (birefringence, the principal azimuth (one of the principal residual stresses in the case of Z-cut wafers), and transmission)^{5,6}, and on automated spectropolarimeter used for mapping of parameters associated with birefringence dispersion on wafer area⁷.

In this work due to the shortage of space we show only some characteristic results. In Fig.3 one can see the circular polariscope pictures of the wafer cut out from the top (Fig.3a), and from the bottom (Fig.3b) parts of the crystal doped with Ho 0.3 at.%. Besides the crack one can not observe any particular defects in Fig.3a. On the other hand, however, a core region is clearly visible in Fig.3b at the center of the wafer originating from the bottom part of the crystal. Moreover, one can also see the characteristic growth ridges on this picture at the perimeter of the wafer. The core region itself, as well as, the growth ridges and their neighborhood are the areas of mechanical stress, whereas the remaining part of the wafer is almost free from layer residual stress. Such is also the wafer cut from the top part of the crystal (Fig.3a) where only a few traces of the growth ridges can be observed.

In Fig.4 one can see the horizontal cross-section (along the horizontal diameter) of the BCD map (not shown in this work) measured for 770 nm wavelength in the automated spectropolarimeter. In the case of Z-cut wafer, like here, the BDC (Birefringence Dispersion Coefficient) equals to the ratio of the stress-optic coefficients⁸, i.e.

$$BDC = \frac{C_i(\lambda_i)}{C(\lambda_{i+1})}$$

where λ_i is 770 nm, and λ_{i+1} is incremented by 10 nm. A good, quasi-radial BDC distribution seen on this figure, as well as on BDC maps, and cross-sections of another wafers well corresponding with the plane and circular polariscope pictures, also showing a quasi-radial residual stress distributions. However in the remaining wafers one could always observe the core region of their centers.

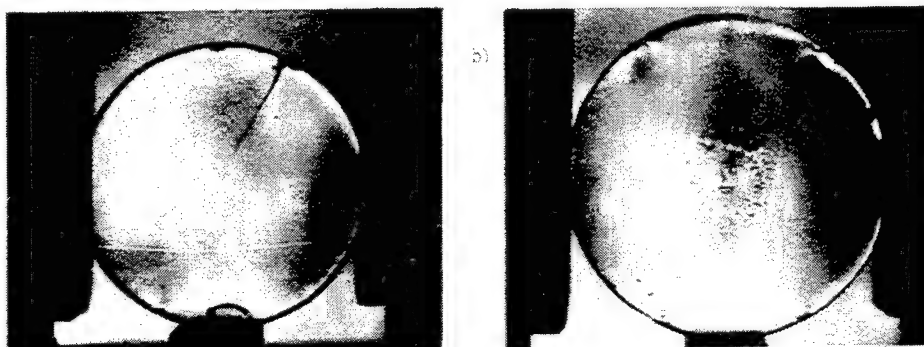


Fig.3. Circular polariscope pictures (quarterwave plates crossed) for 656nm wavelength of the wafer cut out from the top (Fig.3a), and the bottom (Fig.3b) parts of SrLaGa₃O₇ no 1 crystal doped with Ho 0.3 at.%

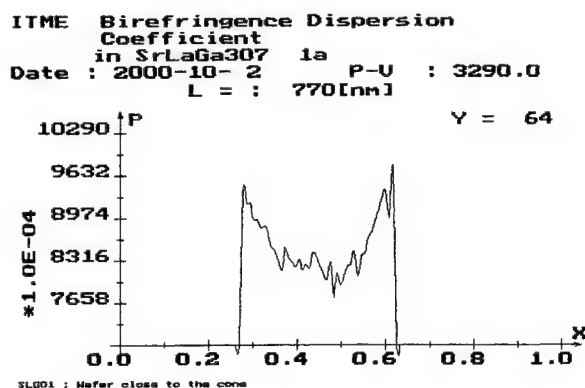


Fig.4. Horizontal cross-section of the BDC map (unshown in this work), corresponding to Fig.3a.

4. CONDUCTIVITY AND CAPACITANCE MEASUREMENTS

Temperature dependence of capacitance and conductivity of SrLaGa₃O₇ single crystals for different holmium concentrations was also measured. In Fig.5a conductivity dependence versus temperature is presented for undoped and SrLaGa₃O₇: Ho single crystals. For comparison, in Fig. 5b the similar dependence for other rare-earth dopants is presented. The band gap value calculated from the slopes of the presented curves is equal to about 2.4eV for undoped and rare-rarth doped specimens.

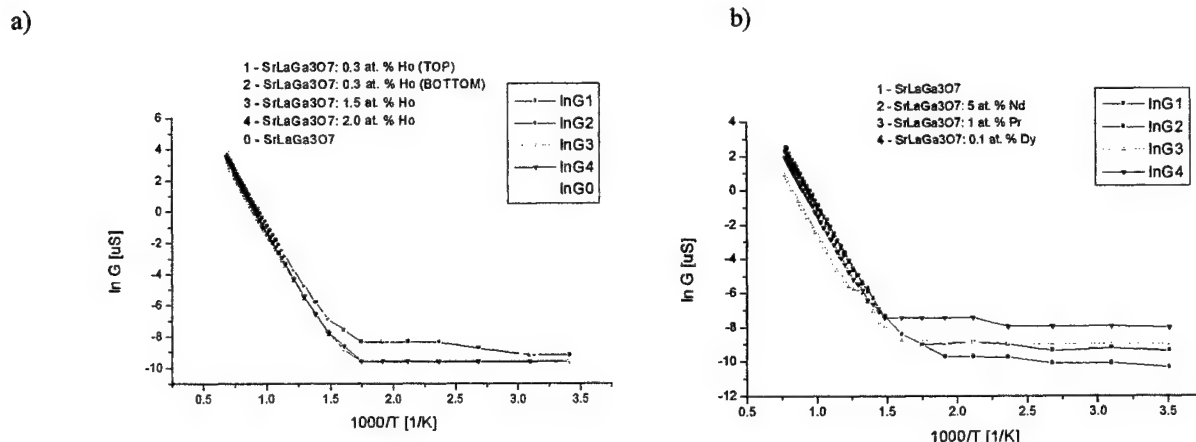


Fig. 5. Conductivity of SrLaGa₃O₇ in dependence on reciprocal temperature. (Fig. 5a – for holmium doped crystals, Fig. 5b – for other rare -earth dopands).

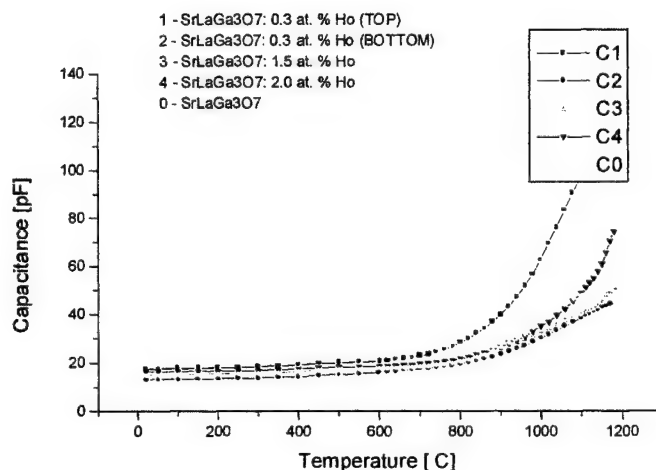


Fig. 6. Capacitance of SrLaGa₃O₇ in dependence on temperature.

5. CONCLUSIONS

Single crystals of SrLaGa₃O₇ doped with holmium were obtained by the Czochralski method. Optical homogeneity of crystals was examined by computer controlled imaging polarimeter.

The optical absorption at the temperature 300K and 12K was measured. It can be seen that more defective structure is observed for crystals with higher concentration of holmium. These results are well consistent with EPMA investigations which suggest that distribution coefficient of Ho in SrLaGa₃O₇ is relatively low and was estimated as close to $k \approx 0.22$. Therefore, due to dopant rejection at interface its concentration increases during growth and crystal quality decreases, especially at the tail part.

According to conductivity measurements as function of temperature it can be concluded that doping with holmium and other rare-earths does not influence the conductance properties of material. Dielectric constant is stable and independent on temperature till 600°C.

REFERENCES

1. L.F. Johnson, H.G. Guggenheim, T.C. Rich, and F.W. Ostermayer, *J.Appl. Phys.* **43**, p. 1125, 1972.
2. D.W. Hart, M. Jani, and N.P. Barnes, *Optics Lett.* **21**, p. 728, 1996.
3. J.B. Gruber, M.J. Hills, M.D. Seltzer, S.B. Stevens, C.A. Morrison, G.A. Turner, and M.R.Kokta, *J.Appl.Phys* **69**, p.8183, 1991.
4. J.B. Gruber, M.J. Hills, M.D. Seltzer, S.B. Steven and C.A. Morrison, *J.Appl.Phys.* **72**, p. 5253, 1992.
5. A.L. Bajor, "Automated polarimeter-microscope for optical mapping of birefringence, azimuths, and transmission in large area wafers. Part I. Theory of the measurement", *Rev. Sci. Instrum.*, **66**, p. 2977, 1995.
6. A.L. Bajor, M.J. Kukla, T. Piątkowski, L. Sałbut, A. Spik, and A. Szwedowski, "ibid. Part II. Measurement setup and results", *Rev. Sci. Instrum.*, **66**, p. 2991, 1995.
7. A.L. Bajor, "Birefringence dispersion inhomogeneity testing in optical materials by imaging polarimetry", in book "Optics and Optoelectronics. Theory, Devices and Applications", **2**, 1312, Ed. O.P. Nijhawan, A.K. Gupta, A.K. Musla, K. Singh, Narosa Publ. House, N. Delhi, Madras, Bombay, Calcutta, London 1998.
8. P.K. Ajmera, B. Huner, A.K. Dutta, and C.S. Hartley, "Simulation and observation of infrared piezobirefringent images in diametrically compressed semiconductor discs", *Appl. Opt.*, **27**, p. 752, 1988.

Relaxation dynamics of excited states of Er^{3+} in YVO_4 single crystals

S.Gołąb^a, G.Dominiak-Dzik^a, P.Solarz^a, T.Łukasiewicz^b, M.Świrkowicz^b,
I. Sokólska^a, W.Ryba-Romanowski^a

^a Institute of Low Temperature and Structure Research, Polish Academy of Sciences,
Okólna 2 Street, 50-950 Wrocław, Poland

^b Institute of Electronic Materials Technology, Wólczyńska 133 Street, 01-919 Warsaw, Poland

ABSTRACT

Crystals of Er:YVO_4 were grown by Czochralski method. Uniformly doped and good quality crystals have been obtained. The lifetimes of the $^4\text{S}_{3/2}$, and the luminescence dynamics were studied as a function of temperature in the region 5–500K. The green luminescence around 550 nm has been observed in excitation by the Ti:sapphire laser into $^4\text{I}_{11/2}$ level. The excitation spectrum recorded for $^4\text{S}_{3/2}$ has been compared with absorption cross section spectrum and calculated ESA spectrum for $^4\text{I}_{11/2} \rightarrow ^4\text{F}_{7/2}$ transition. The contribution of ESA process in upconversion phenomenon under excitation into $^4\text{I}_{11/2}$ has been assessed. The emission cross-section and the gain coefficient for $^4\text{I}_{13/2} \rightarrow ^4\text{I}_{15/2}$ transition of Er^{3+} in YVO_4 have been calculated.

Keywords: Er:YVO_4 crystals, absorption spectrum, green luminescence, doping.

1. INTRODUCTION

In the last few years Er^{3+} doped YVO_4 has been considered as a potential laser material in the IR spectral region¹. However, that real potential strongly depends on the relaxation dynamics of excited states to lower states and upconversion processes. For Er:YVO_4 the ESA and SE cross-section spectra for $^4\text{I}_{13/2} \rightarrow ^4\text{I}_{15/2}$ the transition do not overlap². Accordingly, losses of radiation by ESA at potential laser transition should be negligible but no laser emission of $\text{Er}^{3+}:\text{YVO}_4$ has been observed yet. The absorption spectra, emission spectra and fluorescence dynamics of $\text{Er}^{3+}:\text{YVO}_4$ have been reported³. Upconverted green luminescence has been observed by excitation into $^4\text{F}_{9/2}$, $^4\text{I}_{9/2}$, and $^4\text{I}_{11/2}$ ¹. The absorption cross-section (σ_{ESA}) from $^4\text{I}_{13/2}$ level of Er:YVO_4 have been determined experimentally³. In this study, the temperature dependence of $^4\text{S}_{3/2}$ decay in the range 5–500K was investigated and compared with predictions of multiphonon relaxation model. The contribution of ESA process to the upconversion phenomenon under excitation into $^4\text{I}_{11/2}$ was considered. The emission cross-section and the gain coefficient for $^4\text{I}_{13/2} \rightarrow ^4\text{I}_{15/2}$ transition of Er^{3+} in YVO_4 were calculated.

2. EXPERIMENTAL

Crystals of Er:YVO_4 were grown by Czochralski method. Uniformly doped and good quality crystals have been obtained. The concentration of Er^{3+} in the crystals studied was 0.5, 2, and 4 at %. Absorption spectra were measured with a Varian model 2300 absorption spectrophotometer. The sample luminescence was excited by a Ti:sapphire laser emitting at 970 nm or by Continuum OPO model Surelite I pumped by third harmonic of Nd:YAG laser and dispersed by 1m double grating monochromator, detected by photomultiplier or InSb detector and analysed by a Stanford Model SRS 250 Boxcar integrator. In luminescence decay measurements a digital oscilloscope Tektronix model TDS 3052 has been used. For low temperature measurements, the samples were mounted in Oxford Model CF 1204 continuous flow liquid helium cryostat equipped with a temperature controller.

3. RESULTS AND DISCUSSION

Room temperature absorption spectrum of Er^{3+} ions on YVO_4 is shown in Fig.1. The observed absorption lines are not fully resolved and inhomogeneously broadened.

The temperature dependence of luminescence lifetime of the $^4S_{3/2}$ level of Er^{3+} in YVO_4 for samples containing 0.5at % and 4 at % of erbium is shown by solid circles and squares respectively in Fig.2. The samples were excited by OPO at 523 nm into the level $^2H_{11/2}$. The obtained data are consistent with data presented previously for room temperature and at 77K ^{3,4}. In the phenomenological approach of Riseberg and Moos ⁵ the expected temperature dependence of $^4S_{3/2}$ lifetime has been drawn according to the formula:

$$\tau = \frac{12A_r(^2H_{11/2})\exp\left(-\frac{\Delta E}{kT}\right) + 4A_r(^4S_{3/2})}{12\exp\left(-\frac{\Delta E}{kT}\right) + 4} + A_0 \left(\frac{\exp \frac{\hbar\omega}{kT}}{\exp \frac{\hbar\omega}{kT} - 1} \right)^p \quad (1)$$

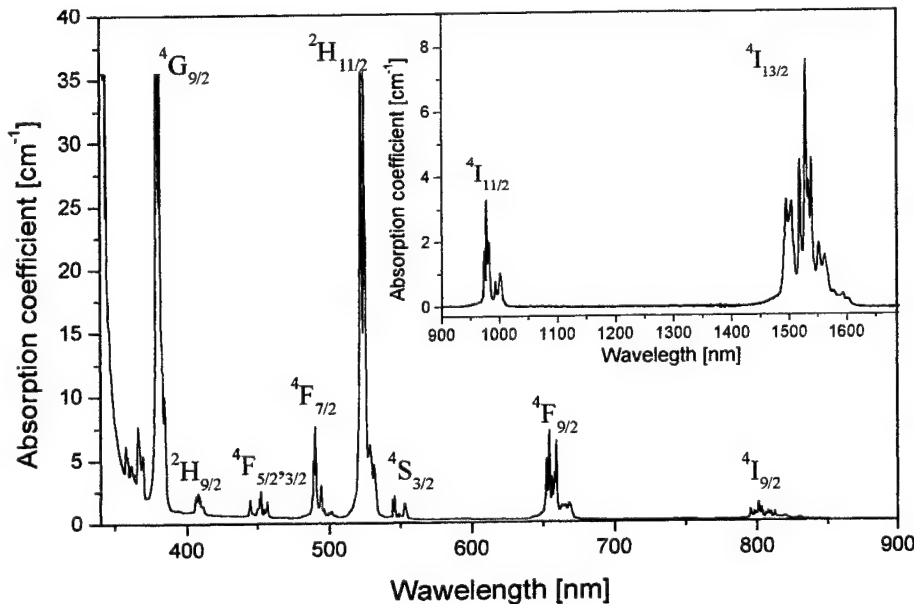


Fig. 1 Absorption spectrum of Er^{3+} ions in YVO_4 crystal recorded at room temperature.

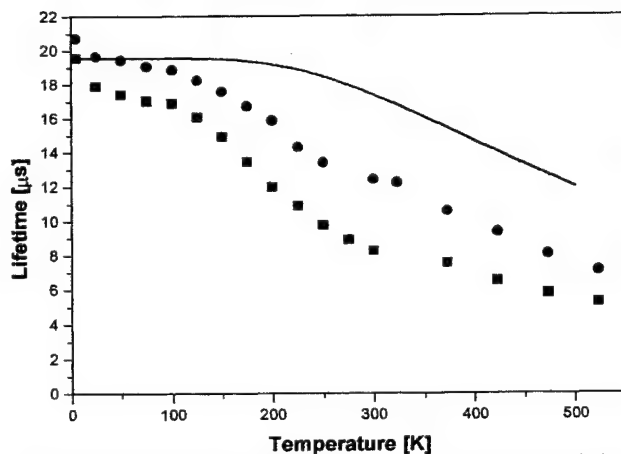


Fig. 2 Temperature dependence of luminescence lifetime of the $^4S_{3/2}$ level of Er^{3+} in YVO_4 crystal. Data indicated by solid circles and squares for samples containing 0.5 at % and 4 at % of erbium, respectively. See text for the explanation of theoretical line.

where: $A(^2H_{11/2})$, $A_r(^4S_{3/2})$ denote the values of the radiative transition rates as given in ⁴, $\Delta E=709 \text{ cm}^{-1}$ is the energy gap between $^2H_{11/2}$ and $^4S_{3/2}$ levels. A_0 denotes the spontaneous multiphonon transition rate, $\hbar\omega=890 \text{ cm}^{-1}$ is the phonon energy ⁶ and $p=4$ is the number of phonons needed to cover the energy gap between $^4S_{3/2}$ and $^4F_{9/2}$ levels. A_0 has been calculated from the inverse of luminescence lifetime measured and 5K. The solid line in Fig.2 presents the theoretical approach derived from equation (1). It cannot predict the experimental temperature dependence of lifetime for the $^4S_{3/2}$ level because the experimentally determined lifetime decreases quickly with increasing temperature. The reason of

observed discrepancy is not clear yet. This may be caused by interaction of active ions with structural defects.

To elucidate a mechanism of upconversion the excitation spectrum of $^4S_{3/2}$ luminescence was recorded at room temperature. The sample was excited by tuneable Ti:sapphire laser in the range 968-988 nm and detected at 552.5nm. The resulting excitation spectrum is presented in Fig.3 by solid line with the σ_{GSA} spectrum (dotted line) in the same wavelength domain. From the analysis of the energy level diagram of Er^{3+} in YVO_4 presented in ³, we have built the σ_{ESA} spectra corresponding to $^4I_{11/2}-^4F_{7/2}$ transition after pumping around 970 nm using the expression ⁷.

$$\sigma_{ESA}^{J \rightarrow J'}(\lambda) = \lambda S_{calc} (J - J') \sum_{i,j} \frac{f_i}{2J+1} \frac{1}{\pi} \frac{\Delta\lambda/2}{(\lambda - \lambda_{ij})^2 + (\Delta\lambda/2)^2} \quad (2)$$

where: f_i is the Boltzmann factor for i -th crystal field level of the starting multiplet J of ESA transition. This factor has been approximated by $1/(2J+1)$; λ_{ij} are the expected wavelength position of ESA lines. In order to calculate λ_{ij} , the experimentally observed crystal-field energy levels of Er^{3+} ion in YVO_4 , for the ${}^4I_{11/2}$ and ${}^4F_{7/2}$ were taken from Table 3 in³. $\Delta\lambda$ is the linewidth of ESA line assumed to has a Lorentzian profile and the same as of GSA line around 970 nm i.e. $\Delta\lambda=1\text{nm}$; λ is the average wavelength of the transition $\lambda=9.74 \times 10^{-5}\text{cm}$. S_{calc} has been calculated by using expression:

$$S_{calc} = C(n) S({}^4I_{11/2} - J') \quad (3)$$

$$\text{where: } C(n) = \frac{(n^2 + 2)^2}{9n} \frac{2\pi^3 e^2}{3hc} \quad (4)$$

$$\text{and } S({}^4I_{11/2} - J') = \sum_{t=2,4,6} \Omega_t \left| \langle {}^4I_{11/2} \| U^{(t)} \| J' \rangle \right|^2 \quad (5)$$

S is the electric - dipole transition strength, $U^{(t)}$ are matrix elements and Ω_t are Judd-Ofelt parameters. S_{calc} was calculated taking to account Ω_t parameters from³, $S_{calc}=0.893$ and $C(n)=0.0283$ for YVO_4 ($n=2.02$). In this calculation it is assumed that all transitions between the Stark components have the same intensity and the same polarisation.

The resulting spectrum is presented in Fig.3 by bold line. It can be seen that the excitation spectrum coincides with both the ESA transition and GSA transition lines. The overlap with the σ_{GSA} is weaker than with σ_{ESA} . Thus, we conclude that the losses by ESA from ${}^4I_{11/2}$ when exciting at 970nm may be appreciable. It was reported⁸ that in Er^{3+} doped fluorozirconate glasses, ESA processes were the principal processes for the upconversion emission near 550nm.

To determine the emission cross section for ${}^4I_{13/2} - {}^4I_{15/2}$ transition of Er^{3+} in YVO_4 we have used the reciprocity method⁹. This method is based on the relation between absorption cross section $\sigma_a(\lambda)$ and emission cross section $\sigma_{em}(\lambda)$ by the following relation

$$\sigma_{em}(\lambda) = \frac{Z_{low}}{Z_{up}} \sigma_a(\lambda) \exp\left(\frac{Z_{LZ} - E(\lambda)}{k_B T}\right) \quad (6)$$

where: Z_{low} , Z_{up} are the partition functions of lower and upper level, respectively, defined as

$$Z_{low} = \sum_{i=1}^n g_i \exp\left(\frac{-E_i}{k_B T}\right) \quad Z_{up} = \sum_{j=1}^n g_j \exp\left(\frac{-(E_j - E(\lambda))}{k_B T}\right)$$

where: $g_i(g_j)$ is a degeneration of sublevel, $E_i(E_j)$ is the energy of the sublevel, E_{LZ} is an energy separation between the lowest crystal field components of the upper and lower multiplets, and k_B is the Boltzmann constant. The ratio Z_{low}/Z_{up} calculated using the above values is equal to 1.06. The energies of E_i and E_j Stark sublevels for ${}^4I_{15/2}$ and ${}^4I_{13/2}$ were taken from Table 3 in³. Calculated

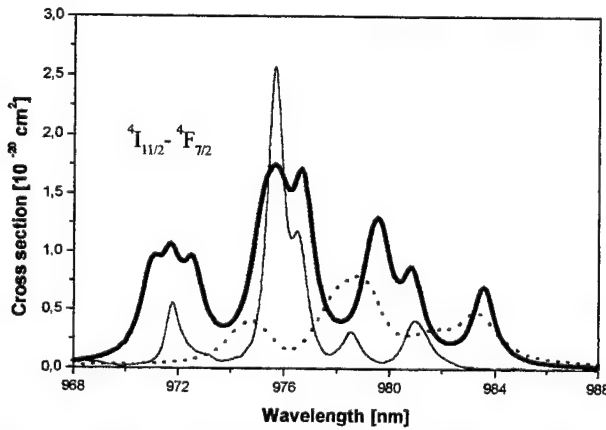


Fig. 3 Room temperature excitation spectrum of ${}^4S_{3/2}$ luminescence of Er^{3+} in YVO_4 - solid line with σ_{GSA} spectrum for ${}^4I_{15/2} - {}^4I_{13/2}$ (dotted line). For the comparison, the calculated spectrum for σ_{ESA} ${}^4I_{11/2} - {}^4F_{7/2}$ transition is presented - bold line.

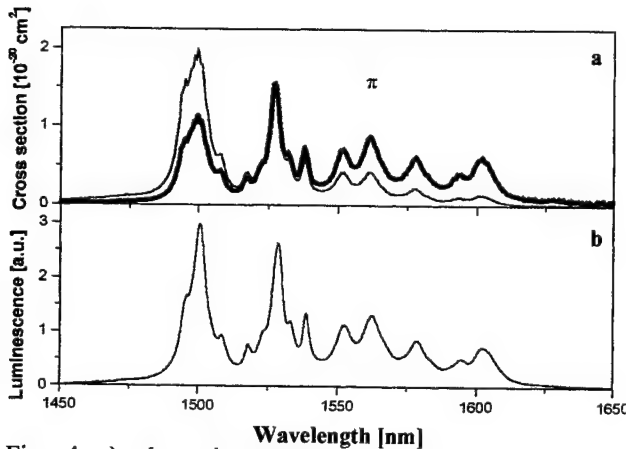


Fig. 4 a) absorption cross section (solid line) and calculated spectra and emission cross section (bold line) b) luminescence spectra recorded for ${}^4I_{13/2} - {}^4I_{15/2}$ under excitation by Ti:sapphire laser emitting at 970 nm. All spectra for π polarisation

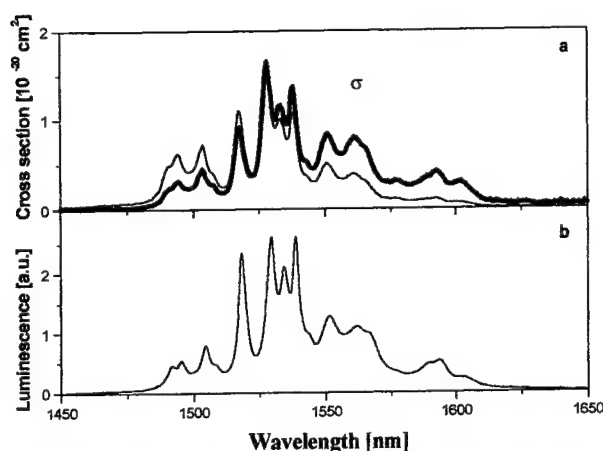


Fig. 5 a) absorption cross section (solid line) and calculated spectra and emission cross section (bold line) b) luminescence spectra recorded for $4I_{13/2} - 4I_{15/2}$ under excitation by Ti:sapphire laser emitting at 970 nm. All spectra for σ polarisation

cross section $\sigma_{em}(\lambda)$ for π and σ polarisation is indicated by bold lines in Fig. 4a and Fig. 5a, respectively. Corresponding $\sigma_a(\lambda)$ spectra are also given by solid lines in those figures. The luminescence spectra for π and σ polarisation recorded under excitation by Ti:sapphire laser emitting at 970 nm are presented in Fig. 4b and Fig. 5b. It can be seen that spectra derived by reciprocity method are in a good agreement with luminescence spectra recorded for both π and σ polarisation. From the estimated $\sigma_a(\lambda)$ and $\sigma_{em}(\lambda)$ the gain coefficient $G(\lambda)$ was calculated using formula¹⁰:

$$G(\lambda) = N[P\sigma_{em}(\lambda) - (1 - P)\sigma_a(\lambda)] \quad (7)$$

where N is the Er^{3+} concentration, P is a population inversion parameter defined as a density of ions in upper state divided by N . Results of calculation for several reasonable values of P are shown in Fig. 6. The presented results are consistent with that presented by F.S. Ermeneux et al.¹ and suggest the possible application of Er:YVO_4 as a laser material operating near $1.6 \mu\text{m}$.

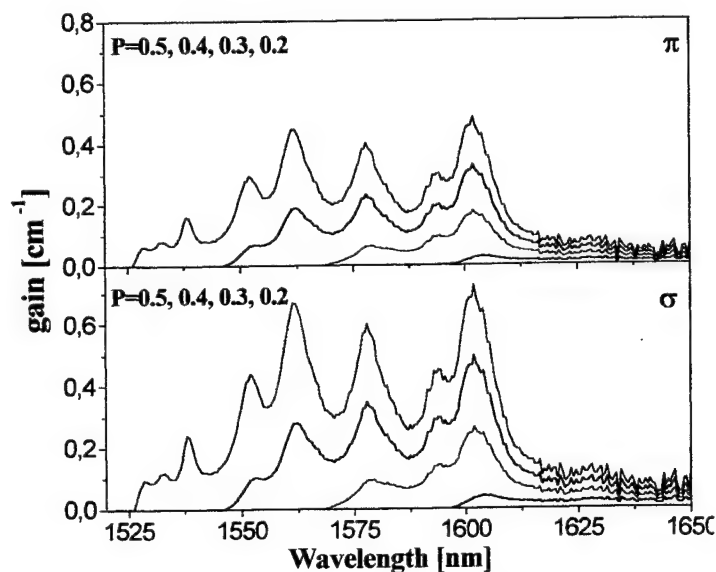


Fig. 6 Gain coefficient calculated for several reasonable values of P for $4I_{13/2} - 4I_{15/2}$ transition Er^{3+} in YVO_4

4. CONCLUSION

The theoretical approach based on multiphonon relaxation model cannot predict the experimental temperature dependence of lifetime for the $4S_{3/2}$ level. The participation of the ESA process from $4I_{13/2}$ in upconverted green phenomenon under excitation at 970 nm is appreciable. The emission cross section spectra derived by reciprocity method are consistent with recorded luminescence spectra of $4I_{13/2} - 4I_{15/2}$ transition for both π and σ polarisation. The positive gain coefficient for $4I_{13/2} - 4I_{15/2}$ transition suggests the possible application of Er:YVO_4 as a laser material operating near $1.6 \mu\text{m}$.

ACKNOWLEDGMENTS

This work is supported by The Polish Committee for Scientific Research under grant No. 8T 11B 021 17

REFERENCES

1. F. S. Ermeneux, R. Moncorgé, P. Kabro, J. A. Capoblanco, M. Bettinelli, and E. Cavalli. "Crystal Growth and Luminescence properties of Er^{3+} doped YVO_4 single crystals", *OSA Trends in Optics and Photonics an ASSL* 1, pp. 498-502, 1996.

2. P. Le Boulanger, J. L. Doualan, S. Girard, J. Margerie and Moncorgé, "Excited state absorption spectroscopy of Er^{3+} doped $\text{Y}_3\text{Al}_5\text{O}_{12}$, YVO_4 and phosphate glass" *Phys. Rev. B* **60**, pp. 11380–11390, 1999.
3. J.A. Capobianco, P. Kabro, F.S. Ermeneux, Moncorgé, M. Bettinelli, E. Cavalli, "Optical Spectroscopy dynamics and crystal-field analysis of Er^{3+} in YVO_4 ", *Chem. Phys.* **214**, pp. 329–340, 1997.
4. F.S. Ermeneux, C. Goutaudier, R. Moncorgé Y. Sun, R. I. Cone, E. Zannoni, E. Cavalli, M. Bettinelli, "Multiphonon relaxation in YVO_4 single crystal", *Phys. Rev. B* **61**, pp. 3915–3920, 2000.
5. L.A. Risberg, W.H. Moos, "Multiphonon orbit-lattice relaxation of excited states of rare-earth ions in crystals" *Phys. Rev.* **174**, pp. 429–438, 1968.
6. S.A. Miller, H.H. Caspers, H.E. Rast, "Lattice vibrations of yttrium vanadate", *Phys. Rev.* **168**, pp. 964–969, 1968.
7. Y. Guyot, H. Manaa, J.Y. Rivoire, R. Moncorgé, N. Garnier, E. Descoix, M. Bon, P. Laporte, "Excited-state absorption and upconversion studies of Nd^{3+} - doped single crystals $\text{Y}_3\text{Al}_5\text{O}_{12}$, YLiF_4 and $\text{LaMgAl}_{11}\text{O}_{19}$ " *Phys. Rev. B* **51**, pp. 784–798, 1995.
8. M. Takahashi, M. Shojiya, R. Kanno, Y. Kawamoto, K. Kadono, T. Ohtsuki, N. Peyghambarian, "Nonradiative decay processes and mechanisms of frequency upconversion in $\text{ZnF}_4\text{--BaF}_2\text{--LaF}_3$ glass" *J. Appl. Phys.* **81**, pp. 2940–2845, 1997.
9. S.A. Payne, L.L. Chase, L.K. Smith, W. L. Kway and W.F. Krupke, *IEEE J. Quantum Electron.* **28**, p. 2619, 1992.
10. K. Ohta, H. Saito, M. Obara, " Tm^{3+} : YVO_4 crystal as an efficient diode pumped laser source near 2000 nm", *J. Appl. Phys.* **73**, pp. 3148–3152, 1993.

Stokes and anti Stokes luminescence in LiTaO₃:Ho

W.Ryba-Romanowski^a, S.Gołąb^a, I.Sokołska^a, G.Dominiak-Dzik^a, P.Solarz^a, T.Łukasiewicz^b,
M.Świrkowicz^b

^a Institute of Low Temperature and Structure Research, Polish Academy of Sciences,
Okólna 2 Street, 50-950 Wrocław, Poland

^b Institute of Electronic Materials Technology, Wólczyńska 133 Street, 01-919 Warsaw, Poland

ABSTRACT

The paper deals with the excitation and decay of excited states of holmium in LiTaO₃ single crystals. Particular attention is paid to processes governing a population build up on the ³S₂ and ⁵I₇ metastable states whose quantum efficiencies are sufficiently high to be considered as initial levels for a laser transition. We observed for the first time, to our knowledge, an efficient conversion of the 647.1 nm light of a krypton ion laser into green luminescence in the material studied. Based upon analysis of excited state relaxation dynamics it is concluded that the mechanism involved is the excited state absorption from the long lived ⁵I₇ level. Efficient single wavelength excitation is due to coincidence of transition energies of the ground state absorption and excited state absorption.

Keywords: Stokes luminescence, LiTaO₃ single crystals, green luminescence.

1. INTRODUCTION

Anti Stokes luminescence, frequently referred as upconverted luminescence in rare earth doped solid matrices attracts much attention recently because it offers a potential of a visible laser emission. Numerous works deal with crystals and glasses doped with thulium or erbium. Upconversion in holmium doped matrices has been studied less extensively. Upconversion lasing in fluoride crystals doped with Ho + Yb¹, and in fluoride glass ZBLAN: Ho² has been achieved. Very recently upconversion phenomena in YAlO₃:Ho have been studied³.

In this paper we report on luminescence of LiTaO₃ crystals with special attention paid to the red-to-green conversion processes.

2. EXPERIMENTAL

Single crystals of LiTaO₃:Ho were grown from congruent melt by the Czochralski method. Uniformly doped and good quality crystals have been obtained. The concentration of Ho³⁺ in the crystals studied was 0.3 and 0.5 at %. Absorption spectra were measured with a Varian model 2300 absorption spectrophotometer. The sample luminescence was excited by Argon laser emitting at 488 nm and Ti:sapphire laser emitting at 751 nm or by Krypton laser at 647.1 nm and dispersed by 1m double grating monochromator, detected by photomultiplier or InSb detector and analyzed by a Stanford Model SRS 250 Boxcar integrator.

3. RESULTS AND DISCUSSION

Room temperature luminescence spectrum of Ho³⁺ ion in LiTaO₃ is shown in Fig.1. The observed lines are not fully resolved and all are strongly inhomogeneously broadened. The electronic structure of Ho³⁺ ions is such that the visible and infrared transitions involve levels having a high multiplicity (2J+1) which gives a high number of Stark levels. This leads to strong levels overlapping. For some multiplets, additional peak splitting has been detected suggesting a multi-site occupancy of Ho³⁺ ions in LiTaO₃ lattice⁴. Green luminescence under the excitation by a krypton ion laser tuned to $\lambda=647.1$ nm was observed at room temperature. Obtained luminescence spectrum was identical as that recorded previously, when exciting into levels above ³S₂ level, and it was associated undoubtedly with the ²S₂ – ⁵I₈ transition of Ho³⁺ presented in Fig.1. In Fig.2 we present log-log plot of intensity of upconverted luminescence versus excitation power, recorded at 300K with a sample containing 0.5 % of holmium. Experimental data are shown by points whereas solid line indicates the power

law behavior. Luminescence intensity is a nearly quadratic function of the excitation power (Slope $\cong 2$), up to maximum available excitation power equal to 72 mW.

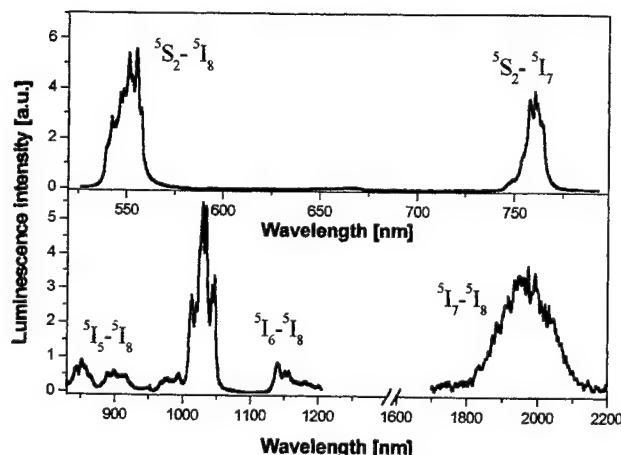


Fig. 1. Room temperature luminescence spectrum of Ho^{3+} ion in LiTaO_3 .

In principle three mechanisms may be involved in the upconversion process, namely an absorption from an excited state (ESA), an excitation by energy transfer between activators and finally a photon avalanche, which combines ESA and an efficient cross relaxation. The latter mechanism is characterized by an excitation power threshold, above which the upconverted luminescence grows by orders of magnitude⁶. It can be seen in Fig. 2 that such a threshold has not been attained. Therefore a photon avalanche mechanism may be neglected in our case. We may neglect also the upconversion by energy transfer based on the observation that the lifetimes of excited states of Ho^{3+} in investigated samples do not differ indicating that an ion-ion interaction is weak. Thus, we consider mechanisms of upconversion processes from excited states.

To elucidate these mechanisms, from the analysis of the energy level diagram of Ho^{3+} in LiTaO_3 presented in⁴, we have built the σ_{ESA} spectra corresponding to $^5\text{I}_7-^5\text{F}_2$ and $^5\text{I}_7-^5\text{F}_3$ transitions around 647 nm using the expression⁵.

$$\sigma_{\text{ESA}}^{J-J'}(\lambda) = \lambda S_{\text{calc}}(J-J') \sum_{i,j} \frac{f_i}{2J+1} \frac{1}{\pi} \frac{\Delta\lambda/2}{(\lambda - \lambda_{ij})^2 + (\Delta\lambda/2)^2} \quad (1)$$

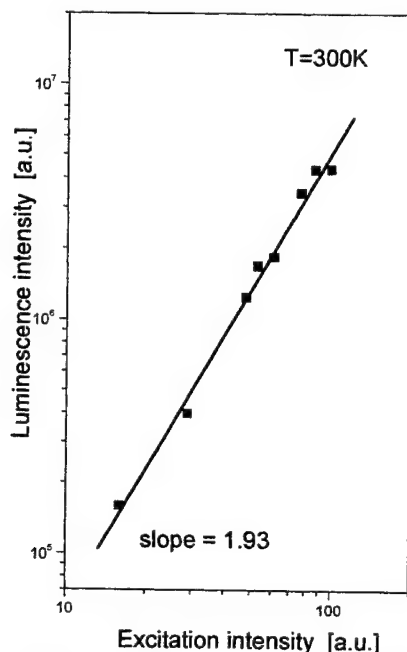


Fig. 2. Log-log plot of intensity of upconverted luminescence versus excitation power, recorded at 300K with a sample containing 0.5 % of holmium. The experimental data are shown by points whereas solid line indicates the power law behavior.

where: f_i is the Boltzmann factor for i -th crystal field level of the starting multiplet J of ESA transition. This factor has been approximated by $1/(2J+1)$; λ_{ij} are the expected wavelength position of ESA lines. In order to calculate λ_{ij} , the experimentally observed crystal-field energy levels of Ho^{3+} ion in LiTaO_3 , for the $^5\text{I}_7-^5\text{F}_2$ and $^5\text{I}_7-^5\text{F}_3$ were taken from Table 3 in⁴. $\Delta\lambda$ is the linewidth of ESA line assumed to have a Lorentzian profile and the same as of GSA line around 647 nm i.e. $\Delta\lambda=1\text{nm}$; λ is the average wavelength of the transition $\lambda = 6,34 \times 10^{-5}\text{cm}$ and $\lambda = 6,55 \times 10^{-5}\text{cm}$ for the $^5\text{I}_7-^5\text{F}_2$ and $^5\text{I}_7-^5\text{F}_3$ respectively. S_{calc} has been calculated by using expression:

$$S_{\text{calc}} = C(n)S(J-J') \quad (2)$$

where:
$$C(n) = \frac{(n^2 + 2)^2}{9n} \frac{2\pi^3 e^2}{3hc} \quad (3)$$

and
$$S(J-J') = \sum_{i=2,4,6} \Omega_i \left| \langle J \| U^{(i)} \| J' \rangle \right|^2 \quad (4)$$

S is the electric - dipole transition strength, $U^{(i)}$ are matrix elements and Ω_i are Judd-Ofelt parameters. S_{calc} was calculated taking to account Ω_i parameters from⁴, $S_{\text{calc}}=0,3393$ and $3,5824$ for the $^5\text{I}_7-^5\text{F}_2$ and $^5\text{I}_7-^5\text{F}_3$ transitions respectively. $C(n)=0,3219$ for LiTaO_3 ($n=2,175$). In this calculation it is assumed that all transitions between the Stark components have the same intensity and the same polarization.

Calculated spectra are presented in Fig.3 by dashed line and solid line for the $^5\text{I}_7-^5\text{F}_2$ and $^5\text{I}_7-^5\text{F}_3$ transitions respectively. It can be seen

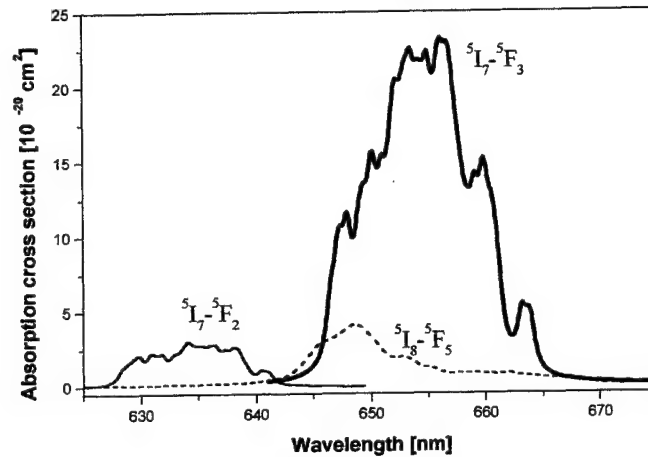


Fig. 3. Spectra of σ_{ESA} for the $^5\text{I}_7 - ^5\text{F}_3$ transition (bold line) and σ_{ESA} for the $^5\text{I}_7 - ^5\text{F}_2$ transition (solid line) with σ_{GSA} for the $^5\text{I}_8 - ^5\text{F}_5$ transition (dash line) of Ho^{3+} in LiTaO_3 .

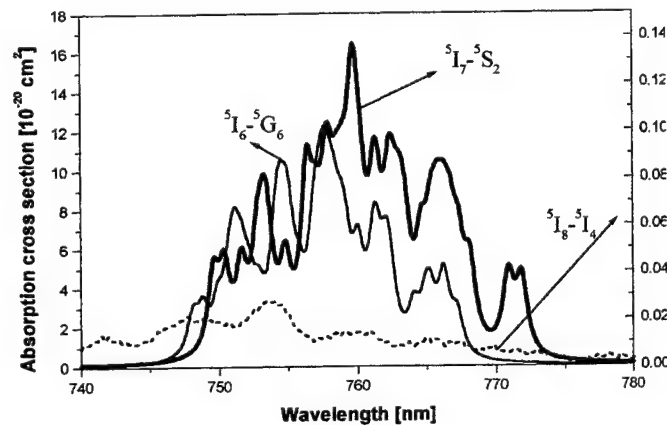


Fig. 4. Spectra of σ_{ESA} for the $^5\text{I}_7 - ^5\text{S}_2$ transition (bold line) and σ_{ESA} for the $^5\text{I}_6 - ^5\text{G}_6$ transition (solid line) with σ_{GSA} for the $^5\text{I}_8 - ^5\text{I}_4$ transition (dashed line) of Ho^{3+} in LiTaO_3 .

that the σ_{ESA} spectrum for the $^5\text{I}_7 - ^5\text{F}_3$ transition overlaps that of σ_{GSA} for $^5\text{I}_8 - ^5\text{F}_5$ transition, which is presented by dotted line in Fig.3. The overlap of σ_{GSA} with σ_{ESA} for the $^5\text{I}_7 - ^5\text{F}_2$ transition is weaker. Thus, we conclude that the ESA process from $^5\text{I}_7$ when exciting at 647nm may be appreciable. In order to assess the possibility of a mechanism of upconversion after pumping at 751nm into $^5\text{I}_4$ level, we have built the σ_{ESA} spectra corresponding to $^5\text{I}_6 - ^5\text{G}_6$ and $^5\text{I}_7 - ^5\text{S}_2$ transitions using the method described above. The resulting σ_{ESA} spectra for $^5\text{I}_7 - ^5\text{S}_2$ (solid line) and for $^5\text{I}_6 - ^5\text{G}_6$ (dashed line) transitions with the σ_{GSA} for $^5\text{I}_8 - ^5\text{I}_4$ transition (dotted line) are reported in Fig.4. Both σ_{ESA} spectra for $^5\text{I}_7 - ^5\text{S}_2$ and σ_{ESA} for $^5\text{I}_6 - ^5\text{G}_6$ transitions overlap the σ_{GSA} spectrum, thus this mechanism of upconversion is likely to occur. The efficiency of this process is expected to be weak because the σ_{GSA} for $^5\text{I}_8 - ^5\text{I}_4$ transition is very small. However, a green luminescence under the excitation by cw Ti:sapphire laser emitting at 751nm was observed. Two proposed mechanisms of upconverted green luminescence by ESA after excitations at 647.1 and at 751 nm are presented in Fig.5.

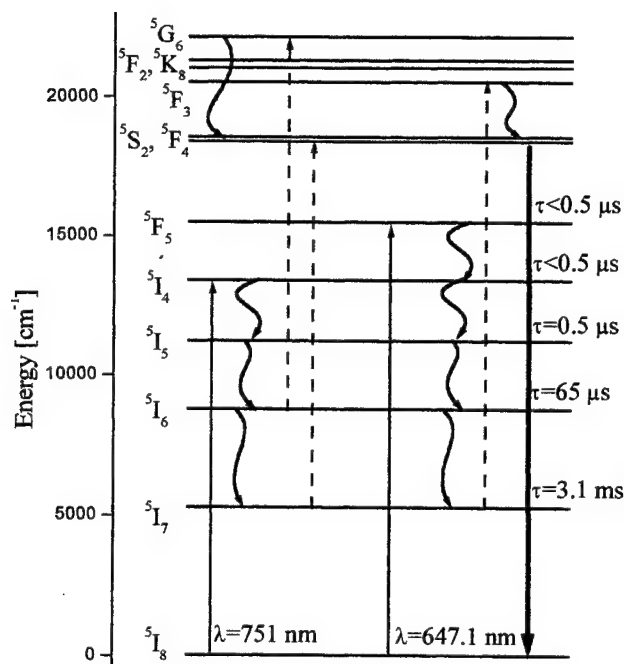


Fig. 5. Energy levels scheme of Ho^{3+} in LiTaO_3 crystal, and proposed mechanisms for upconversion green luminescence. GSA is indicated by solid arrows, non-radiative transitions by wavy arrows, and ESA transitions by dashed arrows.

4. CONCLUSION

Excited state absorption of pumping light at 647 nm and 750 nm contributes adversely to population build up on the initial level of the $^5\text{I}_7 - ^5\text{I}_8$ laser transition around 2 μm . On the other hand a strong ESA at 647 nm provides an excitation of the potential $^5\text{S}_2 - ^5\text{I}_8$ laser transition in the visible.

ACKNOWLEDGMENTS

This work is supported by The Polish Committee for Scientific Research under grant No. 8T 11B 081 17

REFERENCES

1. F. Johnson, H. Guggenheim, "Infrared-Pumped Visible Laser", *Appl. Phys. Lett.* **19**, pp. 44-47, 1971.
2. D. S. Funk, S. B. Stevens, S. S. Wu, and J. G. Eden. "Tuning, temporal, and spectral characteristics of the green ($\lambda \sim 549 \text{ nm}$), holmium-doped fluorozirconate glass fiber laser", *J. Quantum Electron.*, **32**, pp. 638-645, 1996.
3. M. Malinowski, R. Piramidowicz, Z. Frukacz, G. Chadeyron, R. Mahiou, M. F. Joubert, "Spectroscopy and upconversion processes in $\text{YAlO}_3:\text{Ho}^{3+}$ crystals." *Optical Materials* **12**, pp. 409-423, 1999.
4. G. Dominiak-Dzik, S. Gołab, J. Zawadzka, W. Ryba-Romanowski, T. Łukasiewicz, and M. Świrkowicz, "Spectroscopic properties of holmium doped LiTaO_3 ", *J. Phys. Condens. Matter* **10**, pp. 10291-10306, 1998.
5. M.F. Joubert, "Photon avalanche upconversion in rare earth laser materials", *Optical Materials*, **11**, pp. 181-203, 1999.
6. Y. Guyot, H. Manaa, J.Y. Rivoire, R. Moncorgé, N. Garnier, E. Descoix, M. Bon, P. Laporte, "Excited-state absorption and upconversion studies of Nd^{3+} - doped single crystals $\text{Y}_3\text{Al}_5\text{O}_{12}$, YLiF_4 and $\text{LaMgAl}_{11}\text{O}_{19}$ ", *Phys. Rev. B* **51**, pp. 784-798, 1995.

Optical properties of $\text{Li}_2\text{B}_4\text{O}_7$ glasses doped with rare-earths and transition metal ions

S.M. Kaczmarek^a, Cz. Koepke^b, M. Grinberg^c, A. Majchrowski^d, K. Wiśniewski^b, M. Czuba^a

^aInstitute of Optoelectronics, Military University of Technology, 2 Kaliski Str., 00-908 Warsaw, Poland

^bInstitute of Physics, N. Copernicus University, Grudziądzka 5/7, 87-100 Toruń, Poland

^cInstitute of Experimental Physics, University of Gdańsk, Wita Stwosza 57, 80-952 Gdańsk, Poland

^dInstitute of Physics, Military University of Technology, 2 Kaliski Str., 00-908 Warsaw, Poland

ABSTRACT

Absorption and emission spectra of Cr, Eu and Dy ions in $\text{Li}_2\text{B}_4\text{O}_7$ glasses melted in oxygen and hydrogen were measured for valency states and excited states analysis. It was stated that the presence of Cr^{6+} ion is limited by composition of the starting mixture and atmosphere of the melting and that this ion arises as Cr^{6+}O_4 complex. The 308 nm line excites the $\text{Li}_2\text{B}_4\text{O}_7:\text{Cr}$ glass within the highest absorption peak which can be ascribed to the following charge transfer transition: $\text{Cr}^{6+}\text{O}_4(3d^0 2p^6) \rightarrow \text{Cr}^{5+}\text{O}(3d^1 2p^5)$. Under gamma irradiation Cr^{6+}O_4 complex of $3d^0$ configuration can be disintegrated giving additional absorption bands of Cr^{3+} and may be Cr^{4+} centers at tetrahedral sites. One of these additional absorption bands is responsible for 430 nm emission.

Keywords: $\text{Li}_2\text{B}_4\text{O}_7$, absorption and emission spectra, gamma irradiation.

1. INTRODUCTION

In the last four decades a great effort has been devoted to the study of glasses containing transition metal and rare-earth impurities¹⁻⁵. Glasses as laser hosts have advantages such as mass production at low cost and form fibers more easily than single crystals. The emission properties in the glasses are characterized by broader emission spectra, a radiation lifetime with a non-exponential decay law, a peculiar temperature dependence of the quantum efficiency⁶.

Lithium tetraborate ($\text{Li}_2\text{B}_4\text{O}_7$ or LBO) is a congruently melting compound with a melting point 917°C. Single crystals of this material are used as substrates for surface acoustic wave (SAW) devices. The material has cuts with temperature stability of acoustic wave velocity and relatively high electromechanical coupling coefficient for SAW. Polycrystals of $\text{Li}_2\text{B}_4\text{O}_7$ with some dopants find also applications in thermoluminescent personal dosimeters⁷.

Owing to small ionic radii of lithium and boron it is impossible to introduce dopants into $\text{Li}_2\text{B}_4\text{O}_7$ single crystals at high levels. Relatively high viscosity of molten lithium tetraborate, like other borates, is a source of serious problems during single crystals growth of this material. On the other hand this viscosity allows to obtain the material in a form of glass containing much higher amounts of dopants than in case of single crystals.

One of the most investigated impurity ions also in glasses is chromium, and the large number of review articles and papers testifies to the high level of interest in this field^{4,5,8}, even in connection with the development of lasers. Europium and dysprosium doped glasses exhibit wide application in gamma dosimetry and as scintillators.

In this paper we point out the possibility of hosting easily impurity ions: Cr, Eu, Dy in a $\text{Li}_2\text{B}_4\text{O}_7$ glassy matrix. The purpose of this work is also to investigate possible valency states and excited states of Cr, Eu and Dy ions in $\text{Li}_2\text{B}_4\text{O}_7$ glasses.

2. EXPERIMENTAL PROCEDURE

2.1. Glass preparation

The synthesis of lithium tetraborate was carried out from lithium carbonate Li_2CO_3 , and boric oxide H_3BO_3 (Merck, extra pure) in platinum crucibles in air. After reaction of starting materials at 950°C the obtained compound was overheated to 1150°C to remove traces of water and carbon dioxide, which were present in the melt. Because of B_2O_3 losses, due to evaporation, 1 mol% surplus of H_3BO_3 was added to the starting composition. After rapid cooling below 550°C the melt formed glass which did not show any tendency to crystallise. Prolonged heating of obtained glass at

*Further author information

S. M. K. (correspondence): Email: skaczmar@wat.waw.pl.; Telephone: (022) 6859019

temperatures higher than 600°C led to its crystallisation and subsequent formation of polycrystalline material. Cr_2O_3 was dissolved in lithium tetraborate at the level of 0.13 mol% and 2.5 mol%. The addition of chromium oxide, Cr_2O_3 , caused green coloration of the glass. The glasses were obtained in oxidizing atmosphere.

Almost completely transparent $\text{Li}_2\text{B}_4\text{O}_7$ glasses doped with Eu, Dy were obtained in oxidizing and reducing atmosphere of hydrogen.

The following $\text{Li}_2\text{B}_4\text{O}_7$ glasses were obtained: doped with Cr (0.13 wt. % and 2.5 wt. %), and Eu, Dy (2wt.%, 2wt.%).

2.2. Absorption and photoluminescence measurements

The samples were polished to the thickness of about 1 mm. They were also irradiated by gamma photons immediately after growth process. The ^{60}Co gamma source with a power of 1.5 Gy/sec was used. Optical transmission was measured before and after γ treatment using LAMBDA-900 Perkin-Elmer spectrophotometer in UV-VIS range and FTIR-1725 in the IR range. Additional absorption was calculated according to the formula:

$$\Delta K(\lambda) = (1/d) \ln(T_1/T_2) \quad (1)$$

where K is the absorption, λ is the wavelength, d is the sample thickness and T_1 and T_2 are transmissions of the sample before and after a treatment, respectively.

Photoluminescence (PL) was recorded using Perkin-Elmer spectrofluorimeter from 200-900 nm and He-Ne laser excitation of 630 nm.

2.3. Excited state absorption investigations

The excited state absorption (ESA) spectra were measured using a setup which utilized a RD-EXC-150/25 XeCl excimer laser (308 nm) as a source of excitation, a Hamamatsu Xe flash lamp as a source of probe beam and ORIEL InstaSpec II photodiode array detector coupled to MultiSpec 1/8 m spectrograph in the detection branch. The setup operated in pulsed regime and transverse geometry (like in ⁹).

3. RESULTS AND DISCUSSION

3.1 Absorption and photoluminescence

3.1.1 Absorption and the additional absorption measurements

Figs 1-5 show absorption spectra of representative samples obtained at 300K.

In the case of pure $\text{Li}_2\text{B}_4\text{O}_7$ glass (Fig. 1, curve 1) the range of transparency origins at 190 nm (fundamental absorption edge - FAE) and ends at about 2700 nm (lattice absorption). Curve 2 shows absorption of this glass after γ -irradiation with a dose of $5 \cdot 10^4$ Gy.

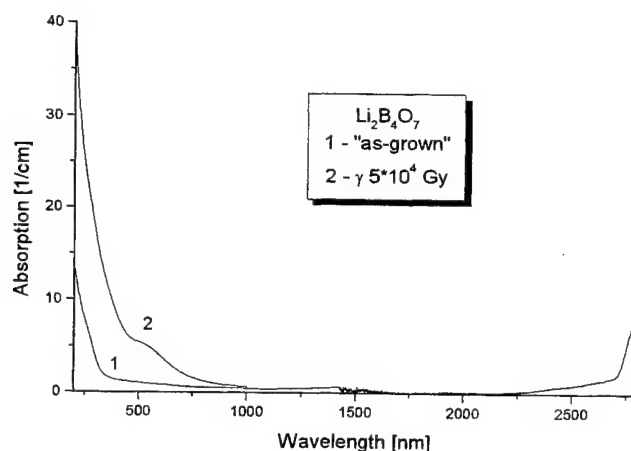


Fig. 1. Absorption of $\text{Li}_2\text{B}_4\text{O}_7$ glass before (1) and after (2) γ -irradiation with a dose of $5 \cdot 10^4$ Gy

In the 0.15wt% chromium doped $\text{Li}_2\text{B}_4\text{O}_7$ glass (Fig. 2a and 2b, curve 1) we observe Cr^{3+} and Cr^{6+} ions spectra. FAE of the glass is equal to 245 nm and lattice absorption origin at 2700 nm. The Cr^{3+} ion has two absorption bands

centered at about 430 and 614 nm due to d-d transition: the former was attributed to the spin-allowed but parity forbidden $^4A_2-^4T_1$ transition and the latter to the spin-allowed but parity-forbidden $^4A_2-^4T_2$ transition. The Cr^{6+} ion has strong absorption band centered at 358 nm and a weak one at 318 nm. It seems that these bands refer to $Cr^{6+}O_4$ complex of $3d^0$ configuration rather than to Cr^{6+} ion⁵. Curve 2 shows absorption of the glass after 10^5 Gy γ -rays while curve 3 the additional absorption. There are seen at least two bands in the additional absorption centered at about 297 and 450 nm. Curve 4 in Fig. 2b shows the absorption of highly doped with Cr (2.5wt.%) $Li_2B_4O_7$ glass. One can see that in case of high doping only 614 nm band due to $^4A_2-^4T_2$ transition in Cr^{3+} ions is present.

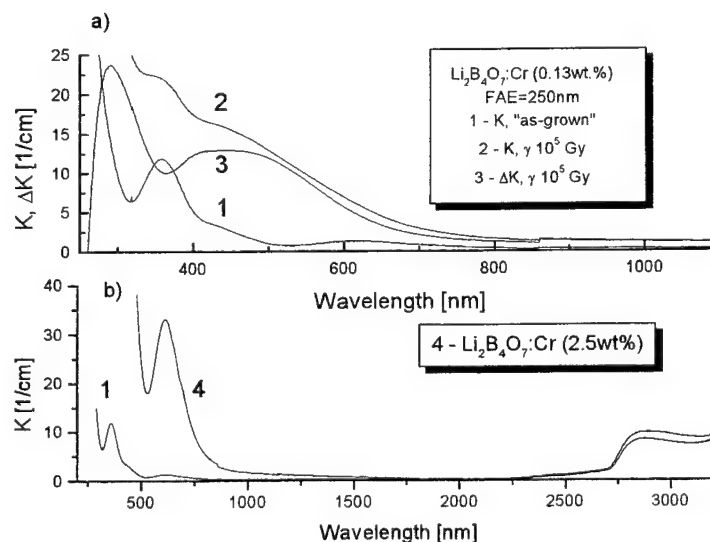


Fig. 2. Absorption before (1) and after γ -irradiation (2) and additional absorption (3) of $Li_2B_4O_7:Cr$ (0.13wt.%) glass, and absorption of $Li_2B_4O_7:Cr$ (2.5wt.%) glass (4)

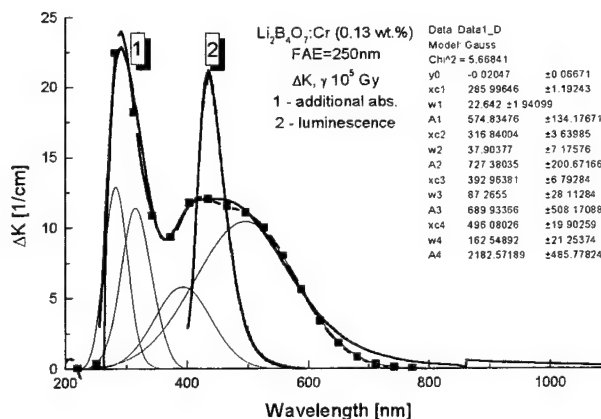


Fig. 3. Gauss distribution of the additional absorption in $\gamma 10^5$ Gy irradiated $Li_2B_4O_7:Cr$ (0.13wt.%) glass (1) and photoluminescence of the glass (2) excited with 260 nm.

Detailed analysis using the fitting with Gauss curves have shown that there are at least four bands in the additional absorption centered at about 285 nm, 316 nm, 392 nm and 496 nm (Fig. 3) which are responsible for 297 nm and 450 nm additional absorptions. Three of them seem correspond to previously described color centers in $Li_2B_4O_7$ glasses. Fourth, at about 392 nm, seems to be responsible for 430 nm emission observed after 260 nm excitation. This broad-band 450 nm

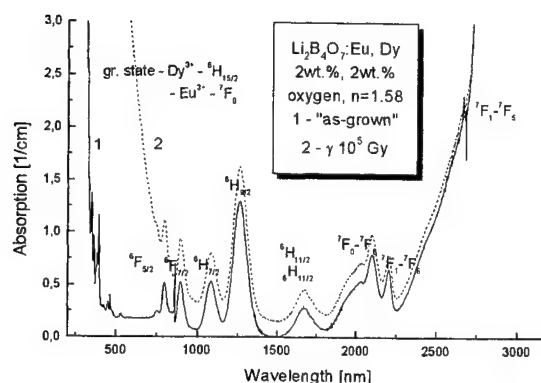


Fig. 4. The absorption of $\text{Li}_2\text{B}_4\text{O}_7:\text{Eu}, \text{Dy}$ (2wt.%, 2wt.%) glass obtained in oxygen atmosphere at 300K before (1) and after (2) γ -irradiation with a dose of 10^5 Gy

additional absorption may be due to $^4\text{A}_2-^4\text{T}_2$, $^4\text{T}_1$ transitions in Cr^{3+} and/or $^3\text{A}_2-^3\text{T}_2$, $^3\text{T}_1-^3\text{T}_2$ transitions in Cr^{4+10} . Parameters of the fitting are listed in a table inside the figure.

Fig. 4 presents the absorption (1) from two ground states: $\text{Dy}^{3+} - ^6\text{H}_{15/2}$ and $\text{Eu}^{3+} - ^7\text{F}_0$ of $\text{Li}_2\text{B}_4\text{O}_7:\text{Eu}, \text{Dy}$ (2wt.%, 2wt.%) glass. As one can see FAE in this case is equal to 270 nm. Refraction coefficient is equal to 1.58. Curve 2 show the absorption after γ -irradiation with a dose of 10^5 Gy. Fig. 5 shows the absorption of Dy^{3+} from $^6\text{H}_{15/2}$ ground state and Eu^{2+} transitions $4f^7-4f^65d^{111}$. FAE is equal to about 355 nm and refraction coefficient 1.62.

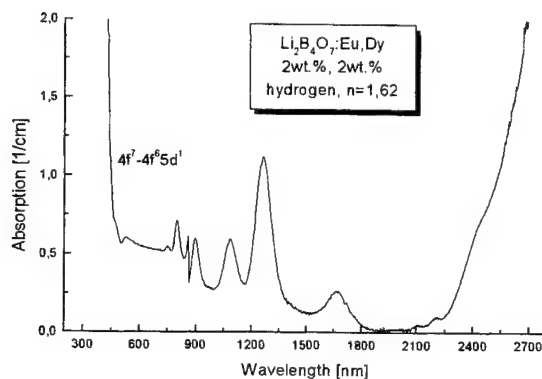


Fig. 5. Absorption of $\text{Li}_2\text{B}_4\text{O}_7:\text{Eu}, \text{Dy}$ (2wt.%, 2wt.%) glass obtained in hydrogen atmosphere

3.1.2. Photoluminescence measurements

Fig. 6 presents photoluminescence of $\text{Li}_2\text{B}_4\text{O}_7:\text{Cr}$ glasses excited with 630 nm He-Ne laser. As one can see gamma irradiation leads to the increase in Cr^{3+} PL intensity.

Fig. 7 shows excitation-emission spectra of $\text{Li}_2\text{B}_4\text{O}_7:\text{Cr}$ (0.13wt.%) glass after γ -exposure with a dose of 10^5 Gy (a) and emission from $\text{Li}_2\text{B}_4\text{O}_7:\text{Cr}$ (2.5wt.%) glass (b) under 270 nm excitation. As one can see emission at 430 nm is due to excitation at 362 nm and 385 nm. This same type of emission is observed also in case of high doping of the glass with Cr (Fig. 7b).

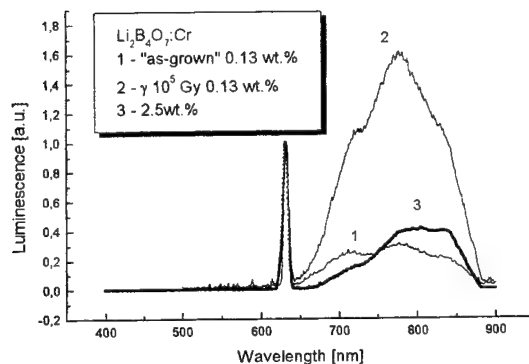


Fig. 6. Photoluminescence of $\text{Li}_2\text{B}_4\text{O}_7:\text{Cr}$ glasses excited by 630 nm He-Ne laser: 0.13wt.%Cr “as-grown” (1), 0.13wt.%Cr γ -irradiated with a dose of 10^5 Gy and 2.5wt.%Cr (3)

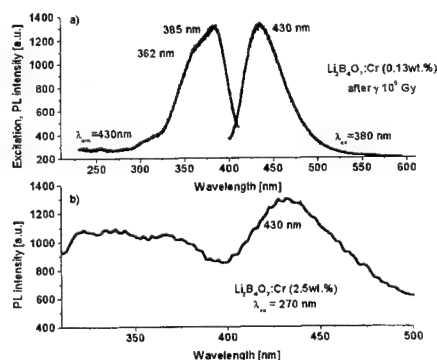


Fig. 7. Excitation-emission spectra of $\text{Li}_2\text{B}_4\text{O}_7:\text{Cr}$ (0.13wt.%) glass after γ -exposure with a dose of 10^5 Gy (a) and emission from $\text{Li}_2\text{B}_4\text{O}_7:\text{Cr}$ (2.5wt.%) glass (b) under 270 nm excitation

The shape of emission spectrum from $\text{Li}_2\text{B}_4\text{O}_7:\text{Eu}$, Dy (2wt.%, 2wt.%) glass strongly depend on the type of growth atmosphere. Fig. 8 shows characteristic emissions for the two basic cases of the obtaining of the glasses: oxidizing (a) and reducing (b) atmospheres¹¹.

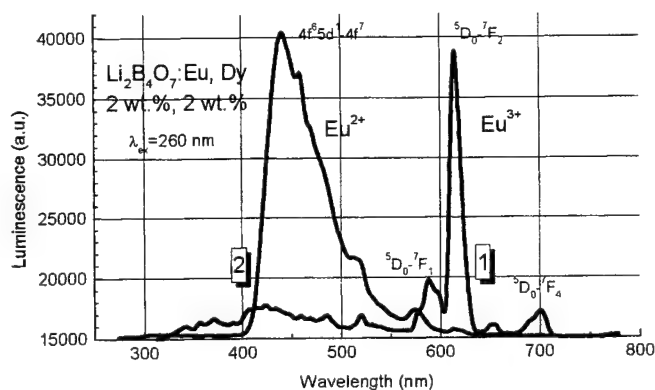


Fig. 8. Emission spectra of $\text{Li}_2\text{B}_4\text{O}_7:\text{Eu}$, Dy (2wt.%, 2wt.%) glasses obtained in oxidizing (1) and reducing (2) atmosphere

3.1.3. Discussion

As one can see in Fig. 1 the absorption spectrum of pure $\text{Li}_2\text{B}_4\text{O}_7$ glass shows a transmission range larger than of other glasses¹. The relevant feature of the glass, as it take place also in case of other glasses, is its high susceptibility to gamma irradiation. Wide, almost non-structural additional absorption in the UV-VIS and NIR of the absorption spectrum (190-1000 nm) is seen with weakly distinguished bands centered at about: 250 nm, 360 nm and 530 nm.

As one can see from Fig. 2 some changes under gamma radiation may be positive one. Our experimental data cannot be interpreted in terms of Cr^{3+} alone, but have to be analyzed in view of the coexistence of Cr ions of different valences. Low chromium doped $\text{Li}_2\text{B}_4\text{O}_7$ glass shows presence of Cr^{3+} and Cr^{6+} ions. The former like exist octahedrally coordinated while the latter tetrahedrally coordinated. The former give well known emission, which is clearly seen in Fig. 6 for $\lambda_{\text{ex}}=630$ nm of He-Ne laser. The latter does not give emission because Cr^{6+}O_4 complex of $3d^0$ configuration seem to be responsible for the 318 and 358 nm absorption. But under gamma irradiation with a dose of 10^5 Gy Cr^{6+}O_4 complex disintegrates giving additional absorption connected with the above mentioned, specific for $\text{Li}_2\text{B}_4\text{O}_7$ color centers and 392 nm band which may be attributed to ${}^3\text{A}_2\text{-}{}^3\text{T}_2$, ${}^3\text{T}_1\text{-}{}^3\text{T}_2$ transitions in Cr^{4+} and/or ${}^4\text{A}_2\text{-}{}^4\text{T}_2$, ${}^4\text{T}_1$ transitions in Cr^{3+} (Fig. 3). Emission spectrum of the gamma irradiated glass reveal an increase in PL intensity of Cr^{3+} ions (Fig. 6), while excitation-emission spectra presented in Fig. 7a suggests presence of other luminescence center. It was previously reported that the Cr^{4+} ion exists in aluminate based glasses¹². The mechanism of forming Cr^{4+} ions was detail discussed in⁵ based on point defects in the glasses. It was stated that Cr^{4+} is observed only in glasses in which oxygen excess defects such as super oxide ion radicals and peroxy linkages are observed. It is possible that in our case Cr^{6+}O_4 complex disintegrates simultaneously to Cr^{4+} and Cr^{3+} . But it demand more and detailed investigations.

Highly doped with chromium $\text{Li}_2\text{B}_4\text{O}_7$ glasses show presence only ${}^4\text{A}_2\text{-}{}^4\text{T}_2$ absorption band (Fig. 2b) although 430 nm emission is also observed (Fig. 7b). Analyzing low and high doping in case of $\text{Li}_2\text{B}_4\text{O}_7$ glass one can state that there exists compositional dependence of the valency states of Cr ions in the glasses. In⁵ it was stated that the contents of Cr^{3+} and Cr^{6+} vary systematically with basicity in the silicate and borate glasses.

Europium¹¹ and dysprosium co-doping characterizes dependency of Eu valence on growth atmosphere. As one can see in Fig. 4 absorption of $\text{Li}_2\text{B}_4\text{O}_7\text{:Eu, Dy}$ glass obtained in oxidizing atmosphere shows many transitions from ground state of Dy^{3+} (${}^6\text{H}_{15/2}$) and ground state of Eu^{3+} (${}^7\text{F}_0$) to higher states. Gamma irradiation does not change a valence of the impurities, but leads to strong additional absorption in the range 270-1000 nm. In case of $\text{Li}_2\text{B}_4\text{O}_7\text{:Eu, Dy}$ glass obtained in reducing atmosphere of hydrogen (Fig. 5) well known transitions of Dy^{3+} ions are seen in the absorption spectrum and the new one $4f^7\text{-}4f^65d^1$ of Eu^{2+} ions. Emission of both types Eu ions is clearly seen in Fig. 8. As it follows from emission measurements both types of Eu ions exists in both types of the obtained glasses, but one of them dominates giving characteristic emission.

3.2 Excited state absorption measurements of Cr:LBO (0.15wt.%) glass

The ESA spectrum of the Cr:LBO (0.15wt.%) glass sample is presented in figure 9. As it is seen, there is no chance to fit this ESA spectrum by a single Gaussian function, whereas two Gaussians {one relatively narrow (2800 cm^{-1}) and another much broader (8200 cm^{-1})} fit the spectrum perfectly. This strongly suggests that the observed ESA under UV excitation consists of transitions to two distinctly defined excited states.

The single configuration coordinate (SCC) diagram can be used to reproduce a characteristic ESA spectrum comparable to that obtained with 308 nm excitation (figure 9). To achieve this, certain assumption has to be made, namely - the existence of additional excited electronic manifold, strongly coupled to the lattice, not detectable in the ground state absorption (GSA) spectrum. Such a state can be related to the $3d^22p^4$ electronic configuration of the central ion - ligand system. The $3d^22p^4$ excited electronic configuration origins from the consecutive excitation of two electrons from the valence band (made mostly of ligands orbitals) to the d orbitals of the central ion. The resulting SCC diagram is presented in Fig. 10 together with definitions of energies taken from the experiment. It shows two positions of the state $|3\rangle$ ($3d^22p^4$) (dashed and solid) corresponding to two qualitatively different situations described in the caption.

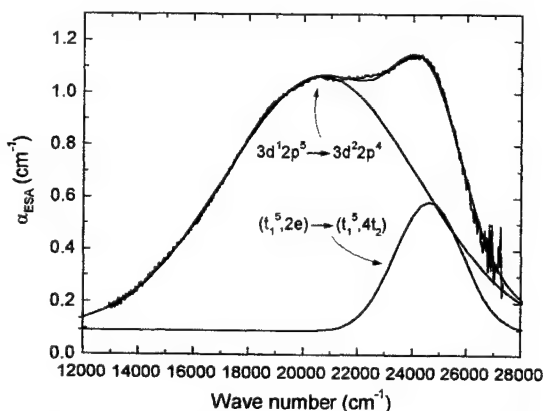


Fig. 9. Experimental ESA spectrum obtained for 308 nm excitation, fit by two Gaussians, and assignation of the contributing ESA bands.

Considering the nature of the electronic configurations which the SCC diagram is constructed from, one should remember that Cr^{6+}O_4 centre is a typical d^0 complex (of approximated T_d symmetry). Then it is possible to write formally the electronic configuration of the central ion-ligand system as $3d^0 2p^6$ ¹³.

4. CONCLUSIONS

It was shown that in case of $\text{Li}_2\text{B}_4\text{O}_7$ glasses it is possible high doping with transition metal and rare-earth element impurities. Obtained compounds are good optical quality, giving clear luminescence especially for Cr^{3+} and Eu^{3+} and Eu^{2+} ions.

It was stated that the presence of Cr^{6+} ion is limited by composition of the starting mixture and atmosphere of the melting (oxidizing). Independently on the above factors in all the glasses there were present Cr^{3+} ions. The 308 nm line excites the $\text{Li}_2\text{B}_4\text{O}_7:\text{Cr}$ (0.13 wt.%) glass within the highest absorption peak which can be ascribed to the following charge transfer transition: $\text{Cr}^{6+}\text{O}_4(3d^0 2p^6) \rightarrow \text{Cr}^{5+}\text{O}^-(3d^1 2p^5)$. Under gamma irradiation Cr^{6+}O_4 complex of $3d^0$ configuration can be disintegrated giving additional absorption band of Cr^{3+} and may be Cr^{4+} ions. There arises luminescence centered at about 430 nm. Gamma irradiation leads to arising of strong additional absorption in the range of 190-1000 nm with weakly distinguished bands peaked at about: 250 nm, 360 nm and 530 nm.

The content and optical characteristics of Eu^{2+} and Eu^{3+} doped $\text{Li}_2\text{B}_4\text{O}_7$ glasses are dependent of the growth atmosphere.

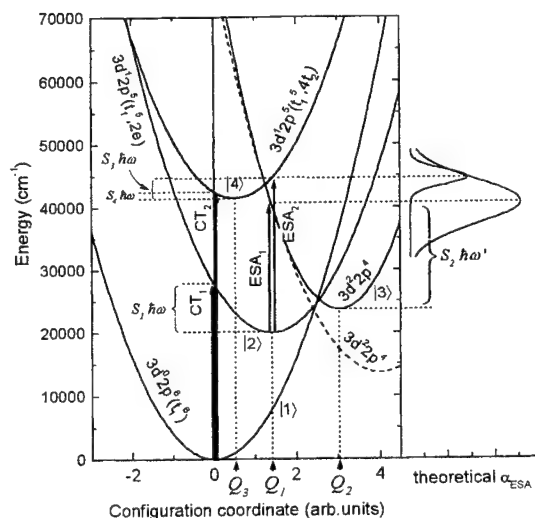


Fig. 10 SCC diagram quantitatively reproducing the ESA spectrum obtained with 308 nm excitation. Right side of the figure shows two Gaussian ESA spectra (of the widths corresponding to the respective relaxation energies) whose composition fits the experiment. The dashed parabola corresponds to the $3d^2 2p^4$ state of linear coupling to the lattice i.e. with the same phonon energy as all remaining states ($\eta\omega = 250 \text{ cm}^{-1}$). The solid parabola of the $3d^2 2p^4$ state corresponds to the different phonon energy $\eta\omega' = 400 \text{ cm}^{-1}$.

ACKNOWLEDGMENT

This work was supported by the State Committee for Scientific Research (KBN) under grants numbers: 2 P03B 117 16 and 2 P03B 063 16 and by Gdańsk University Grant no 5200-5-0299-0.

REFERENCES

1. H.L. Smith and A. Cohen, *J. Phys. Chem. Glasses* **4**, p. 173, 1963.
2. P.C. Schultz, *J. Am. Ceram. Soc.* **57**, p. 307, 1974.
3. A. Lempicki, L. Andrews, S.J. Nettel, B.C. McCollum and E.I. Solomon, *Phys. Rev. Lett.* **44**, p. 1234, 1980.
4. M. Casalboni, V. Ciafardonne, G. Giuli, B. Izzi, E. Paris and P. Proposito, "An optical study of silicate glass containing Cr^{3+} and Cr^{6+} ions", *J. Phys.: Condens. Matter* **8**, pp. 9059-9069, 1996.
5. T. Murata, M. Torisaka, H. Takebe and K. Morinaga, "Compositional dependence of the valency state of Cr ions in oxide glasses", *J. Non-Cryst. Solids* **220**, pp. 139-146, 1997.
6. M. Yamaga, B. Henderson, K.P. O'Donnell and Y. Gao, *Phys. Rev. B* **44**, p. 4853, 1991.
7. A. Majchrowski, "Thermoluminescence in ionising radiation dosimetry", *Proc. SPIE* **2373**, pp. 397-400, 1995.
8. F. Rasheed, K.P. O'Donnell, B. Henderson and D. Hollis, "Disorder and the optical spectroscopy of Cr^{3+} -doped glasses: II. Glasses with high and low ligand fields", *J. Phys.: Condens. Matter* **3**, p. 3825, 1991.
9. Cz. Koepke, A. J. Wojtowicz, and A. Lempicki, "Excited-state absorption in excimer-pumped CaWO_4 crystals", *J. Luminescence* **54**, p. 345, 1993.
10. N.A. Kulagin, W.A. Sandulenko, "Ab initio theory of electronic centers of doped crystals. Chromium ions in oxide compounds", *Fiz. Tverd. Tela*, **31**(1), pp. 243-249, 1989.
11. W. Chen, J.O. Malm, V. Zwiller, Y. Huang, S. Liu, R. Wallenberg, J.O. Bovin and L. Samuelson, "Energy structure and fluorescence of Eu^{2+} in $\text{ZnS}:\text{Eu}$ nanoparticles", *Phys. Rev. B*, **61**(16), p. 11021, 2000.
12. X. Wu, S. Huang, U. Hommerich, W.M. Yen, B.G. Aitken and M. Newhouse, *Chem. Phys. Lett.* **233**, p. 28, 1995.
13. H. Yuan, W. Jia, D. Cohen, W. M. Yen, and B. G. Aitken, "Optical spectroscopy of pentavalent chromium ions in glass", *Mat. Res. Soc. Symp. Proc.* **455**, p. 483, 1997.

X-ray study of Nd:YAG on (111)-oriented Si obtained by pulsed laser deposition

Roman Rumianowski^a, Roman S. Dygdała^b, Franciszek Rozpłoch^b, Andrzej J. Wojtowicz^b,
Monika Wiśniewska^b, and Sławomir Kulesza^b

^a Płock Branch of Warsaw University of Technology, Łukasiewicza 17, 09-400 Płock, Poland

^b Institute of Physics, N. Copernicus University, Grudziądzka 5/7, 87-100 Toruń, Poland

ABSTRACT

Yttrium aluminium garnet ($\text{Y}_3\text{Al}_5\text{O}_{12}$) thin films doped with neodymium have been prepared by Pulsed Laser Deposition (PLD) method on (111)-oriented Si substrates. The substrate was heated up to temperature in the range between 200 and 600 °C. Obtained films were then characterised both by X-ray diffraction (XRD) method using Siemens D5000 diffractometer and radioluminescence spectroscopy.

Keywords: Yttrium aluminium garnet, pulsed laser deposition, XRD, radioluminescence.

1. INTRODUCTION

Pulsed Laser Deposition (PLD) is highly flexible technique for fabrication of thin films. We study Nd:YAG thin films due to their technological applications in optoelectronic systems. Several deposition techniques, such as liquid-phase epitaxy, have been employed to deposit Nd:YAG thin films, but only few publications on pulsed laser deposition of YAG have been reported. These films have been singled out for studies because of their significance in optoelectronic systems. The effects of the substrate temperature on the film orientation and composition and annealing in air have been investigated by the X-ray diffraction (XRD). The quality of the film was also assessed by measuring their photo- and radioluminescence spectra. The emission lines due to the $4f^3$ intra-configuration transitions of Nd^{3+} ions have been identified and analysed. The films produced by PLD are non-uniform in thickness and the thickness profile is determined by the angular distribution of the mass flux of evaporated material ¹. The quality of film strongly depends on substrate temperature ². We have also investigated effect of electric field applied between target and substrate.

2. EXPERIMENTAL DETAILS

The films were deposited using the standard experimental set-up ³. The stainless steel vacuum chamber was evacuated to a pressure of $1 \cdot 10^{-5}$ mbar. Powders of Y_2O_3 , Al_2O_3 and Nd_2O_3 (Aldrich Chem. Co.) were used as the target for deposition process. A XeCl excimer laser beam ($\lambda = 308$ nm, $\tau = 20$ ns, repetition: 15 Hz, fluence: 8 J/cm²) was used for ablation. Target was rotating about 18 rpm. The distance between Si substrate and targets was about 6 cm.

3. RESULTS

3.1. XRD spectra

Thin YAG films have been measured by means of X-rays, using D5000 Siemens diffractometer. In that manner some characteristic structural features of the crystals could be determined but as a rule it was not possible to establish relation concerning those features and parameters of the deposition process. The problem is discussed later.

The main goal of performed XRD analysis was to clarify the two major questions as to structural properties of the deposits. At first, long-time stability of the films was investigated, i.e. it was considered whether structural features of the films do alter under ordinary heat treatment, namely annealing. In fact, long-time stability plays the key role from the point of view of fabrication of many various optoelectronic devices, especially high-power ones. Apart from that, XRD measurements have provided data both on the crystal structure of the films and deposit-substrate interlayer. Those could characterise the PLAD method itself, for example as a result of comparison all the spectra and pointing at their common features.

In the case of SAMPLE A four XRD spectra have been recorded, as presented in Fig.1. Those spectra differ both in sample orientation (on the right, sample was turned within 30° with respect to its normal), and in annealing. Detailed analysis provides the following observations:

- (1) thin YAG film seems to be of good quality indicating by a sharp and distinctive peak at $2\theta = 31.45^\circ$ (indexed as YAG(411) or YAG(330)),

- (2) the above results in the lattice constant $a = 12.055 \text{ \AA}$ which proves that there are tensile stresses induced in the layer,
- (3) since the three other peaks permanently appear in the XRD pattern and their intensities do not depend on the sample orientation it implies that some contribution of disordered phase (existing probably at the YAG-substrate interlayer) must be taking into account,
- (4) after annealing XRD signal is no longer detected which may be caused by re-evaporation of the components attesting to poor long-time stability of the deposited film.

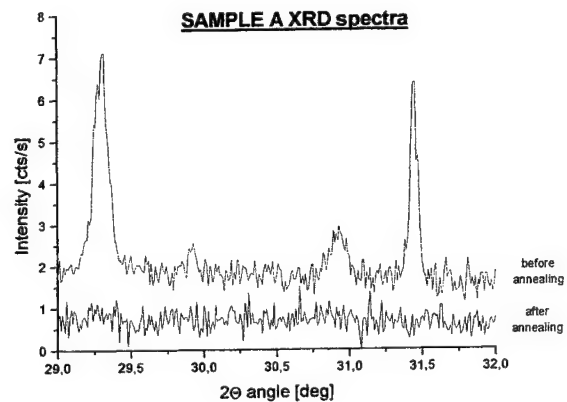
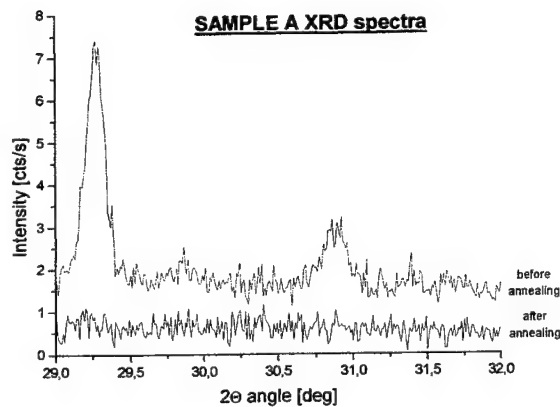


Fig.1. XRD spectra recorded at two different SAMPLE A orientations with respect to its normal: (left) $\phi = 0^\circ$, (right) $\phi = 30^\circ$. Common features are ascribed to strongly disordered structure of the interlayer while sharp peak centred at $2\theta = 31.45^\circ$ is indexed as YAG(411) or YAG(330). Disappearing of the signal after annealing is observed as well.

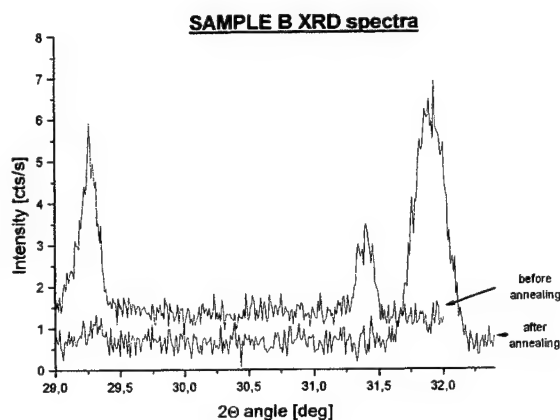


Fig.2. SAMPLE B XRD spectra measured before and after annealing. It appears that under heat treatment peak centred at $2\theta = 31.40^\circ$ both shifts from its un-annealed position within about 0.5° and increases in its intensity.

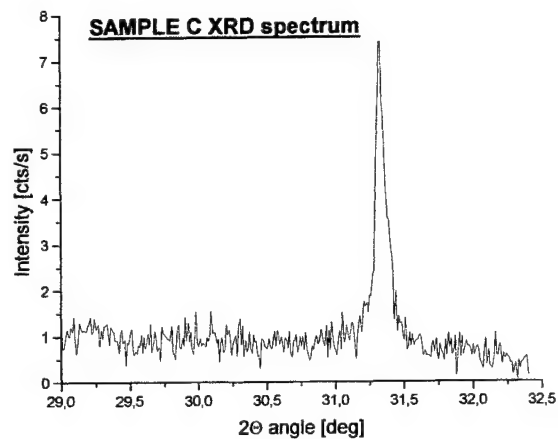


Fig.3. SAMPLE C XRD spectrum coming from un-annealed film in which the only one distinctive feature at $2\theta = 31.32^\circ$ is observed.

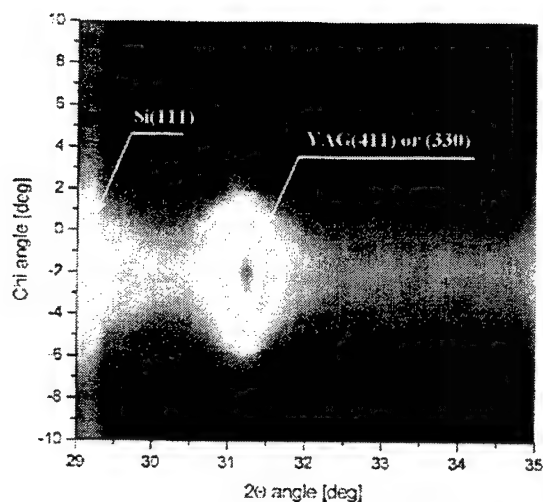


Fig.4. 2-dimensional projection of SAMPLE D XRD pattern plotted both against 2θ as well as χ co-ordinates. Peak shown partly in the left of the figure is Si(111) while that at the centre is YAG(411) or YAG(330). On account of high intensity of the latter (being of the order of magnitude greater than those previously presented) one can state that ordering of the deposit occurs rather than stress-relief behaviour.

Fig.4 shows 2-dimensional projection of XRD pattern of SAMPLE D measured by simultaneous scanning both in 2θ as well as χ co-ordinates. Observed peak is centred at $2\theta = 31.23^\circ$ and $\chi = -2^\circ$. Detailed analysis reveals that Si(111) peak is also centred at $\chi = -2^\circ$ (see on the left of Fig.4). According to that one can conclude that YAG(411) (YAG(330)) planes are parallel to those of Si(111) and therefore heteroepitaxial growth of YAG on Si substrate occurs. Furthermore, predominant orientation of the film is (411) or (330). The highest intensity of the peak (not shown in such projection), being of the order of 200 cts/s, results undoubtedly from considerable thickness of the film. It is not, however, clear whether structure of such thickness is not nearly stress-free (determined lattice constant a is 12.139 Å and is the highest measured). Substantially high FWHM of the peak (about 0.5° and near 3° along 2θ and χ axis, respectively) also points at strong stresses induced in the layer. On the other hand, no signal of the disordered phase is recorded which may be caused by aforementioned heteroepitaxial matching of the two structures.

3.2. Radioluminescence spectra

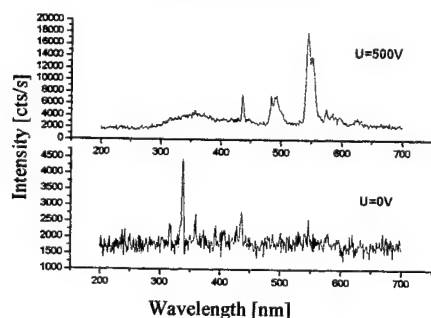


Fig.5. Radioluminescence spectra of Nd:YAG thin films for different voltage between target and substrate. The substrate temperature was 520°C .

In contrast to the previous sample, structure of SAMPLE B seems to be substantially different. It also exhibits quite sharp peak at $2\theta = 31.40^\circ$ indexed as YAG(411) or YAG(330) (before annealing), but another similarities are no further maintained. According to Fig. 2, annealed film reveals very distinctive feature at $2\theta = 31.90^\circ$ so that shift of about 0.5° is observed (with respect to un-annealed sample). In addition, intensity of the peak increases by a factor of 2 after annealing. Assuming that under heat treatment stress-relief behaviour occurs one can expect diminishing of induced stresses. However, observed shift is as high as 0.5° , which indicates that tensile stresses turns into compressive ones (lattice constant a changes from 12.076 to 11.892 Å before and after annealing, respectively). All those suggest that ordering of the growing crystal occurs rather than its stress-relief behaviour. In fact, thermally excited atoms are able to move slightly from their previous positions into new ones in order to decrease energy of the crystal (minimisation of the energy). As a result, rearrangement of the structure is observed.

In the case of SAMPLE C there appears only one diffraction peak in the whole range investigated, centred at $2\theta = 31.33^\circ$ and indexed as YAG(411) or YAG(330). This gives lattice constant as high as 12.103 Å (see Fig.3). Unfortunately, similar heat treatment of the sample was not carried out so that comparison of the results with those previously obtained was not possible.

In Fig.5 we present radioluminescence spectra of Nd:YAG thin films for two different voltages between the target and the substrate. The spectrum of the film obtained under the voltage of 500 V clearly shows sharp lines that are due to $4f^2$ intraconfigurational transitions of the Nd^{3+} ion. The lines, at about 430, 480 and 550 nm, correspond to transitions that originate at lower lying levels. There is, as expected, no $d-f$ emission but there are also some missing $f-f$ emission lines that originate at some higher lying levels of the $4f^2$ configuration and are usually visible in the Nd:YAG monocrystal radioluminescence spectra. The spectrum reveals also some hardly visible broad band emission at 300 to 400 nm that could represent the so-called "host" emission, characteristic of the undoped YAG. Interestingly the second spectrum, of the Nd:YAG film obtained under no voltage, shows no emission at all.

In Fig.6 we show a photoluminescence spectrum of the Nd:YAG thin film that was annealed in air for 1 hour at 800°C . The

exciting light wavelength was set at 186 nm. The spectrum reveals a broad band that resembles the "host" emission band. There also is a rich structure imposed on the broad band that could be due to Nd^{3+} $f-f$ emission lines observed in some Nd:YAG monocrystals.

Finally, in Fig.7 we present radioluminescence spectra obtained at three different spots of the same Nd:YAG film the spectrum of which was shown in Fig.5 (500 V). The differences between the spectra are quite likely indicative of the quality of the local crystalline environment and/or statistical variations of the local Nd concentration.

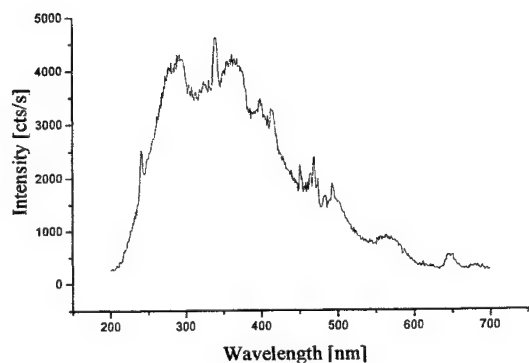


Fig.6. Photoluminescence spectrum of Nd:YAG. The ample was annealed in air for 1hour in 800 °C.

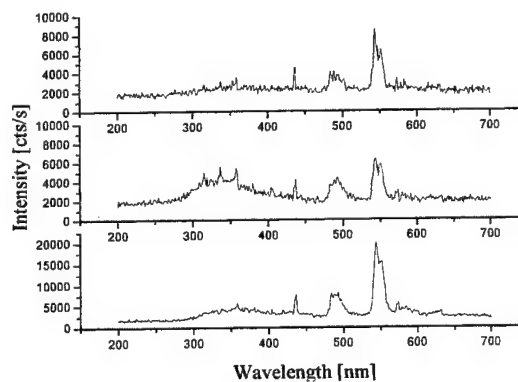


Fig.7. Radioluminescence spectra coming from the three different regions of the same film.

4. CONCLUSIONS

In the present work, the Nd:YAG thin films on (111)-oriented Si substrates have been obtained by two techniques: PLD method with electric field between target and substrate, and PLD method with annealing in air. Those have been proved to possess some interesting structural and electronic properties that have been determined using X-ray diffractometry supported by radioluminescence spectroscopy. XRD patterns reveal that performed annealing may lead either to re-evaporation of the film components or to ordering of atom arrangement in a deposited crystal. In spite of that, however, stress-relief behaviour does not occur. The absence of some $f-f$ emission lines in radioluminescence of Nd:YAG films that are present in the spectrum of Nd:YAG monocrystals calls for further studies. This observation could potentially provide new and interesting information about (quenching, energy transfer) processes that are of importance in the films. It is also interesting to note that radioluminescence can potentially provide a convenient measure of the film quality.

REFERENCES

1. S. I. Anisimov, B.S. Luk'yanchuk, A. Luches, "An analytical model for three-dimensional laser plume expansion into vacuum in hydrodynamic regime", *Applied Surface Science*, Vol. 96-98, pp. 24-32, 1996.
2. M. Ezaki, H. Kumagai, K. Kobayashi, K. Toyoda, M. Obara, "Crystal growth of Nd:YAG laser films on various substrates by pulsed laser deposition". *Japanese Journal of Applied Physics Part 1-Regular Papers Short Notes & Review Papers*, Vol.34, pp. 6838-41, 1995.
3. R. Rumianowski, R. S. Dygdała, W. Bała, J. Sylwisty, "X-ray Characterisation of PbSe/Si Layers Grown by PLD method", ICSSC Zakopane 2000 (to be published in Proc. of SPIE).

Effect of divergence of light wave and alignment of crystal on the response of electrooptic modulators

Marek Izdebski* and Włodzimierz Kucharczyk

Institute of Physics, Technical University of Łódź,
ul. Wólczńska 219, 93-005 Łódź, Poland

ABSTRACT

In this work we report on numerical investigations of the effect of the light beam divergence or imperfect crystal alignment on the response of electrooptic modulators. Resulting nonlinearities are discussed both in terms of nonlinear distortions of modulators and as related to errors in measurements of quadratic electrooptic coefficients. Our calculations based on the Jones calculus have been performed for uniaxial crystals including KDP, and its isomorphs, and LiNbO₃. The results obtained confirm that either the response of the modulators or results of electrooptic measurements can be significantly affected by the light divergence or imperfections in the crystals alignment.

Keywords: Quadratic electrooptic effect, linear electrooptic effect, electrooptic modulators, KDP-type crystals, LiNbO₃, Jones matrices.

1. INTRODUCTION

Electrooptic crystals are widely employed in modulators. In recent years the electrooptic effect is also applied in high-voltage sensors and optical voltage transformers. In all these devices the knowledge of nonlinear distortions of the output signal is very important. Usually, the distortions are sensitive to the divergence of the light beam and crystal alignment. Measurements of the quadratic electrooptic coefficients can be affected by these factors as well (see, for example, Refs ¹⁻⁴).

The aim of this work is to calculate the nonlinear distortions and modulation efficiency in electrooptic modulators related to the light divergence. Our approach is based on the Jones calculus.⁵⁻⁷ In addition, we consider experimental errors that can appear in measurements of the quadratic electrooptic coefficients.

2. METHOD

The intensity of the light passed through the crystal and a quarter-wave plate sandwiched between crossed polarizer and analyzer is analyzed. In this work we take into account modulators with the light beam propagating along the optic axis of uniaxial crystal. The quarter-wave plate is introduced to provide the modulation at the middle point of the linear portion of the dependence of the relative light intensity on the induced phase difference, i.e. at the middle of the transmission characteristic of the modulator.

In our calculations the light entering the crystal plate and that emerging from the modulator is described by one-column Jones vectors^{5,6} ϵ_o and ϵ

$$\epsilon_o = \begin{bmatrix} E_{xo} \\ E_{yo} \end{bmatrix}, \quad \epsilon = \begin{bmatrix} E_x \\ E_y \end{bmatrix}, \quad (1)$$

where E_{xo} , E_x and E_{yo} , E_y are the x- and y-components of the electric field of the light-wave entering the crystal and emerging from the analyzer, respectively. The light intensity can be found as

$$I = |E_x|^2 + |E_y|^2. \quad (2)$$

* Further author information -

MI: Email: izdebski@ck-sg.p.lodz.pl,

WK: Email: kucharcz@ck-sg.p.lodz.pl

Optical elements, i.e. the quarter-wave plate, uniaxial crystal and analyzer, are represented by the Jones matrices J_1 , J_2 and J_3 , respectively. The response of modulator ε is calculated from equation⁵

$$\varepsilon = J_3 J_2 J_1 \varepsilon_0. \quad (3)$$

Jones vectors cannot describe unpolarized light, therefore, in Eq. (3) the vector ε_0 corresponds to the light passed through the polarizer. By omitting an expression connected with the phase of light-wave electric field, the vector ε_0 is given as

$$\varepsilon_0 = \begin{bmatrix} \cos \theta \\ \sin \theta \end{bmatrix}, \quad (4)$$

where θ is the azimuth of polarizer.

General form of the Jones matrices for the objects under consideration can be written as⁷

$$J = \begin{bmatrix} T_f \cos^2 \alpha_f + T_s \sin^2 \alpha_f e^{-i\Gamma} & \sin \alpha_f \cos \alpha_f (T_f - T_s e^{-i\Gamma}) \\ \sin \alpha_f \cos \alpha_f (T_f - T_s e^{-i\Gamma}) & T_f \sin^2 \alpha_f + T_s \cos^2 \alpha_f e^{-i\Gamma} \end{bmatrix}, \quad (5)$$

where T_f and T_s describe the transmission of fast and slow waves, respectively, α_f is the azimuth of the fast wave, and Γ is the phase difference between the slow and fast waves. In our calculations we assumed $T_f = 1$ and $T_s = 0$ for the polarizer and $T_f = T_s = 1$ for other plates. Γ in the quarter-wave plate can be dependent on the light divergence, however, we assumed the quarter-wave plate being thin enough to neglect this.

To investigate the effect of the beam divergence numerical calculations were performed. The deviations of the light propagation vector \mathbf{k} from the optic axis in uniaxial crystals, i.e. from the [001] direction, we expressed in terms of the angles β and γ , as defined in Fig. 1.

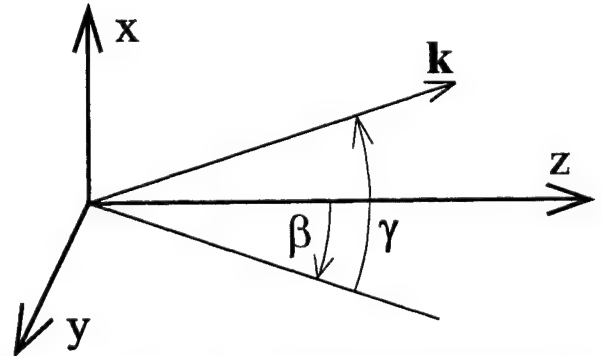


Fig. 1. Angles β and γ describing the deviation of the propagation vector \mathbf{k} from the optic axis direction.

3. ELECTROOPTIC MODULATORS

Many important applications of the linear electrooptic effect involve the use of uniaxial crystals with the light path close to the optic axis. Previously, the effect of deviations of the laser beam from this direction has been considered in terms of the approach employing the optical index ellipsoid. It has been shown that the deviations can affect the depth of modulation at the fundamental frequency and give rise to non-linear distortions of the output signal (see, for example, Refs. ^{1-4, 8-14}).

According to the crystal symmetry and magnitudes of relevant electrooptic coefficients two different kinds of electrooptic modulators may be used. Devices with the electric field applied parallel and perpendicular to the direction of the light beam involve the use of the so-called longitudinal and transverse modulators, respectively. In this work we consider examples of these two types of modulators.

3.1. Longitudinal modulator - the example of the KDP crystal

Well known electrooptic uniaxial crystals that may be used in the longitudinal modulator are members of the potassium dihydrogen phosphate (KDP) family. This is because of relatively large value of the linear electrooptic coefficient r_{63} . It is readily shown that when both the light path and the modulating electric field are exactly parallel to the [001] direction, the relative modulation amplitude of the light intensity at the fundamental frequency I_ω / I_0 is given by

$$I_\omega / I_0 = \pi n_o^3 r_{63} V_o / \lambda \quad (6)$$

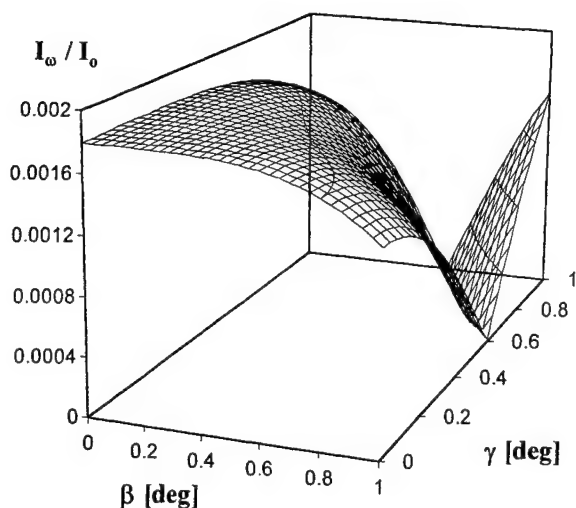


Fig. 2. Dependence of the relative modulation amplitude of the light intensity at the fundamental frequency I_ω / I_0 on the angles β and γ plotted for KDP.

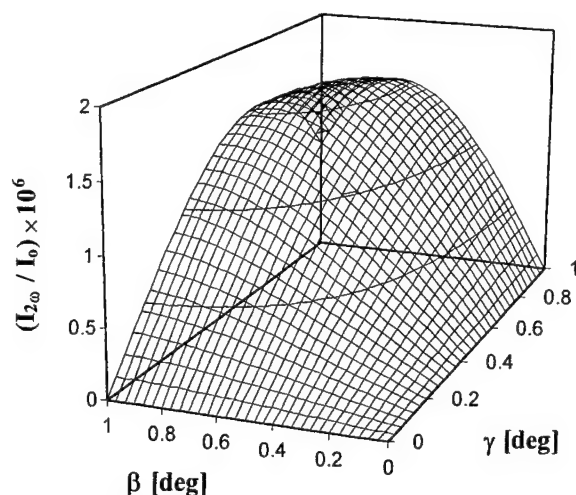


Fig. 3. Dependence of the relative modulation amplitude $I_{2\omega} / I_0$ at the second harmonic on the angles β and γ plotted for KDP.

Here, I_0 is the intensity of the light entering the crystal, n_0 is the ordinary refractive index, V_0 is the voltage amplitude of the modulating electric field and λ is the wavelength. When the light divergence is neglected the relative modulation amplitude of the light intensity at the second harmonic $I_{2\omega} / I_0$ is equal to zero and the modulation efficiency at the fundamental frequency is independent of the crystal length. The higher-order harmonics do not appear in the response of the modulator as well. Any deviation of the light from the [001] direction can lead to a decrease in I_ω and an increase in $I_{2\omega}$. Moreover, when the light divergence cannot be neglected, these factors become to be dependent on the crystal length. The changes in I_ω / I_0 and $I_{2\omega} / I_0$ obtained in this work by using the Jones calculus are illustrated in Figs 2 and 3. The relative nonlinear distortions described by the ratio $I_{2\omega} / I_\omega$ is presented in Fig. 4. Results shown in Figs 2-4 correspond to the crystal length 1 cm, the amplitude of modulating electric field 10^3 V/m, and the wavelength $\lambda = 630$ nm. The transmission axis of the polarizer is taken to be parallel to the [100] direction. The values of linear and quadratic electrooptic coefficients used in our calculations were taken from Refs 13-15.

3.2. Transverse modulator - the example of the LiNbO_3 crystal

The use of transverse modulators is often very convenient. When the thickness and length of the crystal are different, the increase of the ratio length to thickness leads to the decrease in the voltage necessary to drive the modulator. Moreover, relatively easily one can obtain an uniform electric field in electrooptic crystal.

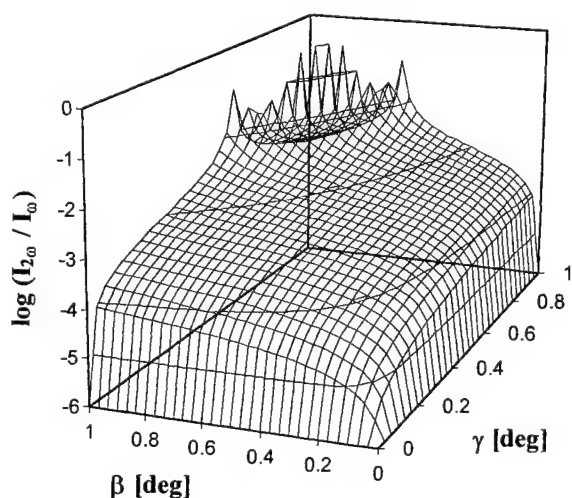


Fig. 4. Dependence of the relative nonlinear distortions $I_{2\omega} / I_\omega$ on the angles β and γ plotted for KDP.

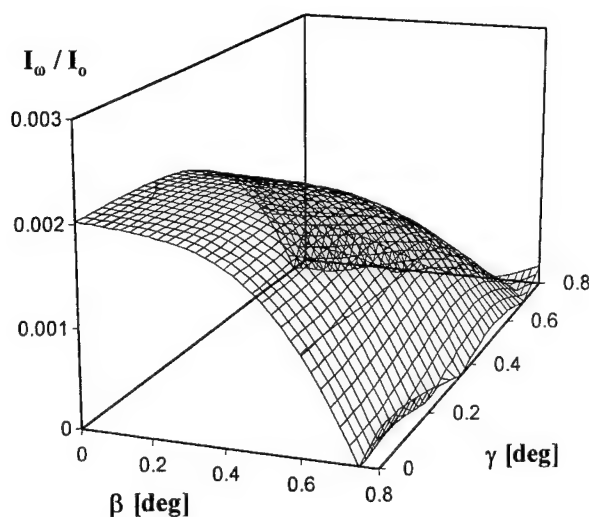


Fig. 5. Dependence of the relative modulation amplitude of the light intensity at the fundamental frequency I_ω / I_0 on the angles β and γ plotted for LiNbO_3 .

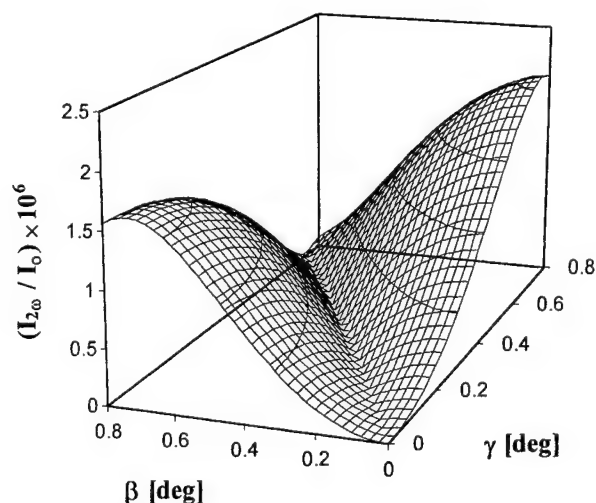


Fig. 6. Dependence of the relative modulation amplitude of the light intensity $I_{2\omega} / I_0$ at the second harmonic on the angles β and γ plotted for LiNbO_3 .

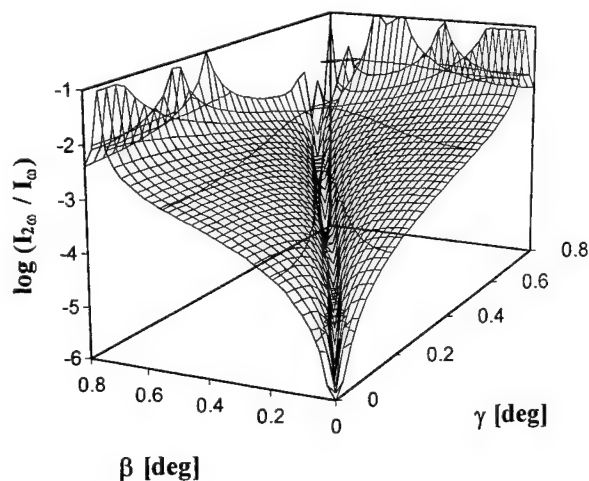


Fig. 7. Dependence of the relative nonlinear distortions $I_{2\omega} / I_0$ on the angles β and γ plotted for LiNbO_3 .

The LiNbO_3 crystal is considered as the example of medium useful in applications in transverse modulators. It may be shown that when the modulating a.c. electric field is applied along the $[010]$ direction and \mathbf{k} is exactly parallel to the $[001]$ direction, the relative modulation amplitude of the light intensity at the fundamental frequency I_ω / I_0 is given by

$$I_\omega / I_0 = \pi n_0^3 r_{12} V_0 L / \lambda t. \quad (7)$$

In Eq. (7) L is the light path in the crystal plate and t is the thickness of the crystal. Here, again, deviations of the light from the $[001]$ direction can lead to the decrease in I_ω / I_0 and increase in $I_{2\omega} / I_0$. The changes in I_ω / I_0 and $I_{2\omega} / I_0$ obtained for the crystal length 1 cm, the amplitude of the modulating electric field 10^3 V/m, and the wavelength $\lambda = 630$ nm are shown in Figs 5-7. The values of linear electrooptic coefficients used in our calculations were taken from Ref. 17. The angle between the transmission axis of the polarizer and the $[100]$ direction was set at $\pi/4$.

4. MEASUREMENTS OF THE QUADRATIC ELECTROOPTIC EFFECT

Studies of electrooptic properties of crystals are of interest from the point of view both applications and an understanding of the nature of relevant nonlinear susceptibilities. The latter is important because the same nonlinearities are responsible for other nonlinear optical effects (see, for example, Refs 9,12-14,18-23). Furthermore, measurements of quadratic electrooptic coefficients allow to investigate the paraelectric-ferroelectric phase transition in ferroelectric crystals.¹⁶

As an example, in this work we present results obtained for the simulation of measurements of the quadratic electrooptic coefficient $g_{11} - g_{12}$. This coefficient may be determined in the KDP crystal with the electric field applied along the $[100]$ direction and the laser beam passed in the $[001]$ direction. Assuming the light divergence to be negligible, the $g_{11} - g_{12}$ coefficient may be experimentally determined as

$$g_{11} - g_{12} = \frac{4\lambda t^2}{\pi L n_o^3 V_o^2} \frac{I_{2\omega}}{I_o} \quad (8)$$

Even small deviations of the light from the optic axis direction can significantly affect the measurement.^{8,9} When allowing for the divergence, an erroneous value, denoted here as $g'_{11} - g'_{12}$ can be predicted from the response of the modulator. Results shown in Fig. 8 confirm earlier predictions drawn from the analysis of the electric field induced changes in the optical indicatrix. Our plot describes the response of the crystal plate of length 1 cm, the amplitude of modulating electric field 10^5 V/m, and the wavelength $\lambda = 630$ nm. The values of linear and quadratic electrooptic coefficients used in our calculations were taken from Refs.¹³⁻¹⁵. The angle between the transmission axis of the polarizer and the [100] direction was set at $\pi/4$.

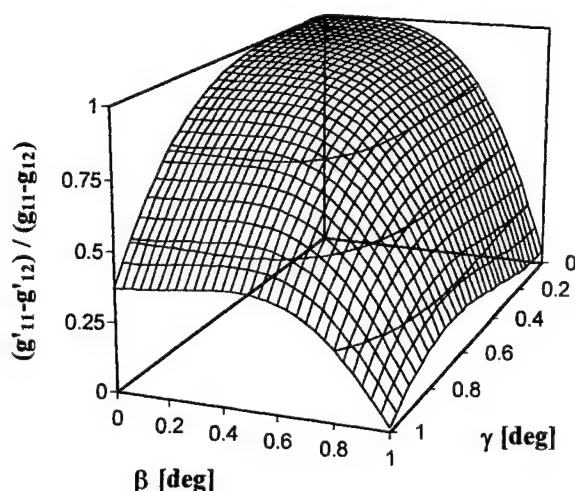


Fig. 8. The relative error in determination $g_{11} - g_{12}$ of KDP plotted against the angles β and γ .

5. CONCLUSIONS

Our results obtained within the framework of the Jones matrices approach support the observations related to the correlation between the efficiency of modulation at the fundamental frequency or non-linear distortions in the response of electrooptic modulators and the divergence of the light beam from the optic axis direction^{1-4,8}. These earlier findings have been obtained employing the optical indicatrix approach. Our numerical calculations confirm previous predictions that in measurements of quadratic electrooptic coefficients the error depends strongly on the divergence of the light. The error may origin from two different sources. Relatively well recognised is the shift from the middle point of the linear part of the transmission characteristic of the modulator. The second one can result from a superposition of two linear in the field effects, namely, changes in the components of the impermeability tensor and the electric field induced changes in the azimuth of the fast wave.

REFERENCES

1. M.S. Ahmed and J.M. Ley, "Defects in the performance of electrooptic modulators using class $\bar{4}2m$ crystals", *J. Phys. D: Appl. Phys.* **4**, pp. 1637-1641, 1974
2. T. Tudor, "Harmonic structure of light modulated by longitudinal electrooptic effect in crystals of class $\bar{4}2m$ ", *J. Optics* **14**, pp. 161-168, 1983
3. P. Górski and W. Kucharczyk, "On the measurement of the quadratic electrooptic effect", *Phys. Stat. Sol. (a)* **100**, pp. K73-76, 1987
4. P. Górski and W. Kucharczyk, "On the measurement of electrooptic coefficients by the static polarimetric technique", *Optik* **83**, pp. 7-10, 1989
5. R.C. Jones, "A new calculus for the treatment of optical systems. I. Description and discussion of the calculus", *J. Opt. Soc. Am.* **31**, pp. 488-493, 1941
6. R.C. Jones, "New calculus for the treatment of optical systems. VIII. Electromagnetic theory", *J. Opt. Soc. Am.* **46**, pp. 126-131, 1956
7. I. Ścierański and F. Ratajczyk, "The Jones matrix of the real dichroic elliptic object", *Optik* **68**, pp. 121-125, 1984
8. P. Górski, W. Kucharczyk, "On the application of uniaxial crystals in modulators", *J. Optics* **20**, pp. 187-192, 1989
9. W. Kucharczyk, "Quadratic electro-optic effect and second-order strain derivatives of electronic susceptibility", *Physica B* **176**, pp. 189-208, 1992
10. M. Izdebski, W. Kucharczyk and R.E. Raab, "Effect of beam divergence from the optic axis in an electrooptic experiment to measure an induced Jones birefringence", to be published

11. M.J. Gunning, R. Ledzion, P. Górski and W. Kucharczyk, "Studies of the quadratic electrooptic effect in KDP-type crystals", International Conf. on Solid State Crystals '98: Single Crystal Growth, Characterization, and Applications, A. Majchrowski; J. Zielinski; Eds. *Proc. SPIE* **3724**, pp. 249-255, 1999
12. W. Kucharczyk, M.J. Gunning, R.E. Raab and C. Graham, "Interferometric investigation of the quadratic electro-optic effect in KDP", *Physica B* **212**, pp. 5-9, 1995
13. M.J. Gunning, R.E. Raab, P. Górski and W. Kucharczyk, "The quadratic electrooptic effect and estimation of antipolarization in ADP", *Ferroelectric Lett.* **24**, pp. 63-68, 1999
14. M.J. Gunning, R.E. Raab and W. Kucharczyk, "Magnitude and nature of the quadratic electro-optic effect in KDP and ADP single crystals", to be published
15. Landolt-Börnstein: *Numerical Data and Functional Relationships in Science and Technology*, New Series, Group III vol. 18, Springer Verlag, Berlin-Heidelberg-New York, 1984
16. P. Górski, R. Ledzion and W. Kucharczyk, "Application of quadratic electrooptic effect to investigate paraelectric-ferroelectric phase transition in KDP-type crystals", *Proceedings of the Fifth International Conference on Intermolecular Interactions in Matter (IIM-5)* Lublin 1999, Politechnika Lubelska, Eds. K. Sangwal, E. Jartych and W. Polak
17. T.A. Maldonado and T.K. Gaylord, "Electrooptic effect calculations: simplified procedure for arbitrary cases", *App. Optics* **27**, pp. 5051-5066, 1988
18. W. Kucharczyk, "A bond-charge calculation of the quadratic electro-optic effect in LiF", *J. Phys. C: Solid State Phys.* **20**, pp. 1875-1880, 1987
19. W. Kucharczyk, "The first- and second-order strain derivatives of electronic dielectric constants in alkali halides", *J. Phys. Chem. Solids* **55**, pp. 237-242, 1994
20. W. Kucharczyk, "Bond polarizability approach to nonlinear phenomena in crystals", International Conf. on Solid State Crystals '98: Single Crystal Growth, Characterization, and Applications, A. Majchrowski; J. Zielinski; Eds. *Proc. SPIE* **3724**, pp. 69-74, 1999
21. W. Kucharczyk and F.L. Castillo-Alvarado, "Calculations of hyper-Raman tensor components of alkali halides", *J. Phys.: Condens. Matter* **11**, pp. 305-309, 1999
22. W. Kucharczyk, F.L. Castillo-Alvarado, P. Górski and R. Ledzion, "Calculations of nonlinear refractive index of alkali halides", *Opt. Quant. Electron.* **32**, in print, 2000
23. W. Kucharczyk, F.L. Castillo-Alvarado, P. Górski and R. Ledzion, "The effective band charge in alkali halides – another manifestation of the crystals ionicity", *J. Phys. Chem. Solids*, accepted to print

Investigations of YAG:Er³⁺, Yb³⁺ and YAG:Co²⁺ crystals for laser application

Z. Mierczyk ^{a,*}, K. Kopczyński ^a, M. Kwaśny ^a, T. Łukasiewicz ^{b,c}, Z. Frukacz ^c and Z. Gałązka ^c

^a Institute of Optoelectronics, Military University of Technology
2 Kaliski Str., 00-908 Warsaw, Poland

^b Institute of Technical Physics, Military University of Technology
2 Kaliski Str., 00-908 Warsaw, Poland

^c Institute of Electronic Materials Technology,
133 Wólczyńska Str., 01-919 Warsaw, Poland

ABSTRACT

The results of examinations of spectroscopic properties and generation parameters of new active media, i.e., Er³⁺ and Yb³⁺ doped YAG crystals are given. Erbium and ytterbium doped YAG single crystals were obtained by the Czochralski method. The spectral properties and laser characteristics were investigated. Absorption spectra of Er³⁺ and Yb³⁺ - doped active media were measured in the spectral range 190÷5000 nm at room temperature. Excitation and luminescence spectra were also recorded at room temperature with a JOBIN-YVON spectrofluorimeter using a diode laser (POLAROID 4300, 980 nm, 1 W) as an excitation source. The measurements of the lifetime of the Er³⁺ ions in the upper laser level (⁴I_{13/2}) of the samples were made by the direct method with pulse excitation.

We present also the results of investigations on spectroscopic properties and non-linear absorption effect in YAG: Co²⁺ crystal - new absorber used for the systems generating giant-pulse radiation at 1.5 μm.

keywords: eyesafe laser, active media, saturable absorbers, erbium doped YAG, ytterbium doped YAG, cobalt doped YAG

1. INTRODUCTION

There is considerable interest in compact pulsed high peak power laser sources emitting at wavelengths near 1.5 μm. Rangefinders and other applications with free space propagation could be strong benefit of such devices. The wavelength of around 1.5 μm is in the eyesafe regime where significantly higher pulse energies can be used without human eyes damaging¹. For wavelength of 1.55 μm there is the minimum of absorption of quartz optical fibres, within the range of 1.5÷2 μm atmosphere transmission is the highest but absorption of biological media and atmospheric pollution of some type are very strong. Thus, „eye-safe” lasers can be applied for telecommunication, optical radars, distance measurements, remote detection of contaminations, and medicine².

In the first laser systems generating eyesafe radiation, a Raman shifter was used in form of a methane cell in which a conversion of radiation, generated by YAG:Nd³⁺ (λ=1064 nm), into radiation of wavelength of 1.54 μm occurred. Molecular crystals (e.g., Ba(NO₃)₂, CaCO₃, or CaSO₄), in which the effect of forced Raman scattering occurs, are competitive with high-pressure gaseous cells. Because the efficiency of this process is not high, these systems have not found practical applications³. Parametric generation of wavelengths near 1.5 μm in nonlinear crystals was practically not used. The main obstacle in this case is the difficulty to ensure stable laser operation within a wide range of temperatures⁴.

At the beginning of the 90's an erbium-ytterbium-phosphate glass was used for the first time for generation of laser radiation at the wavelength of 1.5 μm⁵. The laser systems including this active material have found many practical applications^{6,7}. The drawback of phosphate glass is its low thermal and mechanical stability. So, new search is carried out for new, higher resistant glass matrices and crystalline media⁸.

Efficient materials generating radiation within "eye-safe" range are Cr⁴⁺ doped crystals. Wide luminescence band of Cr⁴⁺ ions within the range of 1.2÷1.6 μm, enables us to obtain tunable generation in this spectral range but absorption within the range of 900÷1100 nm makes possible to pump with laser diode of 980 nm or neodymium laser of 1064 nm.

* e-mail: zmierczy@wat.waw.pl

Pumping YAG:Cr⁴⁺ with diode laser gives tunable generation within the range of 1350-1550 with its maximum at 1450 nm⁹. Other crystals used in systems of generation of eye-safe radiation are active media doped with Er³⁺ and Yb³⁺ ions. Yb³⁺ ions are used in Er³⁺ doped crystalline media in order to increase excitation efficiency, especially in diode pumped laser systems¹⁰.

Searching of non-linear absorbers for laser generating radiation at 1.5 μ m are focused on materials doped with the following ions; U²⁺, Co²⁺, and Er³⁺¹¹⁻¹⁴. The most advantageous spectroscopic parameters [active cross section and saturation energy (intensity)] have media doped with cobalt; LaMgAl₁₁O₁₉:Co²⁺ (LMA:Co) and SiO₂-ZnO-Al₂O₃:Co²⁺ ceramics. Absorbers with bivalent cobalt ions in tetrahedral sites are characterised by various spectroscopic parameters. YAG:Co²⁺ and YSGG:Co²⁺ crystals are so-called "fast absorbers" with relaxation time of about 1 ns¹¹ and ZnSe:Co²⁺ is "slow absorber" with relaxation time of 290 μ s¹⁴.

2. CRYSTAL GROWTH

The crystals were obtained by the Czochralski method, using iridium crucibles of external dimensions ϕ 50×50×1.5 mm. Insulating housing of the crucible was made of alundum ceramics and granular zirconium ceramics stabilised with hafnium (ZrO₂:HfO₂) that filled the space between the crucible, the tube, and alundum base.

The crystallisation processes were carried out in nitrogen atmosphere containing small amount (a fraction of percentage) of oxygen. High purity oxides Y₂O₃(5N) and Al₂O₃(5N) from J.M. & PROD., Er₂O₃(5N), Yb₂O₃(5N) and CoO(4N) from ALDRICH were used as initial materials.

Crystals of a diameter of about 25 mm and a length of 60 mm with following compositions were obtained:

YAG:Er³⁺ (1.5% Er³⁺)

YAG: Er³⁺, Yb³⁺ (0.9% Er³⁺, 9% Yb³⁺)

YAG: Er³⁺, Yb³⁺ (0.5% Er³⁺, 5% Yb³⁺)

YAG:Co²⁺ (2% Co²⁺)

In Fig.1 typical YAG:Er³⁺,Yb³⁺ and YAG:Co²⁺ single crystal grown by Czochralski method is presented. In all obtained crystals the core area of the characteristic threefold symmetry was found. The core has clear, sharp boundaries and its area has a diameter of about 2 mm.

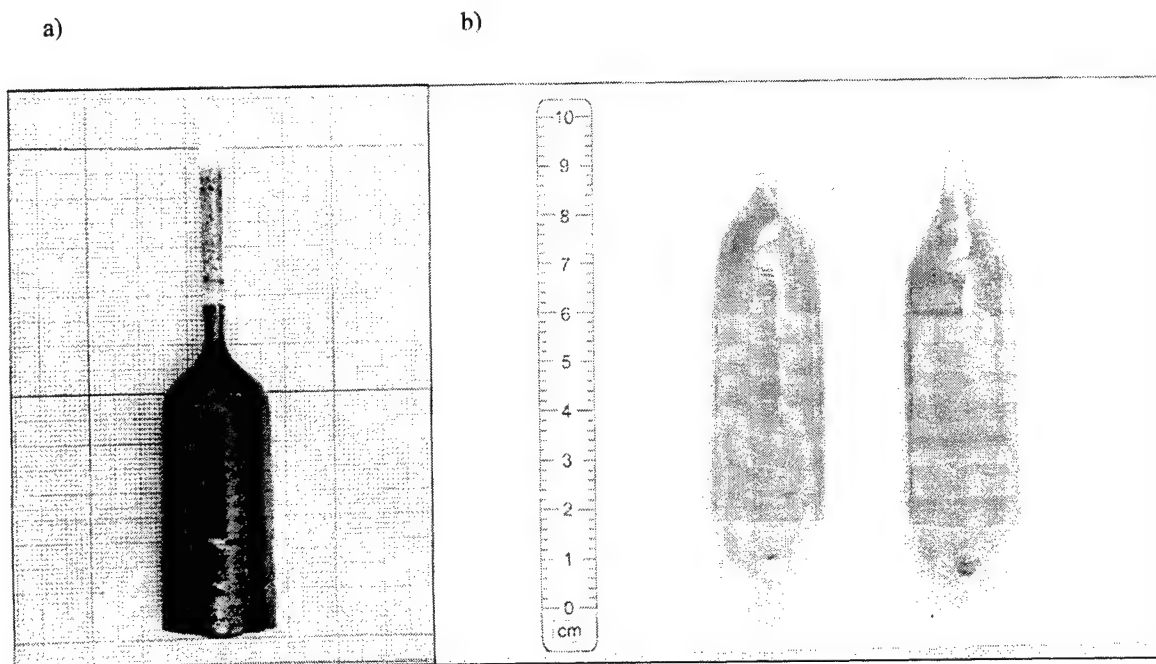


Fig. 1. As-grown YAG:Co²⁺ (a) and YAG:Er³⁺,Yb³⁺ (b) single crystal.

On the basis of the investigations carried out with a Mach-Zender interferometer it was stated that the crystals in the core area are characterised by an inhomogeneity of the refractive index due to defects and stresses. Out of the core area all of crystals were optically homogeneous. The stress in the crystals was examined using the elastoscopic method and registering the picture obtained for crystal, placed between crossed polarisers.

On the basis of the interferometric and elastoscopic investigations the areas of the crystal cuts were determined in order to perform optical elements for the investigations of the spectroscopic characteristics.

3. SPECTROSCOPIC INVESTIGATIONS

From the obtained crystals plane-parallel plates of a thickness of 1 mm were cut, grinded, and polished for spectral measurements. In order to determine the dependence of the absorption coefficient on wavelength $k(\lambda)$, the transmission was measured as a function of the wavelength. The measurements were carried out within the spectral range of 200–3000 nm ($\Delta\lambda=1$ nm) using a LAMBDA900 PERKIN ELMER spectrophotometer and within the range of 1.5–25 μm ($\Delta\lambda/\lambda=1$ cm⁻¹) using a Fourier PERKIN ELMER spectrophotometer 1725-X FT-IR. The spectra of the absorption coefficient for Co²⁺ doped YAG crystals are shown in Fig. 2.

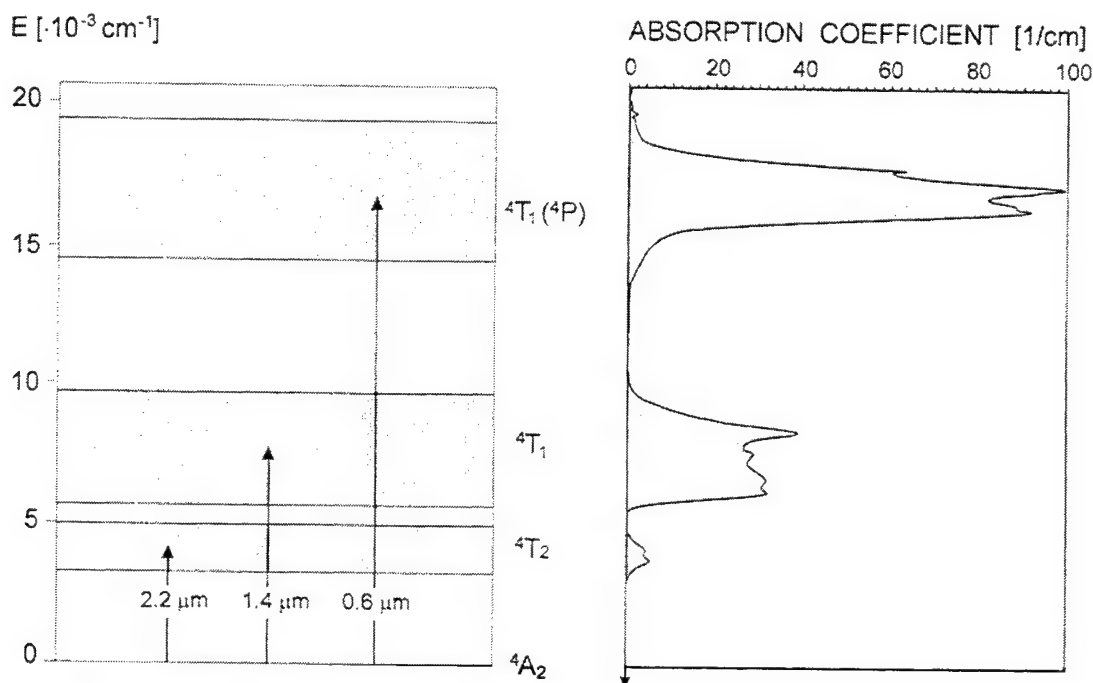


Fig. 2. Energy levels for Co²⁺ in tetrahedral sites and room temperature YAG:Co²⁺ (2 at.% Co²⁺) absorption spectra

The measurements of the luminescence spectra have been performed with a H20 JOBIN YVON monochromator (focal length 200 mm). For excitation a laser diode emitting at 970 nm was used. The luminescence, was registered by means of a LOCK-IN (STANFORD RESEARCH SR510) system with a thermoelectrically cooled InGaAs detector.

The measurements of the lifetime of the ions in the upper laser level ($^4I_{11/2}$) of the samples doped with Er³⁺ and Yb³⁺ were made by the direct method with pulse excitation. The crystal was excited with a radiation pulse significantly shorter than the lifetime τ of the excited level. After excitation the fluorescence decay can be observed.

As source of the exciting pulses of wavelength 970 nm (excitation of Er³⁺ and Yb³⁺ ions) a POLAROID 4300 laser diode was used. The laser was supplied from a power supply SDL800, controlled by a pulse generator and generated pulses of about 8 μs duration at a frequency of about 0.66 kHz. In the detection channel, perpendicular to the excitation channel, a germanium photodiode was used and the fluorescence decay was registered with a digital oscilloscope LeCROY 9350AM (500 MHz). The fluorescence decay times of the investigated samples are listed in Table 1.

Tab. 1. The fluorescence decay times (level $^4I_{11/2}$) of the investigated YAG:Er³⁺ and YAG:Er³⁺,Yb³⁺ crystals

Crystal	Fluorescence decay time
YAG:Er ³⁺ (1.5% Er ³⁺)	5.6 ± 0.1 ms
YAG:Er ³⁺ ,Yb ³⁺ (0.9% Er ³⁺ , 9% Yb ³⁺)	4.3 ± 0.1 ms
YAG:Er ³⁺ ,Yb ³⁺ (0.5% Er ³⁺ , 5% Yb ³⁺)	3.5 ± 0.1 ms

4. NON-LINEAR ABSORPTION INVESTIGATIONS

Investigations of non-linear absorption of YAG:Co²⁺ crystals of various concentrations of Co²⁺ ions were carried out on the basis of analysis of bleaching process dynamics.

Non-linear absorber is characterised by molecular and macroscopic parameters. The molecular parameters are as follows: σ is the absorption cross-section [cm²], τ is the lifetime at the excitation level [s], N_0 is the concentration of absorption centres [cm⁻³], $\Delta N = N_2 - N_1$ is the density of population inversion. The macroscopic parameters: d is the absorber thickness [cm], T is the absorber transmission for the intensity I , I_s is the saturation intensity [W/cm²].

If the relaxation time of absorber is $\tau \ll t_n$, where t_n is the duration of diagnostic pulse, an absorber is of „fast” type and the dependence $T(I)$ describes the equation formulated by Keyes¹⁵ and Hercher¹⁶.

$$(1 - T)^{-1} \ln \frac{T}{T_0} = \frac{I}{I_s} \quad (1)$$

where T_0 is the initial transmission (for small signals), I is the density of incident radiation, I_s is the density of saturation power determined as

$$I_s = \frac{h\nu}{\sigma\tau} \quad (2)$$

where τ is the lifetime of excited absorber.

Relationship (1) can be solved numerically¹⁷ or analytically using special *LambertW* $\equiv W(x)$ function¹⁸⁻²⁰ which is defined as a solution of equation

$$W(x) \cdot \exp(W(x)) = x \quad (3)$$

Analytical solution of equation (1) is dependence

$$T = \frac{I_s}{I} \cdot \text{LambertW} \left(T_0 \cdot \frac{I}{I_s} \cdot \exp \left(\frac{I}{I_s} \right) \right) \quad (4)$$

The changes of transmission of the examined samples as a function of power density of the passing radiation, emitted by the giant-pulse KIGRE MR-253 erbium laser were determined. Laser generated the pulses of 8 mJ energy with duration 25 ns. The power density of a diagnostic pulse was changed within the range of 1÷600 MW/cm². Figure 3 presents the example of application of *LambertW* function for approximation of measurement data of transmission dependence as a function of power density of incident laser radiation wavelength of 1535 nm obtained for YAG:Co²⁺ sample of initial transmission of 24.9%.

As it can be seen from the presented results of analyses, special function *LambertW* allows to correct description of „fast” non-linear absorbers for wide range of their initial transmissions. The results of performed analyses were compared with theoretical models for „fast” absorber as well as with experimental results obtained for non-linear YAG:Co²⁺ absorbers.

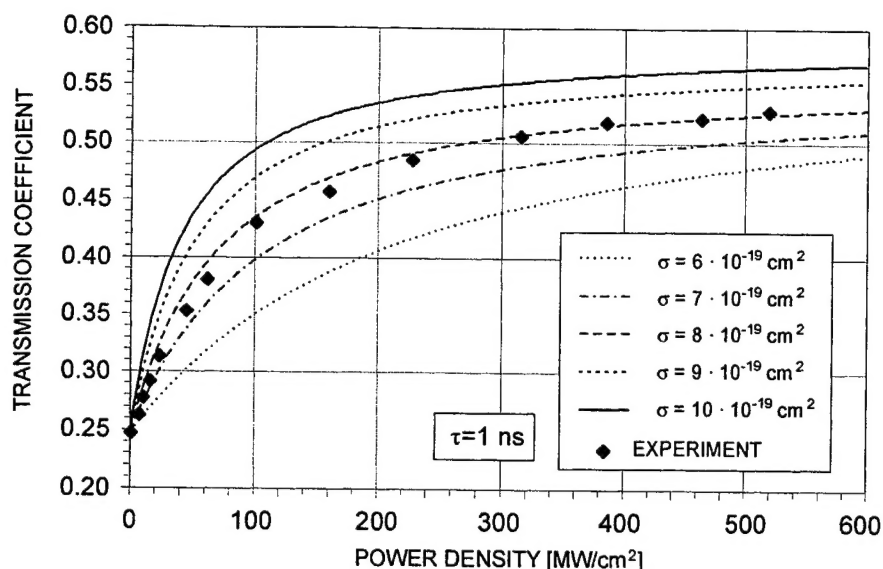


Fig. 3. *LambertW* function applied for approximation of measurement results of transmission as a function of power density of incident laser radiation obtained for YAG:Co²⁺ non-linear absorber

5. LASER ACTION IN YAG:Er³⁺,Yb³⁺

Investigations of longitudinally pumped microlasers generating at 1535 nm made of YAG:Er³⁺,Yb³⁺ were carried out. A schematic of the laser cavity is shown in Fig. 4. The results for YAG:Er³⁺,Yb³⁺ (0.9% Er³⁺, 9% Yb³⁺) are presented in Fig. 5.

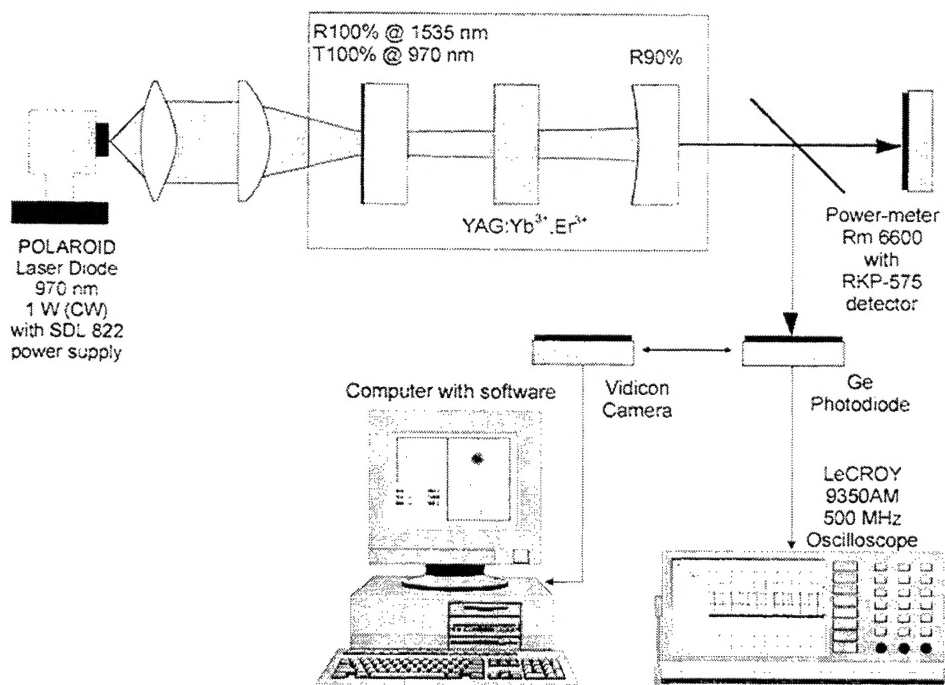


Fig. 4. Experimental setup for the diode pumped YAG:Er³⁺,Yb³⁺ laser

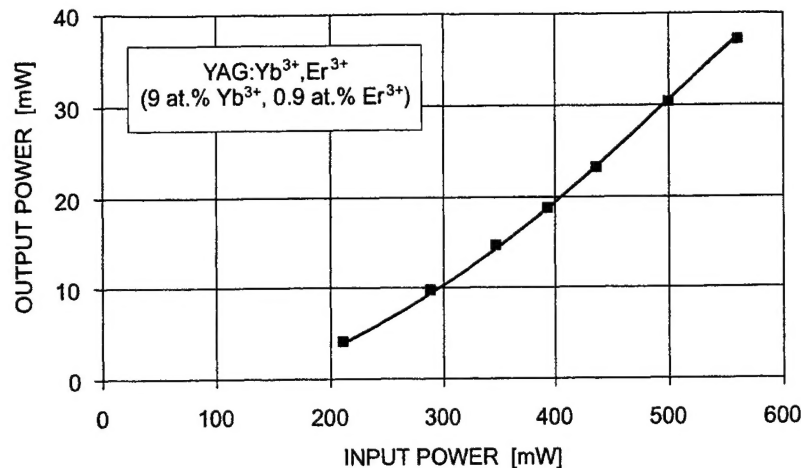


Fig. 5. Generation characteristics of YAG:Er³⁺,Yb³⁺ diode pumped laser (output mirror T=10%, r=40 mm)

6. CONCLUSIONS

The conditions of growing YAG:Er³⁺, YAG:Er³⁺,Yb³⁺ and YAG:Co²⁺ single crystals of various concentrations, devoted to lasers generating eyesafe radiation, were determined. The carried out investigations of the optical and spectroscopic properties of the obtained crystals showed their good optical quality, so they can be applied in laser systems.

Due to the advantageous spectroscopic parameters of YAG:Er³⁺, YAG:Er³⁺, Yb³⁺ and YAG:Co²⁺ crystals and their high thermal and mechanical stability characteristic for garnets, those crystals can be used in laser technology as active materials of lasers generating eyesafe radiation.

REFERENCES

1. D.H. Sliney, Selected papers on laser safety, *SPIE Milestone Series*, Vol. MS-117, Bellingham, Washington, 1995.
2. R. Fluck, U. Keller, E. Gini, H. Melchior, Eyesafe pulsed microchip laser, *OSA TOPS Advanced Solid State Lasers*, Vol. 19, pp. 146-149, 1998.
3. P.G. Zverev, T.T. Basiev, J.T. Murray, R.C. Powell, R.J. Reeves, Stimulated Raman Scattering of Picosecond Pulses in Ba(NO₃)₂ Crystals, *OSA Proc. on Advanced Solid-State Lasers*, vol.15, pp.156-160, (1993),
4. Z.Mierczyk, New materials for coherent pumped laser systems. Active mediums, frequency conversion systems and non-linear elements, *Proc. SPIE*, vol.3186, pp. 22-31, 1997,
5. S.Jiang, J.Myers, D.Rhonehouse, M.Myers, R.Belford, S.Hamlin, Laser and thermal performance of a new erbium doped phosphate glass, Ed. Kigre, Inc. Hilton Head Island, 1990,
6. Laser Rangefinders, JANE's Armour and Artillery Upgrades, Eleventh Edition 1998-99, Jane's Information Group Ltd., Couldson, Surrey UK, 1998,
7. Z.Mierczyk, Investigations of saturable absorbers for „eye safe” giant-pulse laser systems, *Optics and Opto-electronics, Theory, Devices and Applications*, Vol.2, pp. 1033-1036, Narosa Publishing House, New Delhi, 1998,
8. M.B. Camargo, R.D. Stultz, and M. Birnbaum, Passive Q-switching of the Er³⁺:Y₃Al₅O₁₂ laser at 1.64 μ m, *Appl. Phys. Lett.* Vol. 66, pp. 2940-2942, 1995,
9. A.G. Okhrimchuk, A.V. Shestakov, Performance of YAG:Cr⁴⁺ laser crystal, *Optical Materials* 3, pp. 1-13, 1994.
10. Z. Mierczyk, M. Kwaśny, K. Kopczyński, A. Gietka, T. Łukasiewicz, Z. Frukacz, J. Kisieliwski, R. Stępień, K. Jędrzejewski, Er³⁺ and Yb³⁺ doped active media for „eye safe” laser systems, *Journal of Alloys and Compounds* 300-301, pp. 398-406, 2000.
11. R.D.Stultz, M.B.Camargo and M.Birnbaum, Divalent Uranium and Cobalt Saturable Absorber Q-Switches at 1.5 μ m, *OSA Proc. on Advanced Solid-State Lasers*, Vol. 24, pp. 460-464, 1995.
12. M.B. Camargo, R.D. Stultz and M. Birnbaum, Passive Q-switching of the Erbium:Glass Laser using Er³⁺:CaF₂, *OSA TOPS on Advanced Solid-State Lasers*, Vol. 1, pp. 454-457, 1996.
13. R.M.Boiko, A.G.Okhrimchuk, A.V.Shestakov, Glass ceramics Co²⁺ saturable absorber Q-switch for 1.3-1.6 μ m spectral region, *OSA Proc. on Advanced Solid-State Lasers*, TOPS Vol. 19, pp. 24-25, 1998.

Misiuk, Andrzej, 81, 85, 91, 104, 110, 120
 Müller, Anne-D., 191
 Müller, Falk, 191
 Mycielski, Andrzej, 38
 Nguyen Phu, Xuan, 337
 Nowak, Stanisław, 181
 Obodnikov, V. I., 120
 Oganessian, Gagik A., 81
 Padlyak, Bohdan V., 63
 Pajęczkowska, Anna, 289, 369
 Panchenko, L., 211
 Paradowski, Mieczysław L., 242, 246
 Pashchenko, V., 272, 276
 Pavlyuk, A. A., 280
 Pawlaczyk, Czesław, 369
 Piechota, S., 272
 Pluciński, Kazimierz J., 318, 323
 Pődör, Balint, 299
 Polit, J., 263
 Popov, Vladimir P., 120
 Potsidou, M., 91
 Pracka, Izabella, 203, 375
 Prohorov, A., 272
 Prostomolotov, Anatolii I., 97
 Proszak, Władysław, 309
 Prudnikov, Anatolii, 110
 Prujarczyk, M., 91
 Que, Duanlin, 116
 Rak, Mirosława, 156
 Robertz, Bénédicte, 33
 Romano-Rodríguez, A., 120
 Rozpłoch, Franciszek, 396
 Rulmont, André, 33
 Rumianowski, Roman, 396
 Rupp, Romano A., 226
 Ryba-Romanowski, Witold, 380, 385
 Sahraoui, Bouchta, 337
 Šesták, Jaroslav, 46, 161
 Šestáková, Věra, 46, 161
 Shapovalov, V., 272
 Sharmila, B. H., 250
 Shen, Yijun, 116
 Sheregii, Eugen M., 263
 Sherwood, John N., 9
 Shestac, Anatolii S., 259
 Shimamura, Kiyoshi, 18
 Shiryayev, Sergei V., 259
 Shishkova, Natalya V., 104, 110
 Słoma, Piotr, 166, 231
 Sokólska, I., 236, 380, 385
 Solarz, P., 380, 385
 Štěpánek, Bedřich, 46, 161
 Surma, B., 375
 Świrkowicz, Marek, 203, 375, 380, 385
 Szadkowski, A., 38
 Szatkowski, Jacek, 304
 Szybowski, Mirosław, 295, 304
 Szymczak, Henryk, 268, 272, 276, 280, 357
 Thenot, I., 342
 Tian, Daxi, 116
 Tomaszewski, Janusz, 166, 231
 Triboulet, Robert, 1
 Trybus, Mariusz, 309
 Ubizskii, Sergii B., 63
 Verezub, Natalia A., 97
 Villora, E. G., 18
 Wiśniewska, Monika, 351, 396
 Wiśniewski, Krzysztof, 314, 389
 Witkowska, B., 38
 Wojtanowski, J., 69
 Wojtowicz, Andrzej J., 216, 221, 351, 396
 Wolf, Krystyna, 126, 137
 Wróbel, Danuta, 187
 Wronkowska, A., 289
 Wrońska, Teresa, 203
 Yang, Deren, 116
 Yelissev, Alexander P., 342
 Yoshikawa, A., 18
 Zapałowski, Michał, 126
 Zayarnyuk, T., 268, 280
 Ziobrowski, P., 304
 Żmija, Józef, 69
 Zondy, Jean-Jacques, 342
 Zubko, Konrad, 331
 Zubov, E., 268, 276, 280